

Lecture Notes in Civil Engineering

A. Rama Mohan Rao · K. Ramanjaneyulu  
*Editors*

# Recent Advances in Structural Engineering, Volume 2

Select Proceedings of SEC 2016

 Springer

# **Lecture Notes in Civil Engineering**

Volume 12

## **Series editors**

Marco di Prisco, Politecnico di Milano, Milano, Italy

Sheng-Hong Chen, School of Water Resources and Hydropower, Wuhan University, Wuhan, China

Giovanni Solari, University of Genoa, Genova, Italy

Ioannis Vayas, National Technical University of Athens, Athens, Greece

**Lecture Notes in Civil Engineering (LNCE)** publishes the latest developments in Civil Engineering - quickly, informally and in top quality. Though original research reported in proceedings and post-proceedings represents the core of LNCE, edited volumes of exceptionally high quality and interest may also be considered for publication. Volumes published in LNCE embrace all aspects and subfields of, as well as new challenges in, Civil Engineering. Topics in the series include:

- Construction and Structural Mechanics
- Building Materials
- Concrete, Steel and Timber Structures
- Geotechnical Engineering
- Earthquake Engineering
- Coastal Engineering
- Hydraulics, Hydrology and Water Resources Engineering
- Environmental Engineering and Sustainability
- Structural Health and Monitoring
- Surveying and Geographical Information Systems
- Heating, Ventilation and Air Conditioning (HVAC)
- Transportation and Traffic
- Risk Analysis
- Safety and Security

To submit a proposal or request further information, please contact the appropriate Springer Editor:

- Mr. Pierpaolo Riva at [pierpaolo.riva@springer.com](mailto:pierpaolo.riva@springer.com) (Europe and Americas);
- Ms. Swati Meherishi at [swati.meherishi@springer.com](mailto:swati.meherishi@springer.com) (India);
- Ms. Li Shen at [li.shen@springer.com](mailto:li.shen@springer.com) (China);
- Dr. Loyola D'Silva at [loyola.dsilva@springer.com](mailto:loyola.dsilva@springer.com) (Southeast Asia and Australia/NZ).

More information about this series at <http://www.springer.com/series/15087>

A. Rama Mohan Rao · K. Ramanjaneyulu  
Editors

# Recent Advances in Structural Engineering, Volume 2

Select Proceedings of SEC 2016

*Editors*

A. Rama Mohan Rao  
Structural Health Monitoring Laboratory  
CSIR-Structural Engineering Research  
Centre  
Chennai, Tamil Nadu  
India

K. Ramanjaneyulu  
Advanced Concrete Testing & Evaluation  
Laboratory (ACTEL)  
CSIR-Structural Engineering Research  
Centre  
Chennai, Tamil Nadu  
India

ISSN 2366-2557                      ISSN 2366-2565 (electronic)  
Lecture Notes in Civil Engineering  
ISBN 978-981-13-0364-7            ISBN 978-981-13-0365-4 (eBook)  
<https://doi.org/10.1007/978-981-13-0365-4>

Library of Congress Control Number: 2018939461

© Springer Nature Singapore Pte Ltd. 2019

This work is subject to copyright. All rights are reserved by the Publisher, whether the whole or part of the material is concerned, specifically the rights of translation, reprinting, reuse of illustrations, recitation, broadcasting, reproduction on microfilms or in any other physical way, and transmission or information storage and retrieval, electronic adaptation, computer software, or by similar or dissimilar methodology now known or hereafter developed.

The use of general descriptive names, registered names, trademarks, service marks, etc. in this publication does not imply, even in the absence of a specific statement, that such names are exempt from the relevant protective laws and regulations and therefore free for general use.

The publisher, the authors and the editors are safe to assume that the advice and information in this book are believed to be true and accurate at the date of publication. Neither the publisher nor the authors or the editors give a warranty, express or implied, with respect to the material contained herein or for any errors or omissions that may have been made. The publisher remains neutral with regard to jurisdictional claims in published maps and institutional affiliations.

Printed on acid-free paper

This Springer imprint is published by the registered company Springer Nature Singapore Pte Ltd. The registered company address is: 152 Beach Road, #21-01/04 Gateway East, Singapore 189721, Singapore

# Preface

The Tenth Structural Engineering Convention 2016 (SEC 2016) was organized by CSIR-Structural Engineering Research Centre jointly with IIT Madras and Anna University, Chennai, during 21–23 December 2016 at CSIR-SERC, Chennai, India. SEC 2016 provided a common platform for professional structural engineers, academicians and researchers in the broad fields of engineering mechanics and structural engineering to exchange ideas for enriching the research and development activities in the area of structural engineering.

The papers contributed in this convention are a reflection of the diverse research activities in this area and represent the recent developments and futuristic trends in the fundamental understanding of behaviour of materials and structures, computational structural mechanics, health monitoring, mitigation strategies against natural hazards, performance- and durability-based design methodologies, repair and retrofit methods, and technologies for sustainable development. More than four hundred delegates from research organizations, academia and industry participated and presented their papers, making this conference a real great success. All the papers presented are double-blind peer-reviewed. This lecture series in Civil Engineering with the theme of *Recent Advances in Structural Engineering* is brought out in two volumes and contains the select papers presented in SEC 2016. This volume (Volume 2) contains 71 contributions in the following parts:

- Part 1: Structural Dynamics—Wind, Impact and Earthquake Loads
- Part 2: Vibration Control and Smart Structures
- Part 3: Condition Assessment and Performance Evaluation
- Part 4: Repair, Rehabilitation and Retrofit of Structures
- Part 5: Composite Materials and Structures
- Part 6: Structures for Non-conventional Energy (Wind and Solar)

We believe that the collection of papers included in this volume will contribute to scientific developments in the field of structural engineering in a global sense and will be a useful reference work for the academicians, researchers and also most importantly the student community pursuing research in the area of structural engineering.

The success of the conference, SEC 2016, was due to the collective efforts of a large number of individuals, members of the various organizing committees and sponsors. We should take this opportunity to thank all of them for making SEC 2016 a great success. We would like to especially thank all the reviewers, the majority of them from CSIR-SERC who have spent their quality time for reviewing more than five hundred papers received.

Chennai, India

A. Rama Mohan Rao  
K. Ramanjaneyulu

# Contents

<b>Part I Structural Dynamics—Wind, Impact and Earthquake Loads</b>	
<b>Sloshing in Liquid Storage Tanks with Internal Obstructions . . . . .</b>	<b>3</b>
M. Z. Kangda, S. S. Sawant and O. R. Jaiswal	
<b>Nonlinear Static Behaviour of RC Frame Buildings During Construction Stages . . . . .</b>	<b>13</b>
Ankush Gogoi, Bhargav Bhuyan, Nishant Sharma and Kaustubh Dasgupta	
<b>Dynamic Modelling of Ujjayanta Palace—A Heritage Load-Bearing Masonry Building . . . . .</b>	<b>25</b>
S. Raghunath and K. S. Jagadish	
<b>Hybrid Testing of Concrete Bridge Piers with Different Detailing at Column–Foundation Interface . . . . .</b>	<b>39</b>
Needhi Kotoky, Anjan Dutta and Sajal K. Deb	
<b>CFD and Wind Tunnel Investigations on Rectangular Building with Corner Cuts . . . . .</b>	<b>53</b>
A. Monica, P. Harikrishna, K. Nagamani and G. Ramesh Babu	
<b>Correlating Peak Ground A/V Ratio with Ground Motion Frequency Content . . . . .</b>	<b>69</b>
Rahul Garg, Jaya Prakash Vemuri and Kolluru V. L. Subramaniam	
<b>Along Wind Response of Communication Tower . . . . .</b>	<b>81</b>
Nikhil Dhandar, A. Y. Vyavahare and Trupti Nikose	
<b>Predictive Models for Ground Motion Parameters Using Artificial Neural Network . . . . .</b>	<b>93</b>
J. Dhanya, Dwijesh Sagar and S. T. G. Raghukanth	
<b>Effect of Topography on Earthquake Ground Motions . . . . .</b>	<b>107</b>
Anjali Dhabu, J. Dhanya and S. T. G. Raghukanth	



<b>Real-time Hybrid Simulation Using an Electromagnetic Shaker</b> . . . . .	119
Mohit Verma, M. V. Sivaselvan and J. Rajasankar	
<b>Dynamic Behavior of Freestanding Spent Fuel Trays-Stack Without Base Locator During Earthquake Event</b> . . . . .	129
Binu Kumar, O. P. Singh, G. R. Reddy, K. M. Singh, K. Agarwal and N. Gopalakrishnan	
<b>Free Vibration Analysis of Functionally Graded Plates Under Thermal Environment Using Four-Node Quadrilateral Element</b> . . . . .	141
G. A. Deshpande and S. D. Kulkarni	
<b>A Comparative Study of the Seismic Provisions of Indian Seismic Code IS 1893-2002 and Draft Indian Code IS 1893:2016</b> . . . . .	151
Rita Debnath and Lipika Halder	
<b>Analytical Model for Failure of Clamped Beam Subjected to Projectile Impact</b> . . . . .	161
S. Sen and A. Shaw	
<b>Estimation of Peak Factors for Tall Buildings Subjected to Wind-Induced Pressures</b> . . . . .	173
M. Keerthana and P. Harikrishna	
<b>Seismic Behavior of Beam-Column Sub-assemblages Designed According to Different Evolution Stages of Design Philosophies</b> . . . . .	185
A. Kanchana Devi and K. Ramanjaneyulu	
<b>Crushing Analysis of Tapered Circular Corrugated Tubes Subjected to Impact Loading</b> . . . . .	197
Sharad Rawat, A. K. Upadhyay and K. K. Shukla	
<b>Effect of Noise on Vortex-Induced Vibrations of Circular Cylinders</b> . . . . .	207
M. S. Aswathy and Sunetra Sarkar	
<b>Seismic Behaviour of RC Slab–Shear Wall Assemblage Using Nonlinear Static and Dynamic Analyses</b> . . . . .	219
Snehal Kaushik and Kaustubh Dasgupta	
<b>Importance of Inclusion of Soil–Structure Interaction Studies in Design Codes</b> . . . . .	233
Nishant Sharma, Kaustubh Dasgupta and Arindam Dey	
<b>Comparison of Modal Behaviour of Integral Abutment Bridge With and Without Soil–Structure Interaction</b> . . . . .	245
Sreya Dhar and Kaustubh Dasgupta	

**Assessment of Response Reduction Factor for Reinforced Concrete Frame Buildings in a Probabilistic Seismic Risk Framework . . . . .** 255  
 Prakash S. Badal and Ravi Sinha

**Numerical Investigation on the Flexural Performance of Laced Steel–Concrete Composite (LSCC) One-Way Slab System . . . . .** 269  
 G. Gobinath, Mohit Verma and N. Anandavalli

**Wind Tunnel Investigations on a Tall Building With Elliptic Cross Section . . . . .** 281  
 A. Abraham, S. Selvi Rajan, P. Harikrishna and G. Ramesh Babu

**Influence of Bracing Systems on the Seismic Pounding of High-Rise Structure . . . . .** 295  
 Pallerla Sai Krishna and J. S. Kalyana Rama

**Coherency Model for Dense Seismic Array . . . . .** 303  
 Gopala Krishna Rodda and Dhiman Basu

**Seismic Performance of a Heritage Rubble Stone Masonry Building—A Case Study . . . . .** 317  
 Hina Gupta, Debdutta Ghosh and Achal K. Mittal

**Part II Vibration Control and Smart Structures**

**Seismic Vibration Control for 20-Story Nonlinear Benchmark Building Installed with Shape Memory Alloy Damper . . . . .** 331  
 Raghav Moyade and Suhasini Madhekar

**Inelastic Seismic Behaviour of Asymmetric RC Buildings Using Base Shear and Torque (BST) Surface . . . . .** 343  
 Rushikesh. M. Raut and Suhasini. N. Madhekar

**Seismic Retrofitting Using the Concept of Coupling Two Adjacent Buildings . . . . .** 355  
 M. Abdeddaim, A. Ounis, S. D. Bharti and M. K. Shrimali

**Seismic Response Control of Smart Base-Isolated Benchmark Building Using Hybrid Control Strategy (Viscous Fluid Damper with MR Damper) . . . . .** 365  
 Rini Dey and Purnachandra Saha

**Numerical Investigation on the Effectiveness of Double Tuned Mass Dampers in Structural Vibration Control . . . . .** 375  
 Mohammed Fasil and R. Sajeeb

**Three-Dimensional Finite Element Simulation of Isolated Floor Slab with Friction Contact Surface . . . . .** 389  
 P. Kamatchi, S. Cheran Pandian, N. Ezhilarasi and K. Balaji Rao

<b>Performance of Semi-actively Controlled Building Frame Using MR Damper for Near-Field Earthquakes</b> . . . . .	397
Vishisht Bhaiya, S. D. Bharti, M. K. Shrimali and T. K. Datta	
<b>Cyclone Wind Response Mitigation of Transmission Towers by SMA Dampers</b> . . . . .	409
Madhusree Roy and Aparna (Dey) Ghosh	
<b>Linearized Dynamic Analysis of Weightless Sagging Planar Elastic Cables</b> . . . . .	419
Pankaj Kumar, Abhijit Ganguli and Gurmail Benipal	
<b>Experimental Investigations of the Effect of Temperature on the Characteristics of MR Damper</b> . . . . .	435
C. Bharathi Priya and N. Gopalakrishnan	
<b>Semi-active Control of Structures Using Magnetorheological Elastomer-Based Seismic Isolators and Sliding Mode Control</b> . . . . .	445
K. Balamonica, K. Sathish Kumar and N. Gopalakrishnan	
<b>Seismic Response of Single Degree of Freedom System with Shape Memory Alloy (SMA) Damper</b> . . . . .	457
K. Thamaraiselvi and N. Gopalakrishnan	
<b>Energy Harvesting From Dynamic Vibration Pendulum Absorber</b> . . . . .	467
P. V. Malaji, M. Rajarathinam, V. Jaiswal, S. F. Ali and I. M. Howard	
<b>Part III Condition Assessment and Performance Evaluation</b>	
<b>Seismic Fragility Analysis of Highway Bridges in India Considering Evolution of Seismic Code Provisions—A Case Study</b> . . . . .	481
Shivang Shekhar and Jayadipta Ghosh	
<b>Effect of Fire on Reinforced Concrete Slab—Numerical Simulation</b> . . . . .	493
M. K. Haridharan and C. Natarajan	
<b>Change in Microstructure Properties of Concrete on Accelerated Carbonation</b> . . . . .	507
Vineet Shah, Geetika Mishra, Anuj Parashar and Shashank Bishnoi	
<b>An Assessment of the Deterioration of Flexural Capacity of a Pretensioned Concrete Girder Due to Strand Corrosion</b> . . . . .	515
G. Resmi, Amlan K. Sengupta and Radhakrishna G. Pillai	
<b>Reliability Study of Railway Bridge Circular Pier Using Monte Carlo Simulation</b> . . . . .	527
A. Abishek and B. Nageswara Rao	

<b>Evaluation of IS 1893-Based Design Using the Performance Based Earthquake Engineering Framework</b> . . . . .	537
G. Bharat Reddy and B. Radhika	
<b>Corrosion Performance of Steel in Self-compacting Concrete Exposed to Chloride Environment</b> . . . . .	549
Smrati Jain and Bulu Pradhan	
<b>Seismic Damage Evaluation of RC Buildings Using Nonlinear Static Method</b> . . . . .	559
Santanu Paul and Suman Debnath	
<b>Seismic Fragility of Reinforced Concrete Frames with Vertical Irregularities</b> . . . . .	571
T. Choudhury and H. B. Kaushik	
<b>Partial Factors for Safety Assessment of T-Girder of RC Bridges Subjected to Chloride-Induced Corrosion Against Shear Limit State</b> . . . . .	585
N. J. Yogalakshmi, K. Balaji Rao and M. B. Anoop	
<b>Estimation of Residual Crack Widths in Post-Yield Response Range</b> . . . . .	597
Saurabh Shiradhonkar and Ravi Sinha	
<b>Influence of Variation of Material Properties on Interstorey Drift of RC Frame Buildings</b> . . . . .	609
Ashish Sapre and Ravi Sinha	
<b>Influence of Corrosion on the Seismic Vulnerability of a Low-Rise, Poorly Constructed RCC Building</b> . . . . .	623
Jenson Daniel and Ravi Sinha	
<b>Part IV Repair, Rehabilitation and Retrofit of Structures</b>	
<b>Studies on Strengthening Techniques for Existing Transmission Line and Communication Towers</b> . . . . .	639
R. Balagopal, N. Prasad Rao, R. P. Rokade and P. K. Umesha	
<b>Rehabilitation of Post-Tensioned Flat Slab Affected by Fire</b> . . . . .	649
D. Prabu and L. S. Kannan	
<b>Behavior of FRP-Strengthened Reinforced Concrete Columns Under Pure Compression—Experimental and Numerical Studies</b> . . . . .	663
M. Chellapandian and S. Suriya Prakash	
<b>A Numerical Study on the Behaviour of Reinforced Concrete Slab Strengthened with FRP Laminates Using Finite Element Approach</b> . . . . .	675
F. Shit and S. Roychowdhury	

<b>Numerical Evaluation of Cyclic Performance of Damaged RC Frames Using Passive Devices</b> . . . . .	687
Romanbabu M. Oinam and Dipti Ranjan Sahoo	
<b>Flexural Behaviour of Severely Damaged RC Beams Strengthened with Ultra-High Strength Concrete</b> . . . . .	699
A. Ramachandra Murthy, P. Ganesh and G. N. Sakthi Priya	
<b>Performance of RC Columns Strengthened with Prestressed CFRP Bands</b> . . . . .	709
Ambadas Waghmare, Daniel Koothoor, Dhruv Shah, Kinal Bid, Raghav Agarwal, Rahul Ghadwal, Snehal Sonawane, Viraj Sanghvi and Abhay Bambole	
<b>Part V Composite Materials and Structures</b>	
<b>Static Response of Thin-Walled CNT-Reinforced-Laminated Composite Box Beam</b> . . . . .	723
Tushar Sharma, V. Murari and K. K. Shukla	
<b>Dynamic Buckling of Laminated Composite Curved Panels Subjected to In-plane Compression</b> . . . . .	735
V. Keshav and S. N. Patel	
<b>The Interfacial Transition Zone: Microstructure, Properties, and Its Modification</b> . . . . .	745
Meenakshi Sharma and Shashank Bishnoi	
<b>Experimental and Analytical Studies of Failure Characteristics of FRP Connections</b> . . . . .	755
S. B. Singh, Himanshu Chawla and Sudhir Vummadisetti	
<b>Effect of Shear Lag on Buckling of FRP Box-Beams</b> . . . . .	759
M. Kasiviswanathan and Akhil Upadhyay	
<b>Flexural Behavior of Concrete Sandwich Panels Under Punching Load and Four-Point Bending—Experimental and Analytical Study</b> . . . . .	771
J. Daniel Ronald Joseph, J. Prabakar and P. Alagusundaramoorthy	
<b>Bond Behaviour of Externally Bonded FRP Under Cyclic Loading</b> . . . .	783
G. Ramesh, Ravindra Gettu and B. H. Bharatkumar	
<b>Exact Analysis of Layered Plates Using Mixed Form of Hooke's Law</b> . . . . .	797
Ambadas Waghmare, Daniel Koothoor, Dhruv Shah, Kinal Bid, Raghav Agarwal, Rahul Ghadwal, Snehal Sonawane, Viraj Sanghvi and Abhay Bambole	

**Part VI Structures for Non-conventional Energy (Wind and Solar)**

**Hydroelectric Flow Optimization of a Dam:  
A Kriging-Based Approach** ..... 813  
Subhadip Biswas, Souvik Chakraborty, Rajib Chowdhury  
and Indrajit Ghosh

**Effect of Nanosilica and Microsilica on Bond and Flexural Behaviour  
of Reinforced Concrete**..... 825  
Lincy Varghese, V. V. L. Kanta Rao and Lakshmy Parameswaran

**Interaction of a Flexible Splitter Plate with Vortex Shedding  
Past a Rigid Circular Cylinder**..... 841  
Chandan Bose, S. Krishna Kumar, Sunetra Sarkar and Sayan Gupta

# List of Figures

<b>Sloshing in Liquid Storage Tanks with Internal Obstructions</b>	
Fig. 1	ANSYS model of cylindrical tank with obstruction . . . . . 5
Fig. 2	First-mode sloshing frequency ratio of annular tanks . . . . . 9
Fig. 3	Second-mode sloshing frequency ratio of annular tanks . . . . . 10
Fig. 4	First-mode sloshing mass ratio of annular tanks . . . . . 10
Fig. 5	Second-mode sloshing mass ratio of annular tanks . . . . . 10
<b>Nonlinear Static Behaviour of RC Frame Buildings During Construction Stages</b>	
Fig. 1	Floor plan of the building models . . . . . 15
Fig. 2	<b>a</b> Comparative pushover curves during intermediate and final stages, and <b>b</b> final hinge formation for two-storied building . . . . . 18
Fig. 3	<b>a</b> Comparative pushover curves during intermediate and final stages, <b>b</b> final hinge formation in end bay and <b>c</b> for the entire frame in the four-storied building . . . . . 19
Fig. 4	<b>a</b> Comparative pushover curves during intermediate and final stages, <b>b</b> final hinge formation in end bay and <b>c</b> for the entire frame for the six-storied building . . . . . 20
Fig. 5	<b>a</b> Comparative pushover curves during intermediate and final stages, and <b>b</b> final hinge formation for eight-storied building . . . . . 22
Fig. 6	<b>a</b> Comparative pushover curves during intermediate and final stages, and <b>b</b> final hinge formation for ten-storied building . . . . . 23
<b>Dynamic Modelling of Ujjayanta Palace—A Heritage Load-Bearing Masonry Building</b>	
Fig. 1	Ground-floor plan view of Ujjayanta Palace . . . . . 26
Fig. 2	Front view of Ujjayanta Palace . . . . . 27
Fig. 3	Coordinates of masonry piers . . . . . 27

Fig. 4 **a** Schematic representation of sway mode, **b** Schematic representation of torsion mode. . . . . 31

Fig. 5 Acceleration time history response at the surface. . . . . 32

Fig. 6 Linear elastic stress distribution across the thickness of the pier . . . . . 33

Fig. 7 Aluminium flats used for vertical containment reinforcement. . . . . 35

Fig. 8 Typical seismic retrofitting scheme for masonry piers . . . . . 35

Fig. 9 Vertical reinforcement and horizontal GFRP wraps for masonry pier heads . . . . . 36

**Hybrid Testing of Concrete Bridge Piers with Different Detailing at Column–Foundation Interface**

Fig. 1 Reinforcement detailing of the specimen . . . . . 42

Fig. 2 Location of strain gauges on the longitudinal reinforcement . . . . . 44

Fig. 3 Schematic representation of laboratory set-up . . . . . 44

Fig. 4 Key components of hybrid simulation . . . . . 46

Fig. 5 Scaled simulation of El Centro (1940) acceleration time histories with four different intensity levels . . . . . 47

Fig. 6 Damage state of the specimens . . . . . 47

Fig. 7 Lateral force versus lateral displacement of different specimens . . . . . 48

Fig. 8 Strain profile of longitudinal reinforcement C1 at **a** 0.5MCE **b** 1MCE **c** 2MCE **d** 3MCE levels of excitation. . . . . 49

Fig. 9 Damage pattern at the end of cyclic test . . . . . 50

Fig. 10 Energy dissipation at different drift ratio in cyclic test. . . . . 50

**CFD and Wind Tunnel Investigations on Rectangular Building with Corner Cuts**

Fig. 1 Four types of buildings under consideration . . . . . 55

Fig. 2 Schematic diagram of plan of model with pressure tap locations . . . . . 56

Fig. 3 Comparison of mean pressure coefficient at Level 5 for 0° angle of wind incidence (reference pressure =  $p_z$ ). . . . . 58

Fig. 4 Comparison of mean pressure coefficient at Level 5 for 45° angle of wind incidence (reference pressure =  $p_z$ ). . . . . 59

Fig. 5 Comparison of mean pressure coefficient at Level 5 for 90° angle of wind incidence (reference pressure =  $p_z$ ). . . . . 59

Fig. 6 Variation of mean local drag coefficient with  $z/H$  for 0°, 45°, 90° angle of wind incidence, respectively, (reference pressure =  $p_z$ ) . . . . . 60

Fig. 7 Variation of mean local lift coefficient with  $z/H$  for 0°, 45°, 90° angle of wind incidence (reference pressure =  $p_H$ ). . . . . 60



Fig. 8 Variation of mean pressure coefficient for 0° angle of wind incidence at Level 4 for full-height corner cut. . . . . 61

Fig. 9 Variation of mean pressure coefficient for 90° angle of wind incidence at Level 4 for full-height corner cut. . . . . 64

Fig. 10 Variation of mean pressure coefficient for 0° angle of wind incidence at Level 4 for half-height corner cut . . . . . 65

Fig. 11 Variation of mean pressure coefficient for 90° angle of wind incidence at Level 4 for half-height corner cut . . . . . 66

Fig. 12 Variation of mean pressure coefficient for 0° angle of wind incidence at Level 5 for one-third-height corner cut . . . . . 66

Fig. 13 Variation of mean pressure coefficient for 90° angle of wind incidence at Level 5 for one-third-height corner cut . . . . . 67

**Correlating Peak Ground A/V Ratio with Ground Motion Frequency Content**

Fig. 1 Gopeshwar—L record (rich in low frequencies) . . . . . 71

Fig. 2 Gopeshwar—T record (rich in low frequencies) . . . . . 71

Fig. 3 FFTs of Gopeshwar—L and T records—rich in low frequencies . . . . . 72

Fig. 4 Ukhimath—L record (rich in high frequencies) . . . . . 72

Fig. 5 Ukhimath—T record (rich in high frequencies) . . . . . 73

Fig. 6 FFTs of Ukhimath—L and T records (rich in high frequencies) . . . . . 73

Fig. 7 Identification of predominant period parameter,  $T_p$ , from response spectrum . . . . . 74

Fig. 8 Mean period of a seismic wave,  $T_m$ . . . . . 74

Fig. 9 Peak ground A/V ratio versus mean period,  $T_m$  (moderate correlation) . . . . . 79

Fig. 10 Peak ground A/V ratio versus predominant period,  $T_p$  (poor correlation). . . . . 79

**Along Wind Response of Communication Tower**

Fig. 1 Variation of force coefficient with respect to height. . . . . 86

Fig. 2 Microwave tower details of 21 m height . . . . . 87

Fig. 3 Details of microwave lattice tower of 30 m height . . . . . 88

Fig. 4 Details of microwave lattice tower of 50 m height . . . . . 89

Fig. 5 Variation of shear forces of 21 m tower for wind velocity 39 m/s . . . . . 90

Fig. 6 Variation of base bending moment of 21 m tower for wind velocity 39 m/s . . . . . 90

Fig. 7 Variation of shear forces of 30 m tower for wind velocity 39 m/s . . . . . 90

Fig. 8 Variation of base bending moment of 30 m tower for wind velocity 39 m/s . . . . . 91

Fig. 9 Variation of shear forces of 50 m tower for wind velocity 39 m/s . . . . . 91

Fig. 10 Variation of base bending moment of 50 m tower for wind velocity 39 m/s . . . . . 91

**Predictive Models for Ground Motion Parameters Using Artificial Neural Network**

Fig. 1 Typical architecture of artificial neural network. . . . . 94

Fig. 2 Histogram of the input variables . . . . . 96

Fig. 3 Histogram of output variables . . . . . 96

Fig. 4 Regression fit of the model with data . . . . . 99

Fig. 5 Comparison of variation of PGA with respect to distance for 1990 Mw7.6 Chi-Chi earthquake. . . . . 99

Fig. 6 Comparison of variation of PGV with respect to distance for 1990 Mw7.6 Chi-Chi earthquake. . . . . 100

Fig. 7 Comparison of variation of  $S_a$  ( $T = 0.2$  s) with respect to distance for 1990 Mw7.6 Chi-Chi earthquake . . . . . 100

Fig. 8 Comparison of variation of  $S_a$  ( $T = 1$  s) with respect to distance for 1990 Mw7.6 Chi-Chi earthquake. . . . . 100

Fig. 9 Variation of PGA with respect to distance ( $R_{cd}$ ) for different magnitude and soil type. . . . . 101

Fig. 10 Variation of PGV with respect to distance ( $R_{cd}$ ) for different magnitude and soil type. . . . . 102

Fig. 11 Variation of  $S_a$  ( $T$  0.2 s) with respect to distance ( $R_{cd}$ ) for different magnitude and soil type. . . . . 102

Fig. 12 Variation of PGD with respect to distance ( $R_{cd}$ ) for different magnitude and soil type. . . . . 103

Fig. 13 Contributions of input variable on the ANN model developed according to Garson’s method . . . . . 103

Fig. 14 Variation of  $S_a$  ( $T$  1 s) with respect to distance ( $R_{cd}$ ) for different magnitude and soil type. . . . . 104

**Effect of Topography on Earthquake Ground Motions**

Fig. 1 Schematic representation of conical topography considered. . . . . 110

Fig. 2 Topography profiles considered in the study  
**a** ridge **b** valley. . . . . 111

Fig. 3 Mesh created by SPEC-FEM for **a** ridge **b** valley . . . . . 112

Fig. 4 Amplification ratios for horizontal displacement  
**a** case 1 **b** case 2. . . . . 113

Fig. 5 Amplification ratios for vertical displacement  
**a** case 1 **b** case 2. . . . . 113

Fig. 6 Horizontal amplification ratios for case 3  
**a** displacement **b** velocity . . . . . 114

Fig. 7 Vertical amplification ratios for case 3  
**a** displacement **b** velocity . . . . . 114

Fig. 8 Horizontal amplification ratios for case 4  
**a** displacement **b** velocity . . . . . 115

Fig. 9 Horizontal amplification ratio versus gradient  
**a** displacement **b** velocity . . . . . 116

**Real-time Hybrid Simulation Using an Electromagnetic Shaker**

Fig. 1 Schematic of an electromagnetic shaker. . . . . 120

Fig. 2 Test set-up for parameter estimation . . . . . 123

Fig. 3 Frequency response of the electromagnetic shaker  
in voltage mode. . . . . 124

Fig. 4 Schematics of the emulated and hybrid system . . . . . 125

Fig. 5 Comparison of the force transferred by NS and shaker in  
frequency domain . . . . . 126

Fig. 6 Test set-up for hybrid simulation. . . . . 127

Fig. 7 Comparison of the bottom storey acceleration in emulated and  
hybrid system . . . . . 127

**Dynamic Behavior of Freestanding Spent Fuel Trays-Stack Without  
Base Locator During Earthquake Event**

Fig. 1 Target and Achieved Response Spectra with Design Response  
Spectra along *x*-axis. . . . . 131

Fig. 2 Shake table setup for 30 trays-stack system. . . . . 131

Fig. 3 Details of gauges in experiment. . . . . 132

Fig. 4 Displacement of trays at 30th trays height. . . . . 133

Fig. 5 FFT of displacement time histories at 18th and 30th trays height  
for 30 trays stack system. . . . . 133

Fig. 6 Acceleration time history of tank at top wall location . . . . . 133

Fig. 7 FFT of displacement time histories for 25 and  
30 trays-stack system. . . . . 134

Fig. 8 FFT of acceleration time history of tank top . . . . . 134

Fig. 9 Simplified methodology for fluid–structure interaction analysis  
in Kumar . . . . . 135

Fig. 10 Finite element model of SFSWT with submerged  
trays-stacks . . . . . 136

Fig. 11 Slosh frequency of free surface . . . . . 136

Fig. 12 Typical slosh mode shape of free surface . . . . . 137

Fig. 13 Pressure variation along tank left wall. . . . . 137

**Free Vibration Analysis of Functionally Graded Plates Under Thermal  
Environment Using Four-Node Quadrilateral Element**

Fig. 1 First three mode shapes for FGM plate under  
thermal environment . . . . . 149

**A Comparative Study of the Seismic Provisions of Indian Seismic Code IS 1893-2002 and Draft Indian Code IS 1893:2016**

Fig. 1 **a** Response spectra for rock and soil sites for 5% damping, as per existing graph and **b** design acceleration coefficient ( $S_a/g$ ) (corresponding to 5% damping) as per draft code . . . . . 155

**Analytical Model for Failure of Clamped Beam Subjected to Projectile Impact**

Fig. 1 Clamped beam struck transversely by projectile of mass  $G$  and width  $2r$  . . . . . 163  
Fig. 2 Phase 1; **a** velocity profile, **b** generalized forces and moments . . . . . 164  
Fig. 3 Phase 2; **a** velocity profile, **b** generalized forces and moments . . . . . 165  
Fig. 4 Phase 3; **a** velocity profile, **b** generalized forces and moments . . . . . 166  
Fig. 5 Displacement time history of midpoint of the beam struck by projectile having mass 2 kg and width 10 mm with impact velocity; **a** 1 m/s, **b** 3 m/s . . . . . 169  
Fig. 6 Comparison of residual velocities of projectile having width 5 mm and mass; **a** 5 kg, **b** 2 kg, **c** 1 kg, **d** 0.5 kg. . . . . 170

**Estimation of Peak Factors for Tall Buildings Subjected to Wind-Induced Pressures**

Fig. 1 **a** Rigid model of tall building. **b** Flow behavior at separation (after Cook 1990) . . . . . 179  
Fig. 2 Pressure tap layout at level-1 . . . . . 179  
Fig. 3 Model of tall building in wind tunnel under simulated open terrain . . . . . 179  
Fig. 4 Time history of pressure coefficients and standardized pressure coefficients from a pressure tap . . . . . 180  
Fig. 5 Skewness and excess kurtosis values. . . . . 180  
Fig. 6 Skewness and excess kurtosis contours . . . . . 181  
Fig. 7 Effective region of applicability of Hermite method . . . . . 181  
Fig. 8 PDF of data based on the Hermite models . . . . . 182  
Fig. 9 CDF of extremes based on the Hermite models. . . . . 182  
Fig. 10 Ratio of observed and model-based peak factors for pressure taps on the side faces . . . . . 182  
Fig. 11 Ratio of observed and model-based peak factors for pressure taps on the leeward face . . . . . 183

**Seismic Behavior of Beam-Column Sub-assemblages Designed According to Different Evolution Stages of Design Philosophies**

Fig. 1 **a** Building chosen for study. **b** Choosing typical exterior beam-column sub-assemblage . . . . . 187

Fig. 2 **a** Details of gravity load specimen (SP1), **b** details of non-ductile specimen (SP2), **c** details of ductile specimen (SP3) . . . . . 188

Fig. 3 Casting of specimen . . . . . 189

Fig. 4 Schematic test setup. . . . . 190

Fig. 5 Reverse cyclic loading history . . . . . 190

Fig. 6 Layout of LVDTs . . . . . 191

Fig. 7 Crack pattern **a** at +2.94% (left) and **b** at -2.94% (right) drift ratio—SP1 . . . . . 191

Fig. 8 Crack pattern at +5.88% (left) and -5.88% (right) drift ratio—SP2 . . . . . 192

Fig. 9 Crack pattern at +7.05% (left) and -7.05% (right) drift ratio—SP3 . . . . . 192

Fig. 10 **a** Load–displacement hysteresis of SP1. **b** Load–displacement hysteresis of SP2. **c** Load–displacement hysteresis of SP3. . . . . 194

Fig. 11 Load envelope of specimens SP1, SP2, and SP3. . . . . 194

Fig. 12 Cumulative energy dissipation of the specimens . . . . . 195

**Crushing Analysis of Tapered Circular Corrugated Tubes Subjected to Impact Loading**

Fig. 1 Simulation model. . . . . 199

Fig. 2 Tube specifications . . . . . 200

Fig. 3 Tubes incorporated in the study. . . . . 201

Fig. 4 **a** Load–displacement curves of tubes with corrugation pattern and simple tapered tube impacted at smaller end. **b** Load–displacement curves of tubes with corrugation pattern showing the effect of impacting end . . . . . 202

Fig. 5 Comparative force–displacement for amplitude-graded tubes with  $T(c, c)_{B_B}$ . . . . . 202

Fig. 6 **a** Comparative load–displacement of tubes at axial and 5° loading. **b** Comparative load–displacement of tubes at axial and 10° loading. . . . . 203

Fig. 7 Collapse mode of the  $St_{0_B}$  and tapered tube  $T(c, p)_{B_B}$  and tube  $T(c, p)_{B_B-10^\circ}$ , respectively. . . . . 204

**Effect of Noise on Vortex-Induced Vibrations of Circular Cylinders**

Fig. 1 Typical time histories for deterministic system: **a** before lock-in, **b** at lock-in, and **c** after lock-in . . . . . 210

Fig. 2 Bifurcation diagram for deterministic system. . . . . 210

Fig. 3 Structural amplitude versus mean reduced velocity at  $c = 1$  . . . . 211

Fig. 4 Changes in pdfs of the structural response with increasing reduced velocity. . . . . 212

Fig. 5 Response time history at  $Um = 4.5, c = 2$ . . . . . 213

Fig. 6 Trimodal pdf for  $Um = 4.5, c = 2$ . . . . . 214

Fig. 7 Topological changes in joint pdfs for  $Um = 3, 4.1$  and  $5$  corresponding to **a–c** indicating the presence of different attractors and hence p-bifurcations. . . . . 214

Fig. 8 Shannon entropy versus mean reduced velocity in the presence of noise for  $c = 1$  and  $c = 1.5$ . . . . . 215

**Seismic Behaviour of RC Slab–Shear Wall Assemblage Using Nonlinear Static and Dynamic Analyses**

Fig. 1 A typical shear wall–slab assemblage . . . . . 221

Fig. 2 FE model of the shear wall–slab junction subjected to horizontal displacement at the top . . . . . 223

Fig. 3 **a** Recorded horizontal ground motion at Jellapur station during 1997 Indo–Burma earthquake and **b** Fourier spectrum of the ground motion. . . . . 224

Fig. 4 Pushover curve for FE model using CDP . . . . . 224

Fig. 5 **a** Axial stress, S11 in reinforcement and **b** tensile damage pattern at maximum base shear . . . . . 225

Fig. 6 Axial stress, S11 in reinforcement for pushover analysis at: **a** 0.17 mm, **b** 5.84 mm and **c** 100 mm . . . . . 226

Fig. 7 Tensile damage pattern for pushover analysis at: **a** 0.17 mm, **b** 5.84 mm and **c** 100 mm . . . . . 227

Fig. 8 Axial stress in reinforcement for time history analysis at: **a** 0.86 s; **b** 7.80 s and **c** 26 s. . . . . 228

Fig. 9 Tensile damage pattern for time history analysis at: **a** 0.86 s, **b** 7.80 s and **c** 26 s. . . . . 229

**Importance of Inclusion of Soil–Structure Interaction Studies in Design Codes**

Fig. 1 Structural system with loading details . . . . . 235

Fig. 2 Validation of the numerical model. . . . . 237

Fig. 3 **a** Response spectrum and **b** corresponding spectrum compatible ground motion used. . . . . 238

Fig. 4 Storey shear for various analysis cases . . . . . 239

Fig. 5 Percentage drift for various analysis cases. . . . . 240

Fig. 6 Absolute maximum moment profile for **a** exterior columns and **b** interior columns. . . . . 241

Fig. 7 Instantaneous moment profile for **a** exterior columns and **b** interior columns . . . . . 241

Fig. 8 Base shear comparison for various analysis cases . . . . . 242

Fig. 9 Motions used for FBA and FBFFM. . . . . 242

**Comparison of Modal Behaviour of Integral Abutment Bridge With and Without Soil–Structure Interaction**

Fig. 1 Modified Humboldt Bay Middle Channel Bridge with soil–structure interaction modelled in SAP2000 . . . . . 247

Fig. 2 **a** One-noded horizontal and vertical link elements at different depths of piles, **b** two-noded link element at the tip of each pile and **c** two-noded link elements for modelling abutment–backfill interaction . . . . . 248

Fig. 3 Initial stiffness ( $K_{initial}$ ) from the generic force–displacement curve of soil spring . . . . . 248

Fig. 4 Plan views of first mode shape of vibration for **a** fixed base bridge model and **b** bridge with SSI model . . . . . 250

Fig. 5 Plan views of second mode shape of vibration for **a** fixed base bridge model and **b** bridge with SSI model . . . . . 250

Fig. 6 Plan views of third mode shape of vibration for **a** fixed base bridge model and **b** bridge with SSI model . . . . . 250

Fig. 7 Longitudinal mode of vibration for **a** fixed base bridge model and **b** bridge with SSI model . . . . . 251

Fig. 8 Transverse mode of vibration for **a** Case (i) and **b** Case (ii) models . . . . . 252

**Assessment of Response Reduction Factor for Reinforced Concrete Frame Buildings in a Probabilistic Seismic Risk Framework**

Fig. 1 Quantification of seismic performance factors using pushover analysis based on Ref. [10] . . . . . 258

Fig. 2 **a** Plan of the sample building; reinforcement and column sizes for **b** special RCMRF variant and **c** ordinary RCMRF variant on grid 9. All beams are of size  $350 \times 750$  and  $400 \times 750$ , respectively . . . . . 261

Fig. 3 Modified Ibarra–Medina–Krawinkler backbone curve . . . . . 262

Fig. 4 Pushover curve (IS 1893 loading pattern) for SMRF. OMRF variant not shown due to lack of space . . . . . 263

Fig. 5 Controlling IDA curves for FEMA P695 far-field ground motion suite for SMRF . . . . . 264

Fig. 6 Assessment of *RRF* using nonlinear time history analysis for **a** SMRF and **b** OMRF variant. . . . . 265

**Numerical Investigation on the Flexural Performance of Laced Steel–Concrete Composite (LSCC) One-Way Slab System**

Fig. 1 Laced steel–concrete composite . . . . . 270

Fig. 2 Schematics of LSCC one-way slab system . . . . . 272

Fig. 3 Mesh for different parts of LSCC . . . . . 274

Fig. 4 Deflection profile of LSCC slab. . . . . 275

Fig. 5	Equivalent plastic strain. . . . .	275
Fig. 6	Load–deflection curve for LSCC slab . . . . .	275

### **Wind Tunnel Investigations on a Tall Building With Elliptic Cross Section**

Fig. 1	Details of pressure ports around circumferential direction at level 1 and along the height of the model showing body axes with wind direction . . . . .	283
Fig. 2	Simulated mean velocity and turbulence intensity profiles under suburban terrain. . . . .	284
Fig. 3	Elliptic tall building model kept inside the wind tunnel for $\theta = 0^\circ$ and $90^\circ$ under suburban terrain . . . . .	284
Fig. 4	Typical instantaneous pressure traces. . . . .	285
Fig. 5	Comparison on variation of mean pressure coefficients for $\theta = 0^\circ, 15^\circ, 30^\circ, 45^\circ, 60^\circ, 75^\circ,$ and $90^\circ$ . . . . .	286
Fig. 6	Variation of mean force coefficients . . . . .	288
Fig. 7	Comparison on variation of mean drag, lift, and torsion coefficients. . . . .	288
Fig. 8	Comparison on variation of mean pressure coefficients for $\theta = 0^\circ, 30^\circ, 60^\circ,$ and $90^\circ$ . . . . .	289
Fig. 9	Comparison on variation of mean drag force coefficients . . . . .	290
Fig. 10	Comparison on variation of mean lift force coefficients. . . . .	290

### **Influence of Bracing Systems on the Seismic Pounding of High-Rise Structure**

Fig. 1	<b>a</b> Floor plan of 25 storied building, <b>b</b> Floor plan of 20 storied building . . . . .	297
Fig. 2	Storey drift for 20 and 25 storied structures without bracing. . . . .	299
Fig. 3	Storey drift for 20 and 25 storied structures with V bracings. . . . .	299
Fig. 4	Storey drift for 20 and 25 storied structures with X bracings. . . . .	299
Fig. 5	Storey drift for 20 and 25 storied structures with springs to represent the soil . . . . .	300
Fig. 6	Base shear values for 20 and 25 storied structures for different cases . . . . .	300
Fig. 7	Maximum roof displacement for 20 and 25 storied structures for different cases . . . . .	300

### **Coherency Model for Dense Seismic Array**

Fig. 1	LSST array, Lotung . . . . .	306
Fig. 2	SMART-1 array, Lotung . . . . .	307
Fig. 3	Comparison of derived and original spectra. . . . .	312



Fig. 4 Coherency comparison of different models . . . . . 314

Fig. 5 Coherency between I01-M03 during Event  
25 in vertical direction. . . . . 315

**Seismic Performance of a Heritage Rubble Stone Masonry**

**Building—A Case Study**

Fig. 1 Pant Sadan building. . . . . 319

Fig. 2 Talus deposit on downhill slope . . . . . 319

Fig. 3 Ground floor plan of Pant Sadan building . . . . . 320

Fig. 4 3D model of the building . . . . . 321

Fig. 5 Location of Nainital and Uttarkashi [19] . . . . . 322

Fig. 6 Uttarkashi time history curve [19]. . . . . 322

Fig. 7 Compressive and tensile force distribution due  
to gravity load. . . . . 323

Fig. 8 Shell stress due to gravity load (MPa). . . . . 324

Fig. 9 Shell stresses due to pushover in X direction (MPa) . . . . . 324

Fig. 10 Shell stresses due to pushover in Y direction (MPa) . . . . . 325

Fig. 11 Shell stress under Uttarkashi time history data (MPa) . . . . . 326

Fig. 12 Displacement contours under Uttarkashi time history  
(in mm) . . . . . 326

**Seismic Vibration Control for 20-Story Nonlinear Benchmark**

**Building Installed with Shape Memory Alloy Damper**

Fig. 1 Different cases for damper placement for 20-story benchmark  
problem . . . . . 337

Fig. 2 Time histories and maximum drift ratios for all four earthquakes  
of intensity 1.0. . . . . 340

**Inelastic Seismic Behaviour of Asymmetric RC Buildings Using Base  
Shear and Torque (BST) Surface**

Fig. 1 BST surface showing interior and exterior regions . . . . . 344

Fig. 2 Plan for typical floor of G+3 storey RCC  
symmetric building . . . . . 344

Fig. 3 BST surface for typical floor of G+3 storey RCC symmetric  
building . . . . . 345

Fig. 4 Plan for typical floor of G+3 storey RCC uniaxial asymmetric  
building No. 1 with 6.22% asymmetry in plan . . . . . 346

Fig. 5 BST surface for typical storey of G+3 storey RCC uniaxial  
asymmetric building No. 1 with 6.22% asymmetry  
in plan . . . . . 347

Fig. 6 Plan for typical floor of G+3 storey RCC uniaxial asymmetric  
building No. 2 with 8.85% asymmetry in plan . . . . . 347

Fig. 7	BST surface for typical storey of G+3 storey RCC uniaxial asymmetric building No. 2 with 8.85% asymmetry in plan . . . . .	347
Fig. 8	BST surface for all uniaxial asymmetric RCC buildings over symmetric building in plan . . . . .	348
Fig. 9	Plan for typical floor of G+3 storey RCC biaxial asymmetric building No. 1 with 4.7% asymmetry in plan in each direction . . . . .	349
Fig. 10	BST surface for typical storey of G+3 storey RCC biaxial asymmetric building No. 1 with 4.70% asymmetry in plan in each direction . . . . .	349
Fig. 11	Plan for typical floor of G+3 storey RCC biaxial asymmetric building No. 2 with 5.14% asymmetry in plan in each direction . . . . .	349
Fig. 12	BST surface for typical storey of G+3 storey RCC biaxial asymmetric building No. 2 with 5.14% asymmetry in plan in each direction . . . . .	350
Fig. 13	BST surface for all biaxial asymmetric RCC buildings over symmetric building in plan in each direction . . . . .	350
Fig. 14	Plan for typical floor of G+3 storey RCC biaxial asymmetric building No. 7 with 4.7% asymmetry in plan in each direction . . . . .	351
Fig. 15	BST surface for typical storey of G+3 storey RCC biaxial asymmetric building No. 7 with 4.70% asymmetry in plan in each direction . . . . .	351
Fig. 16	Plan for typical floor of G+3 storey RCC biaxial asymmetric building No. 8 with 5.14% asymmetry in plan in each direction . . . . .	352
Fig. 17	BST surface for typical storey of G+3 storey RCC biaxial asymmetric building No. 8 with 5.14% asymmetry in plan in each direction . . . . .	352
Fig. 18	BST surface for all biaxial asymmetric RCC buildings over symmetric building in plan . . . . .	353

### **Seismic Retrofitting Using the Concept of Coupling Two Adjacent Buildings**

Fig. 1	Dynamic modelling of coupled system . . . . .	357
Fig. 2	Percentage variation in ( $\Delta_{max}$ ) with respect to frequency ratio under Northridge earthquake, 1994 . . . . .	360
Fig. 3	Percentage variation ( $V_{base}$ ) with respect to frequency ration under Northridge earthquake, 1994 . . . . .	360
Fig. 4	Percentage variation in ( $D_{max}$ ) with respect to frequency ratio under Northridge earthquake, 1994 . . . . .	361

**Seismic Response Control of Smart Base-Isolated Benchmark Building Using Hybrid Control Strategy (Viscous Fluid Damper with MR Damper)**

Fig. 1 Schematic cross-sectional diagram of VFD . . . . . 367

Fig. 2 Force-deformation diagram of VFD. . . . . 368

Fig. 3 Mathematical model of VFD . . . . . 368

Fig. 4 Effect of damping coefficient ( $c_d$ ) . . . . . 369

Fig. 5 Effect of velocity exponent of VFD on building responses for Newhall earthquake ( $c_d = 300$  kN s/m) . . . . . 369

Fig. 6 Force-deformation behavior of hybrid control system incorporating VFD and MRD for the specified earthquakes . . . . 371

Fig. 7 Time history response of base acceleration of Newhall, Sylmar and El-Centro earthquake El-Centro, Rinaldi, Kobe, Jiji Erzincan earthquake (MRD MR damper response, MRD + VFD = MR damper + Viscous fluid damper response; hybrid control). . . . . 372

**Numerical Investigation on the Effectiveness of Double Tuned Mass Dampers in Structural Vibration Control**

Fig. 1 Spring–mass–damper model of the five degrees-of-freedom system . . . . . 377

Fig. 2 Spring–mass–damper model of the five degrees-of-freedom system with single TMD . . . . . 377

Fig. 3 Various placement configurations of Double TMDs . . . . . 379

Fig. 4 Equivalent spring–mass–damper models of Double TMD configurations; **a** A1; **b** A2; **c** A3; **d** A4; **e** A5 . . . . . 380

Fig. 5 Variation of coefficient,  $\alpha$ , with respect to mass ratio,  $r$  . . . . . 380

Fig. 6 Variation of stiffness coefficients with respect to mass ratio,  $r$  . . . . . 381

Fig. 7 Control Effectiveness of double TMD system. FRFS of **a** displacement; **b** acceleration; **c** base shear . . . . . 382

Fig. 8 Control effectiveness of single and Double TMD (A4) systems for a mass ratio of 5%. FRFs of **a** displacement; **b** acceleration; **c** base shear . . . . . 383

Fig. 9 Control effectiveness under El Centro earthquake; **a** displacement; **b** acceleration; **c** base shear . . . . . 384

Fig. 10 Performance of Double TMDs under El Centro earthquake—displacement-time history . . . . . 385

Fig. 11 White noise signal—acceleration-time history. . . . . 385

Fig. 12 Control effectiveness—white noise; **a** displacement; **b** acceleration; **c** base shear . . . . . 386

Fig. 13 Performance of Double TMDs under white noise base excitation—displacement-time history . . . . . 387

Fig. 14 **a** FRFs of Double TMD systems; **b** 2nd mode shape . . . . . 387

**Three-Dimensional Finite Element Simulation of Isolated Floor Slab with Friction Contact Surface**

Fig. 1 Three-dimensional FE wireframe model **a** FSS—single storey **b** FIS—single storey **c** FSS—three stories **d** FIS—three stories. . . . . 391

Fig. 2 Single-storey FSS, FIS base shear **a** El Centro **b** Loma Prieta **c** Northridge **d** IS 1893–2002 spectrum compatible Zone V Medium soil–DBE. . . . . 393

Fig. 3 Single-storey FSS, FIS displacement **a** El Centro **b** Loma Prieta **c** Northridge **d** IS 1893–2002 spectrum compatible zone V medium soil–DBE. . . . . 394

Fig. 4 Three-storey FSS and FIS **a** roof level displacement—El Centro **b** roof level displacement—North Ridge **c** roof level acceleration—El Centro **d** roof level acceleration—Northridge **e** base shear—El Centro **f** base shear—North Ridge **g** storey level peak displacements for El Centro and North Ridge earthquake . . . . . 395

**Performance of Semi-actively Controlled Building Frame Using MR Damper for Near-Field Earthquakes**

Fig. 1 Structural model equipped with three MR dampers . . . . . 399

Fig. 2 Control algorithm . . . . . 400

Fig. 3 Comparison of uncontrolled and controlled time histories of base shear for Bam (2003) earthquake. . . . . 402

Fig. 4 Comparison of uncontrolled and controlled time histories of top floor displacement for Bam (2003) earthquake . . . . . 403

Fig. 5 Comparison of uncontrolled and controlled time histories of base shear for Chichi (1999) earthquake . . . . . 403

Fig. 6 Comparison of uncontrolled and controlled time histories of top floor displacement for Chichi (1999) earthquake . . . . . 404

Fig. 7 Force–displacement plot of MR damper for Bam (2003) earthquake . . . . . 404

Fig. 8 Force–velocity plot of MR damper for Bam (2003) earthquake . . . . . 405

Fig. 9 Force–displacement plot of MR damper for Chichi (1999) earthquake . . . . . 405

Fig. 10 Force–velocity plot of MR damper for Chichi (1999) earthquake . . . . . 406

**Cyclone Wind Response Mitigation of Transmission Towers by SMA Dampers**

Fig. 1 Harris PSDF for wind velocity . . . . . 413

Fig. 2 Time history of cyclonic instantaneous wind velocity at 35 m height . . . . . 414

Fig. 3 Time history of cyclonic wind force in  $X$ -direction acting at a node on windward side of the tower at 35 m height . . . . . 415

Fig. 4 Time history of cyclonic wind force in  $X$ -direction acting at a node on leeward side of the tower at 35 m height. . . . . 415

Fig. 5 Top displacement time history in the  $X$ -direction of the uncontrolled tower . . . . . 416

Fig. 6 Tower with the SMA damper attached to it. . . . . 416

Fig. 7 Top displacement time history in the  $X$ -direction of uncontrolled and passively controlled tower. . . . . 417

**Linearized Dynamic Analysis of Weightless Sagging Planar Elastic Cables**

Fig. 1 Cables under nodal loads fixed at both ends . . . . . 422

Fig. 2 FDR for general harmonic loading . . . . . 424

Fig. 3 FDR of cables having very close natural frequencies . . . . . 425

Fig. 4 Beating phenomenon . . . . . 426

Fig. 5 Typical FDR plots for small sag cable. . . . . 427

Fig. 6 Effect of axial stiffness of the cable on FDR. . . . . 428

Fig. 7 Typical FDR for different sustained loads . . . . . 430

Fig. 8  $z_2$  response for El Centro earthquake. . . . . 431

Fig. 9  $z_2$  response components for nonlinear analysis . . . . . 432

**Experimental Investigations of the Effect of Temperature on the Characteristics of MR Damper**

Fig. 1 Experimental setup for MR damper characterization: **a** loading frame with actuator; **b** close-up view of damper; **c** wonderbox for input current supply; **d** non-contact thermocouple . . . . . 438

Fig. 2 Increase in temperature in long-stroke and short-stroke MR damper for varying input excitations . . . . . 439

Fig. 3 Variation in maximum force observed between first and last cycle for **a** short-stroke and **b** long-stroke damper. . . . . 440

Fig. 4 Energy dissipation observed between first and last cycle for **a** short-stroke and **b** long-stroke damper . . . . . 441

Fig. 5 Characteristics curves of long-stroke and short-stroke damper for a sinusoidal input 1 Hz—10 mm at different input currents. . . . . 442

**Semi-active Control of Structures Using Magnetorheological Elastomer-Based Seismic Isolators and Sliding Mode Control**

Fig. 1 Varying stress–strain graph of magnetorheological elastomers with current . . . . . 446

Fig. 2 Magnetorheological elastomer-based base isolators . . . . . 447

Fig. 3 Force displacement hysteresis plot for smart base isolators . . . . . 447

Fig. 4 Base isolated structure idealized as 2DOF structure. . . . . 451

Fig. 5 Displacement response of fixed base structure . . . . . 452

Fig. 6 Velocity response of fixed base structure . . . . . 452

Fig. 7 Acceleration response of fixed base structure . . . . . 452

Fig. 8 Displacement response of the structure with smart base isolators  
(controlled and uncontrolled) . . . . . 453

Fig. 9 Velocity response of the structure with smart base isolators  
(controlled and uncontrolled) . . . . . 453

Fig. 10 Acceleration response of the structure with smart base isolators  
(controlled and uncontrolled) . . . . . 453

Fig. 11 Control force applied to the structure . . . . . 455

**Seismic Response of Single Degree of Freedom System with Shape Memory Alloy (SMA) Damper**

Fig. 1 Pseudoelastic hysteresis behaviour exhibited by SMA . . . . . 458

Fig. 2 SDOF system incorporated with SMA damper . . . . . 458

Fig. 3 Block diagram of SDOF system with SMA element . . . . . 459

Fig. 4 Displacement response history for harmonic excitation . . . . . 461

Fig. 5 SMA superelastic cycle for harmonic loading . . . . . 461

Fig. 6 Accelerogram (El Centro earthquake) . . . . . 462

Fig. 7 Displacement response history for random excitation  
(El Centro) . . . . . 463

Fig. 8 Velocity response history for random excitation (El Centro) . . . . 463

Fig. 9 Acceleration response history for random excitation  
(El Centro) . . . . . 464

Fig. 10 Restoring force developed in SMA damper . . . . . 464

Fig. 11 Accelerogram (Taft earthquake) . . . . . 464

Fig. 12 Displacement response history for random excitation  
(Taft earthquake) . . . . . 465

Fig. 13 Velocity response history for random excitation  
(Taft earthquake) . . . . . 465

Fig. 14 Acceleration response history for random excitation  
(Taft earthquake) . . . . . 465

**Energy Harvesting From Dynamic Vibration Pendulum Absorber**

Fig. 1 Schematic of DVA energy harvesting system . . . . . 469

Fig. 2 **a** Frequency response curve for primary structure displacement  
for various values of frequency ratio of pendulum to the primary  
mass. **b** Frequency response curve for normalized power  
harvested for various values of frequency ratio of pendulum to  
the primary mass . . . . . 472

Fig. 3 **a** Frequency response curve for primary structure displacement for various values of electrical damping ratio. **b** Frequency response curve for normalized power for various values of electrical damping ratio . . . . . 473

Fig. 4 **a** Primary structure displacement frequency response curve for various values of pendulum damping ratio. **b** Frequency response curve for normalized power for various values of pendulum damping ratio . . . . . 474

Fig. 5 Genetic algorithm flowchart. . . . . 475

Fig. 6 **a** Frequency response curve for normalized displacement of primary structure for optimized values given in Table 1. **b** Frequency response curve for normalized power for optimized values given in Table 1 . . . . . 476

**Seismic Fragility Analysis of Highway Bridges in India Considering Evolution of Seismic Code Provisions—A Case Study**

Fig. 1 Representative case-study single-column integral box girder bridge. . . . . 485

Fig. 2 Classification of column failure modes . . . . . 486

Fig. 3 Comparison of shear strength and flexural strength capacity for Case 1 and Case 2. . . . . 487

Fig. 4 Comparison of mean spectra of scaled ground motions with design response spectrum of Indian seismic code IS: 1893-2002 and histogram of selected ground motion suite . . . . . 489

Fig. 5 Seismic fragility curves for Case 2 shear-critical (SC) and Case 4 flexural-critical (FC) bridge design cases . . . . . 490

**Effect of Fire on Reinforced Concrete Slab—Numerical Simulation**

Fig. 1 Boundary condition—mechanical loading . . . . . 497

Fig. 2 Percentage variation versus number of layers along depth. . . . . 498

Fig. 3 Insulation check for concrete slab . . . . . 501

Fig. 4 Ratio of ultimate deflection during heating phase to BS 476-20:1987 code . . . . . 501

Fig. 5 Normalized load versus displacement of 125-mm-thick concrete slab—air cooled. . . . . 502

Fig. 6 Normalized load versus displacement of 125-mm-thick concrete slab—quench cooled . . . . . 502

Fig. 7 Stiffness reduction in concrete slab for subjected to—air cooled . . . . . 503

Fig. 8 Stiffness reduction in concrete slab subjected to—quench cooled. . . . . 503

### **Change in Microstructure Properties of Concrete on Accelerated Carbonation**

Fig. 1	Porosity of non-carbonated and carbonated concrete samples having w/c of 0.45 at 1% carbon dioxide concentration . . . . .	510
Fig. 2	Porosity of non-carbonated and carbonated concrete samples having w/c of 0.35 at 3% carbon dioxide concentration . . . . .	510
Fig. 3	Sorptivity of non-carbonated and carbonated concrete samples having w/c of 0.45 kept at 1% carbon dioxide concentration . . . . .	511
Fig. 4	Sorptivity of non-carbonated and carbonated concrete samples having w/c of 0.35 kept at 3% carbon dioxide concentration . . . . .	511
Fig. 5	Air permeability of non-carbonated and carbonated concrete exposed in 1% carbon dioxide concentration . . . . .	511

### **An Assessment of the Deterioration of Flexural Capacity of a Pretensioned Concrete Girder Due to Strand Corrosion**

Fig. 1	Hypothetical variation of cross-sectional area of a strand . . . . .	517
Fig. 2	Cross section of girder at mid-span . . . . .	518
Fig. 3	Variation of area of strands with time . . . . .	520
Fig. 4	Variation of effective depth with time . . . . .	520
Fig. 5	Variation of effective prestress with time . . . . .	521
Fig. 6	Simplified section of composite girder . . . . .	522
Fig. 7	Variation of stress in concrete at extreme fibres with time . . . . .	523
Fig. 8	Variation of mid-span flexural capacity with time . . . . .	524

### **Reliability Study of Railway Bridge Circular Pier Using Monte Carlo Simulation**

Fig. 1	Cross section of the pier . . . . .	528
Fig. 2	Design interaction plot for the pier considering random variables . . . . .	531
Fig. 3	Bias factor of axial load versus eccentricity of load on pier . . . . .	531
Fig. 4	Bias factor of moment versus eccentricity of load on pier . . . . .	531
Fig. 5	Effect of diameter of the pier on the reliability index . . . . .	533

### **Evaluation of IS 1893-Based Design Using the Performance Based Earthquake Engineering Framework**

Fig. 1	Hazard curve of the earthquake ground motions used in the analysis of the frame . . . . .	541
Fig. 2	Maximum IDR of the frame, obtained using 27 ground motion records in the incremental dynamic analysis. Each color line corresponds to a ground motion scaled to different PGA values . . . . .	541



Fig. 3 Normal probability paper plot to validate the lognormal assumption of demand fragility curves. . . . . 542

Fig. 4 Frame demand fragility curves obtained assuming lognormal distribution. Series 1–10 denote the PGA values from 0.2 to 2 g with 0.2 g increment . . . . . 542

Fig. 5 Frame damage fragility assuming lognormal distribution. . . . . 542

Fig. 6 POE of damage, quantifying performance of the frame design . . . . . 543

Fig. 7 Maximum deflection of the free end of the beam, obtained using IDA . . . . . 544

Fig. 8 Normal probability paper plot for the EDP values of the beam . . . . . 544

Fig. 9 Beam demand fragility curves . . . . . 545

Fig. 10 Damage fragility curves. . . . . 545

Fig. 11 POE of damage. . . . . 545

**Corrosion Performance of Steel in Self-compacting Concrete Exposed to Chloride Environment**

Fig. 1 Particle size distribution of aggregates. . . . . 551

Fig. 2 Schematic diagram of prismatic reinforced SCC specimen . . . . . 552

Fig. 3 Experimental setup for half-cell potential and LPR measurements on SCC specimens . . . . . 553

Fig. 4 **a** Half-cell potential of steel in SCC specimens exposed to different concentrations of sodium chloride solutions at *w/c* ratio of 0.40 and **b** half-cell potential of steel in SCC specimens exposed to different concentrations of sodium chloride solutions at *w/c* ratio of 0.43 . . . . . 556

Fig. 5 **a** Corrosion current density of steel in SCC specimens exposed to different concentrations of sodium chloride solutions at *w/c* ratio of 0.40 and **b** corrosion current density of steel in SCC specimens exposed to different concentrations of sodium chloride solutions at *w/c* ratio of 0.43 . . . . . 557

**Seismic Damage Evaluation of RC Buildings Using Nonlinear Static Method**

Fig. 1 Capacity curves for RC buildings . . . . . 564

Fig. 2 Fragility curves for RC buildings . . . . . 566

**Seismic Fragility of Reinforced Concrete Frames with Vertical Irregularities**

Fig. 1 **a** An under construction five-storey OGS building severely damaged during 1999 Kocaeli earthquake; **b** a three-storey OGS building collapsed in Port Blair during 2004 Sumatra earthquake . . . . . 572

Fig. 2	<b>a</b> Structural frame—bare and OGS, <b>b</b> sectional details—beams and columns, <b>c</b> RC frame and equivalent strut model with lumped plasticity . . . . .	573
Fig. 3	<b>a</b> Force-deformation relationship of Takeda’s degrading stiffness models, <b>b</b> typical kinematic hysteresis model for reinforcing bars . . . . .	574
Fig. 4	Hysteretic pivot law particularization for the equivalent diagonal strut . . . . .	575
Fig. 5	Displacement and interstorey drift profile (ISD) for bare and OGS frames for El Centro ground motion with increasing PGA (0.3, 0.5, 0.7, 1 g) . . . . .	577
Fig. 6	Comparison of seismic fragility obtained for bare and OGS frame considering top level (TL) or peak roof displacement as the EDP . . . . .	578
Fig. 7	Storey wise fragility profile of bare and OGS frame considering displacement demand at each floor obtained from time history analysis for El Centro ground motion scaled for different PGA (0.3, 0.5, 0.7, 1 g) . . . . .	579
Fig. 8	Storey wise fragility profile of bare and OGS frame considering ISD demand at each floor obtained from time history analysis for El Centro ground motion scaled for different PGA (0.3, 0.5, 0.7, 1 g) . . . . .	580
Fig. 9	Comparison of seismic fragility of bare and OGS frames at the top level (TL) with interstorey drift demand as the EDP . . . . .	581
Fig. 10	Comparison of seismic fragility of bare and OGS frames at the ground level (GL) with interstorey drift demand as the EDP . . . . .	582

**Partial Factors for Safety Assessment of T-Girder of RC Bridges Subjected to Chloride-Induced Corrosion Against Shear Limit State**

Fig. 1	Histogram for initiation time for the considered example . . . . .	591
Fig. 2	Distribution of shear capacities of the girder at 50 years for the design combination of variables . . . . .	592
Fig. 3	Probability of shear failure for the considered design combination of the variables . . . . .	593
Fig. 4	Probability of shear failure of girder for different quality of workmanship . . . . .	594

**Estimation of Residual Crack Widths in Post-Yield Response Range**

Fig. 1	Comparison of measured crack width against maximum drift . . . . .	601
Fig. 2	Comparison of experimental and simulated force–deflection relationship for shear walls, Dazio et al. [13] experimental dataset . . . . .	603

Fig. 3 Comparison of measured and calculated crack widths using Gergely and Lutz formula for Dazio et al. [13] experimental dataset. . . . . 604

Fig. 4 Comparison of measured and calculated crack widths for Chen et al. [12] experimental dataset . . . . . 604

Fig. 5 Relationship between residual ratio ( $R_w$ ) and % drift for Chen et al. [12] experimental dataset . . . . . 605

Fig. 6 Relationship between residual ratio ( $R_w$ ) and curvature ductility . . . . . 606

Fig. 7 Relationship between residual ratio ( $R_w$ ) and curvature ductility for Dazio et al. [13] experimental dataset . . . . . 607

**Influence of Variation of Material Properties on Interstorey Drift of RC Frame Buildings**

Fig. 1 ANSYS nonlinear model of RC frame . . . . . 612

Fig. 2 Earthquake spectra of selected earthquakes . . . . . 613

Fig. 3 Mean Time Period ( $T_m$ ) of selected earthquakes time histories . . . . . 614

Fig. 4 IDR versus PGA for analysis x81A. . . . . 615

Fig. 5 IDR versus PGA for analysis x82A. . . . . 615

Fig. 6 IDR versus PGA for analysis x83A. . . . . 616

Fig. 7 IDR versus PGV for analysis x81A. . . . . 616

Fig. 8 IDR versus PGV for analysis x82A. . . . . 617

Fig. 9 IDR versus PGV for analysis x83A. . . . . 617

Fig. 10 IDR versus PGA for analysis x91A. . . . . 618

Fig. 11 IDR versus PGA for analysis x92A. . . . . 618

Fig. 12 IDR versus PGA for analysis x93A. . . . . 619

Fig. 13 IDR versus PGV for analysis x91A. . . . . 619

Fig. 14 IDR versus PGV for analysis x92A. . . . . 620

Fig. 15 IDR versus PGV for analysis x93A. . . . . 620

**Influence of Corrosion on the Seismic Vulnerability of a Low-Rise, Poorly Constructed RCC Building**

Fig. 1 Stress–strain curve for confined concrete. . . . . 625

Fig. 2 Stress–strain model for the steel . . . . . 626

Fig. 3 **a** Reinforcing bar embedded in concrete; **b** stress distribution; **c** strain distribution; **d** bond stress between concrete and steel . . . . . 627

Fig. 4 Normalized bond strength as a function of corrosion in the analytical form. . . . . 628

Fig. 5 Capacity curve and performance levels . . . . . 631

Fig. 6 Capacity curve and corresponding vulnerability curve of a poorly constructed building with time-dependent deficiency of

	<i>7% (damage state 1, 2, and 3 stands for IO, LS and CP, respectively).</i> . . . . .	632
Fig. 7	Vulnerability for curves of a poorly constructed building with different degrees of corrosion. . . . .	632
Fig. 8	Influence of time-dependent deficiency on the PGA demand of a poorly constructed building . . . . .	633
<b>Studies on Strengthening Techniques for Existing Transmission Line and Communication Towers</b>		
Fig. 1	Schematic view of connection pattern . . . . .	643
Fig. 2	Experimental setup of connection patterns. . . . .	644
Fig. 3	FE models of connection patterns . . . . .	645
Fig. 4	Failure modes for different connection patterns from analytical and experimental investigations . . . . .	646
<b>Rehabilitation of Post-Tensioned Flat Slab Affected by Fire</b>		
Fig. 1	Basement 1 layout plan . . . . .	650
Fig. 2	Part tendon layout plan in the affected area. . . . .	651
Fig. 3	Classification of fire. . . . .	651
Fig. 4	Fire broke out in basement 1 floor, it got damaged and it passed through the ramp opening and affected the first floor slab and soffit of the second floor slab (there is 4 m cantilever in second floor slab) . . . . .	652
Fig. 5	Spalling of concrete with exposed bottom steel with service lines. . . . .	652
Fig. 6	Spalling of concrete with exposed reinforcement, tendon and concrete beyond reinforcement damaged . . . . .	653
Fig. 7	Spalling of concrete and broken ramp slab with exposed reinforcement—view from basement 1 floor . . . . .	653
Fig. 8	Spalling of concrete in column along grid 2A1-6 in basement 1 floor. . . . .	654
Fig. 9	Spalling of concrete in beam supporting ramp slab in basement 1 floor. . . . .	654
Fig. 10	Closer view of column and beam showing spalling of concrete. . . . .	655
Fig. 11	Core sample location in plan . . . . .	655
Fig. 12	PT 3 (0–50 mm) H-1832 (typical DTA–TG curve) . . . . .	658
Fig. 13	Schematic drawing. . . . .	659
Fig. 14	Numeration detail of part PT slab after rectification . . . . .	660
Fig. 15	Tying of reinforcement in progress (before concreting) . . . . .	660
Fig. 16	Concreting through self-compacting concrete (SCC) by making holes in the existing slab (before concreting). . . . .	661
Fig. 17	Concreting through self-compacting concrete (SCC) by making holes in the existing slab (during concreting) . . . . .	661

Fig. 18 Concreting through self-compacting concrete (SCC) by making holes in the existing slab (after concreting) . . . . . 661

Fig. 19 After completion of SCC (view from ground floor). . . . . 661

Fig. 20 After deshuttering (view from basement 1 floor). . . . . 662

**Behavior of FRP-Strengthened Reinforced Concrete Columns Under Pure Compression—Experimental and Numerical Studies**

Fig. 1 Cross-sectional details of column. . . . . 665

Fig. 2 a–h Strengthening of columns by hybrid strengthening technique . . . . . 666

Fig. 3 Experimental setup. 1. 5000 kN CTM, 2. RC column, 3. controls console, 4. HBM DAQ controller, 5. DAQ system . . . . . 667

Fig. 4 Behavior of RC columns under compression. . . . . 670

Fig. 5 Comparison for plain columns. . . . . 670

Fig. 6 Comparison for unstrengthened RC columns. . . . . 670

Fig. 7 Comparison for NSM-strengthened RC columns. . . . . 671

Fig. 8 Comparison for EB-strengthened RC columns. . . . . 671

Fig. 9 Comparison for hybrid-strengthened RC columns . . . . . 671

**A Numerical Study on the Behaviour of Reinforced Concrete Slab Strengthened with FRP Laminates Using Finite Element Approach**

Fig. 1 Details of the unretrofitted RC slab . . . . . 677

Fig. 2 Volume created in ANSYS . . . . . 679

Fig. 3 FRP along the support edge SS2, continuous edge SS3, along the diagonal SS4 (for one-quarter model) . . . . . 679

Fig. 4 Variation of load deformation behaviour of retrofitted simply supported RC slab due to change in location of FRP along continuous edge. . . . . 680

Fig. 5 30, 55, 75, 100% area of slab SS2 covered by FRP . . . . . 681

Fig. 6 Variation of load deformation behaviour with FRP along support edge. . . . . 681

Fig. 7 30, 55, 75, 100% area of slab SS3 covered by FRP . . . . . 682

Fig. 8 Variation of load deformation behaviour with FRP along continuous edge. . . . . 682

Fig. 9 16.6, 33, 50, 66.67 and 100% area of slab SS4 covered by FRP . . . . . 683

Fig. 10 Variation of load deformation behaviour with FRP along both the diagonals . . . . . 683

Fig. 11 Effect of change of thickness of FRP along support edge, continuous edge, and diagonals . . . . . 685

### Numerical Evaluation of Cyclic Performance of Damaged RC Frames Using Passive Devices

Fig. 1	<b>a</b> Detailing of RS-1 frame, <b>b</b> detailing of RS-2 frame, and <b>c</b> RS-1 frame test setup . . . . .	688
Fig. 2	<b>a</b> Distribution of elements and <b>b</b> fiber section elevation and plan . . . . .	689
Fig. 3	Material parameters of concrete, reinforcement, and bond slip models <b>a</b> <i>Concrete02</i> , <b>b</b> <i>Pinching4</i> , and <b>c</b> <i>Bond SP01</i> . . . . .	690
Fig. 4	<b>a</b> Hysteresis behavior of CMD and <b>b</b> ideal load deformation of CMD . . . . .	692
Fig. 5	<b>a</b> Plan and effective confinement of steel cage section, <b>b</b> half body equilibrium of steel cage section, and <b>c</b> confinement strength ratio graph . . . . .	693
Fig. 6	Steel-caged column section capacities <b>a</b> <i>P-M3</i> interaction and <b>b</b> <i>M-φ</i> curve . . . . .	694
Fig. 7	Imposed displacement history . . . . .	694
Fig. 8	Comparisons of experimental and numerical results of <i>RS-1</i> and <i>RS-2</i> specimen . . . . .	695

### Flexural Behaviour of Severely Damaged RC Beams Strengthened with Ultra-High Strength Concrete

Fig. 1	A typical reinforcement details of RC beam . . . . .	703
Fig. 2	Test set-up . . . . .	704
Fig. 3	Typical crack pattern . . . . .	704
Fig. 4	Crack pattern of beams B1 . . . . .	705
Fig. 5	Load versus deflection . . . . .	705
Fig. 6	Rupture in overlay . . . . .	706
Fig. 7	Load versus deflection . . . . .	706

### Performance of RC Columns Strengthened with Prestressed CFRP Bands

Fig. 1	Stress–strain diagram for different fibers . . . . .	710
Fig. 2	Effect of FRP confinement on circular and non-circular cross sections . . . . .	712
Fig. 3	Failure of unwrapped and wrapped columns, respectively (250 × 200, 1400) . . . . .	713
Fig. 4	Stress–strain diagram for unwrapped specimen from strain gauges . . . . .	713
Fig. 5	Stress–strain diagram for unwrapped specimen from LPs . . . . .	713
Fig. 6	Stress–strain diagram for wrapped specimen from strain gauges . . . . .	715

Fig. 7 Stress–strain diagram for wrapped specimen from LPs . . . . . 715

Fig. 8 Cylindrical columns with double- and single-helical CFRP bands, respectively. . . . . 716

Fig. 9 Prestressed CFRP bands for circular and rectangular cross section . . . . . 717

Fig. 10 Representation of equivalent effective area . . . . . 718

Fig. 11 Typical axial load compressive strain curves of confined columns [5] . . . . . 719

**Static Response of Thin-Walled CNT-Reinforced-Laminated Composite Box Beam**

Fig. 1 Thin-walled closed section coordinates . . . . . 725

Fig. 2 Cantilever composite box beam under axial load. . . . . 729

Fig. 3 Effect of CNT % on tip axial displacement and tip twist angle at  $[0_{10}/45_{10}]$ . . . . . 730

Fig. 4 Variation in axial displacement along the length for different CNT % . . . . . 730

Fig. 5 Variation in twist angle along the length for different CNT % . . . . . 730

**Dynamic Buckling of Laminated Composite Curved Panels Subjected to In-plane Compression**

Fig. 1 Geometry of panel with uniform loading . . . . . 738

Fig. 2 Model showing the support conditions . . . . . 738

Fig. 3 Rectangular pulse load. . . . . 739

Fig. 4 **a** Axial displacement versus time plot of loading duration of  $0.055 \times 10^{-3}$  s. **b** Axial displacement versus time plot of loading duration of  $0.055 \times 10^{-3}$  s. **c** Axial displacement versus time plot of loading duration of  $0.055 \times 10^{-3}$  s. **d** Axial displacement versus time plot of loading duration of  $0.055 \times 10^{-3}$  s. **e** Axial displacement versus time plot of loading duration of  $0.055 \times 10^{-3}$  s . . . . . 740

Fig. 5 Effect of aspect ratio on dynamic buckling load . . . . . 742

Fig. 6 Deformed shape of laminated composite curved panel with  $b/a = 2$  and  $R/a = 20$ . . . . . 742

Fig. 7 Effect of radius of curvature on dynamic buckling load . . . . . 743

Fig. 8 Deformed shape of laminated composite curved panel with  $R/a = 2$  and  $b/a = 1$ . . . . . 743

**The Interfacial Transition Zone: Microstructure, Properties, and Its Modification**

Fig. 1 Comparative stress–strain curves for aggregate, paste, and concrete . . . . . 746

Fig. 2 Illustration of wall effect . . . . . 747

Fig. 3 Calculated initial distribution of anhydrous cement and effective water/cement ratio in the interfacial zone. . . . . 747

Fig. 4 Average distribution of calcium hydroxide in ITZ. . . . . 748

Fig. 5 Porosity gradient in the ITZ of model concrete. . . . . 748

Fig. 6 Volume density of successive size fractions (size range in  $\mu\text{m}$ ), by computer simulations . . . . . 750

Fig. 7 Strength activity index of ground fly ash in paste, mortar, and concrete at  $w/b$  0.3 . . . . . 751

Fig. 8 Effects of mineral admixtures on microhardness at 3 days . . . . . 752

Fig. 9 Effects of mineral admixtures on microhardness at 180 days . . . . . 752

**Experimental and Analytical Studies of Failure Characteristics of FRP Connections**

Fig. 1 Response of lap joint in tension. . . . . 756

**Effect of Shear Lag on Buckling of FRP Box-Beams**

Fig. 1 Schematic view of the analyzed girders. . . . . 761

Fig. 2 End constraints of beam model . . . . . 762

Fig. 3 Buckling mode corresponding to first eigenvalue (beam size— $800 \times 600 \times 5000$ ) . . . . . 764

Fig. 4 State of stress of top flange: **a**  $0^\circ (\theta_f) - 0^\circ (\theta_w)$ ; **b**  $\pm 45^\circ (\theta_f) - 0^\circ (\theta_w)$ ; **c**  $90^\circ (\theta_f) - 0^\circ (\theta_w)$  . . . . . 765

Fig. 5 Top flange stress variation across the beam width: **a** Box-beam highlighting section of interest; **b**  $0^\circ (\theta_f) - \pm 45^\circ (\theta_w)$ ; **c**  $\pm 45^\circ (\theta_f) - \pm 45^\circ (\theta_w)$ ; **d**  $90^\circ (\theta_f) - \pm 45^\circ (\theta_w)$ . . . . . 766

Fig. 6 Variation of shear lag factor with  $\theta_f$  for different  $\theta_w$  . . . . . 767

Fig. 7 Variation of buckling coefficient with  $S_F$  for different  $\theta_w$  . . . . . 767

Fig. 8 Variation of shear lag factor with  $(b/t)_f$  for different  $t_w$  . . . . . 768

Fig. 9 Variation of buckling coefficient with  $S_F$  for different  $t_w$ . . . . . 769

**Flexural Behavior of Concrete Sandwich Panels Under Punching Load and Four-Point Bending—Experimental and Analytical Study**

Fig. 1 Sequence of casting a panel. . . . . 775

Fig. 2 Schematic diagram of test setup . . . . . 776

Fig. 3 Typical panel on test setup . . . . . 776

Fig. 4 Tested panels. . . . . 777

Fig. 5 Load–deflection curves . . . . . 778

Fig. 6 Comparison of experimental and numerical load–deflection responses . . . . . 779

Fig. 7 Plastic strain distributions obtained from numerical analysis . . . . . 780



**Bond Behaviour of Externally Bonded FRP Under Cyclic Loading**

Fig. 1 Specimen geometry and test configuration of modified RILEM TC-RC-5 (1982) . . . . . 785

Fig. 2 Closer view of test setup . . . . . 786

Fig. 3 Typical positioning of strain gages for 100 mm bond length and 50 mm bond width . . . . . 787

Fig. 4 Failure in CFRP-bonded specimens (50-100-C) . . . . . 787

Fig. 5 Failure in GFRP-bonded specimens (50-100-G) . . . . . 787

Fig. 6 Tensile force on FRP with slip in CFRP-bonded specimens . . . . . 789

Fig. 7 Tensile force on FRP with slip in GFRP-bonded specimens . . . . . 789

Fig. 8 Cyclic tensile force on FRP with slip in CFRP-bonded specimens . . . . . 790

Fig. 9 Cyclic tensile force on FRP with slip in GFRP-bonded specimens . . . . . 790

Fig. 10 Cyclic and static tensile force versus with slip in CFRP-bonded specimens . . . . . 792

Fig. 11 Cyclic and static tensile force versus with slip in GFRP-bonded specimens . . . . . 792

Fig. 12 Typical cyclic experimental tensile force on FRP per unit width versus strain for externally bonded CFRP specimens. . . . . 793

Fig. 13 Typical cyclic experimental tensile force on FRP per unit width versus strain for externally bonded GFRP specimens . . . . . 794

**Exact Analysis of Layered Plates Using Mixed Form of Hooke’s Law**

Fig. 1 Simply supported plate . . . . . 799

Fig. 2 Laminated/sandwiched plate coordinates system and subjected to bi-directional sinusoidal loading . . . . . 800

Fig. 3 Displacement ( $w$ ) along thickness using CPT and MFHL for isotropic single-layered plate ( $b = 3a$ ) subjected to sinusoidal loading with aspect ratio  $S = 4$  . . . . . 802

Fig. 4 In-plane stress along thickness using PT and MFHL for isotropic single-layered plate ( $b = 3a$ ) subjected to sinusoidal loading with aspect ratio  $S = 4$ . . . . . 803

Fig. 5 Displacement ( $w$ ) along thickness using CPT and MFHL for isotropic single-layered plate ( $b = 3a$ ) subjected to sinusoidal loading with aspect ratio  $S = 10$  . . . . . 803

Fig. 6 In-plane stress along thickness using CPT and MFHL for isotropic single-layered plate ( $b = 3a$ ) subjected to sinusoidal loading with aspect ratio  $S = 10$  . . . . . 804

Fig. 7 Displacement ( $w$ ) along thickness using CPT and MFHL for isotropic single-layered plate ( $b = 3a$ ) subjected to sinusoidal loading with aspect ratio  $S = 20$  . . . . . 804

Fig. 8 In-plane stress along thickness using CPT and MFHL for isotropic single-layered plate ( $b = 3a$ ) subjected to sinusoidal loading with aspect ratio  $S = 20$  . . . . . 805

Fig. 9 Variation of the normalized transverse displacement ( $\bar{w}$ ) with aspect ratio for isotropic single-layered plate ( $b = 3a$ ) subjected to sinusoidal loading . . . . . 806

Fig. 10 Displacement ( $w$ ) along thickness using MFHL for  $S = 20$  for isotropic five-layered plate ( $b = 3a$ ) subjected to sinusoidal loading. . . . . 806

Fig. 11 In-plane stress  $\sigma_{xx}$  along thickness using MFHL for  $S = 20$  for isotropic five-layered plate ( $b = 3a$ ) subjected to sinusoidal loading. . . . . 807

Fig. 12 In-plane stress  $\sigma_{yy}$  along thickness using MFHL for  $S = 20$  for isotropic five-layered plate ( $b = 3a$ ) subjected to sinusoidal loading. . . . . 807

Fig. 13 Transverse normal stress  $\sigma_{zz}$  along thickness using MFHL for  $S = 20$  for isotropic five-layered plate ( $b = 3a$ ) subjected to sinusoidal loading . . . . . 808

Fig. 14 Transverse shear stress  $\tau_{xz}$  along thickness using MFHL for  $S = 20$  for isotropic five-layered plate ( $b = 3a$ ) subjected to sinusoidal loading . . . . . 808

**Hydroelectric Flow Optimization of a Dam: A Kriging-Based Approach**

Fig. 1 Schematic diagram of hydroelectric dam . . . . . 817

Fig. 2 Hourly variation of electricity price for Case 1 . . . . . 820

Fig. 3 Optimized hourly turbine flow and hourly spill flow obtained using **a** conventional GA and **b** Kriging-based GA . . . . . 820

Fig. 4 Hourly variation of electricity price for Case 2 . . . . . 821

Fig. 5 Results for Case 2 obtained using the proposed approach. **a** Optimized turbine flow and spill flow obtained using the proposed approach; **b** comparison of revenue generated by using the optimized turbine flow and spill flow and setting turbine flow to be equal to spill flow. . . . . 821

Fig. 6 Change in storage level of the reservoir during the simulation period . . . . . 822

**Effect of Nanosilica and Microsilica on Bond and Flexural Behaviour of Reinforced Concrete**

Fig. 1 **a** Scanning electron microscopic image of microsilica (M: 400X) **b** Transmission electron microscopic image of nanosilica (M: 25000X) (M = image magnification) . . . . . 827

Fig. 2 Mould set-up for bond stress specimen . . . . . 829

Fig. 3 Reinforcement details of RCC beam . . . . . 830

Fig. 4 Schematic diagram of beam test set-up . . . . . 830

Fig. 5 Load versus slip curve of RefCon . . . . . 831

Fig. 6 Load versus slip curve of mS-HPC . . . . . 832

Fig. 7 Load versus slip curve of nS-HPC. . . . . 832

Fig. 8 Observed crack pattern on specimens after bond stress test  
**a** RefCon, **b** mS-HPC, **c** nS-HPC . . . . . 833

Fig. 9 Crack pattern of RefCon beam (side 1 and 2) . . . . . 834

Fig. 10 Crack pattern of mS-HPC beam (side 1 and 2) . . . . . 835

Fig. 11 Crack pattern of nS-HPC beam (side 1 and 2) *Note* For side 1:  
 right support = rocker; left support = roller and for side 2: right  
 support = roller; left support = rocker . . . . . 835

Fig. 12 Number of cracks initiated with increase in load. . . . . 835

Fig. 13 Crack width versus load . . . . . 836

Fig. 14 Load versus strain at mid-span . . . . . 836

Fig. 15 Load versus strain at quarter-span . . . . . 836

Fig. 16 Load versus deflection at mid-span . . . . . 837

Fig. 17 Load versus deflection at quarter-span. . . . . 837

Fig. 18 Bending moment versus slope at supports . . . . . 838

**Interaction of a Flexible Splitter Plate with Vortex Shedding Past a Rigid Circular Cylinder**

Fig. 1 Schematic of the experimental set-up. . . . . 843

Fig. 2 Photograph of the experimental set-up in the wind tunnel. . . . . 844

Fig. 3  $St_p$  versus  $Re$

Fig. 4 Frequency spectra of plate response **a** before jump and **b**  
 after jump . . . . . 845

Fig. 5 Flow chart of the strong coupling algorithm . . . . . 847

Fig. 6 Schematic of the computational domain (not to scale). . . . . 848

Fig. 7 Computational grid: structured meshing. . . . . 848

Fig. 8 Vorticity contours at  $Re = 500$  at different time instances . . . . . 849

Fig. 9 Vorticity contours at  $Re = 750$  at different time instances . . . . . 849

Fig. 10 Vorticity contours at  $Re = 1000$  at different time instances . . . . . 850

## About the Editors

**Dr. A. Rama Mohan Rao** obtained his doctoral degree on high-performance computing techniques for nonlinear dynamic analysis from the Indian Institute of Science, Bangalore. He joined CSIR-SERC, Chennai, as a scientist in 1989 (after working nearly for a decade in the design and construction sector) and rose to the position of chief scientist. Currently, he heads the Structural Health Monitoring Laboratory, CSIR-SERC. He is also a Professor at the Academy of Scientific and Innovative Research (AcSIR) and has taught several advanced courses for M. Tech. and Ph.D. students. He was co-editor of the *Journal of Structural Engineering* from 2004 to 2007 and was an editorial board member for all the International Conferences on Parallel, Distributed, Grid and Cloud Computing for Engineering (PARENG 2009–2017) held in various European locations between 2009 and 2017. His research interests include computational structural mechanics; high-performance computing; structural system identification, control and health monitoring; nature-inspired computing, systems engineering; and combinatorial optimization. He has authored more than 95 peer-reviewed papers spread over 45 journals as well as 90 conference papers and several technical reports related to sponsored research and consultancy projects. He is a life member of several professional bodies and was awarded a UNDP fellowship for the year 1994–1995. He was a member of the team that won the CSIR Technology Prize in 1999 for scientific contributions to the development of advanced computational methodologies, modelling techniques and software for analysis and design of complex structures. He has also received an award for “excellence in high-performance cluster computing” from Sun Microsystems in February 2004. He was also a Visiting Research Scientist at the University of Berkeley, California, USA; Cornell University, Ithaca, USA; and Swansea University, Swansea, UK, in 1994–1995.

**Dr. K. Ramanjaneyulu** graduated from the Regional Engineering College, Warangal (now NIT Warangal), and obtained his postgraduate degree in structural engineering from the Indian Institute of Science, Bangalore. He obtained his doctoral degree in structural engineering on stability behaviour of wind-loaded natural draught cooling tower shells from the IIT Madras in 1992. He joined SERC,

Madras, as a scientist in 1989 and rose to the position of chief scientist. He currently heads the Advanced Concrete Testing & Evaluation Laboratory (ACTEL), CSIR-SERC. He is also a Professor at the Academy of Scientific and Innovative Research (AcSIR). His research interests include the behaviour of reinforced concrete structures; analysis and design of special structures such as bridges and cooling tower shells; blast-resistant design of structures; nonlinear finite element analysis of reinforced concrete plate and shell structures; and structural health assessment and management of bridges. He has published over 80 papers in refereed national/international journals and over 100 papers at international and national conferences/seminars.

**Part I**  
**Structural Dynamics—Wind, Impact and**  
**Earthquake Loads**

# Sloshing in Liquid Storage Tanks with Internal Obstructions



M. Z. Kangda, S. S. Sawant and O. R. Jaiswal

**Abstract** In the present paper, the effect of a centrally placed circular obstruction on sloshing frequency and sloshing mass is studied for annular tanks. Finite element approach (ANSYS software) is used to model the liquid. For circular tanks without obstruction, sloshing frequency and sloshing mass at first three modes are obtained using finite element analysis which compare well with the available analytical results. Next, a rigid circular obstruction at the center of tank is modeled and sloshing frequency and modal mass in the first three modes are obtained. It is observed that with the increase in the diameter of the circular obstruction, the sloshing frequency and the percentage of liquid in sloshing mode decrease in first mode. The behavior of these sloshing parameters in higher modes is also discussed. A detailed study over wide range of circular tank geometries is performed. Charts for obtaining sloshing parameters for various tank geometries are plotted.

**Keywords** Circular tanks · Hydrodynamic pressure · Internal obstruction  
Sloshing frequency

## 1 Introduction

In the post-earthquake period, uninterrupted functionality of liquid storage tanks is required for water supply and for controlling fire, if any. Further, any damage or leakage to tanks storing toxic chemicals may lead to hazardous consequences.

---

M. Z. Kangda · O. R. Jaiswal (✉)  
Applied Mechanics Department, Visvesvaraya National Institute  
of Technology, Nagpur 440010, India  
e-mail: ojaiswalvnit@yahoo.co.in

M. Z. Kangda  
e-mail: zainkangda@gmail.com

S. S. Sawant  
Walter P Moore, Pune, India  
e-mail: s.sawant113@yahoo.com

Hence, seismic safety of liquid storage tanks, which are lifeline structures, is very important. During seismic ground shaking, liquid inside the tank undergoes sloshing and this exerts hydrodynamic pressure on container walls. Therefore, one needs to perform proper dynamic analysis of tank-fluid system. Sloshing of liquid depends on various parameters like geometry of container, flexibility of tank wall, obstructions inside.

The sloshing phenomenon has been extensively studied in the past. Housner [1] obtained classical solutions for impulsive and convective parameters of ground-supported rectangular and circular tanks (under horizontal accelerations). The work was further extended to analyze elevated water tanks [2]. The tanks walls are considered rigid. Veletsos and Yang [3] considered the effect of flexibility of cylindrical tanks. Later, parameters like soil-structure interaction, vertical ground shaking component, roof mass, nonuniform wall thickness, and damping of tank foundation system were also considered [4]. A few studies also conducted experimental tests to evaluate the dynamic responses of cylindrical tanks under seismic excitation. Haroun [5] tested full-scale anchored and unanchored cylindrical tanks and compared the responses with the analytical method.

Some researchers have also analyzed tanks with obstruction inside the container. Aslam et al. [6] experimentally investigated annular tanks using small-scale and full-scale models and compared the responses with the developed analytical method. Bauer [7] investigated fluid-structure interaction for annular cylindrical tanks. Abramson [8] compiled the lateral sloshing behavior in annular and sector cylindrical tanks and also included spherical, conical, and oblate tanks. Tang et al. [9] investigated the seismic response of rigid and flexible annular tanks using analytical methods. Gedikli and Erguven [10] proposed a boundary element method (BEM) to evaluate modes of liquid in tanks with rigid baffles. Drake [11] also applied the BEM to analyze circular tanks installed with internal pipes. Biswal et al. [14] validated the results obtained by Gedikli and Erguven [10] using finite element (FE) approach and included the effect of tank-baffle flexibility. Researchers [12, 13] also used finite element approach to evaluate the responses of liquid-filled cylindrical tanks under seismic excitation. Recently, scaled boundary finite element method (SBFEM) was discussed by Lin et al. [15] to study the sloshing phenomenon in annular cylindrical liquid storage tanks.

Nowadays, use of finite element tools to model liquid storage tanks is becoming more and more popular. With the help of this tool, tanks of any shapes and geometries can be analyzed. Moslemi and Kianoush [16] used ANSYS software to analyze ground-supported cylindrical tanks (rigid and flexible) under vertical and horizontal ground acceleration. Kotrasova and Grajciar [17] used ADINA software to evaluate the seismic response of circular tanks. In the present work, finite element approach is used to study the free vibration characteristics of sloshing liquid. The study is focused to obtain sloshing frequency and sloshing mass. Presently, this study is limited to circular tank with rigid circular obstruction at center (i.e., annular container). Once finite element approach is established, then this approach can be extended to tanks of any geometry and any type of obstruction.



## 2 Finite Element Model of Liquid

The liquid is modeled using fluid element FLUID80 from the finite element library of ANSYS. This is a 3-D eight-noded element with three degrees of freedom at each node, i.e., translation in x, y, and z directions, respectively. Tank wall and centrally located obstruction are considered to be rigid. The container is considered to be fixed at the base. Figure 1 shows 3-D and plan view of FE model of container with centrally located rigid circular obstruction. Mesh size plays an important role in the modeling of liquid. A parametric study was performed to arrive at suitable mesh size. It is noted that mesh size depends on aspect ratio of container. Free vibration analysis is done for tanks without obstruction and with obstruction. The bulk modulus of liquid (water) is taken as  $2.18 \times 10^9 \text{ N/m}^2$ , and density of liquid is  $1000 \text{ kg/m}^3$ . Four cylindrical tanks with radius ( $R$ ) of 1, 2.5, 3.5, and 5 m are considered. Height-to-radius ratio ( $H/R$ ) for these tanks is varied from 0.2 to 4. Radius of obstruction ( $R_0$ ) to radius of tank ( $R$ ) ratio ( $k = R_0/R$ ) is varied from 0 to 0.5.

## 3 Results

In the present study, the sloshing frequency ( $\lambda_{n,k}$ ) and sloshing mass ( $m_n$ ) in first three modes are obtained. The effect of size of centrally located rigid circular obstruction on these results is studied. These results are compared with the analytical results on sloshing frequency and sloshing mass. For annular tanks, the sloshing frequency is given by Eq. (1) [3, 8].

$$\lambda_{n,k} = \frac{1}{2\pi} \sqrt{\frac{g}{R} \zeta_{n,k} \tanh\left(\zeta_{n,k} \frac{H}{R}\right)} \quad (1)$$

where  $n$  is the mode number,  $k = R_0/R$ , and  $g =$  gravitational acceleration. The values of  $\zeta_{n,k}$  are obtained by solving a transcendental equation in terms of Bessel's

**Fig. 1** ANSYS model of cylindrical tank with obstruction

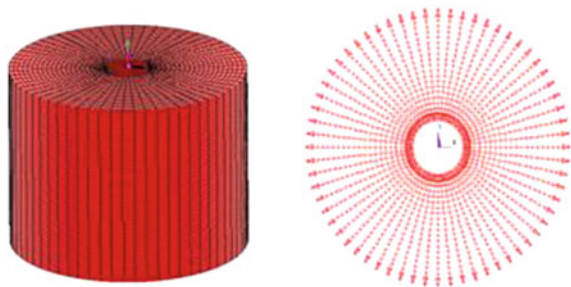


**Table 1** Values of constant  $\zeta_{n,k}$  [8]

$k = R_0/R$	First mode ( $n = 1$ )	Second mode ( $n = 2$ )	Third mode ( $n = 3$ )
0	1.841	5.330	8.530
0.1	1.803	5.137	8.199
0.2	1.705	4.960	8.433
0.3	1.582	5.137	9.308
0.4	1.462	5.660	10.683
0.5	1.355	6.560	12.706

formulations. The values of  $\zeta_{n,k}$  for the first three modes and for some values of  $k$  are given in Table 1.

Likewise, the ratio of sloshing mass in the  $n$ th mode ( $m_n$ ) and total liquid mass ( $m$ ) for tanks without obstruction is given by Eq. (2) [3].

$$\frac{m_n}{m} = \left[ \frac{2}{\zeta_n^2 - 1} \frac{R}{\zeta_n H} \tanh\left(\zeta_n \frac{H}{R}\right) \right] \quad (2)$$

The values of  $\zeta$  in the first three modes are  $\zeta_1 = 1.841$ ,  $\zeta_2 = 5.331$ , and  $\zeta_3 = 8.536$ . It is to be noted that there is no analytical expression for sloshing mass of annular tanks. However, Tang et al. [9] have given expression for sloshing mass coefficients for base shear and moment along with foundation shear for annular tanks.

The sloshing frequency and sloshing mass of circular tank without obstruction are obtained from finite element model of present study and are compared with the analytical results (Eqs. 1 and 2) in Table 2. It is to be noted that  $m_n/m$  depends only on  $H/R$ , whereas  $\lambda_{n,k}$  depends on  $H/R$  and  $R$ . The results of Table 2 are for  $R = 5$  m. It is seen that the results of present study obtained from finite element modeling match well with the analytical results. The results on tanks with obstruction (i.e., annular tanks) are given in Table 3 for  $R = 1$  m and  $R_0 = 0.1$  m and in Table 4 for  $R = 5$  m and  $R_0 = 0.5$  m. The sloshing frequency obtained from present study matches well with the analytical results given by Abramson [8]. From Tables 3 and 4, it is to be noted that the sloshing frequency depends on  $R$  also in addition to  $H/R$  and  $R_0/R$ . However,  $m_n/m$  depends only on  $H/R$  and  $R_0/R$ .

The effect of obstruction size on sloshing frequency and sloshing mass in first three modes is shown in Table 5. The results are for  $R = 5$  m,  $H = 1$  and 5 m, and  $k$  is varied from 0 to 0.5. It is seen that the sloshing frequency and sloshing mass ratio excited in first mode decrease as size of obstruction increases. However, the sloshing frequency in second and third mode initially decreases for  $k = 0$  to 0.2 and gradually increases for  $k = 0.3$  to 0.5.

The sloshing mass ratio in the first and third modes decreases with the size of obstruction. The sloshing mass excited is very large in the first mode. The sloshing mass ratio ( $m_n/m$ ) in the first and third modes decreases with the size of obstruction,

**Table 2** Sloshing frequency and sloshing mass of cylindrical tank without obstruction ( $R = 5\text{ m}$ )

$H/R$	$\lambda_{1,0}$ (Hz)	$\lambda_{2,0}$ (Hz)	$\lambda_{3,0}$ (Hz)	$\lambda_{1,0}$ (Hz)	$\lambda_{2,0}$ (Hz)	$\lambda_{3,0}$ (Hz)	$\frac{mL}{m}$	$\frac{m\lambda}{m}$	$\frac{mL}{m}$	$\frac{m\lambda}{m}$	$\frac{mL}{m}$	$\frac{m\lambda}{m}$
	Present study			Veletsos [3]			Present study			Veletsos [3]		
0.4	0.240	0.510	0.650	0.240	0.508	0.651	0.710	0.0324	0.0074	0.713	0.033	0.0081
0.8	0.287	0.515	0.653	0.287	0.515	0.651	0.512	0.0165	0.0040	0.512	0.017	0.0041
1.2	0.299	0.515	0.653	0.299	0.515	0.651	0.370	0.0120	0.0026	0.370	0.011	0.0027
1.6	0.302	0.515	0.652	0.302	0.515	0.651	0.281	0.0084	0.0020	0.283	0.009	0.0020
2.0	0.302	0.514	0.650	0.302	0.515	0.651	0.226	0.0066	0.0015	0.227	0.007	0.0016
2.4	0.302	0.513	0.647	0.302	0.515	0.651	0.189	0.0056	0.0013	0.189	0.006	0.0014
2.8	0.302	0.513	0.647	0.302	0.515	0.651	0.161	0.0048	0.0011	0.162	0.005	0.0012
3.2	0.302	0.512	0.647	0.302	0.515	0.651	0.141	0.0042	0.0009	0.142	0.004	0.0010
3.6	0.302	0.512	0.646	0.302	0.515	0.651	0.124	0.0037	0.0008	0.126	0.004	0.0009
4	0.302	0.512	0.646	0.302	0.515	0.651	0.113	0.0033	0.0007	0.114	0.003	0.0008

**Table 3** Sloshing frequency and sloshing mass of cylindrical tank with obstruction ( $R = 1$  m,  $R_0 = 0.1$  m, and  $k = 0.1$ )

$H/R$	$\hat{\lambda}_{1,0.1}$ (Hz)	$\hat{\lambda}_{2,0.1}$ (Hz)	$\hat{\lambda}_{3,0.1}$ (Hz)	$\hat{\lambda}_{1,0.1}$ (Hz)	$\hat{\lambda}_{2,0.1}$ (Hz)	$\hat{\lambda}_{3,0.1}$ (Hz)	$\frac{m_1}{m}$	$\frac{m_2}{m}$	$\frac{m_3}{m}$
	Present study			Abramson [8]			Present study		
0.4	0.525	1.111	1.427	0.526	1.111	1.425	0.689	0.046	0.0049
0.8	0.632	1.130	1.426	0.633	1.130	1.427	0.498	0.024	0.0025
1.2	0.657	1.130	1.427	0.661	1.130	1.427	0.361	0.016	0.0016
1.6	0.666	1.130	1.426	0.667	1.130	1.427	0.276	0.012	0.0012
2.0	0.666	1.129	1.428	0.669	1.130	1.427	0.220	0.0095	0.0010
2.4	0.666	1.127	1.429	0.669	1.130	1.427	0.183	0.0079	0.0008
2.8	0.666	1.125	1.426	0.669	1.130	1.427	0.157	0.0066	0.0007
3.2	0.666	1.124	1.424	0.669	1.130	1.427	0.137	0.0059	0.0006
3.6	0.666	1.124	1.422	0.669	1.130	1.427	0.122	0.0052	0.0005
4	0.666	1.125	1.420	0.669	1.130	1.427	0.110	0.0047	0.0005

**Table 4** Sloshing frequency and sloshing mass of cylindrical tank with obstruction ( $R = 5$  m,  $R_0 = 0.5$  m, and  $k = 0.1$ )

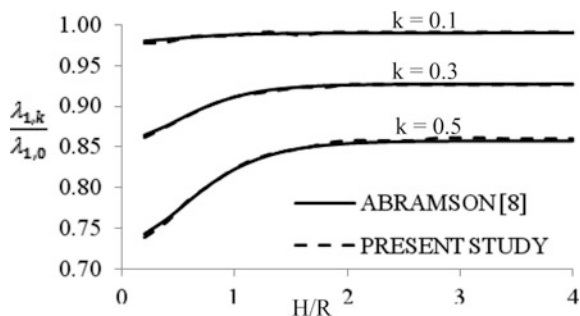
$H/R$	$\hat{\lambda}_{1,0.1}$ (Hz)	$\hat{\lambda}_{2,0.1}$ (Hz)	$\hat{\lambda}_{3,0.1}$ (Hz)	$\hat{\lambda}_{1,0.1}$ (Hz)	$\hat{\lambda}_{2,0.1}$ (Hz)	$\hat{\lambda}_{3,0.1}$ (Hz)	$\frac{m_1}{m}$	$\frac{m_2}{m}$	$\frac{m_3}{m}$
	Present study			Abramson [8]			Present study		
0.4	0.235	0.495	0.637	0.235	0.497	0.637	0.688	0.046	0.0049
0.8	0.283	0.505	0.637	0.283	0.505	0.638	0.498	0.024	0.00246
1.2	0.296	0.505	0.637	0.296	0.505	0.638	0.362	0.016	0.00164
1.6	0.298	0.505	0.637	0.298	0.505	0.638	0.277	0.012	0.00123
2.0	0.299	0.505	0.635	0.299	0.505	0.638	0.221	0.010	0.0010
2.4	0.299	0.505	0.633	0.299	0.505	0.638	0.184	0.0079	0.00080
2.8	0.299	0.504	0.630	0.299	0.505	0.638	0.158	0.0068	0.00070
3.2	0.299	0.504	0.633	0.299	0.505	0.638	0.138	0.0059	0.00060
3.6	0.299	0.504	0.632	0.299	0.505	0.638	0.123	0.0052	0.00054
4	0.299	0.503	0.630	0.299	0.505	0.638	0.110	0.0047	0.00048

whereas sloshing mass ratio in the second mode increases with the size of obstruction.

In the present study, results are obtained for large number of tanks of different  $H/R$  and for different  $R_0/R$ . The results are presented graphically. Since the sloshing frequency depends on  $R$  along with  $H/R$  and  $R_0/R$ , hence for annular tanks the sloshing frequency is presented as a ratio of frequency of annular tanks divided by corresponding frequency of tanks without obstruction (i.e.,  $\lambda_{n,k}/\lambda_{n,0}$ ). In Fig. 2, results on sloshing frequency in first mode are shown for  $k = 0.1, 0.3$ , and  $0.5$ . Here, comparison with analytical results is also shown. It is interesting to note that the frequency ratio ( $\lambda_{1,k}/\lambda_{1,0}$ ) obtained analytically matches well with present results

**Table 5** Effect of obstruction size on sloshing frequency and sloshing mass of cylindrical tank [( $R$ ) = 5 m and  $H$  = 1 m]

$k = R_0/R$	$\hat{\lambda}_{1,k}$ (Hz)	$\hat{\lambda}_{2,k}$ (Hz)	$\hat{\lambda}_{3,k}$ (Hz)	$\hat{\lambda}_{1,k}$ (Hz)	$\hat{\lambda}_{2,k}$ (Hz)	$\hat{\lambda}_{3,k}$ (Hz)	$\frac{m_1}{m}$	$\frac{m_2}{m}$	$\frac{m_3}{m}$
	Present study			Abramson [8]			Present study		
0	0.180	0.457	0.630	0.180	0.457	0.630	0.800	0.054	0.0144
0.1	0.176	0.443	0.615	0.176	0.444	0.615	0.771	0.073	0.0091
0.2	0.167	0.431	0.627	0.167	0.432	0.626	0.705	0.127	0.0057
0.3	0.155	0.443	0.665	0.155	0.444	0.664	0.636	0.182	0.0035
0.4	0.144	0.478	0.718	0.144	0.478	0.719	0.581	0.217	0.0020
0.5	0.133	0.532	0.788	0.133	0.532	0.790	0.543	0.226	0.0010
$R = 5$ m and $H = 5$ m									
0	0.295	0.515	0.653	0.295	0.515	0.651	0.431	0.0132	0.0031
0.1	0.291	0.505	0.637	0.291	0.505	0.638	0.422	0.019	0.0020
0.2	0.282	0.496	0.646	0.282	0.496	0.647	0.400	0.034	0.0012
0.3	0.269	0.505	0.679	0.269	0.505	0.680	0.380	0.0473	0.00074
0.4	0.255	0.530	0.724	0.255	0.530	0.729	0.367	0.0533	0.0004
0.5	0.243	0.571	0.790	0.243	0.572	0.795	0.360	0.0521	0.00021

**Fig. 2** First-mode sloshing frequency ratio of annular tanks

and this ratio is independent of value of  $R$  and depends only on  $H/R$  and  $R_0/R$ . Analytically, the ratio of frequency is given by Eq. (3).

$$\frac{\lambda_{n,k}}{\lambda_{n,0}} = \sqrt{\frac{\xi_{n,k} \tanh(\xi_{n,k} \frac{H}{R})}{\xi_{n,0} \tanh(\xi_{n,0} \frac{H}{R})}} \quad (3)$$

Here,  $\xi_{n,k}$  depend on  $R_0/R$  and  $\xi_{n,0}$  are constants, and hence, it is clear that the frequency ratio value does not depend on individual value of  $R$ . From Fig. 2, it is seen that as the size of obstruction increases, the first sloshing frequency decreases. Similar results for second-mode sloshing frequency are given in Fig. 3. From Fig. 3, it is seen that that for second-mode frequency ratio first decreases with  $k$  and then increases. The effect of obstruction on sloshing mass of first mode is depicted

**Fig. 3** Second-mode sloshing frequency ratio of annular tanks

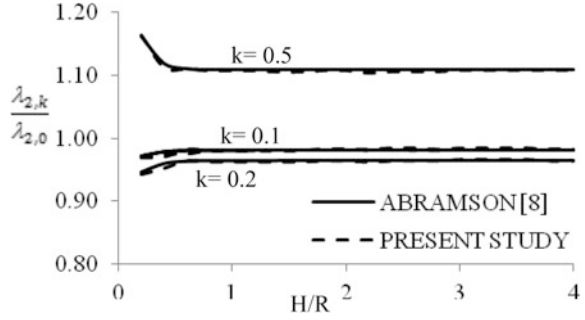


**Fig. 4** First-mode sloshing mass ratio of annular tanks

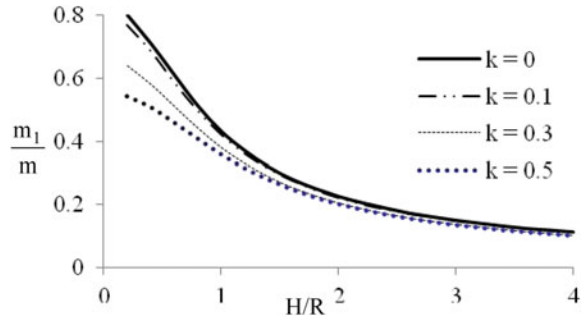
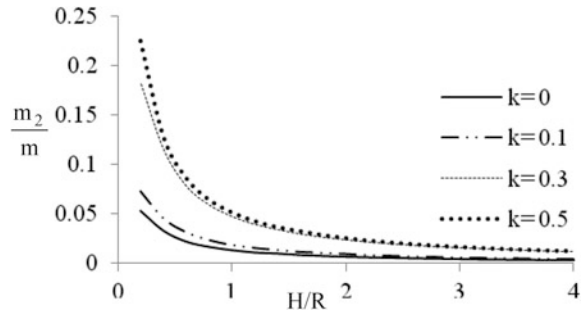


**Fig. 5** Second-mode sloshing mass ratio of annular tanks



in Fig. 4. It is seen that sloshing mass ratio gets affected by obstruction size for shallow tanks, i.e., ( $H/R < 1.0$ ). The sloshing mass of second mode increases with the obstruction size. This increase is significant for shallow tanks. (i.e.,  $H/R < 1.0$ ) as shown in Fig. 5. The sloshing mass ratio obtained in the three modes is represented by  $m_1/m$ ,  $m_2/m$ , and  $m_3/m$ , respectively. Figures 4 and 5 show sloshing mass ratio in first and second mode for the selected tank geometries. The results compare well between present study and available analytical approach. It can be concluded that the convective mass ratio is independent of the  $R_0$ ,  $R$ , and  $H$  of tank alone and, however, depends on radius of obstruction,  $R_0$ , and  $H/R$  ratios.

## 4 Discussion and Conclusions

In the present study, finite element approach is used to quantify the effect of centrally located circular rigid obstruction on sloshing frequency and sloshing mass of circular tank (i.e., for annular tank). Tank walls are considered rigid with fixity at the base. For sloshing frequency of such annular tanks, closed-form expressions are available [8, 9]. However, for sloshing mass such closed-form expressions are not available. The sloshing frequency results of present study match well with analytical results [3, 8].

In the finite element model, suitable mesh size is used to arrive at reasonably converged results. Liquid is considered to be inviscid and incompressible and modeled using the FLUID 80 element from the finite element library of ANSYS having properties of water. The finite element results are first validated with the available results for tanks without obstruction. Then, the results for annular tanks are obtained. The sloshing frequency and sloshing mass are obtained for first three modes. It is seen that with increase in obstruction size, the frequency of first sloshing mode decreases. However, in second and third mode the frequency reduces up to certain value of  $R_0/R$  and then increases (Table 5). The sloshing mass in first mode decreases with increase in size of obstruction. However, in the second mode altogether opposite behavior is seen; i.e., sloshing mass increases with size of obstruction. Further, the mass excited in second and third mode is much less as compared to the amount of mass excited in first mode. However, the mass excited in second mode is quite large for shallow tanks. The effect of obstruction size on sloshing frequency is significant for shallow tanks.

The finite element approach used in this study is quite robust and can be extended to further study the effect of obstruction of any shape at any location. Moreover, the flexibility of obstruction can also be included. Such studies will find applications in nuclear reactors also.

## References

1. Housner GW (1957) Dynamic pressures on accelerated fluid containers. *Bull Seismol Soc Am* 47(1):15–35
2. Housner GW (1963) Dynamic behavior of water tanks. *Bull Soc Am* 53(2):381–387
3. Veletsos AS, Yang JY (1976) Dynamics of fixed-base liquid-storage tanks. In: *Proceedings of U.S.–Japan seminar on Earthquake engineering research with emphasis on lifeline systems*, Tokyo, Japan, Nov 8–12, pp 317–341
4. Velesos AS (1984) Seismic Response and design of liquid storage tanks. In *Guidelines for the seismic design of oil and gas pipeline systems*, pp 255–370
5. Haroun MA (1983) Vibration studies and tests of liquid storage tanks. *Earthquake Eng Struct Dynam* 11(2):179–206
6. Aslam M, Godden WG, Scalise DT (1979) Earthquake sloshing in annular and cylindrical tanks. *J Eng Mech Div* 105(EM3):371–389

7. Bauer HF (1964) Fluid oscillations in the containers of a space vehicle and their influence upon stability. National aeronautics and space administration technical report (NASA TR R-187)
8. Abramson HN (1966) The dynamic behavior of liquids in moving containers, NASA SP-106
9. Tang Y, Grandy C, Seidensticker R (2010) Seismic response of annular cylindrical tanks. *Nucl Eng Des* 240(10):2614–2625
10. Gedikli A, Ergüven ME (1999) Seismic analysis of a liquid storage tank with a baffle. *J Sound Vib* 223(1):141–155
11. Drake KR (1999) The Effect of internal pipes on fundamental frequency of liquid sloshing in a circular tank. *Appl Ocean Res* 21:133–143
12. Balendra T, Ang KK, Paramasivam P, Lee SL (1982) Seismic design of flexible cylindrical liquid storage tanks. *Earthquake Eng Struct Dynam* 10:477–496
13. Babu SS, Bhattacharyya SK (1996) Finite element analysis of fluid-structure interaction effect on liquid retaining structures due to sloshing. *Comput Struct* 59(6):1165–1171
14. Biswal KC, Bhattacharyya SK, Sinha PK (2003) Free-vibration analysis of liquid-filled tank with baffles. *J Sound Vib* 259(1):177–192
15. Lin G, Liu J, Li J, Hu Z (2015) A scaled boundary finite element approach for sloshing analysis of liquid storage tanks. *Eng Anal Boundary Elem* 56:70–80
16. Moslemi M, Kianoush MR (2012) Parametric study on dynamic behavior of cylindrical ground-supported tanks. *Eng Struct* 42:214–230
17. Kotrasová K, Grajciar I (2014) Dynamic analysis of liquid storage cylindrical tanks due to earthquake. *Adv Mater Res* 969:119–124



# Nonlinear Static Behaviour of RC Frame Buildings During Construction Stages



**Ankush Gogoi, Bhargav Bhuyan, Nishant Sharma  
and Kaustubh Dasgupta**

**Abstract** Multi-storied reinforced concrete (RC) frame buildings nowadays constitute a large extent of the building stock in urban India. Usually, multi-storey buildings are analysed at the final stage but in reality loads are sequentially applied at every stage of construction. So in the present study, the influence of the story height on capacity has been attempted to be investigated through analysis of five RC frame buildings during their intermediate construction stages. Here earthquake force is considered to be applied in all the full buildings along with their intermediate stages and pushover analysis is carried out to determine possible damage of structural members with increase in height of the buildings. The present study gives an insight on the vulnerability of the structural members of building liable to seismic damage.

**Keywords** Moment-rotation data · Pushover analysis · Staged construction  
Plastic hinge

---

A. Gogoi · B. Bhuyan  
Department of Civil Engineering, National Institute of Technology Silchar,  
Silchar 788010, India  
e-mail: ankushgogoi1@gmail.com

B. Bhuyan  
e-mail: bhargavbistima@gmail.com

N. Sharma · K. Dasgupta (✉)  
Department of Civil Engineering, Indian Institute of Technology Guwahati,  
Guwahati 781039, India  
e-mail: kd@iitg.ac.in

N. Sharma  
e-mail: nsharmanishant@gmail.com

## 1 Introduction

Multi-storied Reinforced Concrete (RC) frame buildings constitute a large part of the urban building stock in our country. As approximately 60% of the country is under moderate to severe seismic hazard, earthquake-resistant design of RC buildings is a subject of extreme importance in the current scenario. Although past studies have focused extensively on the seismic behaviour and the possible design aspects in detail, most of the investigations have focussed on the building behaviour at its functional stage. Very few studies have focussed on the building behaviour during the different stages of its construction. In Ref. [1], the effect of self-weight was only studied during construction process of buildings. In Ref. [2], rigid frame structures of both concrete and steel model of different configurations were considered for sequential analyses and the structural response against the various loads compared under linear static analyses. In Ref. [3], the effect of construction sequence was studied by carrying out nonlinear static analyses of rigid RC frames of different configurations and compared with the results of single-step analysis. The structural response and the required reinforcement tend to increase for the interior columns for the different stages of construction. In another study [4], several buildings were analysed under different loads in construction stages. Although the design of columns was not much influenced, the designs of interior beam and the edge columns turned out to be critical during the construction stages. A thirty-storied building was analysed under construction sequence loadings in various stages, and critical design aspects in components were identified [5].

In the present study, seismic behaviour of five different buildings at their respective intermediate stages of construction is investigated under the combined effects of dead load, live load and earthquake load. Nonlinear static analysis is carried out for the different stages of construction to assess their seismic behaviour and possible failure modes in the members.

## 2 Input Details and Modelling

The following sections explain the modelling and input details.

### 2.1 Description of the Model

Five RC framed symmetric buildings of different heights and having same plan are considered to be located in Seismic Zone V as per the Indian earthquake code [6]. Their intermediate stages of construction have been considered for the present study. The typical floor plan of the buildings is shown in Fig. 1. Details of the number of intermediate stories taken for the study are shown in Table 1 along with

**Fig. 1** Floor plan of the building models



the model names. The building plan has length and width as 15.52 and 9.14 m, respectively. The typical storey height is considered as 3.04 m for all the buildings.

## 2.2 *Input Details*

The beams and the columns are modelled using 2-noded frame elements (with 3 translational and 3 rotational degrees of freedom at each node) and the slabs are modelled using 4-noded shell elements (with 3 translational and 3 rotational degrees of freedom at each node) using the computer program SAP2000 [7]. The design of the beam and column sections is carried out based on under-reinforced failure mode and using the relevant Indian Standards [8, 9]. Further, ductile detailing of the beam and column sections is carried out and checked against possible seismic shear failure as per the Indian Ductile Detailing Code [10]. The thickness of all the floor slabs is taken as 125 mm. Unreinforced masonry infill walls are not considered in the analyses. The buildings are assumed to be having foundation on rocky stratum, thus the translational and rotational degrees of freedom at the bottom ends of the columns are restrained.

## 2.3 *Load Calculations*

The dead load and live load for the structural elements are adopted as per the provisions in the Indian Standards [11, 12]. As per the Indian Code [6], the important factor and response reduction factor for all the buildings are considered as 1 and 5, respectively. The design lateral force is then calculated and the following load combinations are adopted:

- $1.5 \times (DL + LL)$
- $1.2 \times (DL + LL \pm EL)$

**Table 1** Model details

Model name	No. of stories	No. of stories in intermediate stage
2S	2	1
4S	4	2
6S	6	2, 4
8S	8	3, 6
10S	10	4, 8

- $1.5 \times (DL \pm EL)$
- $0.9 \times DL \pm 1.5 \times EL$

## 2.4 *Beam Section Details*

The section sizes and reinforcement of the beams are carried out for each model (Table 2) as per the relevant standards [8, 9] considering the flexure and shear design methodologies.

## 2.5 *Column Section Details*

The section sizes and reinforcement of the columns are decided based on the combined axial forces and the bending moments at the relevant sections. The longitudinal reinforcement is kept in the range of 0.8–1.35% for all the column sections considering under-reinforced behaviour and equally distributed reinforcement on all the four sides (Table 2). Flexure and shear design methodologies are used as per the relevant standards [8, 9].

## 3 *Nonlinear Static Analysis*

Nonlinear static analysis or pushover analysis is carried out for all the buildings along the direction of the length of each building. First, force-controlled pushover analysis is carried out for dead and live loads. Then, monotonic displacement-controlled pushover analysis is carried out in the horizontal direction with displacement profile same as that of the fundamental translational mode shape of vibration in that direction. Material nonlinearity is modelled using lumped plastic hinges at appropriate sections in the beams and columns, and these hinges represent flexural mode of failure.

**Table 2** Sectional details of columns and beams and corresponding locations

Size <sup>a</sup>	Main <i>r/f</i>	Transverse <i>r/f</i>	Special confining <i>r/f</i>	Location model/ storey <sup>b</sup>
350 × 350	12 # 12 mm Ø	2 leg 12 mm Ø @ 175 <sup>a</sup> c/c	2 leg 12 mm Ø @ 85 <sup>a</sup> c/c over 450 <sup>a</sup>	2S/1–2; 4S/3–4; 6S/5–6; 8S/7–8;
400 × 400	12 # 12 mm Ø	3 leg 10 mm Ø @ 190 <sup>a</sup> c/c	3 leg 10 mm Ø @ 100 <sup>a</sup> c/c over 450 <sup>*</sup>	4S/1–2; 6S/3–4; 10S/7–10;
450 × 450	16 # 12 mm Ø	3 leg 10 mm Ø @ 190 <sup>a</sup> c/c	3 leg 10 mm Ø @ 100 <sup>a</sup> c/c over 450 <sup>a</sup>	6S/1–2; 8S/4–6;
500 × 500	20 # 12 mm Ø	3 leg 10 mm Ø @ 190 <sup>a</sup> c/c	3 leg 10 mm Ø @ 100 <sup>a</sup> c/c over 500 <sup>a</sup>	10S/4–6
550 × 550	20 # 12 mm Ø	3 leg 10 mm Ø @ 190 <sup>a</sup> c/c	3 leg 10 mm Ø @ 100 <sup>a</sup> c/c over 500 <sup>a</sup>	8S/1–3
600 × 600	28 # 12 mm Ø	3 leg 10 mm Ø @ 190 <sup>a</sup> c/c	3 leg 10 mm Ø @ 100 <sup>a</sup> c/c over 600 <sup>a</sup>	10S/1–3
<i>All beams</i>				
	Main <i>r/f</i>	Transverse <i>r/f</i>		
350 × 250	<sup>c</sup> 3 # 12 mm Ø	2 leg 8 mm Ø @ 100 c/c over 600; @ 150 elsewhere		

<sup>a</sup>In millimetre (mm)<sup>b</sup>Storey intervals corresponding to the model name<sup>c</sup>Detailing for tension side. Same detailing is used compression side

### 3.1 Details of Hinge Properties

For locating the plastic hinge section, the plastic hinge length [13] is calculated using Eq. (1)

$$L_p = 0.08L_v + 0.022f_y d_b \quad (1)$$

where  $L_p$  is the length of plastic hinge,  $L_v$  the distance of the point of contraflexure from the support,  $f_y$  the yield strength of longitudinal reinforcement steel and  $d_b$  the mean diameter of longitudinal bars. At each plastic hinge location in the beams, moment–curvature characteristic is assigned to monitor the possibility of flexural failure mode during pushover analysis. For columns, the axial force–bending moment interaction is also assigned at the sections, along with the moment–curvature property, to monitor the failure modes. For both beam and column sections, moment–curvature characteristics are obtained from the section designer module of

SAP2000 program by using the ultimate curvature, yield curvature, ultimate moment and yield moment capacities. For columns, the mentioned parameters are obtained for different axial forces.

For the force-controlled analysis, the models are analysed under dead load first. Then, considering the deformed shape of the model under dead load, pushover analysis was carried out under live load. That was followed by the displacement-controlled pushover analysis. The appropriate displacement profile for displacement-controlled pushover analysis is obtained by carrying out modal analysis of the building models. The mode shape of vibration for the second mode represented required displacement profile along the desired direction.

### 4 Results of Pushover Analysis

For all the buildings, the observed lateral shear capacity is higher for the intermediate construction stage as compared to the lateral capacity obtained for the final stage of construction (Figs. 2a, 3a, 4a, 5a and 6a). For the first stage of construction,

**Fig. 2** **a** Comparative pushover curves during intermediate and final stages, and **b** final hinge formation for two-storied building

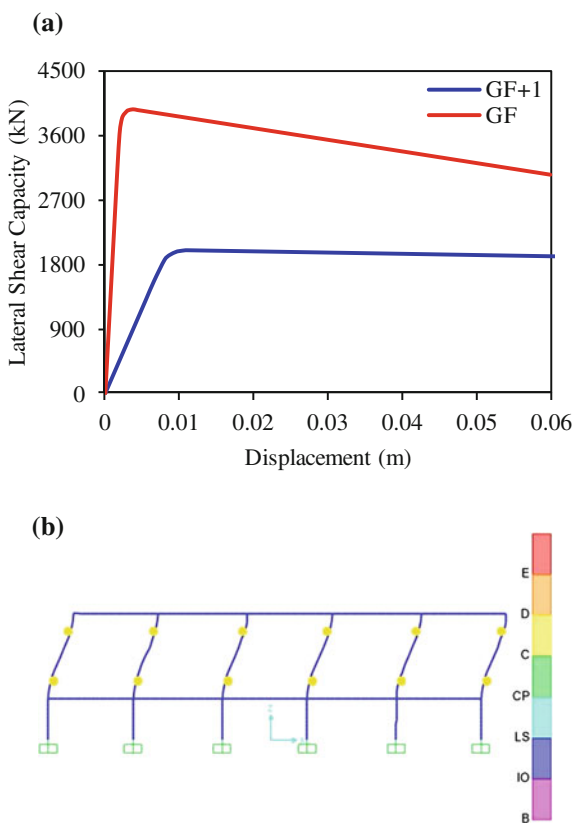


**Fig. 3 a** Comparative pushover curves during intermediate and final stages, **b** final hinge formation in end bay and **c** for the entire frame in the four-storied building

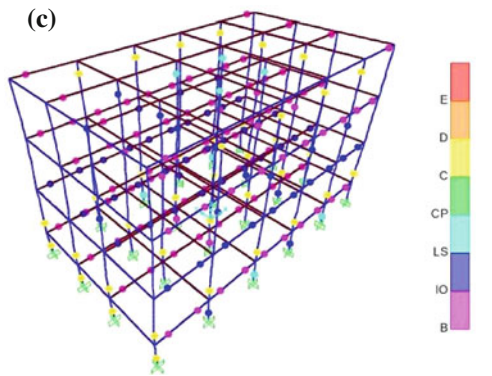
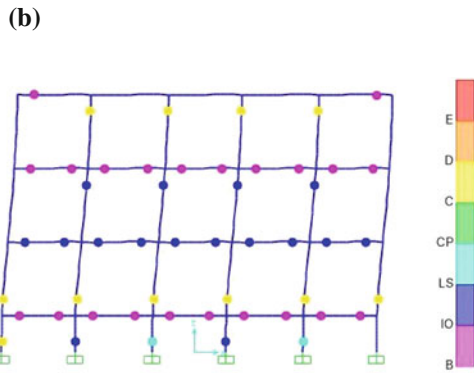
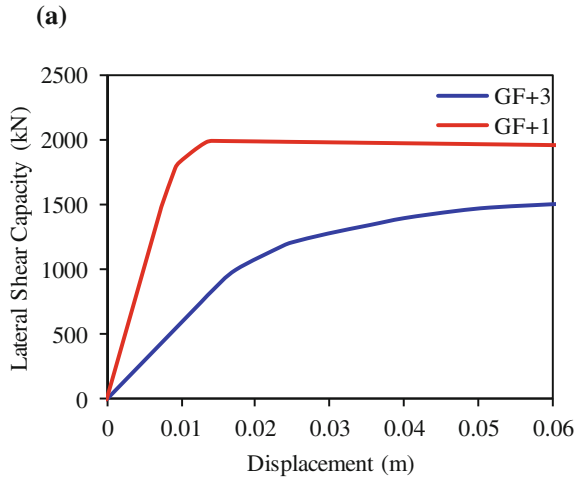
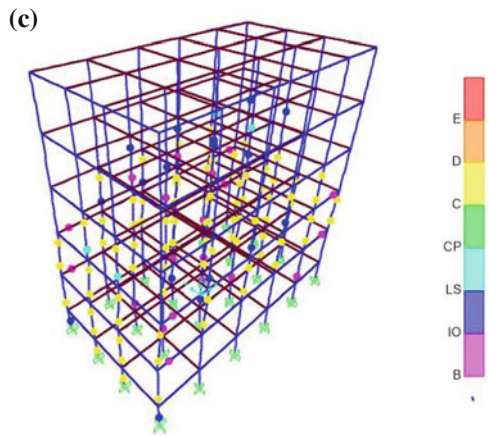
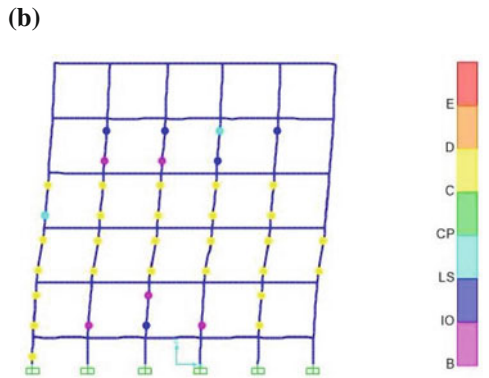
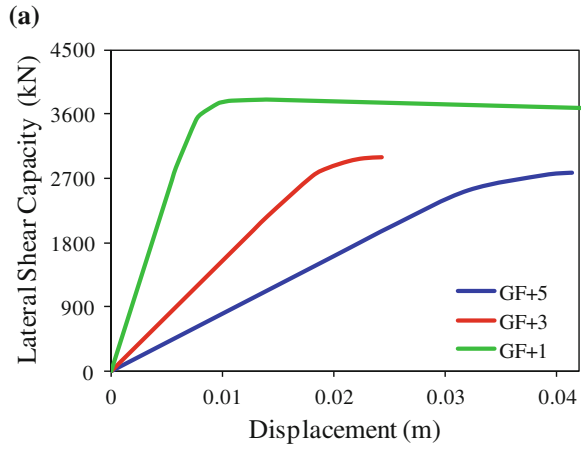


**Fig. 4** **a** Comparative pushover curves during intermediate and final stages, **b** final hinge formation in end bay and **c** for the entire frame for the six-storied building





i.e. with the columns only up to the plinth level, the capacity for the six-storied building is the highest as compared to the two- and four-storied buildings. This is due to the fact that the beams and columns have been designed considering the final structure (excluding any infill wall and floor-finishing load), thus the member capacities are also expected to increase with the final height of the structure.

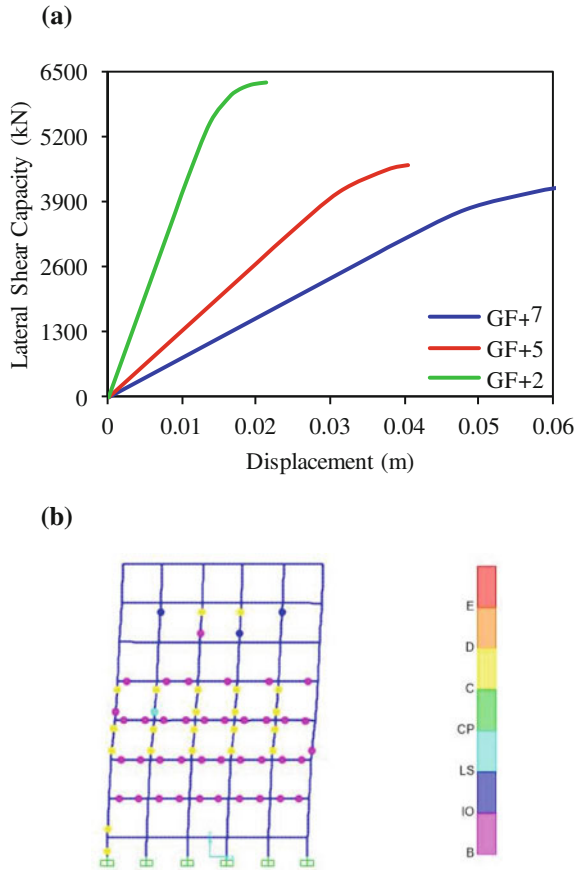
However, the estimated displacement capacities of the buildings are observed to be almost the same for the initial stage. For two-, four- and six-storied buildings, the lateral displacement reduces with increase in height during the construction stages. This is possibly due to the formation of collapse mechanism in the upper stories through mobilization of plastic hinges. For the two-storied building, such a mechanism is formed in the upper story with the hinges reaching the collapse capacities (Fig. 2b). For the four-storied building, mostly beam mechanism is observed in the lower floors with extensive hinge formation at the bottom of the lower story columns (Fig. 3a, b). These possibly lead to lesser displacement capacity in the final stage of construction of the building.

For the final stage two-storied building, the first hinge in the columns is formed at a displacement of 6.5 mm with most of those hinges reaching the collapse stage at a displacement of 8 mm (Fig. 2b). For the final construction stage analysis of the four-storied building, the first hinges are formed in the beams at a lateral displacement of 14 mm, whereas the column hinges start forming at around 35 mm (Fig. 3b, c). Although beam hinges are formed in all the floors, they do not reach the collapse stage in any of the floors. Most of the deformations get concentrated at the column ends and this leads to lesser nonlinearity at the beam ends. For the initial stage analysis of the building, the hinges at the beam and column ends start forming at displacement levels of 7.4 and 12 mm respectively.

For the final stage six-storied building, the first hinges are formed at the column ends at a displacement of 25.6 mm. The hinges are formed in the first- and second-floor beams at a displacement of 38.9 mm but none of the hinges reached the collapse stage. No plastic hinge is formed in the fifth-floor columns as well as in the ground, fourth- and fifth-floor beams (Fig. 4c). For the intermediate stages of construction, the displacement capacity could not be estimated because the non-linear analysis did not proceed after the peak lateral shear capacity was reached. For both the intermediate frames, the first hinges in the beams and columns are formed earlier than the corresponding hinge formations for the final structure. Also, the beam hinges did not reach the collapse level for any of the cases.

For the intermediate construction stages of the eight-storied building, the non-linear static analysis did not proceed beyond the displacement at which peak lateral shear strength was reached. Thus, the displacement capacity could not be estimated for the intermediate six-storied and three-storied structures. For the final stage structure, the first hinges at the beam and the column ends formed at displacements of 48 and 39 mm, respectively. Most of the nonlinearities got concentrated at the column ends of the middle floors (Fig. 5b). Thus, the hinges at the beam ends did not reach the collapse level. For the intermediate stage structures, the hinges at the beam and the column ends formed earlier than those for the final stage structure. Also, hinges at the ends of the columns reached the collapse level, whereas, the

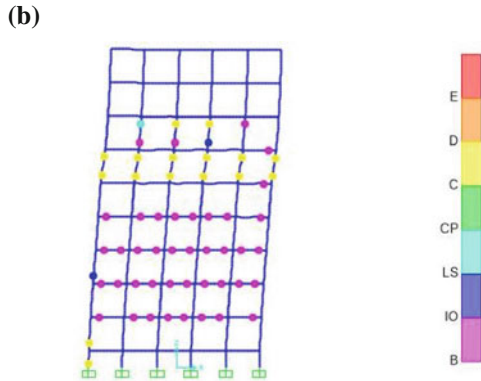
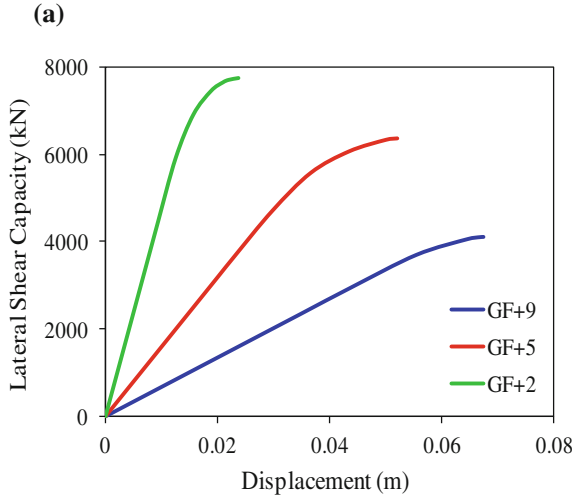
**Fig. 5** **a** Comparative pushover curves during intermediate and final stages, and **b** final hinge formation for eight-storied building



beam hinges did not show significant nonlinearities. For the final stage structure, the peak lateral shear strength could not be observed.

For the ten-storied building, peak lateral shear strength could not be reached for any of the intermediate stage models or the final stage model. The first hinges are formed at the beam end and the column ends at displacement levels of 43.8 and 55.4 mm, respectively. Like the six-storied building, the hinges at the beam and the column ends formed earlier than those for the final stage structure (Fig. 6b). For the final stage structure, the collapse mechanism was observed in the columns of one particular storey. Although hinges were formed at the beam ends for a number of floors, the level of nonlinearity was less as compared to the maximum nonlinearity observed at the column ends. For both six- and eight-storied buildings, very few hinges were formed in the two bottom storey columns (Figs. 5b and 6b).

**Fig. 6 a** Comparative pushover curves during intermediate and final stages, and **b** final hinge formation for ten-storied building



## 5 Conclusions

The following salient conclusions are drawn from the current study:

- (a) With increase in the height of the building, nonlinearities tend to get concentrated at the columns of the middle stories. Also, the beam hinges show lesser levels of nonlinearity.
- (b) With increase in height of the building, hinge formation begins at the column ends and then spreads to the ends of the beams.

Further detailed analyses need to be carried out for final service stage of the buildings to compare the lateral shear strength and displacement capacities with those obtained for the intermediate stages of construction.

**Acknowledgements** The authors are grateful to the Department of Civil Engineering, National Institute of Technology Silchar, and the Department of Civil Engineering, Indian Institute of Technology Guwahati, for providing the resources and facilities to carry out the work.

## References

1. Chakrabarti SC, Nayak GC, Agarwal SK (1978) Effect of sequence of construction in the analysis of multistoried building frame. *Build Environ* 13:1–6
2. Dinar Y, Rasel M, Chowdhury MJA, Ashraf MA (2014) Chronological construction sequence effects on reinforced concrete and steel buildings. *Int J Eng Sci* 3:52–63
3. Dubey N, Sonparote RS, Kumar R (2015) Effect of construction sequence analysis on seismic performance of tall buildings. *J Civil Eng Environ Technol* 2(11):44–49
4. Pathan MK, Ali SW, Khan HT, Mirza MS, Waseem M, Zubair S (2014) Construction stage analysis of RCC frames. *Int J Eng Technol Res* 2(3):54–58
5. Shirhatti TG, Vanakudre SV (2015) The effects of P-Delta and construction sequential analysis of RCC and steel building with respect to linear static analysis. *Int Res J Eng Technol* 2(4):501–505
6. BIS (2002) Criteria for earthquake resistant design of structures—Part1: General provisions and buildings IS 1893 (Part 1): 2002. Bureau of Indian Standards, New Delhi
7. CSI (2014) Structural analysis program SAP2000V 16.0.1. Computers and Structures Inc., Berkeley, U.S.A.
8. BIS (2000) Plain and Reinforced concrete—code of practice IS 456:2000. Bureau of Indian Standards, New Delhi
9. BIS (1980) Design aids for reinforced concrete to IS: 456–1978 SP 16:1980. Bureau of Indian Standards, New Delhi
10. BIS (2003) Ductile detailing of reinforced concrete structures subjected to seismic forces-code of practice IS 13920:1993. Bureau of Indian Standards, New Delhi
11. BIS (1987) Code of practice for design loads (other than earthquake) for buildings and structures: Part 1 Dead loads—unit weights of building material and stored materials IS 875 (Part 1): 1987. Bureau of Indian Standards, New Delhi
12. BIS (1987) Code of practice for design loads (other than earthquake) for buildings and structures: Part 2 Imposed loads IS 875 (Part 2): 1987. Bureau of Indian Standards, New Delhi
13. Paulay T, Priestley MJN (1992) Seismic design of reinforced concrete and masonry buildings. Wiley, USA

# Dynamic Modelling of Ujjayanta Palace—A Heritage Load-Bearing Masonry Building



S. Raghunath and K. S. Jagadish

**Abstract** This paper discusses the modelling of the Ujjayanta Palace building, a highly asymmetrical load-bearing masonry structure, for the purpose of carrying out time history analysis for earthquake inputs. The analysis enabled the ductility-based design, which was a major requirement for seismic retrofitting of the heritage building. The building is situated at Agartala, the capital of the state of Tripura. The building has a number of piers which are assumed to carry the axial gravity loads and the lateral seismic forces. The asymmetry in the plan and elevation necessitated the development of a relatively simple model which includes the lateral sway modes as well as the torsional modes of vibration. Thus, the scheme included calculation of the location of the mass and stiffness centre in each floors. The in-plane and the out-of-plane stiffness of the masonry piers were included in the formulation of the stiffness matrix. The seismic mass lumped at the floor levels were obtained in accordance with the provisions of IS-1893 (2002). After setting up the coupled equations of motion, which included three degrees-of-freedom (translations in the two horizontal directions and rotation about the vertical axis passing through the mass centre) for each floor, the mass matrix and stiffness matrices were obtained. Later, the seismic forces were computed in each of the masonry piers by solving the equations of motion using a numerical integration scheme. The earthquake inputs were taken by considering the site-specific earthquake parameters. This dynamic analysis enabled the crucial computation of the deformation of the masonry piers, following which a containment reinforcement scheme was detailed.

**Keywords** Heritage building · Load-bearing masonry · Dynamic modelling  
Seismic retrofitting · Containment reinforcement

---

S. Raghunath (✉)

Department of Civil Engineering, BMS College of Engineering,  
Bangalore 560019, India  
e-mail: raghunath.smrc@gmail.com

K. S. Jagadish

Department of Civil Engineering, Indian Institute of Science,  
Bangalore 560012, India  
e-mail: ksragadish@gmail.com

© Springer Nature Singapore Pte Ltd. 2019

A. Rama Mohan Rao and K. Ramanjaneyulu (eds.), *Recent Advances in Structural Engineering, Volume 2*, Lecture Notes in Civil Engineering 12,  
[https://doi.org/10.1007/978-981-13-0365-4\\_3](https://doi.org/10.1007/978-981-13-0365-4_3)

## 1 Introduction

Ujjayanta Palace is an important heritage building situated Agartala, the capital city of the state of Tripura, India. At the time of structural assessment, the building served as the Legislative State Assembly of the state. The palace was reported to have been constructed by the then King—Maharaja Radha Kishore Manikya in 1901. The building is styled in Greek architecture and was designed and constructed by Sir. Alexander Martin of M/s Martin Burn co. After the completion of the retrofitting the building is serving as Tripura government museum.

The building is situated in seismic zone V, which has the highest level of seismicity in India. The detailed investigation by M/s BBR (India) Pvt. Ltd, revealed the vulnerability of the building which is predominantly an un-reinforced masonry structure. It was thus decided to carry out the seismic retrofitting.

As the part of the retrofitting project, the condition assessment of the building was carried out. The structure is mainly a two-storey load-bearing building with the walls being 3.3 m high in the ground floor; however the walls in the first floor are of varying heights especially in the durbar hall and ballroom. In addition, there are some components such as front tower, rear tower and the long corridors. The floor heights of these components vary from 4.8 to 6.2 m. Also, at some places, the first floor supports five dominant vertical projections viz. (a) the front tower, (b) the ballroom, (c) the extremely massive central tower with a dome, (d) the durbar hall and (e) the rear tower. The load-bearing walls are made of various sizes and shapes in the two floors. Most of the walls have a good number of openings, majority of which have an arch at the lintel level. The presence of these large openings allows for modelling the walls as a series of piers by neglecting the portion of the walls above the openings. Figures 1 and 2 show the plan view and front elevation of the building.

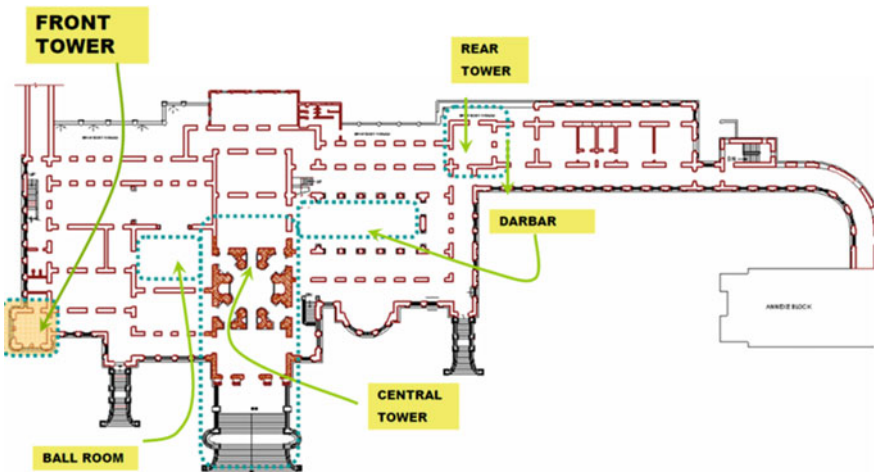


Fig. 1 Ground-floor plan view of Ujjayanta Palace

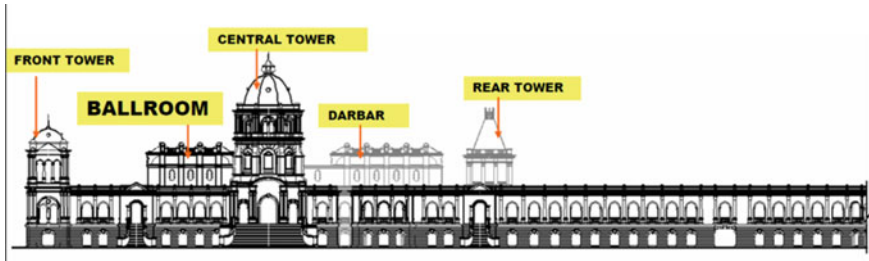


Fig. 2 Front view of Ujjayanta Palace

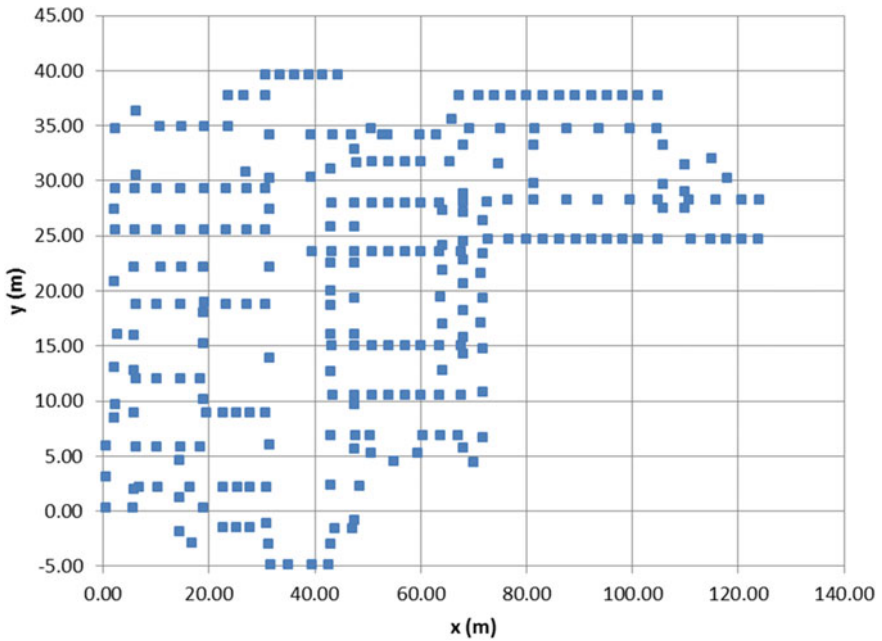


Fig. 3 Coordinates of masonry piers

In total, about 270 piers can be identified. The centroidal location of these piers is shown graphically in Fig. 3. The location and size of the piers were obtained from the measured drawings. In addition to these, there are three single-storey appendages in the front portion of the building to house the steps leading to the first floor of the building. In summary, the building can be described as a highly asymmetric structure both in plan and elevation.

## 2 Design Objectives and Strategy

The major objectives of the seismic retrofitting were to achieve the following

- (i) To permit the structure to undergo inelastic deformations without brittle mode of failure and thus prevent loss of lives.
- (ii) To limit the damage to minor repairable cracks when the structure is subjected to maximum considered earthquake (MCE).

The method of retrofitting followed should be such as not to alter or mar the architectural features of the heritage structure.

The strategy adopted to analyse, design and detail the retrofitting scheme was as follows

- (i) Assess the expected ground motion in the event of MCE, utilizing the characteristics of the local soil strata.
- (ii) Assess the strength and elastic properties of the brick masonry used in the building
- (iii) Develop a dynamic model to analyse the structure.
- (iv) Analyse the structural response of the structure for the suggested earthquake ground motion parameters, using the time history method suggested in IS 1893 (2002) [1]. Obtain the peak displacements and forces in the load-bearing components of the building.
- (v) Develop a heuristic design method for arriving meeting the ductility demand in the masonry elements. Ductile reinforcement in the form of (vertical) aluminium strips to be quantified using a simplified lateral inertial force equivalent to the peak ground acceleration.
- (vi) Heuristic design of horizontal bands and corner vertical reinforcement based on codal recommendations, but using advanced polymer composites (APC) —Epoxy-glass fibre reinforced composite.

The following section discusses the development of the dynamic model.

### 2.1 Development of the Dynamic Model

#### Assumptions

1. It is assumed that the seismic forces shall be taken up by the masonry piers. The floor and roof slab being relatively are considered rigid in its plane and the seismic forces are transmitted to the piers in diaphragm action.
2. The seismic force developed in each masonry pier is proportional to the relative lateral stiffness of the piers. The in-plane shear and bending deformations are considered in computing the stiffness.

The in-plane shear stiffness is taken as  $k_s = btG/h$ , where  $b$  is the length of the pier,  $t$  is the thickness of the pier,  $h$  is the height of the pier and  $G$  is the modulus of rigidity of masonry ( $\sim 0.4E$ ).



The in-plane bending stiffness is taken as  $k_b = \frac{12EI}{h^3}$ , where  $I$  is the moment of inertia,  $E$  is the modulus of elasticity of masonry.

The total in-plane deformation is considered as a linear combination of in-plane shear deformation and in-plane bending deformation. Thus, the in-plane stiffness along an axis works out to  $k = \frac{k_s k_b}{k_s + k_b}$  [2].

3. The masonry wall portions between the openings are assumed to contribute to the mass and not to the stiffness.
4. For the purpose of analysis only two floors are considered (average height of ground floor and first floor is 3.3 and 5.5 m, respectively), although the towers are much taller. However, the appropriate portion of mass of the towers (front, central and the rear towers) is assumed at the roof of the upper floor. It may be noted that the superstructure of the central tower begins at the first-floor level and is inaccessible underneath it. The stiffness of the huge pillars of this tower at the upper floor is also considered.
5. The seismic mass lumped at the floor level is obtained by considering (a) floor/roof slab mass, (b) mass contribution from the live load (as per IS 1893-2002), (c) the mass of the masonry spandrels between the openings (above the opening level) (d) based on the consistent mass approach, 30% of the wall mass is also lumped at the floor level (e) the mass of the parapets and all corbel projections at the roof level
6. Based on the laboratory investigations, the modulus of elasticity of brick masonry in lime-surkhi mortar is taken as 2000.0 MPa. Mass density of masonry is assumed as 1800.0 kg/m<sup>3</sup>, while that of floor slabs as 2400.0 kg/m<sup>3</sup>.
7. Each of the two floors is assumed to possess 3 degrees-of-freedom (d.o.f), viz. translation displacements in the  $x$ - and  $y$ -direction and rotational displacement  $\theta$ , about a vertical axis passing through the mass centre. Hence the total number of d.o.f is 6.
8. The vertical projections (towers, parapets etc.) are designed and checked for stability for five times the design horizontal seismic coefficient, as per the provisions of IS 1893 (2002).

### Step 1 *Setting up the equations of equilibrium*

The following notations are used:

$i$	Masonry pier no. (totally 270 piers are identified)
$x_1, x_2$	Translation of ground floor and first floor lumped mass in $x$ -direction
$y_1, y_2$	Translation of ground floor and first floor lumped mass in $y$ -direction
$\theta_1, \theta_2$	Rotation of the ground floor and first floor lumped mass about the vertical axis passing through the mass centre
$r_{ix}, r_{iy}$	$x$ and $y$ coordinate of the $i$ th masonry pier from the corresponding mass centre
$M_1, M_2$	Lumped mass at the ground-floor and first-floor roof level
$k_{x1i}, k_{x2i}$	Stiffness of the $i$ th ground-floor pier and first-floor pier in the $x$ -direction
$k_{y1i}, k_{y2i}$	Stiffness of the $i$ th ground-floor pier and first-floor pier in the $y$ -direction

$I_{m1}, I_{m2}$  Mass moment of inertia of the ground-floor mass and first-floor mass about the its mass centre

The displacement of a pier can be considered as a combination of sway and rotation about the vertical axis. The net displacement can hence be considered to be a linear summation of the two. This is shown schematically in Fig. 4a, b. Here, counterclockwise rotation is taken as +ve rotation. Of course, the location of the piers from the centre of mass requires that the mass centre has to be computed prior.

$$\begin{aligned}
 M_1 \ddot{x}_1 + \sum k_{x1i}(x_1 - r_{iy}\theta_1) - \sum k_{x2i}(x_2 - r_{iy}\theta_2) &= 0 \\
 M_1 \ddot{y}_1 + \sum k_{y1i}(y_1 + r_{ix}\theta_1) - \sum k_{y2i}(y_2 + r_{ix}\theta_2) &= 0 \\
 I_{M1} \ddot{\theta}_1 + \sum k_{y1i}(y_1 + r_{ix}\theta_1)r_{ix} - \sum k_{x1i}(x_1 - r_{iy}\theta_1)r_{iy} - \sum k_{y2i}(y_2 + r_{ix}\theta_2)r_{ix} \\
 + \sum k_{x2i}(x_2 + r_{iy}\theta_2)r_{iy} &= 0 \\
 M_2 \ddot{x}_2 + \sum k_{x2i}(x_2 - r_{iy}\theta_2) &= 0 \\
 M_2 \ddot{y}_2 + \sum k_{y2i}(y_2 + r_{ix}\theta_2) &= 0 \\
 I_{M2} \ddot{\theta}_2 + \sum k_{y2i}(y_2 + r_{ix}\theta_2)r_{ix} - \sum k_{x2i}(x_2 + r_{iy}\theta_2)r_{iy} &= 0
 \end{aligned} \tag{1}$$

Step-2 Obtaining natural frequencies and mode shapes

These above six equations are used to obtain the natural frequencies and mode shapes. These are computed by obtaining the Eigen value and Eigen vectors. The Eigen vectors are represented in the matrix form as  $[\phi]$

Step-3 *Determination of modal mass and modal stiffness*

The modal mass and modal stiffness matrices are obtained as follows;

$$\bar{M} = \phi^T M \phi \tag{2}$$

$$\bar{K} = \phi^T K \phi \tag{3}$$

Step-4 *Time history analysis*

After uncoupling the equations of equilibrium, for each modal mass and stiffness a time history analysis has been carried out by the well-known Newmark scheme [3]. A time step interval of 0.01 s has been chosen. Analysis has been carried out by choosing damping value of 5%. Three earthquake records considered are from the site-specific ground acceleration time history data based on the geotechnical data. A typical ground motion data (acceleration time history data) is shown in Fig. 5.

Step-5 *Obtaining forces in masonry piers*

The above three cases were studied separately. It may be mentioned that this data was chosen as an input for ground acceleration both in the  $x$ -direction and  $y$ -direction. The peak response quantities were combined

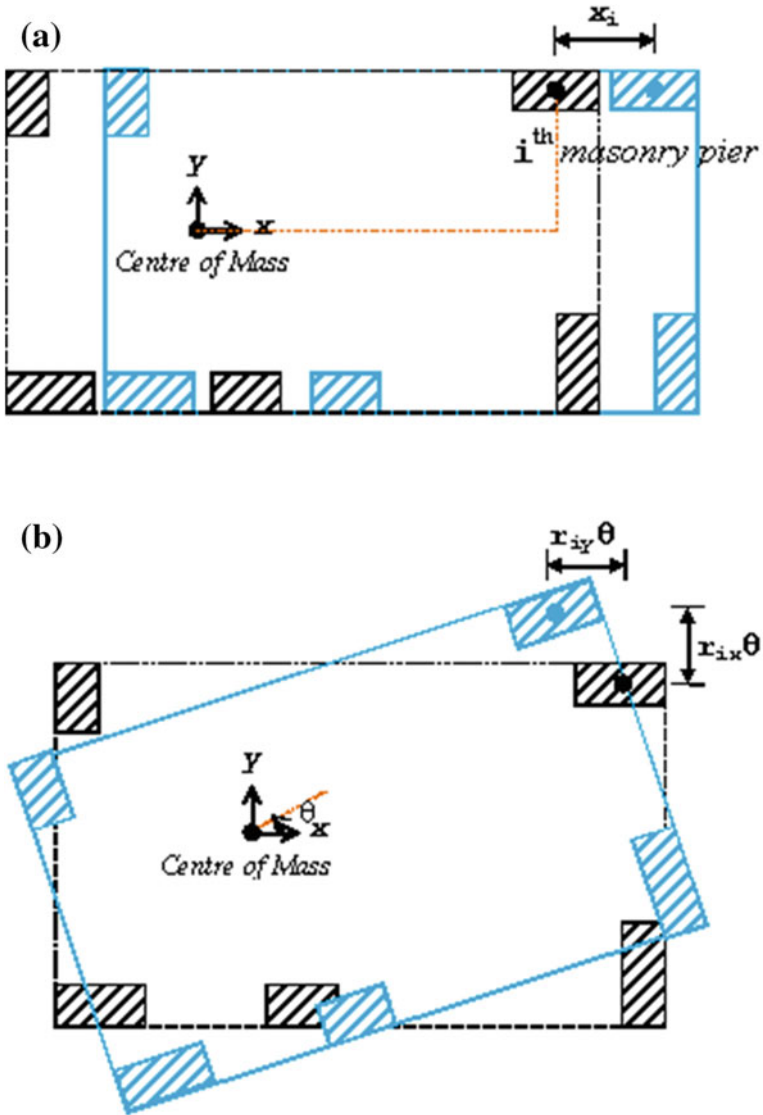


Fig. 4 a Schematic representation of sway mode, b Schematic representation of torsion mode

using modal combination technique as per IS 1893-2002 [1]. The load cases considered are in accordance with cl. 6.3.2 (IS 1893-2002) [1]. The shear force in each masonry piers was obtained by the relative stiffness coefficient, i.e. in proportion to their stiffness.

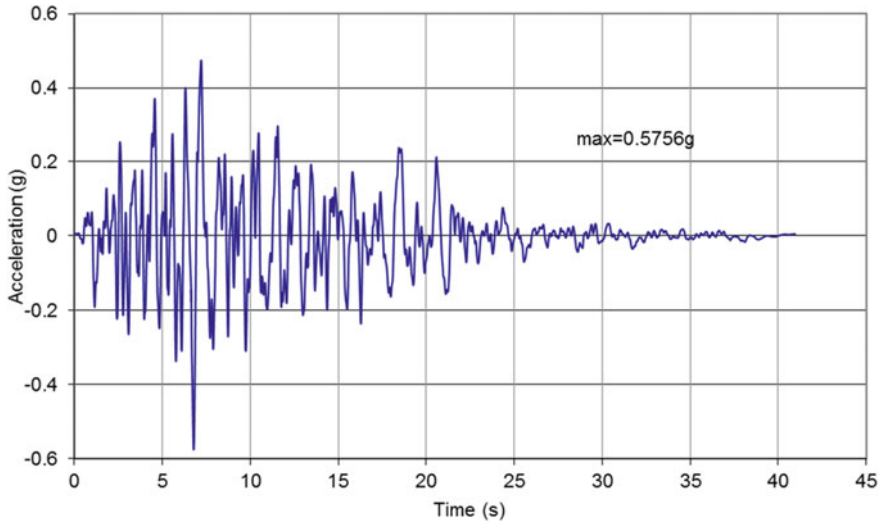


Fig. 5 Acceleration time history response at the surface

### 3 Heuristic Design of Masonry Elements to Resist Lateral Earthquake Loads

Masonry buildings can undergo different types of failures during earthquakes [4]. Some of the typical failures may be classified are: (i) out-of-plane flexural failure, (ii) In-plane shear failure (iii) In-plane flexural rocking of narrow masonry piers between openings, (iv) Shear failure at corners (separation of walls at vertical junctions), (v) Separation of floor/roof and walls, (vi) Buckling of wythes and (vii) Local failures. The mitigation of these damages can be achieved by strategic introduction of reinforcement, for a given geometrical layout of the building. The maximum stress levels reached in each of the masonry pier can be used to compare with the corresponding strengths and this can lead to a design basis. Amongst these, the design to withstand out-of-plane flexural failure has been described in brief.

### 4 Design of Vertical Containment Reinforcement for a Typical Masonry Pier

The design of masonry for ductility requirements was carried out as outlined by Raghunath et al. [5]. This is in the form of containment reinforcement [2, 5]. This is similar to that of a single reinforced concrete beam, the difference being in the stress block. The stress–strain curve of masonry obtained from experiments is considered.

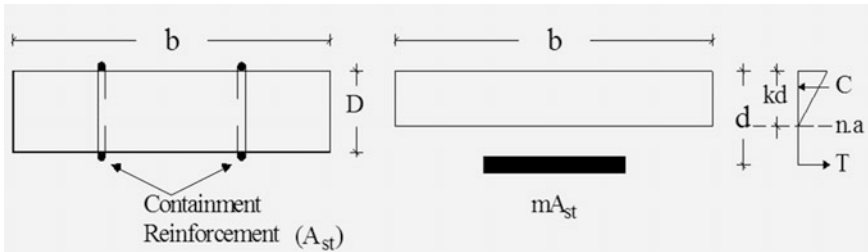


Fig. 6 Linear elastic stress distribution across the thickness of the pier

The design of the walls for out-of-plane flexure is based on the premise that during an earthquake the lateral forces in a masonry building shall be shared by the shear walls, since the cross walls possess relatively very low lateral stiffness. As a result, the cross walls can be expected to experience only out-of-plane inertial forces due to their self-weight. By considering a masonry pier of thickness ‘*d*’ and width ‘*b*’ as shown in Fig. 6, the depth of the neutral axis can be obtained by equating the moment of compression area to the moment of the transformed area.

Thus, using the usual notations and same assumptions as that made for linear elastic analysis of singly reinforced RC beam, we get the following equation;

$$1/2b(kd)^2 + mA_{st}(d - kd) = 0 \tag{4}$$

The tensile strain in steel ( $\epsilon_s$ ) and the compressive strain in extreme fibre of masonry ( $\epsilon_m$ ) can be related by referring to Fig. 5, as

$$\frac{\epsilon_s}{\epsilon_m} = \frac{1 - k}{k} \tag{5}$$

If the yield strain of the reinforcing material is  $\epsilon_{sy}$ , then the compressive strain in extreme fibre of masonry when the reinforcement yields is:

$$\frac{\epsilon_{sy}k}{1 - k} = \epsilon_m \tag{6}$$

If the limiting compressive strain in masonry is  $\epsilon_m$ , then the ductility of masonry in flexure is:

$$\frac{\epsilon_{m(max)}}{\epsilon_m} \tag{7}$$

The moment of resistance of the cross section at yield of steel, assuming a linear stress distribution in compression is:

$$E_s \varepsilon_{sy} A_{st} d (1 - k/3) \quad (8)$$

One can carry out a simple non-linear analysis if the stress distribution is non-linear. As an example;

Consider a masonry pier of width of 1300.0 mm ( $b$ ) and depth/thickness ( $d$ ) of 800 mm and a length of  $l$ .

Assuming a modulus of elasticity aluminium  $E_{Al} = 70,000.0$  MPa and modulus of elasticity of masonry  $E_m = 2000.0$  MPa

Cross sectional area of aluminium  $A_{Al} = 2\text{strips} \times 50 \text{ mm} \times 2 \text{ mm}$

Tensile strain in aluminium =  $\varepsilon_{Al}$

Tensile strain in masonry =  $\varepsilon_m$

Modular ratio =  $m$

The neutral axis depth is now obtained assuming linear variation of stress in masonry by the following equation;

$$\frac{1}{2} b (kd)^2 + mA_{Al} kd - mA_{AL} d = 0 \quad (9)$$

Solving for  $k$ , we get  $k = 0.11$ .

Assuming a linear strain variation in masonry,

$$\frac{\varepsilon_m}{\varepsilon_{Al}} = \frac{0.11}{0.89} = \frac{1}{8} \quad (10)$$

Assuming an inertial horizontal load due to an acceleration of  $0.57g$ , the maximum bending moment = 14,525.0 Nm (for  $l = 3.3$  m) and 40,346.0 Nm (for  $l = 5.5$  m).

Now stress in Aluminium reinforcement is given by obtaining the lever arm (771.0 mm) and hence the total tension in Aluminium = 14,525.0/0.771 = 18,839.0 N (for the case of  $l = 3.3$  m) and similarly it is 52,329.0 N for the case of  $l = 5.5$  m.

The corresponding stress in Aluminium is thus obtained (= 94.2 MPa for  $l = 3.3$  m and 262.0 MPa for  $l = 5.5$  m). Since the yield strength of aluminium is about 100.0 MPa, it will remain in elastic range for  $l = 3.3$  m and will go into elasto-plastic range for  $l = 5.5$  m. The strain in aluminium at yield = 0.014 and the corresponding strain in masonry will be  $0.0014/8 = 0.00,018$ . Various measurements have shown that the peak compressive strain (limiting strain) in masonry to be 0.006–0.008.

Thus the masonry with such reinforcement will maintain ductile behaviour till the peak strain in masonry reaches 0.006. The ductile capacity of the masonry with containment reinforcement is hence =  $0.006/0.00018 = 33.3$ .

The aim of the design here is to maintain the ductile capacity at as high a level as possible. Similar calculations are made for all the piers of the palace structure.

Containment reinforcement is an external reinforcement and the strain compatibility needs to be established by ensuring that the reinforcement is hugging the

masonry element by the provision of special shear connector keys which are anchored into the masonry by anchor plugs and screws.

It was noticed that the minimum ductility capacity is about 19.3, which is generally considered as adequate. Similar analysis was performed by choosing (a) Glass fibre reinforced plastic (GFRP) strips and (b) stainless steel flats as a material for vertical containment reinforcement. The choice of the material was then based on the cost considerations and ease with which the containment reinforcement can be introduced.

Aluminium flats being provided as vertical containment reinforcement is shown in Fig. 7. The typical seismic retrofitting scheme for masonry piers is shown in Fig. 8. Vertical reinforcement and horizontal GFRP wrap for ornate column heads are shown in Fig. 9.

**Fig. 7** Aluminium flats used for vertical containment reinforcement. Source <http://english.cctv.com>



**Fig. 8** Typical seismic retrofitting scheme for masonry piers

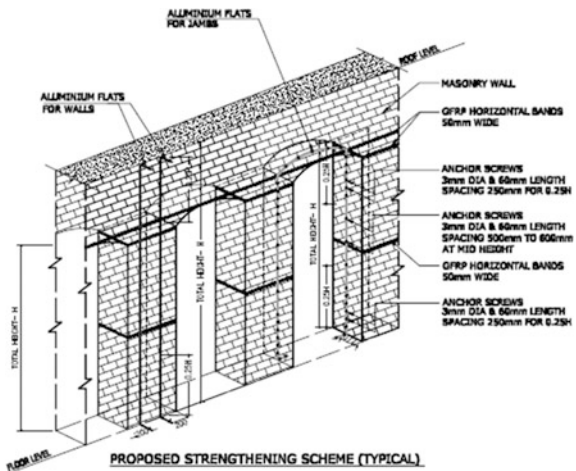


**Fig. 9** Vertical reinforcement and horizontal GFRP wraps for masonry pier heads. Source <http://english.cctv.com>



## 5 Concluding Remarks

Ujjayanta Palace at Agartala is a heritage building situated in seismic Zone V and hence the need for seismic retrofitting. The equations of motion for the highly un-symmetric 2-storeyed building have been set-up by considering the coupled effects of lateral sway and torsion of the masonry piers. After obtaining the natural frequencies and mode shapes, the time history analysis was performed to obtain the maximum forces in each of the masonry piers by considering a series of site-specific ground motion records. This output of the analysis was used to carry out the ductility-based design and detailing using the concept of containment reinforcement with aluminium flats and/or surface wrapping using GFRP strips. This type of ductile detailing helped in ensuring the retaining the architectural embellishments of the heritage building. The seismic retrofitting was completed in 2013.

**Acknowledgements** The authors thank Sri. M. N. Ramesh, formerly Principal Coordinator of the retrofitting project, representing M/s BBR (India) Pvt. Ltd., for giving the opportunity to assist them in the analysis and design. The ground motion data based on the geotechnical data provided was generated by Dr. K. V. Vijayendra, Department of Civil Engineering, Bangalore Institute of Technology, Bangalore. His crucial inputs are gratefully acknowledged.

## References

1. IS 1893 (Part 1) (2002) Indian Standard criteria for earthquake resistant design of structures, Part 1: General provisions and buildings. BIS, New Delhi
2. Raghunath S (2003) Static and dynamic behaviour of brick masonry with containment reinforcement. Ph.D. thesis, Department of Civil Engineering, IISc, Bangalore
3. Chopra AK (2001) Dynamics of structures—theory and applications to earthquake engineering, 2nd edn. Pearson Education Asia Publishing, India



4. Jagadish KS, Raghunath S, Nanjunda Rao KS (2003) Behaviour of masonry structures during Bhuj earthquake of January 2001. *J Indian Acad Sci Earth Planet Sci* 112(30):431–440
5. Raghunath S, Nanjunda Rao KS, Jagadish KS (2012) Ductility of brick masonry beams with containment reinforcement. *J Struct Eng* 39(4, 39–43):399–408

# Hybrid Testing of Concrete Bridge Piers with Different Detailing at Column–Foundation Interface



Needhi Kotoky, Anjan Dutta and Sajal K. Deb

**Abstract** In failures of bridges, damages in piers are mostly localized in the vicinity of pier–foundation interface region. It is preferred to shift the damage from the interface zone to make rehabilitation relatively easier. One possible approach is to incorporate some additional features at interface to shift the likely damage zone. The paper is an experimental investigation to evaluate the role of additional detailing introduced at the interface. Two strategies were tried through incorporation of dowel bar at the interface region and use of corrugated sheet pipe in the foundation below the pier–foundation interface. The performances of these two specimens were compared with a pier having conventional detailing. An advanced seismic testing technique, known as hybrid simulation, was used for the present study to test the performance of the specimens when subjected to earthquake excitation. The specimen with dowel bar was found to be better for all the parameters concerning seismic performance.

**Keywords** Bridge pier · Pier–foundation interface detailing · Earthquake load  
Hybrid simulation · Damage location

## 1 Introduction

A bridge structure should function adequately during and after an earthquake as any failure will seriously hamper the relief and rehabilitation activity in the neighbourhood. Deficiencies in the behaviour of bridges were observed during many

---

N. Kotoky · A. Dutta · S. K. Deb (✉)

Department of Civil Engineering, Indian Institute of Technology Guwahati,  
781039 Guwahati, India

e-mail: skdeb@iitg.ernet.in

N. Kotoky

e-mail: needhi.iitg@gmail.com

A. Dutta

e-mail: adutta@iitg.ernet.in

© Springer Nature Singapore Pte Ltd. 2019

A. Rama Mohan Rao and K. Ramanjaneyulu (eds.), *Recent Advances in Structural*

*Engineering, Volume 2*, Lecture Notes in Civil Engineering 12,

[https://doi.org/10.1007/978-981-13-0365-4\\_4](https://doi.org/10.1007/978-981-13-0365-4_4)

earthquakes all over the world. In these failures of bridges, the reinforced concrete piers were mostly observed to be considerably damaged, which implies that the detailed understanding of nonlinear behaviour of these structural elements during intense earthquakes is an important issue.

It is known that damage in a bridge pier is mostly localized around the plastic hinge and the plastic hinge region is mostly concentrated in the column–foundation interface region. Post-earthquake rehabilitation work becomes difficult if the damage extends deep into the foundation. Thus, it is preferred to shift the damage from the interface zone to make rehabilitation relatively easier. One possible approach is to incorporate some additional features at column–foundation interface to shift the likely damage zone. Aviram et al. [1] used dowel reinforcement at the column–foundation interface to force most of the inelastic deformation to occur within the column. Greizic et al. [2] provided the connection between the column and the footing with dowel bars which matched the column vertical reinforcement in order to shift the location of plastic hinging. Dowel bars were extended a distance of 1.7 times the effective width of the column into the column section resulting in a lap splice length of 42 times of the diameter of the reinforcement. The dowel bars were anchored into the thick footing with 90° standard hooks. Another possible way to shift the damage zone is by embedding a corrugated sheet pipe in the foundation. Corrugated sheet pipe is a tube with a series of parallel ridges and grooves on its surface. The diameter of the sheet pipe may be similar to pier. The use of such corrugated sheet pipe enhances the confinement effect on pier. Ghobarah et al. [3] used corrugated steel to upgrade beam–column joints as it provides both lateral confinement and shear reinforcement. The corrugated jacket adds shear strength and ductility to the connection. Kumar et al. [4] incorporated corrugated steel duct to prevent crack localization at the cold joint at the column base–foundation interface. Two strategies were tried in the presented work through incorporation of dowel bar in the plastic hinge region and use of corrugated sheet pipe in the foundation below the pier foundation interface.

The present work was executed by a new seismic testing technique called hybrid simulation which attracted attention of the researchers in the recent past. Hybrid simulation reduces modelling uncertainties by replacing numerical modelling of highly nonlinear element by physical test of the element. The hybrid simulation methodology is known to be a reliable cost-effective way for evaluating performance assessment of structures [5]. Hybrid simulation technique is executed by physically testing critical elements of a structure (such as bridge piers) while the remaining elements are concurrently simulated numerically using a step-by-step integration of the governing equations of motion for a model formulated considering both the numerical and physical components [6]. The first official publication on hybrid simulation appeared in 1975 when Takanashi [7] proposed “online test” method as an alternative experimental technique to shaking table tests. It is easier to observe specimen behaviour to previously recorded earthquake and measure specimen deflection in hybrid simulation as compared to test on shake table. Further, conventional quasi-static testing, which is a widely used structural testing method, does not account for the ductility demand imposed on earthquake ground

motion on a structural specimen. It also suffers from the difficulty of interpreting the results with respect to the structure it represents. Such problems can be resolved with the hybrid simulation method, in which the displacements applied to a structure are determined from the solution of equation of motion of the structural system.

Real-time hybrid simulation was not carried out in order to inspect the specimen during the course of testing and thus having better insight into the growth of damage throughout the test. As such, pseudo-dynamic testing was performed to evaluate the performance of the specimens. Three scaled bridge piers were constructed in the laboratory. Two bridge piers were provided with additional detailing at the pier–foundation interface. This was done to achieve some modifications of crack distribution from the pier–foundation interface zone. The performances of these piers under seismic loadings are assessed based on the data obtained from the hybrid tests. Further, cyclic tests were also performed after the completion of hybrid tests to compare their ultimate capacities.

## 2 Research Significance

Post-earthquake rehabilitation works of bridge piers become easier if the damage is distributed and shifts away from the pier–foundation interface zone. This is likely to be achieved by some additional features at column–foundation interface. In this paper, detailed strain measurements in reinforcing bars were made to appreciate the seismic performance of different test specimens. The proposed strategies for detailing near the likely damaged zone may provide effective means for crack relocalization and ease of rehabilitation. Advanced hybrid simulation technique can integrate efficiently the seismic behaviour of entire bridge including structural elements with behavioural uncertainties

## 3 Test Program

The test specimens consist of three 1:5 scaled models of pier of a prototype bridge in Tripura, India. These specimens were cast in the Structural Engineering laboratory of Civil Engineering Department of IIT Guwahati. Details of the scaled-down test models and their reinforcement details are shown in Table 1 and Fig. 1. These three test specimens were identical in terms of their geometry and longitudinal reinforcement details. However, they had difference in the details of column–foundation interface portion, which was done targeting a shift in the major damage location away from the pier foundation interface. While specimen Type 1 had conventional reinforcement detailing, dowel bars of length 390 mm (1.1 times the plastic hinge length) were introduced in specimen Type 2. The numbers of dowel bars were equal to the main longitudinal reinforcement and these bars were

**Table 1** Details of scaled-down test models

Item	Prototype	Model	Remarks
Longitudinal steel ratio	1.12%	1.12%	Conserved during scaling
Longitudinal steel reinforcement	36 mm Ø— 38 nos	16 mm Ø— 8 nos	Conserved during scaling
Transverse reinforcement dia	8 mm	8 mm	—
Spacing of transverse reinforcement	300 mm	60 mm	1/5 scale
Pier dia	2100 mm	420 mm	1/5 scale
Pier height	9000 mm	1800 mm	1/5 scale
Cover	40 mm	20 mm	1/2 scale

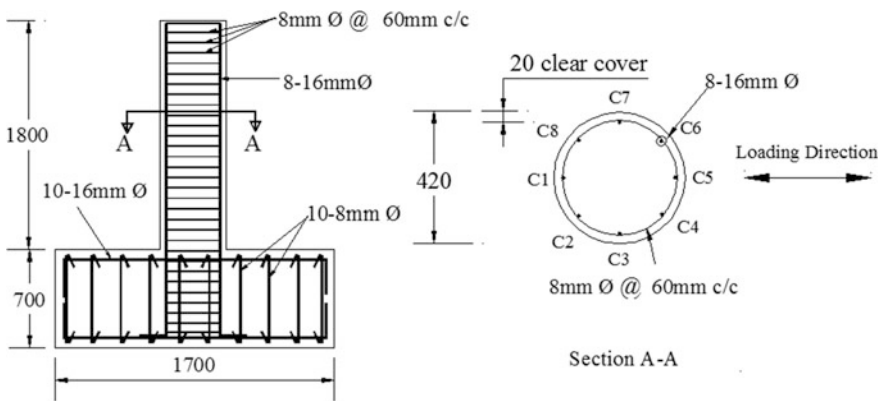




**Fig. 1** Reinforcement detailing of the specimen

distributed equally in the region above and below the pier foundation interface. The third type of detailing at the interface was through the use of corrugated sheet. Specimen Type 3 used corrugated sheet pipe embedded into the foundation with diameter about 10% more than that of the bridge pier. The differences among these specimens are shown in Table 2. The specimens were cast with designed mix having target cube compressive strength of 30 MPa. The specimens were cast in stages. The foundations of piers were cast prior to the casting of the main piers.

### 3.1 Instrumentation

A total of eighteen electrical strain gauges were fixed on longitudinal reinforcement in each of the test specimens at predefined location. The pier was instrumented internally with five strain gauges on each of the longitudinal bars C1 and C5, while

**Table 2** Details of special features

Specimen and their Additional features
Type 1 Conventional reinforcement details as shown in Fig. 1
Type 2 16 mm Ø additional longitudinal bars were used over 175 mm above and below the pier–foundation interface

Type 3 A corrugated sheet pipe over the depth of foundation


four strain gauges were fixed on each of C2 and C6. Figure 2 shows location of strain gauges on the longitudinal reinforcement. All these strain gauges helped to visualize the difference in growth of strain in three types of specimens and compare their performances. The lateral displacements were recorded using three LVDT located at 80, 160 and 320 mm, respectively, from the pier foundation interface and is shown in Fig. 3.

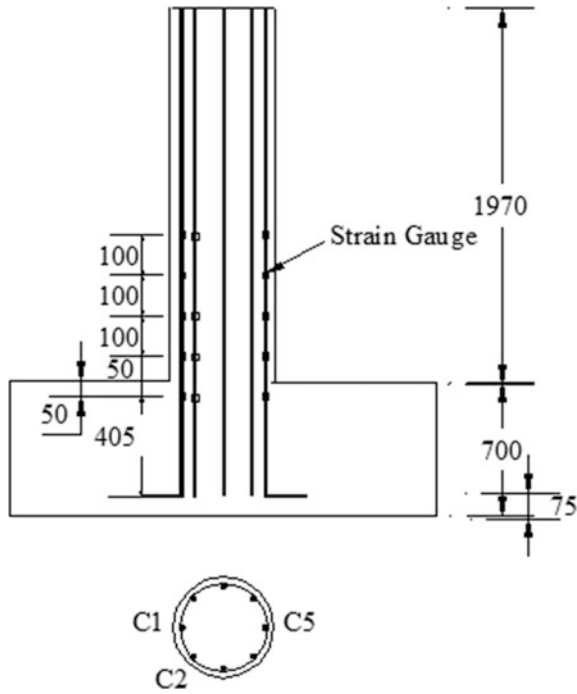


Fig. 2 Location of strain gauges on the longitudinal reinforcement

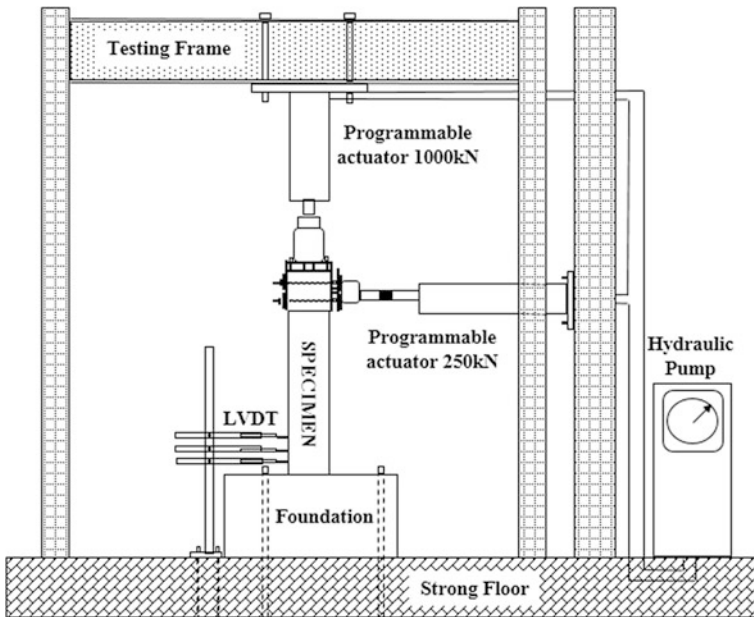


Fig. 3 Schematic representation of laboratory set-up

### ***3.2 Loading Arrangement***

The self-weight of the bridge deck was calculated from the detailed drawing of the prototype bridge deck and its  $1/25^{\text{th}}$  ( $1/S^2$ ,  $S$  is the scale factor) value was applied through a loading arrangement using 1000 kN capacity servo-hydraulic actuator (make: MTS Inc., USA) having stroke length of  $\pm 250$  mm. The actuator was supported by the test frame as shown in Fig. 3. The lateral displacement was imposed on the specimen by 250 kN dynamic actuator with stroke length of  $\pm 250$  mm and this actuator was supported against the strong wall of the laboratory. The arrangement at the pier head ensured free lateral movement of the specimen, while verticality of the applied dead load was maintained throughout the tests. The specimen was fixed to the strong floor by means of four numbers of high-tension bolt.

### ***3.3 Hybrid Test Procedure***

Hybrid simulation of structural system consists of numerical simulation module and experimental module along with an interface for effective communication between these two modules as shown in Fig. 4. Critical elements of a structural system, which are likely to experience nonlinear behaviour and thereby may lead to increased uncertainty in modelling (e.g. bridge piers) are physically tested while the remaining elements are simultaneously simulated numerically. Few experimental studies of RC bridge system by hybrid simulation are available in literature [8, 9]. 3D numerical model of the bridge was created using the analysis platform OpenSees developed by McKenna [10]. Full-scale numerical model of non-critical components are created in the numerical module. The experimental module consists of physical dynamic testing of scaled model of the critical element(s), i.e. bridge pier in this study. Hybrid simulation technique utilizes OpenFresco interface platform [6] to communicate between these two modules. MTS FlexTest GT controller was used for hybrid testing through integration of numerical simulation module and physical testing module.

### ***3.4 Selection of Earthquake Time History***

A past earthquake ground motion which is commonly used for seismic assessment study was selected and matched to response spectra for maximum credible earthquake (MCE) of Zone V in India as per IS 1893 Part I (2002). The north-south component of the El Centro ground acceleration history recorded during the 1940 Imperial Valley earthquake was used to dynamically excite the model. This record was scaled to four different MCE levels. These four levels were selected to study



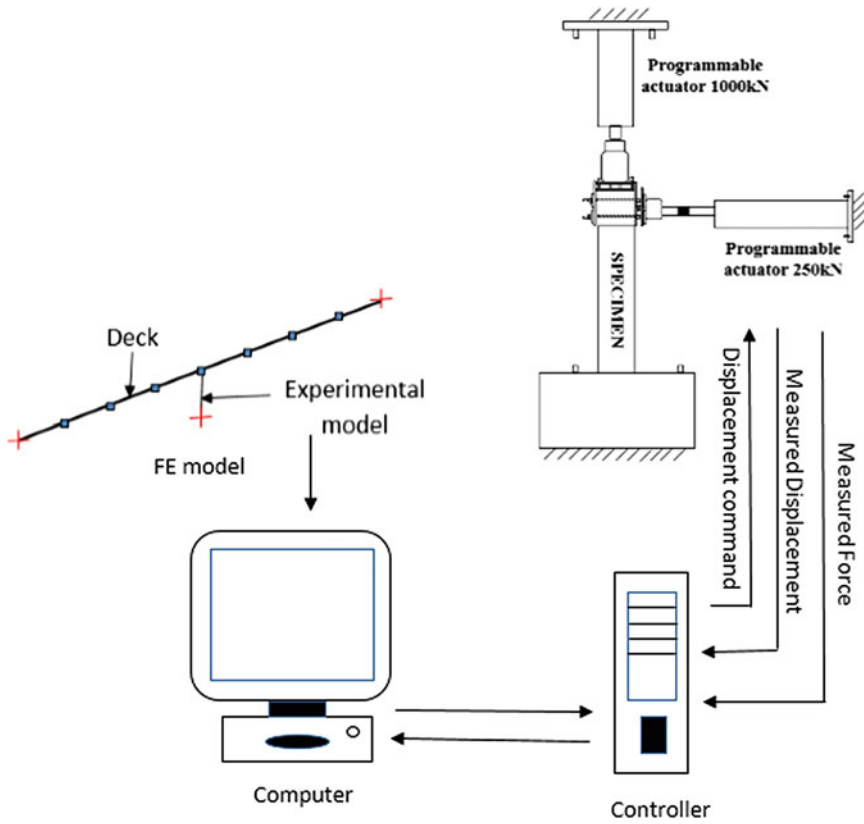
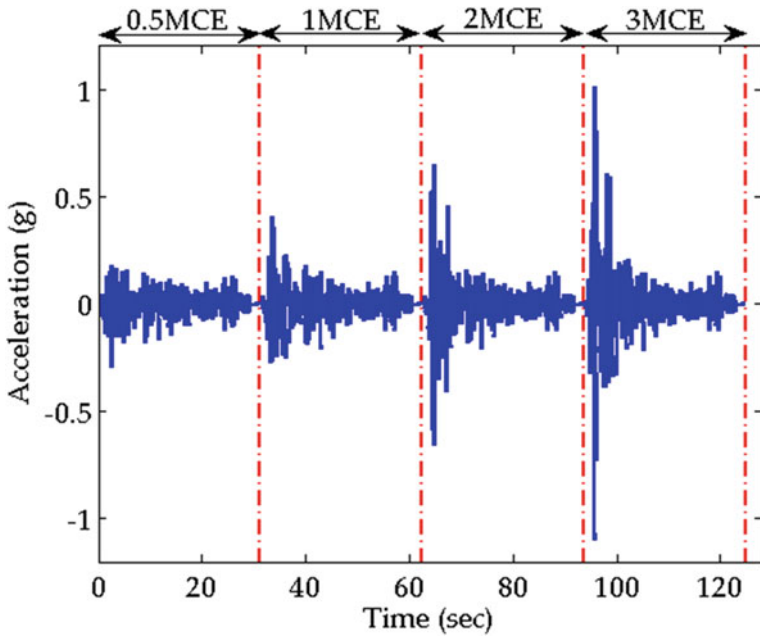


Fig. 4 Key components of hybrid simulation

structural behaviour in the entire spectrum of damage levels commencing from minor cracking to major damage. Thus, the sample earthquake records in the hybrid test consisted of the four scaled 32 s segments applied in sequence as shown in Fig. 5. The response spectra of the scaled records matched the respective target spectrum for Zone V as per IS 1893 Part I (2002).

## 4 Results

The damage states of specimen Type 1–3 at various displacement levels are shown in Fig. 6a, b. At the end of test under 0.5MCE, hairline cracks were seen near the base of the column for specimen Type 1. However, a clear shift in the initial crack location from column–foundation interface could be seen for Type 2 and 3 specimens. The hairline crack subsequently coalesced at the end of 1MCE test and became more visible for all the specimens.



**Fig. 5** Scaled simulation of El Centro (1940) acceleration time histories with four different intensity levels

**Fig. 6** Damage state of the specimens

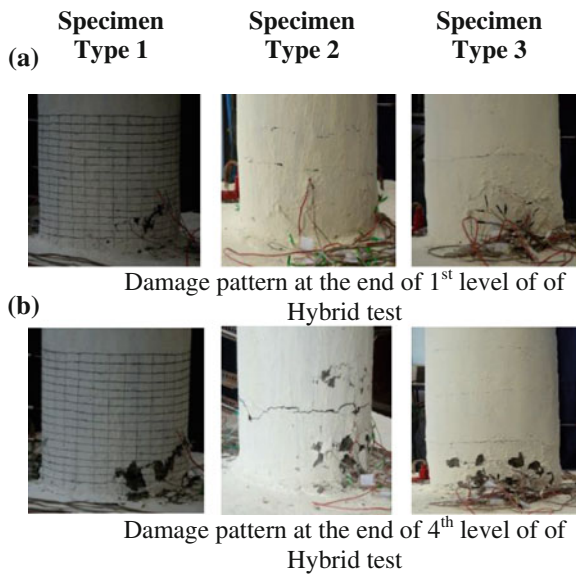
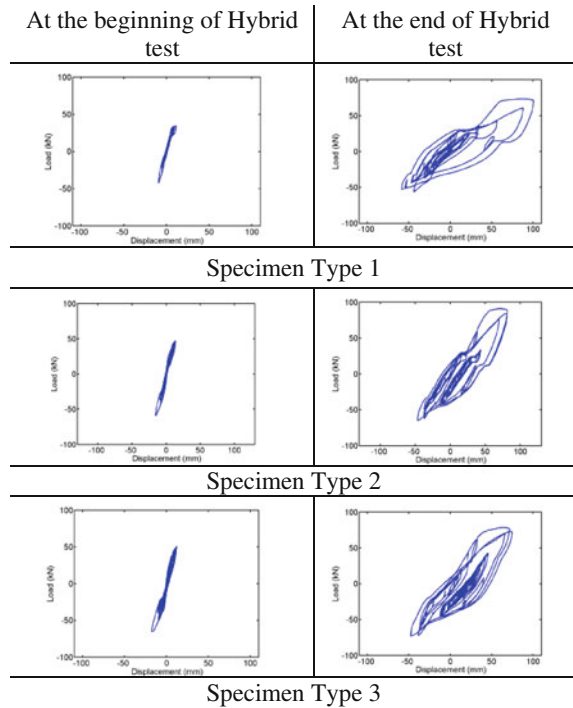


**Fig. 7** Lateral force versus lateral displacement of different specimens

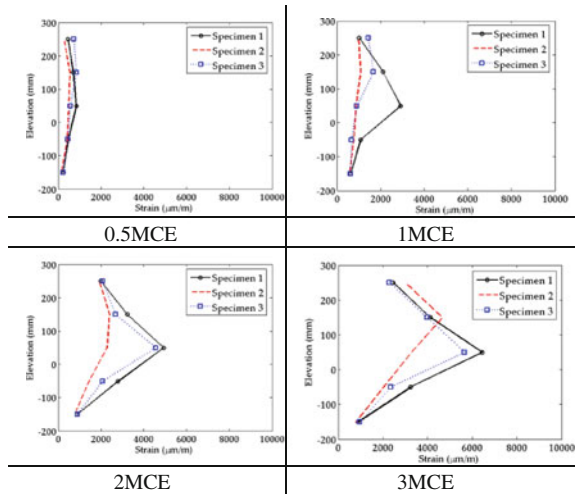


Multiple cracks were also observed distributed over the column–foundation interface region. The position of first crack for specimen Type 2 was at the location where dowels were terminated. Interestingly, specimen Type 3 also had first crack almost at similar location. However, on further increase in the intensity of excitation, the crack location in specimen Type 3 shifted towards column–foundation interface region. Concrete spalling occurred in the zone of initial crack in Type 1 and 2, while in Type 3 spalling occurred near the pier–foundation interface during the test under 2MCE intensity level. At the end of 3MCE intensity level test, the concrete spalling was more prominent. Amongst all the specimen types, Type 2 performed relatively better with lesser damage than rest of the specimens.

At early loading stage, all the types of specimen performed in a similar fashion. The measured lateral force versus lateral displacement responses of Type 1, 2 and 3 are presented in Fig. 7 for excitation with intensity level as 0.5MCE and 3MCE, respectively. The size and shape of hysteresis loops are observed to vary as the intensity of excitation level increases. Areas of these loops are indicative of energy dissipation capability of the model pier. Specimen Type 2 showed higher load carrying capacity than other specimen types. This establishes that dowels provide additional resistance to the imposed displacement.

Strain profile along the height of the pier for longitudinal reinforcement, C1 is plotted in Fig. 8. It was observed that specimen Type 2 had lower growth of strain in all the stages of loading. In Type 1 specimen, the strain gauge at position 50 mm

**Fig. 8** Strain profile of longitudinal reinforcement C1 at **a** 0.5MCE **b** 1MCE **c** 2MCE **d** 3MCE levels of excitation



from pier–foundation interface was observed to show highest strain in comparison to the other four strain gauges in the longitudinal reinforcement. Thus, due to strain compatibility, concrete in that zone also must be having maximum strain developed leading to the formation of damaged zone, which was also evident from Fig. 6.

However, in the rest of the two specimens, the strain gauge at position 150 mm from the pier–foundation interface showed maximum strain during 0.5 and 1MCE intensity levels of excitation. It can be seen from the crack pattern in Fig. 6 that the crack location was at 150 mm from pier–foundation interface during the same stages of loading. However, during 2 and 3MCE intensity level, the crack location in Type 3 specimen got shifted near the pier–foundation interface. This strain pattern for Type 3 also showed maximum value at the interface zone. Further, Type 3 showed lower strain for all intensity levels in comparison to Type 1 specimen.

In order to determine the ultimate capacity, cyclic loading tests were carried out after the completion of hybrid testing. This test program was performed as quasi-static test with a cyclic loading frequency of 0.025 Hz. The first three cycles of applied displacement amplitudes were  $\pm 10$  mm and thereafter displacement amplitude increment of 10 mm was implemented till the end of the test. The tests were stopped, when the reinforcement got snapped off and/or the degraded load carrying capacities of specimens were in the range of 70–80% of the peak load. Further, the damage pattern in the pier–foundation interface zone was monitored (Fig. 9) and the test was stopped when the damage in that zone was serious enough from the viewpoint of overall safety of the set-up. Energy dissipation for each amplitude level was computed as the average area enclosed under the hysteresis loops and the cumulative energy dissipation at a particular displacement level is calculated by summing the individual areas of preceding displacement level with current displacement level. Specimen Type 2 performed better compared to other two specimens as can be seen from Figs. 9 and 10.

**Fig. 9** Damage pattern at the end of cyclic test

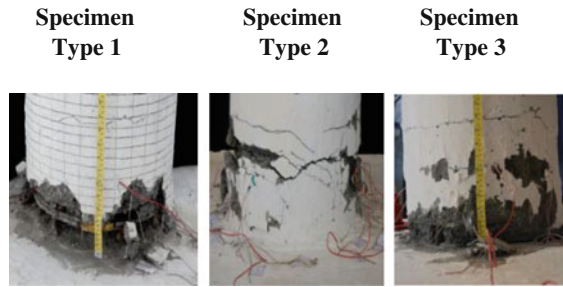
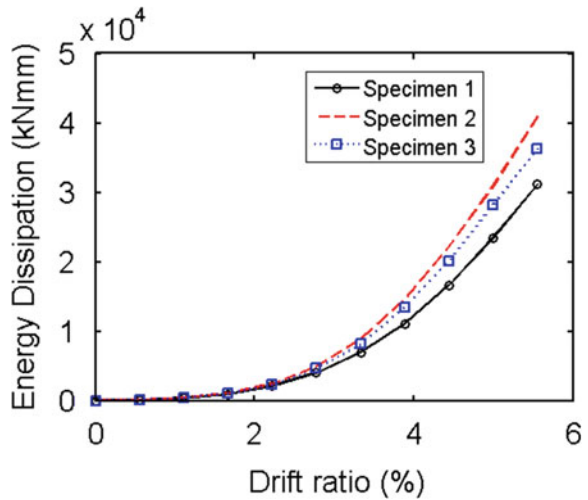


**Fig. 10** Energy dissipation at different drift ratio in cyclic test



## 5 Conclusions

The results obtained from hybrid testing of three types of scaled pier specimens were examined to explore the efficiency of additional features in the column–foundation interface region in bridge structure. Out of the three piers, one pier contains dowel reinforcement in the plastic hinge region and the other one contains corrugated sheet at the foundation in an attempt to shift the crack location from pier–foundation interface region. Strain gauges were used to measure strain in reinforcement in all the specimens. Based on the results of this study, the following important conclusions are drawn:

1. Dowel reinforcements in bridge pier are effective in re-localization of damage away from pier–foundation interface zone. Rehabilitation work would thus be easier.
2. The profile of growth of strain development along the height of the pier is highly demonstrative of such shift in damaged zone.

3. Use of corrugated sheet also has the potential for crack re-localization by appropriate selection of gauge size of sheet.
4. The experimental investigation using hybrid simulation is an efficient technique for the evaluation of seismic performance of a complete structural system.

**Acknowledgements** The financial support provided by the Department of Science and Technology, India, and M/S D2S Infrastructure Pvt. Ltd., Guwahati, India, is gratefully acknowledged.

## References

1. Aviram A, Stojadinovic B, Parra-Montesinos GJ (2014) High performance fiber reinforced concrete bridge column under bidirectional cyclic loading. *ACI Structural J* 111(2), March–April, 303–312
2. Grezic A, Cook WD, Mitchell D (1996a) Seismic retrofit of bridge column-footing connections. In: Eleventh world conference on earthquake engineering, Mexico
3. Ghobarah A, Aziz TS, Biddah A (1996b) Rehabilitation of reinforced concrete beam-column joints. In: Eleventh world conference on earthquake engineering, Mexico
4. Kumar P, Jen G, Trono W, Panagiotou M, Ostertag CP (2011) Self-compacting hybrid fiber reinforced concrete composites for bridge columns. PEER report no. 106
5. Abdelnaby AE, Frankie TM, Elnashai AS, Spencer BF, Kuchma DA, Silva P, Chang CM (2014) Numerical and hybrid analysis of a curved bridge and methods of numerical model calibration. *Eng Struct* 70:234–245
6. Schellenberg AH, Mahin SA, Fenves GL (2009) Advanced implementation of hybrid simulation. PEER report no. 104
7. Takanashi K (1975) Non-linear earthquake response analysis of structures by a computer-actuator online system part 1: detail of the system. *Transactions of the Architectural Institute of Japan* 229:77–83
8. Pinto AV, Pegon P, Magonette G, Tsionis G (2004) Pseudo-dynamic testing of bridges using non-linear substructuring. *Earthquake Eng Struct Dynam* 33:1125–1146
9. Kim SJ, Holub CJ, Elnashai AS (2011) Experimental investigation of the behavior of RC bridge piers subjected to horizontal and vertical earthquake motion. *Eng Struct* 33:2221–2235
10. McKenna FT (1997) Object-oriented finite element programming: frameworks for analysis, algorithms and parallel computing. Ph.D. thesis, University of California, Berkeley

# CFD and Wind Tunnel Investigations on Rectangular Building with Corner Cuts



A. Monica, P. Harikrishna, K. Nagamani and G. Ramesh Babu

**Abstract** Aerodynamic modifications at corners are considered an effective countermeasure to minimize the wind-induced load and load effects. One of the effective corner modification measures is provision of corner cuts to reduce wind-induced along-wind loads and cross-wind vibrations of the building. However, the corner modifications are provided usually throughout the height of the building. The present study deals with the effect of providing corner cuts over limited heights from top of the building. A 1:2:5 rectangular building has been considered for the present study. A corner cut size of 7.5% has been considered. To study the effect of spread over of corner cut over the height of the building, a total number of four cases have been considered, viz. (i) building with full-height corner cut, (ii) building with half-height corner cut, (iii) building with one-third-height corner cut and (iv) building with no corner cut. The study is carried out by using both computational fluid dynamics and wind tunnel experiments. CFD studies included angles of wind incidence of  $0^\circ$  and  $90^\circ$  under open terrain condition. The wind tunnel investigations included pressure measurements on a rigid model with 1:300 geometric scale under simulated open terrain condition for angles of wind incidence of  $0^\circ$ ,  $45^\circ$  and  $90^\circ$ . Using the measured pressures, pressure coefficients, drag and lift force coefficients have been evaluated. The effectiveness of the corner

---

A. Monica

Structural Engineering Division, Department of Civil Engineering,  
College of Engineering, Anna University, Guindy Campus, Chennai 600025,  
Tamil Nadu, India  
e-mail: maruljay@nd.edu

P. Harikrishna (✉) · G. R. Babu

Wind Engineering Laboratory, CSIR-Structural Engineering Research Centre,  
Chennai 600113, Tamil Nadu, India  
e-mail: hari@serc.res.in

G. R. Babu

e-mail: gramesh@serc.res.in

K. Nagamani

Department of Civil Engineering, College of Engineering, Anna University,  
Guindy Campus, Chennai 600025, Tamil Nadu, India  
e-mail: nagamani@annauniv.edu

© Springer Nature Singapore Pte Ltd. 2019

A. Rama Mohan Rao and K. Ramanjaneyulu (eds.), *Recent Advances in Structural Engineering, Volume 2*, Lecture Notes in Civil Engineering 12,  
[https://doi.org/10.1007/978-981-13-0365-4\\_5](https://doi.org/10.1007/978-981-13-0365-4_5)

cut over different heights of the building model has been studied by comparing the evaluated aerodynamic coefficients. Further, numerical results are compared with experimental results for validation purpose.

**Keywords** Rectangular building · Corner cut · Angle of attack  
Wind tunnel experiment · CFD · Aerodynamic coefficients

## 1 Introduction

Wind-induced motion of a tall building can be controlled either by reduction at the source, i.e. geometry, or by reducing the response by using dampers/controllers. An appropriate choice of building shape and aerodynamic modifications can result in the reduction of motion by altering the flow pattern around a building. The aerodynamic modifications of a building's cross-sectional shape, variation of its cross-section along the height, or even its size, can significantly reduce building response in along wind as well as across wind direction by altering the wind flow pattern around the building. Aerodynamically efficient plan shapes are shown to be an effective means of suppressing wind-induced loads. Among the aerodynamic modifications for building corners, the corner cut (or) corner recession has been considered for the present study. The corner cut is defined as the ratio of  $b/B$  where  $b$  indicates the cutting width of corner cut and  $B$  indicates the section width of the building in plan. Usually, these corner modifications are provided throughout the building height to reduce various aerodynamic loads and their effects. Many investigations have been carried out in the past regarding aerodynamic modifications. In Ref. [1], the study of aerodynamic stability of rectangular cylinders with various corner cuts and attack angles under uniform flow condition, giving importance to the effect on Strouhal number, was carried out. Ref. [2] used various aerodynamic modifications to reduce the wind excitation of tall flexible buildings and concluded that modifications to the building corners need to be applied to the corner region greater than about 10% of the building breadth to be beneficial. In Ref. [3], the study of 14 square tall building with recessed corners using high-frequency force balance (HFFB) technique was carried out and concluded that a corner recession ratio of 7.5% is best to reduce aerodynamic force coefficients and is most effective and optimal.

However, most of the aforementioned studies on aerodynamic modifications carried out by previous investigators were based on changes in plan dimensions of the modifications. Virtually, no work has been reported in the previous literature regarding the effects of providing corner cuts over specific heights from top of a building. Therefore, the present study is intended to investigate the effect of corner cut over limited heights of a rectangular building by carrying out experimental studies using wind tunnel and numerical simulation studies using computational fluid dynamics and to validate the numerically obtained aerodynamic coefficients with experimental results.



## 2 Experimental Setup

The boundary layer wind tunnel facility at CSIR-SERC was used for the present study. The size of the test section of the wind tunnel is  $18 \text{ m} \times 2.5 \text{ m} \times 1.8 \text{ m}$  (adjustable ceiling) with a variable speed of 0.5 to 55 m/s. The data has been collected for wind speed of  $\bar{U}_H = 13 \text{ m/s}$ . The data was measured using ESP pressure scanners which were in turn connected to the pressure tubes at each level. The sampling rate was 695 samples per second per channel with an acquisition time of 16 s. The measured pressure data has been processed to evaluate various aerodynamic coefficients, viz. pressure coefficients, local aerodynamic force coefficients, which are time-varying. From these coefficients, mean and standard deviation values have been calculated for further comparison.

### 2.1 Test Model and Conditions

In the present study, a 1:2:5 rectangular building has been considered to investigate the effect of variation of specific height of the corner cut portion from the top of the building through wind tunnel investigations. It is proposed to carry out pressure measurements on 1:300 geometric-scaled model of the rectangular building with (i) full-height corner cut, (ii) half-height corner cut, (iii) one-third-height corner cut and (iv) no corner cut under simulated open terrain condition for three angles of wind incidence ( $0^\circ$ ,  $45^\circ$  and  $90^\circ$ ) as shown in Fig. 1. A corner cut ratio of 7.5% has been adopted for the present study [3].

In the present study, a geometrically reduced rigid model of the rectangular building is considered for the measurement of surface pressures on the building model to derive pressure coefficients, force coefficients, moment. The model is made of

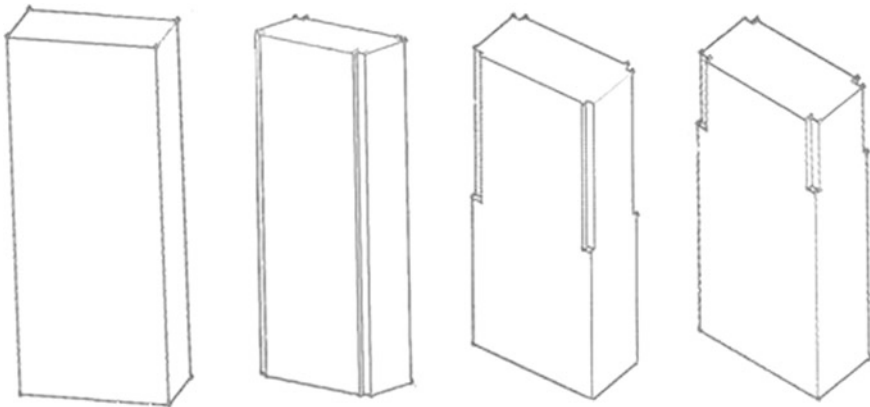


**Fig. 1** Four types of buildings under consideration

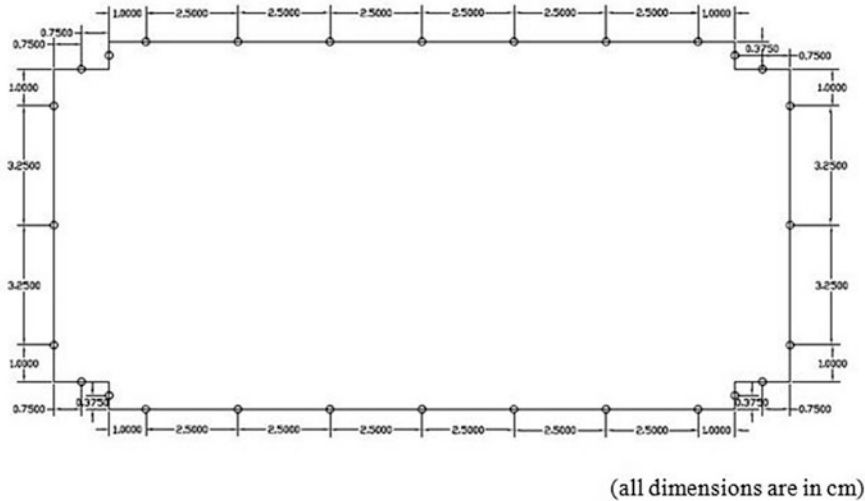


**Fig. 2** Schematic diagram of plan of model with pressure tap locations

3-mm-thick acrylic material. Geometric similarity is maintained between the model and prototype by keeping the ratio of length dimensions, projected areas and volumes of the model equal. The model dimensions are  $0.1 \text{ m} \times 0.2 \text{ m} \times 0.5 \text{ m}$ . The model is instrumented at six different levels (viz. at  $0.1H$ ,  $0.3H$ ,  $0.5H$ ,  $0.7H$ ,  $0.9H$  and  $0.95H$ ) along the height. At each level, 28 pressure ports have been provided circumferentially with one port each at corner cut region as shown in Fig. 2.

A restrictor tubing system is attached to each of the ports which in turn are connected to ESP pressure scanners with digital temperature compensation and mounted inside the wind tunnel. In the present study, it is proposed to make the pressure measurements on the instrumented building model under simulated open terrain condition. The necessary flow conditions in the wind tunnel were generated using vortex generators such as trip board of 30 cm height and seven boards of smaller wooden roughness cubes placed on the test section. The mean velocity profile with the power law coefficient of 0.14 and turbulence intensity profile and spectrum of turbulent horizontal wind speed corresponding to an open terrain condition were simulated to a scale ratio of 1:300. In this study, the effect of Reynolds number is not considered. The present investigation focused on the comparison of aerodynamic coefficients between the buildings with various corner cuts.

## 2.2 Evaluation of Aerodynamic Coefficients

A standard pitot tube is positioned at a height  $H$  (height of the model) on the upstream side of the scaled model. Initially, the reference static pressure measured using the pitot tube has been deducted from all instantaneous pressure measured

from all the pressure taps on the building model. All the pressure coefficients were subsequently deduced with respect to the reference pressure  $\bar{p}_z$ , at heights ( $z/H$ ) of 0.1, 0.3, 0.5, 0.7, 0.9 and 0.95 for Level 1, Level 2, Level 3, Level 4, Level 5 and Level 6, respectively.

The pressure coefficient is calculated as the ratio of wind-induced pressure (=measure pressure – mean static pressure) to the reference pressure,  $\bar{p}_{\text{ref}}$ . Further, statistical analysis of these evaluated pressure coefficients has been carried out to calculate mean and standard deviation values. The local forces per unit height  $F_x$  and  $F_y$  along the  $X$ -axis and  $Y$ -axis, respectively, are computed by integrating the measured instantaneous pressures along with respective tributary widths corresponding to each pressure port. Further, the local drag force ( $F_d$ ) and lift force ( $F_l$ ) at each level are deduced by resolving the evaluated instantaneous local  $F_x$  and  $F_y$  along the aerodynamic axis parallel to the wind direction and along the aerodynamic axis perpendicular to wind direction, respectively. Using these deduced local drag and lift forces, the local drag and lift force coefficients at each level have been obtained.

### 3 Experimental Test Results

#### 3.1 Comparison of Mean Pressure Coefficients for Angle of Wind Incidence $0^\circ$

For the purpose of plotting the pressure coefficient distributions along the circumference of the rectangular building model, the chord length is incremented with the spaces provided between the individual pressure taps in the anticlockwise direction to a maximum of 0.6 m (=0.2 + 0.1 + 0.2 + 0.1 m). For angle of wind incidence of  $0^\circ$ , the distributions of mean pressure coefficient obtained from four cases of corner cut spread over the height of the building, viz. (i) building with full-height corner cut, (ii) building with half-height corner cut, (iii) building with one-third-height corner cut (from top of the building model) and (iv) building with no corner cut, have been compared in Fig. 3 for Level 5 (a typical case).

It can be seen from these figures that the on the windward face (chord length between 0.5 and 0.6 m), there is little difference in the mean pressure coefficient values among all the four cases of corner cut regions. In the base pressure region (chord length between 0.2 and 0.3 m), the base pressure coefficient values are observed to be nearly same for three cases of half-height corner cut, one-third-height corner cut and no corner cut. On both the side faces (chord lengths between 0.0 and 0.2 m and 0.3 and 0.5 m), the mean suction pressure coefficients are significantly less for the case of building with full-height corner cut than those for the other three cases.

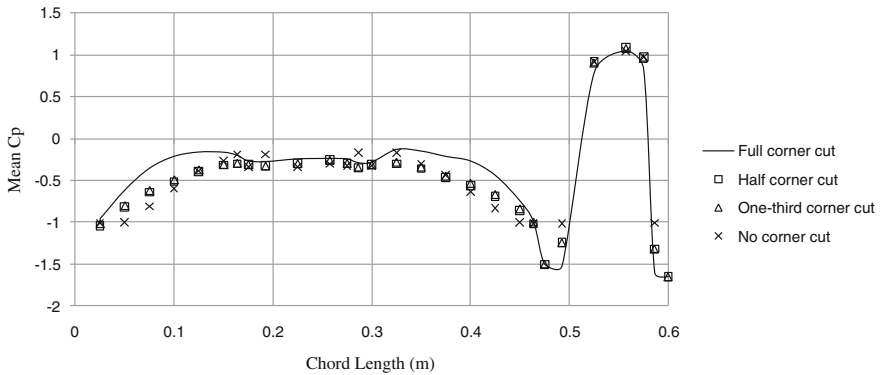


**Fig. 3** Comparison of mean pressure coefficient at Level 5 for  $0^\circ$  angle of wind incidence (reference pressure =  $p_z$ )

### 3.2 Comparison of Mean Pressure Coefficients for Angle of Wind Incidence $45^\circ$

For angle of wind incidence of  $45^\circ$ , the distributions of mean pressure coefficient obtained from four cases of corner cut spread over different heights of the building have been compared in Fig. 4 for Level 5 (a typical case). In general, for most of the levels, the mean pressure coefficients are well comparable, except for no corner cut case. This indicates that for oblique angle of wind incidence, building with one-third-height (from top) corner cut is as effective as building with full-height corner cut.

### 3.3 Comparison of Mean Pressure Coefficients for Angle of Wind Incidence $90^\circ$

For angle of wind incidence of  $90^\circ$ , the distributions of mean pressure coefficient obtained from four cases of corner cut spread over different heights of the building have been compared in Fig. 5 for Level 5 (a typical case). In general, for most of the levels, the mean pressure coefficients are well comparable on the windward (chord length between 0.0 and 0.2 m) and leeward faces (chord length between 0.3 and 0.5 m). However, on both the side faces (chord lengths between 0.2 and 0.3 m and 0.5 and 0.6 m), the mean suction pressure coefficients are observed to be reducing with increase in corner cut region along the height.

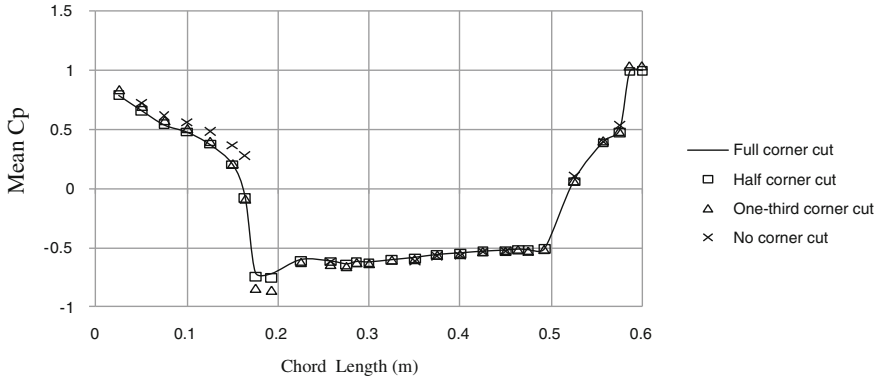


**Fig. 4** Comparison of mean pressure coefficient at Level 5 for 45° angle of wind incidence (reference pressure =  $p_z$ )

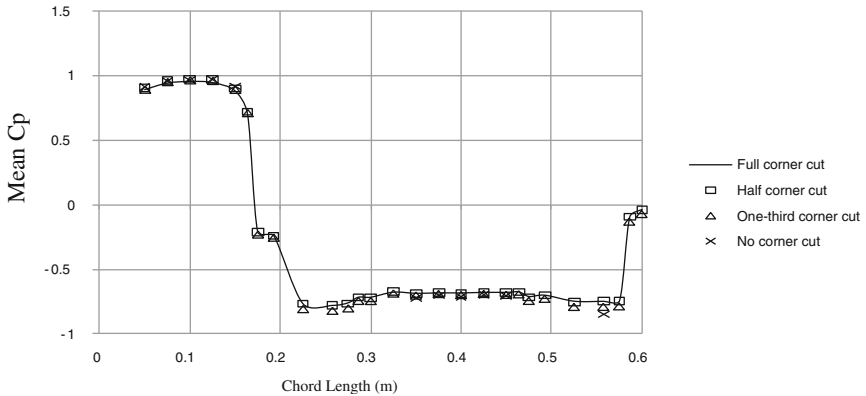


**Fig. 5** Comparison of mean pressure coefficient at Level 5 for 90° angle of wind incidence (reference pressure =  $p_z$ )

### 3.4 Local Force Coefficients

The variations of mean local drag coefficients with height are shown in Fig. 6 for angles of wind incidence of 0°, 45° and 90°, respectively. It can be seen from Fig. 6 (for 0° case) that the mean local drag coefficient is nearly uniform about 0.8, whereas for angles of wind incidence of 45° and 90° (Figs. 7 and 8), the mean local drag coefficient values are observed to be around 1.0 and around 1.5, respectively. These values are observed to be nearly uniform between 0.3H and 0.7H with edge effects near the bottom and top regions. The standard deviation of local lift force

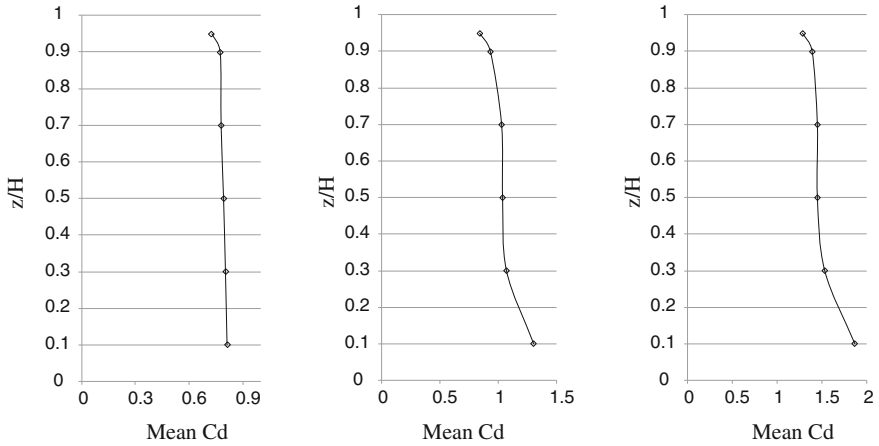


**Fig. 6** Variation of mean local drag coefficient with  $z/H$  for  $0^\circ$ ,  $45^\circ$ ,  $90^\circ$  angle of wind incidence, respectively, (reference pressure =  $p_z$ )

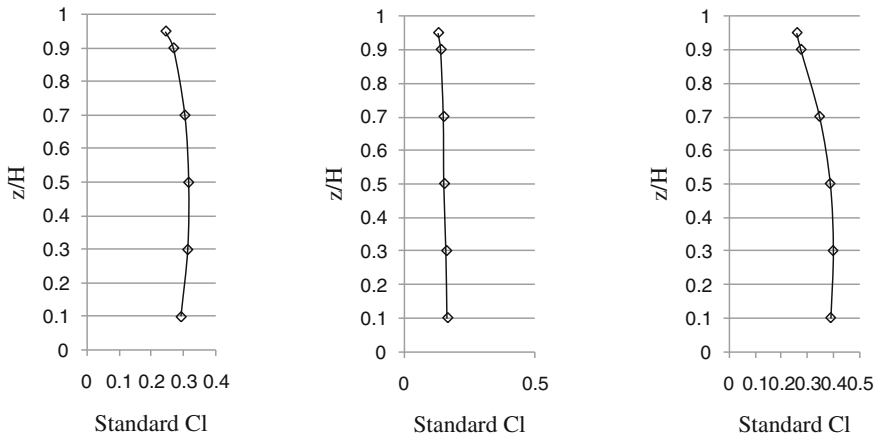


**Fig. 7** Variation of mean local lift coefficient with  $z/H$  for  $0^\circ$ ,  $45^\circ$ ,  $90^\circ$  angle of wind incidence (reference pressure =  $p_H$ )

coefficient values referenced to  $p_H$  has been plotted in Fig. 7 for angles of wind incidence of  $0^\circ$ ,  $45^\circ$  and  $90^\circ$ , respectively. It can be seen from these figures that the standard deviation of local lift force coefficient values referenced to  $p_H$  is nearly uniform over major portion of the height.

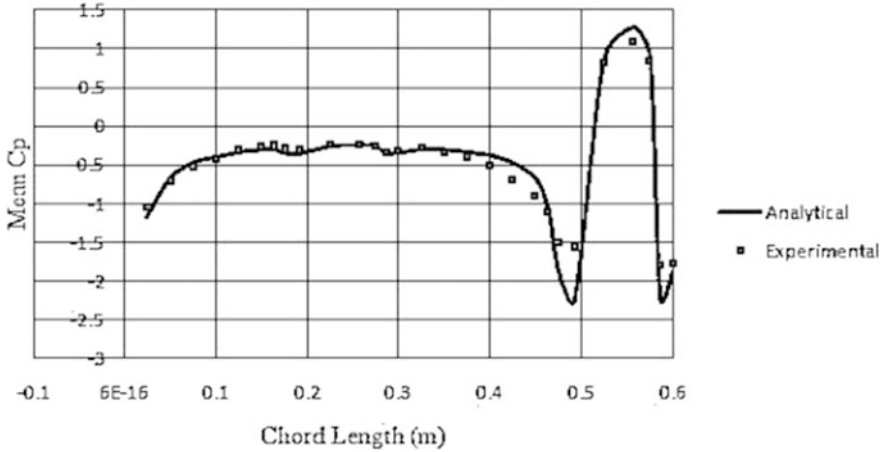


**Fig. 8** Variation of mean pressure coefficient for 0° angle of wind incidence at Level 4 for full-height corner cut

### 3.5 Comparison of Overall Force Coefficients

In the present study, the effectiveness of spread of the corner cut over the height of the building is investigated by comparing the overall force coefficients, which are evaluated by considering  $p_H$  as reference pressure for both overall drag and lift force coefficients. Further,  $(B' \times H)$  has been considered as reference area for drag force coefficients and  $(D' \times H)$  as reference area for lift force coefficients.

Table 1 provides mean and standard deviation of overall drag and lift force coefficients of buildings models corresponding to all the four cases of corner cut for angles of wind incidence of 0°, 45° and 90°. It can be observed from this table that with reference to building with full-height corner cut, building with one-third-height corner cut is observed to be nearly effective (with about 15% difference) in reducing most of the coefficients except for mean and standard deviation of overall drag coefficient for angle of wind incidence of 0°, and for standard deviation of overall lift force coefficient for angles of wind incidence of 45° and 90°. For these specific coefficients, the full-height corner cut is observed to be maximum effective.

## 4 Numerical Investigations

### 4.1 Computational Domain and Meshing

In the present study, a 1:2:5 rectangular building model of dimensions 0.1 m ( $B$ )  $\times$  0.2 m ( $D$ ) in plan and 0.5 m in height, which are identical to the dimensions

**Table 1** Comparison of overall force coefficients

Parameter	Building with full-height corner cut		Building with half-height corner cut		Building with one-third-height corner cut			Building with no corner cut				
	0°	45°	90°	0°	45°	90°	0°	45°	90°	0°	45°	90°
Angle of attack												
Mean $C_d$	0.614	0.814	1.17	0.892	0.899	1.33	0.955	0.932	1.35	1.112	0.991	1.411
Std $C_d$	0.137	0.153	0.236	0.201	0.163	0.278	0.213	0.174	0.278	0.247	0.183	0.289
Std $C_1$	0.265	0.127	0.309	0.285	0.143	0.399	0.281	0.144	0.428	0.267	0.155	0.472



of the building model considered for the wind tunnel investigations, has been chosen for numerical simulation. Angles of wind incidence include  $0^\circ$  and  $90^\circ$ . The total height of the problem domain is  $18B$  which is same as that of the wind tunnel in which experimental studies were carried out. The overall width of the problem domain perpendicular to the flow direction is  $25B$  which is same as that of the width of wind tunnel. Wall (no-slip) boundaries were chosen for building surface and also for top and bottom boundaries of the computational domain. Both the side boundaries of the computational domain are defined as symmetry boundary.

The computational domain has been meshed by choosing the first cell width near the walls of the prism as  $0.02B$ . The distance of grid lines from the face of the building is varied with a geometric series using a stretching ratio of 1:1 for smooth variation.

## 4.2 *Boundary Conditions*

At the inlet boundary, a mean wind velocity profile with  $\alpha$  of 0.14 and turbulence intensity profile ( $I_u(z)$ ) are used as per the wind tunnel simulations. The mean wind velocity at the top of building has been defined as 10 m/s. At the symmetry (free-slip) boundaries, i.e. both the side boundaries of the computational domain, the velocity in the direction normal to the boundary was set equal to zero and also the derivatives of all the flow variables in the direction normal to the boundary were set equal to zero.

At wall boundaries, i.e. on the top and bottom of computational domain, the velocities in all three directions are set equal to zero by default. Standard wall function was used for wall boundaries to model the near-wall turbulence. Second-order upwind differencing scheme was used for momentum,  $k$  and  $\varepsilon$  transport equations. Semi-Implicit Method for Pressure-Linked Equations (SIMPLE) algorithm was used for coupling the pressure and velocity terms.

## 4.3 *Numerical Simulations*

Numerical simulations have been carried out for four cases of corner cut, viz. (i) building with full-height corner cut, (ii) building with half-height corner cut, (iii) building with one-third-height corner cut and (iv) building with no corner cut. The simulations have been carried out for two angles of wind incidence of  $0^\circ$  (wind direction perpendicular to shorter face of the building) and  $90^\circ$  (wind direction perpendicular to longer face of the building).

Realizable  $k$ - $\varepsilon$  turbulence model has been considered in the present study. Unsteady simulations have been carried out with time step of 0.000125 s. Flow analysis has been carried out by adopting iterative approach till a stabilized solution is achieved with convergence. However, due to the limitations in the turbulence

model while using high magnitudes of turbulence intensities, the solution was observed to be converged to steady-state solution. Hence, only mean pressure coefficients and mean overall drag force coefficients have been obtained from the numerical simulations.

#### 4.4 Validation of Numerical Simulations

The numerically obtained pressure coefficient and mean overall drag coefficient values at the selected levels of  $0.1H$ ,  $0.3H$ ,  $0.5H$ ,  $0.7H$ ,  $0.9H$  and  $0.95H$  have been compared with the experimental values.

##### 4.4.1 Comparison of Mean Pressure Coefficients for Building with Full-Height Corner Cut

For angle of wind incidence of  $0^\circ$  and  $90^\circ$ , the numerically obtained mean pressure coefficients of the building with full-height corner cut are compared with the respective experimental values in Figs. 8 and 9, respectively, at Level 4 (a typical case). For angle of wind incidence  $0^\circ$ , the numerically obtained mean pressure coefficients are compared well with the experimental values at all the chord length locations except near stagnation point, where the numerical values are observed to be over-predicted by about 20%.

For angle of wind incidence of  $90^\circ$ , the numerically obtained mean pressure coefficients on the windward face are observed to be over-predicted by about 40%

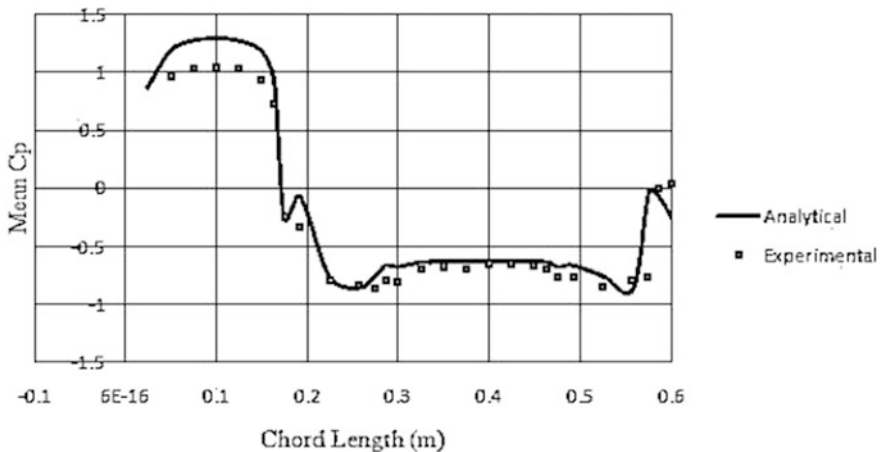


**Fig. 9** Variation of mean pressure coefficient for  $90^\circ$  angle of wind incidence at Level 4 for full-height corner cut

in comparison with experimental values. The base pressure coefficient values are observed to be under-predicted by at least 15% in comparison with experimental values.

#### 4.4.2 Comparison of Mean Pressure Coefficients for Building with Half-Height Corner Cut

For angle of wind incidence of  $0^\circ$  and  $90^\circ$ , the numerically obtained mean pressure coefficients of the building with half-height corner cut are compared with the respective experimental values in Figs. 10 and 11, respectively, at Level 4 (a typical case). For angle of wind incidence  $0^\circ$ , the numerically obtained mean pressure coefficients are compared well with the experimental values.

For angle of wind incidence of  $90^\circ$ , the numerically obtained mean pressure coefficients on the windward face are observed to be over-predicted by at least 15% in comparison with experimental values, whereas the mean base pressure coefficients are observed to be under-predicted by about 40%.

#### 4.4.3 Comparison of Mean Pressure Coefficients for Building with One-Third-Height Corner Cut

The numerically obtained mean pressure coefficients for  $0^\circ$  angle of wind incidence are compared well with the experimental values as shown in Fig. 12 at Level 5 (a typical case). For  $90^\circ$  angle of wind incidence, the numerically evaluated mean pressure coefficients are observed to be over-predicted by at least 20% in comparison with experimental values (Fig. 13).

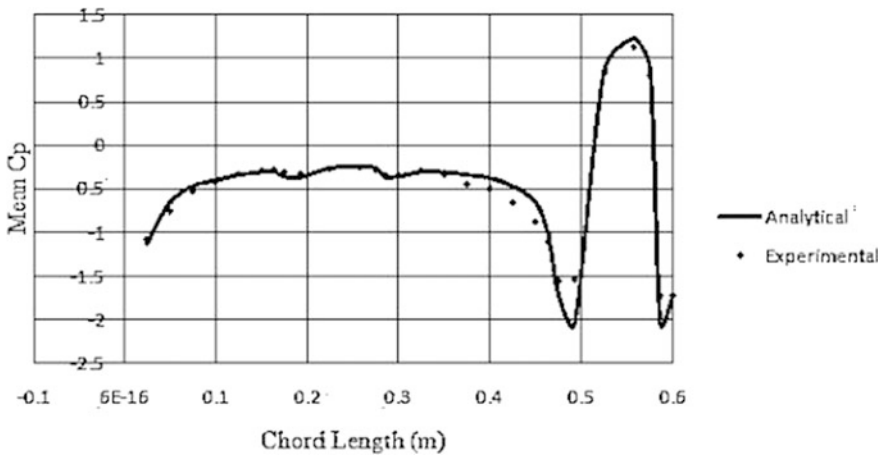


**Fig. 10** Variation of mean pressure coefficient for  $0^\circ$  angle of wind incidence at Level 4 for half-height corner cut

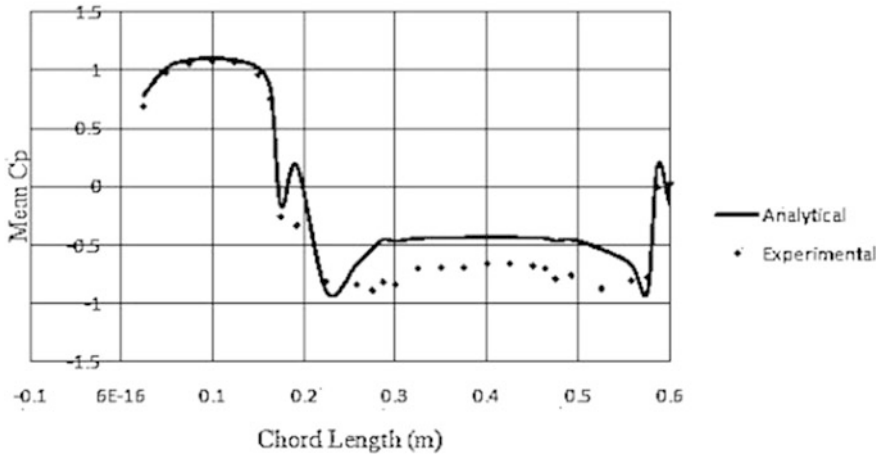


**Fig. 11** Variation of mean pressure coefficient for 90° angle of wind incidence at Level 4 for half-height corner cut

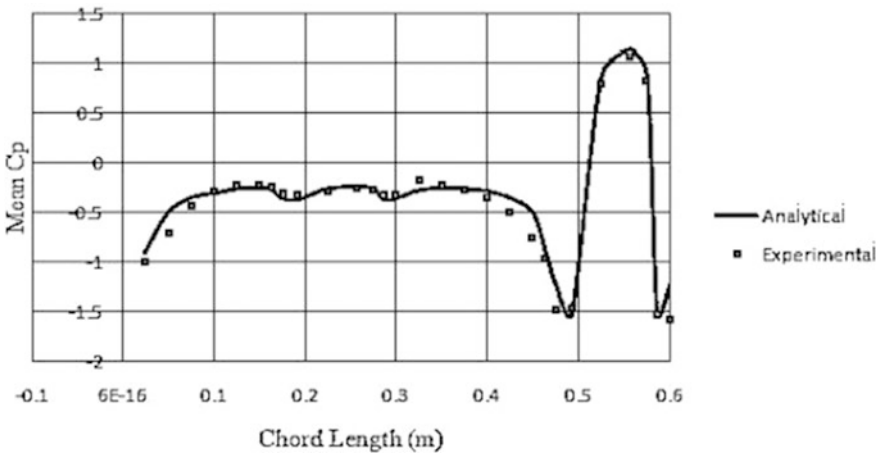


**Fig. 12** Variation of mean pressure coefficient for 0° angle of wind incidence at Level 5 for one-third-height corner cut

#### 4.4.4 Comparison of Mean Overall Drag Force Coefficient

The numerically obtained mean overall drag force coefficients are compared with the experimental values in Table 2. It can be seen from Table 2 that the numerically obtained mean overall drag coefficient is compared well with the experimental values with about ±10% difference.

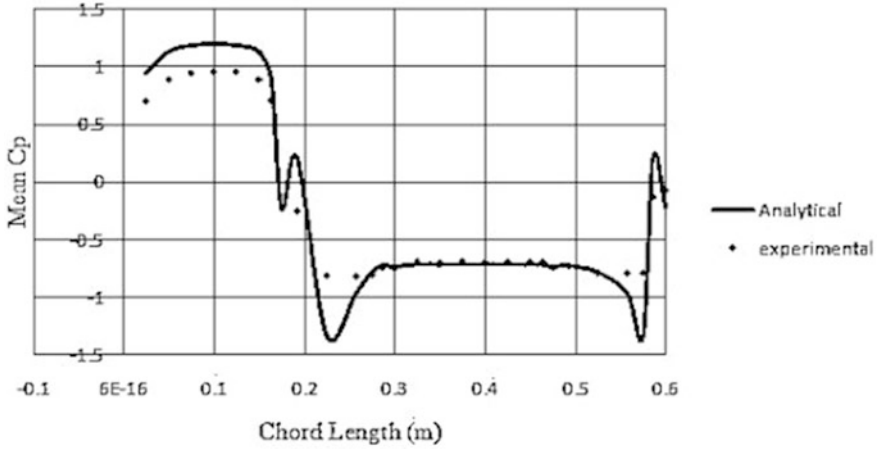


**Fig. 13** Variation of mean pressure coefficient for 90° angle of wind incidence at Level 5 for one-third-height corner cut

**Table 2** Comparison of overall force coefficients

	Experimental	Numerical
<i>0° angle of wind incidence</i>		
No corner cut	1.112	1.08
Full corner cut	0.614	0.73
Half corner cut	0.892	0.90
One-third corner cut	0.955	0.958
<i>90° angle of wind incidence</i>		
No corner cut	1.41	1.225
Full corner cut	1.17	1.126
Half corner cut	1.33	1.168
One-third corner cut	1.35	1.18

## 5 Conclusion

Based on the observations, the following conclusions have been made:

1. The optimization of height over which corner cut needs to be provided has partial benefit in reducing a few overall force coefficients, as much as corner cut over full-height of the building
2. The numerical simulations can be used for sensitivity studies on mean overall drag coefficient value (with expected differences of about ±10% in relation to experimental results).

## References

1. Choi C-K, Kwon D-K (2001) The characteristics of Strouhal number of rectangular cylinders with various corner cuts
2. Amin JA, Ahuja AK (2010) Aerodynamic modification to the shape of the buildings: a review of the state of the art. *Asian J Civ Eng Build Hous* 11(4):433–450
3. Zhengwei Z, Yong Q, Ming G, Nankun T, Yong X (2012b) Effects of corner recession modification on aerodynamic coefficients of square tall buildings. In: *The seventh international colloquium on bluff body aerodynamics and applications (BBAA7)* by International Association for Wind Engineering, Shanghai, China, 2–6 September 2012

# Correlating Peak Ground $A/V$ Ratio with Ground Motion Frequency Content



Rahul Garg, Jaya Prakash Vemuri and Kolluru V. L. Subramaniam

**Abstract** Peak ground  $A/V$  ratio has been used an empirical parameter to estimate ground motion frequency content and categorize ground motion suites for performing nonlinear time history analyses of structures. Ground motions are usually classified into three subjective categories: low  $A/V$ , intermediate  $A/V$ , and high  $A/V$  to reflect low-, moderate-, and high-frequency contents, respectively. However, the relationship between  $A/V$  and frequency is very complex as the  $A/V$  ratio depends on faulting processes, distance from source to recording station, and local geological conditions. Frequency content of earthquake waves is represented by single-frequency parameters, such as mean period,  $T_m$ , and predominant period,  $T_p$ . In this paper, the relationship between  $A/V$  and frequency parameters is explored. Linear regression analyses are performed on data obtained from three major earthquakes. Regression analyses indicate that the predominant frequency content of the ground motion exhibits little or no correlation with  $A/V$  ratio. The  $A/V$  ratio may be used as an empirical parameter to obtain an estimate of only the mean frequency content of the ground motion.

**Keywords** Mean frequency · Predominant frequency ·  $A/V$  · Fast Fourier transform · Regression

## 1 Introduction

Dynamic response of structures is sensitive to the ground motion frequency. Apart from the peak ground acceleration, the frequency content of the earthquake has been recognized as a key parameter contributing to structural damage [1]. High-frequency earthquakes cause resonance in structures with high natural frequencies which are usually low-rise buildings. Similarly, low-frequency earthquakes cause resonance for structures with low natural frequencies which are

---

R. Garg · J. P. Vemuri · K. V. L. Subramaniam (✉)  
Department of Civil Engineering, IIT Hyderabad, Hyderabad, India  
e-mail: kvls@iith.ac.in

© Springer Nature Singapore Pte Ltd. 2019  
A. Rama Mohan Rao and K. Ramanjaneyulu (eds.), *Recent Advances in Structural Engineering, Volume 2*, Lecture Notes in Civil Engineering 12,  
[https://doi.org/10.1007/978-981-13-0365-4\\_6](https://doi.org/10.1007/978-981-13-0365-4_6)

usually moderate height/tall buildings. Gradation of soils may also influence whether low- or high-frequency waves are more damaging to the structure. Fine-grained soils deform more under high-frequency motions, and coarse-grained soils deform more under low-frequency motions.

For a proper seismic assessment, it is therefore important to estimate frequency content. However, an earthquake wave consists of several frequencies and it is essential to understand the distribution of amplitude among different frequencies. This frequency distribution is typically understood from observations of the frequency content obtained using fast Fourier transforms (FFTs). As the computation of FFTs is tedious, a single parameter that characterizes the frequency content of an input ground motion is considered useful. Single-frequency parameters, such as mean period,  $T_m$ , and predominant period,  $T_p$ , have been employed to meaningfully represent frequency content.

The  $A/V$  ratio has been used as an empirical parameter to estimate the ground motion frequency content [2] and also to categorize ground motion suites for performing nonlinear time history analyses of structures. As a seismic wave travels through the earth's layers, the peak acceleration of the observed ground motion attenuates faster as compared to the peak velocity. The peak ground  $A/V$  ratio has been suggested as an empirical parameter to observe the effect of the transmission path on seismic wave characteristics such as amplitude, frequency content, and significant duration. In particular, the peak ground ratio,  $A/V$ , has also been used to approximate frequency content in seismic waves [2]. Zhu et al. [3] categorized ground motions into three categories and discussed its seismological significance. Sawada et al. [4] concluded that low  $A/V$  ratios signify earthquakes with low predominant frequencies, broader response spectra, longer durations, long epicentral distances, and site periods. Ground motions were classified as follows: low, with  $A/V < 0.8$  g/m/s; intermediate, with  $0.8$  g/m/s  $< A/V < 1.2$  g/m/s; and high, with  $1.2$  g/m/s  $< A/V$ . This classification of ground motions is subjective because low  $A/V$ , intermediate  $A/V$  ratio, and high  $A/V$  ground motions are assumed to subjectively reflect low-, moderate-, and high-frequency contents, respectively. However, the relationship between  $A/V$  and frequency is complex as the  $A/V$  ratio depends on faulting processes, distance from source to recording station, and local geological conditions. The relationship between  $A/V$ ,  $T_m$ , and  $T_p$  has not been properly quantified in the literature. This paper explores this relationship based on seismic data recorded in Himalayan earthquakes.

## 2 Fast Fourier Transforms

FFTs are commonly used to transform seismic time history into frequency domain, and the Fourier amplitude spectrum shows the distribution of ground motion amplitude with respect to frequency. Fourier amplitude is computed as the square root of the sum of the squares of the real and imaginary parts of the Fourier



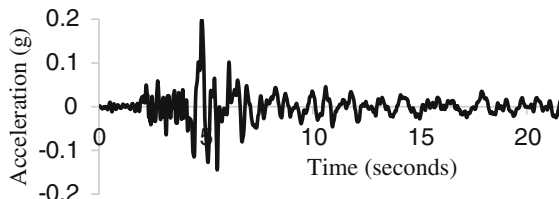


**Fig. 1** Gopeshwar—L record (rich in low frequencies)

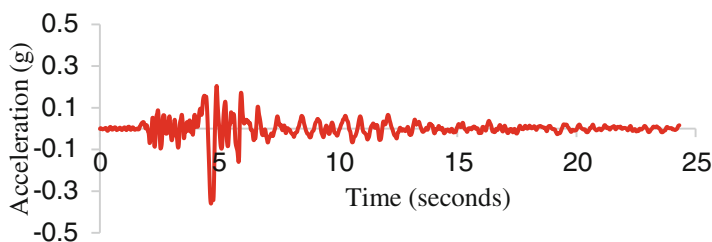


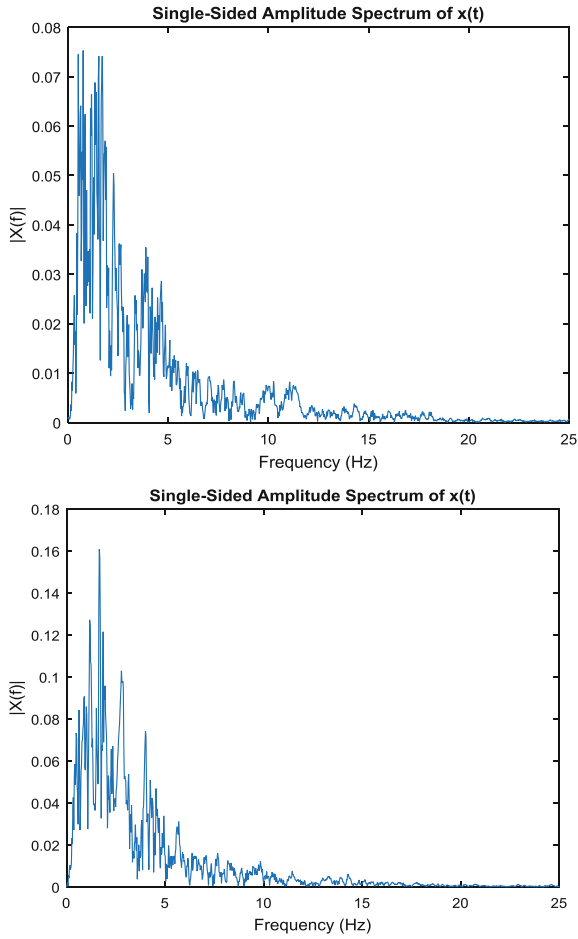
**Fig. 2** Gopeshwar—T record (rich in low frequencies)

transform. FFTs highlight the frequency ranges at which seismic energy is concentrated. As an example, the characteristic frequency of the motions recorded in the 1999 Chamoli Earthquake shows considerable fluctuations, indicating the influence of local geology and topography. In particular, the ground motions at Gopeshwar, situated near the valley, are unusually rich in low frequencies (see Fig. 3) for the near-field motions and the energy is concentrated in a narrow band. On the other hand, the ground motion recorded at Ukhimath, situated on a hill top, is rich in high frequencies (see Fig. 6). Figures 1, 2, 4, and 5 show the horizontal acceleration time histories.

### 3 Predominant and Mean Period

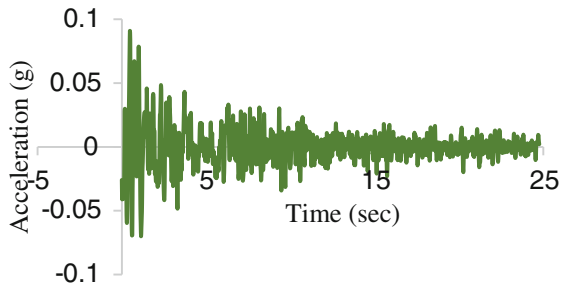
The predominant period is defined as the period at which the maximum spectral acceleration occurs in a 5% damped acceleration response spectrum. It can also be obtained as the period of vibration corresponding to the maximum value of the Fourier amplitude spectrum. Figure 7 shows the predominant period identified from the response spectrum.

The mean period,  $T_m$ , represents the average frequency content and is estimated by Eq. (1) where  $C_i$  are the Fourier amplitudes, and  $f_i$  represent the discrete Fourier transform frequencies between 0.25 and 20 Hz [5]. The mean square frequency is



**Fig. 3** FFTs of Gopeshwar—L and T records—rich in low frequencies

**Fig. 4** Ukhimath—L record (rich in high frequencies)



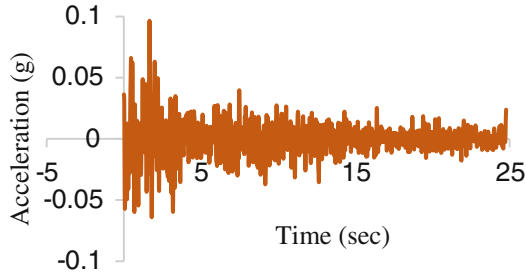


Fig. 5 Ukhimath—T record (rich in high frequencies)

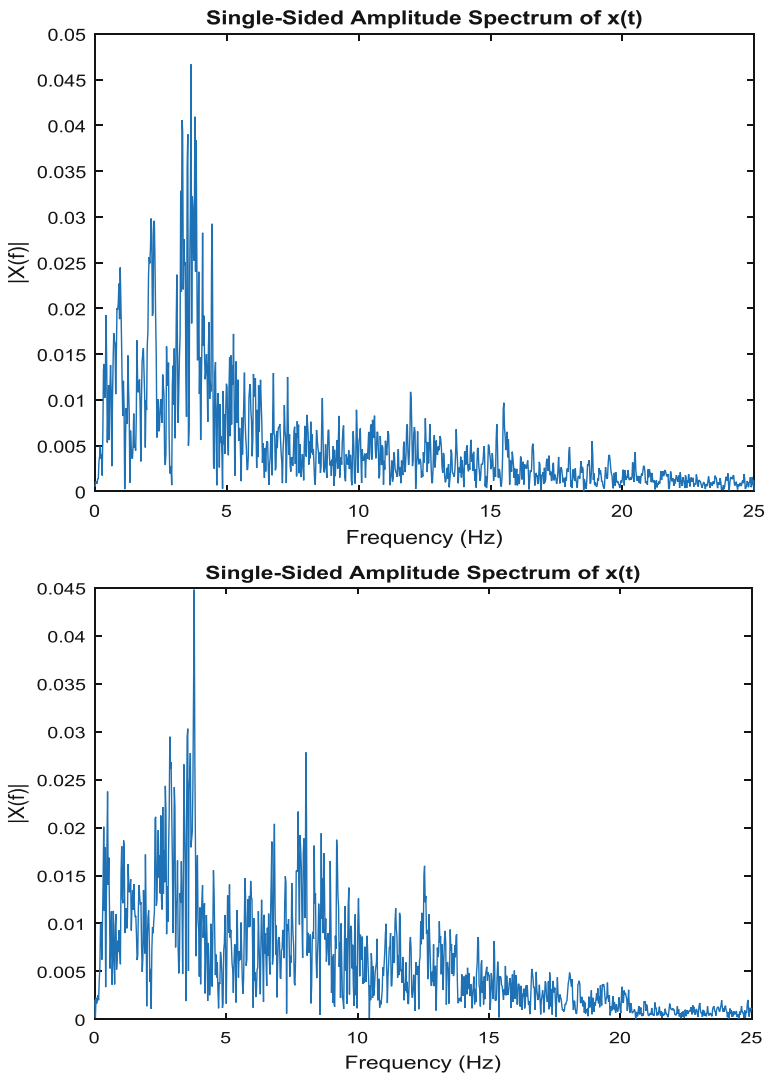
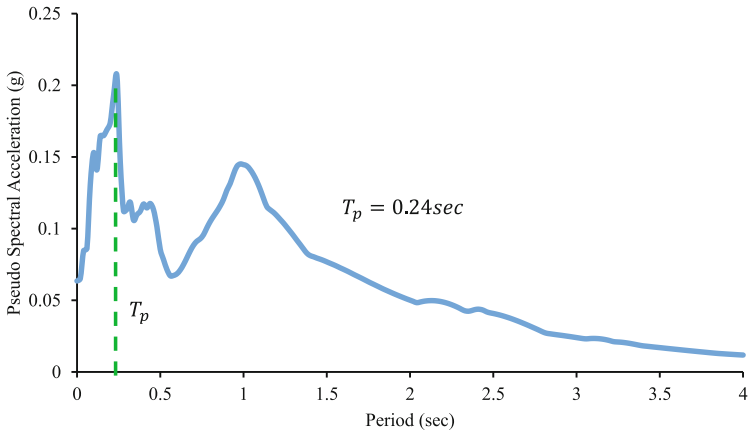
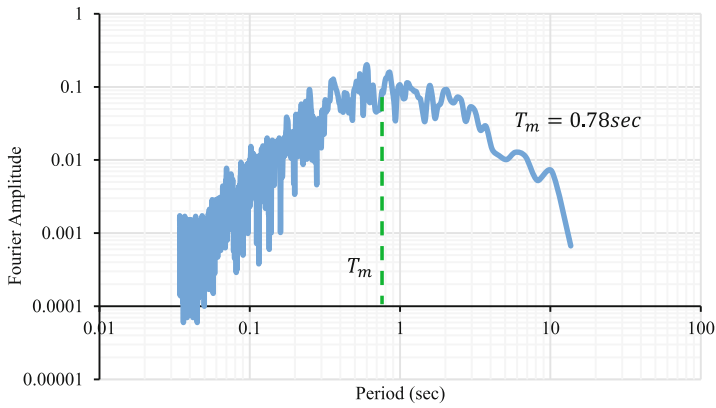


Fig. 6 FFTs of Ukhimath—L and T records (rich in high frequencies)



**Fig. 7** Identification of predominant period parameter,  $T_p$ , from response spectrum



**Fig. 8** Mean period of a seismic wave,  $T_m$

estimated using Eq. (1) with the term  $1/f_i$  replaced by  $f_i$ . Figure 8 shows mean period,  $T_m$ , computed using Eq. (1).

$$T_m = \sum \left( \frac{C_i^2}{f_i} \right) / \sum C_i^2 \tag{1}$$

The mean period, predominant period, and  $A/V$  ratio for the 1991 Uttarkashi, 1988 Indo-Bangladesh, and 1988 Indo-Burma quakes are tabulated in Tables 1, 2, and 3.

**Table 1** Seismic parameters from 1991 Uttarkashi Earthquake

S. No.	Record	A/V (g/m/s)	$T_p$ (s)	$T_m$ (s)
1.	Almora—L	1.33	0.26	0.39
2.	Almora—T	1.7	0.22	0.40
3.	Barkot—L	1.83	0.12	0.23
4.	Barkot—T	1.64	0.26	0.25
5.	Bhatwari—L	0.83	0.28	0.42
6.	Bhatwari—T	1.41	0.62	0.54
7.	Ghansiali—L	1.5	0.2	0.30
8.	Ghansiali—T	1.47	0.18	0.26
9.	Karnprayag—L	1.69	0.34	0.34
10.	Karnprayag—T	2.11	0.34	0.33
11.	Kosani—L	1.54	0.2	0.25
12.	Kosani—T	2.07	0.18	0.24
13.	Koteshwar—L	1.95	0.24	0.30
14.	Koteshwar—T	1.69	0.28	0.33
15.	Koti—L	1.46	0.34	0.54
16.	Koti—T	0.9	0.36	0.45
17.	Purola—L	1.57	0.2	0.29
18.	Purola—T	2.04	0.2	0.29
19.	Rudraprayag—L	2.58	0.12	0.15
20.	Rudraprayag—T	1.91	0.12	0.17
21.	Srinagar—L	3.44	0.08	0.16
22.	Srinagar—T	2.5	0.08	0.19
23.	Tehri—L	1.73	0.32	0.42
24.	Tehri—T	0.68	0.26	0.71
25.	Uttarkashi—L	1.42	0.24	0.29
26.	Uttarkashi—T	1.59	0.24	0.29

**Table 2** Seismic parameters from 1988 Indo-Bangladesh Earthquake

S. No.	Record	A/V (g/m/s)	$T_p$ (s)	$T_m$ (s)
1.	Baigao—L	1.44	0.20	0.28
2.	Baigao—T	1.10	0.12	0.56
3.	Baithalangso—L	1.77	0.10	0.35
4.	Baithalangso—T	1.66	0.18	0.39
5.	Bamungao—L	1.93	0.08	0.25
6.	Bamungao—T	1.18	0.18	0.37
7.	Dauki—L	1.72	0.28	0.29
8.	Dauki—T	2.43	0.16	0.28
9.	Gunjung—L	1.28	0.20	0.43
10.	Gunjung—T	1.47	0.28	0.38

(continued)

**Table 2** (continued)

S. No.	Record	$A/V$ (g/m/s)	$T_p$ (s)	$T_m$ (s)
11.	Haflong—L	1.60	0.12	0.30
12.	Haflong—T	1.60	0.18	0.31
13.	Hatikhali—L	2.00	0.14	0.19
14.	Hatikhali—T	1.67	0.12	0.22
15.	Katakhal—L	0.76	0.32	0.65
16.	Katakhal—T	0.97	0.28	0.45
17.	Kheliehriat—L	1.53	0.30	0.35
18.	Kheliehriat—T	2.05	0.26	0.30
19.	Mawphlang—L	1.43	0.18	0.20
20.	Mawphlang—T	1.65	0.16	0.21
21.	Nongkhlaw—L	1.82	0.20	0.24
22.	Nongkhlaw—T	2.42	0.24	0.28
23.	Nongpoh—L	1.49	0.16	0.22
24.	Nongpoh—T	3.42	0.18	0.19
25.	Pynursla—L	2.21	0.16	0.21
26.	Pynursla—T	2.23	0.18	0.21
27.	Saitsama—L	2.82	0.26	0.23
28.	Saitsama—T	1.97	0.30	0.25
29.	Shillong—L	2.38	0.10	0.18
30.	Shillong—T	1.93	0.12	0.24
31.	Ummulong—L	2.79	0.08	0.15
32.	Ummulong—T	2.01	0.10	0.17
33.	Umrongso—L	1.42	0.28	0.29
34.	Umrongso—T	1.04	0.16	0.36
35.	Umsning—L	2.14	0.24	0.22
36.	Umsning—T	1.93	0.26	0.25

**Table 3** Seismic parameters from 1988 Indo-Burma Earthquake

S. No.	Record	$A/V$ (g/m/s)	$T_p$ (s)	$T_m$ (s)
1.	Baigao—L	3.39	0.12	0.15
2.	Baigao—T	1.19	0.14	0.17
3.	Baithalangso—L	1.11	0.20	0.22
4.	Baithalangso—T	1.13	0.16	0.30
5.	Bamungao—L	1.44	0.26	0.29
6.	Bamungao—T	1.35	0.24	0.33
7.	Berlongfer—L	1.48	0.34	0.41
8.	Berlongfer—T	1.37	0.44	0.40
9.	Bokajan—L	1.72	0.18	0.31

(continued)

**Table 3** (continued)

S. No.	Record	$A/V$ (g/m/s)	$T_p$ (s)	$T_m$ (s)
10.	Bokajan—T	2.06	0.08	0.29
11.	Cherrapunji—L	1.95	0.14	0.26
12.	Cherrapunji—T	1.16	0.20	0.27
13.	Dauki—L	2.58	0.24	0.29
14.	Dauki—T	1.99	0.30	0.35
15.	Diphu—L	1.01	0.12	0.29
16.	Diphu—T	1.25	0.44	0.31
17.	Doloo—L	1.18	0.22	0.56
18.	Doloo—T	1.12	0.22	0.57
19.	Gunjung—L	1.53	0.24	0.30
20.	Gunjung—T	2.13	0.32	0.30
21.	Hajadisa—L	1.55	0.22	0.25
22.	Hajadisa—T	1.26	0.14	0.23
23.	Harengajao—L	1.62	0.22	0.32
24.	Harengajao—T	1.47	0.16	0.31
25.	Hojai—L	1.95	0.18	0.25
26.	Hojai—T	1.12	0.16	0.28
27.	Jellalpur—L	0.95	0.32	0.63
28.	Jellalpur—T	0.88	0.40	0.48
29.	Jhirighat—L	1.04	0.38	0.53
30.	Jhirighat—T	1.25	0.32	0.53
31.	Kalain—L	0.72	0.76	0.74
32.	Kalain—T	1.02	0.26	0.60
33.	Umsning—L	3.15	0.18	0.19
34.	Umsning—T	2.41	0.20	0.21
35.	Umrongso—L	1.49	0.16	0.31
36.	Umrongso—T	1.94	0.18	0.31
37.	Ummulong—L	3.03	0.10	0.12
38.	Ummulong—T	2.58	0.10	0.13
39.	Silchar—L	0.90	0.38	0.62
40.	Silchar—T	0.92	0.50	0.67
41.	Shillong—L	3.67	0.10	0.15
42.	Shillong—T	3.27	0.10	0.15
43.	Saitsama—L	2.42	0.24	0.23
44.	Saitsama—T	2.23	0.30	0.26
45.	Pynursla—L	1.14	0.16	0.25
46.	Pynursla—T	1.60	0.12	0.23
47.	Panimur—L	3.05	0.18	0.18
48.	Panimur—T	2.80	0.18	0.17
49.	Nongstoin—L	2.87	0.24	0.22

(continued)

**Table 3** (continued)

S. No.	Record	$A/V$ (g/m/s)	$T_p$ (s)	$T_m$ (s)
50.	Nongstoin—T	1.59	0.24	0.24
51.	Nongkhlaw—L	1.80	0.32	0.28
52.	Nongkhlaw—T	2.27	0.32	0.26
53.	Mawsynram—L	2.53	0.08	0.17
54.	Mawsynram—T	2.26	0.08	0.18
55.	Mawphlng—L	3.07	0.20	0.21
56.	Mawphlang—T	2.63	0.22	0.21
57.	Mawkyrwat—L	1.82	0.10	0.16
58.	Mawkyrwat—T	2.10	0.10	0.19
59.	Loharghat—L	1.58	0.26	0.53
60.	Loharghat—T	1.12	0.26	0.57
61.	Koomber—L	1.26	0.48	0.54
62.	Koomber—T	1.05	0.24	0.54
63.	Khlieriat—L	2.40	0.30	0.23
64.	Khlieriat—T	2.25	0.20	0.26
65.	Katakhal—L	0.63	0.76	0.90
66.	Katakhal—T	0.71	0.42	0.73

#### 4 Plots of Peak Ground $A/V$ Ratio

Figure 9 shows the plot of  $A/V$  ratio versus mean period,  $T_m$ , for records obtained from three earthquakes: the 1991 Uttarkashi Earthquake, 1988 Indo-Bangladesh Earthquake, and 1988 Indo-Burma Earthquake. The moderate values of  $R^2$  indicate a clear correlation between peak ground  $A/V$  ratio and mean period,  $T_m$ . Figure 10 shows a plot of the  $A/V$  ratio and the predominant period,  $T_p$ , for the same set of seismic records. A poor correlation with high scatter is observed, indicating little or no relationship between these parameters.

In both cases, a scatter is observed in the high-frequency region, indicating that the linear relationship is stronger for earthquakes containing lower-frequency content. The scatter in the high-frequency region is explained using other seismic parameters such as distance, strong motion duration, local site conditions, and Arias intensity. Statistical analyses of seismic data from other major Himalayan earthquakes indicate similar trends.



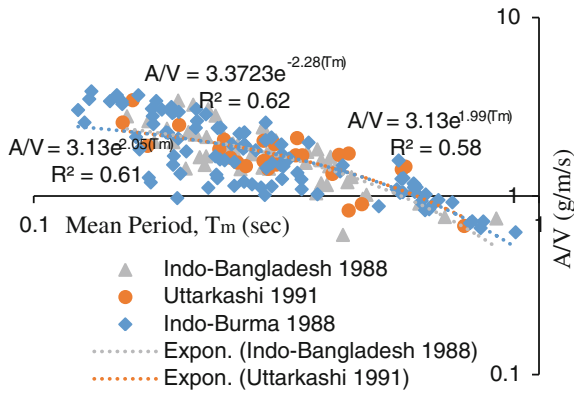


Fig. 9 Peak ground A/V ratio versus mean period,  $T_m$  (moderate correlation)

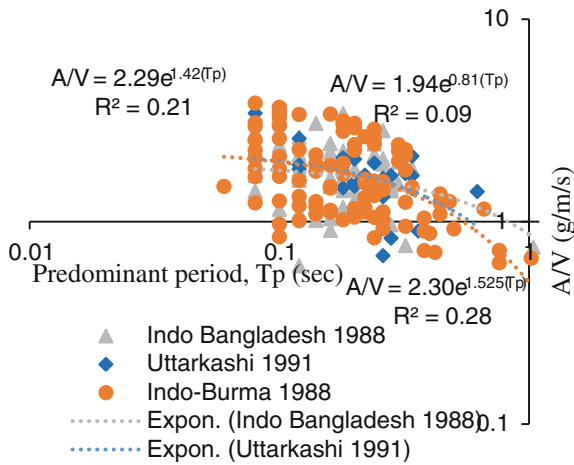


Fig. 10 Peak ground A/V ratio versus predominant period,  $T_p$  (poor correlation)

## 5 Conclusions

In this study, a database of strong ground motions from major Himalayan ground motions is analyzed. Ground motions are characterized using parameters such as peak ground acceleration, peak ground velocity, epicentral distance, mean frequency content, predominant frequency content, strong motion duration, and Arias intensity. The predominant frequency is represented by the predominant period,  $T_p$ , which is the period at which the maximum spectral acceleration occurs in an acceleration spectrum. The mean frequency content is represented by the mean period,  $T_m$ , which is estimated using Fourier amplitudes. To explore the relationship

between various ground motion parameters, correlation analyses are performed on the tabulated data. The range of  $A/V$  in these data sets varies from 0.5 (low) to 4.0 (very high).

It is clear that motions with different frequency content can have the same predominant frequency. Hence,  $T_p$  can only indicate the location of the peak in the acceleration response spectrum but cannot explain the dispersion of the frequency content around the peak. It is concluded that the  $A/V$  ratio is a useful parameter to obtain an estimate of only the mean frequency content of the ground motion.

## References

1. Jafarian Y, Kermani E, Baziar MH (2010) Empirical predictive model for the  $V_{max}/A_{max}$  ratio of strong ground motions using genetic programming. *Comput Geosci* 36:1523–1531
2. McGuire RK (1978) Seismic ground motion parameter relations. *J Geotech Eng Div* 104:481–490
3. Zhu TJ, Heidebrecht AC, Tso WK (1988) Effect of peak ground acceleration to velocity ration on ductility demands of inelastic systems. *Earthquake Eng Struct Dynam* 16:63–79
4. Sawada T, Hirao K, Yamamoto H, Tsujihara O (1992) Relation between maximum amplitude ratio ( $A/V$ ,  $AD/V^2$ ) and spectral parameters of earthquake ground motion. In: 10th world conference on earthquake engineering, Balkema, Rotterdam
5. Rathje EM, Abrahamson NA, Bray JD (1998) Simplified frequency content estimate of earthquake ground motions. *J Geotech Geo-Environ Eng* 124(2):150–159

# Along Wind Response of Communication Tower



Nikhil Dhandar, A. Y. Vyavahare and Trupti Nikose

**Abstract** Presently, communication technology has become significantly important. The need for tall towers has been increasing with the requirements for effective communication, particularly for television, radio, GSM, and Internet traffic. Analysis and design of these dynamically sensitive towers are generally governed by the wind loads. Wind excitation induces fluctuating stresses in the members of the tower leading to fatigue damages of the members. In achieving safety with economy for construction, accurate determination of wind load is important. Design wind loads are calculated from the provisions given in the codes and standards. Communication towers subject to vibrations due to wind gusts, which are analyzed using the gust load factor method. This method gives an accurate estimation of wind response of the structure as it considers the resonant component of wind loads. In this paper, microwave lattice tower heights of 21, 30, and 50 m are considered and wind forces are determined using IS 875-1987, IS 875 (Draft), ASCE 7-2010, AS-NZS 1170.2-2011, and HK-2004 design codes and standards. These towers are analyzed for wind velocity of 39 m/s under terrain category-I, terrain category-II, and terrain category-III, and results are compared. It is observed that there is variation in the wind loads and this is primarily due to the difference in definition of wind field features in the compared codes and standards.

**Keywords** Along wind · Lattice tower · Gust factor · Terrain category

---

N. Dhandar · A. Y. Vyavahare (✉) · T. Nikose  
Applied Mechanics Department, Visvesvaraya National Institute  
of Technology, Nagpur 440010, India  
e-mail: ayv@apm.vnit.ac.in

N. Dhandar  
e-mail: nikhilnd@gmail.com

T. Nikose  
e-mail: truptinikose@gmail.com

## 1 Introduction

In current century, communication technology is at peak. Due to the growth in use of mobile phones had increased the demand in design and implementation of communication towers. In case of emergency (natural disasters), communication towers play a vital role in transfer of emergency protocols. Further, another predominant application is in military (defense) where these towers use radar technology. These towers are used to broadcast or to send and receive data (information) through radio waves such as radio, television, cell phones. They send and receive the information through antennas which are supported on these towers. They are generally made up of steel sections.

The towers are analyzed for self-weight, wind load, earthquake load, and ice load if any. Wind loads are most predominant loads governing on the towers. Wind excitation induces fluctuating stresses in the tower with different amplitudes which will be developing fatigue damages in the members. Hence, it is necessary to do wind analysis and know the response of structure. The response of structure to wind depends on wind characteristics. These structures are sensitive to wind, and therefore along wind response is important.

In the previous studies, Venkateswarlu et al. [1] had done the stochastic analysis to calculate dynamic wind response on microwave lattice tower. The gust response factor computed was compared, with values obtained by formulae recommended by Indian, Australian, British, and ASCE standards with derived simplified expressions. Harikrishna et al. [2] have done analytical and experimental studies on the gust response of a 52-m-tall steel lattice tower under wind loading. Analytical comparison of calculation of gust factor is done by different codes, i.e., Indian, Australian, and British codes. British standards and Australian standards for steel lattice towers recommend different GRFs for the design of main leg members and main bracings, and for serviceability criteria.

In this paper, procedure given for calculating wind load is reviewed and compared with different international wind codes and standards. To highlight the comparison, examples on microwave lattice tower of heights 21, 30, and 50 m have been selected and the responses had been obtained according to IS 875-1987 (Indian code) [3], IS 875 (Indian Draft code) [4], ASCE 7-2010 (American code) [5], AS-NZS 1170.2-2011 (Australian code) [6], and HK-2004 (Hong Kong code) [7].

## 2 Provision for Wind Load

Most of the international codes have given procedures to calculate wind load by gust factor method. As per Indian Wind Code, building and closed structures with a height to minimum lateral dimension ratio of more than 5 or building and structures whose natural frequency in the first mode is less than 1.0 Hz shall be examined for dynamic effects of wind.

For calculation of wind loads, codes and standards have given different parameters which affect the wind loads. Important parameters include basic wind velocity, risk factor/terrain categories, design wind speed, design wind pressure, force coefficient, and gust factor. The codal comparison is tabulated in Table 2.

## ***2.1 Terrain Category***

Terrain category is the characteristic of the surface irregularities of an area which arises from natural or constructed features. In Indian and Australian codes, terrain is classified into four categories. American code terrain is classified into three different categories. Hong Kong code has only one category. In this study for comparison of codes, three categories are considered and explained as follows.

Terrain Category 1—Exposed open terrain with few or no obstructions and in which the average height of any height of any object surrounding the structure is less than 1.5 m (includes sea coast regions and flat treeless plains).

Terrain Category 2—Open terrain with well-scattered obstructions having height between 1.5 and 10 m.

Terrain Category 3—Terrain with numerous large high closely spaced obstructions.

## ***2.2 Basic Wind Velocity***

Basic wind speed ( $V_b$ ) depending on the location of tower is required for analysis. In every code, there are maps or predetermined basic wind velocity according to location. This basic wind velocity is calculated by taking average gust time of 3 s; 10 min; or 1 h. In IS875(Part 3), ASCE 2010, and AS-NZS 2011, the average gust speed is 3 s for height of 10 m above the ground, and in Hong Kong code, the average gust speed is given for 1 h.

## ***2.3 Averaging Time***

Different codes and standards have different average interval time. Generally, three averaging values adopted in codes and standards are 3 s, 10 min, and 1 h. A summary of averaging time for basic wind speed, gust loading factor, and wind-induced response given in codes and standards is tabulated in Table 1.

**Table 1** Averaging time in codes/standards

Code	IS 875-1987	Draft Code IS 875	AS/NZ 1170	ASCE7-2010	HK-2004
$V_b$	3 s	3 s	3 s	3 s	1 h
GLF	1 h	1 h	1 h	3 s	1 h

## 2.4 Design Wind Speed

The basic wind speed is converted to design wind speed by considering the effects of terrain, topography, importance of structure, ground roughness, return period and size of the structure, and local topography. General design wind speed is given as

$$\text{Design Wind Speed } (V_z) = V_b \times k_1 \times k_2 \times k_3 \quad (1)$$

where  $V_b$  is basic wind speed and  $k_1$ ,  $k_2$ , and  $k_3$  are factors for topography, importance of structure, return period of structure, and directionality factor.

## 2.5 Design Wind Pressure

Design wind pressure is calculated by multiplying design wind speed multiplied with factor to convert it to pressure. For design wind pressure, Hong Kong code is giving direct values with respect to height. In other country codes, it is generalized as stated in Eq. (2).

$$P_z = 0.5 \times \rho \times V_z^2 \quad (2)$$

where  $\rho$  is density of air.

## 2.6 Force Coefficient

Force coefficient is calculated by calculating solidity ratio. Solidity ratio is equal to the effective area (projected area of all the individual elements) of a frame normal to the wind direction divided by the area enclosed by the boundary of the frame normal to the wind direction.

Force coefficient for lattice towers of square or equilateral triangle section with flat-sided members for wind blowing against any face is given in codes. In this paper, flat-sided members are considered.

Force coefficient variation for 21 m tower is given in Fig. 1.

**Table 2** Comparative code standards for determining wind response

Parameter/codes	IS 875-1987	AS/NZS 1170.2.2011	ASCE.7.2010	HK 2004	Draft code IS 875
Z	H	H	0.6H	H	H
g	Figure 8 of code	$g_R = \sqrt{2 \ln(600m_0^a)}$ $g_v = 3.7$	$g_R = \sqrt{2 \ln(3600m_1)} + \frac{0.577}{2 \ln(3600m_1)}$ $g_v = 3.4$	$g_R = \sqrt{2 \ln(3600H_0)}$ $g_v = 3.7$	$g_R = \sqrt{2 \ln(3600I_0^d)}$ $g_v = 3.5$
B	Figure 9 of code	$1 + \frac{\sqrt{0.26(h-m)^2 + 0.4b^2}}{L_h}$	-	$\frac{1}{1 + \frac{\sqrt{8(h-v)^2 + 6a^2}}{4H}}$	$\frac{1}{1 + \frac{\sqrt{8(h-v)^2 + 6a^2}}{2H_0}}$
E	Figure 11 of code	$\frac{\pi N}{(1 + 70.8N^2)^{0.6}}$	$\frac{7.47N_0}{(1 + 10.3M)^{0.75}}$	$\frac{0.47}{(2 + N^2)^{0.6}}$	$\frac{\pi N}{(1 + 70N^2)^{0.6}}$
S	Figure 10 of Code	$\frac{1}{1 + \frac{3.5e_0(1 + e_0/h)}{V_{des,0}}} \left[ \frac{1 + \frac{m_0 g_{R1}(1 + e_0/h)}{V_{des,0}}}{1 + \frac{m_0 g_{R2}}{V_{des,0}}} \right]^d$	$R_H R_B (0.53 + 0.74R_L)^f$	$\frac{1 + \frac{3.5e_0 h}{V_{des,0}}}{1 + \frac{4e_0 h}{V_{des,0}}}$	$\frac{1}{1 + \frac{4e_0 h(1 + e_0/h)}{V_{des,0}}} \left[ \frac{1 + \frac{4e_0 h(1 + e_0/h)}{V_{des,0}}}{1 + \frac{4e_0 h(1 + e_0/h)}{V_{des,0}}} \right]$
G <sub>f</sub> /C <sub>dyn</sub>	$1 + g_f r \sqrt{B(1 + \phi)^2 + \frac{g_f^2}{\beta}}$	$\frac{1 + 2h_0 \sqrt{g_f^2 B_0 + \frac{m_0 g_{R2}^2}{2}}}{(1 + 2g_f h_0)}$	$G_f = 0.925 \left[ \frac{1 + 1.7I_z \sqrt{g_f^2 G_0 + g_f^2}}{1 + 1.7R_f I_z} \right]^g$	$1 + 2I_h \sqrt{g_f^2 B + \frac{g_f^2 S F}{\gamma}}$	$1 + 2I_h \sqrt{g_f^2 B_0 + \frac{m_0 g_{R2}^2}{2}} \frac{1}{(1 + 2g_f h_0)}$
F	$C_f A_f P_z C_{dyn}$	$(0.5 \rho_{air})^2 C_{fig} C_{dyn} A_z$	$q_z C_f A_f$	$C_f A_f \bar{q}_z G$	$C_f A_f P_z C_{dyn}$

where <sup>a</sup> $n_{0z}$ ,  $\eta_1$ , and  $f_0$  first-mode natural frequency

<sup>b</sup> $L_{th} = 85(h/10)^{0.25}$  a measure of the integral turbulence length scale at height  $h$  in m

<sup>c</sup> $N = n_d L_h [1 + (g_f h)] / V_{des,0}$  reduced frequency

<sup>d</sup> $I_h$  turbulence intensity, obtained from Table 6.1 of AS-NZS 1170.2: 2011 by setting  $z = h$

<sup>e</sup> $N_1 = \frac{n_d L_h}{V_z}$  where  $L_z = (\frac{z}{f_0})^6$  and  $V_z$  is the mean hourly wind speed at height  $z$

<sup>f</sup> $R_f = \frac{1}{\eta} \frac{1}{2\beta} (1 - e^{-2\beta})$  for  $\eta > 0$ ,  $R_l = R_0$ , setting  $\eta = 4.6\eta_1 h \bar{V}_z$ ,  $R_l = R_B$  setting  $\eta = 4.6\eta_1 h \bar{V}_z$ , and  $R_l = R_z$  setting  $\eta = 15.4\eta_1 L \bar{V}_z$

<sup>g</sup> $Q = \sqrt{\frac{1}{1 + 0.63 \left( \frac{g_f h}{V_z} \right)^{0.67}}}$

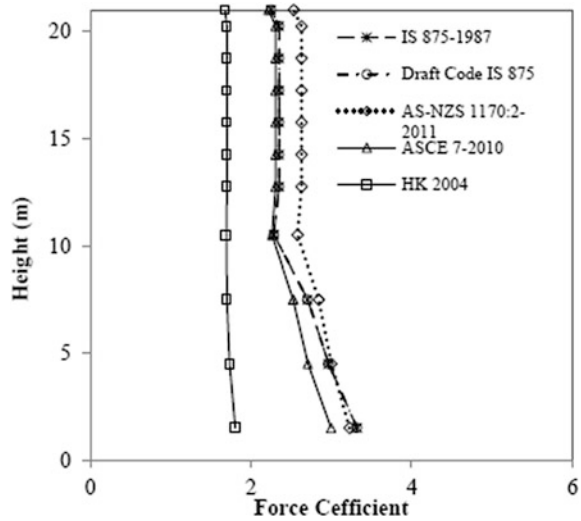
<sup>h</sup> $L_{th} = 1000 \left( \frac{h}{10} \right)^{0.25}$  the effective turbulence length scale

<sup>i</sup> $N = n_d L_h / V_h N$  reduced frequency (non-dimensional)

<sup>j</sup> $L_{th} = 100 \left( \frac{h}{10} \right)^{0.25}$

<sup>k</sup> $N = f_0 L_h [1 + (g_f h)] / V_h$  reduced frequency

**Fig. 1** Variation of force coefficient with respect to height



### 2.7 Gust Loading Factor

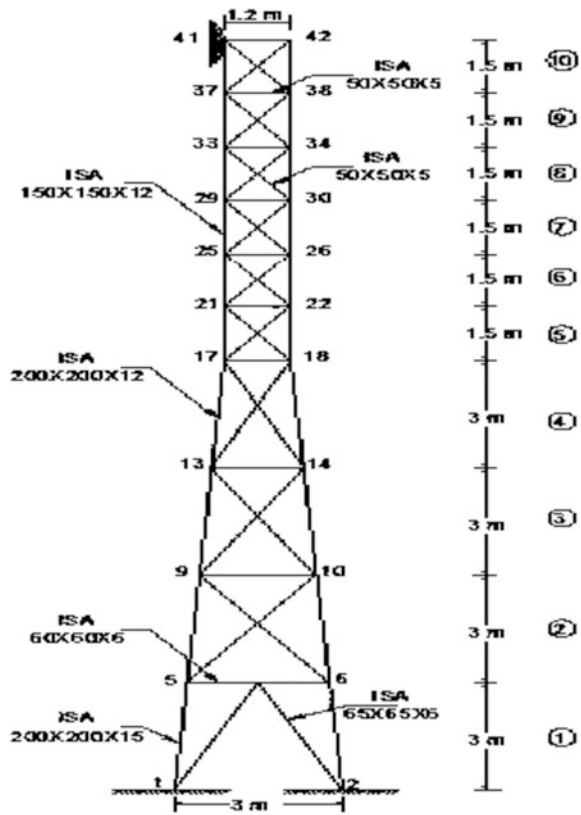
In general, wind speed in the atmosphere increases as increase in the height from zero at ground level to maximum at the required height. For calculation purpose, this wind variation is separated into two parts, i.e., mean and fluctuating components. Mean wind load component is calculated from average wind speed decided for particular region recommended in different codes. Fluctuating component is evaluated by considering dynamic amplifications, size reduction effects, and turbulence in wind. This is taken into account in determining gust average time as considered in codes and the gust factor. The gust factor converts the dynamic response phenomena of wind into static one for effective and easy design of structure. It is the ratio of peak wind gust and average wind speed over a period of time. Gust factor is calculated by the equations given in codes.

## 3 Results and Discussion

To compare the international codes/standards considered in this study, example towers are analyzed using each standard. Microwave square lattice towers of 21 m height as shown in Fig. 2, 30 m height as shown in Fig. 3, and 50 m height as shown in Fig. 4 are considered.

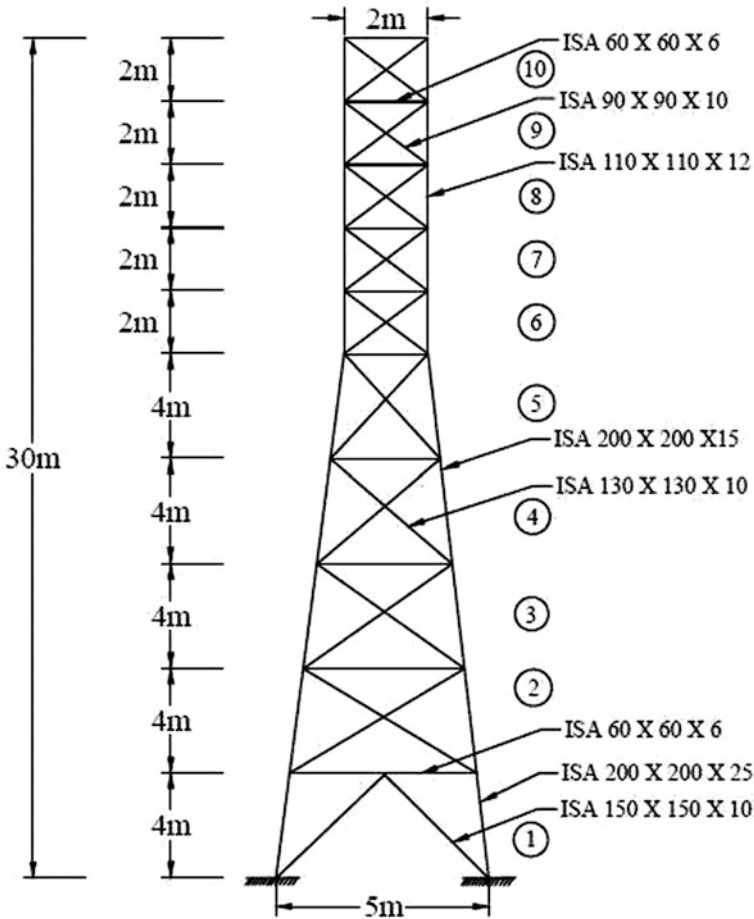


Fig. 2 Microwave tower details of 21 m height



Wind loads are calculated for terrain category-I, terrain category-II, and terrain category-III. The wind force is calculated for basic wind velocity of 39 m/s with damping ratio as 0.02. As per Indian code provision, the risk coefficient ( $k_1$ ) is taken as 1.06 and topography factor ( $k_3$ ) as 1, whereas the terrain height factor ( $k_2$ ) varies with respect to height.

The along wind force response for towers under three terrain categories as per Indian code, Australian code, American and Hong Kong code is calculated. The shear forces and base bending moments due to wind force in along wind direction are compared and are given in Figs. 5, 6, 7, 8, 9, and 10.



**Fig. 3** Details of microwave lattice tower of 30 m height

From the comparison, it is observed that for terrain category 1 and terrain category 2 IS 875-1987 code is giving higher values for all three heights of tower whereas for terrain category 3 American code is giving higher values for all three heights of the illustrated tower.

**Fig. 4** Details of microwave lattice tower of 50 m height

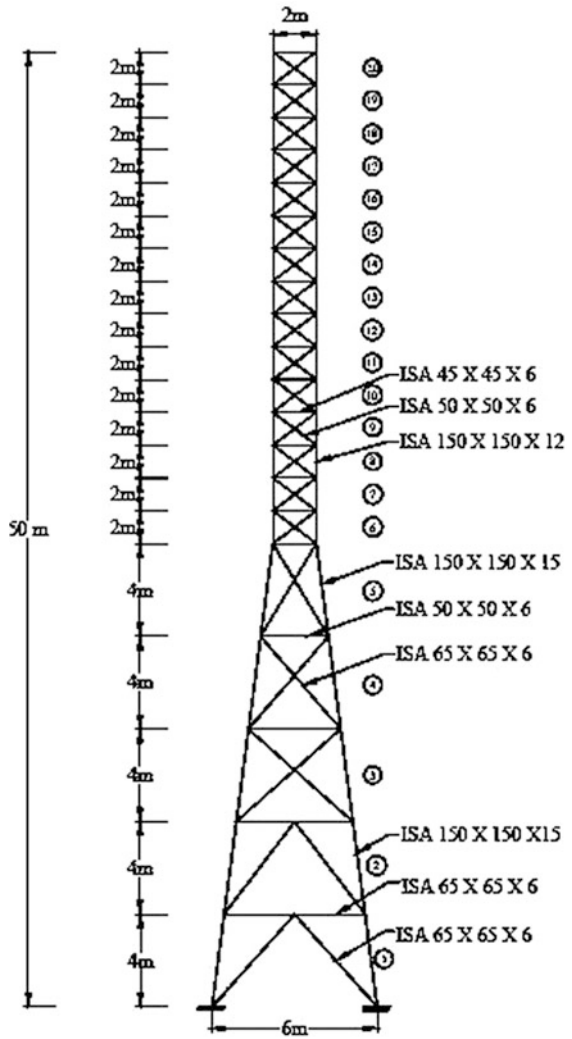


**Fig. 5** Variation of shear forces of 21 m tower for wind velocity 39 m/s

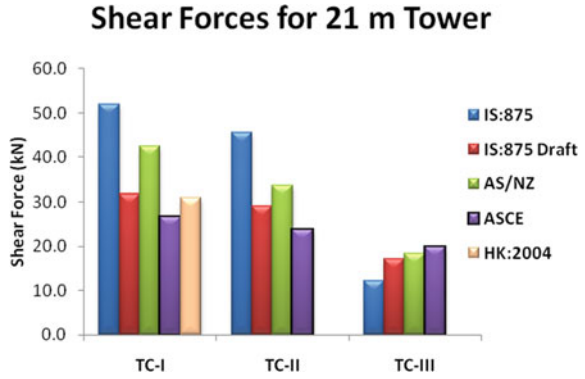


**Fig. 6** Variation of base bending moment of 21 m tower for wind velocity 39 m/s

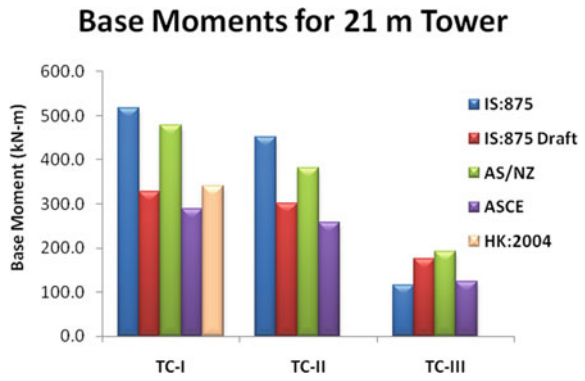


**Fig. 7** Variation of shear forces of 30 m tower for wind velocity 39 m/s

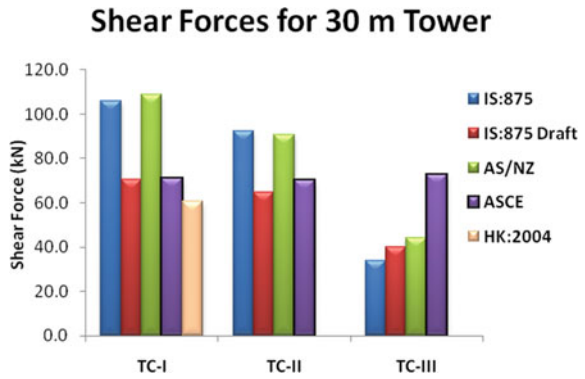


**Fig. 8** Variation of base bending moment of 30 m tower for wind velocity 39 m/s

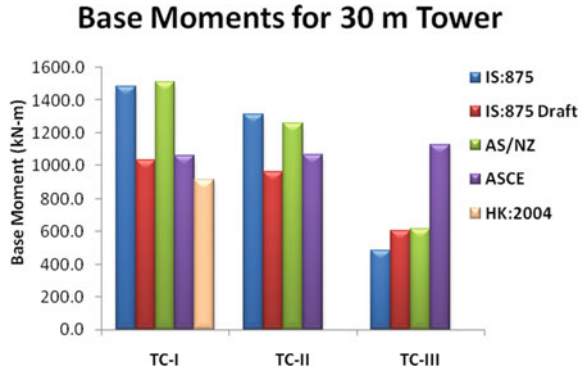


**Fig. 9** Variation of shear forces of 50 m tower for wind velocity 39 m/s

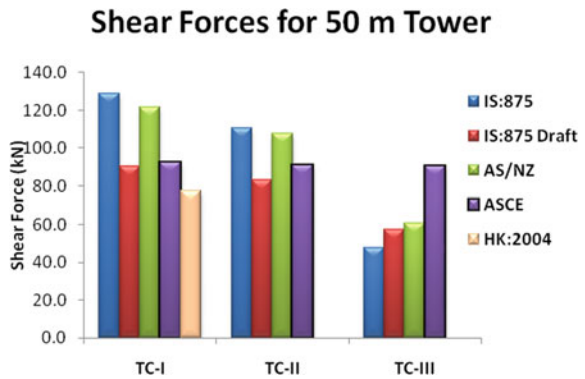
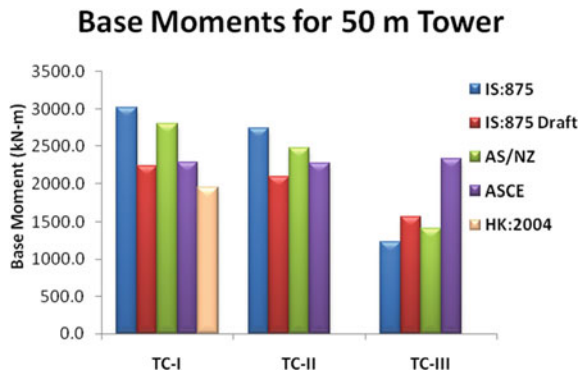


**Fig. 10** Variation of base bending moment of 50 m tower for wind velocity 39 m/s



## 4 Conclusion

All international codes and standards use gust factor method for estimating the wind loads in along wind direction for slender structures like towers. Each code gives its unique definition for different parameters like mean velocity, wind pressure, wind field characteristics, risk factor, gust factor, and force coefficient. These differences lead to variation in the wind load calculations for each code. However, the comparison is achieved by determining the factors affecting the along wind loads for category 1, 2, and 3.

In category 1 and 2, IS 875 code gives nearly twice the value when compared with results calculated using other codes. This may lead to uneconomical design of towers. AS-NZS code and IS 875 draft code give nearly same value of forces due to similar gust factor equations, whereas Hong Kong code gives varying force.

Force coefficient purely depends on the solidity ratio. As the tower height increases, the tower width becomes less and thereby exposed area becomes more and the solidity ratio increases which result in decreases in force coefficient values. Gust factor also decreases as the height of tower increases in all the cases considered.

## References

1. Venkateswarlu B, Harikrishna P, Rajan SS, Kumar MSR (1994) Stochastic gust response of microwave lattice towers. *Comput Struct* 52(5):1031–1041
2. Harikrishna P, Shanmugasundaram J, Gomathinayagam S, Lakshmanan N (1999) Analytical and experimental studies on the gust response of a 52 m tall steel lattice tower under wind loading. *Comput Struct* 70:149–160
3. IS 875 Part-3 (1987) Code of practice for design loads (other than earthquake loads) for buildings and structures
4. Krishna P, Kumar K, Bhandari NM (2002) IS: 875 (Part3): Wind loads on buildings and structures-proposed draft & commentary. Document No.: IITK-GSDMA-Wind (2002): 02-V5
5. ASCE 7 (2010) Minimum design loads for buildings and other structures
6. AS-NZS 1170: Part 2 (2011) structural design actions (wind actions)
7. HK (2004) code of practice for wind effects in Hong Kong

# Predictive Models for Ground Motion Parameters Using Artificial Neural Network



J. Dhanya, Dwijesh Sagar and S. T. G. Raghukanth

**Abstract** In this article, a predictive model for ground motion characteristics is developed using the artificial neural network (ANN) technique. This model is developed to predict peak ground acceleration (PGA), peak ground velocity (PGV), peak ground displacement (PGD), spectral acceleration at 0.2 and 1 s. The input parameters of the model are moment magnitude ( $M_w$ ), closest distance to rupture plane ( $R_{cd}$ ), shear wave velocity in the region ( $V_{s30}$ ), and focal mechanism ( $F$ ). The updated NGA-West2 database released by Pacific Engineering Research Center (PEER) is employed to develop the model. A total of 13,678 ground motion records are used to develop the model. The ANN architecture considered in the study has four input nodes in the input layer, three neurons in the hidden layer, and three output nodes in the output layer. The ANN is trained by a hybrid technique combining genetic algorithm and Levenberg–Marquardt technique. The results of the study are found to be comparable with the existing relation in the global database. The model developed can be further used to estimate seismic hazard.

**Keywords** Ground motion · Genetic algorithm · ANN · Attenuation relationship

## 1 Introduction

Ground motion prediction equations (GMPE) are essential in hazard estimation as well as for the seismic analysis of the structures. There are several ground motion prediction equations available across the globe using various regression techniques [1].

---

J. Dhanya · D. Sagar · S. T. G. Raghukanth (✉)  
Department of Civil Engineering, Indian Institute  
of Technology Madras, Chennai 600036, India  
e-mail: raghukanth@iitm.ac.in

J. Dhanya  
e-mail: dhanyaj17@gmail.com

D. Sagar  
e-mail: dwijeshsagar@gmail.com

Recently, artificial neural network (ANN) technique is adopted in the field of earthquake engineering [2, 3]. The advantage of this method is that it is simple and efficient in capturing the complex characteristics of earthquake ground motion in comparison with other methods. But established ANN methodology might tend to converge at local minimum [4]. This drawback is addressed by a hybrid technique combining global optimization techniques like genetic algorithm ( $G_a$ ) along with Levenberg–Marquardt (LM) technique to train the ANN model developed [5]. Thus, this algorithm shares both global and local search methods and thereby explores the full modal space. Another constraint is that the efficiency of model in accurately predicting the physical phenomenon depends on the number of ground motion data.

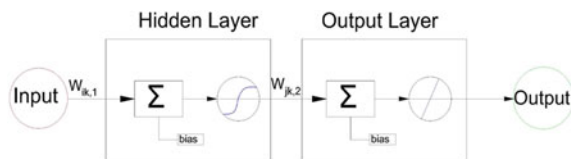
In the present study, the database available in the Pacific Engineering Research Center (PEER) and Next Generation Attenuation (NGA)-West 2 is used. This is a global database and hence is applicable for seismically active regions like Himalayas as well. This work focuses on developing a ground motion prediction model using ANN to determine peak ground acceleration (PGA), peak ground velocity (PGV), peak ground displacement (PGD), and the spectral acceleration (Sa) for 5% damping at time period 0.2 and 1 s. These values of spectral accelerations can be used to construct the design response spectra by following the approach given in the international code [6]. Since the ground motion is mainly influenced by the source, path, and site characteristic, moment magnitude ( $M_w$ ), fault mechanism ( $F$ ), closest distance to fault plane ( $R_{cd}$ ), and shear wave velocity ( $V_{s30}$ ) are chosen as input parameters. The ground motion prediction model so developed is compared with the existing relation [7]. The sensitivity of each input variable on the prediction is determined using Garson’s algorithm [8].

## 2 Methodology

### 2.1 Artificial Neural Network

Artificial neural network is developed in the early 1940s by McCulloch and co-workers [9]. The basic architecture of a feed-forward, which does not have any cyclic loop, ANN is illustrated in Fig. 1. It is clear that ANN architecture has an input layer, hidden layer, and output layer. The number of nodes in the input and output layers is equal to the number of input and output parameters, respectively, that need to be modeled. The number of hidden layers and the number of neurons in

**Fig. 1** Typical architecture of artificial neural network





the hidden layer vary depending on the complexity of the problem. The nodes in the model are fully interconnected with connection weights. To determine these connection weights, the data available for the modeling is split into three parts, respectively, for training, validation, and testing. The training of ANN follows a standard back-propagation algorithm. Thus, determination of connection weight is an iterative process where first a set of weights are obtained by using training dataset and then it is validated with the corresponding validation dataset. The connection weights are updated using the training dataset only after comparing the model with the validation dataset. This process helps to prevent the network from over-fitting the model with respect to training dataset. One full training cycle is termed as epochs. Thus, the connection weights are optimized after suitable iterations and are checked for accuracy with the test dataset.

## 2.2 Hybrid Training Technique

Generally, Levenberg–Marquardt (LM) technique which locates local minima of complex function through iterative procedure is used for training the data. The solution of LM technique, which is a combination of steepest decent and Gauss–Newton method [10], is known to converge relatively faster, but results are dependent on the initial value. Hence, this method faces the disadvantage of getting converged to local minima if the initial values are assumed incorrectly. Therefore, in the present study, genetic algorithm, which is a global optimization technique, formulated by bio-inspired operators such as mutation, crossover, and selection, is used to determine the initial weights. The method is developed during the 1960s–1970s in University of Michigan [11]. This is a stochastic search algorithm which repeatedly modifies the population of individual solutions. Thus, each step individual is selected at random from the current population and uses them as parents to produce children for next generation. This is continued until the optimization criterion is met [12]. Thus, hereby combining the local and global search techniques, full modal space is investigated.

## 3 Statistics of Database Used to Develop Model

The PEER-NGA-West2 database [13] is used to develop the model in the present study. A total of 13,678 ground motion records are selected from the database, depending upon data quality. The magnitudes reported as surface wave magnitude ( $M_s$ ) and body wave magnitude ( $m_b$ ) are converted to moment magnitude ( $M_w$ ) using the expressions available in the literature [14]. Thus, there are 13,678 data points for each input parameters of the model, viz. moment magnitude ( $M_w$ ), closest distance to rupture plane ( $R_{cd}$ ), shear wave velocity in the region ( $V_{s30}$ ), and focal Mechanism ( $F$ ) and for output parameters, viz. PGA, PGV, PGD, and spectral

**Table 1** Statistics of the input and output variables used in the development of model

Parameter	$M_w$	$R_{cd}$ (km)	$V_{s30}$ (m/s)	$F$	PGA (cm/s <sup>2</sup> )	PGV (cm/s)	PGD (cm)	$Sa_{0.20s}$ (cm/s <sup>2</sup> )	$Sa_{1.00s}$ (cm/s <sup>2</sup> )
Mean	5.47	444.62	118.86	2.08	41.05	4.17	2.25	92.33	40.49
Std. Dev.	1.27	178.35	111.77	1.26	92.99	10.04	6.67	213.98	103.38
Kurtosis	1.76	7.74	26.36	2.00	57.74	69.55	640.97	67.80	61.54
Skewness	0.003	1.41	3.25	0.60	5.84	6.20	16.43	6.2	6.19
Minimum	3.20	89.32	0.05	1.00	0	0	0	0	0
Maximum	7.90	2100	1532.66	5.00	1734.70	256.62	365.92	4723.35	2057.14

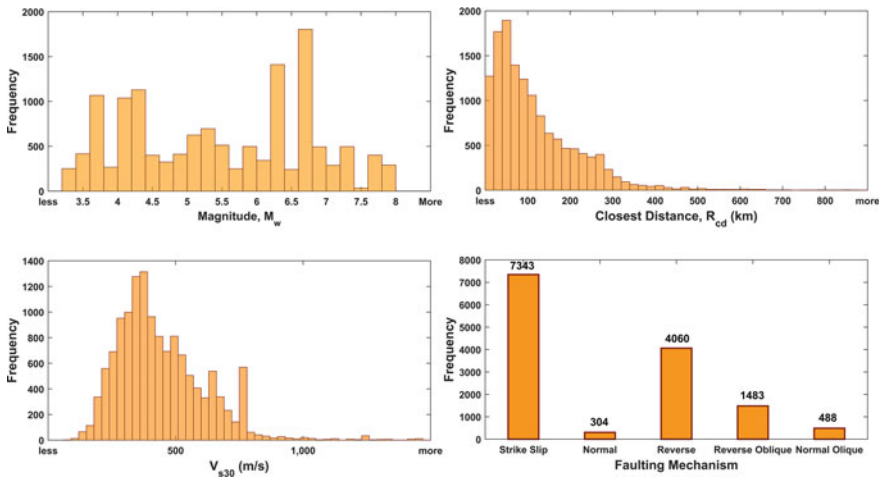


**Fig. 2** Histogram of the input variables

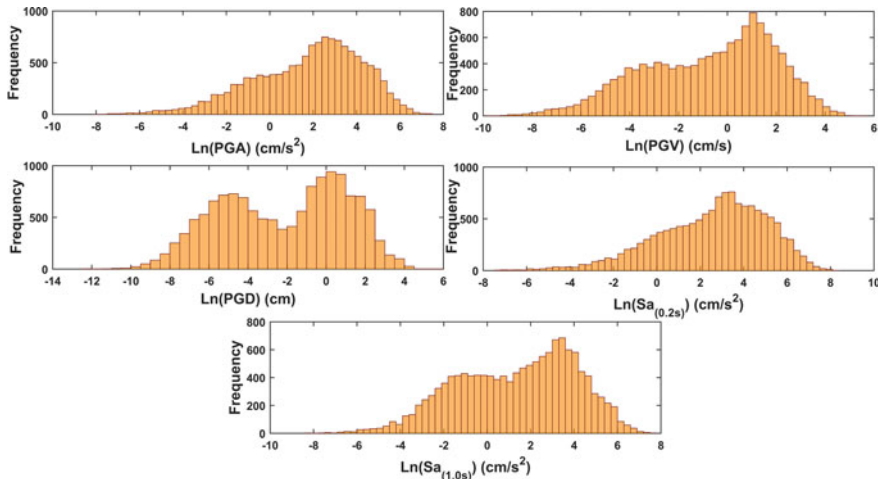


**Fig. 3** Histogram of output variables

acceleration at 0.2 and 1 s. The statistics of each of the parameter considered in the model is summarized in Table 1. It is clear from the high value of kurtosis for output variables that it follows a heavy-tailed distribution. The frequency distribution of the respective parameters is shown in Figs. 2 and 3 for input and output variables, respectively. The bin width of the distribution is according to Scott’s rule.

### 4 Ground Motion Predictions

The formulation considered for the development of ground motion prediction equation in the present study is as follows:

$$\begin{pmatrix} \ln(\text{PGA}) \\ \ln(\text{PGV}) \\ \ln(\text{PGD}) \\ \ln(\text{Sa}_{0.2\text{s}}) \\ \ln(\text{Sa}_{1\text{s}}) \end{pmatrix} = f(M_w \quad \ln(R_{cd}) \quad V_{s30} \quad F) \tag{1}$$

This functional form is modeled using suitable ANN architecture. According to universal approximation theorem, a single hidden layer can sufficiently capture any continuous and nonlinear function [15]. The number of hidden nodes is chosen as three for the present model after due trial and error. The resultant mathematical expression connecting the input and output parameters can be expressed as:

$$Y_j = f_2 \left( \text{bias}_{j,2} + \sum_{k=1}^m W_{jk,2} f_1 \left( \text{bias}_{k,2} + \sum_{i=1}^n W_{ik,1} X_i \right) \right) \tag{2}$$

where  $f_1$  and  $f_2$  are the transfer function between input–hidden nodes and hidden–output nodes, respectively,  $X_i$  and  $Y_j$  are the input and output parameters,  $W_{ik,1}$  and  $W_{jk,2}$  are the connection weight between input–hidden nodes and hidden–output nodes, respectively. Since the present work belongs to regression or function approximation, tanh function is a better choice as a transfer function  $f_1$ . A linear transfer function is adopted for  $f_2$ . The corresponding functional forms are as follows:

$$f_1(x) = \frac{1 - e^{-2x}}{1 + e^{-2x}} \quad \text{and} \quad f_2(x) = x \tag{3}$$

Here, since tanh function is used, input and output parameters are scaled between -1 and +1 using the following expression:

**Table 2** Weights and bias between input and hidden layers

Weights	Input (i)	Number of hidden neurons (k)		
		1	2	3
$W_{ik,1}$	$M_w$	5.7341	-2.3226	-1.3656
	$R_{cd}$ (km)	-0.8715	15.2744	-2.6368
	$V_{s30}$ (m/s)	-0.3220	-3.3960	2.0168
	$F$	-0.9922	3.2470	-2.3971
$bias_{k,1}$		7.3858	33.5215	-8.1236

**Table 3** Weights and bias between hidden and output layers

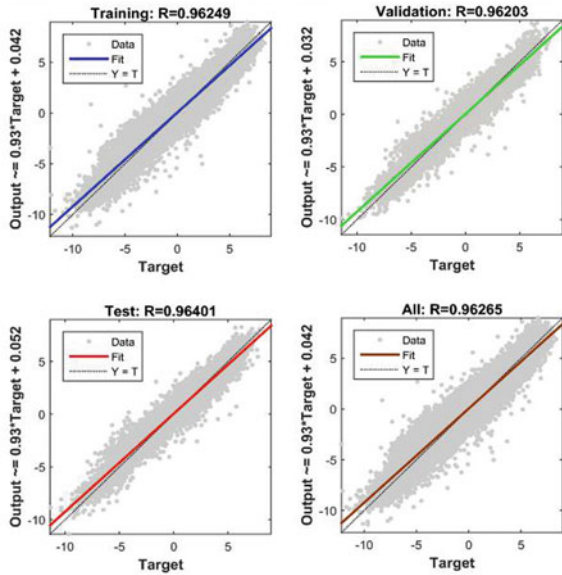
Weights	Input (i)	Number of hidden neurons (k)			
		1	2	3	$bias_{j,2}$
$W_{jk,2}$	PGA	-0.6453	0.0747	-1.5183	-0.9400
	PGV	4.8889	-3.0605	1.4563	0.1360
	PGD	4.0965	4.2706	0.4316	-8.5381
	$Sa_{0,20s}$	0.3001	-1.3003	-3.4404	-2.3211
	$Sa_{1,00s}$	-4.6001	1.1775	1.0026	4.6201

$$Y = a(Y - y_{\min}) + x_{\min}; \quad \text{where } a = \frac{x_{\max} - x_{\min}}{y_{\max} - y_{\min}} \quad (4)$$

where  $x_{\min}$  and  $x_{\max}$  have the value  $-1$  and  $+1$ , respectively, and  $y_{\min}$  and  $y_{\max}$  correspond to the minimum and maximum values of the parameter that is mapped. The minimum and maximum values of each parameter considered are shown in Table 1. In the present study, 70% of the data is used for training 15% for validation and 15% for testing. As explained, a hybrid method is adopted to train the model; thereby, first, Ga technique is employed to determine the initial weights of the network. Then, with these initial weights Levenberg–Marquardt technique is employed to determine optimum connection weights. This hybrid process improves accuracy of prediction model. The best performance of the model is obtained at 86 epochs. The final connection weights and bias for each link are summarized in Tables 2 and 3. These weights can be used in Eq. (2) to obtain predictor variables. Since the data is scaled, the actual prediction is obtained by substituting  $Y_j$  of Eq. (2) in the following expression:

$$Y_j = \frac{Y_j + 1}{a} + y_{\min} \quad (5)$$

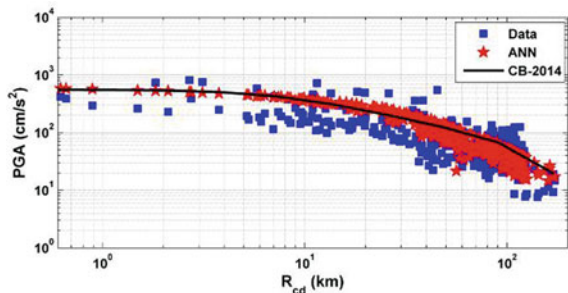
**Fig. 4** Regression fit of the model with data



### 4.1 Model Performance

According to hypothesis [16], a model is said to have strong correlation with the input and output values if correlation coefficient  $|R| > 0.8$  and the error values are minimum. It can be observed from Fig. 4 that the model is having a high value of  $R$  of the order 0.96 for the data used for training validation and testing. The normalized root mean square errors, between observed and predicted data, are estimated. The corresponding values for PGA, PGV, PGD,  $S_a$  ( $T = 0.2$  s), and  $S_a$  ( $T = 1$  s) are only 0.061, 0.052, 0.060, 0.065, and 0.059, respectively. Hence, the present model is observed to be efficient having good predictive ability.

**Fig. 5** Comparison of variation of PGA with respect to distance for 1990 Mw7.6 Chi-Chi earthquake



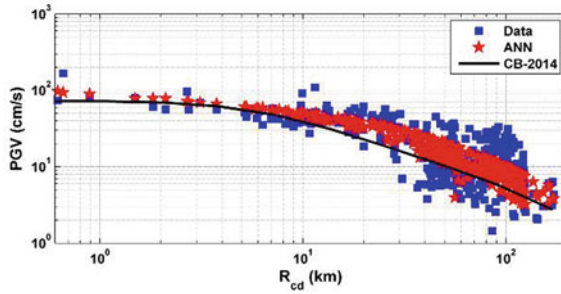


**Fig. 6** Comparison of variation of PGV with respect to distance for 1990 Mw7.6 Chi-Chi earthquake

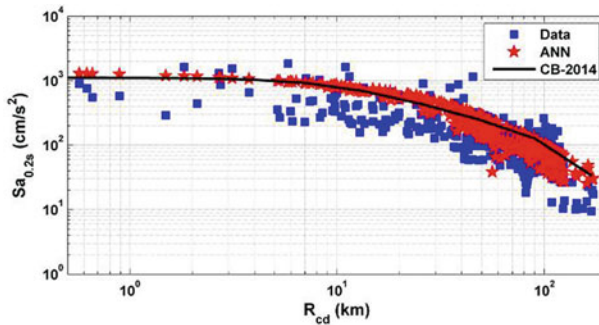


**Fig. 7** Comparison of variation of Sa ( $T = 0.2$  s) with respect to distance for 1990 Mw7.6 Chi-Chi earthquake

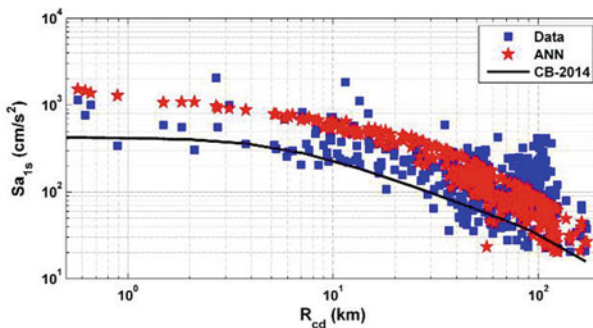


**Fig. 8** Comparison of variation of Sa ( $T = 1$  s) with respect to distance for 1990 Mw7.6 Chi-Chi earthquake

### 5 Comparison with Existing GMPE

The efficiency of the model can be better derived by comparing with the existing GMPE. The present ANN model is compared with, one of the GMPE developed from NGA-West2 database, Campbell and Bozorgnia [7] (CB-2014). Figures. 5, 6, 7, and 8 show the comparison of recorded data, present ANN model, and Campbell and Bozorgnia [7] (named as CB-2014) relation for 1990 Mw7.6 Chi-Chi earthquake. It is clear from the figure that the present model is able to capture the data efficiently and it is also following the same trend as that of the Campbell and Bozorgnia [7]. Further, it is clear from Fig. 8, showing the variation of Sa at time period 1 s with respect to distance, that the present model is better in predicting the data at higher periods than that of Campbell and Bozorgnia [7]. The normalized root mean square error of the present model is also observed to be less than that from existing GMPE. Thus, the present model is observed to be better capable in comparison with the existing relation for predicting data.

### 6 Parametric Analysis

In order to check the robustness of the present model, a parametric analysis is performed. Several combinations of input parameters are chosen for this purpose. Thus, the variation of PGA, PGV, PGD, Sa ( $T 0.2 s$ ), and Sa ( $T1 s$ ) for strike-slip focal mechanism is plotted with respect to distance for A Type ( $V_{s30}$ —1500 m/s) and C Type ( $V_{s30}$ —560 m/s) soil conditions for earthquakes of magnitude 5.5, 6.5, and 7.5 as shown in Figs. 9, 10, 11, 12, and 13. It is clear from the plots that the ground motion parameters considered in the study are higher for higher magnitude and the values are

**Fig. 9** Variation of PGA with respect to distance ( $R_{cd}$ ) for different magnitude and soil type

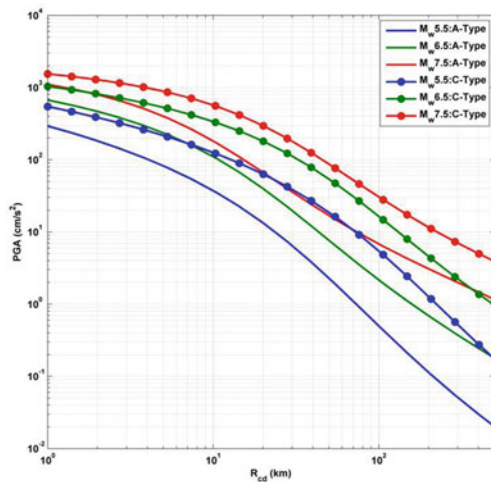


**Fig. 10** Variation of PGV with respect to distance ( $R_{cd}$ ) for different magnitude and soil type

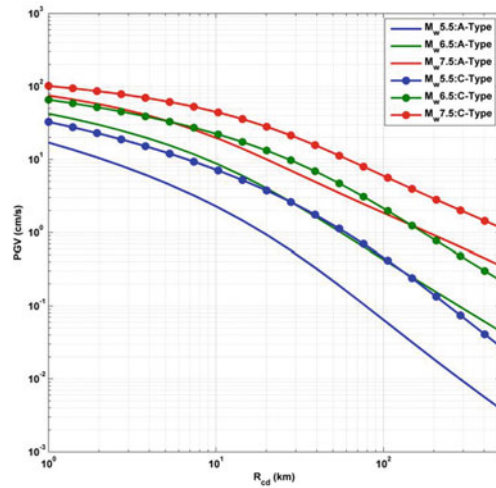
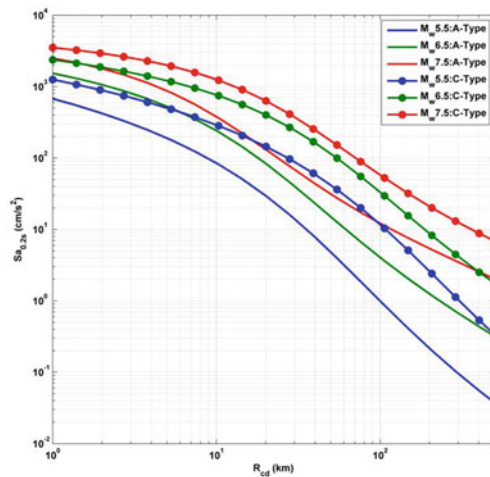


**Fig. 11** Variation of  $S_a$  ( $T$  0.2 s) with respect to distance ( $R_{cd}$ ) for different magnitude and soil type



attenuating with respect to distance conforming to the physical observations. It is known that the ground motion parameters get amplified for soft soil with respect to hard rock. The plots clearly show that the present model is able to capture this phenomenon as well. Thus, the present model is in close agreement with the observed ground motion characteristics and can be applied to get reliable estimates for a given earthquake magnitude, distance to rupture plane, soil type, and focal mechanism.



**Fig. 12** Variation of PGD with respect to distance ( $R_{cd}$ ) for different magnitude and soil type

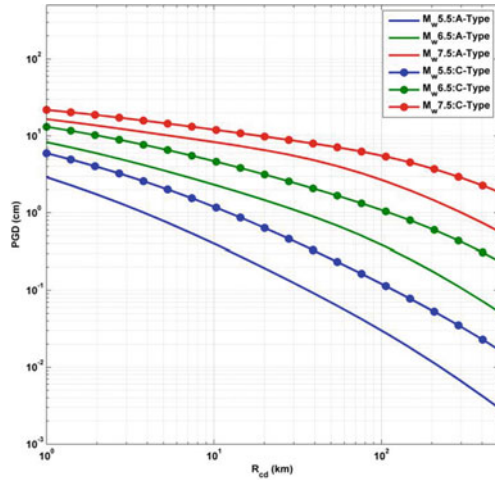
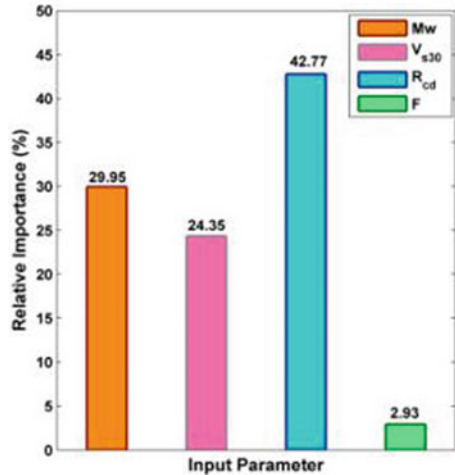


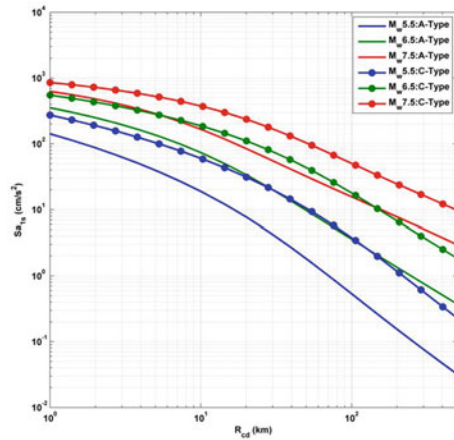
**Fig. 13** Contributions of input variable on the ANN model developed according to Garson’s method



## 7 Sensitivity Analysis

To understand the sensitivity of each input variable on output, relative importance values are calculated using Garson’s algorithm [8]. This method essentially partitions the hidden–output connection weights of the hidden neurons to that associated with input nodes. The relative importance value of the input parameters is illustrated in Fig. 14. It is clear that  $R_{cd}$  exerts higher influence on the variation of ground motion parameters. Further,  $M_w$  and  $V_{s30}$  also have significant effects.

**Fig. 14** Variation of  $S_a$  ( $T = 1$  s) with respect to distance ( $R_{cd}$ ) for different magnitude and soil type



## 8 Summary and Conclusions

In the present study, a feed-forward ANN model is developed to predict peak ground acceleration (PGA), peak ground velocity (PGV), peak ground displacement (PGD), spectral accelerations at 0.2 and 1 s. The predictions are performed for a given earthquake magnitude ( $M_w$ ), closest distance to rupture plane ( $R_{cd}$ ), shear wave velocity ( $V_{s30}$ ), and focal mechanism ( $F$ ). The susceptibility of the model to get captured in local minimum during the data training is addressed by assigning initial weights obtained from, the established global optimization technique, genetic algorithm. The comparison of the predicted model with the data and the existing ground motion relation is observed to be consistent. The parametric study with different combination of input parameters showed that the developed ANN model is able to capture the physical characteristics of ground motion. Thus, the present model is observed to be robust and can be easily applied to determine spectral ground motion characteristics. This model can be applied for the determination of seismic hazard and to obtain design response spectra.

## References

1. Douglas J (2011) Ground-motion prediction equations 1964–2010. Pacific Earthquake Engineering Research Center, Berkeley, CA
2. Alavi, AH, Gandomi AH (2011) Prediction of principal ground-motion parameters using a hybrid method coupling artificial neural networks and simulated annealing. *Comput Struct* 89(23):2176–2194

3. Chu D, Kerh T, Wu CH (2003) Analysis of strong motion information at checking stations of Kaohsiung area by back-propagation neural networks. *J Civil Eng Technol* 7(2):45–62
4. Hamm L, Brorsen BW, Hagan MT (2007) Comparison of stochastic global optimization methods to estimate neural network weights. *Neural Process Lett* 26(3):145–158
5. Matilla-García M, Argüello C (2005) A hybrid approach based on neural networks and genetic algorithms to the study of profitability in the Spanish stock market. *Appl Econ Lett* 12(5):303–308
6. IBC (2009) International building code. International Code Council
7. Campbell KW, Bozorgnia Y (2014) NGA-West2 ground motion model for the average horizontal components of PGA, PGV, and 5% damped linear acceleration response spectra. *Earthquake Spectra* 30(3):1087–1115
8. Garson GD (1991) Interpreting neural-network connection weights. *AI Expert* 6:47–51
9. Perlovsky LI (2001) *Neural networks and intellect*. Oxford University Press
10. Levenberg K (1944) A method for the solution of certain non-linear problems in least squares. *The Quarterly of Applied Mathematics* 2:164–168
11. Holland JH (1975) *Adaption in natural and artificial systems*. University of Michigan Press, Ann Harbor
12. Whitley D (1988) Applying genetic algorithms to neural network problems. International Neural Network Society
13. Ancheta TD, Darragh RB, Stewart JP, Seyhan E, Silva WJ, Chiou BS-J, Wooddell KE et al (2014) NGA-West2 database. *Earthquake Spectra* 30(3):989–1005
14. Scordilis EM (2006) Empirical global relations converting  $M_S$  and  $m_b$  to moment magnitude. *J Seismolog* 10(2):225–236
15. Alavi AH, Gandomi AH, Mollahasani A, Heshmati AAR, Rashed A (2010) Modeling of maximum dry density and optimum moisture content of stabilized soil using artificial neural networks. *J Plant Nutr Soil Sci* 173(3):368–379
16. Smith GN (1986) *Probability and statistics in civil engineering*. Collins, London

# Effect of Topography on Earthquake Ground Motions



Anjali Dhabu, J. Dhanya and S. T. G. Raghukanth

**Abstract** The topography of a region significantly affects the ground motions generated during an earthquake. Due to the computational complexities involved, complete three-dimensional analysis of the effect of topography is not studied in detail. The present study tries to understand this effect by simulating ground motions on three-dimensional ridge and valley using a finite element methodology. Here, first the simulated results from the developed model are compared with the existing analytical expressions for wave propagation in two dimensions (2D). Then, a study is performed with topography profile considered as Gaussian with different source locations. The comparison between the cases is performed based on peak ground displacement (PGD) and peak ground velocity (PGV) amplification ratios. It is noted that the location and amplitude of amplification are related to the relative position and depth of source with respect to topography. The study also attempts to develop a relationship between the amplification ratios and topographic gradient. The developed models can be used as a basis to estimate the possible amplification that can occur at a site due to an earthquake.

**Keywords** Earthquake ground motion · Topography · Amplification

---

A. Dhabu · J. Dhanya · S. T. G. Raghukanth (✉)  
Department of Civil Engineering, Indian Institute  
of Technology Madras, Chennai 600036, India  
e-mail: raghukanth@iitm.ac.in

A. Dhabu  
e-mail: anjalidhabu@gmail.com

J. Dhanya  
e-mail: dhanyaj17@gmail.com

## 1 Introduction

Regions with varying topography are subjected to colossal destruction when struck by an earthquake. The earthquake ground motions in such regions lead to several other natural hazards like landslides, soil liquefaction and further intensify resulting in damage. These damaging effects are clearly exemplified during the 2015 Nepal earthquake of moment magnitude ( $M_w$ ) 7.86, 2011 Sikkim earthquake of  $M_w$ , 6.9, 1934 Bihar–Nepal earthquake of  $M_w$ , 8.1, that occurred in the Himalayan region. Therefore, studying the effect of topography on earthquake-induced ground motions becomes important. The characteristics of ground motion are primarily governed by (i) location and type of seismic source, (ii) the medium through which the waves are propagating, and (iii) boundary condition. Topography of a region forms the free-surface boundary condition. Several studies have been carried out in the past to study the significance of topography on ground motions [1, 2] and to understand its effects on wave propagation in 2D analytically [3, 4]. However, very limited studies dealt with three dimensional (3D) modeling incorporating the topography, due to complexities in representing the surface undulations [5]. Recently, the development in finite element method has facilitated techniques that can model complex domain with lesser numerical complexities and computational cost [6, 7]. These methods are thus capable of incorporating the details of ground topography and material anisotropy for simulation of three-dimensional wave propagation.

The present study aims at analyzing the effect of topography on ground motions more extensively. Here, two types of topographies, namely ridge and valley, are considered. The modeling and simulation are performed with the aid of an established spectral finite element method (SPECFEM). The obtained results are analyzed in terms of peak ground displacement (PGD) and peak ground velocity (PGV) amplification ratios.

## 2 SPECFEM

SPECFEM method is introduced for simulations in computational fluid dynamics [6] and is later developed for simulating wave propagation in 3D earth model [7]. It is more realistic for ground motion simulations because of its ability to consider the actual surface topography and material anisotropy. Thus, it considers the effects due to lateral variation in the compression wave and shear wave speeds due to changing material property [8].

In this method, the region considered is first discretized into non-overlapping hexahedral elements. Here, the high-degree Lagrange interpolant is used to represent functions on the element. The control points needed to define polynomial of order  $n$  are  $(n + 1)^3$  Gauss–Lobatto–Legendre (GLL) points per element. After that, each of these elements is mapped to a reference cube using Jacobian matrix. While mapping, the method ensures non-singularity of the Jacobian matrix, particularly

for boundary elements. The stability of numerical simulation is ensured by Courant–Friedrichs–Lewy condition. According to this condition, the maximum time step should be such that it is always less than the time taken by the wave to travel through the smallest element. Finally, the equation of motion for all the elements is assembled to form the global equation of motion as:

$$\mathbf{M}\ddot{u} + \mathbf{C}\dot{u} + \mathbf{K}u = \mathbf{F} \quad (1)$$

where  $\mathbf{M}$  is the global mass matrix,  $\mathbf{C}$  is the global damping or absorbing boundary matrix,  $\mathbf{K}$  is the global stiffness matrix,  $\mathbf{F}$  represents the force or the source term, and  $u$  is displacement. The method uses the Newmark  $\beta$  integration method to march forward in time [8]. The detailed description of the method can be found in the literature [7]. In the present work, SPEC-FEM3D Cartesian package, a collection of FORTRAN subroutines, is used to simulate ground motions [9, 10]. These are executed using parallel programming based on message passing interface (MPI). For present study, the simulations are carried out in Rocks 6.1 (Emerald Boa) Cluster with AMD Opteron (TM) processor installed with CentOS 6.3 operating system. The machine has two nodes with 32 processors per node. Time required to generate synthetic ground motions for each case considered is 24 h approximately.

### 3 Simulation of Ground Motions

A region of 300 km  $\times$  300 km  $\times$  80 km is considered to simulate ground motions and thus study the effect of topography on it. The material property along the depth of the region is, deliberated as per that for Himalayan region, summarized in Table 1. In Table 1,  $V_p$  and  $V_s$  are the longitudinal wave and shear wave velocities, respectively, and  $Q_p$  and  $Q_s$  are the corresponding quality factors.

Topography of a region can be characterized by its slope. A gentle slope signifies a smaller elevation spread out over a larger region, while a steep slope signifies a topography of higher altitude spread out over a comparatively smaller region. Thus, elevation and span of the topography are two features which can

**Table 1** Material properties in Himalayan region

Depth (km)	$V_p$ (km/s)	$V_s$ (km/s)	Density (gm/cm <sup>3</sup> )	$Q_p$	$Q_s$
0–0.4	3.5	2.00	1.8	50	25
0.4–1.0	5.0	2.86	2.40	80	50
1.0–15.0	5.2	2.97	2.6	4000	2000
15.0–30.0	6.0	3.43	2.90	4000	2000
>30.0	8.33	4.83	3.30	1000	500

Source [17]

geometrically describe topography. Therefore, in this study topographies are categorized in terms of different height ( $h$ ) to length ( $l$ ) ratio ( $h/l$  ratio).

In present work, first the synthetic ground motions are simulated with topographies of specified  $h/l$  ratios and are compared with the available analytical results. Then, a parametric study varying the topography and source location is carried out to understand the variability of resultant ground motion and to establish a preliminary relation between the amplifications observed in ground motions with the slope of topography.

### 3.1 Comparison with Analytical Results

The diffraction of P, SV, and SH waves independently subjected to 2D topography with different  $h/l$  ratio has been studied analytically in the past [11, 12]. The present simulations being three-dimensional, a conical profile equivalent to the 2D triangular profile considered for analytical studies are chosen. The schematic representation of the conical topography with height  $h$  and length  $l$  considered for comparison is shown in Fig. 1.

Thus, ground motions are generated for three cases with  $h/l$  ratios, viz. 0.375, 0.5, and 0.75. The region is discretized into 246 spectral elements along each surface direction. The simulations are carried out with source of moment magnitude  $M_w$  7.5 and focal characteristic as strike angle  $0^\circ$ , dip angle  $45^\circ$ , and rake angle  $90^\circ$ . This source is considered at a depth of 10 km from the flat surface and is placed beneath the peak. The source is represented in terms of central moment tensor (CMT) solution equivalent to the chosen earthquake characteristics [13]. Table 2 presents a comparison of the analytical amplification ratios [11] and the obtained amplification ratios, the ratio of PGD at the peak to that obtained for a station far from the peak.

It is clear from Table 2 that horizontal amplification ratios are increasing with respect to the increase of  $h/l$  ratio of topography. The large variation in the values is attributed to the difference in source, medium characteristics, and wave scattering phenomenon that occurs. At the same time, it should be noted that the amplification ratios are showing similar trend. Thereby, the present model can be said to be comparable with the analytical results.

**Fig. 1** Schematic representation of conical topography considered

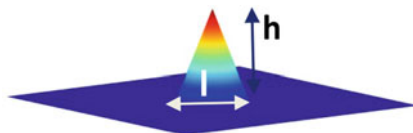


**Table 2** Comparison of amplification ratios

<i>h/l</i> ratio	0.375	0.5	0.75
Horizontal amplification ratio	11.06	11.89	18.34
<i>P</i> wave amplification ratio [11]	1.1	1.4	2
SV wave amplification ratio [11]	2.7	3.1	2.4

### 3.2 Effect of Topography on Ground Motion

A parametric study is performed with topographies considered as Gaussian distribution, with zero mean and different standard deviations, and by varying source locations with respect to peak. The layout of topographies considered, viz. ridge and valley, along with the different source locations chosen is shown in Fig. 2a, b, respectively. The four cases hence chosen for the study are summarized in Table 3. It should be noted that the depth of source from the flat surface is 5 km in the first case while it is 10 km in the next three cases.

It is also clear from Fig. 2 that the topographies are chosen to have a maximum elevation of 8000 m and a height to length ratio of 0.05. This particular elevation and aspect ratio are taken so that it resembles to that observed in Himalayas. The material property is assigned as that shown in Table 1. The region is discretized into 246 spectral elements along each surface direction. The final discretized region for ridge and valley is shown in Fig. 3a, b, respectively.

The source characteristics are same as mentioned in the previous section, but placed at different location in conversant with the cases considered. Using this model, synthetic ground motions are generated for duration of 135 s on a grid of size 151 × 151, with each station approximately 10 km apart.

**Fig. 2** Topography profiles considered in the study  
**a** ridge **b** valley

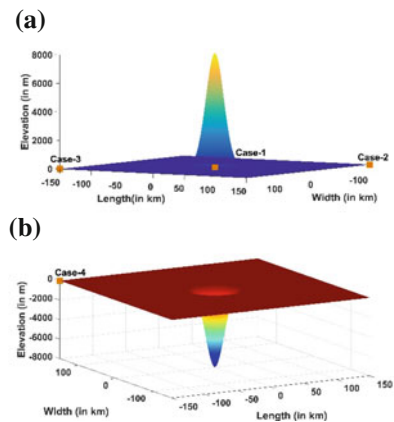
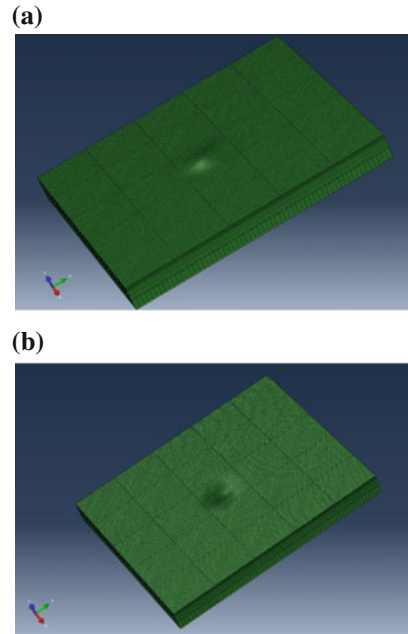




**Table 3** Cases considered in this study

Type of topography	Source parameters		Displacement amplification ratio	
	Distance (km) from peak of topography	Depth (km)	Horizontal	Vertical
Case 1: Ridge	0	5	58.41	185.5
Case 2: Ridge	90	10	8.078	6.275
Case 3: Ridge	90	10	8.355	6.552
Case 4: Valley	90	10	1.372	1.272

**Fig. 3** Mesh created by SPEC-FEM for **a** ridge  
**b** valley



## 4 Results and Discussion

The synthetic ground motion, from the models, is studied in terms of amplification ratio. Here, this ratio is defined as the ratio of PGD and PGV obtained at stations when topography is considered to the PGD and PGV at the same station when topography is not considered. A detailed illustration on the observations is discussed further.

### 4.1 Analysis of the Obtained Synthetic Data

The horizontal and vertical displacement amplification ratios for the cases mentioned in the earlier section are tabulated in Table 3. In first case, the earthquake source is located exactly beneath the peak of the ridge, 10 km deep from the flat surface. While in second case, the source is placed far away (approximately 250 km) from the peak. It can be noticed from Table 3 that the horizontal and vertical displacement amplification ratios undergo a sudden decrease in case 2 as compared to case 1. This is because of diminishing source effect as the distance between source and topography increases. The horizontal and vertical amplification patterns for cases 1 and 2 are shown in Figs. 4 and 5.

**Fig. 4** Amplification ratios for horizontal displacement  
a case 1 b case 2

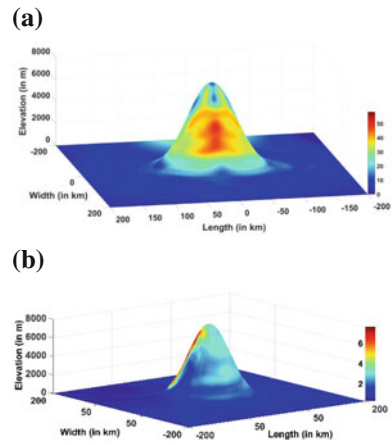


**Fig. 5** Amplification ratios for vertical displacement  
a case 1 b case 2

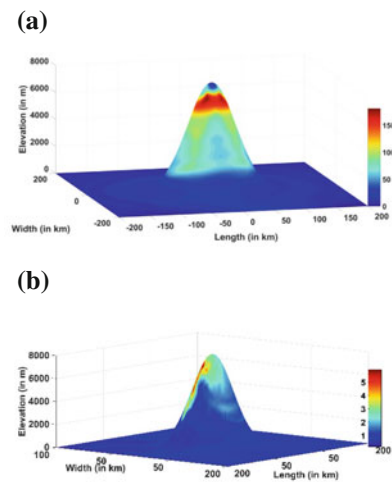


**Fig. 6** Horizontal amplification ratios for case 3  
**a** displacement **b** velocity

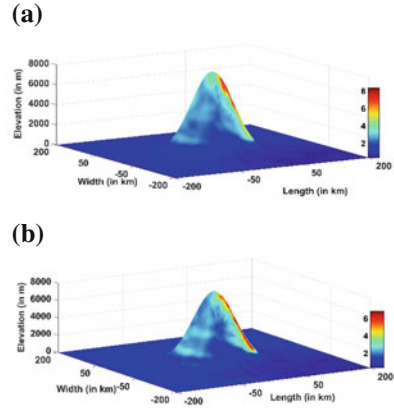
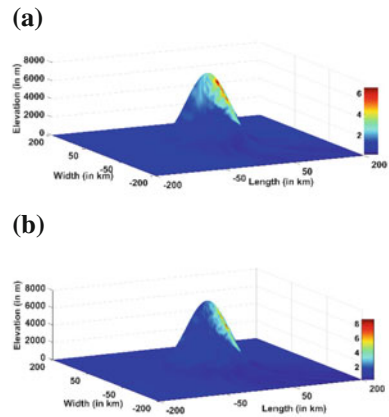


**Fig. 7** Vertical amplification ratios for case 3  
**a** displacement **b** velocity

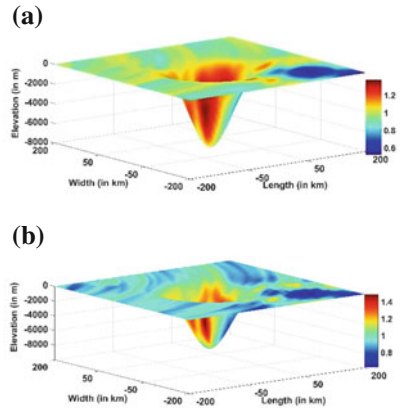


It can be observed from Figs. 4a and 5a that the region of maximum amplification is symmetric to the topography. This is because the source is located right below the peak, whereas the maximum amplification for case 2 is observed on the face of the profile away from the source location. This characteristic is confirmed by simulations with source in a different location (case-3) and is shown in Figs. 6 and 7.

Further, the simulation is performed for valley (case-4) and the maximum amplification is observed on the side closer to the source as shown in Fig. 8. These phenomenon observed in the cases considered might be due to the focusing and defocusing of waves during its traveling through the medium [14].

The amplification ratios for ground displacement obtained in this work are comparable to the amplifications obtained for ground accelerations for the numerical analysis carried out to study the response of three-dimensional hill near Tarzana, California when subjected to shear waves polarized in different directions [15].

**Fig. 8** Horizontal amplification ratios for case 4  
**a** displacement **b** velocity



### 4.2 Relation Between Amplification Ratio and Gradient of Topography

It is observed in the literature that soil properties like shear wave velocity are related to the slope of topography [16]. Hence, for the present study it will be interesting to check whether the amplification ratio also follows a similar trend. Hence, in this paper, a regression analysis is carried out to determine functional relationship between observed displacement and velocity amplification ratios with gradient of topography, which can be used as an empirical relation to estimate amplification factor at a site. Since in the analysis of structures the ground motion in horizontal direction is mostly considered, the regression analysis currently carried out for horizontal amplification ratios. Thus, amplification ratio is taken as dependent variable which is influenced by the gradient of topography. Amplification ratios of horizontal components of displacement and velocity are plotted against gradient (Fig. 9).

The data points are fitted with a best fit line, and it is found that the displacement and velocity amplification ratio for a given topography and source increase linearly with the increase in gradient. The equation of best fit line and the standard deviation in error is presented in Table 4. In the expression, DAR, VAR, and G correspond to displacement amplification ratio, velocity amplification ratio, and gradient of topography, respectively. This developed expression can be applied to estimate the possible amplification factor at a site of given gradient.

**Fig. 9** Horizontal amplification ratio versus gradient **a** displacement **b** velocity

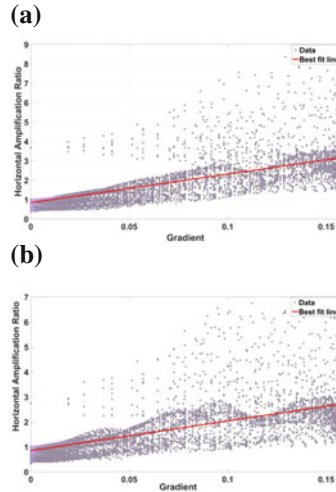


**Table 4** Derived relation between amplification factor and gradient of topography

Parameter	Amplification ratio	
	Displacement	Velocity
Model equation	DAR = 15G + 0.84	VAR = 12G + 0.85
$\sigma (\epsilon)$	0.417	0.394

## 5 Summary and Conclusion

The paper has tried to study the effect of three-dimensional topography on ground motions. This is achieved by performing simulations using different cases of topography profiles and source locations. It is observed that the region of maximum amplification depends on the relative position of source with respect to topography; i.e., in the case of ridge, maximum amplification occurs on the side away from the source, while in the case of valley, maximum amplification is observed on the side near the source.

Thus, the profile of topography and the position of source with respect to topography play a significant role in deciding the region of maximum amplification ratios. Further, amplification ratio is observed to follow an increasing trend with increasing gradient of the topography. This study can be further extended to find a generalized relation between the geographical features of the topography and the amplification ratios for a given position and mechanism of source.

## References

1. Bouchon M, Barker JS (1996) Seismic response of a hill: the example of Tarzana, California. *Bulletin of the Seismological Society of America* 86(1A):66–72
2. Bouchon M (1973) Effect of topography on surface motion. *Bull Seismol Soc Am* 63(2):615–632
3. Aki K, Larner KL (1970) Surface motion of a layered medium having an irregular interface due to incident plane SH waves. *J Geophys Res* 75(5):933–954
4. Sills LB (1978) Scattering of horizontally-polarized shear waves by surface irregularities. *Geophys J Int* 54(2):319–348
5. Lee SJ, Komatitsch D, Huang BS, Tromp J (2009) Effects of topography on seismic-wave propagation: an example from northern Taiwan. *Bull Seismol Soc Am* 99(1):314–325
6. Patera AT (1984) A spectral element method for fluid dynamics: laminar flow in a channel expansion. *J Comput Phys* 54(3):468–488
7. Komatitsch D, Tromp J (1999) Introduction to the spectral element method for three-dimensional seismic wave propagation. *Geophys J Int* 139(3):806–822
8. Pavlov V 3D Partitioning in SPECfEM3D Internal Mesher. Available online at [http://www.prace-ri.eu/IMG/pdf/3D\\_Partitioning\\_in\\_SPECfEM3D\\_Internal\\_Mesher.pdf](http://www.prace-ri.eu/IMG/pdf/3D_Partitioning_in_SPECfEM3D_Internal_Mesher.pdf)
9. <https://geodynamics.org/cig/software/specfem3d>
10. Komatitsch D, Vilotte JP, Tromp J (2015) Development team SPECfEM 3D cartesian user manual version 3. Princeton University, CNRS, University of Marseille and ETH Zürich
11. Gaffet S, Bouchon M (1989) Effects of two-dimensional topographies using the discrete wavenumber-boundary integral equation method in P-SV cases. *J Acoust Soc Am* 85(6):2277–2283
12. Bouchon M (1985) A simple, complete numerical solution to the problem of diffraction of SH waves by an irregular surface. *J Acoust Soc Am* 77(1):1–5
13. Aki K, Richards PG (1980) *Quantitative seismology: theory and methods*
14. Anggraeni D (2010) Modelling the impact of topography on seismic amplification at regional scale. Enschede, UT-ITC 46
15. Bouchon M, Baker SJ (1996) Seismic response of a hill: the example of Tarzana, California. *Bull Seismol Soc Am* 86(1A):66–72
16. Trevor IA, Wald DJ (2007) Topographic slope as a proxy for seismic site-conditions (VS30) and amplification around the globe. Geological Survey (US), No 2007-1357
17. Yu G, Khattri KN, Anderson JG, Brune JN, Zeng Y (1995) Strong ground motion from the Uttarkashi, Himalaya, India, earthquake: comparison of observations with synthetics using the composite source model. *Bull Seismol Soc Am* 85(1):31–50

# Real-time Hybrid Simulation Using an Electromagnetic Shaker



Mohit Verma, M. V. Sivaselvan and J. Rajasankar

**Abstract** This paper discusses a controller design strategy for the real-time hybrid simulation using an electromagnetic shaker. A two-storey shear building is adopted as the system whose response is emulated using hybrid simulation. The bottom storey is taken as the physical subsystem while the top storey is taken as the virtual subsystem. A control law is derived such that the mechanical impedance of the electromagnetic shaker matches to that of the virtual subsystem. The control law is validated by comparing the frequency responses of the virtual subsystem and the electromagnetic shaker from the physical subsystem acceleration to the force transferred. Finally, the experimental validation of the controller design strategy is carried out by the hybrid simulation of the two-storey structure. The frequency response obtained from the experiment and emulated system is found to be in good agreement with each other.

**Keywords** Hybrid simulation · Controller · Electromagnetic shaker  
Impedance · Real-time · Substructuring

---

M. Verma (✉)

Advanced Seismic Testing and Research Laboratory, CSIR-Structural Engineering  
Research Centre, Chennai 600113, India  
e-mail: mohitverma@serc.res.in

M. Verma · J. Rajasankar

Academy of Scientific and Innovative Research, Chennai, India  
e-mail: sankar@serc.res.in

M. V. Sivaselvan

Department of Civil, Structural and Environmental Engineering,  
University at Buffalo, Buffalo, NY, USA  
e-mail: mvs@buffalo.edu

J. Rajasankar

Theoretical & Computational Mechanics Laboratory, CSIR-Structural  
Engineering Research Centre, Chennai 600113, India

© Springer Nature Singapore Pte Ltd. 2019

A. Rama Mohan Rao and K. Ramanjaneyulu (eds.), *Recent Advances in Structural Engineering, Volume 2*, Lecture Notes in Civil Engineering 12,  
[https://doi.org/10.1007/978-981-13-0365-4\\_10](https://doi.org/10.1007/978-981-13-0365-4_10)

## 1 Introduction

Hybrid simulation is used to study the dynamic response of a structure by partitioning it into two substructures—physical (PS) and virtual (VS). The interface boundary condition is imposed on the PS by means of an actuator or shaker, and the corresponding work conjugate is measured and fed back to the VS. Hybrid simulation can be displacement-based or force-based depending on whether a displacement or force from the VS is applied at the boundary on the PS. Correspondingly, conventional hybrid simulation approaches use a displacement- or force-tracking controller. In this paper, we use a control strategy for hybrid simulation, which does not explicitly use a tracking controller. A shaker is used to apply forces on the PS. The control input to the shaker is computed so that it produces the same force on the PS as the VS would. This concept was developed by Stefanaki [1] (see also [2]) in the context of a hydraulic shaker. Here, we apply it with an electromagnetic shaker. Importantly, we use a very lightly damped PS, which poses major stability challenges using conventional approaches. The control law is experimentally validated through real-time hybrid simulation of a two-storey structure.

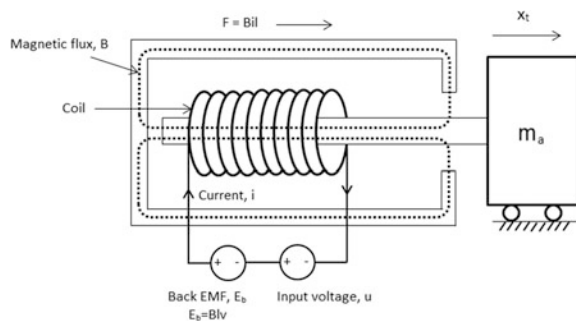
## 2 Mathematical Model of Electromagnetic Shaker

The schematic of an electromagnetic shaker is shown in Fig. 1. A mathematical model of electromagnetic shaker presented in this section has been adopted from [3, 4].

### 2.1 Principle of Force Generation

The electromagnetic shaker works on the principle that when a conductor carrying a current is placed in a magnetic field, it experiences a magnetic force. The force produced is proportional to the magnetic flux passing through the coil, the current flowing through the coil and to the length of wire within the flux field.

**Fig. 1** Schematic of an electromagnetic shaker





Mathematically,

$$F = Bil \quad (1)$$

where  $B$  is the magnetic flux density,  $i$  is the current, and  $l$  is the length of the conductor.

## 2.2 Back Electromotive Force (EMF)

According to Faraday's law, the relative motion between the armature and the magnetic field generates an EMF. The induced EMF resulting from a changing magnetic flux due to the relative motion has a polarity that leads to an induced current whose direction is such that the induced magnetic field opposes the original flux change (Lenz's law).

$$E_b = -Blv \quad (2)$$

where  $E_b$  is the back EMF and  $v$  is the velocity of the armature.

## 2.3 Electrical Impedance of the Coil

Electrical impedance is the measure of the opposition that a circuit offers to a current when a voltage is applied to it. If  $R$  and  $L$  are the resistance and inductance of the coil, then the voltage  $E$  and current across the circuit are related by:

$$E = Ri + L \frac{di}{dt} \quad (3)$$

## 2.4 Dynamic Equilibrium

The equation of motion of the armature of the electromagnetic shaker is given by:

$$m_a \ddot{x}_t + k_a x_t + c \dot{x}_t = Bil \quad (4)$$

where  $m_a$  is the total moving mass of armature assembly,  $k_a$  is the stiffness of the rubber bands in the shaker, and  $c$  is the equivalent viscous damping accounting for the mechanical and eddy current damping in the shaker. If the control input voltage is  $u$ , then the following equation can be obtained using Kirchoff's voltage law:

$$u - Bl\dot{x}_t = Ri + L \frac{di}{dt} \quad (5)$$

The model of the electromagnetic shaker is represented in the state-space form given by the following set of equations:

$$\begin{bmatrix} \dot{x}_1 \\ \dot{x}_2 \\ \dot{x}_3 \end{bmatrix} = \begin{bmatrix} 0 & 1 & 0 \\ -\frac{k_a}{m_a} & -\frac{c}{m_a} & \frac{Bl}{m_a} \\ 0 & -\frac{Bl}{L} & -\frac{R}{L} \end{bmatrix} \begin{bmatrix} x_1 \\ x_2 \\ x_3 \end{bmatrix} + \begin{bmatrix} 0 \\ 0 \\ \frac{1}{L} \end{bmatrix} u \quad (6)$$

where  $x_1$ ,  $x_2$  represent the displacement and velocity of armature assembly and  $x_3$  is the current.

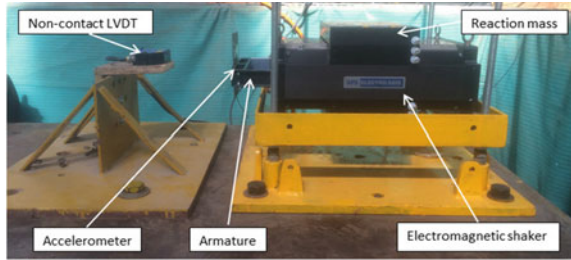
### 3 Parameter Estimation of Electromagnetic Shaker

In this section, the parameters describing the dynamics of the electromagnetic shaker are estimated. The experimental procedure described in [5, 6] was followed for the estimation of the shaker parameters. After the estimation of the parameters, the model of the electromagnetic shaker is validated to ensure that it sufficiently captures the actual dynamics of the shaker. These parameters are then used for deriving control law for hybrid simulation.

#### 3.1 Test Set-up

The test set-up for the parameter estimation of the electromagnetic shaker is shown in Fig. 2. APS 400 ELECTRO-SEIS shaker with the APS 0412—REACTION MASS ASSEMBLY was used in the experiments. A non-contact laser-based LVDT was used to measure the displacement of the shaker. An accelerometer was also attached to the armature to record the acceleration of the reaction mass. The command signals were sent to shaker using DATA PHYSICS dynamic signal analyser which was amplified by APS 145 power amplifier. The amplified signal is then fed as input to the electromagnetic shaker. The input to the shaker can be either voltage or current depending upon the mode in which it is operated. The voltage and current driving the electromagnetic shaker were read from the monitor output from the power amplifier box. The displacement, acceleration, monitor voltage and monitor current were fed back to the DATA PHYSICS to obtain the frequency response.

**Fig. 2** Test set-up for parameter estimation



### 3.2 Parameter Estimation

The mechanical damping and stiffness of the rubber bands in the shaker are obtained from the free vibration response of the shaker in the current off mode. The shaker was perturbed from its equilibrium position. The displacement response of the shaker was measured using LVDT. The amplifier gain was evaluated by relating the magnitude of the input voltage to the monitor voltage tapped from the power amplifier. The inductance of the coil is obtained by approximating the transfer function from input voltage to the current in voltage mode at higher frequencies. For evaluating the eddy current damping, the shaker was operated in the voltage mode. The frequency response of the shaker in voltage mode was measured from the current in the coil to the displacement. The overall damping ( $c$ ) in the system was attributed to both mechanical and eddy current damping. The overall damping of the shaker in voltage mode was obtained by fitting a value of damping such that the frequency response of the theoretically obtained transfer function matches with that obtained experimentally. The rest of the parameters of the electromagnetic shaker were adopted from the data sheet. The values of the electromagnetic shaker parameters are given in Table 1.

### 3.3 Validation

In order to validate the numerical model, the frequency response of the shaker was obtained theoretically using the identified parameters. The frequency response thus

**Table 1** Parameters of electromagnetic shaker

Parameter	Value
Force-to-current ratio ( $Bl$ ) (N/A)	19.62
Mass of the shaker ( $m_a$ ) (kg)	17.90
Damping in voltage mode ( $c$ ) (Ns/m)	25
Stiffness of the rubber bands ( $k_a$ ) (N/m)	175
Coil inductance ( $L$ ) (H)	0.022
Coil resistance ( $R$ ) ( $\Omega$ )	1.5
Amplifier gain ( $G_v$ )	4

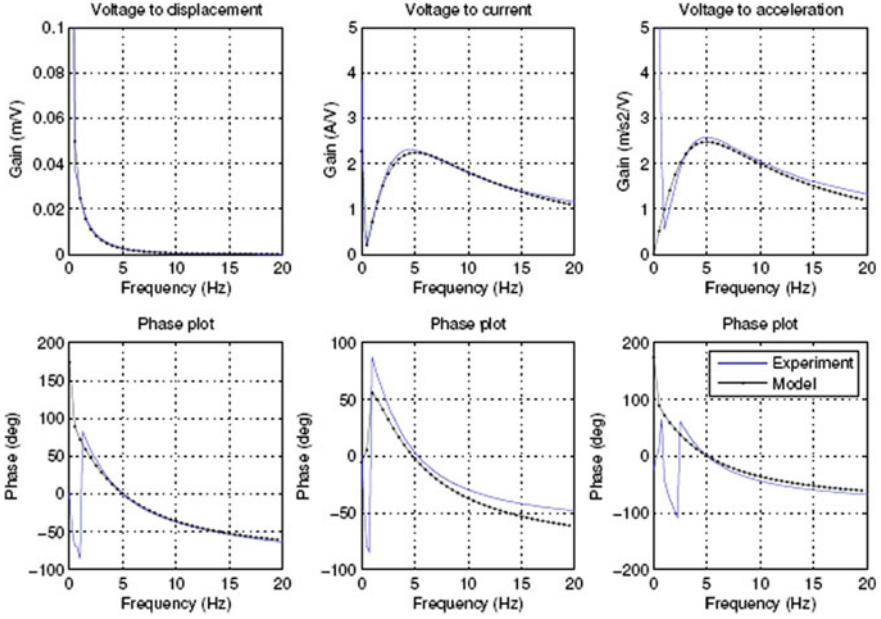


Fig. 3 Frequency response of the electromagnetic shaker in voltage mode

obtained is compared with that of experimentally obtained. The frequency response of the shaker in voltage mode is shown in Fig. 3. The measured and the numerically evaluated frequency response are found to be in close agreement.

#### 4 Mathematical Model of Hybrid System

The emulated system whose response we want to evaluate using hybrid simulation consists of a two-storey structure. The properties of the emulated system are given in Table 2. The hybrid system consists of shaker resting on top of the bottom storey (Fig. 4).

The state-space model of the hybrid system is given by:

$$\begin{aligned}
 \dot{x}_1 &= x_2 \\
 \dot{x}_2 &= -\frac{k_1}{m_1}x_1 - \frac{c_1}{m_1}x_2 + \frac{k_a}{m_1}x_3 + \frac{c_a}{m_1}x_4 - \frac{Bl}{m_1}x_5 - w \\
 \dot{x}_3 &= x_4 \\
 \dot{x}_4 &= \frac{k_1}{m_1}x_1 + \frac{c_1}{m_1}x_2 - \frac{k_a}{m_{eff}}x_3 - \frac{c_a}{m_{eff}}x_4 + \frac{Bl}{m_{eff}}x_5 \\
 \dot{x}_5 &= -\frac{Bl}{L}x_4 - \frac{R}{L}x_5 + \frac{u}{L}
 \end{aligned} \tag{7}$$

**Table 2** Properties of emulated system

Parameter	Value
$m_1$ (kg)	94
$k_1$ (N/m)	$3 \times 10^5$
$c_1$ (Ns/m)	106
$m_2$ (kg)	17.9
$k_2$ (N/m)	$3 \times 10^4$
$c_2$ (Ns/m)	42

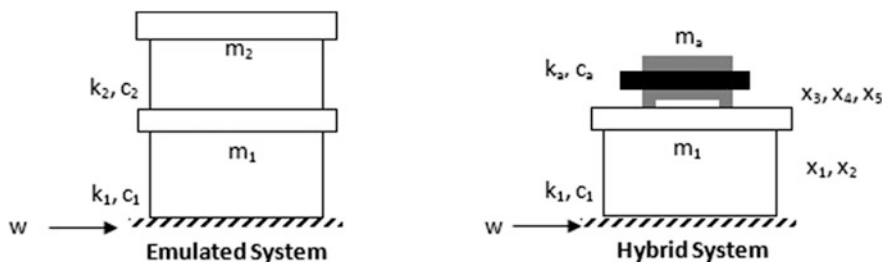


**Fig. 4** Schematics of the emulated and hybrid system

where  $x_1, x_2$  are the displacement and velocity of first storey relative to the ground,  $x_3, x_4$  are the displacement and velocity of armature relative to first storey,  $x_5$  is the current in the armature coil,  $m, k, c$  are the respective mass, stiffness and damping,  $Bl, R, L$  are the force-to-current ratio, resistance and the inductance of the armature and  $m_{eff} = m_1 m_a / (m_1 + m_a)$ .

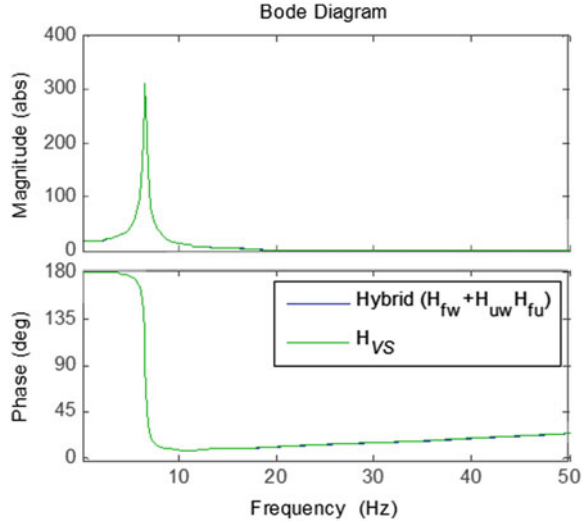
## 5 Control Law

The electromagnetic shaker has two inputs—PS acceleration and control input. Shaker needs to transfer the same amount of force as the VS will transfer in the emulated system [1, 2, 7]. The controller is evaluated using the following equation:

$$H_{uw} = \frac{H_{VS} - H_{fw}}{H_{fu}} \tag{8}$$

where  $H_{uw}$  is the controller,  $H_{VS}$  is the transfer function from bottom storey acceleration to force transferred by numerical substructure in emulated system,  $H_{fw}$  is the transfer function from bottom storey acceleration to force transferred by electromagnetic shaker in hybrid system, and  $H_{fu}$  is the transfer function from control input to the force transferred by electromagnetic shaker in hybrid system.

**Fig. 5** Comparison of the force transferred by NS and shaker in frequency domain



The frequency response of the electromagnetic shaker and VS from bottom storey acceleration to the force transferred is compared in Fig. 5. The electromagnetic shaker is able to emulate the dynamics of the VS.

## 6 Experimental Validation

The electromagnetic shaker was placed on top of a SDOF system represented by a frame (Fig. 6). In order to limit the out-of-plane motion, braces were provided in the transverse direction on both the sides of the frame.

The frequency response of the hybrid system was obtained by subjecting it to a sweep sinusoidal base excitation whose frequency varied from 1 to 30 Hz in 300 s. The acceleration of the bottom storey was measured. The bottom storey acceleration obtained from the experiments is compared with that obtained from the emulated system in Fig. 7. The responses obtained are found to be in good agreement with each other.

## 7 Conclusions

The experimental validation of the controller design strategy for real-time hybrid simulation using electromagnetic shaker was carried out. The parameters of the electromagnetic shaker were estimated. The frequency response of the electromagnetic shaker obtained from the mathematical model using the estimated

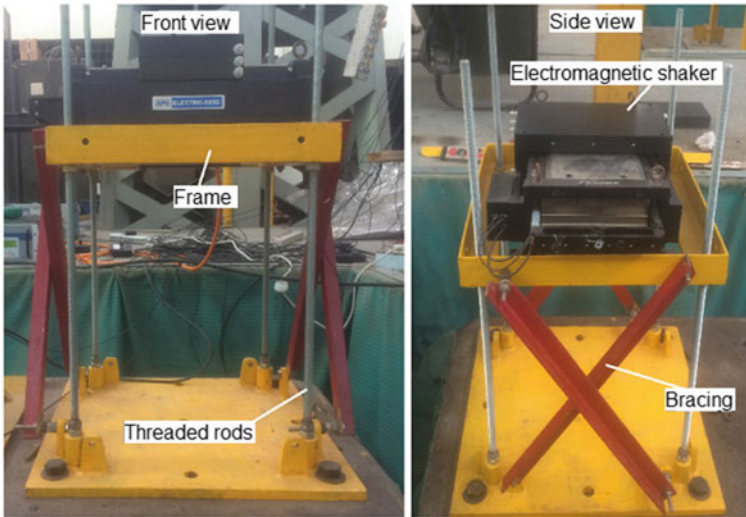
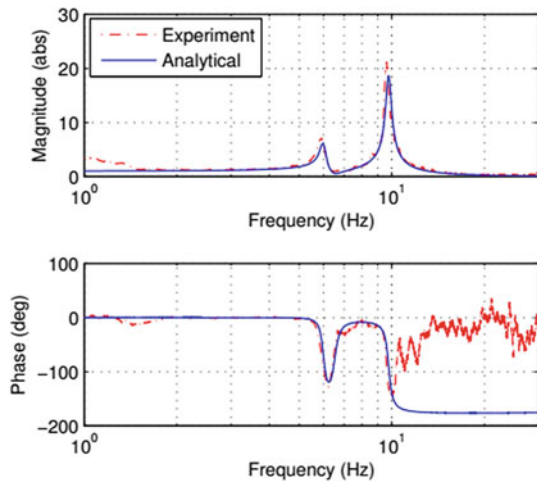


Fig. 6 Test set-up for hybrid simulation

Fig. 7 Comparison of the bottom storey acceleration in emulated and hybrid system



parameters was found to match well with that obtained experimentally. Hybrid simulation of a two-storey emulated system was carried out by taking the bottom storey as physical substructure (PS) and top storey as virtual substructure (VS). The top storey was replaced by the electromagnetic shaker in the hybrid system. The frequency response of the hybrid system was obtained by subjecting it to a sweep sinusoidal base excitation. It was found that the results obtained from the hybrid simulation were in good agreement with the analytical response obtained from the

emulated system. This validates the controller design strategy for the real-time hybrid simulation using electromagnetic shaker.

**Acknowledgements** The first author acknowledges the support received from Fulbright-Nehru Doctoral and Professional Research Fellowship under IIE Grant No. 15130894.

The first and third authors acknowledge the help and support provided by the staff of Astar laboratory, CSIR–SERC.

## References

1. Stefanaki A (2016) A simple strategy for dynamic substructuring—application to soil-foundation-structure interaction. Ph.D. Thesis, University at Buffalo, Buffalo
2. Sivaselvan M (2016) A strategy for dynamic substructuring—application to soil-foundation structure-interaction. Hybrid 2020, ETH Zurich, Switzerland
3. Lang GF (1997) Electrodynamic shaker fundamentals. *Sound Vibr* 31(4):14–23
4. Lang GF, Snyder D (2001) Understanding the physics of electrodynamic shaker performance. *Sound Vibr* 35(10):24–33
5. Carl J (2008) Improved dynamic testing by impedance control. Ph.D. Thesis, University of Colorado, Boulder
6. Carl J, Sivaselvan MV (2011) Improved dynamic testing of structures using impedance control. *Earthquake Eng Eng Vibr* 10(3):423–435. <https://doi.org/10.1007/s11803-011-0078-9>
7. Sivaselvan M (2006) A unified view of hybrid simulation algorithms. NEES Hybrid Simulation Workshop, Berkeley, California, USA



# Dynamic Behavior of Freestanding Spent Fuel Trays-Stack Without Base Locator During Earthquake Event



**Binu Kumar, O. P. Singh, G. R. Reddy, K. M. Singh, K. Agarwal and N. Gopalakrishnan**

**Abstract** Structural stability of freestanding stacks of trays containing spent fuel bundles submerged in spent fuel water pool during earthquake is of greater concern for safe storing and handling for further reprocessing of spent fuels. In the spent fuel water pool, spent fuel bundles are stacked in 25–30 trays and kept on floor without base locators or guide. Analytical procedures are not well developed to analyze the complex phenomena accounting sliding, rocking, impact of these freestanding trays-stack along with hydrodynamic effects of water mass. An experimental setup was made, and a series of shake table experiment has been performed with 25 and 30 trays-stacks submerged in spent fuel water tank. Design ground earthquake excitation of 0.1 and 0.156 g Peak Ground Acceleration (PGA) has been used in the experiment. The dynamic responses of trays-stack and tank, namely displacement and acceleration of stacked trays and tank wall, at different elevation recorded in the shake table test are analyzed and compared with numerical method.

**Keywords** Spent fuel pool · Sloshing · Shake table test · Seismic

---

B. Kumar (✉) · O. P. Singh · G. R. Reddy · K. M. Singh · K. Agarwal  
Bhabha Atomic Research Centre, Trombay, Mumbai 400085, India  
e-mail: binu@barc.gov.in

O. P. Singh  
e-mail: opsingh@barc.gov.in

G. R. Reddy  
e-mail: rssred@barc.gov.in

K. M. Singh  
e-mail: kmsingh@barc.gov.in

K. Agarwal  
e-mail: kagar@barc.gov.in

N. Gopalakrishnan  
CSIR-Structural Engineering Research Centre, Chennai 600113, India  
e-mail: ng@sercm.org

© Springer Nature Singapore Pte Ltd. 2019

A. Rama Mohan Rao and K. Ramanjaneyulu (eds.), *Recent Advances in Structural Engineering, Volume 2*, Lecture Notes in Civil Engineering 12,  
[https://doi.org/10.1007/978-981-13-0365-4\\_11](https://doi.org/10.1007/978-981-13-0365-4_11)

## 1 Introduction

The seismic response of liquid storage tank/pool system has been studied extensively in the past several decades. However, studies are limited to sloshing behavior analysis of water contained in the tank/pool with or without submerged rigid block system. Liu [1] has presented method for 2D analysis of a rectangular tank with an internal rigid block to determine sloshing characteristics of contained liquid using linear potential wave theory. Subsequently, Mitra [2] extended the study for different rigid block size using pressure wave theory without detailed analysis of impulsive and convective pressure effect on the submerged block. Koh [3] presented finite element procedures for slosh dynamics analysis of water tank without any submerged block. Chen [4] explained finite difference technique for nonlinear sloshing analysis of two-dimensional rectangular water tank system under random excitation.

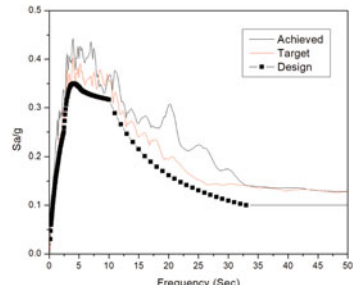
Spent fuels received from reactor are kept in Trays-stacks submerged in water pool for removal of thermal heat and radiation shielding. In a spent fuel storage pool of a nuclear power plant or reprocessing plant, the hydrodynamic pressure of spent fuel pool with stacks of tray is different from those in case of spent fuel pool without stacks of trays.

The stacks of trays are freestanding over pool floor without bottom locators. Under the seismic event, stacks of trays may slide and collide with neighboring stacks or may topple. However, there is no literature on three-dimensional nonlinear analysis of submerged multitrays-stack incorporating gap, friction, and sliding between tray and floor and among trays including slosh dynamic effect of water.

In this paper, tri-axial nonlinear dynamic behavior of 25 and 30 spent fuel trays-stack without bottom locators submerged in Spent Fuel Water Storage Tank (SFWS) during shake table experiments is analyzed and discussed in details. Simplified finite element methodology developed in Kumar [5, 6] is used for numerical analysis of trays-stack with hydrodynamic pressure of sloshing water mass. Gap, contact, and friction elements were modeled to simulate sliding and uplifting/impacting of freestanding trays-stacks during seismic excitation.

The tri-axial shake table testing and finite element analysis are performed for Design Basis Peak Ground Acceleration (DBPGA) [7] of 0.1 and 0.156 g along  $x$ -,  $y$ -, and  $z$ -axis. The response spectra along vertical direction ( $z$ -axis) is two-thirds of horizontal spectra ( $x$ - and  $y$ -axis). The design, target, and achieved spectra along  $x$ -axis used in the shake table test are shown in Fig. 1. Various response parameters such as slosh height, acceleration and displacement of trays, response frequency of the system were measured, and details of the same are discussed below.

**Fig. 1** Target and Achieved Response Spectra with Design Response Spectra along x-axis



## 2 Shake Table Testing

Shake table test has been performed considering two stacks of 25 and 30 trays containing dummy fuel bundles submerged in water in Spent Fuel Storage Water Tank (SFSWT) mounted on shake table at Advanced Seismic Testing and Research Laboratory of Structural Engineering Research Centre (SERC), Chennai.

The servo-controlled shake table of size 4 m × 4 m has payload capacity of 50 tons. The Spent Fuel Storage Water Tank (SFSWT) of 22,500 liter full capacity with two stacks of dummy fuel bundles submerged in water mounted on shake table is shown in Fig. 2.

Instrumentations like displacement sensor, accelerometer, and underwater pressure transducer have been mounted at different elevations to capture displacement, acceleration, and hydrodynamic pressure, respectively. The location and arrangements of sensors and gauges in the experiments are shown in Fig. 3.

Displacement sensors are used to capture the dynamic displacements of stack of trays at different elevations and relative displacement between two stacks. This strain gauge-based displacement sensor is calibrated using standard calibration rig. Laser displacement sensor is also used to measure displacement of 30 trays-stack and movement between two stacks during experiment.

**Fig. 2** Shake table setup for 30 trays-stack system

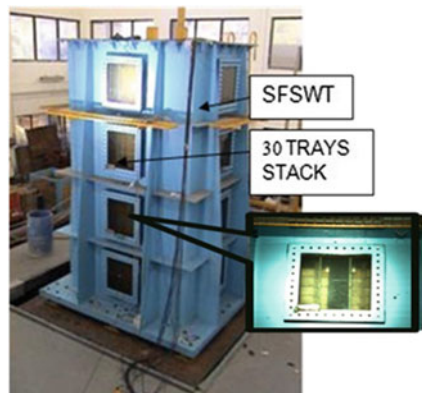
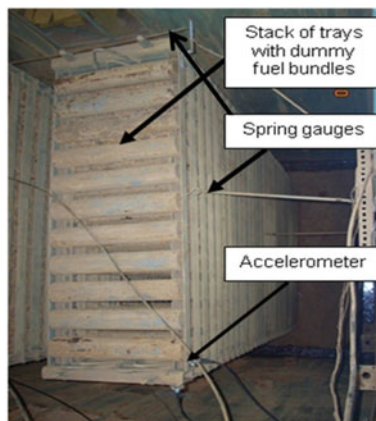


**Fig. 3** Details of gauges in experiment



PW-500 kPa-type dynamic pressure transducer of Tokyo Sokki Kenkyuio Co., ltd make were used to measure hydrodynamic pressure typically at bottom and top location. Pressure transducer is strain gauge-based hydrodynamic pressure sensor. Two ICP-type accelerometers having 941 mv/g sensitivity are fixed on the SFWST wall to record the response of the tank in *X*- and *Y*-direction at top location.

The test was performed for stack trays without locators between bottommost tray and floor. Table 1 shows the maximum displacement and acceleration of trays-stack and tank wall at different stacks height observed during shake table testing for 0.1 and 0.156 g PGA.

Figure 4 shows the displacement time history for 30 trays-stack system submerged in water without locator at bottom, respectively, for 0.1 and 0.156 g PGA seismic excitation. The maximum displacement of 30th tray is 47.14 and 67.77 for 0.1 and 0.156 g PGA seismic excitation, respectively. Whereas, maximum 4.54 and 4.98 m/sec<sup>2</sup> acceleration are recorded at top tray location for 0.1 and 0.156 g PGA seismic excitation, respectively.

Figure 5 shows Fast Fourier Transformation (FFT) of displacement time histories of trays-stack recorded during the shake table testing. The dominant response frequencies of the 30th and 18th trays are 0.56 and 0.53 Hz, respectively. Hence,

**Table 1** Maximum responses of 30 trays-stack and tank

Location	Earthquake excitation of peak acceleration 0.1 g		Earthquake excitation of peak acceleration 0.156 g	
	Displacement (mm)	Acceleration (m/sec <sup>2</sup> )	Displacement (mm)	Acceleration (m/sec <sup>2</sup> )
18th Tray	30.03	N.R.	39.08	N.R.
30th Tray	47.14	4.54	67.77	4.98
Tank top	N.R.	2.24	N.R.	2.95

*N.R.*—not recorded

**Fig. 4** Displacement of trays at 30th trays height

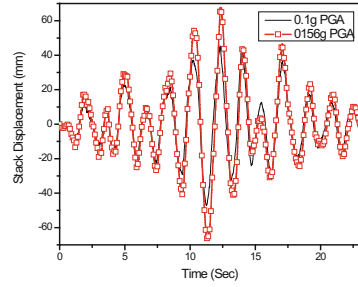


**Fig. 5** FFT of displacement time histories at 18th and 30th trays height for 30 trays stack system

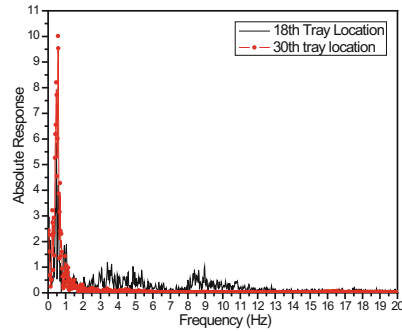
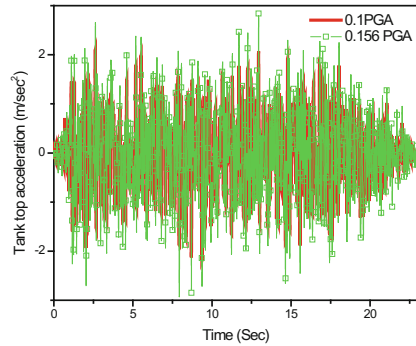


**Fig. 6** Acceleration time history of tank at top wall location



it can be inferred that the top 30th tray containing spent fuel bundles is under the influence of convective pressure of the sloshing water. However, the 18th tray is under the influence of convective and impulsive sloshing pressure.

Figure 6 shows the acceleration time histories of tank wall at top location for 0.1 and 0.156 g PGA seismic excitation. During shake table testing, maximum 2.24 and 2.95 m/sec<sup>2</sup> accelerations are recorded at top tank wall location for 0.1 and 0.156 g PGA seismic excitation, respectively.

**Fig. 7** FFT of displacement time histories for 25 and 30 trays-stack system

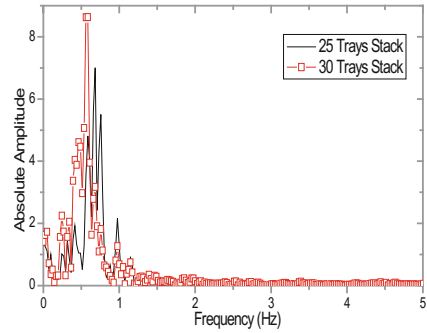


**Fig. 8** FFT of acceleration time history of tank top

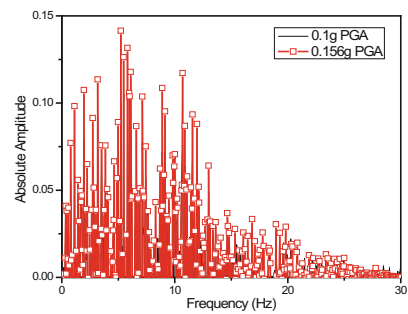


Figure 7 shows the FFT of displacement time histories of 25 and 30 trays-stack recorded during the shake table testing. The dominant response frequencies of the 30 and 25 trays are 0.56 and 0.67 Hz, respectively.

The FFT of acceleration time histories of tank top wall is shown in Fig. 8. The resonance frequency of the tank wall is 7.93 Hz.

During shake table testing, no slipping or permanent movement of the tank trays at the bottom was observed. Only displacement of stacks is observed due to convective water mass and seismic excitation. During experiment, both stacks move in phase with each other. Hence, gap of minimum 150 mm is maintained during test, and collision or impact of two stacks of trays is not found. Hydrodynamic pressure at different elevations on spent fuel water tank wall is also measured. At 0.51 m above bottom, maximum pressure recorded is 15,523 Pa whereas at 2.71 m from bottom of tank maximum pressure, 10,392.12 Pa is observed at 2.5-m-wide tank side wall.

### 3 Numerical Analysis

The simplified decoupled methodology developed in Kumar [5, 6] has been formulated to analyze the trays-stack submerged in water tank. The flowchart of the developed simplified decoupled methodology is shown in Fig. 9. As shown in the Fig. 9, the analysis was carried out in three steps. First step comprises the dynamic analysis of trays-stack without considering hydrodynamic effects. In the second step, hydrodynamic pressure on the stack is estimated considering rigid stack submerged in tank. In third step, the stacks have been analyzed for pressure time histories obtained in second step. The results obtained in these steps were combined to get final results which are compared with experiments.

The contained water in SFSWT is modeled using in-house Finite Element Acoustic Field Analysis Code (FEAFAC) as given in Kumar [5, 6]. The discretized structural dynamics equation is formulated using standard structural elements, i.e., beam, contact, gap, and sliding elements. The water mass is modeled using acoustic wave equation. The acoustic wave equation is derived from fluid momentum (Navier–Stokes) and continuity equations. In acoustic formulation, it is assumed that the fluid is compressible, inviscid, and non-flowing medium. Also, the mean density and pressure are assumed to be uniform throughout the fluid.

Figure 10 represents the finite element model of SFSWT with submerged trays-stack used in the nonlinear numerical analysis. The numerical results obtained are compared and validated with experimental results. The freestanding stack of 25 and 30 trays has been analyzed for 0.1 value friction coefficient ( $\mu$ ) using hydrodynamic pressure time history and seismic base excitation.

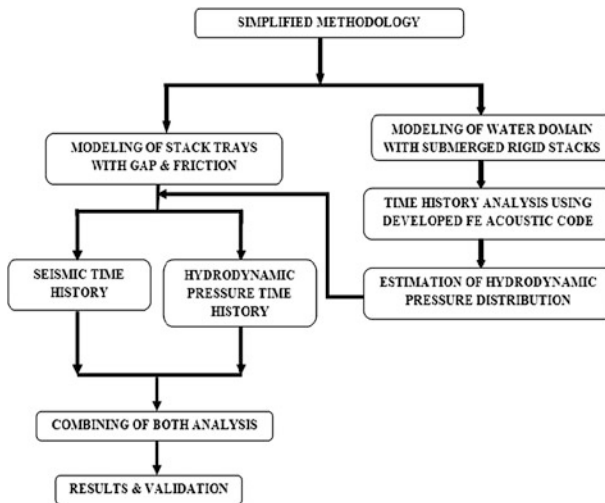
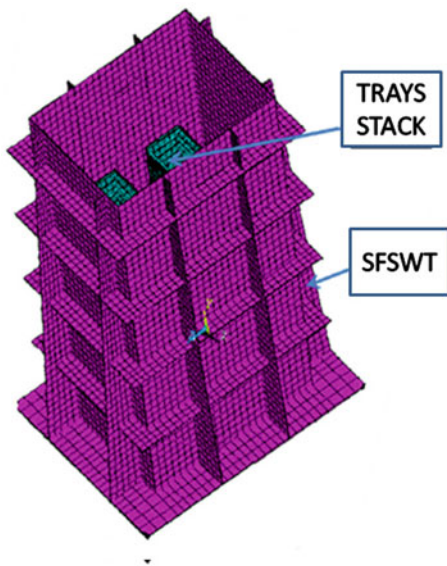


Fig. 9 Simplified methodology for fluid–structure interaction analysis in Kumar [5, 6]

**Fig. 10** Finite element model of SFSWT with submerged trays-stacks



The general finite element equation solved in the analysis is shown in Eq. (1). Newmark method [8] has been used for the time integration. Newton–Raphson iterative scheme [9] has been used at each time step.

$$[M]\{\ddot{X}\} + [C]\{\dot{X}\} + [K]\{X\} = \{F_{EQ}\} + \{F_{hydrodynamic}\} \quad (1)$$

FFT of free surface displacement time history of 25 trays-stack system is shown in Fig. 11. The slosh frequency of the water is 0.56 Hz. A typical mode shape of the free surface is shown in Fig. 12. The slosh frequency computed from the present code matches agreeable with experiment.

Figure 13 shows the hydrodynamic pressure variation along tank left wall at different time. Maximum hydrodynamic pressure is observed at 20 s time.

**Fig. 11** Slosh frequency of free surface

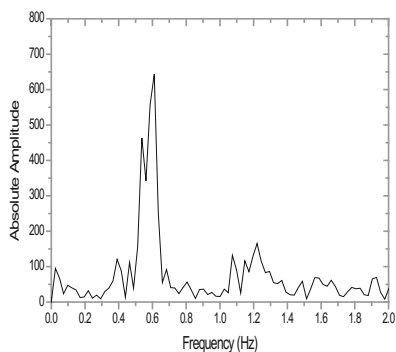




**Fig. 12** Typical slosh mode shape of free surface

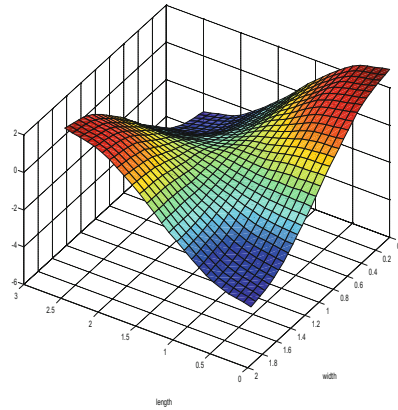
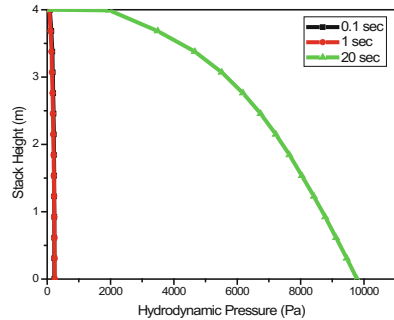


**Fig. 13** Pressure variation along tank left wall



This is due to seismic excitation which is maximum around 20 s that induces more convective and impulsive pressure on tank wall.

### 4 Results and Conclusion

Table 2 shows that maximum displacement and acceleration of 25 and 30 trays-stack systems are recorded in tri-axial shake table test and obtained in numerical analysis for 0.1 and 0.156 g Peak Ground Acceleration (PGA).

In the shake table experiment and numerical analysis, impact of adjacent tray-stack is not observed. Also, no significant slipping of the tray-stacks at the bottom was observed during the tests and finite element analysis.

Displacements of stacks generally increase with increase in base accelerations. In phase motion (i.e. both Trays-Stack move in same direction) of trays-stack is observed during the experiment and also observed in numerical analysis. Hence, relative displacement between two stacks at top location is approximately  $150^{\pm 10}$  mm in shake table testing and numerical analysis. Maximum 11,800.10 and

**Table 2** Maximum displacement of trays in test and finite element (FE) analysis

Sr. No.	Maximum response	0.1 g PGA		0.156 g PGA	
		Test	FE	Test	FE
1.	Displacement (mm) of 25 trays-stacks system	41.88	40.09	60.10	58.23
2.	Displacement (mm) of 30 trays-stacks system	47.14	44.12	67.77	63.77
3.	Acceleration (m/sec <sup>2</sup> ) of 25 trays-stacks system	4.18	4.20	4.59	4.30
4.	Acceleration (m/sec <sup>2</sup> ) of 30 trays-stacks system	4.54	3.96	4.98	4.67

9097.18 Pa hydrodynamic pressure was recorded at bottom and top locations, respectively, for 30 trays-stack for 0.156 g PGA. During shake table experiment and numerical simulation, the 25 and 30 trays-stack system submerged in water tank/pool are found safe and displacements are within safe limit. Slosh frequency and mode shapes computed from developed code are in good comparison with the shake table experiment results. It is observed from Table 2 that the maximum 12% difference is estimated between shake table test and present code analysis for displacement of 25 trays-stacks system. It is also observed that here stacks lie in the region of convective waves; hence, the hydrodynamic pressure on the stacks will induce more displacement of stack than in the case of without water.

The developed finite element code is capable of finding various essential parameters like convective and impulsive frequencies, mode shape, hydrodynamic pressure, and stack displacement. The developed simplified method is able to predict the complex behavior of submerged stacks. Hence, the procedure evolved is quite useful. Analysis gives reasonably acceptable results of displacement and pressure.

## References

1. Liu WK (1981) Finite element procedures for fluid-structure interactions and applications to liquid storage tanks. *J Nucl Eng Des* 65(2):221–238
2. Mitra S, Sinhamahapatra KP (2007) Slosh dynamics of liquid-filled containers with submerged components using pressure-based finite element method. *J Sound Vib* 304:361–381
3. Koh HM, Kim JK, Park JH (1998) Fluid-structure interaction analysis of 3-D rectangular tanks by a variationally coupled BEM-FEM and comparison with test results. *J Earthq Eng Struct Dyn* 27:109–124
4. Chen W (1996) Large amplitude liquid sloshing in seismically excited tanks. *J Earthq Eng Struct Dyn* 25:653–669
5. Kumar B, Singh OP, Reddy GR, Nair KNS (2011) Experimental and numerical analysis of stacked spent fuel trays submerged in water pool subjected to earthquake loading. *SMiRT* 21 240:1–8

6. Kumar B, Singh OP, Reddy GR, Nair KNS, Krishnan NG, Muthumani K (2012) Hydrodynamic effect on stability of tray stacks incorporating simplified fluid structure analysis. ICCMS
7. Envelope of Spectra for 540 MWe Plant on rocky site at NPP, Department of earth quake engineering, EQ 86.6, 1986
8. Newmark NM (1959) A method of computation for structural dynamics. ASCE J Eng Mech Div 85:67–194
9. Cook RD, Malkus DS, Plesha ME (1989) Concepts and applications of finite element analysis, 3rd edn. Wiley

# Free Vibration Analysis of Functionally Graded Plates Under Thermal Environment Using Four-Node Quadrilateral Element



G. A. Deshpande and S. D. Kulkarni

**Abstract** In this work, the four-node quadrilateral element having seven degrees of freedom per node developed earlier by the second author and his co-workers is modified for free vibration analysis of functionally graded plates under thermal environment. The performance of the modified element is assessed by comparing the present results of non-dimensionalised natural frequencies with the available analytical as well as the finite element results. It is observed that the performance of the present element is quite satisfactory for the isotropic FGM plates under thermal environment considered in this study with all edges simply supported as well as with all edges clamped boundary conditions.

**Keywords** Functionally graded material · Finite · Discrete · Quadrilateral

## 1 Introduction

In many engineering fields, nowadays functionally graded materials are used for structural applications. Functionally graded materials normally consist of two phases, namely the metal phase and the ceramic phase. The ceramic phase can resist the severe thermal loading and the metal phase prevents fracture caused by stresses due to high temperature. Due to the special manufacturing process, these materials are macroscopically homogeneous in spite of being microscopically inhomogeneous. Since functionally graded structures are most commonly used in high-temperature environment, changes in mechanical properties of constituent materials are expected. The material properties  $P$  that are temperature dependent can be written as

---

G. A. Deshpande · S. D. Kulkarni (✉)

Department of Civil Engineering, College of Engineering Pune, Pune, India  
e-mail: sdk.civil@coep.ac.in

G. A. Deshpande

e-mail: girijakaranjekar@yahoo.co.uk

© Springer Nature Singapore Pte Ltd. 2019

A. Rama Mohan Rao and K. Ramanjaneyulu (eds.), *Recent Advances in Structural Engineering, Volume 2*, Lecture Notes in Civil Engineering 12,  
[https://doi.org/10.1007/978-981-13-0365-4\\_12](https://doi.org/10.1007/978-981-13-0365-4_12)

$$P = P_0(P_{-1}T^{-1} + 1 + P_1T + P_2T^2 + P_3T^3) \quad (1)$$

where  $P_0, P_{-1}, P_1, P_2$  and  $P_3$  are the coefficients of temperature  $T(K)$  and are unique to the constituent materials. The effective material property through the thickness is normally assumed to be according to the following power law,

$$P(z, T) = P_b(T) + (P_t(T) - P_b(T)) \left[ \frac{2z+h}{2h} \right]^n \quad (2)$$

where ‘ $n$ ’ is the volume fraction index,  $P_b$  and  $P_t$  are the material properties at the bottom and the top surface of the plate, respectively, and ‘ $h$ ’ is the total thickness of the plate. Poisson’s ratio depends weakly on temperature change and is assumed to be constant.

In the present work, the element developed by the second author and his co-workers Ref. [1]; for the analysis of single layer, functionally graded plate is modified for the free vibration analysis of isotropic functionally graded plate under thermal environment. The element presented in Ref. [1] has seven degrees of freedom per node and is based on Reddy’s third-order theory. The  $C^1$  continuity problem posed by Reddy’s third-order theory is circumvented by using the improved Kirchhoff interpolation functions of Jeychandrabose et al. [2]. The performance of the modified element is assessed for the free vibration analysis of two types of isotropic FGM plates under thermal environment in comparison with the available analytical as well as finite element results for the non-dimensionalised natural frequencies. It is observed that for all the cases of FGM plates considered in this study, performance of the modified four-node quadrilateral element based on Reddy’s theory is quite satisfactory.

## 2 Formulation

### 2.1 Temperature Field Approximation

Temperature field is assumed to be uniform over the plate surface and varies only in the thickness direction. The temperature distribution along the thickness direction can be obtained by solving a steady-state heat transfer equation

$$-\frac{d}{dz} \left[ K(z) \frac{dT}{dz} \right] = 0, \quad (3)$$

$$T = T_u \text{ at } z = h/2; T = T_L \text{ at } z = -h/2.$$

where ‘ $T_u$ ’ and ‘ $T_L$ ’ are the temperatures at the top and the bottom surface of the plate, respectively. The solution of this equation, by means of polynomial series,

$$T(Z) = T_u + (T_L - T_u) \eta(Z, h) \quad (4)$$

where

$$\begin{aligned} \frac{2Z + h}{2h} &= m \\ \eta(Z, h) &= \frac{1}{C} \left[ m - \frac{k_{mc}}{(n+1)k_c} (m)^{n+1} \right. \\ &\quad + \frac{k_{mc}^2}{(2n+1)k_c^2} (m)^{2n+1} \\ &\quad - \frac{k_{mc}^3}{(3n+1)k_c^3} (m)^{3n+1} \\ &\quad + \frac{k_{mc}^4}{(4n+1)k_c^4} (m)^{4n+1} \\ &\quad \left. - \frac{k_{mc}^5}{(5n+1)k_c^5} (m)^{5n+1} \right] \end{aligned} \quad (5)$$

$$\begin{aligned} C &= 1 - \frac{k_{mc}}{(n+1)k_c} + \frac{k_{mc}^2}{(2n+1)k_c^2} \\ &\quad - \frac{k_{mc}^3}{(3n+1)k_c^3} \\ &\quad + \frac{k_{mc}^4}{(4n+1)k_c^4} \\ &\quad - \frac{k_{mc}^5}{(5n+1)k_c^5} \end{aligned} \quad (6)$$

$$k_{mc} = k_m - k_c \quad (7)$$

$$E(z, T) = [E_m(T) - E_c(T)]m^n + E_c(T) \quad (8)$$

## 2.2 Displacement Field Approximation

The four-node quadrilateral element formulation is based on Reddy's third-order theory for which the displacement field approximation is

$$\begin{aligned} w(x, y, z, t) &= w_0(x, y, t) \\ u(x, y, z, t) &= u_0(x, y, t) - zw_{0d} + R(z)\varphi_0(x, y, t) \end{aligned} \quad (9)$$

where  $R(z) = z - \frac{4z^3}{3h^2}$

The constitutive relations  $\sigma$  can be expressed as

$$\sigma = \bar{Q}_{ij}[\varepsilon - \bar{\varepsilon}_t] \quad (10)$$

where  $\bar{\varepsilon}_t$  is thermal strain.

Stiffness coefficients  $\bar{Q}_{ij}$  are defined as:

$$\begin{aligned} \bar{Q}_{11} = \bar{Q}_{22} &= \frac{E(z, T)}{1 - \nu^2}; \bar{Q}_{12} = \bar{Q}_{21} = \frac{\nu E(z, T)}{1 - \nu^2}; \\ \bar{Q}_{16} = \bar{Q}_{26} &= 0; \bar{Q}_{44} = \bar{Q}_{55} = \bar{Q}_{66} = \frac{E(z, T)}{2(1 + \nu)} \end{aligned} \quad (11)$$

### 2.3 Finite Element Formulation

Principle of virtual work is used for obtaining stiffness matrix and mass matrix. Details regarding the interpolation functions are given in Ref. [1].

## 3 Numerical Results

Square FGM plates with two types of material mixture are considered. The top surface of the plate is ceramic rich while the bottom surface contains metal.

Type 1: The top surface of the plate is silicon nitride ( $\text{Si}_3\text{N}_4$ ) while the bottom surface contains stainless steel (SUS304), referred as  $\text{Si}_3\text{N}_4/\text{SUS304}$ .

Type 2: The top surface of the plate is zirconium oxide ( $\text{ZrO}_2$ ) while the bottom surface contains titanium alloy (Ti-6Al-4V), referred as  $\text{ZrO}_2/\text{Ti-6Al-4V}$ .

Temperature-dependent coefficients for metal and ceramic are listed in Table 1 as given in Ref. [3] where  $E$  is Young's modulus,  $\alpha$  is thermal expansion coefficient,  $\rho$  is density and  $k$  is thermal conductivity. Poisson's ratio is assumed to be 0.28 and 0.3 for Type 1 plate and Type 2 plate, respectively.

Numerical results presented in Tables 2 and 3 are obtained by using following non-dimensional frequency formula:

$$\bar{\omega} = \frac{\omega \alpha^2}{\pi^2} \sqrt{\frac{I_0}{D_0}} \text{ Where, } I_0 = h\rho, D_0 = \frac{Eh^3}{12(1 - \nu^2)}$$

The material properties  $\rho$  and  $E$  are chosen to be the values of stainless steel at reference temperature  $T_0 = 300$  K.

Rests of the numerical results are obtained by using non-dimensionalised frequency formula given below:

**Table 1** Temperature-dependent coefficient for ceramic and metal

Material	$P_0$	$P_{-1}$	$P_1$	$P_2$	$P_3$
<i>Si<sub>3</sub>N<sub>4</sub>—Silicon nitride</i>					
$E$ (Pa)	$348.43 \times 10^9$	0.0	$3.070 \times 10^{-4}$	$2.160 \times 10^{-7}$	$8.946 \times 10^{-11}$
$\alpha$ (1/K)	$5.8723 \times 10^{-6}$	0.0	$9.095 \times 10^{-4}$	0.0	0.0
$\rho$ (kg/m <sup>3</sup> )	2370	0.0	0.0	0.0	0.0
$k$	9.19	0.0	0.0	0.0	0.0
<i>SUS304—Stainless steel</i>					
$E$ (Pa)	$201.04 \times 10^9$	0.0	$3.076 \times 10^{-4}$	$-6.534 \times 10^{-7}$	0.0
$\alpha$ (1/K)	$12.330 \times 10^{-6}$	0.0	$8.086 \times 10^{-4}$	0.0	0.0
$\rho$ (kg/m <sup>3</sup> )	8166	0.0	0.0	0.0	0.0
$k$	12.04	0.0	0.0	0.0	0.0
<i>ZrO<sub>2</sub>—Zirconia</i>					
$E$ (Pa)	$244.27 \times 10^9$	0.0	$-1.371 \times 10^{-3}$	$1.214 \times 10^{-6}$	$-3.681 \times 10^{-10}$
$\alpha$ (1/K)	$12.766 \times 10^{-6}$	0.0	$-1.491 \times 10^{-3}$	$1.006 \times 10^{-5}$	$-6.778 \times 10^{-11}$
$\rho$ (kg/m <sup>3</sup> )	3000	0.0	0.0	0.0	0.0
$k$	1.80	0.0	0.0	0.0	0.0
<i>Ti-6Al-4V—Titanium alloy</i>					
$E$ (Pa)	$122.56 \times 10^9$	0.0	$-4.5681 \times 10^{-4}$	0.0	0.0
$\alpha$ (1/K)	$7.5788 \times 10^{-6}$	0.0	$6.638 \times 10^{-4}$	$-3.1476 \times 10^{-6}$	0.0
$\rho$ (kg/m <sup>3</sup> )	8166	0.0	0.0	0.0	0.0
$k$	7.82	0.0	0.0	0.0	0.0

$$\bar{\omega} = \frac{\omega a^2}{h} \sqrt{\frac{\rho_0(1-\nu^2)}{E_0}}$$

The material properties  $\rho_0$  and  $E_0$  are chosen to be the values of metal at reference temperature  $T_0 = 300$  K

### 3.1 All-Round Simply Supported (SSSS) and All-Round Clamped (CCCC) Type 1 FGM Plate

The numerical results of non-dimensional frequencies for the first seven modes for all-round simply supported and all-round clamped type 1 FGM square plates with span to thickness ratio of  $S = 10$  are compared with the 3D results presented by Li et al. [4] in Tables 2 and 3, respectively. Though present results are based on two-dimensional theories, they are quite comparable with the 3D results presented by Li et al. [4]. It is also observed that the present results are in close agreement with 3D results.



**Table 2**  $\bar{\omega}$  for Type 1 FGM plate subjected to nonlinear temperature rise  $\Delta T = 300$  K with SSSS boundary condition

Volume fraction	Mesh size	$\bar{\omega}_1$	$\bar{\omega}_2$	$\bar{\omega}_3$	$\bar{\omega}_4$	$\bar{\omega}_5$	$\bar{\omega}_6$	$\bar{\omega}_7$
1	$8 \times 8$	2.6496	6.3146	6.3146	9.2189	9.2189	9.6139	11.8343
	$16 \times 16$	2.6575	6.3408	6.3408	9.1747	9.1747	9.7134	11.8678
	$20 \times 20$	2.6584	6.3442	6.3442	9.1694	9.1694	9.7267	11.8738
	Li et al. [4]	2.6576	6.3764	6.3764	8.9707	8.9707	9.7992	11.9555
2	$8 \times 8$	2.3788	5.6646	5.6646	8.1652	8.1652	8.6182	10.6051
	$16 \times 16$	2.3858	5.6881	5.6881	8.1261	8.1261	8.7077	10.6350
	$20 \times 20$	2.3866	5.6912	5.6912	8.1214	8.1214	8.7196	10.6404
	Li et al. [4]	2.3727	5.6933	5.6933	7.9300	7.9300	8.7468	10.6709
5	$8 \times 8$	2.1603	5.1392	5.1392	7.2991	7.2991	7.8126	9.6076
	$16 \times 16$	2.1668	5.1611	5.1611	7.2641	7.2641	7.8948	9.6374
	$20 \times 20$	2.1676	5.1640	5.1640	7.2599	7.2599	7.9058	9.6427
	Li et al. [4]	2.1424	5.1419	5.1419	7.0806	7.0806	7.8970	9.6331

**Table 3**  $\bar{\omega}$  for Type 1 FGM plate subjected to nonlinear temperature rise  $\Delta T = 300$  K with CCCC boundary condition

Volume fraction	Mesh size	$\bar{\omega}_1$	$\bar{\omega}_2$	$\bar{\omega}_3$	$\bar{\omega}_4$	$\bar{\omega}_5$	$\bar{\omega}_6$	$\bar{\omega}_7$
1	$8 \times 8$	4.5913	8.8613	8.8613	12.4557	14.9302	15.0255	17.4949
	$16 \times 16$	4.5753	8.7832	8.7832	12.3509	14.6288	14.7473	17.3649
	$20 \times 20$	4.5713	8.7674	8.7674	12.3263	14.5809	14.7033	17.3484
	Li et al. [4]	4.4904	8.6443	8.6443	12.1559	14.3412	14.4836	17.0433
2	$8 \times 8$	4.1145	7.9341	7.9341	11.1479	13.3580	13.4423	15.5025
	$16 \times 16$	4.0990	7.8600	7.8600	11.0467	13.0775	13.1833	15.3884
	$20 \times 20$	4.0952	7.8452	7.8452	11.0234	13.0331	13.1424	15.3743
	Li et al. [4]	3.9965	7.6961	7.6961	10.8220	12.7653	12.8934	15.1611
5	$8 \times 8$	3.7283	7.1808	7.1808	10.0846	12.0759	12.1507	13.8749
	$16 \times 16$	3.7136	7.1120	7.1120	9.9891	11.8183	11.9131	13.7728
	$20 \times 20$	3.7101	7.0981	7.0981	9.9672	11.7772	11.8755	13.7603
	Li et al. [4]	3.5941	6.9264	6.9264	9.7400	11.4873	11.6043	13.6331

The temperature effects on non-dimensionalised frequencies of clamped plates are greater than those of simply supported plates.

### 3.2 All-Round Simply Supported (SSSS) Type 2 Square FGM Plate with $S = 8$

Tables 4 and 5 give results of non-dimensional frequencies for type 2 (ZrO<sub>2</sub>/Ti-6Al-4V) FGM plate with zero and 100 K temperature rise, respectively. The comparison of results for all-round simply supported plate obtained with a mesh size of  $8 \times 8$  with different volume fractions with 2D analytical results presented by Huang and Shen [5] based on higher order shear deformation theory for  $\Delta T = 0$  K and  $\Delta T = 100$  K, respectively, in Tables 4 and 5 where  $T_c$  is the temperature at the top surface and  $T_m$  at the bottom surface of the plate. It is observed from both the tables that the results obtained using present elements even with a coarser mesh are matching with those given by Huang and Shen [5]. It is also observed that as the volume fraction increases non-dimensionalised fundamental frequency decreases.

### 3.3 All-Round Simply Supported (SSSS) Type 1 Square FGM Plate with $S = 8$

Table 6 gives comparison of non-dimensionalised frequencies of type 1 square FGM plate with the results presented by Huang and Shen [5]. For this case thermal loading condition,  $T_c = 300$  K and  $T_m = 300$  K is considered. It is observed from Table 6 that results obtained using present elements even with a coarser mesh of

**Table 4**  $\bar{\omega}$  for Type 2 square FGM plate with  $T_c = 300$  K and  $T_m = 300$  K ( $\Delta T = 0$ ) with SSSS boundary condition

Volume fraction	Results	Mode				
		(1,1)	(1,2)	(2,2)	(1,3)	(2,3)
0	Huang and Shen [5]	8.273	19.216	28.962	34.873	43.07
	Present	8.247	19.232	28.802	35.118	43.046
0.5	Huang and Shen [5]	7.139	16.643	25.048	30.174	37.288
	Present	7.086	16.540	24.789	30.244	37.089
1	Huang and Shen [5]	6.657	15.514	23.345	28.12	34.747
	Present	6.632	15.473	23.178	28.278	34.665
2	Huang and Shen [5]	6.286	14.625	21.978	26.454	32.659
	Present	6.264	14.588	21.822	26.606	32.583

**Table 5**  $\bar{\omega}$  for Type 2 square FGM plate with  $T_c = 400$  K and  $T_m = 300$  K ( $\Delta T = 100$ ) with SSSS boundary condition

Volume fraction	Results	Mode				
		(1,1)	(1,2)	(2,2)	(1,3)	(2,3)
0	Huang and Shen [5]	7.868	18.659	28.203	34.015	42.045
	Present	8.039	18.746	28.074	34.231	41.959
0.5	Huang and Shen [5]	6.876	16.264	24.578	29.651	36.664
	Present	6.934	16.191	24.270	29.611	36.319
1	Huang and Shen [5]	6.437	15.202	22.956	27.696	34.236
	Present	6.499	15.168	22.727	27.727	33.996
2	Huang and Shen [5]	6.101	14.372	21.653	26.113	32.239
	Present	6.145	14.317	21.423	26.119	31.995

size  $8 \times 8$  are in close agreement with those given by Huang and Shen [5]. Percentage difference in present results and results presented in Ref. [5] are less than 1%.

### 3.4 All-Round Simply Supported (SSSS) Type 1 Square FGM Plate with Other Finite Element Results with $S = 8$

The results for four different volume fractions for all-round simply supported type 1 square FGM plate with a mesh size of  $8 \times 8$  are given in Table 7. Temperature

**Table 6**  $\bar{\omega}$  for Type 1 square FGM plate with  $T_c = 300$  K and  $T_m = 300$  K ( $\Delta T = 0$ )

Volume fraction	Results	Mode				
		(1, 1)	(1, 2)	(2, 2)	(1, 3)	(2, 3)
0	Huang and Shen [5]	12.495	29.131	43.845	52.822	65.281
	Present	12.457	29.085	43.599	53.186	65.236
0.5	Huang and Shen [5]	8.675	20.262	30.359	36.819	45.546
	Present	8.576	20.022	30.014	36.625	44.924
1	Huang and Shen [5]	7.555	17.649	26.606	32.081	39.692
	Present	7.515	17.542	26.289	32.082	39.341
2	Huang and Shen [5]	6.777	15.809	23.806	28.687	35.466
	Present	6.744	15.725	23.545	28.721	35.195

**Table 7** Comparison of non-dimensionalised frequencies for Type 1 square FGM plate SSSS boundary condition under

Reference	Mode	Volume fraction			
		$n = 0$	$n = 0.5$	$n = 1$	$n = 2$
Huang and Shen [5]	1	12.397	8.615	7.474	6.639
	2	29.083	20.212	17.607	15.762
Sundararaian et al. [6]	1	12.311	8.276	7.302	6.572
	2	29.016	19.772	17.369	15.599
Present	1	12.392	8.535	7.481	6.715
	2	28.933	19.928	17.463	15.659

change  $\Delta T = 100$  K is considered for the analysis. For comparison, the finite element results of fundamental natural frequencies presented by Sundararaian et al. [6] by using 8 node  $C^0$  continuous shear flexible element with 5 degrees of freedom per node based on FSDT are also given along with the results presented by Huang and Shen [5]. The superiority of the present element is clearly indicated from the fact that the number of degrees of freedom required for almost the same accuracy is much less than that required for the element of Ref. [6].

### 3.5 Additional Results

In Fig. 1a, b, the first three mode shapes are plotted for Type 2 and Type 1 FGM plates with all-round simply supported boundary conditions with volume fraction  $n = 5$  with  $S = 8$ . Temperature at the top is 400 K and that at bottom is 300 K. These results can be used as benchmark for further research.

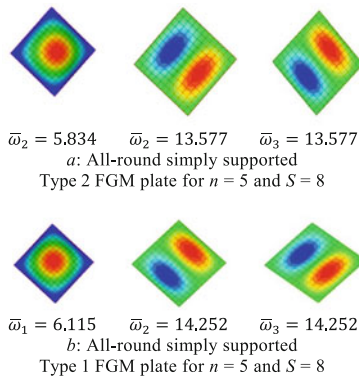


**Fig. 1** First three mode shapes for FGM plate under thermal environment

## 4 Conclusions

The present element based on Reddy's third-order theory observed to give quite satisfactory results for all the cases of FGM plates under thermal environment considered in this study. It is also observed that even the results obtained with a coarser mesh size are also close to the 3D results reported in the literature. This establishes the suitability of the present element for the free vibration analysis of functionally graded plates under thermal environment, and its use is recommended for the further research.

## References

1. Kulkarni SD, Trivedi CJ, Ishi RG (2015) Static and free vibration analysis of functionally graded skew plates using a four node quadrilateral element. In: *Advances in structural engineering*, Springer India Publications, pp. 15–24
2. Jeychandrabose C, Kirkhope J, Meekioshi L (1987) An improved discrete Kirchhoff quadrilateral thin plate bending element. *Int J Numer Methods Eng* 24:635–654
3. Reddy JN, Chin C (1998) Thermomechanical analysis of functionally graded cylinders and plates. *J Thermal Stress* 21(6):593–626
4. Li Q, Iu VP, Kou KP (2009) Three dimensional vibration analysis of functionally graded material plates in thermal environment. *Int J Sound Vib* 324:733–750
5. Huang XL, Shen HS (2004) Nonlinear vibration and dynamic response of functionally graded plates in thermal environments. *Int J Solids Struct* 41:2403–2427
6. Sundarrarajan N, Prakash T, Ganapathi M (2005) Nonlinear free flexural vibration of functionally graded rectangular and skew plates under thermal environments. *Finite Elem Anal Des* 42:152–168

# A Comparative Study of the Seismic Provisions of Indian Seismic Code IS 1893-2002 and Draft Indian Code IS 1893:2016



Rita Debnath and Lipika Halder

**Abstract** This paper compares the seismic design provisions of the existing Indian Seismic Code IS 1893 (part 1): 2002 [1] and the current draft version of Indian Seismic Code IS 1893 (part 1): 2016 [2] to address the differences in their philosophies and applicability. Significant differences are observed in these documents for specifying different parameters such as empirical formulas for calculating time period, building importance factor, response reduction factor, design acceleration coefficient. Moreover, in draft code, additional clarity regarding different types of irregularity of structural systems, effect of masonry infill works on design of framed building, simplifying torsional provisions and simplified method of liquefaction potential analysis are carried out as extra items. Similarities and differences among both codes are illustrated here in the form of tables and graphs.

**Keywords** IS 1893 (part 1): 2002 · IS 1893 (part 1): 2016 · Buildings  
Seismic design provision · Comparative study

## 1 Introduction

Codes and standards are the conventional source of information to the designers of civil engineering structures. The seismic codes are primarily based on comprehensive data on ground motion that are erratic in direction, magnitude, duration and sequence and the results of the research were carried out to understand the consequence of these ground motion on the structures. In the last several decades, the seismic codes are becoming sophisticated with rapid development in earthquake engineering practice. The first Indian Seismic Code was published in 1962 and it

---

R. Debnath · L. Halder (✉)  
Department of Civil Engineering, National Institute  
of Technology Agartala, Agartala 799046, India  
e-mail: erlhalder@yahoo.co.in

R. Debnath  
e-mail: rita7219@gmail.com

had since been revised in 1966, 1970, 1975 and 1984. The said code again revised in 2002 as a fifth revision after the devastating effect of the 2001 Bhuj earthquake. In this fifth revision, the Earthquake Engineering Sectional Committee has decided to cover the provisions for different types of structures in separate parts splitting the seismic code into five parts and in part 1, general provisions and buildings were discussed. However, the last few years have witnessed substantial progress in the understanding of the earthquake, as well as the response to the various kinds of structures and several modifications have also been suggested in the literature.

It is seen that as and when earthquake occurs in any country, building code of that country or region reviewed based on the analysis of the failure of the structure due to the lack of standards to the structure. As evident that the developing countries like Bangladesh first published Bangladesh National Building Code, i.e. BNBC in 1993 to provide guidelines for design and construction of new structures subject to earthquake ground motion in order to minimize the risk of life for all structures. Again in 2010, this code has been reviewed and prepared the draft BNBC comparing the standards of other countries. This has been reported by Bari and Das [3]. Similarly, a comparison was made among seismic design codes of buildings of eight Asian countries such as Japan, India, Turkey, China, Korea, Nepal, Indonesia and Iran being reported by Xiao Guang et al. [4]. Dogangun and Livaoglu have comparatively studied the design spectra of Eurocode 8, UBC, IBC and Turkish Earthquake Code (TEC) on R/C sample buildings [5]. They reported that TEC was revised on 1997 and effective on 1998 but two destructive earthquakes in 1999 forced to re-revise the said code. Imashi and Massumi [6] have done a comparative study of the seismic provisions of Iranian Seismic Code (Standard No.2800) and International Building Code 2003 wherein they provided a comparison process on how to calculate seismic forces by the static analysis method by the International Building Code (IBC) 2003 and the Iranian Seismic Code (IS 2800-05).

It is pertinent to revise the seismic code based on the experience gathered due to the different earthquakes occurred and it is also fact that the comparison between the existing code and draft code is very much essential to understand similarities and de-similarities of both the codes, so that the codes/standards are made with a strong and reliable manner. Accordingly, Indian Seismic Code IS 1893 (part 1): 2002 [1] has been reviewed and proposed draft code IS 1893 (part 1): 2016 [2] has been prepared by BIS.

This paper presents a comparative study of the provision of the existing Indian Seismic Code IS 1893 (part 1): 2002 [1] and the draft code IS 1893 (part 1): 2016 [2] to address the differences in their philosophies and applicability, keeping the language and notation presented in each standard unchanged.

## 2 Methodology

The calculation procedure of seismic loading is more or less similar in both codes. The earthquake force is considered as a lateral force in both codes.

## 2.1 Calculation of Design Earthquake Loads

Effects of design earthquake loads on structures can be considered in two ways, namely Equivalent Static Method and Dynamic Analysis Method.

### 2.1.1 Equivalent Static Method

In existing code, the applicability of Equivalent Static Method is not directly mentioned. However, in the draft code, the applicability of the said method is explicitly mentioned. As per draft code, the method shall be applicable for (i) regular buildings with height less than 48 m and (ii) regular buildings with height greater than 48 m and fundamental translation natural period less than 3.5 s.

### 2.1.2 Dynamic Analysis Method

Dynamic Analysis Method shall be performed in three ways, namely (i) Response Spectrum Method, (ii) Modal Time History Method and (iii) Time History Method

Modal Time History Method is newly added in draft code for calculation of lateral forces.

However, Dynamic Analysis Method shall be performed to the design seismic force and its distribution to different levels along the height of the building and to the various load resisting elements for the buildings mentioned in Table 1 as per existing and proposed code.

**Table 1** Applicability of Dynamic Analysis Method of regular and irregular buildings as per existing and draft code

Particulars	IS 1893 (part 1): 2002 [1]	IS 1893 (part 1): 2016 [2]
Regular buildings	Those greater than 40 m in height in Zones IV and V and those greater than 90 m in height in Zones II and III	Those taller than 48 m in Seismic Zones III, IV and V and taller than 70 m in Seismic Zones II. For buildings not taller than 48 m in Seismic Zones III, IV and V and those not taller than 70 m in Seismic Zones II, Equivalent Static Method may be adopted
Irregular buildings	All framed buildings higher than 12 m in Zones IV and V and those greater than 40 m in height in Zones II and III	Those taller than 12 m in Seismic Zones III, IV and V and taller than 48 m in Seismic Zones II. This method is recommended for irregular buildings of lower height, even though it may not be mandatory as above



It is to be mentioned here that as per proposed code the applicability of Equivalent Static Method is contradictory as the same thing was discussed in the proposed code in Dynamic Analysis Method wherein it has been clearly stated that the Equivalent Static Method may be adopted in case of regular building not taller than 70 m in Seismic Zone II. But, as per point no (ii) of Equivalent Static Method as discussed above, the height required to be approximately 168 m to get fundamental translation natural period as 3.5 s, which does not match with the condition of Dynamic Analysis Method regarding the use of Equivalent Static Method in case of regular building. So in draft code, clarification of the second point of Equivalent Static Method is necessary.

In case of regular building in existing code, Dynamic Analysis Method is applicable for the buildings taller than 40 m in height in zones IV and V, but in proposed code, the said method is applicable for the buildings taller than 48 m in height in Seismic Zones III, IV and V. Again, in existing code, the same method is applicable for the buildings taller than 90 m in height in Zones II and III, but in proposed code, the said method is applicable for the buildings taller than 70 m in height in Seismic Zones II only. In proposed code, it has been clearly mentioned that the Equivalent Static Method may be adopted for buildings not taller than 48 m in Seismic Zones III, IV and those not taller than 70 m in Seismic Zones II. But in existing code, nothing is mentioned regarding this.

Again, in case of irregular building in existing code, the Dynamic Analysis Method is applicable for all framed buildings higher than 12 m in height in zones IV and V, but in proposed code, it is included for Zone III also. Similarly, for Zones II and III, this method is applicable for buildings greater than 40 m in height in existing code and in proposed code, it is 48 m for Zone II only. In proposed code, it is mentioned that the same method is recommended for irregular buildings of lower height also. But in existing code, nothing is mentioned regarding lower height.

However, in most earthquake design codes, the Equivalent Static Method is used to establish design forces and due to this Equivalent Static Method is discussed elaborately in this paper. The forces are determined on the basis of a base shear by Equivalent Static Method. Calculation procedure of base shear is expressed through Eq. (1) as per existing and draft code.

$$V_B = A_h W = \frac{ZI(S_a/g)}{2R} W \quad (1)$$

where  $V_B$  = Base shear;  $A_h$  = Design horizontal acceleration spectrum value using the fundamental natural period  $T_a$  in the considered direction of vibration;  $W$  = Seismic weight of the building;  $Z$  = Seismic zone factor;  $I$  = Importance factor;  $R$  = Response reduction factor and  $S_a/g$  = Design acceleration coefficient.

### 3 Comparison of Various Parameters

#### 3.1 Seismic Zone Factor (*Z*)

According to the distribution of earthquake epicentres, ground motion attenuation, geophysical and tectonic data, India was mapped dividing into four generalized seismic zones. Each zone has a seismic zone factor (*Z*) that represents a reasonable estimate of peak ground acceleration (PGA) in the respective zone. The north-eastern folded regions of India are the most active zones and have a maximum PGA value of 0.36 g.

#### 3.2 Importance Factor (*I*)

According to existing code, importance factor is 1.5 for important service and community buildings and emergency buildings such as hospitals; schools; monumental structures; telephone exchange; television stations; fire station buildings; cinema halls; assembly halls; power station etc. The value of this factor kept 1 for all other Buildings. However, as per draft code along with the existing importance factor, an additional coefficient of importance factor as 1.2 is considered for the residential or the commercial buildings or structures, with occupancy more than 200 persons.

#### 3.3 Design Acceleration Coefficient (*S<sub>a</sub>/g*)

It is a factor denoting the acceleration response spectrum of the structure subjected to earthquake ground vibrations and depends on natural period of vibration and

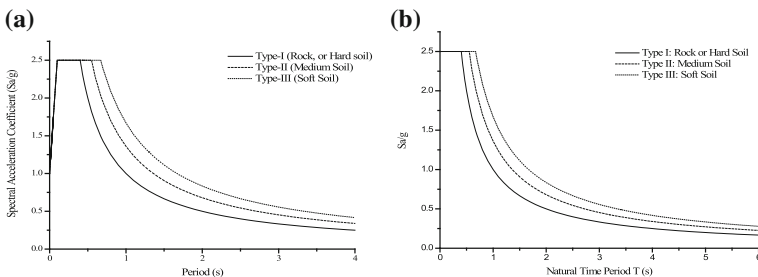


**Fig. 1** a Response spectra for rock and soil sites for 5% damping, as per existing graph and b design acceleration coefficient (*S<sub>a</sub>/g*) (corresponding to 5% damping) as per draft code

**Table 2** Comparison of design acceleration coefficient ( $S_a/g$ ) as per existing and draft code

IS 1893 (part 1): 2002 [1]	IS 1893 (part 1): 2016 [2]
For rocky or hard soil $S_a/g = \begin{cases} 1 + 15T & 0.00 \leq T \leq 0.10 \\ 2.5 & 0.10 \leq T \leq 0.40 \\ 1.00/T & 0.40 \leq T \leq 4.0 \end{cases}$	For rocky or hard soil $S_a/g = \begin{cases} 2.5 & 0 < T < 0.40 \text{ s} \\ 1/T & 0.40 \text{ s} < T < 6.00 \text{ s} \end{cases}$
For medium soil sites $S_a/g = \begin{cases} 1 + 15T & 0.00 \leq T \leq 0.10 \\ 2.5 & 0.10 \leq T \leq 0.55 \\ 1.36/T & 0.55 \leq T \leq 4.0 \end{cases}$	For medium soil sites $S_a/g = \begin{cases} 2.5 & 0 < T < 0.55 \text{ s} \\ 1.36/T & 0.55 \text{ s} < T < 6.00 \text{ s} \end{cases}$
For soft soil sites $S_a/g = \begin{cases} 1 + 15T & 0.00 \leq T \leq 0.10 \\ 2.5 & 0.10 \leq T \leq 0.67 \\ 1.67/T & 0.67 \leq T \leq 4.0 \end{cases}$	For soft soil sites $S_a/g = \begin{cases} 2.5 & 0 < T < 0.67 \text{ s} \\ 1.67/T & 0.67 \text{ s} < T < 6.00 \text{ s} \end{cases}$

damping of the structures. In existing code, three parameters are there in three types of soil but in draft code, two parameters are there in three types of soil. It is a coefficient corresponding to 5% damping for different soil types normalized to PGA corresponding to natural period ( $T$ ) of structure considering soil–structure interaction given by Fig. 1 and the associated expressions are shown in Table 2.

### 3.4 *Fundamental Natural Period (as per IS 1893 (part 1): 2002 [1])/Fundamental Translation Natural Period (as per IS 1893 (part 1): 2016 [2]) ( $T_a$ )*

The most common method to estimate vibration period of a building is from empirical relations considering building specifications (structure type) and its height ( $h$ ) in m, from base level and the base dimension ( $d$ ) of the building at the plinth level, in m, along the considered direction of the lateral force. Empirical relations of fundamental period are shown in Table 3 for both the codes.

### 3.5 *Response Reduction Factor( $R$ )*

Response reduction factor is used in the code to implicitly account for the nonlinear response of structure. It is expressed as a function of various parameters of the structural system, such as strength, ductility damping and redundancy. The response reduction factor is more or less same in existing code as well as in draft code for various lateral loads resisting system. Moreover, few more structural systems are incorporated in the draft version as shown in Table 4.

**Table 3** Comparison of fundamental natural time period ( $T_a$ ) in existing and draft codes

Structural system	Empirical expressions	
	IS 1893 (part 1): 2002 [1]	IS 1893 (part 1): 2016 [2]
RC frame building	$0.075h^{0.75}$	$0.075h^{0.75}$
RC-steel composite MRF building	Not mentioned	$0.080h^{0.75}$
Steel frame building	$0.085h^{0.75}$	$0.085h^{0.75}$
Moment-resisting frame buildings with brick infill panels	$\frac{0.09h}{\sqrt{d}}$	$\frac{0.09h}{\sqrt{d}}$
Buildings with concrete structural walls or un-reinforced masonry infill walls	Not mentioned	$\frac{0.075h^{0.75}a}{\sqrt{A_w}}$

<sup>a</sup> $A_w$  = total effective area ( $m^2$ ) of walls in the first storey of the building calculated by  $A_w = \sum_{i=1}^{N_w} \left[ A_{wi} \left\{ 0.2 + \left( \frac{L_{wi}}{h} \right)^2 \right\} \right]$ ;  $A_{wi}$  = effective cross-sectional area ( $m^2$ ) of wall  $i$  in first storey of building;  $L_{wi}$  = length (m) of structural wall  $i$  in first storey in the considered direction of lateral forces;  $N_w$  = number of direction walls in the considered direction of lateral forces; the value of  $L_{wi}/h$  to be used in this equation shall not exceed 0.9

**Table 4** Response reduction factor  $R$  (proposed and modified) as per draft code

System	Lateral load resisting system	R-Value
Moment frame systems	Steel Building with Ordinary Moment Resisting Frame (OMRF)	4.0
	Steel Building with Special Moment Resisting Frame (SMRF)	5.0
Braced frame systems	Steel Building with Special Braced Frame with Concentric Braces	4.5
	Steel Building with Ordinary Braced Frame with Eccentric Braces	4.5
Structural wall systems	Un-reinforced Masonry (Design as per IS 1905) with horizontal RC Seismic Bands	2.0
	Un-reinforced Masonry (Design as per IS 1905) with horizontal RC Seismic Bands and vertical reinforcing bars at corners of rooms and Jambes of opening (with reinforcement as per IS 4326)	2.5
	For Confined Masonry	3.0
Dual systems	RC Buildings with Ductile RC Structural wall with RC OMRF	4.0 instead of 4.5

It is well-known fact that redundant structures are performing well during earthquake. However, it has been observed that buildings which performed well in past earthquakes have redundancy factor ( $r$ ) more than 2.5. So, in the draft code it is suggested that for buildings with redundancy factor less than 2.5 (i.e. in the range 1.0–2.5) design engineer shall adopt modified values  $R_m$  of response reduction factor given by the expression:

$$R_m = \left[ 0.5 + 0.5 \left( \frac{r-1}{1.5} \right) \right] R \quad (2)$$

where  $r$  is redundancy factor and can be estimated as ratio of ultimate load to first yield load and  $R$  is the response reduction factor as mentioned in Table 6 of Draft Indian Standard IS 1893 (part 1): 2016 [2].

### 3.6 Seismic Weight ( $W$ )

Calculation procedure of seismic weight is more or less same in both the codes.

### 3.7 Base Shear

Calculation procedure of base shear is more or less same in both the codes.

## 4 Regular and Irregular Configuration

A building is said to be earthquake-resistant if it possesses four main attributes and the differences of these in both the codes are shown in Table 5. The differences of plan irregularities and vertical irregularities as per existing and draft code are shown in Tables 6 and 7, respectively.

It is to be mentioned here that in the paper of Valumundsson and Nau [7], it has been clearly stated regarding mass, strength and stiffness irregularities as per Uniform Building Code (UBC). In Indian existing seismic code, it is mentioned that there are some limitations for consideration of soft storey of a building, whereas in draft code, it is mentioned that a building will be a soft storey in which the lateral stiffness is less than that in the storey above.

Mass irregularity is considered to exist where the seismic weight of any storey is more than 200% of its adjacent storeys in case of existing code and it has decreased to 150% in case of draft code which is also used in UBC and the reason also mentioned in the said paper.

**Table 5** Comparison of four main attributes

IS 1893 (part 1): 2002 [1]	IS 1893 (part 1): 2016 [2]
Simple and regular attribution	Simple and regular structural attribution
Adequate lateral strength	At least a minimum lateral strength
Adequate lateral stiffness	At least a minimum initial lateral stiffness
Adequate ductility	Adequate ductility

**Table 6** Comparison of plan irregularities as per existing and draft code

Irregularity type	Description	
	IS 1893 (part 1): 2002 [1]	IS 1893 (part 1): 2016 [2]
Torsional irregularities	Torsional irregularity to be considered to exist when the maximum storey drift, computed with design eccentricity, at one end of the structures transverse to an axis is more than 1.2 times the average of the storey drifts at the two end of the structure	A building is said to be torsionally irregular, when maximum horizontal displacement of any floor in the direction of the lateral force at one end of the floor is more than 1.5 times its minimum horizontal displacement at the far end in that direction

**Table 7** Comparison of vertical irregularities as per existing and draft code

Irregularity type	Description	
	IS 1893 (part 1): 2002 [1]	IS 1893 (part 1): 2016 [2]
Stiffness irregularity—soft storey	A soft storey is one in which the lateral stiffness is less than 70% of that in the storey above or less than 80% of the average lateral stiffness of the three storeys above	A soft storey is one in which the lateral stiffness is less than that in the storey above
Stiffness irregularity—extreme soft storey	A extreme soft storey is one in which the lateral stiffness is less than 60% of that in the storey above or less than 70% of the average stiffness of the three storeys above	Nothing is mentioned regarding this
Lateral stiffness irregularity in two principal plan directions	Nothing is mentioned regarding this	Lateral stiffness of beams, columns, braces and structural walls determine the lateral stiffness of a building in each principal plan direction
Mass irregularity	Mass irregularity shall be considered to exist where the seismic weight of any storey is more than 200% of its adjacent storeys. The irregularity need not be considered in case of roofs	Mass irregularity shall be considered to exist where the seismic weight of any storey is more than 150% of its adjacent storeys. This provision of 150% may be relaxed in case of roofs
Vertical geometric irregularity	Vertical geometric irregularity shall be considered to exist where the horizontal dimension of the lateral force resisting system in any storey is more than 150% of that in its adjacent storey	Vertical geometric irregularity shall be considered to exist, when the horizontal dimension of the lateral force resisting system in any storey is more than 125% of that in its adjacent storey
Discontinuity in capacity—weak storey	A weak storey is one in which the storey lateral strength is less than 50% of that in the storey above	A weak storey is one in which the storey lateral strength is less than that in the storey above

In case of weak storey, some bar is there in existing code but in case of draft code, a soft storey is that where the lateral stiffness is less than that in the storey above.

In existing code, vertical geometric irregularity shall be considered to exist where the horizontal dimension of the lateral force resisting system in any storey is more than 150% of that in its adjacent storey, but in draft code, it has been mentioned that vertical geometric irregularity shall be considered to exist, when the horizontal dimension of the lateral force resisting system in any storey is more than 125% of that in its adjacent storey. Regarding lateral stiffness irregularity in two principal plan directions, nothing is mentioned in the existing code.

## 5 Conclusions

In this paper, after detailed study of IS 1893 (part 1): 2002 [1] and IS 1893 (part 1): 2016 [2] it is observed that IS 1893 (part 1): 2016 [2] is more sophisticated giving more realistic values for time period, importance factor, response reduction factor, design acceleration coefficient, definitions for regular and irregular buildings, etc., in comparison with IS 1893 (part 1): 2002 [1]. Proposed seismic code, i.e. IS 1893 (part 1): 2016 [2], will lead to more rational approach in the seismic design of buildings in India. The study also shows the difference between the codes for seismic design depending on location and occupancy use and the difference between the response spectra graph as per existing and draft code.

## References

1. BIS (2002) IS 1893 (part 1): 2002—Indian standard criteria for earthquake resistant design of structures, part 1: general provisions and buildings (Fifth Revision). Bureau of Indian Standards, New Delhi
2. BIS (2016) IS 1893 (part 1): 2016 (Draft)—Indian standard criteria for earthquake resistant design of structures, part 1: general provisions and buildings (Sixth Revision). Bureau of Indian Standards, New Delhi
3. Bari MdS, Das T (2013) A comparative study on seismic analysis of Bangladesh National Building Code (BNBC) with other building codes. *J Inst Eng India Ser A* 94(3):131–137
4. Xiaoguang C, Jingshan B, Youwei S, Jianyi Z, Yudong, Z (2012) Comparison of seismic fortification criterion of eight Asian countries. 15WCEE, Lisboa
5. Dogangiin A, Livaoglu R (2006) A comparative study of the design spectra defined by Eurocode 8, UBC, IBC, and Turkish Earthquake Code on R/C sample buildings. *J Seismol* 10:335–351
6. Imashi N, Massumi A (2011) A comparative study of the seismic provisions of Iranian Seismic Code (Standard No. 2800) and international building code 2003. *Asian J Civ Eng (Building and Housing)* 12(5):579–596
7. Valumundsson EVB, Nau JM (1997) Seismic response of building frames with vertical structural irregularities. *ASCE J Struct Eng* 1(30):30–41

# Analytical Model for Failure of Clamped Beam Subjected to Projectile Impact



S. Sen and A. Shaw

**Abstract** In the present study, an analytical model is presented for predicting different deformation modes (mode I–IV) that a rigid-plastic clamped beam may undergo when struck symmetrically by a rigid projectile having a finite width. Herein, the plastic deformation (mode I) of the beam is modeled using three basic phase of motion (phase 1–3) and the material failure (mode II–IV) is predicted using an energy criterion. The derived analytical model is validated via numerical solutions.

**Keywords** Clamped beam · Plastic analysis · Failure · Projectile impact  
Plastic hinge

## 1 Introduction

A proper understanding of structural behavior under impact loading is very important in order to design improved impact-resistant structural systems. Impact on beams and plates is the classical problems through which various physical processes (traveling plastic hinge, interaction of elastic and plastic fronts, various failure mechanisms such as ricochet, embedment, plugging, spalling, scabbing, radial fracture, petaling, fragmentation) may be explained [1]. Therefore, behavior of plates and beams under high-velocity impact plays a very important role in characterizing the dynamic behavior of materials or structures. The characterization can be obtained either experimentally, numerically, or analytically. In order to have a quick estimate of ballistic limit and sensitivity of various parameters (material, geometric, and initial conditions), analytical models are very useful. Analytical models, developed based on

---

S. Sen · A. Shaw (✉)  
Civil Engineering Department, Indian Institute of Technology Kharagpur, Kharagpur  
721302, India  
e-mail: abshaw@civil.iitkgp.ernet.in

S. Sen  
e-mail: ssen73@iitkgp.ac.in



simplified assumptions and idealization of an actual impact event, are also useful in forming design provisions of impact-resistant structures.

Several researches were carried out in order to understand the behavior of beam subjected to impact loading both experimentally [2–6] and theoretically [7–16]. Initially, major focus was on the dynamic deformation [7–10] of structures. In last few decades, focus of the research has been gradually shifted from dynamic deformation to dynamic failure [11–15].

Depending upon the nature of dynamic loading, structures may fail in different failure modes. Through experimental studies, Menkes and Opat [4] identified three basic failure modes of clamped beam subjected to impulsive loading, viz large inelastic deformation of the beam (mode I), tensile tearing at the supports (mode II), and shear failure of the beam at support (mode III). Liu and Jones [5] and Yu and Jones [6] studied the response of fully clamped beams subjected to impact loads. In addition to the three failure modes, they observed another mode of failure, viz shear failure at the impact point (mode IV) when the beam is struck near the mid-span.

Liu and Jones [10] developed an analytical model to study the mode I behavior of fully clamped beam, struck by a rigid mass at any point of the span, where the target material is considered as rigid plastic. Shen and Jones [12, 13] developed an energy criterion for studying the failure behavior of clamped beam. Later, Wen et al. [14] suggested a quasi-static approach for calculating the plastic response and failure pattern of clamped beam struck by heavy mass at low speed. In this study, strain and energy criteria are used for predicting the failure of the beam.

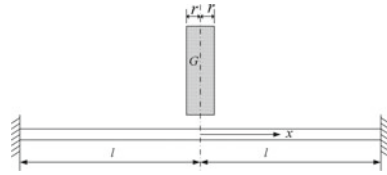
In the available literature, the response of beam has been studied mainly for two types of loading condition, viz impulsive loading and impact by mass (point impact load). Effect of finite width of the projectile (i.e., impact load spread over some portion of the beam) has not been considered. Analytical models were developed for predicting mode I, mode II, and mode III failures. However, these models did not consider the mode IV failure at the mid-span of the beam. In the present study, an analytical model is presented for predicting different deformation modes (mode I–IV) that a clamped beam may undergo when struck symmetrically by a rigid projectile.

## 2 Theory

Let us consider a clamped beam of length  $2l$  and mass  $m$  per unit length. The beam is struck by a rigid projectile having mass  $G$ , width  $2r$  with an initial velocity  $V_0$  as shown in Fig. 1. Followings are the assumptions which constitute the basis of the present model,

- i. The beam is fully clamped and is struck symmetrically at its mid-span by a rigid projectile.
- ii. The beam behaves as rigid perfectly plastic material. Elastic response of beam is negligible compared to its plastic counterpart.
- iii. The projectile remains in contact with the beam throughout the deformation process.

**Fig. 1** Clamped beam struck transversely by projectile of mass  $G$  and width  $2r$



### 2.1 Plastic Deformation

The dynamic plastic response of the beam is modeled with three basic phases of motion, viz phase 1—indentation or shear sliding at impact zone, phase 2—movement of traveling plastic hinges, and phase 3—rotation. As the beam is struck symmetrically by the projectile, only one half is considered for the analysis.

#### 2.1.1 Phase 1: $0 \leq t \leq t_1$

After the beam is struck by the projectile (mass =  $G$  and width =  $2r$ ), two stationary plastic hinges developed at  $x = r$  and  $x = -r$ ; and two traveling plastic hinges developed at  $x = a$  and  $x = -a$ . Transverse shear sliding takes place on both sides of impact zone (i.e.,  $x = r^+$  and  $x = -r^-$ ) where the shear forces reach their plastic capacity ( $Q = Q_0$ ). In the indentation phase, movement of the traveling plastic hinges does not take place, i.e.,  $a' = 0$ . It is assumed that rigid rotation of the part of the beam (AC), between the stationary plastic hinge (A) and traveling plastic hinge (C), takes place about the traveling plastic hinge (C). The remaining part of the beam between traveling hinge and support remains un-deformed. This assumption leads to a linear variation of velocity between the stationary plastic hinge and traveling hinge as shown in Fig. 2a. Plastic yielding of beam is controlled by an interaction yield condition, expressed in terms of bending moment ( $M$ ), membrane force ( $N$ ), and shear force ( $Q$ ) given by

$$|m| \sqrt{1 - q^2} + n^2 + q^2 = 1 \tag{1}$$

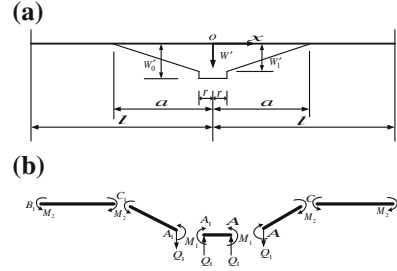
where  $m = M/M_0$ ;  $n = N/N_0$ ;  $q = Q/Q_0$ .  $M_0 = 0.25\sigma_0bh^2$ ;  $N_0 = \sigma_0bh$  and  $Q_0 = \sigma_0bh/\sqrt{3}$  are the plastic moment, membrane, and shear capacity of the beam section of width  $b$  and thickness  $h$ .  $\sigma_0$  is the yield strength of beam material.

Transverse force equilibrium equations for impact zone (AA1) and region AC and moment equilibrium equation for the region AC about point A are given by

$$\ddot{W}_0 = -8uvq_1 \tag{2}$$

$$g(z_1 - k) \ddot{W}_1 = 8uvq_1 \tag{3}$$

**Fig. 2** Phase 1; **a** velocity profile, **b** generalized forces and moments



$$g(z_1 - k)^2 \ddot{W}_1 = 12u(m_1 + m_2) \tag{4}$$

where  $z = x/l$ ,  $z_1 = a_1/l$ ,  $k = r/l$ ,  $\bar{W} = W/l$ ,  $x' = \partial x/\partial T$ ,  $\dot{x} = \partial x/\partial t$ ,  $t = M_0 T/GV_0 l$ ,  $u = Q_0 l/2M_0$ ,  $v = GV_0^2/2M_0$  and  $g = G/ml$ . According to the interaction equation (Eq. 1), in this phase  $m_1 = 0$ ,  $q_1 = 1$ ,  $m_2 = 1$ ,  $q_2 = 0$  and  $n = 0$ .

Now solving Eqs. (2–4) with the initial conditions  $\dot{W}_1 = 0$ ,  $\bar{W}_1 = 0$ ,  $\dot{W}_0 = 2u$  and  $\bar{W}_0 = 0$  at  $t = 0$ , we obtain

$$\begin{aligned} z_1 &= \frac{3}{2v} + k, & \dot{W}_1 &= \frac{16uv^2 t}{3g}, & \bar{W}_1 &= \frac{8uv^2 t^2}{3g} \\ \dot{W}_0 &= 2u - 8uvt, & \bar{W}_0 &= 2ut - 4uvt^2 \end{aligned} \tag{5}$$

Transverse shear sliding ceases when  $\dot{W}_1 = \dot{W}_0$  which occurs at  $t_1 = 3g/[4v(2v + 3g)]$ . Transverse shear sliding ( $\bar{W}_{sf}$ ) accumulated during this phase in impact zone is given as  $\bar{W}_{sf} = \bar{W}_0(t_1) - \bar{W}_1(t_1)$ .

**2.1.2 Phase 2:  $t_1 \leq t \leq t_2$**

In the second phase, traveling plastic hinges move toward the supports. So, ‘ $a$ ’ becomes a function of time ( $T$ ). This phase is completed (at  $t_2$ ) when plastic hinges reach the supports. The velocity profile, the generalized forces, and moments developed in the beam are shown in Fig. 3. Yield condition for point A and C is given by Eq. (1) with  $q_2 = 0$ .

Transverse force equilibrium equations for the region (AA1) and region AC and moment equilibrium equation for the region AC about point A are given by

$$\ddot{W}_1 = -8uvq_1 \tag{6}$$

$$g(z_1 - k) \ddot{W}_1 + g\dot{z}_1 \dot{W}_1 = 8uvq_1 \tag{7}$$

$$(z_1 - k)\ddot{\bar{W}}_1 + 2\dot{z}_1\dot{\bar{W}}_1 = \frac{12u}{g(z_1 - k)} (m_1 + m_2 + n\gamma\bar{W}_1) \tag{8}$$

where  $\gamma = N_0l/M_0$ . Solving Eqs. (6-8), following expressions for  $\ddot{\bar{W}}_1$  and  $\dot{z}_1$  are obtained

$$\ddot{\bar{W}}_1 = -\frac{12u(m_1 + m_2 + n\gamma\bar{W}_1)}{(z_1 - k)[g(z_1 - k) + 2]} \tag{9}$$

$$\dot{z}_1 = -\frac{\ddot{\bar{W}}_1[g(z_1 - k) + 1]}{g\dot{\bar{W}}_1} \tag{10}$$

Normality requirement (suggested by Shen and Jones [13]) of plasticity for transverse velocity profile (Fig. 3a) and yield condition is given by

$$\frac{\dot{\Delta}_1(z_1 - k)}{\dot{\bar{W}}_1} = -\frac{1}{\gamma} \frac{\partial m_1}{\partial n} = \frac{2n}{\gamma\sqrt{1 - q_1^2}} \tag{11}$$

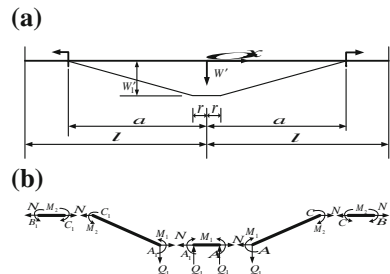
$$\frac{\dot{\Delta}_2(z_1 - k)}{\dot{\bar{W}}_1} = -\frac{1}{\gamma} \frac{\partial m_2}{\partial n} = \frac{2n}{\gamma} \tag{12}$$

where  $\bar{\Delta} = \Delta/l$ ;  $\Delta_1, \Delta_2$  are the axial stretch of the beam at point A and C, respectively. By means of approximate geometric relation [ $\Delta'_1 + \Delta'_2 \cong W_1W'_1/(a - r)$ ], normality equations are expressed as

$$\bar{W}_1 = \frac{2n}{\gamma} \left[ 1 + \frac{1}{\sqrt{1 - q_1^2}} \right] \tag{13}$$

$\dot{\bar{W}}_1, \bar{W}_1,$  and  $z_1$  are estimated by numerically integrating Eqs. (9) and (10) with the initial conditions obtained at the end of Phase 1. During the numerical integration, at each time step  $q_1, m_1$  and  $n$  are estimated from Eqs. (1), (6), and (13).

**Fig. 3** Phase 2; **a** velocity profile, **b** generalized forces and moments



**2.1.3 Phase 3:**  $t_2 \leq t \leq t_f$

At the beginning of the third phase, traveling plastic hinge reaches the support and  $z_1$  becomes 1. During this phase, only rigid rotation of the beam takes place. Velocity profile and the generalized forces and moments developed in the beam are shown in Fig. 4. Yield condition for point A and B is given by Eq. 1.

Transverse force equilibrium equations for impact zone (AA1) and region AB and moment equilibrium equation for the region AB about point B are given by

$$\ddot{W}_1 = -8uvq_1 \tag{14}$$

$$g(1-k)\ddot{W}_1 = 8uv(q_1 - q_2) \tag{15}$$

$$\ddot{W}_1 = -\frac{6u[m_1 + m_2 + n\gamma\bar{W}_1 - 2vq_1(1-k)]}{g(1-k)^2} \tag{16}$$

Solving Eqs. (14) and (16), following expression for  $\ddot{W}_1$  is obtained

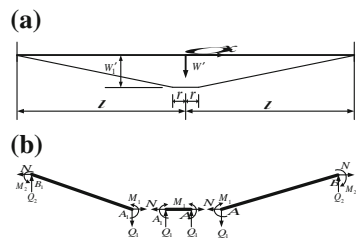
$$\ddot{W}_1 = -\frac{12u(m_1 + m_2 + n\gamma\bar{W}_1)}{(1-k)[2g(1-k) + 3]} \tag{17}$$

By means of approximate geometric relation, normality equations for Phase 3 are expressed as

$$\bar{W}_1 = \frac{2n}{\gamma} \left[ \frac{1}{\sqrt{1-q_1^2}} + \frac{1}{\sqrt{1-q_2^2}} \right] \tag{18}$$

$\dot{\bar{W}}_1$  and  $\bar{W}_1$  are estimated by numerically integrating Eq. (17) with the initial condition obtained at the end of Phase 2. During the numerical integration, at each time step  $q_1, m_1, q_2, m_2$  and  $n$  are estimated from Eqs. (14), (15), (18) and yielding equation (Eq. 1) for A and B section. At the end of this phase (at  $t_f$ ), the beam comes at rest (i.e.,  $\dot{\bar{W}}_1 = 0$ ).

**Fig. 4** Phase 3; **a** velocity profile, **b** generalized forces and moments



In Phase 2–3, dimensionless displacement of the beam at point O ( $\bar{W}_0$ ) is estimated by adding the accumulated shear sliding ( $\bar{W}_{sf}$ ) obtained at the end of Phase 1 with  $\bar{W}_1$ , i.e.,  $\bar{W}_0 = \bar{W}_1 + \bar{W}_{sf}$ .

This analytical model is applicable for beam having  $\nu > 1.5/(1 - k)$ ; otherwise at the first phase, traveling hinge will develop at support ( $z = 1$ ) and there will be no movement of the plastic hinge. With  $M_0 = 0.25\sigma_0bh^2$  and  $Q_0 = \sigma_0bh^2/\sqrt{3}$ , this condition implies that clear half span ( $l - r$ ) of the beam should be greater than 1.3 times the beam thickness, i.e.,  $(l - r)/h > 1.3$ . This condition is generally satisfied in an actual beam.

## 2.2 Failure Modeling

In the present study, failure of the beam is predicted using an energy criterion. According to this energy criterion, beam fails when the amount of energy dissipated ( $E_d$ ) at any critical section of the beam exceeds the energy capacity ( $E_c$ ) of the same section. Energy can be dissipated through bending ( $E_{dm}$ ), shear ( $E_{ds}$ ), and membrane action ( $E_{dn}$ ). The amount of the energy dissipation is calculated in an incremental way. Formulations for energy dissipation through different modes are given as

for bending action

$$\delta E_{dm} = m_1 M_0 \delta \theta \quad (19)$$

for shear action

$$\delta E_{ds} = q_1 Q_0 \delta W_s \quad (20)$$

for membrane action

$$\delta E_{dn} = n N_0 \delta \Delta \quad (21)$$

where  $\delta$  indicates the changes in  $E_{dm}$ ,  $E_{ds}$ ,  $E_{dn}$ ,  $\theta$ ,  $W_s$  and  $\Delta$  for each time increment  $\delta T$ .  $\theta$ ,  $W_s$  and  $\Delta$  represent the rotation, shear sliding, and axial stretch, respectively, and calculated as

$$\theta = \frac{\bar{W}_1}{z_1 - k} \quad (22)$$

$$W_s = (\bar{W}_0 - \bar{W}_1) l \quad (23)$$

$$\Delta = l(z_1 - k) \sqrt{1 + \left(\frac{\bar{W}_1}{z_1 - k}\right)^2} \quad (24)$$

Total dissipated energy and energy capacity of the critical section are calculated using Eqs. (25) and (26). Failure of the beam at support and the middle portion is differentiated using the location of traveling hinge. It is considered that the failure will take place in the middle portion of the beam when failure occurs before the traveling plastic hinge reaches the supports. In the other case, when the traveling hinge reaches the support first, velocity (inertia effect) of projectile reduced. This reduced inertia force can cause the failure of the beam at the support instead of the middle portion.

$$E_d = \sum (\delta E_{dm} + \delta E_{ds} + \delta E_{dn}) \quad (25)$$

$$E_c = \sigma_0 \varepsilon_f b h l_h \quad (26)$$

where  $\sigma_0$  and  $\varepsilon_f$  are the yield strength and rupture strain of beam material;  $b$ ,  $h$ , and  $l_h$  represent the width and depth of the beam cross section and length of the plastic hinge. Plastic hinge length of the beam is estimated using the equations (Eqs. 27–29) given by Shen and Jones [12, 13]. According to these equations, length of plastic hinge depends on the beam thickness and ratio of shear dissipation to total energy dissipation ( $\beta$ ).

$$l_h = \alpha h \quad (27)$$

$$\alpha = 1.3 - 1.2\beta \quad (28)$$

$$\beta = \frac{E_{ds}}{E_d} \quad (29)$$

### 3 Validation

In this section, the derived analytical model is validated via numerical solutions. The response of an aluminum beam having width ( $b$ ) 6.35 mm, thickness ( $h$ ) 6.35 mm and total length ( $2l$ ) 142 mm, struck by steel projectile, is determined using the proposed analytical model. These responses (plastic deformation, residual velocity, and failure behavior) are compared with the results of numerical analysis of the same beam performed in ABAQUS [17]. This study is carried out for three different projectile widths (i.e., 5, 10, and 14.45 mm) and four projectile masses (i.e., 5, 2, 1 and 0.5 kg). Material properties of aluminum and steel are taken from

**Table 1** Mechanical properties of target material

Young's modulus (GPa)	Poisson ratio	Yield strength (MPa)	Density (kg/m <sup>3</sup> )	Rupture strain
68.9	0.33	277.8	2680	0.17

**Table 2** Mechanical properties of projectile material

Young's modulus (GPa)	Poisson ratio	Yield strength (MPa)	Density (kg/m <sup>3</sup> )
200	0.25	600	7850

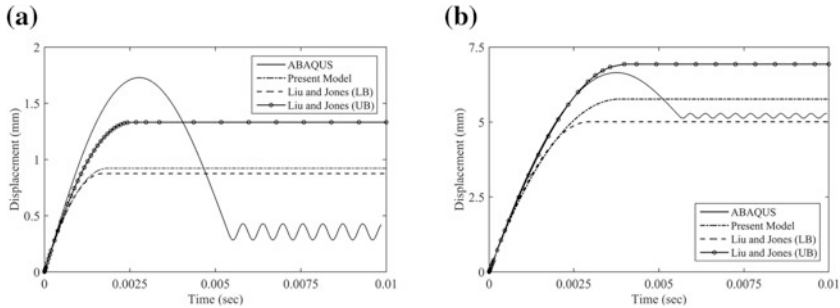


**Fig. 5** Displacement time history of midpoint of the beam struck by projectile having mass 2 kg and width 10 mm with impact velocity; **a** 1 m/s, **b** 3 m/s

the study of Chen and Yu [18] and are tabulated in Tables 1 and 2. This study is carried out for impact velocity varying from 1 to 150 m/s.

For velocities lower than ballistic limits, material failure of the beam does not take place. In these cases, plastic displacement of the beam at point O is compared with the ABAQUS result. Comparison of displacement time histories obtained from proposed analytical model, ABAQUS, and analytical model given by Liu and Jones [10] for 2 kg projectile mass is shown in Fig. 5. Plastic deformations obtained from the proposed analytical model shows better agreement with the ABAQUS results compared to the upper bound results of Liu and Jones's model. Plastic deformations obtained for different projectile width, mass, and impact velocity are tabulated in Table 3.

**Table 3** Midpoint displacement of the clamped beam in mm for different projectile mass, width, and impact velocity

Projectile mass (kg)	Impact velocity (m/s)	Liu and Jones [10]		Present model			ABAQUS [17]		
		LB	UB	5 mm	10 mm	14.45 mm	5 mm	10 mm	14.45 mm
5.0	1	1.90	2.80	2.30	2.20	2.10	1.51	1.40	1.17
5.0	2	5.40	7.40	6.90	6.80	6.60	5.73	5.71	5.69
2.0	1	0.88	1.30	0.95	0.92	0.89	0.60	0.43	0.22
2.0	3	5.00	6.90	6.50	6.30	6.20	5.30	5.29	5.23
1.0	3	3.00	4.30	3.80	3.70	3.60	2.75	2.70	2.60
1.0	5	6.30	8.60	7.90	7.80	7.60	6.87	6.85	6.80
0.5	4	2.80	4.00	3.50	3.40	3.30	2.45	2.40	2.35
0.5	7	6.20	8.40	7.80	7.70	7.50	6.80	6.75	6.70

LB—Lower Bound, UB—Upper Bound



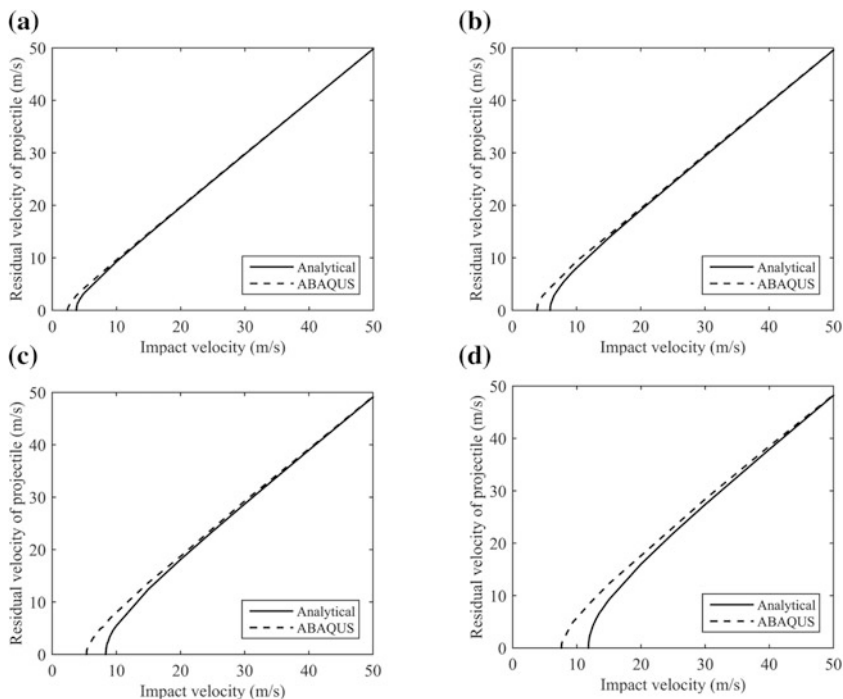


**Fig. 6** Comparison of residual velocities of projectile having width 5 mm and mass; **a** 5 kg, **b** 2 kg, **c** 1 kg, **d** 0.5 kg

**Table 4** Impact velocity (m/s) ranges for different failure mode of clamped beam struck by a 14.45-mm-wide projectile

Projectile mass (kg)	Failure at support		Failure at middle	
	Present model	ABAQUS [17]	Present model	ABAQUS [17]
5.0	$4.0 \leq V_0 < 80.0$	$3.0 \leq V_0 < 85.0$	$V_0 \geq 80.0$	$V_0 \geq 85.0$
2.0	$6.0 \leq V_0 < 80.0$	$4.0 \leq V_0 < 85.0$	$V_0 \geq 80.0$	$V_0 \geq 85.0$
1.0	$8.5 \leq V_0 < 80.0$	$6.0 \leq V_0 < 85.0$	$V_0 \geq 80.0$	$V_0 \geq 85.0$
0.5	$12.0 \leq V_0 < 80.0$	$8.0 \leq V_0 < 87.0$	$V_0 \geq 80.0$	$V_0 \geq 87.0$

For impact velocity higher than the ballistic limit, material failure (mode II, III, and IV) of beam takes place. In such cases, the residual velocity of the projectile and the failure behavior of the beam are studied both analytically and numerically. Residual velocity for 5-mm-wide projectile obtained from analytical model shows good agreement with the numerical results as shown in Fig. 6. Impact velocities associated with the support and middle failure of the beam, struck by a

14.45-mm-wide projectile, obtained both from present model and numerical analysis are tabulated in Table 4. Limit velocities for both support and middle failure estimated from the present model show good agreement with the numerically obtained limit velocities.

## 4 Conclusion

An analytical model is presented for predicting different deformation modes (mode I–IV) that a clamped beam may undergo when struck symmetrically by a rigid projectile. Plastic deformation obtained using this model shows good agreement with the numerical result for impact velocity closer to the ballistic limit. In the case of much lower velocity, the elastic response is not negligible compared to the plastic response. Thus, rigid-plastic analysis of the beam is unable to predict the plastic deformation of the beam at lower velocity. The residual velocity of the projectile and the failure behavior of the beam at different impact velocity are studied when failure of the beam takes place. The residual velocity of the projectile obtained from the analytical and numerical studies shows good agreement. Also, the impact velocity ranges associated with different failure modes obtained both from analytical model and numerical analysis is found to be almost similar.

## References

1. Stronge WJ, Yu TX (1993) *Dynamic models for structural plasticity*. Springer, New York
2. Parkes EW (1958) The permanent deformation of an encastré beam struck transversely at any point in its span. *Proc Inst Civ Eng* 10:227–304
3. Nonaka T (1967) Some interaction effects in a problem of plastic beam dynamics—Part 1: Interaction analysis of a rigid, perfectly plastic beam. *J Appl Mech* 34(3):623–630
4. Menkes SB, Opat HJ (1973) Broken beams. *Exp Mech* 13:480–486
5. Liu J, Jones J (1987) Experimental investigation of clamped beams struck transversely by a mass. *Int J Impact Eng* 6(4):303–335
6. Yu J, Jones N (1991) Further experimental investigations on the failure of clamped beams under impact loads. *Int J Solids Struct* 27(9):1113–1137
7. Symonds P, Mentel T (1958) Impulsive loading of plastic beams with axial constraints. *J Mech Phys Solids* 6(3):186–202
8. Jones N (1971) A theoretical study of the dynamic plastic behavior of beams and plates with finite-deflections. *Int J Solids Struct* 7(8):1007–1029
9. Symonds P, Jones N (1972) Impulsive loading of fully clamped beams with finite plastic deflections and strain-rate sensitivity. *Int J Mech Sci* 14(1):49–69
10. Liu J, Jones N (1988) Dynamic response of a rigid plastic clamped beam struck by a mass at any point on the span. *Int J Solids Struct* 24(3):251–270
11. Jones N (1976) Plastic failure of ductile beams loaded dynamically. *J Eng Ind* 98(1):131–136
12. Shen WQ, Jones N (1992) A failure criterion for beams under impulsive loading. *Int J Impact Eng* 12(1):101–121

13. Shen WQ, Jones N (1993) Dynamic plastic response and failure of a clamped beam struck transversely by a mass. *Int J Solids Struct* 30(12):1631–1648
14. Wen H, Reddy TY, Reid SR (1995) Deformation and failure of clamped beams under low speed impact loading. *Int J Impact Eng* 16(3):435–454
15. Jones N, Shen WQ (2010) Criteria for the inelastic rupture of ductile metal beams subjected to large dynamic loads. In: Jones N, Wierzbicki T (eds) *Structural crashworthiness and failure*. Taylor and Francis, London, pp 82–112
16. Jones N (2011) *Structural impact*. Cambridge University Press, Cambridge
17. Hibbitt D, Karlsson B, Sorensen P (2011) *Abaqus 6.11: a computer software for finite element analysis*. Dassault Systems Simulia
18. Chen F, Yu T (2004) An experimental study of pre-notched clamped beams under impact loading. *Int J Solids Struct* 41(24–25):6699–6724

# Estimation of Peak Factors for Tall Buildings Subjected to Wind-Induced Pressures



M. Keerthana and P. Harikrishna

**Abstract** The peak factor for non-Gaussian fluctuating pressures occurring in the flow-separated regions of a rectangular tall building has been evaluated based on three translation-based Hermite methods, basic Hermite Model (HM), Revised Hermite Model (RHM), and Modified Hermite Model (MHM), with parameters evaluated from Yang (MHM-Yang). The evaluated peak factors have been compared with observed values from the data and other Hermite-based models of peak factors available in the literature. The relative performance of the models toward evaluation of peak factors, especially in the regions of flow separation, has been assessed. It has been observed that use of data-driven Hermite-based models could provide a better and realistic estimate of peak factor, as compared to that offered by Gaussian framework.

**Keywords** Pressures · Gaussianity · Peak factor · Tall building  
Hermite models · Skewness · Kurtosis

## 1 Introduction

Multivariate pressure fluctuations on buildings are characterized by instant peak pressures that are localized in nature. These peak pressures govern the design of components of a structure, e.g., roof cladding of a low-rise building, facades/glass cladding of high-rise buildings. Appropriate evaluation of such peak pressures is one of the important aspects in the performance-based design of such structures/structural components. In the traditional design philosophy, the random process of pressure fluctuations has been assumed to be of Gaussian nature, wherein the peak

---

M. Keerthana (✉) · P. Harikrishna  
Wind Engineering Laboratory, CSIR-Structural Engineering Research Centre,  
Chennai 600113, India  
e-mail: keerthana@serc.res.in

P. Harikrishna  
e-mail: hari@serc.res.in

pressures have been obtained using mean and standard deviation of the data along with the statistical peak factor. This statistical peak factor was well defined as the mean extrema of standardized process for Gaussian processes. Further, the cumulative distribution function (CDF) of the extremes was also derived. However, in regions of flow separation like roof of low-rise building and corners/side faces of high-rise buildings, the statistical description of the measured pressure shows significant deviation from Gaussian nature, with higher order statistical moments, viz., skewness and kurtosis significantly deviating from values of 0 and 3, respectively. The probability density functions (PDFs) of such non-Gaussian pressure fluctuations are characterized by heavy tails, especially in the negative portion. Using the Gaussian framework, as adopted even till date, will lead to unconservative design. This has been demonstrated by various researchers. For example, Kwon and Kareem [8] demonstrated that for the pressures measured at the corner of full-scale low-rise building, the Gaussian peak factor was 4.017, whereas that based on non-Gaussian framework was 8.39. Estimation of peak factors for wind-induced pressures on low-rise and high-rise buildings still continues to be an active area of research [1, 2, 5, 9, 10]. There are two approaches for estimation of peak factor. One is parametric, where the peaks from selected samples are fitted with extreme value distribution to get the parameters of the distribution, using which CDF of the extremes is obtained. Further, the peak value corresponding to a specific fractile level of probability of non-exceedance is evaluated from these extrema of CDF. Another approach is nonparametric and data-driven, where higher order statistical moments are used in analytical expressions to evaluate PDF and CDF of data and its extremes. From the CDF of extremes, a similar procedure as in parametric models is adopted to get peak factor.

In order to accurately model the extremes of pressures using parametric models, long duration data from wind tunnel or full-scale measurements are required. From such records, only a subset of information (on extrema) will be used for probabilistic modeling. The extrema of wind pressures were fitted from 1200 samples of repeated long duration wind tunnel data, to Gumbel (extreme value type I) and Weibull (extreme value type III) distributions [7]. It was reported that Gumbel distribution gave a conservative estimate of the peak pressures with small set of samples of extrema, in comparison with Weibull distribution, which needs about 5000 independent samples to accurately quantify the finite upper tail [4]. Gavanski et al. [3] made an assessment of the uncertainty in peak pressure coefficient with duration of time series and number of subsets used for fitting Gumbel method. Balaji Rao et al. [1] first applied alpha-stable distribution to the peak pressure coefficients from corners of low-rise building. A variety of other extreme value distributions like gamma and lognormal distributions have been used in the literature to model pressure extremes of non-Gaussian processes. It has been observed that a single PDF model cannot cater to strongly non-Gaussianity (especially in the tail region of the distribution), owing to which a combination of models has been attempted in the literature. Sadek and Simiu [13] used three-parameter gamma distribution for long tails and standard Gaussian distribution for short tail using a mapping transformation (MT).

The next class of nonparametric models that rationally treat non-Gaussian nature of pressure fields is Hermite Models (HM). They have been developed based on the framework of translation process, which convert the non-Gaussian process to Gaussian process through a nonlinear transformation. These models work on raw data and its higher order moments, in contrast to the parametric models. Kareem and Zhao [6], analytical expressions for peak factors were derived based on HM and applied to the response of tension leg platform to evaluate the negative peak response. Kwon and Kareem [8] revisited the HM and elucidated two modifications to overcome its inherent limitations. Yang et al. [14] proposed closed-form solutions to evaluate the parameters of improved HM used by Kwon and Kareem [8], making the applicability of improved HM toward probabilistic modeling of wind pressures easier, which otherwise would require solution of coupled nonlinear equations. Peng et al. [10] has suggested a mapping procedure to overcome the limitation on the working range of skewness and kurtosis for these models. Based on HM, a generalized peak factor (GP) was proposed by Pillai and Tamura [11], which considered the non-Gaussianity and bandwidth, i.e., whether it is narrow-banded or broad-banded phenomenon. A further simplified form of the expressions for peak factor in the aforementioned literature, 'skewness-dependent peak factor,' was derived by Huang et al. [5], which is based only on skewness as opposed to other models that considered both skewness and kurtosis. Recently, researchers are developing efficient methodologies to simulate and represent non-Gaussian processes based on third-order HM.

With such continuing research efforts toward evaluation of peak factors via probabilistic modeling toward reliability-based load modeling, the present study aims to evaluate peak factors from multi-channel wind tunnel pressure measurements carried out on a tall building model with rectangular plan ratio of 1:2 and aspect ratio of 9 (based on shorter dimension in plan) tested under turbulent flow (open terrain with power-law coefficient  $\alpha$  of 0.165). Toward this, three Hermite models, basic Hermite Model [8], referred hereafter as **HM**, Revised Hermite Model [8], referred hereafter as **RHM**, and Modified Hermite Model (MHM) [8], referred hereafter as **MHM-Yang**, with parameter estimates from [14] have been used. The peak factors from the aforementioned models have been presented and compared with the observed values from data. Toward completeness, a brief description of the models has been presented in the succeeding section.

## 2 Hermite Model for Non-Gaussian Process

### 2.1 Basic Hermite Model (HM)

With the need to develop more rational models to treat non-Gaussian nature of pressure fields, a model has been developed, by a framework offered by translation process and moment-based HM [8]. The basis of translation process is to use a

univariate nonlinear translation to express non-Gaussian process in terms of underlying Gaussian process as given by Eq. (1).

$$y = \frac{x - \bar{x}}{\sigma_x} = P_Y^{-1}[\Phi(u)] = g(u) \quad (1)$$

where

$y$  is a standardized (zero mean, unit normal) non-Gaussian random variable;  
 $P_Y$  a distribution of non-Gaussian random variable  $y$ ;  
 $\Phi(u)$  the distribution of the standard normal variable  $u$ ;  
 $g(u)$  a nonlinear function of  $u$  that is assumed to increase monotonically; and  
 $u$  a Gaussian random variable.

The nonlinear function  $g(u)$  has been analytically described by ‘moment-based Hermite’ model. This facilitates the description of PDF in an analytical form. For softening process (kurtosis  $> 3$ ), PDF of the process  $y$  is given by

$$y = g(u) = u + h_3(u^2 - 1) + h_4(u^3 - 3u) \quad (2)$$

where  $u(y) = \left[ \sqrt{\xi^2(y) + c + \xi(y)} \right]^{1/3} - \left[ \sqrt{\xi^2(y) + c - \xi(y)} \right]^{1/3} - a$ ;

$$\xi(y) = 1.5b \left( a + \frac{y}{\kappa} \right) - a^3; \quad a = \frac{h_3}{3h_4}; \quad b = \frac{1}{3h_4}; \quad c = (b - 1 - a^2)^3$$

$$h_3 = \frac{\gamma_3}{4 + 2\sqrt{1 + 1.5\gamma_4}}; \quad h_4 = \frac{\sqrt{1 + 1.5\gamma_4} - 1}{18}; \quad \kappa = \frac{1}{\sqrt{1 + 2h_3^2 + 6h_4^2}}$$

where  $\gamma_3$  and  $\gamma_4$  are the skewness and excess kurtosis (kurtosis-3) of the process  $y$ .  $u(y)$  is the solution of Eq. (2) for random variable  $u$ .  $h_3$ ,  $h_4$ , and  $\kappa$  are the coefficients of moment-based HM. Hence, the nonlinear function  $g(u)$  and  $u(y)$  depends on higher order statistical moments, which can be obtained from standardized process  $y$ , with the available time history of data. Hence, the PDF of a standardized non-Gaussian process is given by

$$P_Y(y) = \frac{1}{\sqrt{2\pi}} \exp \left[ -\frac{u^2(y)}{2} \right] \frac{du(y)}{dy} \quad (3)$$

## 2.2 Improved Hermite Models

The HM has been developed for univariate case (i.e., single random variable) and mild non-Gaussian process. It tends to be conservative in situations when the

process exhibits strong non-Gaussianity. Improvements to overcome this limitation of HM have been suggested as follows.

**2.2.1 Modified Hermite Model (MHM-Yang)**

The MHM [8] facilitated improvement in evaluation of a non-Gaussian process  $y$  through modified polynomial coefficients  $h_3$  and  $h_4$  given by

$$\gamma_3 = \kappa^3 (8h_3^3 + 108h_3h_4^2 + 36h_3h_4 + 6h_3) \tag{4}$$

$$\begin{aligned} \gamma_4 + 3 = \kappa^4 (60h_3^4 + 3348h_4^4 + 2232h_3^2h_4^2 + 60h_3^2 + 252h_4^2 \\ + 1296h_4^3 + 576h_3^2h_4 + 24h_4 + 3) \end{aligned} \tag{5}$$

These equations have been designed to obtain nonlinear solution of  $h_3$  and  $h_4$ , by taking  $\gamma_3$  and  $\gamma_4$  from the standardized process  $y$ . Even though this has been observed to improve the accuracy of HM as well as estimation of probability distribution function [8], solution of the equations to obtain  $h_3$  and  $h_4$  involves inversion, which is difficult to achieve analytically. Yang et al. [14] has presented an approximate closed-form solution to these equations, which simplified the use of MHM. These equations have been used in the present study.

**2.2.2 Revised Hermite Model (RHM)**

To make the MHM practically viable, without having to solve coupled nonlinear equations in Eqs. (4) and (5), simplified expressions for  $h_3$  and  $h_4$  based on optimal results that minimize the lack of fit errors for skewness and kurtosis of HM have been proposed [8] as given below.

$$h_3 = \frac{\gamma_3}{6} \left[ \frac{1 - 0.015|\gamma_3| + 0.3\gamma_3^2}{1 + 0.2\gamma_4} \right] \tag{6}$$

$$h_4 = h_{40} \left[ 1 - \frac{1.43 \gamma_3^2}{\gamma_4} \right]^{1-0.1(\gamma_4+3)^{0.8}} ; \quad h_{40} = \frac{[1 + 1.25 \gamma_4]^{1/3} - 1}{10} \tag{7}$$

These expressions are applicable for skewness and kurtosis in the range of  $0 \leq \gamma_3^2 < \frac{2\gamma_4}{3}$  and  $0 < \gamma_4 < 12$ .

The PDF of extremes is given by

$$P_{Y,ext}(y) = \exp(-\psi) \frac{d\psi}{dy}; \quad \psi = v_0 T \exp\left(-\frac{u^2(y)}{2}\right) \tag{8}$$



From the PDF, the peak factor has been obtained as

$$g_{\text{ng}} = \kappa \left\{ \begin{aligned} & \left( \beta + \frac{z}{\beta} \right) + h_3 \left[ \beta^2 + (2\gamma - 1) + \frac{1.98}{\beta^2} \right] \\ & + h_4 \left[ \beta^3 + 3\beta(2\gamma - 1) + \frac{3}{\beta} \left( \frac{\pi^2}{6} - \gamma + \gamma^2 \right) + \frac{5.44}{\beta^3} \right] \end{aligned} \right\} \quad (9)$$

The above equation has been formulated for positive extremes. To get negative extreme, the sign of the raw data needs to be reversed. The positive and negative extremes of the process have been evaluated by using the peak factor (Eq. 9) in the following expressions.

$$\begin{aligned} x_{\text{ext}} &= \bar{x} + \sigma_x \cdot g_{\text{ng}} \\ x_{\text{ext}} &= \bar{x} - \sigma_x \cdot g_{\text{ng}} \end{aligned} \quad (10)$$

### 3 Wind Tunnel Pressure Measurement

Wind-induced pressures on the surface of a 1:300 scale rigid model of a rectangular tall building with full-scale dimensions of 30 m × 60 m in plan and height of 270 m have been measured. The model was instrumented with pressure taps at five levels (with  $z/H$  of 0.1, 0.3, 0.5, 0.7 and 0.9) as shown in Fig. 1a, with 28 pressure taps at each level. The layout of same is shown in Fig. 2. Wind incident on the longer face of the rectangular tall building has been considered in the present study (Fig. 1b).

The wind tunnel tests have been carried out in the boundary layer wind tunnel of CSIR-Structural Engineering Research Centre (Fig. 3), under simulated open terrain with power-law coefficient of 0.165. The fluctuating wind pressures have been measured at a sampling frequency of 650 Hz, for duration of 24 s. This corresponds to full-scale duration of 2 h (based on geometric scale of 1:300 and velocity scale of 1:1). The measured pressures have been represented in the form of pressure coefficient given by

$$C_p = \frac{P}{1/2\rho U^2} \quad (11)$$

where  $U$  is the reference wind speed measured at the model height and  $\rho$  is the density of air. The time history of pressure coefficients from the pressure taps has been standardized, making it zero mean and unit variance trace (Fig. 4) as the Hermite-based methods operate over standardized data. Higher order moments, viz., skewness and kurtosis, have been evaluated for the standardized pressure coefficients.

**Fig. 1** a Rigid model of tall building. b Flow behavior at separation (after Cook 1990)

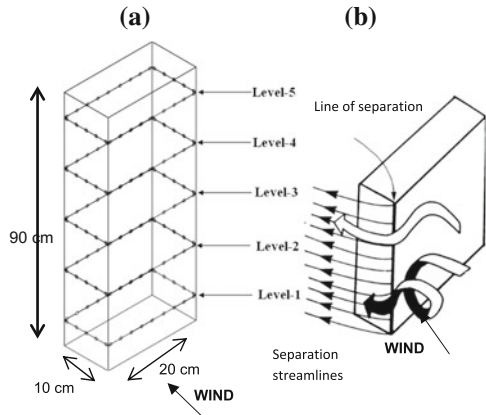


**Fig. 2** Pressure tap layout at level-1

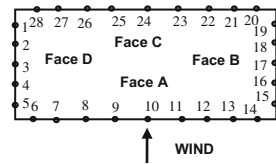


**Fig. 3** Model of tall building in wind tunnel under simulated open terrain



## 4 Results and Discussions

The flow pattern caused on the side walls of a rectangular tall building has been shown in Fig. 1b. The two side walls are subjected to high suction due to separation of flow along the edges of the windward face. A highly complex flow behavior occurs in the separated flow regions as well as in the wake. Further, the probabilistic characteristics of the pressures in that region significantly deviate from Gaussian nature. This is evident from the values of skewness and excess kurtosis (kurtosis-3) of standardized pressures coefficients shown in Fig. 5.

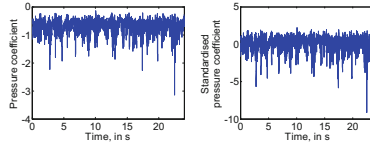


**Fig. 4** Time history of pressure coefficients and standardized pressure coefficients from a pressure tap

The values of higher order moments have been observed to significantly deviate from the value of 0 corresponding to Gaussian process. The contours of skewness and excess kurtosis on the four faces of the rectangular building have been shown in Fig. 6. The deviations have been observed to be more in case of pressure taps on side faces (faces B and D) and leeward face (face C). The negative skewness for the pressure taps on these three faces is indicative of heavy-tailed probability distribution in the suction side. Excess kurtosis is also observed to be positive in these three faces. Such characteristics mandated for non-Gaussian modeling of the extreme of pressure coefficients.

The applicability of Hermite-based models toward evaluation of peak factor has been assessed from the plot of skewness versus kurtosis in Fig. 7. Most of the points fall within the application range of HMs as pointed by Kwon and Kareem [8] for practical cases. The points that fall outside the range mostly correspond to the pressure taps on the windward face (face A) of the rectangular building. Similar observation has been reported in Huang et al. [5]. Since the peak factors to evaluate peak negative wind pressure coefficients in the separated flow regions that exhibit

**Fig. 5** Skewness and excess kurtosis values

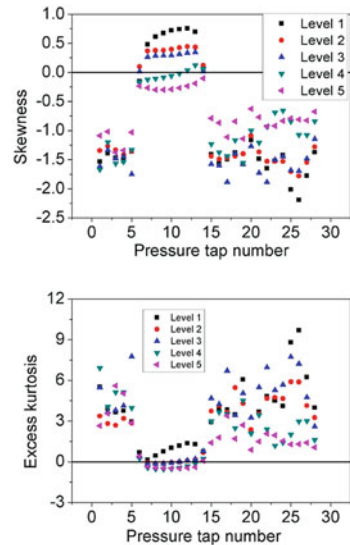


**Fig. 6** Skewness and excess kurtosis contours

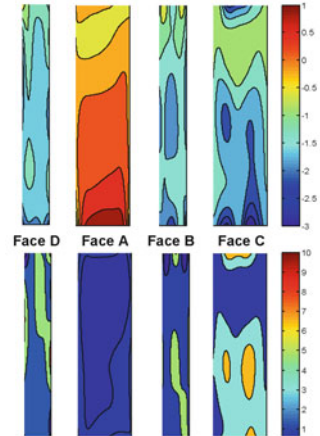
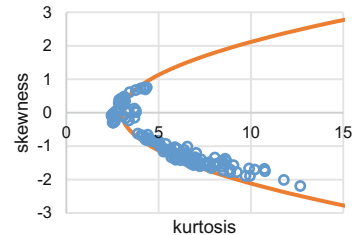


**Fig. 7** Effective region of applicability of Hermite method



strong non-Gaussianity are the major focus of research, the same have been evaluated for the pressure taps in the separated flow regions.

The typical results have been presented for a representative pressure tap at level 2, immediately after flow separation (Fig. 8). The PDF has been evaluated based on the considered HMs and plotted over histogram of the standardized pressure coefficient as shown in Fig. 8. It has been observed that Gaussian distribution does not fit to the wind pressure data in the separated flow regions, as expected. RHM and MHM-Yang provide better description of the non-Gaussianity in the separated flow, with HM being conservative, as reported in the literature. Further, the CDF of extremes as shown in Fig. 9 has been evaluated by numerical integration from the corresponding PDF of extremes computed using Eq. (8).

The peak factors have been evaluated based on the considered HMs (Eq. 9) for separated flow regions, which included side faces and leeward face of the rectangular tall building. Also, two other peak factors, skewness-dependent peak factor (Sk dep) [5] and generalized peak factor (GP) [11] available in the literature, have been evaluated for the purpose of comparison. Figures 10 and 11 show the ratio between observed and model-based peak factors for side faces and leeward face of the rectangular building. It is noteworthy that the observed value has been considered as the average of maximum values of standardized pressure coefficients

**Fig. 8** PDF of data based on the Hermite models

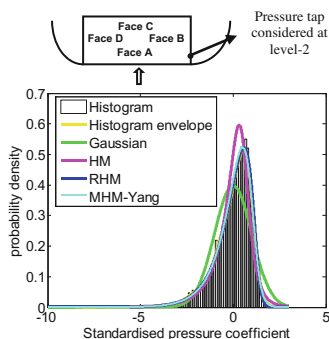


**Fig. 9** CDF of extremes based on the Hermite models

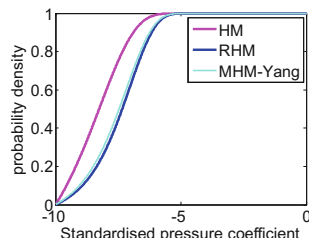
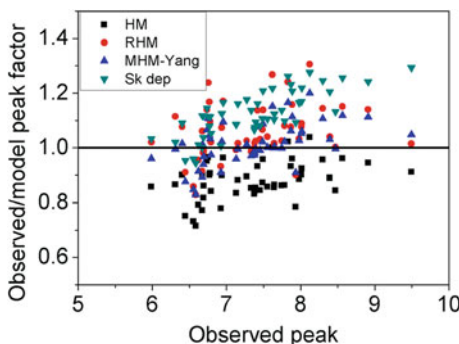


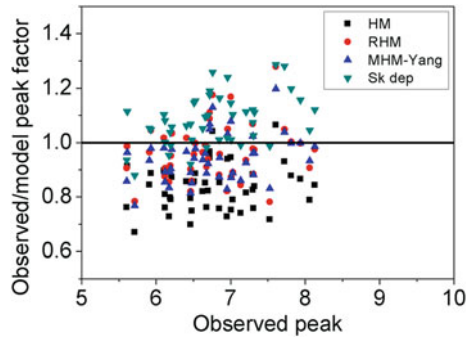
**Fig. 10** Ratio of observed and model-based peak factors for pressure taps on the side faces



from multiple trials of wind tunnel experimental data as considered by Ma et al. [9] (Fig. 11).

The values corresponding to GP [11] were significantly less compared to the observed as well as other model-based peak factors, with the ratio greater than 2, and hence have not been included in the plots. HM has been observed to provide conservative estimates of peak factor among all the models with the aforementioned ratio less than 1.0 as reported in the literature [5, 8]. For the pressure taps on the side faces, peak factors from RHM, MHM-Yang, and Sk dep have been observed to be comparable. But, the values have been observed to be less than the observed value for certain pressure taps and more than the observed values for certain

**Fig. 11** Ratio of observed and model-based peak factors for pressure taps on the leeward face



pressure taps. For pressure taps in the leeward face, RHM and MHM-Yang provided conservative estimate of the peak factor. However, ‘Sk dep’ peak factor has been observed to be less than that of RHM and MHM-Yang by about 10%, which could be attributed to the fact that the model takes into account of skewness only. The evaluated peak factors have to be used in Eq. (10) to evaluate the peak negative wind pressure coefficients.

## 5 Summary

The peak factors associated with wind-induced pressures on a tall rectangular building model in the regions after flow separation, which may not be appropriately modeled and estimated by conventional assumption of Gaussianity, have been evaluated based on three data-driven Hermite-based models, viz., HM, RHM, and MHM-Yang. Comparison has been made with the observed values from wind tunnel experiments and two other models of evaluation of peak factor, viz., skewness-dependent peak factor and generalized peak factor. GP has been observed to significantly underestimate the peak factors. HM has always been observed to provide conservative estimate of peak factor. The performance of MHM and RHM-Yang is comparable with each other and provides conservative estimate for pressure taps on the leeward face of the building. In case of pressure taps on the side faces of the building, MHM and RHM-Yang have been observed to be on either side of the observed values. ‘Sk dep’ peak factor is comparable with MHM and RHM-Yang for side faces, whereas for leeward faces, the values are less than that of MHM and RHM-Yang by about 10%. It has been observed that such HM-based peak factors provide rational estimation of peak effects, close to that of observed values on tall buildings.

**Acknowledgements** This paper is being published with the kind permission of the Director, CSIR-SERC. The support rendered by staff of Wind Engineering Laboratory is gratefully acknowledged.

## References

1. Balaji Rao K, Anoop MB, Harikrishna P, Selvi Rajan S, Iyer NR (2014) Prediction of negative peak wind pressures on roofs of low-rise building. *Wind Struct* 19(6):623–647
2. Ding J, Chen X (2014) Assessment of methods for extreme value analysis of non-Gaussian wind effects with short-term time history samples. *Eng Struct* 80:75–88
3. Gavanski E, Gurley KR, Kopp GA (2016) Uncertainties in the estimation of local peak pressures on low-rise buildings by using the Gumbel distribution fitting approach. *ASCE J Struct Eng* 142(11):04016106-1-14
4. Holmes JD, Cochran LS (2003) Probability distributions of extreme pressure coefficients. *J Wind Eng Ind Aerodyn* 91(7):893–901
5. Huang MF, Lou WJ, Chan CM, Lin N, Pan X (2013) Peak distributions and peak factors of wind-induced pressure processes on tall buildings. *ASCE J Struct Eng* 139(12):1744–1756
6. Kareem A, Zhao J (1994) Analysis of non-Gaussian surge response of tension leg platforms under wind loads. *ASME J Offshore Mech Arct Eng* 116(3):137–144
7. Kasperski M (2003) Specification of the design wind load based on wind tunnel experiments. *J Wind Eng Ind Aerodyn* 91(4):527–541
8. Kwon DK, Kareem A (2011) Peak factors for non-gaussian load effects revisited. *ASCE J Struct Eng* 137(12):1611–1619
9. Ma X, Xu F, Kareem A, Chen T (2016) Estimation of surface pressure extremes: hybrid data and simulation-based approach. *ASCE J Eng Mech* 142(10):04016068-1-9
10. Peng X, Yang L, Gavanski E, Gurley K, Prevatt D (2014) A comparison of methods to estimate peak wind loads on buildings. *J Wind Eng Ind Aerodyn* 126:11–23
11. Pillai SN, Tamura Y (2009) Generalized peak factor and its application to stationary random processes in wind engineering applications. *J Wind Eng* 6(1):1–10
12. Quan Y, Wang F, Gu M (2014) A method for estimation of extreme values of wind pressure on buildings based on the generalized extreme-value theory. *Math Probl Eng* Article ID 926253:1–22
13. Sadek F, Simiu E (2002) Peak non-Gaussian wind effects for database-assisted low-rise building design. *ASCE J Eng Mech* 128(5):530–539
14. Yang L, Gurley KR, Prevatt DO (2013) Probabilistic modeling of wind pressure on low-rise buildings. *J Wind Eng Ind Aerodyn* 114:18–26

# Seismic Behavior of Beam-Column Sub-assemblages Designed According to Different Evolution Stages of Design Philosophies



A. Kanchana Devi and K. Ramanjaneyulu

**Abstract** Over decades, the design philosophy of framed structures had undergone changes from the ordinary gravity load-designed frames to special moment-resisting frames with ductility detailing. Most of the older buildings were designed only for gravity loads. The past earthquakes produced devastating damages to the gravity load-designed structures. This resulted in the remarkable changes in the seismic design philosophy in the form of introducing ductility detailing in the codes of practices. Different codes of practices, namely EURO, ACI, NZ, IS codes, prescribe appropriate detailing practices so as to ensure desired seismic performance. Hence, in the present study, an attempt is made to compare the seismic performance of gravity load designed, seismic load designed without ductility detailing, seismic load designed with ductility detailing which represent the evolution of design philosophies adopted in codes of practices. An exterior beam-column sub-assemblage of typical three-story building is taken up for the study and designed according to the evolution of design philosophies of Indian standard. Experimental investigations are carried out on beam-column sub-assemblages designed according to different evolution stages of design philosophy. The seismic performance of beam-column sub-assemblages of three different design levels, under reverse cyclic loading, is compared in terms of the hysteretic behavior and energy dissipation capacity.

**Keywords** Beam-column sub-assemblage · Energy dissipation  
Hysteretic behavior · Ductility detailing

---

A. Kanchana Devi (✉) · K. Ramanjaneyulu  
ACT&EL, CSIR-Structural Engineering Research Centre, Chennai 600113, India  
e-mail: kanchana@serc.res.in

K. Ramanjaneyulu  
e-mail: rams@serc.res.in

A. Kanchana Devi · K. Ramanjaneyulu  
Academy of Scientific and Innovative Research, Chennai 600113, India

© Springer Nature Singapore Pte Ltd. 2019  
A. Rama Mohan Rao and K. Ramanjaneyulu (eds.), *Recent Advances in Structural Engineering, Volume 2*, Lecture Notes in Civil Engineering 12,  
[https://doi.org/10.1007/978-981-13-0365-4\\_16](https://doi.org/10.1007/978-981-13-0365-4_16)



## 1 Introduction

Beam-column joints of the framed building are the critical components under the action of earthquake, as they are subjected to huge shear demand nearly 4–6 times larger than the adjoining members. The degradation of the joint under seismic activity hinders the force flow from the beam to the column. The joint failures are often associated with the strength degradation behavior. Further, it is difficult to repair a joint region if they fail. Hence, evaluation of seismic performance of the beam-column sub-assemblages becomes vital to ensure the safety of the framed structures under seismic loading.

The existing reinforced concrete building which was built a few decades ago is of gravity load designed. They were not designed for seismic loading and also have exhibited poor seismic performance in the past earthquakes. Then comes the concept of ductility detailing during the late 1970s and the relevant guidelines were incorporated in the codes of practices during the 1980s. Remarkable change in the design philosophies of RC framed structures for seismic resistance was made after the pioneering works of Megget and Park [1], Park and Paulay [2], Blakeley et al. [3], Paulay et al. [4], Park and Keong [5], Park and Scarpas [6], Ehsani and Wight [7]. Numerous research studies were carried out to investigate the seismic performance of gravity load-designed buildings and also bring out efficient joint detailing to enhance the seismic performance. Aycardi et al. [8] studied the performance of gravity load-designed (GLD) sub-assemblages under seismic loading. They attempted to analytically model the seismic behavior and identify the parameters which play the key role under seismic loading. Murty et al. [9] conducted experimental investigations on the exterior RC joint with four details of longitudinal beam bar anchorage and three details of transverse joint reinforcement. The longitudinal bars of beam are provided as U bars, standard ACI 90 hook, full anchorage of beam top and bottom bars, and full anchorage of beam top bars and straight beam bottom bars. The transverse reinforcements are varied as closed ties, hair clips, and no ties in the joint region. It was reported that the seismic performance of non-seismically designed structures could be improved by proper anchorage of longitudinal reinforcement and providing lateral reinforcement. It was also observed that ACI standard hook with hair clip-type transverse reinforcement is preferable as it was easy to construct and effective when compared to the other schemes considered. Dhakal et al. [10] carried out an experimental study on dynamic response of GLD RC connections. It was observed that though the connection zones are the most important parts in dissipating energy during earthquake, most of the GLD connections are weaker than the adjoining structure and failed in shear.

## 2 Details of Beam-Column Specimens

Three levels of design are identified for present study to evaluate seismic performance of reinforced concrete structures that were constructed so far in Indian subcontinent. Three levels of design considered are: (i) gravity load designed (SP1), (ii) designed for seismic force but not provided with ductility detailing (SP2) (non-ductile specimen), and iii) designed for lesser seismic force and provided with code-specified ductility detailing (SP3). An exterior joint without transverse beams of a typical three-storied RC framed building with 6 m span in one direction and 4 m span in the orthogonal direction and floor height of 3.5 m each as shown in Fig. 1 is taken for the study. A 3D model of the building is created using standard analysis package. The support conditions are assigned as fixed at the bottom of the column. The linear elastic analysis is performed for loads according to different levels of design and for the load combinations of dead load (DL), live load (LL), and seismic load (SL) as  $1.5DL + 1.5LL$ ,  $1.5DL + 1.5SL$ ,  $1.2DL + 1.2LL + 1.2SL$ , and  $0.9DL + 1.5SL$ . The seismic loads are arrived according to IS1893 based on equivalent seismic load method corresponding to Zone III with the importance factor of 1. For the computation of base shears due to seismic load, the horizontal seismic acceleration coefficient is estimated with the response reduction factor of 3 and 5, respectively, for non-ductile and ductile specimens. The lateral force thus calculated amounts to 6.67 and 4% of the total weight of the structure for ordinary moment-resisting frame (OMRF) and special moment-resisting frames (SMRF), respectively. The moments and shear forces are obtained for different stages of design. The specimens are designed for limit state of collapse according to IS 456(2000). Beams and columns are designed for three levels

**Fig. 1** a Building chosen for study. b Choosing typical exterior beam-column sub-assemblage

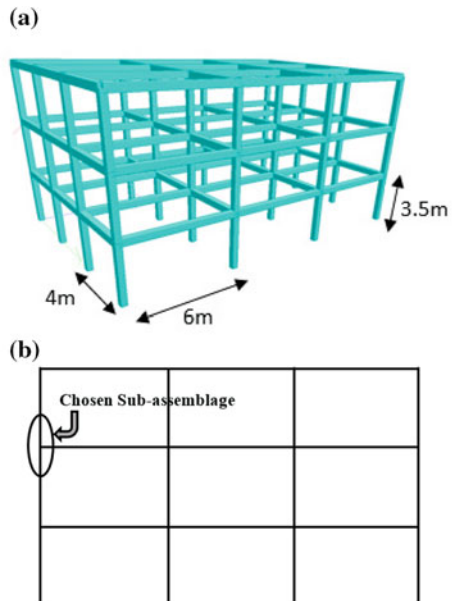
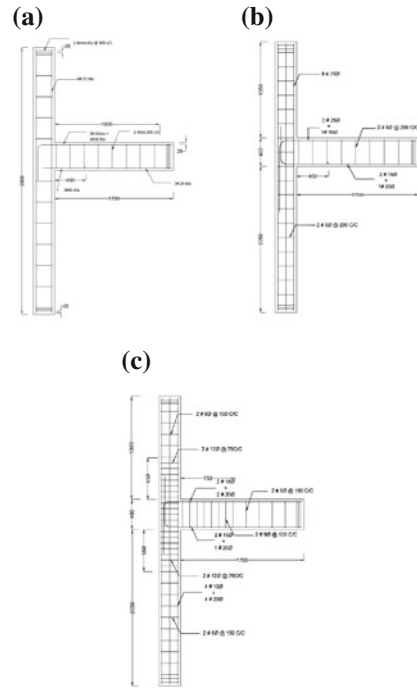


**Fig. 2** **a** Details of gravity load specimen (SP1), **b** details of non-ductile specimen (SP2), **c** details of ductile specimen (SP3)



of design. The cross-sectional dimensions of 300 mm x 400 mm and 300 mm x 300 mm are adopted for beam and column, respectively, for all the specimens, and the reinforcement details of the specimens are arrived as shown in Fig. 2. For gravity load-designed specimen (SP1), beam bottom bars project straight into the joint region. The non-ductile specimen (SP2) is detailed according to SP 34, whereas ductile specimen (SP3) is detailed according to the IS13920. The general dimensions of beam-column sub-assembly are as follows: Height of column is 3800 mm, and length of beam is 1700 mm. The length of beam is arrived based on the point of contra-flexure under the action of load combinations specified in IS code. The lengths of column segments above and below the joint are arrived according to the proportioning of moments at the joint for the combination of loads.

The specimens are instrumented extensively by affixing strain gages at critical locations identified on the reinforcement bars. Strain gages are affixed on the main reinforcement bars of the beam near the junction up to the distance ' $d$ ', i.e., the depth of the beam and on the column main bars, column ties, and beam stirrups. The strain gages are grouped into various bundles and routed to outside of the cage. Functionality of the strain gages is verified before instrumentation, after instrumentation, and after casting. The concrete of mixed proportions 1:1.695:3.013 with water-cement ratio of 0.5 is used for casting of the specimens. The reinforcement cages of specimens are placed inside the steel mold. The steel molds are oiled properly before the placement of concrete. The specimens are compacted by means

**Fig. 3** Casting of specimen

of needle vibrator. The specimen is concreted as shown in Fig. 3 and is cured for 28 days using wet curing. The reinforcement steel of Fe500D grade is used. The average yield strength of the steel reinforcement of 25, 20, 16, and 8 mm diameter is found to be 535, 545, 520, and 527 Mpa, respectively, from the tests carried out on the reinforcement bars. The average compressive strength of concrete is 50 Mpa, and average split tensile strength of concrete is 3.8 Mpa.

### 3 Details of Experimental Investigations Carried Out

The test setup is arranged on the test floor such that the beam-column joint is positioned horizontally parallel to the floor and the cyclic load is applied in the plane of the test floor. The schematic diagram of test setup and positioning of test specimen is shown in Fig. 4. An axial load of 300 kN is applied to the column by hydraulic jack at one end of the column against the reaction block at the other end. The level of axial load in column is arrived from the analysis of the global system of the three-story three-bay building. The axial load to the column is applied prior the application of lateral load. The lateral load is applied at the beam tip in displacement control mode using 25t actuator, according to the load history shown in Fig. 5. Reverse cyclic load is applied in terms of drift ratio (%) of the component where the drift is calculated as per Eq. (1).

$$\text{Drift ratio (\%)} = (\Delta l / l_b) \quad (1)$$

where  $\Delta l$  and  $l_b$  are the applied displacement at the beam tip and the length of the beam from column face to the application point of the displacement, respectively. Three complete cycles are applied for each drift increment. Reverse cyclic displacements of equal magnitude are applied on all the specimens, where positive

Fig. 4 Schematic test setup

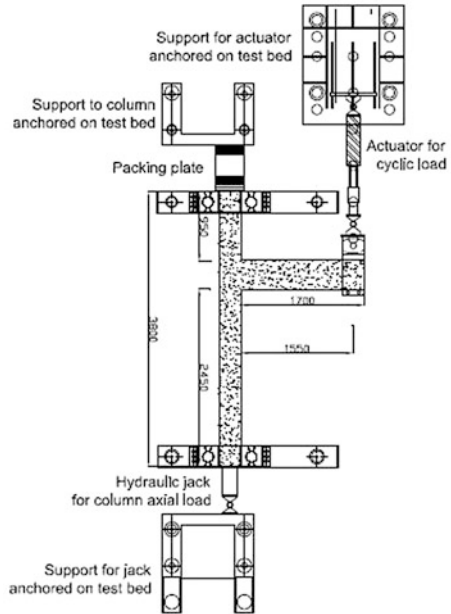
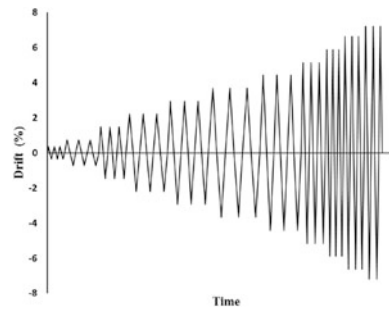
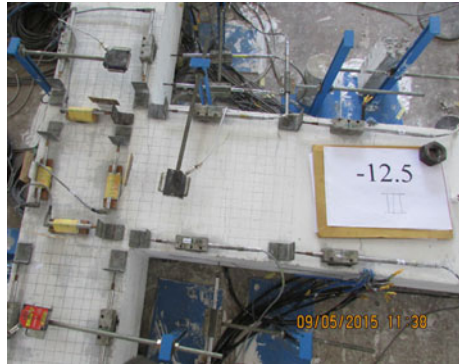


Fig. 5 Reverse cyclic loading history



drift produces tension in the beam bottom and negative drift produces tension in beam top. The test was stopped when the load dropped either in the positive or negative drift ratio by 50% of that maximum load. The test specimens are also instrumented with linear variable displacement transducers (LVDTs), which are mounted on the joint surface as well as attached to the beam and the column segments to measure deflections along the length of beam and column segments and to calculate the rotation of the joint. The layout of LVDTs are shown in Fig. 6.

**Fig. 6** Layout of LVDTs



## 4 Results and Discussion

### 4.1 Damage Progression

Upon application of loading, flexural cracks are developed at both top and bottom faces of beam portion of GLD specimen SP1, up to the drift ratio of +0.737%. At drift ratio of +1.47%, a joint crack of 3 mm width is developed due to the absence of proper anchorage of beam bottom reinforcement and this joint crack got widened with increase in drift ratio. At a drift ratio of +2.94%, the joint crack width is found to be 13 mm and can be seen in Fig. 7a. During the negative cycles of specimen SP1, upon further increment of drift the major damage is shifted toward the joint region by exhibiting diagonal cracks in the joint. The diagonal shear cracking of the joint at drift ratio of -2.94% is shown in Fig. 7b.

In non-ductile specimen SP2, flexural cracks developed along the beam are widened till drift ratio of  $\pm 2.2\%$  beyond which the flexural cracks in the beam remain dormant. After the drift ratio of  $\pm 2.2\%$ , the growth of joint shear crack is observed to be drastic, propagated into the column, and extended beyond the depth

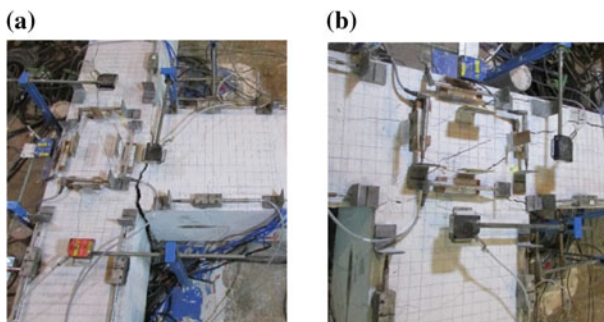


**Fig. 7** Crack pattern **a** at +2.94% (left) and **b** at -2.94% (right) drift ratio—SP1

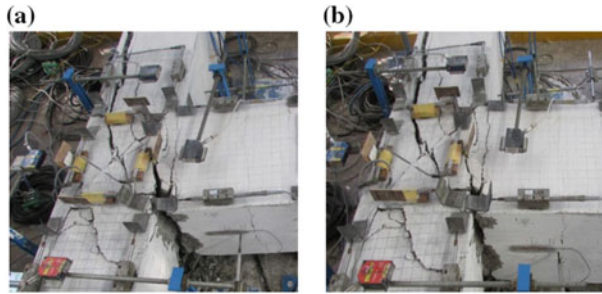
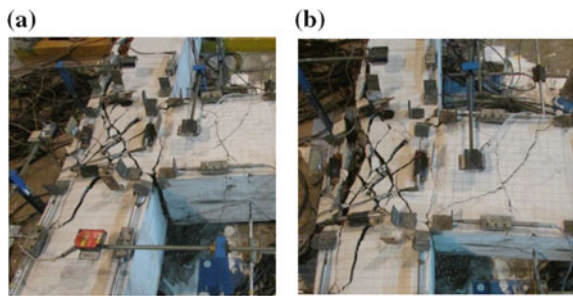


**Fig. 8** Crack pattern at +5.88% (left) and -5.88% (right) drift ratio—SP2

**Fig. 9** Crack pattern at +7.05% (left) and -7.05% (right) drift ratio—SP3



of the column. During the final stage of loading, at drift ratio of  $\pm 5.88\%$  upheaval of concrete in the joint region and opening of joint is observed as shown in Fig. 8.

For ductile specimen SP3, the flexural cracks spread throughout the length of beam in both positive and negative cycles during initial drift increments. Two predominate cracks, one at the face of joint and other at distance of  $D/2$  from the face of joint, formed and widened during the positive cycles up to the drift ratio of 4.4%. Even though the diagonal shear cracks are developed at the drift ratio of +1.47%, the crack widths are smaller and the widening and propagation of diagonal shear cracks are active only after the drift ratio of +4.4% and -3.67% in the positive and negative cycles, respectively. At the final stage of loading, at the drift ratio of 7.05%, column cover concrete at the outer face of column spalled-off and upheaval of joint concrete is also observed as shown in Fig. 9 due to excessive shear cracking in joint region.

It is also found from the experimental studies that with the evolution of the code provisions from gravity load designed to non-ductile and then to ductile specimens, a marked improvement in damage resilience is observed. From experimental investigation of non-ductile (SP2) and ductile (SP3) specimens, it is noted that with appropriate reinforcement detailing and proper confinement, damage can be initially concentrated in beam portion and the joint deterioration can be delayed to an extent. Proper confinement (as provided in the case of SP3) resulted in the formation of wider and stronger concrete strut joining the corners of the joint to transfer the force

at initial stage. Further, with increase in load level, truss mechanism is developed in the joint region of ductile specimen (SP3) and the column reinforcement bars and ties participated in force transfer mechanism. This mechanism delayed the crack propagation and dilatation of the joint region.

## 4.2 Load–Displacement Behavior

The load versus displacement hysteresis curves obtained from reverse cyclic tests carried out on specimens SP1, SP2, and SP3 are shown in Fig. 10a–c. From the load–displacement hysteresis curves, it is evident that specimen SP1, which was designed only for gravity loads, exhibited poor seismic performance when compared to that of the other specimens. The poor seismic performance of specimen SP1 is due to lack of anchorage and inadequate reinforcement at beam bottom. The maximum load carried by specimen SP1 during the positive cycles is 54% lesser than the maximum load carried by the same specimen during the negative cycles. In the positive cycle of specimen SP1, the load is dropped at the displacement cycle of 25 mm (1.47% drift ratio) due to the slippage of beam bottom reinforcement, which could be witnessed by the formation of prominent wide crack at the joint. During negative cycle of loading on specimen SP1, the load increased with the increase in displacement until the yielding of beam top reinforcement had taken place. Beyond this with the further increment of drift, degradation in global strength is observed.

The presence of intermediate column bars and proper anchorage of beam bottom reinforcement facilitated better performance of SP2. Even though SP1 and SP2 had same reinforcement at the beam bottom, improper anchorage of beam bottom bars in SP1 resulted in anchorage failure, whereas proper anchorage of rebars in SP2 improves its hysteresis performance. Specimen SP3 (with ductile detailing) carried more load than SP2 even though it is designed for lesser seismic force. In the positive cycle, the maximum strength is attained in SP3 at a displacement level of 37.5 mm (drift of 2.2%) and the load is sustained up to the displacement level of 87.5 mm (drift of 5.15%). This may be due to the presence of confinement of joint due to the presence of ties in the joint region. Beyond this displacement level, strength degradation is observed. In negative cycles of SP3, after attaining the maximum strength at drift ratio of 2.2% the load sustained for subsequent displacement levels (from drift ratio of 2.2–3.68%) and then strength begins to decrease. The load–displacement hysteresis is observed to be unsymmetrical for positive and negative cycles in all specimens since the beam main reinforcement at the top and bottom is unequal.

The load envelope obtained for specimens SP1, SP2, and SP3 is depicted in Fig. 11. The maximum loads carried by the specimens SP2 and SP3 in the positive cycle are 58 and 94 kN, respectively. This higher load carried by ductile specimen is due to provision of positive steel at the joint face equal to at least 50% of negative steel at that face from ductility detailing consideration, but the provided steel was



**Fig. 10** **a** Load–displacement hysteresis of SP1. **b** Load–displacement hysteresis of SP2. **c** Load–displacement hysteresis of SP3

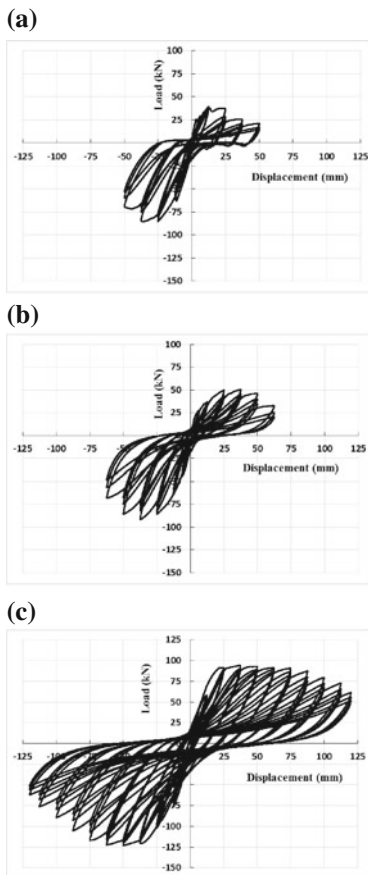
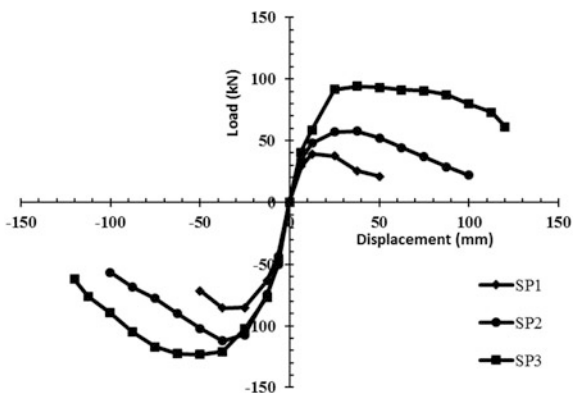


**Fig. 11** Load envelope of specimens SP1, SP2, and SP3

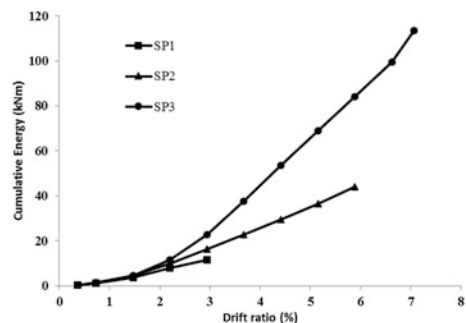


higher than 50% of the negative steel as the tension steel at beam bottom is extended. In the negative cycle, maximum load carried by the non-ductile (SP2) and ductile specimens (SP3) is 112 and 123 kN, respectively. Even though the non-ductile specimen has slightly higher reinforcement than the ductile specimen at beam top, the ductile specimen carried higher load than the non-ductile specimen. This could be due to the fact that proper force transfer mechanism took place in ductile specimen from beam to column through joint and reduced degradation of joint due to confinement of joint due to provision of ductile detailing of joint region. The maximum load carried by SP3 in the positive cycle is 58 and 39% higher than that of SP1 and SP2, respectively. Similarly, the maximum load carried by SP3 in the negative cycle is 31 and 9% higher than that of SP1 and SP2, respectively. This signifies the importance and underlines the need for providing ductility detailing.

### 4.3 Energy Dissipation

The energy dissipation is one of the crucial performance parameters, as the energy imparted to system during earthquake has to be dissipated by the system either elastically or through elastic-plastic response. The cumulative energy dissipation capacities of specimens SP1, SP2, and SP3 are shown in Fig. 12. Till the drift ratio of 1.47%, the cumulative energy is same for the specimens SP1, SP2, and SP3, i.e., till the anchorage failure of beam bottom bars. Beyond this drift ratio, SP2 dissipated more energy through large inelastic deformation which is absent in the gravity load-designed specimens SP1. The cumulative energy dissipated by the SP3 is much higher when compared to SP1 and SP2. The maximum cumulative energy dissipated by SP3 is 89 and 61% higher than that of SP1 and SP2, respectively. The presence of confinement reinforcement in the form of stirrups in the joint region resulted in sustaining load and undergoes huge inelastic deformation resulting in the remarkable improvement in the energy dissipation in the case of SP3. This signifies the superior performance of ductile-detailed specimen SP3.

**Fig. 12** Cumulative energy dissipation of the specimens



## 5 Conclusions

From the experimental investigations carried out on beam-column sub-assemblages of three different design evolutions, the following conclusions are drawn: It is found from the experimental studies that with the evolution of the code provisions from gravity load designed to non-ductile and then to ductile specimens, a marked improvement in damage resilience is observed. The gravity load specimen (SP1) exhibited poor seismic performance when compared to that of the other specimens due to improper anchorage of beam bottom bars. Even though the non-ductile specimen has slightly higher reinforcement than the ductile specimen at beam top, the ductile specimen carried higher load than the non-ductile specimen. This could be due to the reduced degradation of joint by the provision of confinement reinforcement in the joint region as per ductility detailing. The ductile specimen exhibited better seismic performance when compared to other specimens in terms of better damage resilience, hysteretic behavior, and enormous improvement in the energy dissipation. However, even in specimen SP3, weak beam mode of failure was not observed and the specimen encountered joint shear failure.

## References

1. Megget LM, Park R (1971) Reinforced concrete exterior beam-column joints under seismic loading. *NZ Eng* 26(11):341–353
2. Park R, Paulay T (1973) Behaviour of reinforced concrete external beam column joints under cyclic loading. In: *Proceedings, fifth world conference on earthquake engineering paper 88*, vol 1, Session 2D, Rome, June 1973, pp. 772–781
3. Blakeley RWG, Megget LM, Priestley MJN (1975) Seismic performance of two full size reinforced concrete beam-column joint units. *Bull N Z Nat Soc Earthquake Eng* 8(1):38–69
4. Paulay T, Park R, Priestley MJN (1978) Reinforced concrete beam column joints under seismic actions. *J Am Concr Inst Proc* 75(11):585–593
5. Park R, Keong YS (1979) Tests on structural concrete beam-column joints with intermediate column bars. *Bull N Z Nat Soc Earthquake Eng* 12(3):2361–2376
6. Paulay T, Scarpas A (1981) The behaviour of exterior beam-column joints. *Bull N Z Nat soc Earthquake Eng* 14(3):131–144
7. Ehsani MR, Wight JK (1985) Exterior reinforced concrete beam to column connections subjected to Earthquake-type loading. *ACI J* 492–499
8. Aycardi LE, Mander JB, Reinhorn AM (1994) Seismic resistance of reinforced concrete frame structures designed only for gravity loads: experimental performance of sub assemblages. *ACI Struct J* 91(5):552–563
9. Murty CVR, Rai DC, Bajpai KK, Jain SK (2003) Effectiveness of reinforcement details in exterior reinforced concrete beam-column joints for earthquake resistance. *ACI Struct J* 100(2):149–156
10. Dhakal RP, Pan TC, Irawan P, Tsai KC, Lin KC, Chen CH (2005) Experimental study on the dynamic response of gravity-designed reinforced concrete connections. *Eng Struct* 27(1):75–87

# Crushing Analysis of Tapered Circular Corrugated Tubes Subjected to Impact Loading



Sharad Rawat, A. K. Upadhyay and K. K. Shukla

**Abstract** The study investigates the crashworthiness of Magnesium AZ31 tapered circular corrugated tubes under axial and oblique impact. Nonlinear FEM code LS-DYNA is used for simulations with Belytschko–Tsay four-node shell elements on thin-walled tapered tubes. The study aims to analyse the effect of varying corrugations along the length of the tube on initial peak force and specific energy absorption (SEA). It is observed that the graded corrugations in amplitude facilitate the progressive collapse and uniform load–displacement behaviour of tapered tubes.

**Keywords** Impact · Corrugated tubes · Thin-walled structures  
Crashworthiness · Oblique loading

## 1 Introduction

Due to an exponential increase in the road accidents, safety has become of paramount concern for the automotive industry. Thin-walled tubes are extensively used as energy absorbers. Corrugated thin-walled tubes have also become an attractive area of research. Singace and Sobky [1] reported their study in corrugated tubes by concluding that the decrease in stiffness of the tube leads to load uniformity. Dependency of mode of deformation on  $D/t$  ratio was also established. Different modes of deformation and the influence of amplitude and wavelength of corruga-

---

S. Rawat  
Mechanical Engineering Department, Motilal Nehru National  
Institute of Technology Allahabad, Allahabad, India  
e-mail: sharad.me16@mnnit.ac.in

A. K. Upadhyay · K. K. Shukla (✉)  
Applied Mechanics Department, Motilal Nehru National Institute  
of Technology Allahabad, Allahabad, India  
e-mail: kkshukla@mnnit.ac.in

A. K. Upadhyay  
e-mail: ashutosh@mnnit.ac.in

tions on these modes are studied by Chen and Ozaki [2]. In case of tapered tubes [3], a large taper angle is not suggested due to space limitations which hinders maximum utilization of tapered structures. In the book [4], dependency of non-compact and compact mode was discussed on side to thickness ratio [5]. The dependency of energy absorption characteristic on thickness of tube and angle of impactor was established [5]. Karagiozova et al. [6] observed the increase in the energy absorption and mean force on crushing the tube with high impact velocity numerically. El-Hage et al. [7] examined various trigger mechanisms and reported their influence on initial folding force. For simple tubes, increase in thickness decreases the number of natural lobes during deformation and higher impact velocities leading to irregularities were reported [8]. Strain concentration during deformation of square corrugated tubes was also studied [9] where proportional and inversely proportional relation between thickness–strain concentration and corner radius/side length–strain concentration respectively. This study aims to analyse and compare the corrugated tapered circular tubes against the simple tapered tube and how the characteristics would improve on varying the corrugation amplitude/wavelength along the length of the tube.

## 2 Methodology

In the present study, corrugations are graded for their amplitudes and wavelengths using mathematical equations. The tubes are modelled in CATIA using equation editor. Nomenclature is as follows: The first word gives information about corrugated ( $T(\lambda, a)$ ) or simple (St) nature of the tubes. The notation  $T(c, l)_{X_Y}$  means corrugated tube with constant degree of wavelength ( $c$ ) and linear function of amplitude ( $l$ ). The alphabet ( $X$ ) tells about the corrugations: A means corrugation starts at larger diameter side, B means at smaller diameter, and 0 means no corrugations. The alphabet ( $Y$ ) represents impact side: A means that the impact is at higher diameter and B means at lower diameter. Configuration of tube  $T(c, c)$  is same for alphabet ( $X$ ) whether A or B. Therefore, alphabet is used for  $T(c, c)$ . For instance, for  $T(c, l)_{A_A}$ , the equation is  $y = 1 \text{ mm} * X * \sin(2 * \text{Pi} * 8 * X)$ . The respective equations are mentioned in Table 1. Further, LS-DYNA is used to carry out numerical simulations. The tubes have a smaller diameter of 50 mm, taper angle of  $5^\circ$ , and length of 150 mm. It has a thickness of 2 mm, amplitude of corrugated tubes is 1 mm, and there are eight corrugations along the length. Convergence study has been carried out, and the mesh size of 1.8 mm was determined with a corrugated tube as shown in Table 3. The nonlinear code used in the present study is also validated with several results available in the open literature and found to be in good agreement. The material properties of Magnesium AZ31 [10] are considered in the analysis.

Figure 1 schematically shows the configuration and boundary conditions of the model. One end is constrained (DOFs 0), and impact has been done on the other end.

**Table 1** Tube nomenclature

Tube	Amplitude	Wavelength	Governing equation
St	No corrugations 4	No corrugations	$y = 0$
$T(c, c)$	Constant	Constant	$y = \sin(2\pi.8(t))$
$T(l, c)$	Constant	Linear	$y = \sin(2\pi.8(t^2))$
$T(p, c)$	Constant	Parabolic	$y = \sin(2\pi.8(t^3))$
$T(c, l)$	Linear	Constant	$y = t \sin(2\pi.8(t))$
$T(c, p)$	Parabolic	Constant	$y = t^2 \sin(2\pi.8(t))$

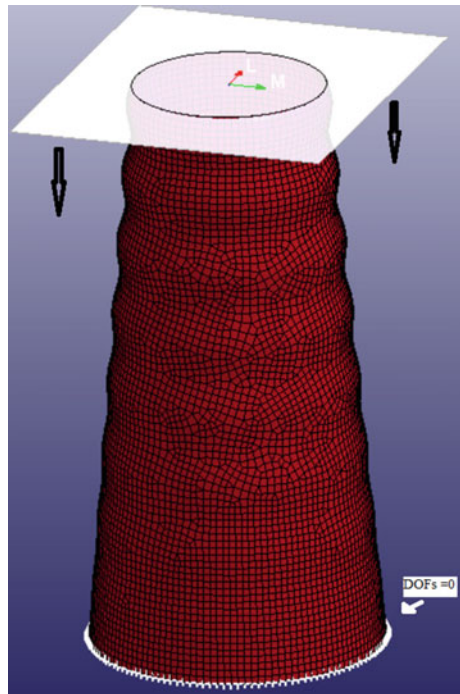
**Table 2** Material properties

Material grade	Stress at 0.2% yield (MPa)	Ultimate strength	Young's modulus (GPA)	Density (kg/m <sup>3</sup> )
AZ31	115	380	42	1780

**Table 3** Mesh size and convergence behaviour of tapered corrugated tube

Mesh	2.4	2.2	2.0	1.8
Peak force (kN)	20.47	20.52	20.48	20.49
Energy absorbed (J)	1691.42	1710.88	1692.42	1698.91

**Fig. 1** Simulation model



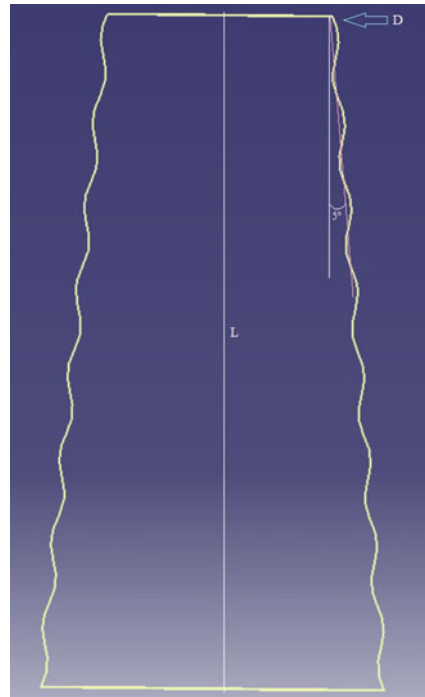
The amplitude of these corrugations is equal to 1 mm. Parabolic and linear functions of wavelength ( $2\lambda$ ) as well as amplitude ( $a$ ) have been studied along. The tubes have undergone axial as well as oblique impact. A comparative study of all the responses of the aforementioned tubes has been done in the next section. Properties of Magnesium AZ31 have been mentioned in Table 2. Strain rate was not taken into consideration.

Figure 2 shows the tube specifications pictorially. Figure 3 a, b shows the various corrugated circular tapered tubes incorporated in the present study.

In LS-DYNA, Belytschko–Tsay four-node shell element is used to model the tubes. The simulation was carried out using the material card MAT-24, MAT\_PIECEWISE\_LINEAR\_PLASTICITY. MAT-24, simultaneously, completely displays characteristics of plastic phase and elasto–plastic material with any arbitrary stress–strain curve defined. Five intergeneration points across the wall thickness were adopted which was effective in buckling response. An imaginary rigid wall with mass and velocity is made to impact on the non-constrained end of the tube with the interface friction set to 0.1. CONTACT\_AUTOMATIC\_SINGLE\_SURFACE with  $\mu = 0.1$  is used to prevent self-penetration during deformation process.

The nonlinear code used in the present study has also been validated with the works of Kumar et al. [11], and the results obtained are in good agreement as shown in Table 4. Tube specifications used for the validation were:  $L = 90$  mm,  $D = 45$  mm,  $t = 1.4$  mm. Mass = 60 kg and velocity = 7 m/s were used for dynamic loading.

**Fig. 2** Tube specifications



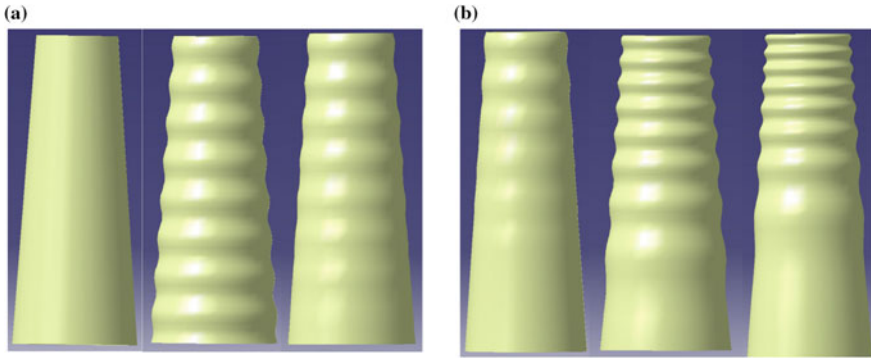


**Fig. 3** Tubes incorporated in the study

**Table 4** Comparison of the peak force and energy absorbed

Model	$F_{avg}$ (kN)	$E_{absorbed}$ (J)
Kumar et al. [11]	23.98	1123.68
Present study	23.33	1100

### 3 Results and Discussions

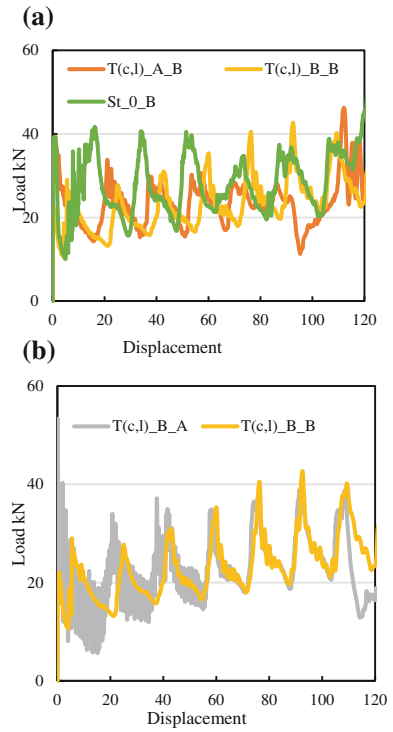
First of all, the side of impact and side where the corrugation should begin are developed. Figure 4a shows the advantage of a tapered circular corrugated over simple circular tapered tube. The corrugated tube  $T(c, l)_{B_B}$  shows significant reduction of 46% initial peak force in the tube over  $St_{0_B}$  and also an improvement over the tube  $T(c, l)_{A_B}$ . But there is 20% reduction in SEA of  $T(c, l)_{B_B}$  than  $St_{0_B}$ , the uniformity in load–displacement curve is better. Figure 4b shows improved characteristics in the case where the impact is done on a lower diameter side. There is a reduction of 60% in initial peak force. Thus when the corrugations begin from the lower diameter side and impact is made on side with lower diameter, then better response of energy-absorbing structure is obtained.

### 4 Amplitude Grading

Amplitude of corrugation is graded for the tube  $T(c, l)_{B_B}$  and  $T(c, p)_{B_B}$  from the non-graded tube  $T(c, c)_{B_B}$ . Figure 5 shows their comparative reaction force variation with displacement. It can be seen that the peak

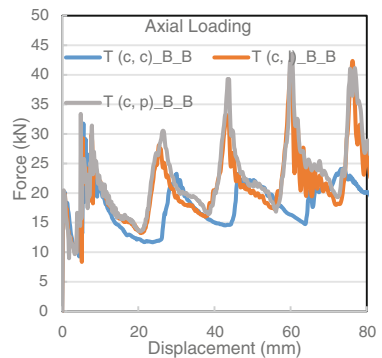


**Fig. 4 a** Load–displacement curves of tubes with corrugation pattern and simple tapered tube impacted at smaller end. **b** Load–displacement curves of tubes with corrugation pattern showing the effect of impacting end



force of  $T(c, c)_{B_B}$  and  $T(c, p)_{B_B}$  is more or less near to that of the tube  $T(c, l)_{B_B}$ . The peak forces and SEA for the tube  $T(c, c)_{B_B}$ ,  $T(c, l)_{B_B}$  and  $T(c, p)_{B_B}$  are 20.12, 19.62, and 19.66 kN and 13.52, 15.57, and 16.83 kJ/kg. Therefore, the tube  $T(c, p)_{B_B}$  is superior to the other mentioned tubes. This can be inferred that as the degree of amplitude is increased, the tube provides an advantage of lower peak force like a corrugated tube in early stages of deformation and also higher energy absorption like a normal tube in the later deformation stages.

**Fig. 5** Comparative force–displacement for amplitude-graded tubes with  $T(c, c)_{B_B}$



### 5 Wavelength Grading

The peak force and specific energy absorption (SEA) of linear and parabolic graded tubes  $T(l, c)_{\_B\_B}$  and  $T(p, c)_{\_B\_B}$  along with the nongraded tube  $T(c, c)_{\_B\_B}$  is shown in Table 5. It can be observed that as the degree of wavelength in corrugation function is increased the peak force increases and SEA decreases credited to increase in the mass of the tube with increase in the degree. Therefore, wavelength grading may not be an improvement over  $T(c, c)_{\_B\_B}$ .

The tube  $T(c, p)_{\_B\_B}$  is the most superior of all the tubes studied in the study. Hence, for further study, only this tube is considered. Since majority of the real-life impacts are oblique in nature, a comparative study of the responses of the tubes in oblique loading at different angles ( $5^\circ$  and  $10^\circ$ ) was also conducted. Figure 6a, b represents the load–displacement of tubes at oblique angles.

It can be observed that as the angle of impact is increased, the peak force, mean force, and hence the SEA decrease. As the angle is increased, the response of tube

**Table 5** Comparative peak force and SEA of various tubes

Tube	Peak force (kN)	SEA (kJ/kg)
$T(c, c)_{\_B\_B}$	20.12	13.52
$T(l, c)_{\_B\_B}$	21.57	14.40
$T(p, c)_{\_B\_B}$	22.81	13.65

**Fig. 6 a** Comparative load–displacement of tubes at axial and  $5^\circ$  loading.  
**b** Comparative load–displacement of tubes at axial and  $10^\circ$  loading

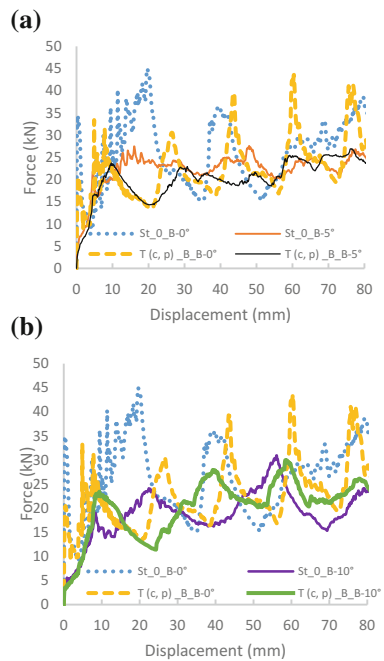
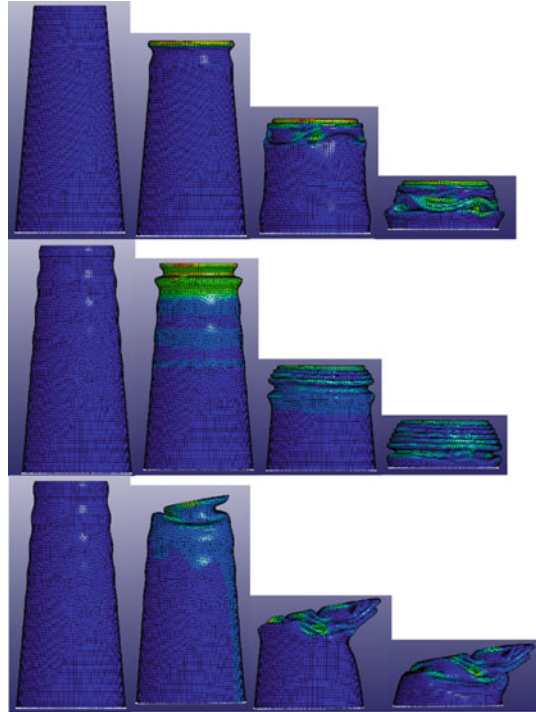


**Table 6** Comparative SEA of tubes at oblique impact angles

Tube	Angle (°)	SEA (kJ/kg)
St_0_B	0	19.54
St_0_B	5	16.04
St_0_B	10	14.35
T (c, p) _B_B	0	16.72
T (c, p) _B_B	5	15.11
T (c, p) _B_B	10	15.10

**Fig. 7** Collapse mode of the St\_0\_B and tapered tube T (c, p) \_B\_B and tube T (c, p) \_B\_B-10°, respectively



T (c, p) \_B\_B shifts closer to the tube St\_0\_B. A clear inference can be made from Table 6. T (c, p) \_B\_B has higher SEA than St\_0\_B at 10°. This is because corrugated tube prevents bending more effectively than the normal tube because of an increased bending moment.

Figure 7 shows the collapse mode of the tube St\_0\_B and T (c, p) \_B\_B. The progressive buckling in concertina mode throughout its deformation clearly shows the advantage of using graded corrugations. Also, tube St\_0\_B shows mixed mode of deformation. Concertina mode has highest energy absorption per unit length of material deformed. At higher angle of impact, mixed mode of deformation can be observed in T (c, p) \_B\_B. Therefore, energy absorption characteristics can further be improved at higher angles where concertina mode of deformation is achieved, which is the future scope of the current study.

## 6 Conclusions

Finite element method is used to study the effect of variation of degrees of amplitude and wavelength of corrugations on crashworthiness of tapered circular tube. The tube  $T(c, l)_{B_B}$ , where corrugations begin and impact is made on the end with lower diameter, shows significantly higher reduction in initial peak force than the reduction in SEA when compared to other tubes with linear amplitude variation and simple tapered tube. The tube  $T(c, p)_{B_B}$  shows better energy absorption characteristics than tubes with grading in amplitude and wavelength in axial and oblique impact angles. Therefore, parabolic degree of amplitude in corrugation function has better crashworthiness.

## References

1. Singace AA, El-Sobky H (1997) Behaviour of axially crushed corrugated tubes. *Int J Mech Sci* 39:249–268
2. Chen DH, Ozaki S (2009) Circumferential strain concentration in axial crushing of cylindrical and square tubes with corrugated surfaces. *Thin-Walled Struct* 47:547–554
3. Nagel GM, Thambiratnam DP (2004) Dynamic simulation and energy absorption of tapered tubes under impact loading. *Int J Crashworthiness* 9:389–399
4. Lu G, Yu T (2003) *Energy absorption of structures and materials*. Woodhead Publishing Limited, England
5. Reyes A, Langseth M, Hopperstad OS (2003) Square aluminium tubes subjected to oblique loading. *Int J Impact Eng* 28:1077–1106
6. Karagiozova D, Nurick GN, Yuen SCK (2005) Thin walled structures 43:956–982
7. El-Hage H, Mallick PK, Zamani N (2005) A numerical study on the quasi-static axial crush characteristics of square aluminum tubes with chamfering and other triggering mechanisms. *Int J Crashworthiness* 10(2):183–195
8. Tarigopula V, Langseth M, Hopperstad OS, Clausen AH (2006) Axial crushing of thin-walled high-strength steel sections. *Int J Impact Eng* 32:847–882
9. Chen DH, Ozaki S (2009) Circumferential strain concentration in axial crushing of cylindrical and square tubes with corrugated surfaces. *Thin-Walled Struct* 47:547–554
10. Agrawal D, Rawat S, Upadhyay AK (2016) Crashworthiness of circular tubes with structurally graded corrugations. *SAE Technical Paper* 2016–28-0050. <https://doi.org/10.4271/2016-28-0050>
11. Kumar P, Rao CL, Simhachalam B (2014) Comparative study of energy absorption characteristics of magnesium and aluminium alloy tubes. In: *International conference on multifunctional materials, structures and applications (ICMMSA-2014)*, MNNIT Allahabad, India

# Effect of Noise on Vortex-Induced Vibrations of Circular Cylinders



M. S. Aswathy and Sunetra Sarkar

**Abstract** In this study, we examine the effect of uniformly distributed noise superimposed on a steady, incompressible mean flow, past a circular cylinder undergoing transverse oscillations. We use a Duffing–Van der pol combined system for the present investigation in order to model the associated nonlinear behavior. We observe that as we vary the mean velocity as the bifurcation parameter, noise brings in major qualitative and quantitative changes on the structural response of the system compared to the deterministic cases. Noise induces new dynamical states in this vortex-induced vibration (VIV) system. The noise, depending on its coefficient of intensity, has a role in advancing the lock-in regime. The time histories of the response prior and post lock-in show different dynamics compared to the deterministic cases. Also, depending on the intensity of the noise coefficient, the probability density functions of the response amplitude also undergo qualitative and quantitative changes. We investigate the existence of P (phenomenological)-bifurcations in the VIV system by analyzing the joint probability density functions and quantify the response using Shannon entropy.

**Keywords** Vortex-induced vibrations · Bifurcation · Uniformly distributed Probability density function

## 1 Introduction

Vortex-induced vibrations of circular cylinders are an important area of research in many practical situations, especially in heat exchangers, bridges, tall buildings, riser tubes, towing pipes, power transmission lines, etc. Flow around circular cylinders

---

M. S. Aswathy · S. Sarkar (✉)  
Department of Aerospace Engineering, Indian Institute of Technology Madras,  
Chennai 600036, India  
e-mail: sunetra.sarkar@gmail.com

M. S. Aswathy  
e-mail: aswathymek@gmail.com

stands as the first step in understanding such flows. Analytical formulations have been found useful to study such scenarios to understand the underlying physics of the problem. The dependence of structural response on the flow and other parameters can be better understood through such formulations.

In the present study, we make efforts to capture the effect of noise superimposed on a uniform incoming flow on the dynamics of an elastically mounted rigid cylinder undergoing transverse oscillations. A combined Duffing–Van der pol oscillator system is used to do this study for cylinders. Williamson et al. [1] and Feng [2] presented interesting experimental results for low mass and high mass to damping cases, respectively. Analytical formulations which have marked themselves as phenomenological are those based on wake oscillators in the form of Van der pol or Rayleigh equations such as that presented by Bishop and Hassan [3], Hartlen and Curie [4]. Fachinetti et al's. [5] model was a major breakthrough since they brought an effective coupling model to characterize VIV due to circular cylinders.

Though lots of studies have been made to study system responses under deterministic environment, not much of studies have been done to understand the effect of stochastic fluctuations on the system dynamics. Noise can be inherently present or externally induced. So, it is important that we have an idea on the impact they will have on the system dynamics which would be different from our deterministic studies. It is also important to extend our study to the stochastic bifurcations, which can occur in the VIV system.

In our current Duffing–Van der pol model, at each time step, we add a multiplicative noise on the mean flow, which is uniformly distributed. Then, the system response and their changes are studied with increasing reduced velocity. Pankaj et al. [6] have made a study on the P (phenomenological)-bifurcations occurring in a simple Duffing–Van der pol oscillator subjected to additive noise. Drawing inspiration from this work, we analyze our stochastic VIV system based on their pdfs and Shannon entropy.

## 2 Methodology

The model consists of a single degree of freedom elastically supported circular cylinder subjected to incompressible constant flow with uniformly distributed noise superimposed on it. The Strouhal number is assumed to be 0.2, as suggested by Blevins [7], in the subcritical range of Reynolds number,  $300 < Re < 1.5 \times 10^5$ . This physical model is captured using an analytical model, wherein we propose a mechanical spring–mass system of the Duffing type to model the transverse vibrations of an infinitely long cylinder. Along with this, a Van der pol oscillator is used to describe the wake dynamics. The final forms of non-dimensional equations of motion are

$$\ddot{y} + \lambda\dot{y} + y + \alpha y^3 = M\Omega^2 q$$

$$\ddot{q} + \epsilon\Omega(q^2 - 1)\dot{q} + \Omega^2 q = A\ddot{y}$$

where  $y$  is the non-dimensional structural amplitude and  $q$  is the wake variable associated with a fluctuating lift coefficient; the damping term  $\lambda$  is the sum of structural viscous damping and the fluid added damping, where  $\lambda = 2\zeta + \gamma\Omega/\mu$  and  $\zeta$  is the structural reduced damping coefficient, taken as 0.0000524 [4]; the values of  $\gamma$  which is a stall parameter assumed a value of 0.8 [5];  $\Omega$  is the ratio of the vortex shedding frequency to the cylinder natural frequency in the medium;  $\mu$  is the mass ratio;  $\epsilon$  and  $A$  are empirical coefficients to be determined.  $M$  is a mass number, which is a function of the mass ratio [5]. The coupling model used for the wake in the present work is an acceleration-coupling model [5]. The Strouhal number for the present study is assumed to be 0.2, as suggested by Blevins [7], in the subcritical range of Reynolds numbers.  $\epsilon$  and  $A$  values have been chosen as 0.3 and 12, respectively [5]. In the present case, we add a fluctuation to the mean value of reduced velocity as  $u = Um + (c * u')$ , where  $u$  is total reduced velocity,  $Um$  is the mean flow reduced velocity,  $c$  is the intensity of noise coefficient, and  $u'$  is either a uniformly distributed fluctuation.

### 3 Results and Observations

The value of Duffing coefficient is taken as 0.7 in the present case. Figure 1 shows the time histories of deterministic system just before lock-in, at lock-in, and just after lock-in. Figure 2 is the bifurcation diagram showing variation of non-dimensional amplitude  $y$  with respect to reduced velocity  $Um$ . It is seen that small amplitude limit cycle oscillations exist until  $Um = 4.5$ . At  $Um = 4.6$ , high-amplitude LCOs exist. The lock-in regime exists until  $Um = 4.5$ , where the oscillations again jump back to small amplitude LCOs.

#### 3.1 Effect of Uniformly Distributed Noise

Firstly, we investigate the effect of a uniformly distributed parametric noise in the incoming flow on the system response. The intensity of noise is slowly changed from smaller to larger values to study how it influences the system dynamics. The noise intensity is increased from 0.5 to 4 in steps of 0.5. It is seen that the noise intensity has a major role in advancing the lock-in regime and in affecting the system dynamics.

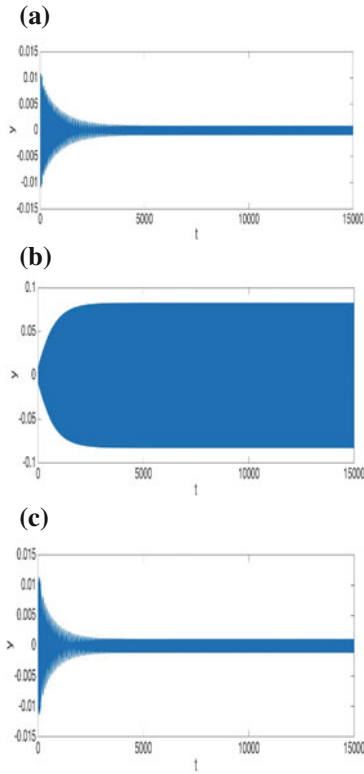


**Fig. 1** Typical time histories for deterministic system: **a** before lock-in, **b** at lock-in, and **c** after lock-in

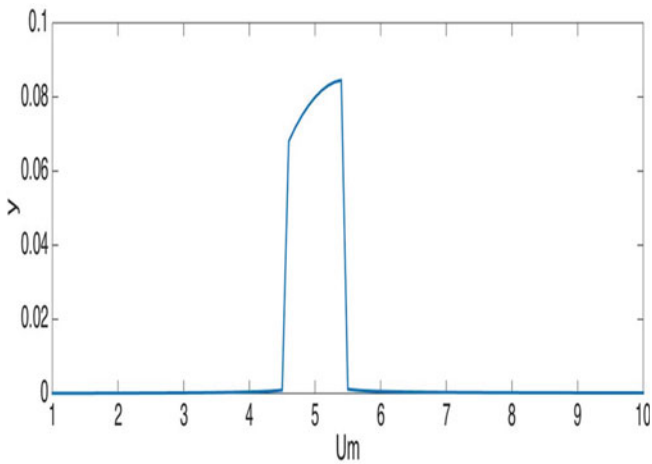


**Fig. 2** Bifurcation diagram for deterministic system



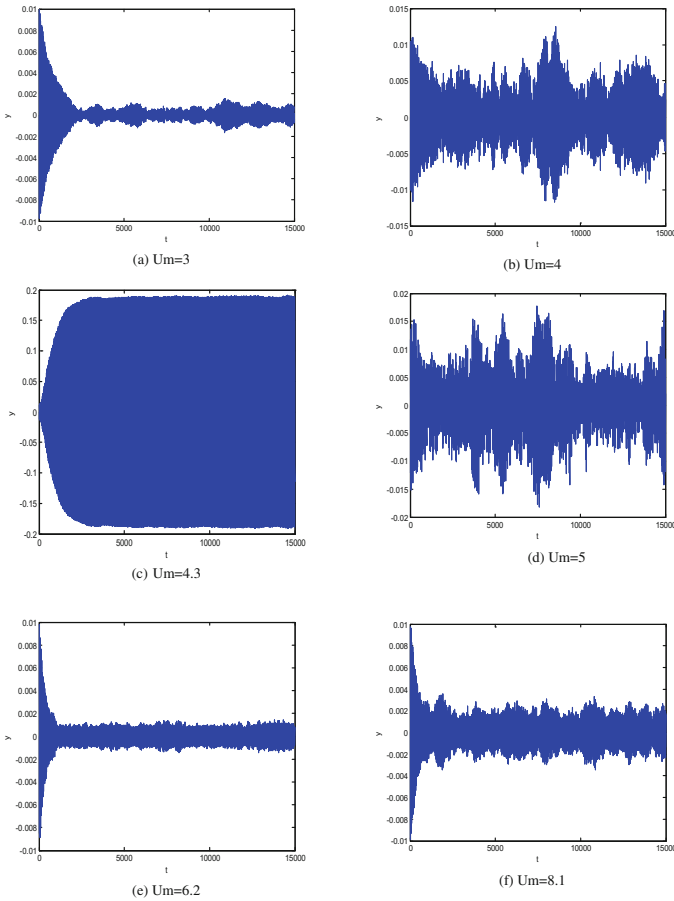


**Fig. 3** Structural amplitude versus mean reduced velocity at  $c = 1$

We start with a noise coefficient value of 0.5. It is seen that the response is almost similar to that of the deterministic case except for the fact that the response has become random limit cycle oscillations and does not have a defined pattern of repetition of signals. Still, it very much resembles the deterministic case, with respect to maximum amplitude, onset of lock-in, etc.

Now, the noise intensity is increased to 1. Though the value has been increased by just 0.5 from the previous case, this has brought out major changes in the responses of the system. We discuss it as follows.

Figure 3a corresponds to the system response at a mean reduced velocity of 3, where the oscillations are seen to be of small amplitude and always bounded within a range. As the reduced velocity reaches 4, the behavior of the system changes instantly. Apart from the fact, the signals are highly irregular compared to the deterministic cases; the structural response is characterized by amplitudes which

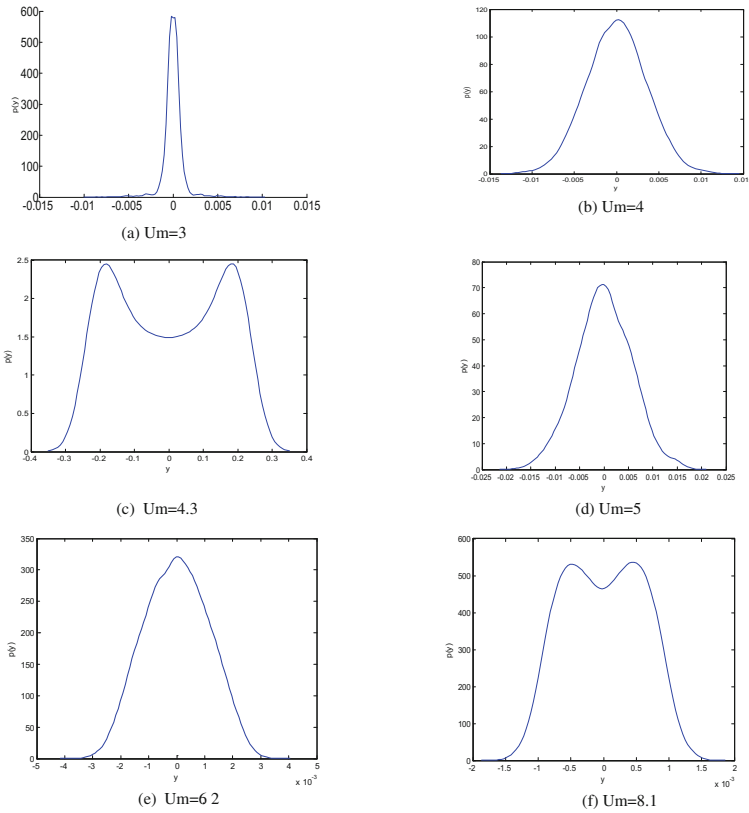


**Fig. 4** Changes in pdfs of the structural response with increasing reduced velocity

differ by orders of magnitude for a reduced velocity. Figure 3b illustrates such a state depicting the time response at reduced velocity of 4 (just before lock-in). Though the response looks erratic at one glance, they are intermittent limit cycle oscillations switching between high and low amplitudes. There are response values as high as 0.01 and as low as 0.001. But this response does not occur in a predictable way, meaning we do not know ‘when’ the high or low-amplitude oscillations might occur. It can be referred to as a state, which is shuttling between the lock-out and lock-in zones. This state of the system is worth noting due to the fact that it is an indicator of the approaching lock-in state.

Figure 4a, b represents pdfs of the above-mentioned two states. It is seen that except for some quantitative changes, where the latter pdf has grown broader, both states show unimodal pdfs.

At a mean reduced velocity of 4.3, we see regular high-amplitude random LCOs as seen in Fig. 3c. The pdf for this case is shown in Fig. 4c. It is a bimodal pdf indicative of the two ends of the random limit cycle oscillations present in the

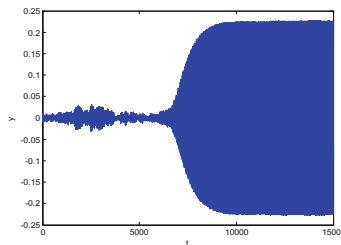
system. It is also to be noted that lock-in has occurred at much earlier velocities in the presence of noise compared to the deterministic cases.

Soon after this, system passes through intermittent LCO state, and at farther velocities away from the lock-in, we have a bimodal pdf again indicative of a small amplitude limit cycle oscillations whose maximum amplitude is of the order of 0.001 as shown in Fig. 3f. The pdf of this state is a bimodal one. So, the system seems to be crossing different dynamical states of whose pdfs are not exactly indicative of the type of response always.

The discussed results establish that there is clearly a qualitative change in the behavior of the system, which is reflected in the pdfs also. But it is not always possible to comment on the type of response just by the qualitative look of the pdf. For example, Fig. 3a, b represents time responses having two different dynamics. But both have unimodal pdfs where the spread of the latter is wider as seen in Fig. 4b.

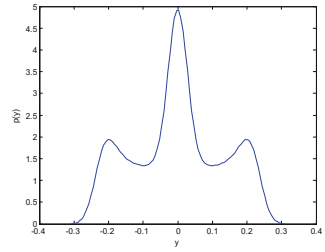
In order to study if a further increase in noise coefficient can bring about any changes, the intensity has been made to 2. Apart from the previously mentioned states, we observe another interesting type of response for this case discussed as follows (Fig. 5).

Figure 5 represents the system response for mean reduced velocity of 4.5, for  $c = 2$ . At 4.6, it moves out of the lock-in regime. So, just before the lock-out zone is approached, it has a response which includes a long transient which is bounded (neither growing nor decaying) and of very small amplitudes. So, an analysis of the system up to just 6000 s, which is a very long interval compared to the previous cases, makes it seem as though the system has already reached the lock-out zone. But, it is seen that, after this long interval, system suddenly settles into high-amplitude RLCOs corresponding to the lock-in zone again. This can be a potentially dangerous situation in real-life situations. We consider it important to account for the small amplitude value oscillations in the beginning due to the fact that they are neither growing nor decaying oscillations and that they stay for a considerable amount of time in the system. Figure 6 shows the pdf for this case. As can be seen, it is a trimodal pdf whereby it has come out as a combination of the bimodal and unimodal states corresponding to the high-amplitude RLCOs in the lock-in zone and low-amplitude LCOs in the lock-out zones, respectively.



**Fig. 5** Response time history at  $Um = 4.5$ ,  $c = 2$

**Fig. 6** Trimodal pdf for  $Um = 4.5, c = 2$



### 3.2 Joint Probability Density Function and Shannon Entropy

We have already seen that a circular cylinder undergoing VIV has different dynamical states characterized by qualitatively and quantitatively different probability density functions. These results are seen similar under effect of Gaussian noise too. But confirmation of P-bifurcations is incomplete without examining the

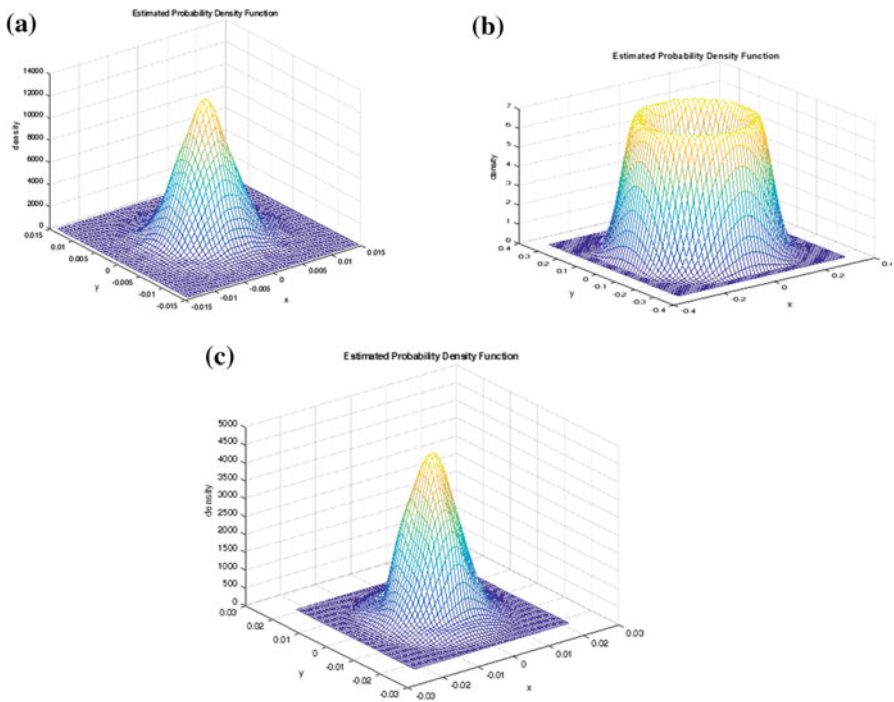


**Fig. 7** Topological changes in joint pdfs for  $Um = 3, 4.1$  and  $5$  corresponding to **a-c** indicating the presence of different attractors and hence p-bifurcations

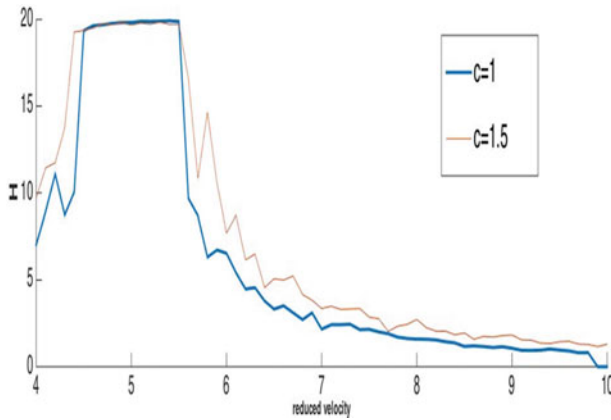


**Fig. 8** Shannon entropy versus mean reduced velocity in the presence of noise for  $c = 1$  and  $c = 1.5$

joint pdfs. Figure 7a–c shows the joint pdfs for three different velocities:  $Um = 3, 4.1,$  and  $5$  (for Gaussian noise with intensity coefficient 1). It is seen that at  $Um = 4.1$  the topological behavior of the pdf has completely changed implying the existence of a different attractor compared to the previous cases.

Now that the presence of P-bifurcation is confirmed, we look forward to invoking a measure which can quantify the randomness of the system. This is done through studying Shannon entropy. Entropy is defined as the amount of disorder present in the system. Shannon entropy of a process  $X(t)$  is defined as [8]

$$H(X, t) = \int_{-\infty}^{\infty} p(X, t) \log_{10} p(X, t) dX$$

We calculate the Shannon entropy based on our joint pdfs. For a particular noise and noise intensity, it is seen that as velocity is increased, the entropy also is increased till lock-in. The entropy is seen to remain constant throughout the lock-in regime. Later, entropy decreases when the system crosses the lock-in regime. It is also observed that increase in noise intensity leads to more fluctuating entropies, especially in the lock-out zone. This feature is illustrated in Fig. 8. For  $c = 1.5$ , the decrease in entropy values is not as smooth as  $c = 1$  case. We see more fluctuating entropies as intensity of noise coefficient is increased. Lower values of entropy indicate small amplitude oscillations, and a non-changing entropy value represents the lock-in zone.

## 4 Conclusion

In this work, we present the effect of noise on the structural amplitude of a cylinder undergoing vortex-induced vibrations. It is observed that uniformly distributed fluctuations imposed on uniform incoming flow are capable of bringing major qualitative changes in the structural response of the system. The onset and regime of lock-in also get advanced in the presence of noise. The existence of P-bifurcations in this stochastic system is confirmed through the topological changes undergone by pdfs. It is seen that, as the velocity is increased, the system passes through different dynamical states depending on the type and intensity of noise. They are as follows: (1) small amplitude-bounded oscillations, (2) intermittent LCOs whose amplitudes shuttle between high and low amplitudes, (3) regular high-amplitude RLCOs in the lock-in state, (4) response with small amplitude-bounded oscillations which stay for a large amount of time and suddenly settle into high-amplitude oscillations thereafter, (5) small amplitude-bounded oscillations. Cases 1, 3, 5 occur in all systems irrespective of the coefficient of intensity or type of noise. Cases 2 and 4 occur for certain values of noise intensities only. It is seen that 1, 3, and 5 are characterized by unimodal pdfs in majority of cases. Case 3 is characterized by a bimodal pdf indicating two amplitude extremes of the random LCOs. Case 4 is an interesting state characterized by a trimodal pdf, which represents a combination of the two types of dynamical states present in the system. In order to further confirm the existence of P-bifurcations, we consider the joint pdfs of these responses. They also undergo topological changes indicating the creation and destruction of new attractors. Further, we investigate on Shannon entropy of the system as a measure to quantify the disorder in the system. It is seen that as velocity is increased, entropy also increases till lock-in regime where it remains constant. After the lock-in, entropy again decreases either smoothly or with heavy fluctuations depending on the intensity and type of noise. Thus, a very high and non-changing entropy value can tell us that the system is in the lock-in state.

In short, the current study establishes the existence of P-bifurcation in stochastically excited VIV system. The effect and influence of other types of stochastic fluctuations and different set of parameters are also under study by the authors.

## References

1. Govardhan R, Williamson CHK (2000) Modes of vortex formation and frequency response of a freely vibrating cylinder. *J Fluid Mech* 420:85–130
2. Feng CC (1968) The measurement of vortex-induced effects in flow past a stationary and oscillating circular and D-section cylinders, PhD thesis, University of British Columbia, Vancouver
3. Bishop RED, Hassan AY (1964) The lift and drag forces on a circular cylinder oscillating in a flowing fluid. *Proc Royal Soc London A* 277:51–75

4. Hartlen RT, Currie IG (1970) Lift-oscillator model of vortex-induced vibration. *J Eng Mech Div, EM5* 577–591
5. Fachinetti ML, De Langre E, Biolley F (2004) Coupling of structure and wake oscillators in vortex-induced vibrations. *J Fluids Struct* 19(2):123–140
6. Kumar Pankaj, Narayanan S, Gupta Sayan (2016) Investigations on the bifurcation of a noisy Duffing–van der Pol oscillator. *Probab Eng Mech* 45:70–86
7. Blevins RD (1990) *Flow-induced vibrations*. Van Nostrand Reinhold, New York
8. Phillis Yannis A (1982) Entropy stability of continuous dynamic systems. *Int J Control* 35 (2):323–340

# Seismic Behaviour of RC Slab–Shear Wall Assemblage Using Nonlinear Static and Dynamic Analyses



Snehal Kaushik and Kaustubh Dasgupta

**Abstract** Extensive research has been carried out in the past on the behaviour of shear walls for earthquake loading. The junction region of reinforced concrete (RC) wall and floor slab in multistoried buildings plays an important role in transfer of forces to the wall during earthquake shaking. However, extensive investigations on seismic behaviour of structural wall–slab assemblage have not been carried out. In the current study, the possible seismic response of an exterior shear wall–slab junction is investigated through nonlinear static and dynamic analyses of RC wall–slab assemblage. The stresses developed in the wall–slab junction are monitored to investigate the tensile damage. Nonlinear static analysis showed higher values of stresses and tensile damage at the junction region than the dynamic analyses under the selected ground motions.

**Keywords** Shear wall · Floor slab · Slab wall junction · Nonlinear static analysis  
Dynamic analysis

## 1 Introduction

Reinforced concrete (RC) structural walls are widely used in multistoried RC frame buildings to provide lateral strength and lateral stiffness during strong earthquake shaking. In most of the tall buildings, wall–slab junction plays a very important role in transferring forces from each floor level to the wall during earthquake shaking. Although various studies have been carried out in the past on isolated shear wall and floor slab–column junctions, shear wall–floor slab junction has not been studied extensively.

---

S. Kaushik · K. Dasgupta (✉)  
Department of Civil Engineering, Indian Institute of Technology Guwahati,  
Guwahati 781039, India  
e-mail: kd@iitg.ernet.in

S. Kaushik  
e-mail: k.snehal@iitg.ernet.in



In the past studies, the strength and stiffness of RC wall–slab junction have been investigated using 3D finite element method. It was observed that the theoretical strains, deflections, and failure loads were in good agreement with the experimental values [1–3]. Some researchers have also carried out modelling of composite beam–RC wall junction [4]. Apart from monolithic wall–slab junctions, behaviour of precast wall–slab junction has been investigated experimentally. The mathematical models, strut and tie model, and modified stiffness matrix method are proposed in order to analyse both monolithic and precast type of connections [5]. Experiments have been carried out on RC slab–squat wall panel under monotonic and cyclic lateral forces to obtain the inelastic behaviour of the members [6]. The shear wall–slab assemblage with slab shear reinforcement bent at  $90^\circ$  at the joint works very well in the moderate to high seismic risk regions [7]. During strong earthquake shaking, the dynamic force may lead to high-stress concentration at the shear wall–slab junction and subsequent localized failure [8].

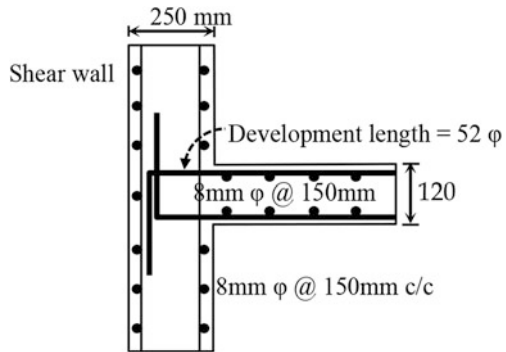
Considering the limited research carried out on seismic behaviour of shear wall–slab junction, the main aim of this study is to investigate the stress concentration and study the damage pattern at the wall–slab junction region caused due to earthquake shaking. Nonlinear static and time history analyses of the shear wall–slab assemblage are carried out to study the behaviour under earthquake loading. To investigate the seismic behaviour of the structure under earthquake action, a refined finite element model is developed using the computer program ABAQUS [9]. Nonlinear time history analyses are conducted using implicit integration method to study the tensile damage at the shear wall–slab junction. The stresses in the wall–slab junction are monitored to see the failure mode in both shear wall and floor slab along with the crack propagation in the concrete.

## 2 Finite Element Modelling

A symmetrical five storied RC wall–frame building is considered to carry out the nonlinear static and dynamic analyses [10]. Reinforcement is embedded in the assemblage (Fig. 1) for the analysis. Both top and bottom bars of the slab are bent at  $90^\circ$  and extended to the exterior face of the shear wall. The reinforcement in the RC shear wall consists of 8 mm diameter rebar spaced at 150 mm *c/c*. The reinforcement is provided in two layers along both the horizontal and vertical directions. Equal reinforcement percentage is provided along the height and width of the wall. The reinforcement provided in the slab is 8 mm diameter bar placed at 300 mm *c/c* in both directions.

The wall–slab assemblage is modelled using eight-noded solid element with reduced integration (C3D8R) using the finite element program ABAQUS [9]. Reinforcement bars are modelled with 2D truss linear element (T3D2) embedded in the solid element. The interaction between wall and slab is modelled as a rigid link (tie constraint), which is based on master node–slave node interaction; however, no sliding is allowed and the parts are rigidly connected.

**Fig. 1** A typical shear wall–slab assemblage



### 3 Material Properties

In the present study, bilinear stress–strain curve is used for the reinforcing steel to provide nonlinearity in the material. A realistic nonlinear stress–strain curve is used for concrete along with the concrete damaged plasticity (CDP) model. Concrete damage plasticity model is chosen to assign the concrete properties to the structure. The material properties of concrete and steel are shown in Table 1.

#### 3.1 Concrete Damage Plasticity Model (CDP)

The Concrete damaged plasticity (CDP) model in ABAQUS uses the concepts of isotropic damaged elasticity and hardening plasticity to represent the behaviour of plain and reinforced concrete [11]. The model uses the yield function of Lubliner et al. [12] with the modifications proposed by Lee and Fenves [13] to account for the multiple damage states (compression and tension damage). The flow potential is defined using a Drucker–Prager function of the hyperbolic type. The model is a continuum, plasticity-based, damage model for concrete with the two principal failure mechanisms as tensile cracking and compressive crushing of concrete. The evolution of the yield (or failure) surface is controlled by two hardening variables,

**Table 1** Material properties for concrete and steel

	Concrete	Steel
Density (kg/m <sup>3</sup> )	2,500	7,800
Elastic modulus (MPa)	25,000	200,000
Poisson's ratio	0.2	0.3
Compressive strength (MPa)	25	–
Tensile strength (MPa)	3.5	–
Yield stress (MPa)	–	415
Ultimate stress (MPa)	–	527

tensile and compressive equivalent plastic strains, linked to failure mechanisms under tension and compression loading.

Among the input parameters for CDP, the modulus of elasticity, Poisson's ratio, yield stresses in compression and tension are considered as 25,000 MPa, 0.2 MPa, 25 MPa and 3.5 MPa, respectively. The dilation angle, eccentricity, viscosity parameter, shape factor ( $K_c$ ) and stress ratio  $\sigma_{b0}/\sigma_{c0}$  are assumed as  $55^\circ$ , 0.1 [14], 0.01, 0.667 and 1.16, respectively. The CDP model and the detailed behaviour of concrete in compression and tension are the same as discussed by Kaushik and Dasgupta [15]. The same equations are used here to develop the stress–strain relationship for concrete in compression and tension.

## 4 Steel Reinforcement

For carrying out analysis in ABAQUS, the material stress–strain data are expressed in “true” stress (Cauchy stress) and logarithmic strain. Most materials exhibit ductile behaviour at yield stress level at the end of elastic range; in such cases, the material data should be given in true form. For nominal stress–strain data under uniaxial test and isotropic material, a simple conversion to true stress and logarithmic plastic strain is given by,

$$\sigma_{\text{true}} = \sigma_{\text{nom}}(1 + \varepsilon_{\text{nom}}) \quad (1)$$

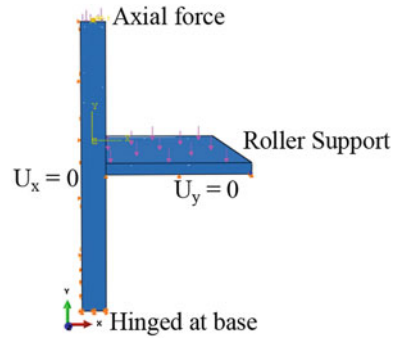
$$\varepsilon_{\text{ln}}^{\text{pl}} = \ln(1 + \varepsilon_{\text{nom}}) \quad (2)$$

Steel reinforcement is modelled as plasticity model in ABAQUS for both tension and compression. Plastic strain values (Eqs. 1 and 2) are used in defining the hardening behaviour. Furthermore, the first data pair must correspond with the onset of plasticity; that is, the plastic strain value must be zero in the first pair. These concepts are applicable when hardening data are defined in a tabular form for plasticity models in ABAQUS/Standard.

## 5 Nonlinear Static Analysis

Pushover analysis of shear wall–slab assemblage, as shown in Fig. 1, was carried out using ABAQUS program. The traditional Newton–Raphson method (static general) is applied together with the material models (concrete and steel), boundary conditions, interaction properties and bond behaviour. The shear wall and the face of the slab are assigned the master surface and slave surface, respectively. The interaction between concrete and steel is modelled using embedded constraint method. In this method, the embedded node is placed at a desired location with the

**Fig. 2** FE model of the shear wall–slab junction subjected to horizontal displacement at the top



constraints imposed by the host element on the translational degrees of freedom of the embedded element. Rebars are modelled as the embedded region in concrete using constraints in the interaction module and making the concrete the host. Thus, rebar elements can only have translations/rotations equal to those of the host elements surrounding them.

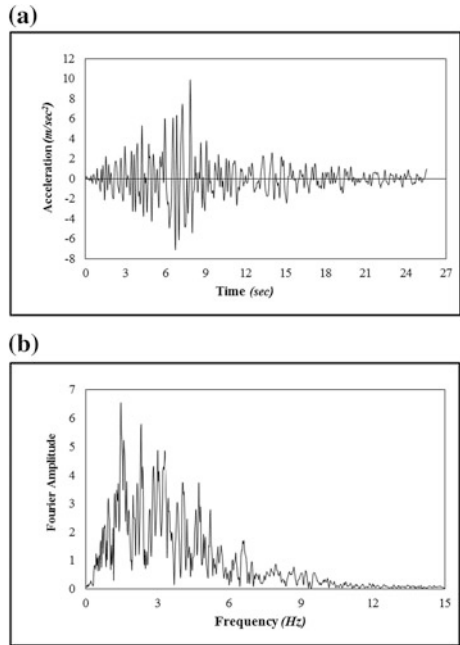
A lateral displacement of 100 mm is applied at the top node in the plane of the shear wall. Translational restraints are imposed on the bottom nodes of the wall to simulate the hinged boundary condition. At the free end of the slab, all the degrees of freedom (DOFs) are constrained except in-plane displacement and rotations about  $X$  and  $Z$  axes. The gravity loads on slab and the axial force on wall are assigned as pressure loads. The slab is loaded with a live load and floor finish of 4 kPa. The out-of-plane bending of shear wall and the vertical bending of slab are restrained. The finite element (FE) model considered for the nonlinear static analysis is represented in Fig. 2.

## 6 Dynamic Analysis

The same model, as shown in Fig. 2, is considered for the nonlinear time history analysis. In this case, the base of the shear wall is fixed at the bottom and ground motions are applied at base. A ground motion, recorded during 1997 Indo-Burma earthquake at station Jellapur with a peak ground acceleration (PGA) of 0.14 g (Fig. 3a, b), is selected for dynamic analysis.

During the analysis, no damage is observed in the models with PGA of 0.14 g. Thus, the same motion is scaled up twice to generate another two ground motions with PGA of 0.56 and 1.12 g. All the three ground motions are applied at the base of the model in the in-plane direction to carry out nonlinear time history analyses.

**Fig. 3** **a** Recorded horizontal ground motion at Jellapur station during 1997 Indo-Burma earthquake and **b** Fourier spectrum of the ground motion



## 7 Comparison and Discussion

The pushover curve obtained from the nonlinear static analysis is shown in Fig. 4. The maximum base shear obtained is 843 kN at a displacement of 34.9 mm. At the ultimate load, most of the reinforcing bars in the shear wall are observed to yield (Fig. 5a). Figure 5b presents the tensile damage pattern at the maximum base shear (34.9 mm displacement).

Yielding of the reinforcement in case of nonlinear pushover analysis appeared first at the shear wall–slab junction region. The vertical reinforcement in the shear wall at the junction region yielded first. Similarly, the tensile damage started at the junction region first at lateral displacement of 0.17 mm. The reinforcement at the

**Fig. 4** Pushover curve for FE model using CDP

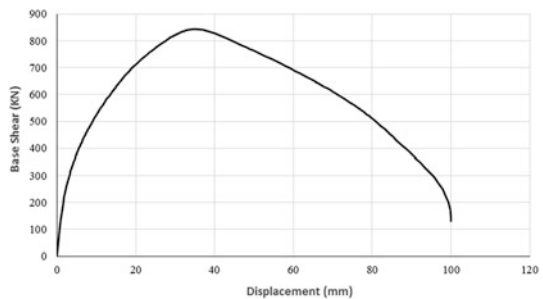
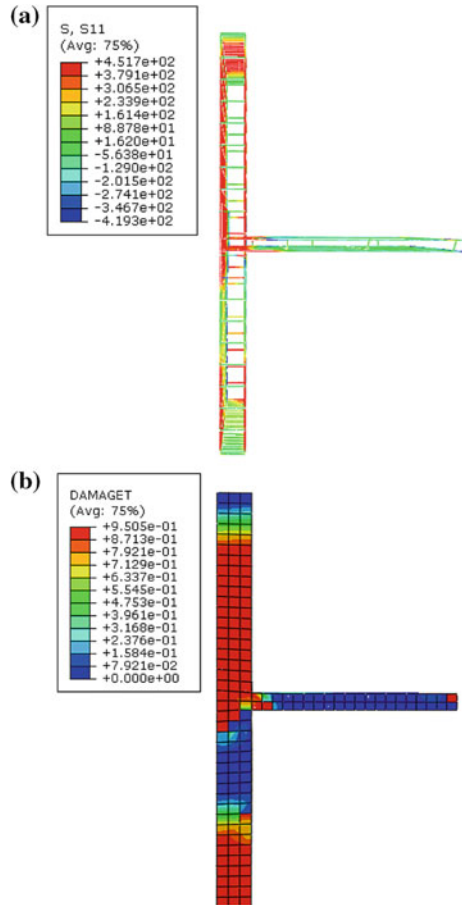


**Fig. 5 a** Axial stress, S11 in reinforcement and **b** tensile damage pattern at maximum damage pattern at maximum base shear



base of the shear wall started yielding at 5.84 mm lateral displacement and propagated upwards in the shear wall region as the displacement increased. Cracks were observed to form in the wall-slab junction region also. Subsequently, flexural reinforcement in that part started yielding, and the damage propagated inside the slab adjacent to the shear wall.

Figure 6 represents the axial stress (S11) in reinforcement, and Fig. 7 shows the tensile damage pattern, at different displacement stages of nonlinear static analysis.

During nonlinear time history analysis, the rebar started yielding at the base of shear wall. The vertical reinforcement in the shear wall yielded first at the time instance of 5.2 s. The tensile stresses observed at 5.2 and 7.8 s (PGA level) time instances were 437 and 496 MPa, respectively. Figure 8 represents the axial stress (S11) developed in the embedded reinforcement of the shear wall–slab junction assemblage.

**Fig. 6** Axial stress, S11 in reinforcement for pushover analysis at: **a** 0.17 mm, **b** 5.84 mm and **c** 100 mm

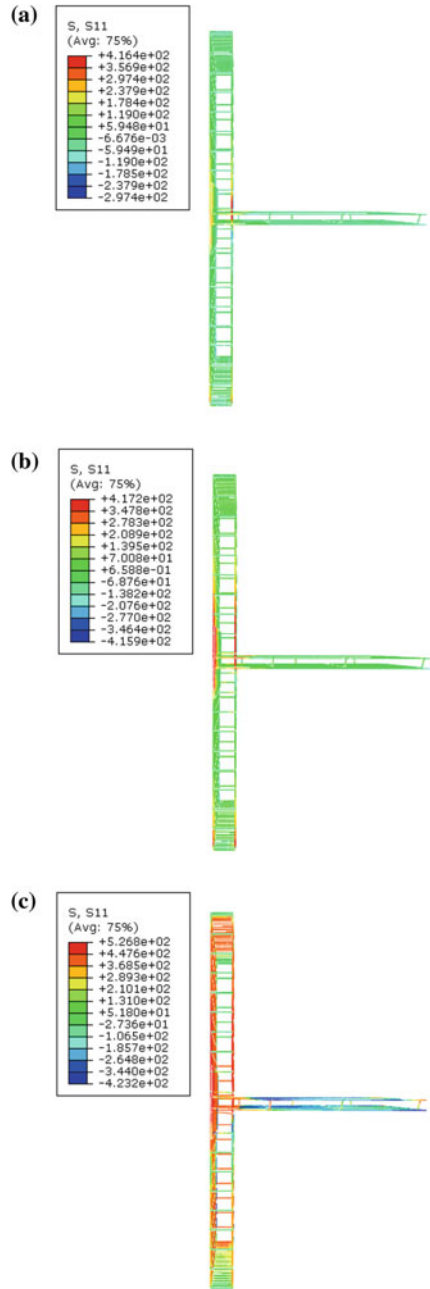


**Fig. 7** Tensile damage pattern for pushover analysis at: **a** 0.17 mm, **b** 5.84 mm and **c** 100 mm

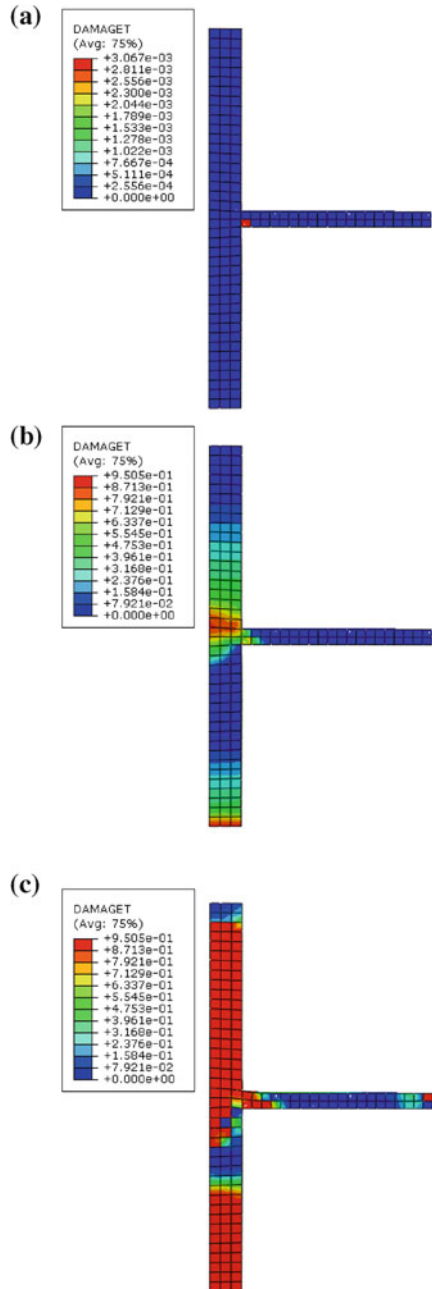




**Fig. 8** Axial stress in reinforcement for time history analysis at: **a** 0.86 s; **b** 7.80 s and **c** 26 s

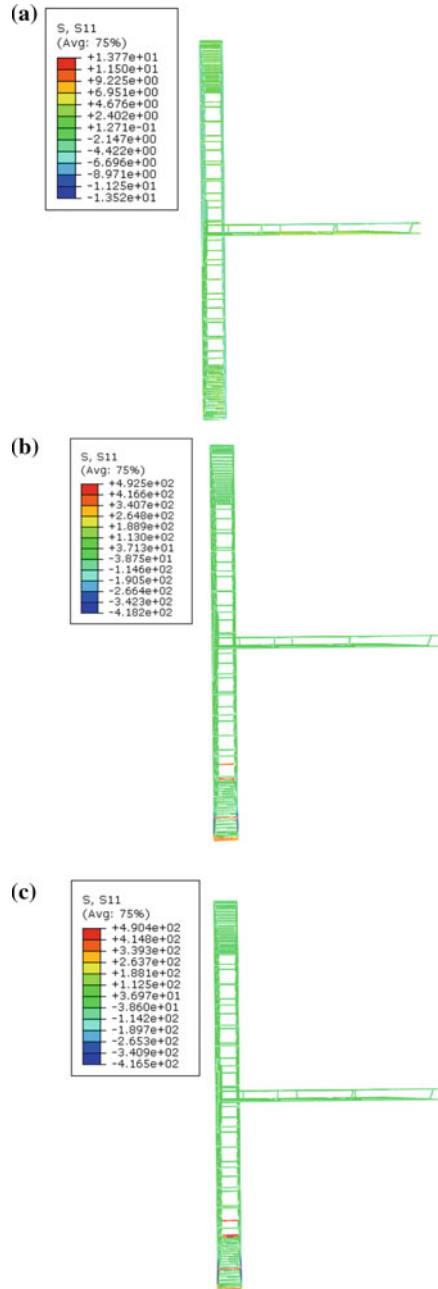
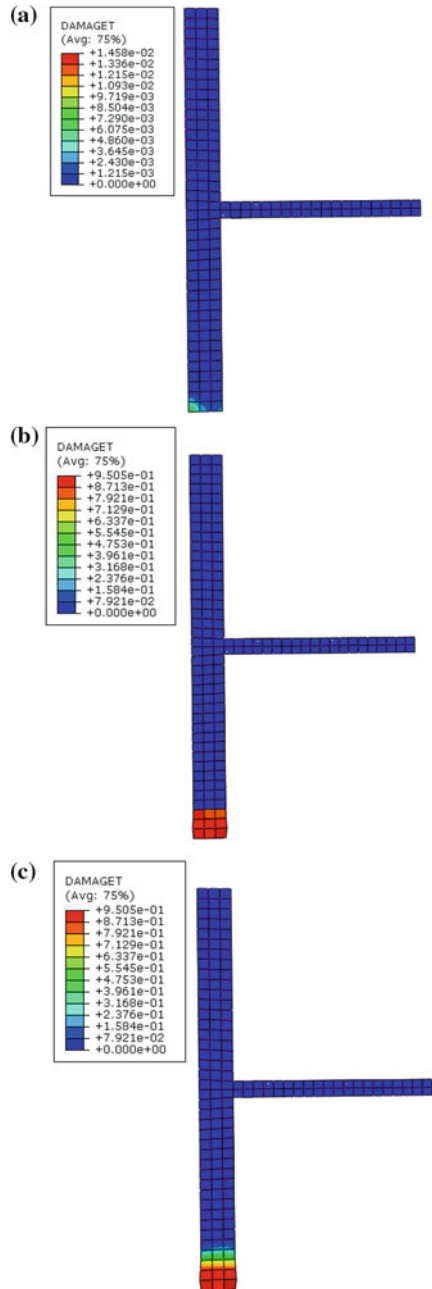


**Fig. 9** Tensile damage pattern for time history analysis at: **a** 0.86 s, **b** 7.80 s and **c** 26 s



As the acceleration is applied in the plane of the shear wall, maximum principal stresses are developed at the base of the wall leading to cracking of concrete. Nonlinear dynamic analysis was carried out using ground motions scaled to three PGA values (0.14, 0.56 and 1.12 g). It was observed that the damage depends on the magnitude of acceleration with the maximum damage incurred for PGA of 1.12 g. Hence, the results for PGA of 1.12 g are compared with those for nonlinear static analysis, and the same has been presented. The damage increases till the attainment of PGA of the ground motion; thereafter, it remains constant. The tensile damage started at the base of the shear wall at 0.86 s time instance and reaches the maximum level at 7.80 s (PGA level). Figure 9 explains the variation of tensile damage at different time instances of ground motion during nonlinear time history analysis.

## 8 Conclusions

In this paper, nonlinear static and dynamic analyses are carried out and compared to study the response of shear wall–slab assemblage. From the nonlinear static analysis it is observed that the hinges formed at the junction region result in the yielding of reinforcing bar at the joint region. As per the dynamic analysis with the input acceleration applied at the base of the specimen, the reinforcement at the base of the shear wall started yielding during dynamic analysis. As the possible damage during time history analysis depends significantly on the characteristics of ground motion, more analyses need to be carried out under various ground motions to develop more insight into dynamic behaviour and spreading of damage at the wall–slab junction region.

**Acknowledgements** The support and resources provided by Department of Civil Engineering, Indian Institute of Technology Guwahati and Ministry of Human Resources and Development, are gratefully acknowledged by the authors.

## References

1. Bari MS (1996) Nonlinear finite element study of shear wall–floor slab connections. *J Civil Eng CE* 24(2):137–145
2. Bari MS (1987) Design of shear wall connection using shear reinforcement, Ph.D. thesis, University of Glasgow
3. Mahmood M (1984) Strength and stiffness of shear wall floor slab connection, Ph.D. thesis, University of Glasgow
4. Henriques J, Simoes da Silva L, Valente IB (2013) Numerical modeling of composite beam to reinforced concrete wall joints part I: global behavior. *Eng Struct* 52:734–746
5. Zenunovic D, Folic R (2012) Models for behaviour analysis of monolithic wall and precast or monolithic floor slab connections. *Eng Struct* 40:466–478

6. Pantazopoulou S, Imran I (1992) Slab-wall connections under lateral forces. *ACI Struct J* 89 (5):515–527
7. Greeshma S, Jaya KP (2013) Effect of slab shear reinforcement on the performance of shear wall-floor slab connection. *J Perform Constr Facil ASCE* 27(4):391–401
8. Coull A, Wong YC (1985) Effect of local elastic wall deformations on the interaction between floor slabs and flanged shear walls. *J Build Environ* 20:169–179
9. Hibbit Karlsson and Sorensen, Inc. (2010) ABAQUS/Standard user's manual (Version 6.11–3), Pawtucket, RI
10. Kaushik S, Dasgupta K (2013) Seismic behavior of slab-structural wall junction in RC building. In: International conference on structural engineering and mechanics, Rourkela, India, Paper No.: 054, Dec 20–22
11. Li, ZJ, Balendra T, Tan TKH, Kong KH (2005) Finite element modeling of cyclic behavior of shear wall structure retrofitted using GFRP. In: SP-230: 7th international symposium on fiber-reinforced (FRP) polymer reinforcement for concrete structures, ACI
12. Lubliner J, Oliver J, Oller S, Onate E (1989) A Plastic-damage model for concrete. *Int J Solids Struct* 25(3):299–326
13. Lee J, Fenves GL (1998) Plastic-damage model for cyclic loading of reinforced concrete structures. *J Eng Mech ASCE* 124(8):892–900
14. Gulec CK, Whittaker AS (2009) Performance-based assessment and design of squat reinforced concrete shear walls, Technical Report, MCEER-09-0010. MCEER, Buffalo
15. Kaushik S, Dasgupta K (2016) Seismic damages in shear wall-slab junction in RC buildings. *Proc Eng Elsevier* 144:1332–1339

# Importance of Inclusion of Soil–Structure Interaction Studies in Design Codes



Nishant Sharma, Kaustubh Dasgupta and Arindam Dey

**Abstract** The Indian seismic design code IS:1893 (Part 1) (BIS, 2002) suggests ignoring soil–structure interaction (SSI) studies for seismic design of structures located on rock or rock-like material. However, for a structure resting on soil, it is imperative that the interaction effects be considered during its analysis. The current study is aimed to assess the differences in the design response and analysis outputs arising due to inconsideration of SSI in the analysis for building frames. Reinforced Concrete (RC) building frames supported on pile foundation and embedded in loose sand are considered and finite element analysis is performed using the OpenSees program. Five types of analysis have been carried out to estimate the different design response and analysis output parameters. The study highlights that it may not always be feasible to ignore time history analysis in cases where site response influences the overall response of the building–foundation–soil system. Thus, detailed investigation is required on possible incorporation of dynamic analysis in code-prescribed seismic design procedure.

**Keywords** Time history analysis · Soil–structure interaction · Equivalent static method of design

---

N. Sharma · K. Dasgupta (✉) · A. Dey  
Department of Civil Engineering, Indian Institute of Technology Guwahati,  
Guwahati 781039, India  
e-mail: kd@iitg.ac.in

N. Sharma  
e-mail: nsharmanishant@gmail.com

A. Dey  
e-mail: arindamdeyiitk@gmail.com

## 1 Introduction

The Indian seismic design code IS:1893 (Part 1) [1] suggests ignoring soil–structure interaction (SSI) studies for seismic analysis and design of structures located on rock or rock-like material. Moreover, the equivalent static method of design is suggested for the estimation of design base shear for the structure. The code is silent on whether to consider or ignore SSI for soft/medium hard soil, and the general practice is to design the structure by ignoring SSI. Evidently, the code provides the design spectrum for these classes of soils, the sole use of which is supposed to cater for the prevalent site conditions. However, for a flexible foundation–soil system it is imperative that the interaction mechanism would play a role in the behaviour of the structure in the event of an earthquake. Therefore, to properly account for SSI effects in the design, it becomes necessary to model the soil domain along with the structure and conduct a dynamic time history analysis using spectrum compatible ground motion data, which would yield realistic estimate of the design forces.

The use of appropriate ground motions, suggested by the code, creates the need to consider the effect of the presence of soil on the modification of the seismic motion as it reaches the ground surface. Time history analysis of a structure with bottom restrained against all possible translations and rotations, under site-specific ground motions, would indirectly consider the effect of the presence of the soil at the site. Thus, there could be various methods for estimation of design forces in the structure. Unfortunately, there exists a lack of clarity on which method would be suitable for cases, wherein there is a large possibility of development of SSI effects. Hence, the objective of the current study is to assess the differences in the design response and analysis outputs arising due to the inconsideration of SSI in the analysis of RC building frames.

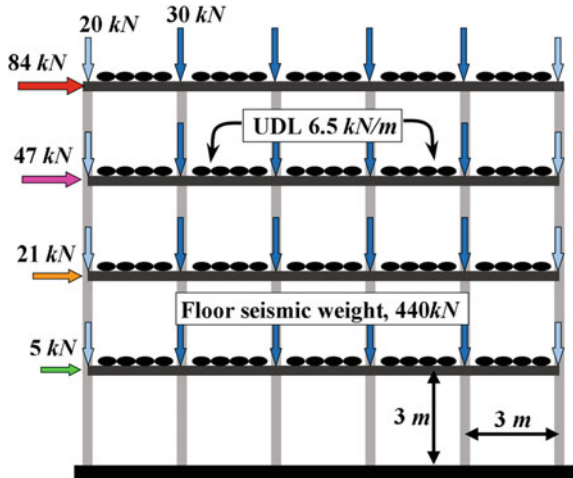
## 2 Modelling and Input

The present study involves two-dimensional modelling of the structure, soil, and foundation system using a finite element-based software framework, OpenSees [2]. The following sections explain in detail the modelling and inputs considered for the study.

### 2.1 Structural System

The structural system, considered in the present study, is a four-storeyed RC frame with a uniform bay length and storey height. The structure is assumed to be located on a soft soil site in Seismic Zone V of the seismic map of India [1]. For the purpose of design and analysis of the structure, relevant Indian standards have been

**Fig. 1** Structural system with loading details



referred. The details of the gravity and lateral loading are shown in Fig. 1. The estimation of the seismic design forces (lateral load) on the structure has been carried out using the equivalent static method (ESM) of analysis as outlined in Ref. [1]. Using the appropriate load combinations, the sizes of the beam and columns have been arrived at Table 1. The modelling of the structural components has been done using two noded frame elements with three translational and three rotational degrees of freedom (DoFs) at each node. M25 grade of concrete and Fe415 grade of rebar are used for design of the frame members, and the material property for the structural element is kept elastic for the present study, as the objective of the current study is not to carry out a performance-based design but to ascertain the differences that arise while adopting different methods to estimate the design forces for the structure.

## 2.2 Soil–Foundation System

For modelling SSI in the present study, a rectangular soil domain is considered and four noded quadrilateral elements with bilinear isoparametric formulation are used to represent the soil. The design forces on the pile foundation have been obtained by determining the design forces at the base of the ground storey columns. For estimation of the flexural and lateral design forces on the piles, Broms’ method is used [1, 3, 4]. The grade of concrete used for piles is M30. Equivalent monopiles have been provided to resist the estimated forces as it is not possible to model pile group in 2D. The sectional details of the pile foundations are shown in Table 1.

The structure and foundation considered are supported on a sandy soil layer of depth 30 m from the base of the superstructure. The sandy layer is assumed to be located above bedrock. The width of the soil domain considered is 20 times the

**Table 1** Frame and pile member details

Beam section (mm × mm)	Column section (mm × mm)	Column r/f, main	Pile diameter (mm)	Pile length (m)
250 × 350	400 × 400	12 # 12 mm $\varnothing$	1000	15

width of the structure [5]. Driven concrete pile foundations support the framed structure and are also modelled using two noded frame elements. The pile nodes are connected to the soil system using a zero-length rigid link member. Interface nonlinearity has not been considered in the study. The structure–foundation system is placed at the central region of the soil domain. Modelling of the pile cap has not been considered, and the material properties of the pile have been kept linear in the study.

### 2.3 *Nonlinear Properties of Soil*

For simulating the nonlinear behaviour of the soil, pressure-dependent multi-yield material model, available in OpenSees, is used. The plastic behaviour in this material model is accounted by using Drucker–Prager yield surface (nested yield surface) criteria. Moreover, a non-associative flow rule exists to capture the effect of dilatancy [6]. Table 2 shows the basic parameters considered for the soil used in the present study. Twenty numbers of nested yield surfaces are used for the simulation of the constitutive behaviour of the material.

### 2.4 *Modelling of Absorbent Boundaries*

For SSI studies, radiation damping is incorporated by proper modelling of vertical and horizontal boundaries of the soil domain. It also allows truncation of the soil domain to a finite extent. In the present study, the vertical and horizontal boundaries have been modelled using Lysmer–Kuhlemeyer viscous dashpots (using appropriate coefficients) [7] to arrest the waves at the boundary along the transverse and longitudinal directions, and preventing the same from reflecting back into the soil

**Table 2** Basic properties of soil

Density of soil (kg/m <sup>3</sup> )	Friction angle of sand ( $\varphi$ )	Poisson's ratio ( $\nu$ )	Shear wave velocity (m/s)
1700	29	0.34	180



medium after being incident at the far-off boundaries. The ground motion input, for SSI cases, has been applied in the form of equivalent nodal forces using the procedure outlined in [8].

## 2.5 Gravity Analysis and Validation

To carry out dynamic analysis of the structure–soil system, it is a prerequisite to carry out static gravity analysis in a staged manner. This staged analysis procedure has been presented in [9]. Moreover, before conducting a full-fledged analysis of the soil–structure system, it is necessary to accurately incorporate the boundary conditions. For this, a linear elastic soil model (without structure) with sine wavelet as input has been analysed and the model validated for the response in the centre of the soil domain as shown in Fig. 2.

## 2.6 Rayleigh Damping

The presence of nonlinearity in soil produces high-frequency spurious oscillations in the numerical solution of the SSI system. It is possibly due to the excitation of high-frequency modes which are undamped. To overcome this issue, the HHT- $\alpha$  method for time step integration may be used [10]. For cases wherein the HHT- $\alpha$  method is ineffective for removal of the spurious oscillations, incorporation of a small amount of Rayleigh damping is useful. Moreover, for the fixed base analysis it is important to incorporate some amount of damping to obtain a realistic response of the structure. Therefore, in the present study, Rayleigh damping has been considered. All contributing modes are assumed to have near about the same damping ratio of 5%. For the fixed base analysis, the frequencies of the various modes of the structure are estimated using the conventional eigenanalysis. However, for the

**Fig. 2** Validation of the numerical model

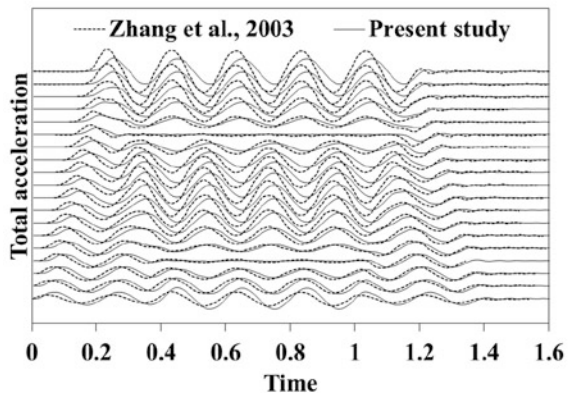


**Table 3** Rayleigh coefficients

Soil		Structure	
$\omega_1 = 9.42$	$a_0 = 0.85$	$\omega_1 = 13.08$	$a_0 = 1.16$
$\omega_4 = 9.42$	$a_1 = 0.0088$	$\omega_4 = 104.7$	$a_1 = 0.0085$

soil–structure system, the conventional eigenanalysis cannot be applied. Hence, a theoretical relationship mentioned in Ref. [11] is used. The frequencies corresponding to the first and the fourth mode are chosen for estimation of Rayleigh coefficients using the relationships mentioned in Ref. [12]. Based on the damping ratios and the frequency of the modes, the coefficients are estimated, and these are used to form the damping matrix (Table 3).

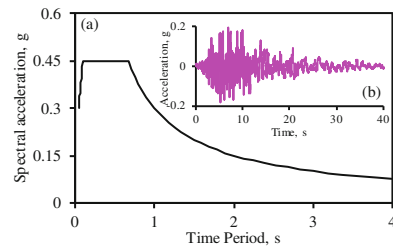
### 2.7 Ground Motion Input and Scaling

The ground motion input selected for the time history analysis is the same as one of the recorded motions during the 1995 Kobe earthquake. The PGA level of the motion considered is that corresponding to the design basis earthquake (DBE) on a soft soil site located in the Seismic Zone V of India and the corresponding response spectrum (Fig. 3). To make the original motion relevant for the chosen site, the original time history is made compatible with the design spectrum using wavelet-based scaling [13] (Fig. 3).

## 3 Analysis Cases

In the present study, the design forces on the structure are estimated using five different methods each representing an analysis case. The description of the five cases is as follows:

**Fig. 3** **a** Response spectrum and **b** corresponding spectrum compatible ground motion used



1. **Equivalent Static Method (ESM):** In this method, the design forces are estimated using the procedure outlined in Ref. [1]. The base of the structure is kept fixed (restrained in all DoF) for this method.
2. **Fixed Base Analysis (FBA):** In this method, the design forces are estimated using the spectrum compatible motion keeping the structure fixed at the base.
3. **Linear Soil–Structure Interaction (LSSI):** In this method, the pile foundation and the supporting soil medium are modelled along with the superstructure. The spectrum compatible motion with half the PGA value is used to provide the input motion at the base of the structure–soil system [11].
4. **Nonlinear Soil–Structure Interaction (NLSSI):** This method is similar to the LSSI case, with the only difference being in the use of nonlinear properties of soil for the analysis.
5. **Fixed Base with Free Field Motion (FBFFM):** In this method, the effect of soil is considered by using the modified motion, recorded at the surface of the soil domain which is obtained by conducting a free field analysis of the soil domain while keeping the structure fixed at the base.

### 4 Results and Discussion

The present section discusses the prime results of the various analysis cases. Base shear is a design parameter that could provide appropriate estimate of the amount of lateral force being induced into the system resulting from the various analysis cases. In the present study, storey-wise absolute maximum shear force, encountered over the entire time history duration, is obtained by summing the shear forces at the base of the column corresponding to each storey level (Fig. 4). From the figure, it is observed that FBA and ESM produce the largest and the smallest shear forces in the lower storey columns. Moreover, LSSI produces values greater than that produced by ESM but less than that produced by NLSSI. For the lower stories, the difference

**Fig. 4** Storey shear for various analysis cases

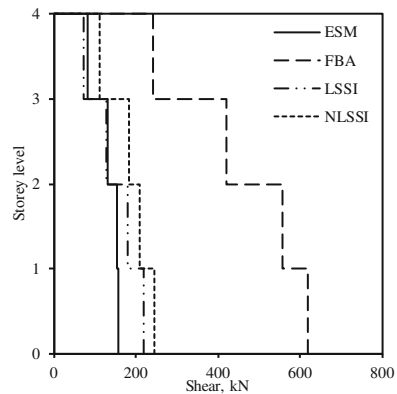
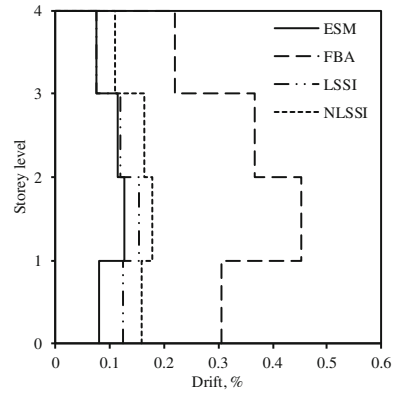


**Fig. 5** Percentage drift for various analysis cases



between the ESM and LSSI cases is high whereas for the higher stories, the difference diminishes. The difference between LSSI and NLSSI values is lower for lower stories but increases for higher stories.

The inter-storey drift ratios (in %) for all the stories show similar trend as observed for storey shear (Fig. 5); i.e. FBA produces largest and ESM produces smallest drift for each storey level. NLSSI produces drift larger than LSSI. For the ground storey, the drift is smaller with respect to other stories even as the shear is higher due to the fixity of the structure at the base.

The comparison of absolute maximum moment profile, induced over the entire duration of each analysis, at the base of each storey level is shown in Fig. 6a (exterior most column) and Fig. 6b (interior most column). Moreover, the storey-wise moment capacity of the column is also plotted in Fig. 6b. It can be seen that the induced forces corresponding to FBA profusely exceed the design moment capacity in exterior columns for lower stories and in interior columns for all the stories. The moment induced corresponding to LSSI and NLSSI also exceeds the design flexural capacity of the columns but for ground storey only for exterior columns. For interior columns, the induced moment is very close to the column capacity.

The instantaneous moment distribution corresponding to the time instant when the maximum bending moment developed in the ground storey columns is shown in Fig. 7. The observations corresponding to Fig. 6 are very much applicable for Fig. 7 as well. In both the figures, it can be seen that at the ground storey level there is a sharp increase in the moment induced for all the analysis cases. This is possibly due to the fact that in the interior columns there is one additional beam member present. This is not so for the exterior columns, and hence, additional moments are induced onto the exterior columns.

Moreover, for the ground storey column, the difference in the moments shared by the exterior and the interior columns is less and it increased for the upper stories. This may be possibly due to the same boundary condition at the base of ground storey for the exterior and the interior columns being same. However, at the top of

**Fig. 6** Absolute maximum moment profile for **a** exterior columns and **b** interior columns

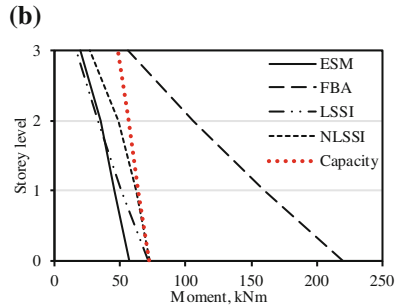
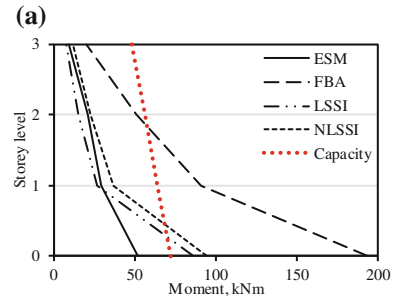
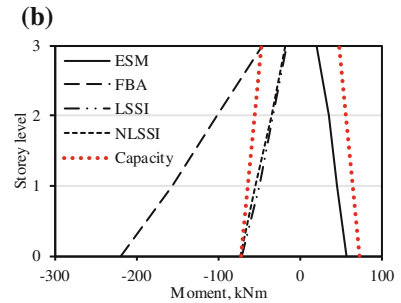
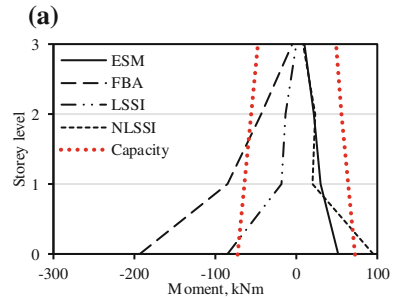


**Fig. 7** Instantaneous moment profile for **a** exterior columns and **b** interior columns



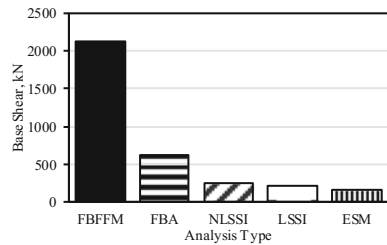
the ground storey level, the exterior columns have the boundary condition which is less stiff in comparison with that of internal column due to the absence of one beam member. This leads to the reduction of moments in the exterior columns above ground storey.

### 5 Importance of Soil–Structure Interaction

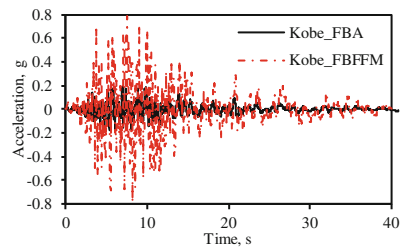
Apart from the four types of analysis discussed so far, another fixed base analysis is also carried out using the motion obtained by conducting a free field analysis of the soil domain (FBFFM). Spectrum compatible motion obtained for SSI analysis is applied at the base of the free field soil domain and analysed. The acceleration response obtained at the surface is noted, and that motion is applied at the base of the building frame with fixed base. Time history analysis using this motion was carried out, and various response entities were noted. Figure 8 shows the comparison of the base shear obtained for this analysis case with other cases. It can be seen that the estimation of base shear for FBFFM analysis case is extremely large and is attributed to the motion obtained from the free field analysis.

Figure 9 shows the original motion used for fixed base analysis and the free field motion (FFM) obtained from free field analysis of the soil domain. It can be seen that there is a large amplification of the acceleration and it is due to the presence of the soft soil deposit. Although the amplified motion considers the modification in the acceleration due to the presence of the soil, the interaction mechanism between the soil and the structure is absent while generating the ground motion. Thus,

**Fig. 8** Base shear comparison for various analysis cases



**Fig. 9** Motions used for FBA and FBFFM



overestimated member forces in the structure are observed. Hence, if the modified ground motions due to the presence of soil domain are to be used, then, in such cases, it becomes imperative to consider the interaction mechanism by suitable modelling of the soil–foundation system along with the superstructure to get a realistic estimate.

The present study clearly highlights how ESM would fall short of estimation of the actual design forces that would arise by considering the actual interaction between the soil and the structure. Moreover, FBA, with or without modified ground motions, as per the sites, could produce forces that may be very large compared to the actual scenario. This is because of the absence of huge energy dissipation that exists due to the interaction mechanism and also due to the radiation phenomenon inherent in the soil. It is also to be noted that the forces produced corresponding to LSSI and NLSSI are slightly higher with respect to ESM which may render a structure unsafe in the event of an earthquake. Hence, this advocates the importance of considering soil–structure interaction studies for the design of structure located at soft soil sites.

## 6 Summary and Conclusions

The present article highlights the importance of inclusion of SSI studies for estimation of design forces on the structure. In the present study, five different types of methods for estimation of design forces on the structure are considered and the differences arising in the design forces using these methods are presented. It has been found that the most widely used method, ESM, produces the lowest estimate of forces and drift values, and FBA, using spectrum compatible ground motion, produces the largest values. The estimates of force obtained using LSSI and NLSSI are significantly lesser than that obtained by FBA but moderately larger than ESM. The margin is sufficient to push the structure into an unsafe zone, especially making the exterior bay columns vulnerable to damage. Although the effect of soil deposit is considered by modifying the ground motion, direct application of motion is not recommended for estimating the design forces. The foundation–soil medium should be modelled to obtain the realistic estimate of design forces. Hence, ESM and FBA may not always provide a realistic estimate and it may sometimes not be possible to ignore dynamic SSI studies for the design of structures located on soft soil. The present study highlights the need of detailed investigation on possible incorporation of dynamic SSI analysis in code-prescribed seismic design procedure. Detailed parametric studies are required to be carried out in this regard.

**Acknowledgements** The support and resources provided by Department of Civil Engineering, Indian Institute of Technology Guwahati, and Ministry of Human Resources and Development (MHRD, Government of India) are gratefully acknowledged by the authors.

## References

1. IS: 1893 (Part I)-2002 (2002) Indian standard criteria for earthquake resistant design of structures, fifth revision, Part-1. Bureau of Indian Standards, New Delhi
2. Mazzoni S, McKenna F, Scott MH, Fenves GL (2006) OpenSees command language manual. Pacific Earthquake Engineering Research (PEER) Center
3. IS: 456-2000 (2002) Indian standard plain and reinforced concrete- code of practice, fourth revision. Bureau of Indian Standards, New Delhi
4. IS: 2911 (Part I/Sec 1)-1979 (1979) Indian standard code of practice for design and construction of pile foundations, first revision, Part-1, Section 1. Bureau of Indian Standards, New Delhi
5. Sharma N, Dasgupta K, Dey A (2016) Finite element modelling studies for SSI studies. In: Proceedings 6th international conference on recent advances in geotechnical earthquake engineering and soil dynamics, 43. IIT Roorkee Extension Center, Greater Noida, India
6. Elgamal A, Yang Z, Parra E, Ragheb A (2003) Modeling of cyclic mobility in saturated cohesionless soils. *Int J Plast* 19(6):883–905
7. Kuhlemeyer RL, Lysmer J (1973) Finite element method accuracy for wave propagation problems. *J Soil Mech Found Div ASCE* 99(SM5):421–427
8. Joyner WB (1975) Method for calculating nonlinear seismic response in 2- dimensions. *Bull Seismol Soc Am* 65(5):1337–1357
9. Zhang Y, Yang Z, Bielak J, Conte JP, Elgamal A (2003) Treatment of seismic input and boundary conditions in nonlinear seismic analysis of a bridge ground system. In: Proceedings of the 16th ASCE engineering mechanics conference, pp 16–18. University of Washington, Seattle, USA
10. Hilber HM, Hughes TJ, Taylor RL (1977) Improved numerical dissipation for time integration algorithms in structural dynamics. *Earthquake Eng Struct Dynam* 5(3):283–292
11. Kramer SL (1996) Geotechnical earthquake engineering. Prentice Hall, New Jersey, USA
12. Chopra AK (1995) Dynamics of structures-theory and applications to earthquake engineering. Pearson Education Inc, Noida, U.P., India
13. Mukherjee S, Gupta VK (2002) Wavelet-based generation of spectrum compatible ground motions. *Soil Dyn Earthquake Eng* 22(9):799–804



# Comparison of Modal Behaviour of Integral Abutment Bridge With and Without Soil–Structure Interaction



Sreya Dhar and Kaustubh Dasgupta

**Abstract** Integral abutment bridges (IABs) have gained popularity over past few years. The main advantage of IAB over conventional bridges is the absence of any bearing at the deck–abutment junction which leads to reduced possibility of unseating of bridge deck during strong earthquake shaking. The seismic response of bridges with integral abutments depends significantly on the abutment–soil interaction in the longitudinal direction and soil–pile interaction in the transverse direction. In the present study, the modal behaviour of IAB is investigated with and without the presence of soil–structure interaction (SSI). The soil flexibility for soil–pile and abutment–backfill interactions is represented by springs. This leads to significant increase in the overall flexibility of the bridge system as compared to the model with all the degrees of freedom (DOFs) restrained at the bottom of pier. Due to higher longitudinal stiffness contributed by both the deck and the abutments, the SSI bridge model shows complete longitudinal mode of vibration in higher mode. By removing the abutments and end spans of the deck, the first longitudinal mode of vibration occurs in one of the lower modes. Hence, the numbers of spans in the bridge play an important role in the modal behaviour of the bridge. The importance of SSI in modal analysis highlights its need for inclusion in the seismic design of IABs.

**Keywords** Integral abutment bridge · Soil–structure interaction  
Modal analysis

---

S. Dhar (✉) · K. Dasgupta  
Department of Civil Engineering, Indian Institute of Technology Guwahati,  
Guwahati 781039, India  
e-mail: sreya.dhar@gmail.com

K. Dasgupta  
e-mail: kd@iitg.ernet.in

## 1 Introduction

Soil–structure interaction is an important aspect in the investigations of structural behaviour for carrying out performance-based earthquake engineering studies. Particularly, in the case of bridges, SSI along with multi-support excitations during earthquake shaking plays an important role in the seismic behaviour of a bridge. In urban areas, IABs are now becoming very popular due to minimal maintenance costs over their service periods. In typical bridges, the repair and maintenance of the joints and the bearings affect the life cycle cost of the bridge and overall economy [1, 2]. One of the most common problems of traditional bridge construction in seismic zone is unseating of the superstructure from the support bearings. This problem is eliminated in integral abutment construction as there are no support bearings [3]. Past studies on integral abutment bridges have accounted for the stresses in different components arising from creep, shrinkage and temperature effects [4]. The length of the integral bridge mainly depends on the pile capacity, soil type and abutment movement due to intensity of temperature and seismic load and other factors [5]. Backfill soil properties influence the IAB behaviour significantly [4, 6]. The contribution of bridge abutments in the natural vibration behaviour of IAB was also observed to be significant [7].

The present study mainly focuses on the natural behaviour of IAB with and without considering the effect of SSI. The effect of the abutment on the modal behaviour of the structure has also been investigated.

## 2 Description of Model

### 2.1 Bridge Model

In the present study, the previously studied Humboldt Bay Middle Channel Bridge [8, 9] has been considered with certain modified characteristics. The modelling of the bridge is carried out using the computer program SAP2000 V16.0.0 [10] (Fig. 1). The bridge is 330 m long, 10 m wide and 12 m in height. The bridge superstructure is integrally connected to the abutments at the two ends. The height, width and the thickness of the abutments are 12 m, 10 m and 1.2 m, respectively. The superstructure consists of concrete deck slab which is resting on four precast prestressed concrete symmetric I-shaped girders. The cross-sectional area and the second moments of the areas are taken as  $0.73 \text{ m}^2$ ,  $0.49 \text{ m}^4$  (major axis) and  $0.0094 \text{ m}^4$  (minor axis), respectively. The deck slab is 165 mm thick, and it is rigidly connected with girders by rigid links. The superstructure is resting on piers which are connected to deck by pier caps. The length and cross-sectional area of pier cap are 10 m and  $4 \text{ m}^2$ , respectively. The height and cross-sectional area of each pier are 12 m and  $3.4 \text{ m}^2$ , respectively. Each pier is supported on pile foundation with each pile group having five precast driven piles. Pile foundations are

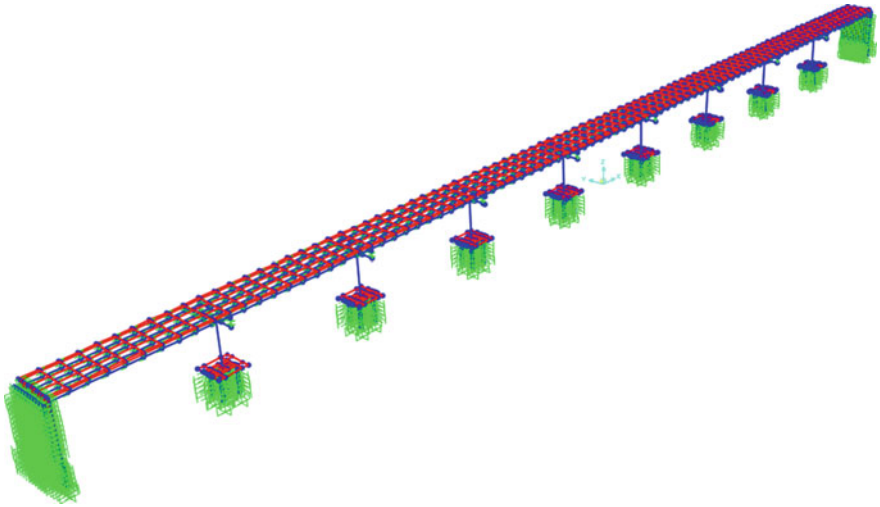


**Fig. 1** Modified Humboldt Bay Middle Channel Bridge with soil–structure interaction modelled in SAP2000

assumed to extend up to 5.2 m depth from ground level. The superstructure, pier and piles are discretized using two-noded frame elements with 6 degrees of freedom (DOFs) at each node, namely (a) three translational and (b) three rotational DOFs at each node. Each individual deck span is discretized into ten elements. Abutments and pilecaps have been modelled by linear elastic four-noded shell elements. Abutment piles have been modelled in the same way as the as pier piles, with a spacing of 1 m. The modulus of elasticity and unit weight of concrete are taken as 28 GPa and 24 kN/m<sup>3</sup>, respectively.

## 2.2 *Foundation and Abutment–Backfill*

Springs have been used to model the flexibility of the backfill soil behind the abutments and the cohesive soil surrounding the piles (Fig. 1). For each spring, force–displacement curves have been used as per API-RP2 [11]. Piles are friction type or floating piles and have been incorporated with skin friction and lateral load resisting capacity due to surrounding soil. Both the lateral stiffness of the soil and the initial skin friction increase with the depth of the piles. The springs are also assigned to account for both the aspects. Each soil spring is modelled using one-noded link element in the program SAP2000 (Fig. 2a). At each pile tip, the end bearing resistance has been modelled by two-noded link element in SAP2000 (Fig. 2b). As the piles are of only 5.2 m in depth, they are considered to be short piles. Soil mass has not been considered for the present study while modelling soil–structure interaction of the IAB.

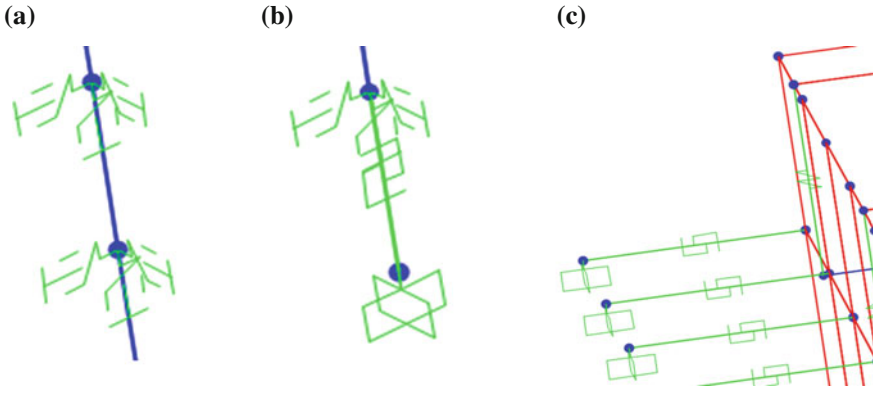
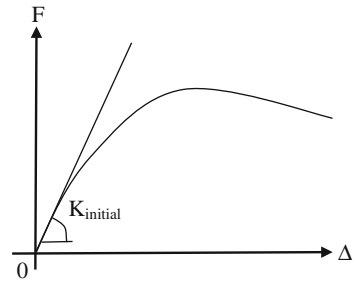


**Fig. 2** **a** One-noded horizontal and vertical link elements at different depths of piles, **b** two-noded link element at the tip of each pile and **c** two-noded link elements for modelling abutment–backfill interaction

**Fig. 3** Initial stiffness ( $K_{initial}$ ) from the generic force–displacement curve of soil spring



Each abutment has been designed against the passive earth pressure during seismic excitation or temperature increment, since the active earth pressure is considered to be negligible [12]. Abutment–backfill behaviour has been modelled considering dense sand properties [8]. The lateral passive pressure exerted by the backfill soil tends to increase with the depth of abutment backwall. Abutment–backfill interaction has been modelled as per BA 42/96 [13] curves for end screen abutments of IAB. These properties have been assigned to the two-noded link elements (Fig. 2c). As linear elastic behaviour is required for the modal analysis, the initial stiffness has been considered for the soil spring elements from their nonlinear force–deformation curves (Fig. 3). For soil–pile interaction, initial lateral stiffness and skin friction are shown in Table 1. The initial lateral stiffness for abutment–backfill interaction is shown in Table 2. Only near-field soil–pile interaction has been considered.

Modal analysis of the bridge model has been carried out without the presence of piles, pilecap and soil and by considering the bottom nodes of pier as fully restrained. This model will be henceforth called as fixed base model. The same

**Table 1** Initial lateral stiffness of the soil and skin friction on pile at different depths

Depth, m	Lateral stiffness, kN/m	Skin friction, kN/m <sup>2</sup>
1.0	250	2,497
2.0	250	3,248
3.0	250	3,973
4.0	748	4,587
5.2	748	5,228

**Table 2** Initial lateral stiffness for abutment–backfill interaction at different depths of abutment

Depth, m	Initial lateral stiffness ( <i>K</i> ), kN/m
1	6,042
2	12,083
3	18,125
4	24,166
5	30,208
6	32,429
7	42,291
8	48,332
9	54,374
10	60,415
11	66,456
12	72,498

analysis has been carried out for the other model considering the soil–pile and backfill–abutment interactions. Modal analysis is carried out with initial zero-stress condition in soil which implies the absence of any other preceding static/dynamic analysis. Further, modal behaviour of IAB is also studied by removing end spans and abutments.

Hence, four cases have been considered to compare the modal behaviour of the bridge which are (a) only bridge model, (b) complete SSI model, (c) Case (i), where both the end spans with abutments have been removed from bridge and (d) Case (ii), where further end spans have been removed.

### 3 Comparison of Modal Analysis Results

For both the SSI model and the fixed base model, the natural periods and the mode shapes of the first 12 modes of vibration have been compared. The mode shapes of vibration for the first 3 modes are shown in Figs. 4, 5 and 6. The first modes are along the transverse direction of the bridge for both the models. Due to soil–pile interaction and increased flexibility, the entire pier cap–pier–pilecap–pile group system deforms along the height of the bridge. This results in less relative transverse deformation of the deck with respect to the bottom of pier in the

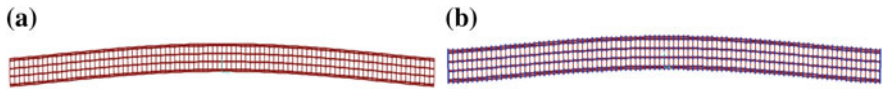


**Fig. 4** Plan views of first mode shape of vibration for **a** fixed base bridge model and **b** bridge with SSI model

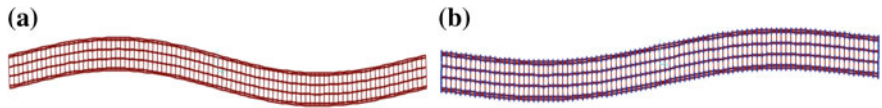


**Fig. 5** Plan views of second mode shape of vibration for **a** fixed base bridge model and **b** bridge with SSI model

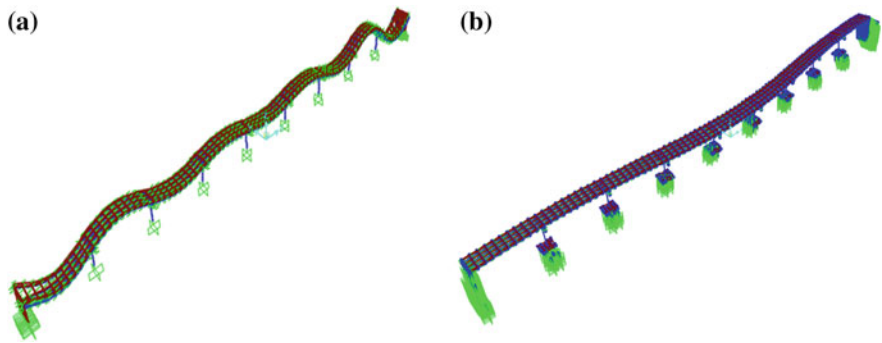


**Fig. 6** Plan views of third mode shape of vibration for **a** fixed base bridge model and **b** bridge with SSI model

corresponding mode shapes. However, in case of fixed base model, the variation of transverse deformation is steeper due to the large relative transverse deformations of deck with respect to the restrained bottom node of pier. For both the models, the second modes involve twisting of the bridge deck.

In the third and the fourth modes, the deck deforms in a wave-shaped profile in the vertical direction for both the models. For both the models, the contribution of longitudinal stiffness by the deck and the two abutments remains the same. However, in SSI model, the flexibility is increased due to the presence of pile cap–pile group–soil system below each pier. Further, the abutments of SSI model become relatively stiffer due to the presence of abutment–backfill interaction springs. The observation of the first longitudinal mode of vibration of the bridge depends on the relative influence of the combined longitudinal bridge stiffness (for the mentioned components) and the bridge stiffness along the transverse direction. Due to large difference between the two stiffness, the first longitudinal mode of vibration occurs in the 11th mode for the bridge model with SSI (Fig. 7).

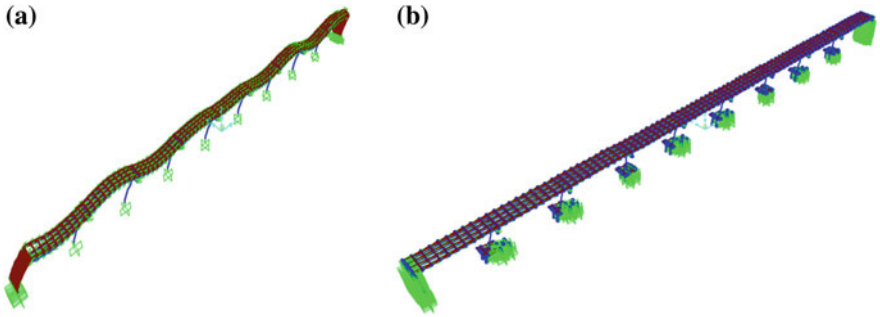


**Fig. 7** Longitudinal mode of vibration for **a** fixed base bridge model and **b** bridge with SSI model

**Table 3** Comparison of natural periods between fixed base bridge model and bridge with SSI model

Mode no.	Time period, s			
	(a) Bridge model	(b) Full SSI model	(c) Case (i)	(d) Case (ii)
1	0.697	2.136	2.216	2.190
2	0.651	1.654	2.070	2.020
3	0.549	1.282	1.897	1.864
4	0.547	1.066	1.651	1.274
5	0.540	0.912	1.060	0.900
6	0.494	0.865	0.891	0.860
7	0.493	0.852	0.858	0.840
8	0.464	0.840	0.849	0.774
9	0.457	0.833	0.838	0.764
10	0.452	0.815	0.777	0.761
11	0.434	0.802	0.767	0.760
12	0.410	0.776	0.762	0.747

As compared to the bridge with SSI model, the difference between the transverse bridge stiffness and the longitudinal bridge stiffness is lesser for the fixed base bridge model. This leads to the occurrence of the first longitudinal mode of vibration in seventh mode for the fixed base bridge model. For two-span integral bridge in underlying clayey soils, longitudinal modes of vibration were also observed in early modes in Ref. [6].

It is observed that the range of natural periods for the bridge model with SSI is higher than the entire range for the fixed base bridge model for the first 12 modes of natural vibration (Table 3). For higher modes, the natural periods are closely spaced for both the models. The presently studied bridge is expected to show significantly large response under earthquake ground motions with dominant period in the range of 0.8–2.1 s. However, the analysis of fixed base model shows an entirely different (lower) range for dominant periods of ground motions. Thus, using fixed base

bridge model for estimation of design forces may lead to unsafe design. Considering more realistic behaviour, SSI needs to be considered in performance-based bridge engineering studies.

#### 4 Removal of End Spans in Bridge with SSI Model

Bridge abutments contribute more to the bridge stiffness along the transverse direction than the longitudinal direction due to their large length. In the present study, the contribution of abutments to the bridge stiffness is investigated by first removing the end spans of the bridge and the abutments (Case (i)). The increase in flexibility is observed for the first nine modes (Table 3) of the new bridge with increase in the natural periods. The bridge natural vibrations occur in transverse, torsional and longitudinal modes of vibration for the first three modes, respectively. Next, the two end spans of the reduced bridge were further removed (Case (ii)). However, the bridge response showed increase in stiffness for all the modes of vibration (Table 3). This is due to the reduction in the ratio of mass/stiffness for the entire bridge on removal of the spans. The nature of mode shapes of vibration for Case (ii) remains the same as in Case (i) (Fig. 8). Hence, the abutments and the number of spans of a bridge contribute to the relative magnitudes of transverse and longitudinal stiffness and hence play an important role in the modal behaviour of the bridge.

#### 5 Summary

The present study is intended to compare the modal behaviour of an integral abutment bridge for two conditions, namely (a) the absence of SSI and (b) the presence of SSI. In the presence of pile cap–pile group–system and abutment–backfill interaction, the natural vibration characteristics of the bridge are quite different from those obtained through the conventional modelling approach, i.e., by restraining the bottom nodes of the piers. The contribution of abutments and the number of spans of the bridge have also been illustrated.

For both the cases, stiffness of the bridge along the transverse direction was lower as compared to the bridge stiffness along the longitudinal direction. This resulted in occurrence of transverse vibration configurations in the lower modes.

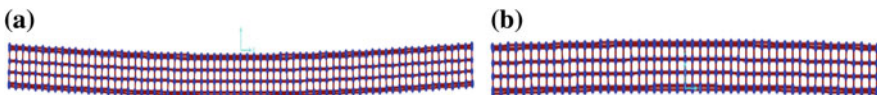


**Fig. 8** Transverse mode of vibration for **a** Case (i) and **b** Case (ii) models



Also, the components contributing to the SSI response of bridge influence the occurrence of longitudinal mode of vibration in the lower or the higher modes. The removal of abutments and the end spans brings changes to the mass/stiffness ratio of the overall bridge. This leads to some modes becoming stiffer and a few modes becoming more flexible.

The present study is carried out on the modified model of a real bridge for which extensive studies had been carried out in the past [8, 9]. To have more generalized conclusions, further studies need to be carried out on different bridge configurations with parametric variations. For longer bridges with more number of spans, heterogeneity of underlying soil becomes an important issue.

## References

1. Mistry V (2005) Integral abutment and jointless bridges. In: The 2005-FHWA conference, Integral Abutment and Jointless Bridges (IAJB 2005), Baltimore, Maryland, USA, March 16–18, pp 3–11, 2005
2. Yannotti AP, Alampalli S, White HL (2005) New York state department of transportation's experience with integral abutment bridges. In: The 2005-FHWA conference, Integral Abutment and Jointless Bridges (IAJB 2005), Baltimore, Maryland, USA, March 16–18, pp 41–49, 2005
3. Wasserman E, Walker J (1996) Integral abutments for steel bridges. Technical report, Tennessee Department of Transportation, American Iron and Steel Institute
4. Kumari P (2013) Seismic analysis of integral abutment bridges. M. Tech thesis, Department of Civil Engineering, IIT Guwahati
5. Greimann LF, Yang PS, Edmunds SK, Worlde-Tinsae AM (1984) Design of piles for integral abutment bridges, Final report, IOWA department of Transportation, ISUERI-Ames 84228
6. Farahani RV, Zhao Q, Burdette EG (2010) Seismic analysis of integral abutment bridge in Tennessee including soil-structure interaction. *J Transp Res Board* 2201:70–79
7. Goel RK (1997) Earthquake characteristics of bridges with integral abutments. *J Struct Eng, ASCE* 123(11):1435–1443
8. Zhang Y, Conte JP, Yang Z, Elgamal A, Bielak J, Acero G (2008) Two dimensional nonlinear earthquake response analysis of a bridge-foundation ground system. *Earthquake Spectra* 24(2):343–386
9. Elgamal A, Yan L, Yang Z, Conte JP (2008) Three-dimensional seismic response of Humboldt Bay Bridge-foundation-ground system. *J Struct Eng, ASCE* 134(7):1165–1176
10. CSI (2013) Integrated software for structural analysis and design SAP2000 version 16.0.0. Computers and Structures Inc. Berkeley, USA
11. American Petroleum Institute (API RP2A-WSD: 2000) (2000) Recommended practice for planning, designing and constructing fixed offshore platforms-working stress design, Washington, D.C.
12. Clough GM, Duncan JM (1991). In: Fang HY Foundation engineering handbook, Indian Edition, CBS Publishers, New Delhi, India
13. BA 42/96 Highway Agency (1993) Design manual for integral bridges: design manual for road and bridges, vol 1, The Stationery office, London

# Assessment of Response Reduction Factor for Reinforced Concrete Frame Buildings in a Probabilistic Seismic Risk Framework



Prakash S. Badal and Ravi Sinha

**Abstract** Response reduction factor (*RRF*) was first introduced in 1978 NEHRP provisions. These factors split the earthquake-resistant design process into two independent segments—first, quantification of the actual seismic demand assuming that structure remains elastic during the expected level of excitation and second, prediction of reserved capacity of a structural system. The *RRF* values were largely assigned with the intent to avoid significant deviation in the prevalent design base shear due to modifications in the code. For regions of moderate seismicity, selection from the alternatives of constructing a limited-ductile building or a fully ductile building is governed by the cost of material and execution. Ideally, the two available choices for the structural systems should result in similar building performance levels. Extending this requirement in a probabilistic seismic risk framework, the paper presents the quantification of *RRF* values for both alternative structural systems. The results obtained from sample midrise reinforced concrete moment-resisting frame (RCMRF) building located in Mumbai and designed as per Indian standards have been presented. It is found that both variants exceed their respective *RRF* values assumed by the code. It is also found that the fully ductile building offers better performance level than the limited-ductile building. The results have implications for the specification of *RRF* in the current Indian standards.

**Keywords** Response reduction factor · Seismic risk · Performance-based design Design standards

---

P. S. Badal · R. Sinha (✉)  
Department of Civil Engineering, Indian Institute of Technology Bombay,  
Mumbai 400076, India  
e-mail: rsinha@civil.iitb.ac.in

P. S. Badal  
e-mail: aprakashn@gmail.com

## 1 Introduction

Buildings following design codes are expected to withstand a rare earthquake without collapsing. This level of earthquake usually corresponds to maximum considered earthquake (MCE). In addition, it is also desirable that buildings perform fairly during a design basis earthquake (DBE). Since the level of these forces, even in the areas of moderate and low seismicity, results in actions that are significantly higher than that due to regular loads, it becomes inevitable to include the inelastic strength of buildings. To indirectly consider this effect while continuing to perform an elastic analysis, building codes include a response reduction factor (*RRF*). In other words, *RRF* represents the cumulative effects of inherent overstrength, ductility capacity, and redundancy of the structure. Various sources contribute to the reserved capacity of a structure. Some of these—such as material safety factors, load factors in design load combinations, higher expected material properties than nominal material properties used in design, conservatism in section sizes, and reinforcement—are effective before the elastic limit of a structure is reached. Others—like energy dissipation mechanisms due to hysteresis and opening–closing of cracks—contribute in the inelastic range.

From the inception of *RRF* values in ATC-3-06 [1], their nature has been empirical and judgment-based. With the expansion of design codes to include various lateral-load-resisting systems, a series of such values have been assigned to each system [2–4]. Attempts to calibrate *RRF* values were made along with the development of the first generation of nonlinear structural assessment guidelines [5–7]. These documents established benchmarks for multiple components of nonlinear analysis, for instance, inelastic capacities of structural elements, design requirements, soil–structure interaction, analysis techniques, damage definitions, and performance objectives.

Assessment of *RRF* values done in the past is primarily based on the nonlinear static analysis. Although this procedure gives an estimate of the inelastic building performance when subjected to high level of lateral loads, it fails to capture many actions such as

1. Effect arising out of the dynamic behavior of the building when subjected to time history records.
2. Ground motion variability in terms of the time history records, which are different even for a chosen magnitude–distance–mechanism tuple.
3. Effects of uncertainty in the analytical modeling, design requirements, and test data.

The objective of this manuscript is to assess *RRF* values for a sample midrise reinforced concrete building located in a moderate seismic region. Focus is also laid on the relative performance offered by the two variants of the buildings, namely fully ductile special RCMRF and limited-ductile ordinary RCMRF. Nonlinear dynamic approach with consideration to the deterioration due to cyclic excitation has been used as the analytical tool. In the moderate seismic regions, design code permits

construction of both kinds of buildings—with full ductility and with limited ductility. On the one hand, limited ductility induces increased sections and flexural reinforcements, and on the other, it evades the cumbersome ductility criteria from structural design and more significantly from the construction. Therefore, depending on the governing criteria and ease of construction, both kinds of buildings are found in these regions. The current manuscript investigates the premise of equal performance by these two design variants in moderate seismic regions.

## 2 Design Provisions and Assessment of *RRF*

Moment-resisting frame is considered to be fully ductile per Indian standards, when all the guidelines from IS 456, IS 1893, and IS 13920 [2, 8, 9] are followed. Design base shear for equivalent lateral force method is defined as follows:

$$V_b = (Z/2)(I/R)(S_a/g)W_e \quad (1)$$

where  $Z$  is the PGA corresponding to MCE (also called zone factor);  $I$  is importance factor of the building ( $=1.0$  for the common buildings);  $S_a/g$  is the spectral ordinate (a function of time period and damping ratio of the building); and  $W_e$  is seismic weight of the building.

### 2.1 *RRF Assessment Using Static Pushover Analysis*

Based on Ref. [10], Fig. 1 illustrates different seismic performance factors. Even though the symbols have been taken from Ref. [3], other codes follow a similar procedure as discussed below. This methodology has been developed with the pushover analysis at its core.  $V_E$  is the base shear corresponding to earthquake ground motion.  $V_{des}$  is the design base shear.  $V_{max}$  is the base shear capacity of the building. Deflection amplification factor,  $C_d$ , and overstrength factor,  $\Omega_0$ , are two other seismic performance factors used for the permissible deflection criteria and element-level forces in “weak” story, respectively. IS 1893 does not recognize these performance factors explicitly; however, it considers them indirectly. Table 1 gives the summary of seismic performance factors for RCMRF as recommended by IS 1893, ASCE 7, and EC 8. Different terms have been used across the design codes, and some factors are not directly defined. Nevertheless, the design processes including the load reduction, deformation check, and use of overstrength factors remain same in all three codes.

Based on the research in the 1990s, notably Ref. [11], Whittaker et al. [12] proposed the expression to split *RRF* as follows:

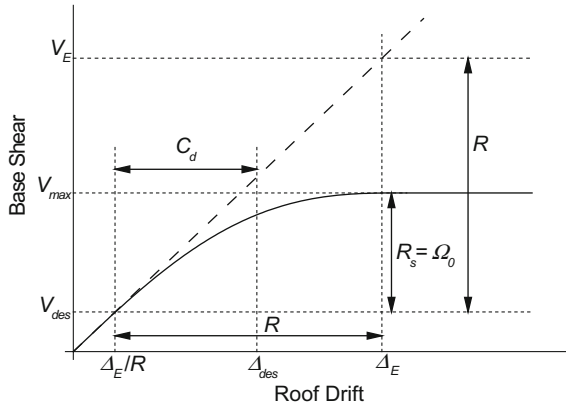


**Fig. 1** Quantification of seismic performance factors using pushover analysis based on Ref. [10]

**Table 1** Seismic performance factors for RCMRF per IS 1893, ASCE 7, and EC 8

System	Code	$R$	$\Omega_0$	$C_d$
<i>Fully ductile RCMRF</i>	IS1893	5.0	2.5 <sup>a</sup>	5.0 <sup>b</sup>
	ASCE7	8.0	3.0	5.5
	EC8 <sup>c</sup>	5.85 <sup>d,f</sup>	4.68 <sup>g</sup>	5.85
<i>Limited-ductile RCMRF</i>	IS1893	3.0	2.5	5.0
	ASCE7	3.0	3.0	2.5
	EC8 <sup>c</sup>	3.90 <sup>e,f</sup>	3.12 <sup>g</sup>	3.90

<sup>a</sup>Defined indirectly for soft-story shear amplification

<sup>b</sup>Determined from the reduced level of  $IDR_{max}$  of 0.4% (treating 2.0% as a benchmark from ASCE 7)

<sup>c</sup>EC8 uses the terminology of *behavior factor*, *magnification factor* and *displacement behavior factor* for  $R$ ,  $\Omega_0$ , and  $C_d$ , respectively

<sup>d</sup>For high-ductility class (DCH)

<sup>e</sup>For medium-ductility class (DCM)

<sup>f</sup>Factor  $\alpha_u/\alpha_1$  taken as 1.30 for multi-story multi-bay structure

<sup>g</sup>(= 0.80R). Not applicable for the infill-discontinuity weak story

$$R = R_s R_\mu R_R R_\xi \tag{2}$$

where  $R_s$  is the strength factor;  $R_\mu$  is the ductility factor;  $R_R$  is the redundancy factor, and  $R_\xi$  is the damping factor.  $R_s$  represents the reserve strength due to a combination of safety factors and design conservatism.  $R_\mu$  depicts inelastic deformation capacity of the structure.  $R_\mu-\mu-T$  relations are used to determine  $R_\mu$  from displacement ductility and time period of the structure [13]. These relations were fitted based on the recorded inelastic response of single-degree-of-freedom systems located on various soil conditions. Suitable modifications for extending these results to multi-degree of freedom are required as proposed in [13].  $R_R$  factor penalizes the absence of redundancy.  $R_\xi$  considers the effect of damping when it is different from 5%.

## 2.2 RRF Assessment Using Time History Analysis

FEMA P695 [14] sets recommendations for assessment of seismic performance factors based on nonlinear time history analysis (NLTHA). Despite a few noted drawbacks, this document serves as a guiding tool. In the recommended methodology, a static pushover analysis is accompanied by a series of incremental dynamic analyses (IDA) consisting of NLTHA for a suite of  $22 \times 2$  far-field normalized strong ground motions. Apart from the analytical consideration of record-to-record variability, uncertainties arising from the quality of test data, design requirements, and modeling have been treated empirically.

Ground motion suite has been maintained to be same for all sites and structures (unless the site is near-field, for which different set of 28 pairs of records are used). To consider the effects of the spectral shape of rare ground motions, spectral shape factor (SSF) has been used. SSF modifies the median collapse intensity parameter while keeping the uncertainties intact. Regression analysis has been performed to correlate SSF with the period-based ductility, time period of the structure, and the expected PGA level. Period-based ductility is a measure of the displacement ductility of the structures. It is derived from the pushover analysis. Adjusted median collapse capacity is given by:

$$S_{CTI} = S_{CT} \exp(\beta_1(\bar{\varepsilon}_0(T) - \bar{\varepsilon}(T)_{\text{records}})) \quad (3)$$

where  $S_{CT}$  is the calculated median collapse capacity;  $\varepsilon_0(T)$  is the expected spectral shape variation at the site, and  $\varepsilon(T)_{\text{records}}$  is the average spectral shape variation in the ground motion records.  $T$  is the fundamental time period of the building.

The current study considers the difference in MCE-DBE design base shear factors in IS 1893 and ASCE 7. Factor for conversion of MCE to DBE ground motion is 0.50 per IS 1893 and 2/3 per ASCE 7.

## 2.3 Performance Objectives for the Assessment

Selection of the performance objective is one of the most critical steps of seismic assessment. Procedures using either SPO or NLTHA involve such decision. For the regions of high seismicity, this choice is easily made in terms of the collapse prevention at MCE ground motion. However, in the regions of the moderate or low seismicity, a stricter performance objective is usually sought. Collapse prevention performance level of the structures is easily demarcated by the structural stability criterion. However, other performance levels require detailed computations and more importantly standardization of damage measure definitions. Simple engineering demand parameters like maximum inter-story drifts have been frequently used in the recent past but for the regions of moderate seismicity they may be misleading. Shirandhokar and Sinha [15] showed that well-calibrated damage

measure definition, capable of identifying cyclic energy dissipation, is required for better prediction of moderate levels of damage. The current study, however, utilizes collapse prevention at MCE as the performance objective. Collapse is defined by the sidesway condition when the structure becomes unstable due to  $P-\Delta$  effects.

### 3 Building Selection, Modeling, and Analysis

In the present manuscript, for the purpose of demonstration and due to lack of space, two variants of the sample building—special RCMRF and ordinary RCMRF—were considered. Design and detailing of both these building have been performed per Ref. [8, 2]. Ductile detailing for special MRF has been performed per [9]. Recommended  $RRF$  values as per IS 1893 for full ductility and limited ductility buildings are 5 and 3, respectively (Table 1).

#### 3.1 Building Details, Design, and Detailing

Based on the real building drawings, a sample midrise bare RCMRF (seven-storied) representative of a typical office building, located in Mumbai, has been chosen. Mumbai is classified in zone-III, a moderate seismic region with peak ground acceleration corresponding to MCE given as 0.16 g.

Typical floor plan and elevation of both buildings have been shown in Fig. 2. The ground floor of the building is 4.50 m high, whereas all the above floors are 3.90 m high. There are three bays, each of span 8.20 m, in the building along  $X$ -direction. Figure 2 also shows required reinforcement along with column sizes. All beams of the ductile building are 350 mm  $\times$  750 mm in size, whereas the size of beams in OMRF building is 400 mm  $\times$  750 mm. The geotechnical condition for the site has been considered to be rocky.

Following the standard practice in the region, design of the building using equivalent lateral force method through a 3-D frame was carried out. Horizontal torsion arising out of accidental eccentricity has been taken as 5%. This makes the frames on grid 9–9 and 2–2 most critical since they have full tributary area and are farthest from the center of mass of the building. Ductile detailing for the beams and columns has been performed per IS 13920 [9] for the fully ductile variant. It is worth noting that IS 13920 does not specify any criteria with regard to the relative moment carrying capacity of the columns and the beams (i.e., SCWB factor).

The thickness of the slab is 250 mm. Loads from the partition, services, and floor finish have been considered as 2 kPa. Since the utility of the slabs can be variable in nature ranging from office space to storeroom, especially due to the symmetry of the building, the live load has been considered as 4 kPa on all the slabs. Concrete grade used is M40 ( $f_{ck} = 40$  MPa) for the columns and beams. Definition of  $f_{ck}$  is based on the strength of cube. A factor of 0.80 has been used for

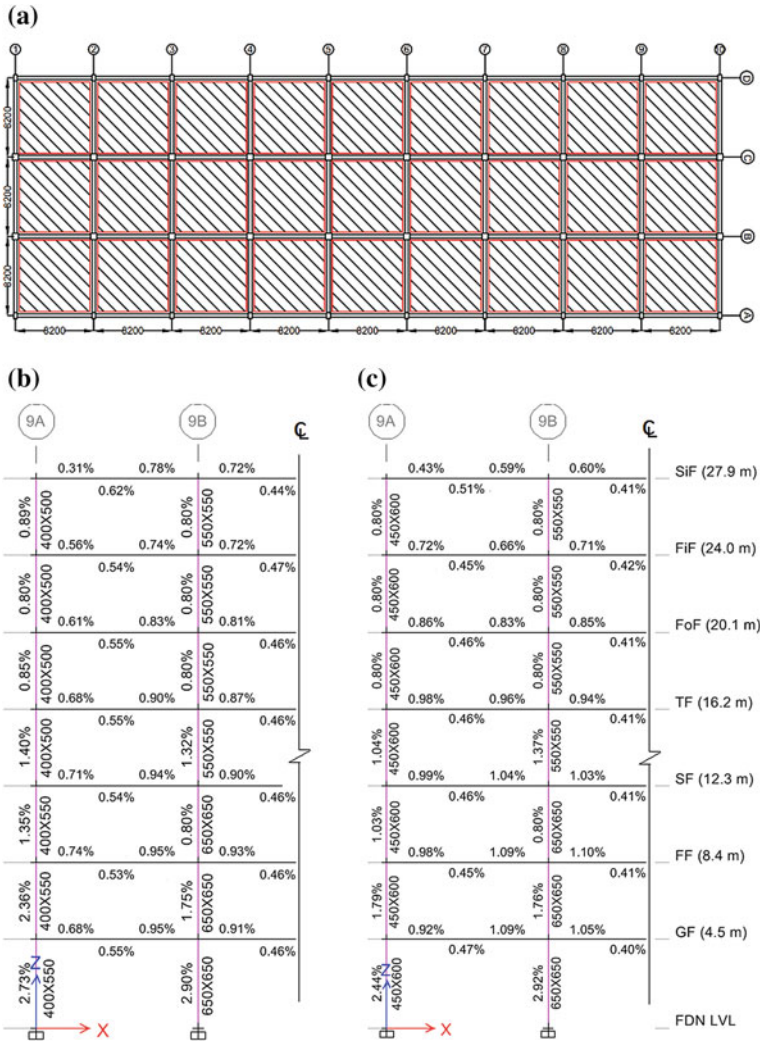


**Fig. 2** a Plan of the sample building; reinforcement and column sizes for b special RCMRF variant and c ordinary RCMRF variant on grid 9. All beams are of size 350 × 750 and 400 × 750, respectively

converting cube strength,  $f_{ck}$ , to cylinder strength,  $f'_c$ , for normal-weight concrete. Reinforcement grade used is Fe500 grade. Both variants have a codal time period of 0.91 s. Seismic base shear was found to be 2.9 and 1.8% of the seismic weight for SMRF and OMRF buildings.



### 3.2 Analytical Modeling and Components

The building is regular and can be idealized as two-dimensional frames along both the orthogonal directions. However, the building is very long in E–W direction and hence strength along this direction is not expected to govern the seismic performance. Therefore, a typical frame along N–S direction was modeled for the current study. As described above, the most critical frame along grid 9–9 was chosen for the performance assessment. It is recognized that 2-D model is incapable of capturing torsional eccentricity in the building. Nonetheless, due to the inherent symmetry of the building under study, this is not a concern.

The 2-D frame was modeled in *OpenSees* with concentrated plasticity, which has been shown to be efficient and accurate for collapse assessment [16]. The model proposed by Ibarra et al. [17] is one of the widely used deterioration models in the last decade for assessment of collapse. An important aspect of IMK model is that it includes the segment with negative stiffness after capping point. This part of the model captures strain-softening of the element. Strain-softening in an element occurs when a combination of concrete crushing in compression, buckling of rebar, and loss of steel–concrete bond takes place. This branch thereby enables the delayed collapse prediction of nonlinear systems subjected to dynamic loads. Based on the correlation and stability of observed parameters from experiments across the globe, [18] modified the parameters. Figure 3 shows the parameters of the backbone curve. Backbone curve is the envelope of hysteretic model for the case when the load is applied in quasi-statically. Details of deterioration parameters have been avoided due to the lack of the space.

Parameters of the backbone curve were derived using empirical relations [19, 20]. Expected properties of the concrete and steel were taken as  $(f_{ck} + 1.645\sigma)$  and  $1.2 f_y$ , respectively [8, 20].

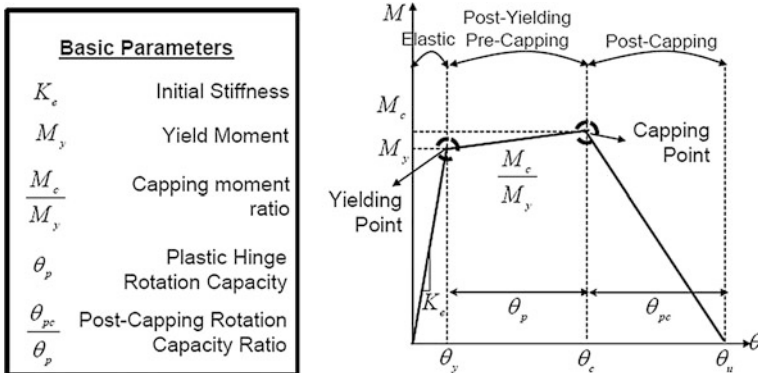


Fig. 3 Modified Ibarra–Medina–Krawinkler backbone curve [18]

### 3.3 Joint Modeling

Joints were modeled based on diagonal compression strut mechanism, which has been shown to comply with the observed data [21]. For ductile variant, shear panel spring was modeled as elastic spring with the stiffness recommended by [22]. Cracking was considered at 25% of the yield stress and at a shear strain of 0.0002 radians. Such simplified model is acceptable for ductile frames, where flexural failure precedes the shear failure due to capacity-based design. For non-ductile variant, shear failure of the joints may result in the eventual collapse of the building. A limited research has been done on the calibration of parameters of the non-ductile joints. The current manuscript used the research carried out by Moehle et al. [23] and Mitra et al. [21] to define non-ductile joints.

### 3.4 Nonlinear Static and Time History Analysis

Using the loading pattern per IS 1893, static pushover (SPO) analysis was performed on both variants of the building. SPO quickly gives an estimate of building performance against lateral loads. Figure 4 shows the results of SPO analysis for SMRF building. Pushover curve continues to be used as an important tool, for instance, period-based ductility,  $\mu_T$ , has been used to estimate the spectral shape factor [14]. Table 2 summarizes the results of SPO analyses for both variants.

IDA was performed using the FEMA P695 far-field ground motion suite. To ensure the unchanged relative values of orthogonal components of ground motion, geometric means was used for scaling. To consider the effects of the three-dimensional model, controlling components of each pair is used. Lognormal fragility function was fitted based on the least-squared error solution. Spectral

**Fig. 4** Pushover curve (IS 1893 loading pattern) for SMRF. OMRF variant not shown due to lack of space

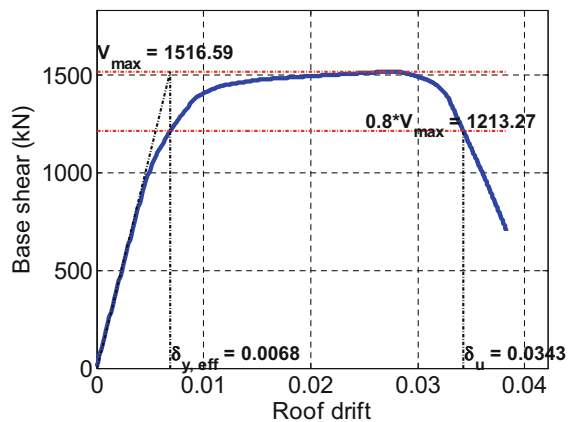
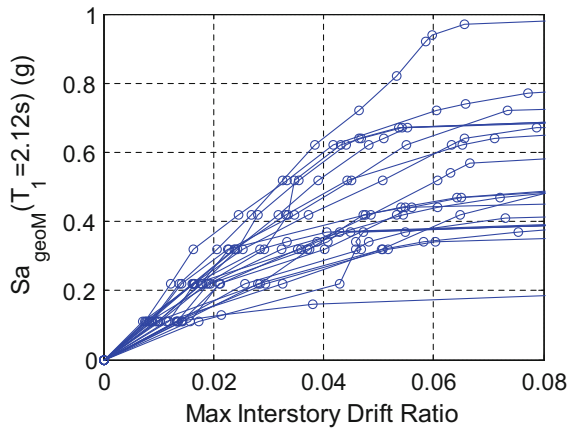


**Table 2** Results of static pushover analyses

System	$R_{des}$	$T_{code}$ (s)	$T_{eig}$ (s)	$\alpha_h$	$Vb_{des}$ (kN)	$\delta_y$	$Vb_{max}$ (kN)	$\delta_{ult}$	$V_y$ (kN)	$\Omega_s$	$R_{eff}$
SMRF	5	0.91	2.12	1.8%	314	0.0068	1517	0.0343	1368	4.83	4.4
OMRF	3	0.91	1.95	2.9%	536	0.0075	1848	0.0251	1657	3.45	3.1

**Fig. 5** Controlling IDA curves for FEMA P695 far-field ground motion suite for SMRF



acceleration at the fundamental time period was chosen as the intensity measure. IDA curves for the SMRF variants of the building are shown in Fig. 5.

### 3.5 Treatment of Uncertainties

Uncertainties are introduced at each step of the probabilistic seismic risk framework. Record-to-record variability is estimated by analyzing the structures for different time history records. However, modeling uncertainties incurred due to the use of median structural properties can be computationally costly to assess even with the efficient algorithms and powerful tools at hand. Limited research and guidelines of FEMA P695 have been used to select the suitable values of these uncertainty components. Total uncertainty in the collapse is assumed as the product of statistically independent components. Total system collapse uncertainty is given by:

$$\beta_{TOT} = \sqrt{(\beta_{RTR}^2 + \beta_{DR}^2 + \beta_{TD}^2 + \beta_{MDL}^2)} \tag{4}$$

where subscripts represent record-to-record variability, design requirement, test data, and modeling uncertainty, respectively. For the current analysis, values of the uncertainty were chosen as  $\beta_{DR} = 0.20$ ,  $\beta_{TD} = 0.10$ , and  $\beta_{MDL} = 0.35$ .

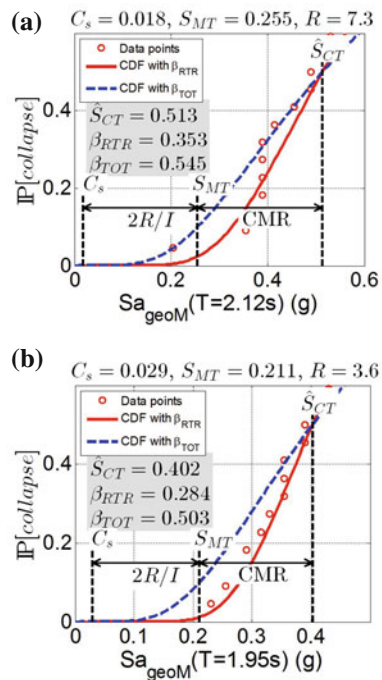
### 4 Results and Conclusions

Figure 6 shows the quantified *RRF* values of 7.3 and 3.6 for SMRF and OMRF variants, respectively. These results suggest that for the chosen building, both OMRF and SMRF systems outperform the expected code-specific level of inelastic capacity. Table 3 gives further details of the results from NLTHA and fragility functions for the two variants of the building.

The methodology assumes that buildings designed in accordance with the codes will have a low probability of collapse in case they are subjected to MCE ground motion. The value of this low probability is adopted from Ref. [14] as approximately 10%. For the current study, this limit is assumed to remain unaltered.

Buildings in the moderate seismic regions, designed for even smaller lateral force due to ductility criterion, tend to have extra reserve strength for the seismic force. Since many vertical members have governing load case as gravity, buildings develop additional resistance against lateral loads.

**Fig. 6** Assessment of *RRF* using nonlinear time history analysis for **a** SMRF and **b** OMRF variant



**Table 3** Results of nonlinear time history analyses for FEMA P 695 far-field ground motion suite

System	$C_s$	$T_I$ (s)	$\mu_T$	$S_{CT}$ (g)	$\beta_{RTR}$	$\beta_{TOT}$	Margin against MCE	$P$ [collapse] MCE]	$R$ w/o SSF	SSF	$R$ with SSF
SMRF	0.018	2.12	5.01	0.513	0.353	0.545	2.92	0.025	7.3	1.285	9.3
OMRF	0.029	1.95	3.36	0.402	0.284	0.503	2.29	0.050	3.6	1.224	4.4

The work presented here does not discuss the effects of ground motion suite. An ongoing study by the authors suggests that this can lead to significant changes in the assessment of *RRF* values. Besides, this study examines only one building. Conventionally, *RRF* values are assigned to lateral-load-resisting systems. An extensive study with archetype structures is required to assess *RRF* values in a generic sense. These archetype buildings must represent the stock of buildings in the given typology adequately. Finally, performance objective has been taken as collapse prevention at MCE for the present study. Other more desirable performance objectives, especially with reference to the moderate seismic regions, shall be considered for a better evaluation of the *RRF* values.

## References

1. Applied Technology Council (1978) Tentative provisions for the development of seismic regulations for buildings. Report no. ATC-3-06. Redwood City, California
2. IS 1893 (2002) Criteria for earthquake resistant design of structures, part 1. Bureau of Indian Standards, New Delhi, India
3. ASCE SEI/ASCE 7-10 (2010) Minimum design loads for buildings and other structures. American Society of Civil Engineers, Reston, Virginia
4. Eurocode 8 (2004) Design provisions for earthquake resistance of structures. Comité Européen de Normalisation, Brussels (Belgium)
5. Applied Technology Council (1996) Seismic evaluation and retrofit of concrete building, vol. 1. Report no. ATC-40. Redwood City, California
6. FEMA (1994) NEHRP provisions for the seismic rehabilitation of buildings (FEMA-273), Federal Emergency Management Agency, Washington, D.C.
7. FEMA (2000) Prestandard and commentary for the seismic rehabilitation of buildings (FEMA-356). Federal Emergency Management Agency, Washington, D.C.
8. IS 456 (2000) Plain and reinforced concrete—code of practice. Bureau of Indian Standards, New Delhi, India
9. IS 13920 (1993) Ductile detailing of reinforced concrete structures subjected to seismic forces. Bureau of Indian Standards, New Delhi, India
10. FEMA (2004) NEHRP Recommended provisions for seismic regulations for new buildings and other Structures, (FEMA-450-2). Federal Emergency Management Agency, Washington, D.C.
11. Applied Technology Council (ATC) (1995) Structural response modification factors. Report no. ATC-19, Redwood City, California
12. Whittaker A, Hart G, Rojahn C (1999) Seismic response modification factors. J Struct Eng 125(4):438–444

13. Krawinkler H, Nassar AA (1992) Seismic design based on ductility and cumulative damage demands and capacities. In: Fajfar P, Krawinkler H (eds) *Nonlinear seismic analysis and design of reinforced concrete buildings*. Elsevier Applied Science, New York
14. FEMA (2009) *Quantification of building seismic performance factors (FEMA-P695)*. Federal Emergency Management Agency, Washington, D.C.
15. Shiradhonkar S, Sinha R (2016) *Seismic damage categorization and damage index for RC buildings*. IIT Bombay, Mumbai
16. Haselton CB (2006) *Assessing seismic collapse safety of modern reinforced concrete moment frame buildings*, Stanford University
17. Ibarra LF, Medina RA, Krawinkler H (2005) Hysteretic models that incorporate strength and stiffness deterioration. *Earthquake Eng Struct Dynam* 34(12):1489–1511
18. Zareian F, Krawinkler H (2006) *Simplified performance-based earthquake engineering*, Stanford University
19. Panagiotakos TB, Fardis MN (2001) Deformations of reinforced concrete members at yielding and ultimate. *Struct J* 98(2):135–148
20. Applied Technology Council, PEER (2010) *Modeling and acceptance criteria for seismic design and analysis of tall buildings, vol. 1*. Report no. PEER/ATC-72-1. Redwood City, California
21. Mitra N, Lowes LN (2007) Evaluation, calibration, and verification of a reinforced concrete beam–column joint model. *J Struct Eng* 133(1):105–120
22. Meinheit DF, Jirsa JO (1981) Shear strength of R/Cs beam-column connections. *J Struct Div* 107(11):2227–2244
23. Moehle J, Lehman D, Lowes L (2006) *Beam-column connections. New information on the seismic performance of existing buildings*, EERI Technical Seminar

# Numerical Investigation on the Flexural Performance of Laced Steel–Concrete Composite (LSCC) One-Way Slab System



G. Gobinath, Mohit Verma and N. Anandavalli

**Abstract** In this paper, numerical investigations are carried out to assess the flexural performance of laced steel–concrete composite (LSCC) one-way slab system subjected to monotonic loading. The individual LSCC units are modelled as L-shaped beams. Flanges of two LSCC units are then connected using high strength steel bolts. Finite element analysis of the LSCC slab system is carried out in ABAQUS. Concrete damaged plasticity (CDP) model is used for concrete in both tension and compression including damage characteristics. Nonlinear behaviour of steel is modelled using plasticity model available in the software. The LSCC slab system is then subjected to two-point loading under displacement control mode. The LSCC slab system is found to take the load up to 333 kN for 200-mm deflection. The composite action of the two LSCC units is evident from the deformed shape. Therefore, the proposed integration scheme for LSCC one-way slab system using bolts is found to be effective. An analytical procedure is also described to estimate the strength of the LSCC one-way slab system based on the different failure criteria. The strength obtained from the analytical model is found to be in close agreement with those obtained from ABAQUS.

**Keywords** Laced reinforced concrete · Monotonic loading · Bolted connections One-way slab · Finite element analysis

---

G. Gobinath · N. Anandavalli  
Theoretical & Computational Mechanics Laboratory,  
CSIR-Structural Engineering Research Centre, Chennai 600113, India  
e-mail: gobig25@gmail.com

N. Anandavalli  
e-mail: anandi@serc.res.in

M. Verma (✉)  
Advanced Seismic Testing and Research Laboratory,  
CSIR-Structural Engineering Research Centre, Chennai 600113, India  
e-mail: mohitverma@serc.res.in

## 1 Introduction

Shear reinforcement is usually provided in the conventional reinforced concrete (RC) to improve its shear capacity and ductility. Many researchers have proposed different types of shear reinforcement strategies to improve the ductility of conventional RC like wire rope [1], continuous spiral reinforcement [2] and inclined crossbars [3]. In the recent years, many steel–concrete composites have been developed which exhibits improved shear capacity and ductility compared to conventional RC. Steel–concrete composite consists of a concrete core sandwiched between the steel cover plates. The two plates are connected to each other with the help of shear connectors. Three different types of shear connectors commonly used are headed shear connectors [4], through–through connector [5] and J-hook connectors [6]. Laced steel–concrete composite (LSCC) system is composite system developed by Anandavalli et al. [7]. LSCC consists of perforated steel cover plates, which are connected using reinforcing members, cross-rods and infilled with concrete as shown in Fig. 1. The reinforcing members are in the form of lacings which transfer the force between steel and concrete. This system is devoid of welding due to particular arrangement of lacings being inserted through the silts at appropriate places and made to stay in place by using cross-rods. The experimental investigations on LSCC beams exhibited large deformation and improved post-peak behaviour. Later on, a finite element (FE) model for LSCC beam was developed [8] to predict its deformation capacity and mode of failure. The developed FE model was found to be effective in terms of predicting load–deflection response, post-peak behaviour and failure mode of LSCC beam. A parametric study was also carried out to identify the effect of different parameters on the response of LSCC beam under monotonic loading.

The construction of LSCC slab system is subjected to some practical difficulties. In order to overcome those difficulties, an integration strategy of two LSCC units using bolted connections is proposed in this paper. Effectiveness of the proposed scheme is brought out through numerical investigation using finite elements. The individual units of LSCC are modelled as L-shaped beams. The flanges of the LSCC units are then connected with the bolts to form one-way slab system. Such integration scheme ensures the composite action of the LSCC units. A FE model is created for the proposed LSCC one-way slab system. The displacement profile obtained clearly

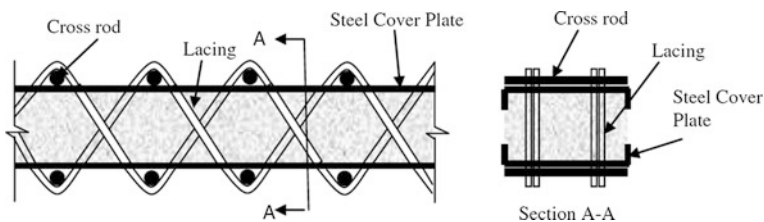


**Fig. 1** Laced steel–concrete composite [7]



shows composite action and verifies the effectiveness of the connection scheme. An analytical model is also described to predict the response of the LSCC slab system in the linear range. The response obtained from the FE and analytical model is found to corroborate well with each other.

## 2 Finite Element Analysis

The section describes the procedure for the modelling and analysis of LSCC one-way slab system. The finite element model is created in ABAQUS.

### 2.1 Geometry and Boundary Condition

The geometrical details of the different components of LSCC are given in Table 1. The schematics of the LSCC one-way slab system are shown in Fig. 1. The slab system is simply supported on both the ends. The slab is subjected to two-point loading (Fig. 2).

### 2.2 Material Modelling

Concrete damaged plasticity (CDP) model is used in the present study to model complete inelastic behaviour of concrete in both tension and compression including

**Table 1** Geometrical details of LSCC beam

Details	Description	Value
LSCC panel	Length, mm	2400
	Span (b/w supports), mm	2000
	Shear span, mm	666
Concrete core	Width (top/bottom), mm	300/375
	Depth, mm	150
Steel cover plate	Width (top/bottom), mm	300/375
	Thickness, mm	3
Lacing	Diameter, mm	8
	Transverse spacing, mm	192
	Angle of lacing, degree	45
Bolts	Diameter, mm	16
	Spacing, mm	150
Cross-rod	Diameter, mm	8
	Total number of cross-rod (on top and bottom)	48

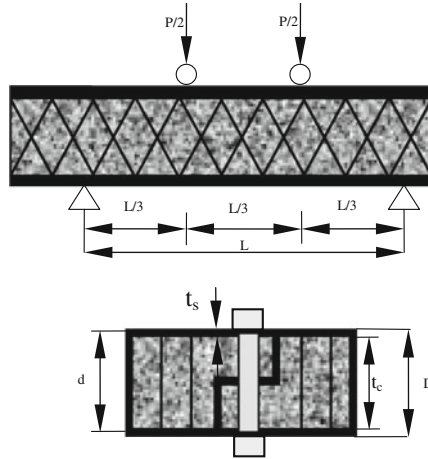


**Fig. 2** Schematics of LSCC one-way slab system

**Table 2** Material properties

Details	Description	Value
Concrete core	Elastic modulus, (MPa)	19,700
	Poisson's ratio	0.19
	Compressive strength, (MPa)	30
Steel cover plate	Elastic modulus, (MPa)	113,419
	Poisson's ratio	0.15
	Average yield stress, (MPa)	113
	Ultimate stress, (MPa)	190
Lacing and cross-rod (high strength bars)	Average yield stress, (MPa)	400
	Ultimate stress, (MPa)	540
Bolts	Average yield stress, (MPa)	400
	Ultimate stress, (MPa)	540

damage characteristics. Nonlinear behaviour of steel is modelled using plasticity model available in the software. Material behaviour of steel cover plate is employed based on the nominal stress–strain behaviour of steel. Bi-linear stress–strain behaviour is adopted to model the lacings, cross-rods and bolts. The material properties used in the analysis are given in Table 2.

### 2.3 Interactions and Constraints

Mechanical interaction between the steel cover plate and concrete surfaces is modelled by surface to surface contact interactions using a friction formulation in a

**Table 3** Interactions and constraints used in FE model

Description	Constraint/interaction
B/w cross-rod and cover plate	Tie constraint
B/w lacing to cross-rod	Merge common nodes
B/w lacings and cover plate	Tie constraint
Concrete and cover plate	Surface to surface Interaction property: contact Tangential and normal Frictional coefficient: 0.4
Lacings and concrete	Embedded constraint
Cover plate and cover plate	Normal (hard contact)
B/w bolt and plate	Tie constraint
B/w bolt and concrete	Tie constraints

tangential direction and hard contact in normal direction. Hard contact is provided in the normal direction to avoid penetration of steel surface into concrete surfaces. Common nodes of the cross-rods and cover plates tied together using tie constraint. The lacing and cross-rods are merged together. Normal contact is provided between the steel cover plates of the two adjacent units of LSCC. The bolt heads are tied to the cover plate, and shank is embedded in the concrete. Lacings are embedded in concrete. The details of the interaction properties and constraints used in the FE model are summarized in Table 3.

### 2.4 Meshing

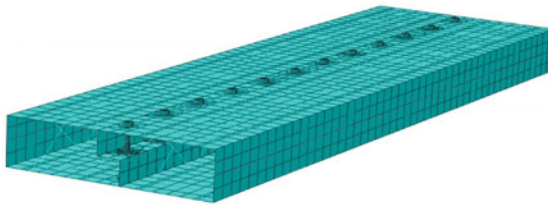
All the components are meshed using part by part basis instead of using global or sweep features. Thus, a regular structured mesh is generated. Solid element is used to make a core of concrete, and shell element is used to make a thin sheet of cold-formed steel as cover plate (skin), lacing and cross-rod are taken as a beam element. The details of the elements used in the FE model are given in Table 4. The mesh for the different components of LSCC is shown in Fig. 3.

## 3 Results

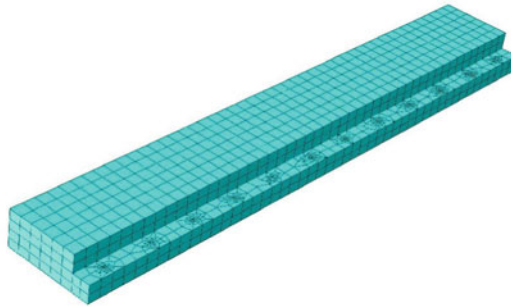
Nonlinear static analysis is carried out to obtain its static response under monotonic loading. Newton–Raphson solution technique is adopted. The deformed shape of the LSCC slab is shown in Fig. 4. The equivalent plastic strain contours in Fig. 5 highlight the parts of the model which have reached the plastic stage. The load versus deflection (at the mid-point of the LSCC slab) behaviour obtained is shown in Fig. 6. The integrated LSCC beam is found to take the load up to 333 kN for 200 mm deflection. The composite action of the two LSCC units is evident from the

**Table 4** Elements details

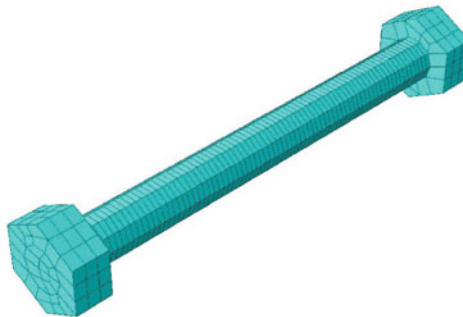
Description	Element type
Lacing and cross-rod	B31: A 2-node linear beam in space
Bolts and nuts	C3D8R: An 8-node linear brick, reduced integration, hourglass control
Bottom plates	S4R: A 4-node doubly curved thin or thick shell, reduced integration, hourglass control, finite membrane strains
Top plates	S4R: A 4-node doubly curved thin or thick shell, reduced integration, hourglass control, finite membrane strains
Concrete (L-shape)	C3D8R: An 8-node linear brick, reduced integration, hourglass control



(a) Cover plate, lacing and cross-rods



(b) Concrete core



(c) Bolt

**Fig. 3** Mesh for different parts of LSCC

**Fig. 4** Deflection profile of LSSC slab

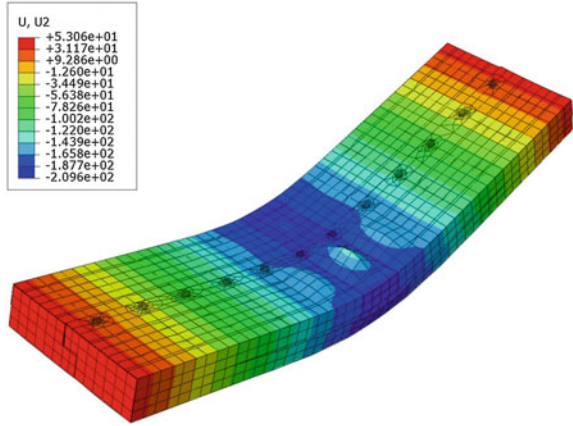


**Fig. 5** Equivalent plastic strain

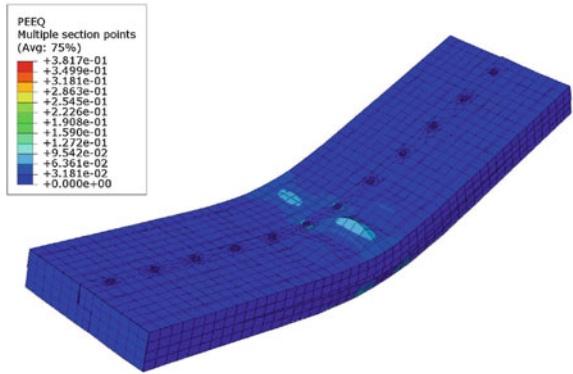


**Fig. 6** Load–deflection curve for LSSC slab

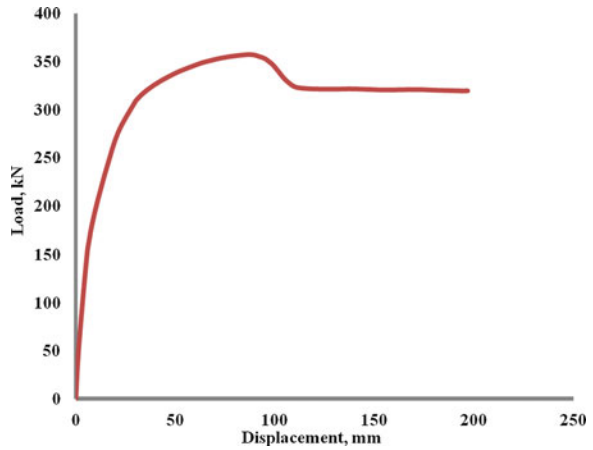


**Table 5** Response obtained from FE analysis

Details	Values
Peak strength, kN	354.11
Displacement at peak strength, mm	86.38
Ultimate load, kN	319
Ultimate displacement, mm	196.6
Support rotation angle, $\phi$	10.18°

deformed shape. Therefore, the proposed integration scheme is found to be effective and can be used to assemble individual units of LSCC. The key response parameters obtained from FE analysis are summarized in Table 5.

## 4 Analytical Model

The flexural capacity of the LSCC one-way slab system is predicted using the mechanics of materials. It is assumed that the steel cover plates and concrete core behaves linearly up to the failure based on classical beam theory. The modes of failure for the LSCC considered are compression failure of the top steel cover plate, shear failure of the concrete core and compression failure of the concrete core. The method described here is adopted from [9]. The peak load at which these three different types of failure occur is evaluated. The lowest of these failure loads will govern the design of the LSCC one-way slab system.

### 4.1 Compression Failure of the Top Cover Plate

The top and bottom cover plates are subjected to compression and tension during flexure. The tensile capacity of steel plate is more than the compression. Therefore, it is expected the failure of the top plate under compression will occur first. The peak load at which the compression failure of the top cover plate occurs is given by:

$$F_s = \frac{12EI\sigma_s}{LE_s D} \quad (1)$$

where  $EI$  is flexural stiffness,  $\sigma_s$  is maximum compressive strength of the skin,  $D$  is the total height,  $L$  is the clear span and  $E_s$  is modulus of elasticity of the steel cover plate. The flexural stiffness,  $EI$  is calculated using Eq. (2).

$$EI = \frac{Bt_s^3}{6} E_s + \frac{Bt_s d^2}{2} E_s + \frac{Bt_c^3}{12} E_c \quad (2)$$

where  $t_s$  and  $t_c$  are the thickness of the cover plate and concrete core,  $E_c$  is modulus of elasticity of the concrete core and  $d$  is the distance between the centre of the top and bottom cover plates.

### 4.2 Shear Failure of the Concrete Core

The maximum shear stress occurs at neutral axis and is zero at the top and bottom cover plates. The peak load at which the shear failure of the concrete core occurs is given by:

$$F_c = \frac{2\tau_c EI}{\left(E_s \frac{t_s d}{2} + E_c \frac{t_c^2}{8}\right)} \tag{3}$$

where  $\tau_c$  is shear strength of the concrete core. The shear stress in the concrete core is evaluated as per [10] and is given by:

$$\tau_c = \sigma_t \sqrt{1 + \left(\frac{\sigma_c}{\sigma_t}\right)^2} \tag{4}$$

$$\sigma_c = \left(\frac{2A_s f_y}{bd}\right) \sin \alpha \cdot \tan \alpha \tag{5}$$

$$\sigma_t = 0.3 \sqrt{f_{ck}} \tag{6}$$

where  $\sigma_c$  is the compressive and  $\sigma_t$  is the tensile strength of the concrete core. The peak load was also calculated using the shear modulus of the cover plates and concrete core. The peak load using the shear modulus is given by:

$$F_{cs} = \frac{2\tau_c GI}{\left(G_s \frac{t_s d}{2} + G_c \frac{t_c^2}{8}\right)} \tag{7}$$

$$GI = \frac{Bt_s^3}{6} G_s + \frac{Bt_s d^2}{2} G_s + \frac{Bt_c^3}{12} G_c \tag{8}$$

where  $G_s$  is shear modulus of the steel cover plate and  $G_c$  is shear modulus of the concrete core.

### 4.3 Compression Failure of the Concrete Core

The concrete core fails once the normal stress in compression exceeds the maximum compressive strength of the concrete. The peak load for this failure mode is given by:

**Table 6** Peak load for different failure modes

Failure mode	Peak load, kN
Compression failure of cover plate	388
Shear failure of the concrete core ( $F_s/F_{cs}$ )	382.15/ 383.15
Compression failure of the concrete core ( $F_{cc}$ )	367

$$F_{ca} = \frac{12EI\sigma_{cc}}{LE_c t_c} \quad (9)$$

where  $\sigma_{cc}$  is the maximum compressive strength of the concrete core.

#### 4.4 Peak Loads for Different Failure Modes

The value of the peak loads at which different modes of failure occur in LSCC is obtained from the analytical model. The results obtained are summarized in Table 6.

## 5 Conclusions

The flexural performance of the LSCC one-way slab system with the bolted connections is analysed using FE method and elastic beam theory. The FE model verifies the effectiveness of the connection scheme used for the integration of the individual LSCC units. An analytical model based on the linear elastic beam theory is also described to arrive at the preliminary loading capacity of LSCC one-way slab system. The results obtained from FE analysis and analytical model are found to corroborate with each other by about 6%.

## References

1. Yang KH, Kim GH, Yang HS (2011) Shear behavior of continuous reinforced concrete T-beams using wire rope as internal shear reinforcement. *Constr Build Mater* 25(2):911–918
2. Sheikh SA, Toklucu MT (1993) Reinforced concrete columns confined by circular spirals and hoops. *ACI Struct J* 90:542
3. Chalioris CE, Favvata MJ, Karayannis CG (2008) Reinforced concrete beam–column joints with crossed inclined bars under cyclic deformations. *Earthquake Eng Struct Dynam* 37(6): 881–897
4. Wright HD, Oduyemi TOS, Evans HR (1991) The experimental behaviour of double skin composite elements. *J Constr Steel Res* 19(2):97–110



5. Xie M, Foundoukos N, Chapman JC (2007) Static tests on steel–concrete–steel sandwich beams. *J Constr Steel Res* 63(6):735–750
6. Liew JR, Sohel KMA (2009) Lightweight steel–concrete–steel sandwich system with J-hook connectors. *Eng Struct* 31(5):1166–1178
7. Anandavalli N, Lakshmanan N, Knight GS, Iyer NR, Rajasankar J (2012) Performance of laced steel–concrete composite (LSCC) beams under monotonic loading. *Eng Struct* 41:177–185
8. Thirumalaiselvi A, Anandavalli N, Rajasankar J, Iyer NR (2016) Numerical evaluation of deformation capacity of laced steel-concrete composite beams under monotonic loading. *Steel Compos Struct* 20(1):167–184
9. Mostafa A, Shankar K, Morozov EV (2014) Experimental, theoretical and numerical investigation of the flexural behaviour of the composite sandwich panels with PVC foam core. *Appl Compos Mater* 21(4):661–675
10. Anandavalli N, Lakshmanan N, Rajasankar J, Samuel Knight GM (2016) Shear capacity of doubly skinned composite beams with lacings. *J Struct Eng* 142(12):04016122

# Wind Tunnel Investigations on a Tall Building With Elliptic Cross Section



A. Abraham, S. Selvi Rajan, P. Harikrishna and G. Ramesh Babu

**Abstract** According to a statistics revealed by Council of Tall Building and Urban Habitat [1] that for every 11.5 millions of global population, there is one tall building with 200 m+ in height available globally. Tall building constructions are paving ways for rapid urbanization worldwide including India, especially during the last one decade and will be continued over next few decades. Wind loads are one of the most important loads that govern the design of tall buildings. Published data on pressure and force coefficients for 3-D building with elliptic cross section under boundary layer flows are very scanty. This paper presents the results on mean force coefficients obtained through wind tunnel pressure measurements carried out on a 3-D tall building with elliptic cross section for various angles of wind incidence under suburban terrain. It is found that the mean pressure distributions and force coefficients depend significantly upon the angle of wind incidence.

**Keywords** Boundary layer wind tunnel · Pressure measurement  
3-D elliptic tall building · Angles of wind incidence · Force coefficients

---

A. Abraham (✉) · S. Selvi Rajan · P. Harikrishna · G. Ramesh Babu  
Wind Engineering Laboratory, CSIR-Structural Engineering Research Centre,  
Chennai 600113, India  
e-mail: abraham@serc.res.in

S. Selvi Rajan  
e-mail: sselvi@serc.res.in

P. Harikrishna  
e-mail: hari@serc.res.in

G. Ramesh Babu  
e-mail: gramesh@serc.res.in

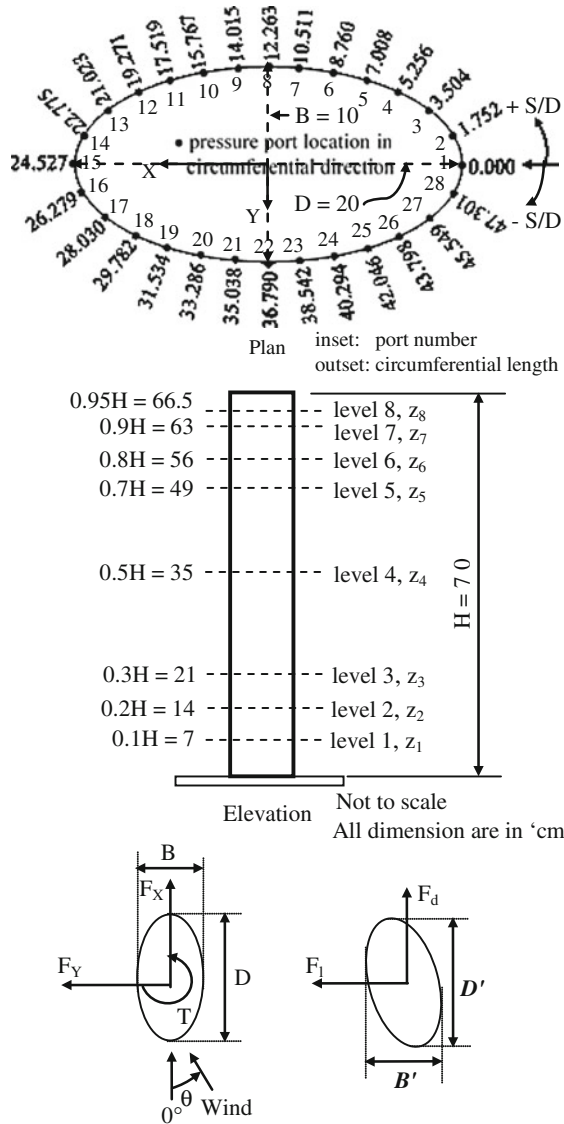
## 1 Introduction

Demand for tall buildings is rapidly increasing worldwide including in India due to their significant economic benefits in dense urban land use. Wind loads are one of the most important loads that influence the design of tall buildings. Using wind tunnel, different techniques are being adopted for quantification of wind loads and its associated dynamic responses on tall buildings. One such technique is measuring the wind-induced pressures on the surface of the tall building models using pressure sensors, and the importance of this technique is felt by the many researchers worldwide even today. But the information on force coefficients using the pressure measurement technique on 3-D tall building with elliptic cross section under boundary layer flows is very scanty. Galloping instability characteristics on 2-D bluff bodies with elliptic cross section using pressure measurement/six component base balance techniques for angles of wind incidence from  $0^\circ$  to  $90^\circ$  were studied through wind tunnel testing [2]. The effect of plan ratio, angle of wind incidence on mean and unsteady pressure coefficients, Strouhal number and wake geometry on 2-D bluff bodies with elliptic cross section using pressure measurement technique were studied through wind tunnel testing [3]. Identification of boundary layer detachments, re-circulations, vortex shedding phenomenon and other flow structures on elliptic cross section having different plan ratios using flow visualisation technique was studied through vertical hydrodynamic tunnel testing [4]. Dynamic wind-induced response analyses were carried out [5] on tall building models including elliptic plan through aerodynamic pressure/force measurements to investigate the relationships among structural properties, aerodynamic modifications, and aerodynamic force characteristics. Wind tunnel experiment on elliptic building model was carried out for various angles of wind incidence to find optimal and critical wind direction through pressure measurement on the external surface [6]. Codes of practice [7, 8] specify the force coefficients for building with elliptic cross section corresponding to a specific plan ratio and for two important angles of wind incidence.

Earlier wind tunnel pressure measurements study on a 3-D tall building model with elliptic cross section having the plan dimensions of  $10\text{ cm} \times 20\text{ cm}$  and height of  $70\text{ cm}$  was carried out for different angles of wind incidence. The fabrication of the model, its instrumentation (Fig. 1), simulation of wind characteristics correspond to open terrain, data collection/analysis, and the results on aerodynamic pressure/force coefficients based on statistical analysis of measured data were reported elsewhere [9]. In addition, a comparison on aerodynamic mean pressure/force coefficients was made between the values obtained from wind tunnel model study and the values reported in the literature.

Further, wind tunnel pressure measurements study on the same tall building model was carried out under suburban terrain condition in order to investigate the effect of terrain conditions on aerodynamic pressure/force coefficients. Accordingly, profiles of mean velocity and turbulence intensity (Fig. 2) to a length scale of 1:300 are simulated in the boundary layer wind tunnel by using a trip board followed by

**Fig. 1** Details of pressure ports around circumferential direction at level 1 and along the height of the model showing body axes with wind direction



set of wooden boards with roughness elements, as vortex generators. Typical views of the model tested in wind tunnel for wind normal to minor and major axes ( $\theta = 0^\circ$  and  $90^\circ$ ) under simulated suburban terrain are shown in Fig. 3.

This paper presents comparison on variation of mean pressure/force coefficients at a typical level for different angles of wind incidence between open and suburban terrain conditions. Further, comparison on aerodynamic mean pressure/force coefficients is made between the values obtained from the present study and the

**Fig. 2** Simulated mean velocity and turbulence intensity profiles under suburban terrain

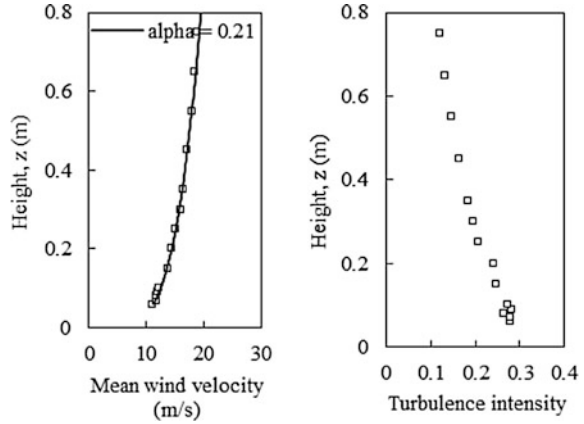


**Fig. 3** Elliptic tall building model kept inside the wind tunnel for  $\theta = 0^\circ$  and  $90^\circ$  under suburban terrain



values reported in the literature. For comparison purpose, the results on mean pressure/force coefficients obtained based on wind tunnel pressure measurements under open terrain are considered in this paper.

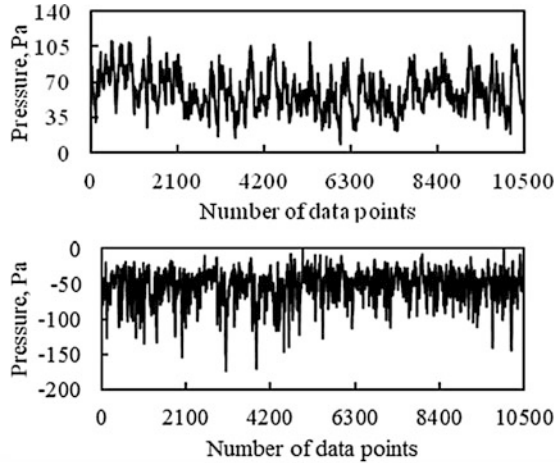
## 2 Results and Discussions

Typical traces of instantaneous pressures at level 4 for port numbers 92 (windward) and 86 (side) for  $\theta = 90^\circ$  are shown in Fig. 4. It is observed that the instantaneous pressures for port numbers 92 and 86 are found to be positive pressures and negative pressures.

### 2.1 Comparison on Mean Pressure Coefficients

Comparison between the distributions of mean pressure/force coefficients obtained under open and suburban terrains for  $\theta = 0^\circ, 10^\circ, 15^\circ, 20^\circ, 30^\circ, 40^\circ, 45^\circ, 50^\circ, 60^\circ, 70^\circ, 75^\circ, 80^\circ,$  and  $90^\circ$  at eight different levels are compiled elsewhere [10]. Figure 5 shows the variation of mean pressure coefficients with respect to

**Fig. 4** Typical instantaneous pressure traces



normalized distance  $S/D$  (port location on the surface to major axis) obtained at level 4 for  $\theta = 0^\circ$  to  $90^\circ$  at  $15^\circ$  interval. Based on the comparison, the following observations are made.

- In general, the variation of mean pressure coefficients is found to be different for different angles of wind incidence. The variation of mean pressure coefficients under open and suburban terrain conditions for all the angles of wind incidence is similar but varying in magnitudes.
- As the angle of wind incidence progresses from  $\theta = 0^\circ$  to  $30^\circ$ , the difference between the variation of mean pressure coefficients (both positive and negative) obtained at most of the levels under open and suburban terrain conditions found similar except at bottom and top levels.
- Beyond  $\theta = 30^\circ$  and as the levels progress from bottom to top, the scatter in the variation of mean suction coefficients under suburban terrain found to be higher than those for open terrain in the circumferential length between 21.023 and 47.301 cm.
- The magnitudes of mean suction coefficients at all the levels under suburban terrain found to be relatively higher than those under open terrain up to  $\theta = 30^\circ$ . As the angle of incidence progresses further, the magnitudes of mean suction coefficients under open terrain up to level 3 found to be relatively higher than those under suburban terrain in the circumferential length between 21.023 and 47.301 cm.
- At level 4, the variation of mean pressure coefficients under open terrain equal to the variation under suburban terrain over the entire circumferential length of the model.
- As the level progresses from level 4 to top level, the magnitudes of mean pressure coefficients obtained under suburban terrain are found to be relatively higher than those for open terrain in the circumferential length between 21.023 and 47.301 cm.

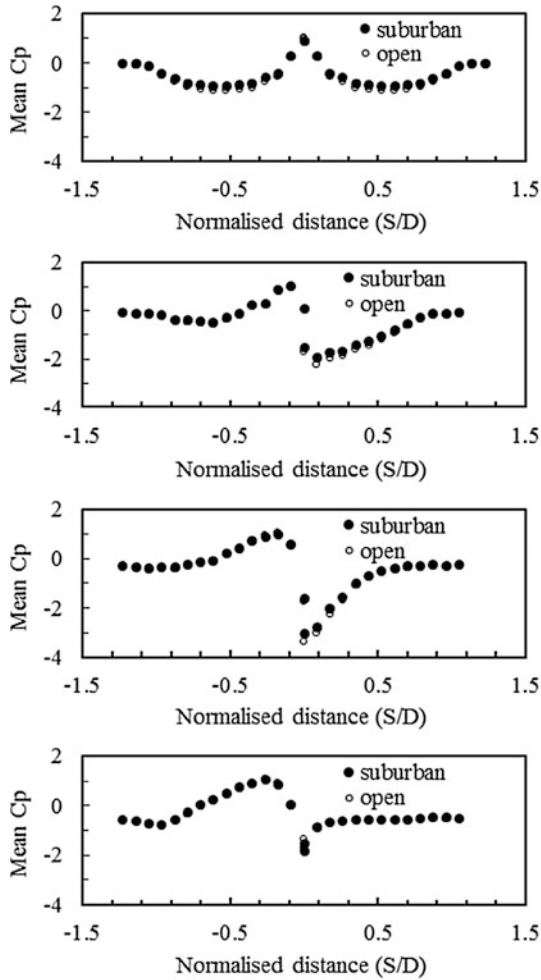


**Fig. 5** Comparison on variation of mean pressure coefficients for  $\theta = 0^\circ, 15^\circ, 30^\circ, 45^\circ, 60^\circ, 75^\circ,$  and  $90^\circ$

With reference to a fixed set of body axes ( $X$  and  $Y$ ), orientations for forces  $F_x$ ,  $F_y$ , and Torsion ( $T$ ), along with drag and lift directions corresponding to angle of wind incidence “ $\theta$ ” are defined in Fig. 1. The forces  $F_x$  and  $F_y$  per unit height along the body-fixed axes  $X$  and  $Y$ , respectively, are computed with respect to respective heights by integrating the circumferentially measured pressures accounting the reference widths (minor and major axis). By resolving  $F_x$  and  $F_y$  in the direction of wind and perpendicular to the direction of wind, the drag force  $F_D$  and the lift force  $F_L$  are evaluated accounting the projected widths. Typical variation of mean force coefficients in body axes  $X$  and  $Y$  (based on the minor axis) at level 4 under

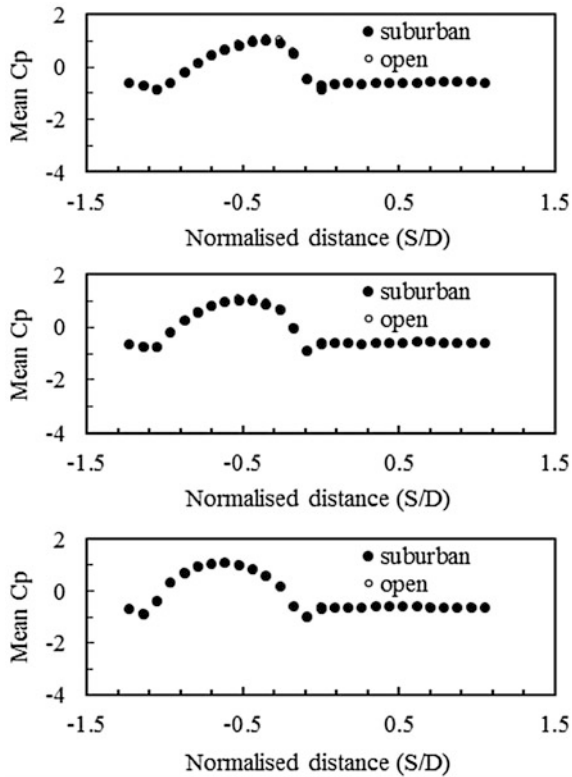


Fig. 5 (continued)

suburban terrain is shown in Fig. 6. Obviously, for most of the angles of wind incidence, the magnitude of force in *Y* direction found to be higher than those obtained in *X* direction.

### 2.2 Comparison on Mean Force/Torsion Coefficients

Comparison on mean drag, lift, and torsion coefficients obtained under open and suburban terrain conditions for all the angles of wind incidence at all levels by accounting the projected widths of *D'*, *B'*, and *D'B'* are made. Typical distributions of mean drag, lift, and torsion coefficients at level 4 are shown in Fig. 7.

The following observations are made:

- The variation of mean drag/lift force and torsion coefficients obtained at levels 4 and 8 found to well compare under both the terrain conditions.



**Fig. 6** Variation of mean force coefficients

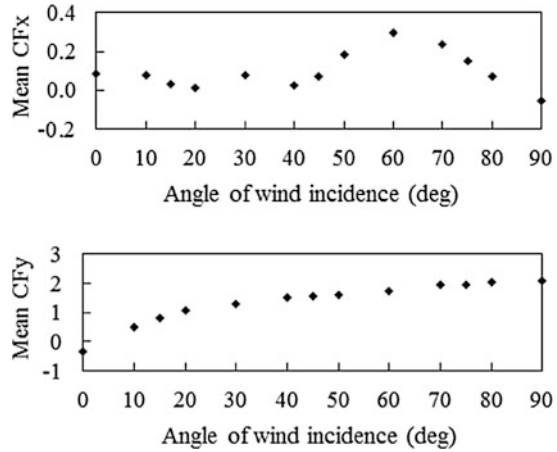
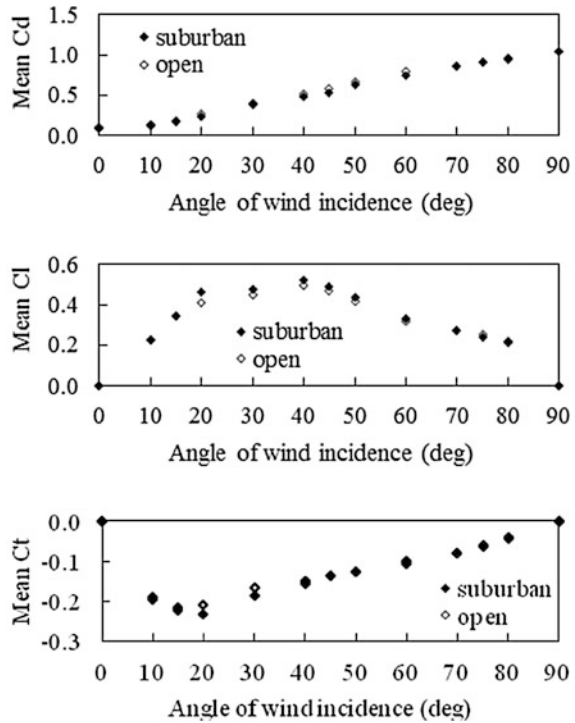


**Fig. 7** Comparison on variation of mean drag, lift, and torsion coefficients



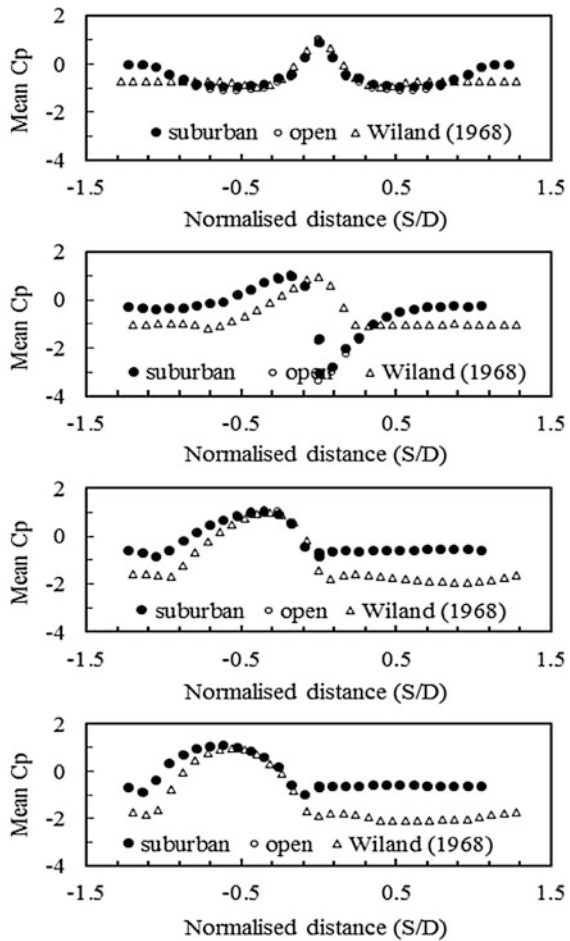
- At level 1, the values of mean drag/lift force and torsion coefficients correspond to suburban terrain found to be higher than those for open terrain in the range of  $\theta = 60^\circ$  to  $90^\circ$ ,  $20^\circ$  to  $80^\circ$ , and  $10^\circ$  to  $60^\circ$ , respectively.

### 3 Comparison Between Present Study and Literature

#### 3.1 Mean Pressure Coefficients

Comparison on variation of mean  $C_p$  between the present study ( $B/D = 0.5$ , under open and suburban terrain conditions) on 3-D elliptical bluff body at level 4 and the literature [3] on 2-D elliptical cylinder ( $B/D = 0.6$ , under uniform flow) are made for  $\theta = 0^\circ, 30^\circ, 60^\circ,$  and  $90^\circ$  and are shown in Fig. 8. Except for  $\theta = 0^\circ$ , for all other angles of incidence, the values of mean suction coefficients reported in the literature [3] are found to be higher than those values obtained from the present study, whereas the values of mean positive pressure coefficients reported in the literature [3] are found to be less than those values obtained from the present study. The above differences could be due to 3-D flow effects in the present study.

Fig. 8 Comparison on variation of mean pressure coefficients for  $\theta = 0^\circ, 30^\circ, 60^\circ,$  and  $90^\circ$



### 3.2 Mean Force/Torsion Coefficients

Comparison on variation of mean  $C_d$  and  $C_l$  between the present study and on long elliptical cylinder reported in the literature [11] and on 2-D elliptical cylinder reported elsewhere [3] are made and are shown in Figs. 9 and 10. The results plotted in Fig. 9 as the variation of mean drag force coefficients are obtained by substituting the evaluated values of mean  $C_d$  for  $\theta = 0^\circ$  and  $90^\circ$  in the empirical relation given in the literature [11]. From Fig. 9, it is found that the values of mean  $C_d$  are minimum at  $0^\circ$  and maximum at  $90^\circ$ ; i.e., values of mean  $C_d$  increase with change in angle of wind incidence from  $0^\circ$  to  $90^\circ$ . The value of mean  $C_d$  reported in [3] for  $0^\circ$  is 0.43, which is found to be relatively higher than those evaluated values under both the terrain conditions and the value obtained using the empirical relation given in the literature [11]. For  $\theta = 90^\circ$ , the evaluated values and the value obtained using the empirical relation given in the literature [11] are found to be relatively less than the value reported in [3].

Comparison on variation of mean  $C_l$  is shown in Fig. 10. The results plotted in Fig. 10 as the variation of mean lift force coefficients are obtained by substituting the evaluated values of mean  $C_l$  for  $\theta = 45^\circ$  in the empirical relation given in the literature [11]. From Fig. 10, it is observed that the values of mean  $C_l$  reported in the literature [3, 11] and the evaluated values are found to be 0 for  $0^\circ$  and  $90^\circ$ . The values of mean  $C_l$  increase with change in angle of wind incidence up to a certain angle of wind incidence and beyond which it decreases with change in angle of wind incidence. The maximum values of mean  $C_l$  reported in [11] and [3] are found to be 0.47 ( $\theta = 45^\circ$ ) and 0.41 ( $\theta = 50^\circ$ ), respectively, whereas from the present study under open and suburban terrain conditions, it is observed to be 0.49 and 0.53 ( $\theta = 40^\circ$ ), respectively.

**Fig. 9** Comparison on variation of mean drag force coefficients

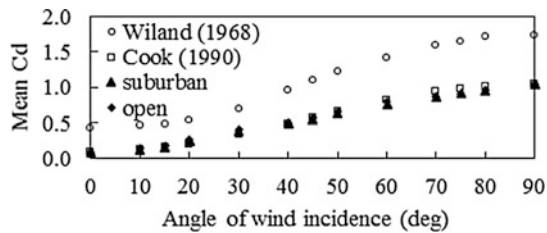


**Fig. 10** Comparison on variation of mean lift force coefficients

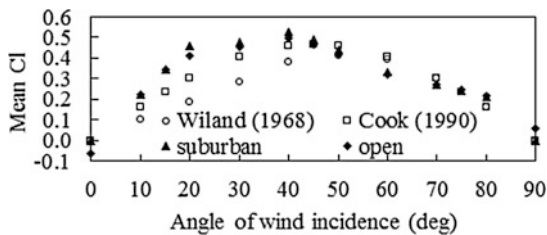


**Table 1** Comparison on mean drag force coefficients

Description	$\theta = 0^\circ$	$\theta = 90^\circ$
IS:875 [7]	0.2	0.95
AS/NZS:1170.2 [8]	0.3	1.5
Present study (both terrains)	0.1	1.05

### 3.3 Comparison Between Present Study and Codes of Practice

Comparison on values of mean  $C_d$  between the present study and the values reported in codes of practice [7, 8] are made and are given in Table 1 for  $\theta = 0^\circ$  and  $90^\circ$ , respectively. From Table 1 for  $\theta = 0^\circ$ , it is found that the evaluated value of mean  $C_d$  is 50 and 67% less than those values reported in codes of practice [7, 8]. For  $\theta = 90^\circ$ , the evaluated value of mean  $C_d$  is 10% higher than the value reported in [7], whereas the evaluated value is 30% less than the value reported in [8], which corresponds to individual members with aspect ratio  $\geq 40$ .

## 4 Summary and Concluding Remarks

Wind tunnel experiments were conducted on a tall building model (scale of 1:300) with elliptical cross section having major and minor axis of 20 cm and 10 cm with height of 70 cm under suburban terrain for 13 different angles of wind incidence of  $0^\circ$  (wind normal to minor axis),  $10^\circ$ ,  $15^\circ$ ,  $25^\circ$ ,  $30^\circ$ ,  $40^\circ$ ,  $45^\circ$ ,  $50^\circ$ ,  $60^\circ$ ,  $70^\circ$ ,  $75^\circ$ ,  $80^\circ$ , and  $90^\circ$  (wind normal to major axis). The model was instrumented with pressure ports in the circumferential direction at eight levels along the height of model, denoted as level 1–8 corresponding to the height ratio of  $z/H = 0.1, 0.2, 0.3, 0.5, 0.7, 0.8, 0.9,$  and  $0.95$ , respectively. The datasets were acquired at a sampling frequency of 700 samples/sec/channel for a sampling duration of 15 s. Static pressure data had been collected by a pitot tube placed at 70 cm height. The measured pressures were processed (using MATLAB script) to obtain statistical parameters of aerodynamic pressure/force coefficients with respect to measurement level. The results obtained from the present study are compared with the earlier wind tunnel pressure measurement study carried out on the same model with same instrumentation scheme under open terrain. Further, the results obtained from the present wind tunnel study are compared with those reported in the literature/codes of practice. Based on the comparison study, the following concluding remarks are made:

- In general, the variation of mean pressure coefficients is found to be different for different angle of wind incidence. The variation of mean pressure coefficients under open and suburban terrain conditions for all the angles of wind incidence is similar but varying in magnitudes.

- The mean pressure distribution around the ellipse is symmetric about major axis for  $\theta = 0^\circ$  and about minor axis for  $\theta = 90^\circ$ . The values of mean pressure coefficients at stagnation points at all levels are found to be unity. In the wake region, the magnitude of suction pressure coefficients for  $\theta = 0^\circ$  is relatively less than those magnitudes for  $\theta = 90^\circ$ , due to large wake created behind the model. Hence, the scatter in mean pressure coefficients is insignificant at the windward region, whereas more scatter is observed in wake region along the height. This is applicable for both open and suburban terrain conditions.
- As the angle of wind incidence progresses from  $\theta = 0^\circ$  to  $30^\circ$ , the difference between the variation of mean pressure coefficients (both positive and negative) obtained at most of the levels under open and suburban terrain conditions found similar except at bottom and top levels.
- As the angle of incidence progresses further, the magnitudes of mean suction coefficients under open terrain up to level 3 found to be relatively higher than those under suburban terrain in the circumferential length between 21.023 and 47.301 cm.
- At level 4, the variation of mean pressure coefficients under open terrain equal to the variation under suburban terrain over the entire circumferential length of the model.
- As the level progresses from level 4 to top level, the magnitudes of mean pressure coefficients obtained under suburban terrain are found to be relatively higher than those for open terrain in the circumferential length between 21.023 cm and 47.301 cm.
- The component of force acted in  $Y$  axis is mostly contributing to drag and it increases with increase in angle of wind incidence, as observed under both terrain conditions.
- The variation of mean lift/torsion coefficients peaks at  $30^\circ$ , which could be a critical angle of wind incidence, as observed under both terrain conditions.
- The variation of mean drag/lift force and torsion coefficients obtained at levels 4 and 8 found to well compare under both the terrain conditions.
- At level 1, the values of mean drag/lift force and torsion coefficients correspond to suburban terrain found to be higher than those for open terrain in the range of  $\theta = 60^\circ$  to  $90^\circ$ ,  $20^\circ$  to  $80^\circ$ , and  $10^\circ$  to  $60^\circ$ , respectively.
- Based on the comparison on mean suction coefficients between evaluated values and values reported in literature, the evaluated values are found to be less than those values reported in the literature for the angles of wind incidence examined.
- Based on the comparison on mean drag force coefficients between evaluated values and values reported in codes of practice, the values reported in codes of practice are found to be conservative.

**Acknowledgements** This full length paper is published with kind permission of Director, CSIR-SERC, Chennai. First author thanks all the staff of Wind Engg. Lab., for their suggestions and successful conduct of experiment.

## References

1. Tall and Urban: An analysis of global population and tall buildings. Counc Tall Build Urban Habitat J Issue II (2011)
2. Alonso G, Meseguer J, Sanz-Andrés A, Valero E (2010) On the galloping instability of two-dimensional bodies having elliptical cross-sections. *J Wind Eng Ind Aerodyn* 98(8–9):438–448
3. Wiland E (1968) Unsteady aerodynamics of stationary elliptic cylinder in subcritical flow, M. A. Sc. Dissertation
4. Fonseca FB, Mansur SS, Vieira EDR (2013) Flow around elliptical cylinders in moderate Reynolds numbers. In: Proceedings of the 22nd international congress of mechanical engineering, November 3–7, Ribeirão Preto, SP, Brazil, pp 4089–4100
5. Tamura Y, Tanaka H, Ohtake K, Nakai M, Kim Y (2010) Aerodynamic characteristics of tall building models with various unconventional configurations. In: Proceedings of the structures congress, May 12–15, Orlando, Florida, pp 3104–3113
6. Franek M, Konečná L, Hubová O, Žilinský J (2016) Experimental pressure measurement on elliptic cylinder. *Appl Mech Mater* 820:332–337
7. IS: 875 (part 3)-1987 (1989) Code of practice for design loads (other than Earthquake) for buildings and structures—Part 3: Wind loads, BIS
8. AS/NZS: 1170.2:2011 (2011) Structural design actions, Part 2: Wind actions, Australian/New Zealand Standard
9. Afreen SA, Abraham A, Selvi Rajan S, Iyer NR, Gomez SM (2015) Wind tunnel pressure measurement studies on a tall building with elliptic cross-section: effect of angle of wind incidence. In: Proceedings of the international conference on innovations in structural engineering, December 14–16, Hyderabad, India, pp 109–128
10. Abraham A, Harikrishna P, Selvi Rajan S, Ramesh Babu G, Chitra Ganapathi S, Keerthana M (2016) Wind tunnel pressure measurement studies on 1:2:7 elliptic building model. CSIR-SERC research report no. R&D 01-MLP 18741-RR-04, March 2016
11. Cook NJ (1990) The designer's guide to wind loading of building structures, Part 2 static structures. Butterworths, London

# Influence of Bracing Systems on the Seismic Pounding of High-Rise Structure



Pallerla Sai Krishna and J. S. Kalyana Rama

**Abstract** Earthquakes are natural hazards where the shaking of the ground occurs due to the seismic waves produced by a release of energy. This nature of earthquakes may cause disasters by the collapse of structures and buildings. The amount of damage during an earthquake depends on many parameters, including intensity, duration and frequency content of ground motion, geologic and soil condition, quality of construction. We need to ensure that the design of building should have adequate strength and be ductile enough to remain as one unit, even while subjected to very large deformations. The present study deals with the assessment of pounding effects on the behavior of two adjacent structures. Suitable resisting techniques were also adopted for addressing the gap required for adjacent structures.

**Keywords** Bracing systems · Seismic pounding · High-rise structure  
Earthquake · Storey drift · Displacement

## 1 Introduction

It is not always possible to increase the separation between buildings to the extent that we need in all practical situations. So an alternative in such a case would be to compensate the gap needed in the structural design with the decreasing lateral motion of the structure which can be done by employing different techniques (bracings, shear walls, dampers, etc.). The separation or gap required to minimize pounding depends on the dynamic characteristics such as mass, stiffness, and strength of the two buildings. This depends on the peak displacement response of adjacent structures. Daniela Dobre et al. investigated the damages after a strong earthquake due to the

---

P. Sai Krishna · J. S. Kalyana Rama (✉)  
Department of Civil Engineering, BITS-Pilani, Hyderabad Campus,  
Hyderabad, Telangana State, India  
e-mail: kalyan@hyderabad.bits-pilani.ac.in

P. Sai Krishna  
e-mail: f2013550@hyderabad.bits-pilani.ac.in

pounding effect between adjacent buildings is observed. Also an analysis is performed to determine the behavior of buildings due to structural pounding, with and without considering the soil-structure interaction (SSI). Winkler springs were used to define the properties of underlying soil. They observed that a frame building located next to a shear wall structure suffered no serious external damage. The damage due to pounding was severe in a case where collision between taller frame and shorter frame building with adjacent corners. Nawawi Chouw et al. carried out numerical analysis to observe the pounding effects between adjacent buildings considering soil-structure interaction. The two structures were described by finite elements whereas the soil underlying them was described by boundary elements. They observed that due to near-source ground motion, there were strong excitations at the low-frequency range. So, it led to a conclusion that high-rise buildings are strongly affected when compared to low-rise buildings. Pounding may not increase the force on the structural members but will surely lead to higher modes of the buildings [1].

Dobre et al. presented some of the related to the Vrancea seismic motions pattern. An analytical and numerical study was carried out to assess the effects of pounding during an earthquake with and without soil-structure interaction. They observed that the damage is concentrated at the roof of the shorter building and stiffer structures suffer detrimentally compared to a flexible structure. Impact forces decrease as the separation gap increases.

Shehata carried out a parametric study on building pounding response along with seismic hazard mitigation for adjacent buildings for three categories of recorded earthquake excitation. He concluded that the seismic poundings between adjacent buildings may induce unwanted damages even though each individual structure might have been designed properly to withstand the strike of credible earthquake events. He suggested an increasing gap width to eliminate the contact between two adjacent structures.

Rahman investigated the dynamic structural response of reinforced concrete moment resistant frames considering soil flexibility effects. Pounding phenomenon of a twelve-storied and six-storied subjected to two recorded earthquake excitations is assessed. He developed suitable numerical models with soil-structure interaction phenomenon. The pounding response in which soil flexibility was accounted for was compared to the fixed base response for each of the separation gaps incorporated. He observed through his analysis that the relative storey accelerations were more dependent on the characteristics of the excitation rather than on the magnitudes of the impact forces.

The present study was done for two scenarios: one for a 20 floors structure and the other for 25 floors structure, and the results obtained were used to arrive at the conclusions. Figure 1 shows the plan configurations of the two structures.



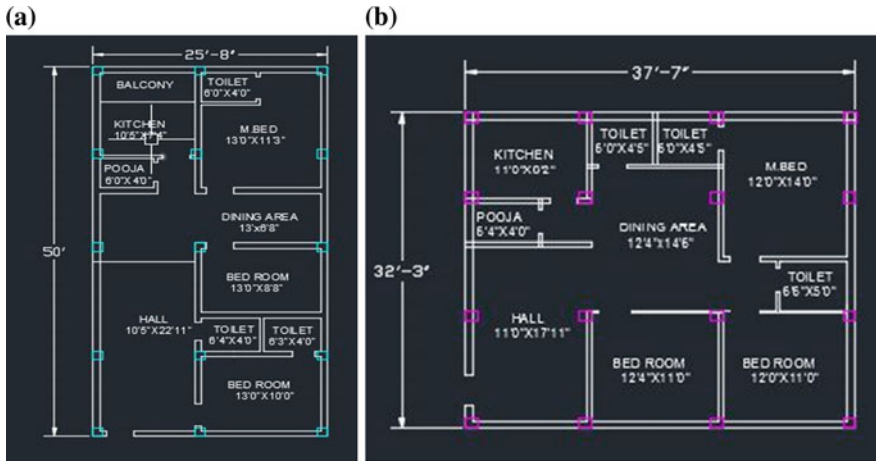


Fig. 1 a Floor plan of 25 storied building, b Floor plan of 20 storied building

## 2 Observations and Results

SAP2000 was used for the modeling and analysis of the structures.

Two structures, one with 20 floors and the other with 25 floors were placed adjacent to each other to discern the effect of seismic pounding. Floor to floor height for both the structures is taken as 3.1 m. Plinth floor height above ground level is taken as 0.55 m. Beams and columns of size 450 mm × 450 mm were adopted. The material used is M20 grade of concrete and Fe415 grade of steel for reinforcement.

A uniformly distributed live load of 4.5 kN/m<sup>2</sup> is considered. Equivalent lateral force procedure is followed to first calculate the design base shear. It is then distributed throughout the height of building at various floor levels.

Equivalent static lateral force method which is a nonlinear static analysis technique is used for the seismic analysis of both the structures. The steps involved in the process are stated below:

1. Seismic weight of the buildings are calculated using the lumped mass concept
2. The design base shear is then calculated based on the equation

$$V_B = A_h * W$$

where

$$A_h = Z * I * S_a / (2 * R * g)$$

- $Z$  Zone factor;  
 $I$  Importance factor;  
 $R$  Response reduction factor;  
 $S_a/g$  Average response acceleration coefficient.

3. This is then distributed throughout the height of building using the equation

$$Q_i = V_B W_i h_i^2 / \sum_{i=1}^n W_i h_i^2$$

where

- $W_i$  Seismic weight of floor  $i$ ;  
 $h_i$  Height of floor  $i$  measured from base;  
 $N$  Number of stories in the building.

The maximum displacement of the structures was found out to be 0.083 and 0.161 m for 20 and 25 floors structure, respectively. When X bracings were provided, lateral displacements of the structures were reduced significantly to 0.08 and 0.154 m for 20 and 25 floors structure, respectively. This implies that, in practice, when the required seismic gap cannot be maintained between structures, provision of bracings, and shear walls would reduce the storey drift of the structures as shown in Figs. 2 and 3.

- Storey drift of structures without bracings (Fig. 2);  
 Storey drift of structures with V bracings (Fig. 3);  
 Storey drift of structures with X bracings (Fig. 4);  
 Storey drift of structures with springs to represent the soil profile (Fig. 5);  
 Base shear of structures for different cases considered (Fig. 6);  
 Maximum roof displacement of structures for different cases considered (Fig. 7).

Figures 6 and 7, case 1 indicates storey drift without bracings; case 2 indicates storey drift with V bracings; case 3 indicates storey drift with X bracings; case 4 indicates storey drift when springs are used to represent the soil profile below the foundation. From the above observations of various cases for both 20 and 25 floors structures, maximum displacement, i.e. roof displacement was observed to be increasing with an increase in the number of floors of the building, considering all other factors remains same. For the above-considered scenario, when buildings are constructed adjacent to each other, a minimum seismic gap of 0.2 m should be provided to avoid the effect of pounding between structures. This maximum roof displacement can be reduced by providing bracings to the structure.

Providing bracings of V shape has reduced the displacement a little higher than by providing X bracings. When springs are used to represent the soil profile below the building by removing the fixity from fixed as in earlier cases, the maximum

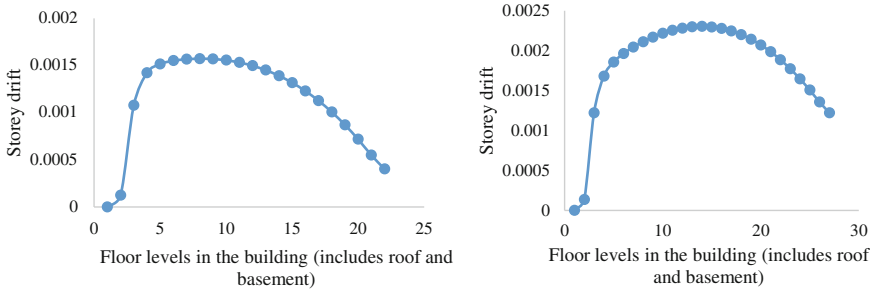


**Fig. 2** Storey drift for 20 and 25 storied structures without bracing

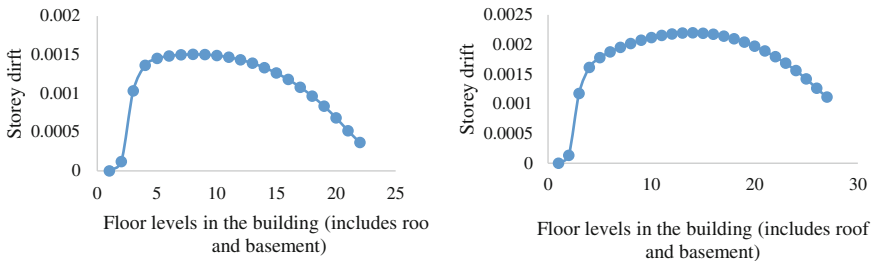


**Fig. 3** Storey drift for 20 and 25 storied structures with V bracings

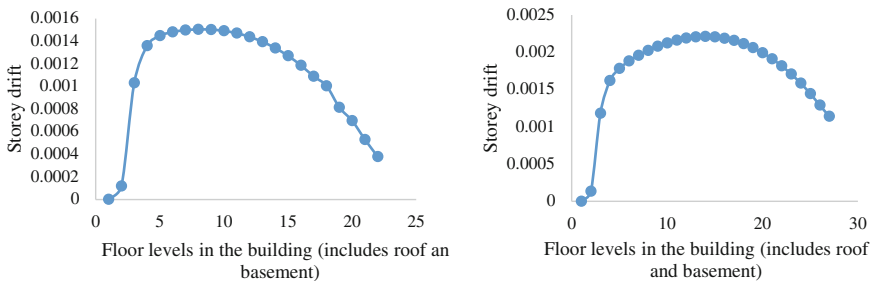


**Fig. 4** Storey drift for 20 and 25 storied structures with X bracings

displacement has seen an increase for both 20 and 25 floors structure. This approach of using springs instead of assuming a fixed support at the base of the column makes our model even more realistic. The model prepared can be further strengthened by designing a foundation by using the base forces and moments obtained earlier.

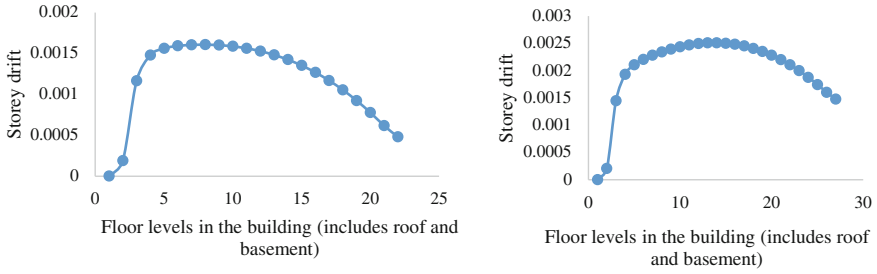


Fig. 5 Storey drift for 20 and 25 storied structures with springs to represent the soil

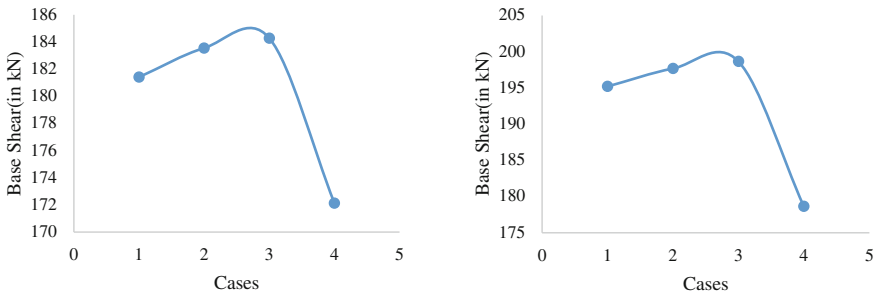


Fig. 6 Base shear values for 20 and 25 storied structures for different cases

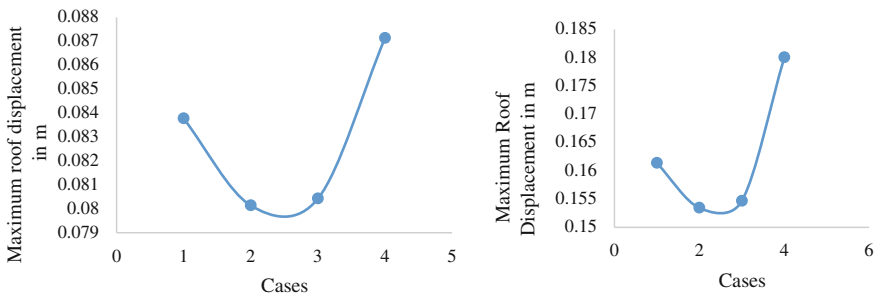


Fig. 7 Maximum roof displacement for 20 and 25 storied structures for different cases

The results thus obtained after that will serve as a good estimate in representing the practical scenario of a structure subjected to seismic load in an earthquake zone. Thereon, we observe if the structure is going to fail in any of the members and thus change the design accordingly.

According to IS:4326, for buildings of height greater than 40 m, the sum of the dynamic deflections at any floor level should be less than the gap width provided between the adjoining structures. Our problem meets those requirements for any floor level considered.

## References

1. Chow N (2002) Influence of soil-structure interaction on pounding response of adjacent buildings due to near-source earthquakes. *J Appl Mech*
2. Dobre D (2014) Pounding effects during an earthquake, with and without consideration of soil-structure interaction. In: *Second European conference on earthquake engineering*
3. Raheem SE (2006) Seismic Pounding between adjacent building structures. *Electron J Struct Eng*
4. Rahman A (2001) Seismic pounding of a case of adjacent multiple-storey buildings of different total heights considering soil flexibility effects. *Bull NZ Soc Earthq Eng*

# Coherency Model for Dense Seismic Array



Gopala Krishna Rodda and Dhiman Basu

**Abstract** The recorded translational motions represent characteristics of the seismic excitation at one single point. Most foundation systems have finite, but considerable dimension, and it may offer rigidity constraint over the underlying soil. However, the extent of rigidity depends on the foundation footprint. Therefore, free-field ground motions are in general preferred in seismic design and effect of foundation flexibility is separately accounted for in a case-by-case. Hence, information about the spatial variability of translational motion is needed for seismic design of structures. Coherency is the best descriptor of spatial variability quantitatively. Moreover, description of the ground motion input cannot be completed without specifying the rotational ground motion. Since direct measurement of the rotational excitations is not feasible, these components must be extracted from the recorded translational data under suitable assumptions so as to account for their effects in an approximate sense in seismic design. Once the coherency is estimated, a number of procedures are available to generate spatially varying ground motion conditioned upon a seed event and coherency model. Objectives of this study are to obtain a coherency model for translational and rotational motion to completely specify the appropriate ground motion fields.

**Keywords** Lagged coherency · Dense seismic array · Rotational motion  
Appropriate translational components

---

G. K. Rodda (✉) · D. Basu  
Department of Civil Engineering, Indian Institute of Technology Gandhinagar,  
Gandhinagar, India  
e-mail: gopalakrishna.rodha@iitgn.ac.in

D. Basu  
e-mail: dbasu@iitgn.ac.in

© Springer Nature Singapore Pte Ltd. 2019  
A. Rama Mohan Rao and K. Ramanjaneyulu (eds.), *Recent Advances in Structural Engineering, Volume 2*, Lecture Notes in Civil Engineering 12,  
[https://doi.org/10.1007/978-981-13-0365-4\\_26](https://doi.org/10.1007/978-981-13-0365-4_26)

## 1 Introduction

Dense seismic array provides a unique opportunity to study the spatial variability. Based on the analysis of strong motion events recorded, many researchers reported that the spatial variability of free-field translational ground motion could be significant within the dimension of a typical engineered structure. Therefore, spatial variability of translational and, especially, rotational ground motion is required to completely specify the appropriate ground motion inputs. This has led to considerable research in the last decade on modeling spatially varying earthquake ground motion. Coherency is generally used as a measure of the spatial variability. Coherency can be obtained by normalizing the cross-spectral density (CSD) with the auto-spectral density (ASD), and lagged coherency is given by its absolute value. Denoting  $f$  as the frequency in Hz, mathematically, coherency between the two ground motions,  $x_1(t)$  and  $x_2(t)$ , can be expressed as

$$\gamma(f) = \frac{S_{x_1x_2}(f)}{\sqrt{S_{x_1x_1}(f)S_{x_2x_2}(f)}} \quad (1)$$

$S_{x_1x_2}$ --CSD between  $x_1(t)$  and  $x_2(t)$

It is immediately obvious that the coherency will have the value of 1 for all the frequencies for any pair of ground motions. This is avoided in practice by performing smoothening operation on the ASD and CSD. Hamming window is used to carry out smoothening in this paper. Lagged coherency was reported to be reducing with the increasing separation distance and frequency. A number of researchers have studied the characteristics of translational ground motion, its spatial variability, and its effect on the seismic response of structures.

Lagged coherency for a particular ground motion component was computed by taking all possible pairs of array elements. Computed numerical coherency is then fitted through a predefined functional form using least squares approximation to get the coefficients of curve fitting.

Different empirical forms have been suggested for approximating the coherency. The sum of two exponentials has been suggested in Ref. [4]:

$$|\gamma(v, f)| = A \exp \left[ -\frac{2v}{\alpha\theta(f)} (1 - A + \alpha A) \right] + (1 - A) \exp \left[ -\frac{2v}{\theta(f)} (1 - A + \alpha A) \right] \quad (2)$$

where  $\theta(f) = k(1 + f/f_o)^b)^{-1/2}$  is the frequency-dependent spatial scale of fluctuation,  $v$  is the distance, and all other parameters ( $A, \alpha, f_o, b$  and  $k$ ) have to be estimated by regression analysis.

Another coherency form has been suggested in Ref. [3] which is:

$$\begin{aligned} \gamma(x, y, \omega) &= \exp(-\alpha_1(\omega)x^2 - \alpha_2(\omega)y^2) * \exp\left(-\frac{i\omega x}{v_a}\right) \\ \alpha_i(\omega) &= \frac{a_i}{b_i + \ln(\omega)}, \quad \omega \geq 0.314 \text{ rad/s}, \quad i = 1, 2 \end{aligned} \quad (3)$$

where  $\omega$  is the circular frequency,  $v_a$  is the apparent propagation velocity,  $x$  and  $y$  are distances between stations along and perpendicular to the wave propagation, and  $a_i$  and  $b_i$  are to be determined by regression analysis, respectively.

References [5, 6] and [8] and others have proposed more complex models. But all these models were proposed for array with comparatively large separation distances and may not match accurately with numerical coherency calculated with dense seismic array. Reference [1] proposed a new coherency model for dense seismic array which is

$$\tanh^{-1}|\gamma(f, \xi)| = (a_1 + a_2\xi) \left[ \exp\{(b_1 + b_2\xi)\} + \frac{1}{3}f^c \right] + k \quad (4)$$

where  $a_1, a_2, k, b_1, b_2$  and  $c$  are model parameters,  $f$  is frequency in Hz, and  $\xi$  is the separation distance in meters. Even though the fitting might be satisfactory in inverse hyperbolic form, deviation will be significant once model is compared with numerical coherency in normal scale. Hence, a new coherency model is proposed for small size array like LSST array and it is as follows. Also, all the coherency models proposed to date lack the theoretical transparency. Therefore, the objective of the present study is to arrive at a coherency model from the first principles and consistent with the theory.

The description of the parameters given till now is limited to the introductory part. The parameters needed will be defined wherever required which will be valid for the rest of sections.

## 2 Description of the Array and Events Considered

### 2.1 LSST Array

The Lotung-LSST (LLSST) site is a part of the much larger SMART-1 array. Figure 1 shows the surface stations of the LSST array to be considered in this paper. All fifteen free-surface accelerometers at the LSST are positioned along three arms at approximately  $120^\circ$  intervals. Each arm extends for about 50 m, and the spacing between the surface stations varies from 3 to 90 m. Each arm contains five stations that are designated here as 1 through 5, starting at the center of the array. For example, FA1\_1 and FA2\_5 denote the innermost and outermost stations located on arm 1 and 2, respectively.



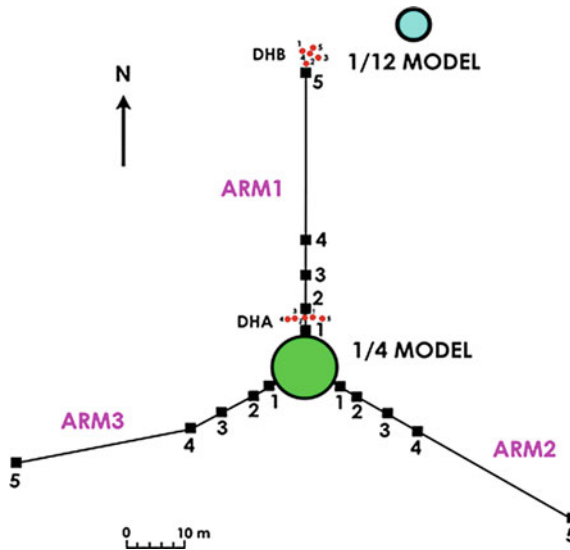


Fig. 1 LSST array, Lotung

Table 1 Events considered

Description	Event-1	Event-2	Event-3
Date	May 20, 1986	November 14, 1986	January 16, 1986
Latitude	24° 4' 54"	23° 59' 30.5"	24° 45' 46.2"
Longitude	121° 35' 29.4"	121° 49' 59.4"	121° 57' 40.1"
Focal depth (km)	15.8	15	10.2
Local magnitude	6.2	6.5	6.1
Epicentral distance (km)	66	75	24

Three strong motions events recorded at the LSST array are considered for analysis in this paper. Brief description of each event is presented in Table 1. Detailed description of the recorded data is provided later in this paper. Note that Event-3 may have some near-field effects as the epicentral distance is approximately 24 km. Only surface stations are considered in the analysis, and out of 15, usually, 10–14 actually functioned during the events. Hence, number of surface stations analyzed varies from one event to another.

Ground motion is recorded in LSST array along the East-West (EW), North-South (NS), and vertical directions. Recorded horizontal accelerations (EW and NS) are rotated along and normal to the principal plane to facilitate extraction of rotational components. These two rotated components, i.e., along and normal to the principal planes, are denoted in this paper as  $a_{g1}$  and  $a_{g3}$ , respectively; for completeness, vertical acceleration is denoted as  $a_{g2}$ .

## 2.2 SMART-1 Array

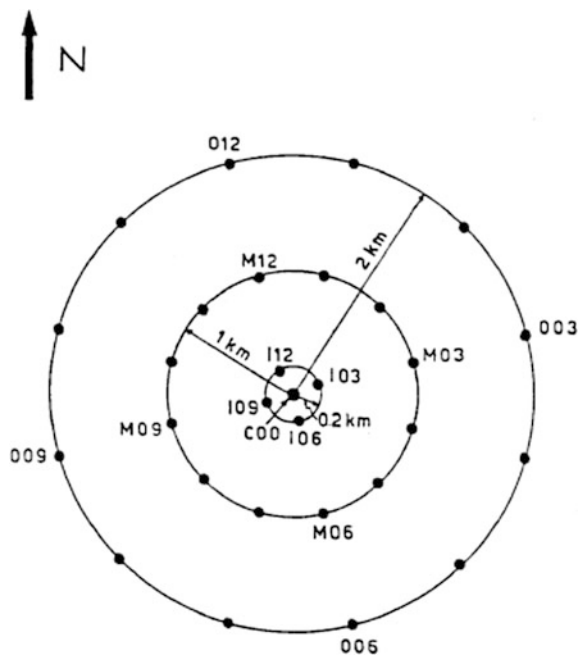
SMART-1 array is a strong motion array located in Lotung, in the northeast corner of Taiwan. It consists of 37 force-balanced triaxial accelerometers arranged on three concentric circles and a center station. The inner ring is denoted by I, the middle by M, and the outer by O. Twelve equi-spaced stations were located on each ring, numbered 1–12, and station C00 was located at the center of the array as shown in Fig. 2. Event considered in this study is the Event 45 information which can be found in <http://www.earth.sinica.edu.tw/~smdmc/smart1/smart1>.

## 3 Methodology

### 3.1 Empirical Coherency Model for Rotational Motion

Let  $j$  and  $k$  be two stations, separated by some distance. Seismic waves are assumed to be propagating like plane waves. During the propagation, it is assumed that seismic waves will reach station  $j$  first and then proceed to reach station  $k$ . Direction of propagation of wave is not along the direction of line joining the two stations. Depending on the direction of propagation and speed of propagation, seismic waves will reach station  $k$  from station  $j$  with some time delay ( $t_o$ ). There will be decay in

Fig. 2 SMART-1 array, Lotung



amplitude ( $h$ ), and random motion will be added during the course of propagation. Hence, translational acceleration at station  $k$  ( $a_k(t)$ ) can be estimated through the following equation.

$$a_k(t) = ha_j(t - t_o) + r(t)$$

$$\text{where } t_o = \frac{\bar{c} \cdot \bar{u}}{|\bar{c}|^2} \quad (5)$$

Using the principles of Fourier transform, Eq. (5) can be written in frequency domain as

$$X_k(f) = he^{-j2\pi ft_o} X_j(f) + R(f) \quad (6)$$

where  $f$  is the frequency, and  $X_j$ ,  $X_k$ , and  $R$  are Fourier transforms of motions at stations  $j$ ,  $k$ , and random motion, respectively.

Using Eq. (6), the ASD at station  $k$  ( $S_{kk}$ ) can be estimated as

$$S_{kk}(f) = \frac{1}{T} X_k^*(f) X_k(f)$$

$$= \frac{1}{T} \left( he^{j2\pi ft_o} X_j^*(f) + R^*(f) \right) \left( he^{-j2\pi ft_o} X_j(f) + R(f) \right) \quad (7)$$

Further simplification of Eq. (7) will lead to

$$S_{kk}(f) = \left( h^2 S_{jj}(f) + 2h \text{Re} \left( e^{-j2\pi ft_o} C_{ar}(f) \right) + S_{rr}(f) \right) \quad (8)$$

$C_{ar}$  is the CSD between motion at station  $j$  and random motion.

Now, the random motion is assumed to be uncorrelated with ground motion i.e.,  $C_{ar} = 0$ . Then, Eq. (6) will be further simplified to

$$S_{kk}(f) = \left( h^2 S_{jj}(f) + S_{rr}(f) \right) \quad (9)$$

Similarly, the CSD between the ground motions at stations  $j$  and  $k$  ( $S_{jk}$ ) is given by

$$S_{jk}(f) = X_j^*(f) X_k(f) / T$$

$$= X_j^*(f) \left( he^{-j2\pi ft_o} X_j(f) + R(f) \right) / T \quad (10)$$

After considering the assumption  $C_{ar} = 0$ , Eq. (10) will lead to

$$S_{jk}(f) = he^{-j2\pi ft_o} S_{jj}(f) \quad (11)$$

Substituting Eqs. (9) and (11) into Eq. (1), coherency is simplified to

$$\begin{aligned}\gamma_{jk}(f) &= \frac{S_{jk}(f)}{\sqrt{S_{jj}(f)S_{kk}(f)}} \\ &= \frac{he^{-j2\pi ft_o} S_{jj}(f)}{\sqrt{S_{jj}(f)(h^2 S_{jj}(f) + S_{rr}(f))}}\end{aligned}\quad (12)$$

It is also to be noted that when distance between the stations is close to zero, there will be no decay in amplitude ( $h \approx 1$ ) and random motion ceases to exist ( $S_{rr} \approx 0$ ). If the stations are well separated, decay in amplitude and random motion will be significant ( $h \approx 0$ ). Satisfying these conditions, ASD of random motion is assumed to be a function of both distance and frequency and is approximated as below.

$$S_{rr}(f, u) = (1 - h^2(u))S_o(f) \quad (13)$$

Substitution of Eq. (13) into Eq. (12) will lead to

$$\begin{aligned}\gamma_{jk}(f, u) &= \frac{he^{-j2\pi ft_o} S_{jj}(f)}{\sqrt{S_{jj}(f)(h^2 S_{jj}(f) + (1 - h^2)S_o(f))}} \\ &= e^{-j2\pi ft_o} (1 + (1/h^2 - 1)S_o(f)/S_{jj}(f))^{-0.5}\end{aligned}\quad (14)$$

From Eq. (14), lagged coherency, which is defined as absolute value of coherency, is estimated as

$$\begin{aligned}|\gamma_{jk}(f, u)| &= (1 + (1/h^2 - 1)S_o(f)/S_{jj}(f))^{-0.5} \\ &= (1 + g_1(u)g_2(f))^{-0.5}\end{aligned}\quad (15)$$

where  $g_1(u)$  and  $g_2(f)$  are defined as

$$\begin{aligned}g_1(u) &= 1/h^2 - 1 \\ g_2(f) &= S_o(f)/S_{jj}(f)\end{aligned}\quad (16)$$

Amplitude decay ( $h$ ) approximation should be such that when distance between the station is close to zero,  $h \approx 1$ , and when distance is very large  $h \approx 0$ . Hence, a decaying exponential has been assumed to represent the decay.

$$h(u) = e^{-\beta u} \rightarrow \beta > 0 \quad (17)$$

Then,  $g_1(u)$  can be expressed as

$$g_1(u) = (1/h^2(u) - 1) = (e^{2\beta u} - 1) \quad (18)$$

The only function left to be estimated is  $g_2(f)$ . So, lagged coherency is calculated numerically and then  $g_2(f)$  is computed from it. Gaussian curve seemed to represent the data the best. Hence, Gaussian curve is assumed to represent the function  $g_2(f)$ , whose coefficients are to be determined from regression analysis of numerical coherency.

$$g_2(f) = Ae^{-\frac{(f-\mu)^2}{2\sigma^2}}$$

$$|\gamma_{jk}(f, u)| = \left(1 + (e^{2\beta u} - 1)Ae^{-\frac{(f-\mu)^2}{2\sigma^2}}\right)^{-0.5} \quad (19)$$

In case of significant curvature changes within the frequency band of interest, it is recommended that Gaussian curve of higher order will represent the function  $g_2(f)$  the best.

$$|\gamma_{jk}(f, u)| = \left(1 + (e^{2\beta u} - 1) \sum_{i=1}^n A_i e^{-\frac{(f-\mu_i)^2}{2\sigma_i^2}}\right)^{-0.5} \quad (20)$$

$$\gamma_{jk}(f, u) = |\gamma_{jk}(f)|e^{-j2\pi f t_0}$$

This multimodal behavior can be explained by the fact that if the stations are far away from each other, attenuation will be significant and higher frequencies will be filtered (single mode), whereas if the stations are close, attenuation will be sporadic (multimode). This completes the estimation of coherency model for translational motion.

### 3.2 Empirical Coherency Model for Rotational Motion

Rotational ground motions are not being measured by the accelerographs deployed. Hence, the effect of rotational motion on structural response is largely ignored despite the studies done by many researchers showing its significance. This lack of consensus can be attributed to the use of different interpretations of rotation, namely the free-field or point rotation, chord rotation, and averaged rotation. Free-field rotation is defined as the spatial derivative of the displacement field at that instant; chord rotation is the ratio of the difference in displacements between two closely spaced, adjacent stations measured along a direction perpendicular to the line joining the two stations; average rotation is the average of chord rotations of several station pairs with one common station. A rigid foundation will filter the high-frequency components of free-field motion, although foundations are never

infinitely stiff. Accordingly, average rotation may be the best choice because chord rotation is usually sensitive to separation distance and point rotation ignores the presence of a foundation. Regardless of the choice of rotation, free-field ground motions are in general preferred in seismic design and effect of foundation flexibility is separately accounted for in a case-by-case. Theoretically, rotation does not propagate like translational waves, and hence, it may be inappropriate to estimate the spatial variation of rotational motion using coherency models which does not exist theoretically. But if the rotational motion is estimated in terms of temporal derivative of translational motion with due scaling, it is possible to estimate the spatial variability of rotational motion completely in terms of spatial variability of the respective translational motion. The simplified procedure for estimation of rotational motion reported by Ref. [7] will facilitate the estimation of spatial variability of rotational motion. The simplified procedure is based on the following constraints: (i) plane wave propagation; (ii) existence of principal plane; (iii) either body or surface wave dominance based on near-fault or far-field recording; (iv) with only body wave, either incidence of only P-wave or only S-wave or both; (v) wave dispersion or scattering; (vi) frequency-independent wave characteristics such as incident angle, apparent wave velocity or their frequency dependency; and (vii) point source or finite fault size with a given set of rupture information, etc.

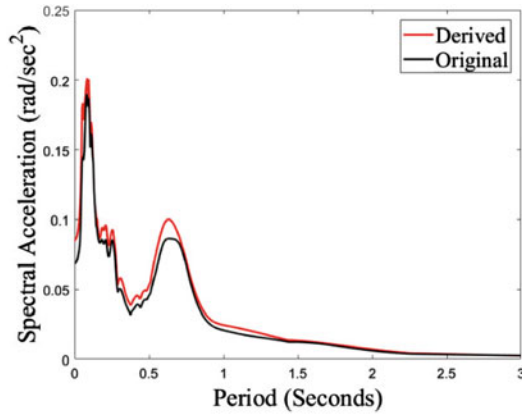
By definition, rotational motion is a spatial derivative of appropriate translational component (ATC), which can be converted to time derivative of that translational motion with due scaling through apparent wave velocity as shown in Eq. (21).

$$\begin{aligned}\ddot{\theta}(t) &= \frac{\dot{a}(t)}{c} \\ \dot{a}(t)_{\text{rocking}} &= - \left\{ \frac{1}{\alpha} [\dot{a}_{g2}(t)]^{\text{if}} - [\dot{a}_{g1}(t)]^{\text{if}} \right\} \\ \dot{a}(t)_{\text{torsion}} &= \dot{a}_{g3}(t)\end{aligned}\quad (21)$$

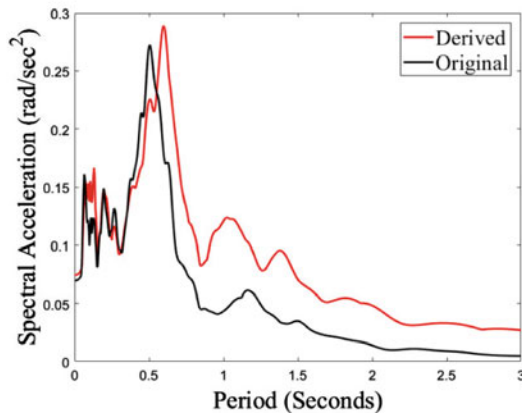
The detailed description of extraction of rotational motion from translational motion is beyond the scope of this study, and it can be found extensively [7]. Response spectral comparison of torsional spectra (taken from Ref. [2] which is rigorous method and requires body wave decomposition) against the spectra of torsional motion extracted from Ref. [7] is shown in Fig. 3a where close resemblance can be observed between both the spectra. Similar, comparison is shown for rocking spectra (taken from Ref. [2]) against the derived rocking spectra in Fig. 3b where close resemblance can be observed between both the spectra. The resemblance is strong in case of torsional motion, whereas it is acceptable in case of rocking motion. Even though limited number of figures are shown here, the conclusion holds well for all the events.

Similar to the coherency estimation of translational motion, coherency for rotational motion has also to be estimated. Even though rotation does not propagate

**Fig. 3** Comparison of derived and original spectra



(a) Torsional spectral comparison at station FA2\_1 for Event 3



(b) Rocking spectral comparison at station FA3\_5 for Event 2

like displacement wave does coherency for rotation can be calculated numerically from spectral densities of rotational motion.

$$\gamma_{jk}^r(f) = \frac{S_{jk}^r(f)}{\sqrt{S_{jj}^r(f)S_{kk}^r(f)}} \quad (22)$$

'r' denotes rotational motion

Using the principles of Fourier transform (FT) and Eq. (21), the FT of rotational motion can be written as

$$X_{\theta}(f) = \frac{X_{\dot{a}}(f)}{c} = \frac{i2\pi f X_a(f)}{c} \quad (23)$$

$X_{\theta}$  and  $X_a$  are FTs of rotational motion and ATC. Hence, auto- and cross-spectral densities are rewritten as

$$\begin{aligned} X_{\theta,j}(f) &= \frac{X_{a,j}(f)}{c_j} = \frac{i2\pi f X_{a,j}(f)}{c_j} \\ S_{jj}^r(f) &= X_{\theta,j}^*(f) X_{\theta,j}(f) / T = \left( \frac{2\pi f}{c_j} \right)^2 S_{jj}^a(f) \\ \text{where } S_{jj}^a(f) &= X_{a,j}^*(f) X_{a,j}(f) / T \end{aligned} \quad (24)$$

Similarly

$$\begin{aligned} S_{kk}^r(f) &= \left( \frac{2\pi f}{c_k} \right)^2 S_{kk}^a(f) \\ S_{jk}^r(f) &= \left( \frac{(2\pi f)^2}{c_j c_k} \right) S_{jk}^a(f) \end{aligned} \quad (25)$$

Using Eqs. (22), (24) and (25), the coherency can be written as

$$\begin{aligned} \gamma_{jk}^r(f) &= \frac{\left( \frac{(2\pi f)^2}{c_j c_k} \right) S_{jk}^a(f)}{\sqrt{\left( \frac{2\pi f}{c_j} \right)^2 S_{jj}^a(f) \left( \frac{2\pi f}{c_k} \right)^2 S_{kk}^a(f)}} \\ &= \frac{S_{jk}^a(f)}{\sqrt{S_{jj}^a(f) S_{kk}^a(f)}} = \gamma_{jk}^a(f) \end{aligned} \quad (26)$$

It has been shown in Eq. (26) that coherency of rotational motion is same as that of its ATC (translational motion), for which functional form of the coherency is readily available in (Eq. 20).

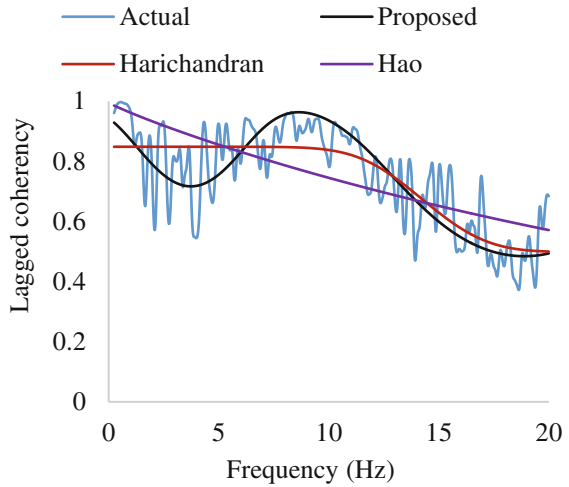
## 4 Results and Discussion

### 4.1 LSST Array

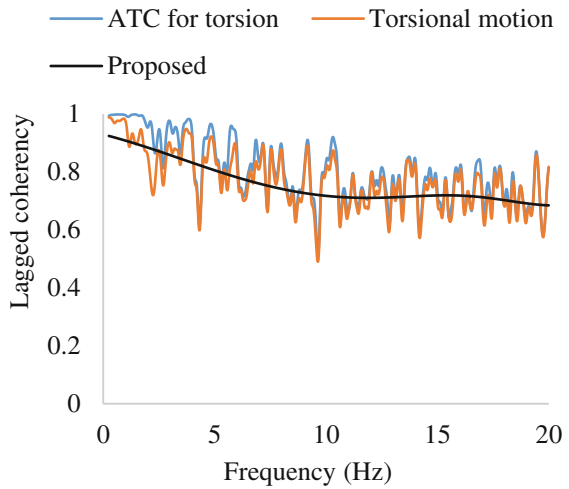
Numerical coherency was calculated for all possible station pairs in LSST array, and distance between them was noted. Station-pairs are divided into different bins (of size 10 m) based on their separation distance, and numerical coherency in a specific bin is averaged. Obtained average coherency was regressed through the



**Fig. 4** Coherency comparison of different models



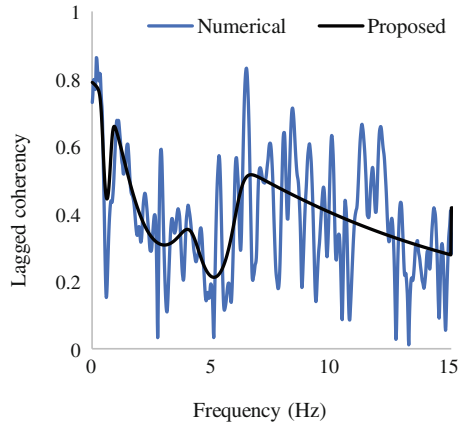
(a) Distance range 10–20 m Event 1 - Vertical



(b) Distance range of 20–30 m Event 3

Harichandran model [4], Hao model [3], and the proposed model to get the coefficients. The lagged coherency from different models was then compared with the numerical coherency in Fig. 4a for translational component and in Fig. 4b for rotational component. It can be seen that the proposed model represents the numerical coherency the best, because the proposed model can account for the multimodal behavior. Also, it can be said that the coherency of rotational motion is same as that of its ATC.

**Fig. 5** Coherency between IO1-M03 during Event 25 in vertical direction



## 4.2 SMART-1 Array

Proposed coherency model is also used to fit the coherency for the data recorded at SMART-1 array during Event 25, and the fitting is found to be satisfactory as it can be seen in Fig. 5 for the station IO1 and MO3.

## 5 Conclusions

The proposed coherency model approximated the numerical coherency very well compared to the widely used existing coherency models in case of dense LSST array. Also, the applicability of the proposed model to the SMART-1 has been examined and found to be satisfactory. Also, it can be seen that multimodal behavior is significant in dense array (LSST) but not in SMART-1 array.

**Acknowledgements** This research is funded by SERB/DST, Government of India, under the Grant No. SB/S3/CEE/012/2013, and the financial support is acknowledged. The authors gratefully acknowledge the Institute of Earth Science, Academia Sinica, Taiwan, for sharing the strong motion data.

## References

1. Abrahamson NA, Schneider JF, Stepp JC (1991) Empirical spatial coherency functions for application to soil-structure interaction analyses. *Earthq Spectra* 7(1):1–27
2. Basu D, Whittaker AS, Constantinou MC (2012) Estimating rotational components of ground motion using data recorded at a single station. *J Eng Mech ASCE* 138(9):1141–1156
3. Hao H (1996) Characteristics of torsional ground motions. *EESD* 25(6):599–610
4. Harichandran RS, Vanmarcke EH (1986) Stochastic variation of earthquake ground motion in space and time. *J Eng Mech* 112(2):154–174

5. Loh CH (1985) Analysis of the spatial variation of seismic waves and ground movements from smart-1 array data. *Earthq Eng Struct Dyn* 13(5):561–581
6. Luco JE, Wong HL (1986) Response of a rigid foundation to a spatially random ground motion. *Earthq Eng Struct Dyn* 14(6):891–908
7. Rodda G, Basu D (2016) On extracting rotational components of ground motion using an empirical rotational window. *Soil Dyn Earthq Eng* (Under review)
8. Ye J, Pan J, Liu X (2011) Vertical coherency function model of spatial ground motion. *Earthq Eng Vib* 10(3):403–415

# Seismic Performance of a Heritage Rubble Stone Masonry Building— A Case Study



Hina Gupta, Debdutta Ghosh and Achal K. Mittal

**Abstract** The old masonry buildings in India are terribly vulnerable to lateral loads especially the buildings lying in the high seismic zones of lower Himalayas. This paper deals with evaluation of the seismic performance of an old unreinforced rubble stone masonry building situated in Uttarakhand. CSIR-CBRI conducted a study on the structural soundness of “Pant Sadan,” the official residence of the Chief Justice of Uttarakhand. After a preliminary survey of the building, architectural plans of the building were developed. A finite element analysis was performed using commercially available SAP2000 software. Linear and nonlinear analysis is performed to assess the present strength of the old structure by computing different stresses in the building under earthquake load. In the modeling, it is assumed that the masonry structure is homogeneous and the material behavior is nonlinear. Subsequently, the static analysis results (stresses) are compared with the values given in masonry code (IS 1905:1987). Pushover analysis and time history analysis for Uttarkashi earthquake (1991) is also performed to assess the performance of building under a Himalayan earthquake. The analysis results show that building response is satisfactory under vertical loading and shows some weak zones for the previous seismic activities. The results of the finite element modeling will help to predict the local and global collapse mechanisms and will reduce the seismic risk by adopting the proper retrofitting strategy.

**Keywords** Unreinforced masonry · Finite element modeling · Time history  
Nonlinear analysis · Heritage building

---

H. Gupta (✉) · D. Ghosh · A. K. Mittal  
Structure Engineering Division, CSIR-Central Building Research Institute,  
Roorkee 247667, India  
e-mail: hina@cbri.res.in

D. Ghosh  
e-mail: debdutta@cbri.res.in

A. K. Mittal  
e-mail: akmittal@cbri.res.in

## 1 Introduction

Masonry is composite, non-homogeneous, and anisotropic material. These buildings consist of stones, bricks, adobe, tiles, stucco, or precast blocks which are bonded together with mortar. Most of the old masonry buildings are load-bearing structures and constructed without any codal provisions.

Masonry being a heterogeneous material, its properties are dependent on many factors like its components which have different mechanical properties, the array and interfaces between the units, etc. Intensive research has been going on to understand these variations in parameters of masonry construction. Homogenization techniques for the analysis of masonry structures have been discussed by [1–4]. On the basis of these homogenization techniques, various techniques like micro-modeling, simplified micro-modeling, and macro-modeling are widely used by different researchers. Analyzing and strengthening of masonry and specially the old structures have always been a challenging task because of the complex geometries, deficient knowledge about the used materials, structural modifications and aging of material [5]. With the development of computational methods, finite element analysis has become the widely accepted tool for the analysis of masonry structures [6, 7]. Finite element analysis of historical buildings in SAP2000 has been performed by [8–11]. The vulnerability of the old buildings situated in the areas of high seismic activities is a matter of concern especially if the building is still being used. Nonlinear analysis is emerging as a powerful tool to assess the strength of the structures under the seismic actions [11, 12].

This paper deals with the detailed analysis of a random rubble masonry building situated at Nainital. Detailed investigation has been carried out by a team of scientists from CSIR-Central Building Research Institute (CSIR-CBRI) [13].

## 2 A Case Study

The building undertaken for study was constructed by Nawab Hamid Ali Khan of Rampur State in the year 1890 and was later named as “Pant Sadan.” In 2002, it became official residence of the Chief Justice of Uttarakhand High Court. This old building is in distress condition and has also developed some cracks. It is a two-storeyed load-bearing random rubble masonry building with wooden trussed roof covered with GI sheets and wall thickness of 18”–24”. The building also has wooden staircase and wooden flooring at first floor. Foundation type and depth are not known and detailed engineering drawings of this old building are not available. Some exposed foundation showed dry random rubble masonry without offset. The building is situated in seismic zone IV of IS: 1893-2002 [14] and located on a talus deposit lying on a sloping hill at different terraces. Some additions and alterations have been carried out in the building as per the need. The recent photograph of the building is shown in Fig. 1. The hill slope and deposit in the downhill, where the

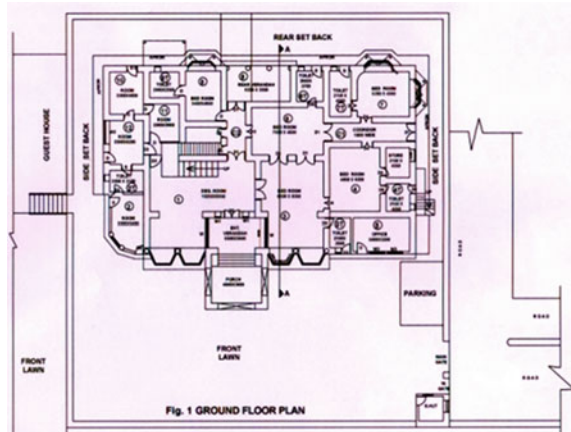
**Fig. 1** Pant Sadan building**Fig. 2** Talus deposit on downhill slope

building is situated is shown in Fig. 2. The ground floor plan of the building and the surrounding area is shown in Fig. 3.

From the visual inspection of the building, several distresses were observed, viz:

- Settlement and tilting of portico pier.
- Cracks in one circular piers of the inner room at the ground floor.
- Cracks in the masonry load-bearing wall and separation of wooden truss/support from masonry at several locations.
- Cracked and decayed wooden roof truss members.
- Vibrations of wooden flooring during movement at the first floor level.
- Decayed wooden false ceiling at some places and separation of joints at various locations.
- Dampness in some portion of the building.
- Sagging chouxhats and separation gaps between wooden beam and masonry.

**Fig. 3** Ground floor plan of Pant Sadan building



### 3 Numerical Modeling

The structure studied here is an unreinforced rubble stone masonry; hence, it is a load-bearing structure. Being a very large structure, heterogeneous modeling of structure is not possible. Therefore, the stone and the mortar are considered as homogeneous units as in the macro-modeling. The floor plans (ground and first) of the building are almost similar.

These homogeneous masonry units are analyzed as macro-model using SAP 2000 FEM numerical package [8]. The material properties for the numerical analysis are taken from chemical analysis of stone, mortar, and wood samples collected from the site by the CBRI team [13] and the available literature on the similar types of material [15–17]. The properties are tabulated in Table 1.

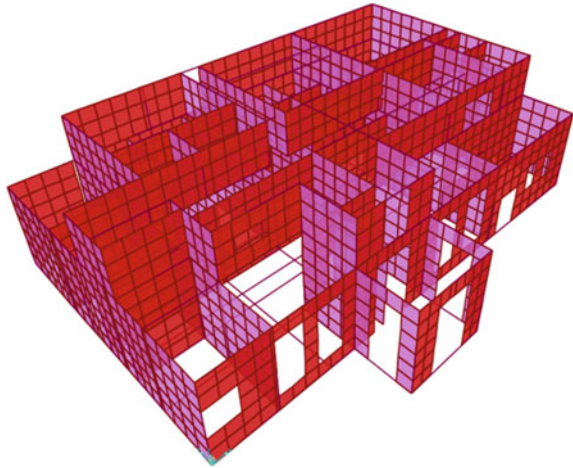
Walls are modeled as SHELL elements while timber beams of the roofs are modeled as FRAME elements.

The building rests on a talus deposit with about 0.8–1.2 m deep masonry strip footing. Hence, the support condition is taken as fixed in the analysis. Building is having GI sheet roofing supported on timber beams which are resting on masonry walls.

**Table 1** Material properties

Properties of material	Value
Unit weight of masonry ( $\text{kN/m}^3$ )	18.5
Prism strength of masonry, $f_m$ (MPa)	3.5
Elastic modulus of masonry, $E$ (MPa)	1925
Shear modulus, $G$ (MPa)	315
Poisson's ratio, $\mu$	0.2

**Fig. 4** 3D model of the building



In the software model, timber beams are taken over walls and roof load is applied. The 3D view of the modeled building is shown in Fig. 4. Values of dead load and imposed load are taken in accordance with IS 875:1987 [18].

## 4 Nonlinear Analysis

The seismic analysis of building is done using nonlinear pushover and time history method as described in the code IS 1893(Part I): 2002 [14]. The 1991 Uttarkashi earthquake is considered for time history analysis. The present structure is analyzed using SAP2000 software.

One of the nearby disastrous earthquake data is taken here for the study of seismic behavior of the building in case of similar events. The time history data of Uttarkashi earthquake, **October 19, 1991, 21:23:15** ( $30^{\circ} 78'N$ ,  $78^{\circ} 77'E$ ) which happened at a hypocentral distance of approximately 200 km from the location of the present building in Nainital ( $29^{\circ} 23'N$ ,  $79^{\circ} 30'E$ ) (Fig. 5). The magnitude of the earthquake was 7.0 on Richter scale with depth of 10 km.

The time history of the Uttarkashi earthquake is shown in Fig. 6 [19].

Both static and dynamic nonlinear analyses have been identified as powerful tools for analysis of masonry buildings [20]. In nonlinear static or pushover analysis, the distribution of lateral forces with the height of the structure is done and the load is increased to push the structure until an ultimate value of displacement is reached. This analysis provides information about the peak response in terms of storey drift, floor displacements, and other deformation quantities [21]. Similarly, parametric studies can be done by dynamic or time history analysis.

Dead load, live load, and earthquake time history of Uttarkashi earthquake are applied to the building, and the response of the building is observed.



**Fig. 5** Location of Nainital and Uttarkashi [19]

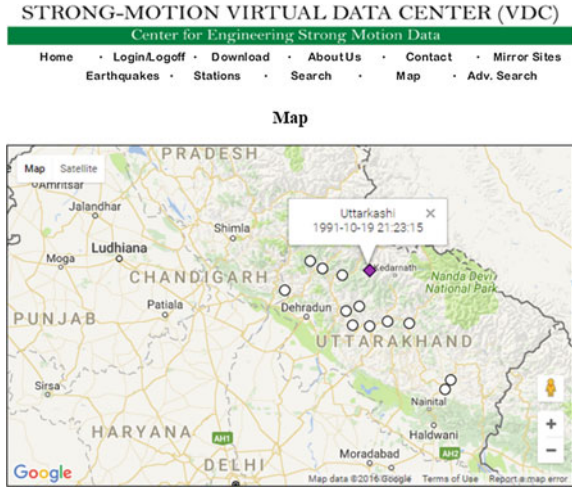
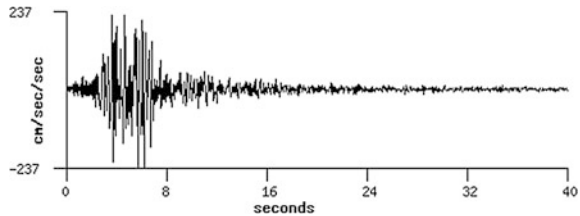


**Fig. 6** Uttarkashi time history curve [19]



## 5 Results

### 5.1 Analysis of Stresses Under Gravity Loading

The building is analyzed for the combination of dead and imposed loads. Fundamental time period of the building for free vibration analysis is 1.893 s.

The force distribution of gravity loads is shown in Fig. 7. The structure is mostly under compressive forces while upper and bottom corners and wall beam junctions seem to have high concentration of tensile forces. As per IS 1905:1987, compressive stresses for the given rubble stone masonry building are taken 0.25 MPa while no tensile stresses are permitted [15]. As seen from Fig. 8, the compressive stresses developed in the building under gravity loading are within permissible limits while tensile stress is exceeded at a very few locations. Beam wall junctions at the roof level, at the bottom, and at the upper corners of walls at each floor lever are subjected to high tensile stress concentration due to combined effect of dead load and imposed load. The maximum value of tensile stress reached is about 0.7 MPa, which is at a beam wall junction showing crack between wall and roof which may be responsible for the cracks in the structure.

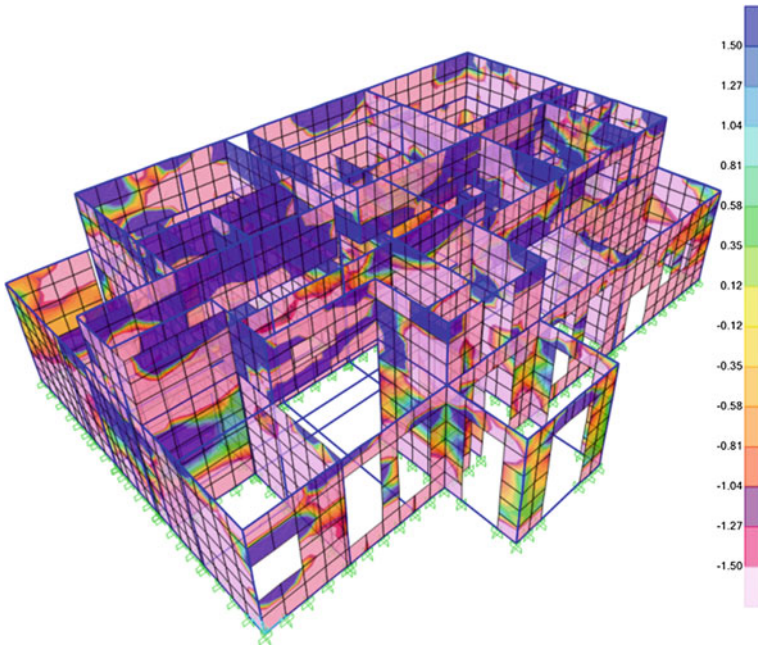


**Fig. 7** Compressive and tensile force distribution due to gravity load

Maximum value of displacement observed is about 12.8 mm under gravity loads.

### 5.2 Analysis of Stresses Under Nonlinear Static Loads (Pushover Analysis)

Figures 9 and 10 show the shell stresses for pushover analysis in X and Y direction, respectively. The out of plane failure of the walls can be clearly observed from the figures as the walls perpendicular to X direction are having maximum stress concentration for pushover in X direction and vice versa for Y direction. The increasing value of tensile stresses in the out of plane walls is indicating the vulnerability of the building under earthquake loads. Maximum value of top displacement observed is about 115.3 mm in X direction while 97.4 mm in Y direction.

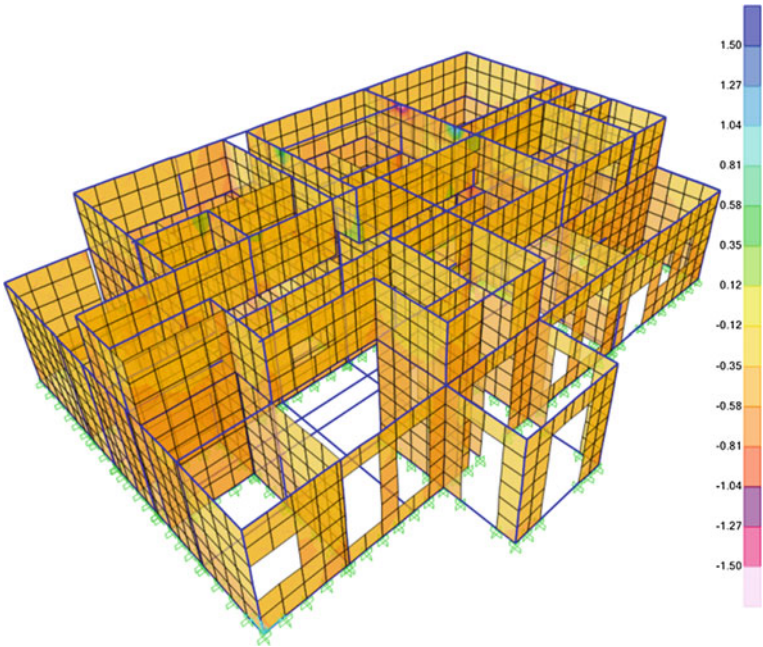


**Fig. 8** Shell stress due to gravity load (MPa)

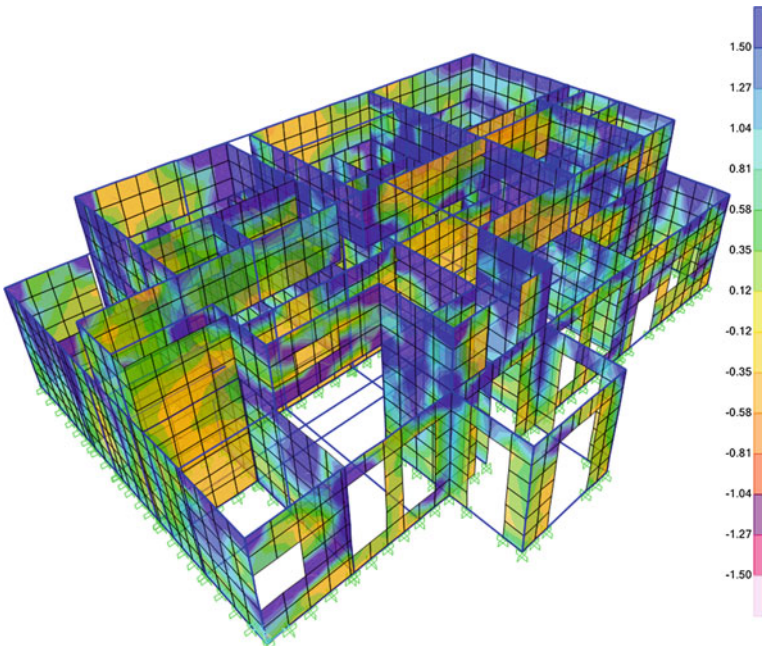


**Fig. 9** Shell stresses due to pushover in X direction (MPa)

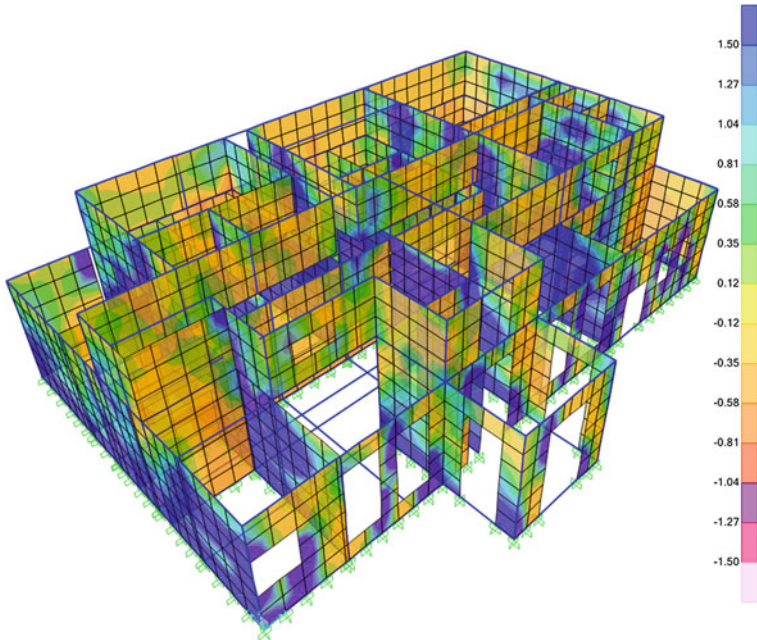


**Fig. 10** Shell stresses due to pushover in *Y* direction (MPa)

### ***5.3 Analysis of Stresses Under Nonlinear Dynamic Loads (Time History Analysis)***

The structure is analyzed for the input ground motion of the Uttarkashi earthquake to determine its seismic performance. As seen from Fig. 11, due to time history applied for the structure, most part of the structure remains under compression within permissible limits. Tensile stress is having high concentration at many locations as seen from figures. This shows that structure may not be able to sustain an earthquake of the same intensity as that of Uttarkashi and it may fail.

As seen from Fig. 12, large portion of building is subjected to a displacement below 30 mm under the Uttarkashi earthquake while maximum displacement observed at the top of the building is about 123.6 mm. Also, the portico piers and area around openings are having large displacement values.

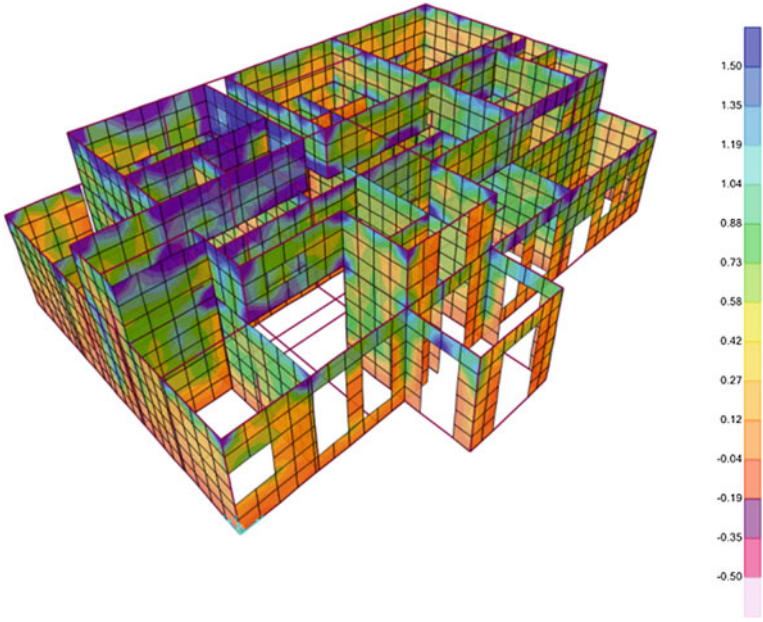


Fig. 11 Shell stress under Uttarkashi time history data (MPa)

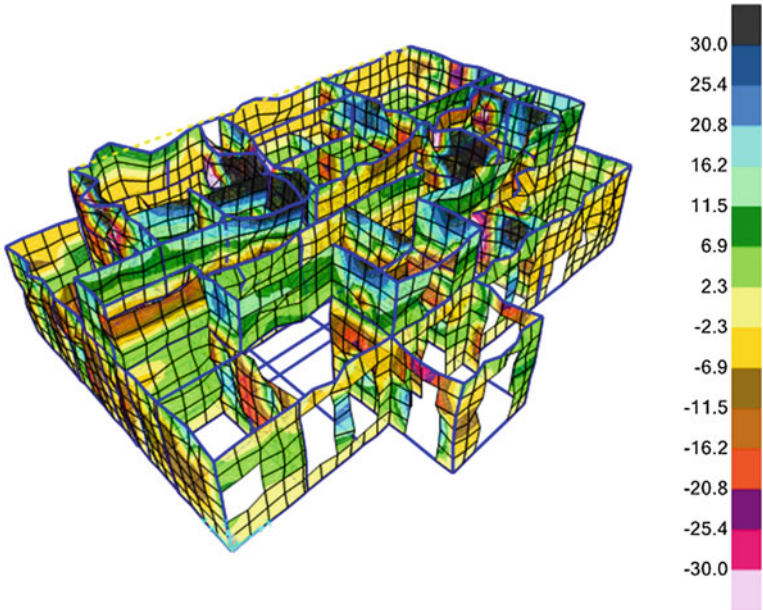


Fig. 12 Displacement contours under Uttarkashi time history (in mm)

## 6 Conclusions

The building is more than 100 years old and is having clear sign of distress in the form of cracks, tilting of piers, decayed wooden structural members and false ceiling, dampness, etc. Further, the test results of the soil samples, bedding mortar, plaster, and wooden samples also show that the building is not in good condition.

The cracks observed from visual inspection are in good agreement with the stress concentration observed from the analysis of finite element model under gravity loading. The results of pushover and time history analysis show that the building is vulnerable during large intensity earthquake. Therefore, adequate repair and rehabilitation works are necessary to make it earthquake resistant.

**Acknowledgements** The authors are grateful to team of CBRI staff associated with Pant Sadan project for providing the details of the visual inspection of the building.

## References

1. Lourenço PB (2002) Computations on historic masonry structures. *Prog Struct Mat Eng* 4 (3):301–319
2. Luciano R, Sacco E (1997) Homogenization technique and damage model for old masonry material. *Int J Solids Struct* 34(24):3191–3208
3. Lourenço PB, Milani G, Tralli A, Zucchini A (2007) Analysis of masonry structures: review of and recent trends in homogenization techniques. *Can J Civ Eng* 34(11):1443–1457
4. Lourenço PB, Rots JG (1997) On the use of homogenisation techniques for the analysis of masonry structures. *Mason Int* 11(1):26–32
5. Roca P, Cervera M, Gariup G, Pela L (2010) Structural analysis of masonry historical constructions. Classical and advanced approaches. *Arch Comput Methods Eng* 17(3):299–325
6. Asteris PG, Chronopoulos MP, Chrysostomou CZ, Varum H, Plevris V, Kyriakides N, Silva V (2014) Seismic vulnerability assessment of historical masonry structural systems. *Eng Struct* 62–63:118–134 (March 2014)
7. Akhaveissy AH (2012) The DSC model for the nonlinear analysis of in-plane loaded masonry structures. *Open Civil Eng J* 6(1):200–214
8. SAP2000 manuals. Available: <http://www.comp-engineering.com/SAPManE.htm>
9. Kappos AJ, Penelis GG, Drakopoulos CG (2002 July) Evaluation of simplified models for lateral load analysis of unreinforced masonry buildings. *J Struct Eng* 128:890
10. Khadka SS (2013) Seismic performance of traditional unreinforced masonry building in Nepal. *Kathmandu Univ J Sci Eng Technol* 9(1):15–28
11. Spyarakos C, Francioso A (2012) Shaking table test and pushover analysis on a scaled masonry building. In: 15th world conference on earthquake engineering
12. Simões A, Bento R, Gago A, Lopes M (2012) Seismic vulnerability of old masonry ‘Gaioleiro’ buildings in Lisbon. In: 15th world conference on earthquake engineering
13. CSIR-CBRI (2010) Detailed project report on suggesting repair cum strengthening measures for Pant Sadan, Nainital. CSIR-Central Building Research Institute, Roorkee
14. IS 1893 (2002) (Part 1) Criteria for earthquake resistant design of structures
15. IS 1905 (1987) Code of practice for structural use of unreinforced masonry
16. Lombillo I, Thomas C, Villegas L, Fernández-Álvarez JP, Norambuena-Contreras J (2013) Mechanical characterization of rubble stone masonry walls using non and minor destructive tests. *Constr Build Mater* 43:266–277

17. Milosevic J, Bento R, Gago AS, Lopes M (2012) Shear tests on rubble stone masonry panels—diagonal compression tests. In: 15th world conference on earthquake engineering
18. IS 875 (1987) (Part 1 & 2) Code of practice for design loads (other than earthquake) for buildings and structures
19. Strong motion virtual data. Available: <http://www.strongmotioncenter.org/vdc/scripts/earthquakes.plx>
20. Galasco A, Lagomarsino S, Penna A, Resemini S (2004) Non-linear seismic analysis of masonry structures Alessandro. In: 13th world conference on earthquake engineering, no. 147
21. Chopra AK (2012) Dynamics of structures, 4th edn

**Part II**  
**Vibration Control and Smart Structures**



# Seismic Vibration Control for 20-Story Nonlinear Benchmark Building Installed with Shape Memory Alloy Damper



Raghav Moyade and Suhasini Madhekar

**Abstract** This paper presents a passive control strategy for 20-story nonlinear benchmark building using Shape Memory Alloy (SMA)-based damper. The problem for seismically excited nonlinear benchmark buildings was published with a goal to provide a clear basis to evaluate the relative merits of various passive, active, or semi-active structural control strategies on seismically excited building. The benchmark problem considers various levels of each of the earthquake records including 0.5, 1.0, and 1.5 times the magnitude of El Centro (1940) and Hachinohe (1968); and 0.5 and 1.0 times the magnitude of Northridge (1994) and Kobe (1995). This makes a total of 10 earthquake records to be considered in the evaluation. The passive control uses a Shape Memory Alloy (SMA)-based device which uses the superelasticity property of SMAs. The SMA wires show hysteresis properties with large recoverable strains which can dissipate energy from the structures. Improved Graesser and Cozzarelli model for SMA wire is used for mathematical modeling of SMAs in MATLAB and Simulink. Six different configurations are used for damper placement. The evaluation results show that SMA-based damper is able to reduce the base shear criteria of the structure effectively. The damper is also able to reduce the occurrence of number of plastic connections in most of the earthquake cases. It also controlled the ductility and dissipated energy criteria effectively. Overall, studying all the evaluation criteria it can be concluded that Shape Memory Alloy damper as a passive device can reduce the responses of the structure moderately and can be used for seismic vibration control.

**Keywords** Benchmark problem · Passive control · Shape memory alloys

---

R. Moyade · S. Madhekar (✉)  
Department of Civil Engineering, College of Engineering Pune,  
Shivajinagar, Pune 411005, India  
e-mail: suhasini.madhekar@gmail.com

R. Moyade  
e-mail: raghavmoyade24@gmail.com

## 1 Introduction

Structural vibration control has become more popular recently, and new smart materials are emerging which are used in dampers. One such smart material is Shape Memory Alloy. SMAs have found applications in civil structures due to their energy dissipation, high fatigue life, superior ductility, and large recoverable strains.

SMA dampers have potential to withstand severe earthquakes efficiently. In general, Shape Memory Alloy-based dampers can reduce permanent deformations in the structure. They can also reduce the plastic deformations and can dissipate large amount of seismic energy.

At a higher temperature, SMAs exhibit the superelasticity. In the superelastic phase, SMAs are initially austenitic. However, upon loading, stress-induced martensite is formed. Upon unloading, the martensite reverts to austenite at a lower stress level, resulting in the hysteretic behavior. These properties make them ideal candidates for seismic energy dissipation devices in structural engineering.

## 2 Twenty-Story Nonlinear Benchmark Problem

The 20-story nonlinear benchmark problem, Ref. [1], used for this study was designed for the Los Angeles region. The benchmark building is 30.48 m  $\times$  36.58 m in plan and 80.77 m in height. Two far-field and two near-field historical ground motion records are selected: El Centro 1940, Hachinohe 1968, Northridge 1994, and Kobe 1995. This benchmark study considers various levels of each of the earthquake records including 0.5, 1.0, and 1.5 times the magnitude of El Centro and Hachinohe; 0.5 and 1.0 times the magnitude of Northridge and Kobe. Thus, in all ten earthquake records are considered in the evaluation of each control strategy.

### 2.1 Evaluation Criteria

The evaluation criteria ( $J_1$ – $J_{17}$ ) are divided into four categories: building responses ( $J_1$ – $J_6$ ), building damage ( $J_7$ – $J_{10}$ ), control devices ( $J_{11}$ – $J_{14}$ ), and control strategy requirements ( $J_{15}$ – $J_{17}$ ).

Various criteria considered are Interstory Drift Ratio ( $J_1$ ); Level Acceleration ( $J_2$ ); Base Shear ( $J_3$ ); Normed Interstory Drift Ratio ( $J_4$ ); Normed Level Acceleration ( $J_5$ ); Normed Base Shear ( $J_6$ ); Ductility ( $J_7$ ); Dissipated Energy ( $J_8$ ); Plastic Connections ( $J_9$ ); Normed Ductility ( $J_{10}$ ); Control Force ( $J_{11}$ ); Control Device Stroke ( $J_{12}$ ); Control Power ( $J_{13}$ ); Normed Control Power ( $J_{14}$ ); Control Devices ( $J_{15}$ ); Sensors ( $J_{16}$ ); and Computational Resources ( $J_{17}$ ). The computational resources are ignored in this study assuming enough computing resources are available. As the damper used in present

study is passive device, the criteria  $J_{13}$ ,  $J_{14}$ , and  $J_{16}$  will be zero. The evaluation criteria are defined as below:

$J_1$  Interstory Drift Ratio

$$J_1 = \max \begin{matrix} \text{El Centro} \\ \text{Hachinohe} \\ \text{Northridge} \\ \text{Kobe} \end{matrix} \left\{ \frac{\max_{t,i} \frac{|d_i(t)|}{h_i}}{\delta^{\max}} \right\} \tag{1}$$

$J_2$  Level Acceleration

$$J_2 = \max \begin{matrix} \text{El Centro} \\ \text{Hachinohe} \\ \text{Northridge} \\ \text{Kobe} \end{matrix} \left\{ \frac{\max_{t,i} |\ddot{x}_{ai}(t)|}{\ddot{x}_a^{\max}} \right\} \tag{2}$$

$J_3$  Base Shear

$$J_3 = \max \begin{matrix} \text{El Centro} \\ \text{Hachinohe} \\ \text{Northridge} \\ \text{Kobe} \end{matrix} \left\{ \frac{\max_t |\sum_i m_i \ddot{x}_{ai}(t)|}{F_b^{\max}} \right\} \tag{3}$$

$J_4$  Normed Interstory Drift Ratio

$$J_4 = \max \begin{matrix} \text{El Centro} \\ \text{Hachinohe} \\ \text{Northridge} \\ \text{Kobe} \end{matrix} \left\{ \frac{\max_{t,i} \frac{\|d_i(t)\|}{h_i}}{\|\delta^{\max}\|} \right\} \tag{4}$$

$J_5$  Normed Level Acceleration

$$J_5 = \max_{\substack{\text{El Centro} \\ \text{Hachinohe} \\ \text{Northridge} \\ \text{Kobe}}} \left\{ \frac{\max_{t,i} \|\ddot{x}_{ai}(t)\|}{\|\ddot{x}_a^{\max}\|} \right\} \quad (5)$$

$J_6$  Normed Base Shear

$$J_6 = \max_{\substack{\text{El Centro} \\ \text{Hachinohe} \\ \text{Northridge} \\ \text{Kobe}}} \left\{ \frac{\max_t \|\sum_i m_i \ddot{x}_{ai}(t)\|}{\|F_b^{\max}\|} \right\} \quad (6)$$

$J_7$  Ductility Factor

$$J_7 = \max_{\substack{\text{El Centro} \\ \text{Hachinohe} \\ \text{Northridge} \\ \text{Kobe}}} \left\{ \frac{\max_{t,j} \frac{|\varphi_j(t)|}{\varphi_{yj}}}{\varphi^{\max}} \right\} \quad (7)$$

$J_8$  Dissipated Energy of the Curvatures at the End of Members

$$J_8 = \max_{\substack{\text{El Centro} \\ \text{Hachinohe} \\ \text{Northridge} \\ \text{Kobe}}} \left\{ \frac{\max_{t,j} \frac{\int dE_j}{F_{yj} \cdot \varphi_{yj}}}{E^{\max}} \right\} \quad (8)$$

$J_9$  Plastic Connections

$$J_9 = \max_{\substack{\text{El Centro} \\ \text{Hachinohe} \\ \text{Northridge} \\ \text{Kobe}}} \left\{ \frac{N_d^c}{N_d} \right\} \quad (9)$$

$J_{10}$  Normed Ductility

$$J_{10} = \max \begin{matrix} \text{El Centro} \\ \text{Hachinohe} \\ \text{Northridge} \\ \text{Kobe} \end{matrix} \left\{ \frac{\max_j \frac{\|\varphi_j(t)\|}{\phi_{vj}}}{\|\varphi^{\max}\|} \right\} \quad (10)$$

$J_{11}$  Control Force

$$J_{11} = \max \begin{matrix} \text{El Centro} \\ \text{Hachinohe} \\ \text{Northridge} \\ \text{Kobe} \end{matrix} \left\{ \frac{\max_{t,l} |f_l(t)|}{W} \right\} \quad (11)$$

$J_{12}$  Control Device Stroke

$$J_{12} = \max \begin{matrix} \text{El Centro} \\ \text{Hachinohe} \\ \text{Northridge} \\ \text{Kobe} \end{matrix} \left\{ \frac{\max_{t,l} |y_l^d(t)|}{x^{\max}} \right\} \quad (12)$$

$J_{13}$  Control Power

$$J_{13} = \max \begin{matrix} \text{El Centro} \\ \text{Hachinohe} \\ \text{Northridge} \\ \text{Kobe} \end{matrix} \left\{ \frac{\max_t \sum P_l(t)}{\dot{x}^{\max} W} \right\} \quad (13)$$

$J_{14}$  Normed Control Power

$$J_{14} = \max \begin{matrix} \text{El Centro} \\ \text{Hachinohe} \\ \text{Northridge} \\ \text{Kobe} \end{matrix} \left\{ \frac{\sum \frac{1}{t_j} \int_0^{t_j} P_l(t)}{\dot{x}^{\max} W} \right\} \quad (14)$$

$J_{15}$  Number of Control Devices

$J_{16}$  Number of Required Sensors

$J_{17}$  Computational Resources

where the norm  $\|\cdot\|$  is computed using the following equation:

$$\|\cdot\| = \sqrt{\frac{1}{t_f} \int_0^{t_f} [\cdot]^2 dt} \quad (15)$$

### 3 Modeling of Shape Memory Alloy-Based Damper

Various models have been proposed for modeling superelasticity property of shape memory alloys. All these models can simulate hysteresis behavior of SMAs. Over the time, superior models have been developed to represent more accurate behavior of SMAs. Ozdemir in year 1976 was the first to model hysteretic properties of SMAs. His model was modified by Graesser and Cozzarelli [2] named as modified Ozdemir's model. Wilde et al. [3] modified the Graesser and Cozzarelli model to include strain hardening effect which means strengthening of metal by plastic deformation due to dislocation in the crystal structure of the material. The present study adopts model by Qian et al. [4] which is an improved Graesser and Cozzarelli model [2] and takes into account the strain hardening effect.

Based on the improved Graesser and Cozzarelli model of SMA wire proposed by Qian et al., differential equations for the model are given as follows:

$$\dot{F} = K_0 \left[ \dot{x} - |\dot{x}| \left| \frac{F - B}{B_c} \right|^{(n-1)} \left( \frac{F - B}{B_c} \right) \right] \quad (16)$$

$$\begin{aligned} B = & K_0 \alpha \{ x_{in} + f_T |x|^c \operatorname{erf}(ax) [u(-x\dot{x})] \\ & + f_m [x - x_{mf} \operatorname{sgn}(x)]^m \\ & \times [u(x\dot{x}) [u(|x| - x_{mf})]] \} \end{aligned} \quad (17)$$

where  $F$  is restoring force;  $x$  is relative interstory displacement;  $\dot{x}$  is the relative interstory velocity;  $B_c$  is the force triggering the forward transformation from austenite to martensite phase;  $\dot{F}$  is the time derivative of the restoring force;  $n$  is the constant that controls sharpness of transition between elastic and plastic phases;  $\alpha$  is the constant controlling the slope of stress-strain curve in the inelastic range;  $B$  is the back force;  $f_T$  is the constant to control the type and size of hysteresis;  $c$  is the slope of unloading stress plateau;  $a$  is the constant controlling the amount of elastic recovery during unloading;  $f_m$  and  $m$  are the material constants controlling the martensitic hardening curve, and  $x_{mf}$  is the martensitic finish strain.  $x_{in}$  is the inelastic displacement which is given by

$$x_{in} = x - \frac{F}{K_0} \tag{18}$$

$u()$  is the unit step function, defined as

$$u(x) = \begin{cases} +1, & x \geq 0 \\ 0, & x < 0 \end{cases} \tag{19}$$

$\text{erf}()$  is the error function, defined by

$$\text{erf}(x) = \frac{2}{\sqrt{\pi}} \int_0^x e^{-t^2} dt \tag{20}$$

$\text{sgn}()$  is the signum function, given by

$$f(x) = \text{sgn}(x) = \begin{cases} +1, & x > 0 \\ 0, & x = 0 \\ -1, & x < 0 \end{cases} \tag{21}$$

The parameters used for the SMA damper are:  $K_0 = 940 \text{ N/mm}$ ;  $B_c = 360 \text{ kN}$ ;  $\alpha = 0.01$ ;  $f_T = 0.34$ ;  $c = 0.0001$ ;  $a = 2500$ ;  $n = 5$ ;  $x_{mf} = 0.015$ ;  $f_m = 100,000$ ; and  $m = 3$ . The SMA wires are given a prestrain of 3% for better dissipation of energy.

Six different configurations for damper placement were chosen in this study which are represented in Fig. 1. These configurations were selected according to Heuristic approach, in which various combinations were studied for reduction of responses and dampers were placed in accordance with it. Main criterion for placing the dampers was to reduce overall responses for maximum number of considered earthquakes.

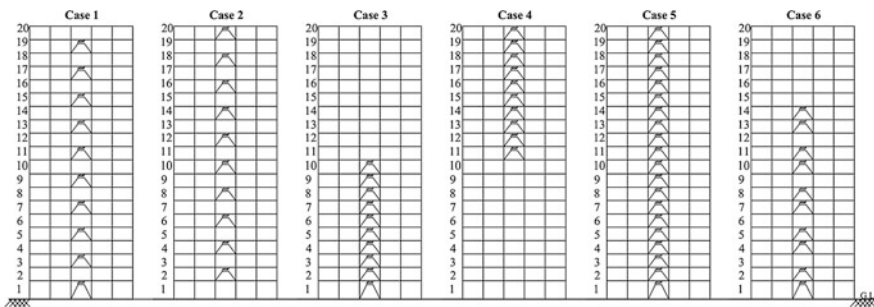


Fig. 1 Different cases for damper placement for 20-story benchmark problem

**Table 1** Percentage reduction in evaluation criteria with number of earthquakes sustained for all six cases

	Case 1			Case 2			Case 3			Case 4			Case 5			Case 6		
	Max (%)	Min (%)	No. of EQ	Max (%)	Min (%)	No. of EQ	Max (%)	Min (%)	No. of EQ	Max (%)	Min (%)	No. of EQ	Max (%)	Min (%)	No. of EQ	Max (%)	Min (%)	No. of EQ
$J_1$	14.5	3.1	4	5.8	3.8	3	10.7	1.8	7	17.6	0.4	3	16.8	11.5	2	10.7	0.1	8
$J_2$	7.4	1.1	6	9.6	0.3	4	4.7	2.4	2	9.5	2.0	3	11.5	1.0	4	6.9	0.6	4
$J_3$	17.1	1.8	9	24.8	0.2	10	27.4	1.0	10	10.0	0.5	9	31.5	0.6	10	26.7	0.9	10
$J_4$	20.5	1.0	2	6.4	0.5	2	21.1	1.9	7	38.7	38.7	1	48.7	48.7	1	25.0	0.9	6
$J_5$	16.2	4.8	9	22.2	0.2	10	11.1	2.0	7	14.1	1.5	8	26.4	1.6	10	10.5	1.0	10
$J_6$	34.6	2.9	10	39.6	3.0	9	31.8	0.3	10	32.4	0.9	10	48.8	7.1	10	31.9	1.7	10
$J_7$	18.5	10.1	8	14.3	5.3	9	10.4	0.5	9	24.1	5.3	7	26.2	7.2	7	14.1	0.3	9
$J_8$	41.6	8.2	2	47.1	5.4	3	28.1	0.2	3	49.6	9.5	2	46.5	23.5	2	33.8	0.7	6
$J_9$	32.6	7.0	2	41.9	9.3	2	25.6	2.1	5	20.9	1.2	3	41.9	18.6	2	34.9	3.1	5
$J_{10}$	25.7	6.5	8	25.7	2.5	7	17.9	1.6	5	33.9	3.5	6	49.1	2.5	6	28.2	1.0	8



**Table 2** Evaluation criteria for Case 6 of SMA damper

Earthquake	El Centro			Hachinohe			Northridge		Kobe		Max
Intensity	0.5	1	1.5	0.5	1	1.5	0.5	1.0	0.5	1.0	
$J_1$	<b>0.971</b>	<b>0.946</b>	<b>0.947</b>	<b>0.910</b>	<b>0.985</b>	<b>0.997</b>	1.079	<b>0.999</b>	1.026	<b>0.893</b>	1.079
$J_2$	1.097	<b>0.982</b>	<b>0.994</b>	1.369	<b>0.969</b>	1.058	1.018	<b>0.931</b>	1.053	1.022	1.369
$J_3$	<b>0.733</b>	<b>0.814</b>	<b>0.929</b>	<b>0.866</b>	<b>0.903</b>	<b>0.936</b>	<b>0.986</b>	<b>0.991</b>	<b>0.969</b>	<b>0.986</b>	<b>0.991</b>
$J_4$	<b>0.839</b>	<b>0.991</b>	<b>0.962</b>	1.048	1.033	1.023	<b>0.938</b>	1.130	<b>0.955</b>	<b>0.750</b>	1.130
$J_5$	<b>0.895</b>	<b>0.942</b>	<b>0.957</b>	<b>0.989</b>	<b>0.965</b>	<b>0.965</b>	<b>0.990</b>	<b>0.989</b>	<b>0.962</b>	<b>0.963</b>	<b>0.990</b>
$J_6$	<b>0.681</b>	<b>0.964</b>	<b>0.983</b>	<b>0.773</b>	<b>0.897</b>	<b>0.927</b>	<b>0.869</b>	<b>0.957</b>	<b>0.943</b>	<b>0.963</b>	<b>0.983</b>
$J_7$	<b>0.872</b>	<b>0.920</b>	<b>0.935</b>	<b>0.936</b>	<b>0.927</b>	<b>0.933</b>	<b>0.944</b>	1.016	<b>0.997</b>	<b>0.859</b>	1.016
$J_8$	–	–	<b>0.826</b>	–	–	<b>0.662</b>	<b>0.799</b>	<b>0.993</b>	<b>0.866</b>	<b>0.965</b>	<b>0.993</b>
$J_9$	–	–	<b>0.651</b>	–	–	<b>0.837</b>	<b>0.958</b>	<b>0.969</b>	<b>0.949</b>	1.000	1.000
$J_{10}$	<b>0.744</b>	<b>0.990</b>	<b>0.949</b>	<b>0.940</b>	<b>0.934</b>	<b>0.926</b>	<b>0.809</b>	1.128	1.147	<b>0.718</b>	1.147
$J_{11}$	0.003	0.003	0.003	0.003	0.003	0.003	0.003	0.003	0.003	0.003	0.003
$J_{12}$	0.089	0.087	0.088	0.066	0.072	0.074	0.095	0.106	0.163	0.140	0.163
$J_{15}$	10										10

### 4 Results from the Simulations

Table 1 presents the percentage reduction in evaluation criteria (minimum and maximum) with number of earthquakes sustained for all six cases. Table 2 presents the evaluation criteria for Case 6. The bold values in this table represent evaluation criteria value less than one, and the particular criteria sustained for that earthquake intensity. Values less than one are desirable.

Graphs presented in Fig. 2 show the time histories and maximum drift ratios for all floors of four earthquakes considered for intensity 1.0. Responses for both: uncontrolled and controlled simulations are shown in Fig. 2.

### 5 Discussions and Conclusions

From the evaluation criteria obtained for the SMA damper for all six cases, it is clear that the Case 6 showed least values of evaluation criteria among all six cases. Case 4 performed the worst among all cases as it made the lower part of the building more stiff giving higher responses to the earthquake. Case 2 reduced peak acceleration effectively than any other case as it provided damping at the top stories. Case 3 reduced the base shear and drift of the structure as it had all the dampers in lower half of the structure.

Case 6 increased the ductility of the structure better than any other case. Energy dissipated from yielding was also reduced in this case. This case also reduced the number of connections going in plastic state. Case 6 reduced the responses of all ten earthquakes considered, for four evaluation criteria as seen in Table 1.

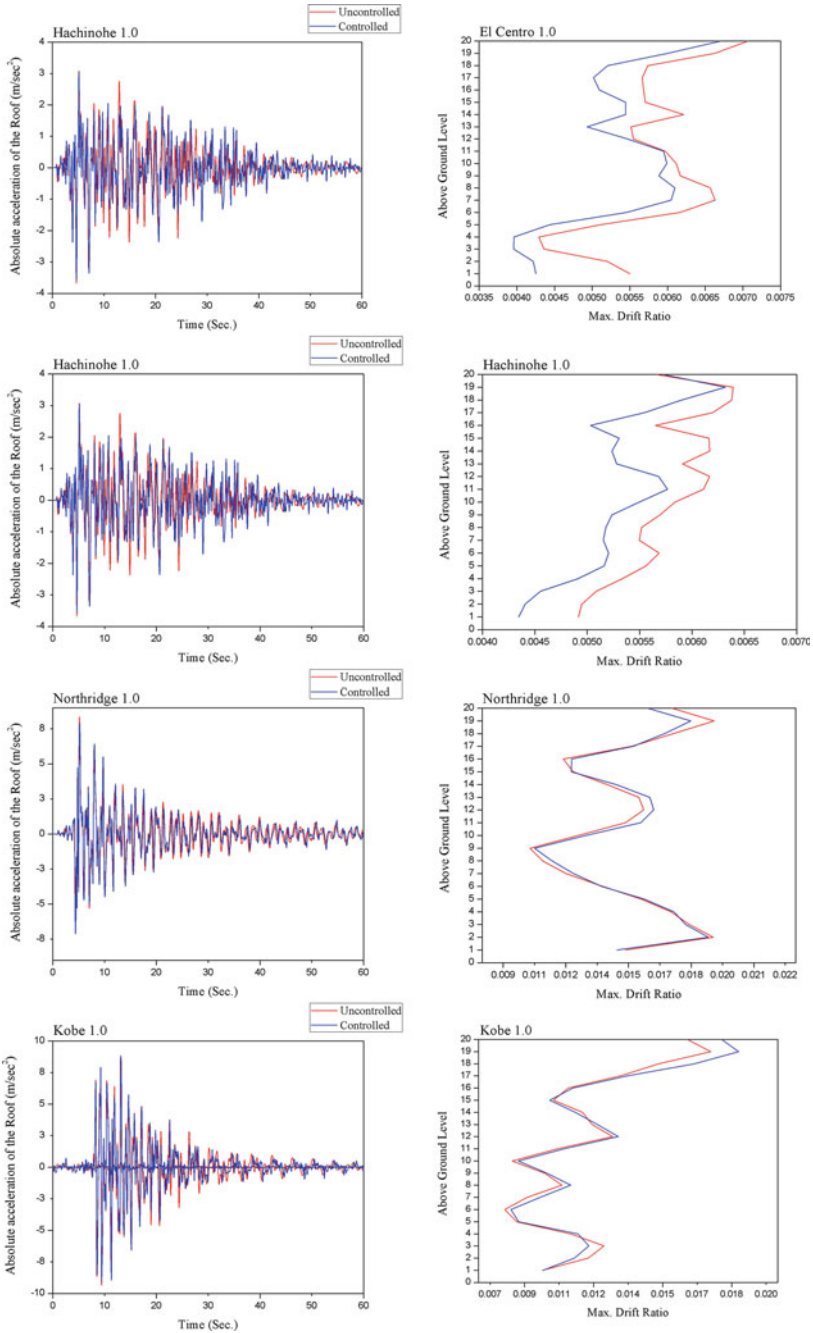


Fig. 2 Time histories and maximum drift ratios for all four earthquakes of intensity 1.0

For the Case 6 evaluation criteria, Peak drift criteria ( $J_1$ ) was reduced by 0.1–10.7% for eight earthquakes; Peak level acceleration ( $J_2$ ) was reduced by 0.6–6.9% for four earthquakes; Peak base shear ( $J_3$ ) was reduced by 0.9–26.7% for all ten earthquakes; Normed drift ( $J_4$ ) was reduced by 0.9–24.2% for six earthquakes; Normed level acceleration ( $J_5$ ) was reduced by 0.5–14% for all ten earthquakes; Normed base shear ( $J_6$ ) was reduced by 1.7–33.5% for all ten earthquakes; Ductility ( $J_7$ ) was reduced by 0.3–14.1% for nine earthquakes; Dissipated energy ( $J_8$ ) was reduced by 0.7–33.8% for six earthquakes; and Plastic connections ( $J_9$ ) was reduced by 3.1–34.9% for five earthquakes; and Normed ductility ( $J_{10}$ ) was reduced by 1–25.4% for eight earthquakes. Strong column and weak beam were used for the structure hence beams would fail first. Beams showed more curvature due to higher acceleration and displacement. More energy was dissipated from higher intensity earthquakes than the lower ones. Responses for the far-field earthquakes El Centro and Hachinohe were controlled better than near-field earthquakes Northridge and Kobe.

Overall, studying all the evaluation criteria it can be concluded that Shape Memory Alloy damper as a passive device can reduce the responses of the structure moderately. It can reduce the base shear effectively for any class of earthquake. Energy dissipation and ductility are increased for most of the cases. Occurrences of number of plastic hinges have been reduced for most of the earthquakes. The amount of energy dissipated through structural yielding is reduced substantially.

## References

1. Ohtori Y, Christenson RE, Spencer BF, Jr., Dyke SJ (2004) Benchmark control problems for seismically excited nonlinear buildings. *J Eng Mech* 130.4:366–385
2. Graesser EJ, Cozzarelli FA (1991) Shape-memory alloys as new materials for aseismic isolation. *J Eng Mech* 117(11):2590–2608
3. Wilde K, Gardoni P, Fujino Y (2000) Base isolation system with shape memory alloy device for elevated highway bridges. *Eng struct* 22(3):222–229
4. Qian H, Li H, Song G, Guo W (2013) Recentring shape memory alloy passive damper for structural vibration control. *Math Probl Eng*

# Inelastic Seismic Behaviour of Asymmetric RC Buildings Using Base Shear and Torque (BST) Surface



Rushikesh M. Raut and Suhasini N. Madhekar

**Abstract** The eccentricity between centre of mass and centre of stiffness produces torsion in asymmetric buildings during earthquakes. In this paper, the inelastic seismic behaviour of asymmetric-plan buildings is studied by using the base shear and torque (BST) surface. BST surface represents all combinations of base shear and torque when applied statically, leading to collapse of the structure. BST surface is a useful tool for the seismic analysis of asymmetrical buildings.

**Keywords** Asymmetric building · BST surface · Inelastic · Seismic

## 1 Introduction

Base shear and torque (BST) surface represents all combinations of base shear and torque when applied statically, leading to collapse of the structure. BST surface is divided into two regions.

**Interior**—combinations of the base shear and torque representing elastic behaviour of the structure.

**Exterior**—containing statically inadmissible base shear and torque combination.

The BST surface is the boundary between these two regions as shown in Fig. 1. All the inelastic action of system takes place on the boundary of this surface. De la Llera and Chopra [1] have presented equations to draw BST surface.

Nineteen number of (One symmetric in plan, six uniaxial asymmetric in plan and twelve biaxial asymmetric in plan) G+3 storey RCC buildings have been analysed using BST surface. The buildings have plan dimensions of 22.5 m × 22.5 m and bay

---

R. M. Raut (✉) · S. N. Madhekar (✉)

Civil Engineering Department, College of Engineering Pune, Shivajinagar,  
Pune 411005, Maharashtra, India  
e-mail: rushikeshr2@gmail.com

S. N. Madhekar

e-mail: suhasini.madhekar@gmail.com

© Springer Nature Singapore Pte Ltd. 2019

A. Rama Mohan Rao and K. Ramanjaneyulu (eds.), *Recent Advances in Structural Engineering, Volume 2*, Lecture Notes in Civil Engineering 12,  
[https://doi.org/10.1007/978-981-13-0365-4\\_29](https://doi.org/10.1007/978-981-13-0365-4_29)

**Fig. 1** BST surface showing interior and exterior regions

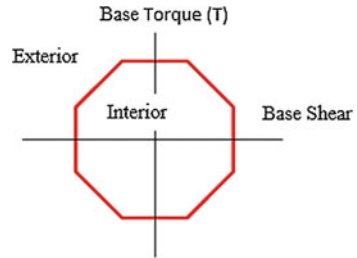
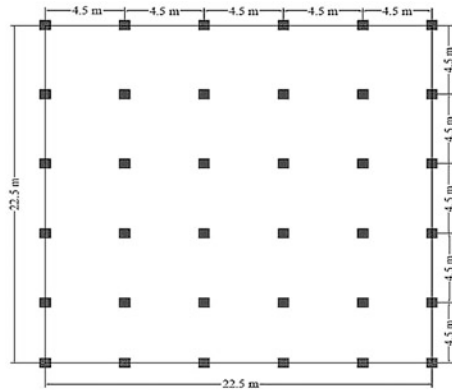


**Fig. 2** Plan for typical floor of G+3 storey RCC symmetric building



width of 4.5 m. as shown in Fig. 2. The RCC buildings have been designed as per IS 456 (2000)

## 2 Developing the BST Surface

BST surface gives the ultimate value for base shear and torque combination; thus, the ultimate shear strength of resisting planes is required. To draw the BST surface, following equations are given by De la Llera and Chopra [2]. The equations are as follows,

$$\begin{aligned}
 X_1 &= V_{yo}, & Y_1 &= V_{yo} X_p + T_1 (1 - \hat{V}_x) \\
 X_2 &= V_{yu} + V_{yc}, & Y_2 &= T_o - T_1 \hat{V}_x \\
 X_3 &= V_{yu} - V_{yc}, & Y_3 &= T_o - T_1 \hat{V}_x \\
 X_4 &= -V_{yo}, & Y_4 &= -V_{yo} X_p + T_1 (1 - \hat{V}_x) \\
 X_5 &= -X_1, & Y_5 &= -Y_1 \\
 X_6 &= -X_2, & Y_6 &= -Y_2 \\
 X_7 &= -X_3, & Y_7 &= -Y_3 \\
 X_8 &= -X_4, & Y_8 &= -Y_4
 \end{aligned} \tag{1}$$

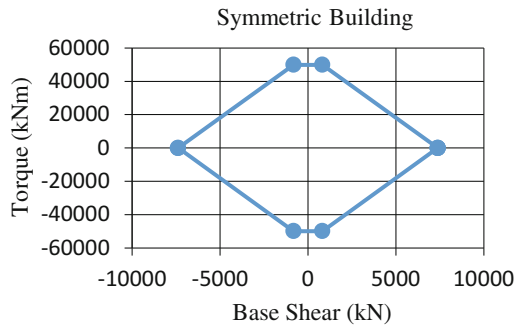
where

1.  $\widehat{V}_x = V_x/V_{xo}$  is the normalized storey shear in the  $x$ -direction;  $V_{xo} = \sum_{i=1}^M f_x^{(i)}$  is the lateral capacity of the storey in the  $x$ -direction;  $f_x^{(i)}$  is the capacity of the  $i$ th resisting plane in  $x$ -direction, and  $M$  is the number of resisting planes in  $x$ -direction.
2.  $V_{yo} = \sum_{i=1}^N f_y^{(i)}$  is the lateral capacity of the storey in the  $y$ -direction;  $f_y^{(i)}$  is the capacity of the  $i$ th resisting plane in  $y$ -direction, and  $N$  is the number of resisting planes in  $y$ -direction.
3.  $V_{yc}$  is the capacity of the resisting planes in the  $y$ -direction passing through the centre of mass (C. M.) of the system.
4.  $T_o = \sum_{i=1}^N |f_y^{(i)} x^{(i)}| + \sum_{i=1}^M |f_x^{(i)} y^{(i)}|$  is the torsional capacity of the system.
5.  $T_1 = \sum_{i=1}^M f_x^{(i)} y^{(i)}$  is the torque provided by the resisting planes in the orthogonal direction.
6.  $X_p = \sum_{i=1}^N f_y^{(i)} x^{(i)} / V_{yo}$  is the strength eccentricity or first moment of strength.
7.  $V_{yu} = \sum_{\substack{i=1 \\ i \neq 2}}^N f_y^{(i)} x^{(i)} / |x^{(i)}|$  is donated as strength imbalance in the storey.

### 2.1 BST Surface for Symmetric RCC Building in Plan

BST surface for symmetric G+3 storey building is drawn by using Eq. (1). The building has plan dimensions of 22.5 m × 22.5 m and bay width of 4.5 m and its BST surface is as shown in Fig. 3. The building has been designed as per IS 456 (2000). The column sizes are in the range of 400 mm × 400 mm to 550 mm × 550 mm after designing. For achieving symmetry in both  $X$ - and  $Y$ -directions, the columns are taken as square in size of dimensions 600 mm × 600 mm. The percentage reinforcement provided in all columns is 0.8%. Hence for 0.8% reinforcement and  $M 25$  grade concrete, shear stress is worked out as 0.57 N/mm<sup>2</sup> (IS 456, 2000). Shear strength of one column is calculated as  $f = 0.57 \times 600 \times 600 \times 10^{-3} = 205.2$  kN.

**Fig. 3** BST surface for typical floor of G+3 storey RCC symmetric building



## 2.2 *BST Surface for Uniaxial Asymmetric RCC Building in Plan*

Six asymmetric buildings are considered for the analysis. The asymmetry is introduced by changing the shear strength of columns by gradually increasing the sizes of some columns from 600 mm × 600 mm to 900 mm × 900 mm.

1. The asymmetric building No. 1 has five lines of columns with column sizes of 600 mm × 600 mm (not selected columns in Fig. 4) and remaining one line of columns with column sizes of 700 mm × 700 mm (selected columns in Fig. 4). The Centre of Mass (C. M.) is at (11.25, 11.25 m). Centre of Stiffness (C. S.) is at (12.65, 11.25 m); thus, percentage asymmetry produced is 6.22%. The shear strength of columns of size 700 mm × 700 mm is calculated similar to that of column size 600 mm × 600 mm;  $f = 0.57 \times 700 \times 700 \times 10^{-3} = 279.3$  kN. The BST surface for this building is shown in Fig. 5.
2. The considered asymmetric building No. 2 has four lines of columns with column sizes of 600 mm × 600 mm (not selected columns in Fig. 6) and remaining two lines of columns with column sizes of 700 mm × 700 mm (selected columns in Fig. 6); hence, percentage asymmetry produced is 8.85%. The BST surface for this building is shown in Fig. 7.

In the similar way, column dimensions are configured for columns of dimensions 800 mm × 800 mm and 900 mm × 900 mm. All uniaxial asymmetric buildings from building No. 3 to building No. 6 have been analysed using BST surface. The BST surface of each uniaxial asymmetric building (No. 1 to No. 6) is superimposed on BST surface of symmetric building (Fig. 3) as shown in Fig. 8.

**Fig. 4** Plan for typical floor of G+3 storey RCC uniaxial asymmetric building No. 1 with 6.22% asymmetry in plan

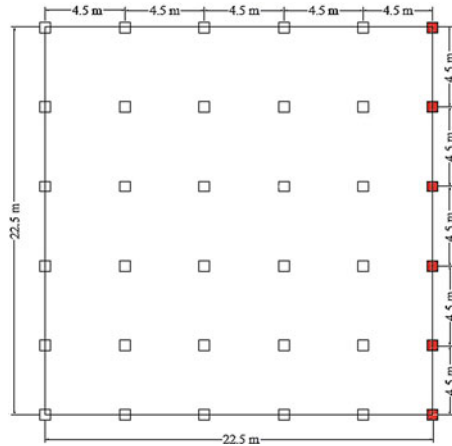


**Fig. 5** BST surface for typical storey of G+3 storey RCC uniaxial asymmetric building No. 1 with 6.22% asymmetry in plan

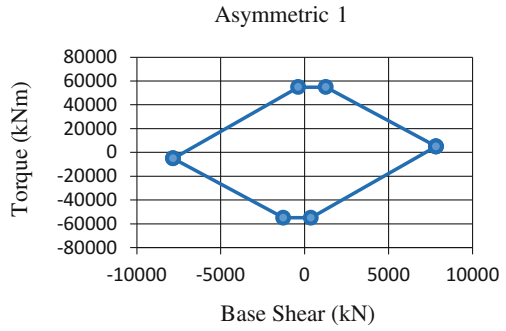


**Fig. 6** Plan for typical floor of G+3 storey RCC uniaxial asymmetric building No. 2 with 8.85% asymmetry in plan

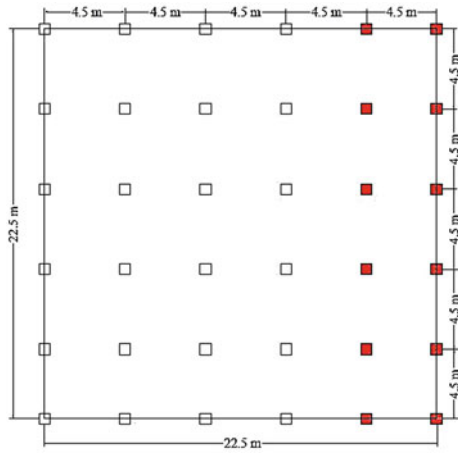


**Fig. 7** BST surface for typical storey of G+3 storey RCC uniaxial asymmetric building No. 2 with 8.85% asymmetry in plan

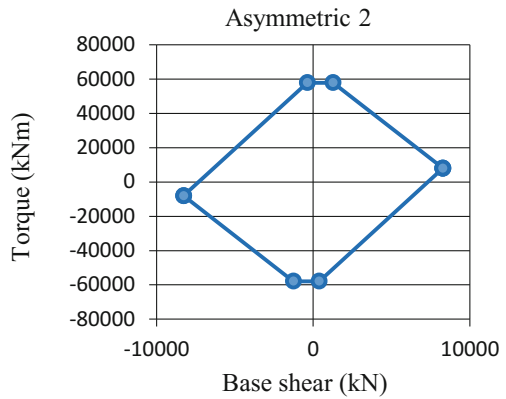
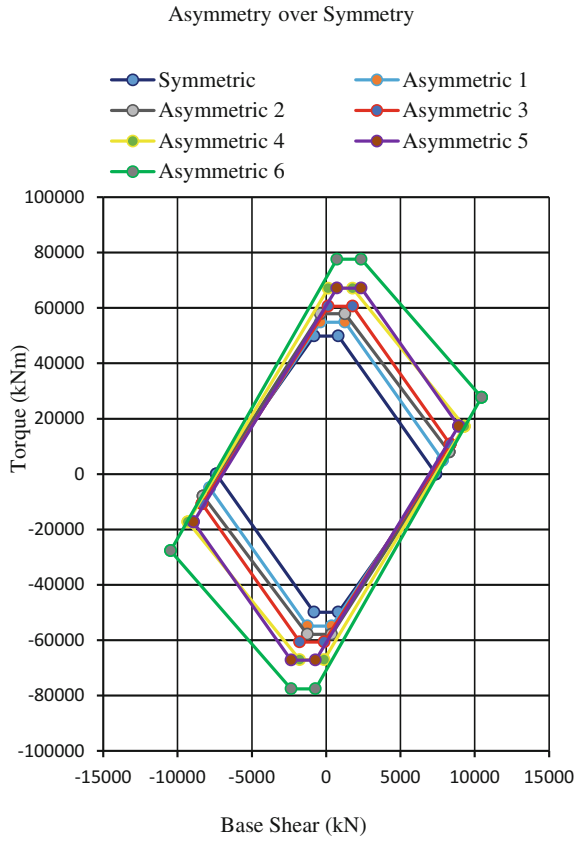




**Fig. 8** BST surface for all uniaxial asymmetric RCC buildings over symmetric building in plan



### 2.3 *BST Surface for Biaxial Asymmetric RCC Building in Plan*

Twelve G+3 storey biaxial asymmetric buildings in plan are considered for the analysis. The asymmetry is introduced by changing the shear strength of columns by gradually increasing the sizes of some columns from 600 mm × 600 mm to 900 mm × 900 mm.

1. The biaxial asymmetric building No. 1 is shown in Fig. 9 with column sizes of 600 mm × 600 mm (not selected columns in Fig. 9) and column sizes of 700 mm × 700 mm (selected columns in Fig. 9); thus, percentage asymmetry produced in X- and Y-directions, respectively, is 4.70% and 4.70%. The BST surface for this building is shown in Fig. 10.
2. The biaxial asymmetric building No. 2 is shown in Fig. 11 with column sizes of 600 mm × 600 mm (not selected columns in Fig. 11) and column sizes of 700 mm × 700 mm (selected columns in Fig. 11); thus, percentage asymmetry

**Fig. 9** Plan for typical floor of G+3 storey RCC biaxial asymmetric building No. 1 with 4.7% asymmetry in plan in each direction

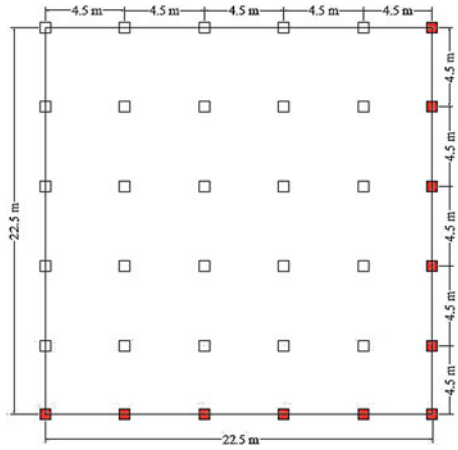


**Fig. 10** BST surface for typical storey of G+3 storey RCC biaxial asymmetric building No. 1 with 4.70% asymmetry in plan in each direction

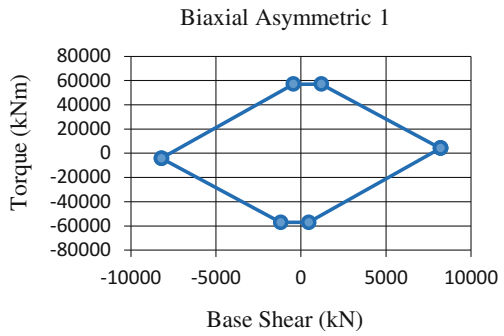


**Fig. 11** Plan for typical floor of G+3 storey RCC biaxial asymmetric building No. 2 with 5.14% asymmetry in plan in each direction

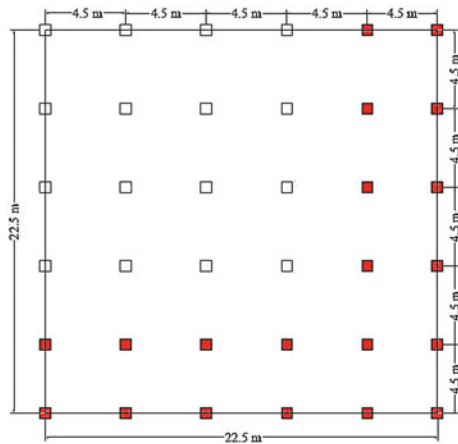


**Fig. 12** BST surface for typical storey of G+3 storey RCC biaxial asymmetric building No. 2 with 5.14% asymmetry in plan in each direction

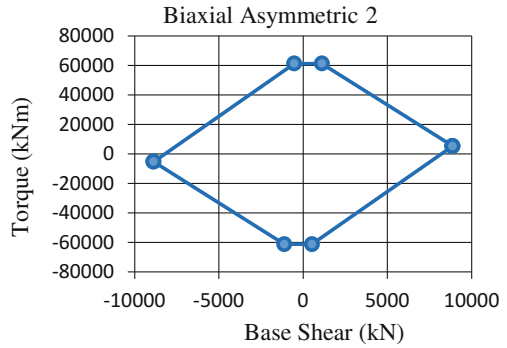
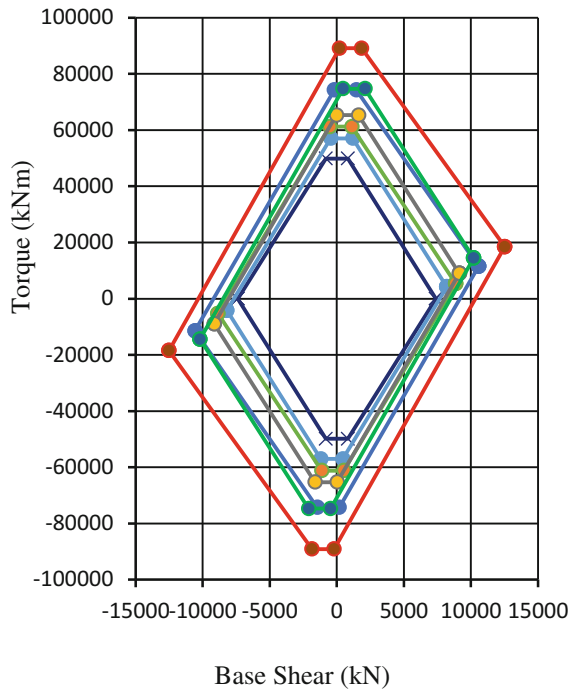


**Fig. 13** BST surface for all biaxial asymmetric RCC buildings over symmetric building in plan in each direction

Asymmetry over Symmetry

- ×— Symmetry
- Biaxial Asymmetry 1
- Biaxial Asymmetry 2
- Biaxial Asymmetry 3
- Biaxial Asymmetry 4
- Biaxial Asymmetry 5



produced in *X*- and *Y*-directions, respectively, is 5.14% and 5.14%. The BST surface for this building is shown in Fig. 12.

In the similar way, column dimensions are configured for columns of dimensions 800 mm × 800 mm and 900 mm × 900 mm. All biaxial asymmetric buildings from building No. 3 to building No. 6 have been analysed using BST surface. The BST surface of each biaxial asymmetric buildings No. 1 to No. 6 is superimposed on BST surface of symmetric building (Fig. 3) as shown in Fig. 13.

3. The biaxial asymmetric building No. 7 is shown in Fig. 14 with column sizes of 600 mm × 600 mm (not selected columns in Fig. 14) and column sizes of 700 mm × 700 mm (selected columns in Fig. 14); thus, percentage asymmetry produced in *X*- and *Y*-directions, respectively, is 4.70%, 4.70%. BST surface for this building is shown in Fig. 15.
4. The biaxial asymmetric building No. 8 is shown in Fig. 16 with column sizes of 600 mm × 600 mm (not selected columns in Fig. 16) and column sizes of 700 mm × 700 mm (selected columns in Fig. 16); thus, percentage asymmetry produced in *X*- and *Y*-directions, respectively, is 5.14%, 5.14%. BST surface for this building is shown in Fig. 17.

**Fig. 14** Plan for typical floor of G+3 storey RCC biaxial asymmetric building No. 7 with 4.7% asymmetry in plan in each direction

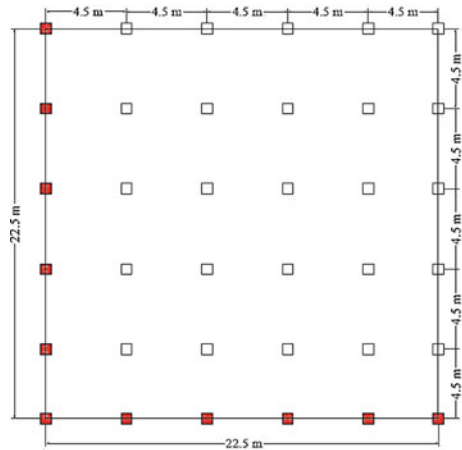


**Fig. 15** BST surface for typical storey of G+3 storey RCC biaxial asymmetric building No. 7 with 4.70% asymmetry in plan in each direction

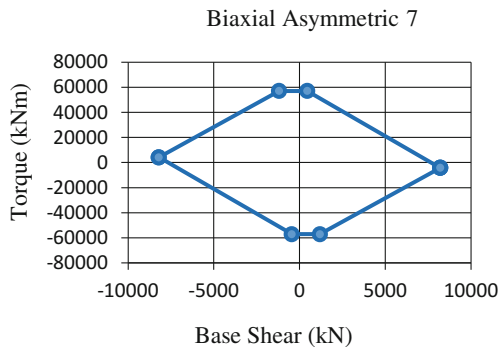


**Fig. 16** Plan for typical floor of G+3 storey RCC biaxial asymmetric building No. 8 with 5.14% asymmetry in plan in each direction

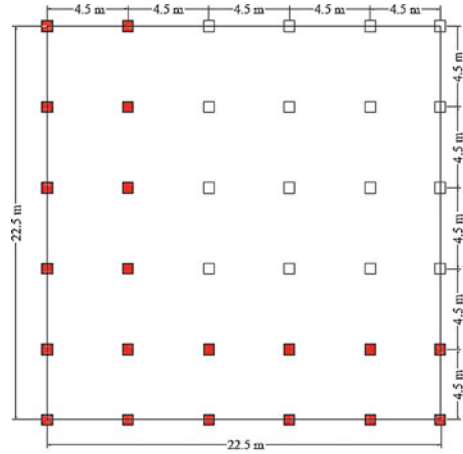
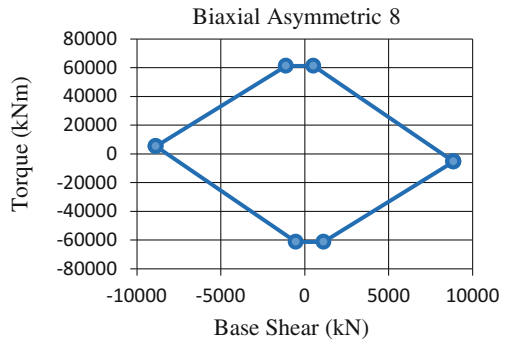


**Fig. 17** BST surface for typical storey of G+3 storey RCC biaxial asymmetric building No. 8 with 5.14% asymmetry in plan in each direction

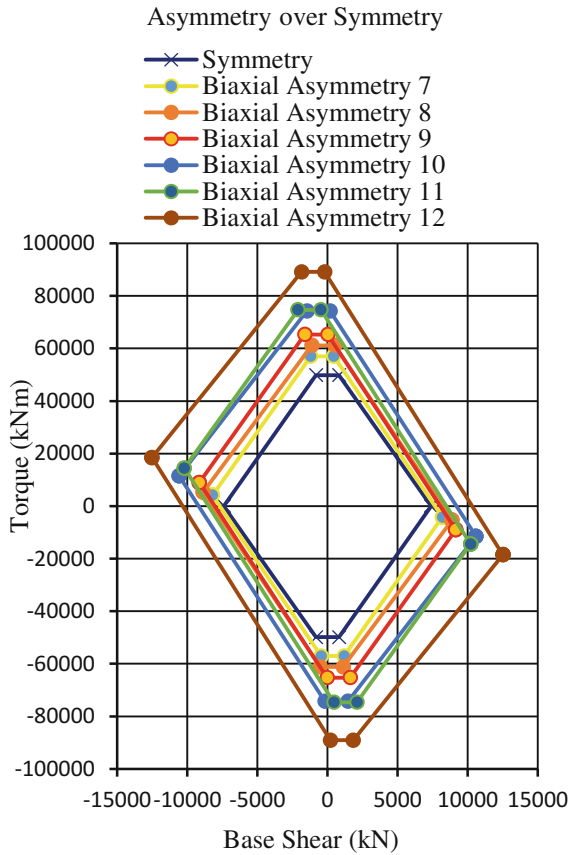


In the similar way, column dimensions are configured for columns of dimensions 800 mm × 800 mm and 900 mm × 900 mm. All biaxial asymmetric buildings from building No. 9 to building No. 12 have been analysed using BST surface. The BST surface of each biaxial asymmetric building No. 7 to No. 12 is superimposed on BST surface of symmetric building (Fig. 3) as shown in Fig. 18.

### 3 Conclusions

1. BST surface gives ultimate values of base shear and torque which give an approximate perception to the designer about strength of building with respect to base shear and torque.
2. As the asymmetry in building increases, the orientation of BST surface changed making it skewed, compared to BST surface of symmetric building.

**Fig. 18** BST surface for all biaxial asymmetric RCC buildings over symmetric building in plan



3. The orientation of BST surface for asymmetric buildings explains that building rotates about those columns, which have higher strength than other columns.
4. Shape of BST surface shows whether building is symmetric or not.
5. Base shear values from linear static or dynamic analysis can be used to find ultimate value of torque by plotting that base shear value on BST surface.
6. By simply calculating the shear strength of building columns, behaviour of any building can be understood by drawing the BST surface.
7. Even without static or dynamic nonlinear analysis, it is possible to compare the expected seismic performance of different structural configurations based on BST surface.

## References

1. De la Llera JC, Chopra AK (1995) Understanding the inelastic seismic behaviour of asymmetric-plan buildings. *Earthq Eng Struct Dyn* 24:549–572
2. De la Llera JC, Chopra AK (1995) A simplified model for analysis and design of asymmetric-plan buildings. *Earthq Eng Struct Dyn* 24:573–594

# Seismic Retrofitting Using the Concept of Coupling Two Adjacent Buildings



M. Abdeddaim, A. Ounis, S. D. Bharti and M. K. Shrimali

**Abstract** Among various retrofitting strategies, use of semi-active control for retrofitting a building structure has gained momentum in recent years. One of the techniques for such retrofitting is to connect a weaker building to an adjacent stronger building by semi-active devices, so that performances of weaker building are significantly improved for seismic forces. In this paper, a ten-storey weaker building is connected to an adjacent stronger building using magneto-rheological (MR) dampers, for primarily improving the performance of the weaker building in terms of displacement, drift and base shear. The results show that there exists a fundamental frequency ratio between the two buildings for which maximum control of the weaker building response takes place with no penalty on the stronger building. There exists also a fundamental frequency ratio where control of the weaker building response is achieved at the expense of the amplification in the stronger building.

**Keywords** Seismic retrofitting · Weaker building · Coupled buildings  
Magneto-rheological (MR) damper

---

M. Abdeddaim · A. Ounis (✉)  
Department of Civil Engineering and Hydraulics, Biskra University, LARGHYDE  
Laboratory, BP 415 RP, 7000 Biskra, Algeria  
e-mail: [ounisafi@gmail.com](mailto:ounisafi@gmail.com)

M. Abdeddaim  
e-mail: [abdeddaim\\_mms@yahoo.fr](mailto:abdeddaim_mms@yahoo.fr)

S. D. Bharti · M. K. Shrimali  
National Center for Disaster Mitigation and Management, Malaviya National Institute  
of Technology, Jaipur 302017, Rajasthan, India  
e-mail: [sdbharti@gmail.com](mailto:sdbharti@gmail.com)

M. K. Shrimali  
e-mail: [shrimali\\_mk@yahoo.co.uk](mailto:shrimali_mk@yahoo.co.uk)



## 1 Introduction

During the lifetime of a building, it can be exposed to several events before the earthquake occurs. Such pre-earthquake events can make the building weaker as compared to a newly built building; such events can be fatigue, previous earthquakes or corrosion. The retrofitting of weaker buildings is an important process especially in high seismic activity zones; this can be a temporary solution to avoid further damages or a permanent solution to upgrade the seismic performance up to a certain level depending on the degree of weakness in the building. The dynamic properties of the damaged building can be greatly changed, thereby generating large displacement, which were not envisaged during the design stage.

A lot of seismic retrofitting technics were introduced during recent years; the use of control devices is one of the most widespread methods for seismic retrofitting. They are basically three types of control devices, which are active, passive and semi-active [1]. Any combination between those three types will be named as hybrid control [2]. The principal aim of those retrofitting technics is to upgrade the behaviour of existing buildings to satisfy new seismic code requirements. Passive devices were introduced for seismic retrofitting in the early 1990s [3]. Passive devices do not need external energy to develop the control force, and it never destabilizes the structure. This motivated researchers to give more importance to this new retrofitting device [4–9]. However, they have low adaptability to change of external loading conditions or usage patterns used in their design. Active control devices are very adaptive different to load cases and usage patterns [10–12]. However, the external energy consumption is still one of the major problems of this kind of devices. This leads other researchers to use semi-active devices that have the advantage of combining passive and active characteristics; those devices use a small source of energy that can be supplied by a battery, avoiding any problem in the case of power cut [13]. Magneto-rheological (MR) dampers are considered as semi-active devices and are widely used in structural vibration control in both civil and mechanical fields [14–16].

The semi-active coupled building strategy is a new control strategy introduced during recent years. The main idea behind this strategy is to couple two or more adjacent buildings using a number of semi-active magneto-rheological (MR) dampers to reduce the response of the coupled system. The investigations of such control strategies were conducted by many researchers for reducing the whipping effects [17] and also for reducing the seismic responses of different height, coupled buildings [18–20]. The coupling strategy was also investigated for pounding reduction between adjacent coupled buildings [21].

All the researches published on coupled buildings using a semi-active device were focusing on response reduction of strong coupled buildings. None of the studies cited previously examined the case of weak buildings, especially for retrofitting a weak building by coupling it with an adjacent stronger building. In this paper, the efficiency of coupling strategy using MR damper is investigated for the retrofitting of a weak building connected to a strong building.

## 2 Dynamic Modelling of the Coupled System

It is assumed that the controlled responses of both structures remain in the elastic range. The governing equation of motion of the coupled system shown in Fig. 1 is expressed as:

$$[M]\{\ddot{x}\} + [C_d]\{\dot{x}\} + [K]\{x\} = [\Gamma]\{f_m\} - [M][r]\{\ddot{x}_g\} \tag{1}$$

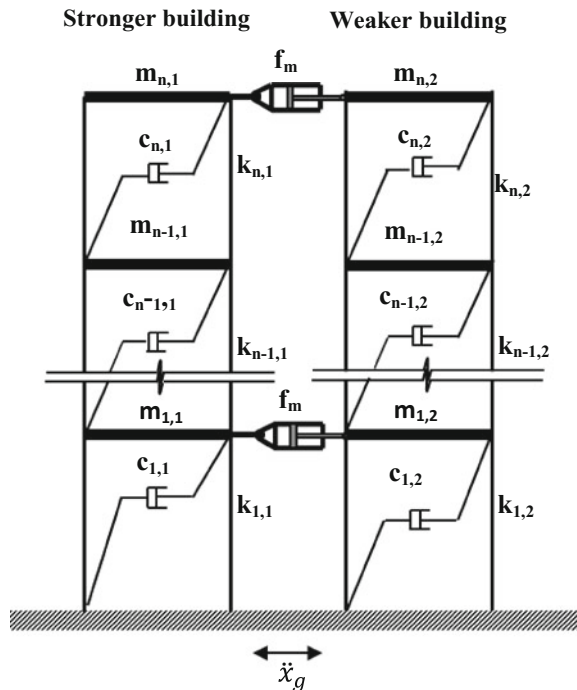
where  $M$ ,  $K$  and  $C_d$ , are mass, stiffness and damping matrices of the coupled system;  $f_m$  is the vector of the input force produced by the MR damper;  $\Gamma$  is the damper location matrix which duly takes into account the control force applied to the buildings;  $r$  is an influence coefficient vector which contains elements equal to unity;  $\ddot{x}_g$  is the ground acceleration and  $\ddot{x}$ ,  $\dot{x}$  and  $x$  are, respectively, the system acceleration, velocity and displacement vectors.

The governing Eq. (1) can be written in state-space form as:

$$\{\dot{z}\} = [A]\{z\} + [B]\{u\} \tag{2}$$

$$\{y\} = [C]\{z\} + [D]\{u\} \tag{3}$$

**Fig. 1** Dynamic modelling of coupled system



## 2.1 Dynamic Model of MR Damper

In this study, phenomenological model proposed by Spencer et al. is modelled in MATLAB to simulate the dynamic behaviour of MR damper based on the Bouc–Wen modified model [22]. The equations governing the force predicted by this model are:

$$f = c_1 \dot{y} + k_1(x - x_0) \quad (4)$$

$$\dot{y} = \frac{1}{(c_1 + c_0)} + (\alpha z + c_0 \dot{x} + k_0(x - y)) \quad (5)$$

$$\dot{z} = -\gamma |\dot{x} - \dot{y}| z |z|^{n-1} - \beta (\dot{x} - \dot{y}) |z|^n + A(\dot{x} - \dot{y}) \quad (6)$$

$$\alpha = \alpha_a + \alpha_b u \quad (7)$$

$$c_1 = c_{1a} + c_{1b} u \quad (8)$$

$$c_0 = c_{0a} + c_{0b} u \quad (9)$$

$$\dot{u} = -\eta(u - v) \quad (10)$$

In Eqs. (4)–(10), the accumulator stiffness is represented by  $k_1$ , and the viscous damping observed at large and low velocities is represented by  $c_0$  and  $c_1$ , respectively;  $k_0$  is present to control the stiffness at large velocities; and  $x_0$  is the initial displacement of spring  $k_1$  associated with the nominal damper force due to the accumulator;  $\gamma$ ,  $\beta$  and  $A$  are hysteresis parameters for the yield element;  $\alpha$  is the evolutionary coefficient. Equation (10) represents a first-order filter used to simulate rheological equilibrium and driving the electromagnet in the MR damper, where the force is dependent on the voltage applied to the current driver in Eqs. (7)–(9).

## 3 Numerical Study

A system of two adjacent buildings is considered, and each building has ten storeys and considered as a shear building. One building is stronger, and the other is assumed to be weaker; reduced stiffness of the weaker building is uniform along the height. Both structures remain in the elastic range during the vibrations. For this study, two cases of stronger building are considered: one is flexible, and the second one is rigid. For both cases, stiffness remains the same but masses vary. Three cases of weaker building are considered. The weaker buildings have reduced stiffness compared to strong building. Three reductions in stiffness for the weaker building are considered, namely 40, 30 and 20%. A stiffness proportional damping is assumed for both buildings with the damping ratio equal to 5%. Table 1 shows the natural frequencies of the stronger and weaker buildings, respectively.

**Table 1** Natural frequencies of the stronger and weaker buildings

Frequency (Hz)	Stronger building		Weaker building		
	Flexible	Rigid	40% weaker	30% weaker	20% weaker
$f_1$	1.00	1.35	0.77	0.83	0.89
$f_2$	2.98	4.02	2.30	2.49	2.66
$f_3$	4.88	6.59	3.78	4.08	4.37
$f_4$	6.67	8.99	5.16	5.58	5.96
$f_5$	8.29	11.1	6.42	6.93	7.41

The two buildings were coupled using MR dampers installed at different locations (Fig. 1). Three damper locations are investigated as (i) one damper used at the top floor, (ii) three dampers used, at the first, middle and top floors and (iii) five dampers used, at the first, third, fifth, seventh and top floors. The MR dampers are driven by a passive control strategy.

The two buildings were subjected to Northridge earthquake record, 1994, with the PGA scaled to 0.2 g. The numerical analysis was performed using a MATLAB Simulink diagram, and the equation of motion was solved using the state-space toolbox, based on Runge–Kutta solver. Six study cases are considered in order to create different ratios of fundamental periods (stronger/weaker defined by  $\delta$ ):

- Case I: weaker building (40% stiffness loss) coupled with stronger flexible building ( $\delta = 1.29$ ),
- Case II: weaker building (40% stiffness loss) coupled with stronger rigid building ( $\delta = 1.75$ ),
- Case III: weaker building (30% stiffness loss) coupled with stronger flexible building ( $\delta = 1.20$ ),
- Case IV: weaker building (30% stiffness loss) coupled with stronger rigid building ( $\delta = 1.62$ ),
- Case V: weaker building (20% stiffness loss) coupled with stronger flexible building ( $\delta = 1.12$ ),
- Case VI: weaker building (20% stiffness loss) coupled with stronger rigid building ( $\delta = 1.51$ ).

The responses investigated are the maximum top floor displacement ( $\Delta_{\max}$ ), the maximum base shear ( $V_{\text{base}}$ ) and the maximum drift ( $D_{\max}$ ). The percentage variations in responses quantities of interest with the frequency ratio for different cases are shown in Figs. 2, 3 and 4.

From the Figs. 2, 3 and 4, it is observed that the maximum response reduction of the weaker building can be achieved for a particular response quantity of interest at a particular frequency ratio. However, higher reductions in responses are obtained at relatively higher frequency ratios. Further, it is observed that for certain frequency ratios, the reduction in response of the weaker building is obtained at the expense of response amplification in the stronger building. It is also worth noting

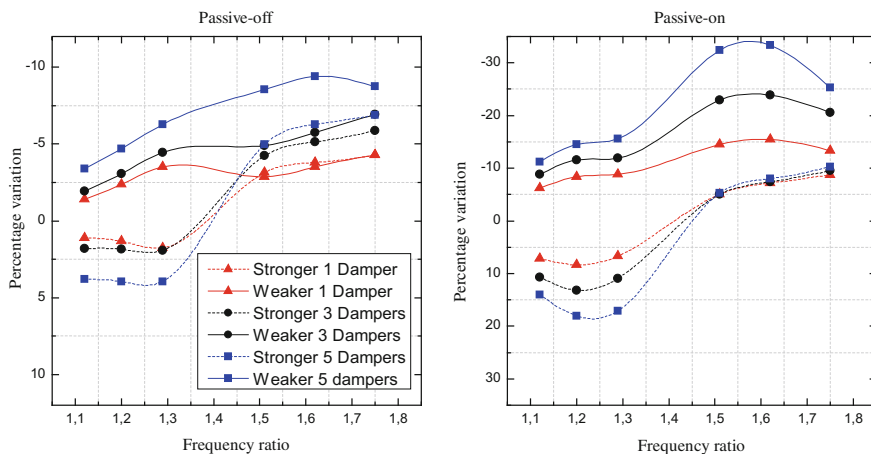


Fig. 2 Percentage variation in ( $\Delta_{max}$ ) with respect to frequency ratio under Northridge earthquake, 1994

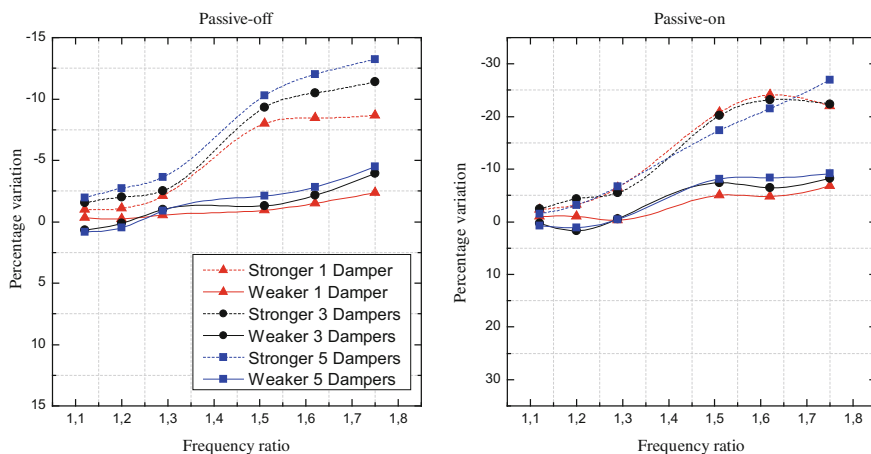
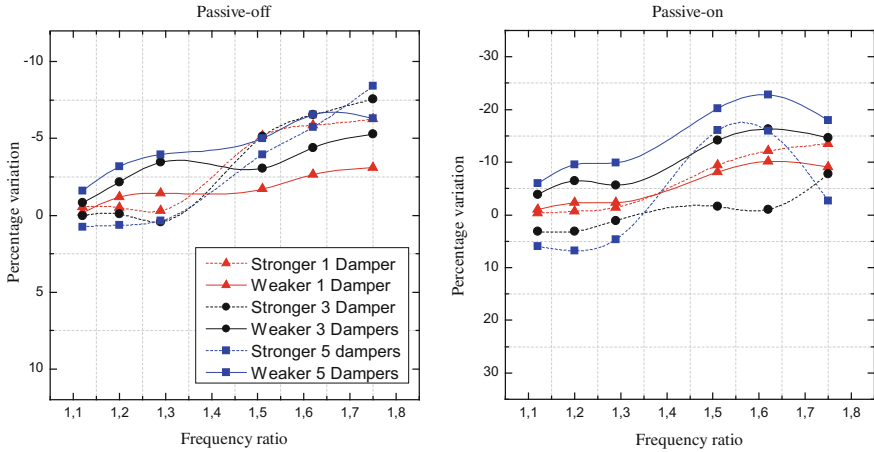


Fig. 3 Percentage variation ( $V_{base}$ ) with respect to frequency ratio under Northridge earthquake, 1994

that, for frequency ratios at which optimum response reduction for weaker building takes place, a reduction in response of stronger building is also attained, nonetheless small it may be.

It is observed from the figures that out of the three responses quantities of interest, the maximum reduction in base shear response is minimal for the weaker building. The corresponding reduction in the base shear of the stronger building is always more than the weaker building.



**Fig. 4** Percentage variation in ( $D_{max}$ ) with respect to frequency ratio under Northridge earthquake, 1994

For the reduction in maximum drift, the pattern of variation remains the same as that of the displacement; the maximum reduction in response in the weaker building is always more, compared to that of the stronger building.

The number of dampers used to couple the two buildings also has significant effect on the reduction of response for the weaker building; better response reduction for weaker building is obtained with greater number of dampers.

The reason for relatively less reduction, even amplification, of response of the stronger building for certain frequency ratios is that it is stiffer than the weaker one. As a result, the weaker building shares some stiffness of the stronger building due to the coupling effect and, thereby, undergoes less vibration compared to the uncoupled state of vibration. Moreover, the MR dampers as connectors between the two buildings dissipate seismic energy leading to less energy input due to the excitation, and hence, less vibration of the buildings takes place. Consequently, the weaker building always has reduction in the response quantities. On the other hand, there is a loss of stiffness in the stronger building due to sharing effect making it more flexible, and therefore, its response increases compared to the uncoupled state of vibration. However, there is a counteracting effect because of the dissipation of energy in the MR dampers. The net result is to decrease the reduction of response, and if the stronger building is flexible, this may even amplify the response rather than controlling it.

## 4 Conclusion

The effectiveness of coupling weaker building with a stronger building is investigated for retrofitting the weaker building. The two buildings are coupled using different numbers of MR dampers. It is observed that the coupling strategy is very effective in retrofitting weaker building in terms of displacement, base shear and drift responses. The coupling strategy is also effective in reducing the possibility of pounding between two adjacent buildings. Results of the numerical study lead to the following conclusions:

- Coupling a stronger building with a weaker building can be very effective for retrofitting the weaker building; knowing the ratio of the fundamental frequency between the two buildings, a rational decision can be made whether coupling strategy would be effective.
- In general, it is found that coupling a weaker building with a rigid stronger building decreases the response of both the weaker and stronger buildings, while coupling a weaker building with a flexible stronger building decreases the response of the weaker building at the expense of the increase in response of the stronger building; there exists a fundamental frequency ratio between the two buildings that provides the optimal results.

## References

1. Fisco N, Adeli H (2011) Smart structures: part I—active and semi-active control. *Sci Iranica* 18(3):275–284
2. Fisco N, Adeli H (2011) Smart structures: part II—hybrid control systems and control strategies. *Sci Iranica* 18(3):285–295
3. Constantinou MC, Symans M (1992) Experimental and analytical investigation of seismic response of structures with supplemental fluid viscous dampers. National Center for Earthquake Engineering Research
4. Zhang R-H, Soong T (1992) Seismic design of viscoelastic dampers for structural applications. *J Struct Eng* 118(5):1375–1392
5. Wu B, Ou J-P, Soong T (1997) Optimal placement of energy dissipation devices for three-dimensional structures. *Eng Struct* 19(2):113–125
6. Lopez Garcia D, Soong T (2002) Efficiency of a simple approach to damper allocation in MDOF structures. *J Struct Control* 9(1):19–30
7. Lavan O, Amir O (2014) Simultaneous topology and sizing optimization of viscous dampers in seismic retrofitting of 3D irregular frame structures. *Earthq Eng Struct Dyn* 43(9): 1325–1342
8. Lavan O (2015) Optimal design of viscous dampers and their supporting members for the seismic retrofitting of 3D irregular frame structures. *J Struct Eng* 04015026
9. Lavan O (2015) A methodology for the integrated seismic design of nonlinear buildings with supplemental damping. *Struct Control Health Monit* 22(3):484–499
10. Adeli H, Saleh A (1997) Optimal control of adaptive/smart bridge structures. *J Struct Eng* 123 (2):218–226

11. Kim H, Adeli H (2004) Hybrid feedback-least mean square algorithm for structural control. *J Struct Eng* 130(1):120–127
12. Hochrainer MJ (2015) Active tuned liquid column gas damper in structural control. In: *Dynamics of civil structures*, vol 2. Springer, Berlin, pp 467–473
13. Symans MD, Constantinou MC (1999) Semi-active control systems for seismic protection of structures: a state-of-the-art review. *Eng Struct* 21(6):469–487
14. Dyke S et al (1998) An experimental study of MR dampers for seismic protection. *Smart Mater Struct* 7(5):693
15. Yang G et al (2002) Large-scale MR fluid dampers: modeling and dynamic performance considerations. *Eng Struct* 24(3):309–323
16. Choi KM et al (2004) Semi-active fuzzy control for seismic response reduction using magnetorheological dampers. *Earthq Eng Struct Dyn* 33(6):723–736
17. Qu W, Xu Y (2001) Semi-active control of seismic response of tall buildings with podium structure using ER/MR dampers. *Struct Des Tall Build* 10(3):179–192
18. Bharti S, Dumne S, Shrimali M (2010) Seismic response analysis of adjacent buildings connected with MR dampers. *Eng Struct* 32(8):2122–2133
19. Mevada SV, Jangid R (2012) Seismic response of torsionally coupled system with semi-active variable dampers. *J Earthq Eng* 16(7):1043–1054
20. Shrimali M, Bharti S, Dumne S (2015) Seismic response analysis of coupled building involving MR damper and elastomeric base isolation. *Ain Shams Eng J* 6(2):457–470
21. Abdeddaim M et al (2016) Pounding hazard mitigation between adjacent planar buildings using coupling strategy. *J Civ Struct Health Monit* 6(3):603–617
22. Jr BS et al (1997) Phenomenological model for magnetorheological dampers. *J Eng Mech* 123(3):230–238



# Seismic Response Control of Smart Base-Isolated Benchmark Building Using Hybrid Control Strategy (Viscous Fluid Damper with MR Damper)



Rini Dey and Purnachandra Saha

**Abstract** Building structures are more susceptible to the ground motion and caused high level of damage to the lives and properties. Hence, the safety parameters and the serviceability have to be maintained by reducing the induced seismic effect on the building structure. The benchmark problem on smart base-isolated benchmark building developed evaluation criteria to compare among the control strategies along with the supplementary devices. A hybrid control strategy consists of semi-active MR damper and passive viscous fluid damper (VFD) which have been proposed in this study for seismic response control of smart base-isolated benchmark building. A set of numerical simulation has been performed in the MATLAB for the specified seven historical earthquakes to investigate the effectiveness of the hybrid control systems for the benchmark problem. The evaluation criteria of the benchmark building of the two control strategies, (a) semi-active system composed of MR damper with Bouc–Wen model and (b) hybrid system composed of MR damper with VFD. From this study, it has been perceived that hybrid control system consisting of MR damper with nonlinear VFD is more robust than the other considered control system.

**Keywords** Benchmark base-isolated building · Viscous fluid damper MR damper

---

R. Dey (✉)  
BBIT, Budge Budge, Kolkata 700137, West Bengal, India  
e-mail: rdey789915@gmail.com

P. Saha  
School of Civil Engineering, KIIT University, Bhubaneswar 751024, India  
e-mail: dr.purnasaha@gmail.com

## 1 Introduction

Base isolation is a technique where the structure is uncoupled from base affected by the horizontal component of earthquake excitation; it is utilized to extricate the force coming from the ground to the structure at the base by providing a flexible device which is enable to lengthen the natural time period of the structure and dissipate the energy by damping. Although a purpose of the base isolation technique is to reduce the forces in the structure due to the random and for near-fault excitation forces. It also increases the displacement responses of the structure. In those cases, semi-active control cannot ensure the displacement response and the safety factor of the structure. Hybrid control system is the ideal one to mitigate the excess displacement response of the structure with the fact of the adaptive control nature of a semi-active device and a reliability of a passive device by its inherent damping nature in the absence of external power resource.

Henceforth, a parametric study has been performed to obtain the optimized value which can ensure the supplement damping of the isolation system to reduce displacement and base shear of the structure. In recent studies, base isolation system such as sliding and elastomeric bearing system is provided to control the structural response but it increases the base displacement response for near-fault ground motion.

Henceforth, to mitigate the displacement response nonlinear devices like MR damper have been initiated; in recent studies due to strong earthquakes, engineers and researchers are keen to find much efficient and reliable methods of vibration control during strong earthquake motion. Methods like hybrid control are developed in this study to have direct research attention on the control system.

In this study, VF damper and MR damper have been employed as a hybrid control strategy.

There have several experimental explorations accompanied on VF damper, Yang and Agarwal [1] have investigated on the response of building structure utilizing the hybrid control system comprising with a laminated rubber bearing with friction damper and viscous dampers against near-fault earthquake excitation. Further experimental studies have been conducted by Constantinou and Symans [2] on the seismic response of building using supplemental fluid damping device. The experimental study shows a simultaneous reduction of base isolation displacement and force transmitted to the superstructure. Markis et al. [3] have studied on the performance of the seismic isolated structure using visco-plastic and friction dampers. Ozbulut et al. [4] have investigated on five-storey structure using VFD as a semi-active device with LRB one with the adaptive fuzzy neural controller and another with the simple adaptive control (SAC) method.

## 2 Structural Model

An idea of the benchmark model leads to a particular benchmark problem which has been adopted from an L-shaped eight-storey building structure of 54.3 m width and 82.4 m length with a bracing of steel which is enabled to the lateral torsional coupling forces, analogues to the USC Hospital in Los Angeles California. The objective of the study of the benchmark problem is to evaluate the performance by comparing different types of control strategies, generalized algorithms with devices under a systematic standardized predefined building structure or a benchmark building subjected to the earthquake excitation (lateral force). The braced supported superstructure at the perimeter of the building resting on the reinforced concrete base slab over the integral concrete beams below that the each columns drop panels are located precisely. The isolation devices are connected between the footing and the drop panels under the column [5–8]. The base and the floor slab of the benchmark building are considered to be rigid and the entire superstructure has been modeled as a linear elastic system. The whole superstructure is simulated on the basis of three masters (DOF) per floor at the mass center. The combination of DOF of the model is précised to be 24 DOF at the superstructure and 3 DOF at the isolation panel composed of 27 DOF. All the twenty-four modes are considered for the fixed base case during the modeling of the superstructure. The benchmark structure is very intricate due to strong coupling effect between the response of the superstructure and the isolation level. The total weight of the structure is 202,000 kN. The damping ratio of the superstructure has been considered to be 5%.

## 3 Viscous Fluid Damper (VFD)

The cross-sectional features of an orifice accomplished damper VFD used in the present study which has been shown in Fig. 1. It consists of a stainless steel piston and the silicon oil fluid in the chamber longitudinally with an accumulator. The piston contains a number of small orifices through which the fluid can be able to pass from one side of the piston to the other [2]. The fluid viscous damper dissipates energy by pushing fluid through an orifice, producing a damping pressure, which creates a force. These damping pressure produced by VFD reduce both stresses and

**Fig. 1** Schematic cross-sectional diagram of VFD

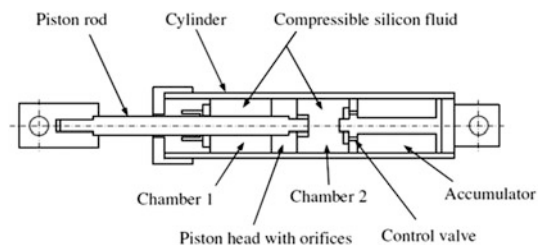


**Fig. 2** Force-deformation diagram of VFD

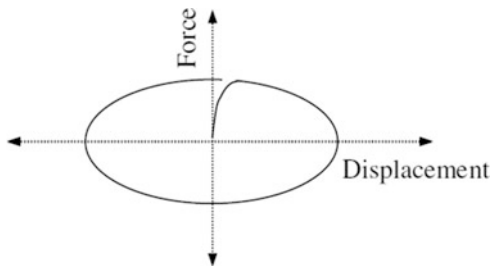
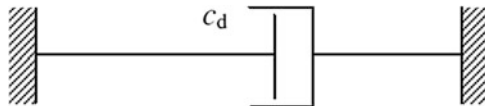


**Fig. 3** Mathematical model of VFD



displacement in the structure. In a viscous damping model, the output of the damper is given by (i.e., damper force  $f$ )

$$f = c_d |\dot{x}_b|^\lambda \text{sgn}(\dot{x}_b) \quad (1)$$

where  $c_d$  = damping coefficient,  $\dot{x}_b$  = velocity across the damper,  $\lambda$  = Velocity exponent  $\dot{x}_b$  is the velocity across the damper”, and  $\lambda$  is mentioned as a velocity exponent. The value of  $\lambda$  ranges from 0.4 to 1.4; a design with equal to 1 results in a linear viscous damper.

The force-deformation behavior and mathematical modeling of the VFD are shown in Figs. 2 and 3, respectively.

## 4 Numerical Study

A set of numerical simulation is performed in the MATLAB for the specified seven historical earthquakes to investigate the effectiveness of the hybrid control systems for the benchmark problem. Time history analysis is performed for the seven earthquake ground motions specified in the benchmark problem to obtain the structural responses of the building. The performance of passive VFD depends upon its damping coefficient ( $c_d$ ) and velocity exponent ( $\lambda$ ). To investigate the optimum values of these two parameters, a parametric study has been carried out and the variation of peak seismic responses of the benchmark building for different values of damping coefficient ( $c_d$ ) of the linear VFD is shown in Fig. 4. It is observed from the figure that minimum value of the evaluation criteria of peak base shear, peak structure shear, base displacement, inter-storey displacement for the seven earthquake excitation is  $c_d = 300$  kN s/m. Therefore, damping coefficient of 300 kN s/m has been chosen to be an optimized value which is good for all the specified earthquakes.

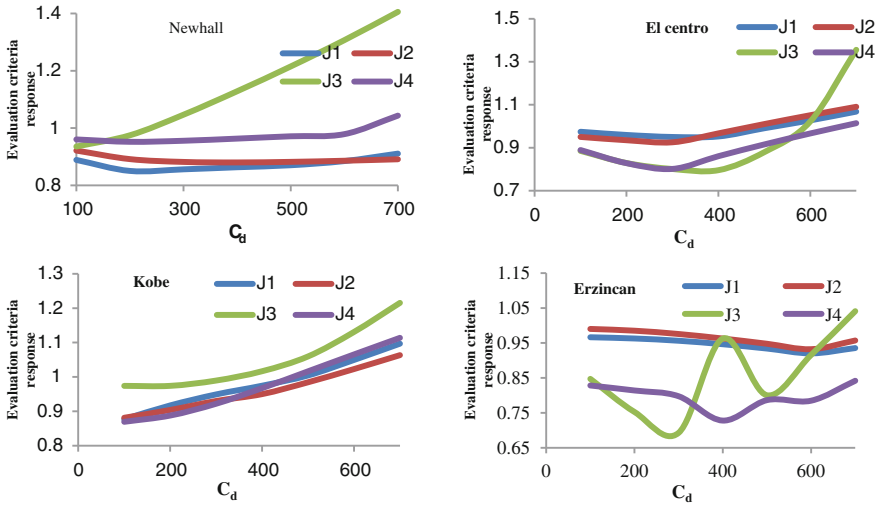
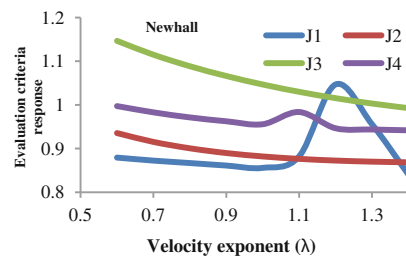


**Fig. 4** Effect of damping coefficient ( $c_d$ )

**Fig. 5** Effect of velocity exponent of VFD on building responses for Newhall earthquake ( $c_d = 300 \text{ kN s/m}$ )



To determine the optimum value of the velocity exponent  $\lambda$ , parametric study has been performed varying the value of damping coefficient as the optimum one (i.e., 300 kN s/m). From Fig. 5, it is observed that optimum value of velocity exponent 1.3 is the optimum which holds good for all the specified earthquakes.

The evaluation criteria of the building considering the above optimum parameters (i.e.,  $c_d = 300 \text{ kN s/m}$  and  $\lambda = 1.3$ ) of the two control strategies, (a) semi-active system composed of MR damper with Bouc–Wen model and (b) hybrid system composed of MR damper with optimized VFD are shown in Table 1. The Main objective of VFD is to provide enough force to reduce the base drift response without much affecting peak base shear response. Due to the energy dissipation capability of reducing excessive Base drift response of VFD the hybrid control system signified to be more effective. From the force-deformation pattern shown in Fig. 6 and from Table 1, it can be observed that the base displacement response J3 (Peak base displacement) is reducing for the Newhall, Sylmar, El-Centro, Rinaldi, Erzincan earthquakes, whereas peak inter-storey drift response

**Table 1** Evaluation criteria for (VFD + MRD) and MRD

Evaluation criteria	Control strategy	Newhall	Sylmar	El-Centro	Rinaldi	Kobe	Jiji	Erzincan
J1	VFD + MRD	0.849	0.8249	0.93	0.9828	0.913	0.764	0.9338
Peak base shear	MRD	0.880	0.9347	0.8993	0.9721	0.8311	0.831	0.9876
J2	VFD + MRD	0.842	0.82	0.881	0.9857	0.8824	0.763	0.9438
Peak structural shear	MRD	0.909	0.9476	0.8864	0.9714	0.8214	0.821	1.0162
J3	VFD + MRD	0.6036	0.6727	0.4121	0.6505	0.6329	0.712	0.4734
Peak base displacement	MRD	0.6754	0.8539	0.4499	0.796	0.5437	0.543	0.5873
J4	VFD + MRD	0.9163	0.7472	0.7232	1.0014	0.8477	0.8001	0.7832
Peak inter-storey drift	MRD	0.9169	0.868	0.7939	0.9487	0.767	0.767	0.8707
J5	VFD + MRD	1.0293	0.9685	1.0505	1.1132	1.1891	0.796	1.0176
Peak floor acceleration	MRD	1.0108	0.9694	0.9043	0.9763	0.9681	0.968	1.0581
J6	VFD + MRD	0.3767	0.3526	0.2462	0.2259	0.2359	0.205	0.262337
Peak control force	MRD	0.1514	0.1339	0.1948	0.1488	0.2025	0.202	0.139787
J7	VFD + MRD	0.4118	0.4483	0.3266	0.4243	0.418	0.493	0.3874
RMS base displacement	MRD	0.4711	0.6088	0.3887	0.5513	0.4817	0.481	0.5564
J8	VFD + MRD	0.7287	0.6129	0.5811	0.5789	0.5613	0.6757	0.5956
RMS floor acceleration	MRD	0.7502	0.7794	0.5729	0.689	0.4817	.4817	0.5564
J9	VFD + MRD	0.4833	0.34277	0.6492	0.5143	0.5798	0.554	0.4669
Energy dissipated by PFD	MRD	0.6553	0.6339	0.7156	0.62319	0.6346	0.6346	0.65971

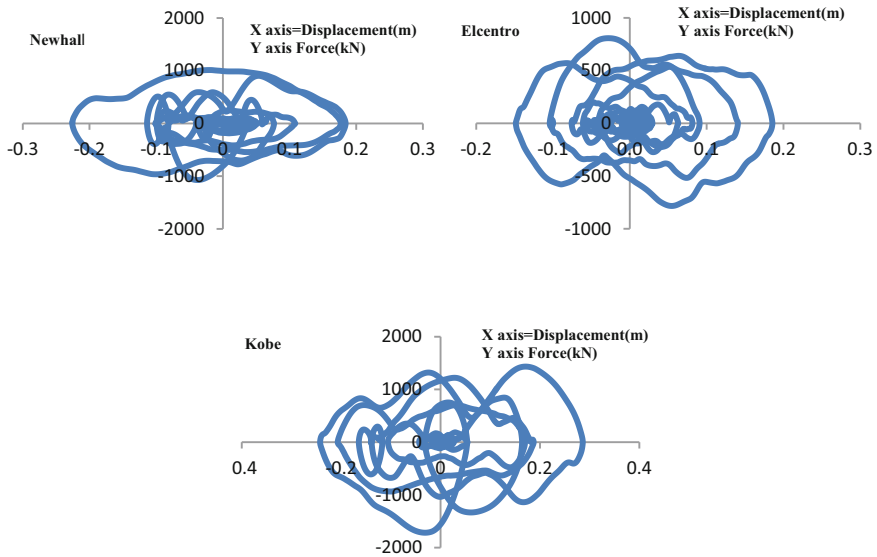


**Fig. 6** Force-deformation behavior of hybrid control system incorporating VFD and MRD for the specified earthquakes

J4 (peak inter-storey drift) has been reduced for Newhall, Sylmar, El-Centro, Kobe, Jiji earthquakes, respectively, for VFD + MR damper. The peak base shear response J1 (peak base shear) of the hybrid control system is achieved with the reduced value for Newhall, Sylmar, Jiji, and Erzincan earthquake compared to the semi-active control, whereas the hybrid control strategy (VFD + MR damper) controlled by clipped optimal control) the peak structural shear response J2 (peak structural shear) appears to be efficient than semi-active control for Newhall, Sylmar, El-Centro, Jiji, and Erzincan earthquakes. From the observation, it can be clearly signified that the base acceleration response for uncontrolled response is having maximum amplitude with respect to time, whereas the base acceleration response of the structure controlled by semi-active device MR damper enables to reduce the structural response due to its adaptive nature of the clipped optimal controller justifying the control force to the MR damper controlling the structure response, whereas the response controlled by MRD + VFD has been proved to be much efficient for Sylmar, Rinaldi, Jiji, Erzincan earthquakes specially due to the involvement of the inherent effect of the energy dissipative nature of the passive device and the adaptive nature of the semi-active control system. Figure 7 shows the time history plot of the base acceleration response for seven specified earthquakes and it can be seen that the effect of a hybrid control system using VFD with MR damper controlled by clipped optimal control gives better control response of the structure. The structural response reduced slightly by 0.96% for semi-active system and for hybrid control system it has reduced by 17.42% with respect to the uncontrolled response of the structure for Sylmar earthquake, similarly for Rinaldi

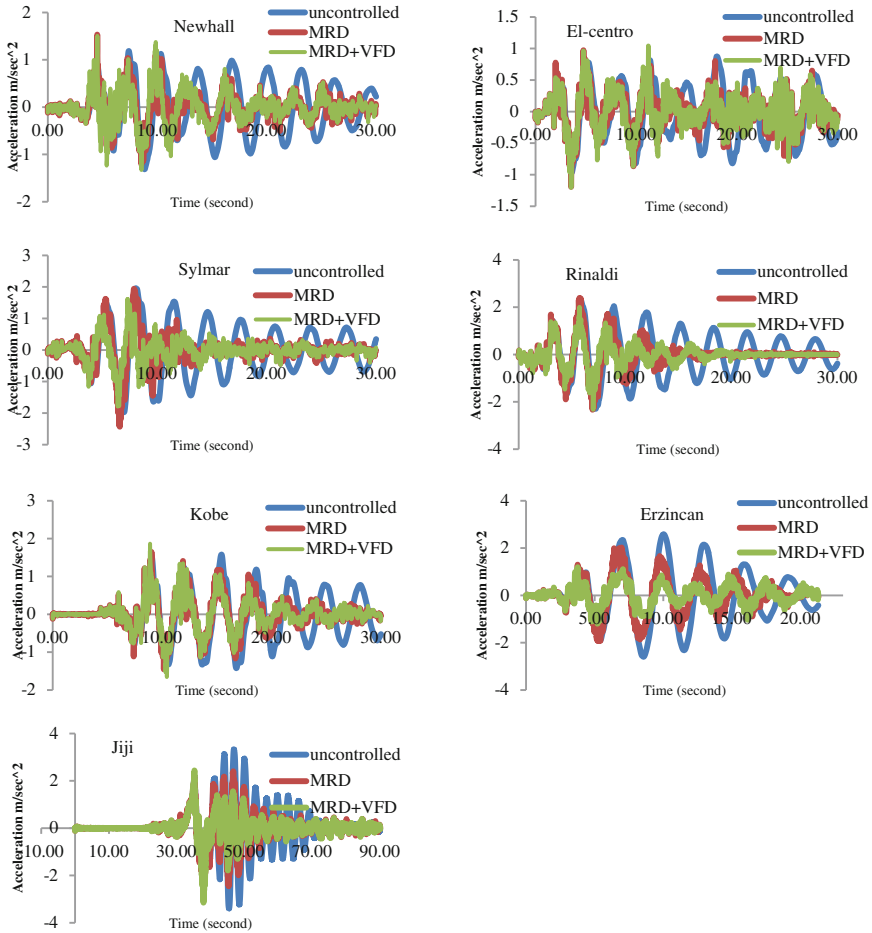


**Fig. 7** Time history response of base acceleration of Newhall, Sylmar and El-Centro earthquake El-Centro, Rinaldi, Kobe, Jiji Erzincan earthquake (MRD MR damper response, MRD + VFD = MR damper + Viscous fluid damper response; hybrid control)

earthquake the base acceleration response has been increased by 4.5% for semi-active control system, whereas for hybrid control system the response reduced up to 12.58%. Correspondingly for Jiji and Erzincan earthquake, the response has been reduced 27.8 and 21.8% for semi-active control system, and for hybrid control system the response reduced by 26.7 and 54.1% to the uncontrolled response.



## 5 Conclusion

In this study, an effort is made to present smart base-isolated benchmark building with hybrid control systems consisting of MR damper of Bouc–Wen model along with clipped optimal control algorithm and passive nonlinear viscous damper. Based on the investigation performed on the seismic response control of the building, the following conclusions are drawn:

1. A parametric study has been performed to obtain the optimized value which can ensure the supplemental damping of the isolation system to reduce displacement and base shear response of the structure.
2. Significant seismic response reduction of the benchmark base-isolated building can be achieved by applying hybrid control system consists of MR damper of Bouc–Wen model along with clipped optimal control algorithm and passive nonlinear viscous damper.
3. Due to the inherent dissipation capability of reducing excessive Base drift response by VFD, hybrid control system signified to be more effective.
4. From the force-deformation behavior for seven earthquakes, a significant amount of energy absorption through the hybrid control system can be observed due to MR damper and VF damper characteristics.
5. Comparing the values of evaluation criteria tabulated, it can be deduced that hybrid control system consisting of MR damper with nonlinear VFD is more robust than the other considered control systems.
6. For Rinaldi earthquake, the base acceleration response has been increased by 4.5% for semi-active control system whereas for hybrid control system the response reduced up to 12.58%. Correspondingly for Jiji and Erzincan earthquake, the response has been reduced 27.8 and 21.8% for semi-active control system and for hybrid control system the response reduced by 26.7 and 54.1% to the uncontrolled response.

## References

1. Yang JN, Agrawal AK (2002) Semi-active hybrid control systems for nonlinear buildings against near fault earthquakes. *Eng Struct* 24:271–280
2. Constantinou MC, Symans MD (1993) Experimental study of seismic response of buildings with supplemental fluid dampers. *Struct Des Tall Build* 2:93–132
3. Makris N, Chang SP, Whittaker AS, Thompson ACT (2002) Experimental and analytical studies on the performance of hybrid isolation systems. *Earthq Eng Struct Dyn* 31:421–443
4. Ozbulut OE, Bitaraf M, Hurlebaus S (2011) Adaptive control of base-isolated structures against near-field earthquakes using variable friction dampers. *Eng Struct* 33:3143–3154
5. Narasimhan S, Nagarajaiah S, Johnson EA, Gavin HP (2006) Smart base-isolated benchmark building. Part I: problem definition. *Struct Control Health Monit* 13:573–578

6. Nagarajaiah S, Narasimhan S (2002) Smart base isolated benchmark building. Part II: phase I sample controllers for linear isolation system. *J Struct Control* 1–6
7. Narasimhan S, Nagarajaiah S, Gavin HP, Johnson EA (2005) Benchmark problem for control of base isolated buildings. In: 15th ASCE engineering mechanics conference, Columbia University, New York, 2–5 June, pp. 1–8
8. Narashiman S (2004) Control of smart base isolated buildings with new semi active devices and novel  $H_2/LQG$ ,  $H_\infty$  and time-frequency controllers, Rice University

# Numerical Investigation on the Effectiveness of Double Tuned Mass Dampers in Structural Vibration Control



Mohammed Fasil and R. Sajeed

**Abstract** The inferior performance of the single tuned mass damper (TMD) and the complexities involved in the implementation of multiple TMDs in the structure is some of the challenges faced in the field of structural vibration control. The present study introduces Double TMDs' control strategy which is simple and is more effective than the conventional single TMD strategy. It essentially consists of two discrete TMD units capable of suppressing vibrations in the neighbourhood of the first and second natural frequencies of the structure to be controlled. Numerical investigations done on a five degrees-of-freedom shear building model with different mass ratios reveal that the proposed strategy is superior to single TMD with regard to effectiveness and wider frequency bandwidth of control of floor displacements, floor accelerations and base shear. An investigation on the placement configurations of the Double TMDs is also conducted.

**Keywords** Vibration control · Double TMDs · Placement configurations

## 1 Introduction

The application of single tuned mass damper (TMD) as a passive control strategy has found great applications in vibration control in structures since its invention in 1909 by Hermann Frahm. Essentially, a single TMD consists of a spring and a mechanism to dissipate energy such as a damper [1]. The great reliability of the system is due to the absence of any active element such as an actuator [2]. From Refs. [3, 4], the lack of robustness to detuning and inferior effectiveness under seismic excitations is often spotted as the major drawbacks of the system. Following the investigations on more than one number of masses in the TMD

---

M. Fasil · R. Sajeed (✉)

Department of Civil Engineering, TKM College of Engineering, Kollam 691005, India  
e-mail: sajeebr.tkm@gmail.com

M. Fasil

e-mail: mohammedfasil@live.in

© Springer Nature Singapore Pte Ltd. 2019

A. Rama Mohan Rao and K. Ramanjaneyulu (eds.), *Recent Advances in Structural Engineering, Volume 2*, Lecture Notes in Civil Engineering 12,  
[https://doi.org/10.1007/978-981-13-0365-4\\_32](https://doi.org/10.1007/978-981-13-0365-4_32)

375

strategy by Iwanami and Seto [5], several researchers focused on the development of multiple TMDs (MTMDs). An MTMD uses several smaller TMD units, instead of a single large TMD tuned to a specific frequency of the structure [6]. Compared to the conventional single TMD system, MTMDs have proven to be more effective and exhibit an enhanced frequency bandwidth of control [4, 6]. From literature, it may be noted that most of the researchers either converted a multi-degree-of-freedom (MDOF) into an equivalent single-degree-of-freedom (SDOF) system [7] or considered only the first resonant mode of vibration [8] of the structure. Since MTMDs consist of several numbers of TMD units distributed either at one location or spatially within the structure [9], the placement of TMDs would adversely affect the architectural appeal, availability of usable area and ease of installation.

The present study investigates the effectiveness of Double TMDs in vibration control of a five degrees-of-freedom shear building frame. The control system consists of two TMD units tuned to the first and second natural frequencies of the frame to be controlled. Equal inertial masses of combined mass ratios (mass of TMDs to the total mass of structure) of 1, 2, 3, 4 and 5% were considered for the study, and comparison of effectiveness with single TMD (with identical mass ratios as above) was considered in the numerical study. Since the Double TMDs consist of two masses, the strategy offers five different placement configurations. The effect of placement configurations was also studied. The Double TMD system performed well under harmonic, seismic and white noise base excitations, proving to be superior to the conventional single TMD.

## 2 Dynamic Analysis

### 2.1 Formulation

Dynamic analysis was carried out using the Runge–Kutta method, formulating the equations of motion in state space. For solution of differential equations in MATLAB, the function ‘ode45’ was used.

For an MDOF system, the equations of motion may be represented in the state space form as,

$$\begin{Bmatrix} \dot{x}_1 \\ \vdots \\ \dot{x}_n \\ \dot{x}_{n+1} \\ \vdots \\ \dot{x}_{2n} \end{Bmatrix} = \begin{bmatrix} 0_{n,n} & I_n \\ -M^{-1}K & -M^{-1}C \end{bmatrix} \begin{Bmatrix} x_1 \\ \vdots \\ x_n \\ x_{n+1} \\ \vdots \\ x_{2n} \end{Bmatrix} + \begin{bmatrix} 0_{n,n} \\ M^{-1} \end{bmatrix} \begin{Bmatrix} f_1(t) \\ \vdots \\ f_n(t) \end{Bmatrix} \quad (1)$$

where  $x_1$  to  $x_n$  represent the displacement of the 1st to  $n$ th masses,  $x_{n+1}$  to  $x_{2n}$  represent velocity of the 1st to  $n$ th masses,  $M$  is the mass matrix of  $n$ th order,  $K$  is

the stiffness matrix of  $n$ th order.  $f_1(t)$  to  $f_n(t)$  represent the dynamic loads acting on 1st to  $n$ th masses. A dot over variable represents differentiation with respect to time.

### 2.2 Problem

The structure chosen for the present study is a five DOF shear building model (Fig. 1) with lumped masses of 40,000 kg at each storey ( $M$ ), total stiffness of  $4 \times 10^7$  N/m per storey ( $K$ ) and 3% damping ratio. Mass ratios of 1, 2, 3, 4 and 5% are chosen to design the mass component of the TMDs.

### 3 Design of Single TMD

Vibration control using a single TMD is implemented by attaching an SDOF system to the top floor of the structure (Fig. 2).

The basic assumption in the design of the single TMD is that the natural frequency of the single TMD is equal to the fundamental frequency of the uncontrolled structure. Mass ratio of the Double TMD system is denoted by ‘ $r$ ’ in the study. Since, the proposed Double TMDs use the same mass, a mass ratio of  $r/2$  is also considered in the study of the single TMD system. For deriving the damper parameters, uniform storey stiffness of  $K$  is assumed.

The following simple assumption is used to design the single TMD:

$$\omega_d = \omega_1 = \sqrt{\frac{\alpha K}{m_d}} \tag{2}$$

where

$$m_d = r \times 5M \tag{3}$$

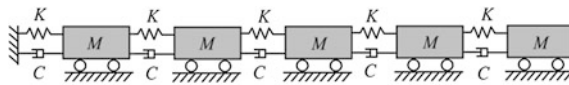


Fig. 1 Spring-mass-damper model of the five degrees-of-freedom system

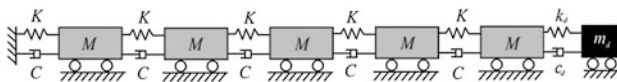


Fig. 2 Spring-mass-damper model of the five degrees-of-freedom system with single TMD

$$m_d = \frac{r}{2} \times 5M \quad (4)$$

Here,  $\omega_d$  is the natural frequency of the single TMD,  $\omega_1$  is the fundamental frequency of the uncontrolled structure,  $\alpha$  is the coefficient to calculate the stiffness of the single TMD,  $m_d$  is the mass of the damper,  $r$  is the mass ratio, and  $M$  is the floor mass.

## 4 Double TMDs

### 4.1 Design

The principle of design of the Double TMDs is to proportion the TMD parameters such that the natural frequencies of the two TMDs match with the first two natural frequencies of the structure to be controlled, *i.e.* natural frequency of first TMD = first natural frequency of the structure and natural frequency of second TMD = second natural frequency of the structure.

For deriving the damper parameters, it is assumed that the storey stiffness is uniform ( $K$ ).

The stiffness of the first damper is taken to be  $\alpha_1 K$  and that of the second damper as  $\alpha_2 K$ , where  $\alpha_1$  and  $\alpha_2$  are stiffness coefficients. The first two natural frequencies of the system may be denoted by  $\omega_1$  and  $\omega_2$ . Damper masses  $m_{d1}$  and  $m_{d2}$  are given by  $(r/2) M_s$ , where  $M_s$  is the total mass of the structure to be controlled.

The stiffness coefficients and damper masses are obtained as follows:

$$\omega_{d1} = \omega_1 = \sqrt{\frac{\alpha_1 K}{m_{d1}}} \text{ or } \alpha_1 = \frac{\omega_1^2 m_{d1}}{K} \quad (5)$$

$$\omega_{d2} = \omega_2 = \sqrt{\frac{\alpha_2 K}{m_{d2}}} \text{ or } \alpha_2 = \frac{\omega_2^2 m_{d2}}{K} \quad (6)$$

The damper masses are given by

$$m_{d1} = m_{d2} = \frac{r}{2} M_s \quad (7)$$

$\omega_{d1}$  is the natural frequency of the TMD to control vibrations in the first natural frequency of the uncontrolled structure,  $\omega_{d2}$  is the natural frequency of the TMD to control vibrations in the second natural frequency of the uncontrolled structure,  $\omega_1$  is the fundamental frequency of the uncontrolled structure, and  $\omega_2$  is the second natural frequency of the uncontrolled structure.  $m_{d1}$  is the mass of the first TMD (which controls the vibrations in the first natural frequency of the uncontrolled structure), and  $m_{d2}$  is the mass of the second TMD (which controls the vibrations in the second natural frequency of the uncontrolled structure).

### 4.2 Placement Configurations of Double TMDs

In the present study, an investigation is also conducted to find the effect of placement of TMDs in the primary structure. The dampers can be arranged in five different configurations as shown in Fig. 3. The different placement configurations are denoted as A1, A2, A3, A4 and A5 as shown in Fig. 3. The spring–mass models of these configurations are provided in Fig. 4.

## 5 Tuning of TMDs

Since the incorporation of TMDs into a structural system results in the variation of mass, stiffening and damping components of the structure, tuning is necessary to obtain optimum displacement, accelerations and base shear responses.

In the present study, tuning of TMDs is done by keeping the mass and damping ratio as constants and varying the stiffness of the individual TMD units.

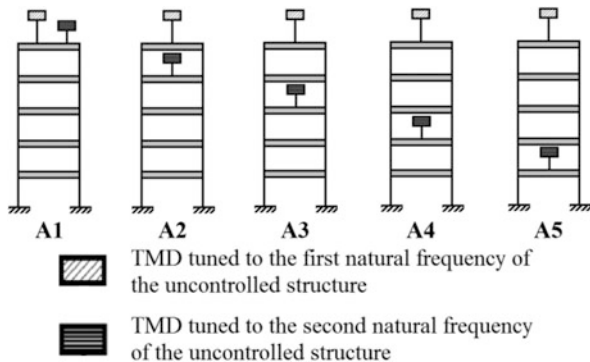
Figure 5 shows the tuned values of  $\alpha$  for various mass ratios of the single TMD.

Since the Double TMD system consists of two TMDs, the coefficients  $\alpha_1$  and  $\alpha_2$  are used to determine the stiffness of the TMDs. The tuned values of  $\alpha_1$  and  $\alpha_2$  for various mass ratios are shown in Fig. 6, corresponding to different Double TMD placement configurations.

## 6 Effectiveness of Double TMDs

Elaborate numerical studies are conducted by subjecting the test structure to various types of base excitations, namely harmonic, seismic and white noise, so as to compare the controlled and uncontrolled responses.

**Fig. 3** Various placement configurations of Double TMDs



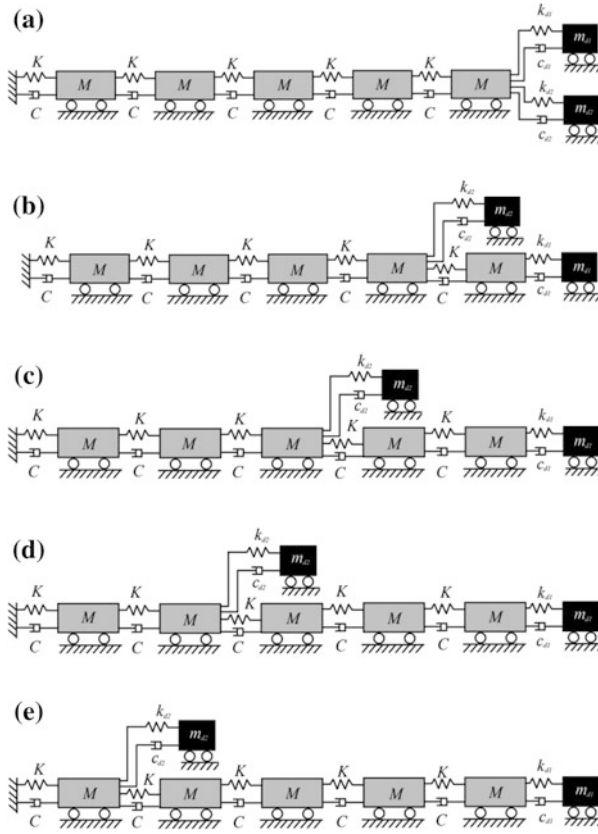


**Fig. 4** Equivalent spring–mass–damper models of Double TMD configurations; **a** A1; **b** A2; **c** A3; **d** A4; **e** A5

**Fig. 5** Variation of coefficient,  $\alpha$ , with respect to mass ratio,  $r$

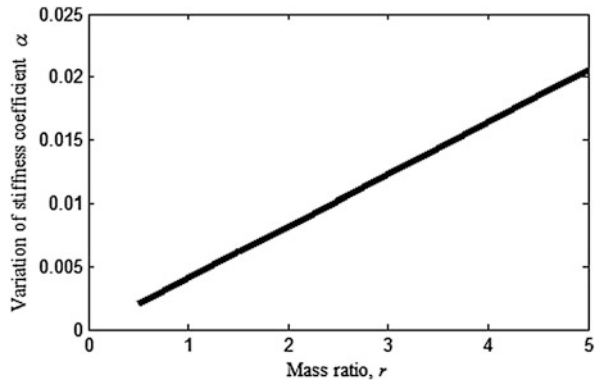
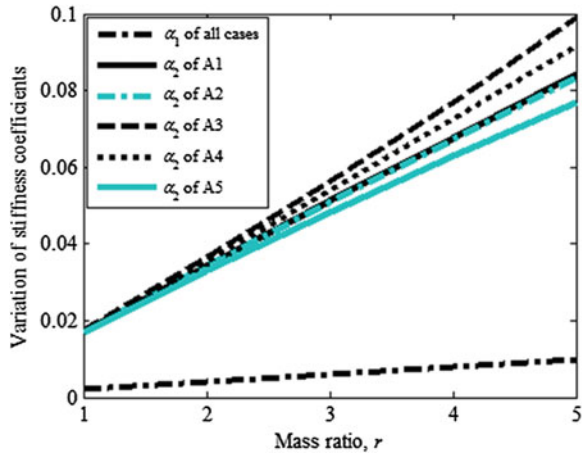




**Fig. 6** Variation of stiffness coefficients with respect to mass ratio,  $r$



### 6.1 Harmonic Base Excitation

Frequency response function (FRF) with frequencies up to 60 rad/s are plotted to study the performance of the Double TMD system. The control effectiveness of the system is studied by plotting the % variation of peak response with reference to the uncontrolled peak response for various mass ratios. Peak response of parameters, i.e. displacement, acceleration and base shear, obtained from FRFs of the corresponding parameters are plotted against various mass ratios of the Double TMDs. This is illustrated in Fig. 7.

It may be observed from the plots above that except A1, all configurations were found to give reasonably good performance for all response parameters considered in the study. Excellent base shear control was observed in Double TMD systems, compared to single TMD systems.

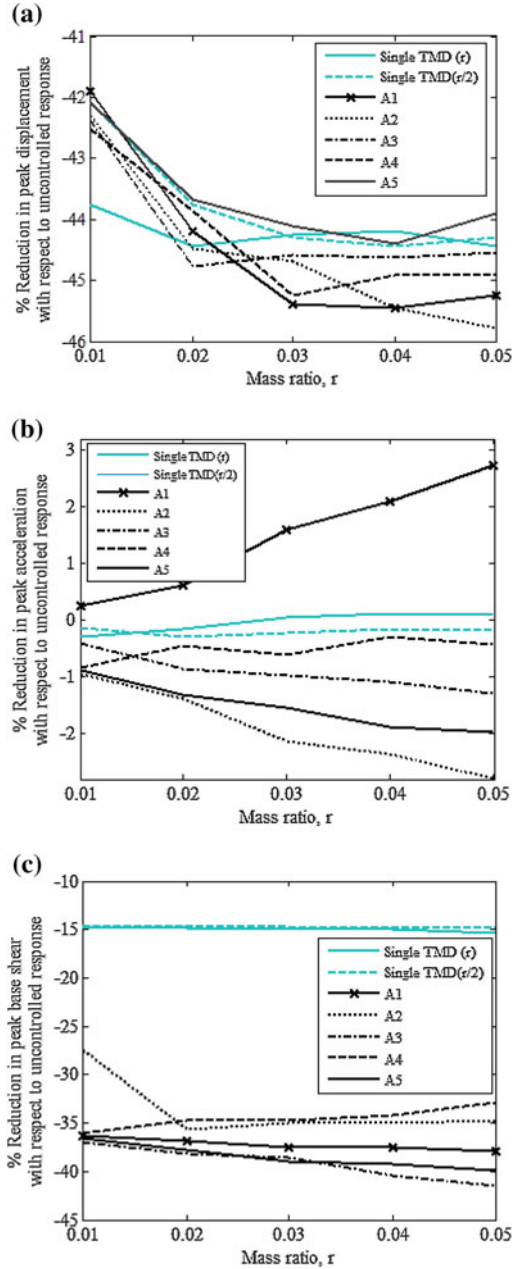
Since only the peak values of responses are noted to study the control effectiveness of the system, even an unusual spike higher than the general response will only be considered. The eccentric behaviour of the system with configuration A1 may be attributed to this fact.

FRFs of various response parameters of uncontrolled and controlled structures corresponding to a mass ratio of 5% are shown in Fig. 8. Placement configuration A4 is considered for the Double TMD system. Peak response reduction attained in the neighbourhood of the second natural frequency of the structure can be observed.

### 6.2 Seismic Base Excitation

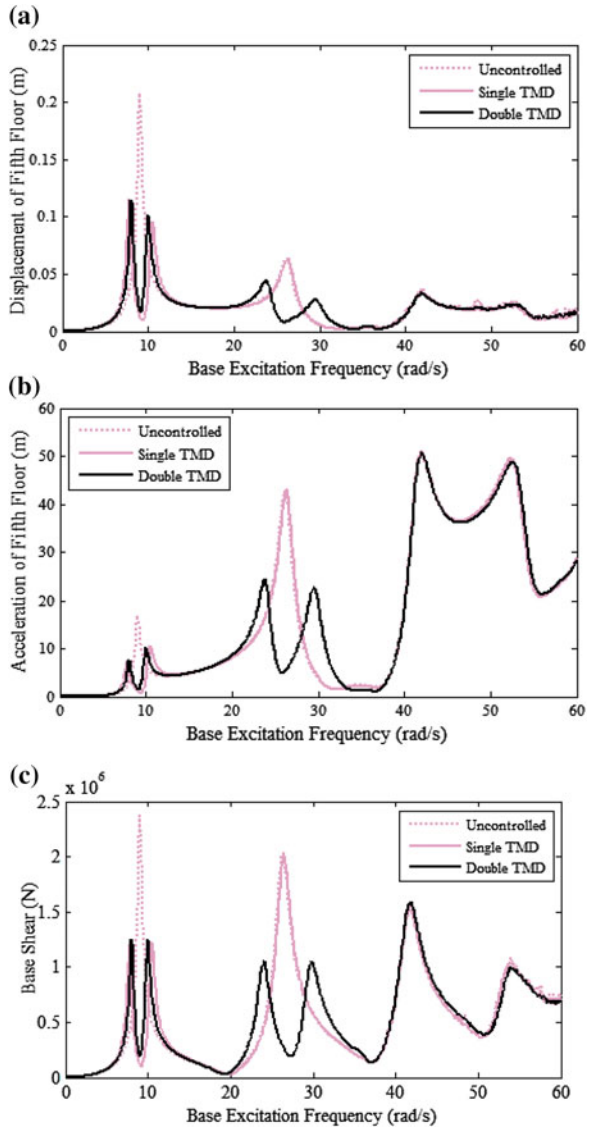
Recorded accelerations in El Centro (1940) earthquake are used to study the effectiveness of the proposed Double TMD system compared to the single TMD

**Fig. 7** Control Effectiveness of double TMD system. FRFS of **a** displacement; **b** acceleration; **c** base shear



topology. From Fig. 9, it may be observed that, with increase in mass ratio, there is a steady reduction in the peak amplitude for the Double TMDs, irrespective of the placement topology used. Placement configuration A1 was found to be superior.

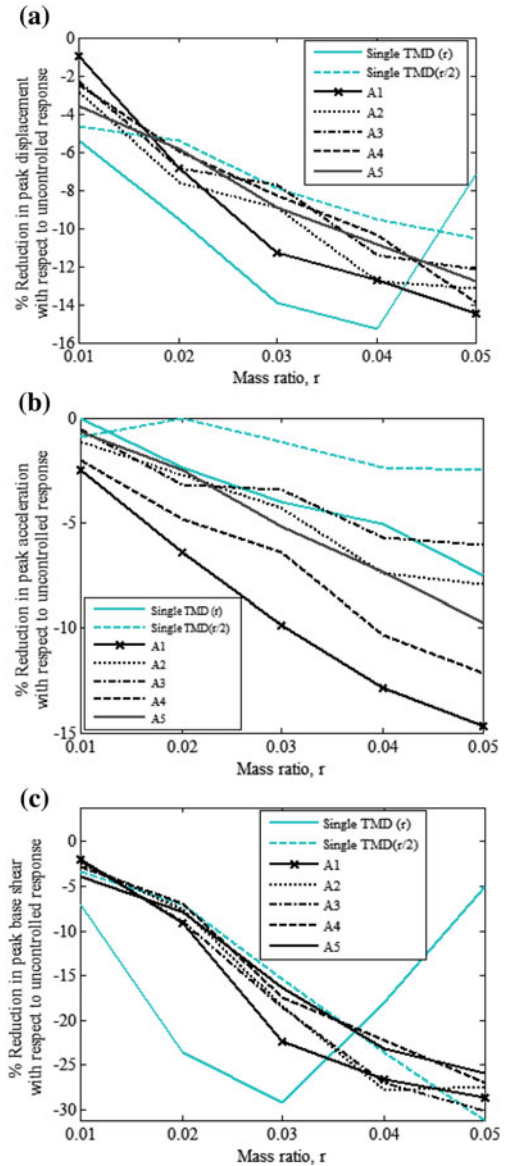
**Fig. 8** Control effectiveness of single and Double TMD (A4) systems for a mass ratio of 5%. FRFs of **a** displacement; **b** acceleration; **c** base shear



Good performance was observed for other configurations also. Here also, the performance of single TMD was found to be inferior.

The comparison of time histories of top floor displacements is shown in Fig. 10. Placement configuration A1 is considered for Double TMDs.

**Fig. 9** Control effectiveness under El Centro earthquake; **a** displacement; **b** acceleration; **c** base shear



### 6.3 White Noise Base Excitation

White noise excitation (Fig. 11) generated in MATLAB, using the function ‘wgn’, normalized to  $1 \text{ m/s}^2$  was given as base acceleration to study the effectiveness of the proposed system under random loading.

**Fig. 10** Performance of Double TMDs under El Centro earthquake—displacement-time history

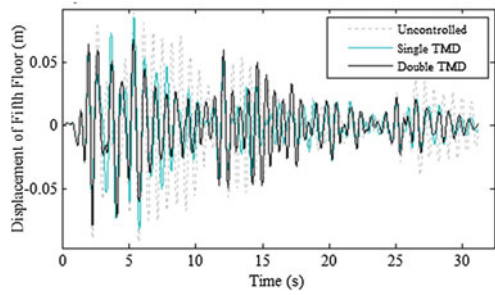
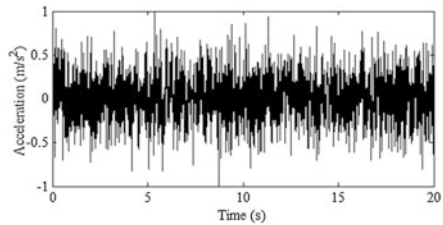


**Fig. 11** White noise signal—acceleration-time history



The variation of response parameters, namely floor displacements, floor accelerations and base shear of the structure controlled by single and Double TMD systems with respect to mass ratios was studied.

From Fig. 12a, b, it may be observed that all control strategies show erratic behaviour. However, it may be noted that the Double TMDs shows enhanced control at higher mass ratios. From Fig. 13, it is definitive that the implementation of Double TMDs into the test structure has exhibited remarkable vibration control under white noise base excitations.

### 6.4 Effect of Placement Configurations

All placement configurations were found to offer better control over single TMD. The levels of control (control effectiveness) offered by the various placement configurations were different for different response quantities. Hence, with the observations made on the reductions in peak responses, it is difficult to pick the best configuration. However, meaningful conclusions are made from the FRFs of systems with different configurations (Fig. 14a) and the second mode shape of the structure (Fig. 14b).

The maximum ordinate of the mode shape is at the second-floor level, and the superior performance of placement configuration A4 (second TMD at second floor) is attributed to this fact. Thus, maximum control will be yielded when the TMD is placed at the floor, where the mode shape ordinate is maximum. Conversely,

**Fig. 12** Control effectiveness—white noise;  
**a** displacement;  
**b** acceleration;  
**c** base shear

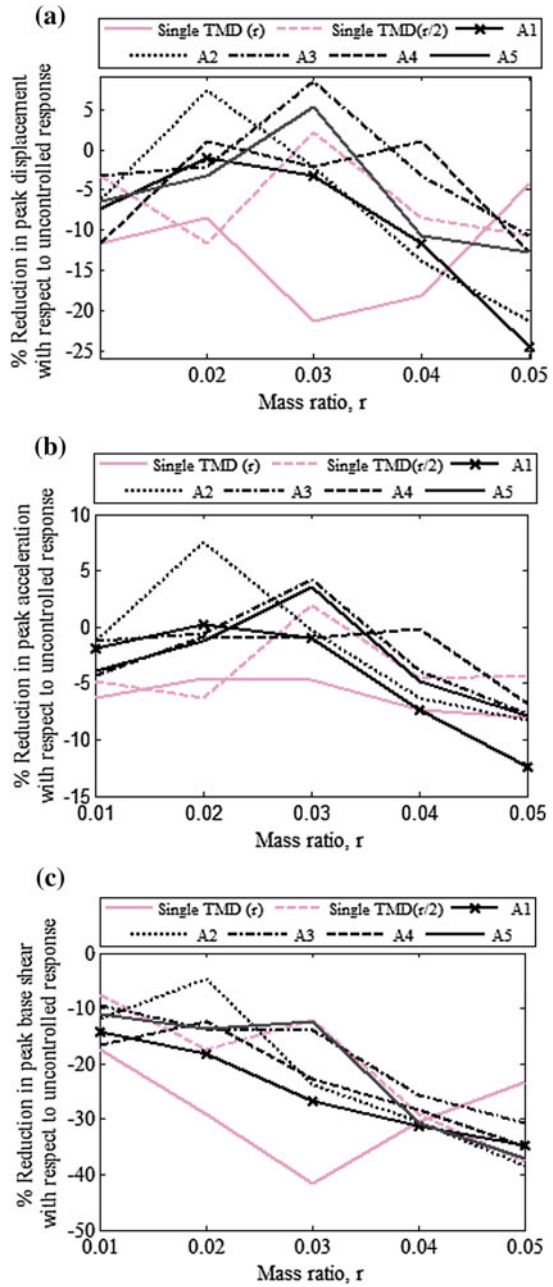


**Fig. 13** Performance of Double TMDs under white noise base excitation—displacement-time history

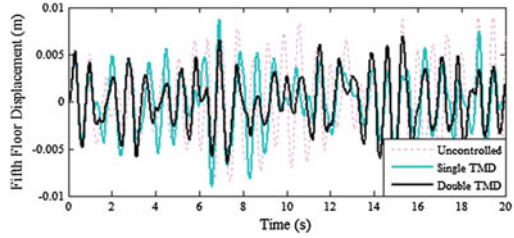
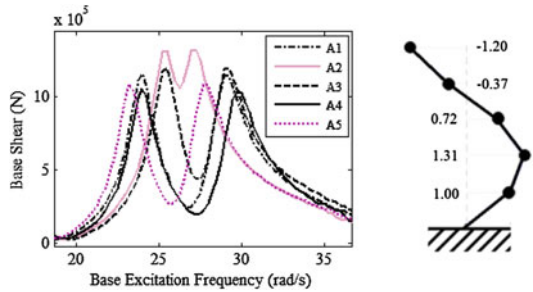


**Fig. 14 a** FRFs of Double TMD systems; **b** 2nd mode shape



control effectiveness of system with damper placed at the floor of minimum mode shape ordinate will be minimum. The inferior performance of configuration A2 (TMD in fourth floor) is affirmative of this observation.

## 7 Conclusions

The numerical study could prove the effectiveness of the proposed Double TMDs in suppressing peak responses to remarkably good level under harmonic, seismic and white noise excitations. The Double TMD system was found to outperform the single TMD systems in vibration control. The study on placement configurations reveals the role of mode shapes on the location of the TMDs. The placement configuration with one damper placed at the top and the other at the floor where the mode shape ordinate is maximum was found offering the most effective vibration control.

One practical issue which may arise due to the installation of a damper system in the intermediate floors is about the usability of the floors due to the excessive vibration of the damper mass. The damper components require a small portion of the floor only and may be enclosed in a separate room. Concealing the components within the structural framework is another option.

## References

1. Connor J (2003) Introduction to structural motion control. Springer
2. Lourenco R (2011) Design, construction and testing of an adaptive tuned mass damper. Thesis report, University of Waterloo
3. Setareh M, Ritchey JK, Baxter AJ, Murray TM (2006) Pendulum tuned mass dampers for floor vibration control. *J Perform Constr Facil* 20(1):64–73
4. Kareem A, Kline S (1995) Performance of multiple mass dampers under random loading. *J Struct Eng* 121:348–361
5. Iwanami K, Seto K (1984) Optimum design of dual tuned mass dampers and their effectiveness. *Jpn Soc Mech Eng* 50(1):44–52
6. Chen G, Wu J (2001) Optimal placement of multiple tuned mass dampers for seismic structures. *J Struct Eng* 127(9):1054–1062
7. Warburton GB (1982) Optimum absorber parameters for minimizing vibration response. *Earthq Eng Struct Dyn* 9:251–262
8. Vakakis AF, Paipetis SA (1986) The effect of a viscously damped dynamic absorber on a linear multi-degree-of-freedom system. *J Sound Vib* 105(1):49–60
9. Debbarma R, Hazari S (2013) Mass distribution of multiple tuned mass dampers for vibration control of structures under earthquake load. *Int J Emerg Technol Adv Eng* 3(8):198–202



# Three-Dimensional Finite Element Simulation of Isolated Floor Slab with Friction Contact Surface



P. Kamatchi, S. Cheran Pandian, N. Ezhilarasi and K. Balaji Rao

**Abstract** Number of studies are reported in literature on the response of structures with different dampers and the combination of more than one damper. An isolated floor slab system, which can move relative to the frame for energy dissipation through friction, is suggested in literature, and a simplified idealization has been adopted for modelling the same. In order to determine the response of the isolated floor slab more realistically, three-dimensional finite element simulation of isolated floor slab with friction contact surface has been demonstrated in the present study. Time history analyses with four earthquake ground motions are carried out for a single-storey and a three-storey frame with solid floor slab and isolated floor slab, and the responses are studied. From the comparison of results, it is observed that frame with isolated floor slab is an efficient passive energy dissipation mechanism and the percentage reductions in responses are different for different ground motions.

**Keywords** Isolated floor slab · Friction contact surface · Response reduction

## 1 Introduction

Number of studies are reported in literature on tuned mass dampers (TMD), combination of friction and tuned mass dampers and pendulum-type tuned mass dampers [1–7]. As it has been reported by many researchers, TMD which is a

---

P. Kamatchi (✉) · S. Cheran Pandian · N. Ezhilarasi · K. Balaji Rao  
CSIR-Structural Engineering Research Centre, Chennai, India  
e-mail: kamat@serc.res.in

S. Cheran Pandian  
e-mail: scheranpandian21@gmail.com

N. Ezhilarasi  
e-mail: ezhilarasi118@gmail.com

K. Balaji Rao  
e-mail: balaji@serc.res.in

dynamic vibration absorbing passive energy dissipation mechanism is effective in response reduction; however, response reduction is directly proportional to mass ratio. Hence, supporting structures need to be designed for additional load. On the other hand, repairing or replacing the bearings provided for base isolation after the earthquake is reported to be very difficult. Engle et al. [8] have introduced an isolated floor slab system which can move relative to the frame. Bottom surface of the floor slab is curved in shape and rests on curved support. Rubber bumpers are installed between the slab and frame, which are compressed and are in contact with the slab always. The spherical curved support interacts with curved slab bottom through the contact surface and dissipates energy by friction. Engle et al. [8] have adopted simplified mathematical idealization of frame and isolated floor slab. In the present study, isolated floor slab with friction contact surface has been modelled using three-dimensional finite element computer program SAP2000 [9]. Time history analysis is carried out, and responses of the single-storey and three-storey frames with solid slab are compared with single- and three-storey frame with isolated floor slabs for different earthquakes.

## 2 Properties and Structural Model

The three-dimensional finite element (FE) models of the single-storey and three-storey FSS and FIS are shown in Fig. 1. The properties adopted in the present study for the frame with solid slab (designated as FSS) and frame with isolated slab (designated as FIS) are given in Table 1. Same properties are adopted for single-storey and three-storey FSS and FIS. Eight-noded 3D solid element with six quadrilateral faces is used for modelling the solid slab. At each node, three translational degrees of freedom are activated in the solid element. Friction–pendulum isolator element is used for the contact surface between sliding curved slab and the curved support. Friction isolator element adopts the hysteretic behaviour proposed by Park et al. [10]. For modelling the bumper stiffness, linear elastic translational joint spring element is adopted.

## 3 Time Periods of the Models

The time period of the single-storey and three-storey FSS and FIS frames are obtained, and it is observed that time periods of FIS are less than the time periods of FSS which indicates FIS to be rigid compared to FSS. However, due to the presence of isolated slab on contact surface, which leads to the generation of lesser inertia force for the same mass, the base shears are less for FIS compared to the base shears obtained for FSS.

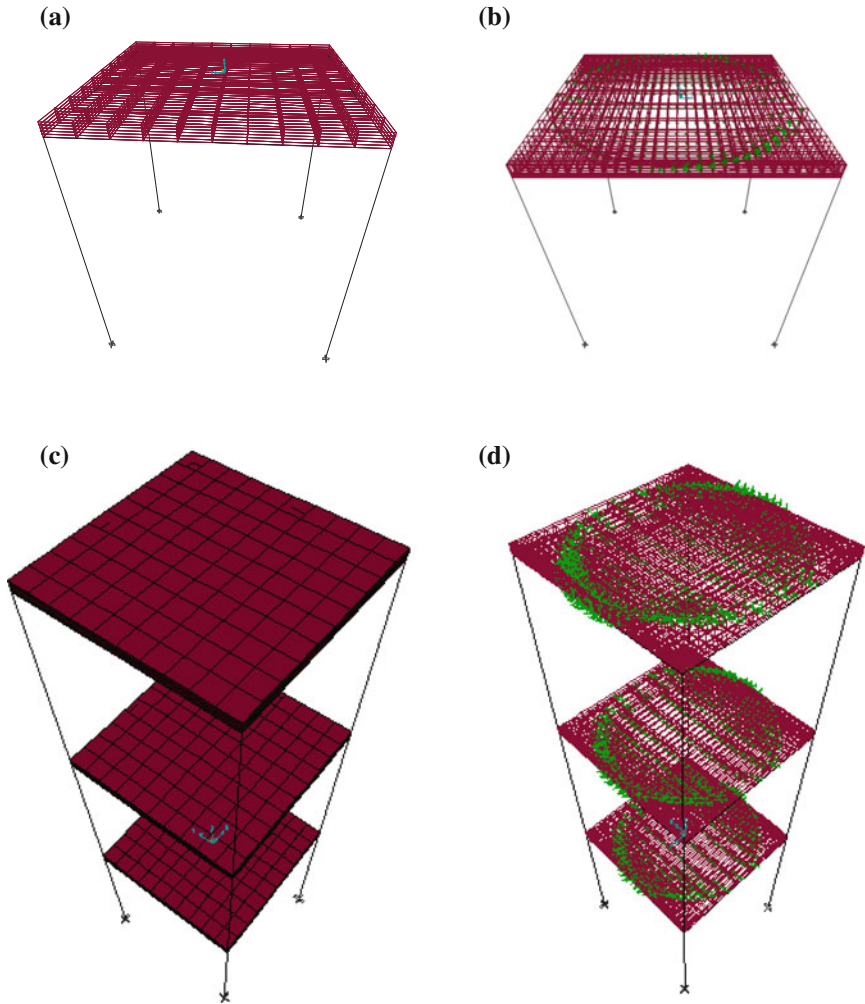


**Fig. 1** Three-dimensional FE wireframe model **a** FSS—single storey **b** FIS—single storey **c** FSS—three stories **d** FIS—three stories

### 4 Linear Time History Analysis

In the present study, linear time history analyses are carried out for the chosen four different earthquakes, viz El Centro (1940), Loma Prieta (1989), Northridge (1994), spectrum compatible ground motions consistent with IS 1893–2002 medium soil spectra for Zone V—design basis earthquake (DBE). The peak base shear, peak acceleration and peak displacement responses, response ratios and percentage reduction in responses for single-storey FSS and FIS are compared as given in

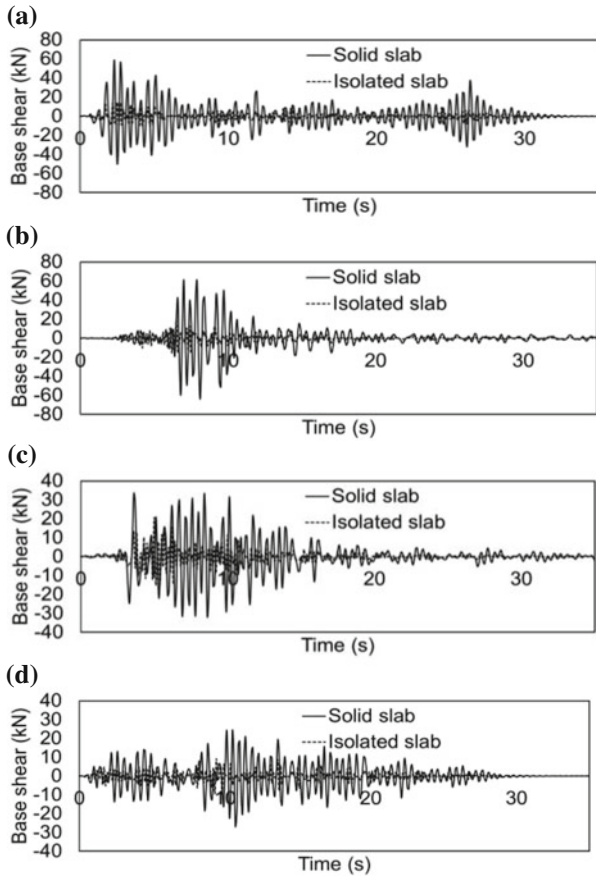
**Table 1** Properties of frame with solid slab and isolated slab

Properties of FSS	Properties of FIS
Dimension: Bay width in plan 2.7 m × 2.7 m	Dimension: Bay width in plan 2.7 m × 2.7 m
Height of storey: 3 m	Storey height: 3 m.
Beam: ISMB 200	Beam: ISMB 200
Column: ISB 113.5 × 113.5 × 4.8	Column: ISB 113.5 × 113.5 × 4.8
Thickness of slab: 130 mm	Thickness of curved slab at middle: 100 mm
Mass source: self-weight plus 50% of live load (3 kN/m <sup>2</sup> )	Thickness of curved slab at edge: 50 mm
	Thickness of supporting slab at middle: 30 mm
	Thickness of supporting slab at edge: 80 mm
	Radius of curved slab = 7.6 m
	Coefficient of friction = 0.3
	Bumper stiffness = 87.4 kN/m
	Stiffness of friction isolation element = 1.99 kN/m
	Mass source: self-weight plus 50% of live load (3 kN/m <sup>2</sup> )

**Table 2** Responses, response ratios and percentage reduction of response for FSS and FIS—single storey

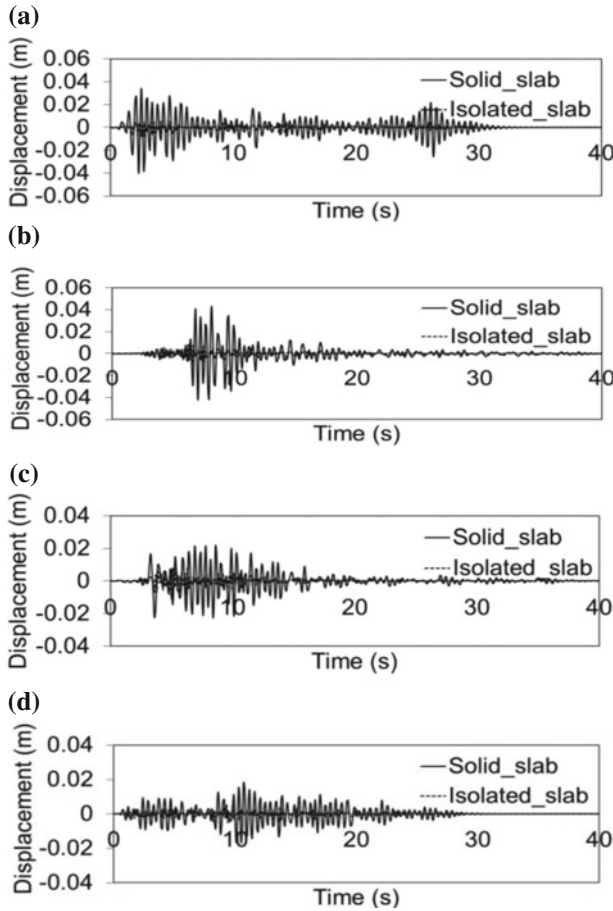
Earthquake	Model	Peak displacement at top (m)	Response ratio (% reduction)	Peak acceleration at top (m/s <sup>2</sup> )	Response ratio (% reduction)	Peak base shear (kN)	Response ratio (% reduction)
El Centro, 1940, NS	FSS	0.0402	0.201	8.198	0.753	58.93	0.251
	FIS	0.0081	(79.9)	6.17	(24.7)	14.77	(74.9)
Loma Prieta, 1989, Arleta, 90	FSS	0.0430	0.249	10.57	0.623	63.78	0.310
	FIS	0.0107	(75.1)	6.59	(33.7)	19.77	(69.0)
North Ridge, 1994, Capitola, 90	FSS	0.0226	0.496	5.00	—	33.53	0.616
	FIS	0.0112	(50.4)	6.64		20.66	(38.4)
IS 1893-2002 Rock Zone 5—DBE	FSS	0.018	0.311	4.00	0.972	26.42	0.390
	FIS	0.0056	(68.9)	3.889	(2.8)	10.31	(61.0)

Table 2. The variations of base shear, roof displacement and acceleration time histories of single-storey FSS and FIS for the four earthquakes are shown in Figs. 2 and 3. It is seen that for Northridge and IS spectrum compatible earthquake, not much of reduction is achieved in acceleration response for the single-storey FSS and FIS systems.



**Fig. 2** Single-storey FSS, FIS base shear **a** El Centro **b** Loma Prieta **c** Northridge **d** IS 1893–2002 spectrum compatible Zone V Medium soil–DBE

Similar studies are carried out for the three-storey FSS and FIS typically for the two earthquakes, viz El Centro and Northridge. The time histories of displacement, acceleration and base shear for the roof level of three-storey FSS and FIS for El Centro and North Ridge earthquakes are shown in Fig. 4a–f. Variations of the storey level peak displacements for the three-storey FSS and FIS for El Centro and Northridge earthquakes are shown in Fig. 4g. It is again seen that reduction of acceleration response is lesser compared to reduction in displacement and base shear for three-storey FIS.



**Fig. 3** Single-storey FSS, FIS displacement **a** El Centro **b** Loma Prieta **c** Northridge **d** IS 1893–2002 spectrum compatible zone V medium soil—DBE

## 5 Conclusions

In this paper, efficiency of isolated floor slab in response reduction is demonstrated through three-dimensional finite element modelling. For the single-storey frame with isolated floor slab, maximum percentage reduction in base shear, displacement and acceleration responses are 75, 80 and 34%, respectively, for the four earthquakes considered. Similarly, for the three-storey frame with isolated floor slab, the maximum percentage reduction in peak base shear, peak roof level displacement and peak acceleration responses are 61, 57 and 30%, respectively, for the El Centro and North Ridge earthquakes. Percentage reduction in acceleration response is

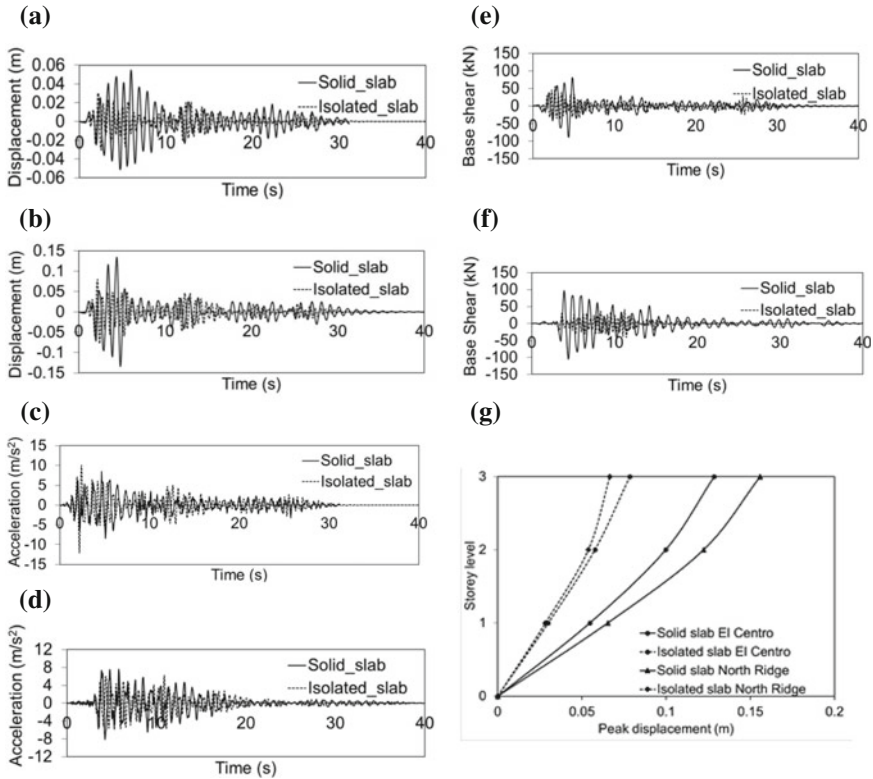


**Fig. 4** Three-storey FSS and FIS **a** roof level displacement—El Centro **b** roof level displacement—North Ridge **c** roof level acceleration—El Centro **d** roof level acceleration—Northridge **e** base shear—El Centro **f** base shear—North Ridge **g** storey level peak displacements for El Centro and North Ridge earthquake

lesser than the percentage reduction in base shear and displacement. Further, the response reductions for different earthquakes are observed to be different.

**Acknowledgements** This paper is published with the kind permission of the Director, CSIR-Structural Engineering Research Centre, Chennai, India. The support extended by Dr. K. Ramanjaneyulu and Dr. K. Rama Raju, Chief Scientists, CSIR-SERC, while carrying out this work is highly acknowledged.

## References

1. Symans M, Charney F, Whittaker A, Constantinou M, Kircher C, Johnson M, McNamara R (2008) Energy dissipation systems for seismic applications: current practice and recent developments. *J Struct Eng ASCE* 134(1(3)):3–21

2. Kamatchi P, Balaji Rao K, Abhishek G (2016) Response reduction of structural system with tuned mass damper for site-specific earthquake including the effect of depth of soil stratum. *Asian J Civ Eng (BHRC)* 17(5):635–650
3. Gewei Z, Basu BA (2010) Study on friction-tuned mass damper: harmonic solution and statistical linearization. *J Vib Control* 17:721–731
4. Pisal YA (2015) Seismic response of multi-story structure with multiple tuned mass friction dampers. *Int J Adv Struct Eng* 7:81–92
5. Lee JH, Berger E, Kim JH (2005) Feasibility study of a tunable friction damper. *J Sound Vib* 283:707–722
6. Lourenco (2011) Design construction and testing of an adaptive pendulum tuned mass damper. University of Waterloo
7. Gerges RR, Vickery BJ (2005) Optimum design of pendulum-type tuned mass dampers. *Struct Des Tall Spec Build* 14:353–368
8. Engle T, Mahmoud H, Chulahwat A (2015) Hybrid tuned mass damper and isolation floor slab system optimized for vibration control. *J Earthq Eng* 19:1197–1221
9. Computers and Structures Inc: SAP 2000. Linear and nonlinear static and dynamic analysis and design of three-dimensional structures. Version 14, California, USA
10. Park YJ, Wn YK, Ang AHS (1986) Random vibration of hysteretic systems under bi-directional ground motions. *Earth Eng St Dyn* 14(4):543–557.



# Performance of Semi-actively Controlled Building Frame Using MR Damper for Near-Field Earthquakes



Vishisht Bhaiya, S. D. Bharti, M. K. Shrimali and T. K. Datta

**Abstract** Most of the studies on the control of building frame using MR damper are investigated for far-field earthquake records, and a considerable reduction in responses is shown. However, MR dampers have some significant drawbacks like the saturation of MR dampers and its performance variability with respect to the ground motions. It has been found that when the predominant frequency of the earthquake is much away from the natural frequency of the structure, the response reduction becomes significantly less. The reason for this may be attributed to the less values of relative displacement and velocities of the floors which primarily influence the force generated in the damper for a given voltage. The characteristics of the near-field ground motion are distinctly different from the far-field ground motion. The performance of the MR damper for the near-field earthquake is not well investigated. In the present study, the performance of the MR dampers is studied for two types of near-field earthquakes, namely Bam (directivity effect) and Chichi (fling step effect) earthquakes. A limited number of MR dampers are employed for response reduction.

**Keywords** MR damper · LQR · Near-field earthquake · Semi-active control

---

V. Bhaiya · S. D. Bharti · M. K. Shrimali · T. K. Datta (✉)  
National Center for Disaster Mitigation and Management, Malaviya  
National Institute of Technology, Jaipur 302017, Rajasthan, India  
e-mail: tushar\_k\_datta@yahoo.co

V. Bhaiya  
e-mail: vishishtbhaiya@gmail.com

S. D. Bharti  
e-mail: sdbharti@gmail.com

M. K. Shrimali  
e-mail: shrimali\_mk@yahoo.co

## 1 Introduction

Controls of structural responses during natural calamities like earthquakes, tsunami, blast, fire, and cyclone have been a favorable research topic for the structural engineers. Many control systems have been proposed and studied by the researchers. The control systems are classified into four categories—passive system, active system, semi-active system, and hybrid system. Out of all the control systems, semi-active control system has gained a considerable attention due to its low power requirement and ability to generate control forces of same order as that produced by active systems. Among all the semi-active devices, MR damper has gained considerable attention as it is fail-safe.

Jansen and Dyke [1] evaluated the performance of different control algorithms using multiple MR dampers. In the numerical example, two MR dampers were installed at lower two floors of a six-story structure and the structure was subjected to El Centro excitation. Xu et al. [2] compared the optimal displacement control strategies with the optimal force control strategy using MR/ER dampers. Yoshida and Dyke [3] investigated the performance of a 20-story nonlinear benchmark building equipped with MR dampers. Kori and Jangid [4] studied the performance of MR dampers under different control algorithms and excitations. Christenson et al. [5] performed a real-time hybrid testing of a large-scale MR damper at University of Colorado, USA. Bahar et al. [6] proposed a hybrid control system combining a nonlinear base isolator and MR damper. In the MR damper, the voltage was updated by a feedback control loop. Chang and Zhou [7] used recurrent neural network models for structural control. They emulated the inverse dynamics of MR damper to produce required command voltage. Two examples of structural control were taken: optimal prediction control of a single degree of freedom system and LQR control of a multi-degree of freedom system to illustrate the proposed scheme. Lee et al. [8] applied the neuro-controller to a base-isolated benchmark problem. The training algorithm based on minimizing the cost function was used. A clipped optimal algorithm was then employed to produce the desired control force. Das et al. [9] used an ANN-cum-fuzzy control scheme for structural response mitigation. Bharti et al. [10] investigated the behavior of an asymmetric building plan with MR dampers.

All the researches published on structural control using MR dampers have mostly used far-field earthquake. In the present study, the performance of the MR dampers is studied for two types of near-field earthquakes, namely Bam (directivity effect) and Chichi (fling step effect) earthquakes. Three MR dampers are employed at the bottom three floors for response reduction.

## 2 Theory

The equation of motion for the building frame fitted with MR dampers in Fig. 1 takes the form:

$$[M]\{\ddot{x}\} + [C]\{\dot{x}\} + [K]\{x\} = [G]\{f_m\} - [M][r]\{\ddot{u}_g\} \tag{1}$$

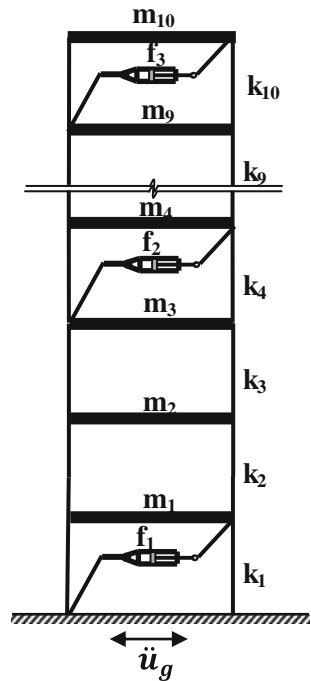
where  $M$ ,  $C$ , and  $K$  are the mass, damping, and stiffness matrices of the system, respectively;  $f_m$  is the MR damper force vector;  $G$  is the damper location matrix of ones and zeroes;  $z$  is the displacement vector with respect to the ground;  $r$  is an influence coefficient vector; and  $\ddot{u}_g$  is the earthquake ground acceleration. The governing Eq. (1) is expressed in the state-space form as below:

$$\{\dot{z}\} = [A]\{z\} + [B]\{f_m\} + [E]\{\ddot{u}_g\} \tag{2}$$

$$y = [C]\{z\} + [D]\{f_m\} + v \tag{3}$$

where  $A$  is a  $2n \times 2n$  system matrix,  $B$  is a  $2n \times n_C$  control matrix,  $E$  is a  $2n \times 1$  disturbance (excitation) matrix,  $C$  is a  $2n \times 2n$  identity matrix,  $D$  is a  $2n \times n_C$  matrix,  $x$  is a  $2n \times 1$  state vector,  $y$  is a  $2n \times 1$  vector of measured outputs, and  $v$  is a  $2n \times 1$  measurement noise vector;  $n$  is the number of states,  $n_C$  is the number of controllers, and  $p$  is the number of measurements.

**Fig. 1** Structural model equipped with three MR dampers



### 2.1 Linear Quadratic Regulator (LQR) Algorithm

The LQR estimates the control force by minimizing the following quadratic cost function:

$$J = E[x^T(T_f)Fx(T_f)] + \int_0^{T_f} x^T(t)Qx(t) + u^T(t)Ru(t)dt \tag{4}$$

where  $E$  denotes the expected value;  $T_f$  denotes the final time which may be finite or infinite, and when  $T_f$  tends to infinity, the first term of the cost function  $x^T(T_f)Fx(T_f)$  becomes negligible;  $Q$  and  $R$  are the positive definite matrices. The control force is given by the following equation:

$$u(t) = -L(t)\hat{x}(t) \tag{5}$$

where  $L(t)$  is the feedback gain matrix and it is defined using  $A$ ,  $B$ ,  $Q$ , and  $R$  matrices and  $F$  by solving the following Riccati equation:

$$-\dot{S}(t) = A^T S(t) + S(t)A - S(t)B^T R^{-1} B^T S(t) + Q \tag{6}$$

$$L(t) = R^{-1} B^T S(t) \text{ and } S(T) = F \tag{7}$$

### 3 Generation of Control Forces Using MR Damper

Force in the MR damper is generated based on the movement of the piston and the viscosity of the MR fluid which is manipulated by applying the voltage to the magnetic coil of the MR damper. While the actuation of the piston is governed by the vibration of the structure, the applied voltage is governed by the control algorithm. The control algorithm is shown in Fig. 2. Modified Bouc–Wen model

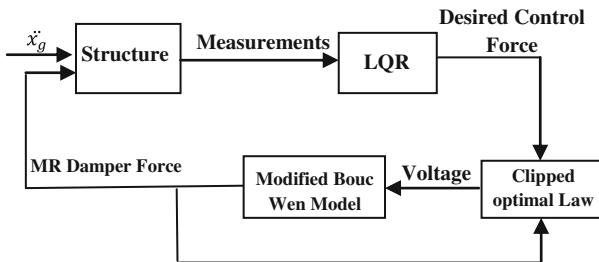


Fig. 2 Control algorithm

[11] is used for predicting the MR damper force. Inputs to the model are the inter-story drifts and velocities. By comparing the generated control force with the desired control force, voltage is held constant or set to zero using clipped optimal control. The reference time history of force used for clipped optimal control is obtained using LQR algorithm. The entire numerical scheme is carried out using Simulink toolbox of MATLAB.

### 3.1 Modified Bouc–Wen Model

Equations governing the MR damper force predicted by this model are given as [11]:

$$\mathbf{f}_m = \mathbf{c}_1 \dot{\mathbf{x}} + \mathbf{k}_1 (\mathbf{u}_d - \mathbf{x}_0) \quad (8)$$

where the evolutionary variable  $z$  is given as:

$$\dot{z} = -\gamma |\mathbf{v}_d - \dot{\mathbf{x}}| |z|^{(n-1)} - \beta (\mathbf{v}_d - \dot{\mathbf{x}}) |z|^n + \mathbf{A}_m (\mathbf{v}_d - \dot{\mathbf{x}}) \quad (9)$$

and  $\dot{\mathbf{x}}$  is given as

$$\dot{\mathbf{x}} = \left\{ \frac{1}{\mathbf{c}_0 + \mathbf{c}_1} \right\} \{ \alpha_0 \mathbf{z} + \mathbf{c}_0 \mathbf{v}_d + \mathbf{k}_0 (\mathbf{u}_d - \mathbf{x}) \} \quad (10)$$

where  $u_d$  is the displacement of the damper;  $x$  is the internal pseudo-displacement of the damper;  $z$  is the evolutionary variable that describes the hysteretic behavior of the damper;  $k_1$  is the accumulator stiffness;  $c_0$  is the viscous damping at large velocities;  $c_1$  is viscous damping for force roll-off at low velocities;  $k_0$  is the stiffness at large velocities; and  $x_0$  is the initial stiffness of spring  $k_1$ ;  $\alpha_0$  is the evolutionary coefficient;  $\gamma$ ,  $\beta$ ,  $\eta$ , and  $A_m$  are shape parameters of the hysteresis loop. The model parameters dependent on command voltage  $c_0$ ,  $c_1$ ,  $\alpha_0$  are expressed as follows:

$$\mathbf{c}_0 = \mathbf{c}_{0a} + \mathbf{c}_{0b} \mathbf{U} \quad (11)$$

$$\mathbf{c}_1 = \mathbf{c}_{1a} + \mathbf{c}_{1b} \mathbf{U} \quad (12)$$

$$\alpha_0 = \alpha_{0a} + \alpha_{0b} \mathbf{U} \quad (13)$$

where  $U$  is given as output of first-order filter following the condition as below

$$\dot{U} = -\eta(U - V) \quad (14)$$

### 3.2 Clipped Optimal Control Law

The input voltage to the MR damper is obtained using clipped optimal law [12]. When the absolute value of MR damper force is greater than the absolute value of LQR force, then the voltage is set to maximum, and when the absolute value of MR damper force is less than the absolute value of LQR force, then the voltage is set to zero. The mathematical form of clipped optimal law is:

$$V = V_{\max} H\{(F_d - F_{mr})F_{mr}\} \tag{15}$$

where  $V$  is the input voltage to the MR damper,  $H$  is the Heaviside function,  $V_{\max}$  is the maximum input voltage,  $F_d$  is the LQR force, and  $F_{mr}$  is the MR damper force. The voltage is maximum when Heaviside function is one and zero when Heaviside function is zero.

## 4 Numerical Study

The details of building frame are shown in Fig. 1. Mass of each story is 18,000 kg, and stiffness of each floor is 24,965 kN/m. Three MR dampers are used to control the response and are placed at the bottom the story of the frame where maximum drifts are expected to take place for uncontrolled vibration. The time histories of uncontrolled and controlled responses of top floor displacement for Bam and Chichi earthquakes are shown in Figs. 4 and 6, respectively. Similarly, time histories of uncontrolled and controlled responses of base shear for Bam and Chichi earthquakes are shown in Figs. 3 and 5, respectively. Force–displacement and force–velocity plots of the MR damper located at third floor are shown in Figs. 7, 8, 9, and 10.

**Fig. 3** Comparison of uncontrolled and controlled time histories of base shear for Bam (2003) earthquake

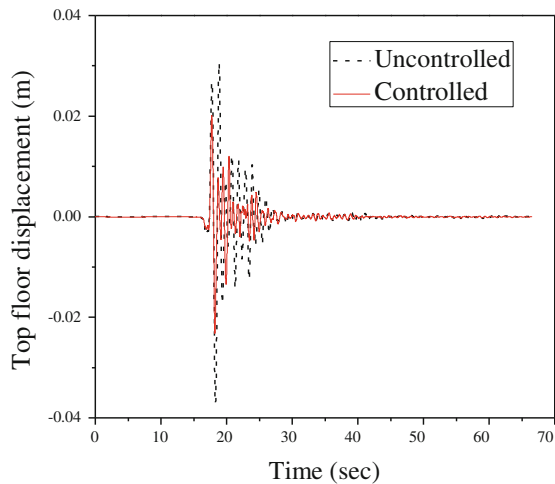


**Fig. 4** Comparison of uncontrolled and controlled time histories of top floor displacement for Bam (2003) earthquake

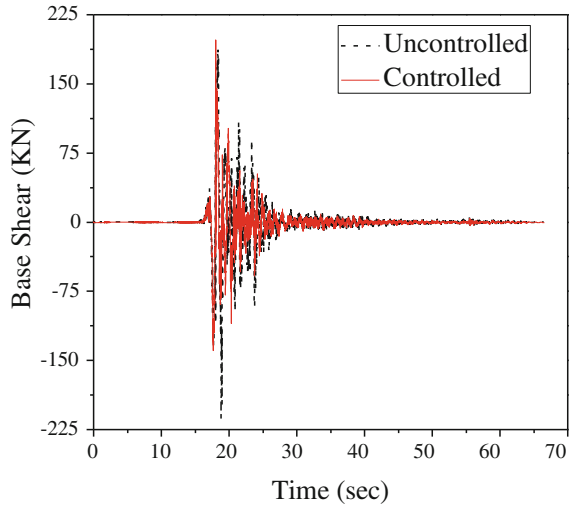
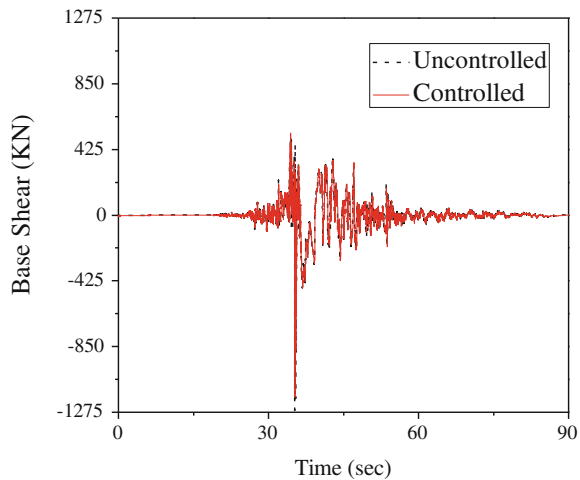


**Fig. 5** Comparison of uncontrolled and controlled time histories of base shear for Chichi (1999) earthquake



It is seen from the above figures that the control characteristics for the two earthquakes are distinctly different. The differences in the two responses are largely due to the presence of the directivity effect in one and the fling step effect in the other. The fling step causes large displacement in the structure. The peak values for different response quantities of interest for uncontrolled and controlled conditions are shown in Table 1. The percentage reductions for different responses of interest are shown in Table 2. The percentage reduction is calculated as shown below

**Fig. 6** Comparison of uncontrolled and controlled time histories of top floor displacement for Chichi (1999) earthquake

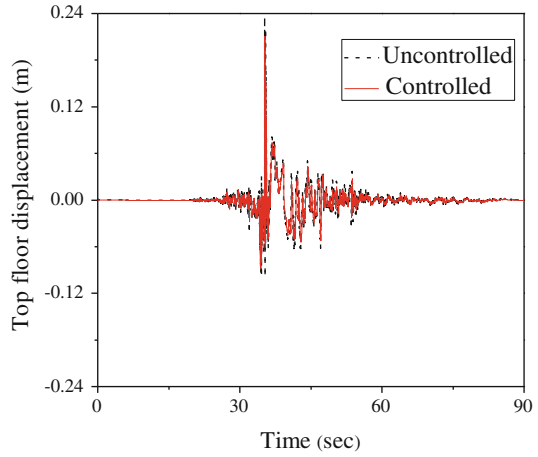
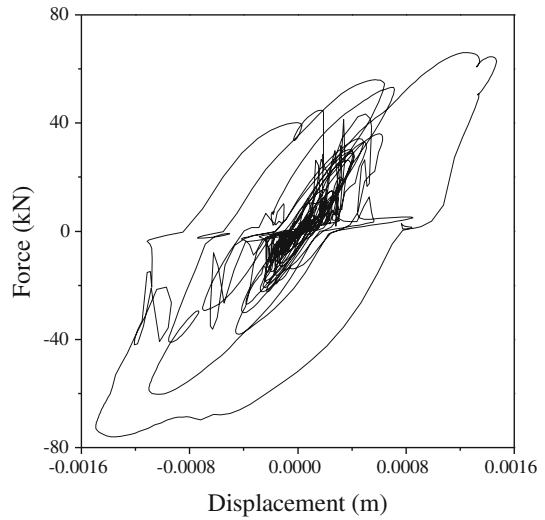


**Fig. 7** Force–displacement plot of MR damper for Bam (2003) earthquake



$$\text{Percentage reduction} = \frac{UN_{pr} - CO_{pr}}{UN_{pr}} \tag{16}$$

where  $UN_{pr}$  is the uncontrolled peak response;  $CO_{pr}$  is the controlled peak response.



**Fig. 8** Force–velocity plot of MR damper for Bam (2003) earthquake

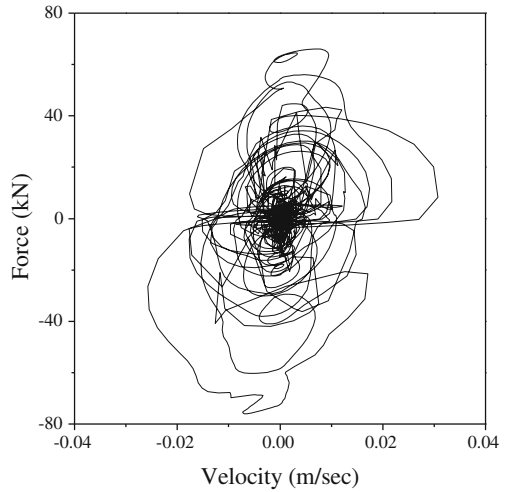
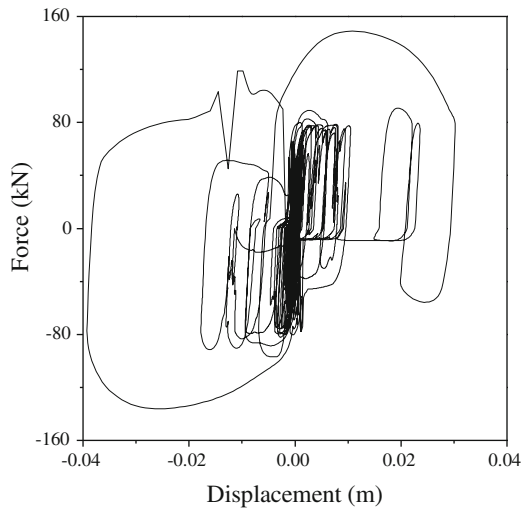


**Fig. 9** Force–displacement plot of MR damper for Chichi (1999) earthquake



## 5 Conclusions

Numerical studies lead to the following conclusion:

1. The controlled responses of the frame for the two earthquakes have distinctly different characteristics.
2. The fling step effect induces a large displacement in the structure as compared to the directivity effect.

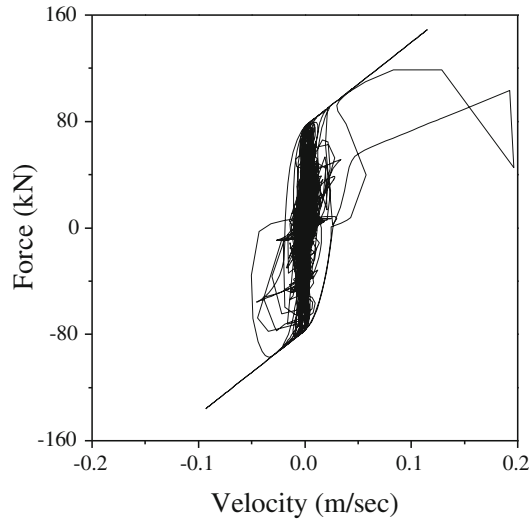


**Fig. 10** Force–velocity plot of MR damper for Chichi (1999) earthquake

**Table 1** Peak responses for Bam and Chichi earthquakes for uncontrolled and controlled conditions

Response quantity	Percentage reduction for Bam earthquake (2003)	Percentage reduction for Chichi earthquake (1999)
$D$	38.6	12.5
$F_d$	12.54	11.5
$d_r$	58.52	15.23

**Table 2** Percentage response reduction for Bam and Chichi earthquakes

Response quantity	Bam earthquake (2003)		Chichi earthquake (1999)	
	UN <sub>pr</sub>	CO <sub>pr</sub>	UN <sub>pr</sub>	CO <sub>pr</sub>
$D$ (cm)	3.43	2.31	23.84	21.09
$F_d$ (kN)	216	197	1263	1177
$d_r$ (cm)	0.59	0.26	4.16	3.55

Note  $D$ ,  $F_d$ , and  $d_r$  denotes the top floor displacement, base shear, and maximum inter-story drift, respectively

3. The percentage reduction of response quantities of interest for an earthquake with directivity effect is comparable to those for far-field earthquake.
4. Fling step effect provides a very less reduction in response quantities of interest, and thus it appears that semi-active control using MR dampers is not suitable for the control of buildings for the near-field earthquake with fling step effect.

## References

1. Jansen LM, Dyke SJ (2000) Semiactive control strategies for MR dampers: comparative study. *J Eng Mech* 126(8):795–803
2. Xu Y, Qu W, Ko J (2000) Seismic response control of frame structures using magnetorheological/electrorheological dampers. *Earthq Eng Struct Dynam* 29(5):557–575
3. Yoshida O, Dyke SJ (2004) Seismic control of a nonlinear benchmark building using smart dampers. *J Eng Mech* 130(4):386–392
4. Kori JG, Jangid R (2009) Semi-active MR dampers for seismic control of structures. *Bull New Zealand Soc Earthq Eng* 42(3):157
5. Christenson R et al (2008) Large-scale experimental verification of semiactive control through real-time hybrid simulation 1. *J Struct Eng* 134(4):522–534
6. Bahar A et al (2010) Hierarchical semi-active control of base-isolated structures using a new inverse model of magnetorheological dampers. *Comput Struct* 88(7):483–496
7. Chang C-C, Zhou L (2002) Neural network emulation of inverse dynamics for a magnetorheological damper. *J Struct Eng* 128(2):231–239
8. Lee H-J et al. (2005) Semi-active neuro-control strategy for a seismic-excited base isolated benchmark structure
9. Das D, Datta T, Madan A (2012) ANN-cum-fuzzy control of seismic response using MR dampers. In: *Proceedings of the 15th World Conference on Earthquake Engineering (15 WCEE)*, Lisbon
10. Bharti S, Dumne S, Shrimali M (2014) Earthquake response of asymmetric building with MR damper. *Earthq Eng Eng Vibr* 13(2):305–316
11. Spencer B et al (1997) Phenomenological model for magnetorheological dampers. *J Eng Mech* 123(3):230–238
12. Dyke S et al (1996) Acceleration feedback control of MDOF structures. *J Eng Mech* 122(9):907–918

# Cyclone Wind Response Mitigation of Transmission Towers by SMA Dampers



Madhusree Roy and Aparna (Dey) Ghosh

**Abstract** The present study focuses on a means of improving the performance of transmission towers under high-intensity winds in the form of cyclonic winds through the use of shape memory alloy (SMA) dampers installed in the bracings of the tower. The cyclonic wind field is modelled as per the guidelines of the World Meteorological Organization, and the Harris power spectral density function (PSDF) is used to characterize the fluctuating component of the cyclonic wind velocity. Nonlinear time history analysis of a single circuit lattice transmission tower is carried out under the cyclonic wind load time histories generated for each node of the tower. Results indicate that the recentering and energy dissipation properties of superelastic SMA bar dampers are capable of significantly mitigating the tower's response to cyclonic wind loads.

**Keywords** Transmission tower · SMA damper · Superelastic effect  
Cyclonic wind load

## 1 Introduction

Over the last few years, in India and elsewhere, the growing demand for an uninterrupted power supply even to distant places, far away from the power generating stations, has spurred an increase in transmission line tower (TLT) construction and their maintenance activities. TLTs are usually tall steel lattice structures with small damping and sensitivity to wind excitation. The vulnerability of these structures to wind loading is very high, and over 80% reported cases of damage to TLTs have been caused by high-intensity winds (HIW) such as

---

M. Roy · A. (Dey) Ghosh (✉)  
Department of Civil Engineering, Indian Institute of Engineering Science  
and Technology, Shibpur, Howrah 711103, India  
e-mail: [aparna@civil.iiests.ac.in](mailto:aparna@civil.iiests.ac.in)

M. Roy  
e-mail: [madhusree.roy16@gmail.com](mailto:madhusree.roy16@gmail.com)

tornadoes, cyclones, microbursts. As the wind structures of HIW are more complex than that of traditional boundary layer winds, TLTs designed against code-specified design wind loads may still suffer heavy damages under extreme weather events. Therefore, it is necessary to investigate such designs and devices that can mitigate the disastrous effect of HIW on transmission towers.

The costly problem of transmission tower failure has led to the development and application of various structural assessment and mitigation techniques, including vibration control devices, for both wind- and seismic-induced responses of these structures. Chen et al. [1] have provided a state-of-the-art review of the vibration control methodologies for transmission towers. Semi-active control strategies using magneto rheological (MR) dampers and friction dampers were investigated for the control of the transmission tower-line system under wind and earthquake excitation, respectively, in [2, 3] and found effective. Viscoelastic dampers were also proposed for the wind-resistant design of the transmission tower-line system [4] while the tuned mass damper (TMD) and pounding tuned mass damper (PTMD) were studied by Tian et al. [5], Zhang et al. [6], respectively, for the seismic vibration control of transmission tower systems.

In this paper, shape memory alloy (SMA)-based control devices are proposed to be installed in the axial members of the truss tower. SMAs have found applications in many areas due to their large elastic strain capacity, energy dissipation capability and excellent fatigue and corrosion resistance. Fukuta et al. [7], Ocel et al. [8], Andrawes et al. [9] have studied the application of SMAs in the vibration control of building structures and bridge systems. SMA control devices include SMA restrainer bars, SMA-assisted elastomeric bearings, SMA rods and SMA braces. The last has been developed using SMA wires by Dolce et al. [10] and their effectiveness reported in studies by Han et al. [11], McCormick et al. [12], among others. The present work considers the replacement of some of the steel braces of the transmission tower by SMA braces.

The TLT considered for the present study is a 35-m-high single circuit tension tower. It is modelled in 3-D in the standard finite element software OpenSees. The cyclonic wind field is modelled by following the guidelines given by the World Meteorological Organization [13]. The Harris power spectral density function (PSDF) is used to characterize the fluctuating component of the cyclonic wind velocity. The cyclonic wind velocity time histories are generated from the Harris PSDF by using the spectral representation method suggested by Shinozuka and Deodatis [14]. The force-velocity relationship for a slender bluff body as provided by Wen [15] is then utilized to obtain the cyclonic force time histories. These are evaluated for and applied at the different nodes of the tower, and the response of the tower is obtained by carrying out a nonlinear time history analysis in OpenSees. Results indicate that the tower undergoes very large deformations due to yielding of some of the members, leading to an unbounded response and consequent failure of the structure. Next, SMA damping devices in the form of superelastic SMA bars are installed in some of the members of the TLT and the response mitigation achieved is evaluated.

## 2 Description of Example Tower

The TLT considered for the present study is a single circuit tension tower of total height 35 m and a square base area of  $6 \times 6$  m. It is a lattice transmission tower fixed at the base. In the considered tower, the tower body is 27 m high, cage of the tower is 3 m high and peak of the tower is 5 m high. The tower is provided with traditional chevron bracing system up to the cross-arm level along the perimeter to provide lateral load resistance. A diagonal bracing system is also provided in the peak, cage and cross-arm portions of the tower.

## 3 Details of SMA Damper

The superelastic property of SMA (here Nitinol) can be exploited in order to operate as a passive control device in structural systems. To mitigate the response of the transmission tower under cyclonic wind load, the SMA damping device used here is in the form of superelastic SMA bars in the bracing members as well as in the horizontal members of the tower. This type of SMA damper was proposed by McCormick et al. for seismically excited steel framed structures. The model of the SMA brace considered here is taken from [16], who studied the cyclic properties of large diameter superelastic SMA bars. The SMA model represents an idealized behaviour for the SMA devices where a complete recovery of the original shape is achieved at the removal of the load. In this model, the strain values at the start and the end of the phase transformation are taken as 1 and 6%, respectively.

## 4 Modelling of Cyclonic Wind Field

In the cyclonic wind field, the instantaneous wind  $V(t)$  can be simply represented as the sum of the mean wind speed  $V_{T_0}$  averaged over a period of  $T_0$  and a fluctuating component  $u(t)$  about the mean [13] such that,

$$V(t) = u(t) + V_{T_0}. \quad (1)$$

The vertical variation in the mean wind speed with height for a typical tropical cyclone can be well approximated by an equilibrium form of the logarithmic boundary layer profile under neutral stability conditions [17, 18] and can be expressed as

$$V(z) = \frac{u_*}{k} \ln\left(\frac{z}{z_0}\right) \approx V_{T_0}(z). \quad (2)$$

in which  $k$  denotes von Karman's constant having a value of 0.41,  $u_*$  is the friction velocity,  $z$  is the height above the ground and  $z_0$  is the surface roughness length.

In practice,  $u_*$  can be expressed in terms of a surface drag coefficient  $C_{10}$  referenced to the standard reference height of +10 m for neutral stability conditions as shown in the equation below,

$$C_{10} = \frac{u_*^2}{V_{T_0}^2(10)}. \quad (3)$$

in which the values of  $C_{10}$  and  $z_0$  are taken as 0.005 and 0.1, respectively [19].

The fluctuating component of velocity  $u(t)$  is assumed to be a stationary random process and is characterized by the standard Harris PSDF in the frequency domain. The simulation procedure suggested by Shinozuka and Deodatis [14] is then used to obtain a time history of wind velocity from the Harris PSDF.

#### 4.1 PSDF Characterizing Wind Velocity

In this study, the Harris PSDF [20] is used to characterize the fluctuating component of the cyclonic wind velocity. In the Harris spectrum for wind, the PSDF of wind velocity is given by,

$$S_V(\omega) = \frac{4\pi K_0 V_{10}^2}{\omega} \frac{X}{[2 + (X^2)]^{5/6}}. \quad (4)$$

$$\text{where, } X = \frac{\omega l_x}{2\pi V_{10}} \quad (5)$$

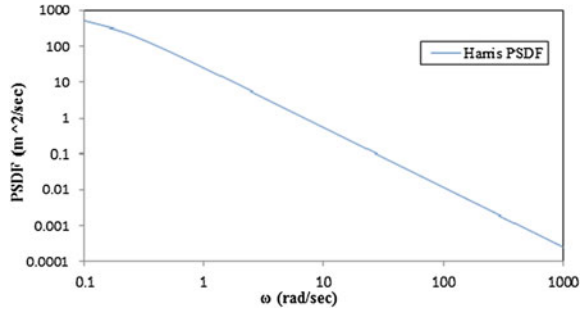
in which  $K_0$  is the ground surface drag coefficient,  $l_x$  is the length constant,  $\omega$  is the frequency in rad/sec and  $V_{10}$  is the mean wind velocity at 10 m height. Here,  $K_0$  and  $l_x$  are taken as 0.03 and 1200 m (Balendra et al. 1995), respectively. As per IMD tropical cyclone intensity scale, for cyclonic storm,  $V_{10}$  is considered as 18 m/s.

A logarithmic plot of the Harris PSDF is shown in Fig. 1. From the plot, it can be seen that the Harris PSDF indicates very high energy content corresponding to a very small frequency ( $\omega$ ) value. It is observed that at the fundamental frequency of the tower (=22 rad/s), the energy is considerably reduced but still significant.

#### 4.2 Simulation of Stochastic Process

A one-dimensional, univariate, stationary, Gaussian stochastic simulation procedure is provided by Shinozuka and Deodatis [14] using the spectral representation

**Fig. 1** Harris PSDF for wind velocity



method. Following this methodology, sample functions of the stochastic process can be generated with great computational efficiency using a cosine series formula.

A one-dimensional, univariate, stationary, zero-mean stochastic process  $f_0(t)$  with PSDF  $S_{f_0f_0}(\omega)$  is considered. Then its simulation  $f(t)$  can be represented as

$$f(t) = \sqrt{2} \sum_{n=0}^{N-1} A_n \cos(\omega_n t + \Phi_n). \tag{6}$$

in which,  $A_n = (2S_{f_0f_0}(\omega_n)\Delta\omega)^{1/2}$  \tag{7}

where  $n = 0, 1, 2, \dots, N - 1$ .

$$\omega_n = n\Delta\omega. \tag{8}$$

$$\Delta\omega = \omega_u/N \tag{9}$$

and  $A_0 = 0$  or  $S_{f_0f_0}(\omega_0 = 0) = 0$ . \tag{10}

In Eq. (9),  $\omega_u$  represents an upper cut-off frequency beyond which the PSDF  $S_{f_0f_0}(\omega)$  may be assumed to be zero for either mathematical or physical reasons. The  $\Phi_0, \Phi_1, \Phi_2, \dots, \Phi_{N-1}$  appearing in Eq. (6) are independent random phase angles distributed uniformly over the interval  $[0, 2\pi]$ .

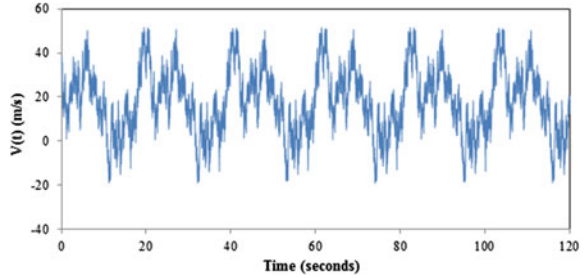
With the help of Eq. (10), it is seen that the simulated stochastic process  $f(t)$  given by Eq. (6) is periodic with period  $T_0$  such that,

$$T_0 = \frac{2\pi}{\Delta\omega}. \tag{11}$$

This indicates that the smaller the value of  $\Delta\omega$  or equivalently larger  $N$  under a specified upper cut-off frequency value  $\omega_u$ , the longer the time period of the simulated stochastic process. It is important to note that while generating sample functions of the simulated stochastic process, the time step  $\Delta t$  separating the generated values in the time domain must obey the following condition in order to avoid aliasing.



**Fig. 2** Time history of cyclonic instantaneous wind velocity at 35 m height



$$\Delta t \leq \frac{2\pi}{2\omega_u} \quad (12)$$

To generate the time history of the fluctuating component of the wind velocity, the value of  $\omega_u$  is considered as 300 rad/sec as beyond this value the Harris PSDF indicates very low amount of energy content (ref. Figure 1). The value of  $N$  is considered as 1000 and  $\Delta\omega$  is obtained as 0.3. In order to satisfy the condition of Eq. (12),  $\Delta t$  is considered as 0.01 s. Using this aforementioned set of values, a sample time history of the fluctuating component of wind velocity for 120 s duration is simulated and the resulting time history of the instantaneous wind velocity  $V(t)$  is shown in Fig. 2.

## 5 Generation of Cyclonic Wind Loads

We consider here both the drag and the inertia force components in the force-velocity relationship. Let  $Q(t)$  denote the force per unit height of the tower. This may be expressed as [15]

$$Q(t) = \frac{1}{2} C_D D \rho U(t)^2 + \frac{\pi}{4} C_m D^2 \rho \frac{dU(t)}{dt}. \quad (13)$$

in which  $C_D$  and  $C_m$  denote the drag and inertia coefficients, respectively.  $\rho$  is the air density,  $D$  is the projected width of the tower normal to the direction being considered and  $U(t)$  is the velocity component in that direction. The values of  $C_D$ ,  $C_m$  and  $\rho$  are considered as 3, 1 and 1.225 kg/m<sup>3</sup>, respectively.

The time history of nodal forces acting on the windward and leeward sides of the tower at a height  $z$  in the X-direction are obtained from the following expressions,

$$F_{WX} = \frac{1}{3} Q_X(z, t) \times h \times S_r. \quad (14)$$

**Fig. 3** Time history of cyclonic wind force in X-direction acting at a node on windward side of the tower at 35 m height

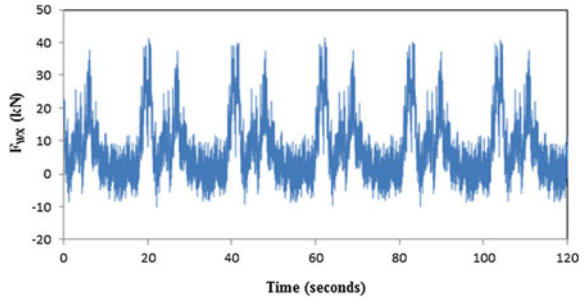
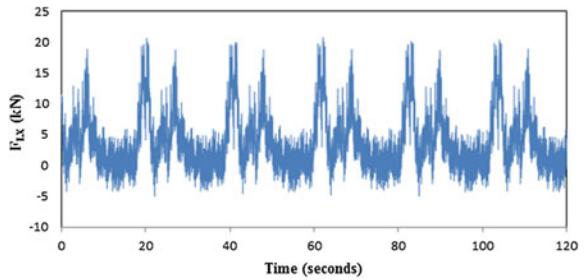


**Fig. 4** Time history of cyclonic wind force in X-direction acting at a node on leeward side of the tower at 35 m height



$$F_{LX} = \frac{1}{6} Q_X(z, t) \times h \times S_r. \tag{15}$$

where  $S_r$  is the solidity ratio, and it is considered as 0.28 for the present study.  $h$  is the projected height of half the panel above and below the node under consideration. Those evaluated at 35 m height of the tower are shown in Figs. 3 and 4.

## 6 Nonlinear Dynamic Time History Analysis of TLT Under Cyclonic Wind Loads

The considered tower model is analysed under the cyclonic wind loading by performing a nonlinear dynamic time history analysis in the finite element software OpenSees [21]. In Fig. 5, the displacement time history at the top of the tower in the X-direction is shown. From the displacement time history, it can be observed that the tower undergoes large oscillations with a significant amount of permanent displacement, which ultimately leads to the failure of the tower. The structural failure of the tower takes place due to the material failure, i.e. yielding of some of the steel chevron braces, some of the horizontal members and some of the cross bracings provided at the cross-arm level of the tower.

**Fig. 5** Top displacement time history in the X-direction of the uncontrolled tower

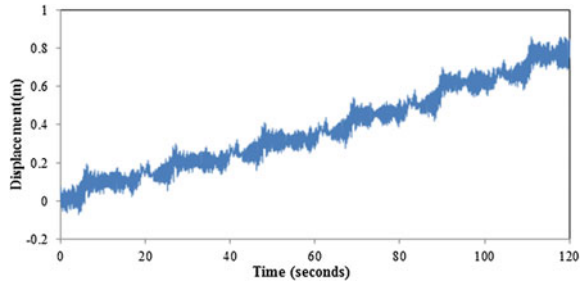
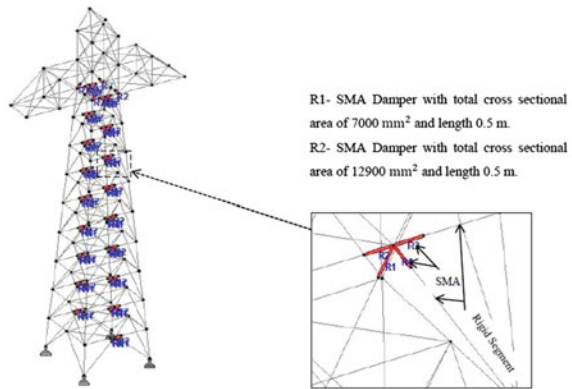
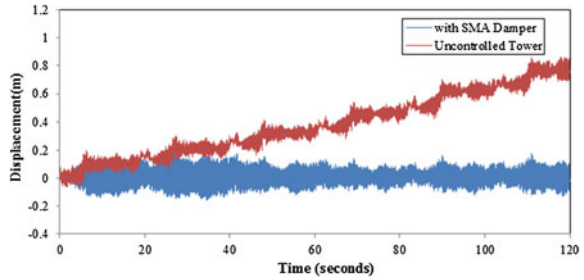


**Fig. 6** Tower with the SMA damper attached to it



Next, the steel chevron braces, the cross bracings in the cage at cross–arm level and the horizontal steel members up to the cross–arm level of the tower under study are replaced with superelastic SMA bar segments as shown in Fig. 6 and are connected to the structure through rigid elements in order to reduce the length of SMA required. The SMA braces are designed to provide the same initial axial stiffness as the steel braces. Here, the steel chevron bracings are provided with a total cross-sectional area of  $0.001612 \text{ m}^2$  (2 nos *ISA 70 × 70 × 6*). The cross bracings in the cage at the cross–arm level and the horizontal steel members up to the cross–arm level of the tower are provided with a total cross-sectional area of  $0.002903 \text{ m}^2$  (*ISA 150 × 150 × 10*). Young’s modulus of elasticity for steel and the austenite elastic stiffness for Nitinol SMA are considered as  $2 \times 10^{11} \text{ N/m}^2$  and  $4.5 \times 10^{10} \text{ N/m}^2$  respectively. From this, it is computed that the SMA bars provided in the chevron bracings should have a total cross-sectional area of  $7000 \text{ mm}^2$  and may consist of 55 numbers of 12.7-mm-diameter individual bars [12] so as to provide the required cross-sectional area. Similarly, for the remaining SMA bars which are provided in the cross bracings and in the horizontal members up to the cross–arm level of the tower, it is evaluated that they should have a total cross-sectional area of  $12,900 \text{ mm}^2$  and may be composed of 100 numbers of 12.7-mm-diameter individual bars [12]. As there is no difference in the stiffness of

**Fig. 7** Top displacement time history in the X-direction of uncontrolled and passively controlled tower



the uncontrolled and controlled towers, both the conventional steel braced tower and the SMA braced tower have the same natural time periods.

In order to compare the performance of the passively controlled tower with the uncontrolled tower, the displacement time histories at the top of the considered tower for the two cases are evaluated and shown in Fig. 7. The uncontrolled steel tower shows an unbounded response with a significant amount of residual displacement in X-direction but the same tower with the SMA braces shows a bounded response with no residual displacement and a maximum top displacement of 0.2 m in X-direction. The energy dissipating capability of the SMA decreases the plastic deformations of the members of the tower. The recentering ability of the SMA causes the tower to return to its original geometry at frequent times during the HIW event, thereby preventing accumulation of inelastic deformations in the structure.

## 7 Conclusions

Through this work, the applicability of superelastic SMA dampers as a control device for the mitigation of the structural response of TLT subjected to cyclonic wind loads is investigated. The cyclonic wind loading creates unbounded responses signifying failure in the uncontrolled tower. However, the same tower after incorporation of superelastic SMA bars in the bracing system shows a bounded response with a complete removal of residual displacement. Hence, it can be concluded that the tower with SMA dampers prevents the failure of the tower by reducing the maximum top displacement and residual displacement of the tower significantly. The ability of the SMA damper to dissipate energy through its flag-shaped hysteresis and to provide recentering is mainly responsible for decrease in the maximum and residual displacements of the tower. Thus, superelastic SMAs have a great potential in controlling the structural response of TLTs due to cyclonic winds.

## References

1. Chen B, Guo W-H, Li P-Y, Xie W-P (2014) Dynamic responses and vibration control of the transmission tower-line system: a state-of-the-art review. *Sci World J* 2014:1–20
2. Chen B, Zheng J, Qu W (2009) Control of wind-induced response of transmission tower-line system by using magnetorheological dampers. *Int J Struct Stab Dyn* 9(4):661–685
3. Chen B, Zheng J, Qu WL (2010) Vibration control and damage detection of transmission tower-line system under earthquake by using friction dampers. In: *Proceedings of the 11th international symposium on structural engineering, Guangzhou, China*, pp 1418–1425
4. Chen B, Zheng J, Qu WL (2007) Practical method for wind resistant design of transmission tower-line system by using viscoelastic dampers. In: *Proceedings of the 2nd international conference on structural condition assessment, monitoring and improvement, Changsha, China*, pp 1028–1034
5. Tian L, Yu QQ, Ma RS (2013) Study on seismic control of power transmission tower-line coupled system under multi component excitations. *Math Probl Eng* 2013(829415): 12
6. Zhang P, Song GB, Li HN, Lin YX (2013) Seismic control of power transmission tower using pounding TMD. *J Eng Mech* 139(10):1395–1406
7. Fukuta T, Iiba M, Kitagawa Y, Sakai Y (2004) Experimental study on stress-strain property of shape memory alloy and its application to self-restoration of structural members. In: *Proceedings of the 13th world conference on earthquake engineering, Canadian Association for Earthquake Engineering, Ottawa*, paper 610
8. Ocel J, DesRoches R, Leon R, Hess W, Krumme R, Hayes J, Sweeney S (2004) Steel beam-column connections using shape memory alloys. *J Struct Eng* 130(5):732–740
9. Andrawes B, DesRoches R (2005) Unseating prevention for multiple frame bridges using superelastic devices. *Smart Mater Struct* 14(3):S60–S67
10. Dolce M, Cardone D, Marnetto R (2000) Implementation and testing of passive control devices based on shape-memory alloys. *Earthquake Eng Struct Dynam* 29:945–968
11. Han Y-L, Li QS, Li A-Q, Leung AYT, Ling P-H (2003) Structural vibration control by shape-memory alloy damper. *Earthquake Eng Struct Dynam* 32(3):483–494
12. McCormick J, ASCE SM, DesRoches R, ASCE M, Fugazza D, Auricchio F (2007) Seismic assessment of concentrically braced steel frames with shape memory alloy braces. *J Struct Eng* 133: 862–870
13. Harper BA, Kepert JD, Ginger JD (2008) Guidelines for converting between various wind averaging periods in tropical cyclone conditions. *World Meteorol Organ*
14. Shinozuka M, Deodatis G (1991) Simulation of stochastic process by spectral representation. *Appl Mech Rev* 44(4):155–190
15. Wen YK (1975) Dynamic tornadic wind loads on tall buildings. *J ASCE Struct Div* 101:169–185
16. DesRoches R, McCormick J, Delemont M (2004) Cyclic properties of superelastic shape memory alloy wires and bars. *J Struct Eng* 130(1):38–46
17. Lumley JL, Panofsky HA (1964) *The Structure of atmospheric turbulence*. Wiley Interscience, New York. p 239
18. Powell MD, Vickery PJ, Reinhold TA (2003) Reduced drag coefficient for high wind speeds in tropical cyclones. *Nature* 279–283
19. Wieringa J, Davenport AG, Grimmond CSB, Oke TR (2001) New revision of Davenport roughness classification. In: *Proceedings of the 3rd European and African conference on wind engineering, Eindhoven, The Netherlands*, 2–6 July, pp 285–292
20. Balendra T, Wang CM, Cheong HF (1995) Effectiveness of tuned liquid column dampers for vibration control of towers. *Eng Struct* 17(9):668–675
21. McKenna F, Fenves GL (2004) *OpenSees command language manual, version 1.5.2*, Pacific Earthquake Engineering Research Center, [<http://opensees.berkeley.edu>]

# Linearized Dynamic Analysis of Weightless Sagging Planar Elastic Cables



Pankaj Kumar, Abhijit Ganguli and Gurmail Benipal

**Abstract** Nonlinear dynamic analysis of elastic structures is known to be much more complex than their linear analysis. There are many sources of nonlinearity of the structural response of elastic cables, viz., physical nonlinearity due to nonlinear tension–extension relations, geometric nonlinearity associated with finite elastic displacements and nonlinearity of nodal load–displacement relations due to the presence of self-weight. Incremental second-order differential equations of motion are used to predict the vibration amplitudes relative to the equilibrium state caused by additional dynamic forces. Generally, the tangent stiffness matrices are determined by adding the tangent elastic and geometric stiffness matrices. Many a time, an approximate linearized dynamic analysis is attempted. In this paper, the initial tangent stiffness matrix corresponding to the equilibrium state is used in the second-order linear differential equation of motion. The dynamic response relative to the equilibrium state of the structure subjected to additional dynamic loads is predicted. The predictions of linearized dynamic analysis are generally considered acceptable for small elastic displacements from the equilibrium state. The validity of such linearized dynamic analysis for elasto-flexible cables obeying third-order differential equation of motion is explored.

**Keywords** Weightless sagging cables · Cable dynamics · Nonlinear analysis  
Configurational response

---

P. Kumar · A. Ganguli · G. Benipal (✉)  
Department of Civil Engineering, IIT Delhi, Hauz Khas, New Delhi 110016, India  
e-mail: gurmail@civil.iitd.ac.in

P. Kumar  
e-mail: pankaj437@gmail.com

A. Ganguli  
e-mail: abhijit.ganguli@civil.iitd.ac.in

© Springer Nature Singapore Pte Ltd. 2019  
A. Rama Mohan Rao and K. Ramanjaneyulu (eds.), *Recent Advances in Structural Engineering, Volume 2*, Lecture Notes in Civil Engineering 12,  
[https://doi.org/10.1007/978-981-13-0365-4\\_36](https://doi.org/10.1007/978-981-13-0365-4_36)

## 1 Introduction

Cables are important components of structures in diverse fields such as transportation, power transmission lines, marine environment, entertainment. First theories of sagging cables were proposed about three centuries ago. Major impetus to research was provided by aeroelastic failure of Tacoma Narrows suspension bridge caused by moderate winds in 1940. Sagging flexible cables differ from the conventional elastic structures in some very important respects. Sagging cables lack unique natural state even though their equilibrium states are uniquely determined by the applied loads. It attests to the complexity of the problem that research papers dealing with the dynamic analysis of the sagging elastic cables keep on appearing even in the recent decades.

There are many sources of nonlinearity of the structural response of elastic cables: physical nonlinearity due to nonlinear tension–extension relations, geometric nonlinearity associated with finite elastic displacements and nonlinearity of nodal load–displacement relations due to the presence of self-weight. As cables lack unique reference state, the equilibrium state under self-weight is generally used as the reference state for stating the additional load–displacement relations [1, 2]. Generally, the Lagrangian coordinate of the material point on the one-dimensional cable along its undeformed length plays the role of reference state for defining the elastic extensions and strains [3, 4]. In the incremental formulations, the tangent stiffness matrix is determined as the sum of tangent elastic and geometric stiffness matrices. Continuous catenary element has been proposed for three-dimensional analyses of cables under distributed loads using a discrete finite element for nonlinear inelastic cables with different segment properties and under concentrated loads. The discrete finite elements are predicted to be better than the continuous cable elements [5]. Conventional stability functions have also been used to incorporate the effects of geometrical nonlinearity, while material yielding is simulated by a plastic hinge model [6]. A spatial two-node catenary cable element has been developed for nonlinear static and dynamic analysis of cables under self-weight and concentrated loads [7]. An elastic catenary finite element was proposed for analysis of planar cables and cable networks [8].

Recently, the authors have proposed rate-type constitutive equations for weightless sagging elastic planar cables. Here, the tangent stiffness matrix is determined as the inverse of tangent flexibility matrix itself obtained as the sum of tangent elastic and configurational flexibility matrices. Third-order equation of motion is derived in terms of deformed nodal coordinates as the primary kinematic variables and loading rates. The proposed theory of sagging elastic cables is then used for determining their dynamic response [7].

Analysis of nonlinear elastic structures is quite complex. Sometimes, it is justified to use the simpler though only approximate linearized analysis of these structures. Conventional elastic structures possess unique passive natural state as well as unique tangent stiffness matrix. The stiffness matrix in this passive state is used for the linearized analysis. In contrast, single sagging elastic cables lack

unique passive natural state. In view of this, the stiffness matrix of these structures in their passive state cannot be defined [7]. However, it is possible to determine their dynamic response to additional dynamic loading if these nonlinear elastic structures are subjected to some sustained loads. The tangent stiffness matrix corresponding to their equilibrium state under sustained loads is used as constant stiffness matrix for conducting their linearized analysis. Incremental second-order differential equations of motion are used to predict the vibration amplitudes relative to the equilibrium state caused by additional dynamic forces. The linearized analysis is considered acceptable for small elastic displacements from the equilibrium reference state.

The above methodology for linearized analysis is developed for conventional nonlinear elastic structures. In this paper, the validity of this linearization scheme is investigated for the weightless elasto-flexible sagging planar cables. The linearized analysis predictions of the structural response are compared with the available nonlinear analysis predictions.

## 2 Scheme Adopted for Linearization

Recently, the present authors have proposed a new theory of weightless sagging planar elastic cables undergoing small elastic displacements under point loads [7]. The cable material is considered to obey linear tension–extension relation, and due to small elastic displacements considered, the structure is also geometrical linear, although the structure shows inherent nonlinearity. This is due to the ‘configurational nonlinearity’ associated with the cable flexibility. Configurational nonlinearity is essentially different from the conventional physical and geometrical nonlinearities, but generally treated as part of the geometric nonlinearity in the available literatures. Here, the natural state corresponding to any equilibrium state of the cable can be obtained by the proportional unloading from the equilibrium state. The natural state plays the role of reference state for defining the elastic displacements. The configuration-defining nodal coordinates and the elastic displacements turn out to be zero and first-order homogeneous functions of the nodal loads, respectively [7].

The investigation for weightless sagging planar elastic cable having two-node and four DOF undergoing small elastic displacements is as shown in Fig. 1. The cable is in equilibrium state under sustained nodal loads  $F_0$  and variable nodal loads  $F_i$ . Also, the nodal elastic displacement ( $u_0$ ) is measured from the equilibrium nodal coordinates ( $x_0$ ), to give the deformed state nodal coordinates ( $y_0 = x_0 + u_0$ ). The initial tangent flexibility matrices like  $D$ ,  $f$  and  $N$  are determined which gives the initial tangent stiffness matrix ( $K^T$ ) described in the authors paper [7]. Then, the third-order differential equation of motion is derived for the dynamic analysis of nonlinear elastic cable and is stated below:



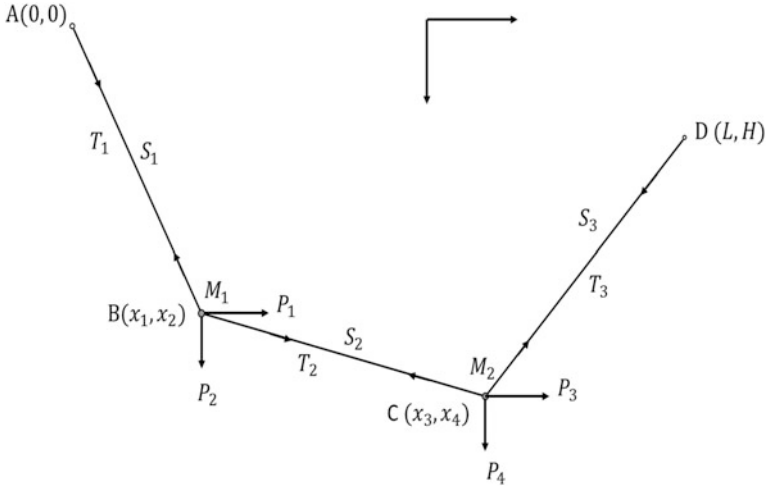


**Fig. 1** Cables under nodal loads fixed at both ends

$$M\ddot{y} + C\dot{y} + Ky = \dot{F}(t) \tag{1}$$

It should be noted that above equation of motion is expressed in terms of the deformed nodal coordinates ( $y = x + u$ ) as primary kinematic variables. The instantaneous tangent stiffness matrix ( $K$ ) used in above equation is determined by the instantaneous cable configuration and nodal loads. Then, predicted dynamic response is presented in terms of displacements from equilibrium state obtained by using the following expression:

$$z(t) = y(t) - y(0) = (x + u) - (x_0 + u_0) \tag{2}$$

In the case of linearized analysis presented in this paper, the second-order differential equation of motion adopted for dynamic analysis is obtained as

$$M\ddot{z} + C\dot{z} + K_0^T z = F_t \tag{3}$$

Here, the dynamic variables ( $z = y - y_0$ ) represent the nodal displacement of the cable from the equilibrium state. For solving the above second-order equation of motion, two initial conditions, viz.  $z(0)$  and  $\dot{z}(0)$ , are needed. Unless otherwise specified, assumed initial conditions are  $z(0) = 0$  and  $\dot{z}(0) = 0$ . Also, the dynamic force is expressed as  $F_t = F_L \sin \omega t \pi$  except in the case of seismic analysis. It should be noted that this analysis is valid only for small elastic displacements. However, there is no restriction on configurational displacements. Also, in both linear and nonlinear analyses, the constant initial damping matrix used is determined as

$$C = a_0M + a_1K \tag{4}$$

The constant damping matrix  $C$  is assumed to be initially classically damped. The values of the coefficients  $a_0$  and  $a_1$  required for establishing the damping matrix are determined by assigning the chosen damping ratios for the two lowest modes of vibration.

### 3 Response of a Single Sagging Cable to General Sinusoidal Loading

Typical sagging elastic cable system is considered for investigation with four DOF systems as shown in Fig. 1. The basic parameters assumed are shown in Table 1.

Here, the symbols  $A_0$  and  $E$  represent, respectively, the area of cross-section and the modulus of elasticity of the cable. The natural frequencies obtained for cable system for typical nodal loads are (2.5552; 12.6818; 27.4331; 46.61) rad/s. The FDR for a general sinusoidal loading covering only lowest natural frequency is presented in Fig. 2.

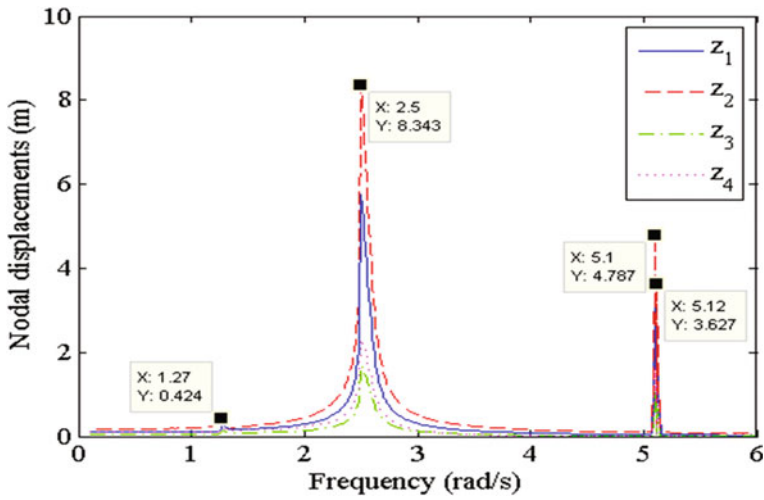
Both linearized and nonlinear analyses [7] predict about the same fundamental resonance frequency (2.5 rad/s) but slightly different peak amplitudes. However, as expected, linearized analysis does not predict the presence of regular and irregular subharmonic resonance phenomenon.

The sagging cables for particular nodal loads and the lower two natural frequencies are found to very close to each other [7]. Typical FDR for a particular sinusoidal loading is presented in Fig. 3 for both nonlinear and linearized analyses. Higher adjacent resonance frequencies but quite different peak amplitudes are predicted by linearized analysis. The FDR plot for  $z_1$  response is observed to be substantially different.

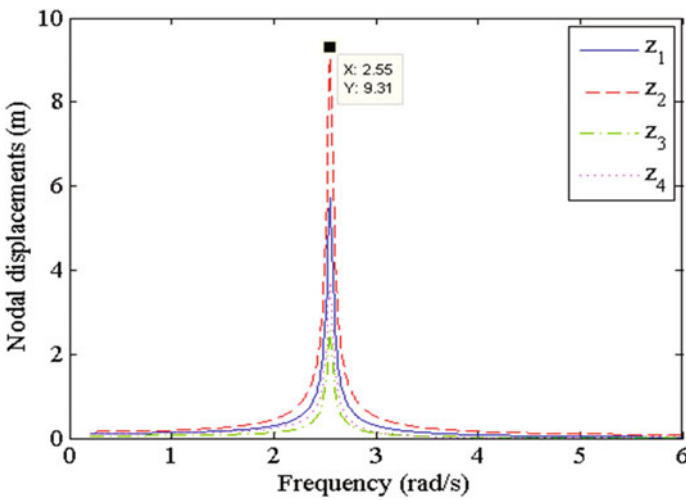
The transient beating phenomenon is also observed at a forcing frequency between the two adjacent peaks. Typical  $z_4$  waveform at forcing frequency 12.63 rad/s shows slightly different beating characteristics for both the analyses as shown in Fig. 4. The linearized analysis predicts sharper beats occurring at higher beating frequency which equals the difference in the adjacent natural frequencies (12.34 and 12.9 rad/s). In contrast, the beating frequency predicted by nonlinear analysis is about half the above value and is unrelated to the adjacent peak response

**Table 1** Cable parameters and equilibrium state coordinates

$L = 300$ m; $H = 20$ m; $S_1 = 130$ m; $S_2 = 100$ m;
$S_3 = 110$ m; $A_0 = 0.005$ m <sup>2</sup> ; $E = 2 \times 10^{11}$ N/m <sup>2</sup> ;
$M_1 = 8000$ kg; $M_2 = 14000$ kg; $P_1 = 30$ kN;
$P_2 = 110$ kN; $P_3 = 45$ kN; $P_4 = 200$ kN;
$x_0 = (111.2167; 67.3116; 208.3953; 90.8990)$ m



(a) Nonlinear analysis [9]

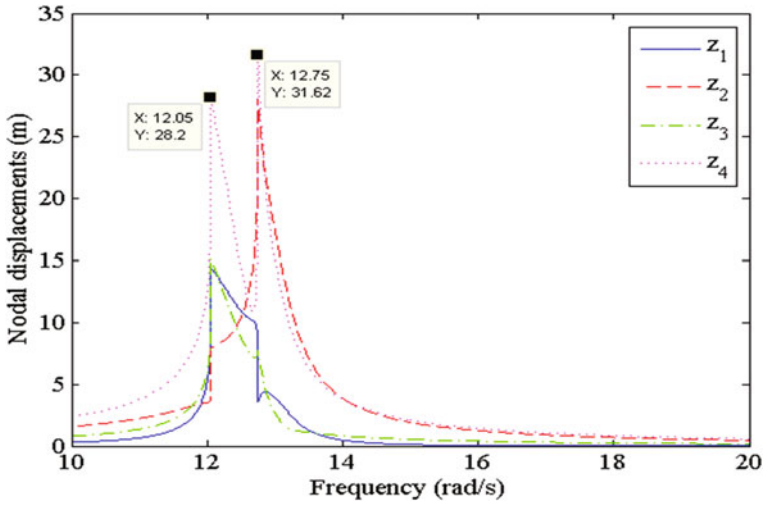


(b) Linearized analysis

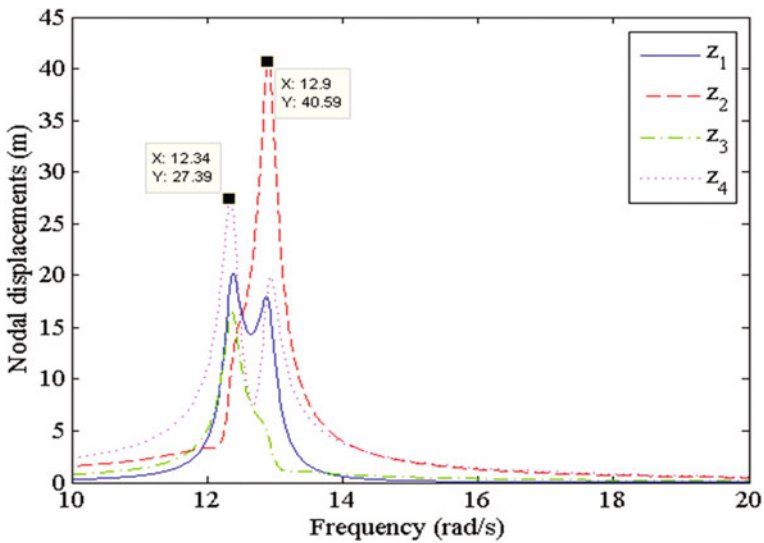
Fig. 2 FDR for general harmonic loading

frequencies (12.05 and 12.75 rad/s). Perhaps, this is because of the expected variation of natural frequencies of the cable structure experiencing such large vibration amplitudes.

Typical FDR plots for cables with small sag with frequency ranges only two lower resonance peaks are plotted in Fig 5. Similar values for the resonance frequencies as well as the peak amplitudes are predicted by the nonlinear analysis and the linearized analysis.



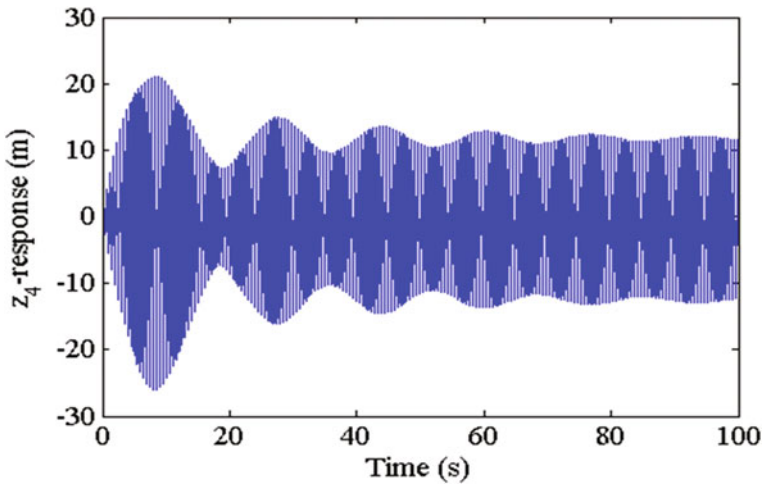
(a) Nonlinear analysis [9]



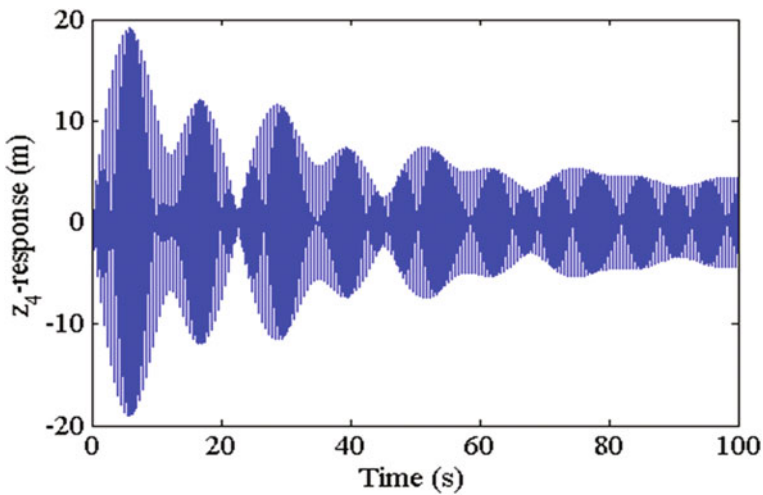
(b) Linearized analysis

Fig. 3 FDR of cables having very close natural frequencies

The inextensible cables are modelled as elastic cables with extremely high axial elastic stiffness [7]. Effect of axial stiffness on typical FDR plots for cables under same loading is depicted in Fig. 6.



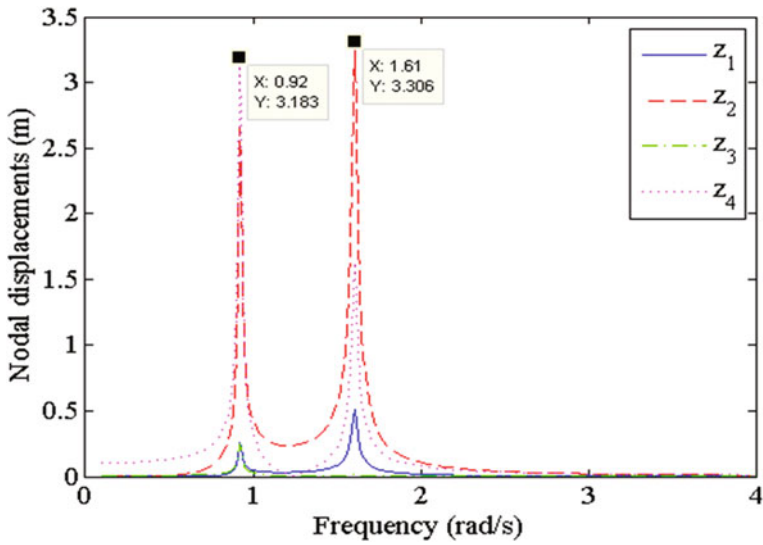
(a) Nonlinear analysis [9]



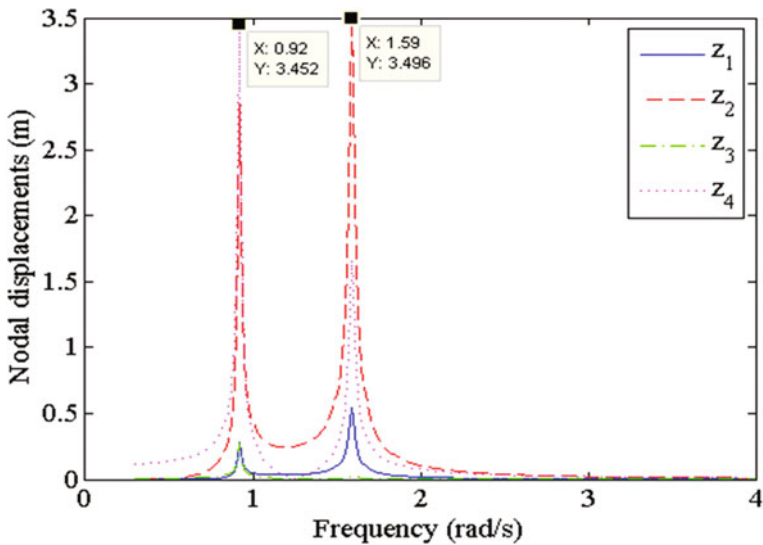
(b) Linearized analysis

**Fig. 4** Beating phenomenon

Entirely different FDR characteristics are observed for different values of their elastic stiffness, for both nonlinear analysis and approximate linearized analysis. Also, no regular or irregular subharmonics are predicted by linearized analysis. For case of nonlinear analysis, the fundamental resonance frequency remains affected from change of the axial elastic stiffness of the cable in FDR plot as shown in Fig. 6a. The FDR range covers only lowest fundamental resonance frequency as the other three resonance frequencies (401.0, 864.3 and 1472.6 rad/s) are infinitely



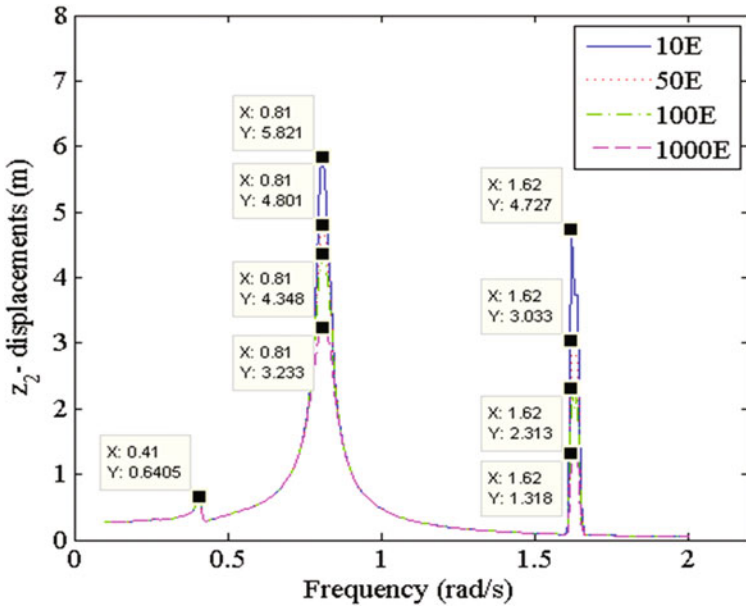
(a) Nonlinear analysis [9]



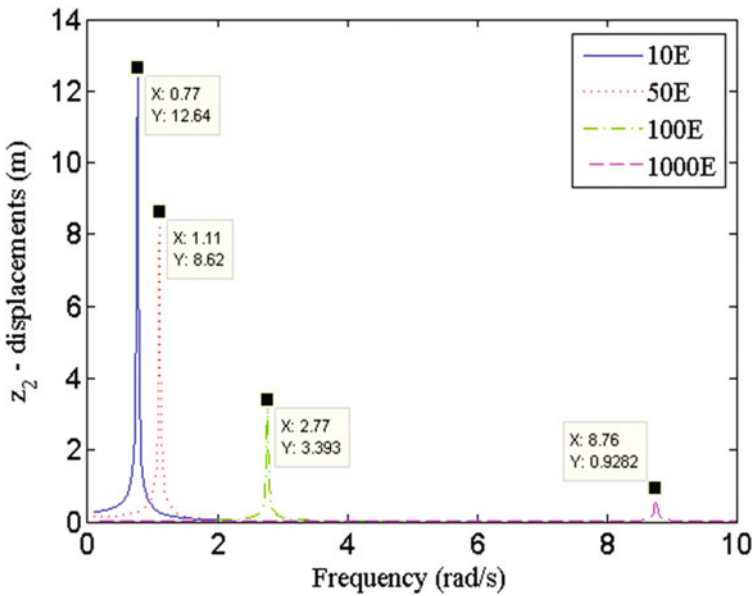
(b) Linearized analysis

Fig. 5 Typical FDR plots for small sag cable

high. However, the peak response frequency is observed to be lower for higher elastic stiffness. In contrast, in linearized analysis the fundamental resonance frequency increases and the corresponding peak response amplitude decreases as the axial stiffness increases as depicted in Fig. 6b.



(a) Nonlinear analysis [9]



(b) Linearized analysis

Fig. 6 Effect of axial stiffness of the cable on FDR

The effect of constant sustained loads upon the dynamic response is also analysed. FDR is plotted for different sustained loads but keeping the amplitude of the applied sinusoidal loading constant. This effect on their FDR is compared in Fig. 7 for nonlinear analysis and linearized analysis. The resonance frequencies as well as resonance peak amplitudes predicted by both the nonlinear and linearized analyses are approximately same under higher sustained loads. However, the difference observed in the linearized analysis than the nonlinear analysis is more at lower magnitudes of the sustained loads.

## 4 Cable Response to Seismic Loading

The seismic responses of a single sagging planar elastic cable to available horizontal and deduced vertical seismic excitation components of El Centro ground acceleration are compared with respect to nonlinear [9] and linearized predictions. It must be noted that the third-order equation of motion for nonlinear analysis demands the deduced rate of ground acceleration in addition to the available ground acceleration input. This is in contrast to the linearized analysis using second-order equation of motion and requiring only ground acceleration input.

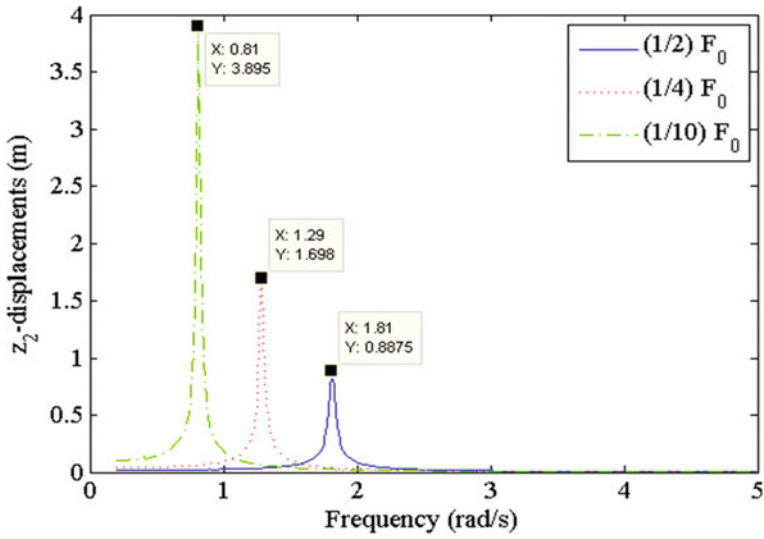
It can be observed from Fig. 8 that the linearized analysis underestimates both the horizontal and vertical seismic responses that too at lower response frequency. However, such underestimation of vibration amplitude as well as response frequency is much higher in the case of horizontal seismic excitation.

The seismic response for both horizontal and vertical excitations as analysed by nonlinear analysis as shown in Fig. 9 represents the elastic components and is marginally more for vertical excitation as compared to horizontal excitation. As cable tension is directly related to the elastic components of the cable response, horizontal excitation leads to lower tension increments. However, the dynamic response predicted by linearized analysis cannot be decomposed into configurational and elastic components.

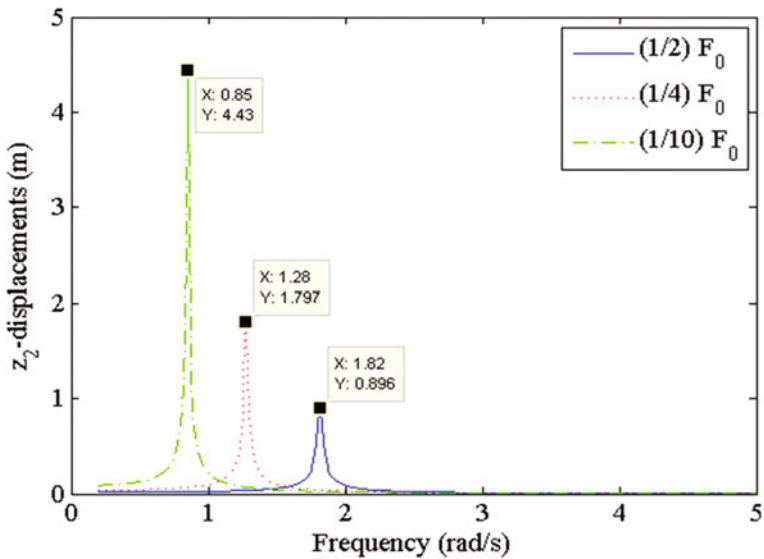
## 5 Discussion

Linearization technique adopted in this paper involves conducting an approximate linear analysis for predicting displacements from an equilibrium state introduced by applied nodal load increments. In nonlinear analysis earlier adopted by authors [7, 9], the tangent flexibility matrix depends on the instantaneous sustained loads. Obviously, the predicted response in linearized analysis is more accurate when the load increments are small. Conventional nonlinear elastic structures are generally considered to be linear at lower loads. Thus, their structural response is believed to differ from the expected initial linear response with increase in loads. Such is not the case with elastic cables. As presented above in Fig. 7, for the same load





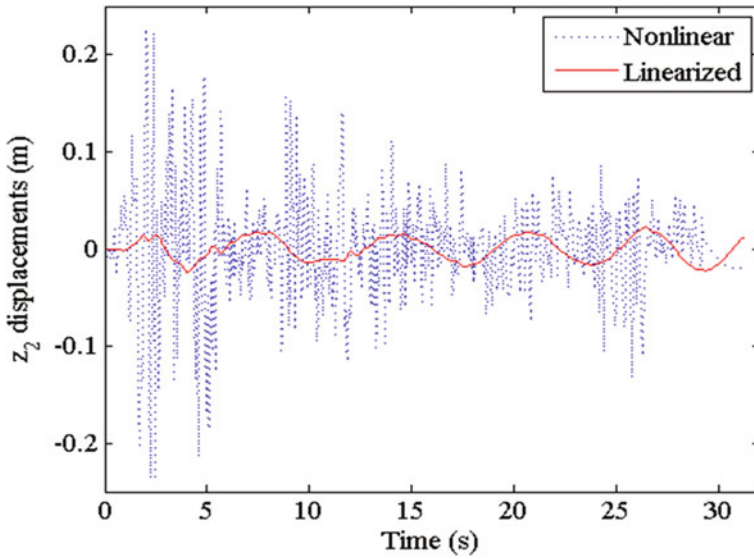
(a) Nonlinear analysis [9]



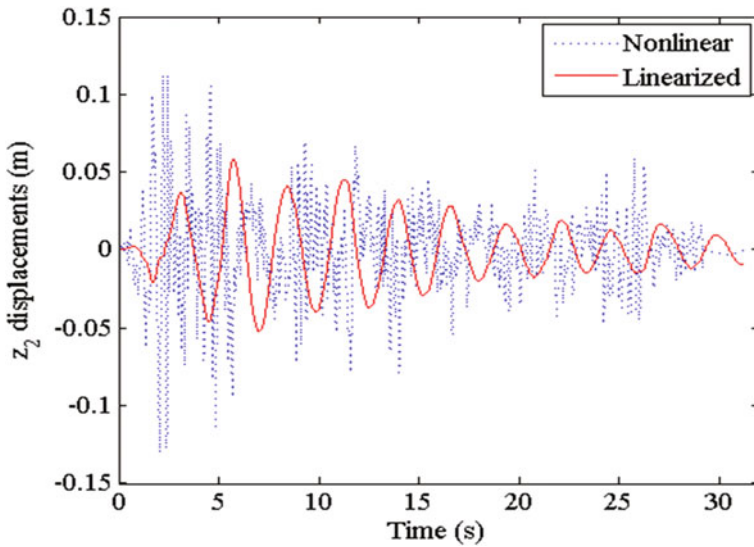
(b) Linearized analysis

Fig. 7 Typical FDR for different sustained loads

increments, the departure from linearized response occurs more at lower sustained loads. At lower sustained loads, the configurational nonlinearity dominates as discussed in author’s paper [7]. Due to this, the conventional nonlinear cables structures are not linearizable at lower sustained loads.



(a) Horizontal seismic excitation



(b) Vertical seismic excitation

**Fig. 8**  $z_2$  response for El Centro earthquake

To recapitulate, in the linearized analysis, the initial tangent stiffness matrix evaluated is assumed as constant for dynamic analysis. In contrast, the tangent stiffness matrix is updated after every time step for predicting the nonlinear dynamic response. It is emphasized that authors approach is used for establishing

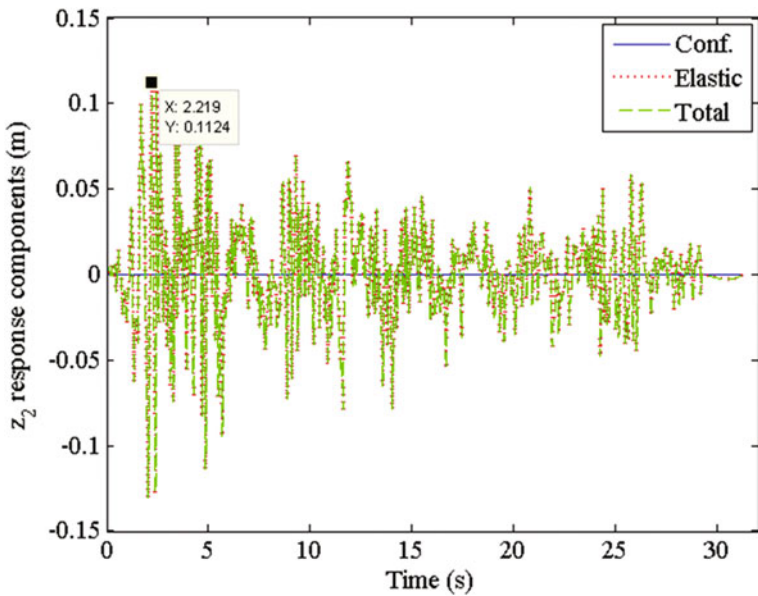
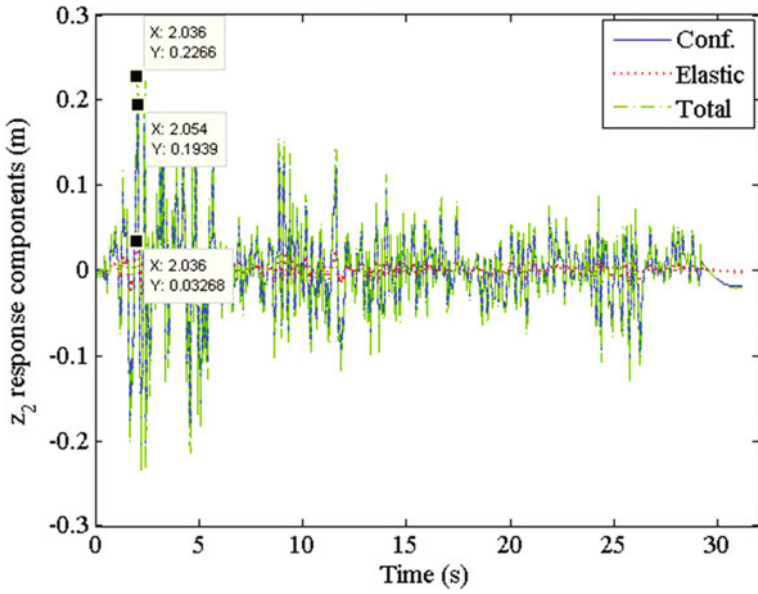


Fig. 9  $z_2$  response components for nonlinear analysis

the initial stiffness matrix even in the linearized analysis. Thus, the effect of sustained loads on the initial stiffness matrix and so the predicted response is already incorporated.

Also, in linearized analysis the primary kinematic variable in the equation of motion is the displacement from equilibrium state, whereas in nonlinear analysis, it is the deformed state nodal coordinates. Although, in both the analyses, the dynamic response is predicted in terms of the nodal displacements from equilibrium states. It is important to note that linearized analysis is valid only for small displacements. The validity of nonlinear analysis is only for small elastic displacements, but there is no such limit on the configurational displacements. Also, the decomposition of total displacement from equilibrium state to elastic and configurational displacement is not possible in case of linearized analysis.

## 6 Conclusion

The effectiveness of linearized analysis for sagging elastic cable structures has been explored in this paper. Predictions of linearized analysis are found to be acceptable only in the case of single sagging cables with small sag and cables with higher sustained loads. The linearized analysis cannot accurately predict either subharmonic resonances of sagging elastic cables under harmonic loading or their seismic response. It is concluded that the linearization scheme developed for conventional nonlinear elastic structures is not sufficiently effective in predicting the dynamic response of elasto-flexible cable structures.

## References

1. Irvine HM, Caughey TK (1974) The linear theory of free vibrations of a suspended cable. *Math Phys Sci* 341(1626):299–315
2. Rega G (2004) Nonlinear vibrations of suspended cables-Part I: modelling and analysis. *Appl Mech Rev* 57(6):443–478
3. Santos HAFA, Paulo CIA (2011) On a pure complementary energy principle and a force-based finite element formulation for non-linear elastic cable. *Int J Non-Linear Mech* 46:395–406
4. Lacarbonara W (2013) *Nonlinear structural mechanics: Theory dynamical phenomenon and modelling*. Springer, Berlin
5. Abad MSA, Shoostari A, Esmaeili V, Riabi AN (2013) Nonlinear analysis of cable structures under general loadings. *Finite Elem Anal Des* 73:11–19
6. Thai HT, Kim SE (2008) Second-order inelastic dynamic analysis of three-dimensional cable-stayed bridges. *Steel Struct* 8:205–214
7. Kumar P, Ganguli A, Benipal GS (2016) Theory of weightless sagging elasto-flexible cables. *Latin Am J Solids Struct* 13:155–174
8. Jayaraman HB, Knudson WC (1981) A curved element for the analysis of cable structures. *Comput Struct* 14(3–4):325–333
9. Kumar P, Ganguli A, Benipal GS (2015) Seismic analysis of weightless sagging elasto-flexible cables. *Adv Struct Eng* 1543–1562

# Experimental Investigations of the Effect of Temperature on the Characteristics of MR Damper



C. Bharathi Priya and N. Gopalakrishnan

**Abstract** This paper presents the experimental studies that are carried out to investigate the effect of temperature on the characteristics of MR damper. Active research has been carried out to study the effect of factors such as input current/voltage, frequency and amplitude of input excitation on the characteristics of the damper, but very limited research has been done on the effect of temperature on the energy dissipation and force characteristics of the damper. This warrants the current study in which the effect of temperature is investigated through experimental characterization of two commercially available dampers with different stroke lengths. It is found that the temperature is found to rise with the increase in input voltage and input frequency of excitation. This in turn affects the maximum force developed by the damper and energy dissipation capacity of the damper. This can affect the performance of dampers when applied to structural control applications.

**Keywords** MR damper · Characterization · Temperature effect  
Energy dissipation

## 1 Introduction

Magnetorheological (MR) dampers are a class of semi-active controllable dampers widely used in automobile, civil and mechanical industries. The controllable property and advantages like low power requirement, high reliability, fast reaction

---

C. Bharathi Priya (✉)

CSIR-Structural Engineering Research Centre, Chennai 600113, Tamil Nadu, India  
e-mail: bharathipriya@serc.res.in

N. Gopalakrishnan

CSIR-Central Building Research Institute, Roorkee, India  
e-mail: ng@cbri.res.in

C. Bharathi Priya · N. Gopalakrishnan

AcSIR-Academy of Scientific and Innovative Research, Ghaziabad, India

© Springer Nature Singapore Pte Ltd. 2019

A. Rama Mohan Rao and K. Ramanjaneyulu (eds.), *Recent Advances in Structural Engineering, Volume 2*, Lecture Notes in Civil Engineering 12,  
[https://doi.org/10.1007/978-981-13-0365-4\\_37](https://doi.org/10.1007/978-981-13-0365-4_37)

time, low maintenance of these dampers offer wide applicability in the dynamic response control of civil engineering buildings and structures. During events like earthquake, the MR dampers attached with a structure act as a secondary device and offer additional damping to the structure to protect it from seismic loads. The challenge in the use of MR damper in structural control is modelling the nonlinear and hysteretic force–displacement, force–velocity characteristics of the damper accurately in order to harness the full potential of the controllable property of the damper.

Several models, parametric and nonparametric, are available in the literature for effective modelling of MR damper. The characteristics of MR damper get altered due to several parameters such as the characteristics of smart MR fluid used, properties of input excitation. Active research has been carried out to study the effect of factors such as input current/voltage, frequency and amplitude of input excitation on the characteristics of the damper. However, very limited research has been done on the effect of temperature on the energy dissipation and force characteristics of the damper.

When an external magnetic field is applied to the damper, under a dynamic excitation, the damper can experience variations in temperature. As the viscosity of the damper fluid changes, the MR fluid is sheared which leads to self-heating of the damper fluid. This can significantly alter the yield force and energy dissipation capacity of the damper.

In this study, the effect of temperature on the characteristics of the damper is investigated through experimental characterization of two commercially available dampers with different stroke lengths. The temperature is found to increase with the increase in input voltage and input frequency of excitation. This in turn affects the maximum force developed by the damper and energy dissipation capacity of the damper. For the same input characteristics, at higher temperature, damper force and energy dissipation are found to reduce considerably. This can affect the performance of dampers when applied to structural control applications.

## 2 Magnetorheological Fluids and Dampers

Smart fluids are the class of fluids which has added micro-/nano-particles that can alter the physical/mechanical properties of fluid like viscosity, surface tension, shear rate typically on application of external stimulus like electric or magnetic field. Examples of smart fluid include electrorheological fluid, magnetorheological fluid. These smart fluids are used across various fields in many practical applications like vibration dampers, shock absorbers and prosthetics.

MR damper is a vibration absorbing damper consisting of piston and a tube filled with MR fluid, which is controlled by a magnetic field, usually using an electromagnet. Commercially available MR dampers are of type monotube, twin tube, double-ended MR damper which are capable of operating on flow mode, shear mode and squeeze flow mode. Depending on the applied magnetic field,

the viscosity of the fluid changes which is used to dissipate energy from the system with which the damper is attached. Since these dampers behave highly nonlinear, the challenge in practical application of these dampers in energy dissipation relies on accurate modelling of the behaviour of the damper under varying input conditions. Although various models are present to model the damper characteristics taking into account, the effect of varying input current, frequency and amplitude, very less focus is given on the effect of temperature. Due to repeated application of input current continuously for few minutes, the temperature of MR fluid is found to increase. This self-heating is found to affect the energy dissipation capacity of the damper, which is a paramount deciding factor for its use in vehicle suspension and semi-active building control applications.

### 3 Literature Review

Gordaninejad and Breese [1] found significantly high temperature rise in MR damper particularly in large force application. Batterbee and Sims [2] developed and validated a dynamic temperature-dependent model for MR damper and found that viscosity, yield stress and damper stiffness are highly affected by temperature by conducting hardware in loop experiments. Sahin et al. [3] found that the modified Bouc–Wen model parameters did not capture the significant temperature effects of MR damper. Wilson and Wereley [4] proposed a new model to better capture stiffness behaviour over a large operating temperature range of MR damper. However, there is still only limited research on the temperature effect in the dampers and most of the existing research is concentrated in research level applications. This is a limitation when using the commercially available dampers in real-world applications. This study concentrates to investigate the effect of temperature in energy dissipation characteristics of two commercially available dampers of different stroke length.

### 4 Experimental Characterization

Experimental characterization studies are carried out on a commercially available short-stroke (RD-8040-1) and long-stroke (RD-8041-1) MR damper in a loading frame designed and built for the purpose. These dampers are of monotube type containing high-pressure nitrogen gas. The typical properties of the damper as supplied by the manufacturer Lord Corporation are presented in Table 1. Desired input current to the damper is supplied using Wonder Box<sup>®</sup> Device Controller from the same manufacturer. Short-stroke and long-stroke MR dampers are subjected to

**Table 1** Damper properties

Property	RD-8040-1	RD-8040-1
Stroke (mm)	55	74
Extended length (mm)	208	248
Body dia (mm)	42.1	42.1
Shaft dia (mm)	10	10
Tensile force (N)	8896	8896
Damper force (N) 5 cm/s @ 1 A 20 cm/s @ 0 A	>2447 <667	>2447 <667
Operating temp (°C)	71 max	71 max

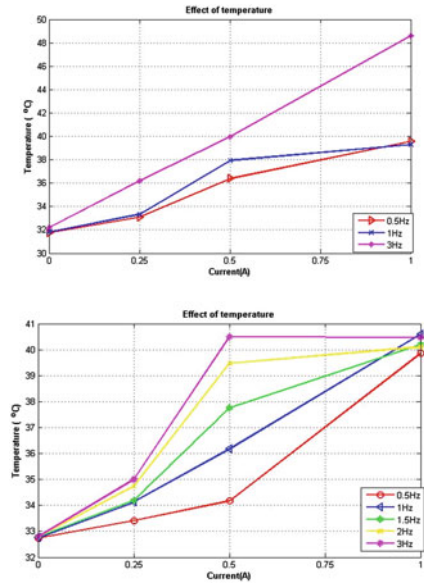
**Fig. 1** Experimental setup for MR damper characterization: **a** loading frame with actuator; **b** close-up view of damper; **c** wonderbox for input current supply; **d** non-contact thermocouple



displacement-controlled sinusoidal displacements at various currents based on their typical properties. The dampers are tested for 0, 0.25, 0.5, 1 A currents with a frequency of 0.5, 1, 1.5, 2 and 3 Hz in each current value. At each displacement, an amplitude of 5, 10 and 15 mm for short stroke and 5, 10, 15 and 20 mm for long-stroke damper is given and values are recorded for ten cycles. Two dampers of each type are tested to ensure repeatability of the results. During the experiments, it is observed that there is an increase in the temperature, between the first and tenth cycle. Since the MR fluid is sealed inside the cylinder and inaccessible, the temperature developed in the outer surface of the cylindrical shaft is measured using a non-contact laser-based thermocouple. Temperature of the shaft at the first and final cycle is recorded using the thermocouple, and in all cases, it is ensured that the initial cycle is done nearly at room temperature. The experimental setup and instrumentation are shown in Fig. 1.



**Fig. 2** Increase in temperature in long-stroke and short-stroke MR damper for varying input excitations



## 5 Results and Observations

One of the initial observations is the temperature increase in the damper between the cycles is more when the input frequency and input current increase.

For 15 mm amplitude, under varying input frequency and current, the temperature recorded at the tenth cycle is shown in Fig. 2, and from the figure, it can be seen that the increase in temperature is nonlinear in nature.

The effect of the temperature increase on the maximum force of the damper is calculated by comparing the force–displacement curve of the first and last cycle. The absolute value of maximum force and the temperature recorded in the first and last cycle under various frequencies for 10 mm amplitude is presented in Fig. 3. From the figure, it is found that, in all cases, the increase in the temperature decreases the maximum force developed by the damper. This decrease is observed in both short-stroke and long-stroke dampers as shown in Fig. 3a, b. For both dampers, the decrease in force is more pronounced at higher input currents. The same trend is observed in energy dissipation characteristics of the dampers. This is shown in Fig. 4a, b for short-stroke and long-stroke dampers.

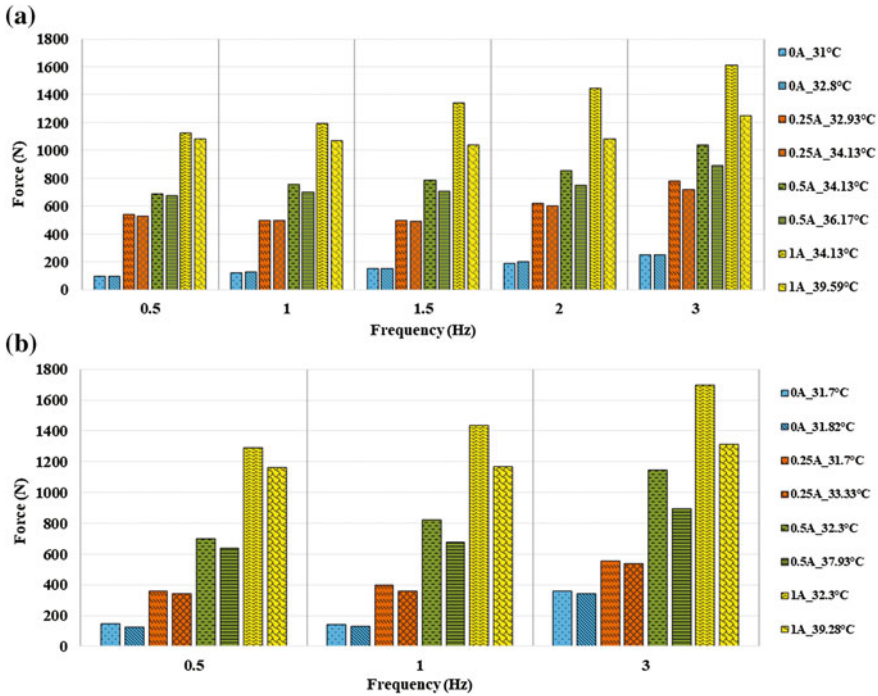


**Fig. 3** Variation in maximum force observed between first and last cycle for **a** short-stroke and **b** long-stroke damper

At a sinusoidal input of 3 Hz frequency with 10 mm amplitude and 1 A input current to the damper, 25% of maximum force variation and 28% of energy dissipation percentage variation is observed for the long-stroke damper due to the increase in temperature. For similar input condition, a 22% decrease is observed in maximum force and 26% decrease is observed in energy dissipation for the short-stroke damper.

The effect of temperature on the damping characteristics affects the characteristic curves of the damper as shown in Fig. 5. From the force–displacement curves, it is found that the stiffness of the damper is altered between the first and last cycle. The force–velocity plots show that at higher currents, the post-yield damping is found to vary more than the pre-yield damping. This is indicated by a slight clockwise rotation of the curves on the force–velocity plot. This is due to the reduction in fluid’s viscosity with increase in temperature.

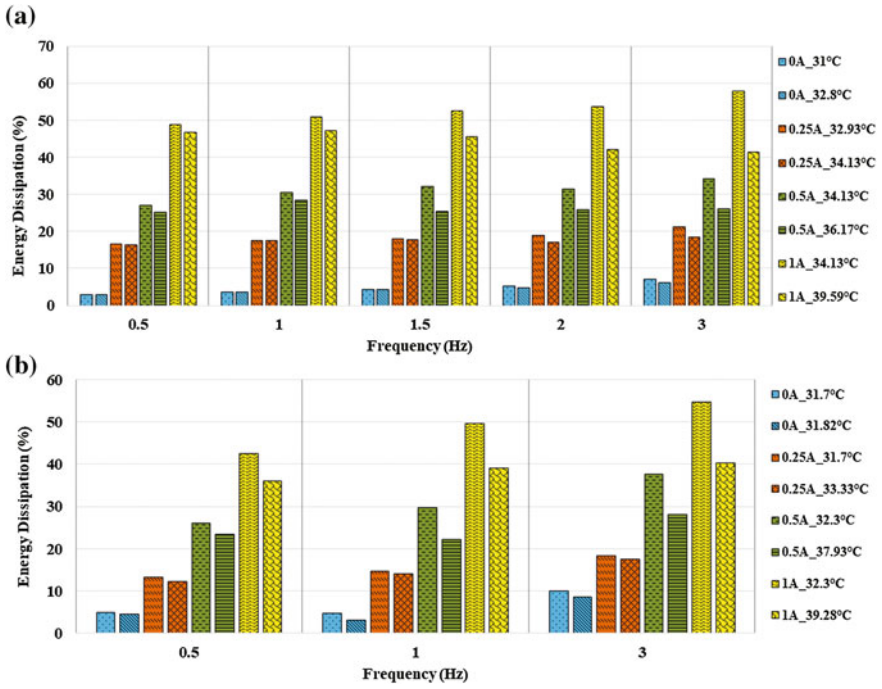


**Fig. 4** Energy dissipation observed between first and last cycle for **a** short-stroke and **b** long-stroke damper

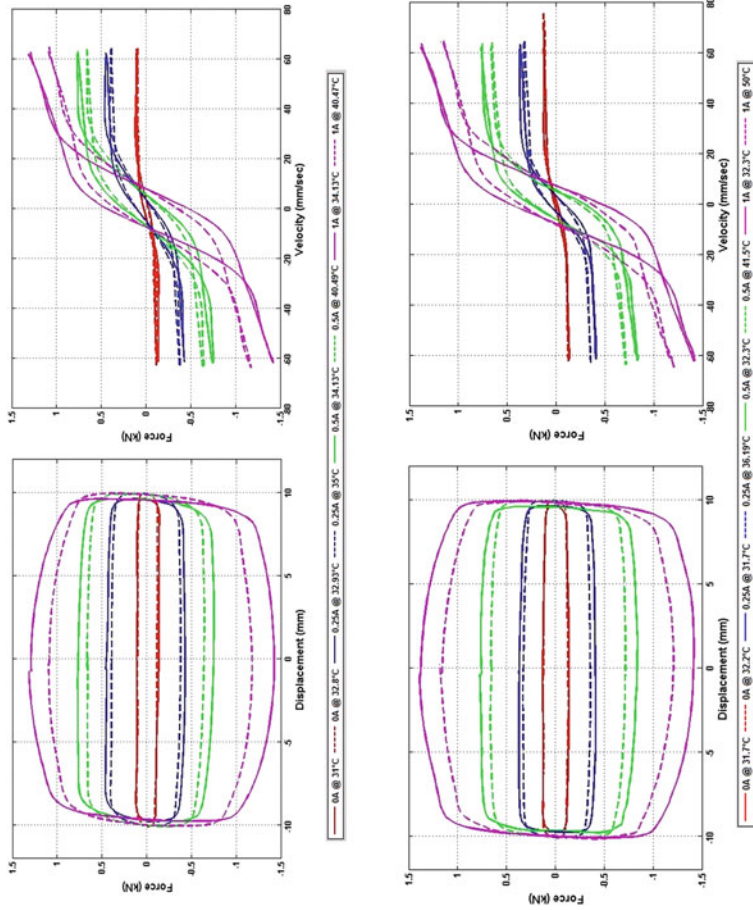


Fig. 5 Characteristics curves of long-stroke and short-stroke damper for a sinusoidal input 1 Hz—10 mm at different input currents

## 6 Conclusions

Experimental studies are carried out to investigate the effect of temperature on the characteristics of MR damper. It is found that rise in temperature with respect to rise in input properties significantly decreases the maximum force developed and energy dissipation characteristics of MR damper. Temperature increase as high as 18 °C is observed within ten cycles of operation of damper. This temperature increase is found to significantly alter the performance of the damper which is crucial in applications like vibration absorbers in buildings and automotives. Hence, an attempt has been made to study the effect of temperature in the hysteresis of the two commercially available dampers with different strokes. It is found that, for same input excitation, at higher temperature, the force and energy dissipation decreases to a considerable extent, especially in post-yield region, which can potentially alter the performance of the damper. For future work, the temperature effect will be further investigated for developing a suitable model of MR damper for its use in seismic response control.

**Acknowledgements** The author sincerely acknowledges all the scientists and technical staff of ASTAR Laboratory, CSIR-SERC.

## References

1. Gordaninejad F, Breese DG (1999) Heating of magnetorheological fluid dampers. *J Intell Mater Syst Struct* 10(8):634–645
2. Batterbee D, Sims ND (2009) Temperature sensitive controller performance of MR dampers. *J Intell Mater Syst Struct* 20(3). <https://doi.org/10.1177/1045389x08093824>
3. Sahin I, Cismeci S, Wilson NL, Wereley NM (2010) Sensitivity of magnetorheological damper behavior to perturbations in temperature via BoucWen model. In Proceedings of 12th International Conference on ER and MR Suspensions, Philadelphia, USA, pp 433–439
4. Wilson NL, Wereley NM (2010) Analysis of a magnetorheological fluid damper incorporating temperature dependence. In Technical paper—51st AIAA/ASME/ASCE/AHS/ASC structures, structural dynamics, and materials conference, AIAA

# Semi-active Control of Structures Using Magnetorheological Elastomer-Based Seismic Isolators and Sliding Mode Control



K. Balamonica, K. Sathish Kumar and N. Gopalakrishnan

**Abstract** Control of structures against the earthquake forces had been a keen topic of interest in research for past decades. Isolator being one such system which works passively to decouple the structure from the earthquake forces has many disadvantages such as large displacements, poor adaptability to varying ground conditions. Recently, magnetorheological (MR) elastomer-based base isolation systems have been actively studied as an alternative smart base isolation systems because MR elastomers are capable of adjusting their modulus or stiffness depending on the magnitude of the applied magnetic field. In this paper, MR elastomer-based isolators have been used to semi-actively control the structure subjected to earthquake excitation. Sliding mode control algorithm has been investigated and used effectively to control the structure semi-actively.

**Keywords** Magnetorheological elastomer · Stiffness · Seismic control  
Isolator · Sliding mode control

## 1 Introduction

The base isolation technique is one of the most widely used seismic performance improvement strategies for civil infrastructures, such as bridges and buildings. The conventional passive base isolators have to be provided with large seismic gaps due to their high horizontal flexibility and exhibit poor adaptability to varying ground

---

K. Balamonica  
National University of Singapore, Singapore, Singapore  
e-mail: balamonica08@gmail.com

K. Sathish Kumar (✉)  
CSIR-Structural Engineering Research Centre, Chennai, India  
e-mail: ksk@serc.res.in

N. Gopalakrishnan  
CSIR-Central Building Research Institute, Roorkee, India  
e-mail: ng@cbri.res.in

excitations. Hence, it becomes necessary to introduce “smartness”, in the conventional base isolators, and enhance their adaptability to varying spectra of input loads. In order to introduce smartness in the passive base isolation systems, a class of smart materials called magnetorheological elastomer (MRE) can be used. MREs are solid analogue of magnetorheological fluids. The materials whose properties can be altered with the passage of magnetic field are called as magnetorheological materials. They consist of micronized iron particles and a non-magnetic medium. Hence on the passage of magnetic field, the elastic modulus of the material can be altered as the particle aligns along the direction of the magnetic field.

The idea of using MR elastomers for civil engineering applications is rarely explored. The conceptual study of using MR elastomers for base isolators was carried out by Hwang et al. [1]. The numerical evaluation of the dynamic performance of the smart base isolation system employing MR elastomer was performed by Usman et al. [2], and the results show that the proposed system outperforms the conventional system in reducing the responses of the structures during seismic excitations. Jung et al. [3] showed that the smart MR elastomer isolator system with fuzzy logic control algorithm gives better results than that of passive isolation device by investigating on a small-scale single-storey building. Opie and Yim [4] proposed the variable stiffness vibration isolator (VSVI), and experimental results showed that the MRE isolator reduces the resonances and payload velocity by 16–30%.

## 2 Smart Base Isolator

Li et al. [5] developed smart base isolators using the MREs made of carbonyl iron particles and silicone rubber. These MREs exhibit variation in their shear modulus as shown in Fig. 1. It could be seen that the stiffness of the MRE increases with the increase in the magnetic field. The isolators were made by sandwiching layers of

**Fig. 1** Varying stress–strain graph of magnetorheological elastomers with current

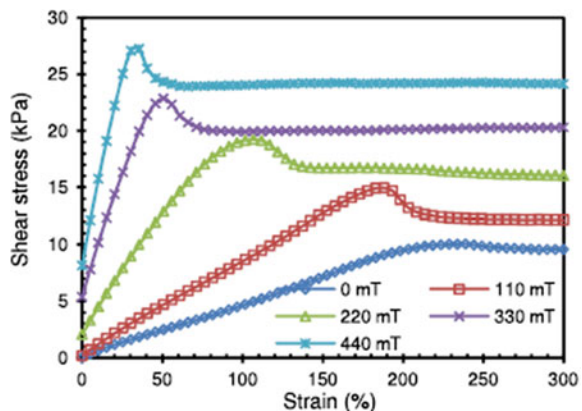


**Fig. 2** Magnetorheological elastomer-based base isolators

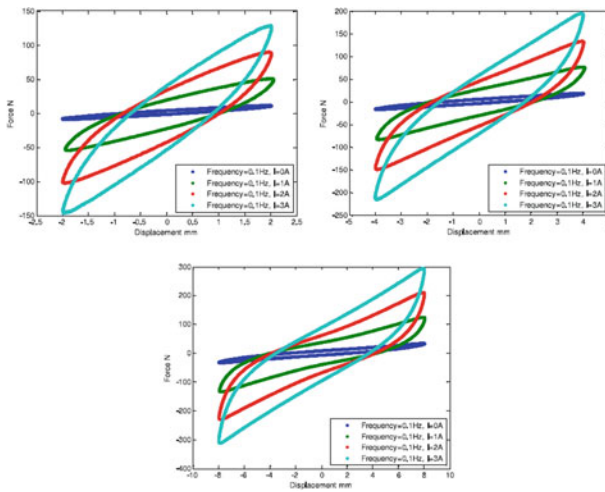
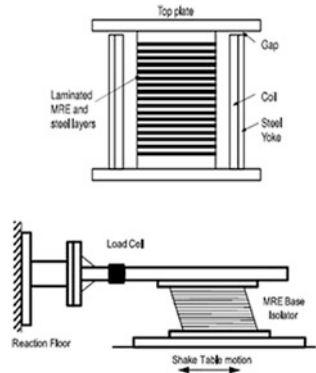


**Fig. 3** Force displacement hysteresis plot for smart base isolators

MRE and steel plates (Fig. 2). The force–displacement curves for various currents and frequencies are given in Fig. 3.

### 3 Sliding Mode Control

Sliding mode control (SMC) is a nonlinear control technique in which systems are designed to drive the system states onto a surface in the state space, named sliding surface [6]. Once the sliding surface is reached, sliding mode control keeps the



states on the close neighbourhood of the sliding surface. The main aim of the SMC method is to design the controller, which leads the sliding function to the manifold and keep the system in desired sliding mode. The SMC design consists of two steps: switching function design and controller design. The switching function is the function of the state and can be obtained either as output or state feedback [7].

### 3.1 Conditions for the Existence of a Sliding Mode

A sliding mode exists, if in the vicinity of the switching surface,  $\sigma(x) = 0$ , the tangent or velocity vectors of the state trajectory always point towards the switching surface [8]. Consider the following  $n$ th order, single input system

$$\dot{x} = f(t, x, u) = Ax + Bu \quad (1)$$

With the following general control strategy,

$$u = \begin{cases} u^+(t, x) & \text{if } \sigma(x) > 0 \\ u^-(t, x) & \text{if } \sigma(x) < 0 \end{cases} \quad (2)$$

Then, sliding mode exists if

$$\frac{d\sigma}{dx}f(t, x, u^+) < 0 \text{ and } \frac{d\sigma}{dx}f(t, x, u^-) > 0$$

Consider a linear system  $\dot{x} = Ax + Bu$

Where  $x$  ( $n \times 1$ ) is the states,  $A$  ( $n \times n$ ) is system matrix and  $B$  ( $n \times r$ ) is the control matrix. The matrix  $B$  is assumed to have full rank, and  $(A, B)$  is controllable. The control law  $u$  is defined

$$u = -K \text{sgn}(\sigma) \quad (3)$$

### 3.2 Switching Function Design

The switching function provides the necessary dynamics to the system to make it slide along the sliding surface [9]. The switching function is assumed to be function of the states.

$$\sigma = Sx \quad (4)$$

That is,  $\sigma = S_1x_1 + S_2x_2 + S_3x_3 + \dots$

The  $S$  ( $n \times r$ ) vector needs to be evaluated to make the system slide in the desired path.

The switching surface  $\sigma(x) = 0$  is a  $(n - m)$ -dimensional manifold in  $R^n$  determined by the intersection of  $m$   $(n - 1)$ -dimensional switching surfaces  $\sigma(x) = 0$ . The switching surfaces are designed such that the system response restricted to  $u(x) = 0$  has a desired behaviour such as stability or tracking.

### 3.3 Equivalent Control Method

The method of equivalent control is a means for determining the system motion restricted to the switching surface  $\sigma(x) = 0$  [6]. Suppose at to, the state trajectory of the plant intercepts the switching surface and a sliding mode exists for  $t > t_0$ . The existence of a sliding mode implies (1)  $\dot{\sigma}(x(t)) = 0$ , and (2)  $\sigma(x) = 0$  for all  $t > t_0$ . From the chain rule,  $[\partial\sigma/\partial x]\dot{x} = 0$

Substituting for  $\dot{x}$  yields

$$\left[\frac{\partial\sigma}{\partial x}\right]\dot{x} = \left[\frac{\partial\sigma}{\partial x}\right][f(t, x) + B(t, x)u_{\text{eq}}] = 0 \quad (5)$$

where  $u_{\text{eq}}$  is the equivalent control which solves the equation. After substituting this  $u_{\text{eq}}$  in Eq. (1), the motion of (5) describes the behaviour of the system restricted to the switching surface provided the initial condition  $x(t_0)$  satisfies  $\sigma(x(t_0)) = 0$ . Thus

$$u_{\text{eq}} = -\left[\left[\frac{\partial\sigma}{\partial x}\right]B(t, x)\right]^{-1}\frac{\partial\sigma}{\partial x}f(t, x) \quad (6)$$

Given that  $\sigma(x(t_0)) = 0$ , the dynamics of the system on the switching surface can be given for time  $t \geq t_0$  as

$$\dot{x} = \left[1 - B(t, x)\left[\left[\frac{\partial\sigma}{\partial x}\right]B(t, x)\right]^{-1}\frac{\partial\sigma}{\partial x}\right]f(t, x) \quad (7)$$

If the switching function is assumed to be linear, i.e.  $\sigma(x) = Sx$ , then  $\partial\sigma/\partial x = S$ ; hence, the above equation is reduced to

$$\dot{x} = \left[1 - B(t, x)[SB(t, x)]^{-1}S\right]f(t, x) \quad (8)$$

Equation (8) governs the motion of the system in the switching surface. In the sliding mode, the equivalent system must not only satisfy the  $n$ -dimensional state dynamics but also the  $m$ -dimensional equations of the sliding surface  $\sigma(x) = 0$ . Since we use both the constraints, the  $n$ th order model gets reduced to  $(n - m)$ th order model.

Equation (8) can be used to find the parameters of the sliding surface by using pole placement methodology or LQR method.

### 3.4 Controller Design

The controller is used to determine the feedback gains that will drive the system to the desired trajectory. Assuming the sliding mode is designed, the feedback controller has to adjust the gains such that the system continues to be in the sliding surface. In general, the control law renders “ $m$ ”-dimensional vectors [10]

$$u_i = \begin{cases} u_i^+(t, x) & \text{for } \sigma_i(x) > 0 \\ u_i^-(t, x) & \text{for } \sigma_i(x) < 0 \end{cases} \tag{9}$$

There are various methods to arrive at the feedback controller design. The essential principle of these methods is to use some diagonalization procedure which converts multiple input problems into  $m$  single input design problem. A new control vector  $u^*$  is formulated by using a non-singular transformation,

$$u^*(t) = Q^{-1} \left[ \frac{\partial \sigma}{\partial x}(x) \right] B(t, x) u(t) \tag{10}$$

where  $Q(t, x)$  is an arbitrary  $m \times m$  diagonal matrix.  $Q^{-1}(t, x)$  is simply a matrix which allows flexibility in the design. It can be a weighting matrix for the various control channels. Often, it is chosen as the identity matrix which provides equal weightage for all the control channels. The state dynamics in terms of  $u^*$  is

$$\dot{x} = f(t, x) + B(t, x) \left[ \left[ \frac{\partial \sigma}{\partial x} \right] B(t, x) \right]^{-1} Q(t, x) u^*(t) \tag{11}$$

Although this new control structure looks more complicated, the structure of  $\sigma(x) = 0$  permits one to independently choose the  $m$ -entries of  $u^*$  to satisfy the sufficient conditions for the existence and reachability of a sliding mode. Once  $u^*$  is known, it can be unravelled by inverting the transformation to yield the required  $u$ . For a sliding mode to exist, it should satisfy  $\sigma^T(x)\dot{\sigma}(x) < 0$ . In terms of  $u^*$

$$\dot{\sigma}(x) = \frac{\partial \sigma}{\partial x}(x) f(t, x) + Q(t, x) u^*(t) \tag{12}$$

Thus, if the entries  $u_i^{*+}$  and  $u_i^{*-}$  are chosen such that

$$q_i(t, x) u_i^{*+} < -\nabla \sigma_i(x) f(t, x) \tag{13}$$

$$= - \sum_{j=1}^n s_{ij} f_j(t, x) \quad \text{when } \sigma_i(x) > 0 \tag{14}$$

$$q_i(t, x) u_i^{*-} > - \nabla \sigma_i(x) f(t, x) \tag{15}$$

$$= - \sum_{j=1}^n s_{ij} f_j(t, x) \quad \text{when } \sigma_i(x) > 0 \tag{16}$$

### 4 Control of Structures Subjected to Dynamic Loads Using MRE-Based Isolators

As described in the previous section, MRE-based isolators can be used effectively to control the response of the structures [11]. Using MRE-based isolators coupled with sliding mode control which is a robust control that does not depend on the system parameters, a structure can be effectively controlled. Consider a structure which is modelled as 2DOF system as shown in Fig. 4.

The equations of motion of the system are

$$m_1 \ddot{x}_1 + c_1 (\dot{x}_1 - \dot{x}_g) + c_2 (\dot{x}_1 - \dot{x}_2) + k_1 (x_1 - x_g) + k_2 (x_1 - x_2) = 0 \tag{17}$$

$$m_2 \ddot{x}_2 + c_2 (\dot{x}_2 - \dot{x}_1) + c_3 (\dot{x}_2) + k_2 (x_2 - x_1) + k_3 (x_2) = 0 \tag{18}$$

where  $x_1$  corresponds to the base isolation degree of freedom and  $x_2$  corresponds to superstructure degree of freedom.

For the below study, it is assumed that the  $K_1 = 20,000$  N/m,  $K_2 = 1,191,200$  N/m,  $m_1 = 680$  kg,  $m_2 = 2490$  kg,  $C_1 = 374$  N s/m,  $C_2 = 2371$  N s/m. For these parameters, the studies are performed for three cases.

#### 4.1 Case 1: Fixed Base Structure

For the fixed base structure, the frequency of the structure was found to be 3.484 Hz. The state space equation is given by

**Fig. 4** Base isolated structure idealized as 2DOF structure

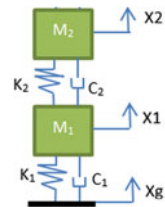


**Fig. 5** Displacement response of fixed base structure

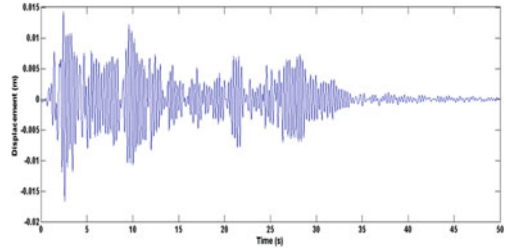


**Fig. 6** Velocity response of fixed base structure

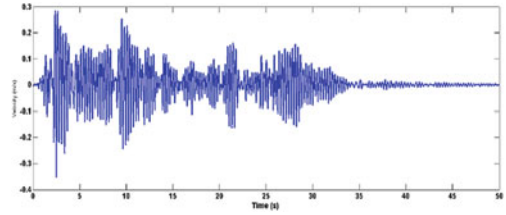
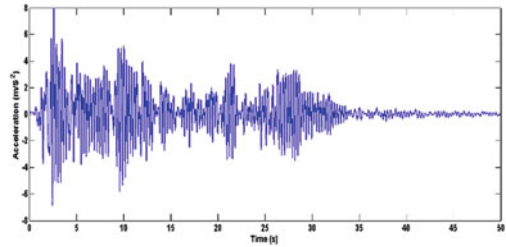


**Fig. 7** Acceleration response of fixed base structure



$$\begin{bmatrix} \dot{X}_1 \\ \dot{X}_2 \end{bmatrix} = \begin{bmatrix} 0 & 1 \\ -478.39 & -0.9522 \end{bmatrix} \begin{bmatrix} X_1 \\ X_2 \end{bmatrix} + \begin{bmatrix} 0 \\ -1 \end{bmatrix} X_g \tag{19}$$

The storey displacement, velocity and acceleration responses for El Centro ground excitation are shown in Figs. 5, 6 and 7, respectively.

#### 4.2 Case 2: Passive Control of Structure Using Base Isolation

Base isolators designed for the structure with the specification given already are modelled which will impart passive control on the structures. The state space equations are given as below

**Fig. 8** Displacement response of the structure with smart base isolators (controlled and uncontrolled)

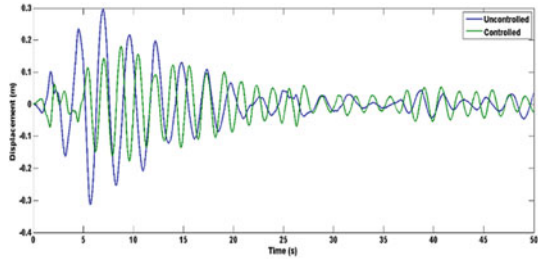


**Fig. 9** Velocity response of the structure with smart base isolators (controlled and uncontrolled)

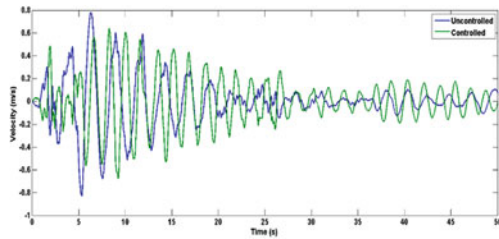
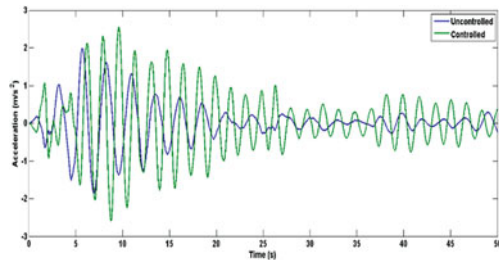


**Fig. 10** Acceleration response of the structure with smart base isolators (controlled and uncontrolled)



$$\begin{bmatrix} \dot{X}_1 \\ \dot{X}_2 \\ \dot{X}_3 \\ \dot{X}_4 \end{bmatrix} = \begin{bmatrix} 0 & 1 & 0 & 0 \\ -1781.17 & -4.036 & 1751.76 & 3.487 \\ 0 & 0 & 0 & 1 \\ 478.39 & 0.9522 & -478.39 & -0.9522 \end{bmatrix} \begin{bmatrix} X_1 \\ X_2 \\ X_3 \\ X_4 \end{bmatrix} + \begin{bmatrix} 0 \\ -1 \\ 0 \\ -1 \end{bmatrix} U_g \tag{20}$$

The displacement, velocity and acceleration of the base isolation (labelled as uncontrolled) are shown in Figs. 8, 9 and 10. Since the superstructure behaves like a rigid body, the responses will be same as that of base isolators. It can be observed clearly that the displacement of the isolator gets doubled approximately. That is, the structure moves twice the displacement compared to case 1. But the acceleration responses are greatly reduced by 75% and the responses in Fig. 10 show smooth behaviour compared to the chaotic behaviour in Fig. 7.

### 4.3 Case 3: Semi-active Control of Structures Using Sliding Mode Control

The MRE-based isolators are capable of altering the stiffness of the isolator based on the applied magnetic field. That is, the structure can be controlled semi-actively. The sliding mode control procedure described above is used to find the feedback forces required to drive the system to the required trajectory.

The poles of the system were assumed to be  $-0.0977$ ,  $-1.019$ ,  $-83.1256$ . These poles are used to arrive at the sliding surface parameters. The sliding surface which is a function of the states can be derived to be

$$\sigma = 841.283X_1 + X_2 - 779.672X_3 + 0.1745X_4 \quad (21)$$

From equations, control force  $U^*$  is given by

$$U^* = [K_{11} \quad K_{12} \quad K_{13} \quad K_{14}] \begin{bmatrix} X_1 \\ X_2 \\ X_3 \\ X_4 \end{bmatrix} \quad (22)$$

where

$$K_{11} = \begin{cases} < -1628.585 & \text{if } \sigma_1 X_1 > 0 \\ > -1628.585 & \text{if } \sigma_1 X_1 < 0 \end{cases} \quad (23)$$

$$K_{12} = \begin{cases} < 1876.83 & \text{if } \sigma_2 X_2 > 0 \\ > 1876.83 & \text{if } \sigma_2 X_2 < 0 \end{cases} \quad (24)$$

$$K_{13} = \begin{cases} < 1835.24 & \text{if } \sigma_3 X_3 > 0 \\ > 1835.24 & \text{if } \sigma_3 X_3 < 0 \end{cases} \quad (25)$$

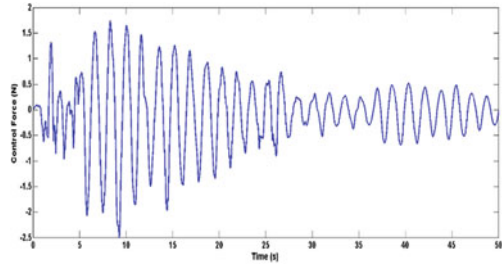
$$K_{14} = \begin{cases} < 776.35 & \text{if } \sigma_4 X_4 > 0 \\ > 776.35 & \text{if } \sigma_4 X_4 < 0 \end{cases} \quad (26)$$

From this, control force is given by

$$U = 1.1886 \times 10^{-3} [K_{11} \quad K_{12} \quad K_{13} \quad K_{14}] \begin{bmatrix} X_1 \\ X_2 \\ X_3 \\ X_4 \end{bmatrix} \quad (27)$$

A Simulink model was modelled to implement the sliding mode control to semi-actively control the structure using smart base isolators. A comparison between the controlled and uncontrolled responses of structure with smart base isolators is shown in Figs. 8, 9 and 10. The displacement response and velocity

**Fig. 11** Control force applied to the structure



response in Fig. 8 shows considerable reduction in the displacements. But the velocity and acceleration in Figs. 9 and 10 shows a marginal increase compared to the uncontrolled state. The control force applied on to the structure is given in Fig. 11. This control force is applied by altering the stiffness of the base isolators which in turn is performed by varying the applied current.

## 5 Conclusion

The acceleration of the structure was observed to be of 8 m/s which gets reduced to 2 m/s when the isolators are used passively. Thus, a reduction of 75% is observed. But the displacement of the structure with fixed base and passively controlled isolators is increased by 50%. This is characteristic of the isolation systems.

The responses are smooth compared to fixed base systems. Smart base isolators aim at reducing the displacements of the isolators by exhibiting a change in stiffness with respect to the applied field. The sliding mode control algorithm drives the system to desired path. The displacement response of the semi-actively controlled and uncontrolled isolators shows that the displacements are reduced considerably with a marginal increase in the acceleration. Thus, smart base isolators coupled with sliding mode control can be used for semi-active control of structures.

## References

1. Hwang IH, Lim JH, Lee JS (2006) A study on base isolation performance of magneto-sensitive rubbers. *J Earthq Eng Soc* 10:77–84
2. Usman M, Sung SH, Jang DD, Jung HJ, Koo JH (2009) Numerical investigation of smart base isolation system employing MR elastomer. *J Phys Conf Ser* 149:1–4
3. Jung H-J et al (2011) Seismic performance analysis of a smart base-isolation system considering dynamics of MR elastomers. *J Intell Mater Syst Struct* 22(13):1439–1450
4. Opie S, Yim W (2009) Design and control of a real-time variable stiffness vibration isolator. In: *IEEE/ASME International conference advanced intelligent mechatronics* (Singapore, July 2009), pp 380–385



5. Li Y et al (2013) Development and characterization of a magnetorheological elastomer based adaptive seismic isolator. *Smart Mater Struct* 22(3):035005
6. Perruquetti W, Barbot JP (2002) Sliding mode control in engineering. CRC Press, Boca Raton
7. Yang JN, Wu JC, Agrawal AK (1995) Sliding mode control for nonlinear and hysteretic structures. *J Eng Mech* 121(12):1330–1339
8. DeCarlo R, Zak SH, Matthews GP (1988) Variable structure control of nonlinear multivariable systems: a tutorial. *Proc IEEE* 76(3):212–232
9. Vadim IU (1977) Survey paper variable structure systems with sliding modes. *IEEE Trans Autom Control* 22(2)
10. Hung JY, Gao W, Hung JC (1993) Variable structure control: a survey. *Indus Electron IEEE Trans* 40(1):2–22
11. Jung H-J, Eem S-H, Jang DD, Koo HH (2011) Seismic performance analysis of a smart base-isolation system considering dynamics of MR elastomer. *J Intell Mater Syst Struct* 22:1439–1450

# Seismic Response of Single Degree of Freedom System with Shape Memory Alloy (SMA) Damper



K. Thamaraiselvi and N. Gopalakrishnan

**Abstract** Shape memory alloys can effectively be used as a damper in structures due to its excellent re-centring (self-restoration) and energy dissipation properties. The distinctive hysteresis exhibited by the shape memory alloys enables it to be used in re-centring devices which can be connected to real structures. Hence, the analysis of a single degree of freedom system coupled with the SMA damper becomes crucial. This paper discusses the nonlinear time history analysis of a SDOF system with SMA damper modelled in MATLAB/SIMULINK subjected to harmonic and random excitation. The responses obtained from the system with and without SMA damper are compared.

**Keywords** Passive control · Time history · Superelasticity · Hysteresis Response history · Vibration control

## 1 Introduction

Seismic protection of structures using re-centring devices made of shape memory alloy (SMA) is a new paradigm shift beyond performance-based design. The hysteretic damping capacity and high recoverable strains (8–10%), the characteristic properties of SMA [1, 2], enable the material to be used in protection system for civil structures subjected to dynamic loads. Hence, the study of shape memory alloy-based passive/semi-active control devices is of immediate necessity in earthquake-resistant design.

---

K. Thamaraiselvi (✉)

Academy of Scientific and Innovative Research, Chennai, Tamil Nadu, India  
e-mail: thamarai.civil1992@gmail.com

N. Gopalakrishnan

CSIR-Structural Engineering Research Centre, Chennai 600113, Tamil Nadu, India  
e-mail: ng@serc.res.in

© Springer Nature Singapore Pte Ltd. 2019

A. Rama Mohan Rao and K. Ramanjaneyulu (eds.), *Recent Advances in Structural Engineering, Volume 2*, Lecture Notes in Civil Engineering 12,  
[https://doi.org/10.1007/978-981-13-0365-4\\_39](https://doi.org/10.1007/978-981-13-0365-4_39)

## 2 SMA as Damper

Pseudoelasticity is a type of hysteresis exhibited by the shape memory alloys (SMA) which helps in complete recovery of very large strains the material is subjected to without external application of heat. This property can be effectively employed in the passive control of structures [3, 4]. Figure 1 shows the typical pseudoelastic hysteresis behaviour of SMA. The NiTiNol (Ni-55%) shape memory alloy is used in the wire form in a specially designed damper device which can be connected to the structure [5, 6]. This device is designed in such a way that it is capable of taking both tension and compression loading and can be incorporated as a damper in the system [7–9].

An idealized SDOF system incorporated with shape memory alloy damper to be modelled in SIMULINK is represented in Fig. 2. The single degree of freedom system (SDOF) consists of a mass ‘ $m$ ’ attached to a spring of stiffness ‘ $k$ ’ and damper of damping coefficient ‘ $c$ ’. This mass is attached to the SMA element through a damper device.

The response of the SDOF system is governed by the following dynamic equilibrium equation

**Fig. 1** Pseudoelastic hysteresis behaviour exhibited by SMA

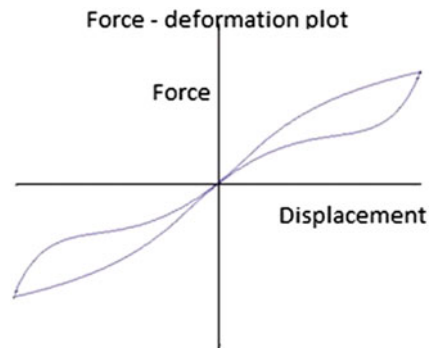
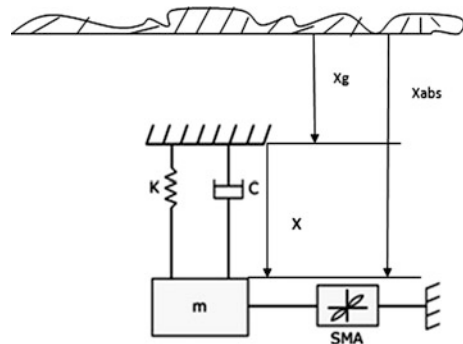


**Fig. 2** SDOF system incorporated with SMA damper



$$m\ddot{x}_{abs} + c\dot{x} + kx + F_{SMA} = 0 \tag{1}$$

where  $\ddot{x}_{abs}$  corresponds to the mass coordinate measured from an inertial reference frame and 'x' refers to the relative displacement.

$$x_{abs} = x + x_g \tag{2}$$

where  $\ddot{x}_g$  refers to the base acceleration, i.e. excitation acceleration given to the structure.  $F_{SMA}$  is the force exerted on the structure by the SMA element. Equation (1) can be written as follows

$$m\ddot{x} + c\dot{x} + kx + F_{SMA} = -m\ddot{x}_g \tag{3}$$

A nonlinear time history analysis must be performed to obtain the response from the system which is discussed in detail in the following section.

### 3 Analysis of SDOF System Coupled with SMA Damper

A time history analysis to numerically evaluate the dynamic response of a one degree of freedom model structure is performed in MATLAB/SIMULINK. The block diagram representing the incorporated SDOF system with SMA element in SIMULINK is shown in Fig. 3. The displacement time history obtained from the SDOF system is fed as input to the SMA element subsystem which characterizes the hysteresis behaviour of shape memory alloys. The SMA subsystem contains the superelastic hysteresis model of shape memory alloy which displays the force developed in SMA as output for the given displacement time history input. This restoring force is given back into the SDOF system, and this completes the loop.

The hysteresis behaviour of SMA damper for the given input is computed using a one-dimensional constitutive model developed by Cozzarelli et al. (1994) as discussed in Ref. [10, 11]. The value of stiffness and yield force of the SMA wires

**Fig. 3** Block diagram of SDOF system with SMA element

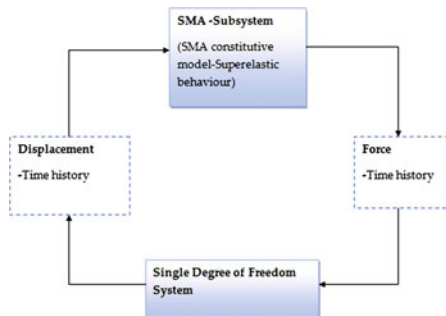


**Table 1** Parameters for the SMA damper model

Parameter	Value
Stiffness, $K$	150 N/mm
Yield force, $F_y$	800 N
$A$	0.1
$f_T$	6
$C$	0.001
$T_d$	0.02 s
$N$	1

used in damper are given as 150 N/mm and 800 N, respectively. Equations (4) and (5) represent the stress–strain relationship of SMA material [11] modelled in SIMULINK.

$$\dot{F} = K \left[ \dot{u} - |\dot{u}| \left( \frac{F - Z}{F_y} \right)^n \right] \tag{4}$$

$$\frac{Z}{K} = \alpha \{ u^{in} + T_d |\dot{u}| f_T |u^c| erf(\alpha u) [f(-ui)] \} \tag{5}$$

The values of material constants and other parameters that control the hysteresis loop are given in Table 1.

### 3.1 Response of the SDOF System

In this section, response of the SDOF system modelled with shape memory alloy element in SIMULINK for different loading conditions is computed. For this purpose, the SDOF system consisting of the following model parameters has been included in the analysis. A steel cantilever model of natural frequency 4 Hz is considered in the investigation. The SDOF model parameters employed in SIMULINK are given in Table 2.

**Table 2** SDOF model parameters

Parameter	Value
Mass ( $m$ )	100 kg
Damping coefficient ( $c$ )	502.6 N s/m
Length of beam ( $L$ )	1 m
Spring stiffness ( $k$ )	63165 N/m
Natural frequency ( $\omega_n$ )	4 Hz
Damping ratio, $\zeta$	0.1

### 3.1.1 Response Due to Harmonic Excitation

A harmonic sinusoidal excitation force of amplitude 500 N and frequency 1 Hz is supplied to the under-damped SDOF system connected to the SMA damper sub-system. The governing differential equation of motion in Eq. (6) is as follows

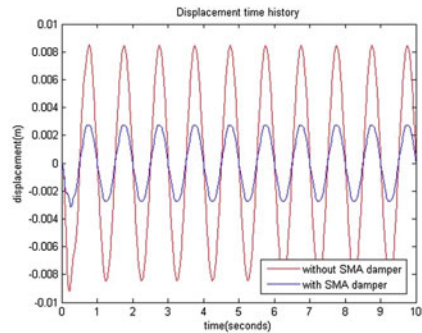
$$m\ddot{x} + c\dot{x} + kx + F_{SMA} = 500\sin(2\pi f)t \tag{6}$$

where ‘ $f$ ’ is the excitation frequency applied to the system.

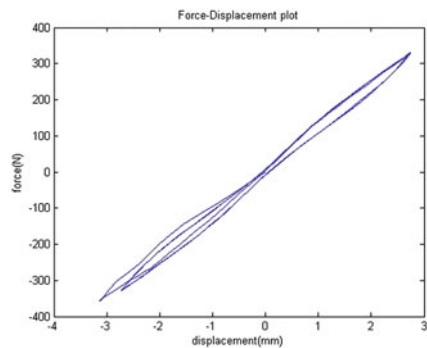
The response obtained from the system is shown in Fig. 4. The figure shows a comparison between the response obtained from the system with and without SMA damper. It can be clearly seen that there is a significant reduction in the peak displacement of the structure from 8.5 to 2.7 mm when SMA damper is attached to the system.

Figure 5 shows the superelastic cycles developed in the shape memory alloy damper system due to the displacement produced by harmonic excitation on the SDOF system. The maximum force developed on the SMA damper for the specified sinusoidal loading is found to be 330 N. This force time history developed in SMA damper is then mass normalized and fed into the SDOF system. The analysis results

**Fig. 4** Displacement response history for harmonic excitation



**Fig. 5** SMA superelastic cycle for harmonic loading



thus show that there is a reduction in peak displacement of the mass when subjected to harmonic loading, for about 68.23% once the SMA damper is attached to the system.

### 3.1.2 Response Due to Random Excitation

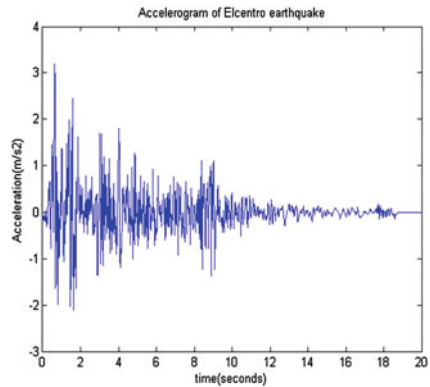
A nonlinear time history analysis is performed on the SDOF system modelled in SIMULINK by applying ground acceleration of  $\ddot{x}_g$ . The governing differential equation of motion is given in Eq. (3). The seismic input for the SDOF system is the accelerogram corresponding to NS component of El Centro earthquake, 18 May 1940, recorded in the Imperial Valley in south-eastern Southern California near the international border of the USA and Mexico. It had a moment magnitude of 6.9. It has a maximum peak ground acceleration of  $3.2 \text{ m/s}^2$ , predominant frequency of 4.5 Hz, and the total duration of the earthquake was 20 s. The model parameters of the SDOF system subjected to accelerogram of El Centro earthquake are given in Table 3.

The accelerogram supplied as input to the analytical model developed in SIMULINK is shown in Fig. 6. The nonlinear analysis performed in SIMULINK shows that the relative peak displacement of the mass gets reduced from 2.5 to 1.3 mm once the SMA damper system is attached to the SDOF system as shown in Fig. 7. It can also be seen that there is a significant reduction in the peak velocity of

**Table 3** SDOF model parameters for random excitation

Parameter	Value
Mass ( $m$ )	100 kg
Damping coefficient ( $c$ )	2000 N s/m
Length of beam ( $L$ )	1 m
Spring stiffness ( $k$ )	63165 N/m
Natural frequency ( $\omega_n$ )	4 Hz
Damping ratio, $\zeta$	0.3

**Fig. 6** Accelerogram (El Centro earthquake)



the mass attached from 0.0025 to 0.0013 m/s (Fig. 8). The absolute peak acceleration of the mass is found to get decreased from 4.1 to 3.9 m/s<sup>2</sup> (Fig. 9).

From the analysis results, it can be seen that there is a 48% reduction in the peak displacement value of the mass when it is connected to the SMA damper system. The average relative displacement of the system is found to be 0.28 mm without any damper, whereas the average relative displacement of the system with SMA damper element is 0.12 mm. This shows a reduction of about 58% in the mean relative displacement.

The restoring force developed in the SMA damper which acts on the SDOF system is shown in Fig. 10. It can be seen that the maximum restoring force developed in the SMA damper for the given accelerogram input is 327.3 N. This restoring force developed in the SMA system is mass normalized and fed into the SDOF system.

The nonlinear time history analysis is again performed on the SDOF model created in SIMULINK for a different earthquake time history to study its behaviour and versatility. The SDOF model parameters remain same which has been used for El Centro earthquake.

**Fig. 7** Displacement response history for random excitation (El Centro)

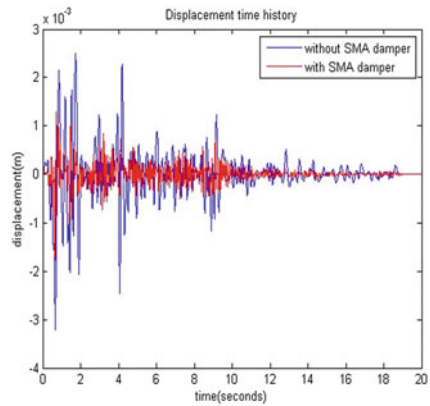


**Fig. 8** Velocity response history for random excitation (El Centro)

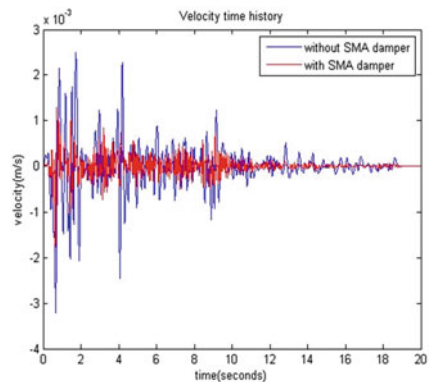




**Fig. 9** Acceleration response history for random excitation (El Centro)

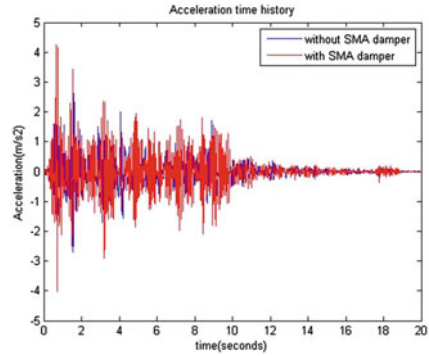


**Fig. 10** Restoring force developed in SMA damper

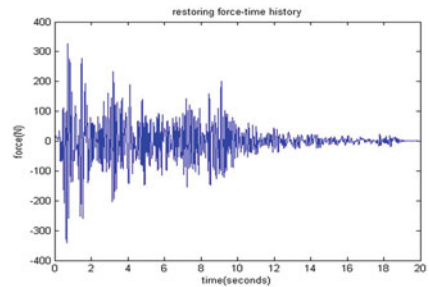
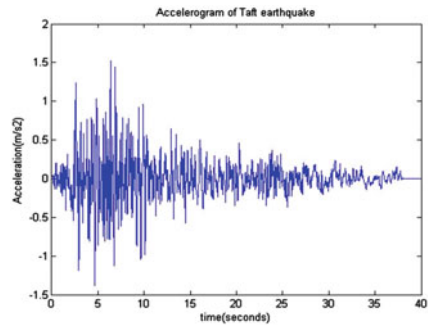


**Fig. 11** Accelerogram (Taft earthquake)



The accelerogram obtained from Taft earthquake (1952) is given as seismic input for the SDOF system modelled in SIMULINK (Fig. 11). The Kern County earthquake occurred on July 21 in the southern San Joaquin Valley and measured 7.3 on the moment magnitude scale. It has a peak ground acceleration of 1.557 m/s<sup>2</sup>, predominant frequency of 1.5 Hz, and the total duration of EQ is about 40 s.

The analysis results show that the relative peak displacement of the mass gets reduced from 2.2 to 0.67 mm once the SMA damper system is attached to the

**Fig. 12** Displacement response history for random excitation (Taft earthquake)

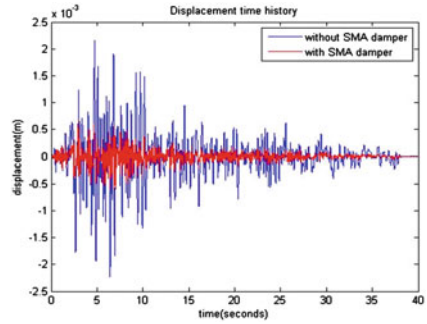


**Fig. 13** Velocity response history for random excitation (Taft earthquake)

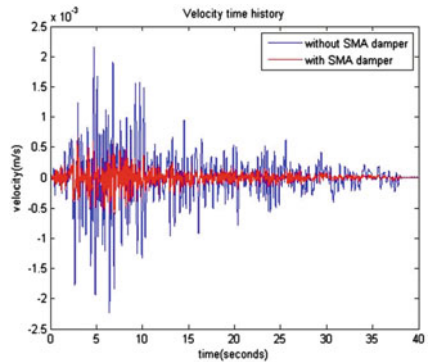
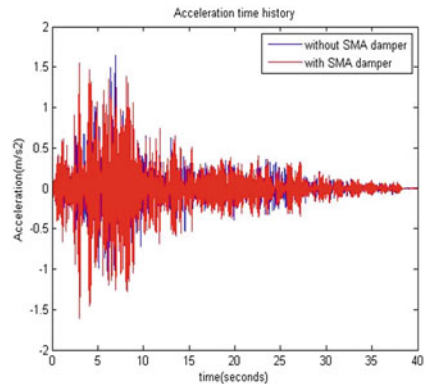


**Fig. 14** Acceleration response history for random excitation (Taft earthquake)



SDOF system (Fig. 12). It can also be seen that there is a significant reduction in the peak velocity of the mass attached from 0.0022 to 0.0067 m/s (Fig. 13). The absolute peak acceleration of the mass is found to get decreased from 1.6419 to 1.5439  $m/s^2$  (Fig. 14).

## 4 Conclusions

A single degree of freedom system is modelled in SIMULINK with SMA damper element exhibiting superelastic hysteresis behaviour. Two earthquake time histories have been supplied as input to the SDOF system modelled in SIMULINK, and the results are studied. It can be seen that the percentage reduction in the peak displacement of the system for El Centro earthquake is comparatively lesser than that of Taft earthquake. This may be due to the fact that the predominant frequency of El Centro earthquake is closer to the natural frequency of the SDOF system. However, the incorporation of SMA damper in a system is found to reduce the peak displacement of the system significantly for both the earthquake time histories.

Thus, the analysis conducted on the single degree of freedom system model in SIMULINK proves that the shape memory alloys can be effectively used in energy dissipation devices.

**Acknowledgements** The authors wish to express their sincere gratitude to the Director, CSIR-SERC, whose support plays a very important role in publishing the paper. We would also like to acknowledge Shri. Sreekala. R, Scientist, CSIR-SERC, for her valuable suggestions.

## References

1. Soul H, Yawny A (2015) Self-centering and damping capabilities of a tension-compression device equipped with superelastic NiTi wires. *Smart Mater Struct*, vol 24
2. Soul H, Isalgue A, Yawny A, Torra V, Lovey FC (2010) Pseudoelastic fatigue of NiTi wires: frequency and size effects on damping capacity. *Smart Mater Struct*, vol 19
3. Attanasi G, Auricchio F (2011) Innovative superelastic isolation device. *J Earthquake Eng* 15:72–89
4. Mayes JJ, Lagoudas D, Henderson BK (2001) An experimental investigation of shape memory alloy pseudoelastic springs for passive vibration isolation. In: *AIAA space 2001 conference and exposition*
5. Dolce M, Cardone D, Marnetto R (2001) SMA re-centering devices for seismic isolation of civil structures. In: *Proceedings of SPIE*, pp 238–249
6. Parulekar YM, Reddy GR, Vaze KK, Guha S, Gupta C, Muthumani K, Sreekala R (2012) Seismic response attenuation of structures using shape memory alloy dampers. *Struct Control Health Monit* 19:102–119
7. Sreekala R, Muthumani, K, Nagesh RI (2011) Seismic response control using smart materials. In: *Francisco B-C. INTECH Open Access Publisher*
8. Sreekala R, Muthumani K, Lakshmanan N, Gopalakrishnan N, Sathishkumar K (2008) Orthodontic arch wires for seismic risk reduction. *Curr Sci*, vol 95
9. Sreekala R, Muthumani K, Meher Prasad A, Gopalakrishnan N, Sathishkumar K (2010) Towards a sustainable infrastructure through smart dampers. *J Struct Eng* 37:61–65
10. Fugazza D (2003) Shape memory alloy devices in earthquake engineering: mechanical properties, constitutive modelling and numerical simulations. Master thesis, ROSE School, Pavia
11. Graesser EJ, Cozzarelli FA (1994) A proposed three dimensional constitutive model for shape memory alloys. *J Intell Mater Syst Struct* 5:78–79

# Energy Harvesting From Dynamic Vibration Pendulum Absorber



P. V. Malaji, M. Rajarathinam, V. Jaiswal, S. F. Ali and I. M. Howard

**Abstract** Dynamic vibration absorbers (DVAs) have proven to be an effective passive technique to suppress device vibration, with many realistic implementations in structures, buildings, and machines. Vibration energy harvesting is a process used to convert unwanted vibrations of a host structure into electrical energy. In this paper, a harmonic single degree-of-freedom system is considered consisting of a pendulum absorber and electromagnetic energy harvesting transduction mechanism. These types of DVAs are suitable for control of multi-story buildings, where for the simplicity of analysis a two degree-of-freedom system which models the building with the absorber is considered. Controlling the vibrations of buildings is the primary objective, and harvesting the energy from the dynamic vibration pendulum absorber at the same time is the secondary objective. Parametric analyses are performed. It is observed that proper system parameter selection is key for reducing the vibration amplitude of the primary system and for enhancing the energy harvested from the secondary system. Optimization analysis based on the genetic algorithm approach is used to optimize the system parameters. It is observed that with a proper selection of parameters, wideband energy can be harvested along with reduction in vibration of the building.

**Keywords** DVA · Energy harvesting · Electromagnetic

---

P. V. Malaji · M. Rajarathinam · V. Jaiswal (✉) · S. F. Ali  
Department of Applied Mechanics, IIT Madras, Chennai 36, India  
e-mail: vishal8005.iitm@gmail.com

P. V. Malaji  
e-mail: pradeepmalaji@gmail.com

M. Rajarathinam  
e-mail: rajiitm@gmail.com

S. F. Ali  
e-mail: sfali@iitm.ac.in

I. M. Howard  
Department of Mechanical Engineering, Curtin University, Perth, Australia  
e-mail: i.howard@curtin.edu.au

## 1 Introduction

Keeping structures safe and improving durability is an essential part of economic progress and sustainability. The use of new sensing and control technologies can be important tools that provide critical information to the engineering community about the health of the structure. These tools can help industry to control a structure or to rapidly identify the inception of structural damage in an instrumented structural system [1].

The area of smart structures has seen manifold developments in the last decade. The design of sensors and actuators, together with controllers that are made to measure and control the dynamic response of structures, can be deployed for structural health monitoring purposes [2]. Active control has often been adopted instead of passive control for effective vibration control. These systems can then be switched to semi-active and even hybrid semi-active systems to include the design of more efficient and less power-demanding systems. Still, the operation and powering up of the sensors and actuators is a challenging task, especially in remote locations. This challenge motivates researchers to look for an alternate way of supplying power to the sensors and actuators including the use of batteries. However, the effective life of batteries still limits the usefulness of the sensors and actuators. Devolvement of smart self-powered or autonomous sensors will enable the sensors to harvest sufficient energy from surroundings like the vibration of the host structure.

Energy harvesting for autonomous sensors and actuator nodes has attracted considerable interest in the recent decade [3, 4]. Ambient resources like solar, thermal, and vibration are being used to harvest the energy for health monitoring implementations. Vibration energy harvesting is one of the best-suited methods of harvesting energy from structures. Electromagnetic and piezoelectric techniques are the two main vibration-based harvesting techniques. Electromagnetic harvesters convert relative motion between the coil and magnet into electrical power [5, 6]. Piezoelectric energy harvesters utilize strain in the piezoelectric material to harvest electrical power [7, 8]. Both techniques have their own pros and cons. Electromagnetic techniques can be suitable for low-frequency applications. Several researchers have explored electromagnetic energy harvesting [5, 6, 9, 10].

Most of the studies on energy harvesting focused on the efficiency of the harvesters. Structural health monitoring has been the main application area for energy harvesting. Very few researchers have focused on devices that can control as well harvest the energy [11, 12]. While controlling structural vibration, the main goal is to reduce the vibration of the structure, which will reduce the energy harvested from it. It is important to find the trade-off between vibration reduction and energy harvested. DVAs are a suitable choice as the device shifts the vibrations from the primary structure to the secondary structure from which energy can be harvested [13].

Ali and Adhikari [13] investigated the linear damped vibration absorber as an energy harvesting device by using a piezoelectric mechanism. Optimal trade-off

parameters were obtained by using the fixed-point theory. Das and Santhosh [14] investigated the possibility of employing a nonlinear absorber for harvesting energy from DVA systems.

Energy harvesting from DVA will give the added advantage of harvesting energy from a secondary mass. This harvested energy can be used for the event-based powering of wireless sensors such as in the case of earthquake vibration, where conventional power supply may be affected. In the present study, a pendulum absorber is used as a secondary mass to reduce the vibration of the building and energy is harvested through the electromagnetic mechanism.

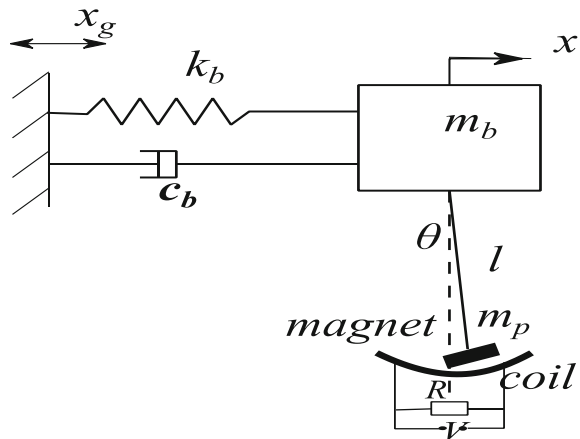
## 2 Mathematical Model

Figure 1 shows the schematic diagram of the proposed dynamic pendulum vibration absorber with energy harvesting. This represents a two degree-of-freedom system with electromagnetic energy conversion. The primary mass ( $m_b$ ) whose vibration has to be suppressed is connected with pendulum absorber of mass  $m_p$ . The pendulum absorber consists of an end magnet below which a copper coil is placed with load resistance as shown in Fig. 1.

The primary system representing the building is modeled as a single degree-of-freedom system with mass  $m_b$ , damping coefficient  $c_b$ , and stiffness  $k_b$  as shown. The pendulum absorber has length  $l$ , end mass (with magnet)  $m_p$ , and damping coefficient  $c_p$ . The magnet has flux density of  $B$  with a copper coil of length  $L$  which is connected to load resistance  $R$  that is placed at a distance  $d$  from the magnet.  $V$  denotes the voltage across the load resistor. The coupling between the mechanical and electrical systems is modeled by electrical damping  $c_e$ .

The electromechanical equations for small displacement are written as:

**Fig. 1** Schematic of DVA energy harvesting system



$$(m_b + m_p)\ddot{x} + m_p l \ddot{\theta} + c_b \dot{x} + k_b x = -(m_b + m_p)\ddot{x}_g \tag{1}$$

$$m_p l \ddot{x} + m_p l^2 \ddot{\theta} + (c_b + c_e) l^2 \dot{\theta} + m_p g l \theta = -m_p l \ddot{x}_g \tag{2}$$

$$V = dBL\dot{\theta} \tag{3}$$

where  $x$  and  $\theta$  denote displacement of the primary mass and pendulum, respectively. The primary structure is subjected to the harmonic base excitation of amplitude  $x_g$ .

For steady-state solution of the system, solutions of Eqs. (1)–(3) can be written as

$$x = X e^{i\omega t}, \theta = \Theta e^{i\omega t}, x_g = X_g e^{i\omega t}, V = V1 e^{i\omega t} \tag{4}$$

The following non-dimensional parameters are introduced to non-dimensionalize Eqs. (1)–(3), where  $h$  indicates the height of the building [].

$$\begin{aligned} \mu &= \frac{m_p}{m_b}, \Omega = \frac{\omega}{\omega_b}, \omega = \sqrt{\frac{k_b}{m_b}} v = \frac{X}{h}, c_e = \frac{BL^2}{R} \\ \beta &= \frac{l}{h}, \alpha = \frac{\omega_p}{\omega_b}, \Gamma_b = \frac{c_b}{2m_b \omega_b}, \Gamma_p = \frac{c_p}{2m_p \omega_p} \\ \Gamma_e &= \frac{c_e}{2m_b \omega_b} \end{aligned} \tag{5}$$

Substituting Eqs. (4) and (5) in Eqs. (1)–(3) results in

$$-(1 + \mu)\Omega^2 + i2\Omega\Gamma_b + 1)v - (\mu\beta\Omega^2)\Theta = (1 + \mu)\Omega^2 v_g \tag{6}$$

$$-\Omega^2 v + (-\beta\Omega^2 + i2\Omega\beta\alpha(\Gamma_p + \Gamma_e) + \alpha^2\beta)\Theta = \Omega^2 v_g \tag{7}$$

$$V1 = i\omega dBL\Theta \tag{8}$$

Solving for displacement amplitude  $v$  and  $\Theta$  provides

$$v = \frac{a_1\Omega^8 + a_2\Omega^7 + a_3\Omega^6 + a_4\Omega^5 + a_5\Omega^4 + a_6\Omega^3}{\Delta^2} \tag{9}$$

$$\Theta = \frac{b_1\Omega^7 + b_2\Omega^6 + b_3\Omega^5 + b_4\Omega^4 + b_5\Omega^3}{\Delta^2} \tag{10}$$

where the denominator is given as

$$\Delta = d_1\Omega^4 + d_2\Omega^3 + d_3\Omega^2 + d_4\Omega + d_5 \quad (11)$$

The coefficients in Eqs. (9)–(11) are given by

$$\begin{aligned} a_1 &= -2v_g\beta^2, a_2 = -i2\beta((\Gamma_p + \Gamma_e)(1 + \mu)\alpha + \Gamma_b) \\ a_3 &= -\alpha^2v_g(1 + \mu)\beta^2((1 + \mu)\alpha^2 + 8\Gamma_b(\Gamma_p + \Gamma_e)\alpha \\ &\quad + 4\Gamma_p^28\Gamma_e\Gamma_p + 1) \\ a_4 &= -i4\beta^2\alpha v_g((1 + \mu)^2(\Gamma_p + \Gamma_e)\alpha^2 + 2\Gamma_b(((\Gamma_p + \Gamma_e)^2 + \frac{1}{4})\mu((\Gamma_p + \Gamma_e)^2 + \frac{1}{2})\alpha) \\ &\quad + \frac{1}{2}(\Gamma_p + \Gamma_e)(\mu + 2)) \\ a_5 &= (\frac{1}{4} + ((\Gamma_p + \Gamma_e)^2\mu + 2\Gamma_e\Gamma_p + \Gamma_p^2 + \frac{3}{4} + \Gamma_e^2)(1 + \mu)\alpha^2 \\ &\quad + \Gamma_b(\Gamma_p + \Gamma_e)(2 + \mu)\alpha)4v_g\beta^2 \\ b_1 &= i4v_g\Gamma_b\beta, b_2 = 4v_g\beta(\frac{1}{2} + \Gamma_b^2 + \alpha(\Gamma_p + \Gamma_e)(1 + \mu)\Gamma_b) \\ b_3 &= i2v_g\beta(\Gamma_b(1 + \mu)\alpha^2 + (\Gamma_p + \Gamma_e)(4\Gamma_b^2 + 1 + \mu)\alpha + 2\Gamma_b) \\ b_4 &= -\beta v_g(1 + (4\Gamma_b^2 + 1 + \mu)\alpha^2 + 8\Gamma_b(\Gamma_p + \Gamma_e)\alpha) \\ b_5 &= i2\beta v_g\alpha(\Gamma_p + \Gamma_e + \Gamma_b\alpha) \\ d_1 &= \beta, d_2 = -i2\beta((\Gamma_p + \Gamma_e)(1 + \mu)\alpha + \Gamma_b) \\ d_3 &= -\alpha^2\beta - 4\Gamma_b\Gamma_p\beta\alpha - \mu\alpha^2\beta - \beta - 4\beta\Gamma_e\alpha \\ d_4 &= i2\beta\alpha(\alpha\Gamma_b + \Gamma_p + \Gamma_e), d_5 = \beta\alpha^2 \end{aligned}$$

The power harvested by the pendulum absorber is given by

$$p = \frac{V1^2}{R} \quad (12)$$

The normalizing power with respect to mass and frequency of the pendulum and distance between coil and magnet results in

$$P = \frac{p}{m_p\omega_p^3d^2} = \Omega^2\Gamma_e\Theta^2 \quad (13)$$

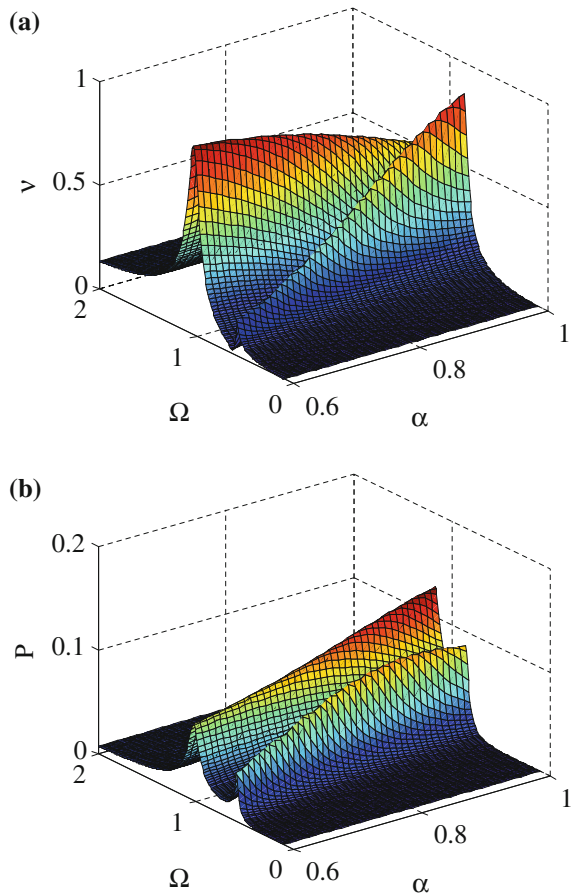


### 3 Parametric Study

Equations (9) and (12) are simulated over a range of parameters to study the effect of displacement of the primary structure and power harvested from the secondary system. The excitation amplitude  $v_g$  is taken as 0.1, ratio of pendulum length to building height  $\beta$  is taken as 0.1, and damping ratio of primary mass  $\Gamma_b$  is taken as 0.05.

Figure 2a, b shows the frequency response curves for displacement of the primary structure and power harvested for the various values of frequency ratio of pendulum to the primary mass. Pendulum damping ratio and electrical damping ratios are taken as 0.01 and 0.005, respectively. From the frequency response curves, one can observe that for lower values of frequency ratio  $\alpha$ , the amplitude of the primary mass nearer to the resonance will be of higher magnitude than that which is away from resonance, whereas the power curve will have two peaks of equal magnitude. With the increase in frequency ratio  $\alpha$ , opposite behavior in the

**Fig. 2** **a** Frequency response curve for primary structure displacement for various values of frequency ratio of pendulum to the primary mass. **b** Frequency response curve for normalized power harvested for various values of frequency ratio of pendulum to the primary mass



two peaks of amplitudes of the primary structure is observed. The magnitude of the power peaks increases with increase in the frequency ratio  $\alpha$  initially, while further increase in the frequency ratio magnitude results in a slight decrease of one of the peak powers.

The normalized displacement of the primary mass and normalized power for different values of electrical damping  $\Gamma_e$  are ( $\Gamma_p = 0.01$ ) shown in Fig. 3a, b, respectively.

Reduction in amplitude of the primary mass is observed with an increase in electrical damping ratio as shown in Fig. 3a. The power harvested increases with increase in electrical damping, where theoretically the harvested power can become infinite for infinite value of electrical damping [10] as shown in Fig. 3b. This is because the electrical damping has much less effect on the relative velocity between the primary structure and the absorber. It is very difficult to obtain optimum values of electrical damping, where generally electrical damping cannot be taken too high as the mass of pendulum is much less. Electrical damping value which is equal to or

**Fig. 3** a Frequency response curve for primary structure displacement for various values of electrical damping ratio. b Frequency response curve for normalized power for various values of electrical damping ratio

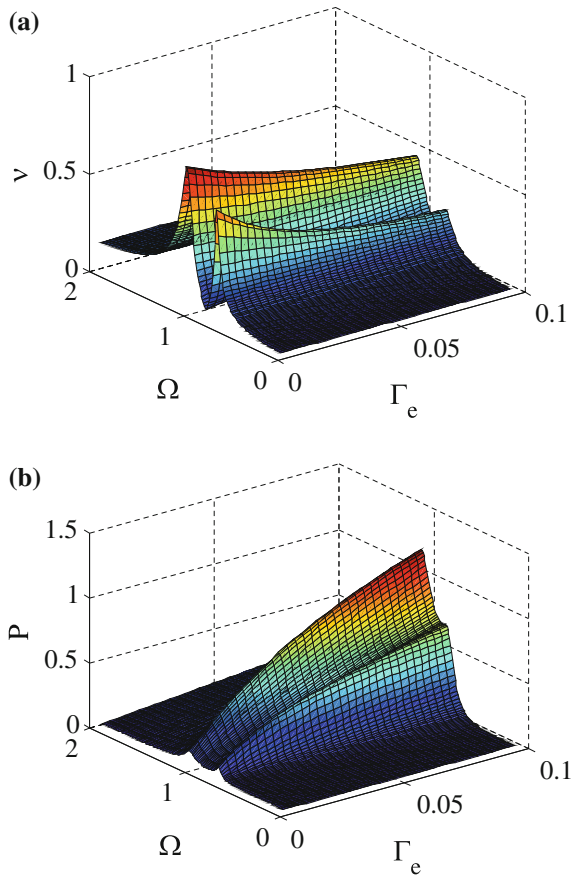
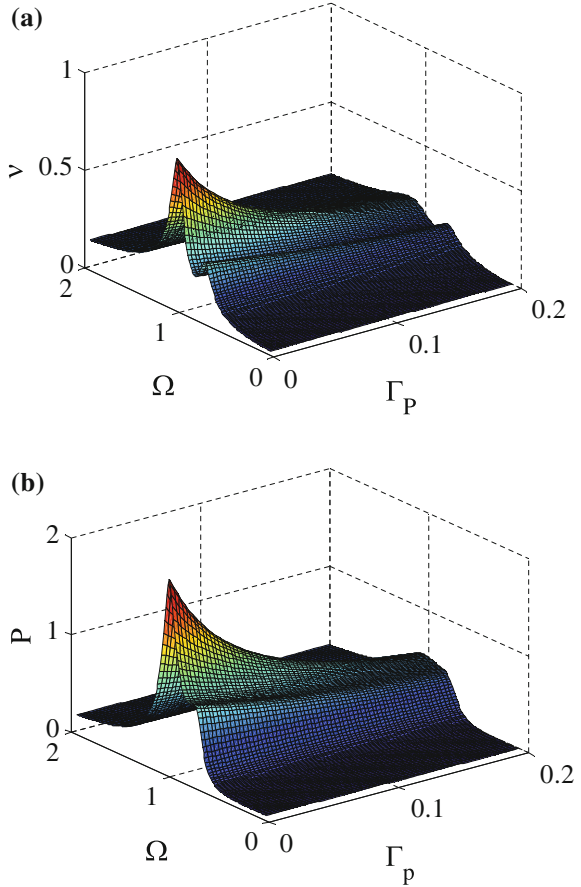


**Fig. 4** **a** Primary structure displacement frequency response curve for various values of pendulum damping ratio. **b** Frequency response curve for normalized power for various values of pendulum damping ratio



slightly more than the pendulum damping value is considered as the optimal value. In the present work, we will consider electrical and pendulum damping to be equal for the optimum power.

The amplitude of both the primary structure and power magnitude decreases with the increase in pendulum absorber damping ratio  $\Gamma_p$  ( $\Gamma_e = 0.005$ ) as shown in Fig. 4a, b. The power peaks merge into one as the damping ratio increases with decrease in power.

### 4 Optimization

The objectives of harvesting energy from the DVA are conflicting, as the response amplitude of the primary mass has to be reduced while the power harvested by the pendulum absorber has to be increased. Therefore, an optimization is necessary to

obtain optimal parameters which can satisfy both requirements. The parameters to be optimized are the frequency ratio  $\alpha$  and pendulum damping  $\Gamma_e$ . As the optimization involves both minimization and maximization of objective functions  $f_1$  and  $f_2$ , the problem can be converted into minimization of the cost function  $f$ :

$$\text{Min} f = f_1 - f_2 \tag{14}$$

$$f_1 = \min(\mathbf{v}) \tag{15}$$

$$f_2 = \max(P) \tag{16}$$

The parameter constraints are defined as

$$0.5 < \alpha < 1 \text{ and } 0.005 < \Gamma_p < 0.04$$

Genetic algorithm (GA) which optimizes the bounded parameters was used to solve the bi-objective optimization problem. GA is a computerized search and optimized algorithm based on natural selection. The GA process starts with a population of random strings representing the judgment variables. Later, this population is operated on by the three operators of reproduction, crossover, and mutation to create new population of points. Furthermore, each new population is evaluated, and this process continues until the termination criteria is met. Figure 5 shows the flowchart representing the working of GA.

Two different cases with different mass ratios are considered. The optimized parameters are shown in Table 1.

Fig. 5 Genetic algorithm flowchart

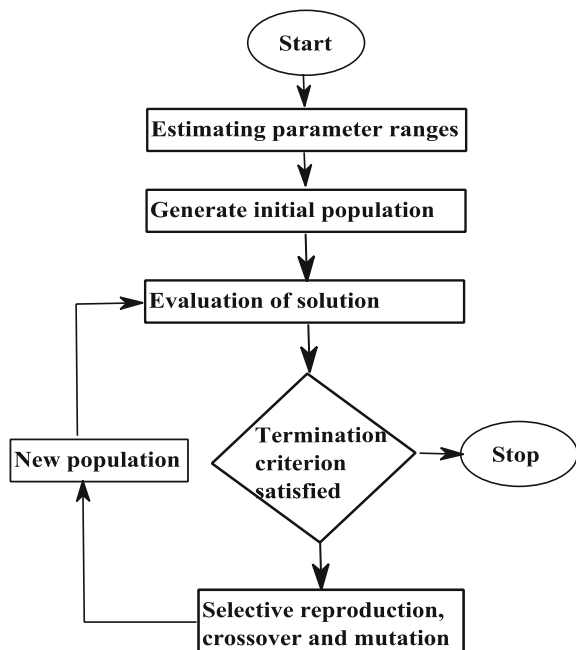
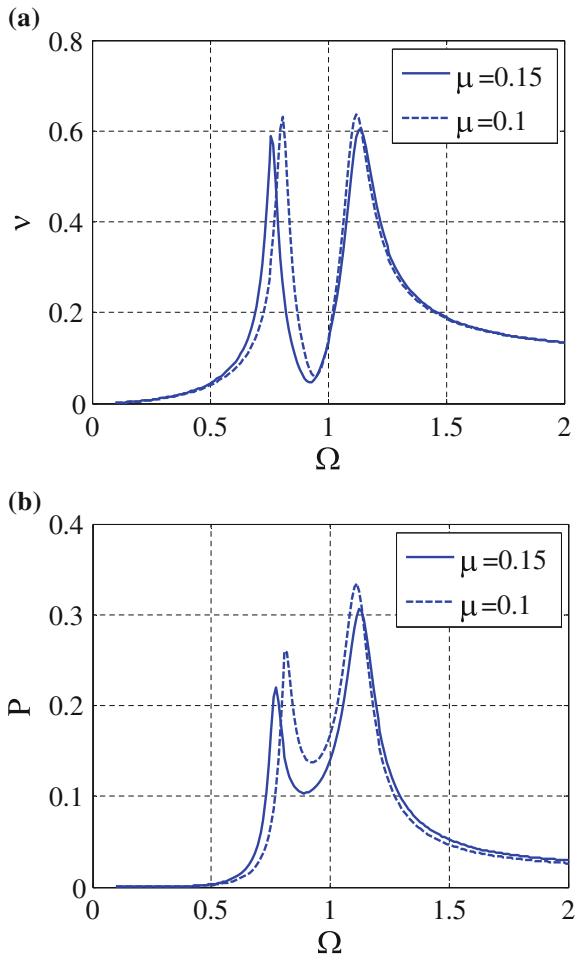


**Table 1** Optimal parameters

Case	$\alpha$	$\Gamma_p = \Gamma_e$
$\mu = 0.1$	0.9	0.015
$\mu = 0.15$	0.882	0.01

**Fig. 6 a** Frequency response curve for normalized displacement of primary structure for optimized values given in Table 1. **b** Frequency response curve for normalized power for optimized values given in Table 1



The normalized amplitude and normalized power as a function of normalized frequency are shown in Fig. 6a, b. With optimal parameters, the analysis shows that the amplitude of the primary structure can be reduced substantially while at the same time allowing for harvesting of energy from the absorber across a wide band of frequencies.

## 5 Conclusion

In this work, a pendulum dynamic absorber for buildings as an energy harvesting device is analyzed. The objective is to reduce the building (primary structure) vibration while also harvesting energy from the pendulum absorber. Parametric analysis of the frequency ratio of the pendulum with the primary structure, pendulum damping ratio, and electrical damping ratio was carried out. Optimal parameters were then obtained from GA optimization. The following points can be noted from the present study.

1. The power curve of the pendulum harvester shows a double peak, which indicates broadband energy harvesting possibilities.
2. The harvested power can theoretically reach infinite value for infinite electrical damping ratio. However for practical cases, where the pendulum absorber mass is much less compared to the primary mass, maximum electrical damping can be chosen equal to the pendulum damping.
3. Energy harvesting introduces electrical damping, which reduces the high damping requirement of the pendulum absorber to reduce the building (primary mass) amplitude.

Future work will include the effect of pendulum nonlinearity on optimal performance and the experimental demonstration with a building model.

## References

1. Ali SF, Ramaswamy A (2009) Optimal dynamic inversion based semi-active control of benchmark bridge using MR dampers. *Struct Control Health Monit* 16:564–585
2. Ali SF, Ramaswamy A (2009) Testing and modeling of MR damper and its application to MDOF systems using integral backstepping technique. *ASME J Dyn Syst Meas Contr* 131(2):021009
3. Sodano HA, Inman DJ, Park G (2004) A review of power harvesting from vibration using piezoelectric materials. *Shock Vib Dig* 36(3):197–205
4. Beeby SP, Tudor MJ, White NM (2006) Energy harvesting vibration sources for microsystems applications. *Meas Sci Technol* 17(12):175–195
5. Williams C, Yates R (1996) Analysis of a micro-electric generator for microsystems. *Sens Actuators A Phys* 52:8–11
6. Kulkarni S, Koukharenko E, Torah R, Tudor J, Beeby S, O'Donnell T, Roy S (2008) Design, fabrication and test of integrated micro-scale vibration-based electromagnetic generator. *Sens Actuators A Phys* 145:336–342
7. Adhikari S, Friswell MI, Inman DJ (2009) Piezoelectric energy harvesting from broadband random vibrations. *Smart Mater Struct* 18(11):115005
8. Lumentut MF, Howard IM (2013) Analytical and experimental comparison of electromechanical vibration response of a piezoelectric bimorph beam for power harvesting. *Mech Syst Signal Process* 36:66–86
9. Malaji PV, Ali SF (2015) Analysis of energy harvesting from multiple pendulums with and without mechanical coupling. *Eur Phys J Spec Top* 23:411–420

10. Xiudong T, Lei Z (2011) Enhanced vibration energy harvesting using dual-mass systems. *J Sound Vib* 330:5199–5209
11. Nakano K, Suda Y, Nakadai S (2003) Self powered active controlled using electric actuator. *J Sound Vib* 260:213–235
12. Chio YT, Wereley NM (2009) Self powered magnetorheological dampers. *ASME J Vib Acoust* 131:044501
13. Ali SF, Adhikari S (2013) Energy harvesting dynamic vibration absorbers. *J Appl Mech* 80(4)
14. Das AS, Santhosh B (2016) Energy harvesting from nonlinear vibration absorbers. *Procedia Eng* 144:653–659

**Part III**  
**Condition Assessment and Performance**  
**Evaluation**



# Seismic Fragility Analysis of Highway Bridges in India Considering Evolution of Seismic Code Provisions— A Case Study



Shivang Shekhar and Jayadipta Ghosh

**Abstract** Periodic advances in seismic design codes, and bridge detailing and construction practices across different nations are a common manifestation of the lessons learned from past earthquakes. The structural deficiencies are addressed in prevailing design standards through improved estimates of seismic forces and reinforcement detailing to better withstand the next seismic event. Similarly, a history of damaging earthquakes in the Indian subcontinent has led to significant upgradation in provisions of seismic code for highway bridge design. Bridges designed as per such varied design methods must be evaluated for vulnerability estimation for future earthquakes. However, there is a marked absence of such seismic vulnerability evaluation frameworks for highway bridges within the country. The present study investigates the impact of seismic code provisions on seismic performance and probability of failure using fragility curves. Significant improvement in performance is observed compared to non-seismic design for the case-study bridge when seismic design principles are adopted.

**Keywords** Seismic design codes · Ground motions · Fragility curves  
IRC provisions

## 1 Introduction

Over the past several decades, seismic design principles for highway bridges in India have undergone substantial changes, ranging from a little to no consideration of earthquake effects to the adoption of modern ductile detailing principles. Bridges designed as per such varied design methods must be evaluated to review the dif-

---

S. Shekhar · J. Ghosh (✉)  
Department of Civil Engineering, Indian Institute of Technology Bombay,  
Powai, Mumbai 400076, India  
e-mail: jghosh@iitb.ac.in

S. Shekhar  
e-mail: shivangshekhar@iitb.ac.in

© Springer Nature Singapore Pte Ltd. 2019  
A. Rama Mohan Rao and K. Ramanjaneyulu (eds.), *Recent Advances in Structural Engineering, Volume 2*, Lecture Notes in Civil Engineering 12,  
[https://doi.org/10.1007/978-981-13-0365-4\\_41](https://doi.org/10.1007/978-981-13-0365-4_41)

ferences in their seismic performance as well as failure probability through a systematic comparison of seismic fragility curves. The poor performance of highway bridges within India has been revealed multiple times during past earthquake events, for example during the 1984 Cachar earthquake in Assam, the 1997 Jabalpur earthquake, the 1999 Chamoli earthquake and the 2001 Bhuj earthquake, among others. Given the uncertainty associated with ground motions, it is critical to estimate the seismic vulnerability of highway bridges built across different design eras using probabilistic methods and develop a framework to aid bridge infrastructure owners for bridge rehabilitation and retrofit prioritization. However, seismic reliability assessment of highway bridges in India using probabilistic methods is still in its infancy. Among the limited literature available, only recently Goswami and Murty [1] have reviewed, albeit deterministically, the seismic vulnerability of reinforced concrete (RC) bridge piers designed with IRC provisions.

Addressing such drawbacks and present needs, this paper traces the evolution of seismic code provisions within India and conducts subsequent impact assessment on the seismic vulnerability of highway bridges using fragility curves. These curves are conditional probabilistic statements which indicate the likelihood of bridge failure given the intensity of seismic shaking. In this study, seismic fragility curves corresponding to different design eras are developed and compared for a representative two-span single-column integral box girder case-study bridge located in the high seismic zone (Zone V).

The next section of the paper elaborates on the evolution of seismic codes for highway bridges in India. Next, the representative case-study bridge along with its analytical model is introduced, followed by the identification of the characteristic failure modes during earthquake events. Subsequently, seismic fragility curves are developed and compared across different design cases. The paper ends with key conclusions and recommendations for future work.

## **2 Evolution of Seismic Design Codes for Highway Bridges in India**

The extensive damage of bridges all over the world has greatly influenced the earthquake design principles and seismic code provisions. Within India, while the Indian standards IS 1893 published by Bureau of Indian Standards historically provides the general seismic loading criteria for structures, design and construction of highway bridges in India have been primarily governed by the Indian Road Congress (IRC) Specifications. The IRC: 6 publication, which provides guidelines for loads and stresses (including seismic loads) for highway bridges, has undergone several revisions in the last five decades. The first three versions of IRC: 6 till IRC: 6-1966 [2] did not perceive the seismic provisions of IS 1893 code and only specified a lateral force of 5–10% of total gravity loads in earthquake-prone regions of the country. The IRC: 6-1966 was amended in the year 1981, and seismic zone

map and provisions were adopted from IS: 1893-1975 code. The horizontal design earthquake load on the bridges was now calculated based on seismic coefficient method. The equivalent static horizontal seismic force ( $F_{eq}$ ) on the bridge is specified as follows:

$$F_{eq} = \alpha_o \beta \lambda W \quad (1)$$

where  $\alpha_o$  is the horizontal seismic coefficient (recommended as 0.01, 0.02, 0.03, 0.04 and 0.08, respectively, for zones I to V),  $\lambda$  is the importance factor (1.0 for regular and 1.5 for important bridges),  $\beta$  is the soil-foundation system factor and  $W$  is the seismic weight. The fourth revision of IRC: 6 came in the year 2000 without any further modifications to the existing seismic provisions. Goswami and Murty [1] have critically reviewed the clauses of IRC: 6-2000 [3] and the respective concrete design code IRC: 21-2000 and IRC: 78-2000 [4, 5] and concluded that the Indian bridges are under-designed for seismic load as per IRC provisions due to low level of design force as compared to other international provisions. The flexibility and dynamic behaviour of the bridge were also not considered while calculating design seismic force for bridges. Additionally, the general design specifications were based on the working stress method (WSM) were not adequate. While provisions for shear design for column and compression member even under lateral loading were absent, detailing provisions were included for transverse reinforcement. A closer look reveals that such detailing provisions were inadequate, thereby rendering the performance of bridges inadequate under seismic loading. Thus, design specifications until 2000 advocated only flexural strength design, and ductile detailing and capacity-based design remained unaddressed.

Following the Bhuj earthquake in 2001, the IRC: 6-2000 [3] was amended in 2003 with interim provisions [6], following the IS: 1893-2002 [7] seismic provisions. As per this code, the Indian land mass is divided into four zones and the horizontal seismic coefficient is modified depending on the flexibility of the structure. The design horizontal seismic force is calculated as follows:

$$F_{eq} = A_h W, \text{ where } A_h = \frac{Z I S_a}{2 R g} \quad (2)$$

where  $A_h$  is the design seismic coefficient,  $Z$  is the zone factor,  $I$  is the importance factor and  $S_a/g$  is the average response acceleration coefficient which depends on the time period of the structure and soil condition. The response reduction factor ( $R$ ) which depends on the ductility of the member is assigned a value of 2.5, regardless of the bridge component. It is noted that this code still followed the WSM design philosophy (IRC: 21-2000 and IRC: 78-2000), but for ductile detailing, IS: 13920-1993 was recommended which specifies ductile detailing criteria for buildings.

The fifth revision of IRC: 6 came in the year 2010 wherein the value of  $R$  was rationalized depending upon type of substructure and bearing and also the bridge importance factor. This code, however, still followed the WSM design philosophy.

**Table 1** Classification of design cases

Cases	Level of seismic force	Design principle	Reinforcement detailing philosophy	Codes/guidelines
Case 1	Nil	WSM	Non-ductile	IRC: 6-1966
Case 2	Low	WSM	Non-ductile	IRC: 6-2000 IRC: 21, 78-2000
Case 3	High	WSM	Ductile	IRC: 6-2000 (Amended in 2003) IRC: 21, 78-2000 IS 13920
Case 4	High	LSM	Ductile	IRC: 6-2014 IRC: 112-2011

The sixth and latest revisions of IRC: 6 [8] came in the year 2014 after the publication of IRC: 112-2011 [9] which is based on limit state method (LSM) of design in the year 2011. The response reduction factor  $R$  was further rationalized depending on the ductility of the member, and furthermore, the cracked moment of inertia is used for the calculation of the time period. Ductile detailing of bridges, in line with the provision of IRC: 112-2011 [9], was also introduced for the first time. A description of representative cases considered in this study depending on the level of seismic force, method of design and detailing practices is summarized in Table 1.

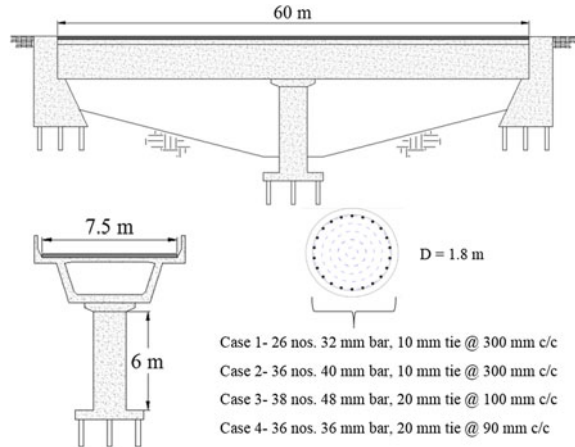
To investigate the impact of different design provisions on seismic vulnerability, this study considers a representative case-study bridge. The bridge description, analytical modelling and fragility assessment are discussed next.

### 3 Representative Case-Study Bridge

#### 3.1 Bridge Description and Geometry

This study considers a two-span single-column box girder integral bridge having span length of 30 m as shown in Fig. 1. The nominal (i.e. design) concrete strength of the substructure and superstructure is 35 and 40 MPa, respectively. The dead weight of superstructure is 166.67 kN/m which produces a gravity load of 5000 kN on the reinforced concrete bridge column. The diameter of the column is 1.8 m, and reinforcement layout is shown in Fig. 1. The lateral seismic forces are determined as per different version of IRCs with an assumption that the bridge lies in seismic Zone V (very severe earthquake risk) and belongs to the seismic class of important bridges. The bridge column is designed for four seismic design cases identified earlier (Table 1).

**Fig. 1** Representative case-study single-column integral box girder bridge



### 3.2 Analytical Modelling of Bridge

As typical of integral bridges, this study assumes that the seismic fragility of the case-study bridge is primarily dictated by the vulnerability of RC columns. The contribution of abutment to the overall bridge fragility is considered to be minimal, and superstructure is assumed to remain elastic during an earthquake. The case-study bridge is modelled as 2D stick/beam-column element with superstructure mass lumped on the top of the bridge column along with its self-weight. The column section is modelled with *NonLinear Beam Column* element in OpenSees [10] using the fibre section approach with distributed plasticity, consisting of circular concrete patches and circular layers of reinforcement. The concrete, both confined and unconfined, is modelled using the *Concrete01* properties in OpenSees. The longitudinal reinforcement is modelled using *Steel02* material properties with strain hardening ratio of 0.018. The fibre-based modelling of RC section can only consider interaction between biaxial bending and axial force, and the effect of shear deformation which can be crucial in case of non-ductile column is not a part of this fibre-based model. The *Section Aggregator* command is used to “add” the shear deformation behaviour to the existing fibre section. An elastic-perfectly plastic shear force-deformation ( $V-\gamma$ ) behaviour is assumed with an elastic slope equal to  $GA_s$ , where  $G$  is the shear modulus and  $A_s$  is the effective shear area. The calculated shear strength ( $V$ ) of a section depends on the grade of concrete and steel, amount of transverse reinforcement (as per the different design eras) and axial load. The aggregated section can accommodate axial, bending and shear behaviour.

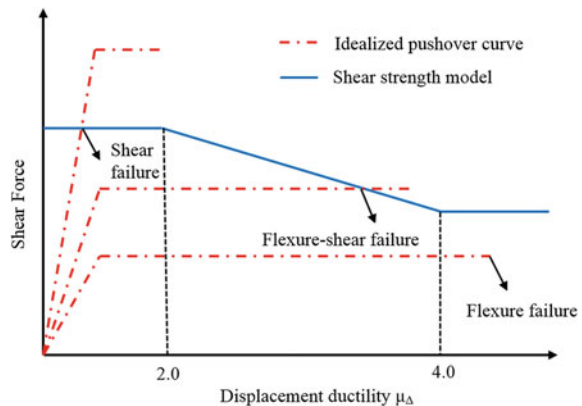
### 3.3 Identification of Failure Modes for Four Different Designed Eras' Bridge Column

In order to identify the type of failure modes for four different designed eras' bridge column, this study utilizes the conceptual model proposed by ATC-6 [11] which describes the relationship between shear strength and displacement ductility. As per this model, as lateral drift increases, the flexure-shear cracks widen and the concrete mechanism of shear transfer degrades due to loss of aggregate interlock, resulting in decrease in shear strength with increasing ductility. Three possible failure modes of columns subjected to lateral displacement can be identified, as shown in Fig. 2. The failure mode can be identified by using the displacement ductility-based predictive shear strength model [12–14] and then comparing with shear force demands obtained from static pushover analysis of the bridge column. It is observed that significant variation exists between various shear strength models and the possibility of failure modes depends on the chosen strength prediction model.

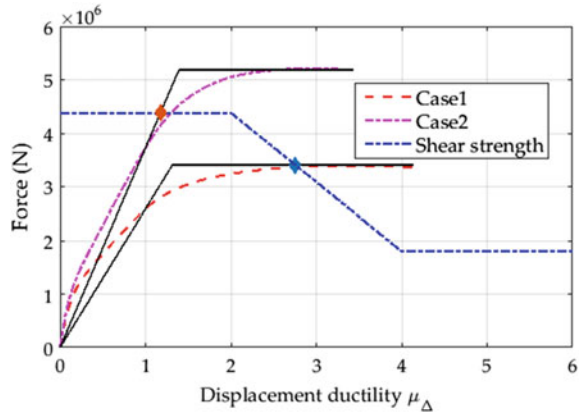
This paper considers the model proposed by Priestley et al. [12] to calculate the shear strength of the bridge column as function of displacement ductility, as commonly adopted by similar other studies [15, 16]. As per this model, the shear strength  $V_n$  is calculated as the summation of shear carried by concrete  $V_c$ , shear carried by transverse reinforcement based on truss mechanism  $V_s$  and shear enhancement due to axial load on the column  $V_p$ .

Figure 3 shows the comparison of shear strength model and flexural strength capacity curve as function of displacement ductility  $\mu_\Delta$  for the case-study bridge column designed as per Case 1 and Case 2 (Table 1). The type of failure mechanism is identified in accordance with the classification of ATC-6 described earlier (Fig. 2). The figure reveals that for Case 1, the bridge column fails in flexure-shear mode, while Case 2 column fails in pure shear mode as displacement ductility demand increases. Due to limited longitudinal rebars in Case 1, the reinforcements initially undergo flexural yielding before shear failure. Although the Case 2 bridge

Fig. 2 Classification of column failure modes [11]



**Fig. 3** Comparison of shear strength and flexural strength capacity for Case 1 and Case 2



column is designed for seismic forces corresponding to the design era, the bridge column primarily fails in shear due to inadequate transverse reinforcement because of non-ductile detailing.

On the contrary, for the Case 3 and Case 4 bridge column the predominant failure mode is flexure due to closely spaced transverse reinforcement (ductile detailing), which in addition to enhancing the shear strength, also confines the core concrete. Analysis also reveals that even though the amount of longitudinal reinforcement is more in Case 3 due to lower value of response reduction factor  $R$  resulting in higher seismic forces, its displacement ductility capacity is less than the Case 4 bridge column; thereby, Case 4 column will respond better than Case 3 column in case of seismic event. For further analysis, this study will examine seismic vulnerability of shear-critical column (non-ductile Case 2) and flexural-critical column (ductile Case 4) using fragility curves.

### 4 Seismic Fragility Analysis

Seismic fragility curves are a fundamental tool for seismic vulnerability assessment methodologies and are used to assess potential seismic damage to bridges for a given seismic hazard level. It describes the probability that the seismic demand ( $D$ ) placed on the structure exceeds the capacity ( $C$ ) conditioned on a chosen intensity measure ( $IM$ ) representative of the seismic loading. The following sections will elaborate on the ground motion selection for nonlinear time-history analysis of bridge models, followed by the fragility analysis using column capacity distributions and probabilistic seismic demand models of bridge columns for shear-critical (non-ductile) and flexural-critical (ductile) bridge columns.

## 4.1 Selection of Ground Motions

Selection of ground motions plays an important role in the development of fragility curves for highway bridges. Several studies have shown that the record-to-record variability of ground motions is the primary contributor to the aleatoric randomness. Thus, fragility curves are likely to be sensitive to the ground motion selection. Since the real recorded ground motion for Northeast India (Zone V) is insufficient in number, additional sources of data need to be explored. In addition to the few available earthquakes records of this region, recorded acceleration time histories from other parts of the world having similar fault mechanism, site condition and seismic potential as that of Northeast India are selected. The initial selection criteria for ground motion is decided based on the maximum earthquake magnitude potential ( $5.0\text{--}7.5 M_w$ ), distance from the nearest fault (10–30 km), fault mechanism (normal, strike-slip, reverse) and site conditions (shear wave velocity 180–1500 m/s). These criteria are representative of the Northeast India and are selected based on past literature. The next criterion is based on the minimum seismic intensity level they have so that a bridge experiences some level of seismic damage under the effect of selected ground motions. Therefore, ground motions having  $\text{PGA} < 0.05 \text{ g}$  and  $\text{PGV} < 15 \text{ cm/s}$  are filtered out. The last criterion is applied on a number of records per event which is limited to four to avoid event-based bias. A total of 48 ground motions are finally selected based on the above-mentioned criteria from the recorded ground motions from different parts of the world available in PEER NGA database [17]. Further 17 records are selected from past earthquakes records of Northeast India applying the criteria that  $\text{PGA} > 0.05 \text{ g}$  and not more than four records are selected from the same event.

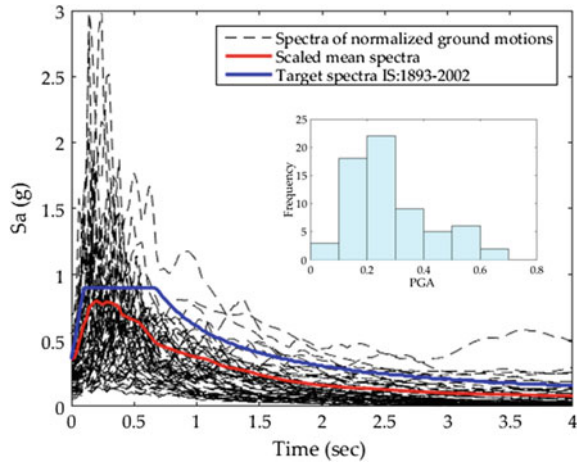
The selected 65 records are normalized based on FEMA guidelines [18]. As per this method, individual records of a given set are normalized by their peak ground velocities (PGV). Normalization by PGV is an easy and simple way to remove unwarranted variability between records due to inherent difference in event magnitude, source type and site condition, distance to source while still maintaining the inherent record-to-record variability necessary for accurately predicting fragility. After normalization, the average response spectrum of all 65 ground motions was scaled so that its PGA matches with the design spectrum PGA specified in Indian seismic code IS: 1893-2002, as shown in Fig. 4. The PGA distribution of selected ground motion is also shown, and it varies from 0.06 to 0.69 g.

## 4.2 Seismic Fragility Curves

Typical of seismic fragility analysis, the seismic demand is compared with the component capacity for different limit states to develop fragility curves. Several researchers [15, 16] have defined limit state capacities of bridge columns. However, these recommendations cannot be used for Indian code-designed bridge columns



**Fig. 4** Comparison of mean spectra of scaled ground motions with design response spectrum of Indian seismic code IS: 1893-2002 and histogram of selected ground motion suite



due to differences in material properties, construction qualities, loading condition and other parameters. Therefore, as per the recommendation of HAZUS [19] pushover analysis was carried out to define limit state capacities. Using the variability in material strength of concrete and steel, random samples were generated and pushover analysis was carried out to determine various limit states.

Since the non-ductile (Case 2) bridge column fails in shear (brittle failure), only one damage state, i.e. collapse, is defined which corresponds to the displacement/drift in pushover curve when force reaches its design shear strength. For the ductile bridge columns, limit states are defined in terms of curvature ductility as the failure mode is flexure. Four damage states are defined viz. slight, moderate, extensive and collapse. Based on the work of Hwang et al. [15], these damage states are characterized with respect to concrete compression and steel tension limits taken from the literature. All the capacity limit states are fitted to a common probability distribution, and it is observed that lognormal distribution fits the data best. The median ( $S_c$ ) and dispersion ( $\beta_c$ ) of each of the four damage states of the two considered cases are shown in Table 2.

The next step is the estimation of seismic demand. Each of the selected 65 ground motions is randomly paired with the 65 bridge models generated using Latin hypercube sampling by considering uncertainty in material properties. A full

**Table 2** Bridge column limit states

Limit states	Slight		Moderate		Extreme		Collapse	
	$S_c$	$\beta_c$	$S_c$	$\beta_c$	$S_c$	$\beta_c$	$S_c$	$\beta_c$
Case 2	–	–	–	–	–	–	0.1	0.47
Case 4	1	0.25	1.46	0.25	3.85	0.47	8.47	0.47

*Note* Limit states in terms of drift (%) for Case 2 (shear-critical) bridge columns and curvature ductility for Case 4 (flexural-critical) bridge columns

**Table 3** Bridge fragility parameters (in units of PGA)

Limit states	Slight		Moderate		Extreme		Collapse	
	med <sub><i>i</i></sub>	ζ <sub><i>i</i></sub>	med <sub><i>i</i></sub>	ζ <sub><i>i</i></sub>	med <sub><i>i</i></sub>	ζ <sub><i>i</i></sub>	med <sub><i>i</i></sub>	ζ <sub><i>i</i></sub>
Case 2	–	–	–	–	–	–	0.33	0.35
Case 4	0.48	0.35	0.63	0.35	1.25	0.45	2.18	0.45

Note med<sub>*i*</sub> and ζ<sub>*i*</sub> are the median PGA and dispersion of *i*th limit state

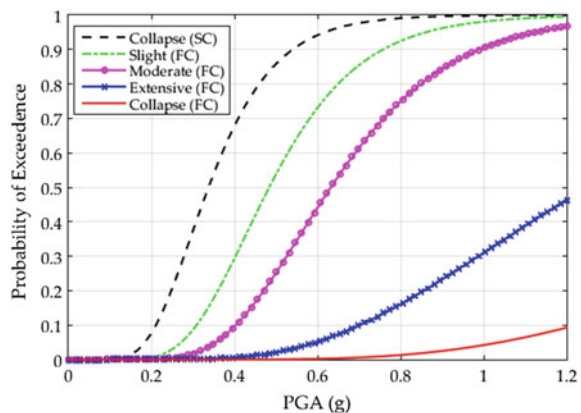
nonlinear time-history analysis is performed for each bridge ground motion pair for both shear-critical (Case 2) and flexural-critical cases (Case 4), and maximum demands on bridge column are recorded. Drift and curvature ductility are considered as demand parameters in non-seismic and seismic cases, respectively. A probabilistic seismic demand model (PSDM) is developed to estimate the median seismic demand using the relation given by [20]. The seismic fragility curves are estimated as a lognormal distribution as shown below.

$$P[D \geq C|IM] = \Phi\left(\frac{\ln(IM) - \ln(\text{med}_i)}{\zeta_i}\right) \tag{3}$$

where med<sub>*i*</sub> is the median of lognormal distribution for fragility and ζ<sub>*i*</sub> is the dispersion of fragility.

Using the results of PSDM and median capacity limit states (Table 2), log-normal parameters of fragility curves (median med and dispersion ζ) are calculated and are shown in Table 3. Seismic fragility curves are plotted for both the cases and are shown in Fig. 5. The median PGA value for collapse damage state in case of shear-critical (Case 2 non-ductile) bridge is 0.33 g which is likely to be exceeded during earthquake occurrences in very high seismic zones. However, significant reduction in the vulnerability is seen in bridge with latest seismic design principle (Case 4). This is primarily due to the ductile detailing of the bridge columns which not only avoids brittle mode of failure (shear) but also enhances its post-yielding deformation characteristics.

**Fig. 5** Seismic fragility curves for Case 2 shear-critical (SC) and Case 4 flexural-critical (FC) bridge design cases



## 5 Conclusions and Future Work

The study presents the impact of evolution of seismic code provisions on seismic vulnerability of highway bridges in India. Firstly, an overview of seismic design practices for highway bridges across four different design eras is presented which tracks the transition from outdated non-ductile to modern ductile detailing practices and adoption of limit state design philosophies. To investigate the impact of seismic code provision on seismic fragility, a representative case-study box girder single-column integral bridge located in high seismic zone is considered. Deterministic analysis on the four considered design cases reveals that the failure mode and load-carrying capacity is governed by the percentage and spacing of transverse reinforcement. Earlier codes which do not advocate ductile detailing, bridge columns fail primarily in shear due to insufficient transverse reinforcement in the potential plastic hinge region. In probabilistic approach also, using fragility curves it is observed that for non-ductile detailed bridge column due to shear failure, the probability of occurrence of collapse damage state is very high even at very low intensity level. The vulnerability of seismic designed bridge is very low even at high level of seismic intensity.

The study on the vulnerability of specific highway bridge reveals the importance of seismic code provisions and highlights the need of vulnerability assessment of class of older highway bridges located in seismically active region of the country. Future studies will develop flexible parameterized fragility models for different types of bridges which can be used for quick and precise assessment of bridge fragility. Additionally, future work will also incorporate effect of ageing and deterioration on the seismic vulnerability of highway bridges.

**Acknowledgements** This research was funded by Grant Number 14IRTAPSG008 from Industrial Research and Consultancy Centre at Indian Institute of Technology Bombay. The support is gratefully acknowledged.

## References

1. Goswami R, Murty CVR (2005) Seismic vulnerability of RC bridge piers designed as per current IRC Codes including Interim IRC : 6-2002 provisions. Indian Concr J
2. IRC: 6-1966 (1996) Standard specifications and code of practice for road bridges, section: II, loads and stresses. The Indian Road Congress, New Delhi
3. IRC: 6-2000 (2000) Standard specifications and code of practice for road bridges, section: II, loads and stresses. The Indian Road Congress, New Delhi
4. IRC: 21-2000 (2000) Standard specifications and code of practice for road bridges, section: III, cement concrete (plain and reinforced). The Indian Road Congress, New Delhi
5. IRC:78-2000 (2000) Standard specifications and code of practice for road bridges, section: VII, foundations and substructure. The Indian Road Congress, New Delhi
6. Interim IRC: 6 (2002) Interim measures of IRC:6-2000 for seismic provisions. The Indian Road Congress, New Delhi

7. IS: 1893-Part 1 (2002) Indian standard criteria for earthquake resistant design of structures: part 1 general provisions and buildings. Bureau of Indian Standards, New Delhi
8. IRC: 6-2014 (2014) Standard specifications and code of practice for road bridges, section: II, loads and stresses. The Indian Road Congress, New Delhi
9. IRC: 112-2011 (2011) Code of practice for concrete road bridges. The Indian Road Congress, New Delhi
10. McKenna F, Fenves G, Scott M (2000) Open system for earthquake engineering simulation. University of California, Berkeley, CA
11. ATC-6-2 (1983) Seismic retrofitting guidelines for highway bridges. Applied Technology Council, Redwood City, California
12. Priestley M, Verma R, Xiao Y (1994) Seismic shear strength of reinforced concrete columns. *J Struct Eng* 120(8):2310–2329
13. Sezen H, Moehle J (2004) Shear strength model for lightly reinforced concrete columns. *J Struct Eng* 130(11):1692–1703
14. Kowalsky MJ, Priestley MN (2000) Improved analytical model for shear strength of circular reinforced concrete columns in seismic regions. *ACI Struct J* 97(3)
15. Hwang H, Liu J, Chiu Y (2001) Seismic fragility analysis of highway bridges. Mid-America Earthquake Center Technical Report CD Release
16. Nielson BG, DesRoches R (2007) Analytical seismic fragility curves for typical bridges in the central and southeastern United States. *Earthq Spectra* 23(3):615–633
17. PEER NGA. Strong motion database. <http://ngawest2.berkeley.edu/>
18. FEMA P695 (2009) Quantification of building seismic performance factors. Applied Technology Council, Redwood City, California
19. FEMA. HAZUS-MH MR 1 (2003) Technical manual. Federal Emergency Management Agency, Washington (D. C.)
20. Cornell C, Jalayer F (2002) Probabilistic basis for 2000 SAC federal emergency management agency steel moment frame guidelines. *J Struct Eng* 128(4):526–533

# Effect of Fire on Reinforced Concrete Slab—Numerical Simulation



M. K. Haridharan and C. Natarajan

**Abstract** Buildings are often exposed to elevated temperature due to lack of fire safety, sabotages, etc. A recent survey about India's risk says that fire has been rated among top three risks by most of sectors across India. The study investigates the influence of cooling condition on concrete slab exposed to fire. The variables considered for the study are thickness of slab 125 mm, retention period of one-hour and four-hour, subjected to temperature of 300, 400 and 500 °C, and two types of cooling regimes like air cooling and quench cooling. The slab which was exposed to temperature of 500 °C for four-hour duration had temperature of 143 °C at the unexposed surface which is marginally less than the allowable limit, but other slabs reveal good resistance to insulation. The reduction in flexural stiffness of concrete slab exposed to 500 °C for four-hour retention period was 28.67 and 37.89% for air cooled and quench-cooled specimens, respectively. The irrecoverable loss in flexural stiffness of concrete slab was influenced by the retention period, exposed temperature and cooling regimes.

**Keywords** Concrete slab · Fire severity · Flames · Heat transmission Serviceability

---

M. K. Haridharan

Department of Civil Engineering, Amrita School of Engineering,  
Amrita Vishwa Vidyapeetham, Coimbatore, Tamil Nadu, India  
e-mail: harai411@gmail.com

C. Natarajan (✉)

Department of Civil Engineering, National Institute of Technology,  
Trichy, Tamil Nadu, India  
e-mail: nataraj@nitt.edu

© Springer Nature Singapore Pte Ltd. 2019

A. Rama Mohan Rao and K. Ramanjaneyulu (eds.), *Recent Advances in Structural Engineering, Volume 2*, Lecture Notes in Civil Engineering 12,  
[https://doi.org/10.1007/978-981-13-0365-4\\_42](https://doi.org/10.1007/978-981-13-0365-4_42)

## 1 Introduction

The development of a nation depends on its infrastructure facilities. India witnessed remarkable development in the infrastructure sector during 2002–2017 with Government investing US \$1.9 trillion [1]. The major fundamental concern during the design of structures is to ensure adequate safety of its occupant under normal as also under accident loads (fire, blast, impact, etc.). Fire risk is ranked as the second after natural hazards in the infrastructure sector in India [2]. During 2014, the total number of people deceased due to fire accident was 19,513 out of 20,377 victims, of which 20% of fire accidents had been taken place in residential/dwelling buildings [3]. Statistical survey indicated an upward trend in the number of incidence of fire almost in all countries of the world and tends to have more incidences in highly populated countries. The efforts made for reduction of the occurrence of fire accidents in residential/dwelling units by the Government agencies and Building Fire Research Centre (BFRC) in the country have been a challenging due to the sudden vertical growth of the country and the proliferation of high-rise buildings due to increasing population.

Several researchers studied the strength variation of concrete cube under various parameters including stressed and unstressed conditions, replacing aggregate and testing the sample during hot and cold condition. These studies constituted the scientific base for developing design curves adopted in design codes [4–11].

An extensive study had been carried out experimentally and numerically by researchers over the last decades on restrained reinforced concrete (RC) slabs [12], involving investigation of the additional load-carrying capacity of the slabs subjected to fire [13–15].

The current design codes and most of the research articles consider the effect of heat up phase only on structural elements but the effect of cool-down phase was not considered. Literature review reveals a paucity of experimental data on the effect of different cooling regimes, the influence on effect of crack formed during heating stage and residual strength of concrete slab exposed to elevated temperature. Concrete specimens cooled with water for a short period showed a drastic variation in residual strength, when the temperature exposed was more than 200 °C [16–18]. Some researchers concluded that if early-aged concrete was fire-damaged, it could regain its strength when placed in proper moist environment [9, 19, 20].

## 2 Finite Element Method and Material

Analytical investigation has been carried out to study the behaviour of reinforced concrete slabs using finite element analysis software ABAQUS 6.11. [21]. An effective mathematical model is one that yields the required solution with satisfactory accuracy and with least cost in terms of computer run-time. The accuracy of modelling depends upon the mathematical model, material properties and appropriate mesh size.

## **2.1 Geometrical Modelling**

In the reinforced concrete slab, concrete has been modelled for the actual dimensions using 3D solid element, and the reinforcement was modelled as the truss element. The usage of 3D beam and 3D shell element was not possible due to constraints and limitations to capture real behaviour. In the 3D beam element, it was unable to perform heat transfer analysis along the cross section. In 3D shell element, the reinforcement was introduced by using a rebar command. Transfer of the temperature degrees of freedom to this rebar layer did not occur in this case.

## **2.2 Material Properties**

Numerical tools are heavily dependent on the material definitions provided as input; hence, to assess the adequacy of numerical methods and to capture the behaviour of reinforced concrete at elevated temperature, a thorough investigation of the material models at ambient and elevated temperatures is required. The temperature-dependent thermal properties of steel such as density, conductivity, specific heat and thermal expansion of steel were considered from the equations, and values provided in the Eurocode 3 [22] are shown in Table 1. Similarly the temperature-dependent thermal properties of concrete were considered from the equations, and values provided Eurocode 2 [23] are also shown in Table 1.

In numerical modelling, the residual mechanical properties of reinforcement were considered from Eurocode 3 [22]. In the case of mechanical properties of concrete, the variation in compressive strength was considered from the previous study [18] for other missing data values specified in Eurocode [22, 23] were considered.

## **2.3 Element Type**

The sequentially coupled analysis method was used for the present study. It is a multiphysics analysis where heat transfer analysis was carried out separately and the temperature from the heat transfer analysis was predefined into the mechanical analysis as a scalar nodal value. An eight node linear heat transfer brick element, DC3D8 for concrete and two node heat transfer link element, DC1D2 for reinforcement were considered for thermal analysis. In the case of stress analysis, an eight node tri linear displacement and temperature, reduced integration 3D solid element, C3D8RT and a two node linear displacement and linear temperature 3D truss elements, T3D2T was considered for concrete and reinforcement respectively.

**Table 1** Thermal properties of steel and concrete

Sl. No.	Temperature (°C)	Thermal properties of steel			Thermal properties of concrete				
		Density ( $\rho_s$ ) (kg/m <sup>3</sup> )	Thermal expansion ( $10^{-3}$ )	Specific heat ( $C_{ps}$ ) (KJ/kg/K)	Conductivity ( $\lambda_s$ ) (W/m/K)	Density ( $\rho_c$ ) (kg/m <sup>3</sup> )	Thermal expansion ( $10^{-5}$ )	Specific heat ( $C_{pc}$ ) (KJ/kg/K)	Conductivity ( $\lambda_c$ ) (W/m/K)
1.	20	7850	0.00	0.440	53.4	2450	0.09	0.90	1.95
2.	100		1.00	0.488	50.7	2450	0.74	0.90	1.77
3.	200		2.32	0.530	47.4	2401	1.80	1.00	1.55
4.	300		3.72	0.564	44.1	2364	3.14	1.05	1.36
5.	400		5.20	0.605	40.7	2328	4.89	1.10	1.19
6.	500		6.76	0.664	37.4	2306	7.20	1.10	1.04
7.	600		8.40	0.760	34.1	2285	10.19	1.10	0.91
8.	700		10.12	1.008	30.7	2263	14.00	1.10	0.81
9.	800		11	0.796	27.3	2242	14.00	1.10	0.72
10.	900		11.8	0.643	27.3	2220	14.00	1.10	0.66
11.	1000		13.8	0.650	27.3	2199	14.00	1.10	0.62
12.	1100		15.8	0.650	27.3	2177	14.00	1.10	0.60
13.	1200		17.8	0.650	27.3	2156	14.00	1.10	0.60



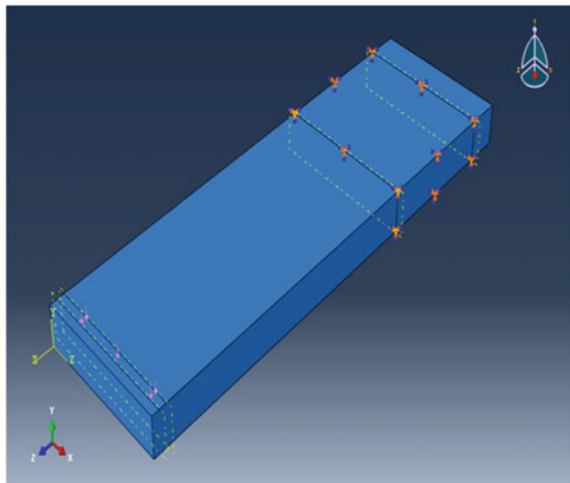
## 2.4 Contact Pair and Interaction Between Concrete and Steel

Interaction: Thermal analysis—Tie constraint was used for contact between steel and concrete. Mechanical analysis—Embedded constraint was used to establish the contact between steel and concrete.

## 2.5 Boundary Conditions and Load Application

Thermal analysis was performed by taking into account of radiation at the exposed and unexposed surface of the slab, convection through air was considered on all the unexposed surfaces, conduction was considered within the concrete element and measured temperature was provided as an input. Temperature at unexposed surface was calculated at any time by considering heat transfer through radiation, convection with air and conduction. The interactions with the environmental temperatures are considered on the unheated (top) surface. The unheated surface interactions for radiation are emissivity of the concrete surface = 0.9 and Stefan–Boltzmann radiation constant =  $5.669 \times 10^{-9} \text{ W/m}^2 \text{ K}^4$ . The convective heat coefficient is defined by the value  $25 \text{ W/m}^2 \text{ K}$ . Reinforced concrete slab with one end free and other end fixed against all rotational and translational degrees of freedom was considered for the mechanical analysis as shown in Fig. 1. The incremental load applied in the form of pressure load on the concrete surface for a small strip is shown in Fig. 1.

**Fig. 1** Boundary condition—mechanical loading



### 2.6 Mesh Convergence Study

Meshing is an important part of finite element analysis. The use of solid elements for modelling structural bending is not as accurate as beam elements. In the process of analysis, special attention should be given to locating the most appropriate and efficient element density for accurate prediction. Finding the most appropriate and efficient mesh size depends largely on computational resources, and as the mesh gets finer more computational resources are needed for the analysis. So the capability of the computer is a main factor to determine mesh density. Finding the most appropriate and efficient mesh size depends largely on computational resources, and as the mesh gets finer, more computational resources are needed for the analysis. So the capability of the computer is a main factor to determine mesh density. A mesh convergence study is done on the reinforced concrete beam. A simply supported beam of span 4.00 m with cross section of 230 mm wide and 300 mm depth was modelled. The beam was subjected to a uniformly distributed load. The beam was then meshed with different mesh densities, and the midspan deflection of experimental and analytical was compared with the variation in results for various mesh sizes as shown in Fig. 2. The mesh size of 25 mm was adopted throughout the modelling.

### 2.7 Validation of Finite Element (FE) Model

The FEA methodology adopted for the present investigation was validated to ensure accuracy of the results obtained from the analysis. The experimental results of Ref.

**Fig. 2** Percentage variation versus number of layers along depth

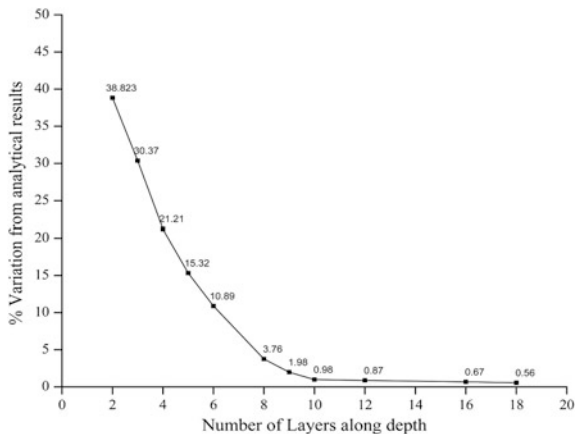


**Table 2** Details of the test specimen used for the validation of FE model

Slab length	4.7 m
Span centre to centre	4.5 m
Exposed length	4.0 m
Cube strength (NWC)	30 N/mm <sup>2</sup>
Live load	1.5 kN/m <sup>2</sup>
Width	0.925 m
Thickness	0.150 m
Rebar	8 mm diameter
No. of bars	10
Yield strength for steel	460 N/mm <sup>2</sup>
Temperature	ISO-834 fire
Support condition	Simply supported on two sides & free on the other two sides

**Table 3** Comparison of FEA results with experimental data [13]

Time (min)	Live load (kN/m <sup>2</sup> )	Midspan deflection (mm)		
		BRE slab	FEM	Error %
30	–	81.92	78.01	4.77
30	1.5	83.73	80.10	4.44
60	–	131.56	130.15	1.08
60	1.5	136.74	138.34	-1.17
90	–	168.86	169.24	-0.22
90	1.5	184.16	185.11	-0.51

[13] were used for validation of mechanical. Numerical modelling was undertaken based on the properties detailed in Table 2, and the midspan deflections are compared and presented in Table 3. All the temperature-dependent materials properties were considered from the Eurocode [22, 23] and for steel and concrete, respectively.

## 2.8 Limitation of the Modelling

The limitation of this study is as follows:

- (a) Spalling effects of concrete are not modelled.
- (b) The slip between the materials concrete and reinforcing steel is not taken into account.

### 3 Results and Discussion

The finite element analysis software ABAQUS was used efficiently to study the influence of temperature, cooling condition and duration of exposure. The modelling considered the influence of material nonlinearity and geometric nonlinearity which were validated by the experimental study. The influence of cooling condition was considered by using appropriate strength reduction factor for concrete and reinforcement.

The detailed identification of slabs exposed to various temperatures and durations is shown in Table 4. After exposure to the desired temperature and duration, the specimens were subjected to cooling regimes.

#### 3.1 Temperature Distribution at Top and Bottom Surfaces of the Slab

In the case of slab element is considered, bottom surface of the specimen was exposed to the fire while the other surfaces were open to atmospheric condition. The variations in the average temperature at top and bottom surfaces of slabs were obtained through the thermal analysis of slabs. The temperature variation within top surface of the slab was very scanty.

Eurocode [23] put forward two sets of failure criterion based on insulation. A slab is said to fail when the following conditions occur: (a) the average temperature rise over the whole of the non-exposed surface is limited to 140 °C. (b) The maximum temperature rise at any point of that surface does not exceed 180 °C. Figure 3 provides information about an insulation check for slabs. The S3-4h slab exceeds the specified limit for insulation, while other specimens show an acceptable performance over insulation criteria.

#### 3.2 Vertical Deflection of Concrete Slab During Heating

The slab started deflecting vertically away once the temperature was applied from the bottom. The magnitude of the vertical deflection depends on exposed temperature

**Table 4** Description and detail of concrete slab

Sl.No	Identification marking	Description
1	S1-D/Q-1 h/4 h	S1—slab of thickness 125 mm subjected to 300 °C
2	S2-D/Q-1 h/4 h	S2—slab of thickness 125 mm subjected to 400 °C
3	S3-D/Q-1 h/4 h	S3—slab of thickness 125 mm subjected to 500 °C

*D* air cooled, *Q* quench cooled, (1 h—one hour, 4 h—four hour)—duration of exposure

**Fig. 3** Insulation check for concrete slab

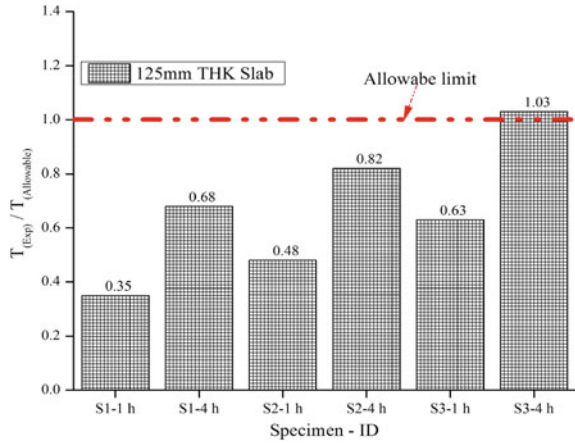
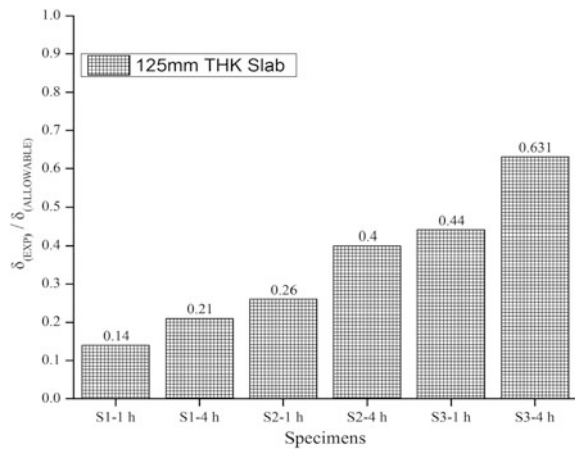


**Fig. 4** Ratio of ultimate deflection during heating phase to BS 476-20:1987 code



and the duration of exposure. The vertical deflection of the 125-mm-thick concrete slab subjected to 300 °C reached 8.01 mm at 155 min. The variation of vertical deflection with times was found to be inconsequential. The failure criteria of flexural members based on deflection was considered in accordance with BS 476–20:1987 [24]. The ratio of ultimate deflection recorded during heating to the allowable deflection criteria as stated above was compared as shown in Fig. 4. The slabs’ ultimate deflections were within the specified limit of British standard limits.

### 3.3 Mechanical Loading—Residual Strength

The residual load versus deflection of 125-mm-thick concrete specimens which was subjected to elevated temperature and subsequently subjected to air cooling and quench cooling is shown in Figs. 5 and 6, respectively. The normalized load versus deflection graph clearly depicts the behaviour changes for 4-h exposure at various temperature and cooling conditions. All the tested slabs achieved the working load and ultimate load equal to the control specimen, but there were variations in the deflection of the slab at a specific load. The reductions in residual flexural stiffness of concrete slab for various heating and cooling conditions were shown in

**Fig. 5** Normalized load versus displacement of 125-mm-thick concrete slab—air cooled

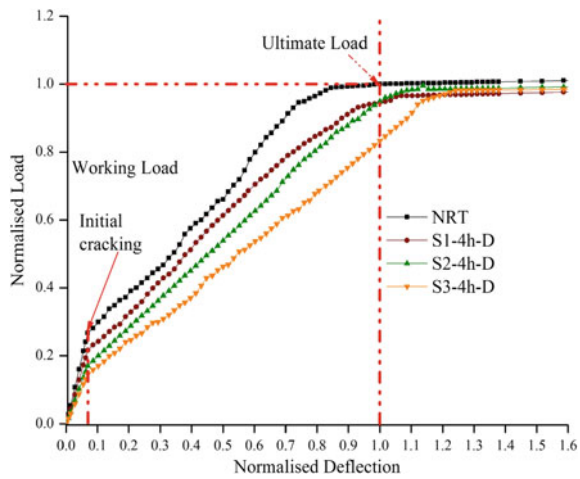


**Fig. 6** Normalized load versus displacement of 125-mm-thick concrete slab—quench cooled

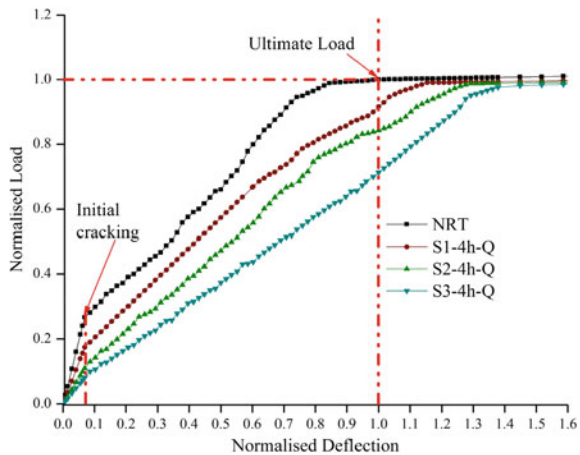


**Fig. 7** Stiffness reduction in concrete slab for subjected to —air cooled

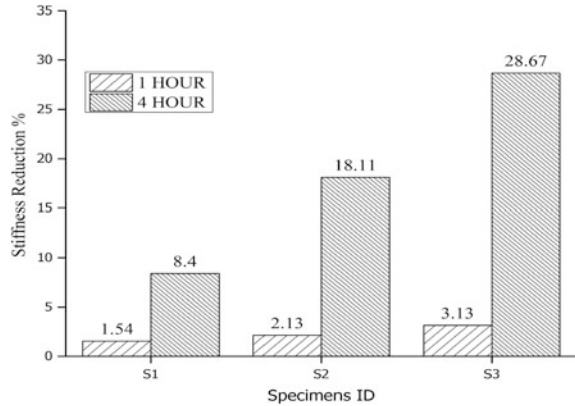
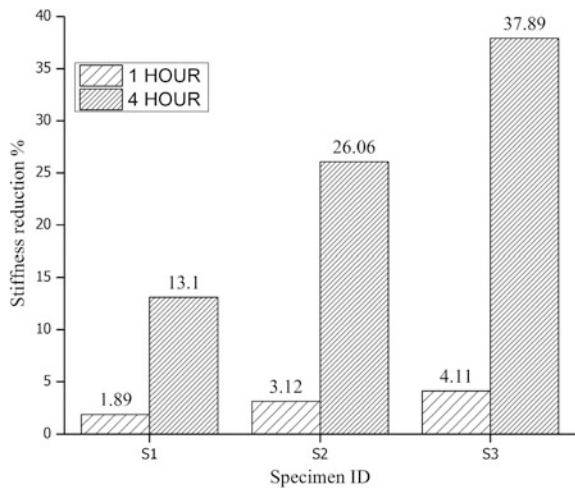


**Fig. 8** Stiffness reduction in concrete slab subjected to —quench cooled



Figs. 7 and 8. The percentage reduction in flexural stiffness was 1.54, 2.13 and 3.13 for S1–S3, respectively, for 1 h of exposure under air cooled condition.

In the case of 4 h of exposure under air cooled condition, the reduction in flexural stiffness was 8.4, 18.11 and 28.67% for S1–S3 slabs, respectively. The reductions in residual flexural stiffness of quench-cooled concrete slabs were 1.89, 3.12, 4.11 for S1–S3 slab, respectively, under quench-cooled condition. Similarly, for 4 h of exposure, the loss in stiffness was 13.10, 26.06 and 37.89% for S1–S3, respectively. The present study shows the cooling regimes having an influence on the residual flexural stiffness. Quench cooling on slabs has adverse effect on the flexural stiffness of the member due to the thermal shock which lead to the development of cracks at unexposed surface during quenching [18, 19].

## 4 Conclusions

The study reveals the reduction in flexural stiffness of concrete slab exposed to various temperature, retention periods and also the influence of cooling regimes.

- An insulation criterion is most important for the slab element as it has to perform as a vertical separation element too. S3-4h-(D&Q) specimen fails in these criteria but other slabs reveal good resistance to insulation.
- The deflection ratio was found to increase from 0.14 to 0.44 for 1 h of exposure under 300–500 °C of temperature. In the case of a 4 h of exposure, the deflection ratio varied from 0.21 to 0.63. The ratio was minimum for 200 °C and maximum for 500 °C.
- In the case of one-hour retention period for temperatures 300–500 °C, loss in stiffness was less than 5% for both the types of cooling conditions.
- The reduction in stiffness percentage for four-hour retention period was 8.4–28.67% for air cooled person. Similarly in the case of quench-cooled specimen, reduction in flexural stiffness percentage was 13.10–37.89% for S1–S3 slab.
- The impact of different cooling methods was observed by the variations found in residual flexural stiffness. The reduction in flexural stiffness depends on the exposed temperature and cooling regimes.

## References

1. Planning Commission link (2002–2016) Link <http://planningcommission.nic.in/plans/planrel/fiveyr/welcome.html>
2. Federation of Indian Chambers of Commerce and Industry (FICCI) (2012) Link <http://www.ficci.com/Sedocument/20186/IndiaRiskSurvey2012.pdf>
3. Accidental Death and Suicides in India (ADSI) (2014) National Crime Records Bureau, Ministry of Home Affairs India. <http://ncrb.nic.in/StatPublications/ADSI/ADSI2014/adsi-2014%20full%20report.pdf>
4. Lea FC (1922) The resistance to fire of concrete and reinforced concrete. *J Soc Chem Ind* 41:395R–396R
5. Malhotra HL (1956) The effect of temperature on the compressive strength of concrete. *Mag Concr Res* 8:85–94
6. Zoldners NG (1960) Effect of high temperatures on concretes incorporating different aggregates (No. NP-9226). Department of Mines and Technical Surveys. Mines Branch, Canada
7. Abrams MS (1971) Compressive strength of concrete at temperatures to 1600F. *Spec Publ* 25:33–58
8. Lankard DR, Birkimer DL, Fondriest FF, Snyder MJ (1972) Effects of moisture content on the structural properties of portland cement concrete exposed to temperatures up to 500F. *Spec Publ* 25:59–102
9. Harada T, Takeda J, Yamane S, Furumura F (1972) Strength, elasticity and thermal properties of concrete subjected to elevated temperatures. *Spec Publ* 34:377–406
10. Mohamedbhai GTG (1986) Effect of exposure time and rates of heating and cooling on residual strength of heated concrete. *Mag Concr Res* 38:151–158



11. Reinhardt HW, Cornelissen HA, Hordijk DA (1972) Tensile tests and failure analysis of concrete. *J Struct Eng* 112:2462–2477
12. Bailey CG, White DS, Moore DB (2000) The tensile membrane action of unrestrained composite slabs simulated under fire conditions. *Eng Struct* 22:1583–1595
13. Cooke GM (2001) Behaviour of precast concrete floor slabs exposed to standardised fires. *Fire Saf J* 36:459–475
14. Bailey C (2002) Holistic behaviour of concrete buildings in fire. *Proc Inst Civil Eng Struct Build* 152:199–212
15. Elghazouli AY, Izzuddin BA (2004) Failure of lightly reinforced concrete members under fire. II: parametric studies and design consideration. *J Struct Eng* 130:18–31
16. Peng GF, Bian SH, Guo ZQ, Zhao J, Peng XL, Jiang YC (2008) Effect of thermal shock due to rapid cooling on residual mechanical properties of fiber concrete exposed to high temperatures. *Constr Build Mater* 22:948–955
17. Bingol AF, Gul R (2009) Effect of elevated temperatures and cooling regimes on normal strength concrete. *Fire Mater* 33:79–88
18. Haridharan MK, Natarajan C, Chen SE (2016) Evaluation of residual strength and durability aspect of concrete cube exposed to elevated temperature. *Int J J Sustain Cem Based Mater* 1–23. <https://doi.org/10.1080/21650373.2016.1230898>
19. Poon CS, Azhar S, Anson M, Wong YL (2001) Comparison of the strength and durability performance of normal-and high-strength pozzolanic concretes at elevated temperatures. *Cem Concr Res* 31:1291–1300
20. Poon CS, Azhar S, Anson M, Wong YL (2001) Strength and durability recovery of fire-damaged concrete after post-fire-curing. *Cem Concr Res* 31:1307–1318
21. Abaqus 6.11(2011) Abaqus analysis user's manual. Providence, Dassault Systems Simulia Corporation
22. EN 1993-1-2 (2005) Eurocode 3 Design of steel structures-part 1–2: general rules—structural fire design. European Committee for Standardization, Brussels
23. EN 1992-1-2 (2004) Eurocode 2 Design of concrete structures-part 1–2: general rules—structural fire design. European Committee for Standardization, Brussels
24. BS 476–20 (1987) British standards institution method for determination of the fire resistance of elements of construction: part 20. BSI; London

# Change in Microstructure Properties of Concrete on Accelerated Carbonation



Vineet Shah, Geetika Mishra, Anuj Parashar and Shashank Bishnoi

**Abstract** Carbonation of concrete is a complex physicochemical process. The overall volume of the system changes due to carbonation of different hydration products. During carbonation,  $t$  products formed on conversion of calcium hydroxide have a higher volume as compared to the initial products, thus the surplus volume fills up the empty space in the capillary system, resulting in a reduced porosity. Supplementary cementitious materials (SCMs) consume calcium hydroxide by pozzolanic reaction, which is the majorly responsible for high alkalinity. Volume change due to CSH transformation is most uncertain, and the type of polymorph formed depends on the calcium-to-silica ratio and water content of the silica gel. Therefore, the change in the microstructure of concrete due to carbonation depends upon the type of cement. In this study, the effect of accelerated carbonation on the microstructure of concrete, made from different cements, was analysed. Change in properties of concrete such as porosity, sorptivity and permeability with carbonation was studied. Accelerated carbonation was carried out at 1 and 3% CO<sub>2</sub> concentration. From the results, it can be inferred that irrespective of the type of cement used, the porosity of the system increases on carbonation. Similarly, results were also obtained for sorptivity and air permeability.

**Keywords** Carbonation · Supplementary cementitious materials (SCMs)  
Porosity · Pore structure

---

V. Shah · G. Mishra (✉) · A. Parashar · S. Bishnoi  
Department of Civil Engineering, Indian Institute of Technology Delhi,  
Delhi 110016, India  
e-mail: geetika.mishra30@gmail.com

V. Shah  
e-mail: vineet.shah9@gmail.com

A. Parashar  
e-mail: anujparashar29@gmail.com

S. Bishnoi  
e-mail: shashank.bishnoi@gmail.com

## 1 Introduction

The hydration reaction of Portland cement produces calcium hydroxide (CH) and calcium silicate hydrate (CSH) as the main hydration phases. The hydration products of cement form a highly alkaline pore solution in concrete. In the alkaline environment, the stable compounds of iron form a thin protective oxide film around reinforced steel embedded in concrete. This layer does not stop the corrosion reaction but reduces the rate of corrosion to an insignificant level [1]. On replacing clinker with supplementary cementitious materials (SCMs), calcium hydroxide produced from clinker hydration is consumed and more CSH is produced, resulting in reduced alkalinity of the system. The reduced alkaline content results in disintegration of protective oxide layer on reinforcement, thus making it susceptible for corrosion because of carbonation. Carbonation is a complex physicochemical process. The carbon dioxide diffuses from the atmosphere into capillary pores of the concrete. Carbon dioxide dissolves in pore water forming carbonic acid which reacts with the dissolved ions of hydration products available in pore solution [2].

The overall volume of the system changes due to carbonation of different hydration products. The change in porosity of the system because of carbonation depends upon the type of phase being carbonated [2, 3]. As a general notion, carbonation is known to reduce the porosity of system by conversion of calcium hydroxide into different polymorphs of calcium carbonate. Carbonation of ettringite leads to increase in pore volume, whereas change in volume because of carbonation of CSH depends upon the Ca/Si ratio [2]. Numerous studies have reported reduction in porosity of Portland cement on carbonation and increase in porosity of blended cement [4–6]. Inconsistency exists in the understanding of changes in microstructure because of carbonation.

This study aims at examining change in microstructure properties of concrete made using different types of cement on carbonation. Ordinary Portland cement (OPC), Portland pozzolana cement (PPC), limestone-calcined clay cement (LC<sup>3</sup>) and composite cement (CC) were used in the study. Porosity, sorptivity and air permeability of the concrete samples were measured before and after carbonation.

## 2 Experimental Procedure

### 2.1 Materials

OPC was produced in laboratory by grinding clinker in a laboratory-scale ball mill. PPC was produced by interblending 70% OPC and 30% fly ash in a ball mill. LC<sup>3</sup> was produced having composition of 50% clinker, 31% calcined clay, 15% limestone and 4% gypsum. All the above materials were ground individually and thereafter intermixed in a ball mill to produce the blend. Similarly, CC was

**Table 1** Chemical analysis of raw materials

	Clinker	Limestone	Gypsum	Clay	Fly ash	Slag
Silica SiO <sub>2</sub>	21.07	11.02	2.77	51.60	58.82	32.26
Iron Fe <sub>2</sub> O <sub>3</sub>	4.32	1.55	0.36	1.15	6.19	1.93
Aluminium	4.65	2.53	0.62	36.13	30.62	23.16
Calcium	65.16	44.24	32.62	0.54	1.01	33.88
Magnesium	2.13	1.96	1.20	0.77	0.41	7.01
Sulphate	0.77	–	38.75	–	0.12	–
Sodium	0.38	0.50	0.06	0.10	0.19	0.010
Potassium	0.20	0.28	0.037	0.04	1.30	0.37
LOI	0.96	36.96	23.02	8.24	1.11	1.08

produced by interblending 50% clinker, 31% slag, 15% fly ash and 4% gypsum. The chemical properties of the raw materials measured using X-ray fluorescence spectroscopy (XRF) is shown in Table 1.

## 2.2 Casting and Exposure Conditions

Concrete was cast using all the four types of cement at two different water-to-cement ratios of 0.45 and 0.35. Cylinder specimens having radius of 5 cm and height of 10 cm were cast. After casting, the concrete samples were cured underwater for 120 days. Prolonged curing period was selected to ensure complete hydration of cement.

After the curing regime, the cylinders were cut in a disc having height of 5 cm. Epoxy was applied on the circumference of the cylinders, leaving only two sides exposed top and the bottom. Thereafter, the specimens were kept in a conditioning room having temperature of 27 °C and relative humidity of 60% for 15 days. After the end of conditioning period, specimens with 0.45 water-to-cement ratio were kept in accelerated carbonation chamber having carbon dioxide concentration of 1%, at 27 °C and relative humidity 60%. Whilst specimens with 0.35 water-to-cement ratio were kept in carbonation chamber having carbon dioxide concentration of 3%, rest all the parameters were same as the other carbonation chamber.

## 2.3 Methodology

The porosity was measured according to the guidelines described in ASTM C642, whereas sorptivity was measured according to the guidelines mentioned in ASTM C1585. The air permeability of the concrete samples was measured according to specifications provided in Durability Index Testing Procedure Manual, South Africa.

### 3 Results

#### 3.1 Porosity

The porosity was measured according to the guidelines described in ASTM C642. The initial porosity of concrete, i.e. non-carbonated sample, was measured after the end of conditioning period. The porosity of carbonated sample was measured at the end of 4 months of exposure to accelerated carbon dioxide condition. The results of porosity are shown in Figs. 1 and 2.

#### 3.2 Sorptivity

Water absorption by concrete due to capillary suction was measured according to guidelines provided in ASTM C1585. Only the primary sorption was measured for the concrete samples. The sorption index was measured for non-carbonated and carbonated samples. The results of the water absorption are shown in Figs. 3 and 4.

**Fig. 1** Porosity of non-carbonated and carbonated concrete samples having w/c of 0.45 at 1% carbon dioxide concentration

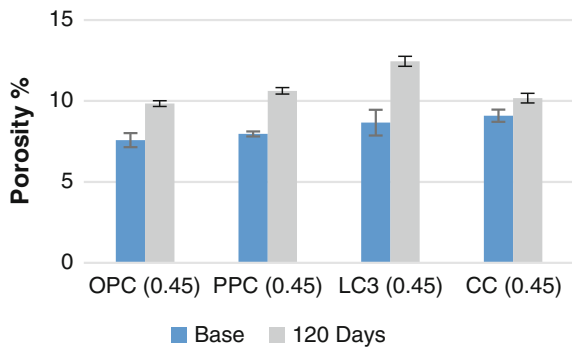


**Fig. 2** Porosity of non-carbonated and carbonated concrete samples having w/c of 0.35 at 3% carbon dioxide concentration

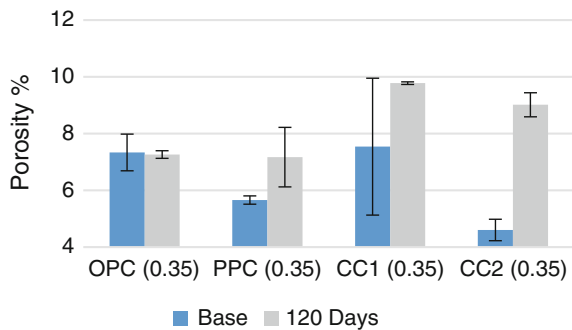


**Fig. 3** Sorptivity of non-carbonated and carbonated concrete samples having w/c of 0.45 kept at 1% carbon dioxide concentration

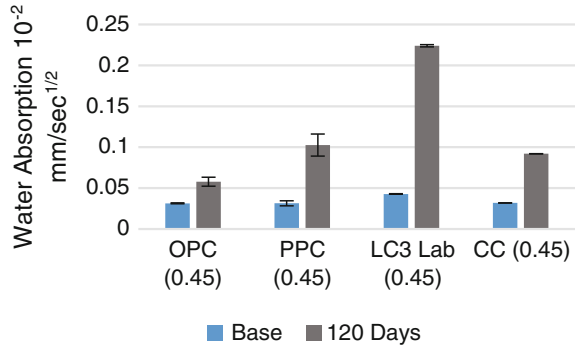


**Fig. 4** Sorptivity of non-carbonated and carbonated concrete samples having w/c of 0.35 kept at 3% carbon dioxide concentration

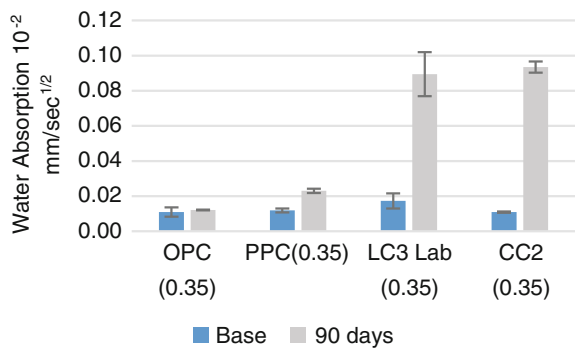
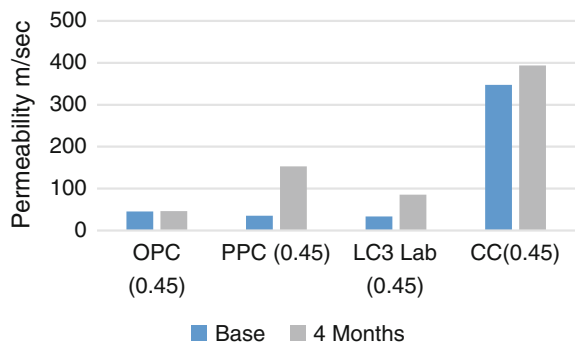


**Fig. 5** Air permeability of non-carbonated and carbonated concrete exposed in 1% carbon dioxide concentration

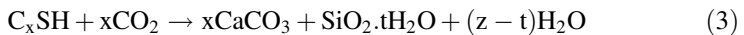
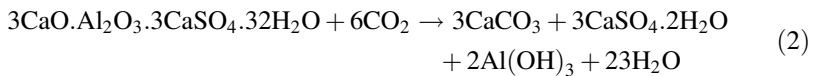
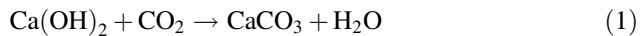


### 3.3 Air Permeability

The air permeability of carbonated and non-carbonated sample was measured according to the procedure described in Durability Index Manual. The results of air permeability are shown in Fig. 5.

## 4 Discussion

Carbonation depends upon numerous parameters such as temperature, relative humidity, carbon dioxide concentration and type of cement. Carbon dioxide concentration and type of cement were varied in this study, keeping all the other factors same. The extent of carbonation in a system along with compressive strength of the concrete depends upon the pore structure characteristics of concrete. From the results, it can be inferred that with carbonation the porosity of the system increases. Irrespective of type of cement and carbon dioxide concentration, there is increase in pore volume of the system. Porosity value of OPC at 0.35 water-to-cement ratio did not change on carbonation. Similarly, results were also obtained from sorptivity and air permeability of the carbonated samples. Sorptivity results of 90 days' carbonated samples are reported instead of 120 days for 3% carbon dioxide exposure condition. Increased air permeability indicates that there is no clogging effect because of deposition of carbonation products in pores, which might result in reduced permeability. Typical carbonation reactions taking place in a cement system are given below:



Carbonation of CH results in increase in volume of the system due to formation of calcium carbonate. The volume of the solid products increases by 11–14% depending upon type of polymorph formed. Ettringite on carbonation reaction produces calcium carbonate, calcium sulphate and alumina gel. The total solid volume of the products formed is less as compared to the solid volume of ettringite. CSH on carbonation forms calcium carbonate and silica gel. The solid volume of the products formed depends upon the initial calcium-to-silica ratio and silica gel formed. The removal of calcium ions from CSH leads to formation of Si–OH groups. These silica chains condense with each other resulting in polymerization [7, 8]. The volume of the silica gel produced depends upon the extent of polymerization. Cement containing CH in the system will lead to reduction of total porosity of system on carbonation. But, as soon as the calcium hydroxide is consumed, the calcium silicate hydrate and other phases present in the hydrated cement start carbonating and result in increase of volume on carbonation. The results obtained are in line with the explanation given above. The volume reduction caused by carbonation of CH is much less as compared to volume increase caused by other hydration products because difference in quantity present initially. Higher carbon dioxide concentration leads to consumption of all the phases present in the hydrated system simultaneously and thus increased porosity is observed even in OPC system

where CH content is high. Also, the carbonation products are deposited on the surface of CH crystals thus with time the amount of CH present in the pore solution decreases.

## 5 Conclusion

Carbonation study was carried out on different types of cement, at different carbon dioxide concentration and water-to-cement ratio, to understand the effect of carbonation on pore structure characteristics of concrete.

- The change in microstructure of concrete because of carbonation is related to all the phases present in the system and not limited to a particular phase.
- Carbonation results in increased porosity of system, irrespective of type of cement used.
- The water absorption of the concrete is increased because of carbonation. Carbonation results in polymerization of silica gel, which results in coarsening of pores. Thus, resulting in increased suction of water by capillary pores.
- The air permeability of the carbonated sample is more as compared to non-carbonated samples; this is due to increased pore volume of the system.

## References

1. Richardson MG (2002) Fundamentals of durable reinforced concrete. Spon Press
2. Lagerblad B (2005) Carbon dioxide uptake during concrete life cycle—state of the art report. *Cem Concr Res CBI* 2005:2
3. Sanjuan MA, Andrade C, Cheyrezy M (2003) Concrete carbonation tests in natural and accelerated conditions. *Adv Cem Res* 15(4):171–180
4. Chindapasirt P, Rukzon S (2010) Pore structure changes of blended cement pastes constraining fly ash, rice husk ash, and palm oil fuel ash caused by carbonation. *J Mater Civil Eng* 21(11):1723–1733
5. Ngala V, Page C (1997) Effects of carbonation on pore structure and diffusional properties of hydrated cement pastes. *Cem Concr Res* 27(7):995–1007
6. Pihlajavaara S (1968) Some results of the effect of carbonation on the porosity and pore size distribution of cement paste. *Mater Constr* 1(6):521–527
7. Borges PHR, Costa JO, Milestone NB, Lynsdale CJ, Streatfield RE (2010) Carbonation of CH and C-S-H in composite cement pastes containing high amounts of BFS. *Cem Concr Res* 40:284–292
8. Chen JJ, Thomas JJ, Jennings HM (2006) Decalcification shrinkage of cement paste. *Cem Concr Res* 36:801–809
9. Brebbia CA, Telles JCF, Wrobel LC (1984) Boundary element techniques. Springer, Berlin, New York



# An Assessment of the Deterioration of Flexural Capacity of a Pretensioned Concrete Girder Due to Strand Corrosion



G. Resmi, Amlan K. Sengupta and Radhakrishna G. Pillai

**Abstract** This paper illustrates the effect of chloride-induced corrosion in the flexural capacity of a pretensioned concrete girder in an existing girder-and-slab deck bridge. The numerical study of the time-wise variation of the flexural capacity is based on a proposed model for the loss of cross-sectional area of the prestressing strands. It was observed that almost 46% of the total area of strands can get affected due to chloride-induced corrosion of the girder, by the end of its service life. The corresponding flexural capacity of the girder gets reduced by 50% of its initial capacity.

**Keywords** Chloride-induced corrosion · Flexural capacity · Girder-and-slab deck bridge · Pretensioned concrete girder

## 1 Introduction

Pretensioned concrete bridge decks in coastal areas are prone to corrosion of strands, which result in the deterioration of their flexural capacities. This may lead to the reduction in estimated service life of a bridge. The bridge structures are designed for a target service life of 100 years as per the codes of the Indian Roads Congress. But many of the existing bridges are showing signs of distress even after a few decades of construction. Several prestressed concrete (PC) bridge girders including post-tensioned girders have failed in different parts of the world due to corrosion of strands such as Ynys-y-Gwas Bridge at Wales (Ref. [1]).

---

G. Resmi · A. K. Sengupta (✉) · R. G. Pillai  
Department of Civil Engineering, Indian Institute  
of Technology Madras, Chennai 600036, India  
e-mail: amlan@iitm.ac.in

G. Resmi  
e-mail: ce13d050@smail.iitm.ac.in

R. G. Pillai  
e-mail: pillai@iitm.ac.in

Normally, a strand in a pretensioned girder is protected against corrosion due to the alkalinity of surrounding concrete ( $\text{pH} > 12.5$ ) (Ref. [2]). However, even in uncracked concrete, the strands are susceptible to corrosion mainly due to diffusion of chloride ions, either from de-icing salts or from ambient atmosphere in bridges located near coastal regions (Ref. [3]). The present study investigates the time-wise variation of the flexural capacity of a pretensioned concrete girder in an existing girder-and-slab deck bridge.

## 2 Research Significance

Pretensioned girders are used in fast-track construction of many bridges, urban flyovers and other elevated transport structures. Assessment of the girders is necessary to estimate the service life of such a structure. In coastal areas, the reduction in the area of strands due to diffusion of chloride ions will lead to reduction of the flexural capacity of a girder. In addition to reduction of area of the strands, there will be losses of prestress due to the effects of elastic shortening, creep and shrinkage of concrete and relaxation of steel. The present study provides a method to quantify the reduction in flexural capacity with time, due to chloride-induced corrosion and variation in concrete stresses due to the effect of losses in prestress. With further validation of the model, the approach can be used in the management of similar existing or newly built bridge decks.

## 3 Model for Corrosion Initiation

Chloride penetration through uncracked concrete can be treated as a diffusion process following Fick's second law of diffusion. The assumptions include concrete to be homogenous, non-reactive and non-absorptive material. Based on the law, for one-dimensional diffusion, the variation of chloride concentration through the cover concrete with respect to time is given as follows (Ref. [4]):

$$\frac{\partial C}{\partial t} = D_c \frac{\partial^2 C}{\partial x^2} \quad (1)$$

Here,  $C(x, t)$  is the chloride concentration ( $\text{kg}/\text{m}^3$ ) at a distance  $x$  (mm) from the surface at time  $t$  (years).  $D_c$  is the chloride diffusion coefficient for concrete ( $\text{mm}^2/\text{year}$ ). The exact solution of Eq. (1) is given as follows:

$$C(x, t) = C_0 \left\{ 1 - \text{erf} \left[ \frac{x}{2\sqrt{D_c t}} \right] \right\} \quad (2)$$

Here,  $C_0$  is the surface chloride concentration ( $\text{kg/m}^3$ ) under equilibrium condition. The symbol erf represents the error function.

The corrosion initiation time ( $t_0$ ) can be estimated from Eq. (2) with  $t = t_0$ ,  $x = c$  (thickness of cover concrete) and  $C(x, t) = C(c, t_0) = C_{th}$  (threshold chloride concentration in  $\text{kg/m}^3$ , for initiation of corrosion). The expression for  $t_0$  can be obtained by transposing the terms of Eq. (2) as shown.

$$t_0 = \frac{c^2 \left[ \text{erf}^{-1} \left( \frac{C_0 - C_{th}}{C_{th}} \right) \right]^{-2}}{4D_c} \tag{3}$$

### 4 Model for Loss of Area of Strand

For modelling the propagation of corrosion, a precise evaluation of the residual area of a 7-wire twisted strand is not possible, considering the formation of random pits along the periphery. A hypothetical model for the loss of area of a strand was adopted as shown in Fig. 1.

It was assumed that corrosion will initially occur uniformly along the exposed circumference of the outer wires of a strand, till 10% of the area of an outer wire gets corroded. Subsequently, the inner portions of the outer wires and the central wire will start corroding. The mathematical model for the same is as given below:

For  $t < t_0$ ;

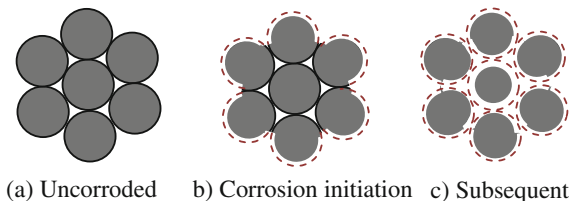
$$A_p = (6 \times \pi \varphi_0^2) + (\pi \varphi_i^2) \tag{4a}$$

For  $t_0 \leq t \leq t_1$

$$A_p = 6 \left( \frac{\sqrt{3}}{4} + \frac{2\pi}{3} \right) (\varphi_0 - \Delta r_1)^2 + 6\varphi_0^2 \left( \frac{\pi}{3} - \frac{\sqrt{3}}{4} \right) + (\pi \varphi_i^2) \tag{4b}$$

For  $t < t_1$

**Fig. 1** Hypothetical variation of cross-sectional area of a strand



$$A_p = 6\left(\frac{\sqrt{3}}{4} + \frac{2\pi}{3}\right)(\varphi_0 - \Delta r_1)^2 + 6\left(\frac{\pi}{3} - \frac{\sqrt{3}}{4}\right)(\varphi_0 - \Delta r_2)^2 + \pi(\varphi_i - \Delta r_2)^2 \tag{4c}$$

where  $t_1 = t_0 + \frac{0.10\varphi_0}{r}$ .

Here,  $A_p$ ,  $\varphi_0$ ,  $\varphi_i$  and  $r$  are area of one strand ( $\text{mm}^2$ ), radius of outer wire (mm), radius of inner wire (mm) and rate of corrosion of prestressing wire (mm/year), respectively.  $\Delta r_1$  and  $\Delta r_2$  represent the reductions in radii of outer and inner wires, respectively.

### 5 Analysis of Girder

The design details of a typical pretensioned girder of the Panipat Elevated Expressway on National Highway No. 1 were used for the analysis. It was assumed that similar type of girders is used in the coastal regions of India. The cross section of the girder at mid-span is shown in Fig. 2. At the mid-span, the girder consists of four layers of strands at bottom (A, B, C and D) and one layer of strand at top (T), having ultimate tensile strength in terms of stress ( $f_{pk}$ ) of 1861 MPa. The nominal diameter of a strand was 15.2 mm. The initial prestress applied on each strand was 76.5% of  $f_{pk}$ . It was observed based on tests that the tensile strength of a strand is not affected by corrosion (Ref. [5]).

**Fig. 2** Cross section of girder at mid-span

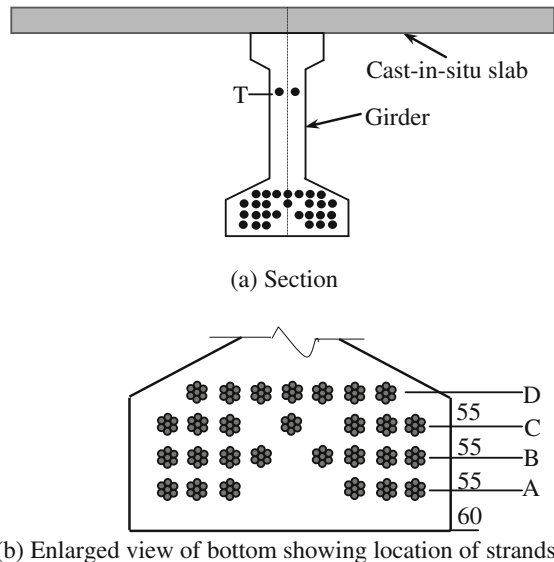


**Table 1** Geometric details of section at mid-span

All dimensions in millimetres	
Effective width of flange	2150
Depth of flange	200
Width of web	230
Depth of web	1800

The section considered was composite, with grade of concrete for the precast girder as M50, and that for the cast in situ slab as M45.

The assumptions made in the analysis of the girder are as follows.

1. The corrosion of strands is due to the ingress of chloride ions from the soffit of the girder.
2. The long-term loss of prestress in strand in terms of stress, is independent of corrosion.
3. Due to prestressing, there is no flexural cracking of the concrete under service condition.
4. Since the area of a strand is small as compared to that of the bars used as primary longitudinal reinforcement in reinforced concrete girders, the tensile stress generated in the concrete cover due to the formation of rust and subsequent spalling of the cover is negligible. The bond between the twisted strands and concrete is retained. However, this assumption may not be valid with deterioration of concrete.

The geometric details of the composite section used for analysis are given in Table 1.

### 5.1 Variation of Area of Stand and Effective Depth

The parameters required for computing the corrosion initiation time as per Eq. (3) were adopted from Ref. [4] for very severe exposure condition (Table 2).

The results obtained from the analysis are as given in Table 3. Layers A and B corrode during the target service life of the bridge.

The rate of corrosion ( $r$ ) of prestressing steel wire was taken from the data of linear polarisation resistance tests of wire specimens embedded in mortar (Ref. [6]). The average corrosion current density ( $i_{corr}$ ) value obtained from the study was converted into rate of corrosion in mm/year and was used in the present analysis.

**Table 2** Input for analysis

Threshold chloride concentration, $C_{th}$	0.83 kg/m <sup>3</sup>
Surface chloride concentration, $C_0$	12 kg/m <sup>3</sup>
Diffusion coefficient of concrete, $D_c$	40 mm <sup>2</sup> /year
Rate of corrosion of prestressing steel, $r$	0.0493 mm/year

**Table 3** Corrosion initiation time

Layer	Effective cover (mm)	No. of strands	Initiation time (yrs)
A	60	6	16
B	115	8	49

**Fig. 3** Variation of area of strands with time

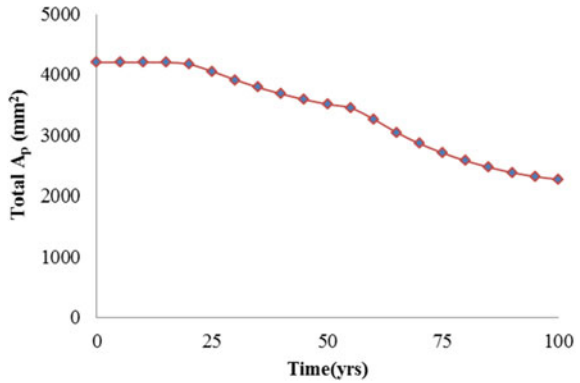
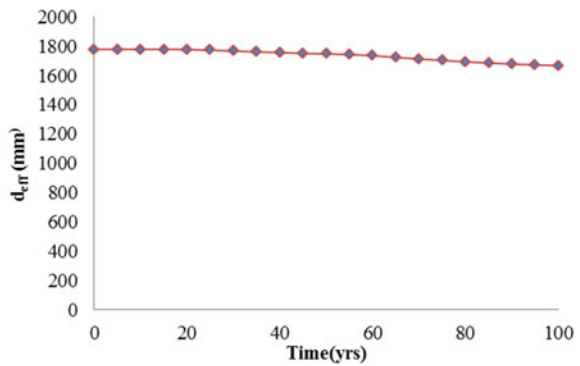


**Fig. 4** Variation of effective depth with time



The model for loss of area as per Eq. (4) was then used to calculate the propagation of corrosion through the service life.

The variation of the total area of strands with time is shown in Fig. 3. The two kinks in the curve correspond to the initiation of corrosion of Layers A and B. Around 46% of the total area gets reduced due to very severe exposure condition over a period of 100 years.

The reduction of total area of prestressing strands resulted in slight reduction of effective depth for the section. The initial effective depth of the section was 1778.5 mm. The variation of effective depth with time is as shown in Fig. 4. The effective depth reduces by 6.2%.

### 5.2 Variation of Prestress with Time

The losses in prestress were computed according to the recommendations of Ref. [7]. In case of the selected girder, the prestress was transferred on the third day after casting of the girder (when concrete attained strength of 40 MPa). The short-term losses due to relaxation in 3 days and elastic shortening at transfer were 1.82% of the initial prestress and 0.94% of updated prestress, respectively.

The deck slab was cast on the 50th day after casting of the girder. Thus, the long-term losses were calculated for the following time periods: 50th day, 1, 5, 50 and 100 years which denotes the time between casting of deck slab and end of target service life of the girder. The values of prestress loss obtained are shown for instances in Table 4.

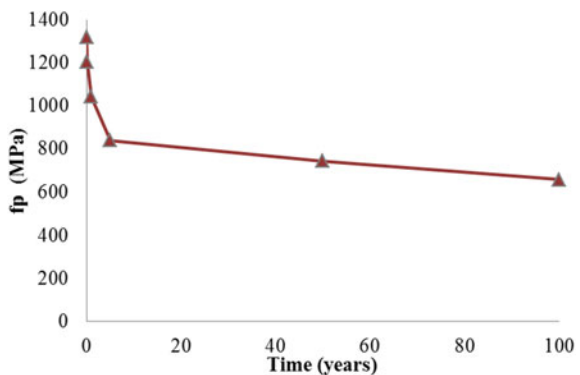
Figure 5 shows the effective prestress reduction with time till 100 years. The losses were evaluated at third day, fifty days, 1, 5 and 50 years. The interactions of losses were also incorporated in the analysis by updating the stresses at each interval.

It was analysed from the graph that the effective prestress got reduced to  $0.35 f_{pk}$  by the end of 100 years as a result of prestress losses.

**Table 4** Total loss of prestress

Time	Effective prestress
3rd day	$0.71 f_{pk}$
50th day	$0.64 f_{pk}$
1 year	$0.56 f_{pk}$
5 years	$0.45 f_{pk}$
50 years	$0.40 f_{pk}$
100 years	$0.35 f_{pk}$

**Fig. 5** Variation of effective prestress with time



### 5.3 Flexural Capacity of Girder

The composite girder shown in Fig. 2 was simplified as shown in Fig. 6. It consists of a deck slab of 2150 mm width and 200 mm depth. The pretensioned girder was assumed to be a rectangular section of 230 mm width. The total of thirty prestressing strands of 15.2 mm nominal diameter was used in five layers. Hence, the total effective area of the strand was obtained as 4200.7 mm<sup>2</sup> at an effective depth of 1778.5 mm from the top of composite girder.

This composite beam can be analysed as a flanged beam. Since the flange of the section is much large compared to the thickness of web, the neutral axis will lie within the flange itself. Hence the portion below the neutral axis will be ineffective in taking any compressive forces. This will justify the simplification done in Fig. 6.

The strain compatibility method was used for estimating the flexural capacity of the composite girder. The steps adopted in this method are stated below:

- (1) According to compatibility condition, strain in concrete and strand at the level of strand are equal. For an ultimate compressive strain of 0.0035 in concrete at extreme top fibre, tensile strain in the strand ( $\epsilon_p$ ) was obtained by using the following relation:

$$\epsilon_p = \left( \frac{x_u - d}{d} \times 0.0035 \right) + \Delta\epsilon \quad (5)$$

where  $\Delta\epsilon = \frac{f_{pi}}{E}$

$x_u$  neutral axis depth (mm)

$d$  effective depth of strand (mm)

$f_{pi}$  initial prestress after deducting relaxation loss at 3 days (MPa)

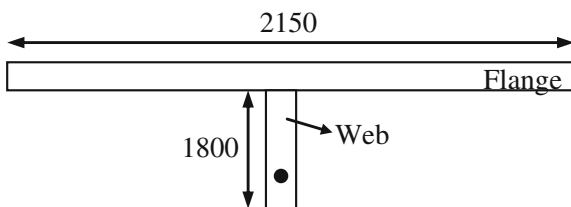
$E$  modulus of elasticity of strand (MPa).

- (2) Stress in strand ( $f_p$ ) was obtained from the constitutive relationship of prestressing strand. The model given in Ref. [8] was used in this analysis.

$$f_p = f(\epsilon_p) \quad (6)$$

- (3) The tensile ( $T$ ) and compressive ( $C$ ) forces in strand and concrete were calculated as:

Fig. 6 Simplified section of composite girder





$$T = f_p \times A_p \tag{7}$$

$$C = 0.362 \times f_{ck} \times b_f \times x_u \tag{8}$$

Equation (8) is valid in this analysis since the neutral axis lies inside the flange always and hence can be used for finding the compressive force.  $x_u$  has to be iterated until the force equilibrium condition is satisfied.

$$C = T \tag{9}$$

(4) The ultimate moment of resistance ( $M_{UR}$ ) was obtained from moment equilibrium relationship:

$$M_{UR} = T \times (d - 0.42x_u) \tag{10}$$

The analysis was done for getting the flexural capacity reduction till 100 years for an increment of five years. The reduction of cross-sectional area and effective depth were incorporated in the analysis. The neutral axis depth was iterated to satisfy the equilibrium condition, and the corresponding moment of resistance was obtained.

## 6 Results and Discussions

The time-dependent stress variation in concrete due to sustained loads is consolidated in Fig. 7. It shows the variation of stress at the top and bottom of composite girder with time. The reduction occurred is due to the incurred prestress losses. The in-service superimposed loads are not considered in the current analysis. It is evident from Fig. 7 that the top fibre of concrete which was under tensile stress initially is shifting to compressive stress with the increase in time, due to the effect of prestress losses. The bottom fibre of girder is losing the compressive stress, while

**Fig. 7** Variation of stress in concrete at extreme fibres with time

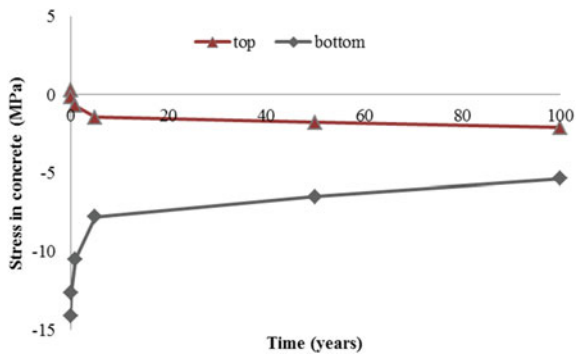
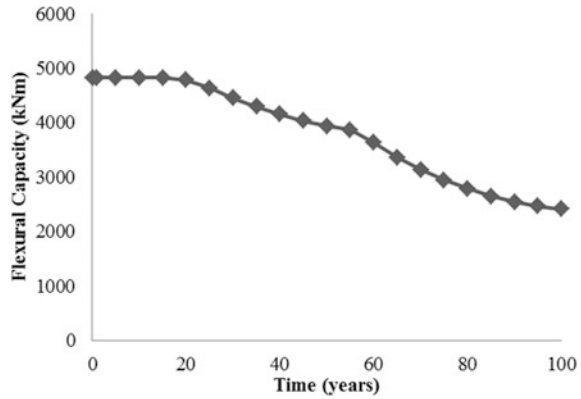


**Fig. 8** Variation of mid-span flexural capacity with time



the top fibre of girder is gaining more compressive stress. This leads to the sagging of member as a whole. The inclusion of service loads will further aggravate the stresses in girder and will deflect more.

The results obtained from the flexural capacity analysis of the section at the mid-span using the strain compatibility method are as shown in Fig. 8.

The major part of subsequent reduction in flexural capacity was contributed by the reduced area of cross section of strand as a result of corrosion. The reduction in effective prestress with time does not contribute to the ultimate capacity reduction of composite girder, but it is affecting the service conditions of the girder. Altogether, by the end of hundred years, the flexural capacity of the composite girder got reduced by 50%.

In this analysis, the bond between strand and concrete was assumed to be perfect, which is not the real scenario once the corrosion of strand occur. More rigorous analysis will be necessary for incorporating that also into the present analysis.

At present, an experimental programme is underway to determine the change in flexural behaviour of pretensioned beams subjected to artificial corrosion of strands. The results from that will be used to update the calculations of time variant flexural capacity and behaviour of the selected bridge girder.

## 7 Conclusions

Based on the analysis discussed in this paper, the following conclusions are drawn:

- In case of prestressed concrete girders, there will be loss due to reduction of effective prestress with time due to various prestress losses. Out of long-term losses, the ones due to creep of concrete, shrinkage of concrete and relaxation of strand play a major role in reduction of the in-service stresses of concrete.

- The ultimate flexural capacity is independent of the prestress losses and was found to be dependent on amount of corrosion occurred in strands.
- It was estimated from the analysis that 46% reduction of total cross-sectional area of strands and 6.2% reduction of effective depth resulted in an ultimate flexural capacity reduction of 50% towards the end of service life of the girder.
- It was also observed that out of thirty strands in the composite girder, only fourteen strands were subjected to corrosion due to severe exposure to chloride ions. In the present analysis, only Layer A and Layer B got affected.

**Acknowledgements** The authors acknowledge the support provided by the Department of Civil Engineering, Indian Institute of Technology, Madras, Chennai, India, to carry out this research. The support given by Larsen and Turbo IEL, Chennai, in giving the design documents of Panipat Express Highway girder, is gratefully acknowledged.

## References

1. Woodward RJ, Williams FW (1988) Collapse of Ynys-s-Gwas Bridge, West Glamorgan. Proc Inst Civil Eng, Part I 84:635–669
2. ACI 222.2R-01 (2001) Corrosion of prestressing steels. American Concrete Institute Committee, 222
3. Podolony W (1992) Corrosion of prestressing steels and its mitigation. PCI J Spec Rep 34–55
4. IRC SP: 60-2002, An approach document for assessment of remaining life of concrete bridges. Indian Road Congress, New Delhi
5. Ranjitha R (2016) Use of digital image correlation to assess the mechanical properties of corroded steel rebars. M. S. Thesis, Indian Institute of Technology Madras
6. Karuppanasamy J, Pillai RG (2014) Probabilistic estimation of corrosion propagation period for prestressed concrete structures exposed to chlorides In: 4th International conferences on the durability of concrete structures, Purdue University, 24–26th July, 2014
7. IRC 112: 2011, Code of practice for concrete road bridges. Indian Road Congress, New Delhi
8. PCI design handbook, Precast/Prestressed Concrete Institute (PCI), Chicago, Illinois, 1999

# Reliability Study of Railway Bridge Circular Pier Using Monte Carlo Simulation



A. Abishek and B. Nageswara Rao

**Abstract** Bridges are one of the important structures that are being used in our day to day lives. The design process of elements of the bridge is a complex procedure and is based on mostly research and experience to arrive at a balance between safety, functionality, and economy. Among all the elements of the bridge, piers are considered as the most important because of the higher stress concentration in them. Hence, the safety and reliability of the pier to satisfy its purpose during its lifetime is of core importance. The purpose of this work is to study the safety of an existing pier of a railway bridge. The resistance of the pier is assumed to be composed of many random variables. Considering them as random variables, reliability analysis is performed to evaluate the probability of failure of the pier by determining whether the limit-state function is exceeded. The study also focuses on the determination of reliability index of the pier when fatigue in concrete is taken into consideration.

**Keywords** Reliability · Railway bridge pier · Fatigue

## 1 Need of Reliability Analysis for Railway Bridges

In railways, which is one of the oldest networks in India, the design of the structural elements are almost standardized. The sections used in their design are almost same irrespective of the place in which the structure is constructed and is dependent only on the span of the bridges, in case of railway bridges. The pre-decided sections are just checked if adequate to carry the required load from the superstructure and live load, and the sections are not decided to carry the required load thus making huge

---

A. Abishek · B. Nageswara Rao (✉)  
Department of Civil Engineering, Indian Institute of Technology Madras,  
Chennai 600036, India  
e-mail: bnrao@iitm.ac.in

A. Abishek  
e-mail: asaithambi.abishek@gmail.com

uneconomical sections. Reliability analysis of those pre-decided sections gives us an idea about the probability of failure of these sections by evaluating whether the limit-state function is exceeded or not and also helps in identifying size of the section that is actually required to carry the load.

## 2 Railway Loads

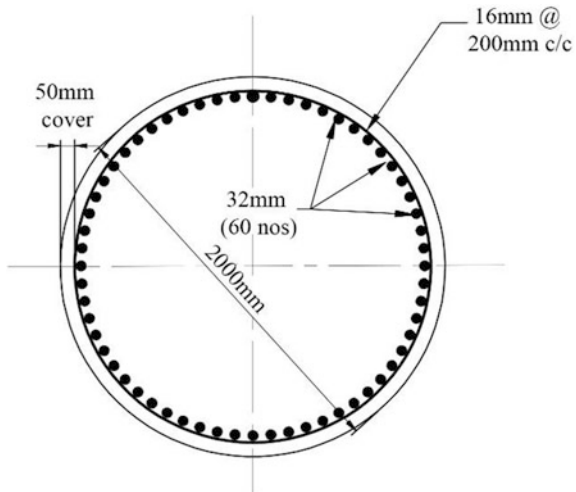
In the current study, railway bridge pier of a new electrified broad-gauge double-line bridge located in between Kharsia and Dharamjaygarh is considered. The overall length of the four-span bridge is 53.2 m. The overall length of each span is 13.3 m. Since the bridge is a double-line meter-gauge bridge, at the junction of two spans, two circular piers are located perpendicular to the direction of the railway line. Each of the two circular piers has a diameter of 2.0 m. The two piers are connected to each other by a pier cap of width 10.5 m and depth of 1.5 m. For the purpose of analysis, it is assumed that the load from one of the two railway lines is completely taken by one of the piers and transferred to the foundation. One of the two piers is considered for the study. The configuration of the pier is as in Table 1.

The cross section of the pier is as in Fig. 1.

**Table 1** Configuration of the pier

S.No.	Parameter	Dimension/No.
1.	Diameter	2000 mm
2.	Main bar diameter	32 mm
3.	Tie bar diameter	16 mm
4.	No. of main bars	60 Nos.
5.	Clear cover	50 mm

**Fig. 1** Cross section of the pier



### 3 Load Calculation

Following types of loads were considered for calculating the actual load on the pier.

- Dead load—Self-weight of the superstructure, SIDL due to track and rail, self-weight of the substructure including pier cap and pier shaft
- Live load
- Centrifugal force—Force in the transverse direction due to the curvature in the track
- Longitudinal forces—Force due to live load; acceleration and braking forces and force due to wind effects on the superstructure and live load
- Forces and effects due to earthquake.

The types of loads considered are in accordance with Bridge Rules of Indian Railway Standards [1]. In the current numerical study, load combination 2 of ultimate limit state and load factors for ultimate limit state as mentioned in Clause 11.3 of IRS Concrete Bridge Code [1] are considered. Forces and moments at the base of the pier shaft were calculated for both normal and seismic case during dry and high flood level conditions. Summary of the forces is in Table 2.

The maximum and minimum loads were obtained by considering all possible combinations of the live load, i.e., the rail, on the tracks.

### 4 Resistance of the Pier

The axial load and moment capacity of the given section of the pier for various possible eccentricities are obtained using the standard algorithms [2–4] with the help of a MATLAB code which is validated with the design interaction curve of SP 16 [5]. Here in the study since the material parameters such as strength of concrete, strength of steel and section parameters, viz. area of steel, dimension of the overall section are considered as random variables, the code is modified in such a way to calculate the design interaction plots for complete range of the random variables. In the current study, the strength and dimension parameters are considered as normally distributed with a bias factor and coefficient of variation. The statistical parameters used are as in Table 3 which are used for code calibration [6].

In order to arrive at the range of design interaction plots, Monte Carlo simulation technique is used in the MATLAB code. The steps involved are as follows:

**Table 2** Loads on the pier

Case/Condition	Final forces and moments		
	$P_{\max}$ (kN)	$P_{\min}$ (kN)	$M_x$ (kNm)
Dry	10,103.603	1409.854	7141.503
HFL	9972.365	1242.260	7160.653

**Table 3** Statistical parameters of random variables

Parameter	Nominal value	Bias factor	Coefficient of variation
Depth of Pier ( $D$ )	2.0 m	1.005	0.040
Height of bar ( $d_i$ )		1.000	0.010
Strength of concrete ( $f_{ck}$ )	35 MPa	1.300	0.134
Yield strength of steel ( $f_y$ )	415 MPa	1.130	0.030
Area of steel ( $A_s$ )	804.25 mm <sup>2</sup>	1.000	0.015

- Generation of random numbers: Random numbers in the range [0,1] are generated using the inbuilt functions of MATLAB. Since the numerical value of  $F_x(x_i)$  is a value within the interval [0,1], the generated random numbers are used to arrive at the random variables where  $F_x(x_i)$  is the cumulative distribution function of random variable  $x_i$ .
- Inverse transformation: Normal inverse transformation technique is used in order to obtain at the normally distributed random variables from the random numbers.

$$F_x(x_i) = v_i \text{ which implies } x_i = F_x^{-1}(v_i)$$

where  $v_i$  is the generated random number of range [0,1].

- Generation of design interaction plot: The generated random variables, compressive strength of concrete, yield strength of steel, area of steel, depth of pier, and height of the bars are used to generate plots in the moment-load axes of the design interaction curve.

In the current study, 10,000 simulations of random variables for the respective bias factor and coefficient of variation were done and plotted for 21 possible eccentricities on the design interaction plot. Hence for each eccentricity value, 10,000 plots are generated based on the randomness of the above-mentioned parameters. The eccentricity ratios ( $e/D$ ) considered are 0.01, 0.02, 0.03, 0.05, 0.07, 0.1, 0.125, 0.15, 0.2, 0.25, 0.3, 0.4, 0.5, 0.6, 0.7, 0.8, 0.9, 1.2, 2, and 50. The generated design interaction plot is as in Fig. 2.

## 5 Bias Factor of the Resistance of Pier

From the obtained interaction plots, the mean and standard deviation of the resistance parameters, i.e., load and moment capacity, are calculated from which the bias factor is arrived at for different eccentricities on the pier. Figures 3 and 4 show the variation of bias factor with respect to eccentricity of the pier.

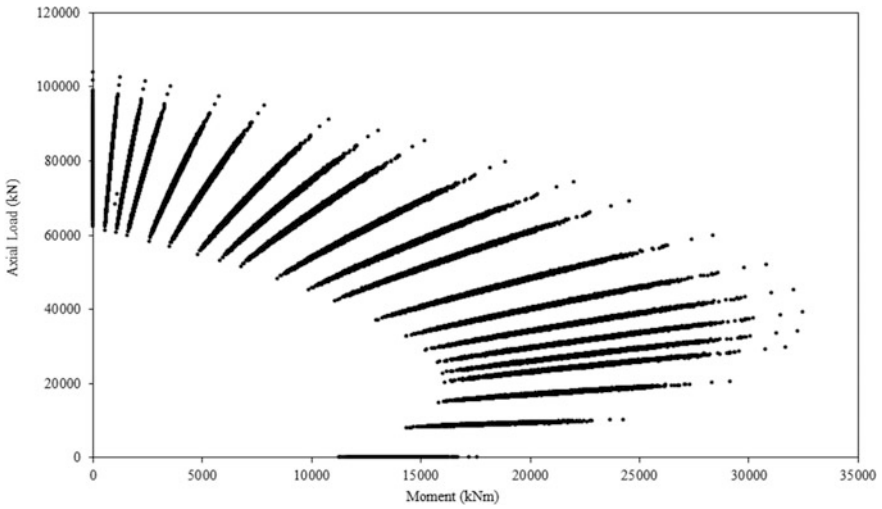


Fig. 2 Design interaction plot for the pier considering random variables

Fig. 3 Bias factor of axial load versus eccentricity of load on pier

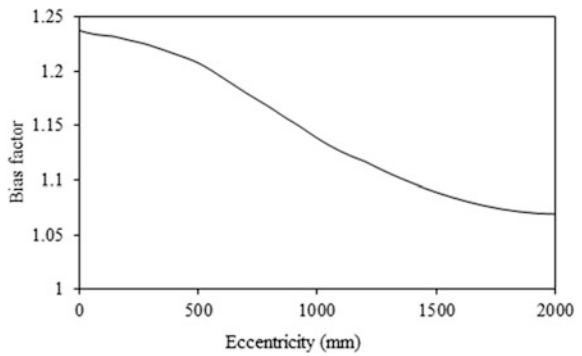
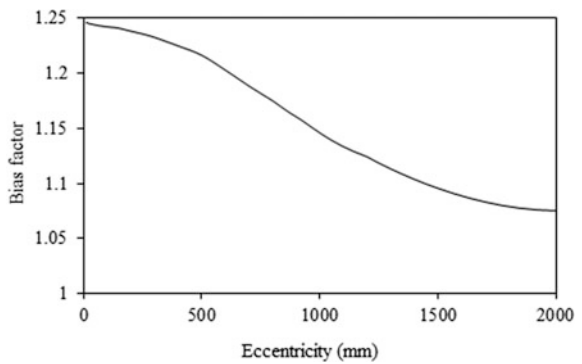


Fig. 4 Bias factor of moment versus eccentricity of load on pier





## 6 Reliability of the Pier

### 6.1 Probability of Failure

Probability of failure ( $P_f$ ) is obtained from the ratio of number of simulations where the limit-state function is exceeding and the total number of simulations is considered as in Eq. (1). Total number of simulations in the current study is 10,000. Reliability index is also determined from the probability of failure.

$$P_f = \frac{N_f}{N} \quad (1)$$

where

$N_f$  is the number of simulations the limit-state function has exceeded  
 $N$  is the total number of simulations; here  $N$  is 10,000.

### 6.2 Determination of Failure Cases

For the load that is transferred onto the pier from the superstructure and live load, allowable moment capacity is interpolated from the obtained design interaction plots. This allowable moment capacity is compared with the actual moment that comes on the pier. Based on whether the actual moment is lesser or higher than the design moment capacity, the number of failure cases  $N_f$  is determined.

### 6.3 Reliability Index

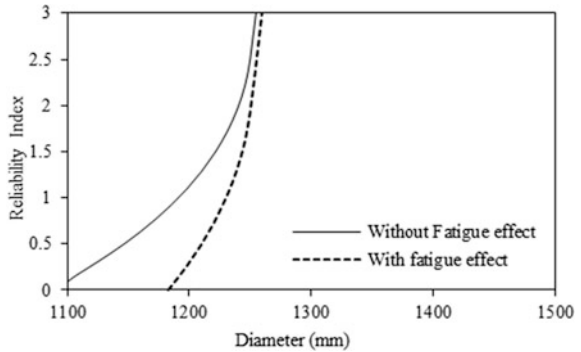
For a normally distributed random variables, the reliability index [7, 8] is calculated as in Eq. (2).

$$\beta = -\Phi(P_f) \quad (2)$$

where  $\Phi$  is the standard normal distribution function.

From the MATLAB code, reliability index of the pier in the particular case considered as well as the effect of diameter of the pier on the reliability of the pier is numerically determined. The effect of diameter on the reliability of pier is as in Fig. 5.

**Fig. 5** Effect of diameter of the pier on the reliability index



### 7 Fatigue Effect on the Pier

Bridge piers are always subjected to different stress levels due to dead and live loads which initiate the fatigue damages in them. Since imperfections such as micro-cracking due to shrinkage or heat of hydration initiates the fatigue damage in concrete, piers become the obvious structural element to be focused on fatigue damages due to its huge mass. Among many fatigue models, Aas-Jakobsen fatigue model [9] is used in the current study. According to the model,

$$S_{\max} = \frac{\sigma_{\max}}{f'_c} = 1 - \beta(1 - R) \log N_f \tag{3}$$

where

- $S_{\max}$  is maximum stress level in concrete,
- $f'_c$  is the compressive strength of concrete under static load,
- $N_f$  is the number of cycles to failure,
- $R$  is  $\sigma_{\min}/\sigma_{\max}$ ,
- $\beta$  is material constant (0.064).

The statistical parameters of concrete subjected to fatigue are taken same as that of the logarithm of  $N_f$  due to its linear relationship with  $\sigma_{\max}/f'_c$  which is then taken for analysis in MATLAB. Using 10,000 simulations, the statistical parameters of  $\log N_f$  are determined. The effect of fatigue on the reliability index is as in Fig. 5.

### 8 Results and Discussions

From the results obtained, it is clear that for the particular configuration that is taken, there has not been any cases of failure in the numerical simulation thus giving zero probability of failure and reliability index of infinity. Even considering the fatigue effect using Aas-Jakobsen fatigue model, the simulation has arrived with

**Table 4** Probability of failure for different diameters of the pier

Diameter of the pier (mm)	Probability of failure (%)	
	Without fatigue effect	With fatigue effect
2000	0	0
1600	0	0
1250	0.61	2.74
1100	46.55	85.75
1000	97.04	99.99

zero probability of failure. Figure 5 shows the influence of the diameter of pier on the reliability for the particular loading configuration with and without considering the fatigue effect. Table 4 shows the failure probability of the pier with and without the fatigue effect for various considered diameters.

When the diameter considered is 1250 mm, the failure probability considering fatigue increases by around 3.5 times the failure probability without considering fatigue, while for 1000 mm diameter of pier, the increase is only around 3%.

## 9 Conclusions

Results clearly indicate that the specific configuration is free from failure but still from Fig. 5 it is obvious that the actual section is bigger than what is required for the available loading conditions. Thus, Fig. 5 can be used to identify the approximate section that is required. More economical sections can be arrived at.

Even in fatigue case, the section turned out to be safe in the simulation. For smaller diameter of the pier, the probability of failure was more when fatigue effect is considered, and it is observed from Fig. 5.

From the simulation, it is evident that as the diameter of the pier is increased the reliability indices are coinciding irrespective of whether fatigue effect is considered or not.

Considering fatigue of concrete increases the failure probability of the pier. The percentage of increase in probability of failure decreases as the diameter of pier decreases.

## References

1. IRS Bridge Rules: 2005 Indian railway standard, Rules specifying the loads for design of super-structure and sub-structure of bridges
2. Wight JK, MacGregor JG (2009) Reinforced concrete. Mechanics and design, 5th edn. Pearson Education, Inc
3. Unnikrishna Pillai S, Devdas M (2009) Reinforced concrete design, 3rd edn. Tata McGraw Hill

4. IS 456: 2000, Indian standard code of practice for plain and reinforced concrete. Bureau of Indian Standards, New Delhi
5. Design Aids (for Reinforced Concrete) to IS 456: 1978 (1980) Special Publication SP:16, Bureau of Indian Standards, New Delhi
6. Nowak AS, Szerszen MM (2003) Calibration of design code for buildings (ACI 318): Part 1—Statistical models for resistance. *ACI Struct J* 100(3):377–382
7. Choi S-K, Grandhi RV, Canfield RA (2006) Reliability-based structural design. Springer, Berlin
8. Nowak AS, Collins KR (2000) Reliability of structures. McGraw-Hill
9. Aas-Jakobsen K (1970) Fatigue of concrete beams and columns, vol 70. Division of Concrete Structures, The Norwegian Institute of Technology, The University of Trondheim, Norway, September 1970

# Evaluation of IS 1893-Based Design Using the Performance Based Earthquake Engineering Framework



G. Bharat Reddy and B. Radhika

**Abstract** The performance-based earthquake engineering (PBEE) approach provides a framework to evaluate the performance of a structural system accounting for the uncertainties present in the different stages of modeling, design, and analysis. The framework typically comprises four stages of analysis—hazard, demand, damage and loss analyses—to evaluate performance. In the present study, the earthquake-resistant design of a frame and beam conforming to IS 1893–2000 is considered, and their performance is evaluated and presented in the form of probability of exceedance of damage. The first three stages of the performance evaluation are demonstrated using the method of incremental dynamic analysis to account for the record-to-record variability and further assuming the demand and damage fragility curves to have a lognormal distribution. The methodology presented to evaluate the performance of these structure helps in making decisions by accounting for the uncertainties present in each stage.

**Keywords** Performance-based engineering · Incremental dynamic analysis  
Earthquake-resistant design

## 1 Introduction

The performance evaluation of a code-based design using the performance-based earthquake engineering (PBEE) framework is explored in the present work. For any design method, it would involve analyzing the hazard which could be loads like earthquake, wind, wave forces, vehicle axle load; followed by analyzing the

---

G. Bharat Reddy  
Promarg Consultants Pvt. Ltd., Hyderabad, Telangana, India  
e-mail: bharatreddy06@gmail.com

B. Radhika (✉)  
School of Infrastructure, Indian Institute of Technology  
Bhubaneswar, DST-INSPIRE Faculty, Odisha, India  
e-mail: radhika@iitbbs.ac.in

proposed structure for the given hazard levels, and subsequently comparing with the desired strength and deformation criteria; a violation of which would require iterating the design. If the loss associated with a structure is defined in terms of socioeconomic parameters like death, downtime, or monetary loss, it would comprise the fourth step of loss analysis. Furthermore, in achieving this, the role of uncertainties needs to be acknowledged; the source of which could be any one or often a combination of factors such as variable material properties, loads, boundary conditions, methods adopted for analysis and capacity estimation, choice of structural models, to name a few. In the evolution of design methods, uncertainty has been addressed by the factor of safety in allowable stress design (ASD) and load and resistant factors in load and resistance factor design (LRFD) methods. The structural design codes have been developed over the years according to these design formats. The choice of factor in the ASD is more heuristic and banks on professional judgment in comparison with LRFD format which is motivated by the reliability-based design philosophy. Cornell and Krawinkler [1] of the Pacific Earthquake Engineering Research (PEER) group at University of California, Berkeley, had proposed a unified framework for performance-based earthquake engineering (PBEE) in which all the four steps discussed above are combined using the total probability theorem of probability theory, making it suitable to address problems of structural design, assessment of alternative designs, evaluation of existing structures, and retrofit strategies. Mathematically, the framework translates to [2].

$$\lambda(dv) = \iiint G(dv|dm)dG(dm|edp)dG(edp|im)d\lambda(im) \quad (1)$$

where  $\lambda(x)$  is the mean annual frequency (MAF) of exceedance of  $x$ ,  $G(\cdot|\cdot)$  is the conditional complementary probability distribution function, and  $dv, dm, edp$  and  $im$  are the decision variable (DV, monetary, death, and downtime), damage measure (DM, e.g., light, moderate, and severe with respect to repair of a component), engineering design parameter (EDP, e.g., inter-story drift ratio, roof acceleration), and intensity measure of the hazard (IM, e.g., peak ground acceleration, spectral acceleration), respectively. The uppercase letters denote the random variables (DV, DM, EDP, and IM) and the lowercase letters denote the values that the random variables assume ( $dv, dm, edp$ , and  $im$ ).

The main objective of the present study is to quantify the performance of an IS code-based design of a structure using the PBEE framework. This is represented by the probability of exceedance (POE) of damage or of the decision variable of the structure being studied. For a given hazard description, the performance-based framework involves four analysis phases and the details of the methods proposed to be used in different phases (only first three considered in the present study) for the design evaluation of a structure are outlined in the next section.

## **2 Methodology of PBEE**

The PBEE framework comprises of four stages of analysis, namely hazard, demand, damage, and loss analyses. The last step in the framework involves computation of loss fragility curves which requires understanding on relation between engineering quantities and socioeconomic parameters which lie outside the scope of the present work. The analysis therefore is limited to the first three stages, and the performance is reported by the probability of exceedance of damage in terms of structural demand parameters. The details of each step in the analysis are discussed next.

### **2.1 Hazard Analysis**

The ground motions that a site of interest may experience are characterized by their peak ground responses, spectral accelerations, Mercalli intensity, etc., collectively known as intensity measures (IMs). Hazard curve provides a quantitative estimate of the occurrence of a particular IM. This is obtained by considering uncertainties in earthquake source, distance from site, soil properties, and magnitude of earthquake. A performance-based approach to quantify the earthquake hazard is within the realm of probabilistic seismic hazard analysis (PSHA), the output of which is the hazard curve which may be the probability of exceedance or mean annual frequency of exceedance of an IM. Hazard curve compatible ground motions are selected to account for record-to-record variability either by simulation or from database of existing records. These time histories are used in the subsequent analysis as input to the structural system.

### **2.2 Demand Analysis**

Given the random input in the form of hazard compatible ground motions, the response of the frame structure is computed by performing an incremental dynamic analysis (IDA) [3] assuming a nonlinear model for the frame behavior. The response quantities governing the design are known as engineering design parameters (EDPs) which could be the maximum of the inter-story drift for structural elements and maximum of the acceleration response for non-structural elements or a combination of parameters. The conditional distribution of the EDPs given the hazard information is obtained in the form of a demand fragility curve which is used in the next phase of damage analysis. These fragility functions are assumed to be lognormally distributed with parameter values evaluated using the IDA results corresponding to each IM value.

### **2.3 Damage Analysis**

The capacity of structural and non-structural elements obtained either by experimental or analytical studies would be useful in identifying damage measures (DMs) for the respective components. For example, an IDA-based drift capacity can

be used to delineate damage measures for structural elements, with respect to inter-story drift, as slight, moderate, or severe damage. Similarly, DMs for non-structural elements like partition units can be defined as visible or significant, depending on whether the units would need patching up or complete replacement. In order to quantify the damage in the system, the relation of the DM given the EDP is established in the form of a damage fragility curve. Again, a lognormal assumption for these curves is found acceptable in literature. Alternatively, models based on IDA and Monte Carlo simulation-based estimation are also possible. In the present study, a lognormal distribution for the fragility curves is assumed.

The earthquake record generation, structural analysis, and computation of structural capacity will be carried out by writing codes in MATLAB and SAP. For illustration, in the following sections, the performance evaluation of a RC frame and beam designed as per IS 456 using the method outlined above is presented.

### 3 Performance Evaluation of a Code-Based Design

The PBEE framework provides an approach to evaluate a codal design and quantify the performance of the same by estimating the POE of damage. A code-based design of a two-story two-bay frame and a cantilever beam is considered, and their performance has been evaluated using the method discussed in the previous section.

#### 3.1 Performance Evaluation of a RC Frame

To illustrate the methodology discussed in the previous section, a two-bay two-story RC frame with bay length 6 m and each story height 3 m with fixed supports at the base is considered. M25 grade concrete and Fe 415 steel are used in the design. The beams have a cross section of 0.5 m  $\times$  0.5 m, and 12 numbers of 10-mm-diameter steel reinforcement are provided. The columns have a dimension of 0.5 m  $\times$  0.5 m with 8 numbers of 8-mm-diameter bars. A live load of 5 kN/m is taken to be distributed on each beam. The material model proposed by Mander et al. [4] is assumed in modeling the frame. The modeling of the frame and subsequent IDA analysis is performed on commercial software SAP2000.

It is assumed that the frame is subjected to earthquake loads whose hazard curve is shown in Fig. 1. A suite of 27 ground motion records compatible with the hazard curve was chosen from the PEER database [5]. The intensity measure was assumed to be the peak ground acceleration (PGA) of the time histories. Each of these records was scaled to PGA values ranging from 0.2 to 2 g with 0.2 g increment and used in the nonlinear structural analysis for IDA. The ground accelerations are applied as input in the analysis by taking the equivalent floor loads.

The maximum of the inter-story drift ratio (IDR) in each analysis was taken to be the EDP. Figure 2 shows the plot of the EDP versus IM obtained by IDA. The



**Fig. 1** Hazard curve of the earthquake ground motions used in the analysis of the frame

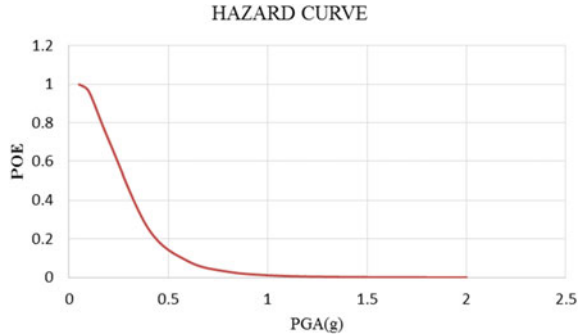
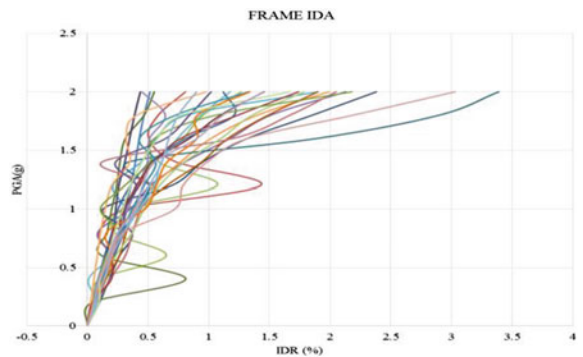


**Fig. 2** Maximum IDR of the frame, obtained using 27 ground motion records in the incremental dynamic analysis. Each color line corresponds to a ground motion scaled to different PGA values



weaving pattern is observed owing to the record-to-record variability which essentially is captured by IDA. Corresponding to each IM value, a lognormal distribution for the EDP is assumed, and the median ( $m$ ) and coefficient of variation (COV) are accordingly computed using the 27 data points. These are substituted in the lognormal distribution given by

$$P(EDP > edp|IM) = 1 - \Phi\left(\frac{\ln EDP - m}{COV}\right) \tag{2}$$

This assumption is validated by plotting the logarithm of maximum IDR values on a normal probability paper as shown in Fig. 3. A linear plot conforms to the values following the lognormal distribution.

The curves obtained using Eq. (2) serve as demand fragility curves (Fig. 4) which are subsequently used along with the damage fragility curves (Fig. 5) to obtain the POE of the damage. The damage fragility curves in turn are assumed to be lognormally distributed and the POE of damage is computed as

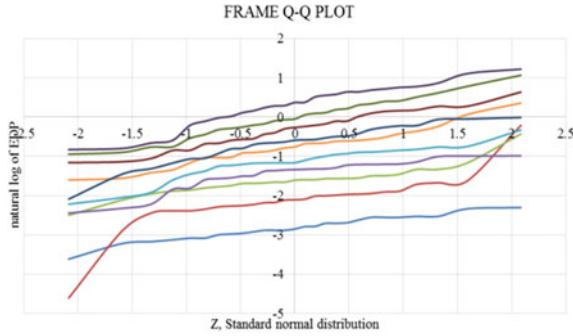


**Fig. 3** Normal probability paper plot to validate the lognormal assumption of demand fragility curves

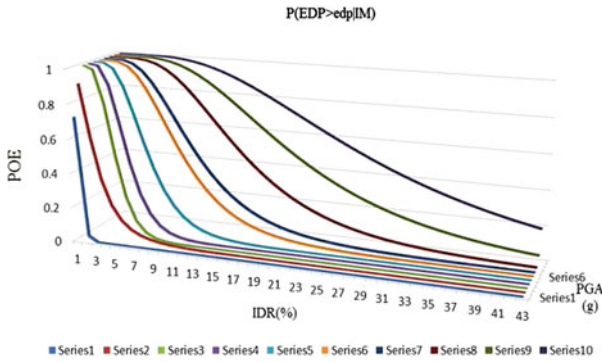


**Fig. 4** Frame demand fragility curves obtained assuming lognormal distribution. Series 1–10 denote the PGA values from 0.2 to 2 g with 0.2 g increment

**Fig. 5** Frame damage fragility assuming lognormal distribution

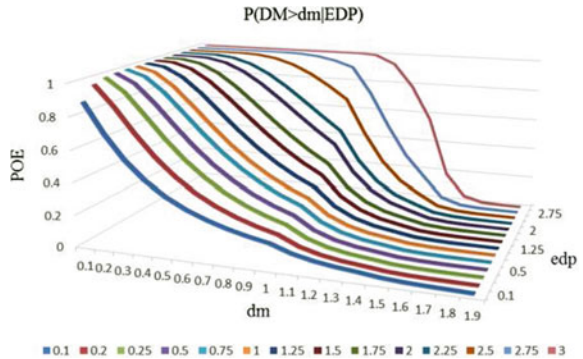
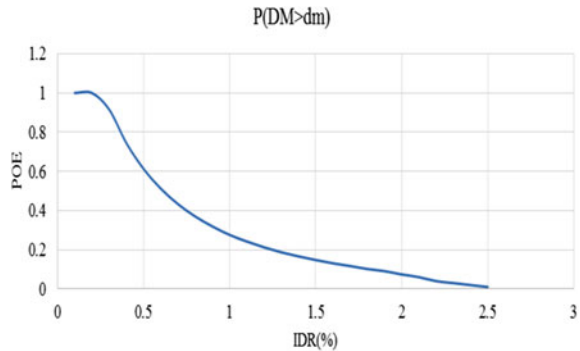


**Table 1** POE of damage of the RC frame

S. No	Limit state	POE
1.	Immediate occupancy (<1%)	>0.24
2.	Damage control (1–2%)	0.24–0.04
3.	Life safety (>2%)	<0.04

**Fig. 6** POE of damage, quantifying performance of the frame design



$$P(DM > dm) = \sum_{i=1}^{14} \sum_{j=1}^{10} P(DM > dm|EDP)P(EDP > edp_i|IM)P(im_j) \quad (3)$$

where the damage and demand fragility curves derived above are the first two quantities inside the summation and the hazard curve information the third probability. The POE of the damage obtained using Eq. (3) is shown in Fig. 5. ATC-40 [6] specifies the limit states; immediate occupancy, damage control, and life safety in terms of the IDR. This has been adopted in the present study, and the POE of the limit states is given in Table 1. This quantitative information on the performance of the frame with respect to the chosen limit states and the hazard information will be useful in decision making (Fig. 6).

### 3.2 Performance Evaluation of a RC Beam

An RC cantilever beam of size 0.5 m × 0.5 m × 6 m with #12, 10 mm Fe 415 steel reinforcement designed as per IS 456 (2007) for dead and live loads (5 kN/m) is considered for performance evaluation with respect to earthquake hazard. It is assumed that the beam is subjected to earthquake loads whose hazard curve is shown in Fig. 1. The ground motion input was given to the structure taking the equivalent load to act at the free end. The maximum of the free end deflection in each analysis was taken to be the EDP. Figure 7 shows the plot of the EDP versus IM obtained by IDA.

**Fig. 7** Maximum deflection of the free end of the beam, obtained using IDA

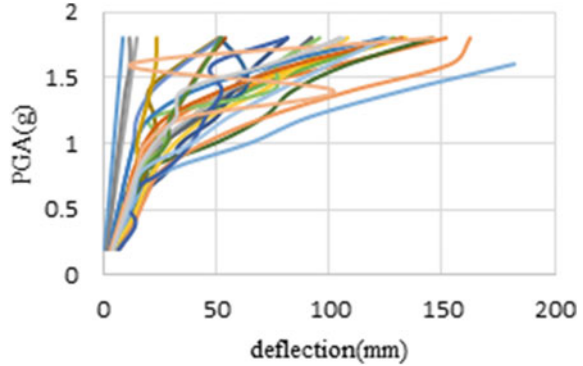
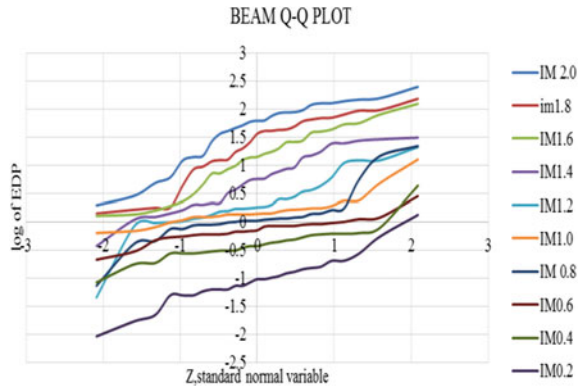


**Fig. 8** Normal probability paper plot for the EDP values of the beam



Corresponding to each IM value, a lognormal distribution for the EDP is assumed, and the median and coefficient of variation (COV) are accordingly computed using the 27 data points. This assumption is validated by plotting the logarithm of the EDP values on the probability paper shown in Fig. 8.

These serve as demand fragility curves (Fig. 9) which are subsequently used along with the damage fragility curves (assuming lognormal distribution, Fig. 10) to obtain the POE of the damage as shown in Fig. 11. As per IS 456, Clause 22.3, the limit state is assumed to be maximum deflection which is minimum (span/250, 20 mm). For the beam considered, 20 mm is the maximum permissible deflection, and the POE of this limit state from Fig. 10 is obtained as 0.9. Therefore, for the assumed hazard description, the designed beam is found to be unsafe and a re-design is recommended.

**Fig. 9** Beam demand fragility curves

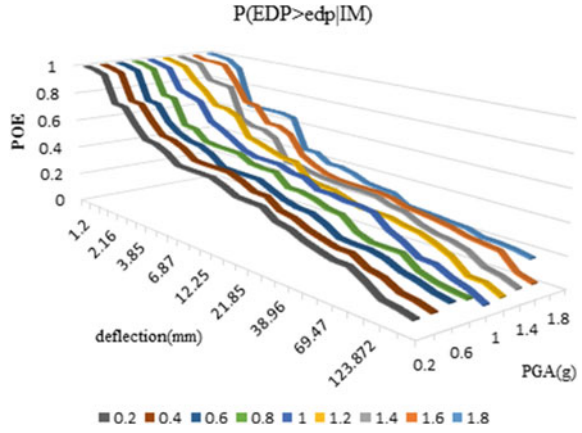


**Fig. 10** Damage fragility curves

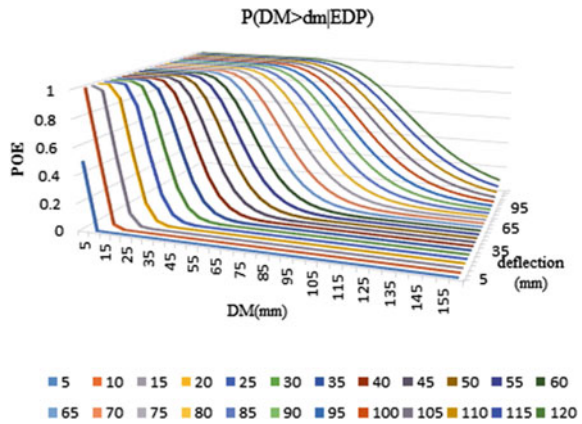
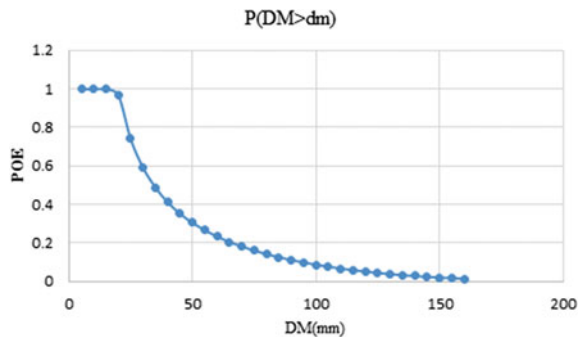


**Fig. 11** POE of damage



## 4 Note on the Methods and Models Adopted in the PBEE Analysis

The performance analysis of the frame design discussed in the paper highlights the steps adopted in the PBEE framework. Following are observations on the methods adopted:

1. The assumption of a lognormal distribution for the demand fragility curves is inspired from literature which is based on a statistical observation. But the same can be perceived as a problem in random vibration wherein the distribution of extremes of a non-stationary process (maximum of IDR) is of interest. This approach to modeling of the fragility curves would require application of the extreme value theory to determine the distribution of the fragility curves. The work by Naess and his co-workers [7, 8] proposes an asymptotic solution to this problem in the form of the average conditional exceedance rate (ACER) method.
2. The damage fragility curves in the present study have also been assumed to be lognormally distributed which again is adopted from literature. But a more rigorous study would involve deriving them using experimental data or Monte Carlo simulations.
3. The EDPs considered in the illustration are scalar, but a more general problem would be to handle a vector of dependent EDPs. The validity of joint lognormal distributions and the proposal for alternate models need to be examined.
4. Furthermore, an analytical solution to the PBEE problem (Eq. 1) has been proposed by Jalayer and Cornell [9] assuming lognormal models for the fragility curves. A similar solution considering alternate models for fragility using the theory of extreme values can also be derived.

## 5 Closure

The paper presents a method for quantifying the performance of a prescriptive-based frame design using the PBEE framework. Scalar IMs and EDPs were chosen to demonstrate the different stages of analyses. The choice of IMs, EDPs, modeling of the frame, and fragility curves is open to improvement, within the confines of the proposed method. Some of the above aspects along with the observations made in Sect. 4 are intended to be addressed by the authors in their future work.

## References

1. Cornell CA, Krawinkler H (2000) Progress and challenges in seismic performance assessment. PEER Cent News 3(2):1–4
2. Deierlein GG, Krawinkler H, Cornell CA (2003) A framework for performance based earthquake engineering. In: 7th Pacific conference on earthquake engineering, Christchurch, New Zealand
3. Vamvatsikos D, Cornell CA (2002) Incremental dynamic analysis. Earthq Eng Struct Dyn 31:491–514
4. Mander JB, Priestley MJN, Park R (1988) Theoretical stress-strain model for confined concrete. J Struct Eng ASCE 114(8):1804–1823
5. PEER Ground Motion Database, Pacific Earthquake Engineering Research Centre. <http://ngawest2.berkeley.edu/>
6. ATC-40 (1996) Seismic evaluation and retrofit of concrete buildings. Applied Technology Council Report, California Seismic Safety Commission Report
7. Naess A, Gaidai O, Karpa O (2013) Estimation of extreme values by the average conditional exceedance method. J Probab Stat 2013, pp 15, Article ID 797014. <https://doi.org/10.1155/2013/797014>
8. Naess A, Karpa O (2015) Statistics of bivariate extreme wind speeds by the ACER method. J Wind Eng Ind Aerodyn 139:82–88
9. Jalayer F, Cornell CA (2003) A technical framework for probability-based demand and capacity factor design (DCFD) seismic formats, PEER report, University of Berkeley

# Corrosion Performance of Steel in Self-compacting Concrete Exposed to Chloride Environment



Smrati Jain and Bulu Pradhan

**Abstract** The objective of this paper is to investigate the durability performance of self-compacting concrete (SCC) in terms of corrosion performance of steel reinforcement. The corrosion performance was evaluated by half-cell potential measurement, which provides information about the probability of occurrence of steel reinforcement corrosion and determining the corrosion current density by linear polarization resistance (LPR) measurement, which indicates the corrosion rate of steel reinforcement. Keeping this in view, in the present work prismatic reinforced concrete specimens with a centrally embedded steel bar were made from SCC mixes. Ordinary Portland cement (OPC) was used as a binder, and two  $w/c$  ratios of 0.40 and 0.43 were used for the preparation of concrete mixes. The fresh properties of SCC were evaluated by conducting slump flow,  $T_{50\text{cm}}$  time, V-funnel flow time, L-box, and sieve segregation tests, and the compressive strength was determined for the hardened property. The prismatic reinforced concrete specimens were exposed to sodium chloride solutions for 180 days with alternate wetting–drying cycles. The fresh concrete test results revealed satisfactory filling ability, passing ability, and segregation resistance at both the water–cement ( $w/c$ ) ratios. From results of corrosion parameters, it is observed that higher concentration of chloride ions increased the corrosion current density at longer exposure period. Further, higher corrosion current density was observed at  $w/c$  ratio of 0.43 as compared to that at  $w/c$  ratio of 0.40 at the longer exposure period.

**Keywords** SCC · Fresh properties · Chloride · Half-cell potential  
Corrosion current density

---

S. Jain · B. Pradhan (✉)

Department of Civil Engineering, Indian Institute of Technology Guwahati, Guwahati  
781039, India  
e-mail: bulu@iitg.ernet.in

© Springer Nature Singapore Pte Ltd. 2019

A. Rama Mohan Rao and K. Ramanjaneyulu (eds.), *Recent Advances in Structural Engineering, Volume 2*, Lecture Notes in Civil Engineering 12,  
[https://doi.org/10.1007/978-981-13-0365-4\\_47](https://doi.org/10.1007/978-981-13-0365-4_47)



## 1 Introduction

Concrete is the mostly widely used construction material in the world because of many reasons with one of them being its flexibility of converting into any desired shape. Self-compacting concrete (SCC) is a special type of concrete with characteristics of high fluidity or deformability, which can reach any corner of the formwork and is compacted by its own weight, without any vibration [1]. Improvement in the quality of concrete structures is a reason behind the invention of SCC because it has good consolidation without segregation and bleeding, even in the structures with congested steel reinforcement and narrow openings [2].

For better durability performance, concrete must resist physical and chemical attacks when exposed to aggressive environmental conditions. The durability of reinforced concrete structures is affected by deleterious chemical reactions between hardened cement matrix and different aggressive ions and subsequently affecting the embedded steel reinforcement. Steel reinforcement corrosion in concrete is the major durability problem faced by various reinforced concrete structures. Steel bars embedded in concrete are protected from corrosion by a passive layer (thin oxide layer of  $\gamma\text{-Fe}_2\text{O}_3$ ) that is formed and maintained on their surfaces because of the highly alkaline environment of concrete pore solution ( $\text{pH} > 13.5$ ) [3]. This passive film is destroyed either by reduction in pore solution pH due to carbonation or by ingress of chloride ions to steel–concrete interface [4]. Out of these causes, chloride attack is the primary cause of steel reinforcement corrosion in concrete. Chloride ions enter into concrete in the fresh state (through contaminated aggregates, mixing water, and admixtures that are added during preparation of concrete) and from external environment into the hardened concrete [5].

When concrete is subjected to chloride-rich environment, the chloride ions penetrate through the concrete cover, ultimately reaching the vicinity of steel bars, and result in corrosion of steel reinforcement. Out of two forms of chloride in concrete, i.e., free chloride and bound chloride, free chloride ions are mainly responsible for initiating steel reinforcement corrosion in concrete [6]. The corrosion of reinforced concrete structures is highly dependent on many factors such as moisture content, temperature of concrete, concentration of salts, ohmic resistivity, and supply of oxygen to the cathode site [7]. For evaluating the corrosion performance of steel reinforcement, different corrosion parameters, namely corrosion potential and corrosion current density, are generally determined.

From the review of the literature, it is observed that numerous studies have been carried out on corrosion performance of steel reinforcement in normal vibrated concrete exposed to the chloride environment [4, 8–10]. However in the reported literature, the studies on corrosion behavior of steel reinforcement in self-compacting concrete are scanty [11–14]. The objective of the present research work is to investigate the corrosion performance of reinforcing steel in self-compacting concrete (SCC) exposed to external chloride environment. For this

purpose, test specimens were prepared from SCC mixes. The fresh properties of SCC mixes were evaluated by slump flow,  $T_{50\text{cm}}$  time, V-funnel flow time, L-box, and sieve segregation tests. The SCC specimens were exposed to sodium chloride solution, and corrosion behavior of steel bar was evaluated by half-cell potential and linear polarization resistance (LPR) measurements.

## 2 Experimental Work

### 2.1 Materials and Mixture Proportion of SCC

In the present experimental work, self-compacting concrete (SCC) mixes were prepared using 43 grade ordinary Portland cement (OPC) with two  $w/c$  ratios of 0.40 and 0.43. The specific gravity of cement is 3.12. Locally available 20 mm maximum size of aggregate (MSA) and 10 mm MSA coarse aggregates in equal proportion (by mass) and locally available river sand as fine aggregate were used for the preparation of SCC mixes. The fine aggregate and both coarse aggregates have specific gravity of 2.62 and 2.65 (each), respectively. The grain size distributions of the aggregates are shown in Fig. 1. A water content of  $195 \text{ kg/m}^3$  was used in the preparation of SCC mixes at both  $w/c$  ratios. A polycarboxylate ether-based superplasticizer was used as water-reducing admixture. The quantities of the ingredients of SCC mixes were obtained by trail tests, as per the guidelines mentioned in ACI 237R-07 [15]. The mixture proportions of SCC are shown in Table 1.

**Fig. 1** Particle size distribution of aggregates

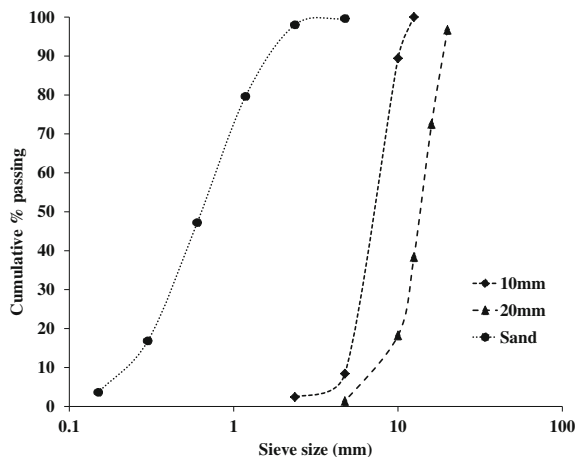


**Table 1** Mixture proportion of SCC ( $\text{kg/m}^3$ )

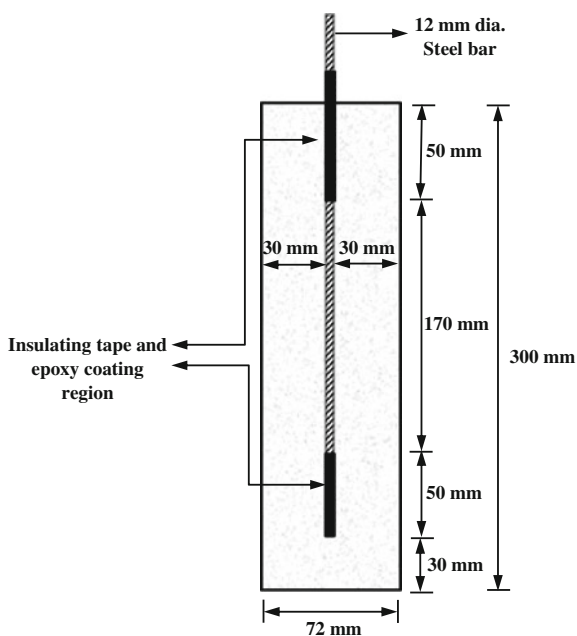
w/c ratio	Cement	Water	Aggregates		SP <sup>c</sup>
			CA <sup>a</sup>	FA <sup>b</sup>	
0.40	487.5	195	755.3	786.1	3.90
0.43	453.5				3.63

<sup>a</sup>Coarse aggregate<sup>b</sup>Fine aggregate<sup>c</sup>Superplasticizer

## 2.2 Tests on Fresh SCC and Specimen Preparation

Slump flow,  $T_{50\text{cm}}$  time, V-funnel flow time, L-box, and sieve segregation tests were conducted on the fresh SCC mixes to evaluate essential properties of SCC such as filling ability, passing ability, and segregation resistance. The tests for evaluating fresh property of SCC mixes were conducted as per EFNARC guidelines [16]. In order to determine compressive strength, cube specimens of size 150 mm were prepared from SCC mixes. For measurement of corrosion parameters, prismatic reinforced concrete specimens of size 300 mm  $\times$  72 mm  $\times$  72 mm with a centrally embedded steel bar (Tempcore TMT Steel) of 12 mm diameter were made from SCC mixes. The schematic diagram of prismatic reinforced concrete specimen is shown in Fig. 2. The steel bar was coated with insulating tape followed by epoxy coating at the bottom of the steel bar and at the concrete–air interface (Fig. 2) to avoid crevice corrosion. The exposed length of steel bar inside the prismatic

**Fig. 2** Schematic diagram of prismatic reinforced SCC specimen



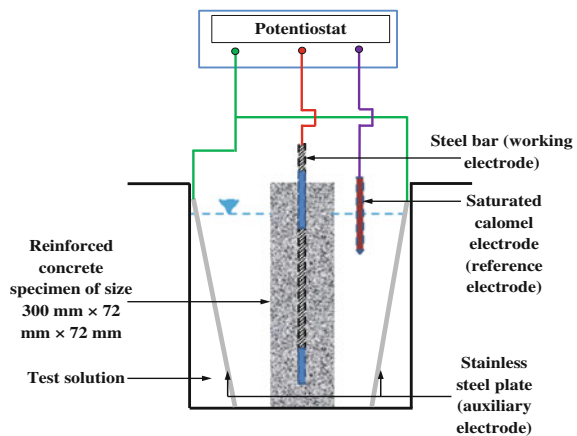
specimen was 170 mm, and a concrete cover depth of 30 mm was provided at the bottom and on all sides in the prismatic specimen.

### 2.3 Tests on Hardened SCC

After 24 h of preparation, the cube and prismatic reinforced concrete specimens prepared from SCC mixes were subjected to water curing in a curing tank till 28 days from the day of preparation. After completion of moist curing, the 28-day compressive strength of SCC cubes was determined in a compression testing machine. After removal from curing tank at the completion of curing, the prismatic reinforced specimens were kept in laboratory dry condition for a period of 14 days and were then exposed to sodium chloride (NaCl) solutions of concentrations 0, 1, and 3% with alternate wetting–drying cycles for an exposure period of 180 days. The alternate wetting–drying cycle consists of 3 days of wetting (i.e., partially immersing the specimen in NaCl solution up to a height of 255 mm from its bottom in a plastic tank) followed by 7 days of laboratory drying. Corrosion parameters such as half-cell potential and corrosion current density by linear polarization resistance (LPR) technique were measured for all prismatic reinforced concrete specimens at the end of exposure periods of 90 and 180 days. Corrosion monitoring instrument (make: ACM, Gill AC serial no. 1542) was used for the measurement of corrosion parameters. The schematic representation of experimental setup is shown in Fig. 3.

The experimental setup consists of a plastic container filled with sodium chloride solution with concentration same as the exposure solution, three electrode system, and corrosion monitoring instrument (potentiostat). The three electrode systems consist of working electrode (steel bar embedded in prismatic specimen), auxiliary electrode (stainless steel plates), and reference electrode (saturated calomel electrode). These electrodes were connected to the potentiostat. The half-cell potential of steel bar embedded in SCC specimen was measured with reference to saturated

**Fig. 3** Experimental setup for half-cell potential and LPR measurements on SCC specimens



calomel electrode (SCE). For determining corrosion current density of steel reinforcement in SCC specimen, linear polarization resistance (LPR) measurement was carried out. During LPR measurement, the steel reinforcement embedded in concrete was polarized to  $\pm 20$  mV from the equilibrium potential at a scan rate of 6 mV per min. For calculation of corrosion current density ( $I_{\text{corr}}$ ), Stern–Geary equation was used [4].

$$I_{\text{corr}} = \frac{B}{R_p} \quad (1)$$

where

$I_{\text{corr}}$  Corrosion current density,

$B$  Stern–Geary constant,

$R_p$  Polarization resistance of steel reinforcement.

The Stern–Geary constant ‘ $B$ ’ is given by

$$B = \frac{\beta_a \times \beta_c}{2.3[\beta_a + \beta_c]} \quad (2)$$

where

$\beta_a$  Anodic Tafel constant

$\beta_c$  Cathodic Tafel constant.

The value of ‘ $B$ ’ was taken as 26 mV considering steel reinforcement in active condition [5].

### 3 Results and Discussion

The results of fresh properties and 28-day compressive strength of SCC mixes are shown in Table 2.

From the results presented in Table 2, it is observed that the SCC mixes are satisfying the acceptance criteria in terms of filling ability, passing ability, and segregation resistance as per EFNARC guidelines [16]. The slump flow,  $T_{50\text{cm}}$  time,

**Table 2** Properties of SCC in fresh and hardened state

Properties	w/c ratio of 0.40	w/c ratio of 0.43
Slump flow (mm)	675	670
$T_{50\text{cm}}$ time (s)	1.6	1.06
V-funnel flow time (s)	3.89	3.42
Passing ratio	0.82	0.82
Segregation index (%)	6.68	10.22
Compressive strength (N/mm <sup>2</sup> )	43.7	41.33

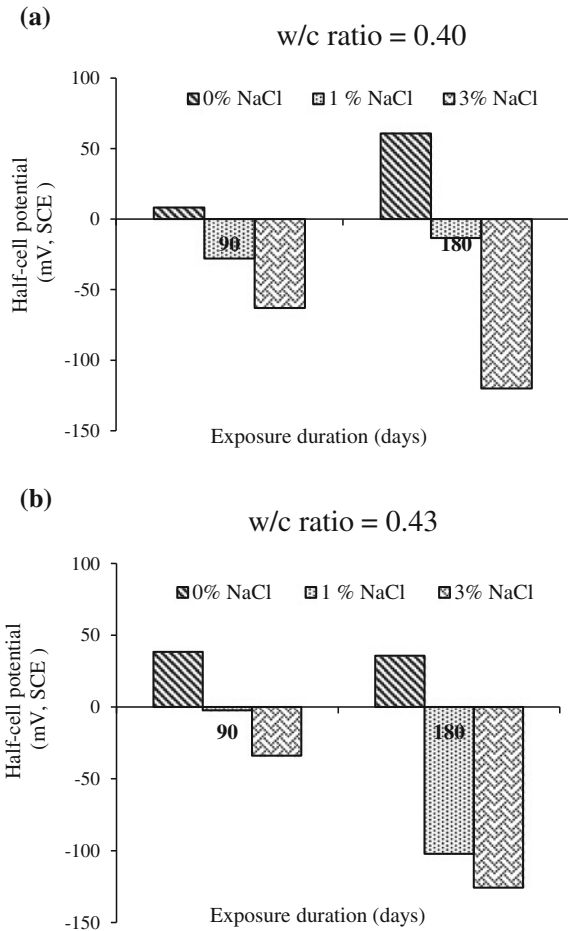
and V-funnel flow time of SCC mixes decreased with increase in  $w/c$  ratio. The passing ratio (L-box test) is same at both  $w/c$  ratios, and segregation resistance is higher at lower  $w/c$  ratio (0.40) as compared to that at higher  $w/c$  ratio (0.43).

The 28-day compressive strength of SCC mix shown in Table 2 is the average value of three replicate cube specimens. From Table 2, it is observed that the 28-day compressive strength of SCC mixes decreased with increase in  $w/c$  ratio.

The half-cell potential values of steel reinforcement in SCC specimens are shown in Fig. 4a, b for  $w/c$  ratios of 0.40 and 0.43, respectively. The potential values shown in these figures are the average values of three replicate specimens. As per ASTM C876 guidelines [17], the potential values more negative than  $-350$  mV (Cu/CuSO<sub>4</sub>)/ $-270$  mV (SCE) correspond to a greater probability of occurrence of steel reinforcement corrosion. From Fig. 4a, b, it is observed that the half-cell potential values are less negative than  $-270$  mV (SCE) for both exposure durations, which indicate lower probability of occurrence of steel reinforcement corrosion. Further, the half-cell potential values were more negative in the specimens exposed to NaCl solutions (1 and 3%) as compared to those exposed normal water (0% NaCl) for both  $w/c$  ratios and both exposure periods. In addition, it is observed that the half-cell potential values became less negative with increase in  $w/c$  ratio (i.e., from 0.40 to 0.43) for different exposure solutions at the exposure period of 90 days. However, at the exposure period of 180 days, the half-cell potential values decreased (i.e., became more negative) with increase in  $w/c$  ratio for different exposure solutions and especially, there was a significant decrease in the half-cell potential value for the specimens exposed to 1% NaCl solution as compared to those exposed to other solutions as the  $w/c$  ratio increased from 0.40 to 0.43. This may be attributed to polarization phenomena induced by limited oxygen diffusion [5], resulting in a significant decrease in half-cell potential value with increase in  $w/c$  ratio from 0.40 to 0.43 for 1% NaCl solution at the exposure period of 180 days, although the half-cell potential values are less negative than  $-270$  mV (SCE).

The corrosion current density of steel reinforcement in SCC specimens is shown in Fig. 5a, b for  $w/c$  ratios of 0.40 and 0.43, respectively. Each value of corrosion current density shown in these figures is the average value of three replicate specimens. From these figures, it is noted that there is no systematic variation in corrosion current density with concentration of NaCl in the exposure solution at the exposure period of 90 days. However at the exposure period of 180 days, the corrosion current density of steel reinforcement in SCC specimens increased with increase in concentration of NaCl in the exposure solution for both  $w/c$  ratios. This may be attributed to increase in conductivity of concrete due to penetration of higher amount of chloride ions when exposed to NaCl solutions of higher concentration. Further, the corrosion current density of steel bar in SCC mixes increased with increase in  $w/c$  ratio at the exposure period of 180 days as observed from Fig. 5a, b. However, there is no systematic variation in corrosion current density with  $w/c$  ratio at the exposure period of 90 days.

**Fig. 4 a** Half-cell potential of steel in SCC specimens exposed to different concentrations of sodium chloride solutions at *w/c* ratio of 0.40 and **b** half-cell potential of steel in SCC specimens exposed to different concentrations of sodium chloride solutions at *w/c* ratio of 0.43



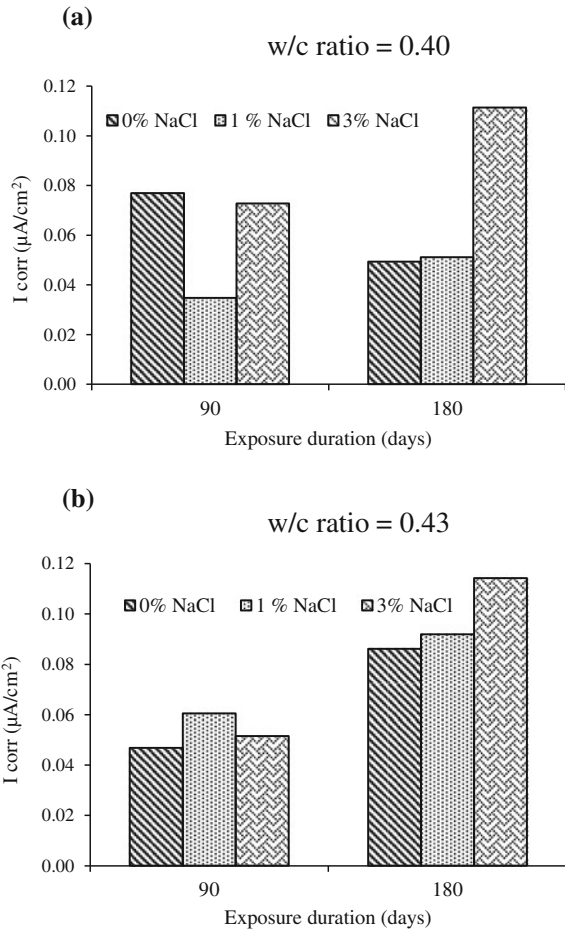
### 4 Conclusions

The present study was carried out to evaluate the fresh, hardened, and durability properties of self-compacting concrete (SCC) made with OPC at *w/c* ratios of 0.40 and 0.43. From the obtained results of this study, the following conclusions were drawn.

The SCC mixes satisfied the acceptance criteria for fresh properties in terms of filling ability, passing ability, and segregation resistance as per EFNARC guidelines.

The measured half-cell potential values indicated lower probability of occurrence of steel reinforcement corrosion in SCC specimens exposed to NaCl solutions of different concentrations, as the potential values were less negative than  $-270$  mV (SCE) at both *w/c* ratios and both exposure durations.

**Fig. 5 a** Corrosion current density of steel in SCC specimens exposed to different concentrations of sodium chloride solutions at  $w/c$  ratio of 0.40 and **b** corrosion current density of steel in SCC specimens exposed to different concentrations of sodium chloride solutions at  $w/c$  ratio of 0.43



The corrosion current density of steel reinforcement in SCC specimens increased with increase in NaCl concentration in the exposure solution and with increase in  $w/c$  ratio at the longer exposure period (i.e., 180 days). Further, there was no systematic variation in corrosion current density with NaCl concentration in the exposure solution and with  $w/c$  ratio at the exposure period of 90 days.

## References

1. Madandoust R, Mousavi SY (2012) Fresh and hardened properties of self-compacting concrete containing metakaolin. *Constr Build Mater* 35:752–760
2. Melo KA, Carneiro AMP (2010) Effect of Metakaolin's finesses and content in self-consolidating concrete. *Constr Build Mater* 24:1529–1535



3. Dehwah HAF, Maslehuddin M, Austin SA (2003) Effect of sulfate ions and associated cation type on the pore solution chemistry in chloride-contaminated plain and blended cements. *Cem Concr Compos* 25:513–525
4. Al-Amondi OSB, Maslehuddin M (1993) The effect of chloride and sulfate ions on reinforcement corrosion. *Cement Concr Res* 23:139–146
5. Pradhan B (2014) Corrosion behavior of steel reinforcement in concrete exposed to composite chloride–sulfate environment. *Constr Build Mater* 72:398–410
6. Maes M, Belie ND (2014) Resistance of concrete and mortar against combined attack of chloride and sodium sulphate. *Cem Concr Compos* 53:59–72
7. Liu T, Weyers RW (1998) Modeling the dynamic corrosion process in chloride contaminated concrete structures. *Cem Concr Res* 28:365–379
8. Kayali O, Zhu B (2005) Corrosion performance of medium-strength and silica fume high-strength reinforced concrete in a chloride solution. *Cem Concr Compos* 27:117–124
9. Aguirre-Guerrero AM, Mejía-de-Gutiérrez R, Montês-Correia MJR (2016) Corrosion performance of blended concretes exposed to different aggressive environments. *Constr Build Mater* 121:704–716
10. Pradhan B, Bhattacharjee B (2007) Role of steel and cement type on chloride-induced corrosion in concrete. *ACI Mater J* 104:612–619, November–December 2007
11. Ahmad S, Adekunle SK, Maslehuddin M, Azad AK (2014) Properties of self-consolidating concrete made utilizing alternative mineral fillers. *Constr Build Mater* 68:268–276
12. Dinakar P, Babu KG, Santhanam M (2009) Corrosion resistance performance of high-volume fly-ash self-compacting concretes. *Mag Concr Res* 61:77–85
13. Dehwah HAF (2012) Corrosion resistance of self-compacting concrete incorporating quarry dust powder, silica fume and fly ash. *Constr Build Mater* 37:277–282
14. Hassan AAA, Hossain KMA, Lachemi M (2009) Corrosion resistance of self-consolidating concrete in full-scale reinforced beams. *Cem Concr Compos* 31:29–38
15. ACI 237R-07 (2007) Self-consolidating concrete
16. EFNARC (2005) The European guidelines for self-compacting concrete: specification, production and use May, 2005
17. ASTM C876-09 (2009) Standard test method for corrosion potentials of uncoated reinforcing steel in concrete. ASTM International, West Conshohocken (PA)

# Seismic Damage Evaluation of RC Buildings Using Nonlinear Static Method



Santanu Paul and Suman Debnath

**Abstract** The main objective of this chapter is to evaluate the expected seismic damage in reinforced concrete buildings from a deterministic point of view. To do that, a typical low-rise and mid-rise RC building is designed for two design cases according to the provisions of Indian codes IS 456 and IS 1893 as a gravity load and earthquake-resistant designed building. These are analyzed using nonlinear static procedure as ATC 40 and fragility analysis by HAZUS methodology. Starting from the determination of capacity curves from capacity spectrum-based method which revealed the nonlinear performances of buildings together with fragility curves, damage probability matrices (DPM) are formed for maximum considered earthquake (MCE) and design basis earthquake (DBE) to evaluate the damage state. The study suggests that the earthquake-resistant designed buildings show better performances and lie in low-level damage as compared to gravity load designed buildings.

**Keywords** Capacity curve · Fragility curve · Damage probability matrices

## 1 Introduction

The very exponential increase in the population of the world, along with the growing big cities which are characterized by the inadequate occupancy of the land, contributes increased damage due to seismic catastrophes. The high concentration of population, high-rise buildings, infrastructures, and exposed values turn these zones into high-risk areas. The Seismic Zone Map of India (2002) emphasizes that about 59% of land area is under moderate-to-very severe earthquake and liable to

---

S. Paul · S. Debnath (✉)

Department of Civil Engineering, National Institute of Technology Agartala,  
Agartala 799046, India  
e-mail: sumantwenty4@gmail.com

S. Paul

e-mail: santanupaul22@gmail.com

© Springer Nature Singapore Pte Ltd. 2019

A. Rama Mohan Rao and K. Ramanjaneyulu (eds.), *Recent Advances in Structural Engineering, Volume 2*, Lecture Notes in Civil Engineering 12,  
[https://doi.org/10.1007/978-981-13-0365-4\\_48](https://doi.org/10.1007/978-981-13-0365-4_48)

559

higher intensity. In past, India has already experienced large damaging earthquakes such as the 1897 Shillong Earthquake ( $M_w$  8.1); the 1918 Srimangal Earthquake ( $M_s$  7.6); the 1950 Assam Earthquake ( $M_w$  8.7). Recently, the 2001 Bhuj Earthquake and 2011 Sikkim Earthquake highlighted the seismic vulnerability and revealed the condition of the RC buildings in India. However, a considerable portion of the building stock of country is low-rise and mid-rise reinforced concrete (RC) buildings which are designed mainly for gravity loads and are few as earthquake-resistant. Hence, special attention has to be given to those large number of gravity load designed RC buildings to execute seismic hazard mitigation strategy along with earthquake-resistant designed buildings.

The aim of seismic vulnerability evaluation is to find the deficiencies in structure before taking appropriate measures to upgrade the system. Several methodologies have been developed to estimate the vulnerability of buildings together with the damage evaluation, and time by time, these methodologies have been improved. The nonlinear static analysis is used to evaluate the seismic performances of RC buildings, which represents structural behavior. A convenient and widely adopted way of determining seismic damages is using the fragility curves and DPM which are derived by different methods and based on various types of data and seismic parameters. The use of DPM for the probabilistic prediction of damage to buildings from earthquakes was first developed in 1974 [1]. Collective efforts have also been made to arrive a simple rationalized procedure for regular use in formulation of fragility curves and damage probability matrices [2, 3] etc.

Here, seismic performance and damage evaluation of a low-rise (three-storied) and mid-rise (seven-storied) RC building, designed under gravity load (GLD) and earthquake-resistant (ERD) as per Indian codes IS 456 2000 [4] and IS 1893 2002 [5], are considered. Nonlinear static analysis [6] is carried out using available computer program SAP2000 (V16) along with fragility analysis using HAZUS<sup>®</sup>-MH MR5 [7] methodology. The main objective of the present study is to find out the damage state of gravity load designed and earthquake-resistant designed three-storied and seven-storied RC framed buildings by developing the capacity curve, fragility curve, and damage probability matrices (DPM), considering two different seismic hazard levels, i.e., maximum considered earthquake (MCE) and design basis earthquake (DBE).

## 2 Capacity Spectrum-Based Method

The capacity spectrum-based method [6] has been used in this study to evaluate the performances of the RC buildings in nonlinear static analysis (pushover) when subjected to earthquake scenarios which are represented by 5% damped elastic response spectra. For performance evaluation of structure, selection of load pattern is vital which represents the distribution of inertia forces imposed on the structure during an earthquake. The vertical distribution of seismic forces as given in FEMA 356 [8] is considered here.

### 3 Fragility Analysis

In fragility analysis, the relationship between ground motion severity (peak ground acceleration or spectral displacement) and structural damage is expressed in terms of probabilistic form. It is represented either in graphical form such as fragility curves or in tabular form such as damage probability matrices. Fragility curve describes the probability that a structure will reach or exceed one particular damage state as a function of seismic ground motion (spectral acceleration, spectral velocity, and spectral displacement). In the present study, spectral displacement is considered. According to HAZUS methodology, it is given as follows:

$$P[ds|S_d] = \phi \left[ \frac{1}{\beta_{ds}} \ln \left( \frac{S_d}{\bar{S}_{d,ds}} \right) \right]$$

where  $S_d$  is spectral displacement,  $\bar{S}_{d,ds}$  is the median value of spectral displacement at which the building reaches the damage-state threshold,  $ds$ ;  $\beta_{ds}$  is the standard deviation of the natural logarithm of spectral displacement for damage state,  $ds$ ;  $\phi$  is the standard normal cumulative distribution function.

The dispersion of fragility curve for a given damage state primarily depends on the lognormal variability associated with the discrete threshold of each damage grade  $\beta_{T,ds}$ , the lognormal variability associated with the capacity curve  $\beta_C$ , and the lognormal variability associated with the demand spectrum  $\beta_D$ . Since the demand spectrum for equivalent damping is dependent on building ductility capacity, a convolution process is required to find out the total variability  $\beta_{ds}$ , but this convolution process involves a complex numerical calculation that would be very difficult to perform as the demand and capacity are correlated. This difficulty is avoided by using the pre-calculated values of damage-state beta values taken from HAZUS<sup>®</sup>-MH MR5 [7], considering moderate condition, corresponding to  $\beta_C = 0.3$ ,  $\beta_{T,ds} = 0.4$  for  $\beta_{ds}$  in case of low-rise building and mid-rise building.

In this study, four damage states are considered as guided by HAZUS<sup>®</sup>-MH MR5 [7] which are based on performances of structures to define the damage-state thresholds. Barbat et al. [2] have proposed damage-state thresholds based on yield and ultimate spectral displacement of the building which is shown in Table 1. The yield spectral displacement ( $S_{dy}$ ) and ultimate spectral displacement ( $S_{du}$ ) are obtained analytically from the bi-linearization of capacity curve. A mean damage index or weighted average damage index ( $DS_m$ ) is considered which is close to the most likely damage state of the structure and can be calculated using this formula  $DS_m = \sum ds_i P[ds_i]$ , where  $ds_i$  takes the values 1, 2, 3, and 4 for the damage states  $i$  considered in the analysis and  $P[ds_i]$  are the corresponding occurrence probabilities. Table 2 shows the most probable damage grade as a function of the mean damage index.

**Table 1** Damage-state thresholds (Barbet et al. [2])

Damage grade	Damage state	Damage-state threshold
DG1	Slight	$S_{d1}^- = 0.7 S_{dy}$
DG2	Moderate	$S_{d2}^- = S_{dy}$
DG3	Severe	$S_{d3}^- = S_{dy} + 0.25$ ( $S_{du} - S_{dy}$ )
DG4	Complete	$S_{d4}^- = S_{du}$

**Table 2** Damage states and mean damage index values (Barbet et al. [2])

Mean damage index intervals	More probable damage state
0–0.5	No damage
0.5–1.5	Slight damage
1.5–2.5	Moderate damage
2.5–3.5	Severe damage
3.5–4.0	Complete damage

### 4 Description of RC Buildings and Seismic Hazards

In the present study, three-dimensional regular three-story and seven-story reinforced concrete bare frame residential buildings are considered which represents low- and mid-rise buildings. These buildings are designed under gravity load and earthquake-resistant as per IS 456 (2000) and IS 1893 (2002) as GLD and ERD RC buildings. These buildings are symmetrical in plan with both directions, and the number of bays considered in each direction is four. The story height of each building has been considered as 3 m having a floor area of 16 m × 16 m. M25 grade concrete, Fe 415 grade for longitudinal steel and Fe 250 grade for transverse steel are considered for the design of building. The thickness of infill wall is considered 0.250 m for exterior and 0.125 m for interior partitions. Only the loads of the infill are considered which are uniformly distributed along the length of beams in the frame. The slab thickness is assumed as 0.125 m at different story levels. The dead loads conforming IS 875 Part-1, 1987a [9] and imposed loads conforming IS 875 Part 2, 1987b [10] of the RC buildings are taken.

To study the seismic performance of these low- and mid-rise RC buildings, two hazard levels such as design basis earthquake (DBE) and maximum considered earthquake (MCE) are taken, considering 5% damped accelerating response spectrum for medium soil site of zone V having peak ground acceleration of 0.36 g.

### 5 Modeling Approaches

In the present study, beam and column elements are modeled as nonlinear frame elements with lumped plasticity by defining plastic hinges accounting for the material nonlinearity. For RC frame buildings subjected to lateral loads such as seismic action, flexural deformations occur near the frame elements' extremities

and hence flexural hinges are assigned to the member ends while modeling. Coupled P-M2-M3 hinges considering the interaction of axial force and bending moments are used for columns, and uncoupled moment or flexural M3 hinges are used for beams. Properties of flexural hinges generate the actual response of reinforced concrete components subjected to lateral load. The hinge properties which are used here according to FEMA-356 [8] are section-dependent.

## 6 Results and Discussions

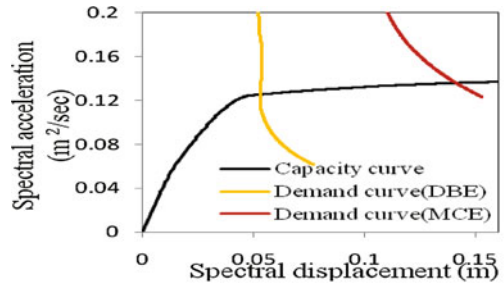
The pushover curve shows the total base shear (in terms of building weight) as a function of roof drift with its bilinear representation. From pushover curve, yield displacement and ultimate displacement defining the bilinear spectra for the modeled RC buildings are evaluated and given in Table 3. The yield point represents the strength level beyond which the response of the building is strongly nonlinear. The ultimate point is related to the maximum strength of the building when the global structural system reached a full plastic mechanism.

Capacity curves (spectral acceleration and spectral displacement) in ADRS format are shown in Fig. 1 for RC buildings considering design basis earthquake (DBE) and maximum considered earthquake (MCE) which are very much useful in ascertaining whether and how a structure is capable of sustaining certain level of seismic load and its behavior in the nonlinear or inelastic range. Performance point is the intersection of the capacity curve with the appropriate demand curve in the capacity spectrum method and is calculated using the iterative method (procedure A) of equal displacement approximation according to ATC-40, 1993 [6]. It represents the inelastic or nonlinear displacement that the structure is going to experience for the given level of earthquake. Using this point, the associated damage state for the structure can be evaluated and this damage state can be compared for different earthquakes. From these capacity curves, it has been observed that the performance points are coming in nonlinear range, i.e., beyond the yield point in both DBE and MCE hazard levels for all the RC buildings. From these capacity curves, it has been observed that the performance points are coming in nonlinear range, i.e., beyond the yield point in both DBE and MCE hazard levels for all the RC buildings.

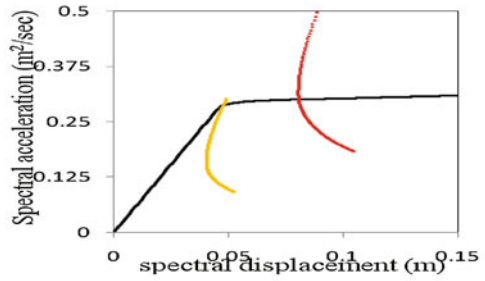
**Table 3** Yield and ultimate spectral displacement for RC buildings

Building class	Displacement (m)		Spectral displacement (m)	
	Yield	Ult	Yield	Ult
Low-rise	0.041	0.236	0.032	0.185
GLD	0.064	0.170	0.048	0.129
ERD				
Mid-rise	0.037	0.317	0.028	0.241
GLD	0.096	0.267	0.096	0.200
ERD				

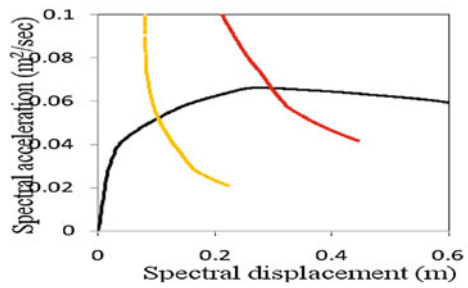
**Fig. 1** Capacity curves for RC buildings



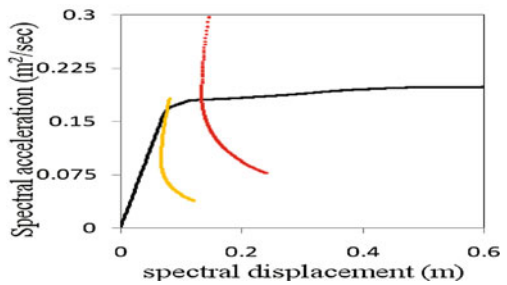
(a) Low rise (GLD)



(b) Low rise (ERD)



(c) Mid rise (GLD)



(d) Mid rise (ERD)

Table 4 shows the spectral acceleration and spectral displacement parameters corresponding to performance point for DBE and MCE of RC buildings. The spectral displacement is coming higher for MCE as compared to DBE with respect to its performance point for low- and mid-rise RC buildings. So, from this it is clear that RC buildings show good performance in DBE as compared to MCE as spectral displacement is very lower in DBE. And it also depicts that in both DBE and MCE hazard levels ERD buildings show good behavior as compared to GLD buildings in both low- and mid-rise categories. In DBE, low-rise GLD RC building is subjected to the spectral displacement of 53 mm, whereas for ERD RC building it is decreasing and subjected to 48 mm. And in MCE, it significantly varies from 141 to 81 mm. Similar trend has been observed in mid-rise RC building for DBE and MCE. It implies that the ERD RC buildings have higher stiffness and strength due to slenderness and failure criterion used in the design of buildings and pushover analysis.

Table 5 shows the median spectral displacement for slight, moderate, extensive, complete damage states of low-rise and mid-rise RC buildings which are obtained from damage-state thresholds that considered after Barbet et al. [2]. Specific fragility curves have been developed for RC buildings and shown in Fig. 2. It shows that, in DBE at 53-mm spectral displacement (performance point), the expected probability of low-rise GLD building for the slight damage is nearly 86%, moderate damage 70%, severe damage 39%, and complete damage 11%, whereas at 48-mm spectral displacement ERD building possesses it 67, 49, 36, and 17%, respectively. For mid-rise GLD building, at 103-mm spectral displacement the slight damage is

**Table 4** Spectral acceleration and spectral displacement at performance point for RC buildings

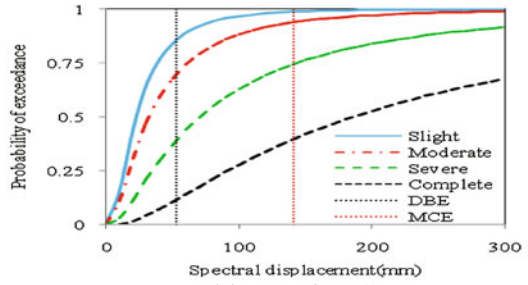
Building class	Spectral acceleration ( $S_a$ ) (m <sup>2</sup> /sec)		Spectral displacement ( $S_d$ ) (m)	
	DBE	MCE	DBE	MCE
Low-rise	0.125	0.136	0.053	0.141
GLD	0.287	0.300	0.048	0.081
ERD				
Mid-rise	0.052	0.066	0.103	0.290
GLD	0.167	0.181	0.077	0.134
ERD				

**Table 5** Median spectral displacement of different damage grades for RC buildings

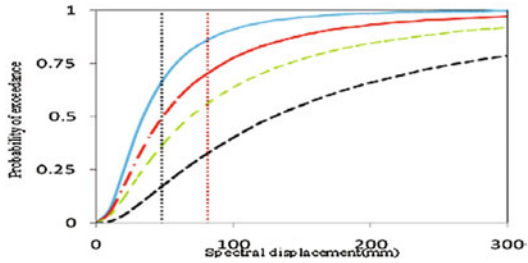
Building class	Median spectral displacement (mm)			
	DG1	DG2	DG3	DG4
Low-rise	22.41	32.02	70.2	184.8
GLD	33.94	48.49	68.7	129.4
ERD				
Mid-rise	19.86	28.38	81.58	241.21
GLD	50.52	72.20	104.2	200.30
ERD				



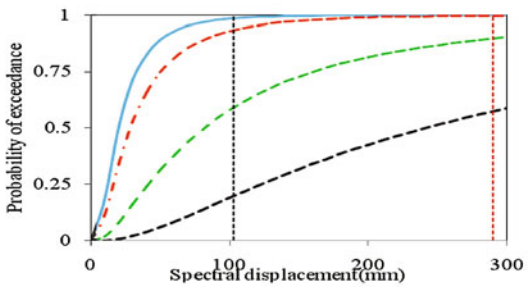
**Fig. 2** Fragility curves for RC buildings



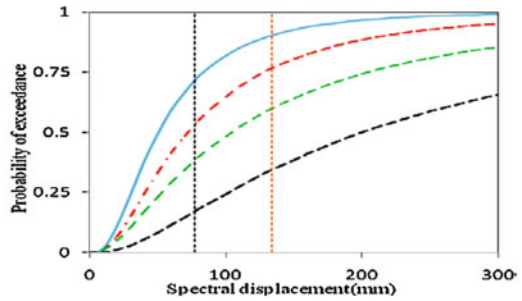
**(a)** Low rise (GLD)



**(b)** Low rise (ERD)



**(c)** Mid rise (GLD)



**(d)** Mid rise (ERD)

**Table 6** Damage probability matrices (DPM) and probable damage state of RC buildings for design basis earthquake (DBE) hazard level

Building class	Damage-state probabilities				DS <sub>m</sub>	Probable damage state
	DG1	DG2	DG3	DG4		
<i>Low-rise</i>						
GLD	0.157	0.308	0.277	0.117	2.07	Moderate
ELD	0.172	0.129	0.194	0.172	1.70	Moderate
<i>Mid-rise</i>						
GLD	0.051	0.343	0.395	0.197	2.71	Severe
ELD	0.193	0.149	0.212	0.169	1.80	Moderate

**Table 7** Damage probability matrices (DPM) and probable damage state of RC buildings for maximum considered earthquake (MCE) hazard level

Building class	Damage-state probabilities				DS <sub>m</sub>	Probable damage state
	DG1	DG2	DG3	DG4		
<i>Low-rise</i>						
GLD	0.049	0.194	0.348	0.398	3.07	Severe
ERD	0.156	0.143	0.235	0.328	2.46	moderate
<i>Mid-rise</i>						
GLD	0.003	0.095	0.319	0.582	3.48	Severe
ERD	0.137	0.167	0.255	0.344	2.61	Severe

98%, moderate damage is 93%, severe damage is 59%, and complete damage is 19%, whereas at 77-mm spectral displacement for ERD building these damages are 72, 53, 38, and 17%.

Similarly in MCE, at 141-mm spectral displacement the low-rise GLD building undergoes slight damage of 98.9%, moderate damage of 94%, severe damage of 74%, and complete damage of 40%, whereas at 81-mm spectral displacement ERD building depicts it 86, 70, 56, and 33%, respectively. For mid-rise GLD building, at 290-mm spectral displacement the slight damage is 99.9%, moderate damage is 99.6%, severe damage is 90%, and complete damage is 58%, whereas for ERD at 134-mm spectral displacement building these damages are 90, 76, 60, and 34%. Therefore, from the above results it is clear that the earthquake-resistant designed buildings depict fewer damages and gravity load designed building experienced higher level of damages in both DBE and MCE levels.

For each case of earthquake hazard level, damage probability matrices (DPM) strongly depend on the spectral displacement at the performance point and the capacity of the building. Tables 6 and 7 show the damage probability matrices and probable damage state of the considered RC buildings for both DBE and MCE hazard levels.

Using the mean damage index intervals from Table 2, in case of DBE it has been observed that both the gravity load designed and earthquake-resistant designed

low-rise RC buildings lie in moderate damage state. Though they lie in moderate damage state, the mean damage index varies significantly for ERD as compared to GLD building, and it is high in case of GLD building. Whereas mid-rise RC building is lie in severe-to-moderate damage state in both GLD and ERD buildings. In case of MCE, the low-rise GLD RC building lies in severe damage state and ERD RC building in moderate damage state. However, the GLD and ERD mid-rise RC buildings lie in severe damage state with significantly varying mean damage index. From the above, it is clear that earthquake-resistant designed (ERD) as ordinary moment-resistant frame buildings show better performance compared to gravity load designed RC buildings and it lies in lower-level damage state.

## 7 Conclusion

In this study, seismic performances and damages of gravity load designed and earthquake-resistant designed low-rise and mid-rise RC bare frame buildings have been evaluated for the lateral load pattern according to FEMA 356 [8] using nonlinear static analysis. Fragility analysis has also been performed to develop fragility curves which characterize the expected structural damage in probabilistic way. The damage probability matrices are developed to identify the damage state of RC buildings. The fragility curves indicate higher damage probability for gravity load designed RC buildings as compared to earthquake-resistant designed buildings. Using damage probability matrices (DPM) and mean damage index intervals, it has been found that the gravity load designed low- and mid-rise RC buildings experience higher damage as compared to earthquake-resistant designed RC buildings under both DBE and MCE hazard levels.

## References

1. Whitman RV, Reed JW, Hong ST (1973) Earthquake damage probability matrices. In: Proceedings of the fifth world conference on earthquake engineering vol 2, Rome, Italy, pp 2531–2540
2. Barbat AH, Pujades LG, Lantada N (2008) Seismic damage evaluation in urban areas using the capacity spectrum method: application to Barcelona. *Soil Dyn Earthquake Eng* 28: 851–865
3. Fajfar P (2000) A non linear analysis method for performance-based seismic design. *Earthquake Spectra* 16(3):573–592
4. BIS 456 (2000) Indian standard for plain and reinforced concrete—code of practice. Bureau of Indian Standards, New Delhi
5. BIS 1893 (1987) Part 1, Indian standard criteria for earthquake resistant design of structures. Bureau of Indian Standards, New Delhi
6. ATC (1996) Seismic evaluation and retrofit of concrete buildings, report ATC-40 (also report no. SSC 96-01. California Seismic Safety Commission), Applied Technology Council. Redwood City, CA, U.S.A.

7. FEMA/NIBS methodology (HAZUS<sup>®</sup>-MH MR5) (2003) Advanced engineering building module: technical and user's manual, Federal Emergency Management Agency, Washington DC, USA
8. FEMA (2000) Pre-standard and commentary for the seismic rehabilitation of buildings, report FEMA-356, Federal Emergency Management Agency, Washington DC, USA
9. BIS 875 (1987) Part 1, design loads (other than earthquake) for buildings and structures. Dead loads—code of practice. Bureau of Indian Standards, New Delhi
10. BIS 875 (1987) Part 2, design loads (other than earthquake) for buildings and structures. Imposed loads—code of practice. Bureau of Indian Standards, New Delhi

# Seismic Fragility of Reinforced Concrete Frames with Vertical Irregularities



T. Choudhury and H. B. Kaushik

**Abstract** Seismic fragility functions are essential for performance-based seismic design of structures. It is a common practice in the past to consider global demand parameters, such as peak roof displacement or drift in a building to estimate its seismic fragility. However, such global demand parameters may not suffice in case of buildings with vertical irregularities, where maximum demand is mostly concentrated at the level of irregularity. To investigate the matter, reinforced concrete frames with and without vertical irregularity (soft storey) are considered in the current study. Nonlinear dynamic analysis of the frames subjected to ground motions scaled-up for different PGA is carried out to estimate the local and global drift demands, also known as engineering demand parameters (EDPs). Seismic fragilities developed for the frames based on both the local and global EDPs are presented. Finally, the importance of component-based fragilities for irregular frames is emphasized.

**Keywords** Reinforced concrete frames · Vertical irregularity · Seismic fragility

## 1 Introduction

This paper provides an investigation into the seismic fragility assessment methodologies for reinforced concrete (RC) frames with and without vertical irregularities (soft storey). The most common engineering demand parameter (EDP) considered in a large-scale fragility assessment of building includes peak roof or top storey displacement. Here, the global displacement or drift response of the building is entirely defined by the top storey displacement. However, such a

---

T. Choudhury · H. B. Kaushik (✉)  
Department of Civil Engineering, Indian Institute of Technology Guwahati,  
Guwahati, India  
e-mail: hemantbk@iitg.ac.in

T. Choudhury  
e-mail: c.trishna@iitg.ac.in

methodology is insufficient to describe exactly the failure mechanism in a building particularly in case of irregular frames, such as open ground storey (OGS) frames, where the failure is mostly concentrated at the level of irregularity. OGS columns lack adequate ductility capacity, stiffness, and strength needed to resist the high demand of storey shear. This leads to an undesirable column-sway failure mechanism in OGS buildings subjected to earthquake excitations, in which failure occurs mostly in the columns of the ground storey. In contrast, the infills present in the upper stories restrain the deformation of the upper storey, and thus, little damage is incurred in the upper storeys. Figure 1 shows two such OGS buildings, which suffered severe damage in the ground storey during 1999 Kocaeli earthquake [1] and 2004 Sumatra earthquake [2]. These buildings were found to be damaged even in a moderate level of earthquake intensity without any noticeable damage in the upper stories of the building.

The existing fragility assessment procedures, e.g., HAZUS [3], require displacement thresholds to be defined for a frame type that specify the limiting capacity of the frame at various damage levels. Several document and literature suggest such limiting values for different frame typologies. HAZUS defines these thresholds based on average interstorey drift ratio, which can be converted to corresponding top storey displacement by multiplying with the height of the building. This procedure provides a good estimate of fragility for regular frames, but distorts the true fragility of irregular frames.

Hence, a component-level fragility analysis is carried out in the current study to estimate the realistic failure fragility of such buildings. For this purpose, an internal frame (Fig. 2) of a three-bay–four-storey (3B–4S) RC building, designed and detailed for the highest seismic zone as per the relevant Indian Standards [4],

**Fig. 1** **a** An under construction five-storey OGS building severely damaged during 1999 Kocaeli earthquake [1]; **b** a three-storey OGS building collapsed in Port Blair during 2004 Sumatra earthquake [2]



**(a)**



**(b)**

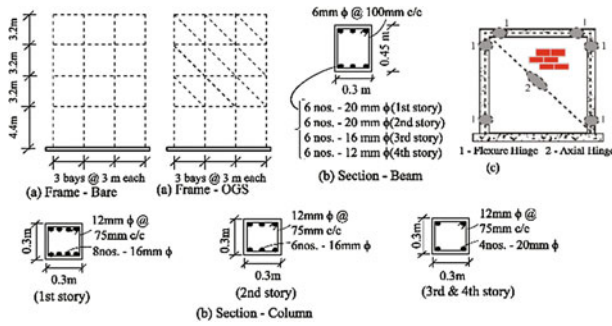


**Fig. 2** a Structural frame—bare and OGS, b sectional details—beams and columns, c RC frame and equivalent strut model with lumped plasticity

is considered. Two different structural configurations representing both regular and irregular frames are considered for the 3B–4S RC frame as listed below:

1. Bare Frame: Masonry infill walls are not provided in any storey (regular frame)
2. Open Ground Storey (OGS) Frame: Masonry infill walls are not provided in the ground storey but provided in all upper storeys (vertically irregular frame)

Nonlinear dynamic analyses of the frames subjected to several ground motions are carried out to obtain the drift demands on the frames both globally, considering roof displacement, and locally, at each storey level. The primary objective of the study is to bring out a favorable engineering demand parameter that defines the failure, and hence the seismic fragility, accurately for RC frames with vertical irregularity.

## 2 Nonlinear Dynamic Analysis

Nonlinear dynamic analyses of the frames are carried out to investigate their dynamic behavior under earthquake excitations. The seismic input is modeled using a time history analysis, which involves time-step-by-time-step evaluation of the building response. For this purpose, 1940 El Centro (Mw 6.9) ground motion scaled for different PGA levels are considered. The peak interstorey drift (ISD) demands and maximum storey displacement for different intensity of ground motion at each floor level is obtained and used as engineering demand parameter (EDP) for seismic fragility estimation.

## 2.1 Generic Buildings and Analytical Modeling

Two different RC building typologies are considered for seismic analysis, namely open ground storey (OGS) frame and bare frame, and modeled in SAP 2000 [5] for dynamic analysis. For the OGS frame, stiffness and strength of masonry infills are considered in the upper stories; however, the ground storey of the frame is kept open, i.e., without masonry infills. For bare frame, masonry infills are not considered in any of the stories.

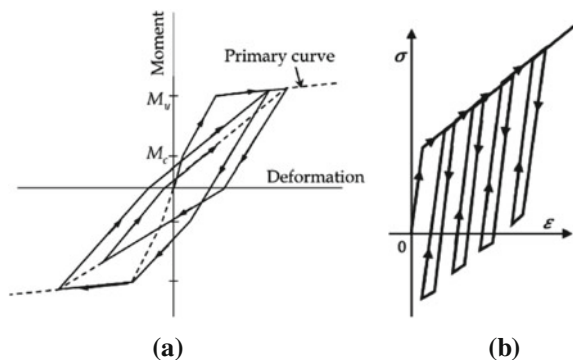
Sectional details of various members of the frame are shown in Fig. 2b. The frames are fixed at the base of ground storey columns. Beams and columns are modeled as line elements with concentrated plasticity defined using fiber sections. The infilled walls are modeled as single equivalent diagonal strut. Length of the strut is determined as diagonal length of the infill panels and width is considered as one-fourth of the diagonal length of the walls.

## 2.2 Material Modeling

The materials considered in the analytical models are concrete, reinforcing steel, and infill. The compressive cube strength of concrete is considered as 25 MPa (Elastic Modulus: 25,000 MPa), and the reinforcing bars have expected yield stress of 450 MPa (Elastic Modulus: 200 GPa). Mander's model [6] is used to characterize the stress–strain curve of concrete. Idealized stress–strain model proposed by [7] is used to model the material nonlinearity in masonry considering masonry prism strength of 4.1 MPa and elastic modulus of 2255 MPa.

The Takeda model [8] as shown in Fig. 3a for hysteresis is considered to model the hysteretic behavior (cyclic degradation) in concrete. This model included stiffness changes at flexural cracking and yielding, and also strain-hardening characteristics. The Takeda model simulates dominantly flexural behavior.

**Fig. 3** **a** Force-deformation relationship of Takeda's degrading stiffness models, **b** typical kinematic hysteresis model for reinforcing bars





The model has a tri-linear envelope curve and is designed to dissipate energy even at low cycles once the cracking point has been exceeded.

Figure 3b shows a typical kinematic hysteresis model [9] used for reinforcing bars. This model is based upon kinematic hardening behavior that is commonly observed in metals. This model dissipates a significant amount of energy and is appropriate for ductile materials. Upon unloading and reverse loading, the curve follows a path made of segments parallel to and of the same length as the previously loaded segments and their opposite-direction counterparts until it rejoins the backbone curve when loading in the opposite direction.

Figure 4 shows the pivot hysteretic model used for equivalent strut model for masonry infill [10]. The pivot model is based mainly on geometrical rules that define loading and unloading branches rather than analytical laws. This reduces not only the computational effort but also the number of hysteretic parameters involved. Moreover, the pivot model has great flexibility in modeling unsymmetrical tension-compression behaviors, as in the case of infill equivalent struts.

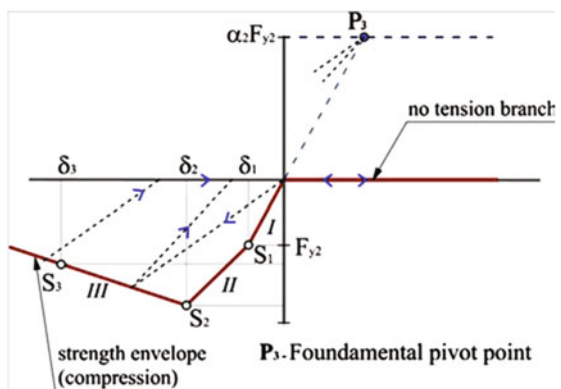
When fiber hinges are used, the cross section is discretized into a series of axial fibers, which extend along the hinge length. Each of these fibers has a stress-strain relationship, and together these give the force-deformation and moment-rotation relationships for the frame section. The fiber hinge is more accurate than the P-M2-M3 hinge, but it is computationally more expensive.

For the frames, first gravity load analysis, as a combination of dead and live loads ( $DL + 0.25 \times LL$ ), is carried out before nonlinear dynamic analysis. P-delta effects are not included in the analyses. Rayleigh damping ( $C$ ) is assumed based on a modal damping ratio of 5% [11] and calculated by using Eq. (1).

$$C = \alpha M + \beta K \tag{1}$$

where  $\alpha$  and  $\beta$  are scale factors calculated from:

**Fig. 4** Hysteretic pivot law particularization for the equivalent diagonal strut [10]



$$\alpha = \frac{2(\xi_i \omega_j - \xi_j \omega_i) \omega_i \omega_j}{\omega_j^2 - \omega_i^2}, \quad \beta = \frac{2(\xi_j \omega_j - \xi_i \omega_i)}{\omega_j^2 - \omega_i^2} \quad (2)$$

Here,  $\omega_i$  and  $\omega_j$  are two of the eigen frequencies of the system and  $\xi_i$  and  $\xi_j$  are their corresponding damping ratios, approximately equal to 0.05. The damping ratio for each mode  $i$  can thereafter be calculated from:

$$\xi_i = \frac{1}{2\omega_i} \alpha + \frac{\omega_i}{2} \beta \quad (3)$$

Nonlinear time history analyses are conducted using El Centro ground motion scaled for different PGA values ranging from 0.3 to 1 g.

### 3 Seismic Damage and Fragility Assessment

Seismic damage and fragility assessment is the numerical quantification of probable damage to a building due to a given hazard. In order to physically categorize the degree of damage to the members of a building under an earthquake of a specific intensity, damage states are specified. The most common form of a seismic fragility function is the lognormal cumulative distribution function and is of the form as shown in Eq. (4).  $P[x \geq \theta_d | \text{IM}]$  represents the conditional probability of exceedance of the EDP (here,  $x$ ) with respect to  $\theta_d$ , given intensity measure (IM).  $\Phi$  represents the standard normal probability,  $\theta_d$  is the median value of EDP, i.e., interstorey drift, assumed according to HAZUS [3] for different damage states considered [Slight (S), Moderate (M), Extreme (E), and Collapse (C)]. The drift thresholds are suitably converted to displacement threshold. The total uncertainty in fragility estimation ( $\beta_d$ ) is taken as 0.7 [12].

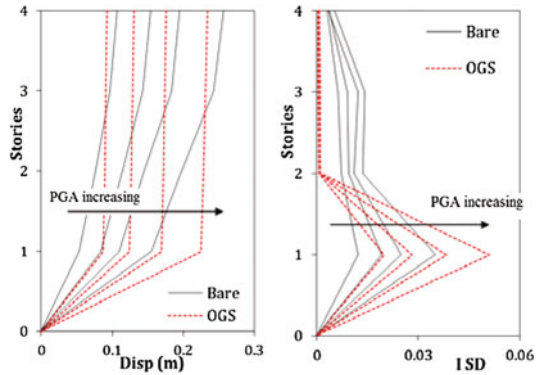
$$P[x \geq \theta_d | \text{IM}] = \Phi\left(\frac{\ln(x/\theta_d)}{\beta_d}\right) \quad (4)$$

## 4 Results

### 4.1 Nonlinear Time History Analysis

Several nonlinear dynamic analyses for both bare and OGS frame are carried out, and displacement time histories of the selected joints at each floor levels are monitored. The peak displacement and interstorey drift (ISD) profiles of the frames for different PGA are shown in Fig. 5. Displacement profile at the ground storey level shows a very high response for OGS frame, compared to bare frame.

**Fig. 5** Displacement and interstorey drift profile (ISD) for bare and OGS frames for El Centro ground motion with increasing PGA (0.3, 0.5, 0.7, 1 g)



The displacement demand gradually goes on increasing from lower stories to upper stories in bare frame, whereas it remains almost constant in case of OGS frame.

ISD profile gives the relative deformation demands on the columns in a storey. As observed from past earthquakes, the OGS columns are subjected to very high drift demand, but there is negligible drift demand in the columns of the upper stories. There is a sudden and drastic change in the ISD profile of upper stories compared to the OGS. The bare frame, however, shows uniform variation in the ISD demands throughout the frame height. Thus, the distribution of damage is also uniform in case of bare frame (or regular frames).

### 4.2 Seismic Fragility

The seismic fragilities are computed using Eq. (4) considering the following EDPs at various floor levels:

- i. *Peak displacement at the top storey*

It is clearly observed from Fig. 6 that the seismic fragility of bare frame is more compared to OGS frame considering the top displacement for both the frames for all PGA and for all damage states.

- ii. *Peak displacements at each floor level*

Fragility with respect to displacement at all the floors is obtained by considering linear distribution of the thresholds. The average interstorey drift is multiplied by the respective height at each floor of the building to obtain the displacement threshold as per HAZUS [3]. In this case, the seismic fragility at the ground floor is observed to be the highest (Fig. 7). Also, the fragility of OGS frame is higher than the bare frame. The fragility of the upper floors is lesser than the adjacent lower floors in each frame. However, the behavior or failure pattern of OGS frames, as shown in Fig. 1, is not observed in the seismic fragility obtained. The upper

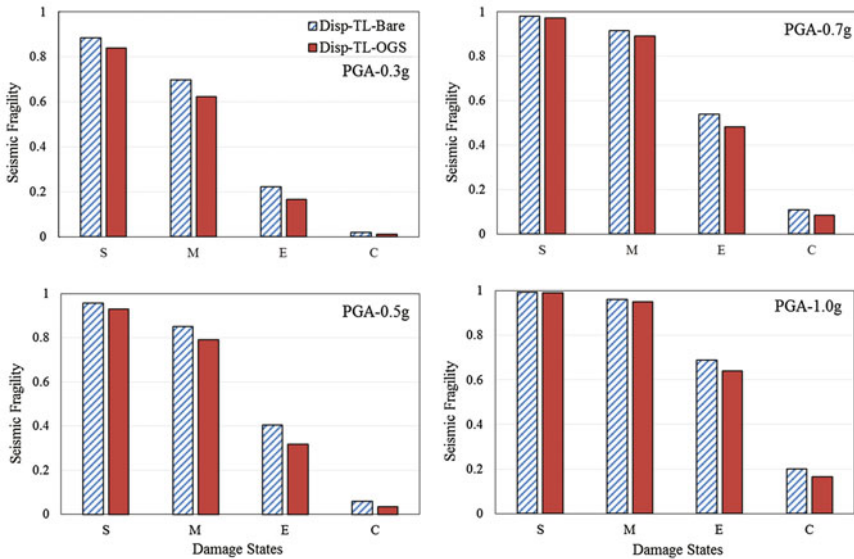


**Fig. 6** Comparison of seismic fragility obtained for bare and OGS frame considering top level (TL) or peak roof displacement as the EDP

stories are least affected during earthquake and, hence, are not vulnerable to damage and remain intact, even after heavy damage to the columns of OGS.

iii. *Interstorey drift (ISD) at each floor level*

Fragility with respect to ISD at each floor level is obtained by considering uniform distribution of the drift thresholds for each damage state. Fragility with respect to ISD clearly shows the failure pattern of the regular and irregular frames. For the OGS frame, seismic fragility is almost nil in case of upper stories, whereas it is maximum at the ground storey level (Fig. 8), which is obvious, since the OGS frames fail due to the failure of the open ground storey columns. In contrast, the fragility of bare frames is uniformly distributed throughout the height of the building. The fragility goes on decreasing from bottom floor to the upper floors. Comparing the fragility at the top node and also at the ground floor shows the clear difference in the behavior of the two frames (Figs. 9 and 10).

Fragility at the top of the OGS frame is almost zero as expected from real damages in structures during previous earthquakes. At the same time, the OGS columns are found to be more vulnerable than the bare frame ground storey columns, which is obvious. Hence, this form of representation can give us a better view of the fragility in terms of damage incurred in irregular frames, such as an OGS frame.

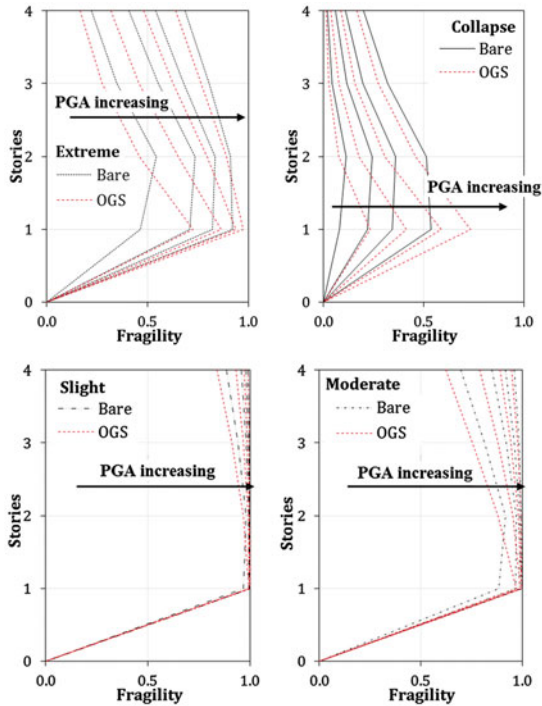


**Fig. 7** Storey wise fragility profile of bare and OGS frame considering displacement demand at each floor obtained from time history analysis for El Centro ground motion scaled for different PGA (0.3, 0.5, 0.7, 1 g)

### 5 Conclusion

Irregular frames, such as OGS frames, show storey collapse mechanism in the weak storey, and in contrast, the regular frames show multistorey collapse mechanism for the same seismic intensity. The current study is dedicated to the fragility estimation of irregular frames such that it furnishes the damage pattern also in the frame. In general, the threshold of infilled frames are reduced by some factors to consider the effect of infill panels on the building displacement capacity. However, the concern is the distribution of infills or its absence in some storey throughout the frame that makes the frame irregular and alters the frame failure mechanism making it vulnerable.

In this regard, the storey wise fragility, i.e., the component-level fragility is found to be more relevant and accurate for irregular frames with one or more flexible storey because the flexible storey has much higher fragility than the adjacent stories. In regular frames, (here, bare frame) the distribution of strength and

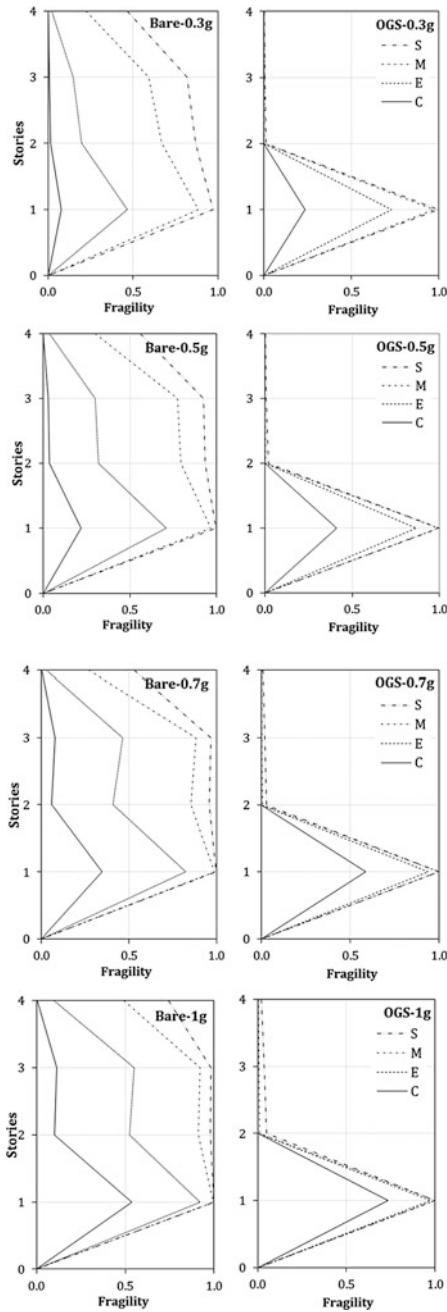


**Fig. 8** Storey wise fragility profile of bare and OGS frame considering ISD demand at each floor obtained from time history analysis for El Centro ground motion scaled for different PGA (0.3, 0.5, 0.7, 1 g)

**Fig. 9** Comparison of seismic fragility of bare and OGS frames at the top level (TL) with interstorey drift demand as the EDP

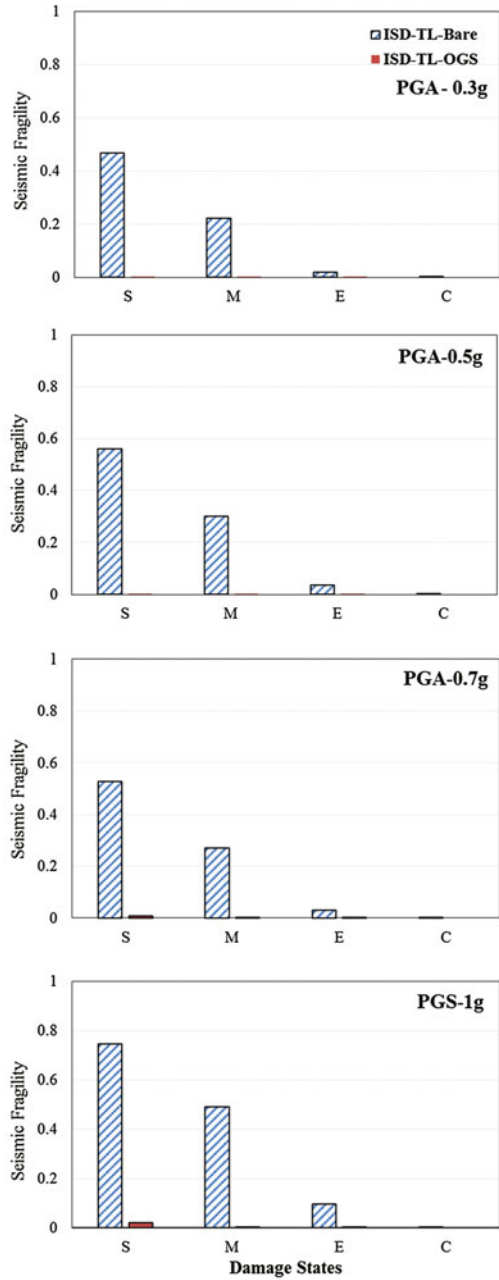
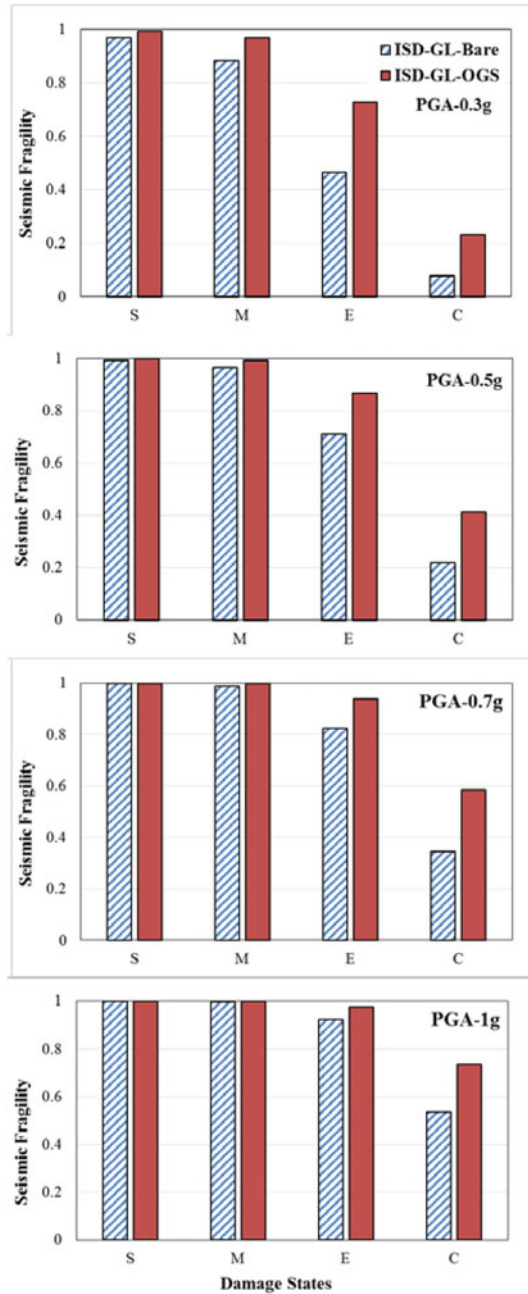


**Fig. 10** Comparison of seismic fragility of bare and OGS frames at the ground level (GL) with interstorey drift demand as the EDP





stiffness is uniform along the height of the frame, and hence, its fragility is also uniform and, therefore, can be conveniently estimated using conventional methods considering peak roof displacement of the building frame as the engineering demand parameter.

**Acknowledgements** The authors acknowledge the financial assistance provided by the Ministry of Human Resource Development (MHRD), Government of India, in the doctoral research work.

## References

1. Aschheim M, Gulkan P, Sezen H, Bruneau M, Elnashai A, Halling M, Love J, Rahnama M (2000) 11 Performance of buildings. *Earthquake Spectra* 16(S1):237–279. EERI
2. Kaushik HB, Jain SK (2007) Impact of great December 26, 2004 Sumatra earthquake and tsunami on structures in Port Blair. *J Perform Constructed Facil ASCE* 21(2):128–142
3. HAZUS-MH MR-4 (2004) Technical manual, multi-hazard loss estimation methodology, Federal Emergency Management Agency, Washington, DC
4. Indian Standard 1893 (Part 1) (2002) Criteria for earthquake resistant design of structures: part 1 general provisions and buildings, 5th Rev, Bureau of Indian Standards, New Delhi, India
5. SAP2000 (2015) Structural analysis program—advanced, static and dynamic finite element analysis of structures. Computers and Structures Inc. (CSI), Berkeley, USA
6. Kaushik HB, Rai DC, Jain SK (2007) Stress-strain characteristics of clay brick masonry under uniaxial compression. *J Mater Civ Eng ASCE* 19(9):728–739
7. Mander JB, Priestley MJ, Park R (1988) Theoretical stress-strain model for confined concrete. *J Struct Eng ASCE* 114(8):1804–1826
8. Takeda T, Sozen MA, Neilsen NN (1970) Reinforced concrete response to simulated earthquakes. *J Struct Div ASCE* 96:2557–2573
9. Hahn GT, Bhargava V, Chen Q (1990) The cyclic stress-strain properties, hysteresis loop shape, and kinematic hardening of two high-strength bearing steels. *Metall Trans A* 21(2): 653–665
10. Cavaleri L, Di Trapani F (2014) Cyclic response of masonry infilled RC frames: Experimental results and simplified modeling. *Soil Dyn Earthquake Eng* 65:224–242
11. Wilson EL (1996) Three-dimensional static and dynamic analysis of structures. Computers and Structures Inc, Berkeley, CA
12. Kaushik HB, Choudhury T (2015) Vulnerability analysis of buildings for seismic risk assessment: a review. *Bridge Struct Eng J Indian Natl Group (ING) Int Assoc Bridge Struct Eng (IABSE)* 45(1)

# Partial Factors for Safety Assessment of T-Girder of RC Bridges Subjected to Chloride-Induced Corrosion Against Shear Limit State



N. J. Yogalakshmi, K. Balaji Rao and M. B. Anoop

**Abstract** The health assessment of bridge is becoming increasingly important in the view of the life extension programs. The main focus of this study is to develop a reliability-based procedure to carry out safety assessment against the shear limit state for a typical T-Girder bridge. Chloride-induced corrosion of reinforcement is considered to be the primary reason for deterioration of shear capacity with time. The girder is modeled by series connection of elements in the shear critical region. The shear capacity is determined by mechanical behavior (brittle or ductile) of each element depending on degree of corrosion in each element. Using the time-variant shear capacity obtained from the stochastic analysis, an attempt has been made to determine the partial factors using first-order reliability method (FORM). These partial factors can be used for safety assessment of similar T-Girder bridges located in marine environment and subjected to similar traffic loading.

**Keywords** Partial factors · Assessment · Chloride-induced corrosion  
T-Girder bridges

## 1 Introduction

Reinforced concrete structures tend to deteriorate with age due to environmental conditions. Structural deterioration affects the performance of structures by strength degradation [1]. The existence of a corrosive environment, cyclic loading, and concrete cracking either in combination or in isolation can cause structural strength

---

N. J. Yogalakshmi · K. Balaji Rao (✉) · M. B. Anoop  
Risk and Reliability of Structures, CSIR-Structural Engineering  
Research Centre, Chennai 600113, India  
e-mail: balaji@serc.res.in

N. J. Yogalakshmi  
e-mail: yoga.engg10@gmail.com

M. B. Anoop  
e-mail: anoop@serc.res.in

degradation. Corrosion of reinforcing steel due to chloride ingress is one of the important reasons of deterioration in structures. This mainly occurs in chloride-rich environment like coastal regions. To ensure safety and durability, such deteriorating structures must be regularly assessed for their strength.

The process of corrosion is complex and involves huge variables in estimating it. By nature, the basic variables describing the corrosion process are also uncertain with spatial and temporal variations. Therefore, the corrosion process also exhibits spatial and temporal variations. This necessitates the use of probabilistic methods to be adopted for assessment [2]. This work presents methodology for assessment of in-service T-Girder bridges subjected to corrosion using stochastic analyses approach for determining the shear capacity of girder. The shear capacity at the end of 50 years is used in deriving the partial factors that can be used in the preliminary level of assessment.

## 2 Corrosion Modeling

The corrosion encountered in steel is of various types. However, the mechanism of corrosion of reinforcement due to chlorides ingress in the cover region of reinforced concrete can be divided into two distinct phases, initiation and propagation.

### 2.1 Corrosion Initiation

The initiation time of corrosion is the period when chloride diffuses from the environment through the concrete cover before chloride iron concentration equals the critical chloride concentration at the surface of reinforcement. The chloride ingress into concrete can be modeled using Fick's second law [3, 4]. The time of initiation of corrosion can be expressed as,

$$T_i = \frac{\bar{c}^2}{4D} \left\{ \operatorname{erf}^{-1} \left( \frac{c_0 - c_{cr}}{c_0} \right) \right\}^{-2} \quad (1)$$

where  $T_i$  is the corrosion initiation time in years;  $\bar{c}$  is the concrete cover in cm;  $c_0$  is the surface chloride concentration as percentage weight of concrete;  $c_{cr}$  is the critical chloride concentration as percentage weight of concrete;  $D$  is the chloride diffusion coefficient in  $\text{cm}^2/\text{year}$ ; erf is the error function.

## 2.2 Corrosion Propagation

The next stage in corrosion after initiation is the propagation stage. For localized corrosion, the maximum penetration of pitting is about four to eight times the average penetration (as that of uniform corrosion) [5]. The maximum pit depth is given by,

$$p(t) = r_{\text{corr}}(t - T_i) \quad (2)$$

where  $\alpha$  is the pitting factor and  $p(t)$  is the maximum pit depth at time  $t$ . The remaining area of the steel in this study is calculated using empirical expression [6–8]. Val [7] proposed a model assuming the formation of pit in hemispherical shape.

## 3 Stochastic Modeling Shear Capacity of Girder

The ultimate shear capacity offered by girder mainly comes from two components: Shear capacity offered by concrete in the cross section and shear capacity offered by stirrups.

$$V_u = V_{uc} + V_{us} \quad (3)$$

The shear capacity of the concrete used in the design calculation is given by,

$$V_{uc} = (\tau_c) \times bd \quad (4)$$

The nominal shear strength is expressed as per EN 1992-1-1 [9]. In addition to the shear capacity of the concrete, stirrups also provide shear resistance and it is given by,

$$V_{us} = \frac{A_{sv}f_yS_v}{d} \quad (5)$$

where  $A_{sv}$  is the cross-sectional area of stirrup;  $S_v$  is the spacing of stirrups;  $d$  is the effective depth of the girder; and  $f_y$  is the yield strength of the steel used.

### 3.1 Discretization of Girder

The girder is discretized into smaller elements. The shear failure causes diagonal cracking which is inclined approximately at angle 45 from support. Therefore, the length of each element is taken as  $d$  which is the effective depth of the girder.

These elements in the girder are connected in series; hence, the failure of one element leads to the failure of the girder. The stirrups inside each element are considered to form a parallel system. The element can be ductile or brittle depending on the degree of corrosion.

### 3.2 Shear Capacity of Ductile and Brittle Elements

It is noted that the degree of corrosion of stirrups within the element can vary with time. The shear capacity of each element depends on the mechanical behavior of the stirrups—ductile and brittle behavior. It is considered in the study that if 20% reduction in area occurs in more than 20% of stirrups present in the element, then the element is brittle [10, 11]. When the element exhibits ductile behavior, the shear capacity of element is the summation of shear capacity of individual stirrups in the element. The shear capacity of individual stirrup in the given element at given time is expressed by,

$$r_j^{(i)}(t) = A_{srj}^{(i)}(t) \times f_{yj}^{(i)}(t) \quad (6)$$

where  $r_j^{(i)}(t)$  represents the shear capacity of  $j$ th stirrup in the  $i$ th element at time  $t$ ;  $f_{yj}^{(i)}(t)$  represents the yield strength of the  $j$ th stirrup in the  $i$ th element at time  $t$ . Similar to the loss in area of the stirrups, loss in yield strength of the stirrup also occurs with corrosion propagation. This is given by,

$$f_{yj}^{(i)}(t) = f_{yj}^{(i)}(0) \times \left( 1 - \beta \frac{A_{srj}^{(i)}(t)}{A_{sv}^{(i)}(0)} \right) \quad (7)$$

where  $A_{sv}(0)$  and  $f_y(0)$  are the cross-sectional area and yield strength of the stirrup at initial time.  $A_{sr}(t)$  and  $f_y(t)$  are the remaining cross-sectional area and yield strength of the stirrup at time  $t$ .  $\beta$  is the empirical coefficient taken as 0.005 as recommended by Du et al. [12].

The shear capacity of ductile element due to stirrups becomes,

$$V_s^{(i)}(t) = \sum_j^{ns} A_{srj}^{(i)}(t) \times f_{yj}^{(i)}(t) \quad (8)$$

The shear capacity of brittle element due to stirrups is given by,

$$V_s^{(i)}(t) = \max \left[ n \cdot r_1^{(i)}, (n-1) \cdot r_2^{(i)}(t), \dots, r_n^{(i)}(t) \right] \quad (9)$$

where  $r_1(t) < r_2(t) < \dots < r_n(t)$ .

## 4 Reliability Analyses

The safety margin equation for assessment against shear capacity is given by,

$$Z(t) = \min_{i=1:N} [V_s(t) + V_c(t) - V] \quad (10)$$

where  $V$  is the shear force on the girder and  $N$  is the number of elements. All basic variables involved in modeling of corrosion initiation time ( $c_0$ ,  $c_{cr}$ , and  $D$ ) and propagation model ( $I_{corr}$ ,  $\alpha$ ) are considered as time-invariant random variables. Similarly, the shear force is also considered to be time-invariant random variables, whereas the shear capacity of the girder becomes time-dependent random variable due to loss in yield strength and loss in area of the reinforcement with time. The girder fails if,

$$Z(t) \leq 0 \quad (11)$$

The probability of failure is calculated by simulating 1000 such realizations,

$$P_f(t) = [\text{no. of cases with } Z(t) \leq 0] / 1000 \quad (12)$$

### 4.1 Partial Factors for Assessment

Using the distribution of shear capacity of girder estimated at a particular instant of time from the stochastic analysis and by using the distribution of prevailing loads on the bridge, the partial factors for assessment can be derived adopting first-order reliability method (FORM) method.

## 5 Illustrative Example

MORT&H [13] recommends standard drawings for bridge design. A typical bridge built according to standard MORT&H drawing is considered as an example in this study. Reinforced concrete T-Girder bridge is of span 10 m and width 12 m, carrying three-lane traffic with four main girders. The bridge girders are assumed to be constructed using M25 and Fe415 grades of concrete and steel, respectively, and considered to be located at Chennai carrying in-service traffic. It is to be noted that although the in-service traffic loads are not 70 R, it is understood that the difference in the reliability index due to the design loads and actual plying commercial loads are not significantly different [14]. Therefore, the design loads are considered as the actual prevailing load and are used in assessment. The structure is assumed to be at a coastal environment and hence subjected to deterioration due to chloride-induced

**Table 1** Statistical properties of basic variables used in the present study [10]

Variables	Units	Distribution	Mean	COV
Diameter of longitudinal rebar $\Phi_1$	mm	LN	30	0.02
Diameter of stirrups $\Phi$	mm	LN	16	0.02
Cover concrete $\bar{c}$	mm	LN	50	0.10
Surface chloride concentration $c_0$	% wt of concrete	U	0.211–0.401	0.18
Critical chloride concentration $c_{cr}$	% wt of concrete	U	0.073–0.182	0.25
Diffusion coefficient $D$	cm <sup>2</sup> /year	LN	0.5	0.2
Current density near support $I_{corr}$	μA/cm <sup>2</sup>	U	1–5	0.38
Current density at interior $I_{corr}$	μA/cm <sup>2</sup>	U	0.2–1	0.38
Pitting factor $\alpha$	–	U	4–8	0.1

**Table 2** Details of random variable sensitive to quality of workmanship [15]

Variables	Varying parameter	Quality of workmanship		
		Good	Medium	Poor
Concrete cover	COV	0.1	0.2	0.3
Diffusion coefficient	Mean	0.5	1.0	1.5
Compressive strength of concrete	COV	0.1	0.2	0.25

corrosion of reinforcement. The random variables used in the study are given in Table 1.

It is more rational to consider variations in quality of workmanship since different bridge/flyovers in cities like Chennai will be constructed by different contractors although the design may be according to MORT&H recommendations. It is known that the variations in the quality of workmanship can be represented by varying COV of cover thickness and compressive strength of concrete (though the average/specified values can still be maintained). However, due to variation in the quality of workmanship the microstructure of concrete is directly affected. This would result in variation in mean value of  $D$ . These observations are also reported in literature [15] and the same is considered in the present study as given in Table 2.

In the present investigation, the girders are assumed to be simply supported. The traffic loading is arranged (in plan) to induce highest shear force. The maximum shear force occurs at the left support. Though the shear force decreases along the span, for the sake of simplicity, the shear force is assumed to be constant over a distance of  $L/4$  in the shear critical region; an assumption that results in conservatives in assessment.

## 6 Results and Discussions

The reliability of a bridge girder which is not maintained and subjected to chloride-induced corrosion of reinforcement, with respect to shear limit state, is very sensitive to the time to corrosion initiation  $T_i$ . Moreover, the life of the girder exposed to marine environment is more or less governed by corrosion initiation time. Keeping these in view, the statistical properties of  $T_i$  of the girder are estimated using Monte Carlo simulation technique. In simulation, different basic variables presented in Table 1 are considered to be random variable and one thousand simulation cycles are considered. The probabilistic distribution of  $T_i$  is shown in Fig. 1. From the results of the simulation, it is found that  $T_i^{\min} = 2$  years and  $T_i^{\text{mean}} = 19$  years. The characteristic time of initiation is estimated as 5 years. This type of information can be useful in design decision. The variation in  $T_i$  is determined for three types of workmanship considered. Mean  $T_i$  decreases with decrease in workmanship quality. The mean  $T_i$  for three cases are 60 years, 30 years, and 21 years, respectively. The COV of  $T_i$  increases with decrease in quality of workmanship.

From the stochastic analysis of the shear capacity, the mean value of shear capacity before corrosion propagation is found to be 1270 kN (which correspond to  $T_i^{\min} = 2$  years). The histogram of shear capacity of the girder at time 50 years (which correspond to approximately service life) is shown in Fig. 2. Figure 2 indicates that the mean of shear capacity of the RC bridge girder has decreased to 929 kN; a 29% reduction in shear capacity due to corrosion in 50 years.

An investigation, similar to the one carried out for  $T_i$ , is carried out to study the effect of quality of workmanship on the degree of variability of shear capacities of girder at various instants of times. For good quality workmanship, the shear capacity falls from approximately 1170 to 900 kN in 50 years. Thus, the percentage decrease in shear capacity over 50 years is 23%. The COV is initially 0.09 and

**Fig. 1** Histogram for initiation time for the considered example

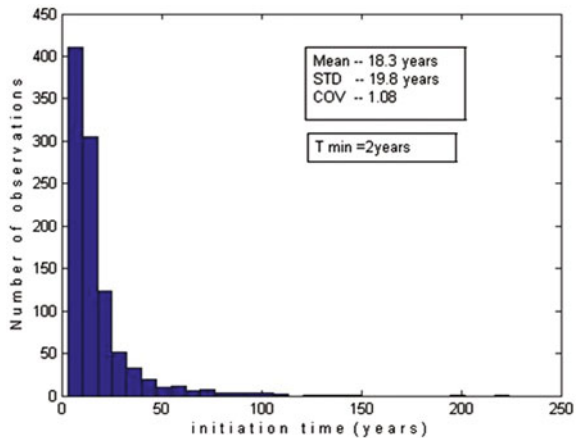
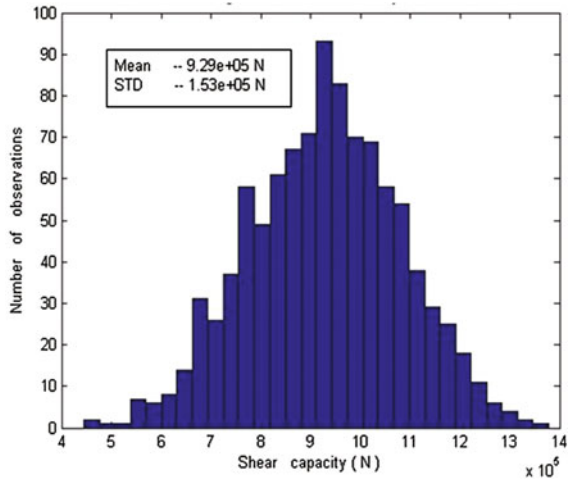




**Fig. 2** Distribution of shear capacities of the girder at 50 years for the design combination of variables



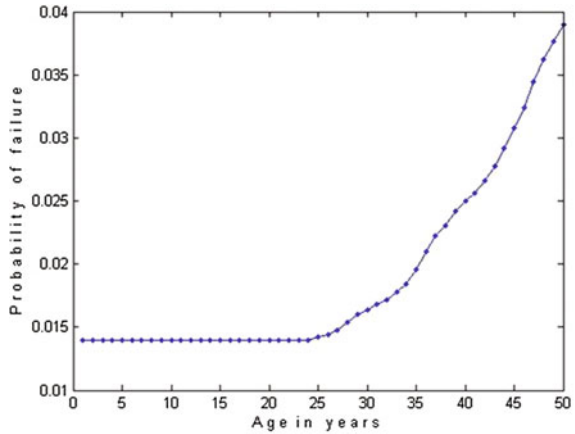
constant up to 25 years, later it increases up to 0.185 at the end of 50 years. For medium quality workmanship, the shear capacity falls from approximately 1150 to 800 kN in 50 years and corresponding decreases is 30.4%. The COV is initially 0.09 and constant up to 20 years, later it increases up to 0.22 at the end of 50 years. Similarly, for poor quality workmanship the shear capacity falls from approximately 1150 to 758 kN in 50 years. This corresponds to a percentage decrease of 34%. The COV is initially 0.1 and constant up to 22 years, later it increases up to 0.23 at the end of 50 years. The quality of workmanship has a significant effect on the shear capacity of the element.

The reduction in the shear capacity of the girder with time also causes the safety margin between the capacity and load effects of the girder to decrease. For the design combination of variables, the mean of safety margin curve decreases from 820 to 640 kN which correspond to about 22% reduction in 50 years. It is observed that reduction in safety margin is lesser than reduction in shear capacity. The COV of the safety margin is initial 0.136 and constant up to 17 years, later it increases up to 0.146 at the end of 50 years.

The safety margin for all the three cases starts approximately from 715 kN and falls to 640, 630, and 620 kN for good, medium, and poor quality of workmanship, respectively. This corresponds to decreases in 10, 11.8, and 13.3% of safety margin at end of 50 years, respectively.

Since the safety margin falls with time, it is evident that the probability of failure increases with time. The probability of failure for the considered design combination at the end of 50 years is estimated as 0.04 as shown in Fig. 3. The corresponding reliability indices is calculated from the expression,

**Fig. 3** Probability of shear failure for the considered design combination of the variables



$$\beta = \Phi^{-1}[-P_f] \tag{13}$$

The reliability index at the end of 50 years becomes 1.75. Similarly, the probability of failure of the girder with time is plotted for different quality of workmanship as shown in Fig. 4. It is observed that variation in probability of failure at the end of 50 years is 0.001 for good quality workmanship, 0.015 for medium quality workmanship, and 0.025 for poor quality workmanship. The corresponding reliability indices are 3.1, 2.2, and 2.0. This does not satisfy the target reliability for ultimate shear capacity limit state (3.3 or 3.8 depending on the consequence of failure) [16, 17]. While it is preferable to meet these target reliabilities, but the structures are located in very severe environments, it may result in costly repairs. However, this type of analyses would help in ration prioritization of repairs for bridges in bridge stock.

The partial factors for resistance and load effects are then derived using the FORM expression,

$$\gamma_i = 1 - \beta_t \alpha_i \Omega_{X_i} \tag{14}$$

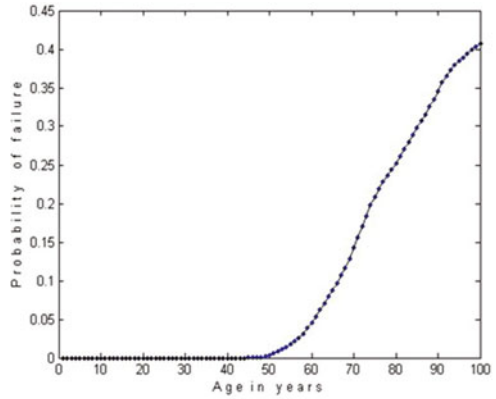
where  $X_i$  represents the basic variables and  $\beta_t$  is taken as 1.6 as suggested in [14]. The values of derived partial factors for assessment against shear capacity are given in Table 3.

These partial factors can be used at the time of assessment to find the minimum resistance required.

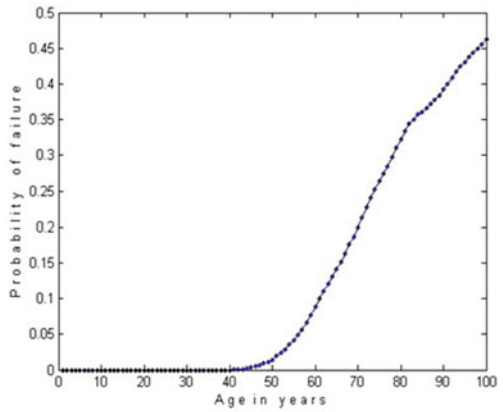
$$R_{\min} = \frac{\sum_i \gamma_i \times \text{Load effect}'i'}{\gamma_\tau} \tag{15}$$

If the resistance of the structure satisfies the minimum resistance, then the structure is safe. If not load posting have to be imposed for normal operation. If the

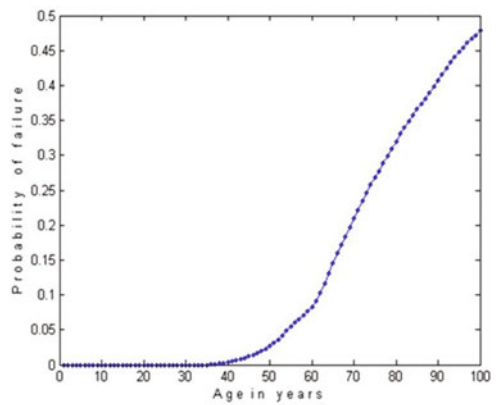
**Fig. 4** Probability of shear failure of girder for different quality of workmanship



**(a)** Good quality



**(b)** Medium quality



**(c)** poor quality

**Table 3** Partial factors for assessment of girder against shear capacity

Quality of workmanship	$\gamma_{Vc}$	$\gamma_{Vs}$	$\gamma_D$	$\gamma_T$
Good	0.998	0.552	1.034	1.068
Medium	0.977	0.449	1.031	1.063
Poor	0.967	0.388	1.030	1.060

margin between the actual resistance minus minimum resistance is very low, then the structure has to be repaired immediately or to be declared/deemed unfit.

## 7 Conclusion

The main focus of this paper is to develop a procedure to carry out stochastic analysis for estimation of shear capacity of T-Girder of a RC bridge. The developed procedure is demonstrated on a typical girder designed according to MORT&H recommendations. The reliability of RC T-Girder bridge of 10 m span which is not maintained and subjected to chloride-induced corrosion of reinforcement is found to sensitive to initiation time of corrosion. The shear capacity of the demonstrated example decreases by 29% at the end of service life due to corrosion. The corresponding reduction in safety margin is 22%. The reliability index is 1.7 at the end of 50 years. The traffic load considered in this study is a time-invariant random variable. 70 R and Class A loadings are used since the reliability of bridge by design loads is similar to in-service loads. However in the future studies, traffic load can be considered as time-variant random variable, provided relevant information is available about the traffic condition.

A parametric study involving variations in quality of workmanship shows that the quality of workmanship has a significant impact on the initiation time, shear capacity, safety margin, and its resulting failure probability. This gets reflected in the derived partial factors for assessment. The resulting partial factors are 0.998 for concrete, 0.552 for steel, 1.034 for dead load, and 1.068 for traffic load for good quality workmanship. 0.977 for concrete, 0.449 for steel, 1.031 for dead load, and 1.063 for traffic load for medium quality workmanship. Similarly, 0.967 for concrete, 0.388 for steel, 1.03 for dead load, and 1.06 for traffic load for poor quality workmanship. These partial factors can be adopted for safety assessment after proper calibration for similar bridges, thus avoiding similar analysis to be repeated.

## References

1. Stewart MG, Rosowsky DV (1998) Structural safety and serviceability of concrete bridges subject to corrosion. *J Infrastruct Syst* 4(4):146–155

2. Enright MP, Frangopol DM (1998) Probabilistic analysis of resistance degradation of reinforced concrete bridge beams under corrosion. *Eng Struct* 20(11):960–971
3. Crank J (1979) *The mathematics of diffusion*. Oxford University Press, Oxford
4. Thoft-Christensen P (1995) Advanced bridge management systems. *Struct Eng Rev* 3(7): 151–163
5. Tuutti K (1982) Corrosion of steel in concrete. Swedish Cement and Concrete Research Institute, Fo4.82, Stockholm
6. Rodriguez J, Ortega LM, Casal J (1997) Load carrying capacity of concrete structures with corroded reinforcement. *Constr Build Mater* 11(4):239–248
7. Val DV (2007) Deterioration of strength of RC beams due to corrosion and its influence on beam reliability. *J Struct Eng* 133(9):1297–1306
8. Andrade C, Alonso C (1996) Corrosion rate monitoring in the laboratory and on-site. *Constr Build Mater* 10(5):315–328
9. EN 1992-1-1 Eurocode 2: design of concrete structures
10. Ahsana PV, Balaji Rao K, Anoop MB (2016) Time-variant reliability analysis of RC bridge girders subjected to corrosion–shear limit state. *Struct Concr* 17(2):162–174
11. Stewart MG (2009) Mechanical behaviour of pitting corrosion of flexural and shear reinforcement and its effect on structural reliability of corroding RC beams. *Struct Saf* 31(1): 19–30
12. Du YG, Clark LA, Chan AH (2005) Residual capacity of corroded reinforcing bars. *Mag Con Res* 57(3):135–148
13. Ministry of Surface Transport (1993) Standard plans for highway bridges: RCC beam and slab superstructure. Indian Roads Congress, Roads Wing
14. Yogalakshmi NJ, Balaji Rao K, Anoop MB (2016) A methodology for reliability assessment of shear capacity of in-service RC T-girder bridges for human safety. Submitted to SADHANA (under review)
15. Chryssanthopoulos MK, Sterritt G (2002) Integration of deterioration modelling and reliability assessment for reinforced concrete bridge structures. In: First ASRA Net international colloquium
16. ISO I (1998) 2394 General principles on reliability for structures. ISO, Zurich
17. Steenbergen RDJM, Vrouwenvelder ACWM (2010) Safety philosophy for existing structures and partial factors for traffic loads on bridges. *Heron* 55(2)

# Estimation of Residual Crack Widths in Post-Yield Response Range



Saurabh Shiradhonkar and Ravi Sinha

**Abstract** Crack width calculation is one of the serviceability requirements in the structural concrete elements. Estimation of maximum crack widths under service loading, when response remains in linear range, is well studied in the literature. However, when an RC building is subjected to extreme loading such as an earthquake, peak response of RC members is usually in the post-yield region. The applicability of available crack width formulation in post-yield response range has not been studied in the literature. Additionally, the relationship between maximum crack width that occurs at peak response, and residual crack width that occurs at the end of loading, is not available in published the literature. Such relationship is useful to trace the peak loading experienced by the member from its condition, observed at the zero force condition. In the present study, the available crack width formulae are reviewed thoroughly and validated in pre- and post-yield response ranges by reproducing observed experimental responses. The simulated experimental responses are also used to develop a relationship between residual and maximum crack widths. The effect of cyclic loading on the residual crack width is also presented in the present paper.

**Keywords** Maximum crack width · Residual crack width · Nonlinear response

## 1 Introduction

Cracking of concrete is a complex phenomenon and mainly caused by the tensile weakness of concrete. Cracking of RC section is characterized by axial tensile strain, bar diameter, bar spacing, fracture energy of the concrete, and modules of

---

S. Shiradhonkar · R. Sinha (✉)  
Department of Civil Engineering, Indian Institute of Technology Bombay,  
Mumbai 400076, India  
e-mail: rsinha@civil.iitb.ac.in

S. Shiradhonkar  
e-mail: saurabh.coep@gmail.com

elasticity of concrete and steel. When an RC section is subjected to an incremental load, initial cracking on tension side occurs as tensile strain at bottom fiber exceeds limiting tensile strain in concrete. The initial cracking in RC section is governed by the tensile strength of the concrete. Strength criterion governs cracking till tensile strain in bar reaches limiting tensile strain in the concrete. After this stage, an additional increase in crack width value is because of slippage of the bond between concrete and reinforcement bar. Generally, strength criterion remains valid for crack widths of the order 0.10–0.50 mm, while bond slippage predominately contributes in higher crack width values. During the initial cracking phase, strains in steel and concrete remain equal for a portion of the element between the cracks and therefore no slippage occurs. If crack spacing is greater than twice the transfer length ( $l_t$ ) of the bond, another crack occurs between initial cracks as concrete stress reaches the tensile capacity. Once crack spacing varies between  $l_t$  and  $2l_t$  crack development stabilizes, and no new cracks are formed. At initial cracking, concrete between cracks remains stress-free at the crack surface and steel carries the entire load; but during crack stabilization phase, concrete between cracks is subjected to tensile stresses due to the bond between steel and concrete. The development of bond stress finally leads to bond slippage and increase in the crack opening. Increase in maximum crack width due to bond slippage is estimated by integration of the steel and concrete strains between initial cracks (or transfer length) and generally found as twice of bond slip for symmetrical cracking behavior. Fracture mechanics models are also studied to capture the increase in cracking caused by bond slippage.

Several formulae have been proposed to estimate the maximum crack width and crack spacing. In the present study, the available crack width formulae are reviewed thoroughly and validated in pre-yield and post-yield response ranges by reproducing observed experimental responses. The simulated experimental responses are then used to develop a relationship between residual and maximum crack widths.

During seismic loading, the members of the building frames experience several cycles of load reversals. Therefore, the effect of cyclic loading on the residual crack width is also studied using published experimental responses.

## **2 Available Formulae to Estimate of Maximum Crack Width**

Several formulae have been proposed to estimate the maximum crack width and crack spacing. Borosnyoi and Balazs [1] extensively reviewed the development of flexural crack and summarized most relevant formulae for crack spacing. The available crack width formulae are either based on mechanics models such as fracture mechanics models [2, 3], bond slip models [4, 5] or empirical relationships developed by fitting of a large number of experimental data [6]. Development of various crack width formulae has been discussed in this section.

Bazant and Oh [2] expressed crack spacing and crack widths as a function of strain energy released due to initial tensile stress exceedance (strength criteria) and bond slip, using fracture theory. This theory differentiates micro- or initial cracks, caused before tensile strain in bar exceeds limiting tensile strain in the concrete, and increase in the crack widths caused by bond slippage. It was mentioned that as the strain is increased, the first cracks appear at a certain strain, and subsequently, further cracks are produced which causes the crack spacing to diminish as the strain grows.

Oh and Kang [3] proposed formulae to estimate crack width and spacing on the basis of cracking theory. Cracking theory was proposed by Bazant and Oh [2] to estimate crack spacing and maximum crack width formula using energy criterion of fracture mechanics as well as the strength criterion. The strength criterion indicates whether the fracture formation can initiate while the energy criterion indicates whether the fracture can actually form. Bazant and Oh [2] expressed crack spacing as the function of axial tensile strain, bar diameter, bar spacing, fracture energy of concrete, and its elastic modulus. Oh and Kang [3] extended this cracking theory and proposed the following formula to estimate the crack width, by minimizing nonlinear function of above-mentioned variables weighted by the constants against experimental data for best prediction.

$$W_{\max} = d_b \beta (\varepsilon_s - 0.0002) \left( \begin{matrix} 159 \left( \frac{t_b}{h-d} \right)^{4.5} \\ + 2.83 \left( \frac{A_c}{n_b A_{s1}} \right)^{\frac{1}{3}} \end{matrix} \right) \tag{1}$$

where  $\beta$  is the ratio of distance between neutral axis and tension face to distance between neutral axis and centroid of reinforcing steel.  $A_c$  is the effective stretched concrete area  $d_b$  and  $A_{s1}$  are diameter of bar and its area, respectively.  $(h-d)$  is distance between neutral axis and tension face,  $\varepsilon_s$  is strain in steel,  $n_b$  is number of reinforcing bars in tension, and  $t_b$  is effective cover.

Balazs [4] presented a method for crack width estimation under monotonic loading using local bond stress–slip relationship together with the evaluation of transfer length and stress distribution between the cracks. The transfer length is necessary for transferring the axial force of reinforcing bar to concrete. The crack width is based on the integration of the steel and concrete strains between cracks as,

$$W_{\max} = \beta \times \frac{s_w f_s}{E_s} \tag{2}$$

where  $f_s$  is stress of reinforcing bar and  $E_s$  is modulus of the elasticity reinforcing bars. Thus after crack stabilization phase, an increase of load causes an increase of the crack widths and maximum crack width at the level of reinforcement is proportional to the strain in the concrete, as explicitly mentioned by Frosch [7].

The Gergely and Lutz [6] crack width formula has been developed by empirical relationships based on fitting of a large number of experimental data. The Gergely and Lutz crack width formula is widely used in design codes such as ACI 318-08



[8] to calculate crack widths at various performance levels. The maximum crack width is estimated as,

$$W_{\max} = 0.076\beta f_s^3 \sqrt[3]{d_c A_c} \times 10^{-3} \quad (2)$$

where  $d_c$  is distance from center of bar to extreme tension fiber.

Eurocode-2 [9] proposed the following equation for predicting the crack width,

$$W_{\max} = \left( 3.4 \times \text{cover} + \frac{0.425k_1k_2d_b}{\rho_{\text{eff}}} \right) \varepsilon_{\text{sm}}\varepsilon_{\text{cm}} \quad (3)$$

$$\begin{aligned} \text{with } \rho_{\text{eff}} &= \frac{A_s}{A_c} \text{ and} \\ (\varepsilon_{\text{sm}}\varepsilon_{\text{cm}}) &= \frac{\left( f_s - k_t \left( \frac{f_{\text{ct}}(1 + \eta\rho_{\text{eff}})}{\rho_{\text{eff}}} \right) \right)}{E_s} \geq 0.6 \frac{f_s}{E_s} \end{aligned} \quad (4)$$

where  $k_1$  is coefficient that accounts bond properties (0.8 for HYSD bars, 1.6 for plain reinforcement) and  $k_2$  is coefficient that accounts the strain distribution. The value of  $k_2$  is equal to 0.5 for sections with pure bending and 1.0 for sections with pure axial tension.  $k_t$  accounts duration of loading (0.4 for long-term and 0.6 for short-term loading).  $f_{\text{ct}}$  is tensile strength of concrete and  $\eta$  is the modular ratio.

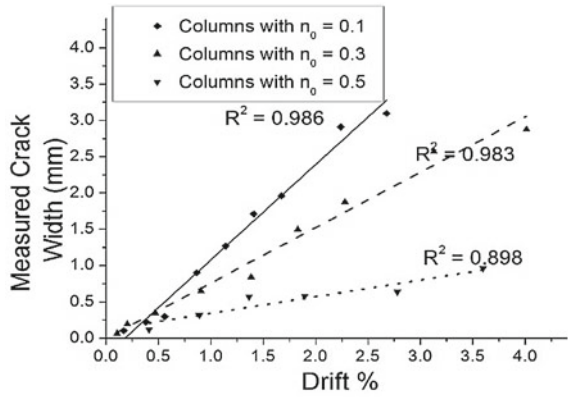
Allam et al. [10] verified Oh and Kang [3] and Gergely and Lutz [6] crack width formulas discussed above and several other empirical formulas available in Egyptian, Eurocode and British codes against the crack widths observed in pre-yield range during experimentations. In the present study, crack widths are estimated, in linear and post-yield response ranges, to visually identify different levels of damage in the RC frame members. It has been seen that, as the maximum crack width is directly proportional to the strain in steel, crack widths for post-yield responses can be estimated from strain in steel. Sezen and Moehle [11] used the concept of slip-based crack width model to determine the increase in deformation of RC member due to bond slippage of development lengths in the linear and post-yield region. The slippage of development length in the post-yield region has been found proportional to strain in steel.

### 3 Validation of Crack Width Formulas in Post-Yield Response Range

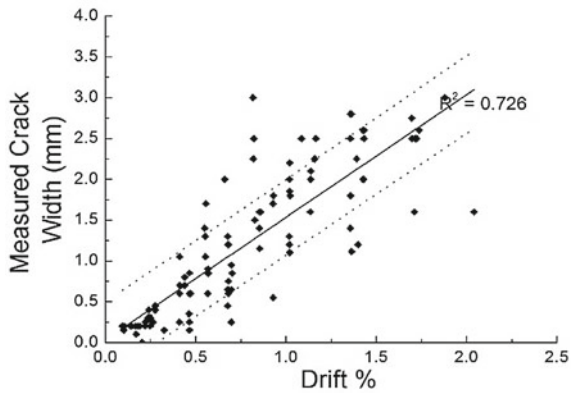
The increase in the crack width for a proportionate increase in the tensile strain of the steel is validated using crack widths observed during quasi-cyclic tests on flexure dominating RC columns and RC shear walls performed by Chen et al. [12] and Dazio et al. [13], respectively.

Maximum flexural crack widths measured during experiments conducted by Chen et al. [12] are plotted against the maximum drift in Fig. 1a for RC columns

**Fig. 1** Comparison of measured crack width against maximum drift



(a) Chen et al. [12] experimental dataset



(b) Dazio et al. [13] experimental dataset

with different axial loads. Values of yield drifts for columns with axial load ratios 0.1, 0.3, and 0.5 are 0.24, 0.42, and 0.35%, respectively. A linear relationship between maximum crack width and maximum drift can be observed in Fig. 1a for both linear (pre-yield) and post-yield responses. Similarly, a linear relationship between maximum crack width and maximum drift is observed in Fig. 1b for RC shear walls measured by Dazio et al. [13] For tested shear walls, the first yield in extreme reinforcement occurs between 0.75 and 1%. Verderame et al. [14, 15] tested RC columns with smooth reinforcement under monotonic and quasi-cyclic loading. It was reported that the crack width increases linearly with the drift in both linear and nonlinear response ranges. However, the crack widths observed in the nonlinear range cannot be used for verifying those estimated by reviewed formulas, as the latter is not applicable to smooth reinforcement.

### 3.1 Analytical Estimation of Crack Widths

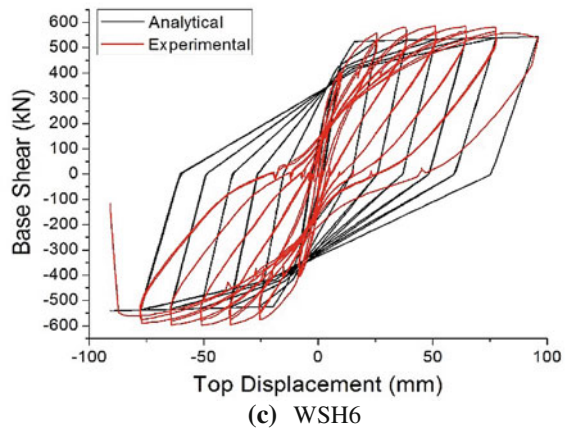
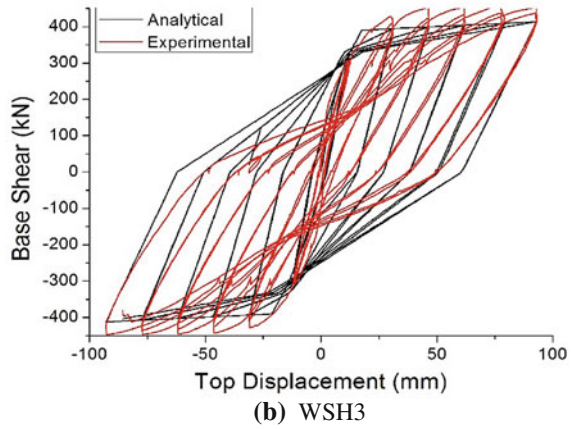
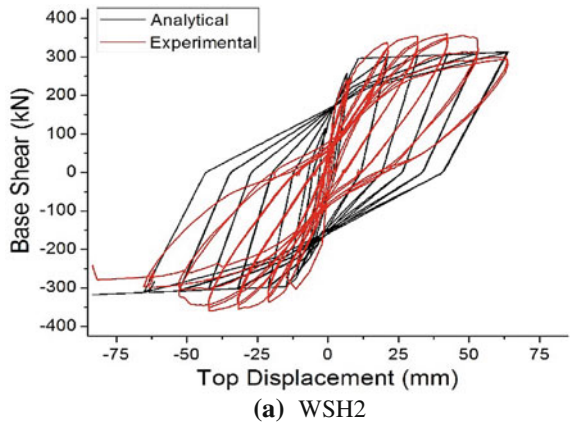
Responses of experiments presented in Chen et al. [12] and Dazio et al. [13] are simulated in IDARC-2D version 7.0. For shear wall specimens of Dazio et al. [13] experimental dataset, trilinear moment-curvature relationship has been used to simulate the experimental response. The concentrated shear hinge has been used to model shear deformation characteristics of the shear wall. The nonlinear shear deformation properties of the shear hinges are estimated as per Krolicki et al. [16]. Different values of hysteretic modeling parameters are tried during simulation for a reasonable match between experimental and simulated force–deflection relationship and yield displacements. Figure 2 compares experimental and simulated force–deflection relationship for WSH-2, WSH-3, and WSH-6, respectively. A reasonable match is observed between experimental and simulated force–deflection relationship from Fig. 2.

Table 1 compares the first yield and nominal yield displacements observed during the experiments with those estimated from the simulations. From this table, it is observed that both first yield displacements from simulated responses are closely related with those observed during experimental studies. Similarly, a reasonable match between experimental and simulated responses has been observed for Chen et al. [12] dataset.

Figure 3 compares maximum crack widths estimated using Gergely and Lutz [6] formula against maximum crack widths measured by Dazio et al. [13] during experimental testing of shear walls. The analytical crack widths are estimated using simulated responses. The analytical estimation of crack widths varies almost linearly with the observed crack widths, for values less than 2 mm.

Figure 4 compares maximum crack widths estimated using Gergely and Lutz [6], Oh and Kang [3] and Eurocode-2 [9] formulas against maximum crack widths measured by Chen et al. [12] for columns with different axial load ratio. It is observed that the analytical estimation of crack widths using Gergely and Lutz [6] and Oh and Kang [3] formulas yield same values and is almost identical to the observed crack widths, for columns with axial load ratios 0.1 and 0.3. Crack widths estimated using Eurocode-2 [9] formula are slightly higher compared to those estimated by Gergely and Lutz [6] formula, for column with axial load ratio 0.1, but slightly lower for column with axial load ratio 0.3. For a column with axial load ratio of 0.5, all three formulas overpredict the observed crack widths. This is due to non-calibration of parameters for higher axial load ratios. However, for axial load ratios in the interest of present study, all three formulas fairly predict maximum crack widths in linear and post-yield response phase. Gergely and Lutz [6] formula is found simpler to use compared to other formulas.

**Fig. 2** Comparison of experimental and simulated force–deflection relationship for shear walls, Dazio et al. [13] experimental dataset



**Table 1** Comparison of simulated and measured yield displacements for Dazio et al. [13]

	At first yield of reinforcement (mm)		Nominal yield disp. (mm)	
	Simulated	Measured	Simulated	Measured
1	8.06	8.40	12.31	11.00
2	9.98	7.80	12.68	10.50
3	11.24	11.30	17.60	16.50
4	11.18	11.40	16.61	15.50
5	7.89	7.80	10.57	9.30
6	10.35	9.90	15.74	12.70

**Fig. 3** Comparison of measured and calculated crack widths using Gergely and Lutz formula for Dazio et al. [13] experimental dataset

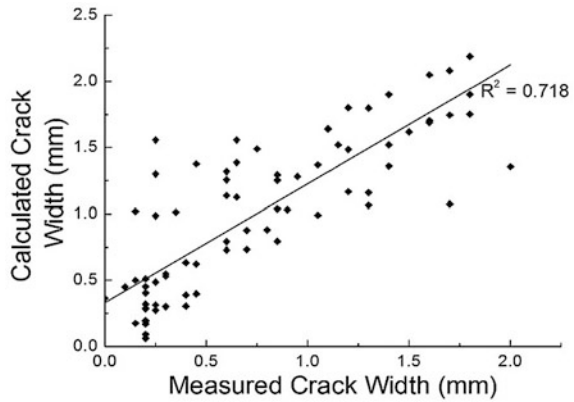
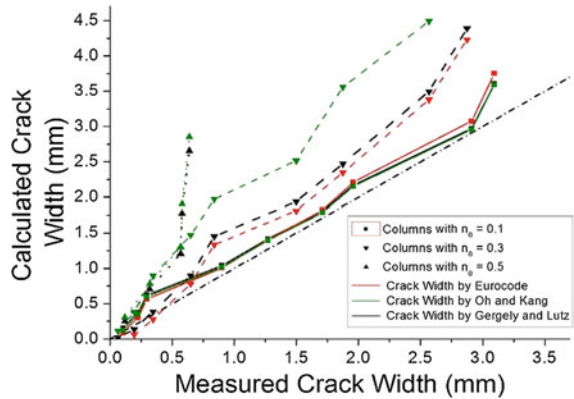


**Fig. 4** Comparison of measured and calculated crack widths for Chen et al. [12] experimental dataset



### 4 Estimation of Residual Crack Width

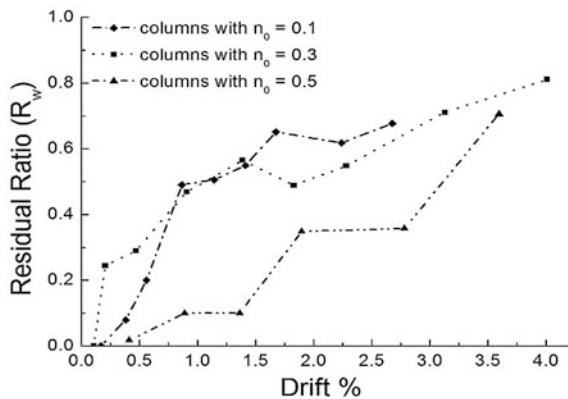
The relationship between peak response parameter and residual crack widths has been developed using the relationship between the residual ratio of maximum crack width and drift as reported by Chen et al. [12]. The residual ratio of maximum crack width ( $R_w$ ) is defined as the ratio of residual width to its maximum crack width.

Figure 5 shows the relationship between  $R_w$  and drift, for columns with different axial load ratios. It is observed that the residual ratio yielded low values for lower drift ratios, but shows a sudden increase after longitudinal reinforcement has yielded. The residual ratio remained constant at high levels after yielding of longitudinal reinforcement.  $R_w$  gradually decreases with increase in the axial load ratio from 0.1 to 0.5. The reduction crack closing capability and effect of axial load on  $R_w$  is due to increase in the contribution of bond slippage in total maximum crack width.

The relationship between maximum and residual crack widths has been studied using local bond stress–slip relationship proposed by Oh and Kim [17]. Oh and Kim [17] conducted several cyclic tests to develop bond slip relation under repeated loading to determine the increase in residual slip with the increase of load cycles. The numbers of constant amplitude load cycles applied before complete pullout tests were 0, 10, 100, 1000, 10,000, and 100,000. Slip and residual slip were measured at 1st, 10th, 100th, 1000th, 10,000th, and 100,000th cycle. Measured values of slip at peak of bond stress and residual slip at the end of first cycle are summarized in Table 2.

From Table 2, it can be observed that residual bond slippage at zero force level is almost same as that of maximum bond slippage in that cycle. Thus, the bond slippage contributes equally in maximum and residual crack widths. On the other hand, cracking caused by strength criterion contributes only in maximum crack width. Cracking governed by strength criteria increases with increase in the tensile strain in extreme concrete fiber and attends constant value once tensile strain in reinforcement bar exceeds limiting tensile strain of concrete. Thus, an increase in

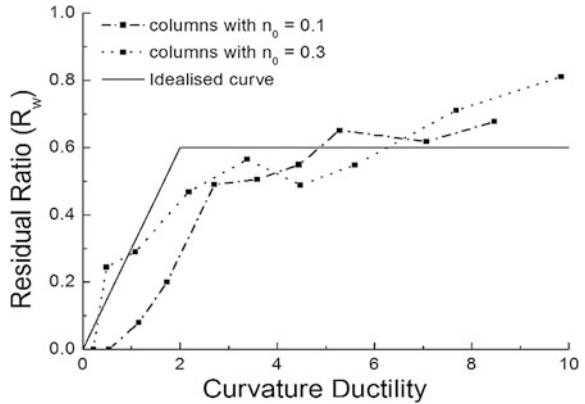
**Fig. 5** Relationship between residual ratio ( $R_w$ ) and % drift for Chen et al. [12] experimental dataset



**Table 2** Measured values of slip at peak of bond stress and residual slip at the end of first cycle for Oh and Kim [17] experimental dataset

	Slip (mm)	Residual slip after first cycle (mm)
0.45	0.278	0.138
0.60	0.472	0.440
0.75	0.528	0.500

**Fig. 6** Relationship between residual ratio ( $R_w$ ) and curvature ductility



the residual ratio  $R_w$  with an increase in drift is due to increase in the contribution of bond slippage in total maximum crack width.

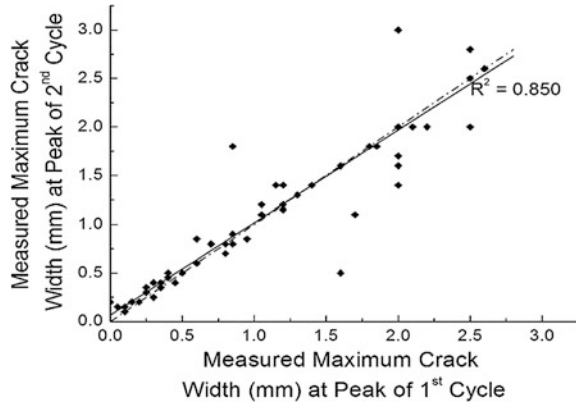
$$\begin{aligned}
 R_w &= 0.3 \times \mu_\phi, & \text{for } \mu_\phi < 2 \\
 R_w &= 0.6, & \text{for } \mu_\phi \geq 2
 \end{aligned}
 \tag{5}$$

A relationship between  $R_w$  and curvature, columns with axial load ratios 0.1 and 0.3 and beams is established using simulated responses. The drift measurements in Fig. 5 are converted into curvature ductilities using simulated responses. Figure 6 illustrates relationship between residual ratio  $R_w$  and curvature ductility. For columns, the residual ratio increases with increase in curvature ductility and attends constant value of 0.6 for curvature ductility more than 2, as shown by the idealized curve.

### 5 Effect of Cyclic Loading on Maximum and Residual Crack Widths

Maximum flexural crack widths observed at the peak of successive cycles, during quasi-cyclic tests on flexure dominating RC shear walls Dazio et al. [13], are plotted in Fig. 7. A linear relationship between maximum crack widths at the peak of the

**Fig. 7** Relationship between residual ratio ( $R_w$ ) and curvature ductility for Dazio et al. [13] experimental dataset



first and second cycle is observed for both linear (pre-yield) and post-yield responses.

Oh and Kim [17] proposed the following relationships to estimate residual slip ( $s_{rN}$ ) after  $N$  cycles from residual slip after first cycle,

$$s_{rN} = s_{r1} \times N^{-0.098} \tag{6}$$

During strong motion earthquakes, structural members are usually subjected to at most 5–10 cycles of load reversals after peak response. Therefore, residual crack widths in the members estimated using Eq. (6) are 15–20% higher at the end of earthquake compared to those at the end of first load reversal. Thus, residual crack width at the end of earthquake motion does not differ substantially compared to the same at the end of first peak load reversal.

## 6 Summary and Conclusions

Substantial work has been carried out to determine the maximum crack width in the RC element. These formulae were calibrated for crack widths measured in linear response range of the member. In order to study the applicability of available formulae in post-yield response range, the available crack width formulae are reviewed thoroughly and then evaluated in pre- and post-yield response ranges using the simulation of observed experimental responses.

From the study, it has been observed that available formulas fairly predict maximum crack widths in linear and post-yield response phase, when axial load ratio in a member is less than 0.3.

The simulated experimental responses are also used to develop a relationship between residual and maximum crack widths and to study the effect of cyclic loading on the residual crack width. For earthquake loading, the residual crack



width at the end of loading is nearly same as that of residual crack width at the end of first peak load reversal, which is estimated from the curvature ductility at peak response and corresponding maximum crack width. The proposed relationship between residual and maximum crack width is useful to trace the peak response experienced by the member from its condition at the end of loading and to predict the residual capacity of the member and that of the building.

## References

1. Borosnyoi A, Balazs GL (2005) Models for flexural cracking in concrete: the state of the art. *Struct Concr* 6(2):53–62
2. Bazant ZP, Oh BH (1983) Spacing of cracks in reinforced concrete. *J Struct Eng ASCE* 109(9):2066–2085
3. Oh BH, Kang YJ (1987) New formulas for maximum crack width and crack spacing in reinforced concrete flexural members. *ACI Struct J* 84(2):103–112
4. Balazs GL (1993) Cracking analysis based on slip and bond stresses. *ACI Mater J* 90(4):340–348
5. Oh BH, Kim SH (2007) Advanced crack width analysis of reinforced concrete beams under repeated loads. *J Struct Eng ASCE* 133(4):411–420
6. Gergely P, Lutz LA (1968) Maximum crack width in reinforced concrete flexural members. *ACI Spec Publ* 20
7. Frosch RJ (1999) Another look at cracking and crack control in reinforced concrete. *ACI Struct J* 96(3):437–442
8. ACI-318 (2008) Building code requirements for structural concrete and commentary. ACI Committee
9. Eurocode-2 (1991) Design of concrete structures: {Part 1}: General rules and rules for buildings. European Committee for Standardization
10. Allam SM, Shoukry MS, Rashad GE, Hassan AS (2012) Crack width evaluation for flexural RC members. *J Alex Eng* 51(3):211–220
11. Sezen H, Moehle JP (2003) Bond-slip behavior of reinforced concrete members. In: *Proceedings of FIB symposium on concrete structures in seismic regions*
12. Chen L, Lu X, Jiang H, Zheng J (2009) Experimental investigation of damage behavior of RC frame members including non-seismically designed columns. *Earthq Eng Eng Vib* 8(2):301–311
13. Dazio A, Beyer K, Bachmann H (2009) Quasi-static cyclic tests and plastic hinge analysis of RC structural walls. *Eng Struct* 31(7):1556–1571
14. Verderame GM, Fabbrocino G, Manfredi G (2008) Seismic response of RC columns with smooth reinforcement. Part I: Monotonic tests. *Eng Struct* 30(9):2277–2288
15. Verderame GM, Fabbrocino G, Manfredi G (2008) Seismic response of RC columns with smooth reinforcement. Part II: Cyclic tests. *Eng Struct* 30(9):2277–2288
16. Krolicki J, Maffei J, Calvi GM (2011) Shear strength of reinforced concrete walls subjected to cyclic loading. *J Earthq Eng* 15(S1):30–71
17. Oh BH, Kim SH (2007) Realistic models for local bond stress-slip of reinforced concrete under repeated loading. *J Struct Eng ASCE* 133(2):216–224

# Influence of Variation of Material Properties on Interstorey Drift of RC Frame Buildings



Ashish Sapre and Ravi Sinha

**Abstract** The main ingredients that provide load-resisting capacity to RCC members are concrete and steel. They possess very different physical properties in elastic as well as inelastic range. Their production processes contribute to variation in their properties, and thereby the resultant behaviour of the RCC members. This paper aims to quantify the effects of material variation on the seismic resistance capacity of RCC buildings. The study uses 3-bay 2D RC frame of two building types, low-rise (G + 3) and mid-rise (G + 7) which are designed as per Indian standards. Both building types are further divided into three categories based on ground floor height. Interstorey drift ratio (IDR) is used to evaluate the influence of variation in steel and concrete properties on the seismic resistance of the buildings. It is observed that at lower and higher IDR, concrete variation governs the structural response. However, at middle range of IDR, it is steel property variation that governs structural behaviour. It is also found from plot of IDR versus PGA and PGV that PGV is a better indicator of IDR, and thus structural damage for both building heights.

**Keywords** Material variation · Nonlinear dynamic analysis · Soft storey Interstorey drift (IDR) · Seismic response

## 1 Introduction

Factors that affect a building's seismic response can broadly be classified into seismic parameters and building parameters. First set deals with shaking characteristics, for example, the peak ground acceleration (PGA), duration, frequency

---

A. Sapre · R. Sinha (✉)  
Department of Civil Engineering, Indian Institute of Technology Bombay,  
Mumbai 400076, India  
e-mail: rsinha@civil.iitb.ac.in

A. Sapre  
e-mail: ashish.sapre@iitb.ac.in

content, source-to-site distance. We have little control over it. The second includes building design, material property, building irregularity, quality of maintenance and can be controlled. To understand seismic response of building, it is important to understand these parameters.

Material variation in a building stock plays important role in deciding its response to seismic excitation. Understanding material variation's effect on post-earthquake damage calls for a probabilistic analysis. Most complex form of such exercise demands nonlinear time history analysis of several buildings for range of earthquake.

Dumova-Jovanoska [1] developed two sets of fragility curves and damage probability matrices for RC structures of Skopje (Macedonia) region. Two representative RC frame structures of 6 storeys and 16 storeys were analysed using nonlinear dynamic analysis for 240 synthetic earthquake time histories. Structural damage was measured using the damage index by Park and Ang [2], and corresponding individual discrete damage states were derived.

Kwon and Elnashai [3] derived vulnerability curves for mid-rise RCC frame and adopted concrete variation as normally distributed with 24 MPa mean strength and 18.6% coefficient of variation. Coefficient of variation was based on the previous study by Barlett and MacGregor [4]. This study was based on large number of tests spanning 6 years from 1988 to 1993. Authors used data from 3756 cylinder tests from 108 mixes with strength less than 55 MPa. Relationship between in-place compressive strength of concrete in structures and specific strength was studied using this vast amount of data. Kwon and Elnashai [3] assumed normal distribution for steel strength with 337 MPa mean strength and 10.7% coefficient of variation based on previous study [5].

Singhal and Kiremidjian [6] derived vulnerability curves for low-rise, mid-rise and high-rise buildings with concrete and steel strength as random variable. A normal distribution for concrete is used with mean strength of  $1.14f_{ck}$  and coefficient of variation as 0.14. Lognormal distribution was used for steel strength with  $1.05f_y$  mean strength and coefficient of variation as 0.11.

Rossetto and Elnashai [7] used sample size of 25 structures to obtain vulnerability curve for RCC frame with infill walls. This study assumed normal distribution for concrete strength with nominal  $f_c$  as mean value and 0.12 as coefficient of variation. It also used masonry infill as a random variable with lognormal distribution, nominal  $f_{cw}$  as mean value of infill strength and 0.2 as coefficient of variation. They considered lognormal distribution for reinforcing steel.

A 25-storey structure was analysed by Tantala and Deodatis [8] to generate fragility curve with random variable as concrete and steel strengths. Concrete strengths were distributed as normal distribution with mean strength of 3.39 ksi and coefficient of variation 18%. This analysis used single model with variable strength of beams and columns. Beam on the same floor was considered to be of same strength because practically they are cast with same batch of concrete. Normal distribution is used for steel strength with 67.5 ksi mean strength and 9.8% coefficient of variation.

Reinforcing steel strength is considered to be more uniform compared to concrete because of better quality control. However, researchers have found variation large enough to be considered as random variable.

Main focus of all such studies has been to develop fragility and/or vulnerability curves. However, there is no comparative study available to show effect on building response due to only concrete variation or only steel variation. Such study will help to understand and quantify, if there is any, relative importance of one material over other for range of seismic excitations.

In an RC building, the concrete is non-homogenous and is produced in not-so-controlled environment. In contrast, steel is factory-produced in controlled environment. So steel has lower variation in its physical and mechanical properties compared to concrete. Behaviour of both materials after yielding also differs significantly. Hence, it is necessary, besides being interesting, to evaluate the influence of properties of concrete and steel on the structural behaviour under seismic base excitations.

A seismic intensity measure (IM) is a parameter chosen to represent strength of earthquake shaking, for example, peak ground acceleration (PGA), peak ground velocity (PGV),  $a/v$  ratio (PGA/PGV), spectral acceleration ( $S_a$ ), spectral velocity ( $S_v$ ). In the past, many of the above-mentioned IMs have been used to represent structural damage. In this study, it is aimed to compare PGA and PGV as a measure of maximum interstorey drift ratio (IDR).

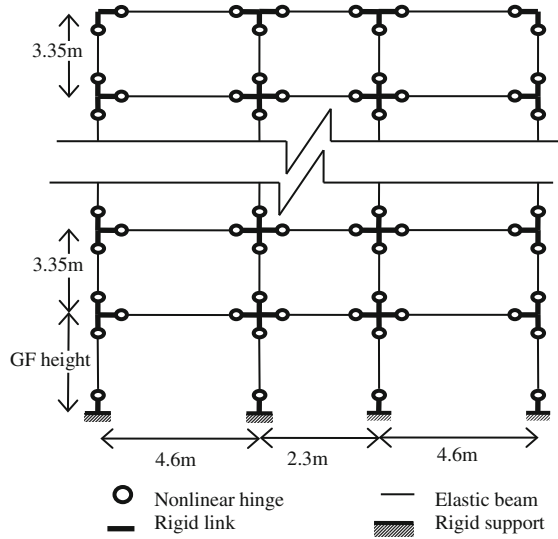
This study has chosen concrete and steel rebar property as variable to understand their relative importance to resist seismic forces. Nonlinear dynamic analysis of several RC frames is conducted for four set of materials: ( $\mu_c, \mu_s \pm \sigma_s$ ) and ( $\mu_c \pm \sigma_c, \mu_s$ ), where  $\mu$  is the average and  $\sigma$  is standard deviation of material property. Subscripts “c” and “s” represent concrete and steel, respectively.

## 2 Building Design and Analysis Model

In the current study, a 3-bay 2D RC frame of low-rise (G + 3 storey) and mid-rise (G + 7) are designed using IS code procedure [9, 10]. Seismic design is done considering building to be located in Zone IV. These building types are further divided into three frames based on ground floor height. First subtype has same ground floor height as above stories, i.e. 3.35 m. Second and third subtypes have 4 m and 5 m high ground floor, respectively. Special provisions of designing for soft storey are not considered, because it is not followed up usually in practice. Building geometry is as per design example in Agarwal and Shrikhande [11].

Nonlinear model of structure, developed in ANSYS software, consists of elastic beam element and nonlinear hinge elements at the end of elastic beam elements. Joints are modelled as rigid, and hinges are considered to be formed at  $d/2$  from the edge, where  $d$  is depth of member. Hinge length is considered to be equal to member depth ( $d$ ). Figure 1 shows nonlinear model of buildings as modelled in ANSYS. Material nonlinearity of concrete and steel is considered as per Indian standards [9, 12].

**Fig. 1** ANSYS nonlinear model of RC frame



Damping in the analysis is defined using Rayleigh model. Damping coefficients  $\alpha$  and  $\beta$  are defined using first and second mode frequency.

Following assumptions are made for creating nonlinear frame model:

- (a) Plastic hinge length is kept constant to beam/column depth.
- (b) Plastic hinge in frame member is assumed to be located at a distance  $d/2$  from the edge of perpendicular frame member, where  $d$  is depth of frame member.
- (c) Hinge property is assumed to be non-degrading bilinear.
- (d) End of member is assumed to be rigid for the portion which is imbedded in other perpendicular member.

Variation in concrete and steel material property is chosen from Indian standards [9] and published literature of previous studies [13]. Mean strength for concrete and steel is 26.6 and 468.9 MPa, and coefficient of variation is 15 and 7.3%, respectively. Table 1 shows building types, and Table 2 shows concrete and steel properties used in analysis.

**Table 1** Building types and analysis Id

Building typology	Number of stories	Ground storey height (m)	Upper storey height (m)	Analysis Id
Low-rise RCC frame	4	3.35	3.35	x81A
	4	4.00	3.35	x82A
	4	5.00	3.35	x83A
Mid-rise RCC frame	8	3.35	3.35	x91A
	8	4.00	3.35	x92A
	8	5.00	3.35	x93A

**Table 2** Young’s modulus of materials

S. No.	Concrete (N/mm <sup>2</sup> )	Rebar steel (N/mm <sup>2</sup> )
1	26.6	503.1
2	26.6	434.7
3	30.6	468.9
4	22.6	468.9

### 3 Earthquake Ground Motion Selection

For this kind of analysis, it is important to select earthquakes which cover entire range of intensity. Seismic time histories are collected from online database [14, 15]. Selection criteria included following parameters:

- (a) Stiff soil;
- (b) Epicentral distance—15 to 1000 km;
- (c) Recording instrument on ground;
- (d) Corrected acceleration time history;
- (e) PGA—0.08 to 1.0 g.

Thirty-two acceleration time histories are selected based on above criteria, and 16 of them were scaled to get uniform PGA distribution between 0.08 and 1.0 g. Maximum scale factor is 1.63. Figure 2 shows spectra and average spectra of selected earthquakes.

Selected earthquakes have wide range of frequency content. This is measured using Mean Time Period ( $T_m$ ) which is the average of time period having weightage as square of the Fourier amplitude. Figure 3 shows the variation of Mean Time Period of selected earthquake time histories with PGA.

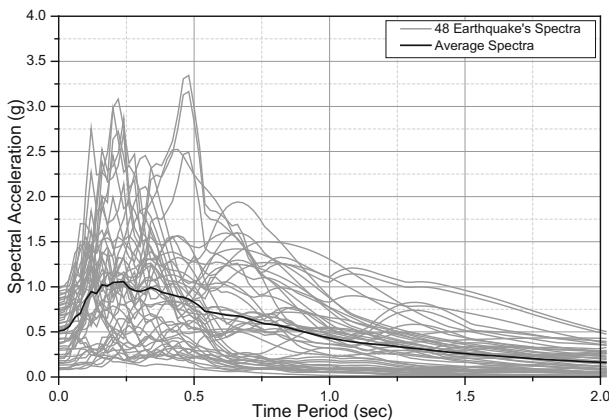


**Fig. 2** Earthquake spectra of selected earthquakes

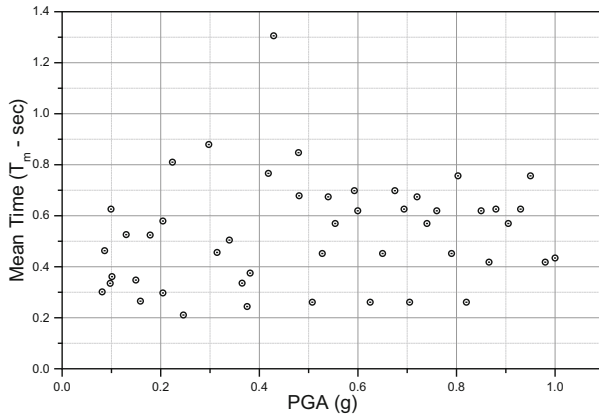


Fig. 3 Mean Time Period ( $T_m$ ) of selected earthquakes time histories

### 4 Results and Discussion

In this study, maximum IDR is selected as engineering demand parameter (EDP). IDR is the commonly used EDP to represent fragility and vulnerability functions because of its direct correlation with building damage and easy for visualisation. The aim of current analysis is to quantify change in IDR due to variation of one material while other is kept constant. Additionally, results are used to compare the better IM, to represent IDR, between PGA and PGV.

Results are plotted such that graph shows spread from minimum IDR to maximum IDR when one material is constant and other varies between mean plus/minus standard deviation.

Concrete variation ( $\Delta_C$ ) for a given PGA (or PGV) is defined as difference between maximum and minimum IDR when steel property is constant. Similarly, steel variation ( $\Delta_S$ ) for a given PGA is defined as difference between maximum and minimum IDR when concrete property is constant.

$$\Delta_C = \left| \text{IDR}_{(\mu_C - \sigma_C, \sigma_S)} - \text{IDR}_{(\mu_C + \sigma_C, \sigma_S)} \right| \tag{1}$$

$$\Delta_S = \left| \text{IDR}_{(\mu_C, \sigma_S - \sigma_S)} - \text{IDR}_{(\mu_C, \sigma_S + \sigma_S)} \right| \tag{2}$$

Figures 4, 5, 6, 7, 8, 9, 10, 11, 12, 13, 14 and 15 show plot of  $\Delta_C$  and  $\Delta_S$  with PGA and PGV. Lower and upper ends of bars show lower and higher IDR, respectively, when one material property is constant and other changes between  $\mu + \sigma$  and  $\mu - \sigma$ .

Several analysis cases of x93A did not converge; hence, there are limited results in Figs. 12 and 15.

Two observations stand out predominantly by looking at graphs. First, the variation in IDR due to concrete property change is higher at lower and higher IDR

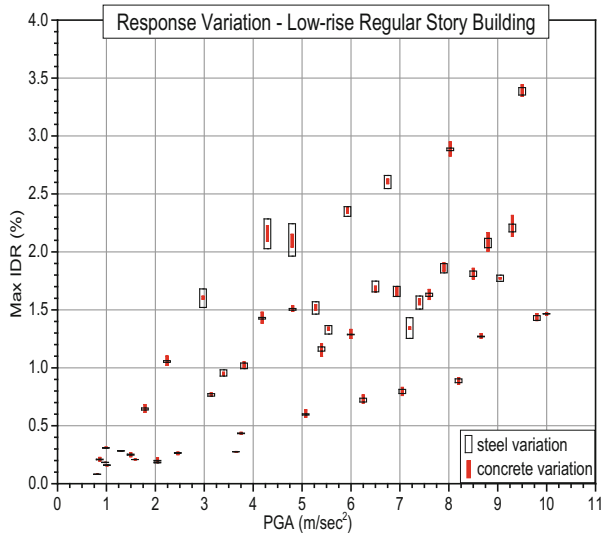


Fig. 4 IDR versus PGA for analysis x81A

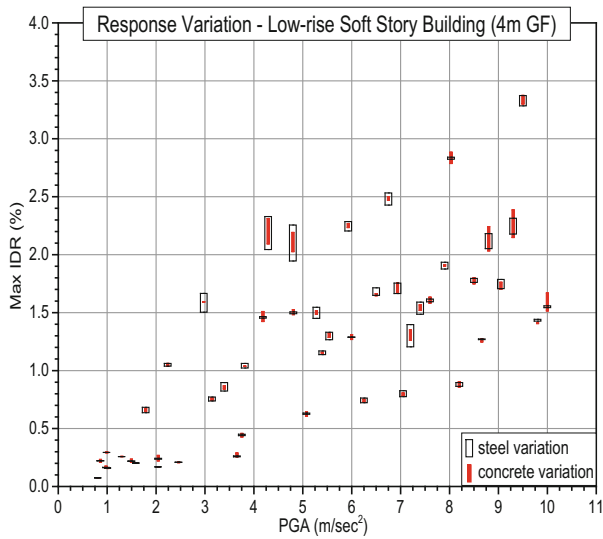


Fig. 5 IDR versus PGA for analysis x82A



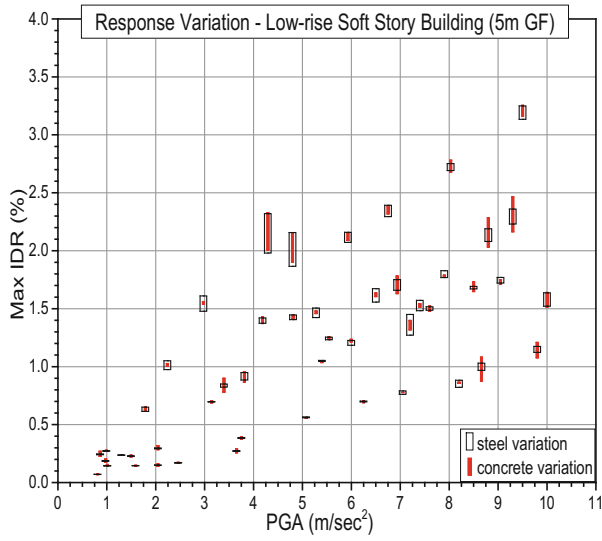


Fig. 6 IDR versus PGA for analysis x83A

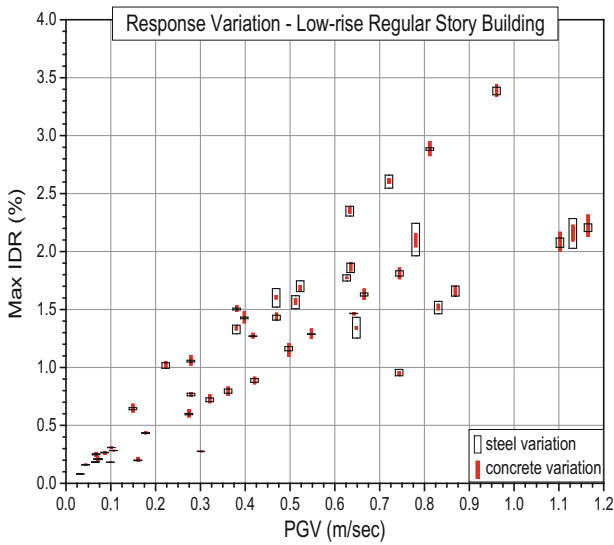


Fig. 7 IDR versus PGV for analysis x81A

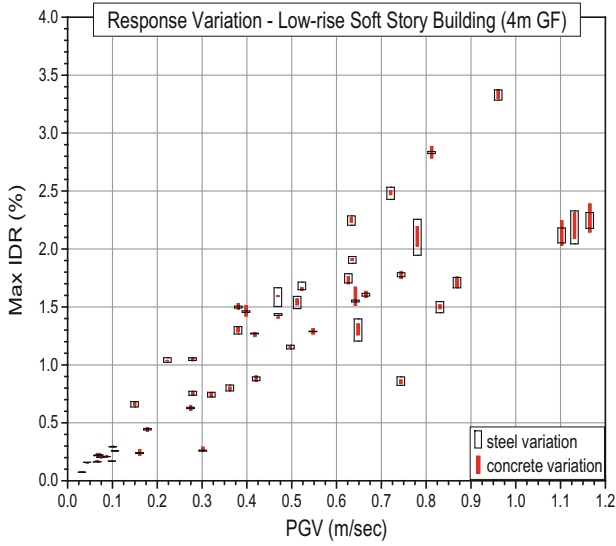


Fig. 8 IDR versus PGV for analysis x82A

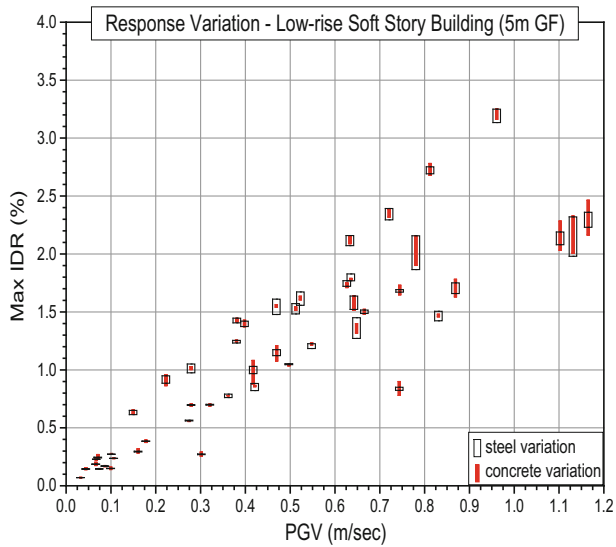


Fig. 9 IDR versus PGV for analysis x83A

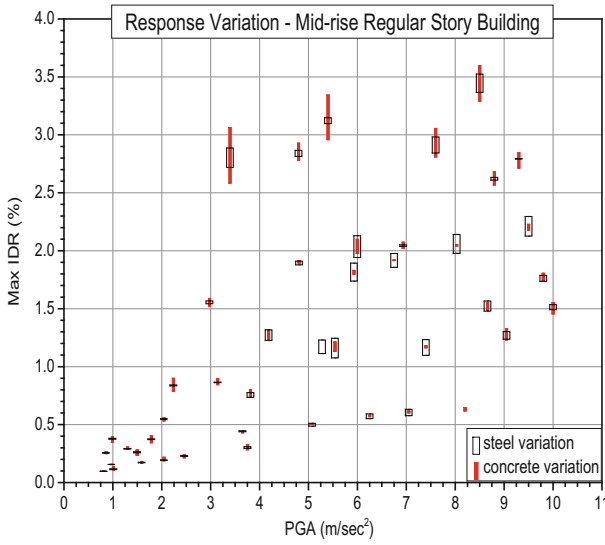


Fig. 10 IDR versus PGA for analysis x91A

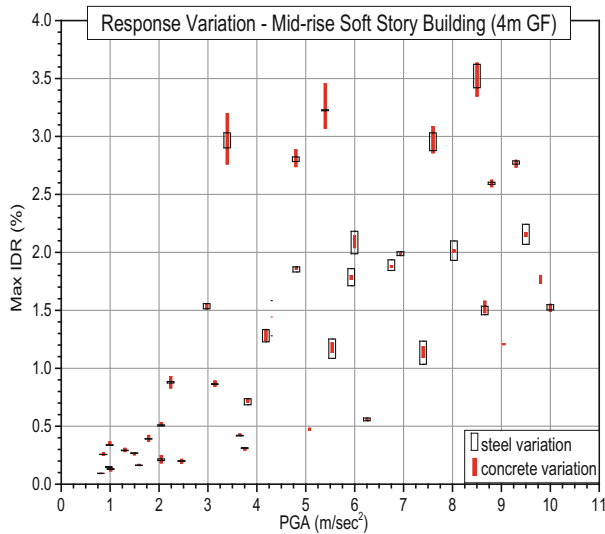


Fig. 11 IDR versus PGA for analysis x92A

levels. In the mid-IDR range, steel variation results in higher IDR variation. This is especially visible in mid-rise structure result where all the results with IDR higher than 2.5% have concrete variation governing over steel variation. In other words, for moderate-to-extensive collapse limit states, change in steel property leads to

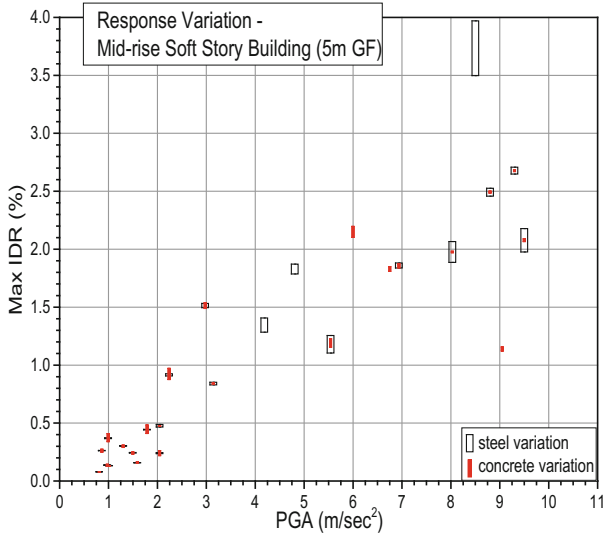


Fig. 12 IDR versus PGA for analysis x93A

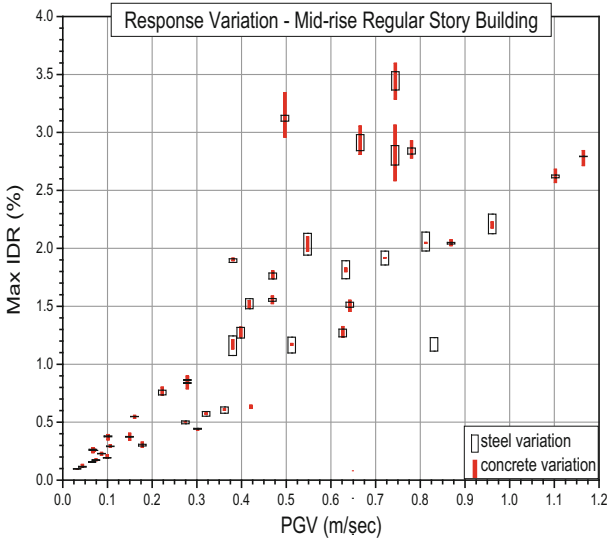


Fig. 13 IDR versus PGV for analysis x91A

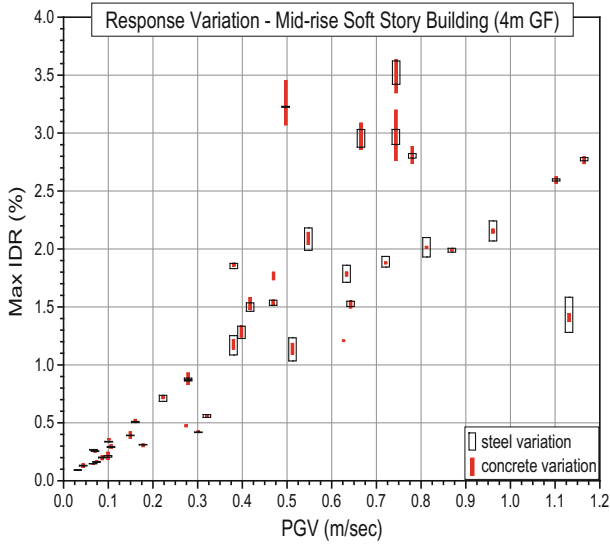


Fig. 14 IDR versus PGV for analysis x92A

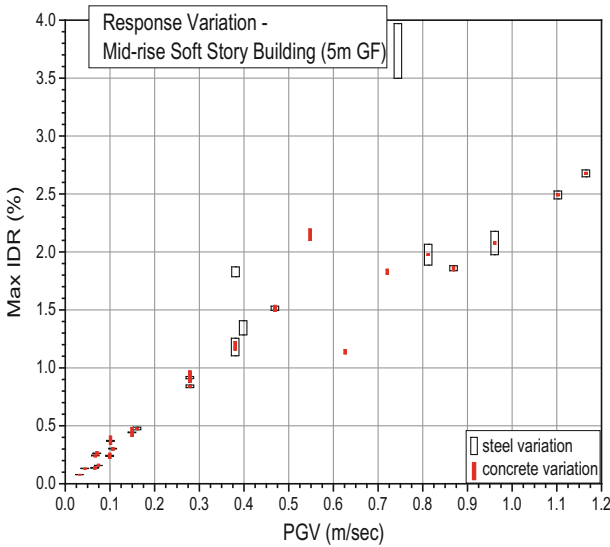


Fig. 15 IDR versus PGV for analysis x93A

higher IDR changes as against similar change in concrete property. When structure's IDR is in range of extensive-to-complete collapse state, concrete property variation leads to higher IDR change.

This result has serious implication in the understanding of building damage. Usually, quality control of concrete is given importance over steel, considering it to be factory-manufactured. However, results show that in the middle IDR range, where property loss and injuries are maximum, steel behaviour governs building response.

Second observation is evident by comparing IDR versus PGA plots with IDR versus PGV plots. Visual observation makes it amply clear that IDR has better correlation with PGV compared to PGA. A clear trend of linear relationship between IDR and PGV is visible at lower values of PGV. This diverges as PGV increases. However for PGA, though linear relationship is clear, scatter in the data is very high as against PGV.

Among both observations, first needs to be looked into mode details. A mathematical relationship for IDR band needs to be established within which steel property governs over concrete. Second observation adds and confirms to various previous studies which advocate PGV to be better indicator of structural damage compared to PGA. However, here also regression analysis is next logical step to establish relationship between IDR and IM.

## References

1. Dumova-Jovanoska E (2000) Fragility curves for reinforced concrete structures in Skopje (Macedonia) Region. *Soil Dyn Earthq Eng* 19(6):455–466
2. Park YJ, Ang AHS (1985) Mechanistic seismic damage model for reinforced concrete. *J Struct Eng* 111(4):722–739
3. Kwon OS, Elnashai A (2006) The effect of material and ground motion uncertainty on the seismic vulnerability curves of RC structure. *Eng Struct* 28:289–303
4. Barlett FM, MacGregor JG (1996) Statistical analysis of the compressive strength of concrete in structures. *ACI Mater J* 93(2):158–168
5. Mirza SA, MacGregor JG (1979) Variability of mechanical properties of reinforcing bars. *J Struct Div* 105(5):921–937
6. Singhal A, Kiremidjian AS (1996) Method for probabilistic evaluation of seismic structural damage. *J Struct Eng ASCE* 122(12):1459–1467
7. Rossetto T, Elnashai A (2005) A new analytical procedure for the derivation of displacement-based vulnerability curves for populations of RC structures. *Eng Struct* 7 (3):397–409
8. Tantala MW, Deodatis GD (2002) Development of seismic fragility curves for tall buildings. In: *Proceedings of 15th ASCE engineering mechanics conference*, Columbia University, New York, June 2002
9. IS 456 (2000) Plain and reinforced concrete—code of practice (Fourth revision). Bureau of Indian Standards, New Delhi
10. IS 1893 (2002) Part-1. Criteria for earthquake resistant design of structures. Part-1, General provisions and buildings. Bureau of Indian Standards, New Delhi
11. Agarwal P, Shrikhande M (2012) Earthquake resistant design of structures. PHI learning, New Delhi, 2012

12. SP16 (1980) Design aids for reinforced concrete to IS 456: 1978. Bureau of Indian Standards, New Delhi
13. Ranganathan R (1999) Structural reliability analysis and design. Jaico Publishing House, Mumbai
14. <http://www.cosmos-eq.org/VDC/index.html> (last accessed on Sept 8, 2016)
15. <http://ngawest2.berkeley.edu> (last accessed on Sept 8, 2016)

# Influence of Corrosion on the Seismic Vulnerability of a Low-Rise, Poorly Constructed RCC Building



Jenson Daniel and Ravi Sinha

**Abstract** Seismic vulnerability assessment methods have been used by engineers and policy-makers as a tool for various engineering and economic applications during the last several decades. These methods were developed for building typologies representing a building stock. Member deficiencies due to poor quality of design, construction or maintenance are not explicitly taken into account in most of these methods. This paper quantifies the influence of member-level deficiencies due to corrosion on the seismic vulnerability of a low-rise, poorly constructed RCC building. Typical design and construction practice prevalent in Andaman and Nicobar Islands have been considered, which is both a highly seismic zone and has highly corrosive environment due to the saline and humid environment.

**Keywords** Member-level deficiency · Corrosion · Seismic vulnerability  
PGA demand · Construction quality

## 1 Introduction

Seismic vulnerability assessment is the measure of damage potential of a building type in a region, subjected to a given intensity of ground shaking. It is carried out by collecting information on building type, occupancy, past earthquakes. This is done to address various engineering, economical or societal requirements [1]. In other words, seismic vulnerability gives the proneness of building to damage in a given earthquake [2].

The domain of seismic vulnerability has been open to much research work for last 5–6 decades with an objective to ascribe a mathematical formulation to it.

---

J. Daniel · R. Sinha (✉)  
Department of Civil Engineering, Indian Institute of Technology Bombay,  
Mumbai 400076, India  
e-mail: rsinha@civil.iitb.ac.in

J. Daniel  
e-mail: jensondaniel@gmail.com



In the past, most of the vulnerability assessments have been carried out on a building stock consisting of different building typologies. Building typologies were generally chosen keeping in mind the type of building construction practices in the region and the materials used [3].

Though a general condition of building's capacity would have been considered for the estimation of seismic vulnerability, not much literature is available wherein member-level deficiencies are explicitly taken into account. In this work, two such deficiencies are considered, viz. *inherent deficiency*, i.e. construction deficiencies due to lack of anchorage length of tension bars in beams or insufficient lap splice length of bars, generally in columns and the other being *time-dependent deficiency*, i.e. deficiencies due to corrosion.

Seismic vulnerability assessment methods are generally three types, viz. empirical, analytical or hybrid. Empirical methods have its limitations due to unavailability of enough and authentic statistical data for all intensity levels. No data exist up to intensity level V as there is practically no damage, and since there are not many earthquakes above the intensity IX and hence not much data available though there is an abundance of data in the intensities between intensities VI and VIII [4].

Hybrid methods also hence have its limitations, like empirical methods, due to non-availability of damage data in all intensity levels. Moreover, the data from elsewhere cannot be taken up effectively, as we do not have the data on the deficiencies in the buildings before the earthquake, unless the same is estimated retrospectively from the available details of collapsed buildings which could be time taking.

Analytical methods had its limitations in the past being computationally intensive; however, with the advent of new computers the same has been taken care of. Analytical methods are advantageous because [2]:

- Availability of seismic hazard maps in terms of PGA and spectral ordinates allows correlation of building damage to the input parameters.
- It allows more detailed and transparent evaluation of vulnerability and can be interpreted more realistically.
- It allows direct tuning up to different hazard and building characteristics.

This paper is based on the work done on the buildings of the Andaman and Nicobar Islands which come under seismic zone V and where MMI IX or bigger earthquakes are expected [5]. Buildings are constructed by default low rise due to regulatory restrictions. RCC buildings there have shown much proneness to corrosion because of the use of sea sand for construction in the past and also due to the ambient marine environment. The region is also known for its excessive rainfall. The constructions in the private sector and the remote islands are generally carried out by untrained workforce with lesser quality control. These facts have been responsible for the occurrence of member-level inherent deficiencies and time-dependent deficiencies in the buildings.

## 2 Methodology

Analytical method has been used for the evaluation of seismic vulnerability of a low-rise RCC building typical of Andaman and Nicobar Islands with inherent and time-dependent deficiencies in this paper.

### 2.1 Member and Material Modelling

A building with members that are well designed and constructed as per latest seismic codal provisions is expected to behave satisfactorily in an earthquake. The properties of members are defined by the ‘ $M-\theta$ ’ curves. These curves, in order to be as close to the actual, are to be based on stress–strain curves of steel and concrete that are more realistic.

The stress–strain model for concrete is taken as suggested by Park, Priestly and Gill [6, 7] for a confined concrete. A typical stress–strain curve for the concrete is shown in Fig. 1. However, the practically possible maximum strain is considered, i.e.  $\epsilon_{cc}85$  which corresponds to 85% of maximum confined strength in the descending branch of the curve. Similarly, the stress–strain curve model for steel with 15% strain hardening after a strain of 3% with a maximum strain of about 14.5% has been considered. A typical stress–strain model for steel used is shown in Fig. 2.

### 2.2 Deficiency Parameters

Pre-code constructions and poorly designed building have deficiencies that are inherent. Dimova and Negro have worked on an experimental setup and have found that inherent deficiencies do influence the seismic response of structures [8].

**Fig. 1** Stress–strain curve for confined concrete [6]

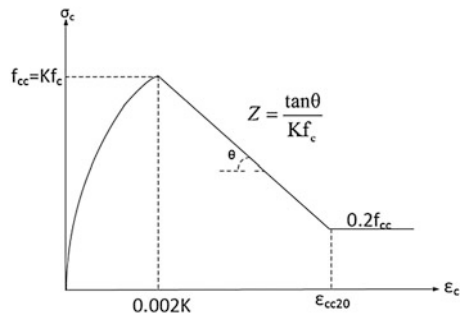
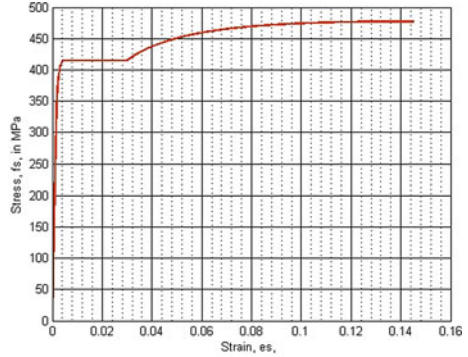


**Fig. 2** Stress–strain model for the steel



Member-level inherent deficiencies that can affect the seismic vulnerability of a concrete building are generally:

- Lack of anchorage length specially at beam-column joints for beams.
- Lack of lap splice length especially for the columns.
- Lack of confining reinforcement specially at plastic hinge zones.

Even if members do not have any inherent deficiencies, it could still have, subsequently, as the building ages, time-variant deficiencies in the members like:

- Loss of bond strength due to corrosion.
- Loss of area of steel due to corrosion.
- Loss of concrete strength due to ageing: Chemical attack/cracks/spalling of concrete due to steel corrosion.

## 2.3 Inherent Deficiencies (ID)

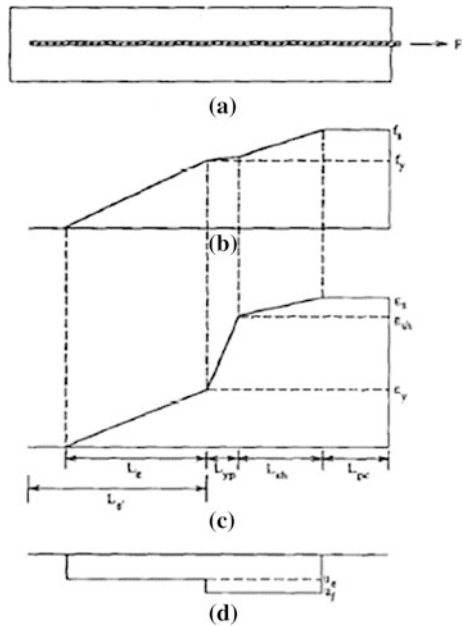
Various inherent deficiencies (ID) that are considered here are:

### 2.3.1 Lack of Anchorage Length

Minimum anchorage length required to develop full strength at a beam-column joint for any bar will be given by the development length (Eq. 1). In some of the collapses that are seen in the past earthquakes, the anchorage length can be as low as 10% of what is required.

$$L_d = \frac{\phi f_s}{4\tau_d} \quad (1)$$

**Fig. 3** **a** Reinforcing bar embedded in concrete; **b** stress distribution; **c** strain distribution; **d** bond stress between concrete and steel [9]



where  $L_d$  = development length,  $\phi$  = diameter of the bar,  $f_s$  = the bar cross section and  $\tau_d$  = bond stress corresponding to  $f_{c,mean}$ .

Reinforcement anchorage slip has been studied and modelled by Alsiwat et al. [9] way back in 1992 and has been adopted by many researchers. Anchorage slip also brings in additional end rotations that are not otherwise reflected in the flexural analysis. The stress–strain in the embedded region is shown by Alsiwat et al. which is shown in Fig. 3.

### 2.3.2 Insufficient Lap Splice Length

Similarly, a column with deficient lap splice length will have adverse effect on the ‘ $M-\theta$ ’ curve. What is generally seen on site is that lap splice length can be as low as 50% of what is required. There has been a work by Traverdilo et al. [10], wherein they have derived fragility curves for reinforced concrete frames with lap-spliced columns. They have given a formula for calculating the force developed in the lap-spliced bar given in Eq. (2).

$$T_b = A_b f_s = F_t P L_s \tag{2}$$

where  $T_b$  = force developed in the lap-spliced bar,  $A_b$  = the bar cross section,  $F_t$  = tensile strength of concrete is equal to  $0.33\sqrt{f'_c}$  and  $f'_c$  is the concrete

compressive strength,  $L_s$  is the lap splice length and  $P$  is the perimeter of cylindrical block, which is given by Eq. (3) for a rectangular column.

$$P = \frac{s}{2} + 2(d_b + c) \leq 2\sqrt{2}(d_b + c) \tag{3}$$

where  $s$  is average distance between spliced bars,  $c$  is the cover and  $d_b$  is the bar diameter.

### 2.4 Time-Dependent Deficiencies (TD)

Time-dependent deficiencies (TD) in the concrete structures are deficiencies brought in by the corrosion of steel reinforcement and deterioration of concrete by chemical attack or by the cracks generated by the corrosion products. There has been significant work that has gone by to understand the various aspects of corrosion and its effects on concrete structures and its behaviour [11–13]. It has been long understood that the corrosion products exert pressure on surrounding concrete causing excessive crack, thereby weakening the anchorage and bond in the interface (Fig. 4).

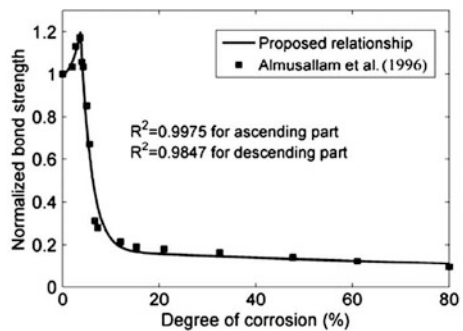
Mangat and Molloy [14] have given a relationship to determine the loss of steel due to corrosion over a period of time which is shown in Eq. (4). This relationship to find the depth of corrosion in re-bars has been used by many researchers.

$$x = 11.6i_{\text{corr}}t \tag{4}$$

where  $x$  is the metal loss in the radial direction in  $\mu\text{m}$ ;  $i_{\text{corr}}$  is the corrosion current density in  $\mu\text{A}/\text{cm}^2$ ;  $t$  is time in years.

Almusallam et al. [15] have established a relationship between degree of corrosion and ultimate bond strength. Li et al. [16] based on data of Almusallam et al. [15] have brought out an analytical relationship between degree of corrosion ‘ $w$ ’ and normalized bond strength given by Eqs. (5) and (6).

**Fig. 4** Normalized bond strength as a function of corrosion in the analytical form [16]



for  $w \leq 4\%$ :

$$\frac{\tau_{\max}^c}{\tau_{\max}} = 0.9959e^{0.0041w} + 0.0069e^{0.7858w} \tag{5}$$

for  $4 < w \leq 80\%$ :

$$\frac{\tau_{\max}^c}{\tau_{\max}} = 9.662e^{-0.5552w} + 0.1887e^{-0.0069w} \tag{6}$$

where  $\tau_{\max}^c$  = corrosion-affected bond stress,  $\tau_{\max}$  = bond strength without corrosion and  $w$  = degree of corrosion by mass loss of original steel.

These deficiencies were modelled as nonlinear rotational spring at the beam-column joints. In the building model, a single equivalent rotational spring, representing the actual ‘ $M-\theta$ ’ curve of the section with all the deficiencies and the additional slips, was adopted, so that the member stiffness remains realistic.

## 2.5 Other Parameters

### 2.5.1 Earthquake Parameter Selection

Response spectrum from IS 1893 was adopted.

### 2.5.2 Damage State Parameters

Inter-storey drift ratios as global displacement limits for various performance levels like ‘IO’, ‘LS’ and ‘CP’ were taken as the damage state parameters [17] shown in Table 1.

**Table 1** Deformation limit [17]

Inter-storey drift limit in %	Performance level		
	Immediate occupancy (IO) (%)	Life safety (LS) (%)	Collapse prevention (CP) (%)
	1	2	4

## 2.6 Building Model and Analysis

A three-bay (both direction), triple-storied structure is considered for analysis. It has three bays of 3.5 m span both ways and a storey height of 3 m. All beams are of size of 300 mm  $\times$  400 mm size with four bars of 16-mm-diameter bars at bottom and four bars of 16-mm-diameter bars at top with four-legged 8-mm-diameter stirrups 100 mm *c/c*. All columns are 350 mm  $\times$  350 mm size with eight bars of 25 mm diameter as longitudinal steel and 8 mm ties at 85 mm *c/c*. Grade of concrete is taken as M15 and grade of steel as Fe415. Lap splices are provided just above first-floor column joints.

### 2.6.1 Deficiencies Considered in This Work

Inherent deficiencies are varied uniformly in the building to represent the average level of the building construction with same deficiency for all beams. And the lap splice deficiency is kept at same level as in beam but only at bottom of first-floor level. Generally, degree of corrosion in a bar varies with the density of corrosion current and the bar diameter as shown in the literature [14, 15]. However, for this work a uniform degree of corrosion has been adopted.

Since shear hinges are not considered for this work as of now, corrosion of stirrups is not considered. The cracking of concrete due to corrosion is though not explicitly considered but implicitly modelled in the bar slip based on the work of Alsawat and Saatcioglu [9] and Almusallam et al. [15].

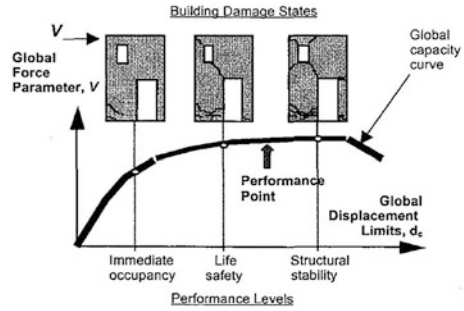
### 2.6.2 Nonlinear Analysis

A number of nonlinear static analyses (pushover) were carried out using capacity spectrum method in *Perform-3D*, on building model taking various combinations of deficiency parameters.

There are many nonlinear static analysis procedures; for the rapid evaluation technique used for seismic vulnerability assessment of buildings in the USA, Capacity Spectrum Method was adopted by ATC40 [18]. In this method, the graphical intersection of pushover curve and demand curve plotted in a specialized format called acceleration–displacement response spectra (*ADRS*) Format estimates the behaviour of the building/structure [19]. A point called the performance point, in this curve, describes a unique damage state for the structure (Fig. 5) [20].

Though there are many software that are available, *Perform 3D* developed by CSI Lab, Berkley, is used for this work. Some of its unique features make it stand out as a powerful tool for the seismic vulnerability assessment of buildings. It implements the procedures of ASCE 41 Seismic Rehabilitation of Existing Buildings, Pre-standard and Commentary for the Seismic Rehabilitation of

**Fig. 5** Capacity curve and performance levels [20]



Buildings [17]; FEMA-356 [21] and ATC 40 Seismic Evaluation and Retrofit of Concrete Buildings [18].

### 2.7 Derivation of Vulnerability Functions

After the pushover analysis, the following were the progression to vulnerability function derivation:

- Obtaining the capacity curve output of Perform-3D in ADRS format.
- Evaluating the spectral displacement corresponding to the three damage states, IO, LS and CP.
- Conversion from  $S_d$  to corresponding PGA in line with method given in HAZUS methodology, Technical Manual MR, Sect. 5.4.4 [22].
- Derived vulnerability curve between the PGA and damage states.

#### 2.7.1 Quantify Influence of Deficiencies on Vulnerability Function

After the vulnerability functions were made, influence of each of the deficiency and the combination thereof on the vulnerability curve were evaluated/estimated and quantified. The probability of PGA demand exceeding in 50 years causing a given damage was estimated.

## 3 Results

Once the above results were obtained, from the modal data, modal participation factor was calculated. Then, roof displacements for each damage state, viz. IO, LS and CP, were evaluated and corresponding spectral displacements were calculated



**Fig. 6** Capacity curve and corresponding vulnerability curve of a poorly constructed building with time-dependent deficiency of 7% (*damage state 1, 2, and 3 stands for IO, LS and CP, respectively*)

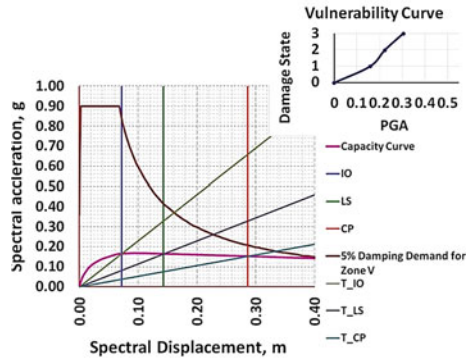
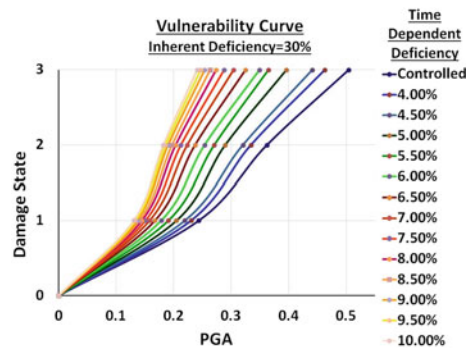


**Fig. 7** Vulnerability for curves of a poorly constructed building with different degrees of corrosion



and were marked on the capacity curve which is in the ADRS format. PGA demand for each of the damage state is evaluated using method mentioned in Sect. 2.6.

Vulnerability curves are then derived [23] for different degrees of deterioration. Figure 6 shows the capacity curve and the corresponding derived vulnerability curve for a typical analysis.

Vulnerability curves of a poorly constructed building with an inherent deficiency of 30% and varying degrees of corrosion is shown in Fig. 7.

The influence of the deficiencies on the PGA demand on each damage state is evaluated and shown for the case discussed earlier in Fig. 8.

The percentage probability of PGA demand exceeding, for each damage state of the poorly constructed building, in 50 years, for various degrees of time dependant deficiency, is shown in Table 2.

**Fig. 8** Influence of time-dependent deficiency on the PGA demand of a poorly constructed building

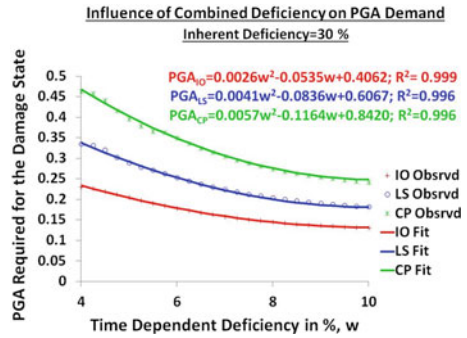


**Table 2** Probability (%) of PGAs being exceeded in 50 years for a set of analyses for each damage state

S. No	Deficiency		% Probability of exceeding in 50 years		
	ID	TD	IO	LS	CP
1	0	0	5.65	1.96	0.55
2	30	4.0	6.37	2.51	0.80
3	30	4.5	7.02	2.85	0.97
4	30	5.0	8.00	3.76	1.45
5	30	5.5	9.06	4.44	1.91
6	30	6.0	10.15	5.18	2.21
7	30	6.5	11.18	6.00	2.74
8	30	7.0	12.13	6.76	3.29
9	30	7.5	12.96	7.47	3.82
10	30	8.0	13.67	8.08	4.31
11	30	8.5	14.24	8.59	4.75
12	30	9.0	14.78	9.09	5.14
13	30	9.5	15.19	9.49	5.50
14	30	10	15.53	9.81	5.80

## 4 Discussions and Conclusions

Seismic deficiency and vulnerability of a low-rise, poorly constructed concrete example building are deliberated. There has not been much work in domain of influence of inherent and time-dependent member-level deficiencies on seismic vulnerability curves.

Most vulnerability assessment methods are made on building typologies, that is typical of a region, construction practice at the time of construction, height of building and material used for construction, and hence generally fail to address realistically, the effect of building specific seismic deficiencies.

The member-level deficiencies are found to greatly affect the seismic capacity and influence the seismic vulnerability curves. Poor workmanship is the reason for

inherent deficiencies, which also make the buildings more susceptible to time dependent deficiencies.

Realistic models validated by experiments and many studies are available to predict the rate of corrosion and degree of corrosion in real timescale. If the corrosion current density is known, then the seismic vulnerability of a building can be estimated at any given age of the building.

Vulnerability curves made considering time-dependent deficiencies will enable policy-makers to see the vulnerability of a building or building stocks in real timescale and make necessary plans for structural intervention/retrofitting at appropriate time.

## References

1. Sapre A, Sinha R (2010) Building seismic vulnerability assessment methods: relevance to India. In: Proceedings of the 14th symposium on earthquake engineering (14SEE)
2. Borzi B, Pinho R, Crowley H (2008) Simplified pushover-based vulnerability analysis for large-scale assessment of RC buildings. *Eng Struct* 30(3):804–820
3. Calvi G, Pinho R, Magenes G, Bommer J, Restrepo-Velez L, Crowley H (2006) Development of seismic vulnerability assessment methodologies over the past 30 years. *ISET J Earthq Technol* 43(3):75–104
4. Kappos AJ, Panagopoulos G, Panagiotopoulos C, Penelis G (2006) A hybrid method for the vulnerability assessment of R/C and URM buildings. *Bull Earthq Eng* 4(4):391–413
5. Murty C, Rai DC (2003) Reconnaissance report North Andaman (Diglipur) earthquake of 14 September 2002. National Information Center for Earthquake Engineering, Indian Institute of Technology Kanpur, Kanpur
6. Park R, Priestley M, Gill WD (1982) Ductility of square-confined concrete columns. *J Struct Div* 108(4):929–950
7. Penelis GG, Kappos AJ (1997) *Earthquake-resistant concrete structures*, 1st edn. Taylor and Francis, Oxon OX14 4RN, UK
8. Dimova S, Negro P (2005) Influence of construction deficiencies on the seismic response of structures. *Earthq Eng Struct Dyn* 34(6):613–635
9. Alsiwat J, Saatcioglu M (1992) Reinforcement anchorage slip under monotonic loading. *J Struct Eng* 118(9):2421–2438
10. Tariverdilo S, Farjadi A, Barkhordary M (2009) Fragility curves for reinforced concrete frames with lap-spliced columns. *Int J Eng Trans A Basics* 22(3):213
11. Cabrera J (1996) Deterioration of concrete due to reinforcement steel corrosion. *Cement Concr Compos* 18(1):47–59
12. Sezen H, Moehle JP (2003) Bond-slip behavior of reinforced concrete members. In: Proceedings of FIB symposium on concrete structures in seismic regions
13. Dekoster M, Buyle-Bodin F, Maurel O, Delmas Y (2003) Modelling of the flexural behaviour of RC beams subjected to localised and uniform corrosion. *Eng Struct* 25(10):1333–1341
14. Mangat P, Molloy B (1992) Factors influencing chloride-induced corrosion of reinforcement in concrete. *Mater Struct* 25(7):404–411
15. Almusallam AA, Al-Gahtani AS, Aziz AR et al (1996) Effect of reinforcement corrosion on bond strength. *Constr Build Mater* 10(2):123–129
16. Li C, Yang S, Saafi M (2014) Numerical simulation of behavior of reinforced concrete structures considering corrosion effects on bonding. *J Struct Eng* 140(12):04014092
17. A. 41 (2006) ASCE 41—seismic rehabilitation of existing buildings. American Society of Civil Engineers Reston, Virginia

18. ATC (1996) Seismic evaluation and retrofit of concrete buildings, Report No. SSC 96-01: ATC-40, 1. ATC
19. Lin Y-Y, Chang K-C (2003) An improved capacity spectrum method for ATC-40. *Earthq Eng Struct Dyn* 32(13):2013–2025
20. Comartin CD, Niewiarowski RW, Freeman SA, Turner FM (2000) Seismic evaluation and retrofit of concrete buildings: a practical overview of the ATC 40 document. *Earthq Spectra* 16(1):241–261
21. E. U. F. E. M. A. FEMA (2000) Prestandard and commentary for the seismic rehabilitation of buildings. FEMA
22. NIBS (2003) Multi-hazard loss estimation methodology. Earthquake model, HAZUS® MH technical manual. National Institute of Building Sciences and Federal Emergency Management Agency, Washington, DC
23. Saeidi A, Deck O, Verdel T (2009) Development of building vulnerability functions in subsidence regions from empirical methods. *Eng Struct* 31(10):2275–2286

**Part IV**  
**Repair, Rehabilitation and Retrofit of**  
**Structures**

# Studies on Strengthening Techniques for Existing Transmission Line and Communication Towers



R. Balagopal, N. Prasad Rao, R. P. Rokade and P. K. Umesha

**Abstract** The transmission and communication towers are subjected to increased loading due to its voltage upgradation and installation of new antennas in existing towers for new line of sight, respectively. Hence, cost-effective structural upgrading scheme has to be developed that can be easily adopted by power and communication industries. In the present study, component level analytical and experimental investigations are carried out to strengthen existing angle section of transmission tower. Experimental investigation is conducted to determine the buckling capacity of single angle section of size  $65 \times 65 \times 5$  mm with slenderness ratio 40 strengthened with different connection patterns such as (i) double cross-plate, (ii) single cross-plate, (iii) friction grip, (iv) double angle, and (v) double cleat angle connections. The compression strength of angle section is increased on an average by 20%. The analytical investigation is carried out using ABAQUS software using C3D8R elements. The numerical and experimental results are in good agreement, and the variation is within 16%.

**Keywords** Retrofitting · Structural upgradation · Strengthening  
Cleat angle · Friction grip · Cross-plate

---

R. Balagopal (✉) · N. Prasad Rao · R. P. Rokade · P. K. Umesha  
TTRS, CSIR-Structural Engineering Research Centre, Chennai 600113, India  
e-mail: bala@serc.res.in

N. Prasad Rao  
e-mail: nprao@serc.res.in

R. P. Rokade  
e-mail: rokade@serc.res.in

P. K. Umesha  
e-mail: pku@serc.res.in

## 1 Introduction

The transmission line towers that are currently in service are 30–50 years old and need to be upgraded. The degradation of the tower material will occur due to adverse environmental conditions. Due to increasing demand for power supply, voltage upgradation of the existing lines is required. This results in additional wind and gravity loads, which lead to overstressing of the existing tower members. The aged tower members also require strengthening. The wind loads are frequently updated due to revision of wind zones. The increased wind loading also requires strengthening of the towers. Due to urbanization, it is difficult to obtain new right of way for installation of new communication towers. The installation of additional antennas in the existing tower may be required to augment the required signal strength. The increased wind and dead load due to these additional antennas will induce higher stresses in the tower members. The tower capacity will exceed their design limit due to additional loading, and this may lead to collapse of several communication towers.

The failure of any of these transmission/communication towers can lead to outage of power/communication interruption and will have huge impact on national economy. To eliminate the failure of the transmission and communication towers due to increased loading and strength degradation, a cost-effective structural upgrading scheme has to be developed that can be easily adopted by power and communication industries.

Experimental investigation was carried out at component level to strengthen  $65 \times 65 \times 5$  mm equal angle section for different connection patterns such as (i) single cross-plate, (ii) double cross-plate, (iii) friction grip, (iv) double angle, and (v) double cleat angle connections. The analytical investigation is carried out using ABAQUS software using C3D8R elements. Based on the results of the investigations on different upgradation schemes, suitable strengthening technique is proposed to upgrade leg member in transmission line/communication tower.

## 2 Current Status of Technology

Albermani et al. [1] developed diaphragm bracing system for upgradation of existing transmission tower. The strength improvement was investigated by adding series of diaphragm bracings at mid-height of the slender diagonal member through experimental investigation on tower substructure assembly. The developed upgrading scheme was successfully implemented on existing 105-m-height TV tower. Sarno and Elnashai [2] studied the seismic performance of steel moment resisting frame retrofitted with different bracing systems. Three different brace configurations such as special concentrically brace frames (SCBFs), buckling-restrained brace frames (BRBFs), and mega-brace frames (MBFs) were investigated. Inelastic time history analysis was carried out to assess the structural

performance of retrofitted steel frame under earthquake loading. Brennan [3] studied the failure of existing transmission lines and the techniques to restore its life by different refurbishment techniques. The increased capacity due to refurbishment and the associated probability of failure are discussed. The influence of conductor and overhead earth wire, bolted connection, and foundation of different refurbishment techniques are also discussed. Shahi [4] explored the feasibility of using glass fiber-reinforced polymer (GFRP) cross-arms in place of wooden cross-arms. The GFRP retrofitting proved to be an effective way of strengthening as it changed the failure mode to pure flexure with increased strength and stiffness. Kabir and Seif [5] presented an analytical solution for lateral-torsional buckling of I-beam, retrofitted using FRP sheets. The analytical solution is formulated based on the total potential energy and Rayleigh–Ritz method. The steel I-beam retrofitted in its top-bottom flange portion with the FRP sheet is considered for the analysis based on classical lamination theory (CLT). Bekey et al. [6] conducted experimental investigation to enhance the buckling strength of steel angle with different slenderness ratio through fiber-reinforced polymer (FRP) reinforcement. The FRP strengthening influences the failure mode and the buckling capacity, ductility behavior of existing angle section. Dostanti [7] studied the strengthening techniques for solid round member using split pipes along with U bolts, and it is recommended that compression capacity of solid pipes can be increased through wrapping with welded split pipe along its length.

Baskaran et al. [8] investigated tower failure based on simple methods to check tower capacity based on available simplified models. The preliminary structural analysis with specialized structural analysis package has to be incorporated into existing steel tower design procedures to assess the failure of these towers. The transmission tower leg retrofitted by steel angles through bolted connection to enhance its capacity is explored by Mills et al. [9]. It was found that bolted-splice connection can transfer axial loads effectively between original and reinforcing angle member. Rao et al. [10] carried out nonlinear analysis of angle compression members through 3D finite element analysis of lattice frames and towers. The member eccentricity, rotational rigidity of connection, and material nonlinearity are considered in the analysis. Xie and Sun [11] conducted experimental investigation on the retrofitting strategy of 500 kV transmission tower failed due to ice disaster in China. It was observed that the addition of diaphragm bracing prevents the out of plane deformation of bracing member, and it enhanced the load carrying capacity of existing leg member. Amiri et al. [12] studied the feasibility of using buckling-restrained bracing as retrofit scheme for existing steel frame structure. Comprehensive nonlinear static and time history analysis were carried out to assess the increased load carrying capacity of this retrofitted steel frame. Lu et al. [13, 14] found that the load displacement behavior of reinforced steel transmission tower legs is influenced by friction coefficient, applied torque, and number of bolts in the bolted connection. From the above literature, it is noticed that there is further scope for optimizing the design of retrofitted steel angle connections in transmission line towers.



### 3 Present Study

To study the strengthening techniques for the existing angle sections in transmission and communication towers, five different strengthening patterns are studied. The strengthening member should be effective in load transfer from existing angle member. Hence in the present study, an equal angle section of size  $65 \times 65 \times 5$  mm with slenderness ratio of 40 is strengthened to examine its increase in compression capacity at component level through different connection patterns such as (a) double cross-plate, (b) single cross-plate, (c) frictional grip, (d) cleat angle, and (e) double angle connections. The analytical investigation is carried out using ABAQUS software for modeling the angle members strengthened through different connection techniques.

### 4 Analytical and Experimental Investigations on Strengthening of Leg Member

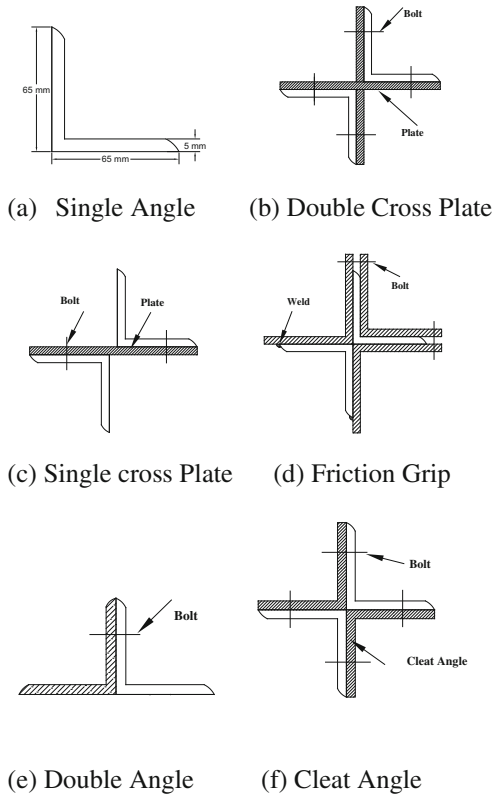
The experimental investigations on strengthening angle section through different connection patterns in the existing leg member are carried out. An equal angle section of L  $65 \times 65 \times 5$  mm size with slenderness ratio 40 is chosen to represent both the existing leg member and retrofitting angle member respectively. These two members are connected back to back through bolted connection to form a compound section. Five different connection patterns like (i) double cross-plate, (ii) single cross-plate, (iii) friction grip, (iv) double angle, and (v) double cleat angle connections are considered. The buckling capacities of these compound sections are compared with the capacity of control specimen of single angle member that represents the existing leg member. For connections, 16 mm diameter of 8.8 grade bolts tightened to a torque level of 110 N m is used. For single and double cross-plate connections,  $140 \times 65$  mm plate is used at a spacing of 300 mm c/c connected through bolts. The schematic view of different connection patterns is shown in Fig. 1.

Five different connections are considered for the present study. The connection patterns are designated as follows.

- Single angle member (control specimen);
- Double cross-plate connection;
- Single cross-plate connection;
- Frictional grip-type connection;
- Double angle connection;
- Double cleat with back-to-back angle connection (cruciform connection).

For friction grip connection, one flange of each cleat angle is welded to the strengthening angle member at a spacing of 300 mm. The outstanding flanges of these cleats are connected to the flanges of the third cleat held at required position in

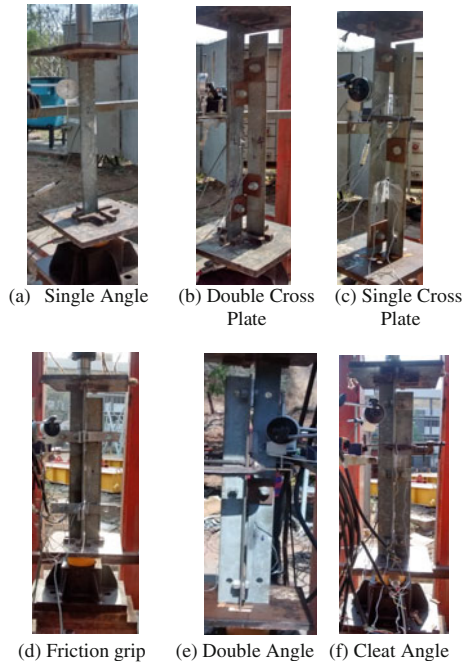
**Fig. 1** Schematic view of connection pattern



the main leg member. The load from main leg member is transferred to the strengthening angle through the friction generated between the cleat contact surfaces with the main leg member. In the case of double cleat connection, i.e., the strengthening and existing leg member, two angle members are connected directly back to back with cleats at a spacing of 300 mm c/c using bolts. Similarly, for double angle connection, the additional strengthening angle member is connected to the main leg member through bolts at a spacing of 300 mm.

The compression load is applied to the main leg (existing) member to simulate the load transfer similar to the existing field condition. The boundary condition is simulated through end plate fitting of size 300 × 300 mm and 20 mm thick with small strips welded to guide the positioning of angle member. The load is applied through the center of gravity of main angle member. The axial load is applied through 30 t capacity compression jack, and the load is measured through 100-tonne capacity digital wigameter. The compression jack is operated through mechanized hydraulic pump. The axial deformation and load transfer between existing and strengthened angle member are monitored using dial and strain gauges. The experimental setup for all the strengthening patterns is shown in Fig. 2a–f,

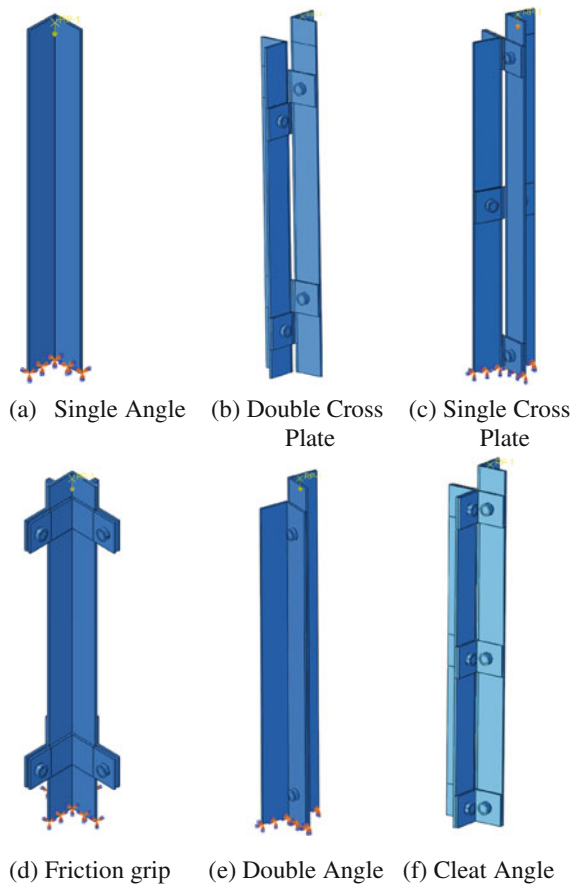
**Fig. 2** Experimental setup of connection patterns



respectively. All the specimens failed due to local buckling because of rotation near the loading end.

The numerical investigation is carried out using ABAQUS software 6.13 version. The steel angle and bolts are modeled using solid C3D8R elements for single and double cross-plate, friction grip, cleat angle, and double angle connections. The frictional contact between steel angle and plate sections is defined through surface-to-surface contact friction with friction coefficient of 0.25. For friction grip connection, the coupling constraint is defined at the bolted connection region, to ensure that the load is transferred through friction. All steel angles, bolts, and the connection plates are modeled with yield stress of 250 MPa, Young's modulus as  $2 \times 10^5$  N/mm<sup>2</sup>, and Poisson's ratio as 0.3. The nonlinear material property is defined through nonlinear stress-strain curve for mild steel. The bottom portion of the compound angle section is assumed to be held in position and restrained against rotation about longitudinal axis, and at the top portion, all DOFs are constrained except the displacement and rotation along axial direction. All the components are meshed using the mesh refinement aspect ratio of 7.5. The FE models of all connection patterns are shown in Fig. 3a–f, respectively. Nonlinear static analysis is carried out. The failure modes of experimental and analytical investigations are shown in Fig. 4a–f respectively. The comparison of failure loads from the experimental and numerical investigations is tabulated in Table 1.

**Fig. 3** FE models of connection patterns



From Table 1, it is observed that the experimental and FE analysis failure loads vary in the range of 10–16% for different types of connections. The FE analysis results deviate from experimental results due to local buckling of the main angle section in its free length portion. The local buckling occurs in the main angle sections occur due to application of load in the centroidal axis of main member. The cleat angle connection for strengthening shows higher enhancement of compression strength compared to other types of connections. The cleat angle and friction grip connection are cost-effective compared to other types of strengthening patterns. From the analytical and experimental results, it is observed that in cleat and friction grip connections, the strengthening angle member shares considerable stress arising from the main member during the application of load. The double angle connection changes the buckling mode of main angle member. It is observed that the strengthening pattern also plays an important role in determining the failure mode of main angle member.

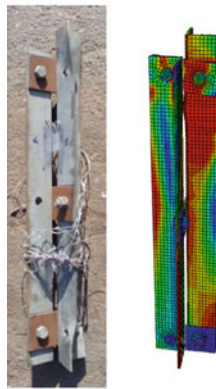
**Fig. 4** Failure modes for different connection patterns from analytical and experimental investigations



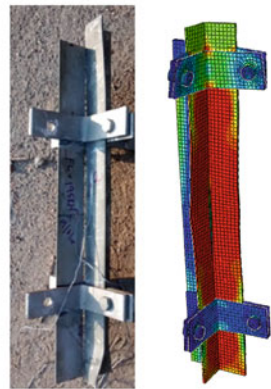
(a) Single Angle



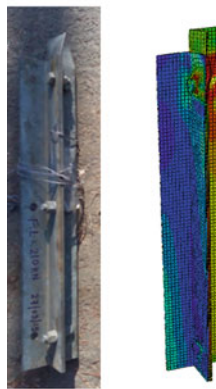
(b) Double Cross Plate



(c) Single cross plate



(d) Friction Grip



(e) Double Angle



(f) Cleat Angle

**Table 1** Summary of analytical and experimental results

Type of specimen	Experimental failure load (kN)	FE analysis failure load (kN)	Increase in compression strength (experimental) % (w. r. t reference specimen)	Increase in compression strength (FEA) % (w. r. t reference specimen)
Single angle (reference specimen)	175	158	–	–
Double cross-plate connection	210	180	20	14
Single cross-plate connection	195	170	12	8
Friction grip connection	197	175	13	11
Double angle connection	195	175	11	11
Cleat angle connection	210	180	20	14

## 5 Summary

From the experimental and analytical investigations, the following conclusions are drawn.

- It is observed that the experimental and analytical failure loads vary in the range of 10–16% for different types of connections. The compression strength is enhanced by 20 and 14% for cleat angle and double cross-plate connection strengthening in the experimental and FE analysis respectively.
- The cleat angle and double cross-plate connection show higher enhancement of compression strength compared to other types of connections. The cleat angle connection is cost-effective compared to other types of strengthening patterns.
- It is observed that in the cleat and friction grip connection, the strengthening angle member shares considerable stress arising from the main member during the application of load. The double angle connection changes the buckling mode of failure of main angle member.

**Acknowledgements** This paper is being published with the kind permission of the Director, CSIR-Structural Engineering Research Centre, Taramani, Chennai-113, India.

## References

1. Albermani F, Mahendran M, Kitipornchai S (2004) Upgrading of transmission towers using a diaphragm bracing system. *Eng Struct* 26:735–744
2. Sarno LD, Elnashai AS (2004) Bracing system for seismic retrofitting of steel frames. In: 13th World conference on earthquake engineering, Canada
3. Brennan G (2004) Refurbishment of existing overhead transmission lines. Integral Energy, Australia, Session 2004. <http://www.cigre.org>
4. Shahi A (2008) Strengthening of wooden cross arms in 230 kV transmission structure using glass fiber reinforced polymer (GFRP) wrap. M.A.Sc. thesis, Department of Civil Engineering, University of Waterloo, Western Ontario, Canada
5. Kabir MZ, Seif AE (2010) Lateral torsional buckling of retrofitted steel I-beams using FRP sheets. CICE 2010, Beijing, China
6. Bekey S, Peng F, Lieping Y (2010) Experimental study on behavior of FRP anti-buckling strengthening steel members. In: Proceedings of the 5th international conference on FRP composites in civil engineering, pp 919–924, Beijing, China
7. Dostanti C (2011) Analysis, design and strengthening of communication towers. Ph.D. thesis, Dept of Civil and Environmental Engineering, University of Windsor, Ontario, Canada
8. Baskaran K, Jayasinghe J, Hettiarachchi (2011) Strength assessment of steel towers. Civil Engineering Research for Industry. M.Sc. thesis, Department of Civil Engineering, University of Moratuwa, Sri Lanka
9. Mills JE, Ma X, Zhuge Y (2012) Experimental study on multi-panel retrofitted steel transmission towers. *J Constr Steel Res* 78:58–67
10. Rao NP, Knight GMS, Mohan SJ, Lakshmanan N (2012) Studies on failure of transmission line towers in testing. *Eng Struct* 35:55–70
11. Xie Q, Sun L (2012) Failure mechanism and retrofitting strategy of transmission tower structures under ice load. *J Constr Steel Res* 74:26–36
12. Amiri JV, Naeef M, Naeef MR (2012) Seismic retrofitting of steel frames with buckling restrained braces. *IJEE* 178–185. ISSN 2079-2115
13. Lu C, Ma X, Mills JE (2014a) Modeling and parametric analysis of bolted connections on retrofitted transmission tower leg member. In: 23rd Australasian conference on the mechanics of structures and materials, Byron Bay, Australia
14. Lu C, Ma X, Mills JE (2014b) The structural effect of bolted splices on retrofitted transmission angle member. *J Constr Steel Res* 95:263–278

# Rehabilitation of Post-Tensioned Flat Slab Affected by Fire



D. Prabu and L. S. Kannan

**Abstract** This paper explains about the evaluation and rehabilitation of a severely fire-affected post-tensioned flat slab without demolition. The portion under rehabilitation was a post-tensioned slab in the ground floor of a tower with 3 Basements + Ground + 13 floors, to be used as office space. The post-tensioned flat slab was designed with isolated drop panels. The building was designed to resist gravity and lateral loading with a combination of reinforced concrete columns and shear walls. The flat slab had suffered various levels of damages including spalling of concrete with the bottom un-tensioned reinforced and pre-stressing tendon exposed. Columns in the affected area also had significant damages due to exposure to the high temperature. The total affected area of the floor was around 500 m<sup>2</sup> including four columns. The damaged face of the flat slab and all faces of the column were chipped to remove the loose and delaminated concrete. The strength of the existing concrete and reinforcement was ascertained with core cuts, TGA and DTA tests and cut samples. Based on the results, a comprehensive retrofit plan was drawn up without the need to pull down the affected slab. The rehabilitation involved change of the design basis from isolated drop panels to formation of a continuous drop connecting the columns in the affected area. The design utilised the residual strength available in the concrete, un-tensioned and pre-tensioned reinforcements. Self-compacting concrete with mineral and chemical admixtures was used for forming the retrofit zone and was placed from above the existing affected slab. Shear connection between existing and new concrete was created with chemical grouted dowel reinforcements. The entire rehabilitated slab and column was grouted with low viscous epoxy grout to seal the micropores and restore normalcy to the slab. The complete rehabilitation of the area was done without any change in the intended design capacity and with the most optimum and economical solution.

---

D. Prabu (✉)

EDRC, B&F IC, L&T Construction, Manapakkam, Chennai 600089, India  
e-mail: dprabu@Intecc.com

L. S. Kannan

TC-II, B&F IC, L&T Construction, Manapakkam, Chennai 600089, India  
e-mail: lsk@Intecc.com

© Springer Nature Singapore Pte Ltd. 2019

A. Rama Mohan Rao and K. Ramanjaneyulu (eds.), *Recent Advances in Structural Engineering, Volume 2*, Lecture Notes in Civil Engineering 12,  
[https://doi.org/10.1007/978-981-13-0365-4\\_55](https://doi.org/10.1007/978-981-13-0365-4_55)



**Keywords** Rehabilitation • PT slab • Concrete affected by fire  
DTA–TG tests • Self-Compacting Concrete (SCC)

## 1 Introduction

An office space (3 Basements + Ground + 13 storied) structure (panel size is 13.5 m × 13.5 m c/c with slab thickness of 275 mm and drop thickness of 525 mm) under construction got affected by fire during non-working hours. The post-tensioned flat slab with isolated drops at Basement 1 floor level, 2 columns, ramp slab connecting ground floor to basement floor 1 and beams adjacent to ramp slab got affected by fire.

The fire was due to the stacked nitrile rubber insulation, APP bitumen sheets, FPS pipe wrapping, SBS and PVC waterproofing material. The slab, beams and columns were studied for extent of damages and DTA–TG tests were performed for evaluation of concrete strength and core tests are taken. An economical and site-friendly method of Rehabilitation is proposed (Figs. 1 and 2).

## 2 The Fire Is Classified, Depending on the Surface and Structural Appearance

Class 1—Slight damage (green colour and no crack with less/no exposure)

Class 2—Noticeable damage (blue colour and no crack with less spalling of concrete)

Class 3—Extensive damage (orange colour and small/minor crack with exposure to reinforcement/tendon) (Fig. 3).

**Fig. 1** Basement 1 layout plan

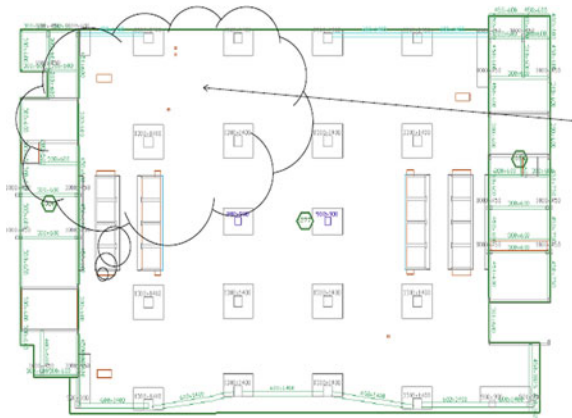


**Fig. 2** Part tendon layout plan in the affected area

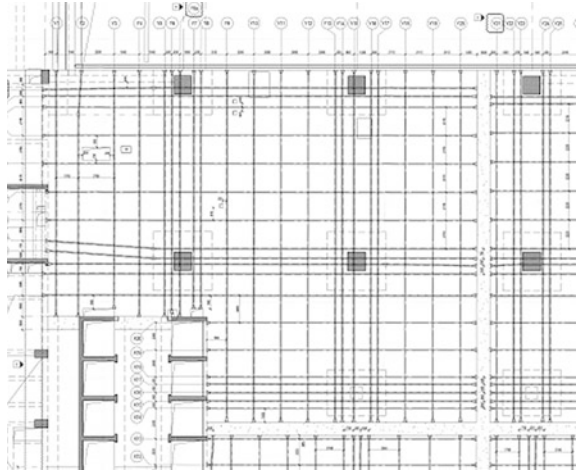
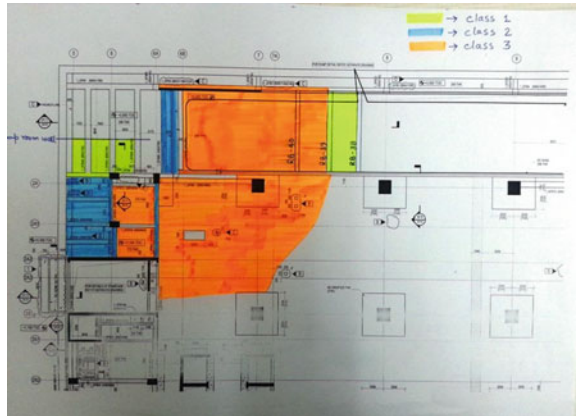


**Fig. 3** Classification of fire



**Pictures showing the extent of fire:**

To assess the existing condition of the structural elements and to determine the extent of damage in the material resulted from exposure to heat, following tests were suggested so as to undertake suitable remedial measures for rehabilitation of the structure (Figs. 4, 5, 6, 7, 8, 9 and 10).

1. Drilled Core Test
2. Test on steel (reinforcement)
3. Differential Thermal Analysis–Thermogravimetric Test.

**Fig. 4** Fire broke out in basement 1 floor, it got damaged and it passed through the ramp opening and affected the first floor slab and soffit of the second floor slab (there is 4 m cantilever in second floor slab)



**Fig. 5** Spalling of concrete with exposed bottom steel with service lines



**Fig. 6** Spalling of concrete with exposed reinforcement, tendon and concrete beyond reinforcement damaged

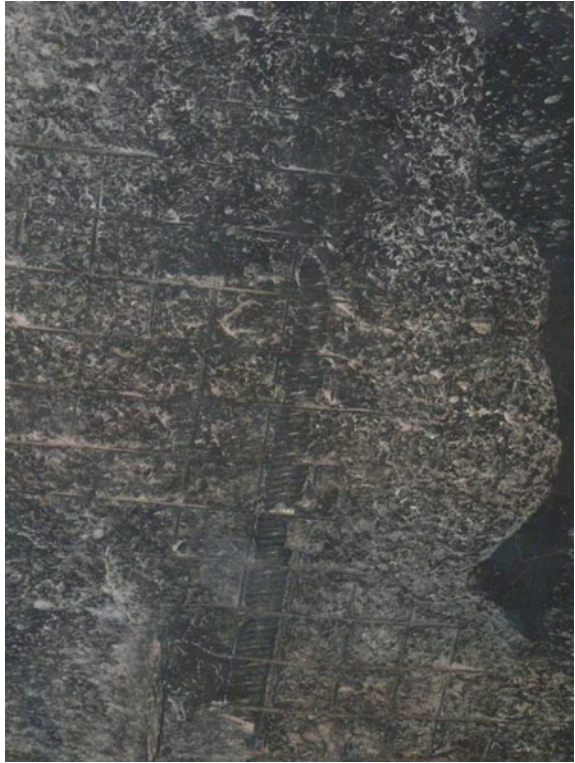


**Fig. 7** Spalling of concrete and broken ramp slab with exposed reinforcement—view from basement 1 floor



**Fig. 8** Spalling of concrete in column along grid 2A1-6 in basement 1 floor



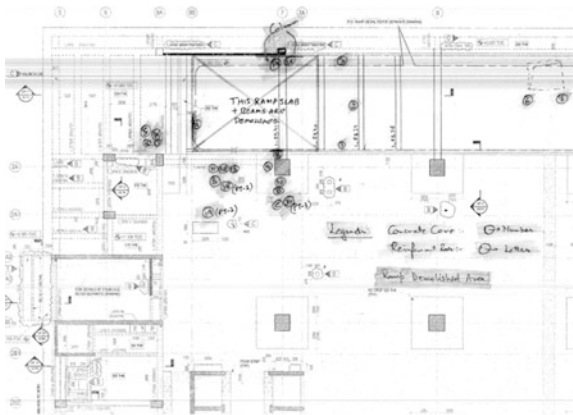
**Fig. 9** Spalling of concrete in beam supporting ramp slab in basement 1 floor



**Fig. 10** Closer view of column and beam showing spalling of concrete



**Fig. 11** Core sample location in plan



## 2.1 Drilled Core Test

See Fig. 11 and Tables 1, 2 and 3.

## 2.2 Thermal Analysis of Samples (Said to Be Concrete Core)

The thermogravimetric analysis (TG) of all the samples (said to be concrete core) show total weight losses in the range 5–7% up to a temperature of 900 °C from ambient.

**Table 1** Compressive strength of extracted concrete core on different portions of the fire-affected area

Sample No.	Compressive strength (N/mm <sup>2</sup> )	Location
1	30.3	Ramp beam
2	36.0	Ramp beam 1_RB 39
3	35.5	Ramp beam
4	36.1	GF beam 1_GFB70
5	31.8	GF beam 1_GFB59
6	30.1	Ramp slab
7	33.5	Ramp slab
8	36.3	Column 2A/7
9	41.1	Column 2A/7
10	40.2	GF beam 1_GFB 9
11	43.3	GF beam 1_GFB 9
12	46.9	Column connecting to ramp near grid 7
13	38.0	Column connecting to ramp near grid 7
14	23.7	Ramp slab near grid 6A & 2A
15	26.7	Ramp slab near grid 6A & 2A
16	37.0	PT slab
17	44.9	PT slab
18	23.6	PT slab

**Table 2** Physical test of steel sample near fire-affected area

Sample ID	Dia. of bar (mm)	Unit weight (kg/m)	Ultimate tensile strength (N/mm <sup>2</sup> )	Yield strength (N/mm <sup>2</sup> )	% Elongation
A	8	0.386	668.43	566.17	22.75
B	8	0.397	624.90	505.93	30.85
C	8	0.394	661.28	558.21	21.60
D	10	0.578	719.80	618.29	24.80

**Table 3** Chemical test of steel sample near fire-affected area

Sample ID	Dia. of bar (mm)	Carbon	Silicon	Manganese	Phosphorus	Sulphur
B	8	0.225	0.16	0.83	0.02	0.013

The DTA pattern clearly represents three endothermic peaks in all the samples except in H-1832 and H-6711 in which only the last two endothermic peaks are evident.

**Table 4** DTA–TG test results

S. no.	Sample code	Total wt. loss (%)	Dissociation of Ca(OH) <sub>2</sub>		Inversion of silica	Decarbonation	
			Peak position (°C)	Wt. loss (%)	Peak position (°C)	Peak position (°C)	Wt. loss (%)
1.	H-8931	7.08	457.2	0.45	570.1	684.1	1.44
2.	H-8805	6.30	455.6	0.37	570.0	681.2	1.32
3.	H-8179	6.28	461.5	0.27	570.4	676.2	0.87
4.	H-1832	5.03	–	–	570.6	667.2	0.75
5.	H-6889	5.63	459.8	0.21	570.2	669.6	0.72
6.	H-8786	5.86	461.2	0.47	571.0	685.5	0.89
7.	H-7089	6.90	458.7	0.33	570.7	677.1	0.84
8.	H-8474	5.51	458.1	0.26	570.5	685.9	1.195
9.	H-4924	6.27	461.1	0.39	570.6	674.5	0.87
10.	H-9918	4.71	458.8	0.31	570.5	678.7	0.71
11.	H-7050	6.50	458.8	0.30	570.4	673.0	0.67
12.	H-9880	5.18	457.3	0.30	570.3	665.1	0.47
13.	H-6711	6.29	–	–	570.8	682.4	0.74
14.	H-1766	6.63	455.8	0.37	570.1	684.2	1.27
15.	H-7044	7.01	458.2	0.38	570.3	678.8	1.07

The first endotherm (Table 1) in all the samples (except H-1832 and H-6711) is observed around 460 °C and is attributed to dissociation of calcium hydroxide. The weight losses associated with these endothermic peaks are in the range of 0.2–0.4%.

The samples depict a prominent and characteristic peak of inversion of silica at around 570 °C.

The last endotherm in the DTA pattern of the samples is around 670–680 °C and is also associated with weight losses. This endothermal peak arises due to decarbonation. The weight losses recorded in TG corresponding to these peaks are in the range 0.7–1.4%.

The peak positions of DTA–TG curve and the corresponding weight losses are taken.

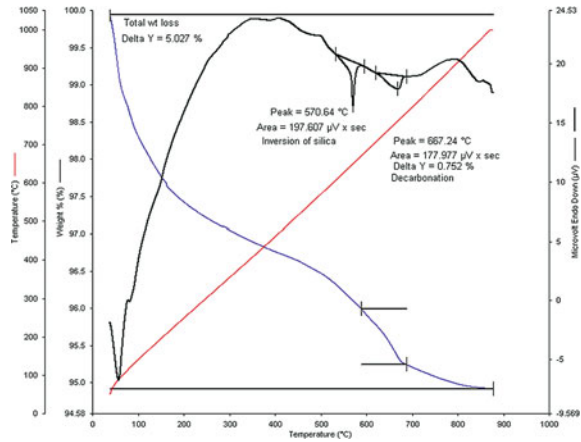
The thermogravimetric analysis (TG) of all the samples (said to be concrete core) shows total weight losses in the range 5–7% up to a temperature of 900 °C from ambient (Table 4; Fig. 12).

### 2.3 Rectification Methodology for Ramp Slab (Class 3 Fire)

Ramp slab was heavily damaged, and hence, it should be totally demolished and constructed again.



**Fig. 12** PT 3 (0–50 mm)  
H-1832 (typical DTA–TG  
curve)



### 2.3.1 Rectification Methodology for RC Conventional Slab/RC Column and RC Beam (Class 1 Fire)

1. Providing necessary scaffolding and working platform for the area to be plastered.
2. Chipping the existing old surface about 5–6 mm to remove the black smoke stain-affected concrete.
3. Cleaning the surface of loose and foreign materials and smoke stain material by means of sandblasting with coarse sand and pressure sufficient to ensure that sand sticks to the surface under air pressure.
4. The above operation shall be followed by the final cleaning of the surface that shall be done with oil-free air blast.
5. The cleaned surface shall be wetted followed by application of cement slurry after wetting the surface and then 6 mm thick (minimum) cement plasterwork of mix 1:3 (1 PPC/masonry cement:3 sand) to build up the even finished mortar surface by means of wooden float to the original concrete surface.
6. The above application shall be followed by 24 h of drying and curing shall be continued for at least 10 days.

### 2.3.2 Rectification Methodology for RC Conventional Slab, RC Column and RC Beam (Class 2 and 3 Fire)

1. In the portions of elements belonging to zone 2, where no spall had occurred, the treatment mentioned in Sect. 2.3.1 can be used for the purpose of repair.
2. The repair procedure given below shall be adopted in places where depth of repair treatment is less 50 mm and where some spalling has occurred.

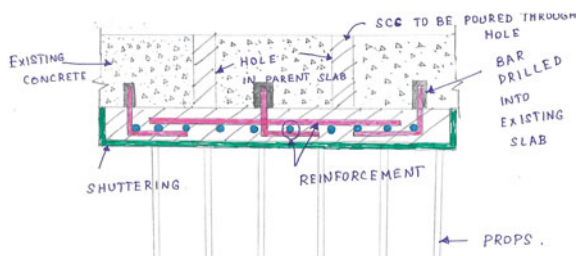
### 2.3.3 Rectification Methodology for PT Slab (Class 3 Fire)

The core cut results show minimum cube strength of  $23.6 \text{ N/mm}^2$  and maximum cube strength of  $43.3 \text{ N/mm}^2$ . Strength of concrete as per core results is considered and by assuming tendon has lost its entire property (for the span portion) the design is carried out.

The rectification methodology is as follows:

1. Providing the necessary scaffolding and working platform for the area to be repaired.
2. In the elements belonging to zone 3, where plaster or concrete has spalled-off, the weak concrete including loose concrete in the area shall be removed up to 25 mm depth (minimum) by chipping off with hammer and chisel/concrete cutting machine. The repair shall include the area of spalling of plaster/concrete and its surrounding (i.e. the area of weak concrete to be removed) extending at least 100 mm beyond the spall in all directions.
3. The surface shall be cleaned by sandblasting followed by cleaning oil-free air blast as mentioned earlier in the repair operations for Zone 1.
4. An anti-corrosive coating of minimum 40–50 microns thick on the surface of exposed rebars, cleaned by sandblasting shall be applied to avoid future anode formation. Sikatop Armatec 108 or Colusal VL of MC-Bauchemie or Nitroprime of Fosroc or equivalent product may be used.
5. “L” shaped RC dowel (maximum 500 mm in length) reinforcements (12 mm dia. bars—approximately 400 mm c/c both ways, as per approved drawing) are chemically grouted by using “Hilti” or equivalent to establish shear connection between old existing concrete and the new concrete (Fig. 13).
6. Mat as per design (12 mm/16 mm dia. bars) is tied with the cover blocks in position over the “L” shaped RC dowels, which was already drilled in the parent slab.
7. Fresh non-shrink, freely flowing, cementitious micro concrete shall be used to repair the cut area after thoroughly cleaning the surface of the steel if exposed. SikaRep—microcrete 2 or Renderroc RG of Fosroc or equivalent that exhibits a strength of 30 MPa in 3 days and 50 MPa in 28 days both measured at  $30^\circ\text{C}$ . Cast-in-situ or any other suitable technique may be used to apply the concrete for a band of 4.5 m width and drop depth of 625 mm connecting the affected

Fig. 13 Schematic drawing



columns (existing drop depth is 525 mm) and slab thickness of 325 mm (existing slab thickness is 275 mm). The mould must be suitable, robust and firmly fixed to withstand the applied pressure without leakage of grout. For the concreting of soffit of slab, holes can be drilled from top to put the freely flowing concrete over the firmly supported mould.

8. The shuttering is removed after the concrete gets strength and entire area is reproped.
9. The entire area of retrofit shall be drilled from bottom to the depth of ne concrete for low viscous epoxy grouting. The grout tubes spacing shall be 1.2 m c/c both ways.
10. All reprops shall be removed after grout attains strength (Fig. 14).

**Pictures during execution:**

See Figs. 15, 16, 17 and 18.

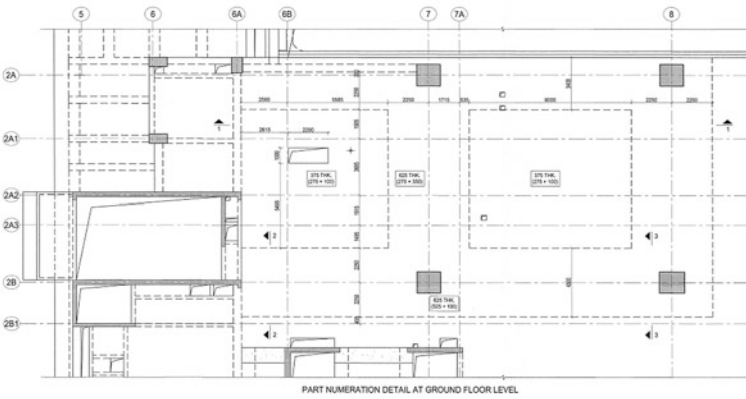


Fig. 14 Numeration detail of part PT slab after rectification

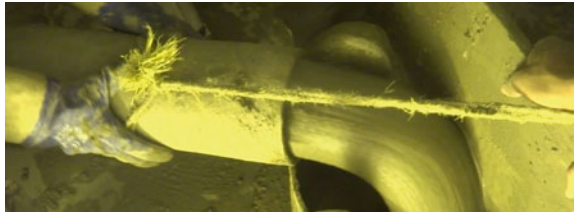


Fig. 15 Tying of reinforcement in progress (before concreting)

**Fig. 16** Concreting through self-compacting concrete (SCC) by making holes in the existing slab (before concreting)



**Fig. 17** Concreting through self-compacting concrete (SCC) by making holes in the existing slab (during concreting)



**Fig. 18** Concreting through self-compacting concrete (SCC) by making holes in the existing slab (after concreting)



**Fig. 19** After completion of SCC (view from ground floor)



**Fig. 20** After deshuttering  
(view from basement 1 floor)



**Pictures after completion:**

SCC shows seventh-day strength as 42 Mpa (Figs. 19 and 20).

### 3 Conclusion

The complete retrofit of the fire damaged area was done without resorting to any external pre-stressing or fibre wraps to reduce the total cost of the retrofit.

This was achieved by complete evaluation of existing structural elements and redesigning the slab.

The entire retrofit was accomplished and the design capacity of the slab was restored.

### References

1. Jones CD (1984) Repair of fire damaged structures. In: Anchor RD, Malhotra HL, Purkess JA (eds) Design of fire against structure. Elsevier
2. Malhotra HL (1982) Design of fire-resisting structure. Surrey University Press
3. The entire scheme was approved by IIT—Delhi Prof. Bishwajit Bhattacharjee before execution

# Behavior of FRP-Strengthened Reinforced Concrete Columns Under Pure Compression—Experimental and Numerical Studies



M. Chellapandian and S. Suriya Prakash

**Abstract** Hybrid strengthening of columns is explored in this study using both near-surface mounting (NSM) of carbon fiber-reinforced polymer (CFRP) laminates and external bonding (EB) of CFRP fabric. A total of ten small-scale square columns were cast and tested to investigate the efficiency of hybrid strengthening of RC columns under pure compression. A nonlinear finite element model was proposed to investigate the behavior of columns with and without FRP strengthening. The experimental results are compared with the finite element predictions to validate the proposed model and the predicted response. Comparisons showed close correlation with the observed behavior. The results indicate the hybrid strengthening was able to increase both the strength and stiffness of columns compared to that of only NSM and CFRP confined columns.

**Keywords** CFRP · Near-surface mounting · External bonding  
RC column · Hybrid strengthening

## 1 Introduction

Strengthening of reinforced concrete structures using fiber-reinforced polymer (FRP) composites has gained relevance in recent years due to the problems encountered in conventional strengthening techniques. Strengthening of structures using steel jacketing technique has been used in the past decades to provide good confinement effect but at a cost of increased weight and handling difficulties. FRP composites consist of fibers used as reinforcing elements and the polymer matrix used for transferring the load between the concrete and fiber interface. FRP

---

M. Chellapandian · S. Suriya Prakash (✉)  
Department of Civil Engineering, Indian Institute of Technology,  
Hyderabad 502285, India  
e-mail: suriyap@iith.ac.in

M. Chellapandian  
e-mail: ce15resch11005@iith.ac.in

composites possess many advantages like lightweight, ease of installation, resistance to corrosion, and high strength. Concrete columns are predominantly subjected to pure compression loading resulting in brittle material failure by crushing of concrete. FRP strengthening of columns can provide passive confinement for improving the strength, ductility, and energy dissipation capacity of the columns. Parvin and Brighton [1] investigated the corrosion repair of concrete columns using FRP and concluded that FRP strengthening not only improves the strength and ductility but also reduces the rate of corrosion significantly.

## 2 FRP Strengthening Technique

In general, the type of strengthening technique will be chosen based on the extent of damage or retrofit required for the particular member or the additional load-carrying capacity required by the structure to account for the increased demand in loads. Near-surface mounting (NSM) technique is used to retrofit the deficit structures that are predominantly subjected to shear and flexure. Olivova and Bilcik [2] carried out experimental study on concrete columns strengthened using carbon FRP laminates and concluded that NSM technique is effective only if the member is subjected to bending. NSM technique is also mainly used for strengthening the members that are prone to fire conditions. External bonding of FRP fabric is the most common method of strengthening the concrete members subjected to axial load. Confining effect in columns using FRP fabric is reduced due to premature de-bonding [2]. In this study, combining the advantage of both NSM and EB techniques, hybrid strengthening technique is proposed where the carbon laminates help in improving post-peak behavior and energy dissipation capacity of columns, whereas the carbon fabric helps in improving the confinement effect and delays the buckling of reinforcement and laminates. As a result, the column possesses higher load capacity that is required to overcome the additional requirement.

## 3 Experimental Investigation

### 3.1 Specification of Test Specimen

Ten small-scale square columns of cross section as shown in Fig. 1 were cast to experimentally investigate the behavior of columns with different strengthening techniques such as near-surface mounting, external bonding, and hybrid strengthening. The dimensions of the column were 230 mm × 230 mm × 450 mm. The columns were tested under pure axial compression loading. The details of the specimen are given in Table 1.

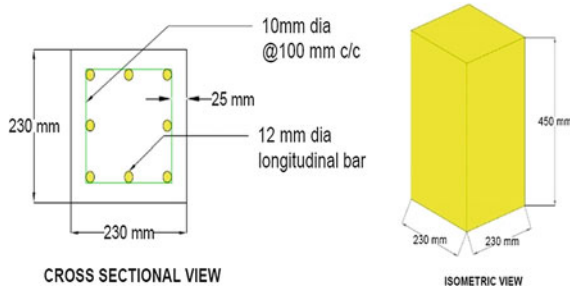


**Fig. 1** Cross-sectional details of column

**Table 1** Details of test specimen and strengthening technique

S. No.	Specimen ID	Loading type	Strengthening details	Concrete strength (MPa)
1.	SQ-PCC	Pure compression	No strengthening	34
2.	SQ-CP	Pure compression	No strengthening	34
3.	SQ-NSM	Pure compression	8 CFRP laminates (12.5 mm × 4.2 mm)	34
4.	SQ-EB	Pure compression	2 layers of CFRP fabric (500 mm × 0.2 mm)	34
5.	SQ-HYBRID	Pure compression	8 CFRP laminates + 2 layers of fabric	34

### 3.2 Material Properties

#### 3.2.1 Concrete

Columns were cast in IIT Hyderabad and water cured for 28 days. The average cylinder compressive strength of the column was found to be 34 MPa.

#### 3.2.2 CFRP Laminates

Laminates used in NSM strengthening were obtained from pultrusion process wherein carbon is used as the fiber material. The dimensions of laminates are 50 mm × 4.2 mm. Coupon test was carried out to determine the tensile strength of the laminate and was found to be 2300 MPa. The modulus of elasticity and rupture strain were 150 GPa and 1.3%, respectively.



### 3.2.3 CFRP Fabric

A 500 mm  $\times$  0.2 mm CFRP fabric of 230 GSM was used. The modulus of elasticity of the fabric was found to be 81.3 GPa with the rupture strain of about 1.4%.

## 3.3 Strengthening Procedure

### 3.3.1 NSM Strengthening

NSM strengthening was carried out as per the ACI 440.2R provisions [3]. A groove was cut in columns with dimensions not lesser than 1.5 times the dimension of the laminates. The groove is cleaned and applied with primer to remove the dust and to provide a good bond between the concrete and the laminate. After 24 h, the laminates are placed in the groove and epoxy resin was filled in the groove. After a curing period of 48 h, the columns were tested. The detailed procedure of NSM strengthening is shown in Fig. 2a–d.

### 3.3.2 Strengthening by External-Bonded FRP

The corners of the square columns are ground in order to provide a smooth contact surface and prevent any edge de-bonding of FRP. The surface of the specimen is



**Fig. 2 a–h** Strengthening of columns by hybrid strengthening technique

cleaned and applied with primer. After 24 h, epoxy resin is applied and CFRP fabric is pasted over the specimen. Minimum overlap is ensured as per ACI 440 provisions [3]. The column surface pasted with CFRP is rolled over with the help of a hand roller to expel the air bubbles. After a curing period of 48 h for the FRP to gain sufficient bond, the columns were tested. The detailed procedure of strengthening by external-bonded FRP is given in Fig. 2e–h.

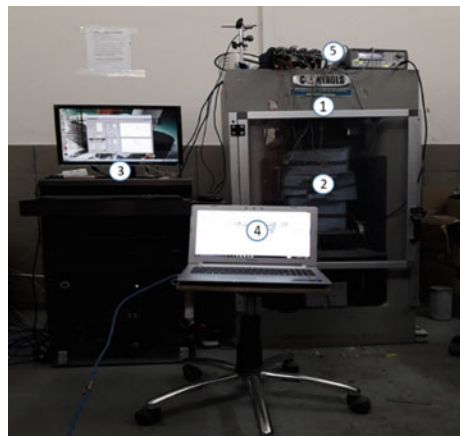
### 3.3.3 Hybrid Strengthening Technique

A hybrid combination of NSM and externally bonded was used for strengthening to prevent the buckling of NSM CFRP laminates under compression. The objective of the hybrid strengthening was to gain increased strength stiffness and ductility. The detailed procedure is explained in Fig. 2. Previous research on NSM and hybrid FRP strengthened RC elements shows the effectiveness under all combinations of axial compression and flexure [4–8].

## 3.4 Experimental Testing

The experimental setup for testing strengthened RC square RC columns under pure compression is shown in Fig. 3. The concrete column is tested under displacement-controlled mode using a servo-controlled compression testing machine (CTM) of 5000 kN capacity. The bottom plate ensures fixity of the column, while the top plate applies uniform compression on the column. The surface undulations are removed by loading and unloading the specimen for 15% of its peak load up to three cycles. Once the initial undulations are removed, the testing is started again in displacement-controlled mode. An average displacement from two

**Fig. 3** Experimental setup.  
1. 5000 kN CTM, 2. RC column, 3. controls console,  
4. HBM DAQ controller,  
5. DAQ system



10 mm LVDTs was used for displacement-controlled testing. Once the displacement exceeds more than 9 mm, the controls are shifted to 50 mm LVDT. Four 20-mm LVDTs are attached to the surface of the column to measure the deformation of the column. The gauge length is fixed as 180 mm for measuring the surface strain in concrete. MX-1615 data acquisition system (DAQ) is used to measure the strains from the strain gauges (120  $\Omega$ ) connected to the steel reinforcements and FRP. Four strain gauges are connected to the steel reinforcements (two in longitudinal and transverse reinforcements), and two strain gauges are connected to both CFRP laminates and CFRP fabric.

## 4 Results and Discussion

### 4.1 Experimental Results

Experimental results of strengthening techniques were compared in Table 2. To understand the efficiency of each technique under pure compression, the ultimate load is considered as the load at which the drop in the peak load exceeds more than 40% and the same is considered as failure.

#### 4.1.1 Behavior and Failure Mechanisms

The overall behavior of columns under axial compression is depicted in Fig. 4. It is clear that hybrid FRP strengthening was able to improve the strength and ductility of columns when compared to only NSM or EB strengthening. The plain concrete specimen (SQ-PCC) had an initial crack at a load of 1336 kN after which there is a change in the slope of curve. The column attained peak load at a displacement of 0.26 mm. The failure occurred due to formation of large compression crack at the center with few small cracks nearby. For the columns with conventional reinforcements (SQ-CP), the load corresponding to spalling of concrete cover was about 1650 kN and peak displacement of 0.39 mm.

**Table 2** Test results of strengthened RC columns

S. No.	Specimen ID	Experimental results				Numerical results	
		Peak load (kN)	Failure load (kN)	Peak disp. (mm)	Ultimate disp. (mm)	Peak load (kN)	Ultimate disp. (mm)
1.	SQ-PCC	1764	1099	0.27	0.72	1913	0.35
2.	SQ-CP	2148	1372	0.39	1.37	2291	0.92
3.	SQ-NSM	2319	1443	0.45	1.92	2202	1.90
4.	SQ-EB	2357	1562	0.49	1.95	2635	2.18
5.	SQ-HYBRID	2590	1630	0.44	2.11	2751	2.25

The column strengthened using NSM CFRP laminates had improvement in the load only up to 8% which is not a significant number, but the mode of failure changed from brittle to ductile. There was a considerable reduction in the spalling of concrete cover and compression cracking. There was considerable improvement in the cracking load of the column about 18% when strengthened using external-bonded technique of CFRP fabric. The peak load and ultimate load-carrying capacity of the column was increased by 10 and 42%, respectively. When the columns are strengthened using hybrid NSM and EB technique, the peak load had an improvement about 21% when compared to the control specimens. The specimen failed at an ultimate displacement of 2.11 mm which was improved 54%. As expected, the buckling of CFRP laminates is prevented in this technique.

## ***4.2 Numerical Modeling***

Using commercial finite element software ABAQUS, nonlinear finite element modeling of concrete is performed using concrete damage plasticity. The procedure of nonlinear analysis is carried out using dynamic explicit method. In meshing, three-dimensional eight-noded brick element C3D8R is used for concrete and two-noded truss element T3D2 is used for reinforcement and laminates. Three-dimensional four-noded shell element S4R is used to model CFRP fabric. Reduced integration technique is used to reduce the computational time for the analysis. Bond definitions are not defined and presented as a part of this study due to high computational time. However, the improved model including the cohesive bond slip behavior between CFRP and concrete is defined and a detailed parametric investigation is carried out in the other paper of authors [9].

## ***4.3 Comparison Graph***

Finite Element (FE) predictions are compared with the test results and shown in Figs. 5, 6, 7, 8, and 9. The FE predictions had a fair correlation with the test results. The variations in post-peak predictions are due to interaction behaviour of concrete and FRP/steel. The results presented in this study is a part of preliminary investigation carried out which is improved further with the cohesive bond slip definitions and presented in the companion paper [9].

**Fig. 4** Behavior of RC columns under compression

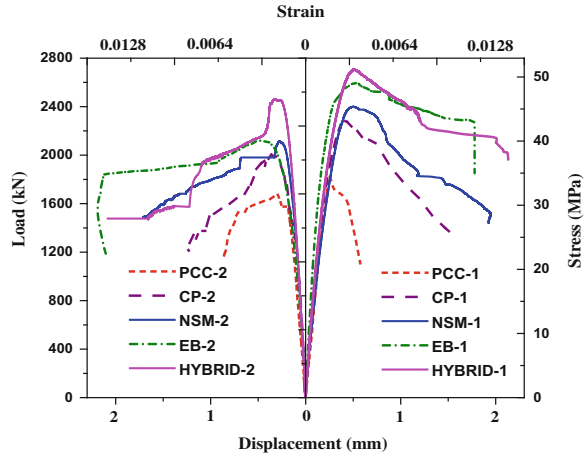


**Fig. 5** Comparison for plain columns

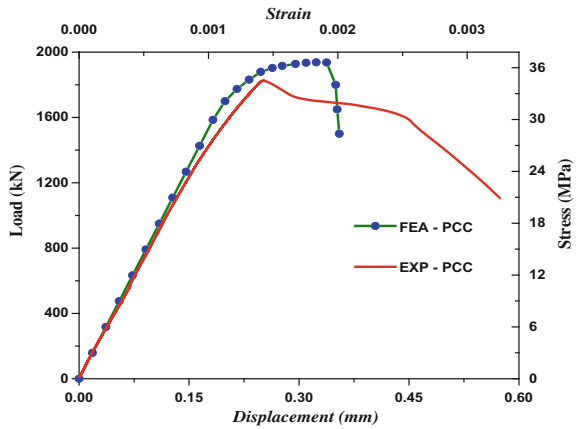


**Fig. 6** Comparison for unstrengthened RC columns

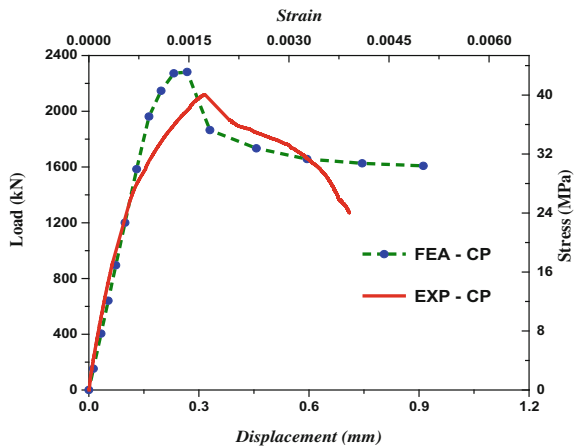


**Fig. 7** Comparison for NSM-strengthened RC columns

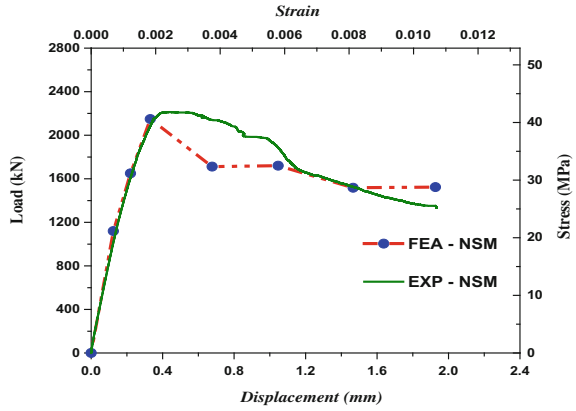


**Fig. 8** Comparison for EB-strengthened RC columns

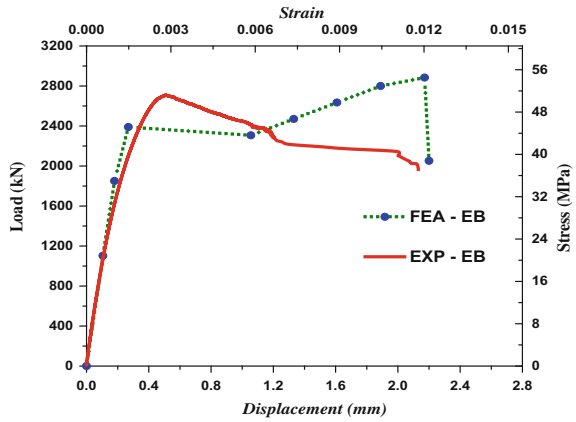
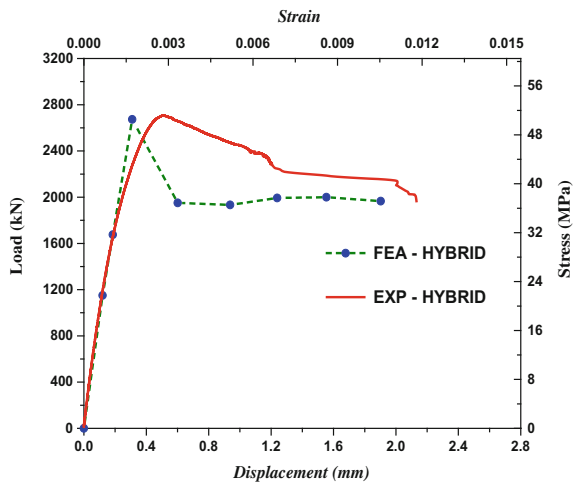


**Fig. 9** Comparison for hybrid-strengthened RC columns



## 5 Conclusions

This paper presents the effectiveness of hybrid strengthening technique in improving the performance of reinforced concrete columns under pure compression. The following important conclusions can be drawn from this study:

- Hybrid FRP strengthening improved strength, ductility, and stiffness of the columns under compression which is significant from the overall behavior and failure mode.
- There is considerable increase in the load-carrying capacity of the hybrid-strengthened column with failure occurring at a higher strain compared to the conventional RC columns.
- Hybrid-strengthened columns failed by rupture of confinement fibers and through de-lamination of NSM CFRP along with the concrete cover.
- Nonlinear finite element model was able to predict the initial stiffness, peak load and failure mechanism of the tested columns with and without FRP strengthening. However, improvements required for accurate prediction of post-peak behavior.

**Acknowledgements** This research work was carried out under the project funded by Department of Science and Technology, India. FRP materials were partially donated by R&M International Ltd. Mumbai. The authors gratefully acknowledge for their generous support.

## References

1. Parvin A, Brighton A (2014) Fiber reinforced polymer composites strengthening of concrete column under various loading conditions. *Polymers* 6:1040–1056
2. Olivova K, Bilcik J (2009) Strengthening of concrete columns with CFRP. *Slovak J Civil Eng* 1–9
3. ACI Committee 440 (2008) Guide for the design and construction of externally bonded FRP systems for strengthening concrete structures. American Concrete Institute
4. Barros JAO, Varma RK, Sena-Cruz JM, Azevedo AFM (2008) Near surface mounted FRP strips for the flexural strengthening of RC columns—experimental and numerical research. *Eng Struct* J 30(12):3412–3425
5. Herwig A, Motavalli M (2012) Axial behavior of square reinforced concrete columns strengthened with lightweight concrete elements and unbonded GFRP wrapping. *J Compos Constr* 16:747–752
6. Song X, Gu X, Li Y, Chen T, Zhang W (2013) Mechanical behavior of FRP strengthened concrete columns subjected to concentric and eccentric compression loading. *J Compos Constr* 17:336–346
7. Chellapandian M, Prakash SS, Sharma A (2017) Strength and ductility of innovative hybrid NSM reinforced and FRP confined short RC columns under axial compression. *J Compos Struct* 176:205–216

8. Chellapandian M, Prakash SS (2018) Rapid repair of severely damaged reinforced concrete columns under combined axial compression and flexure – An experimental study. *J Constr Build Mat* 173:368–380
9. Chellapandian M, Prakash SS, Rajagopal A (2018) Analytical and finite element studies on hybrid FRP strengthened RC column elements under axial and eccentric compression. *J Compos Struct* 184:234–248



# A Numerical Study on the Behaviour of Reinforced Concrete Slab Strengthened with FRP Laminates Using Finite Element Approach



F. Shit and S. Roychowdhury

**Abstract** External wrapping with fibre-reinforced polymer (FRP) sheet has become a promising solution for retrofitting of damaged reinforced concrete slab in reinforced concrete framed structures as well as brick masonry structures due to various advantages. In particular, the flexural strength of a slab can be significantly increased by application of FRP sheets adhesively bonded to the tension face of the slab. It has been tried in the present work to study the behaviour of reinforced concrete slab strengthened with glass fibre-reinforced polymer (GFRP) laminates following the finite element approach using the software ANSYS. Previous research work based on the experimental observation reveals the fact that the extent of repair or strengthening of reinforced concrete slab with FRP laminates in terms of the load-carrying capacity or deformation under service load depends on different parameters such as the location of FRP laminate, the width of the FRP strips and thickness of the FRP.

**Keywords** Reinforced concrete slab · Strengthened RC slabs · FRP fibre-reinforced polymer · ANSYS

## 1 Introduction

The present work is aimed to analyse numerically the reinforced concrete simply supported slab strengthened with FRP laminates using FE method. This involves the proper choice of element, material properties, boundary conditions, solution techniques, etc. In this chapter, different steps of FE modelling of the above-mentioned slab is described with reference to the features available in the FE software ANSYS and models prepared are analysed to obtain load deformation

---

F. Shit · S. Roychowdhury (✉)  
Department of Civil Engineering, Jadavpur University, Kolkata 700032, India  
e-mail: sreceju@yahoo.com

F. Shit  
e-mail: shitfalguni@gmail.com

response analytically. To perform a parametric study, the numerical analysis of a RC slab with or without FRP laminates is done using different FRP position, FRP width and FRP thickness.

## 2 Literature Review

Ebead et al. [1], in their paper, reported the results of six specimens to evaluate the effectiveness of using fibre-reinforced plastics as strengthening materials for two-way slabs against flexural deficiency. Chothani et al. [2] reported that the structural response of slab was improved due to the bonding of FRP laminate with the slab. In their experimental work, three identical reinforced concrete slabs ( $1500 \times 900 \times 50$  mm) were constructed. Mustafa and Agarwal [3] presented a study dealing with the finite element modelling of control RC slabs and strengthened slabs with the help of finite element software ANSYS where the software was used for modelling of RC structures.

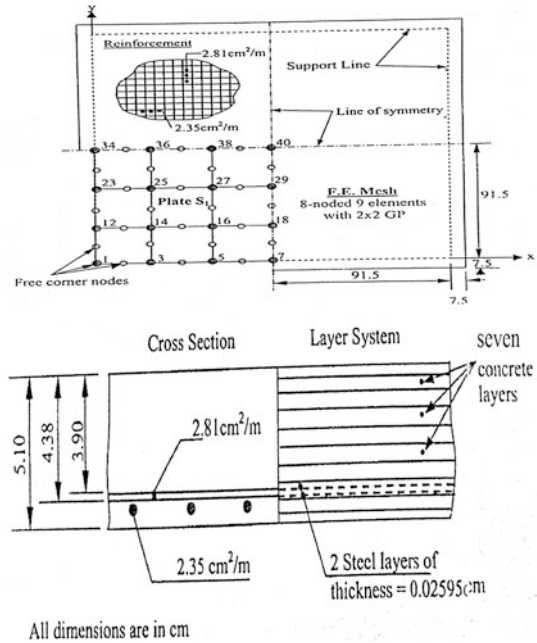
## 3 Model of RC Slab Structure

In the present work, a RC slab is modelled with or without FRP laminates and validation is performed with the analytical solution of the same RC slab without FRP laminates reported in the Ph.D. thesis of S. Roychowdhury and shown in Fig. 1. There are four FE models of the slab out of which one control slab (S1) is without FRP laminates and three retrofitted slab (S2, S3, S4) with FRP laminates. The dimensions of all the slab specimens are identical. The plan dimensions of all the RC slab is 1980 mm (in  $x$ -direction) and 1980 mm (in  $z$ -direction). Thickness of slab is 51 mm. The slab is reinforced with two layers of reinforcing bars (FE 500) of area  $281 \text{ mm}^2/\text{m}$  provided at the bottom face only.

### 3.1 Element Types

While modelling the RC slab in ANSYS, different elements are used to model concrete, steel reinforcement and FRP laminates. SOLID65 element is chosen to model three-dimensional concrete elements; LINK180 is adopted for flexural reinforcement bars. SOLID185 element has been taken to model the layer of FRP. Following are the brief descriptions of these elements along with the real constants required to be provided in ANSYS.

**Fig. 1** Details of the unretrofitted RC slab



### 3.2 Input for Material Properties

Material plays an important role in ANSYS modelling. Cube compressive strength and all other properties of concrete are taken from the previous experimental study by Taylor et al. [4], and the numerical analysis has been conducted by Owen et al. [5].  $E_c = 5000 \sqrt{f_{ck}} = 29,580.39$  MPa,  $f_{ck} = 35$  MPa, Poisson's ratio = 0.18. Parameters needed to define the material properties for the slab models are given in Table 1.

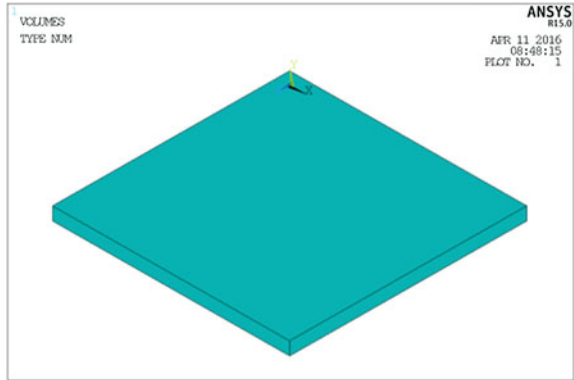
### 3.3 Details of the Present Finite Element Model

The two-way simply supported RC slab is modelled as a volume (Fig. 2). Due to symmetry in geometry of the RC slab and loading, the finite element analysis is done for one-quarter of the slab. For quarter model, the dimensions are as 915 mm  $\times$  915 mm  $\times$  51 mm (Fig. 1).

**Table 1** Material properties for present model

Material model number	Element type	Material properties		
1	SOLID65	<i>Multilinear isotropic</i>		
		Reference point	Strain	Stress (MPa)
		1	0	0
		2	0.0002	0.665
		3	0.0006	1.785
		4	0.001	2.625
		5	0.0014	3.185
		6	0.0018	3.465
		7	0.0035	3.5
		<i>Non-metal plasticity (concrete)</i>		
		Shear transfer coefficient for open crack		0.3
		Shear transfer coefficient for closed crack		1
		Uniaxial tensile cracking stress		3.79 e6
		Uniaxial crushing stress		-1
Biaxial crushing stress, ambient hydrostatic stress state, biaxial crushing stress under ambient hydrostatic stress state, uniaxial crushing stress under ambient hydrostatic stress state, stiffness multiplier for cracked tensile condition		Each of these value is 0		
2	LINK180	<i>Linear isotropic</i>		
		$E_x$	2.069 e11	
		$P_{RXY}$	0.3	
		<i>Bilinear isotropic</i>		
		Yield stress	3.759 e8	
		Tang modulus	3 e10	
3	SOLID185	<i>Linear orthotropic</i>		
		$E_x$ (MPa)	20,700	
		$E_y$ (MPa)	7000	
		$E_z$ (MPa)	7000	
		$V_{xz}$	0.26	
		$V_{xy}$	0.26	
		$V_{yz}$	0.3	
		$G_{xz}$ (MPa)	1520	
		$G_{xy}$ (MPa)	1520	
		$G_{yz}$ (MPa)	2650	

**Fig. 2** Volume created in ANSYS



## 4 Results and Discussions

The results of finite element analysis of control slab and the retrofitted slabs are presented here. Three parametric variations like the variation of location, width and thickness of FRP are considered and the corresponding models are numerically analysed.

### 4.1 Location of FRP

To strengthen the basic reinforced concrete slab (also termed here as control slab SS1), FRP laminates are considered as attached with the bottom surface of the slab. To study the effect, three different locations of the FRP strips are considered (Fig. 3)—(a) along the simply supported edge (SS2), (b) along the continuous edge (SS3) and (c) along the diagonal (SS4).

**Fig. 3** FRP along the support edge SS2, continuous edge SS3, along the diagonal SS4 (for one-quarter model)

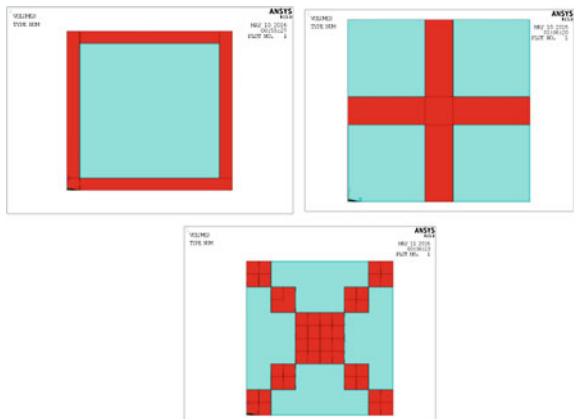
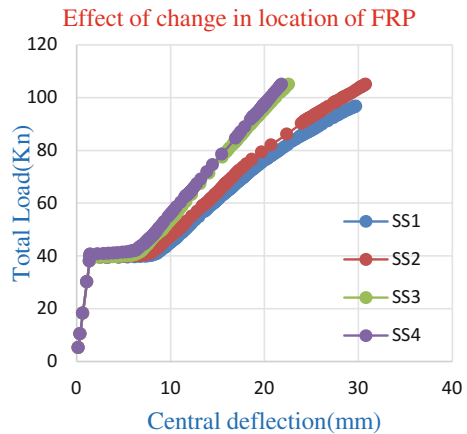


**Fig. 4** Variation of load deformation behaviour of retrofitted simply supported RC slab due to change in location of FRP along continuous edge



The result coming from the analysis of control slab SS1 and the same for retrofitted slab SS2, SS3 and SS4 are compared graphically in the plot of load deflection curve as given in Fig. 4. These three retrofitted slabs carry more load than SS1 slab and also the stiffness is more than that of SS1 slab. Among these three retrofitted slabs, SS3 and SS4 are stiffer than slab SS2 with SS4 being the most stiff. From this, it can be suggested that for simply supported slab, the location of FRP along diagonal is the best alternative.

## 4.2 Width of FRP

The width of FRP laminate in each of the retrofitted slabs SS2, SS3 and SS4 is considered as a variable parameter in this section as this has a considerable effect on the behaviour of the slab.

### 4.2.1 FRP Along the Support Edge of the Simply Supported Slab

In slab SS2, the FRP has been provided along the support edge. But initially in the model, FRP elements are attached with the outermost elements of the model as shown in Fig. 5. Thus, the percentage of slab area covered with FRP are increased to 30, 55, 75 and 100%, respectively. All these models are analysed and the load-deflection plots coming from the analysis are compared as shown in Fig. 6.

The comparison not only shows that the slabs get more stiffer with the increment in the area of FRP laminates but also indicates that the failure load increases with higher FRP area.

**Fig. 5** 30, 55, 75, 100% area of slab SS2 covered by FRP

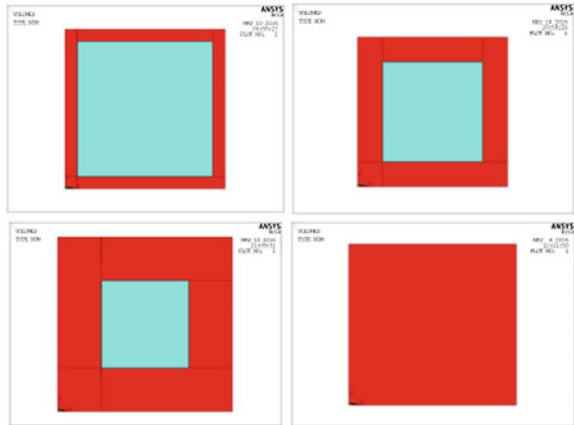
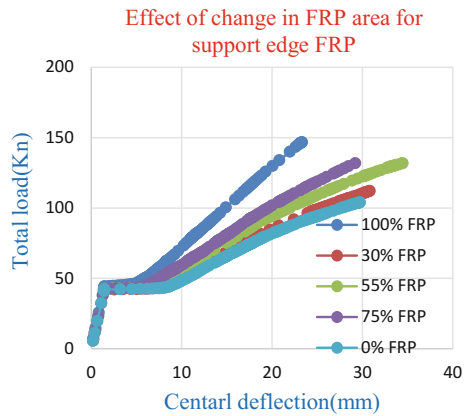


**Fig. 6** Variation of load deformation behaviour with FRP along support edge



**4.2.2 FRP Along the Continuous Edge of the Simply Supported Slab**

Similar to the change of width of FRP along support edge, continuous edge of slab SS3 are retrofitted with increasing FRP. The percentage of slab area covered with FRP are 30, 55, 75 and 100%, respectively, as shown in Fig. 7. All these models are analysed and the load-deflection plots coming from the analysis are compared as shown in Fig. 8. The comparison of load-deflection curve not only shows that the slabs get more stiffer with the increment in the area of FRP laminates but also indicates that the failure load increases with higher FRP area.

**Fig. 7** 30, 55, 75, 100% area of slab SS3 covered by FRP

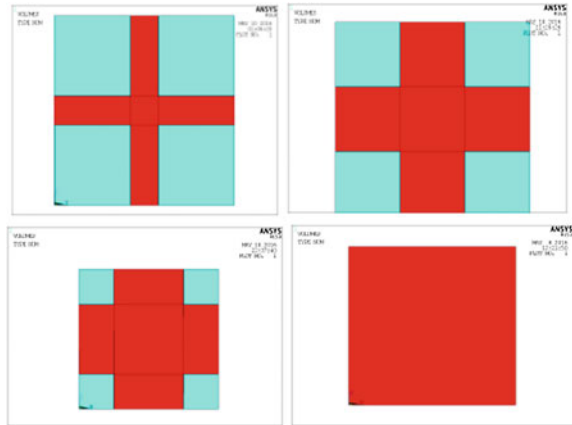
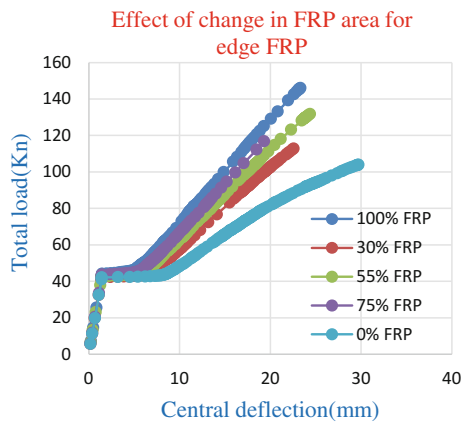


**Fig. 8** Variation of load deformation behaviour with FRP along continuous edge



### 4.2.3 FRP Along the Diagonal of the Simply Supported Slab

Similar to the previous two locations, in slab SS4 the width of FRP is also increased, the FRP has been provided along the diagonal direction of the one-quarter of the slab. Thus, the percentage of slab area covered with FRP are 16.67, 33.33, 50, 66.67 and 100%, respectively, as shown in Fig. 9. The comparison shows that the slabs get more stiffer with the increment in the area of FRP laminates indicating smaller deflection at the ultimate load shown in Fig. 10. It is also observed that there is a variation in the failure load which increases just after increasing the width of FRP area but there is minor changes (reduction in some cases also) when the FRP area is increased further.

In addition to the above, the change of load-carrying capacity of simply supported RC slab retrofitted with FRP at different locations and having different width, i.e. area of FRP, are shown in the following Table 2 and change of



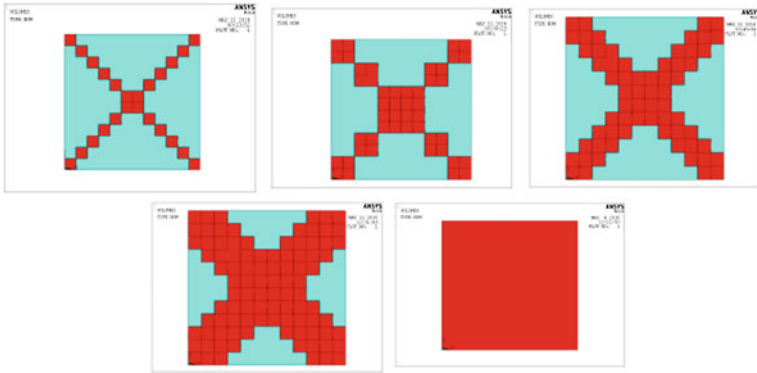


**Fig. 9** 16.6, 33, 50, 66.67 and 100% area of slab SS4 covered by FRP

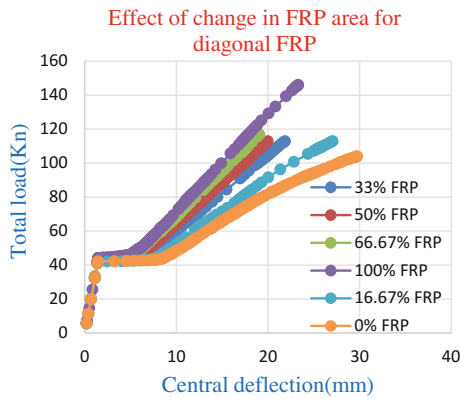


**Fig. 10** Variation of load deformation behaviour with FRP along both the diagonals

**Table 2** Change of load-carrying capacity of RC slab retrofitted with FRP

Percentage of FRP area	Increment of load-carrying capacity in percentage		
	RC slab retrofitted with support edge FRP	RC slab retrofitted with diagonal FRP	RC slab retrofitted with continuous edge FRP
16.67		8.73	
30–33.33	8.73	8.73	8.73
50–55	27.1	8.73	27.1
66.67–75	27.1	12.62	12.62
100	41.75	41.75	41.75

**Table 3** Change of deformation at ultimate load of RC slab retrofitted with FRP

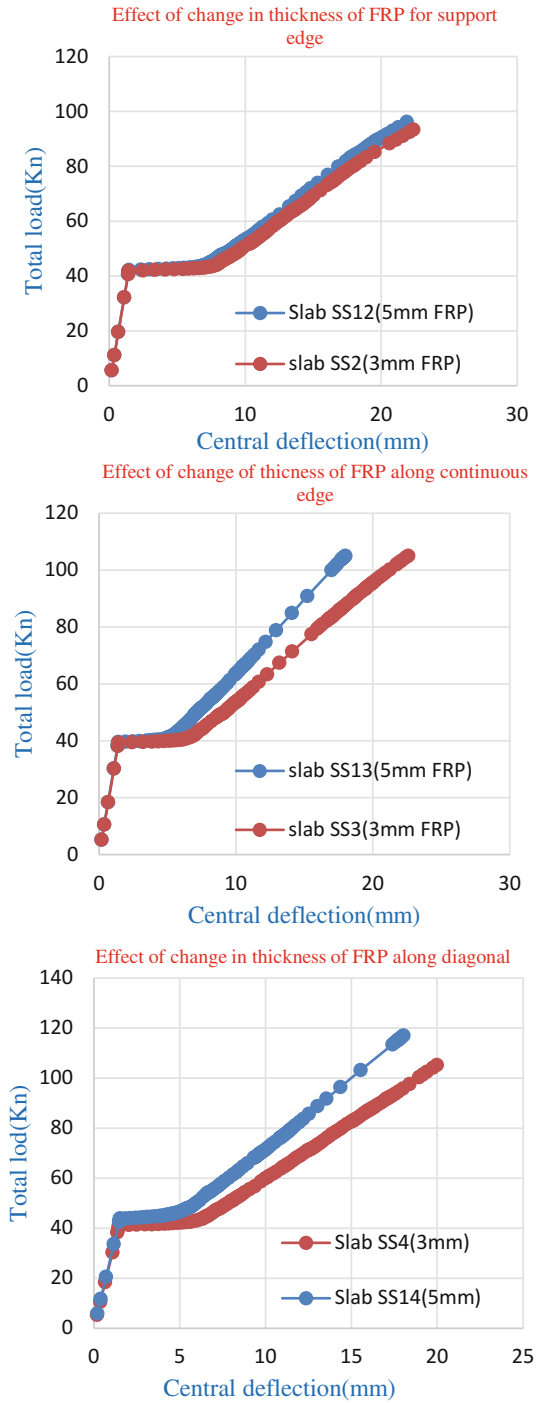
Percentage of FRP area	Deformation at ultimate load (mm)		
	RC slab retrofitted with support edge FRP	RC slab retrofitted with diagonal FRP	RC slab retrofitted with continuous edge FRP
16.67		27.06	
30–33.33	30.79	21.84	22.58
50–55	34.44	20	26.08
66.67–75	29.2	19.07	19.31
100	23.32	23.32	23.32

deformation at ultimate load of those slab retrofitted with FRP are shown in Table 3. It can easily be observed that to achieve maximum benefit 100% of the slab area should be covered with FRP. But in case of location of FRP along support edge or continuous edge, coverage of 50–55% area will give satisfactory improvement. But for the location of FRP along diagonal, the requirement of coverage with FRP is found to be 75%. The deformation at ultimate load has also a tendency to reduce with the increase in the area of slab covered with FRP which is quite obvious.

### 4.3 Thickness of FRP

In this section, an attempt has been made to study the behaviour of the retrofitted slab due to the change in the thickness of the FRP laminates. Initially, the slab models SS2, SS3 and SS4 have been prepared considering the thickness of FRP as 3 mm. Here, this thickness has been increased to 5 mm and the models are S12, S13, and S14. All these models are analysed and the load-deflection plots coming from the analysis are compared as shown in Fig. 11 for the three different locations of FRP, respectively. From the comparisons of three curves, it is observed that due to the increase in the thickness of FRP, the load-deflection curve gets stiffer and gives higher ultimate load compared to that with lower thickness of FRP in all three locations of FRP, i.e. along support edge, along continuous edge and along diagonal. But the change of stiffness is considerably high in case of the location of FRP along continuous edge and diagonal. It is comparatively less in the case of FRP along support edge.

**Fig. 11** Effect of change of thickness of FRP along support edge, continuous edge, and diagonals



## 5 Conclusion

From the above three different parametric studies on simply supported RC slab strengthened with FRP laminates, the following conclusions are made.

- (a) Three different locations of the FRP strips have been considered and observed that the retrofitted slab shows higher stiffness and ultimate load compared to the unretrofitted control slab irrespective of the location of FRP. Among three retrofitted slabs SS2, SS3 and SS4, the diagonal location of FRP giving the highest stiffness and ultimate load becomes the best alternative.
- (b) It can easily be observed from the results of above-mentioned second parametric study that to achieve maximum benefit, 100% of the slab area should be covered with FRP. But in case of location of FRP along support edge or continuous edge, coverage of 50–55% area will give satisfactory improvement.
- (c) It is also observed that due to the increase in the thickness of FRP, the load-deflection curve gets stiffer and gives higher ultimate load compared to that with lower thickness of FRP in all three locations of FRP. The effect of change of stiffness is considerably high in case of the location of FRP along continuous edge and diagonal. It is comparatively less in the case of FRP along support edge.

In fine, it can be stated that the present work will help and provide guideline for the numerical study of strengthening of pre-damaged RC slab by application of FRP laminates which is commonly done in actual practice.

## References

1. Ebead U, Marzouk H, Lye LM (2002) Strengthening of two-way slabs using FRP materials: a simplified analysis based on response surface methodology. In: 2nd World engineering congress, Sarawak, Malaysia, 22–25 July 2002
2. Chothani DG, Arora NK, Dave SP (2012) Effect of anchoring GFRP sheet on ultimate strength of slab. In: Fourth international conference on structural stability and dynamics (ICSSD 2012), 4–6 Jan 2012
3. Mustafa BM, Agarwal VC (2013) Non-linear finite element analysis of RC slabs strengthened with CFRP laminates. *Int J Eng Trends Technol (IJETT)* 5(3)
4. Taylor R, Maher DRH, Hayes B (1966) Effect of arrangement of reinforcement on the behavior of reinforced concrete slab. *Mag Concr Res* 18(55)
5. Owen DRJ, Figueiras JA, Damjanic F (1983) Finite element analysis of reinforced and prestressed concrete structure including thermal loading. *Comput Methods Appl Mech Eng* 41:323–366

# Numerical Evaluation of Cyclic Performance of Damaged RC Frames Using Passive Devices



Romanbabu M. Oinam and Dipti Ranjan Sahoo

**Abstract** Metallic yielding device is one of the passive energy dissipation devices. It has good energy dissipation capacity, high initial stiffness along with high ductility. In this study, 0.4-scale single-story single-bay non-ductile gravity load design frame has been tested under cyclic load; later on, the damaged frame has been strengthened with the help of steel caging and metallic yielding damper. In this paper, the experimental results are validated numerically using *OpenSees*. The numerical model has the capability of predicting of failure and nonlinear behavior of reinforced concrete frame. The numerical model predicted the hysteresis behavior, stiffness, and energy dissipation with adequate accuracy.

**Keywords** Non-ductile reinforced concrete • Metallic yielding damper  
Hysteresis • Stiffness • Energy dissipation

## 1 Introduction

To control excessive damage in highly vulnerable existing non-ductile gravity load design reinforced concrete (RC) buildings, many researchers have performed extensive experimental investigations using various types of passive control device [1, 2]. Modern seismic codes emphasize the requirement of transverse reinforcement with adequate toughness and ductility of structural members during strong ground shakings. However, in existing structures, there is limiting possibility of changing the section sizes or percentage of reinforcement. Hence, the existing RC buildings require strengthening to enhance their seismic performance [3–5].

---

R. M. Oinam  
National Institute of Technology, Warangal 506004, India  
e-mail: romanbabu@gmail.com

D. R. Sahoo (✉)  
Department of Civil Engineering, Indian Institute of Technology Delhi,  
Delhi 110016, New Delhi, India  
e-mail: drsahoo@civil.iitd.ac.in

The seismic performance of RC structure is highly dependent on interaction between the reinforcement bars and concrete. During cyclic displacement (similar to earthquake-induced load profile) tests, bond degradation is accelerated, which leads to significant bar slippage. Hence, bond-slip mechanism is one of the most important reasons for damage or collapse when subjected to earthquake loading [6]. As a result, bond-slip effect should be considered in numerical model to predict the realistic behavior RC structures.

This study describes the numerical modeling of two experimental frames (0.4-scale model), which are strengthened by metallic yielding dampers and steel caging technique (*RS-1 and RS-2*). The combined metallic yielding damper (*CMD*) has been used as global strengthening technique, when the steel caging is used on column as local strengthening technique. The experimental results are used to calibrate the numerical model taking the bond-slip effect into account. The main objectives of this study are to investigate (a) bond-slip effect in the non-ductile gravity load design frame, (b) modeling of the strength and stiffness degradation of reinforced concrete structure during loading and unloading, (c) evaluation of effective concrete confinement due to steel cage, and (d) modeling of *CMD* device.

## 2 Description of Study Frames

A single-story single-bay reinforced concrete (RC) frame representing an interior bay of a prototype open-ground-story-framed structure is considered as the test frame in this study. All the dimensions and percentage of reinforcement of test frame is simulated using 0.4-scale factor. The overall width and height of test frame are taken as 3200 and 2100 mm, respectively. The cross-sectional dimension of beam is taken as  $160 \times 130$  mm, whereas both the columns' dimension is assumed as  $160 \times 160$  mm.

Both the *RS-1* and *RS-2* specimens are damaged test specimens due to previous cyclic test. Due to excessive damage on column, *RS-1* specimen is strengthened using *CMD* and with steel cage on column, while *RS-2* specimen is strengthened with the help of *CMD* only. Figure 1a, b shows clearly the *RS-1* and *RS-2* detailing

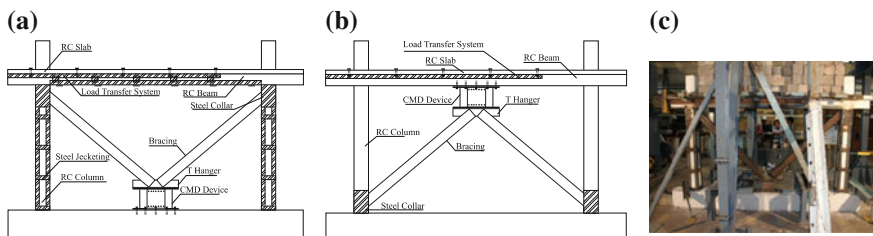


**Fig. 1** a Detailing of *RS-1* frame, b detailing of *RS-2* frame, and c *RS-1* frame test setup

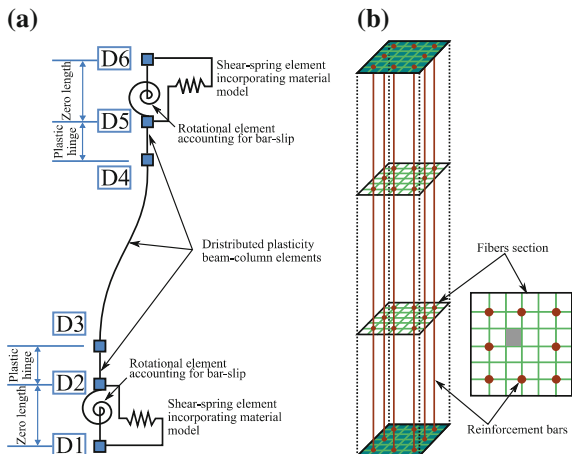
along with test setup. Both the specimens are subjected to the same cyclic displacement up to 6.0% lateral drift under constant gravity load.

### 3 Overview of *OpenSees* Platform and Models

*OpenSees* is a software framework for simulating the seismic response of structural and geotechnical systems subjected to earthquakes and other hazards [7]. This framework software has different type of sections, each of them has own specialty; however, for the frame structural member, fiber-based models are always preferred due to realistic plastic hinge mechanism. Figure 2 shows the distribution of element in frame member considering bond-slip model along with fiber sections. Frame stiffness and strength are obtained numerically by integrating the stiffness and strength of members. Damage level of each fiber section is observed from state of strain, which is recorded using the section deformation. This is based on the plane section assumption. In addition, the stress and stiffness of fiber sections are upgraded based on the material behavior, followed by upgrading of the section resultant force and corresponding stiffness [8, 9].

*OpenSees* has capability of simulating the bond-slip effect on the elements. The fiber section does not take care of shear deformation; however, in practically structural member deformation is the interaction of axial, flexural, and shear force. As a result, to consider shear deformation in model, section aggregator is introduced in fiber section.

**Fig. 2** **a** Distribution of elements and **b** fiber section elevation and plan [7]



### 3.1 Structural Elements' Modeling

The fiber section work based on distributed plasticity and inelasticity can form at any section point along the longitudinal axis of the element, where the points are identified by the numerical integration method. Distributed plasticity model will provide accurate to exact solution; however, this method required a great computational effort [10]. In case of lumped plasticity, there will not be much computational effort; however, result will not be accurate compared to distributed plasticity. In this study, all the structural members are assigned *forced-based distributed plasticity beam-column element*. Figure 2a shows modeling of flexural, shear, and axial behavior RC frame adopted in this study.

### 3.2 Concrete Modeling

Uniaxial material model “Concrete02” has been used to account for the compression as well as tensile behavior of concrete. The tensile strength of the concrete is generally not taken into account in the design of concrete members due to its weakness in tension. However, for validating the experimental result, tensile strength cannot be ignored. Direct tensile strength of M25 grade concrete is 8–11% of compressive strength [11]. The concrete compressive strength used in the numerical model is 34.6 MPa [12]. The tensile strength of the reinforced concrete has been taken as 10% of its mean compressive strengths [11]. The nonlinear monotonic behavior of concrete is characterized by a multi-linear curve, defined by seven parameters as shown in Fig. 3a. These parameters are (a) maximum compressive strength ( $f_{pc}$ ); (b) strain at maximum compressive strength ( $\epsilon_{sc0}$ ); (c) crushing strength ( $f_{pcu}$ ); (d) strain at crushing strength ( $\epsilon_{scu}$ ); (e) ratio of unloading slope and initial slope ( $\lambda$ ); (f) tensile strength of concrete ( $f_t$ ); (g) tension softening stiffness ( $E_{ts}$ ).

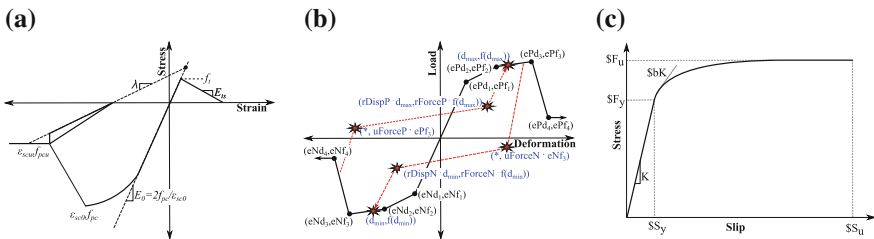


**Fig. 3** Material parameters of concrete, reinforcement, and bond slip models **a** *Concrete02*, **b** *Pinching4*, and **c** *Bond SP01*



**Table 1** Damage parameters of *Pinching4*

<i>Pinching4</i> damage parameters												
$F_y$ (Mpa)	$E_s$ (Mpa)	$rDisp$		$rFoRCe$		$uFoRCe$		$K$	$D$	$F$	$E$	$dam$
		Pos	Neg	Pos	Neg	Pos	Neg					
415	$2.1 \times 10^5$	0.4	0.4	0.1	0.1	0.12	0.12	0.25	0.5	0	10	Energy
								0.35	0.5	0		
								0.4	2	0		
								0.2	2	0		
								0.5	0.5	0		

### 3.3 Reinforcement Bar Modeling

Pinching effect in the hysteretic response of RC members at the higher cyclic excursions is a common phenomenon. This is an inherent property of concrete, and it happens due to the combined effect of stiffness and strength degradation in the nonlinear range while loading and unloading occur. Due to this effect, concrete members dissipate less energy compared to steel structures. To consider the pinching effect in the modeling of concrete members, a uniaxial material called *pinching4* is used from *OpenSees* library. Figure 3b shows the load deformation curve of *pinching4* material. The speciality of *pinching4* material is that it considers material degradation (strength–stiffness). The strength–stiffness cycle degradation occurs in three ways: namely (a) unloading stiffness degradation, (b) reloading stiffness degradation, and (c) strength degradation.

Table 1 shows the damage parameters of *pinching4* material. The damage parameter includes the following factors, (i) ratio of deformation  $rDisp$ , (ii) ratio of force  $rForce$ , (iii) ratio of strength developed  $uForce$ , (iv) cyclic stiffness degradation  $\gamma K$  and  $\gamma D$ , (v) cyclic strength degradation  $\gamma F$ , (vi) maximum energy dissipation under cyclic loading  $\gamma E$ , and (vii) type of damage.

### 3.4 Bond-Slip Model

Bond slippage normally occurs in column–foundation joints and beam–column joints. In this study, bond-slip model is applied to the above-mentioned joints. Location of bond-slip model is shown in Fig. 2a. Due to lateral displacement imposed at beam level, there is high bending moment is developed at all corners because of moment resisting connection, so the probability of bond slip at these joints are very high. In *OpenSees* library, there is a material called *Bond SP01*, which can model the effect of bond slippage. Figure 3c shows the deformation behavior of *Bond SP01* model. In this model, strain penetration is counted at nonlinear deformation, which can generate the effect of bond slippage.

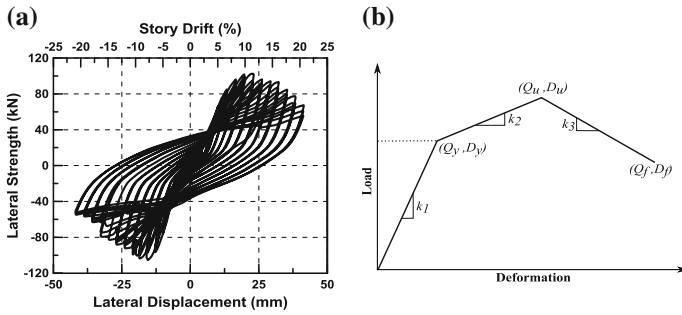


Fig. 4 a Hysteresis behavior of CMD [13] and b ideal load deformation of CMD

### 3.5 CMD Model

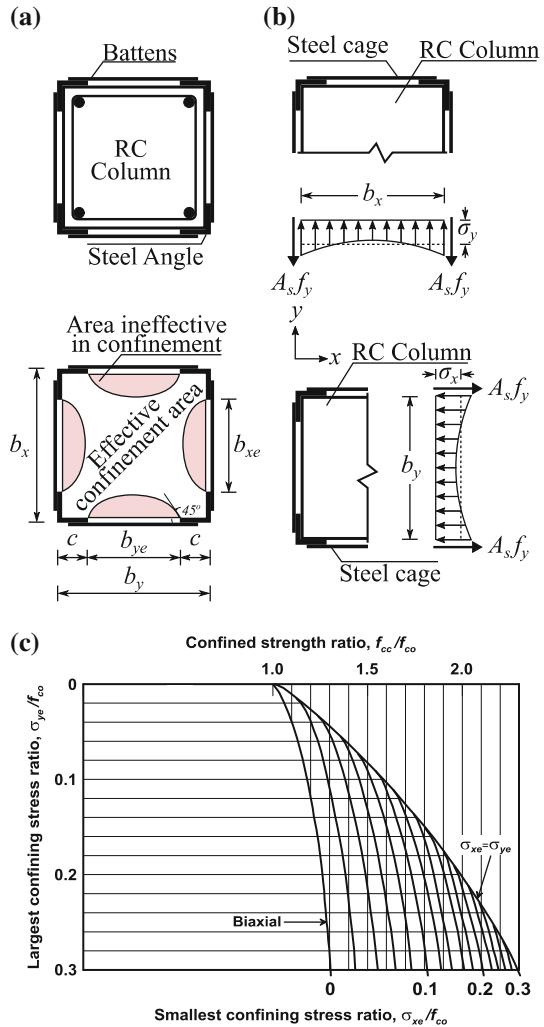
CMD has been modeled as link element, and force deformation data has been used as input. Idealized force deformation for CMD is shown in Fig. 4b, and this deformation behavior has been derived from multiple hystereses of CMD component test [13, 14]. Figure 4a shows one of the hysteresis behavior of CMD. Idealized force deformation curve of CMD has three major coordinates, namely  $Q_y, D_y, Q_u, D_u,$  and  $Q_f, D_f$ . Here,  $Q_y$  and  $D_y$  represent yielding point deformation while  $Q_u$  and  $D_u$  and  $Q_f$  and  $D_f$  represent ultimate and fracture deformation points [15]. This ideal force deformation plot has been modeled in *OpenSees* using “*uniaxial hysteretic material.*”

## 4 Evaluation of Effective Confinement on Steel-Caged Column

While modeling the steel-caged column, the passive confinement of concrete has been taken into account. Passive confinement of the concrete column is developed due to Poisson’s effect, which is generated due to the lateral restraint at corners by steel angles [16]. Figure 5a shows the unconfined concrete present near the battens of the steel cage due to absence of confining pressure, which is comparable to the case of rectangular hoops of shear stirrups in reinforced concrete column where unconfined concrete is present near the side hoops. The theoretical model of confined concrete for rectangular hoop proposed by Mander et al. [17] is used for the confinement action, which is produced by external steel cage.

Figure 5b shows half free body diagram of steel-caged section. The average and effective lateral confined stress can be obtained using balance equilibrium equation from the figure. As well as, Fig. 5c shows the general solution of the multi-axial failure criterion in terms of the two lateral confining stresses (i.e.,  $\sigma_{xc}$  and  $\sigma_{yc}$ ), which has been developed by Mander et al. [17] for rectangular hoops. From this

**Fig. 5** **a** Plan and effective confinement of steel cage section, **b** half body equilibrium of steel cage section, and **c** confinement strength ratio graph [17]



plot, the confined compressive strength of steel-caged concrete can be obtained. To obtain confining stress, peak unconfined strain ( $\epsilon_{cc}$ ) and ultimate confined strain ( $\epsilon_{cu}$ ) are required.

The peak unconfined compressive strain ( $\epsilon_{cc}$ ) and ultimate confined strain ( $\epsilon_{cu}$ ) of concrete have been calculated using equation recommended by Mander et al. [17], and the corresponding strain values are found to be 0.002 and 0.00526, respectively. Using material properties of the confined concrete, section capacities of steel-caged column have been evaluated in terms of axial–moment interaction and moment curvature. Figure 6 shows section capacities of steel-caged column section (RS-I).

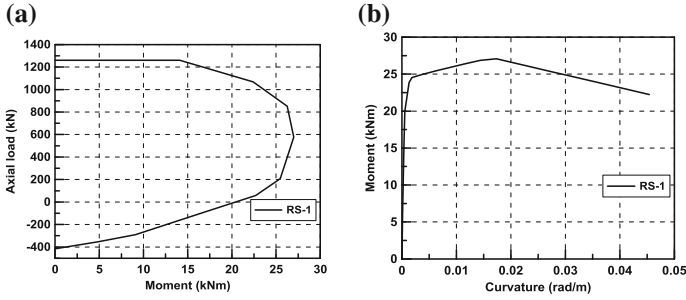


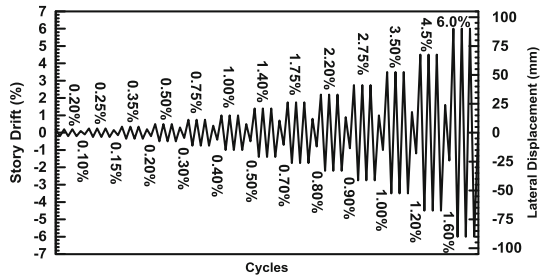
Fig. 6 Steel-caged column section capacities a  $P$ - $M$  interaction and b  $M$ - $\phi$  curve

### 5 Loading Protocol

In both numerical and experimental studies, same loading protocol has been used which is recommended by ACI Committee 374.1-05 [18]. Under this loading protocol, frames are subjected to gradually increase reversed cyclic displacement with constant gravity load. This displacement history consists of drift cycles of 0.20, 0.35, 0.50, 0.75, 1.10, 1.40, 1.75, 2.20, 2.75, 3.50, 4.50, and 6.0%. This imposed displacement profile is shown in Fig. 7.

Story drift (or drift ratio) may be defined as the ratio of the roof displacement to height of the story measured from the bottom level of column to the center line of top beam. Each displacement cycle is repeated for three times at any drift ratio and then, followed by a single drift cycle of the smaller magnitude. A constant gravity load of 7.25 kN is applied at the beam level of the prototype frame. Both the frames have been investigated under cyclic load up to 6.0% lateral drift considering constant gravity load effect [15].

Fig. 7 Imposed displacement history



### 6 Results and Discussion

Figure 8 shows the comparison of experimental and numerical results in terms of hysteresis, backbone, and energy dissipation for *RS-1* specimen. During the experiment, particularly up to 1.0% drift level, *CMD* was behaving elastically. At 1.4% drift, the shear plate buckled (out of plane) and this corresponded to the ultimate load carrying capacity (130.0 and 135.5 kN in tension and in compression, respectively). After this drift level, overall lateral strength of frame was reduced suddenly to 85 and 99 kN in tension and compression, respectively. Same behavior of frame is also observed from numerical study. Similar to experimental study, peak load of numerical frame has been found at 1.4% drift level to be 130.4 and 135.3 kN in tension and compression. At the last cycle (6.0% drift), load carrying capacity of frame has been observed as 87.2 and 109.4 kN in experimental and numerical, respectively, in compression cycle. All these behaviors are clearly visible in the backbone comparison (Fig. 8b). While comparing pinching behavior, numerical model predicted the experimental results accurately. In case of energy dissipation, numerical model has lower energy dissipation in the lower drift cycles; however in higher drift level, it has lower value compared to experimental but difference is not that much. At the final drift level, numerical energy dissipation has bit higher than experimental.

Comparison of experimental and numerical results of *RS-2* frame is shown in Fig. 8d-f. Experimentally, maximum lateral load resistance of *RS-2* was 124.5 and

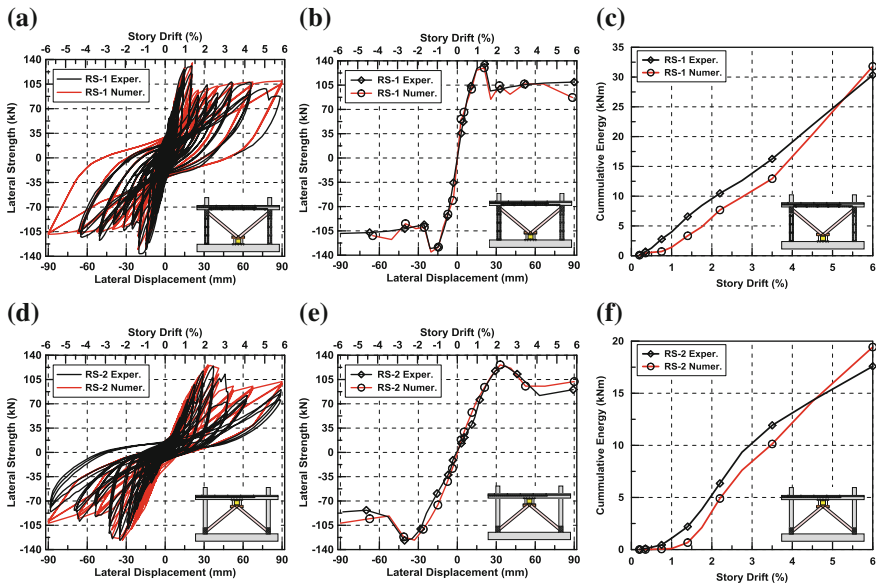


Fig. 8 Comparisons of experimental and numerical results of *RS-1* and *RS-2* specimen

-126.8 kN in tension and compression, respectively, at 2.75% drift level. Numerically, the peak lateral load of 126.2 and 126.5 kN in tension and compression, respectively, is observed at same drift level. In addition, from the comparison it can be observed that both experimental and numerical hysteresis responses are close to each other up to 2.75% drift level in both tension and compression. Last three drift level numerical results show a bit higher load carrying capacity than experimental results. The difference is 13.0% in both compression and tension (90.0 and 102 kN). All these deformation can be observed clearly from backbone curve in each drift cycle. Energy dissipation of numerical *RS-2* model is very close to experimental values in the beginning; after some few cycles, the values are bit lower than experimental results; however, at the higher drift level numerical values are close to experiment results. At final drift level, numerical model predicted higher values of lateral strength than experiment.

## 7 Conclusion

Numerical models of RC frames have been developed using *OpenSees*, and it considers bond slip at all critical moment connection and includes existing concrete weak bond strength. Parameters like lateral load capacity, strength–stiffness degradation during loading unloading and energy dissipation capacity of the numerical model matched with the experimental results. In addition, pinching behavior in both frames is well predicted by numerical model. Experimental and numerical results match each other. For example, difference in peak lateral load capacity of *RS-1* specimen is 0.3%, while *RS-2* specimen shows 1.4%. In case of energy dissipation, numerical model predicted much close values to experimental energy dissipation values and over all numerical energy curve is almost same as the experimental. These results indicate that *OpenSees* software platform has the capability of modeling various effects including pinching, tensile strength of concrete, and bar slip model.

## References

1. Sahoo DR, Rai DC (2010) Seismic strengthening of non-ductile reinforced concrete frames using aluminum shear links as energy-dissipation devices. *Eng Struct* 32:3548–3557
2. Khampanit A, Leelataviwat S, Kochanin J, Warnitchai P (2014) Energy-based seismic strengthening design of non-ductile reinforced concrete frames using buckling-restrained braces. *Eng Struct* 81:110–122
3. ASCE 41-06 (2007) Seismic rehabilitation of existing buildings. American Society of Civil Engineers, Reston Virginia
4. ASCE 41-13 (2007) Seismic evaluation and retrofit of existing buildings. American Society of Civil Engineers, Reston Virginia

5. FEMA-547 (2006) Techniques for the seismic rehabilitation of existing buildings. Applied Technology Council, Washington DC
6. Melo J, Fernandes C, Varum H, Rodrigues H, Costa A, Arêde A (2010) Numerical modelling of the cyclic behaviour of RC elements built with plain reinforcing bars. *Eng Struct* 33: 273–286
7. McKenna F, Fenves G, Scott M, Jeremic B (2000) Open system for earthquake engineering (OpenSees). Berkeley CA
8. Zhao J, Sritharan S (2007) Modeling of strain penetration effects in fiber-based analysis of reinforced concrete structures. *ACI Struct J* 104:133–141
9. Sahoo DR, Prakash A (2015) Seismic behavior of concentric braced frames designed using direct displacement-based design method. In: 8th international conference on behaviour of steel structures in seismic areas (STESSA), Shanghai China
10. Oinam RM, Sahoo DR (2015) Analytical prediction of cyclic performance of RC frame structures. In: Tenth pacific conference on earthquake engineering (10PCEE), Sydney, pp 6–13
11. Shetty MS (2005) Concrete technology: theory and practice. S. Chand and Company Ltd, New Delhi
12. Oinam RM, Sahoo DR, Sindhu R (2014) Cyclic response of non-ductile RC frame with steel fibers at beam-column joints and plastic hinge regions. *J Earthquake Eng* 18:908–928
13. Taraithia SS, Sahoo DR, Madan A (2013) Experimental study of combined yielding metallic passive devices for enhanced energy dissipation of structures. In: The Pacific structural steel conference, Singapore
14. Sahoo DR, Singhal T, Taraithia SS, Saini A (2015) Cyclic behavior of shear-and-flexural yielding metallic dampers. *J Constr Steel Res* 114:247–257
15. Oinam RM, Sahoo DR (2016) Seismic rehabilitation of damaged reinforced concrete frames using combined metallic yielding passive devices. *Struct Infrastruct Eng* 1–15
16. Nagaprasad P, Sahoo DR, Rai DC (2009) Seismic strengthening of RC columns using external steel cage. *Earthquake Eng Struct Dyn* 38:1563–1586
17. Mander JB, Priestley MJN, Park R (1989) Theoretical stress-strain model for confined concrete. *J Struct Eng* 114:1804–1826
18. ACI, Committee, 374.1-05 (2006) Acceptance criteria for moment frames based on structural testing and commentary—An ACI standard. American Concrete Institute, Farmington Hills Michigan

# Flexural Behaviour of Severely Damaged RC Beams Strengthened with Ultra-High Strength Concrete



A. Ramachandra Murthy, P. Ganesh and G. N. Sakthi Priya

**Abstract** RC structures are severely damaged and deteriorated due to various reasons, and it is essential to strengthen it to satisfy the capacity and service conditions. In order to achieve this, an appropriate strengthening technique has been arrived at in the present study for the severely damaged RC beams. In this study, RC beams of size 1500 mm (length)  $\times$  100 mm (wide)  $\times$  200 mm (depth) were cast with M30 grade concrete by providing 2–10 mm dia reinforcement at bottom and 2–8 mm dia at top. The beams were tested under displacement control till failure (control beams) with an ultimate load of about 78 kN and deflection about 27 mm. Later, two beams were preloaded to beyond ultimate load (deflection is about 8 mm) to introduce severe damage. The preloaded beams were strengthened with ultra-high strength concrete (UHSC) strips of 10 mm thickness on the tension face and tested under displacement control and found that responses such as the strength and ductility of the strengthened RC beams are comparable with the control beams. The average ultimate load and maximum deflection of strengthened beams are found to be 93 kN and 23 mm, respectively, indicating that UHSC is one of the promising materials for repair and retrofitting. Further, no debonding/delamination is observed during testing.

**Keywords** RC beam  $\cdot$  Pre-damage  $\cdot$  Ultra-high strength concrete Strip  $\cdot$  Adhesive bonding  $\cdot$  Retrofitting

---

A. R. Murthy (✉)  $\cdot$  G. N. Sakthi Priya  
Computational Structural Mechanics Group, CSIR-Structural  
Engineering Research Centre, Chennai 600113, India  
e-mail: murthyarc@serc.res.in

G. N. Sakthi Priya  
e-mail: sakthi.civilgce@gmail.com

P. Ganesh  
Engineering of Structures-AcSIR, CSIR-Structural  
Engineering Research Centre, Chennai 600113, India  
e-mail: ganesh@acsir.res.in



## 1 Introduction

In recent years, many reinforced concrete (RC) structures are suffering from various deteriorations such as cracks, concrete spalling and large deflection due to which there is reduction in strength and stiffness. The deteriorations are due to unexpected loading, ageing, environment and corrosion of steel reinforcement, etc. Strengthening of existing concrete structures is necessary to enhance the load carrying capacity and satisfy serviceability criteria. Rehabilitation and strengthening has therefore become an acceptable way of improving their load carrying capacity and extending their service life. One of the major challenges in the retrofitting operation is the selection of an appropriate retrofitting material. The popularly employed methods for retrofitting are jacketing, post-tensioning, bonded steel plates and fibre-reinforced plastic [1, 2].

Retrofitting of RC structural members by using externally bonded steel plates has gained popularity due to (i) fast and easy implementation, (ii) minimum site disturbance and (iii) minimal changes in section size. The limitations of this method include (i) undesirable shear failures, (ii) difficulty in handling heavy steel plates, (iii) corrosion of the steel and (iv) the need for butt joint systems as a result of limited workable lengths. The other popularly employed material for retrofitting is FRP. Several extensive studies were carried out in the last few decades on FRP-based strengthening of the RC structures in the form of externally bonded laminates or near-surface mounted rebar. Some of the merits of the FRP material include (i) high strength-to-weight ratio, (ii) stiffness-to-weight ratio and (iii) chemically inert. These merits boosted the growing interests among conventional techniques like steel plates and external pre-stressing. In turn, FRP strengthening has been recognized as an effective solution and gained widespread popularity to enhance structural capacity [3, 4]. However, some drawbacks associated with FRP such as abrupt failure, lesser ductility, high material cost, skilled manpower, emission of toxic fumes, moisture incompatibility and difficulty in application in low temperature knocked researchers to think beyond. The experimental observations made on FRP were revealed a loss of ductility due to the linear elasticity made up to tensile rupture.

The limitation of this technique is brittle failure due to mismatch of tensile strength and stiffness with that of concrete. The drawbacks of the above methods have led to the development of a fibre-reinforced ultra-high strength concrete (UHSC) with high mechanical and durability properties making suitable choice for retrofitting. UHSC is a novel cementitious material consisting of a dense, high-strength matrix containing a large number of evenly embedded steel fibres. It has exceptional mechanical properties and transport characteristics including very high tensile strength, strain hardening, ductility combined with very low permeability making it ideal for the production of thin structural members as well as for the rehabilitation and modification of existing structures [5–8].

Due to enhanced mechanical and excellent durability-related properties of UHSC, it can compete with steel structural members in terms of size, properties and

cost. The ultra-high strength is achieved by optimizing the microstructure of the cement-based composites by an appropriate selection of materials and the use of special process technology such as self-compaction, extrusion, spray/concreting as well as the modification of micromechanical properties [9]. Hence, UHSC has been identified as a promising candidate for repair and retrofitting of RC structures as it possesses excellent bond with normal concrete, i.e. the interface between the new concrete (UHSC) and the old concrete substrate is effectively bonded which reduce distresses like debonding happens in other types of materials used for retrofitting.

In this present study, the severely pre-damaged RC beams were strengthened by the ultra-high strength concrete (UHSC) overlay and tested up to failure. The details of failure modes, crack patterns, effect of retrofitting scheme are presented.

## 2 Materials and Experimental Program

### 2.1 Materials and Properties

Materials used for producing UHSC generally consist of very fine powder comprises cement, sand, quartz powder, silica fume, steel fibres (optional) and superplasticizer [10]. In the present study, cementitious material used is ordinary Portland cement (OPC) conforming to IS 12269 (2013) standard. The chemical and physical properties of the cement are shown in Table 1. In addition, supplementary cementitious materials (SCM), silica fume is used as an additive. A maximum silicon dioxide ( $\text{SiO}_2$ ) content is the property most frequently specified. According to that silica fume is used as powder form with 95%  $\text{SiO}_2$  with a particle size range of 0.2–25  $\mu\text{m}$ .

By the addition of SCM with less water-to-cement ratio, a demand for flow ability or workability is increased due to larger specific surface area. Hence, superplasticizer (SP) is used to decrease the water demand while improving the workability of concrete. A polycarboxylate-ether-based superplasticiser manufactured by BASF (Master Glenium Sky 8233) is used for all mixes. The SP content is

**Table 1** Chemical and physical properties of OPC

$\text{SiO}_2$	5.80
$\text{Al}_2\text{O}_3$	3.30
CaO	64.10
MgO	1.75
$\text{K}_2\text{O}$	0.75
$\text{SO}_3$	1.80
$\text{Na}_2\text{O}$	0.20
$\text{Cl}^-$	0.03
Specific gravity	3.15
SSA ( $\text{m}^2/\text{g}$ )	0.32

adjusted for each mix to ensure that no segregation would occur. Brass-coated steel fibres of length 13 mm and diameter 0.18 mm having yield strength about 1500 MPa are used. Similarly, materials used for producing conventional concrete are ordinary Portland cement 53 grade, natural sand and gravels with aggregate size below 12 mm and potable water.

## 2.2 Mix Proportion

In the absence of well-established comprehensive methods for the mix design of UHSC, mixes are arrived at based on several trials to get the desired strength. Information on UHSC regarding mix design to obtain the required target strength is scarce in the literature. Therefore, several trials were made before the final mix design. The ingredients of final mix proportion of UHSC include cement, silica fume, quartz sand, quartz powder, superplasticizer and water that are given in Table 2. Mix design has been carried out for normal strength concrete (M30 grade) as per Bureau of Indian Standards (BIS) [11]. The mix ratio of normal strength concrete (NSC) by weight of cement, fine aggregate, coarse aggregate and water is 1: 1.67: 1.86: 0.45, and the mix proportions are given in Table 2.

## 2.3 Test Program

Experiments were conducted on severely damaged RC beams retrofitted with UHSC overlay over the bottom phase of the beam which is damaged under flexure. Two-point monotonic loading was considered to evaluate mid-span deflection, crack pattern of the tested RC beam, flexural capacity and flexural stiffness. Also

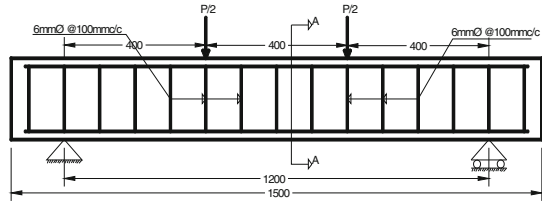
**Table 2** Mix proportion for UHSC

Mix ID/mix ingredients	NSC	UHSC
Water/cement ratio	0.45	0.23
Cement (Kg/m <sup>3</sup> )	442	839
Fine aggregate (Kg/m <sup>3</sup> )	738	–
Coarse aggregate (Kg/m <sup>3</sup> )	822	–
Silica fume (Kg/m <sup>3</sup> )	–	210
Quartz sand (Kg/m <sup>3</sup> )	–	923
Quartz powder (Kg/m <sup>3</sup> )	–	336
Water (Kg/m <sup>3</sup> )	199	193
Superplasticizer <sup>a</sup>	–	3.5%
Steel fibre <sup>b</sup>	–	2%

<sup>a</sup>% weight of binder content in mix

<sup>b</sup>% volume of concrete

**Fig. 1** A typical reinforcement details of RC beam



the mechanical properties like compressive strength and split tensile strength were determined on cubical specimen of size 100 mm and cylindrical specimen of size 150 mm × 300 mm, respectively, for NSC. Similarly, the mechanical properties like compression strength and split tensile strength were determined on cubical specimen of size 70.7 mm and cylindrical specimen of size 75 mm × 150 mm, respectively, for UHSC mix.

The dimension of the RC beam is 1500 mm (length), 200 mm (depth) and 100 mm (breadth). The thickness of the UHSC overlay used for retrofitting is 10 mm. The typical reinforcement of all RC beams was 2–10 mm diameter bars in tension, 2–8 mm diameter bars at compression and 2-legged stirrups of 6 mm diameter bars as shear reinforcement at 100 mm c/c spacing. Sufficient margin of cover to main reinforcement was ensured.

All the three beams were simply supported over an effective span of 1200 mm and tested under four-point bending, as shown in Fig. 1. The load was applied using a servo-controlled hydraulic actuator (400 kN capacity) with a loading rate of 0.5 mm/min for control specimen and 1.0 mm/min for all strengthened beams. Control beam was tested under displacement control till failure to evaluate the ultimate load carrying capacity. The linear varying displacement transducers (LVDTs) are used to measure the vertical displacement at mid-span. Later, two beams were preloaded to beyond ultimate load to introduce severe damage. The preloaded beams were strengthened with UHSC strips of 10 mm thickness on the tension face.

### 3 Results and Discussion

#### 3.1 Control Beam (CB)

The average compressive strength and split tensile strength for NSC are obtained as 35 and 3.2 MPa, respectively. Control beam was tested to failure by displacement control test with a loading rate of 0.5 mm/min. When the tensile stress of RC beam exceeds the modulus of rupture, few cracks were occurred inside of CB and it was visible for the corresponding load of 32.6 kN. Because of loading, cracks were multiplied at flexure and shear zones and extended to top of the section. Figure 2 shows the test set-up at laboratory, and Fig. 3 presents the crack details.

**Fig. 2** Test set-up**Fig. 3** Typical crack pattern

From Fig. 3, it can be observed that CB reveals linear behaviour of load–deflection response till the specimen had reached the first crack load afterwards steel started yielding at the load of 75.67 kN. Successively the deflection increased with respect to load by ductile property of RC section. Finally, the specimen sustained an ultimate load of 78.54 kN and failed in flexure following by concrete crushing at dropping load of 68 kN with gradually increased deflection almost 28 mm.

### 3.2 *Retrofitted Beam 1 (RS1)*

The average compressive strength and split tensile strength of the retrofitting material (UHSC) are obtained as 122.5 and 20.7 MPa, respectively. Beam was loaded under four-point bending beyond the peak load to induce severe damage. Beam was loaded about 81 kN with deflection of 8 mm. In the beginning of loading process, microcracks developed nearby the mid-span and on further loading, and cracks were propagated to the compression zone to the maximum depth of 175 mm (Fig. 4). Figure 5 presents the comparison of load–deflection behaviour of severely pre-damaged beam (S1), strengthened beam (RS1) and control beam CB. Retrofitted beam exhibits linear response of load–deflection up to 90.95 kN. With increasing load, steel yielding taken place. Beyond yielding load, it is clear that retrofitted beam exhibited more stiffness than the control beam.

**Fig. 4** Crack pattern of beams B1

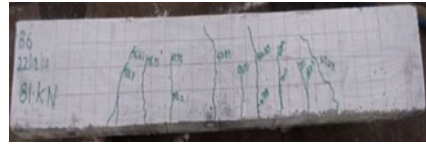
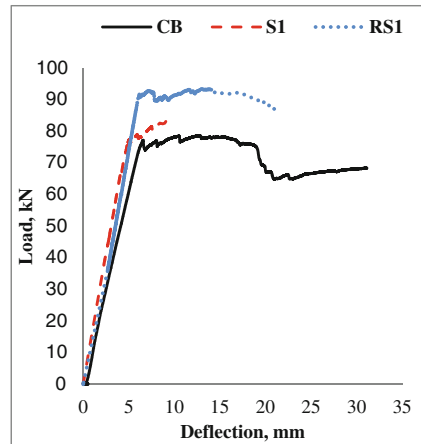


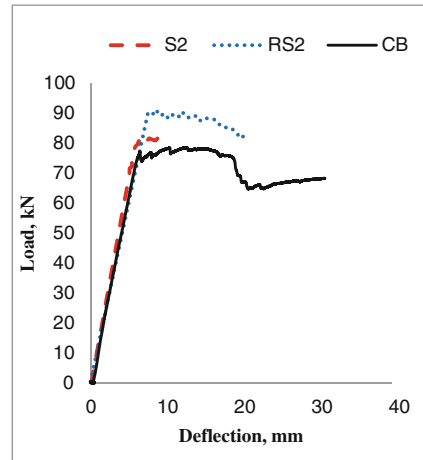
**Fig. 5** Load versus deflection



UHSC strip which was attached to the tensile face acted as barrier for the pre-cracks to grow up to the load of 46.8 kN and then few flexural as well as shear cracks also emerged in beam and strip. After the load of 92.5 kN, the pre-cracks activated to propagate to crack depth of 180 mm. Upon application of further load, RS1 subjected to strain hardening in plastic region with the maximum load of 93.35 kN which is 19% increment of load carrying capacity of control beam CB. Consequently, UHSC strip experienced rupture nearby the mid-span corresponding to post peak load of 91 kN. As observed, the maximum width of widened crack is around 3 mm only; it is the lower value corresponding to the enhanced load carrying capacity and considerably reduced the deflection of about 20% than control beam. As result of retrofitting, it is certain that 10-mm-thick overlay is significant in load carrying capacity as well as ductile behaviour. The failure modes of strengthened beams are typical flexural failure, and there is no debonding or delamination of strip from the severely damaged RC beam substrate proves the excellent interfacial bonding behaviour of composite RC beams.

### 3.3 *Retrofitter Beam 2 (RS2)*

Same as RC beam S1, S2 was damaged severely beyond the ultimate load of control beam of about 81.65kN with corresponding deflection of 9.2 mm. The

**Fig. 6** Rupture in overlay**Fig. 7** Load versus deflection

multiple cracks appeared on the beam, and these cracks propagated to the compression zone due to gradual loading. After damaged, RC beam S2 was strengthened with UHSC overlay and loaded till full failure as control beam. Retrofitted beam RS2 exhibited linear response of load–deflection up to 90.16 kN and steel continued to yield. UHSC overlay restricted the appearance of new cracks on beam, but existing cracks started to propagate and widen. Few cracks appeared at shear zone of beam and overlay also. Due to continuous loading, the overlay experienced rupture in the constant bending zone at the maximum load of 90.78 kN (Fig. 6) with the corresponding deflection of 16.2 mm. From Fig. 7, it is found that retrofitted beam RS2 could not enhance the stiffness as that of control beam due to high magnitude of damage. However, retrofitted beam maintains the stiffness similar to pre-damaged RC beam and control beam. Retrofitted beam enhances the load carrying capacity of 16%.

## 4 Conclusion

An experimental investigation of severely damaged RC beams strengthened and rehabilitated using UHSC overlay was carried out, and the following conclusion is made.

- The load–deflection behaviour of the severely damaged beam retrofitted with UHSC overlay can effectively increase the first crack load, yield load and ultimate flexural capacity of the beam.
- The ultimate load carrying capacity of the beam is enhanced by 19% for RS1 and 16% for RS2.
- There is no significant improvement in stiffness behaviour; these may be due the severe extent of damage induced.
- The failure modes of strengthened beams are typical flexural failure, and there is no debonding/delamination of overlay from the old concrete substrate proves the excellent interfacial bonding behaviour of composite RC beams.

**Acknowledgements** The authors thank the staff of the Computational Structural Mechanics Group of CSIR-SERC for the co-operation and suggestions provided during the investigations. This paper is being published with the kind permission of the Director of CSIR-SERC.

## References

1. Attari N, Amaziane S, Chemrouk M (2012) Flexural strengthening of concrete beams using CFRP, GFRP and hybrid FRP sheets. *J Constr Build Mater* 37:746–775
2. Rabinovitch O, Frostig Y (2003) Experiments and analytical comparison of RC beams strengthened with CFRP composites. *Compos B* 34(8):663–677
3. Teng JG, Chen JF, Smith ST, Lam L (2002) FRP-strengthened RC structures. Wiley, England
4. Nanni A (2003) Concrete repair with externally bonded FRP reinforcement: examples from Japan. *J Concr Int* 97:22–26
5. Alaae FJ, Karihaloo BL (2003) Retrofitting of reinforced concrete beams with CARDIFRC. *J Compos Constr* 7:174–186
6. Shin HO, Yoon YS, Cook WD, Mitchell D (2015) Effect of confinement on the axial load response of ultrahigh-strength concrete columns. *J Struct Eng* 141(6):04014151
7. Karihaloo BL, Benson SDP, Alaae FJ (2004) CARDIFRC: properties and application to retrofitting. In: Proceedings 5th world congress on fracture mechanics of concrete structures (FRAMCOS-5), Vail, USA, Published in: AI, V C Li Et ed., pp 733–742
8. Xu SL, Wang N, Zhang XF (2012) Flexural behavior of plain cement concrete beams strengthened with ultra-high toughness cementitious concrete layer. *Mater Struct* 45(6):851–859
9. Ramachandra Murthy A, Iyer Nagesh R, Raghu Prasad BK (2013) Evaluation of mechanical properties of high strength and ultra high strength concretes. *Adv Concr Constr* 1(4):341–358
10. Richard P, Cheyrezy MH (1995) Composition of reactive powder concretes. *Cem Concr Res* 25:1501–1511
11. Bureau of Indian Standards (2000) IS 456:2000, Indian standard for plain and reinforced concrete code of practice, New Delhi



# Performance of RC Columns Strengthened with Prestressed CFRP Bands



Ambadas Waghmare, Daniel Koothoor, Dhruv Shah, Kinal Bid, Raghav Agarwal, Rahul Ghadwal, Snehal Sonawane, Viraj Sanghvi and Abhay Bambole

**Abstract** This paper investigates the comparison of external passive and active confinement to restore the strength, ductility, and durability of affected RC columns to an acceptance level using carbon fiber reinforced polymer (CFRP) bands. The experimental program included compression load testing of square and circular-shaped reinforced concrete columns to establish the effect of the confinement on the compressive load-carrying capacity and the stress–strain behavior. A number of parameters are investigated in the study including the effect of varying the band spacing, confining pattern, and passive and active confining forces. It has been found analytically that confining the columns with prestressed CFRP bands did optimize the load-carrying capacity economically. It also enhanced the confined column's stress–strain behavior with greater lateral stresses at peak strength observed as well as the ductile property.

**Keywords** RC columns · Prestressed · Confinement · CFRP · Strength

## 1 General Information

### 1.1 Introduction

Many times it is observed that concrete structures reach a state where they can no longer perform their intended function of withstanding the load acting on them safely. This problem can arise due to deterioration of the structure due to environmental

---

A. Waghmare · D. Koothoor · D. Shah · K. Bid · R. Agarwal  
R. Ghadwal · S. Sonawane · V. Sanghvi  
Department of Civil Engineering, VJTI, Mumbai, India

K. Bid  
e-mail: kinalbid95@gmail.com

A. Bambole (✉)  
Department of Structural Engineering, VJTI, Mumbai, India  
e-mail: anbambole@vjti.org.in

**Fig. 1** Stress–strain diagram for different fibers

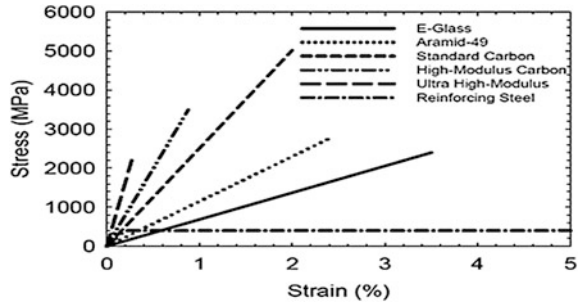


**Table 1** Comparison of typical properties of different fibers

Property	Material		
	GFRP	CFRP	AFRP
Tensile strength (MPa)	517–1207	1200–2410	1200–2068
Yield strength (MPa)	N/A	N/A	N/A
Elastic modulus (GPa)	30–55	147–165	50–74
Specific gravity	1.5–2.0	1.5–1.6	1.25

effects, which leads to loss of strength. The structure may have to carry loads larger than that considered in design due to change of usage demand or revision of code requirements. Also, sometimes structures fail to resist the loads due to deficiency in construction or design. In some extreme cases, the performance of structure may be reduced due to accident or vandalism. Demolition or rebuilding of the structure is not an economically viable option. Hence, there is need for strengthening or retrofitting of the structure.

The various options available for strengthening columns are externally bonded steel plates, steel or concrete jackets, external post-tensioning and use of composite material. But bonding of steel plates to concrete surface is not desirable due to heavy weight, difficulty to shape to fit complex profile like circular and arc shape the possibility of corrosion that may adversely affect bond strength. FRP sheets are convenient than steel plates because of high strength to weight ratio, resistance to corrosion effect, good mechanical strength.

The efficient way of enhancing the load-carrying capacity and/or ductility of RC column is by confining the concrete. The lateral pressure due to dilation of concrete induces triaxial state of stress and consequently causes increment in compressive strength and ultimate strain (Fig. 1; Table 1).

## 1.2 Advantages of Prestressing Over Confinement

- CFRP sheets increase the bearing capacity and overall performance of the structure, but today, only 20–30% of the strength of carbon fiber reinforced polymer is used.
- There exists FRP strain hysteresis, and much lower fracture strain of FRP than of fiber material, and it is very hard to control quality of on-site construction.
- Prestressing FRP is an effective method to reduce the impact of the FRP confinement concrete strain hysteresis.
- Since prestressing of column is done using FRP bands, the pitch can be varied which ultimately saves significant quantity of FRP material without compromising the load-bearing capacity obtained by fully confined column.
- Other advantages are reduced crack widths, reduced deflection, and reduced stress in internal steel and increase-bearing capacity.

## 2 Analytical Studies

### 2.1 Controlled Specimens

Identical columns without confinement were analyzed along with the test samples to evaluate the improvement of the mechanical properties.

From IS 456: 2000 [1], axial compressive force can be given by

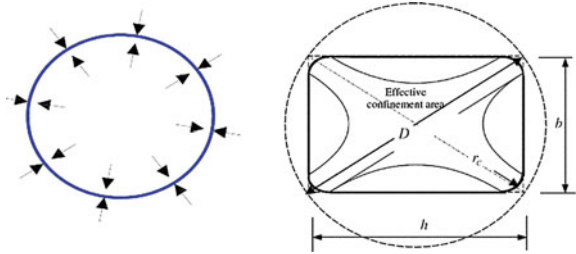
$$P_u = 0.4 f_{ck} A_c + 0.67 f_y A_{sc}$$

$$P_u = 52.5 \text{ Tonne}$$

### 2.2 Wrapped Specimens

Confinement by FRP wraps is achieved by placing fibers transverse to the longitudinal axis of the column providing passive confinement, which is activated when concrete core starts dilating due to Poisson's effect. The confinement of circular column is more efficient than confinement of non-circular column because circumferential pressure acts radially outwards and is uniform in case of circular column. In case of confinement of non-circular columns, the confinement is concentrated at the corners rather than over entire perimeter (Fig. 2).

**Fig. 2** Effect of FRP confinement on circular and non-circular cross sections



From ACI 440.2R 2008 [2],

$$f_l = \frac{2E_f n t_f \epsilon_{fe}}{D}$$

$$f'_{cc} = f'_{ck} + 3.3 \psi_f \kappa_a f_l$$

Substituting  $f'_{cc}$  as  $f_{ck}$  in  $P_u = 0.4 f_{ck} A_c + 0.67 f_y A_{sc}$ , we get

$$P_u = 0.4 f'_{cc} A_c + 0.67 f_y A_{sc}$$

$$P_u = 61.25 \text{ Tonne}$$

**Percentage increase in strength = 16.67%**

### 3 Experimental Studies

All RC columns were tested in reaction frame of 400-ton capacity. The test setup consisted of a reaction frame, hydraulic jack, load cells, four Linear Potentiometers, data acquisition system, and steel plate for packing as per the requirement (Figs. 3, 4, and 5; Table 2).

**Fig. 3** Failure of unwrapped and wrapped columns, respectively (250 × 200, 1400)



**Fig. 4** Stress–strain diagram for unwrapped specimen from strain gauges

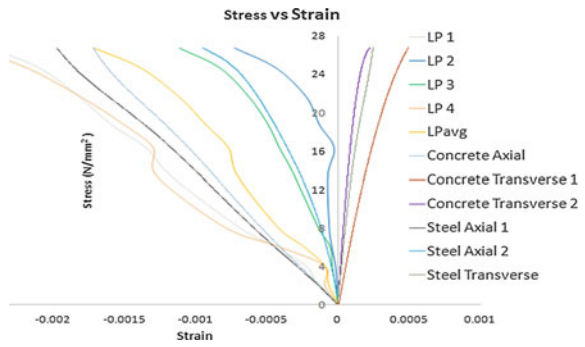


**Fig. 5** Stress–strain diagram for unwrapped specimen from LPs

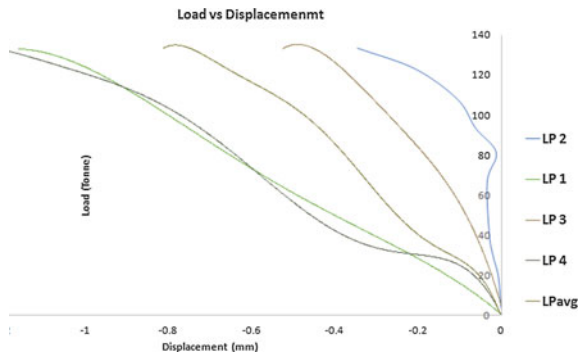


**Table 2** Experimental results

Specimen	Corresponding strain	Average maximum load (Tonne)	Average maximum stress (MPa)	% Increase in LCC
UR-200X250-1200	0.00210	135.79	27.28	33.26
WR-200X250-1200	0.00431	180.95	36.41	
UR-200X250-1400	0.00172	129.34	25.99	38.47
WR-200X250-1400	0.00368	179.10	35.98	

## 4 Proposed Analytical Approach of Columns with CFRP Bands

### 4.1 Non Prestressed Bands Pattern

#### 4.1.1 Horizontal Bands

Higher the pitch, lower is the effective confining pressure. The correction that needs to be incorporated is given by

$$f_l = \alpha \times \frac{2E_f n t_f \varepsilon_{fe}}{d}$$

$$P_u = 0.4 (f_{ck} A_c + 3.3 \psi_f \kappa_a f_l A'_c) + 0.67 f_y A_{sc}$$

where

- \*\*  $\alpha$  is the correction factor
- \*\*  $d$  is equivalent effective diameter
- \*\*  $A'_c$  is equivalent effective cross-sectional area of core

$$\alpha \propto \frac{\text{Confined area}}{\text{Total surface area}}$$

\*\*This has been discussed in the following article (Figs. 6 and 7).

#### 4.1.2 Single- and Double-Helical Bands

As we know that helical stirrups contribute to 5% increase in the shear capacity compared to that of horizontal stirrups, consequently, we expect approximately 5 and 10% increase in the load-bearing capacity of cylindrical column due to single-helical and double-helical CFRP bands, respectively.

For single-helical band pattern,

**Fig. 6** Stress–strain diagram for wrapped specimen from strain gauges

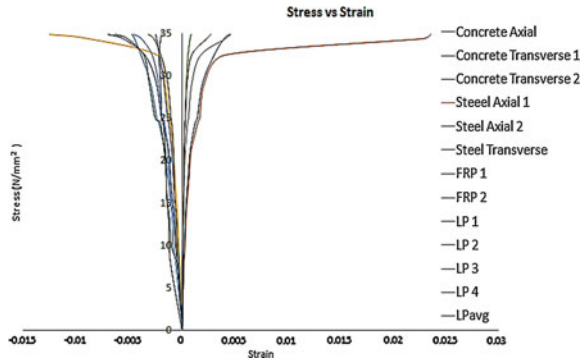
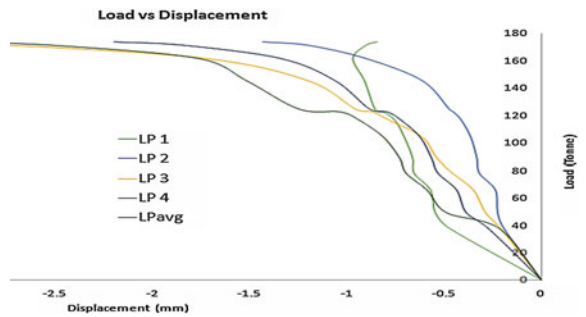


**Fig. 7** Stress–strain diagram for wrapped specimen from LPs



$$f_l = 1.05 \alpha \times \frac{2E_f n t_f \epsilon_{fe}}{d}$$

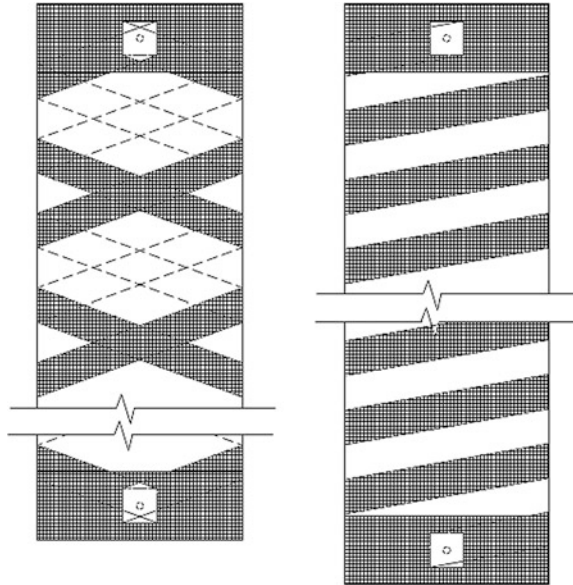
For single-helical band pattern (Fig. 8),

$$f_l = 1.1 \alpha \times \frac{2E_f n t_f \epsilon_{fe}}{d}$$

### 4.2 Externally Prestressed Columns with CFRP Band

The effect of external prestressing using CFRP horizontal bands has been studied analytically, and an empirical formula has been suggested which needs to be authenticated by experimental results. This study has been done to evaluate the optimization of confinement to achieve economy.

**Fig. 8** Cylindrical columns with double- and single-helical CFRP bands, respectively



**4.2.1 Tension Device Design**

The tension device consists of two parts: the hoops and the tension system. The hoops have sufficient strength and stiffness to withstand the deformation and stress. The device’s working principle is as follows: one end of the prestressing CFRP is pasted on one side of the column with epoxy resin, which makes the pasted length satisfy the tension force. The hoops are then fixed on both the sides of CFRP. Pull the screw through the floor and pressure sensor after connection of screw and steel roller. Put the CFRP around the column in a circle and the other end of CFRP around the steel roller and paste a certain length. Then, the CFRP is tensioned after the epoxy resin dries. The screw nut is tightened by wrench, and the CFRP is fastened by screw. In order to measure the tension in CFRP, the tensile stress is monitored by sensor. This prestressing method has been adopted from [3] (Fig. 9).

The effective area for this technique in non-circular section is as shown above [4]. Equivalent confining pressure is given by

$$f_l = \frac{(\beta\sigma_{H1} + \gamma\sigma_{H2}) \times 2nt_f}{d}$$

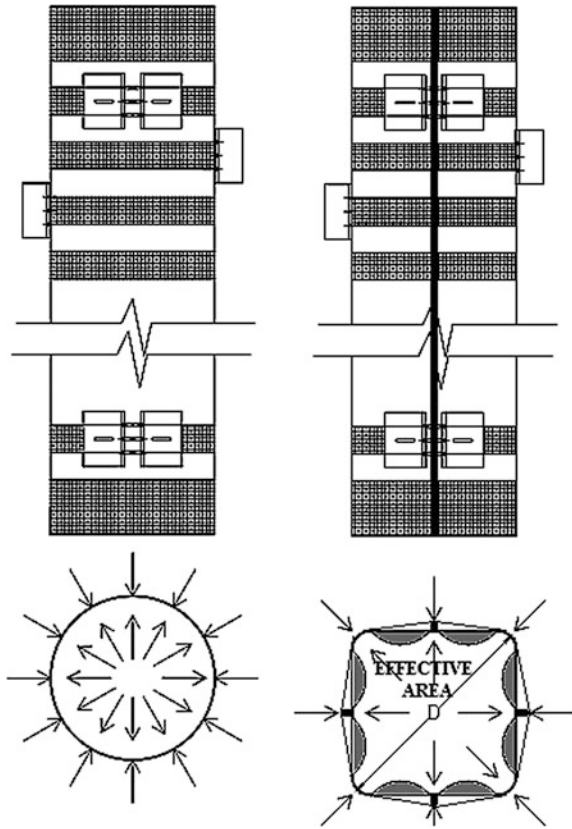
$$P_u = 0.4 (f_{ck}A_c + 3.3\psi_f\kappa_{af}lA'_c) + 0.67f_yA_{sc}$$

where

- \*\*  $d$  is equivalent effective diameter
- \*\*  $A'_c$  is equivalent effective cross-sectional area of core



**Fig. 9** Prestressed CFRP bands for circular and rectangular cross section



$\sigma_{H1}$  is hoop stress because of confinement

$\sigma_{H2}$  is hoop stress because of prestressing

**\*\*  $\beta$  and  $\Upsilon$  are the correction factors for  $\sigma_{H1}$  and  $\sigma_{H2}$ , respectively**

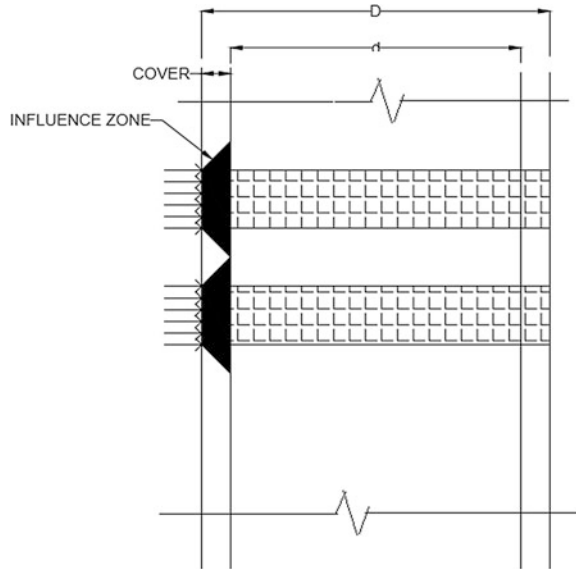
**\*\*This has been discussed in the following article.**

### 4.3 Theory Behind Load-Carrying Capacity of FRP-Banded Columns

The effective-confined area of partially FRP-wrapped column can be calculated by considering an equivalent area of fully confined column by virtue of stress distribution as shown below.

Consider,  
width of band =  $w$

**Fig. 10** Representation of equivalent effective area



pitch =  $s$   
 Assuming ideal condition,  
 therefore,  $d = D - s$  (Fig. 10)

$$\alpha \propto \frac{W}{W + S}, \quad \beta \propto \frac{W}{W + S}, \quad \gamma \propto \frac{W}{W + S}$$

This theoretical formulation needs to be verified using experimental results (Fig. 11).

#### 4.4 Experimental Variable Specifications

See Table 3.

### 5 Analytical Results

See Tables 4 and 5.

**Fig. 11** Typical axial load compressive strain curves of confined columns [5]

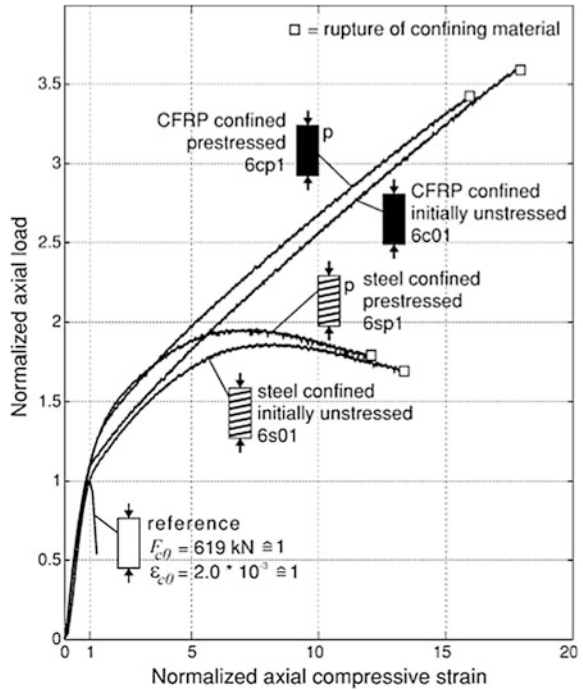


**Table 3** Variable specifications

	Property	Value	Unit
<i>Cross section</i>			
Square	Side	270	mm
	Height	1630	mm
Circular	Side	300	mm
	Height	1800	mm
<i>Material</i>			
Concrete	Grade	20	N/mm <sup>2</sup>
Steel	Grade	415	N/mm <sup>2</sup>
CFRP	Width	50	mm
	Pitch	50	mm
	Prestress	600–950	N/mm <sup>2</sup>

\*Angle for single-helical band = 10°–20°

Angle for single-helical band = 10°–30°

**Table 4** For circular section

Description	Value (tonne)
Controlled specimen	82.36
Fully wrapped specimen	112.68
Partially wrapped specimen	95
Externally prestressed specimen	107.3

**Table 5** For square section

Description	Value (tonne)
Controlled specimen	80.52
Fully wrapped specimen	96.06
Partially wrapped specimen	85.26
Externally prestressed specimen	92.73

## 6 Conclusion

1. Significant increase in structural strength for all the wrapped specimens tested was observed along with significant enhancement in ductility of test specimens.
2. The improvement in load-bearing capacity is more in case of circular section as compared to that of non-circular section.
3. Application of bands is relatively easier on columns. Moreover, the material quantity is expected to reduce by 50% without compromising the strength significantly, as provided by fully wrapped CFRP. Thus, this predicted feature of bands may prove to be of great utility in civil and structural engineering.
4. Prestressing of column using CFRP bands leads to optimization of the fiber used by exploiting the ultimate strength of the CFRP.
5. By initially prestressing the bands, the passive confinement is converted into active confinement thus generating higher confining pressure and greater increase in strength.
6. As the pitch decreases, it leads to higher confining pressures and peak compressive stresses.
7. By externally prestressing columns, the stiffness of the element as compared to controlled and wrapped specimens is predicted to increase.

## References

1. IS 456: 2000 (2002) Plain and reinforced concrete—code for practice
2. American Concrete Institute (ACI) Committee 440 (2008) Guide for the design and construction of externally bonded FRP systems for strengthening concrete structures. ACI Committee Report 440.2R-08
3. Yi Y, Cheng D (2015) Mechanical performance analysis of the columns strengthened with prestressed CFRP sheets. In: 5th international conference on advanced engineering material and technology (AEMT 2015)
4. Wu E, Jiang W, Wang X, Zou Y (2013) Experimental investigation on reinforced RC column with prestressed double helix FRP strip. *Eur J Environ Civil Eng* 17(S1):s53–s64
5. Michels J (2015) Prestressed FRP systems. [https://doi.org/10.1007/978-94-017-7336-2\\_7](https://doi.org/10.1007/978-94-017-7336-2_7)

**Part V**  
**Composite Materials and Structures**

# Static Response of Thin-Walled CNT-Reinforced-Laminated Composite Box Beam



Tushar Sharma, V. Murari and K. K. Shukla

**Abstract** The paper presents the static response of CNT-reinforced thin-walled-laminated composite box beam. The elastic properties of CNT-reinforced three-phase composite are predicted by Halpin–Tsai model and micromechanics approach. Governing equations are derived using CLT and minimum total potential energy principle. Using finite element method, results are obtained for cantilever thin-walled box beam under axial loading. Effect of CNT reinforcement on axial displacement and twist angle for different CNT aspect ratio and laminated stacking sequence are studied.

**Keywords** Thin-walled composite beam · CNT-reinforced · FE method

## 1 Introduction

Thin-walled laminated composite box beam is one of the important structural element being used extensively in aerospace and other engineering structures such as helicopter rotor blades, wind turbine blades, aircraft wings and thus stimulating the interest of researchers working in this area. Vlasov [1] was the first to develop the theory of thin-walled members made of isotropic materials for open and closed section beams. Response of the thin-walled composite box beam is highly dependent on the parameters such as stacking sequences, material coupling, structural coupling, fibre orientation, and arbitrary layups. Previous research focused on improvement of the static response of thin-walled composite box beam through

---

T. Sharma · V. Murari · K. K. Shukla (✉)  
Applied Mechanics Department, Motilal Nehru National Institute  
of Technology Allahabad, Allahabad, India  
e-mail: kkshukla@mnnit.ac.in

T. Sharma  
e-mail: ram0213@mnnit.ac.in

V. Murari  
e-mail: vmurari@mnnit.ac.in

analysing the effects of structural and material parameters, such as pre-twist, taper section, arbitrary cross section, loading and boundary conditions, orthotropy ratio. Chandra et al. [2] carried out experimental investigations on symmetric and antisymmetric laminated composite thin-walled rectangular beams under bending, torsional as well as extensional loads and observed the effects of structural coupling on the structural response. Lee et al. [3] analysed flexural–torsional behaviour of thin-walled composite box beam and explored effects of fibre angle, boundary conditions, and stacking sequence on different load type. Utilizing finite element method, Sheikh et al. [4] developed a model which includes all coupling effects along with shear deformation for thin-walled composite beam having open and closed cross section. The efficient three-noded beam element is used to analyse different numerical example under different loading conditions for I, C, and box sections. Song et al. [5] analytically studied the effect of pre-twist angle, arbitrary cross section, material coupling and spinning speed on vibration and stability response of composite thin-walled beam. Further applying numerical method, Kim et al. [6] predicted the exact solution for twist angle and fibre stresses in thin-walled beams on single- and double-celled section when subjected to torsional loading. Shin et al. [7] focused on the effect of taper on joint structure and on different height-to-width ratio on static behaviour of tapered thin-walled beam under out-of-plane loads and twisting moments.

In order to improve the response of thin-walled beams, either we have to improve structural parameters or improve the material properties it is built off. Nowadays, aerospace industry and other high-performance engineering structures preferred CNT-reinforced composite because of its inherent high strength/weight ratio, in comparison to other reinforced composites. An important study by Qian et al. [8] reported that with addition of 1 wt% (i.e., 1% by weight), multiwall carbon nanotubes to polystyrene resulted in 36–42 and 25% increase in the elastic modulus and the break stress of the nanocomposite properties, respectively. Sharma et al. [9] evaluated Young's modulus of SWCNT and MWCNT using finite element simulation. The effect of diameter, length, chirality, and different type of defect on SWCNT and effect of no. of walls on MWCNT are also studied. Kim et al. [10] evaluated the elastic properties of CNT-reinforced composite using Halpin–Tsai model and compared it with the experimental results. Bhardwaj et al. [11] studied the effect of aspect ratio and CNT % on nonlinear static and dynamic response of CNT-reinforced-laminated composite plates. Rafiee et al. [12] studied the nonlinear static and dynamic response of rotating CNT/fibre-/epoxy-laminated thin-walled multiscale composite beams and blades. For determining the bulk material properties of multiscale nanocomposite, Halpin–Tsai equation with fibre micromechanics is used. Guru et al. [13] studied the effect of interface thickness and stiffness on the elastic properties of CNT nanocomposite using molecular mechanics, molecular dynamics, and FE methods.

In the present study, the effect of CNT % on static response of thin-walled box beam is investigated. The model is based on CLT, and governing equations are derived using minimum total potential energy principle. 1D finite element model is used to investigate the static response of thin-walled box beam. For evaluating the

properties of two-phase and three-phase CNT-reinforced composite, Halpin–Tsai model and rule of mixture are used, respectively. Numerical results are obtained for static analysis of thin-walled box beam under axial loading with effect of different CNT aspect ratio and laminate stacking sequence.

## 2 Mathematical Formulation

The coordinate systems for thin-walled closed section are shown in Fig. 1.  $x$ - and  $y$ -axes lie in plane of cross section, and  $z$ -axis lies parallel to longitudinal axis of the beam.  $n$ - and  $s$ -axes are normal and tangent to the middle surface of a plate element, respectively, and directed along the contour line of the cross section. The above coordinate systems are related to the angle of rotation  $\theta$  as shown in Fig. 1. Point  $P$  is pole, and axis parallel to  $z$ -axis through  $P$  is pole axis.

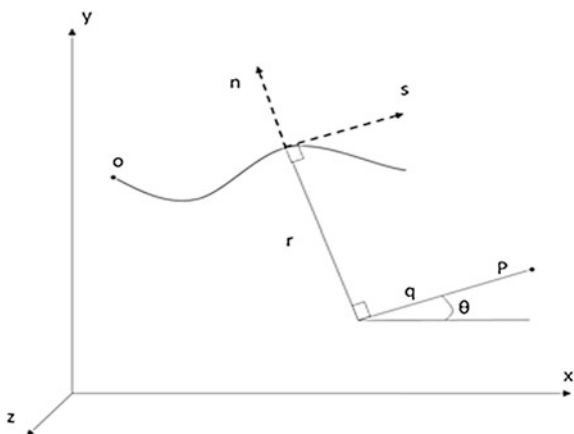
The mid-surface displacement field applied to whole contour is expressed as [3]:

$$\begin{aligned} \bar{u}(s, z) &= U(z) \sin \theta(s) - V(z) \cos \theta(s) - \Phi(z)q(s) \\ \bar{v}(s, z) &= U(z) \cos \theta(s) + V(z) \sin \theta(s) + \Phi(z)r(s) \\ \bar{w}(s, z) &= W(z) - U'(z)x(s) - V'(z)y(s) - \Phi'(z)\omega(s) \end{aligned} \tag{1}$$

where  $U, V, W$  are the displacements of a point in  $x, y,$  and  $z$  directions, respectively. The warping function  $\omega$  is expressed as;

$$\omega(s) = \int_{s_0}^s \left[ r(s) - \frac{F(s)}{t(s)} \right] ds \tag{2}$$

**Fig. 1** Thin-walled closed section coordinates





Deformation at any generic point on profile section is represented as  $u$ ,  $v$ , and  $w$  in terms of mid-surface displacement  $\bar{u}$ ,  $\bar{v}$ , and  $\bar{w}$  as:

$$\begin{aligned} u(s, z, n) &= \bar{u}(s, z) \\ v(s, z, n) &= \bar{v}(s, z) - n \frac{\partial \bar{u}(s, z)}{\partial s} \\ w(s, z, n) &= \bar{w}(s, z) - n \frac{\partial \bar{u}(s, z)}{\partial z} \end{aligned} \quad (3)$$

The resulting strains are:

$$\begin{aligned} \varepsilon_z &= \varepsilon_z^o + (x + n \sin \theta) \kappa_y + (y - n \cos \theta) \kappa_x + (\omega - nq) \kappa_\omega \\ \gamma_{sz} &= \left( n + \frac{F}{2t} \right) \kappa_{sz} \end{aligned} \quad (4)$$

In order to evaluate elastic properties of CNT-reinforced multiscale composites, two steps are required. In first step, CNT-reinforced composite (i.e., two-phase composite) elastic properties are calculated using Halpin–Tsai model. The Halpin–Tsai equations are a set of empirical relationships that predict composite material properties which are expressed in terms of the properties of the matrix and reinforcing phases together with their proportions and geometry [10]. Perfect bonding between the matrix and fibre and no interface between CNT and matrix are assumed.

Thus, the modulus of two-phase CNTR composites is expressed as:

$$\begin{aligned} E_{2\text{-phase}} &= \left[ \frac{3}{8} \times \frac{1 + 2(l_{\text{CNT}}/d_{\text{CNT}})\eta_L V_{\text{NT}}}{1 - \eta_L V_{\text{CNT}}} + \frac{5}{8} \times \frac{1 + 2\eta_D V_{\text{CNT}}}{1 - \eta_D V_{\text{CNT}}} \right] E_{\text{matrix}} \\ \eta_L &= \frac{(E_{\text{NT}}/E_{\text{epoxy}}) - (d_{\text{NT}}/4t)}{(E_{\text{NT}}/E_{\text{epoxy}}) + (l_{\text{NT}}/2t)} \\ \eta_D &= \frac{(E_{\text{NT}}/E_{\text{epoxy}}) - (d_{\text{NT}}/4t)}{(E_{\text{NT}}/E_{\text{epoxy}}) + (d_{\text{NT}}/2t)} \end{aligned} \quad (5)$$

where  $E$ ,  $l_{\text{NT}}$ ,  $d_{\text{NT}}$ ,  $V_{\text{NT}}$ , and  $t$  represent tensile modulus, length and diameter, volume fraction of nanotube, and thickness of graphite layer, respectively.

In second step, the mechanical properties of a CNT/matrix/fibre multiscale composite (i.e., three-phase composite) are predicted using micromechanics approach. CNT-reinforced composite properties are considered to be as modified matrix properties which are further reinforced with E-glass fibre in an orthotropic manner to evaluate three-phase composite properties.

The longitudinal modulus of composite is expressed as:

$$E_1 = E_f V_f + E_m V_m \tag{6}$$

The transverse modulus of composite is expressed using the Halpin–Tsai relationship as [10]:

$$\frac{E_2}{E_m} = \frac{1 + \zeta \eta V_f}{1 - \eta V_f} \tag{7}$$

where

$$\eta = \frac{(E_f/E_m) - 1}{(E_f/E_m) + \zeta} \tag{8}$$

The in-plane shear modulus is determined by using the following relationship:

$$\frac{G_{12}}{G_m} = \frac{1 + \zeta \eta V_f}{1 - \eta V_f} \tag{9}$$

where

$$\eta = \frac{G_{12f}/G_m - 1}{G_{12f}/G_m + 1} \tag{10}$$

Here,

$E_f, E_m$  Young’s modulus of fibre and matrix.

$V_f, V_m$  Volume fraction of fibre and matrix.

$G_f, G_m$  Shear modulus of fibre and matrix.

Finally, the computed longitudinal modulus ( $E_1$ ), transverse modulus of composite ( $E_2$ ), shear modulus ( $G_{12}$ ), and volume fraction ( $v_{12}$ ) as defined above are used as material properties in studying the response of thin-walled-laminated composite box beam. The elastic properties computed from three-phase or multi-phase composite are used to determine ABD matrix for composite which is further used to determine cross-sectional stiffness [ $E_{ij}$ ].

The forces and moments can be expressed as:

$$\begin{Bmatrix} N_z \\ M_y \\ M_x \\ M_\omega \\ M \end{Bmatrix} = \begin{bmatrix} E_{11} & E_{12} & E_{13} & E_{14} & E_{15} \\ & E_{22} & E_{23} & E_{24} & E_{25} \\ & & E_{33} & E_{34} & E_{35} \\ & & & E_{44} & E_{45} \\ sym. & & & & E_{55} \end{bmatrix} \begin{Bmatrix} \epsilon_z^o \\ \kappa_y \\ \kappa_x \\ \kappa_\omega \\ \kappa_{sz} \end{Bmatrix} \tag{11}$$

where [ $E_{ij}$ ] is the stiffness of cross section. The explicit form of coefficient of [ $E_{ij}$ ] can be found in [3].

After utilizing above equations and minimum total potential energy principle, the most general form for flexural and torsional behaviour of CNTR-laminated composite thin-walled box beam is obtained, and the governing differential equations are expressed as:

$$\begin{aligned}
 E_{11}W''' - E_{12}U''' - E_{13}V''' - E_{14}\Phi''' + 2E_{15}\Phi'' &= 0 \\
 E_{12}W''' - E_{22}U^{iv} - E_{23}V^{iv} - E_{24}\Phi^{iv} + 2E_{25}\Phi''' &= 0 \\
 E_{13}W''' - E_{23}U^{iv} - E_{33}V^{iv} - E_{34}\Phi^{iv} + 2E_{35}\Phi''' + q &= 0 \\
 E_{14}W''' + 2E_{15}W'' - E_{24}U^{iv} - 2E_{25}U''' - E_{34}V^{iv} \\
 - 2E_{35}V''' - E_{44}\Phi^{iv} + 4E_{55}\Phi'' + t &= 0
 \end{aligned} \tag{12}$$

### FE formulation

One-dimensional displacement-based finite element method is implemented for describing thin-walled composite beam model, considering combination of interpolation function such as 1D Lagrange interpolation function  $\psi_j$  and Hermite cubic interpolation function  $\Psi_j$ . Associated with node  $j$  and nodal values, the generalized displacements over each element are expressed as:

$$\begin{aligned}
 W &= \sum_{i=1}^n w_i \psi_i \\
 U &= \sum_{i=1}^n u_i \Psi_i \\
 V &= \sum_{i=1}^n v_i \Psi_i \\
 \Phi &= \sum_{j=1}^n \phi_j \Psi_j
 \end{aligned} \tag{13}$$

Substituting Eq. (13) into Eq. (12), the finite element model for a distinctive element can be written as:

$$[K]\{\Delta\} = \{f\} \tag{14}$$

where  $[K]$  is the elemental stiffness matrix,  $\{\Delta\}$  is the nodal displacement vector, and  $\{f\}$  is the element force vector.

One-dimensional displacement-based finite element method is implemented for describing thin-walled composite beam model, considering combination of interpolation function such as 1D Lagrange interpolation function and Hermitecubic interpolation function.

### 3 Result and Discussion

In the present study, static analysis of thin-walled CNT-reinforced composite-laminated box beam is carried out. The Halpin–Tsai model and micromechanics approach are used for evaluating the elastic properties of two-phase and three-phase composite, respectively. The properties of carbon nanotubes used in the analysis are as follows: [11, 13].

$$E_{CNT} = 866.449 \text{ GPa}, E_{matrix} = 4.06 \text{ GPa},$$

$$E_{fibre} = 69 \text{ GPa}, G_{fibre} = 28.29 \text{ GPa},$$

$$\nu_{CNT} = \nu_{matrix} = 0.3, \nu_{fibre} = 0.22,$$

$$l/d = 50$$

The elastic properties of CNT-reinforced composites are evaluated under varying volume fraction and aspect ratio of (8, 8) armchair CNT [13]. The effect of CNT % on the mechanical properties of two-phase and three-phase composite for fixed aspect ratio (i.e.,  $l/d = 50$ ) is shown in Table 1.

In order to study the effect of CNT % on response of thin-walled composite beam, a uniform cross-sectional cantilever composite box beam is chosen with axial loading  $P$  as shown in Fig. 2. The effect of CNT % on axial tip displacement and tip twist angle for  $[0_{10}/45_{10}]$  stacking sequence is shown in Fig. 3. Very minor changes are in  $w_{tip}$  with increase in CNT %, but steep change can be observed in case of  $\theta_{tip}$ . The variation in axial displacement and twist angle along the length for different CNT % is shown in Figs. 4 and 5.

**Table 1** Effect of CNT % on elastic properties of two-phase and three-phase composite at  $l/d = 50$

CNT %	Two-phase		Three-phase		
	$E$	$G$	$E1$	$E2$	$G12$
0	4.06	1.56	56.01	24.05	9.45
0.5	4.64	1.79	56.13	26.23	10.32
1	5.23	2.01	56.25	28.23	11.13
1.5	5.83	2.24	56.37	30.08	11.88
2	6.43	2.47	56.49	31.79	12.57

**Fig. 2** Cantilever composite box beam under axial load

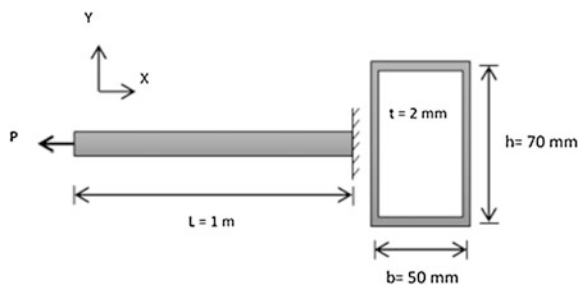


**Fig. 3** Effect of CNT % on tip axial displacement and tip twist angle at  $[0_{10}/45_{10}]$

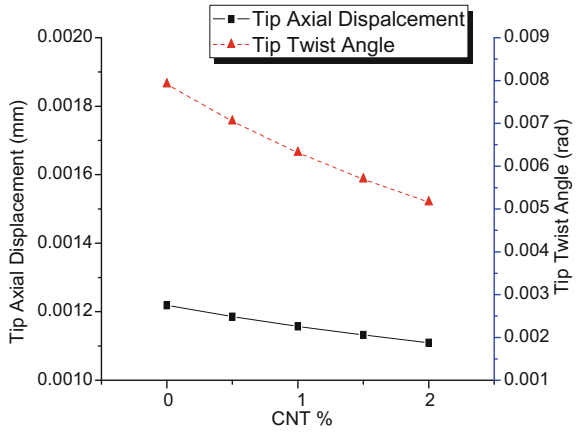


**Fig. 4** Variation in axial displacement along the length for different CNT %

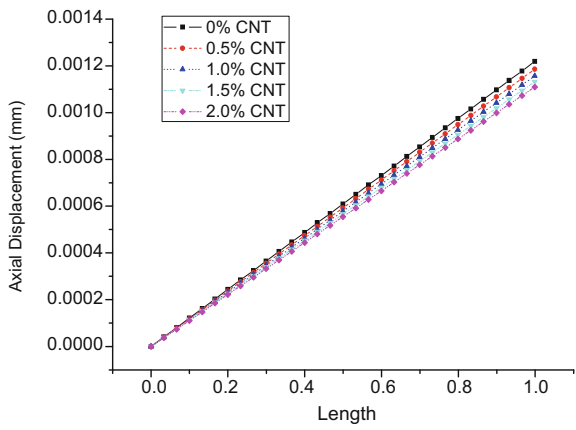


**Fig. 5** Variation in twist angle along the length for different CNT %

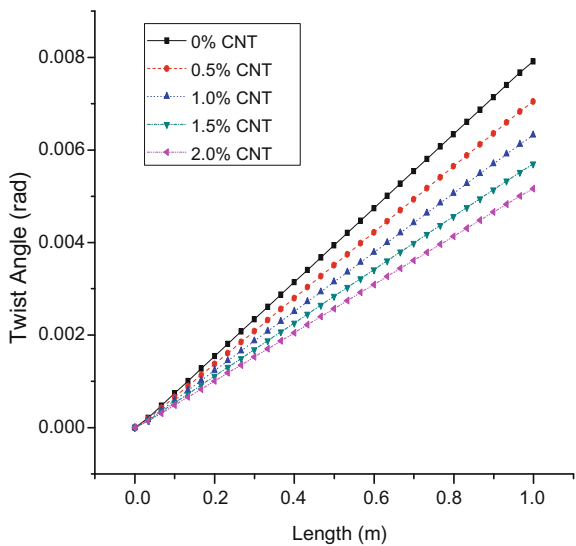


**Table 2** Effect of CNT % on  $w_{tip}$  and  $\theta_{tip}$  with different CNT aspect ratio ( $l/d$ )

$V_{CNT}$	0%		0.5%		1%		1.5%		2%	
	$w_{tip}$ (mm)	$\theta_{tip}$ (rad * $10^{-2}$ )	$w_{tip}$ (mm)	$\theta_{tip}$ (rad * $10^{-2}$ )	$w_{tip}$ (mm)	$\theta_{tip}$ (rad * $10^{-2}$ )	$w_{tip}$ (mm)	$\theta_{tip}$ (rad * $10^{-2}$ )	$w_{tip}$ (mm)	$\theta_{tip}$ (rad * $10^{-2}$ )
$l/d$										
10	0.508	0.329	0.504	0.318	0.499	0.307	0.495	0.297	0.492	0.287
50	0.508	0.329	0.494	0.293	0.482	0.263	0.472	0.237	0.462	0.215
100	0.508	0.329	0.488	0.276	0.471	0.236	0.457	0.203	0.446	0.177
200	0.508	0.329	0.481	0.26	0.46	0.21	0.444	0.174	0.431	0.146
500	0.508	0.329	0.474	0.243	0.45	0.187	0.433	0.148	0.419	0.12
1000	0.508	0.329	0.471	0.235	0.446	0.177	0.428	0.138	0.413	0.11

**Table 3** Effect of CNT % on  $w_{tip}$  and  $\theta_{tip}$  with different stacking sequence

$V_{CNT}$	0%		0.5%		1%		1.5%		2%	
	$w_{tip}$ (mm)	$\theta_{tip}$ (rad * $10^{-2}$ )	$w_{tip}$ (mm)	$\theta_{tip}$ (rad * $10^{-2}$ )	$w_{tip}$ (mm)	$\theta_{tip}$ (rad * $10^{-2}$ )	$w_{tip}$ (mm)	$\theta_{tip}$ (rad * $10^{-2}$ )	$w_{tip}$ (mm)	$\theta_{tip}$ (rad * $10^{-2}$ )
Stacking sequence										
Ply1	0.508	3.292	0.494	2.932	0.482	2.629	0.472	2.371	0.462	2.148
Ply2	0.52	1.60E-02	0.506	1.30E-02	0.493	1.10E-02	0.482	1.00E-02	0.472	8.00E-03
Ply3	0.773	0.273	0.718	0.236	0.674	0.206	0.639	0.182	0.609	0.162
Ply4	0.502	0.00E+00	0.489	1.00E-03	0.478	1.00E-03	0.468	1.00E-03	0.459	1.00E-03
Ply5	0.469	9.00E-03	0.46	8.00E-03	0.452	7.00E-03	0.445	6.00E-03	0.438	6.00E-03

The effect of CNT aspect ratio ( $l/d$ ) along with CNT % ( $v_{\text{CNT}}$ ) on response of thin-walled beam is shown in Table 2. It can be observed that as the  $l/d$  ratio increases  $w_{\text{tip}}$  and  $\theta_{\text{tip}}$  decreases with increase in CNT %. The effect of CNT % on  $w_{\text{tip}}$  and  $\theta_{\text{tip}}$  for different stacking sequence is shown in Table 3.

where

$$\text{Ply1} = [0_{10}/45_{10}],$$

$$\text{Ply2} = [0_{10}/90_{10}],$$

$$\text{Ply3} = [45_{10}/-45_{10}],$$

$$\text{Ply4} = [(45/-45)_5/0_{10}],$$

$$\text{Ply5} = [(45/-45)_2/(0/0)_6/(45/-45)_2].$$

It can be observed that  $w_{\text{tip}}$  and  $\theta_{\text{tip}}$  vary for different stacking sequence and for each stacking sequence  $w_{\text{tip}}$  and  $\theta_{\text{tip}}$  decrease as  $v_{\text{CNT}}$  increases.

## 4 Conclusions

The static response of CNT-reinforced thin-walled laminated composite box beam is obtained using finite element method. Two-phase and three-phase elastic properties of CNT-reinforced composite are evaluated using Halpin–Tsai model and rule of mixture approach, respectively. For constant  $l/d$  ratio, elastic properties of two-phase composite increase about 58% with increase in CNT %, whereas for three-phase CNT-reinforced composite, significant increase of nearly 32% with increase in CNT % is observed in E2 and G2. Axial displacement and twist angle of box beam decrease with increase in CNT % along the length. Tip axial displacement  $w_{\text{tip}}$  and tip twisting angle  $\theta_{\text{tip}}$  decrease by 18 and 66%, respectively, with increase in CNT aspect ratio ( $l/d$ ) along with CNT %. And similar change is observed with different stacking sequence.

## References

1. Vlasov V (1961) Thin-walled elastic beams.pdf, 2nd edn. Jerusalem, Isr Isr Progr Sci Transl
2. Chandra R, Stemple A, Chopra I (1990) Thin-walled composite beams under bending, torsional and extensional loads. *J Od Aircr* 27:619–639
3. Vo TP, Lee J (2007) Flexural–torsional behavior of thin-walled composite beams. *Eng Struct* 29:1774–1782
4. Sheikh AH, Thomsen OT (2008) An efficient beam element for the analysis of laminated composite beams of thin-walled open and closed cross sections. *Compos Sci Technol* 68:2273–2281
5. Song O, Jeong N-H (2000) Vibration and stability of pretwisted spinning thin-walled composite beams featuring bending–bending elastic coupling. *J Sound Vib* 237:513–533
6. Kim NI, Shin DK (2009) Torsional analysis of thin-walled composite beams with single- and double-celled sections. *Eng Struct* 31: 1509–1521



7. Shin D, Choi S, Jang G-W, Kim YY (2016) Finite element beam analysis of tapered thin-walled box beams. *Thin-Walled Struct* 102:205–214
8. Qian D, Dickey EC, Andrews R, Rantell T (2000) Load transfer and deformation mechanisms in carbon nanotube-polystyrene composites. *Appl Phys Lett* 76(20):2868–2870
9. Sharma T, Guru K, Mishra SSB, Shukla KK (2013) Evaluation of mechanical properties of SWCNT and MWCNT using Simulation. In: Indian conference on applied mechanics (INCAM) 2013, IIT Madras, INCAM\_2013\_SM\_75, 4–6 July, 2013, pp 118–119
10. Kim M, Park YB, Okoli OI, Zhang C (2009) Processing, characterization, and modeling of carbon nanotube-reinforced multiscale composites. *Compos Sci Technol* 69:335–342
11. Bhardwaj G, Upadhyay AK, Pandey R, Shukla KK (2013) Non-linear flexural and dynamic response of CNT reinforced laminated composite plates. *Compos B* 45:89–100
12. Rafiee M, Nitzsche F, Labrosse M (2016) Rotating nanocomposite thin-walled beams undergoing large deformation. *Compos Struct* 150:191–199
13. Guru K, Sharma T, Shukla KK, Mishra SB (2016) Effect of interface on the elastic modulus of CNT nanocomposites. *ASCE J Nanomech Micromech* 6(3):04016004

# Dynamic Buckling of Laminated Composite Curved Panels Subjected to In-plane Compression



V. Keshav and S. N. Patel

**Abstract** This paper deals with dynamic buckling of laminated composite curved panels subjected to in-plane dynamic compressive loads. Results from the available literature are used to validate the static buckling load of curved panels, and the dynamic buckling loads of the same panel are predicted using finite element software ABAQUS/Explicit. Volmir's criterion is used to find the dynamic buckling load. Dynamic load of various magnitudes in the form of pulse load is applied on the panel for various duration. The effect of aspect ratio and radius of curvature are studied. It is observed that smaller loads require longer duration of loading and vice versa for dynamic buckling to occur. The dynamic buckling load is observed to be lesser than static buckling load for longer duration of loading which is an important aspect to be considered in designing.

**Keywords** Curved panels · Laminated composite panels · Dynamic buckling Axial compression

## 1 Introduction

Lightweight composite materials are well established in aerospace sector, water transportation, manufacture of high-end cars, bioengineering, composite bridges to name a few. These materials owing to their high strength/stiffness to weight ratio are also being used in repair and rehabilitation works in civil engineering field. The stability of these structures is one of the important parameters to be considered while designing these structures. Bucking phenomenon is critical since it not only affects a particular structural component, but also its neighbouring components as

---

V. Keshav · S. N. Patel (✉)  
Department of Civil Engineering, BITS Pilani, Pilani Campus,  
Pilani 333031, Rajasthan, India  
e-mail: shuvendu@pilani.bits-pilani.ac.in

V. Keshav  
e-mail: keshav.vasanth@gmail.com

well. Investigation of the whole structure is time-consuming, and hence, small structural components are studied simulating the actual phenomenon. Laminated composite curved panels which are one of the major shell structural components made up of composite materials are studied in this paper. The study is focused on nonlinear dynamic buckling of laminated composite curved panels.

It is noted that the dynamic buckling analysis is carried out for thin-walled plate structures which are subjected to compressive loads by Kubiak [1]. The laminated composite curved panels are subjected to in-plane dynamic compressive loads in many instances. The pulse loads can be characterised as sinusoidal, triangular, rectangular, exponential, etc. The current study is restricted to rectangular loads. Linearised equations for anisotropic, laminated, and sandwich cylindrical shell panels are proposed by Sciuva and Carrera [2]. These cylindrical panels are subjected to normal and uniform shear forces. Analytical and finite element displacement approaches are used to develop approximate solution for elastic stability. The dynamic buckling behaviour of thermo-viscoplastic circular shells is studied by Wei et al. [3]. The analysis is carried out both analytically as well as using finite element method. The authors have developed algebraic equations for maximum initial growth rate for small disturbance. Finite element method is used to study the effect of initial imperfections in cylindrical shells which are subjected to low-velocity impacts. Rahman et al. [4] have developed a finite element method for imperfection-sensitive shell structures in order to implement a reduction method for dynamic buckling. The approach is based on Budiansky's approach by incorporating inertial forces. The dynamic buckling of stiffened composite cylindrical shells is studied by Patel et al. [5]. The analysis is carried out using finite element software—ABAQUS/Explicit. The model generated is validated using experimental results of collapse test, and the dynamic buckling analysis is carried out. Priyadarsini et al. [6] investigated the experimental and numerical aspects of dynamic buckling of advanced fibre composite cylindrical shells which are subjected to axial compression. Significant work is taken up by Jensen [7] in the study of parametric excitation, where the pulsating loads act on the structures [8]. Some dynamic buckling criteria available in the literature are Volmir's criterion, Budiansky–Hutchinson criterion, Ari-Gur and Simonetta's criterion, Petry–Fahlbusch criterion [1]. In the current study, Volmir's criterion is used to calculate the dynamic buckling loads. According to this criterion, the critical deflection value is assumed to be equal to the thickness of plate.

## 2 Theory and Formulation

The nonlinear dynamic equilibrium equation solved by ABAQUS/Explicit is given in Eq. (1).

$$[M]\{\ddot{u}\} + [C]\{\dot{u}\} + [K(\{u\})]\{u\} = \{F(t)\} \quad (1)$$

where  $[M]$  is the mass matrix,  $[C]$  the damping matrix,  $[K]$  the stiffness matrix, which depends on the deformations due to the geometric nonlinearity,  $\{u\}$  the nodal displacement vector,  $\{\dot{u}\}$  the nodal velocity vector,  $\{\ddot{u}\}$  the nodal acceleration vector, and  $\{F(t)\}$  the load vector. In the current study, the damping effect is not considered. The nonlinear dynamic equilibrium equation solved is shown in Eq. (2).

$$[M]\{\ddot{u}\} + [K(\{u\})]\{u\} = \{F(t)\} \quad (2)$$

### 3 Results and Discussion

The convergence and validation study is carried out using some of the results reported in the literature. Then, the current problem is then discussed.

#### 3.1 Validation and Convergence

Non-dimensional buckling load is evaluated for a square planed, simply supported, uniformly loaded symmetric cross-ply panel ( $0^\circ/90^\circ/0^\circ/90^\circ/0^\circ$ ) as shown in Fig. 1. The support conditions are shown in Fig. 2. The material properties and other parameters are taken as:  $a/b = 1$ ,  $R/a = 20$ ,  $al/h = 100$ ,  $E_{11} = 40E_{22}$ ,  $G_{12} = G_{13} = 0.5E_{22}$ ,  $G_{23} = 0.6E_{22}$ , and  $\nu_{12} = 0.25$ . The non-dimensional buckling load is calculated as,  $\overline{P}_{cr} = P_{cr}b^2/E_{22}h^3$ . Table 1 shows the non-dimensional static buckling load for the curved panel along with finite element analysis results presented by Sciuva and Carrera [2] and Patel et al. [8].

The buckling analysis is performed by taking different mesh sizes of the panel. The results with  $40 \times 40$  mesh size match well with the results of Sciuva and Carrera [2] and Patel et al. [8] as shown in Table 1. The same mesh size is taken of dynamic buckling analysis.

#### 3.2 Dynamic Buckling

After the static buckling study, the dynamic buckling analysis is carried out for the same panel used for validation. The pulse loads are the loads having a finite duration. These loads can be a trigonometric, exponential, triangular, etc., functions. In the current study, only rectangular loads are taken into consideration. Figure 3 shows the rectangular loading function taken into consideration for this study. For a particular loading duration, the magnitude of loads is varied and the

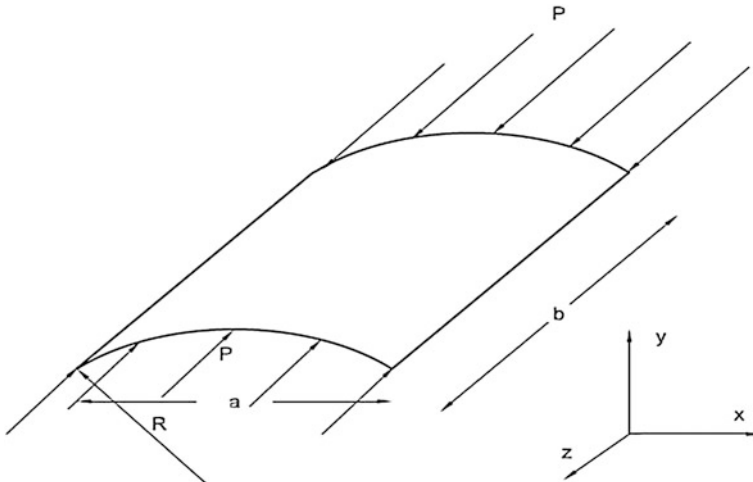


Fig. 1 Geometry of panel with uniform loading

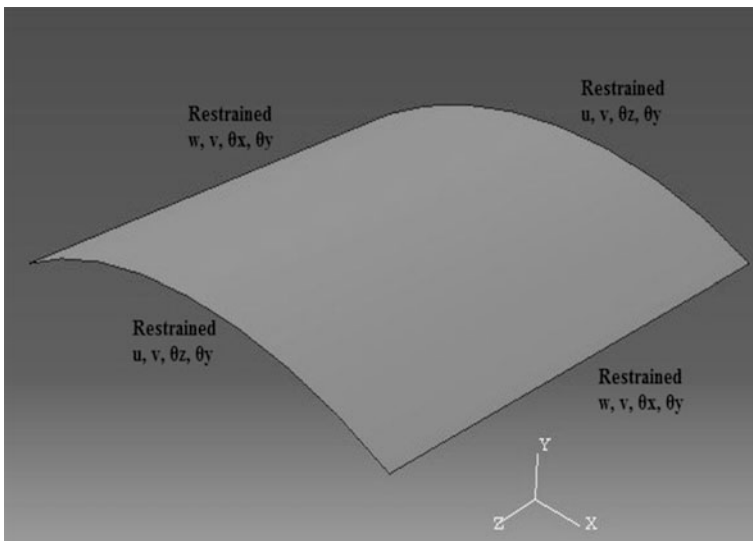


Fig. 2 Model showing the support conditions

Table 1 Non-dimensional static buckling load

Analysis	Mesh size	Non-dimensional buckling load
Present	40 × 40	36.4875
Sciuva and Carrera [2]	5 × 5	36.86
Patel et al. [7]	8 × 8	36.8452

response is observed. In order to perform dynamic analysis, the material properties presented by Priyadarsini et al. [6] are used.  $E_{22} = 9250 \text{ MPa}$  and density =  $1700 \text{ kg/m}^3$ . The value of  $E_{22}$  is substituted in the ratios used for the validation study. Table 2 shows the predicted nonlinear dynamic buckling loads.

Figure 4a–e shows the axial displacement vs time plots for calculating the dynamic buckling load for a loading duration of  $0.055 \times 10^{-3} \text{ s}$ . For various magnitudes of loads, axial displacement responses are observed. The loads are applied for  $0.055 \times 10^{-3} \text{ s}$ , and the responses are observed till 0.5 s. The target axial displacement is set in accordance with Volmir’s criterion as the value of thickness = 1 cm, as prescribed by Kubiak [1]. The load which gives a displacement equal to or almost reaches the target value is the dynamic buckling load according to Volmir’s criterion.

It is observed from Table 2 that in very short duration (0.055 ms), the dynamic buckling load is higher than static buckling load. However, as the loading duration is increased, the dynamic buckling load starts decreasing.

### 3.2.1 Effect of Aspect Ratio

The effect of aspect ratio is studied on laminated composite curved panel in this section. The ratio  $b/a$  is increased keeping  $a$  constant and nonlinear dynamic buckling loads are calculated. The pulse loads are applied for various duration. Tables 3, 4, 5, 6, 7, and 8 show the dynamic buckling loads for laminated composite curved panels with different aspect ratios and various loading duration.

**Fig. 3** Rectangular pulse load

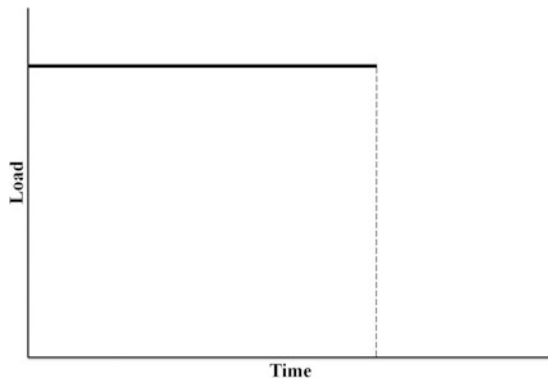


**Table 2** Dynamic buckling loads for laminated composite curved panel

Load (kN/m)	Duration of application( $\times 10^{-3} \text{ s}$ )	Displacement (cm)
40	0.055	1.102
27	0.1	1.047
20	1	1.156
2.08	10	1.050

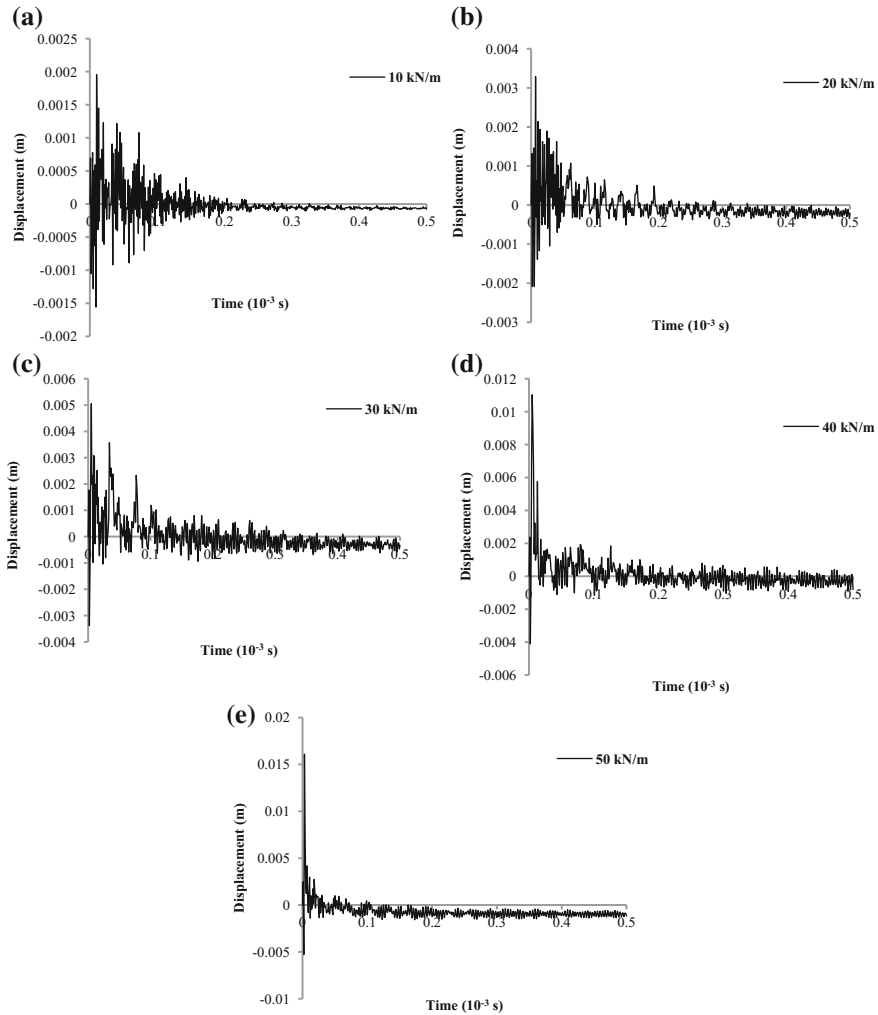


**Fig. 4** **a** Axial displacement versus time plot of loading duration of  $0.055 \times 10^{-3}$  s. **b** Axial displacement versus time plot of loading duration of  $0.055 \times 10^{-3}$  s. **c** Axial displacement versus time plot of loading duration of  $0.055 \times 10^{-3}$  s. **d** Axial displacement versus time plot of loading duration of  $0.055 \times 10^{-3}$  s. **e** Axial displacement versus time plot of loading duration of  $0.055 \times 10^{-3}$  s

Figure 5 shows the effect of aspect ratio on the nonlinear dynamic buckling load of laminated curved panel. It is observed that as the loading duration is increased, the variation of dynamic buckling load is not appreciable. Although for very short durations, 0.1 ms and 1 ms, there is an initial increase in dynamic buckling load,

**Table 3** Dynamic buckling load for  $0.1 \times 10^{-3}$  s

<i>b/a</i>	Load (kN/m)	Displacement (cm)
1	27	1.0479
1.5	47	1.09597
2	27.5	1.04913
2.5	38	1.09774
5	30	1.02507

**Table 4** Dynamic buckling load for  $1 \times 10^{-3}$  s

<i>b/a</i>	Load (kN/m)	Displacement (cm)
1	20	1.15627
1.5	31.5	1.116
2	12	1.04005
2.5	8.5	1.02355
5	4.8	1.05048

**Table 5** Dynamic buckling load for  $2.5 \times 10^{-3}$  s

<i>b/a</i>	Load (kN/m)	Displacement (cm)
1	10.5	1.1011
1.5	9.5	1.05675
2	9.9	1.11087
2.5	7.5	1.06839
5	5.25	1.00174

**Table 6** Dynamic buckling load for  $5 \times 10^{-3}$  s

<i>b/a</i>	Load (kN/m)	Displacement (cm)
1	4.5	1.05047
1.5	4.75	1.03733
2	5.2	1.06425
2.5	5.52	1.17393
5	5.25	1.00174

**Table 7** Dynamic buckling load for  $7.5 \times 10^{-3}$  s

<i>b/a</i>	Load (kN/m)	Displacement (cm)
1	2.88	1.12339
1.5	2.95	1.1697
2	3.05	1.07938
2.5	3.25	1.17211
5	3.25	1.02823

which gradually dissipates as the aspect ratio is increased. Figure 6 shows the deformed shape of the laminated composite curved panel with aspect ratio 2 at point of loading and deformation scale factor = 5.



**Table 8** Dynamic buckling load for  $10 \times 10^{-3}$  s

$b/a$	Load (kN/m)	Displacement (cm)
1	2.08	1.05034
1.5	2.14	1.09281
2	2.24	1.05609
2.5	2.35	1.16029
5	2.35	1.0586

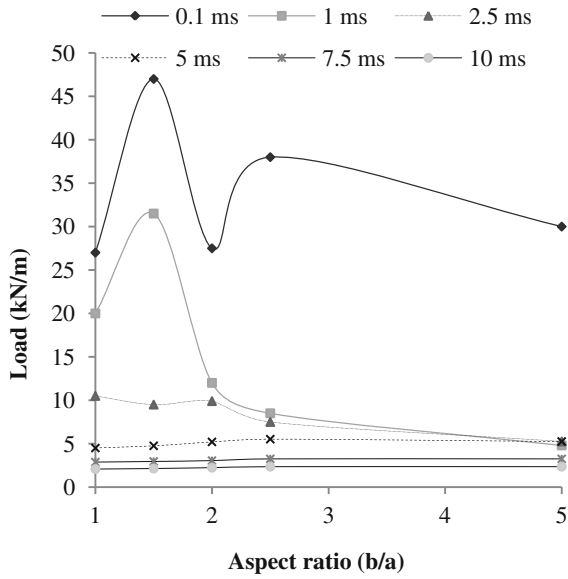


**Fig. 5** Effect of aspect ratio on dynamic buckling load

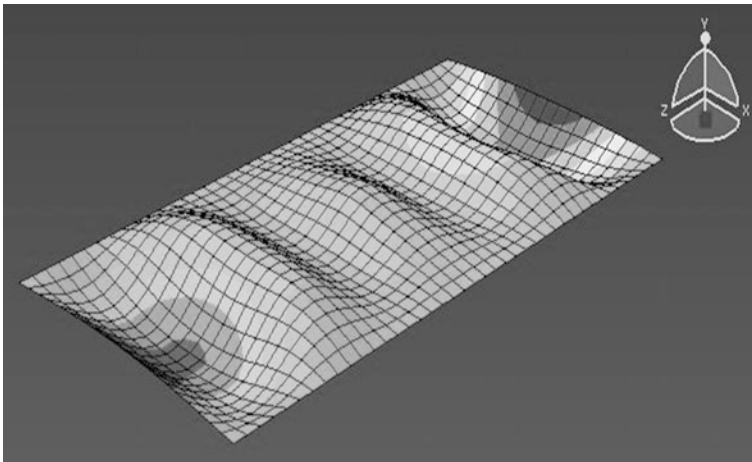


**Fig. 6** Deformed shape of laminated composite curved panel with  $b/a = 2$  and  $R/a = 20$

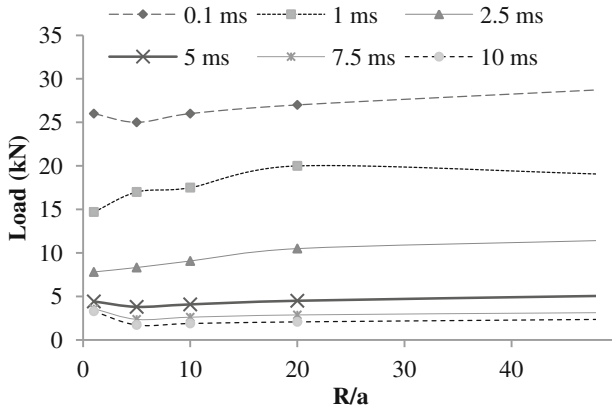


Fig. 7 Effect of radius of curvature on dynamic buckling load

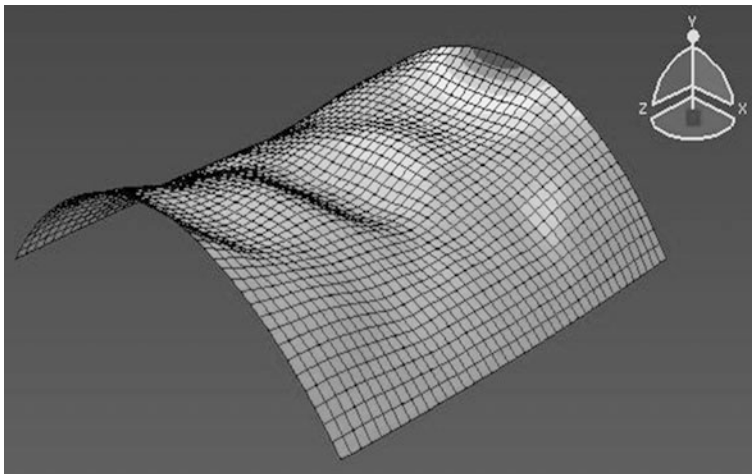


Fig. 8 Deformed shape of laminated composite curved panel with  $R/a = 2$  and  $b/a = 1$

### 3.2.2 Effect of Radius of Curvature

The effect of radius of curvature is studied on nonlinear dynamic buckling behaviour of laminated composite curved panel in this section. The ratio  $R/a$  is varied along with loading duration. For each loading duration, the dynamic buckling loads are calculated.

Figure 7 shows the effect of radius of curvature on nonlinear dynamic buckling behaviour of laminated composite curved panel. It is seen that for a particular loading duration, the variation of dynamic buckling load is less. The variation of dynamic buckling load reduces rapidly for longer duration of application of loads.

Figure 8 shows the deformed shape of laminated composite curved panel with  $R/a = 2$ , at point of loading and deformation scale factor = 3.

## 4 Conclusion

The conclusions of the study are summarised below.

1. The nonlinear dynamic buckling load for a laminated composite curved panel gradually reduces as the loading duration is increased.
2. When the loading duration is small, the nonlinear dynamic buckling load can be higher than static buckling load.
3. For very short duration of loading, the effect of aspect ratio is significant initially. This gradually reduces as the aspect ratio is increased. When the loading duration is increased, the variation in nonlinear dynamic buckling load is insignificant.
4. For a particular loading duration, the effect of radius of curvature on the variation in nonlinear dynamic buckling load is low. With the increase in loading duration, the effect of radius of curvature is minute.

**Acknowledgements** The authors thankfully acknowledge the Council of Scientific and Industrial Research (CSIR), New Delhi, for providing the financial support for this investigation through the project No. 22(0666)/14/EMR-II.

## References

1. Kubiak T (2013) Static and dynamic buckling of thin-walled plate structures. Springer, Switzerland
2. Sciuva DM, Carrera E (1990) Static buckling of moderately thick, anisotropic, laminated and sandwich cylindrical shell panels. *AIAA J* 28(10):1782–1793
3. Wei ZG, Yu JL, Batra RC (2005) Dynamic buckling of thin cylindrical shells under axial impact. *Int J Impact Eng* 32(1):575–592
4. Rahman T, Jansen EL, Gürdal Z (2011) Dynamic buckling analysis of composite cylindrical shells using a finite element based perturbation method. *Nonlinear Dyn* 66(3):389–401
5. Patel SN, Bisagni C, Datta PK (2011) Dynamic buckling analysis of a composite stiffened cylindrical shell. *Struct Eng Mech* 37(5):509–527
6. Priyadarsini RS, Kalyanaraman V, Srinivasan SM (2012) Numerical and experimental study of buckling of advanced fiber composite cylinders under axial compression. *Int J Struct Stab Dyn* 12(04):1250028
7. Jansen EL (2005) Dynamic stability problems of anisotropic cylindrical shells via a simplified analysis. *Nonlinear Dyn* 39:349–367
8. Patel SN, Datta PK, Sheikh AH (2003) Vibration and buckling of composite curved panels using a degenerated shell element. In National conference on emerging trends in structural mechanics and composites (ETSMC-2003), Nov 1–2. Department of Civil Engineering, NIT Rourkela

# The Interfacial Transition Zone: Microstructure, Properties, and Its Modification



Meenakshi Sharma and Shashank Bishnoi

**Abstract** Interfacial transition zone (ITZ) is the region of cement paste adjacent to the aggregate surface. Large size aggregates disturb the packing of cement in their near vicinity due to wall effect and form ITZ. The microstructure of ITZ is more porous and has higher calcium hydroxide (CH) content compared to the bulk cement paste. ITZ has been considered the weakest link in concrete due to its microstructure. The presence of ITZ is the reason of lower strength of concrete compared to its constituents, cement paste, and aggregate. Effect of ITZ on the transport properties of concrete is still a subject of debate. Improving the microstructure of ITZ is a good way of improving mechanical and transport properties of concrete. This paper reviews various alternative methods used for improving the microstructure of ITZ.

**Keywords** Interfacial transition zone · Wall effect · Microstructure

## 1 Interfacial Transition Zone and Its Properties

Concrete, the fundamental building material for infrastructure development around the world, is a composite material made of cement, water, and aggregates (coarse and fine). It is often considered as a two-phase composite material with inert aggregates and hydrated cement paste, and various properties of concrete are different from its constituent materials. Figure 1 shows that both aggregate and cement paste have brittle elastic behavior, while concrete has quasi-ductile behavior; even the strength of concrete is considerably lower than aggregate and cement paste [1]. This signifies the presence of a third phase, interfacial transition zone which is more critical for the properties of concrete.

---

M. Sharma · S. Bishnoi (✉)

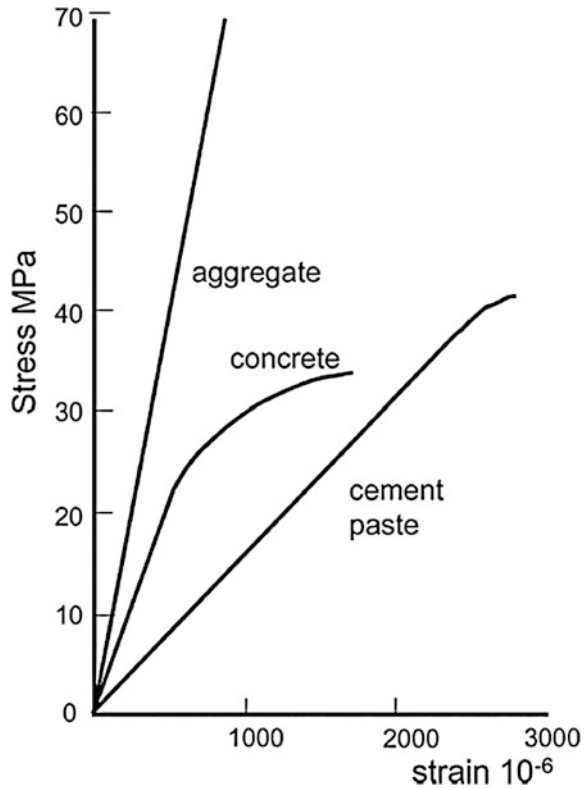
Department of Civil Engineering, Indian Institute of Technology Delhi,  
New Delhi 110016, Delhi, India  
e-mail: shashank.bishnoi@civil.iitd.ac.in

© Springer Nature Singapore Pte Ltd. 2019

A. Rama Mohan Rao and K. Ramanjaneyulu (eds.), *Recent Advances in Structural Engineering, Volume 2*, Lecture Notes in Civil Engineering 12,  
[https://doi.org/10.1007/978-981-13-0365-4\\_63](https://doi.org/10.1007/978-981-13-0365-4_63)

745

**Fig. 1** Comparative stress–strain curves for aggregate, paste, and concrete [1]



ITZ is a thin and heterogeneous region of cement paste adjacent to the aggregate surface. Wall effect is the main reason for the formation of ITZ; large aggregate particles disturb the packing of cement grain resulting in the rearrangement of small grains nearby aggregates and larger grains moves away from the aggregates (Fig. 2) [1]. This reduces cement content and increases water/cement ( $w/c$ ) ratio near the aggregate surface forming a more porous and weaker ITZ compared to bulk cement paste.

Accumulation of bleed water below the aggregate further increases the  $w/c$  ratio below aggregate. Wall effect and bleeding both result in the formation of water-filled spaces around aggregates [2]. These water-filled spaces promote the nucleation of calcium hydroxide (CH) near aggregate surface due to its tendency to nucleate in larger pores [2].

In fresh mixes, the microstructure of ITZ is characterized by higher porosity, higher  $w/c$  ratio, and lower cement content compared to bulk cement matrix, while higher CH content and higher porosity are the characteristics of ITZ in hardened systems. Microstructural composition of ITZ varies from the aggregate surface to bulk cement matrix. Depending on the age, interfacial region is characterized by gradients of microstructural composition such as unhydrated cement content,  $w/c$  ratio, porosity, and CH content [1–3] (Figs. 3, 4 and 5).

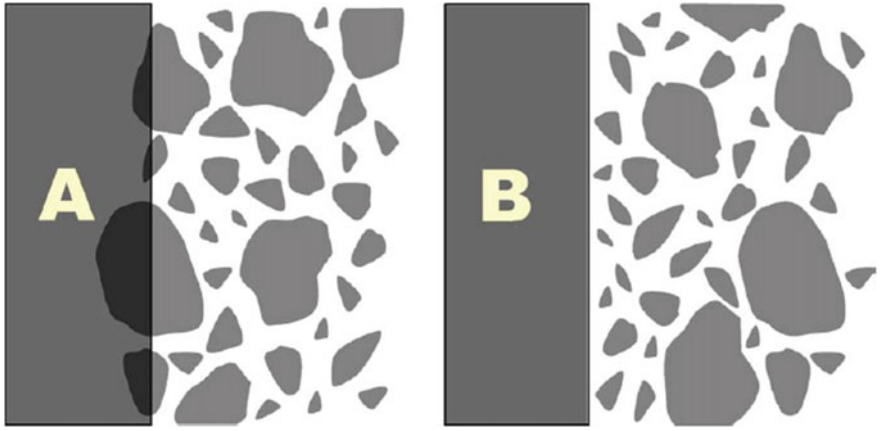


Fig. 2 Illustration of wall effect [1]

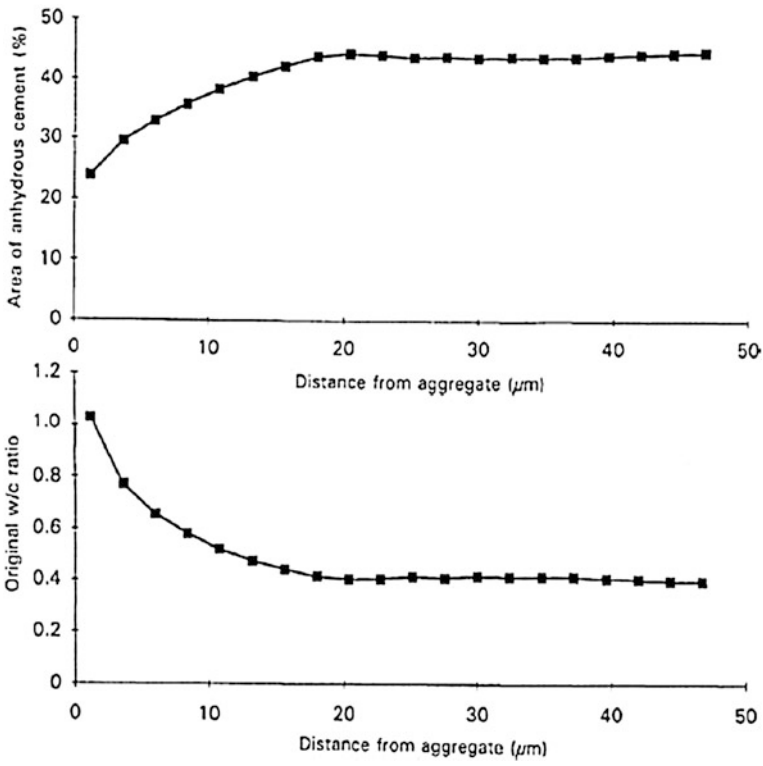


Fig. 3 Calculated initial distribution of anhydrous cement and effective water/cement ratio in the interfacial zone [2]

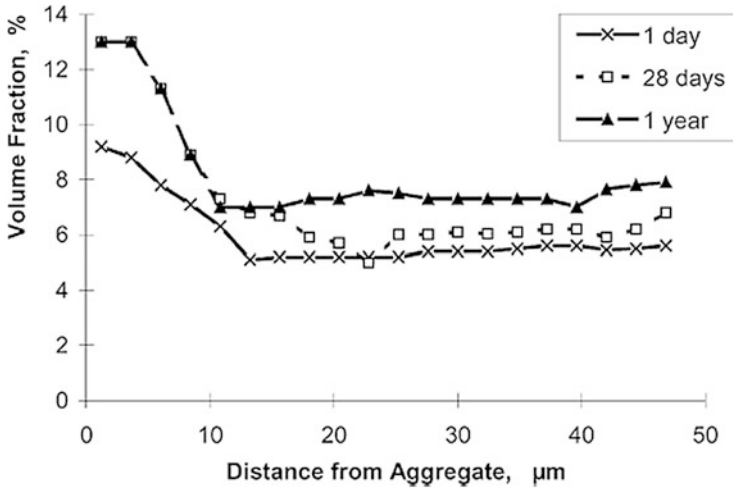


Fig. 4 Average distribution of calcium hydroxide in ITZ [1]

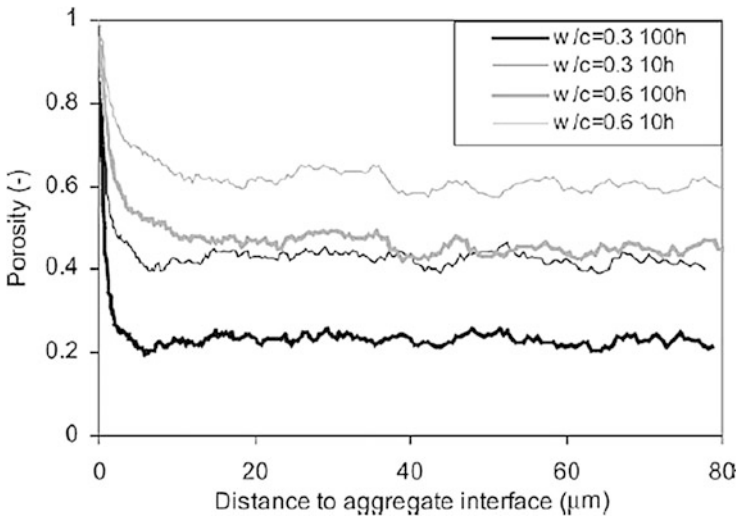


Fig. 5 Porosity gradient in the ITZ of model concrete [3]

The extent of ITZ is usually measured by the distance from aggregate surface to the bulk cement where porosity or density becomes almost equal to the bulk matrix. The extent of “wall effect” and ITZ depends on the size of aggregate and cement grains. Thus, the thickness of ITZ is compared with the size of cement. Bentz and Garboczi using computer simulation found that the thickness of ITZ is equal to the

median size of cement grains [4]. Ollivier et al. reported that the thickness of ITZ is equivalent to the mean diameter of cement grains [5].

Several authors have reported the thickness of ITZ to be around 40–50  $\mu\text{m}$  based on the perturbation caused by aggregate particle [1, 2]. This might be deviating from the results of Scrivener and Nematı revealing that ITZ thickness is around 30–100  $\mu\text{m}$  [6]. The perturbation is most significant within 15–20  $\mu\text{m}$  distance from aggregate surface [1, 5].

## 2 Effect of ITZ on the Properties of Mortar and Concrete

High porosity and microcracks are intrinsic features of ITZ microstructure. This influences the elastic modulus of concrete to a great extent. ITZ serves as a linking chain between aggregate and paste. ITZ has lower elastic modulus compared to aggregate and cement paste, which reduces overall elastic modulus of concrete. Yang using computer simulation showed that elastic modulus of ITZ varies from 0.2 to 0.7 times of elastic modulus of paste, depending on the thickness [7].

Strength of concrete is considerably lower than the strength of either of the two components, aggregate and paste, due to the presence of ITZ only. The formation and expansion of microcracks is easier in ITZ region compared to cement matrix and aggregate. Therefore, fracture path of concrete usually occurs along the aggregate surface.

Several authors have concluded that adding aggregate increases permeability of mortar and concrete [8, 9]. Wong et al. [10] revealed that adding a small amount of aggregate (10% by volume) increases permeability, diffusivity, and sorptivity of mortars, but further addition of aggregates reduces the same. Similar trend was observed by Tumidajski [11] for electrical conductivity of Portland cement mortar, while Princigallo et al. showed that adding aggregates in cement paste continuously reduces electrical conductivity from  $\approx 1.8$  S/m for neat cement paste, to  $\approx 0.3$  S/m for concrete containing 75% aggregates [12]. The effect of aggregate addition is more pronounced on permeability compared to other properties like sorptivity, diffusivity, and electrical conductivity. This shows the permeability is more influenced by pore structure and tortuosity compared to other transport properties.

## 3 Methods of Modifying Microstructure of ITZ

### 3.1 Mix Design Parameter

Changing the mix design parameters modifies the packing of cement particles around aggregates and hence the microstructure of ITZ. Cement particles get packed efficiently at low  $w/c$  ratio, not only in bulk matrix but also in ITZ.



Increasing the aggregate/cement ratio restricts the rearrangement of cement grains only over small distances and resulting in narrower ITZ.

### 3.2 Changing Particle Size Distribution

Efficient packing of cement near aggregate surface reduces the thickness and microstructural gradient of ITZ. Small-sized cement particles pack efficiently near aggregate surface and reduce the thickness of ITZ [1–3]. Figure 6 shows that volume density of small-sized particles is highest within 10  $\mu\text{m}$  distance from the aggregate surface and large size particles are found further away. Thus, gap grading of cementitious materials is an effective method of improving the microstructure of ITZ.

### 3.3 Use of Supplementary Cementitious Materials (SCMs)

Supplementary cementitious materials show different physical and chemical effects depending on the degree of hydration. Adding SCMs have the following physical effects in cementitious systems: dilution, modification of particle size distribution, and heterogeneous nucleation [13]. Pozzolanic reaction, the reaction of reactive

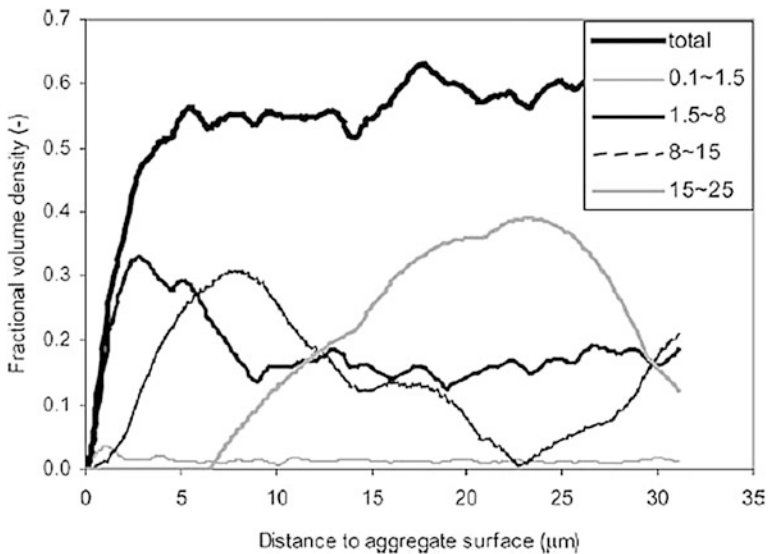


**Fig. 6** Volume density of successive size fractions (size range in  $\mu\text{m}$ ), by computer simulations [3]

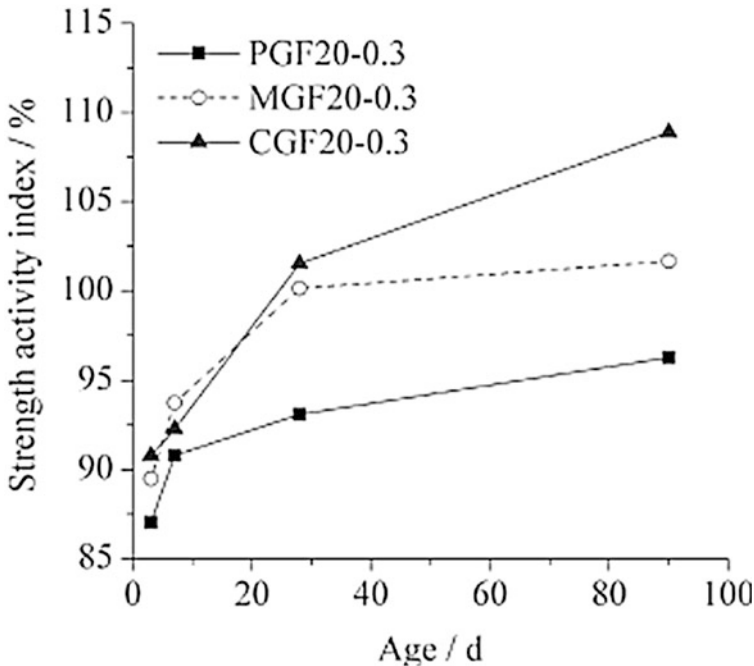


Fig. 7 Strength activity index of ground fly ash in paste, mortar, and concrete at  $w/b$  0.3 [14]

silica with CH, is the chemical effect of SCMs. Thus, SCMs have been extensively used to improve the overall microstructure of cementitious systems. All the effects of SCMs addition are more prominent in interfacial region.

Fangui et al. [14] revealed that the effect of fly-ash addition is more pronounced for mortar and concrete compared to paste. Figure 7 shows that the strength activity index of fly ash is more for mortar and concrete compared to paste. This might be due to microfilling and pozzolanic effect of fly ash, especially in ITZ. Finer ground fly ash can accumulate near aggregate surface at early ages. At later ages, fly ash will react with excess CH available in ITZ and strengthens the ITZ. Duan et al. performed microhardness test on various polished and sliced concrete specimen containing ITZ between aggregate and mortar [15]. Figures 8 and 9 show that concrete containing silica fume (SF), metakaolin (MK), and slag (SL) have higher microhardness compared to normal concrete. At early ages, fine mineral additives have highest positive effect on ITZ microhardness due to microfilling. At later ages, mineral additives improve microhardness of ITZ by pozzolanic reaction.

Xuan et al. performed pullout test on exposed near-surface-zone aggregate to study the interfacial bond strength between aggregate and cement matrix. An increase of around 80% in the pullout force of aggregate was observed on adding 9% SF [16]. Thickness of ITZ also reduces by adding mineral admixtures.

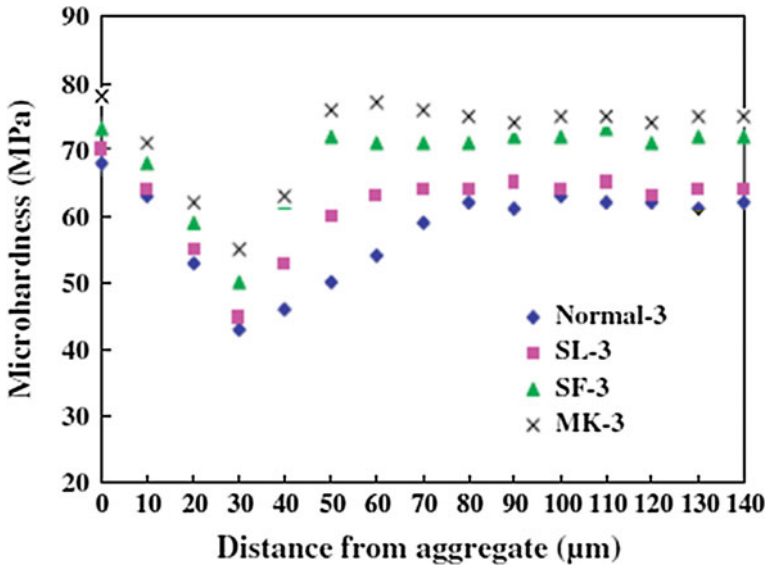


Fig. 8 Effects of mineral admixtures on microhardness at 3 days [15]

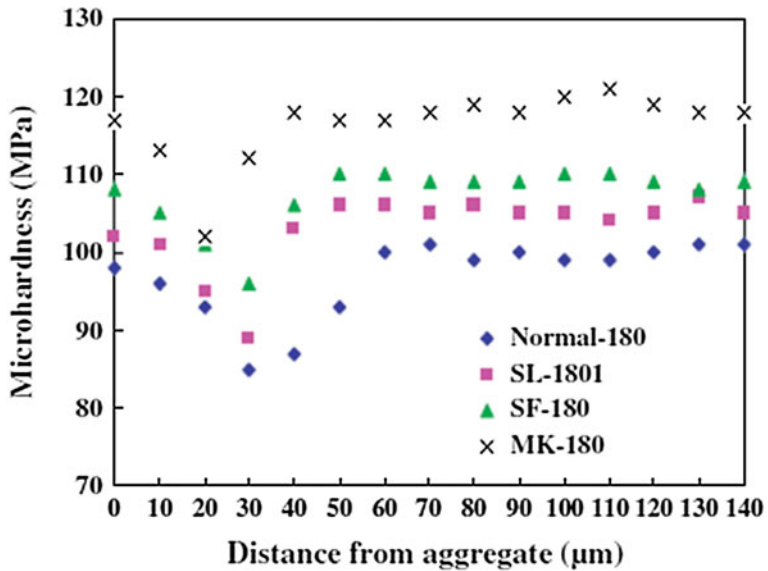


Fig. 9 Effects of mineral admixtures on microhardness at 180 days [15]

It can also be observed in Fig. 9, the thickness of ITZ decreases from almost 70 to 40 µm by the addition of mineral admixtures. Rossignolo also observed 36% reduction in ITZ thickness by addition of 10% SF [17].

### 3.4 Use of Nano-materials (SCMs)

Use of nano-materials in concrete is a more recent approach. Various authors have reported that the use of nano-materials like nano-SiO<sub>2</sub>, nano-TiO<sub>2</sub>, and nano-alumina results in a significant improvement in the microstructure of ITZ. Due to their high surface energy, these nano-materials get absorbed on the sand surface by Vander wall forces and act as filler in ITZ making it denser, which in turn improve elastic modulus and compressive strength of mortar and decrease the thickness of ITZ [18–20]. Nano-SiO<sub>2</sub> also shows pozzolanic reaction and further improves microstructure of ITZ.

## 4 Conclusion

- The ITZ is not a separate phase in concrete but a zone of transition in cement matrix around aggregates. The thickness of this zone depends on w/c ratio, size of aggregates, and cement.
- The microstructure of ITZ is characterized by high porosity, high CH content, and low cement content; thus, its microhardness is lower than bulk cement paste.
- Due to the weak microstructure, ITZ has negative effects on mechanical properties of concrete like compressive strength and elastic modulus.
- The microstructure of ITZ can be improved by using low w/c ratio, high aggregate/cement ratio, and gap grading in the binder. Use of nano-materials is a good alternative of achieving gap grading in cementitious systems.
- SCMs improve the microstructure of ITZ by filling effect and pozzolanic reaction. At early ages, filling effect dominates in the ITZ due to accumulation of small size SCMs. At later ages, pozzolanic reaction is more in ITZ region due to availability of high amount of CH in ITZ.

## References

1. Scrivener KL, Crumbie AK, Laugesen P (2004) The interfacial transition zone (ITZ) between cement paste and aggregate in concrete. *Interface Sci* 12:411–421
2. Maso JC (ed) (1996) *Interfacial transition zone in concrete: RILEM report* (E & FN Spon)
3. Hu J, Stroeven P (2004) Properties of the interfacial transition zone in model concrete. *Interface Sci* 12:389–397
4. Bentz DP, Garboczi EJ (1999) In: Alexander MG et al (eds) *Engineering and transport properties of the interfacial transition zone in cementitious composites*. RILEM Publications SARL
5. Ollivier JP, Maso JC, Bourdette B (1995) Interfacial transition zone in concrete. *Adv Cem Based Mater* 2:30–38

6. Scrivener KL, Nematı KM (1996) The percolation of pore space in the cement paste/ aggregate interfacial zone of concrete. *Cem Concr Res* 26(1):35–40
7. Yang C (2003) Effect of the interfacial transition zone on the transport and the elastic properties of mortar. *Mag Concr Res* 55(4):305–312
8. Nyame BK (1985) Permeability of normal and lightweight mortars. *Mag Concr Res* 37(130): 44–48
9. Halamickova P, Detwiler RJ (1995) Water permeability and chloride ion diffusion in portland cement mortars: relationship to sand content and critical pore diameter. *Cem Concr Res* 25(4): 790–802
10. Wong HS, Zobel M, Buenfeld NR, Zimmerman RW (2009) Influence of the interfacial transition zone and microcracking on the diffusivity, permeability and sorptivity of cement-based materials after drying. *Mag Concr Res* 61(8):571–589
11. Tumidajski PJ (1996) Electrical conductivity of Portland cement mortars. *Cem Concr Res* 26(4):529–534
12. Princigallo A, van Breugel K, Levita G (2003) Influence of the aggregate on the electrical conductivity of Portland cement concretes. *Cem Concr Res* 33:1755–1763
13. Lawrence P, Cyr M, Ringot E (2003) Mineral admixtures in mortars effect of inert materials on short-term hydration. *Cem Concr Res* 33:1939–1947
14. Fanghui H, Qiang W, Jingjing F (2015) The differences among the roles of ground fly ash in the paste, mortar and concrete. *Constr Build Mater* 93:172–179
15. Duan P, Shui Z, Chen W, Shen C (2013) Effects of metakaolin, silica fume and slag on pore structure, interfacial transition zone and compressive strength of concrete. *Constr Build Mater* 44:1–6
16. Xuan DX, Shui ZH, Wu SP (2009) Influence of silica fume on the interfacial bond between aggregate and matrix in near-surface layer of concrete. *Constr Build Mater* 23:2631–2635
17. Rossignolo JA (2009) Interfacial interactions in concretes with silica fume and SBR latex. *Constr Build Mater* 23:817–821
18. Zhenhua L, Wang H, He S, Lu Y, Wang M (2006) Investigations on the preparation and mechanical properties of the nano-alumina reinforced cement composite. *Mater Lett* 60:356–359
19. Ji T (2015) Preliminary study on the water permeability and microstructure of concrete incorporating nano-SiO<sub>2</sub>. *Cem Concr Res* 35:1943–1947
20. Mohseni E, Naseri F, Amjadi R, Khotbehsara MM, Ranjbar MM (2016) Microstructure and durability properties of cement mortars containing nano-TiO<sub>2</sub> and rice husk ash. *Constr Build Mater* 114:656–664

# Experimental and Analytical Studies of Failure Characteristics of FRP Connections



S. B. Singh, Himanshu Chawla and Sudhir Vummadisetti

**Abstract** This study presents the failure characteristics of FRP lap joints in tension using experimental and analytical techniques. The lap joint is made from coupons extruded from laminated plates and pultruded beams. FRP plates are fabricated from different fabrics and stacking sequence of fibers. Extensive study is performed on changing the end distance-to-bolt diameter ratio, bolt diameter-to-thickness ratio, and stacking sequence of the laminates. Coupons are connected through bolts and/or adhesive. It is observed that the failure of the bonded connection is very brittle while those connected by bolt and adhesive have ductile failure. Adhesive joints failed by failure of external layers, while bolted joints have bearing failure of coupons as well as shear failure of coupons and bolt. It is noted that the strength of the joint increases with increase in the overlapping length, while it decreases with increase in bolt diameter. The quasi-isotropic, i.e.,  $(0/90/\pm 45)_s$ , have higher failure strength than cross-ply and angle-ply laminates.

**Keywords** Adhesive joint · Bearing failure · Bolted connection  
FRP lap joint · Shear failure

## 1 Introduction

Connection of beams with bolts or adhesive becomes the weaker portion of a structure, which leads to the primary failure of the structure. Hence, it is very important to study the structural response and failure characteristics of FRP beams and its components connected by bolts. Lap joints are more commonly used for

---

S. B. Singh · H. Chawla (✉) · S. Vummadisetti  
Civil Engineering Department, BITS, Pilani 333031, India  
e-mail: himanshuchawla11@gmail.com

S. B. Singh  
e-mail: sbsinghbits@gmail.com; sbsingh@pilani.bits-pilani.ac.in

S. Vummadisetti  
e-mail: sudhir.vummadisetti@gmail.com

joining the structures. Design of FRP lap joint for FRP beams depends upon the layout of the beam as well as type of the fabrics present in beams.

## 2 Analytical Method

Failure load ( $F$ ) is determined from gross area (or net area of joint) and the strength of coupons ( $\sigma$ ), i.e.,  $F = \sigma \times A$  [1–3]. The failed area ( $A$ ) of joint in bearing, net-tension, and shear failure is  $dt$ ,  $(w - d)t$ , and  $et$ , respectively. Here,  $d$ ,  $e$ ,  $w$ , and  $t$  are diameter of bolt, edge distance (from center of bolt), width, and thickness of coupon, respectively. In case of bearing failure of joints,  $\sigma$  is compressive strength of laminate; in tension failure,  $\sigma$  is tensile strength and in shear out failure,  $\sigma$  is shear strength of laminate.

## 3 Results

Figure 1a shows the response of lap joint fabricated by bolt (L50B), adhesive (L50E), and the both adhesive and bolt (L50EB) in tension. It is noted that failure of adhesive-bonded lap joint is very brittle as compared to the bolted connections. In specimen L50EB, initial load is taken by epoxy (i.e., adhesive), and once the ultimate strength of adhesive or outer lamina is reached, then the load is transferred to bolt but the bearing load decreased slightly due to presence of clearance between bolt and hole. The quasi-isotropic laminates have higher load carrying capacity than those of other laminates as shown in Fig. 1b.

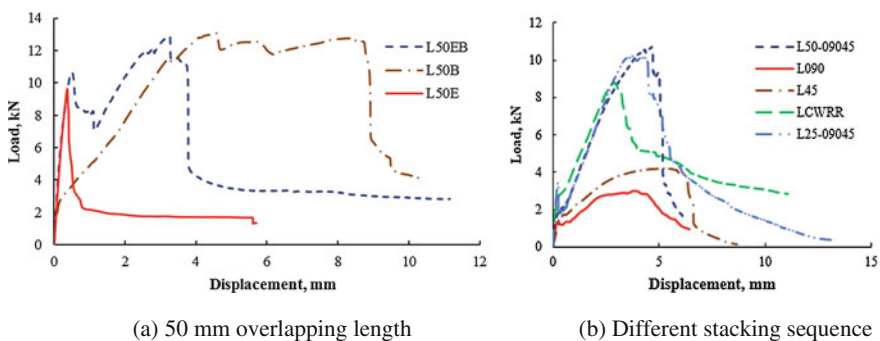


**Fig. 1** Response of lap joint in tension

## 4 Conclusions

1. Adhesive-bonded lap joint decreases the deformation of lap joint due to brittle failure. The strength of the adhesive-bonded lap joint depends upon the strength of adhesive as well as the strength of external lamina. Therefore, external lamina should be of woven fabrics, because it has higher strength than the rovings and continuous strands mat.
2. Lap joint made using epoxy and bolt together gives slightly higher capacity than the joint made with bolt only. Failure of epoxy-bonded joint is sudden, while the failure of joint using bolt and epoxy has high strength with more deformation. Hence, lap joints of combined bolted and epoxy bonded are more suitable than bonded with epoxy only.
3. Based on the strength and failure characteristics of different stacking sequences of lap joints, quasi-isotropic stacking sequence (i.e.,  $(0/90/\pm 45)_s$ ) is recommended for lap joint.

## References

1. DiNicola AJ, Fantle SL (1993) Bearing strength of clearance fit fastener holes in toughened graphite/epoxy laminates. *Compos Mater Test Des* 11:220–237
2. Kelly G, Hallstro S (2004) Bearing strength of carbon fibre/epoxy laminates: effects of bolt-hole clearance. *Composites B* 35:331–343
3. Keller T, Vallee T (2005) Adhesively bonded lap joints from pultruded GFRP profiles. Part I: stress–strain analysis and failure modes. *Composites B* 36:331–340



# Effect of Shear Lag on Buckling of FRP Box-Beams



M. Kasiviswanathan and Akhil Upadhyay

**Abstract** Nowadays, FRP applications have been increased in the various engineering fields because of their numerous mechanical and physical properties, i.e., high strength, lightweight, corrosion resistance, and tailoring ability. The tailoring ability of FRP gives us flexibility to change the configuration and positions of fiber orientation in the laminate; it helps to fulfill the specific design requirements. However, being a thin-walled structure, design of box-beam is governed by stability. Generally, in the FRP box-beam two type of buckling is possible, i.e., web and flange. Flange buckling is caused by both primary and secondary stresses. Primary stresses are caused by bending, and secondary stresses are caused by shear lag, torsion, and distortion. Herein, the effect of shear lag on buckling stress of box-beam has been studied with the help of finite element software 'ANSYS 15' by changing the fiber orientation and geometry of various elements of box-beam.

**Keywords** Flange buckling · FRP box-beam · Stability problems  
Shear lag

## Notations

$b_f, b_w$	Width of the flange and web
$\delta_f$	Rotational restraint parameter of flange
$q$	Uniform line load
$\theta_f, \theta_w$	Fiber orientation of flange and web
$(b/t)_f$	Slenderness ratio of flange
$\sigma_{x,max}$	Maximum bending stress at beam center
$t_f, t_w$	Thickness of the flange and web
$\sigma_{b,f}$	Flange buckling stress

---

M. Kasiviswanathan · A. Upadhyay (✉)  
Department of Civil Engineering, Indian Institute of Technology Roorkee,  
Roorkee, India  
e-mail: Akhilfce@iitr.ac.in

M. Kasiviswanathan  
e-mail: kasiviswacivil@gmail.com

$E_1, E_2, G_{12}$	Lamina modulus
$\nu_{12}, \nu_{21}$	Lamina major and minor poison ratio
$S_F$	Shear lag factor
$\sigma_{x,avg}$	Average bending stress at beam center

## 1 Introduction

Steel box-beams are widely used in aircraft wings due to their light weight and torsional characteristics. Later, these applications are increased in bridges also due to their good bending resistance, section integrity, and better construction adoptability. Applications have been increased to reduce the dead weight as well as to increase the torsional stiffnesses, especially in curved bridges. Replacing of composite box-beams instead of steel box-beams further reduces the dead weight of structure. Fiber orientation and number of plies in the laminate provide a wide number of parameters which help to enhance the performance of structure but increases the design variables. To know the significance of these parameters on structural efficiency further research needs to be conducted.

According to Bernoulli beam theory, span-wise normal stress distribution across the width of solid beam is uniform under pure bending. However, in box-beam, top and bottom flange will be suffered from the effect of shear deformation. Hence, the value of stress at the web flange junction is higher than the value of stresses remote from the web; that is, while going away from the web normal stress lags and results in non-uniform width-wise normal stress distribution. This lag of normal stress distribution across the width is called as shear lag.

Shear lag effect reduces bending strength and stiffness of box-beam as a consequence of non-uniform stress distribution in the flanges. If flanges have low shear stiffness, normal stresses cannot be uniformly distributed across the width of the flanges that has been stated by Salim and Davalos [1]. Gan et al. [2] studied the performance of pultruded I-beams with various web-flange conjunctions. They observed that maximum stress in the flanges is higher than expected value. Visnjic and Nozak [3] have conducted extensive numerical study for I-beams to reduce the shear lag effect. They found parameters which have more influence on shear lag phenomenon. Resser [4], Kristek et al. [5], Evans et al. [6], Lopez-Anido, and GangoRao [7] also studied the shear lag phenomenon but their studies are connected with wide-flange thin-walled beam with high height to length ratio.

Shear lag phenomenon has been studied for many decades by many researchers. But those works are mainly focused about the effect of shear lag on stress distribution and deflection of beam. Lertsima et al. [8], Sa-nguanmanasak et al. [9] have studied the effect of shear lag on stress concentration factor. They conducted detailed parametric study, and as a result of this study, they listed out some key parameters which have influence on shear lag, and based on these parameters, they proposed empirical formula by regression analysis. Similarly, Lertsima et al. [10] have studied the shear lag

effect on deflection of box-beam. Lee and Wu [11] have studied the shear lag effect by finite element method, and based on these studies, they concluded that FEM is the feasible approach for the analysis of thin-walled structures. However, studies about the effect of shear lag on buckling coefficient are meager. So, in this paper, shear lag effect on buckling coefficient of box-beam has been studied by changing the fiber orientation and geometry of various elements of box-beam.

## 2 Finite Element Analysis

Finite element method was employed to study the shear lag effect on buckling coefficient of FRP box-beam. FEM programs help to predict the shear lag effect on flange buckling of box-beam with different geometry and loading constraints. In this study, commercially available finite element tool 'ANSYS 15' was utilized.

### 2.1 Model Geometry

In this step, geometry of various elements of box-beam has been defined. The length and cross section details of box-beam are shown in Fig. 1.

### 2.2 Loading and Boundary Conditions

In this analysis, simply supported box-beam as shown in Fig. 2 was considered. To simulate the hinged support  $X$ ,  $Y$ , and  $Z$  directions were constraints at the one end. Similarly, for roller support,  $y$  and  $z$  directions were constraint at the other end. In all the cases, uniform line load is applied over the length of flange and web junction.

### 2.3 Material Properties

For the analysis of box-beam, material properties as shown in Table 1 are used.

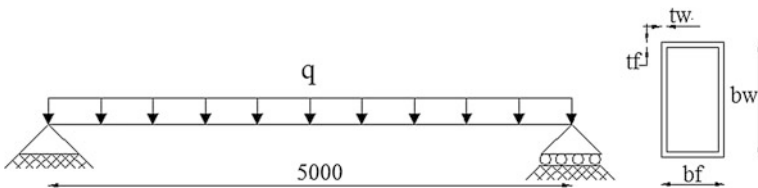


**Fig. 1** Schematic view of the analyzed girders

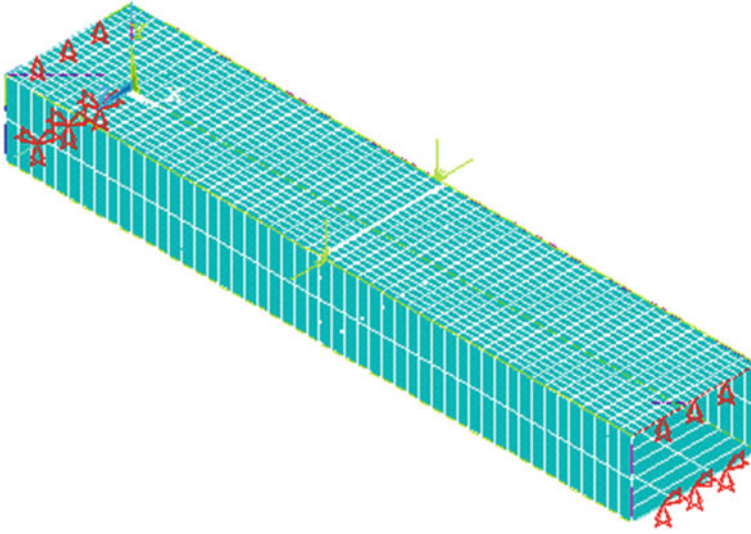


**Fig. 2** End constraints of beam model

## 2.4 Element Type

Shell element 281 was used to model the various elements of box-beam in the finite element analysis. This element has eight nodes, and each node has six degrees of freedom: translation and rotation in  $x$ ,  $y$ , and  $z$  direction. The element has been chosen because it has both bending and membrane capabilities, and it can sustain in-plane load and normal load. Additionally, it is suitable for the large deformation analysis.

## 2.5 Validation Study

Definition of the material properties, constraints, mesh size, and fiber orientation of various elements of beam needs more care, and it is essential to establish the accuracy of modeling before it is used for the analysis. Therefore, results obtained from reference studies and presented by Kollar [12] and Qiao et al. [13] were used to assess the accuracy of the proposed finite element modeling. Beam subjected to uniform compression load was considered for validation. Table 2 shows the

**Table 1** Lamina material properties

$E_1$ (GPa)	$E_2$ (GPa)	$G_{12}$ (GPa)	$\rho$ (kg/m <sup>3</sup> )	$\nu_{12}$	$\nu_{21}$
145	16.5	4.48	1520	0.314	0.037

**Table 2** Validation of FE model

Dimensions in mm $b_w \times b_f \times t_w \times t_f$	$N_{cr}$ (kN/m)		% Difference
	FE analysis		
	Reference studies	Present study	
$203.2 \times 101.6 \times 6.4 \times 6.4$	519 <sup>a</sup>	503.47	-3.08
$152 \times 152 \times 6.4 \times 6.4$	717 <sup>b</sup>	758.9	5.52
$152 \times 102 \times 6.4 \times 6.4$	850.1 <sup>b</sup>	905.763	6.14

<sup>a</sup>Kollar [12], <sup>b</sup>Qiao et al. [13]

dimension and results for the beam used for the validation. The difference between the references studies and numerical model resistance against uniform compression load ranged from -3.08 to 6.14%, and it shows good agreement.

### 2.6 Buckling Coefficient and Mode Shape

In all the cases, buckling coefficient was found by Eigen buckling analysis, and cross sections are proportioned in such a manner that flange buckling is the first mode of buckling. In order to obtain flange buckling coefficient, five buckling modes can be generated for each case and the value corresponding to the first flange buckling mode (lowest) is taken as the flange buckling coefficient. Flange buckling mode of the beam is shown in Fig. 3.

## 3 Need for Study and Basic Plan

Because of highly orthotropic nature of the composite materials, determining shear lag analytically is a difficult task and reliable solution for the design apparently cannot be achieved. Consequently, numerical methods and particularly finite element remain feasible approach for the analysis of shear lag in complex thin-walled structures. So, in the present study, finite element programs have been used to quantify the shear lag factor and buckling coefficient. For that, geometry of box-beam and fiber orientation of various elements are varied. During these studies, geometrical parameters of box-beam, i.e., width and thickness, are varied along with variation of fiber orientation in flange and web. Three fiber orientations 0°, ±45°, and 90° are considered to cover extreme cases of orthotropy. In all the cases, sections are proportioned in such a manner that flange buckling will be the first mode of buckling.

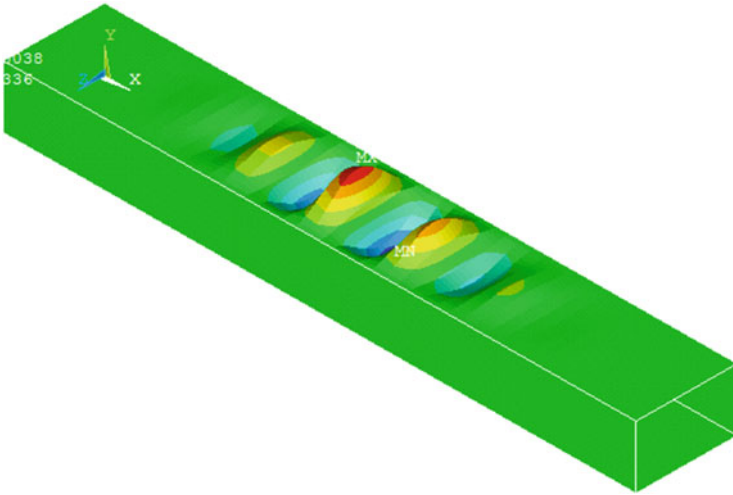


**Fig. 3** Buckling mode corresponding to first eigenvalue (beam size—800 × 600 × 5000)

#### 4 Analysis of Shear Lag Effect

In order to evaluate and compare the magnitude of shear lag effect on buckling coefficient of FRP box-beams, shear lag factor was used. It was calculated by the following equation.

$$S_F = \frac{\sigma_{x,\max}}{\sigma_{x,\text{avg}}} \quad (1)$$

where the trapezoidal rule of integration was used to calculate the average normal stress  $\sigma_{x,\text{avg}}$  and  $\sigma_{x,\max}$  is the maximum stress in the beam width at the  $L/2$ .

#### 5 Effect of Fiber Orientation

In order to show the influence of fiber orientation on shear lag phenomenon, three extreme cases of fiber orientation were considered for both flange and web elements, while geometrical parameters were kept constant. The considered material and geometrical properties for analyzed cases are given in Table 3.

In general, fiber orientation affects the state of stress of box-beam. Particularly, it brings the considerable changes in flange stresses by changing the orientation of fibers, and consequently, it affects the stress variation along the beam width. State of stress of top flange for different flange–web combinations is shown in Fig. 4. In each combination, the distribution of stress differs considerably.

**Table 3** Cross-sectional dimensions and fiber orientations used to display the significance of fiber orientation

$L=5000$ mm, $b_f=500$ mm, $t_w=20$ mm				
$\theta_f$	$\theta_w$	$b_w$ (mm)	$t_f$ (mm)	Load case
$(0^\circ/0^\circ)_s$	$(0^\circ/0^\circ)_s$	500	2.5	Symmetrical load
$(\pm 45^\circ)_s$	$(\pm 45^\circ)_s$	600		
$(90^\circ/90^\circ)_s$	$(90^\circ/90^\circ)_s$	700		

To show the changes in the stress variation along the beam width, for a constant web fiber orientation and geometry, three extreme cases of flange fiber orientation were considered i.e. 0, 45 and 90. Stress values are taken from the beam center ( $L/2$ ) that as mentioned in Fig. 5a. The corresponding stress variation for different flange fiber orientation is shown in Fig. 5b–d. It shows the considerable changes in the stress variation across the beam.

As can be seen from Fig. 5b–d, fiber orientation affects the shear lag phenomenon noticeably. In order to show the effect of fiber orientation on shear lag, shear lag factor can be quantified with the help of Eq. (1). Shear lag factor variations for different flange and web fiber orientations are shown in Fig. 6. From this figure, it can be observed that for the constant web fiber orientation, shear lag factor decreases with increases of flange fiber orientation, but when flange has  $\pm 45^\circ$  fiber orientation, shear lag factor is even lower than  $90^\circ$  because  $\pm 45^\circ$  provide adequate shear stiffness to laminate and the shear lag is almost constant.

The corresponding shear lag factor effect on buckling coefficient is shown in Fig. 7. From this figure, it can be observed that buckling coefficient decreases with increases of shear lag factor. It implies that  $\sigma_{x,avg}$  decreases with decreases of  $\theta_f$  that means stress variation across the beam gets increased at low flange fiber orientation.

Corresponding with  $\theta_f^*$  = corresponding value of  $\theta_f$  for different shear lag factor as given in Fig. 5.

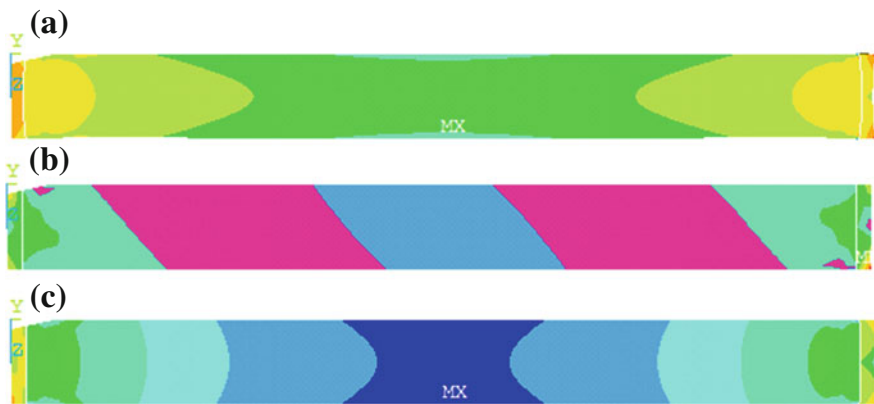
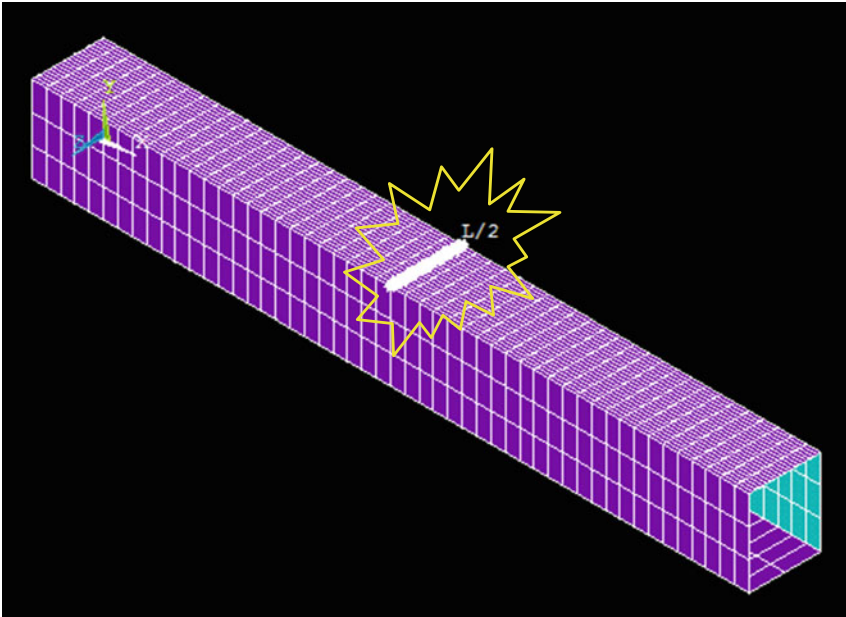


**Fig. 4** State of stress of top flange: **a**  $0^\circ (\theta_f) - 0^\circ (\theta_w)$ ; **b**  $\pm 45^\circ (\theta_f) - 0^\circ (\theta_w)$ ; **c**  $90^\circ (\theta_f) - 0^\circ (\theta_w)$

(a)



(b)



(c)



(d)



**Fig. 5** Top flange stress variation across the beam width: **a** Box-beam highlighting section of interest; **b**  $0^\circ (\theta_f) - \pm 45^\circ (\theta_w)$ ; **c**  $\pm 45^\circ (\theta_f) - \pm 45^\circ (\theta_w)$ ; **d**  $90^\circ (\theta_f) - \pm 45^\circ (\theta_w)$



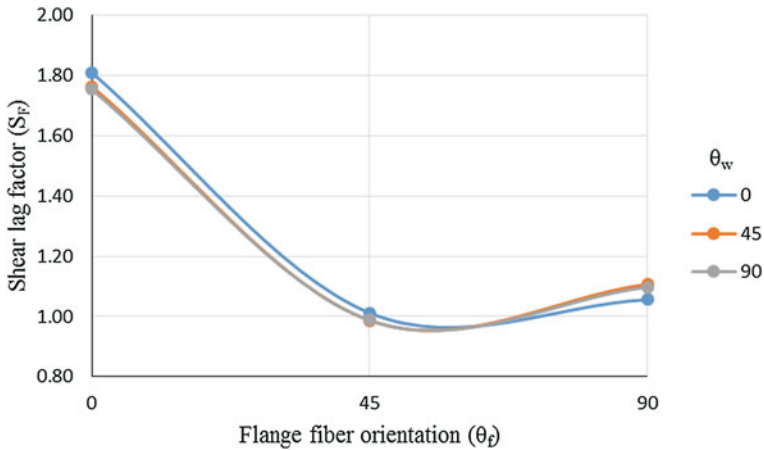


Fig. 6 Variation of shear lag factor with  $\theta_f$  for different  $\theta_w$

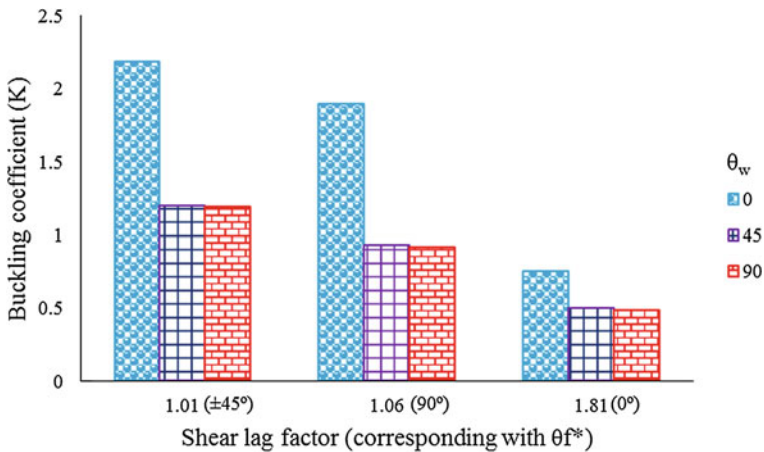


Fig. 7 Variation of buckling coefficient with  $S_F$  for different  $\theta_w$

### 6 Effect of Geometry

The cross section of the analyzed box-beam is shown in Fig. 1. The total beam height used in the analysis was 500 mm. In order to isolate the study from the influence of beam cross section on shear lag effect, cross section along the beam was kept constant. Flanges are mostly subjected to in-plane compressive and tensile loads, so,  $0^\circ$  fiber orientation was chosen for flange. Fifteen different flange widths to thickness ratio were considered. The considered  $b_f$ ,  $t_f$ , and  $(bt)_f$  is given in Table 4. While, web predominantly subjected to shear stress, so  $\pm 45^\circ$  fiber

**Table 4** Correlation between flange thickness ( $t_f$ ) width ( $b_f$ ) and slenderness ratio  $(b/t)_f$

$t_f$ (mm)	$b_f$ (mm)	$(b/t)_f$
10.00	250.00	25.00
8.50	294.11	34.60
7.75	322.58	41.62
6.75	370.37	54.87
6.25	400.00	64.00
5.75	434.78	75.61
5.00	500.00	100.00
4.50	555.55	123.45
4.00	625.00	156.25
3.50	714.28	204.08
3.25	769.23	236.69
3.00	833.33	277.78
2.50	1000.00	400.00
2.00	1250.00	625.00
1.75	1428.57	816.32

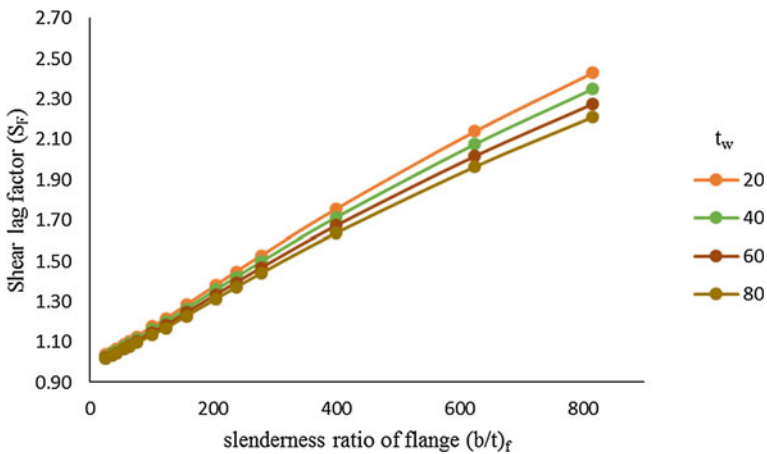


**Fig. 8** Variation of shear lag factor with  $(b/t)_f$  for different  $t_w$

orientation was chosen for web. Four different web thicknesses were used in the analysis.

In Fig. 8, shear lag factor plotted was against  $(b/t)_f$  for different web thicknesses. From this figure, it can be observed that shear lag factor increases with increase in  $(b/t)_f$ . In addition to this, thickness of the web has insignificant effect on the shear lag factor at lower  $(b/t)_f$  value, but at higher  $(b/t)_f$  value, with the increase in thickness of web shear lag factor decreases considerably.

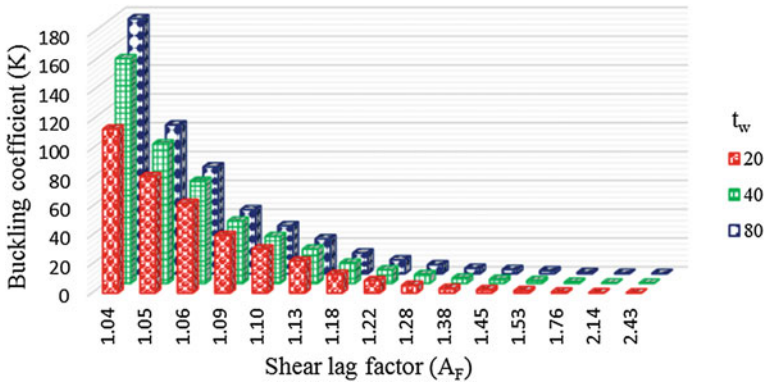


Fig. 9 Variation of buckling coefficient with  $S_F$  for different  $t_w$

The influence of shear lag factor on buckling coefficient is shown in Fig. 9. From this figure, it can be noticed that the buckling coefficient decreases with increase in shear lag factor, the reason is shear stiffness of flange decreases with increase in flange width.

In addition to this, for the same value of shear lag factor, a thicker web gives higher buckling coefficient, because the thicker web reduces the stress level which transmits from web to flange.

## 7 Conclusion

In the present work, effect of shear lag on flange buckling of box-beam has been studied numerically with the help of commercially available package ‘ANSYS 15.’ True state of stress and stress variation of box-beam across the beam width can be obtained easily by this approach. Shear lag effect on buckling coefficient is examined by changing the fiber orientation and geometry of various elements of box-beam. The results clearly bring out the influence of fiber orientation on shear lag. The  $\pm 45^\circ$  and  $90^\circ$  fiber orientation of flange gives low shear lag factor as a consequence of less non-uniform stress variation in beam width, and consequently, due to the combined effect of the fiber orientation and shear lag effect, buckling coefficient increases. In addition to this, the influence of web thickness and slenderness ratio of flange on shear lag also can be observed. The shear lag factor increases with increases of slenderness ratio of flange as a result of reducing stiffness of flange. Meantime, buckling coefficient increases with decreases of shear lag factor. Noteworthy, buckling coefficient value directly proportional to the shear lag factor.

## References

1. Salim HA, Davalos JF (2005) Shear lag of open and closed thin-walled laminated composite beams. *J Reinf Plast Compos* 24(7):633–690
2. Gan LH, Ye L, Mai YW (1999) Simulations of mechanical performance of pultruded I-beams with various flange-web conjunctions. *Compos B Eng* 30(4):423–429
3. Visnjic G, Nozak D (2014) Reducing shear-lag in thin-walled composite I-beam wing spars. *Aircr Eng Aerosp Technol Int J* 86(2):89–98
4. Reissner E (1946) Analysis of shear lag in box beam by the principle of minimum potential energy. *Q Appl Math* 6(3):268–278
5. Kristek V, Evans HR, Ahmad MKM (1990) A shear lag analysis for composite box girders. *J Constr Steel Res* 16(1):1–21
6. Evans HR, Ahmad MKM, Kristek V (1993) Shear lag in composite box girders of complex cross-sections. *J Constr Steel Res* 24(3):183–204
7. Lopez-Anido R, GangaRao HVS (1996) Warping solution for shear lag in thin-walled orthotropic composite beams. *J Eng Mech ASCE* 122(5):449–457
8. Lertsima C, Chaisomphob T, Yamaguchi E (2004) Stress concentration due to shear lag in simply supported box girders. *Eng Struct* 26(8):1093–1101
9. Sa-nguanmanasak J, Chaisomphob T, Yamaguchi E (2007) Stress concentration due to shear lag in continuous box girders. *Eng Struct* 29:1414–1421
10. Lertsima C, Chaisomphob T, Yamaguchi E, Sa-nguanmanasak J (2005) Deflection of simply supported box girder including effect of shear lag. *Comput Struct* 84:11–18
11. Lee CK, Wu GJ (2000) Shear lag analysis by the adaptive finite element method 1: analysis of simple plated structures. *Thin Wall Struct* 38(4):285–309
12. Kollar LP (2003) Local buckling of fiber reinforced plastic composite structural members with open and closed cross sections. *J Struct Eng* 129:1503–1513
13. Qiao P, Shan L (2005) Explicit local buckling analysis and design of fiber-reinforced plastic composite structural shapes. *Compos Struct* 70:468–483

# Flexural Behavior of Concrete Sandwich Panels Under Punching Load and Four-Point Bending—Experimental and Analytical Study



J. Daniel Ronald Joseph, J. Prabakar and P. Alagusundaramoorthy

**Abstract** Concrete sandwich structural panels can serve dual purposes of transferring load and insulating. This paper presents and discusses results of experimental and numerical studies carried out to understand the flexural behavior of concrete sandwich panels under different flexural loading conditions such as four-point bending and punching load. The experimental study consisted of testing two prototype concrete sandwich panels. Wythes of the panels were reinforced using wire mesh and rebars, and shear connectors were used to connect both wythes. Experimental study indicated that flexural behavior of these panels is significantly affected by type of the loading conditions. Though constructional details of both panels tested in this study are same, failure mode of the panels are different under four-point bending and punching load. The panel tested under four-point bending failed by forming inclined shear cracks and the panel tested under punching load failed by forming flexural cracks. Numerical analysis was carried out using finite element package ABAQUS. Numerical models developed are able to approximately predict load-deflection responses of concrete sandwich panels under different loading conditions. Further experimental and numerical studies are required in this area toward developing design guidelines.

**Keywords** Sandwich panel · Insulated structural panel · Lightweight panel Composites · Precast · EPS

---

J. Daniel Ronald Joseph (✉) · J. Prabakar  
ACTEL, CSIR-Structural Engineering Research Centre, Chennai 600113, India  
e-mail: daniel@serc.res.in

J. Prabakar  
e-mail: prabhakar@serc.res.in

P. Alagusundaramoorthy  
Department of Civil Engineering, Indian Institute of Technology Madras,  
Chennai 600036, India  
e-mail: aspara0@iitm.ac.in

## 1 Introduction

Precast concrete structural elements are manufactured under controlled factory conditions, and hence concrete structural elements with good precision in geometry and finishing can be manufactured. Background information on precast technology can be found in the literature [1–3]. Precast concrete elements besides being structurally and economically efficient [4] also have social and environmental benefits [5]. Precast structural elements if light-weighted may also have advantages such as (i) less attraction of seismic forces, (ii) ease of handling and transportation, and (iii) cost effective. Lightweight concrete sandwich panels produced by replacing core concrete using less denser material may consist of two skins of concrete called wythes, one on either side of the core. The core is made of material that provides significant thermal and sound insulation such as Expanded Polystyrene (EPS). In order to achieve composite action of the panel, shear transfer between the wythes is ensured by using shear connectors that connect the wythes. The shear connectors may be discrete provided at specific predefined locations or may be continuous like truss oriented along the longitudinal direction. Wires or conventional steel rebars may be used to reinforce the wythes and as shear connectors.

Bush and Stine [6] reported that under flexural load, 100% composite action may be achieved in the concrete sandwich panels. Composite and non-composite actions of sandwich panels using different numbers of truss connectors were explored. They found that panels with shear connectors exhibited composite action. It was also observed that stripping and handling inserts offered significant shear transfer between the wythes. Einea et al. [7] carried out experimental and analytical studies on the flexural behavior of concrete sandwich panels with hybrid shear connectors using FRP and prestressed steel strands. The panels were found to exhibit thermal and structural efficiency. They recommended mechanical anchorages be provided in shear connectors made of FRP rebars. The authors found that the axial strength of the shear connectors had profound effect on the shear strength of the panels. Also they observed that full-scale size panels achieved more composite action than the small-scale size specimens. Salmon and Einea [8] proposed equations to determine the out-of-plane deflections of partially composite insulated sandwich panels due to temperature difference between the wythes. The authors showed that the deflections are insensitive to stiffness of the connectors, and hence, partially composite panel and fully composite panel will have almost same deflection due to temperature difference.

Salmon et al. [9] tested concrete sandwich panels under lateral loads. Two different types of shear connectors such as FRP connectors and steel connectors were used. The authors reported that the panels achieved semi-composite action under service loads. Panels with FRP shear connectors were found to be efficient in thermal insulation compared to steel shear connectors. Benayoune et al. [10] carried out experimental and theoretical investigations on the behavior of concrete sandwich panels under flexural load. The authors reported that the failure modes of the panels was similar to conventional solid concrete panel behavior. Also, they report

that the shear connectors significantly affected the load carrying capacity and composite action of panels. Gara et al. [11] carried out experimental and numerical analysis of sandwich panels subjected to four-point bending. Concrete with average strength of 34.5 MPa was used for casting the wythes. Totally six numbers of full-scale panels were tested in their study. Flexural tests indicated that the failure of the sandwich panels occurred due to the rupture of the bottom wythe. They reported that the equivalent loads at which failure occurred were lesser than the design loads on floors and hence, these types of panels may be used for practical applications. The authors also reported that increase in the load carrying capacity might be achieved by increasing the thickness of the panel. Literature survey indicates that studies on flexural behavior of concrete sandwich panels under two different loading conditions are not reported. In order to understand the flexural behavior of concrete sandwich panel under two different loading conditions such as punching and four-point bending, this study was carried out.

## 2 Experimental Details

### 2.1 Materials

Two prototype concrete sandwich panels of dimensions  $3000 \times 1220 \times 150$ -mm ( $L \times B \times T$ ) were cast and tested to failure under four-point bending and punching load. Details of the panels are given in Table 1. The size of the wire mesh used as wythe reinforcements is  $50 \times 50$ -mm. The two meshes are connected using truss-like shear connector wires that were inclined at  $70^\circ$ . The shear connectors were welded to wire mesh. The truss-like shear connectors were oriented along the spanning direction and hence are effective in resisting shear only bending along longitudinal axis of the panel. The spacing between trusses is 100-mm. The wires of mesh and the shear connectors were nearly 2.2-mm in dia. The average tensile strength of these wires was  $650\text{-N/mm}^2$ .

Self-compacting concrete was used for casting the wythes. The mix proportion of concrete was arrived based on the guidelines of ACI [12], and it was 1:1.89:2.34:0.3:0.41:0.6% in the order of cement, coarse aggregate, fine aggregate, ground granulated blast furnace slag (GGBFS), water and superplasticizer

**Table 1** Details of panels tested

Sl. No.	ID	Mesh size (mm)	Dimension ( $L \times B \times D$ ) (mm)	Thickness (mm)			Rebars in bottom wythe	$\rho_t$	$\rho_{t, \min}^a$
				Wythe	EPS	Total			
1	PB	$50 \times 50$	$3000 \times 1220 \times 150$	25	100	150	5#8 mm $\phi$	0.191	0.0011
2	PP	$50 \times 50$							

PB panel tested in bending, PP panel tested in punching,  $\rho_t$  percentage of reinforcement provided

<sup>a</sup>Required minimum percentage of reinforcement as per ACI 318-11

(by weight of binder content). In designing the concrete mix, target slump value of >650-mm was chosen (see Table 2.5 of ACI [12]) and the total powder content used was 481-kg/m<sup>3</sup>. The cement and the GGBFS content used were 370 and 111-kg/m<sup>3</sup>, respectively. As per ACI [12], filling ability and passing ability of the concrete were measured using slump flow test and L-box test, respectively. The average slump value was 678 mm. In L-box test, the ratio of the height of concrete in the horizontal section to that of vertical section determined was 1.3. T50 which gives an indication of the viscosity of the concrete was nearly 4-s and hence, according to ACI [12] the concrete mixture was found to have viscosity that lies between low viscosity and high viscosity. It is observed from these tests that the self-compacting concrete mixture satisfied the recommended [12] minimum requirements. Coarse aggregates passing through 10-mm sieve were used. The average cube compressive strength (f<sub>ck</sub>) and flexural tensile strength of SCC were 45.97 and 4.34-MPa, respectively. The flexural tensile strength of concrete was determined using concrete prism specimens of size 150 × 150 × 700-mm as per Indian Standard [13]. The number of trusses as shear connectors present in a panel was 13. The thickness of top and bottom concrete wythes was 25-mm for all the panels.

## 2.2 Casting Process

The sequence of casting a panel is shown in Fig. 1. A steel mold of inner dimension 3000 × 1200 × 150-mm was placed on a level surface, and concrete was poured to a depth of 25-mm to form bottom concrete wythe. EPS panel with welded wire mesh and continuous truss-like shear connectors was placed upon the bottom wythe concrete. Concrete was then poured to form top concrete wythe of 25-mm thickness. Stiffening concrete beams were provided along the supporting edges (shorter edges) to avoid failure due to local crushing of concrete. The panels were cured for 28 days by using gunny bags.

## 2.3 Test Setup and Instrumentation

Schematic diagram of test setup and instrumentation used for four-point bending and punching load is shown in Fig. 2. For both types of loading conditions, one edge of the panel was supported by hinge and the other was supported on a roller. Linear voltage displacement transducer (LVDT) with 50-mm range was used to measure the mid-deflection of the panels. The strains on the wires and concrete were measured using strain gauges with gauge lengths of 2-mm and 30-mm, respectively. Picture of panels ready for testing is shown in Fig. 3.



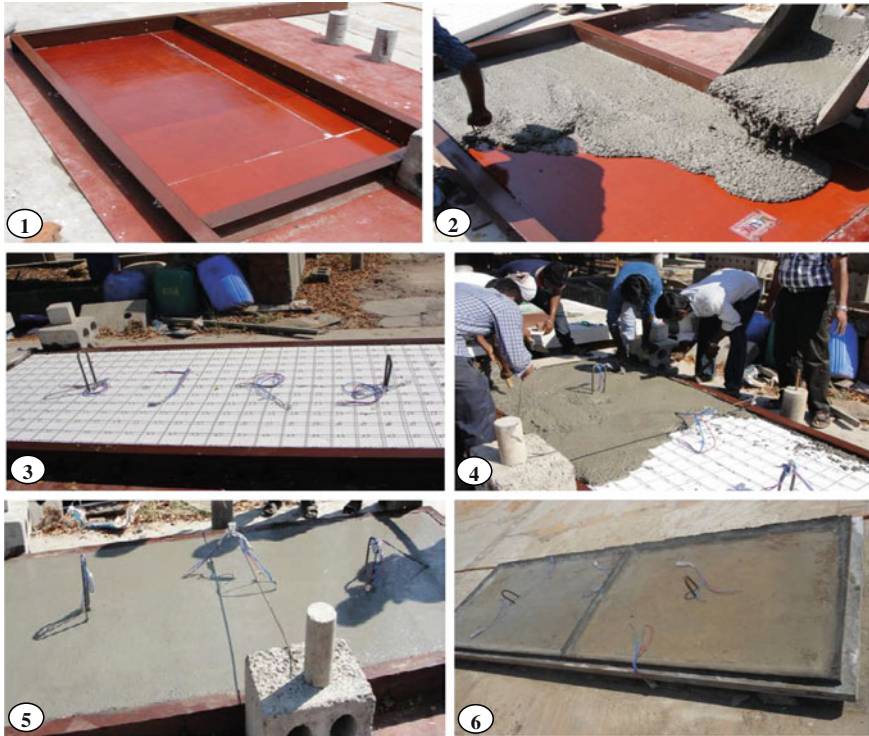


Fig. 1 Sequence of casting a panel

### 3 Numerical Analysis

Static nonlinear numerical analysis was carried out in FE software ABAQUS [14]. Concrete damaged plasticity model was used to simulate the behavior of material concrete. This model takes into consideration the degradation of elastic stiffness, both in tension and compression, by plastic straining of concrete [14]. Concrete is assumed to be isotropic in elastic and inelastic regime both in compression and tension, and the two failure modes assumed are the tensile cracking and crushing under compression [14]. Concrete behavior under compression was modeled using Saenz [15] stress–strain curve. Young’s modulus of concrete was determined using the following equation [16].

$$E = 5000\sqrt{f_{ck}} = 5000\sqrt{45} = 33541\text{-N/mm}^2$$

Tensile behavior of concrete was assumed to be linearly elastic until the failure stress that corresponds to the onset of micro-cracking. The tensile post-peak behavior of concrete was modeled using fracture energy ( $G_f$ ) method. The fracture energy of the concrete was calculated using fib Model Code [17] equation, which is

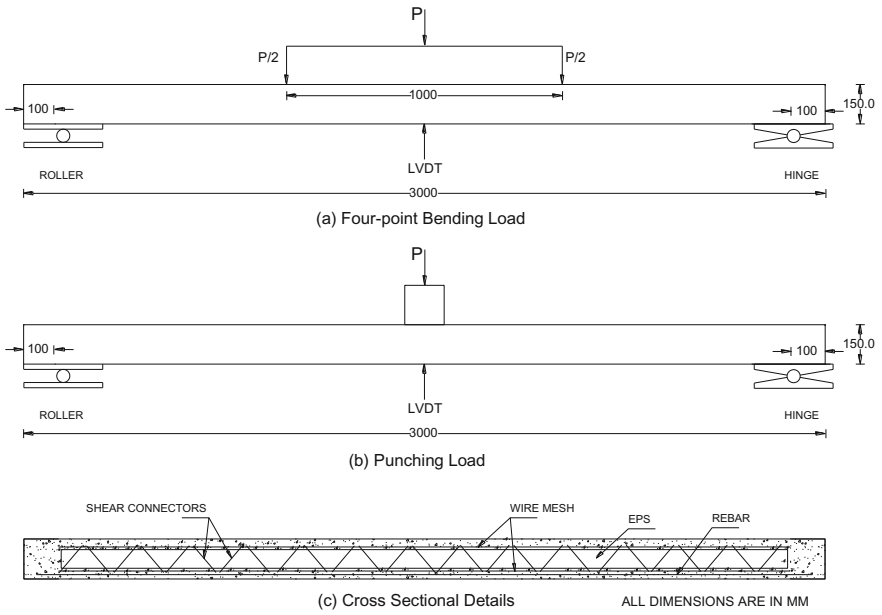


Fig. 2 Schematic diagram of test setup



Fig. 3 Typical panel on test setup

a function of concrete cylinder strength ( $f_{cm}$ ). The concrete cube strength was converted to equivalent cylinder strength by multiplying a factor of 0.8.

Fracture energy,

$$G_f = 73f_{cm}^{0.18} = 73 \times (0.8 \times 45)^{0.18} = 139\text{-Joule/m}^2$$

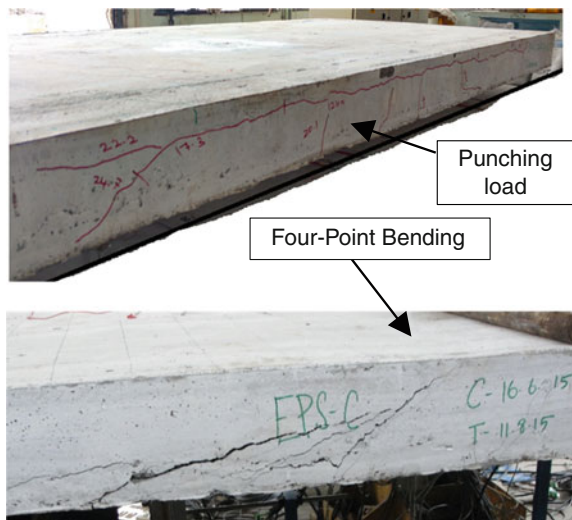
8-noded linear brick elements were used for modeling top and bottom concrete wythes. The wires of the mesh were modeled using 2-noded linear truss elements. Wire meshes were modeled as embedded elements in the concrete wythes and hence, it is inherently assumed in the models that the bond between wire mesh and the concrete was perfect.

### 4 Results and Discussions

In this section, results of the experimental study are presented and discussed first followed by the results of numerical analysis. Figure 4 shows the failed panels.

The panel tested under four-point bending failed by forming inclined shear cracks wherein the panel tested under punching load failed by forming flexural cracks in bottom wythe. It is noted that slabs are not generally governed by the shear failure. Nevertheless, it is found from the present experimental study that the concrete sandwich panel failed by forming inclined cracks that tend to join loading point and nearest support. After formation of the inclined cracks, when the applied load is increased, the width of the inclined crack increased without forming new flexural cracks in the panel. In the case of panel tested under punching load, horizontal cracks along the longitudinal direction at EPS-concrete interface were

Fig. 4 Tested panels



seen. These cracks may be attributed due to negative bending moment developed due to homogenous casting of concrete cover at sides of the panels. The side concrete cover provided partial restraint when top wythe tends to bend along the transverse direction due to punching load. No such cracks were seen in the panel subjected to four-point bending. It is also observed that even though the construction details of both the panels tested are same, ultimate load and ultimate bending moment resisted by the panels under different loading conditions are not same. In general, these observations indicate that the failure mode and flexural behavior of concrete sandwich panels are dependent on type of loading conditions. Figure 5 shows load-deflection curves obtained from the experiments. Corresponding moment-deflection curves are also shown in Fig. 5.

From Fig. 5, it is observed that the panel behavior under both loading conditions considered may be assumed as linear up to 8-kN of applied load magnitude beyond which they behaved nonlinearly until failure. Comparison of load-deflection responses obtained from the experimental and numerical analysis is shown in Fig. 6.

In general, it is observed that the numerical analysis is able to predict the different flexural behavior of concrete sandwich panels under different loading conditions. However, it is to be noted that the finite element models are stiffer compared to experimental analysis. The reasons for this may be attributed to micro-cracks, and possible creep and shrinkage cracks present in panels tested are not considered in the models. Also, possible weld failure at nodes where wire mesh and shear connectors are not considered in finite element models.

In numerical analysis, the tensile strength of concrete was chosen so as to get load-deflection response closer to experimental results. This is due to the fact that the concrete wythes are thin compared to the prism used to determine the flexural strength of the concrete. Also, it is reported that, reduction in tensile strength of

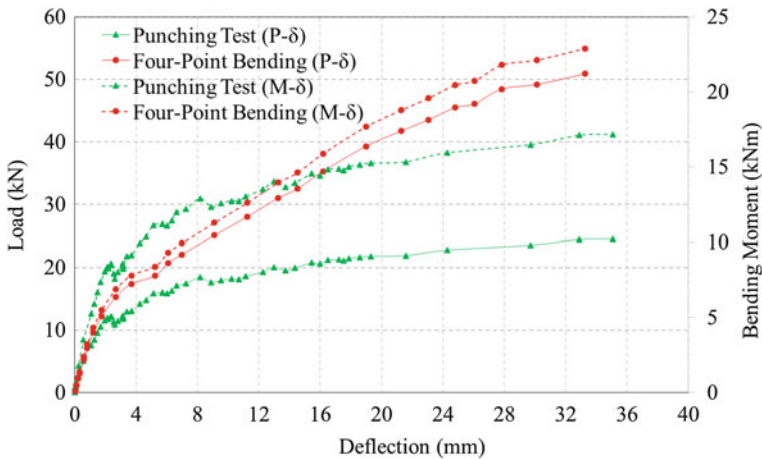


Fig. 5 Load-deflection curves

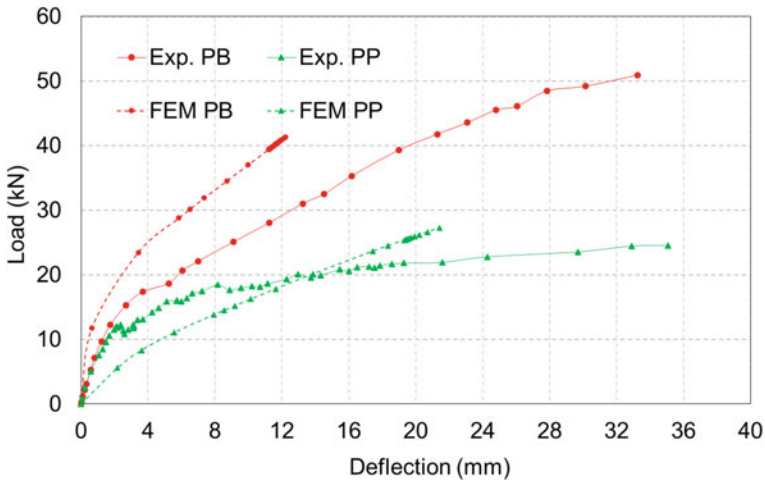


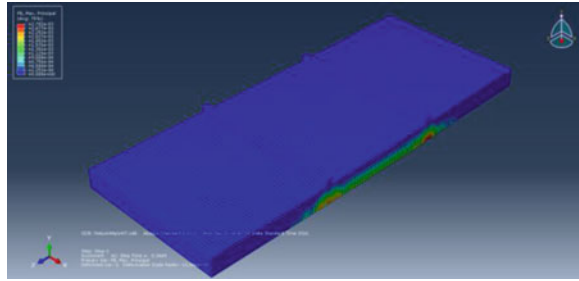
Fig. 6 Comparison of experimental and numerical load–deflection responses

concrete is expected due to size effect [18]. The plastic strain distributions that represent cracking pattern in the panels are shown in Fig. 7.

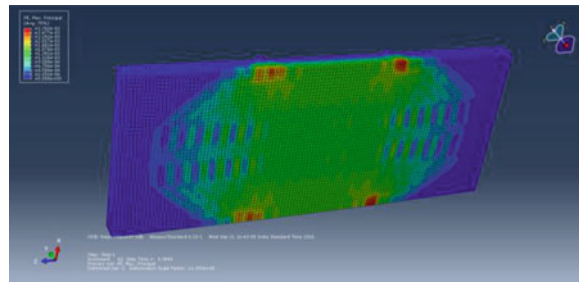
### 5 Summary and Conclusions

Experimental and numerical studies carried out to understand the flexural behavior of concrete sandwich panels under different loading conditions such as four-point bending and punching load are presented and discussed in this paper. Experimental study indicated that the flexural behavior of concrete sandwich panels is significantly affected by the type of loading conditions. The panel tested under punching load failed by forming flexural cracks whereas the panel tested under four-point bending failed by forming inclined shear cracks. Numerical studies indicated that the finite element models developed are able to predict the load–deflection responses of the panels under different loading conditions comparable to experimental results. Further experimental and numerical studies are required in this area toward developing general design guidelines.

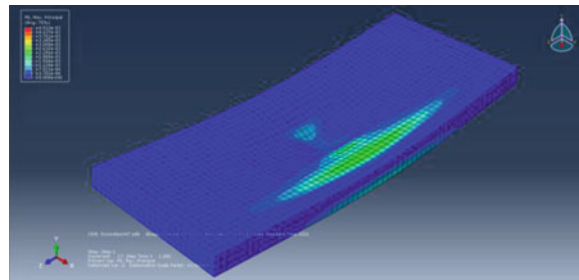
**Fig. 7** Plastic strain distributions obtained from numerical analysis



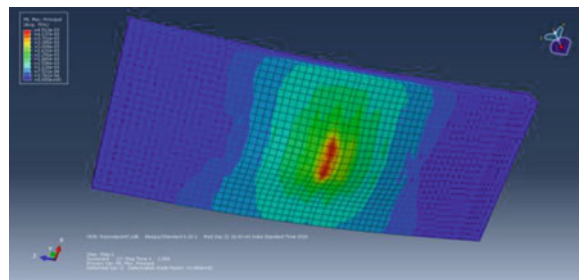
**(a) Four-Point Bending Test (Top Wythe)**



**(b) Four-Point Bending Test (Bottom Wythe)**



**(c) Punching Load Test (Top Wythe)**



**(d) Punching Load Test (Bottom Wythe)**

## References

1. Yee AA (1976) Prestressed concrete for buildings. *PCI J* 24(5):112–157
2. Yee AA, Nai KC (1984) One hundred Washington square: structural design and construction. *PCI J* 29(1):24–48
3. Yee AA (1991) Design considerations for precast prestressed concrete building structures in seismic areas. *PCI J* 36(3):40–55
4. Yee AA (2001) Structural and economic benefits of precast/prestressed concrete construction. *PCI J* 46(4):34–42
5. Yee AA (2001) Social and environmental benefits of precast/prestressed concrete construction. *PCI J* 46(3):14–19
6. Bush TD, Stine GL (1994) Flexural behaviour of composite precast concrete sandwich panels with continuous truss connectors. *PCI J* 39(2):112–121
7. Einea A, Salmon DC, Tadros MK, Culp T (1994) A new structurally and thermally efficient precast sandwich panel system. *PCI J* 39(4):90–101
8. Salmon DC, Einea A (1995) Partially composite sandwich panel deflections. *ASCE J Struct Eng* 121(4):778–783
9. Salmon DC, Einea A, Tadros MK, Culp TD (1997) Full scale testing of precast concrete sandwich panels. *ACI Struct J* 94(4):354–362
10. Benayoune A, Samad AAA, Trikha DN, Ali AAA, Ellinna SHM (2008) Flexural behavior of pre-cast concrete sandwich composite panel—experimental and theoretical investigations. *J Constr Build Mater* 22:580–592
11. Gara F, Ragni L, Roia D, Dezi L (2012) Experimental tests and numerical analysis of floor sandwich panels. *Eng Struct* 36:258–260
12. ACI 237R-07 (2007) Self consolidating concrete, ACI Committee 237
13. IS 516:1959 (2002) Methods of tests for strength of concrete. Bureau of Indian Standards
14. ABAQUS/Standard User's Manual for Version 6.10
15. Saenz LP (1964) Discussion of “Equation for stress-strain curve of concrete” by Desayi P, Krishnan S. *ACI Struct J* 61:1229–1235
16. IS 456:2000 (2005) Plain and reinforced concrete—code of practice, Bureau of Indian Standards
17. Fib Model Code for concrete structures. Ernst & Sohn, 2010
18. Carpinteri A, Chiaia B, Ferro G (1995) Size effects on nominal tensile strength of concrete structures: multifractality of material ligaments and dimensional transition from order to disorder. *Mater Struct* 28:311–317

# Bond Behaviour of Externally Bonded FRP Under Cyclic Loading



G. Ramesh, Ravindra Gettu and B. H. Bharatkumar

**Abstract** Strengthening of concrete structures through external bonding of fibre-reinforced polymer (FRP) composites has become a popular technique due to its advantages such as strength-to-weight and stiffness ratios, etc. In this investigation, a test method similar to RILEM TC-RC5 (used to evaluate the bond strength of rebars in concrete) is extended to evaluate bond behaviour of externally bonded FRP sheets. In the present study, experimental investigations on two types of FRP composites (with carbon and glass fibres) have been carried out, and the tensile force on the FRP versus bond–slip response has been evaluated. Both monotonic and cyclic loadings have been carried out to study the envelope response and debonding process for the chosen bond length and width. The average ultimate slip for CFRP and GFRP for selected bond length under monotonic loading was 2.28 and 2.03 mm, respectively, and in the case of cyclic loading was 1.95 and 1.76 mm, respectively. The reduction in the bond–slip under cyclic loading is due to partial debonding of FRP during repeated loading and unloading cycles.

**Keywords** Bond cyclic · Envelope curve · Bond–slip · Epoxy-concrete interface Debonding

## 1 Introduction

Externally bonded fibre-reinforced polymer (EBFRP) laminates or sheets have been used for strengthening, repair, and retrofitting for more than three decades. EBFRP sheets have benefits such as high strength-to-weight ratio, high stiffness-to-weight ratio, corrosion resistance, easy handling and can be moulded into any shape. The failure of the FRP strengthened RC flexural member is often controlled by the

---

G. Ramesh (✉) · B. H. Bharatkumar  
CSIR-Structural Engineering Research Centre, Chennai 600113, India  
e-mail: grm@serc.res.in

R. Gettu  
Indian Institute of Technology, Madras, Chennai 600036, India

© Springer Nature Singapore Pte Ltd. 2019  
A. Rama Mohan Rao and K. Ramanjaneyulu (eds.), *Recent Advances in Structural Engineering, Volume 2*, Lecture Notes in Civil Engineering 12,  
[https://doi.org/10.1007/978-981-13-0365-4\\_67](https://doi.org/10.1007/978-981-13-0365-4_67)

783



debonding (peeling of the fibre) of FRP from the concrete substrate rather than by crushing of concrete or by tensile rupture of FRP [1–5]. Since the behaviour of EBFPR strengthened members depends on the bonding of FRP to concrete interface and the characteristics of the concrete substrate, it is useful to characterize the bond response adequately.

Many available test methods for the evaluation of FRP bond behaviour are based on single and double shear pull out type of tests [6–10], which do not simulate flexure. To overcome this limitation, a method similar to RILEM TC-RC5 [11–14] (used to evaluate bond strength of rebar in concrete) is used in the present investigation to evaluate the bond behaviour of EBFPR sheets. In this study, the effect of cyclic loading on bond behaviour of FRP strengthened elements has also been evaluated. The experimental results are used to compare the bond behaviour of carbon and glass fibre sheets at the FRP-concrete interface under monotonic and cyclic loading.

## 2 Experimental Details

### 2.1 Materials Used

CFRP and GFRP sheets with unidirectional fibres were used in the study along with the epoxy resin recommended by the manufacturer. The fibre properties given by the manufacturer are shown in Table 1. Steel fibre-reinforced concrete, with a characteristic compressive strength of 50 MPa, was used in this study to cast the test specimens; the steel fibres were used to prevent diagonal shear cracking of the concrete.

Before bonding the FRP to the concrete, the surface was roughened with a powered wire brush. The initial primer coat was applied over the bonded surface to fill the voids and make the surface even. The fibre sheets were saturated with the prescribed epoxy, and the saturated sheet was pressed on to the concrete surface. The pressure was applied using a ribbed roller to ensure the penetration of epoxy between the fibres.

**Table 1** Properties of fibres

Data are given by the manufacturer	E-glass	Carbon
Thickness of the fibre, gsm	900	230
Modulus of elasticity, kN/mm <sup>2</sup>	73	240
Tensile strength, N/mm <sup>2</sup>	3400	3800
Density, g/cm <sup>3</sup>	2.6	1.7
Ultimate strain, %	4.5	1.6

## 2.2 Test Details

The method proposed by RILEM TC-RC5 [7] for assessing bond characteristics of conventional steel rods was adopted with minor modifications in the size of the test specimens. The geometry, test configurations, and schematic of bonded region are shown in Fig. 1. Two separate concrete blocks, designated as A and B, are interconnected by means of a mild steel hinge arrangement located at the central portion of the specimen. At the bottom portion of the specimen, 50-mm-wide FRP composites are bonded over a length of 100 mm. The test region was always kept in block A in this investigation, whereas the FRP bonded to block B is firmly fixed to trigger the failure in the bonded region of A only. The test specimen is placed in a three-point bending frame with a load capacity of 500 kN under piston displacement control mode. The rate of loading was about 0.05 mm/min until failure.

Figure 2 shows the typical test setup. The FRP was instrumented with four strain gauges of 5 mm length at the locations referred to as S1, S2, S3, and S4 (see Fig. 3). Two linear variable differential transformers (LVDTs) with 25 mm span were used for measuring the loaded end slip. In this study, slip refers to the movement of the FRP sheet relative to the concrete. The cyclic test methodology involves two loading and two unloading cycles at each strain level. In this programme, the signal from one of the strain gauges fixed in the bonded zone was used as the controlling parameter for the loading and the reloading cycles. The specimen was loaded until the strain of SG1, the first strain gauge (i.e., nearest to the hinged face), reached a value of 1000 microstrains then unloaded. The reloading point for each unloading cycle was about 1.0 kN. Two loading and two unloading cycles were performed before continuing the loading until 2000 microstrain, when the unloading-reloading is repeated. So on, for every 1000 microstrain increment, till the subsequent strain gauge SG2 reaches 1000 microstrain. When the strain of SG2, the second strain gauge, reaches the strain level of 1000 microstrains, subsequent

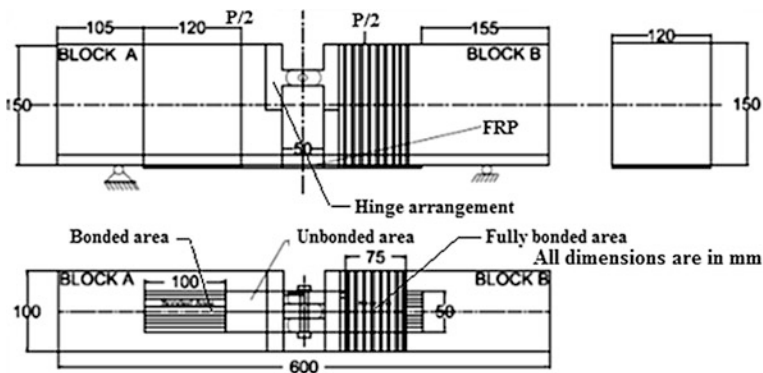


Fig. 1 Specimen geometry and test configuration of modified RILEM TC-RC-5 (1982)



**Fig. 2** Closer view of test setup

cycles were done on the basis of the strain in the second gauge. This was continued till the strains in SG3 and SG4, the third and fourth strain gauges, reached 1000 microstrains. All the sensors were monitored with a data logger.

### **3 Discussions of Test Results**

#### **3.1 Failure Pattern (Cyclic)**

The failure in CFRP-bonded specimens in Series I (with 100 mm bond length) was by peeling and some cracking of the FRP, with debonding in the adhesive layer or in the concrete. Typical debonded specimens can be seen in Fig. 4. Failure occurred along the FRP-epoxy interface or along the concrete-epoxy interface. The CFRP-bonded specimen failed suddenly with an explosive sound, while in the GFRP-bonded specimens, the failure was progressive. The debonded surfaces are shown in Figs. 4 and 5. The failure in CFRP-bonded specimens was peeling and fracture of FRP with explosive sound, while the failure in GFRP-bonded specimen was progressive debonding.

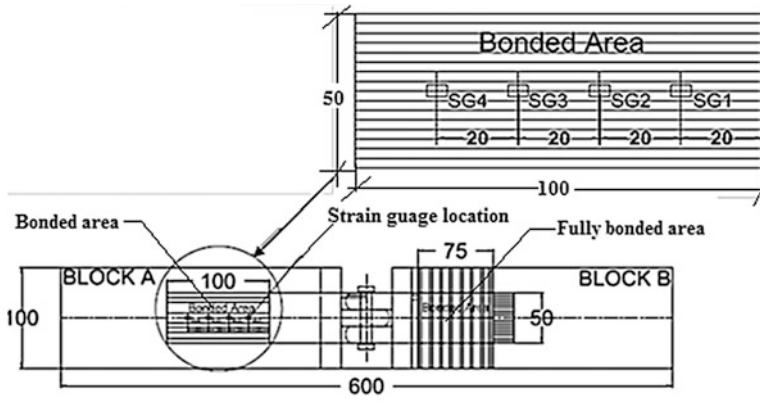


Fig. 3 Typical positioning of strain gages for 100 mm bond length and 50 mm bond width



Fig. 4 Failure in CFRP-bonded specimens (50-100-C)



Fig. 5 Failure in GFRP-bonded specimens (50-100-G)

### 3.2 Monotonic Result Tensile Pullout Force on FRP—Bond–Slip Behaviour

Parameters such as the average maximum tensile force on fibre, peak bond shear stress or bond strength ( $\tau_{\text{umax}}$ ) and average ultimate deflection for each series of specimens have been obtained and reported in Table 2. Figures 6 and 7 show the load–bond–slip behaviour of the CFRP- and GFRP-bonded specimens. The average data from the two LVDTs are used to calculate the bond–slip. It was seen that the average ultimate slip was higher for carbon FRP when compared to glass FRP; the ultimate slip for CFRP is 2.28 mm and for GFRP is 2.03 mm. The average bond pullout force developed, from the three tests, for CFRP is 214 N/mm and for GFRP is 226 N/mm.

### 3.3 Cyclic Result Tensile Pullout Force on FRP—Bond–Slip Behaviour

Figures 8 and 9 show the evolution of the cyclic bond–slip at the loaded end and the tensile force on FRP. Parameters such as the average maximum tensile force on fibre, peak bond shear stress or bond strength ( $\tau_{\text{umax}}$ ) and average ultimate deflection for each series of specimens have been obtained and reported in Table 2. From the experimental bond versus slip curve, it is observed that the curve consists of three regimes. The first part is linear up to a load level of 50–60% of the maximum load attained from the specimen. The tensile force versus slip response has an initial linear regime up to about 6 kN, after which the load increases with a decreasing slope until failure occurs. Beyond that, there is some nonlinearity, at which stage debonding starts from the loaded end. Subsequently, complete debonding occurs throughout the bond length. In the final stage, sudden failure occurs. The maximum tensile force on unit width of CFRP and GFRP was 214 and 226 N/mm, respectively, under monotonic loading and was 212 and 223 N/mm, respectively, under cyclic loading. The influence of cyclic loading is not affecting the tensile forces on FRP much in both the glass and carbon fibres. The tensile force

**Table 2** Parameters of experimental bond–slip loads for monotonic and cyclic loading (mean and std. deviation)

Series	Specimens	Maximum tensile force on unit width of FRP (N/mm)	Bond strength (MPa/mm)	Bond–slip, $\delta_f$ (mm)
I (mono)	50-100-C-1,2,3	214±0.02	0.042±0.02	2.28±0.22
II (mono)	50-100-G-1,2,3	226±0.81	0.045±0.16	2.03±0.46
I (cyc)	50-100-C-1,2,3	212±0.01	0.041±0.004	1.95±0.05
II (cyc)	50-100-G-1,2,3	223±0.02	0.044±0.002	1.76±0.08

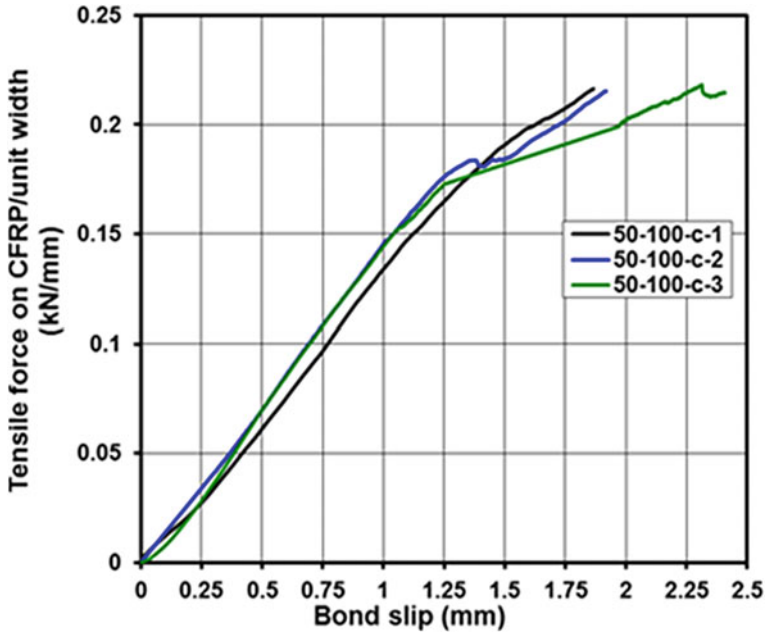


Fig. 6 Tensile force on FRP with slip in CFRP-bonded specimens

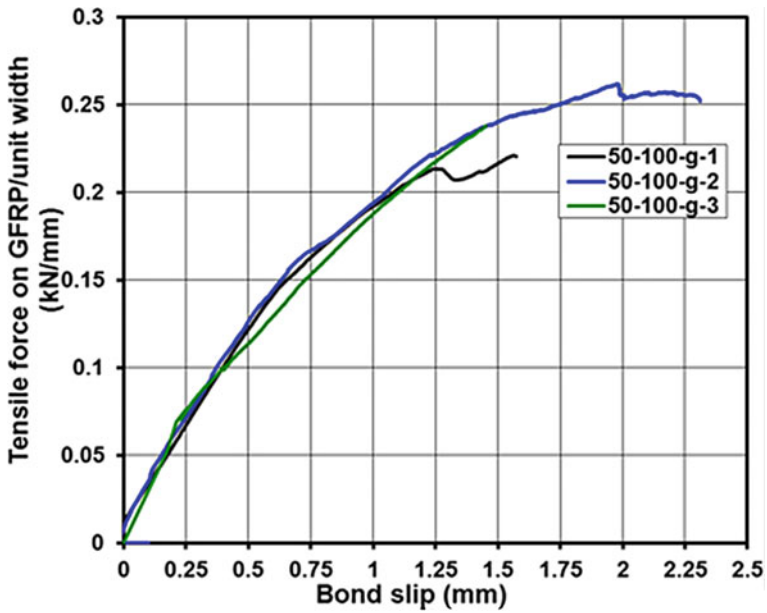


Fig. 7 Tensile force on FRP with slip in GFRP-bonded specimens

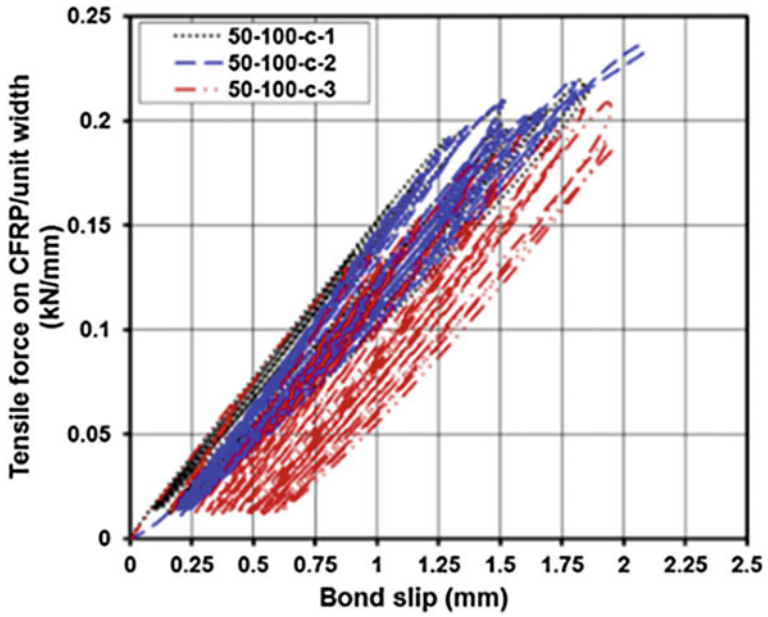


Fig. 8 Cyclic tensile force on FRP with slip in CFRP-bonded specimens

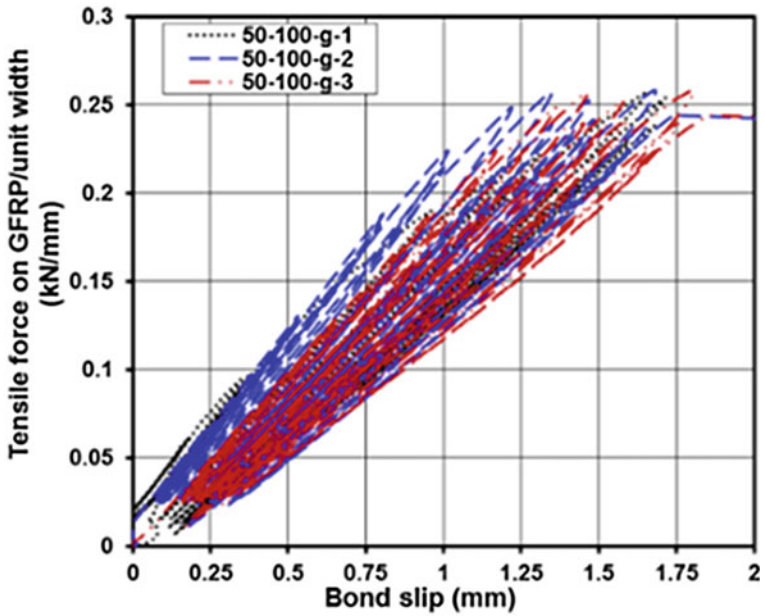


Fig. 9 Cyclic tensile force on FRP with slip in GFRP-bonded specimens

on FRP is not influenced by the type of FRP. This may be due to the fact that the bond behaviour is fully dependent on the interface between the concrete and epoxy.

The average ultimate slip for CFRP and GFRP under monotonic loading was 2.28 and 2.03 mm, respectively, and in the case of cyclic loading was 1.95 and 1.76 mm, respectively. From the experimental observations, it was found that there was a reduction in bond–slip under cyclic loading which is due to partial debonding of FRP due to repeated loading and unloading cycles. The unloading and reloading cycles in this investigation were performed in the pre-peak and post-peak regime to study the bond–stiffness degradation. Stiffness is defined as the slope of the line connecting the points corresponding to the beginning of the unloading and reloading. Bond stiffness is purely governed by friction between the bond surface (concrete), FRP fibre, and the epoxy interface. In the pre-peak region, there is no much degradation in stiffness in the both carbon and glass fibres in the unloading and reloading cycles. In the pre-peak, the number of cycles is not having any influence on debonding due to cyclic loading. The residual bond–slip in the unloading and reloading is minimal for the chosen bond length and width. After reaching the post-peak, the stiffness decreases significantly. This can be attributed to the progressive debonding of the CFRP epoxy and epoxy-concrete interfaces up to the peak force. At that stage, bond between the bond surface and FRP loses friction leads to increase in the bond–slip.

The cyclic tensile force on the fibre versus bond–slip curve traces the monotonic curve till failure in both the carbon and glass fibre. In the strain-based cyclic loading, the tensile force on FRP versus bond–slip traces the monotonic response. In the case of the CFRP-to-concrete joints, for the same cyclic behaviour, lower maximum slip values were observed for GFRP-bonded joints. Similar behaviour is observed for the monotonic specimens in GFRP. The effect of repeated loading and unloading leads to decrease in maximum ultimate slip for both the CFRP- and GFRP-bonded joints for the selected bond length and width. Similar observations were made by Ko and Sato [15] that the monotonic response envelope coincides with the cyclic curves; they also observed that plastic displacement and reduction in stiffness were observed due to partial debonding imposed by repeated unloading and reloading cycles. In terms of bond–slip GFRP, bonded specimens shows significant improvement compared to the CFRP specimens in both the cyclic and monotonic loading.

### 3.4 *Envelope Curve*

Figures 10 and 11 show the cyclic response in terms of the tensile force per unit width of FRP versus bond–slip along with the monotonic response. It can be seen that there is a close correspondence between the load envelope obtained from the monotonic tests and the cyclic response. The envelope curve of cyclic response in terms of tensile force per unit width of FRP versus bond–slip follows the monotonic response till 90% of failure load.



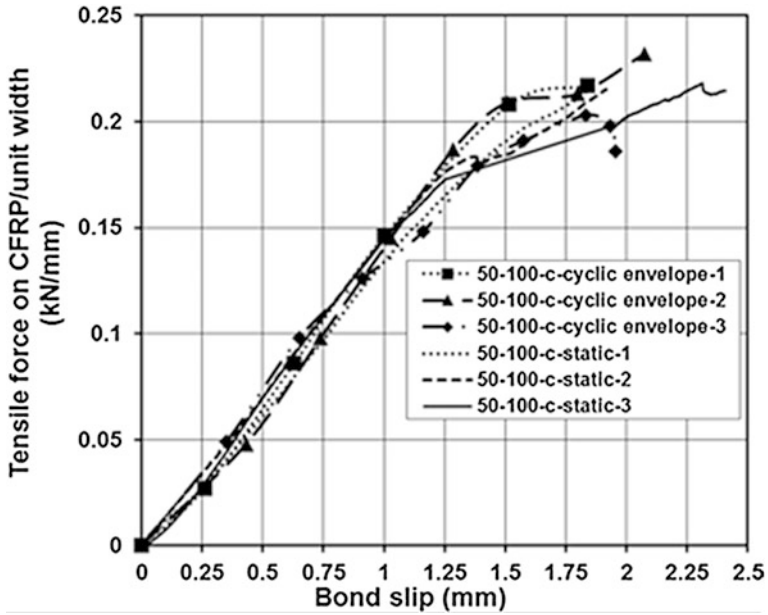


Fig. 10 Cyclic and static tensile force versus with slip in CFRP-bonded specimens

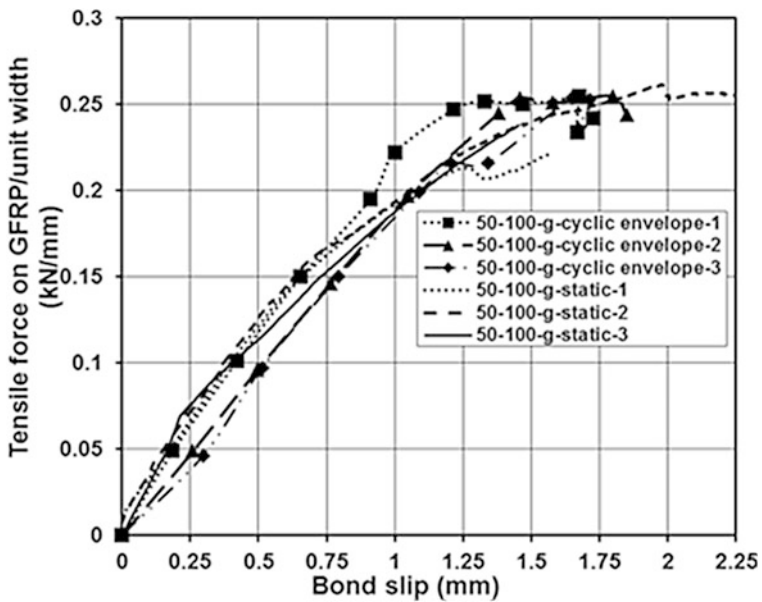
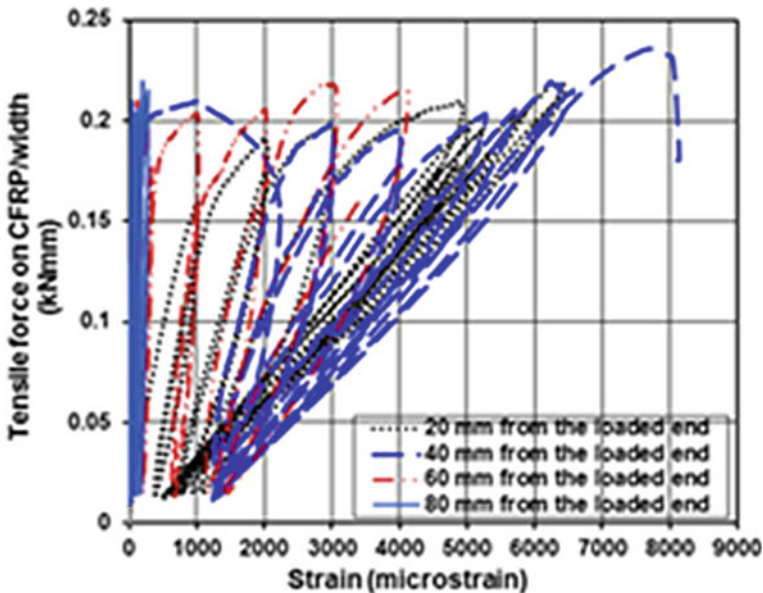


Fig. 11 Cyclic and static tensile force versus with slip in GFRP-bonded specimens

#### 4 Cyclic Strain Distribution of CFRP- and GFRP-Bonded Specimens

Figures 12 and 13 show the tensile force on FRP per unit width versus strain plot of both CFRP- and GFRP-bonded specimens. Strain cycle and the increment of successive strains from all four strain gauges observed during first strain cycles at 1000  $\mu\epsilon$  interval in the first strain gauge reach about 60–70% of debonding force on FRP, and subsequent debonding of FRP sheet (50-100-C) is reported till the second strain gauge reaches the 1000  $\mu\epsilon$  target. Similarly, strain evolution during second strain gauge 1000  $\mu\epsilon$  interval cycles at 85% of debonding force and subsequent debonding for FRP sheet is reported in till the third strain gauge reaches the 1000  $\mu\epsilon$  interval. In the third strain gauge, 1000  $\mu\epsilon$  strain cycle the debonding force is 95% of the tensile force on FRP. Finally, the fourth strain gauge reaches less than 500–700  $\mu\epsilon$  complete debonding occurred in the FRP sheet. FRP strains are very regular showing an exponential decay starting from the loaded section. From the strain distribution, it can be seen that, at early stages of loading, the curves show linear behaviour in the loaded end. It can be assumed that bond failure begins immediately after the point when the curve becomes parabolic shape and leads to uniform distribution of bond stress along the CFRP and GFRP sheet. As expected,



**Fig. 12** Typical cyclic experimental tensile force on FRP per unit width versus strain for externally bonded CFRP specimens

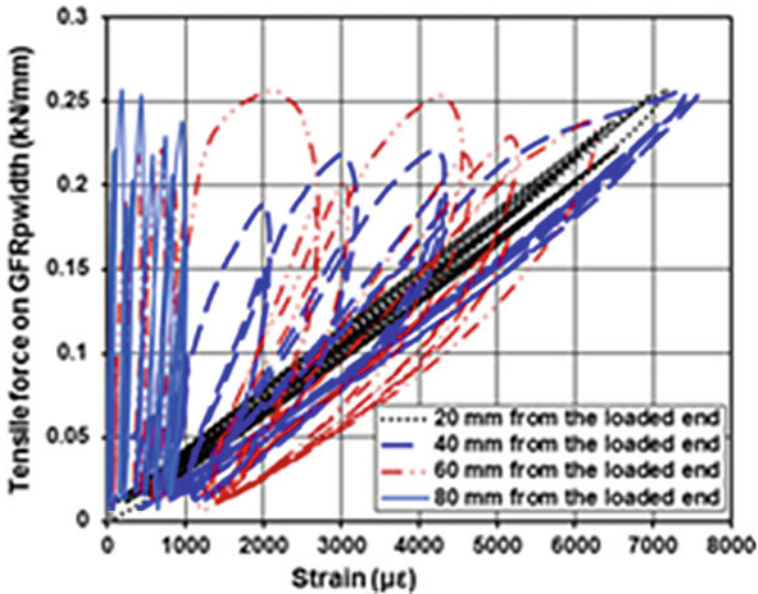


**Fig. 13** Typical cyclic experimental tensile force on FRP per unit width versus strain for externally bonded GFRP specimens

the ultimate slip of CFRP sheet is higher with respect to GFRP ones, but the tensile force on FRP observed during the strain cycles is comparable with that seen under monotonic loading.

## 5 Conclusions

A simple beam bending test was designed for evaluation of FRP bond behaviour by modifying the RILEM TC-85 recommendation for rebar bond test. The following conclusions were drawn from the study carried out for selected bond length and width of FRP bonding under monotonic and cyclic loading:

- The failure in CFRP-bonded specimens was peeling and fracture of FRP with an explosive sound, while the failure in GFRP-bonded specimen was progressive debonding.
- The maximum tensile force on unit width of CFRP and GFRP was 214 and 226 N/mm, respectively, under monotonic loading and was 212 and 223 N/mm, respectively, under cyclic loading. The tensile force on FRP is not influenced by the type FRP. This may be due to the fact that the bond behaviour fully is dependent on the interface between the concrete and epoxy.

- The average ultimate slip for CFRP and GFRP under monotonic loading was 2.28 and 2.03 mm, respectively, and in the case of cyclic loading was 1.95 and 1.76 mm, respectively. The lower slip under cyclic loading is due to partial debonding of FRP due to repeated loading cycles.
- The envelope curve of cyclic response in term of tensile force per unit width of FRP versus bond–slip follows the monotonic response till 90% of failure load.

**Acknowledgements** The author acknowledges the help rendered by the technical staff of Advanced Materials Laboratory, CSIR-SERC.

## References

1. Jones R, Swamy RN, Bloxham J, Bouderalah A (1980) Composite behavior of concrete beams with epoxy bonded external reinforcement. *Int J Cement Compos* 2(2):91–107
2. Van Gemert DA (1980) Repairing of concrete structures by externally bonded steel plates. *Int J Adhes* 2:67–72
3. Oehlers DJ, Moran JP (1990) Premature failure of externally plated reinforced concrete beams. *J Struct Eng* 116(4):978–995
4. Quantrill RJ, Hollaway LC, Thorne AM (1996) Experimental and analytical investigation of FRP strengthened beam response: part I. *Mag Concr Res* 48(177):331–342
5. Triantafillou TC, Plevris N (1992) Strengthening of RC beams with epoxy-bonded fiber-composite materials. *Mater Struct* 25:201–211
6. Chajes MJ, Finch WW Jr, Januszka TF, Theodore Thomson A Jr (1996) Bond and force transfer of composite material plates bonded to concrete. *ACI Struct* 93(2):209–217
7. RILEM TC-RC5 (1982) Bond test for reinforcement steel. 1. Beam test. *Mater Struct* 6(32):213–217
8. Yao J, Teng JG, Chen JF (2005) Experimental study on FRP-to-concrete bonded joints. *J Compos Eng, Part-B* 36(2):99–113
9. Brosens K, Van Gemert D (1997) Anchoring stresses between concrete and carbon fibre reinforced laminates. In: *Non-metallic (FRP) reinforcement for concrete structures*, vol 1. Japan Concrete Institute, pp 271–278
10. Bizindavyi L, Neale KW (1999) Transfer lengths and bond strengths for composites bonded to concrete. *J Compos Constr* 3–4:153–160
11. De Lorenzis L, Miller B, Nanni A (2001) Bond of FRP laminates to concrete. *ACI Mater* 98(3):256–264
12. Miller B, Nanni A (1999) Bond between carbon fiber reinforced polymer sheets and concrete. In: Bank LC (ed) *Proceedings ASCE 5th materials congress*, New York, pp 240–247
13. Harmon TG, Kim YJ, Kardos J, Johnson T, Stark A (2003) Bond of surface-mounted fiber-reinforced polymer reinforcement for concrete structures. *ACI Struct J* 100(5):557–564
14. Ramos G, Casas JR, Alarcón A (2006) Normalized test for prediction of debonding failure in concrete elements strengthened with CFRP. *J Compos Constr* 10(6):509–519
15. Ko H, Sato Y (2007) Bond stress–slip relationship between FRP sheet and concrete under cyclic load. *J Compos Constr* 11(4):419–426

# Exact Analysis of Layered Plates Using Mixed Form of Hooke's Law



**Ambadas Waghmare, Daniel Koothoor, Dhruv Shah, Kinal Bid, Raghav Agarwal, Rahul Ghadwal, Snehal Sonawane, Viraj Sanghvi and Abhay Bambole**

**Abstract** Recent applications of composite materials involve the use of thick-section layered and/or sandwich construction. The complexities of composite materials demand extensive analysis techniques to predict the reliable response of even the simplest of loading conditions. Various theories have been developed for exact analysis of laminated composite plates. The present analysis of laminated plate is based on Mixed Form of Hooke's Law. This approach leads one to write the boundary conditions on the top and bottom surfaces of the plate directly in terms of transverse stresses. The advantage of this theory is that equilibrium conditions and other boundary conditions can be enforced in a simplistic manner so that realistic behavior of layered plates can be predicted.

**Keywords** Exact analysis · Mixed form of Hooke's Law

## 1 Introduction

Fiber-reinforced layered composites are often used in structural members due to better stiffness-to-weight and strength-to-weight ratios than those of conventional monolithic materials. The advantages of layered plates are their high strength-to-weight and stiffness-to-weight ratios, high thermal stability, excellent resistance to environmental and corrosion attack, and high fatigue strength. In addition, these materials can be concurrently designed while designing the structure. However, inherent complexities of composite materials call for detailed analysis techniques to measure the response to different loading conditions.

---

A. Waghmare · D. Koothoor · D. Shah · K. Bid  
R. Agarwal · R. Ghadwal · S. Sonawane · V. Sanghvi  
Department of Civil Engineering, VJTI, Mumbai, India  
e-mail: agarwal59.raghav@gmail.com

A. Bambole (✉)  
Department of Structural Engineering, VJTI, Mumbai, India  
e-mail: anbambole@vjti.org.in

Exact three-dimensional analysis and solutions for simply supported layered plates are of integral importance to predict the exact stresses and displacements of the plates. Moreover, these solutions can be used to validate the accuracy of other numerical methods, such as Finite Element Method as presented by Demasi [1].

Various theories and models have been developed from classical plate theory, shear deformation theories, layerwise theories, and elasticity solutions to 3-D continuum theories for stress analysis of laminated composites and sandwich plates. Kant et al. [2] formulated a two-point boundary value problem for a three-dimensional (3-D) laminate. The problem was governed by a set of first-order coupled ordinary differential equations in terms of displacements and the transverse stresses through the thickness of the laminate. Vinson and Chou [3] and Reddy [4] have presented a historical account of the anisotropic plate analysis using classical and shear deformation theories. A detailed review of the literature related to the structural mechanics of composite plates was presented by Bert and Francis [5], Reddy [4], Mallikarjuna and Kant [6], Altenbach [7], Ghugal and Shimpi [8]. Srinivas et al. [9] have presented elasticity solutions for flexure and free vibration of three-ply laminated plates with isotropic lamina. Srinivas and Rao presented a unified theory for exact solutions of simply supported thick orthotropic rectangular plates and laminates.

This paper compares and validates the results obtained for rectangular single-layered isotropic plates by Mixed Form of Hooke's Law (MFHL) with the analysis of the same by Classical Laminated Plate Theory and addresses exact solution of five-layered isotropic plate subjected to sinusoidal loads.

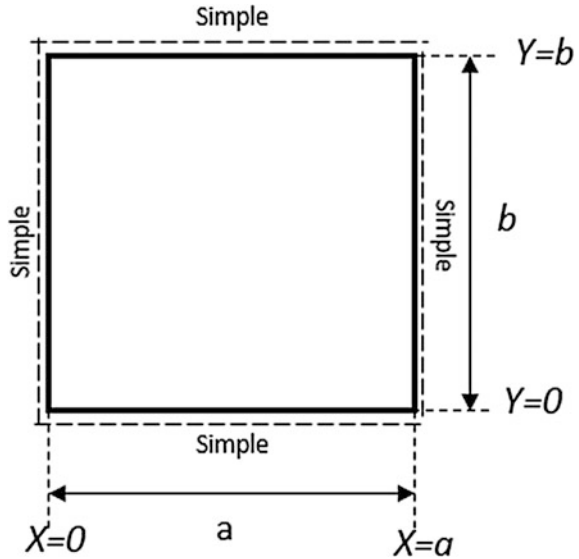
### ***1.1 Advantages of MFHL***

Mixed Form of Hooke's Law helps to evaluate the stresses and displacements of the layered plates by simplifying the stress-strain relation. Boundary conditions are utilized for known input values, to determine the unknown stresses and strains. MFHL not only incorporates displacement conditions, but also interlaminar transverse stress equilibrium and in-plane strains continuity conditions along with surface boundary conditions, implicitly. Thus, MFHL gives accurate results.

## **2 Theoretical Formulation**

A laminate composed of a number of isotropic, linear elastic laminae of uniform thicknesses with plan dimension  $a \times b$ , and thickness ' $h$ ' is considered (Figs. 1 and 2) bounded by the coordinate planes  $x = 0, a, y = 0, b$ , and  $z = -h/2, h/2$ . The plate composed of a finite number  $L$  of homogeneous layers symmetrically disposed with respect to the mid-plane. The layers are considered perfectly bonded. The material of each constituent layer is linearly elastic and isotropic. A normal traction  $\sigma_z = P^z$

**Fig. 1** Simply supported plate



$(x, y)$  is applied on top surface. Let  $u^{(k)}(x, y, z)$ ,  $v^{(k)}(x, y, z)$ ,  $w^{(k)}(x, y, z)$  denote the displacement components of a material point located at  $(x, y, z)$  in the  $k$ th layer of a general laminated plate in the  $x$ -,  $y$ -, and  $z$ -directions, respectively.

Using geometric relations, MFHL becomes:

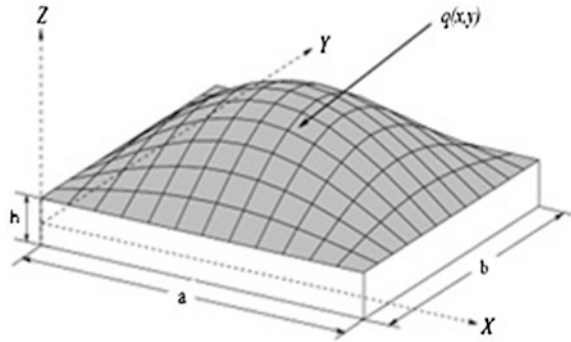
$$\begin{bmatrix} \sigma_p \\ \varepsilon_n \end{bmatrix} = \begin{bmatrix} C_{pp} & C_{pn} \\ C_{np} & C_{nn} \end{bmatrix} \begin{bmatrix} \varepsilon_p \\ \sigma_n \end{bmatrix} \tag{1}$$

On expanding,

$$\begin{bmatrix} \sigma_{xx} \\ \sigma_{yy} \\ \sigma_{xy} \\ \frac{\partial u_x}{\partial x} + \frac{\partial u_x}{\partial z} \\ \frac{\partial u_z}{\partial y} + \frac{\partial u_y}{\partial z} \\ \frac{\partial u_x}{\partial z} \end{bmatrix} = \begin{bmatrix} C_{11} & C_{12} & 0 & 0 & 0 & C_{13} \\ C_{12} & C_{22} & 0 & 0 & 0 & C_{23} \\ 0 & 0 & C_{66} & 0 & 0 & 0 \\ 0 & 0 & 0 & C_{55} & 0 & 0 \\ 0 & 0 & 0 & 0 & C_{44} & 0 \\ -C_{13} & -C_{23} & 0 & 0 & 0 & C_{33} \end{bmatrix} \begin{bmatrix} \frac{\partial u_x}{\partial x} \\ \frac{\partial u_y}{\partial y} \\ \frac{\partial u_x}{\partial y} + \frac{\partial u_y}{\partial x} \\ \sigma_{xz} \\ \sigma_{yz} \\ \sigma_{zz} \end{bmatrix} \tag{2}$$

The displacements and stresses are expressed as a combination of trigonometric functions as given below:

**Fig. 2** Laminated/ sandwiched plate coordinates system and subjected to bi-directional sinusoidal loading



$u^k$  = displacements,

$s^k$  = stresses varying across thickness:  $\sigma_{xz}, \sigma_{yz}, \sigma_{zz}$ ,

$$\left. \begin{aligned} u_x^k(x, y, z^k) &= x U^k(z^k) C_a^{m\pi x} S_b^{n\pi y} \\ u_y^k(x, y, z^k) &= y U^k(z^k) S_a^{m\pi x} C_b^{n\pi y} \\ u_z^k(x, y, z^k) &= z U^k(z^k) S_a^{m\pi x} S_b^{n\pi y} \end{aligned} \right\} \quad (3)$$

$$\left. \begin{aligned} s_x^k(x, y, z^k) &= x S^k(z^k) C_a^{m\pi x} S_b^{n\pi y} \\ s_y^k(x, y, z^k) &= y S^k(z^k) S_a^{m\pi x} C_b^{n\pi y} \\ s_z^k(x, y, z^k) &= z S^k(z^k) S_a^{m\pi x} S_b^{n\pi y} \end{aligned} \right\} \quad (4)$$

where

$$C_a^{m\pi x} = \cos \frac{m\pi x}{a}, C_b^{n\pi y} = \cos \frac{n\pi y}{b}$$

$$S_a^{m\pi x} = \sin \frac{m\pi x}{a}, S_b^{n\pi y} = \sin \frac{n\pi y}{b}$$

The applied pressure at the top surface of the plate is:

$$P_z^t(x, y) = z P^t \sin \frac{m\pi x}{a} \sin \frac{n\pi y}{b} \quad (5)$$

where ‘t’ denotes the top of the layer.

Governing Equation: Because of the variable separability equilibrium, equation can be simplified as below:

$$\left[ \frac{dU^k}{dz} \right] = \frac{dX^k}{dz} = A^k \cdot X^k \quad (6)$$



$$A^k = \begin{bmatrix} 0 & 0 & -\frac{m\pi}{a} C_{55}^k & 0 & 0 \\ 0 & 0 & -\frac{n\pi}{b} C_{44}^k & 0 & 0 \\ \frac{m\pi}{a} C_{13}^k & \frac{n\pi}{b} C_{23}^k & 0 & 0 & C_{33}^k \\ \frac{m^2\pi^2}{a^2} C_{13}^k + \frac{n^2\pi^2}{b^2} C_{66}^k & \frac{mn\pi^2}{ab} C_{12}^k + \frac{mn\pi^2}{ab} C_{66}^k & 0 & 0 & -\frac{m\pi}{a} C_{13}^k \\ \frac{mn\pi^2}{ab} C_{66}^k + \frac{mn\pi^2}{ab} C_{12}^k & \frac{m^2\pi^2}{a^2} C_{66}^k + \frac{n^2\pi^2}{b^2} C_{22}^k & 0 & 0 & -\frac{n\pi}{b} C_{23}^k \\ 0 & 0 & 0 & \frac{m\pi}{a} & \frac{n\pi}{b} \end{bmatrix} \tag{7}$$

$$X^k = c_1^k \overline{X_1^k} \cdot e^{-\frac{m\pi}{a} z^k} + c_2^k \overline{X_2^k} \cdot e^{-\frac{n\pi}{b} z^k} + c_3^k \left( \overline{X_2^k} z^k + \overline{X_3^k} \right) \cdot e^{-\frac{m\pi}{a} z^k} + c_4^k \overline{X_4^k} \cdot e^{\frac{m\pi}{a} z^k} + c_5^k \overline{X_5^k} \cdot e^{\frac{n\pi}{b} z^k} + c_6^k \left( \overline{X_5^k} z^k + \overline{X_6^k} \right) \cdot e^{\frac{m\pi}{a} z^k} \tag{8}$$

To obtain the displacements and stresses of the laminate, the continuity and equilibrium conditions at the interfaces and the transverse stress boundary conditions at the faces surfaces must be satisfied. There are two sets of internal boundary conditions at each interface between the *k*th and (*k* + 1)th layers:

(1) The continuity of displacements

$$\left. \begin{aligned} u^{(k)}(x, y, z) &= u^{(k+1)}(x, y, z) \\ u_y^k(x, y, z^k) &= u_y^{(k+1)}(x, y, z^k) \\ u_x^k(x, y, z^k) &= u_x^{(k+1)}(x, y, z^k) \end{aligned} \right\} \tag{9a}$$

(2) The continuity of transverse stresses

$$\left. \begin{aligned} \sigma_z^{(k)}(x, y, z_k) &= \sigma_z^{(k+1)}(x, y, z_k) \\ \tau_{xz}^{(k)}(x, y, z_k) &= \tau_{xz}^{(k+1)}(x, y, z_k) \\ \tau_{yz}^{(k)}(x, y, z_k) &= \tau_{yz}^{(k+1)}(x, y, z_k) \end{aligned} \right\} \tag{9b}$$

$$X^k \Big|_{z=z^k} = X^{k+1} \Big|_{z=z^{k+1}} \tag{10}$$

Equation (8) is solution for one layer. For five layers, the total solution is obtained by superimposing. It will involve 30 constants. These constants can be found out from boundary condition:

- (a) Displacements and transverse stresses are continuous at the interface. There are 6 \* 4 = 24 equations.
- (b) Stresses at bottom surface = 0. This gives 3 equations.
- (c) Stresses at top surface: one known and other two equal to zero. This gives 3 equations.

It will create a 30 \* 30 simultaneous equation.

### 3 Numerical Results and Discussions

Based on concept of Mixed Form of Hooke’s Law, formulations have been attempted for multilayer laminated plates under bi-directional bending subjected to sinusoidal load. Formulations are applicable to ‘N’ lamina of isotropic laminate subjected to sinusoidal load at any location at top surface. Results obtained from the present formulation have been compared with the available results.

$$\bar{u} = u \frac{E}{p_0 h S^3}, \bar{v} = v \frac{E}{p_0 h S^3}, \bar{w} = w \frac{100E}{p_0 h S^4} \tag{11}$$

Illustrative numerical examples considered in the present work are discussed next.

*Example 3.1* Simply supported single layer (**b = 3a**) isotropic plate subjected to sinusoidal loads has been investigated. Transverse displacement (*w*) for aspect ratios *S* = 4, 10, 20 has been presented in Figs. 3, 5, and 7, respectively. Simultaneously, variation of the in-plane normal stresses ( $\sigma_x$ ) thickness for aspect ratio *S* = 4, 10, 20 has been shown in Figs. 4, 6, and 8, respectively. Maximum values of stress resultants and displacements for various aspect ratios have been tabulated in Tables 1, 2, and 3, respectively. Results obtained using present

**Fig. 3** Displacement (*w*) along thickness using CPT and MFHL for isotropic single-layered plate (*b* = 3*a*) subjected to sinusoidal loading with aspect ratio *S* = 4

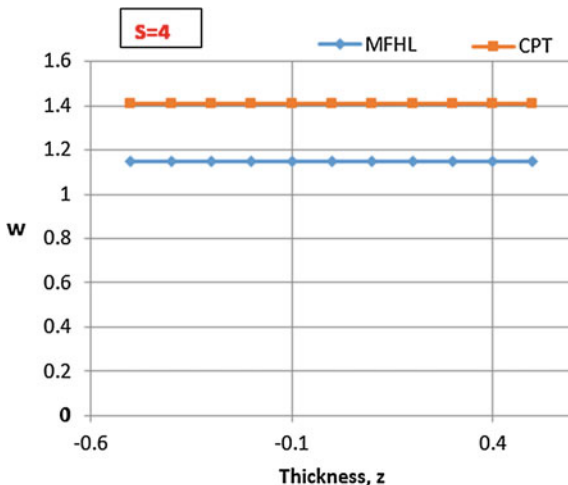


**Fig. 4** In-plane stress along thickness using PT and MFHL for isotropic single-layered plate ( $b = 3a$ ) subjected to sinusoidal loading with aspect ratio  $S = 4$

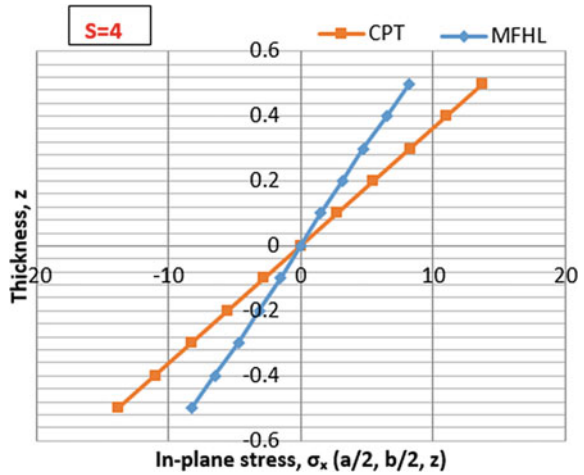
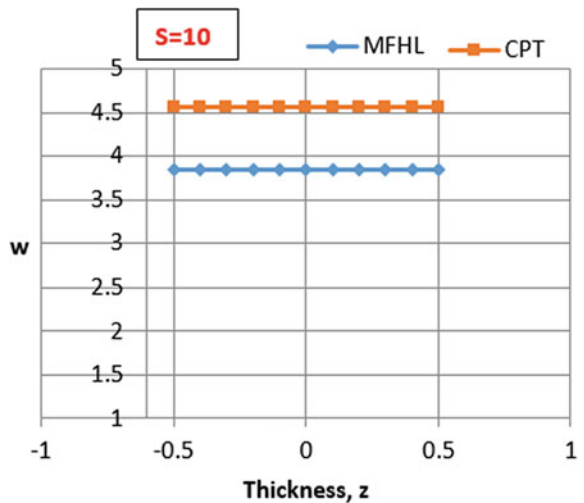


**Fig. 5** Displacement ( $w$ ) along thickness using CPT and MFHL for isotropic single-layered plate ( $b = 3a$ ) subjected to sinusoidal loading with aspect ratio  $S = 10$



formulation are comparable with Classical Plate Theory solutions, thereby validation of logic is attained. Material properties:  $E = 25 \text{ GPa}$ ;  $\nu = 0.25$ . The graphical representation of normalized displacement ( $\bar{w}$ ) with aspect ratio is shown in Fig. 9.

The following results pertain to the analyses based on MFHL run through MATLAB and the Classical Plate Theory  $S = 4, S = 10, S = 20$ .

**Fig. 6** In-plane stress along thickness using CPT and MFHL for isotropic single-layered plate ( $b = 3a$ ) subjected to sinusoidal loading with aspect ratio  $S = 10$

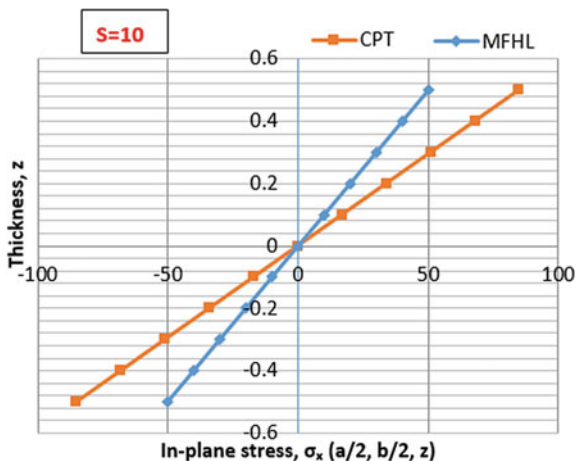
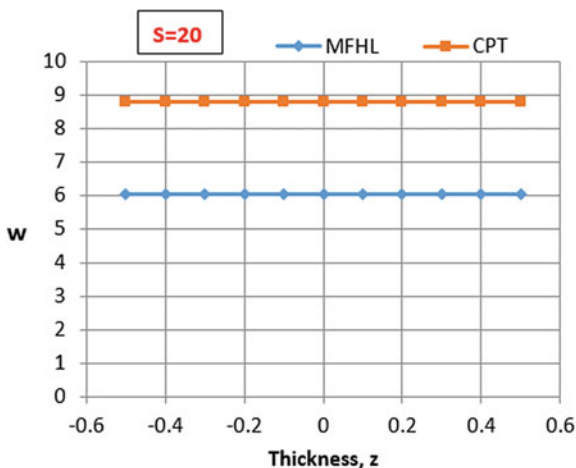


**Fig. 7** Displacement ( $w$ ) along thickness using CPT and MFHL for isotropic single-layered plate ( $b = 3a$ ) subjected to sinusoidal loading with aspect ratio  $S = 20$



*Example 3.2* Simply supported five-layered isotropic plate ( $b = 3a$ ) and  $E_1/E_2 = 25$ ,  $\nu = 0.25$  subjected to sinusoidal loads has been investigated. Transverse displacement ( $w$ ) for aspect ratios  $S = 20$  has been presented in Fig. 10. Simultaneously, variation of the in-plane normal stresses and transverse stresses through the thickness for aspect ratio  $S = 20$  has been shown in Figs. 11, 12, 13 and 14.

The following results pertain to the analyses based on MFHL run through MATLAB and the Classical Plate Theory for  $S = 20$ .

**Fig. 8** In-plane stress along thickness using CPT and MFHL for isotropic single-layered plate ( $b = 3a$ ) subjected to sinusoidal loading with aspect ratio  $S = 20$

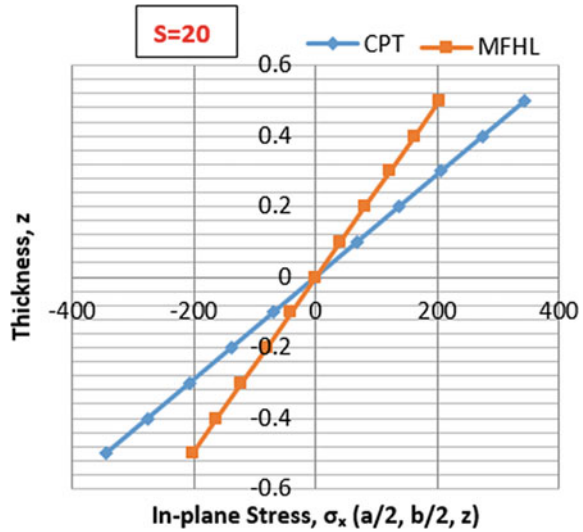


**Table 1** MFHL and CPT results for single layer for  $S = 4$

Method	Displacement ( $w$ ) (m)	In-plane stress ( $\sigma_{xx}$ ) (Pa)
MFHL	$1.15 \times 10^{-9}$	8.244
CPT	$1.41 \times 10^{-9}$	13.735

**Table 2** MFHL and CPT results for single layer for  $S = 10$

Method	Displacement ( $w$ ) (m)	In-plane stress ( $\sigma_{xx}$ ) (Pa)
MFHL	$3.845 \times 10^{-8}$	50.64
CPT	$4.56 \times 10^{-8}$	85.5

**Table 3** MFHL and CPT for single layer for  $S = 20$

Method	Displacement ( $w$ ) (m)	In-plane stress ( $\sigma_{xx}$ ) (Pa)
MFHL	$6.02 \times 10^{-7}$	200
CPT	$8.81 \times 10^{-7}$	343.584

## 4 Conclusion

MFHL formulation for 3-D analysis of layered simply supported rectangular plate and multilayer plate has been developed.

Detailed study of the response of isotropic simply supported rectangular plate and multilayer plate subjected to sinusoidal load revealed for small aspect ratios the response is predominantly 3-D.

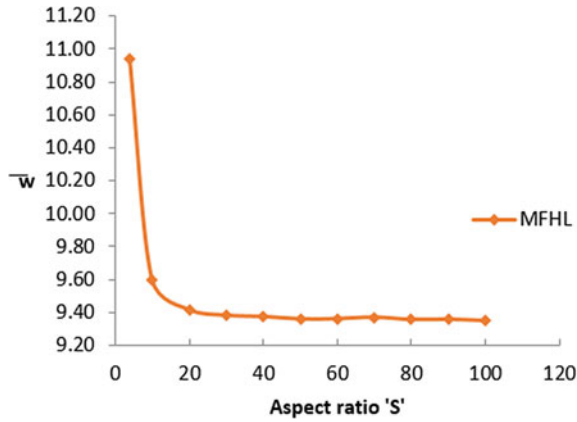


**Fig. 9** Variation of the normalized transverse displacement ( $\bar{w}$ ) with aspect ratio for isotropic single-layered plate ( $b = 3a$ ) subjected to sinusoidal loading

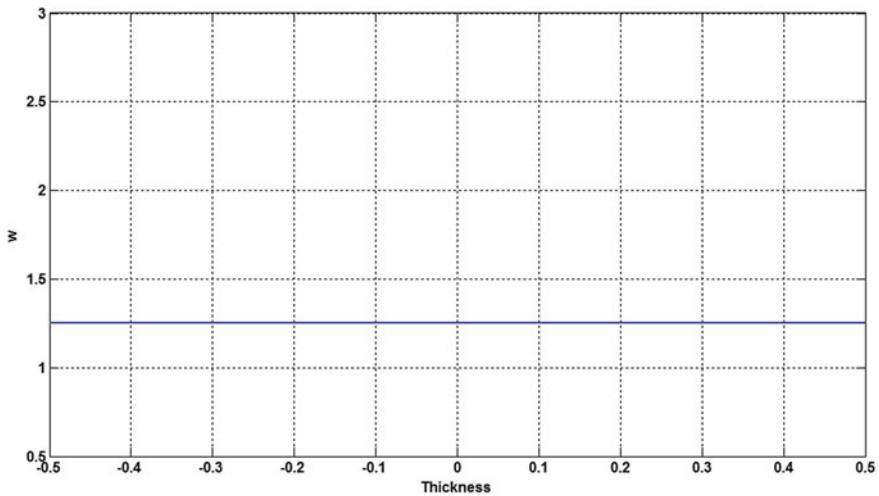


**Fig. 10** Displacement ( $w$ ) along thickness using MFHL for  $S = 20$  for isotropic five-layered plate ( $b = 3a$ ) subjected to sinusoidal loading

As the aspect ratio goes on increasing, the behavior of plates tends to 2-D analysis, which converges with the results obtained from CPT.

Thus, importance of accurate evaluation of 3-D stress state of layered isotropic plates has been established from the results.

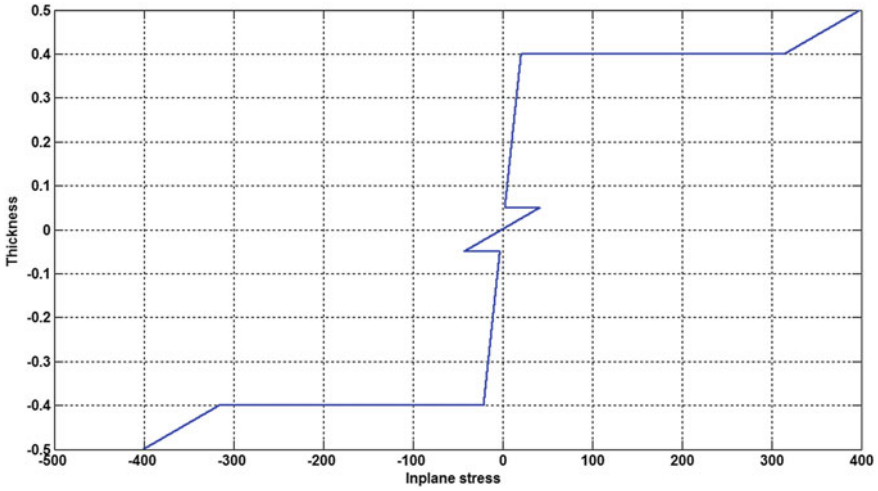


**Fig. 11** In-plane stress  $\sigma_{xx}$  along thickness using MFHL for  $S = 20$  for isotropic five-layered plate ( $b = 3a$ ) subjected to sinusoidal loading

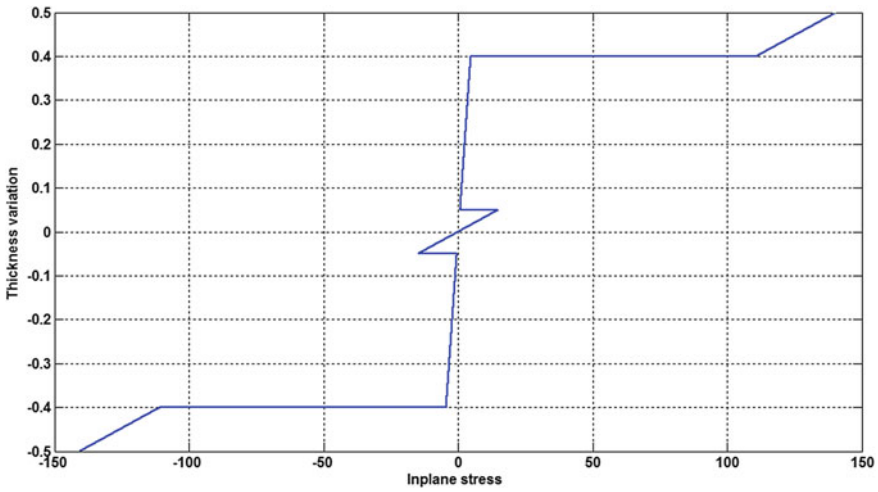


**Fig. 12** In-plane stress  $\sigma_{yy}$  along thickness using MFHL for  $S = 20$  for isotropic five-layered plate ( $b = 3a$ ) subjected to sinusoidal loading

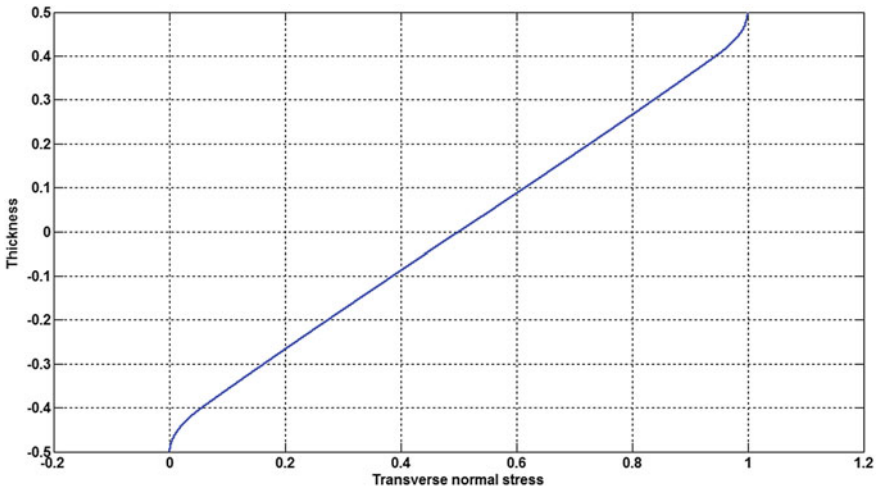


**Fig. 13** Transverse normal stress  $\sigma_{zz}$  along thickness using MFHL for  $S = 20$  for isotropic five-layered plate ( $b = 3a$ ) subjected to sinusoidal loading

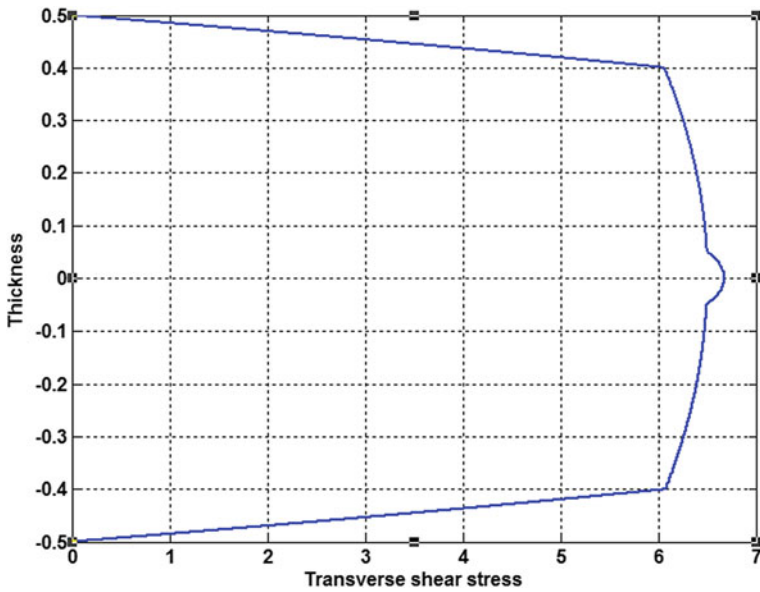


**Fig. 14** Transverse shear stress  $\tau_{xz}$  along thickness using MFHL for  $S = 20$  for isotropic five-layered plate ( $b = 3a$ ) subjected to sinusoidal loading



## References

1. Demasi L (2006) Three-dimensional closed form solutions and exact thin plate theories for isotropic plates. *Sci Direct*
2. Kant T, Pendhari SS, Desai YM (2007) A new partial finite element model for statics of sandwich plates. *J Sandwich Struct Mater* 9:487
3. Vinson JR, Chou TW (1975) Composite materials and their use in structures. Applied Science Publishers Ltd, London
4. Reddy JN (1997) Mechanics of laminated composite plates: theory and analysis. CRS Press, Boca Raton, Florida, p 782
5. Bert CW, Francis PH (1974) Composite materials mechanics: structural mechanics. *AIAA J* 12(9):1173–1186
6. Mallikarjuna, Kant T (1993) A critical review and some results of recently developed refined theories of fibre-reinforced laminated composites and sandwiches. *Compos Struct* 23(4): 293–312
7. Altenbach H (1998) On the theories for laminated and sandwich plates. *Mech Compos Mater* 34(3):243–252
8. Ghugal YM, Shimpi RP (2002) A review of refined shear deformation theories of isotropic and anisotropic laminated plates. *J Reinf Plast Compos* 21(9):775–813
9. Srinivas S, Joga Rao CV, Rao AK (1970) An exact analysis of vibration for simply-supported homogeneous and laminated thick rectangular plates. *J Sound Vib* 12(2):187–119

**Part VI**  
**Structures for Non-conventional Energy**  
**(Wind and Solar)**

# Hydroelectric Flow Optimization of a Dam: A Kriging-Based Approach



Subhadip Biswas, Souvik Chakraborty, Rajib Chowdhury  
and Indrajit Ghosh

**Abstract** This paper presents a novel approach for hydroelectric flow optimization. The proposed approach integrates Kriging into the framework of genetic algorithm (GA). This coupling reduces the computational effort associated with conventional GA without affecting the accuracy. The proposed approach has been used for hydroelectric flow optimization. For the model considered, revenue generated is dependent on (a) hourly turbine flow, (b) hourly spill flow, (c) hourly electricity price and (d) storage level of reservoir. Two case studies have been performed by varying the simulation time considered. For the first case, the simulation is run for 50 h. It is observed that the proposed approach yields accurate result at significantly reduced computational cost. On contrary for the second case, the simulation is run for 20 days. Due to huge computational cost involved, it was not possible to generate benchmark solution. Hence, only the results obtained using the proposed approach have been reported. The results obtained are indicative of the fact that the proposed approach can be utilized for optimization of large-scale system from an affordable computational cost.

**Keywords** Hydroelectric dam · Kriging · Genetic algorithm

---

S. Biswas · S. Chakraborty · R. Chowdhury (✉) · I. Ghosh  
Department of Civil Engineering, Indian Institute of Technology Roorkee,  
Roorkee 247667, India  
e-mail: rajibfce@iitr.ac.in

S. Biswas  
e-mail: subhadipbiswas.in@gmail.com

S. Chakraborty  
e-mail: csouvik41@gmail.com

I. Ghosh  
e-mail: indrafce@iitr.ac.in

## 1 Introduction

Optimization is basically a process to adjust some specified set of parameters without violating certain constraints so that the outcome parameter gets maximized or minimized. Optimization technique is widely utilized in various research fields [1, 2]. A number of optimization techniques that are available in the literature [3] can be classified roughly into two basic forms: (a) conventional optimization techniques (Taguchi method, response surface method, iterative mathematical search technique, etc.) and (b) non-conventional optimization techniques (Heuristic search technique, genetic algorithm, Tabu search, simulated annealing, etc.). The selection of the right technique could be case specific since each of them holds certain advantages under specific circumstances.

Hydroelectric flow optimization of a dam, the prime objective of the study, is a large-scale problem and involves multiple factors which govern the eventual revenue generated by the hydroelectric dam. The present study has adopted a novel approach based on Kriging surrogate for modelling the hydroelectric flow. Compared to conventional techniques, Kriging has the following advantages:

- (i) Kriging performs a bi-level approximation: first on a global scale by using the trend function (polynomial part) and second on a local scale by using an appropriate covariance function [4, 5]. Naturally, the results predicted using Kriging are more accurate as compared to conventional approaches.
- (ii) Kriging provides the best linear unbiased estimator [6].
- (iii) Last but not least, the number of data set required in Kriging is significantly less compared to other conventional approaches [6].

These are the reasons for wide acceptance of Kriging model in the field of structural reliability [5–7], and also it is gaining popularity in some other research domains [8–10]. In the present study, an approach based on Kriging coupled with genetic algorithm (GA) has been adopted in order to optimize the hydroelectric flow.

## 2 Proposed Approach

In this section, the proposed approach has been presented. However, before going into the details of the proposed approach, a brief description of Kriging has first been presented.

### 2.1 Kriging Technique

Theoretical basis for Kriging was first proposed by Krige [11] and subsequently extended by Matheron [12] and Cressie [13]. In the beginning, Kriging was an

interpolation technique where the interpolated values are modelled as a Gaussian process governed by prior covariances. This segment is devoted to briefly describe the Kriging approximation model. It is to be noted that universal Kriging has been utilized in this work. In the first section, the concept regarding constructing a Kriging approximate model is described and then use of the model in predicting response at an unknown input is discussed in the subsequent section.

### 2.1.1 Construction of Kriging Model

Before developing the model, one should have a set of experimental points of design variables  $x$  and corresponding responses  $y(x)$  given as:

$$\mathbf{x} = \begin{bmatrix} x_{11} & x_{12} & \cdots & x_{1p} \\ x_{21} & x_{22} & & \\ \vdots & & \ddots & \vdots \\ x_{n1} & & \cdots & x_{np} \end{bmatrix} \quad \& \quad \mathbf{y}(\mathbf{x}) = \begin{bmatrix} y_1(x) \\ y_2(x) \\ \vdots \\ y_n(x) \end{bmatrix} \tag{1}$$

where  $p$  and  $n$  are the number of design variables and the number of experiments, respectively. In order to model the deterministic response, Sacks et al. [14] suggested the following model (Eq. 2).

$$\mathbf{Y}(\mathbf{x}) = \mathbf{f}^T(\mathbf{x})\mathbf{b} + \mathbf{Z}(\mathbf{x}) \tag{2}$$

The model considers regression  $\mathbf{f}^T(\mathbf{x})\mathbf{b}$ , as well as stochastic process  $\mathbf{Z}(\mathbf{x})$  capturing local variations to arrive at more accurate prediction of the response. In the model,  $\mathbf{f}(\mathbf{x}) = \{f_1(x), f_2(x), \dots, f_m(x)\}^T$  denotes the functional vector and  $\mathbf{b} = \{b_1, b_2, \dots, b_m\}^T$  denotes the coefficient vector, where  $m$  is the number of basic function of  $x$ .  $\mathbf{Z}(\mathbf{x})$  is the covariance of Gaussian stationary process represented as:

$$\mathbf{Z}(\mathbf{x}) = \mathbf{Cov}(\mathbf{x}_i, \mathbf{x}_j) = \sigma^2 \mathbf{R}(\mathbf{x}_i, \mathbf{x}_j); \quad i, j = 1, \dots, p \tag{3}$$

$\sigma^2$  in Eq. (3), is the process variance and  $\mathbf{R}(\mathbf{x}_i, \mathbf{x}_j)$  is the correlation function between two design variables  $x_i$  and  $x_j$ . Therefore in the process, the method approaches towards estimation of two unknown parameters,  $\mathbf{b}$  and  $\sigma^2$  by means of Eqs. (4) and (5), respectively.

$$\mathbf{b} = (\mathbf{F}^T \mathbf{R}^{-1} \mathbf{F})^{-1} \mathbf{F}^T \mathbf{R}^{-1} \mathbf{Y} \tag{4}$$

$$\sigma^2 = 1/n(\mathbf{Y} - \mathbf{Fb})^T \mathbf{R}^{-1} (\mathbf{Y} - \mathbf{Fb}) \tag{5}$$

Here  $\mathbf{F}$  denotes the vector composed of  $f(x)$  values at each experimental point, and  $R$  represents the correlation matrix including correlation functions  $\mathbf{R}$  for all possible combinations of experimental points:

$$\mathbf{R} = \begin{bmatrix} R(x_1, x_1) & R(x_1, x_2) & \cdots & R(x_1, x_n) \\ R(x_2, x_1) & R(x_2, x_2) & & \\ \vdots & & \ddots & \vdots \\ R(x_n, x_1) & & \cdots & R(x_n, x_n) \end{bmatrix} \tag{6}$$

$R(x_i, x_j)$  in Eq. (6) is the correlation function. It is widely acknowledged that the performance of Kriging is dependent on the choice of correlation function. In the present work, commonly used Gaussian correlation function is adopted. Details of the available correlation functions and their performances are discussed in a study conducted by Mukhopadhyay et al. [5].

### 2.1.2 Prediction of the Response Against Given Inputs

Second stage of the methodology deals with the prediction of the response(s) at new set of design variables  $x$  using the model developed in previous stage.

$$\mathbf{y}(\mathbf{x}) = \mathbf{f}^T(\mathbf{x})\mathbf{b} + \mathbf{r}^T(\mathbf{x})\mathbf{R}^{-1}(\mathbf{Y} - \mathbf{F}\mathbf{b}) \tag{7}$$

$\mathbf{b}$  in Eq. (7), the coefficient vector is determined using Eq. (4).  $\mathbf{f}^T(\mathbf{x})$  is quantified by putting the new set of values into the functional vector.  $\mathbf{r}^T(\mathbf{x})$  is a vector representing correlations between the new set of point  $\mathbf{x} = \{x^1, x^2, \dots, x^p\}$  and all given experimental points (Eq. 8).

$$\mathbf{r}^T(\mathbf{x}) = \{R(x, x_1), R(x, x_2), \dots, R(x, x_n)\} \tag{8}$$

$R(x, x_i)$  is defined by the product of the correlations between the individual components of  $\mathbf{x}$  and the components of  $\mathbf{x}_i$  as shown in Eq. (9).

$$R(x, x_i) = \prod_{k=1}^p R(x^k, x_i^k) \tag{9}$$

Thus, it is possible to predict the unknown responses at given sets of design variables using Kriging technique. It is well accepted that regression is much simpler compared to the present technique; however, advantage of the Kriging method over commonly used regression lies in its accuracy to predict the responses. In Kriging, the residuals of the regression model  $\mathbf{y}(\mathbf{x}) - \mathbf{f}^T(\mathbf{x})\mathbf{b}$  are interpolated to arrive at more close predictions of the unknown responses.

## 2.2 Kriging-Based GA

The basic idea of the proposed Kriging-based generic algorithm is to first generate an approximate objective and/or constraint function by using the Kriging approach

and consequently use the GA to solve the problem. Incorporating Kriging within the framework of GA enables the user to address high-dimensional problems with reasonable computational effort. The steps involved are:

- i. formulate approximate objective and constraint by using the Kriging,
- ii. solve the problem by using GA.

It is to be noted that although GA has been considered in this study, the same procedure is applicable with any other optimization tool.

### 3 Problem Definition

One of the most widely used source of electricity, accounting for 6% of world's energy supply and about 15% of the electricity generated is the hydropower [15]. Similar to wind energy, hydropower is also a renewable energy source and hence can never be exhausted. A hydropower plant consists of a generator, a turbine, a penstock and wicket gate. A schematic diagram of a typical hydroelectric dam is shown in Fig. 1.

Present study considers a hydroelectric power plant featured with a reservoir along with an inlet flow from a river to that reservoir. Inlet flow rate and the storage level of the reservoir are predefined. There are two ways through which water can exit the reservoir: either via spillway or through turbine. The water passing through the turbine is utilized to produce electricity. Flow rates through both of the turbine and the spillway can be controlled externally. The energy produced by the dam is simply governed by the two factors: (a) the flow rate through turbine and (b) the storage level of the reservoir. The storage level is again governed by three factors:

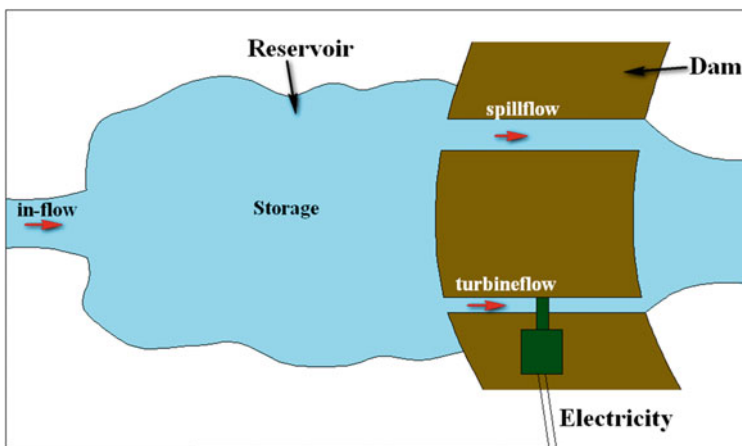


**Fig. 1** Schematic diagram of hydroelectric dam

(a) inflow rate, (b) flow through turbine and (c) flow through spillway. Additionally, the price of electricity may also vary with time depending on several factors. With this background, this paper aims to find the critical values of downstream flow rates for the maximum revenue of the power plant. All the four factors influencing the revenue of the hydroelectric dam are monitored on an hourly basis. Naturally, the number of variables associated with the system varies depending on the time of simulation. There is a constraint on the maximum flow that the turbine can handle and hence,

$$0 \leq f_i(i) \leq f_i^a, \quad \forall i \quad (10)$$

where  $f_i$  denotes the flow at the  $i$ th hour and  $f_i^a$  denotes the maximum flow that the turbine can handle. In this work,

$$f_i^a = 25,000 \text{ CFS} \quad (11)$$

has been considered. Secondly, the total hourly flow from the reservoir should exceed a predefined level, i.e.

$$f_t(i) + f_s(i) \geq \Delta S \quad (12)$$

where  $f_s$  denotes the flow through spillway and  $\Delta S$  denotes the maximum allowed hourly flow from the reservoir. In this work,

$$\Delta S = 500 \text{ AF} \quad (13)$$

has been considered. Thirdly, the difference between the hourly flow of two consecutive hours should be less than a predefined threshold, i.e.

$$|(f_t(i) + f_s(i) - f_t(i-1) - f_s(i-1))| \leq \varepsilon \quad (14)$$

where  $\varepsilon$  is the allowed threshold. This constraint ensures there is no sudden change in the storage level of the reservoir. In this work,

$$\varepsilon = 500 \quad (15)$$

has been considered. Fourthly, the storage of the reservoir should always be within a specific limit. In this work,

$$50,000 \leq S \leq 100,000 \quad (16)$$

has been considered. Here  $S$  denotes the storage level of the reservoir. The lower threshold of  $S$  ensures that it is possible to continuously produce electricity. On contrary, the upper limit ensures that there is overflow in the reservoir. Lastly, an additional constraint that ensures that the storage levels of the reservoir at the start and the end of the simulation should have the same level has been considered:



$$S(\text{end}) = S(\text{start}) = 90,000 \text{ AF} \quad (17)$$

This ensures that the hydroelectric plant can operate in a similar fashion beyond the optimization period. Combining all the above-mentioned equations, the optimization problem reads:

$$\begin{aligned} \arg \max \quad & R(f_t, f_s) \\ \text{s.t.} \quad & 0 \leq f_t(i) \leq 25,000, \quad \forall i \\ & f_t(i) + f_s(i) \geq 500 \\ & |\Delta(f_t(i) + f_s(i) - f_t(i-1) - f_s(i-1))| \leq 500 \\ & 50,000 \leq S \leq 100,000 \\ & S(\text{end}) = 90,000 \end{aligned} \quad (18)$$

where  $R$  denotes the revenue generated.

In order to illustrate the performance of the proposed approach, two case studies have been performed. In the first case, the simulation is run for 50 h and hence the underlying system is having 100 design variables (hourly flow through turbine and hourly flow through spillway). On contrary for the second case, the simulation is run for 20 days and hence the system is having 960 design variables.

## 4 Results and Discussion

This section presents the results obtained corresponding to the two cases described above. For both the cases described above, the proposed Kriging-based GA has been utilized to compute the optimum value of hourly flow through and turbine and hourly flow through spillway. For validating and illustrating the advantage gained by using the proposed approach, results obtained for the first case (i.e. the one for which simulation was run for 50 h) have been compared with results obtained using conventional GA. As for the second case, it was not possible to compare the results owing to the huge computational effort associated with this problem. Next, the results obtained using the two cases have been detailed.

### 4.1 Case 1: Simulation for 50 h

In the first case, the simulation is run for 50 h. Hence, the underlying system is having 100 design variables. For Kriging, the sample points required have been generated by using the Latin hypercube sampling [16]. As for the covariance function involved in Kriging, the Gaussian covariance function has been used in this study. The hourly inflow is considered to be 1070 CFS. The electricity price has been considered to vary on an hourly basis. The hourly variation of electricity price, considered in this study, has been shown in Fig. 2. In order to illustrate the accuracy

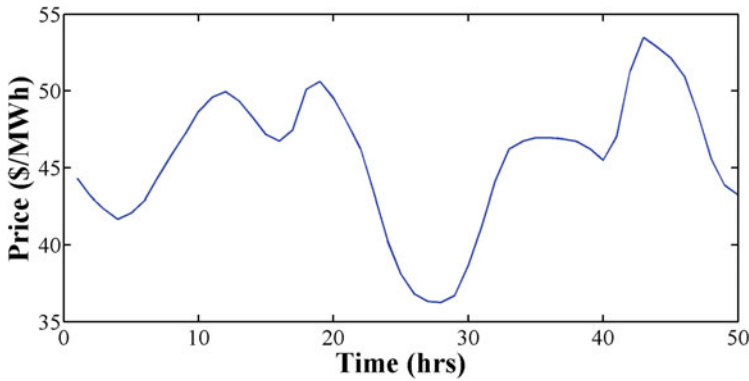


Fig. 2 Hourly variation of electricity price for Case 1

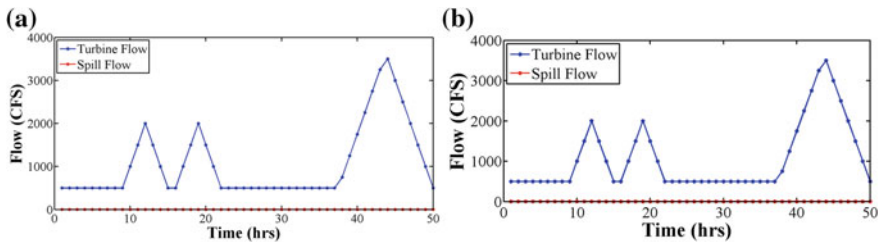


Fig. 3 Optimized hourly turbine flow and hourly spill flow obtained using a conventional GA and b Kriging-based GA

Table 1 Computational effort associated with the conventional GA and the proposed approach

Methods	Number of function evaluation
Conventional GA	≈ 45,000
Kriging-based GA	5000

and efficiency of the proposed approach, results obtained have been compared with results obtained using conventional GA.

Figure 3 shows the optimized hourly flow through turbine and hourly flow through spillway obtained using the proposed approach and conventional GA. However, the number of actual function evaluations using the proposed approach is only 5000 as compared to the 45,000 function evaluation required using the conventional GA (Table 1).

### 4.2 Case 2: Simulation for 20 Days

In the second case, the same problem with the same set-up has been run for 20 days. The primary goal of this case study is to demonstrate the applicability of the proposed approach for a large-scale system involving significant number of design variables system for which conventional GA is difficult to implement. The variation of electricity price over the simulation time is shown in Fig. 4. As a consequence, the number of design variables involved with this problem is 960. Generating benchmark solution by using conventional GA for such a large-scale problem was not possible. Hence, only the results obtained using the proposed approach have been reported.

Figure 5 shows the results obtained using the proposed approach. For this case, 15,000 actual function evaluations are required. Figure 5b illustrates that optimized

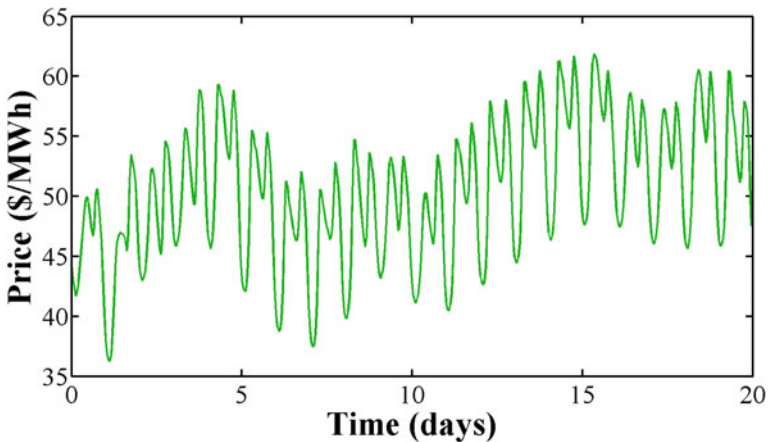


Fig. 4 Hourly variation of electricity price for Case 2

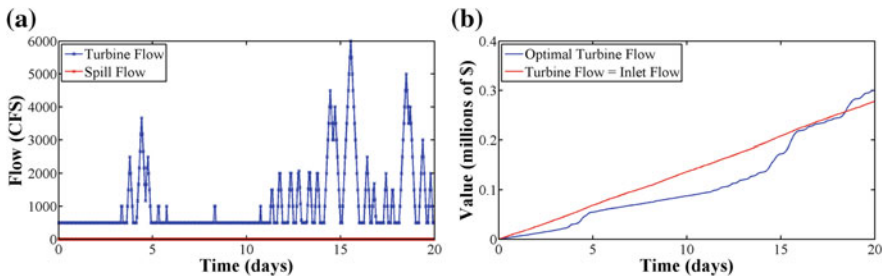
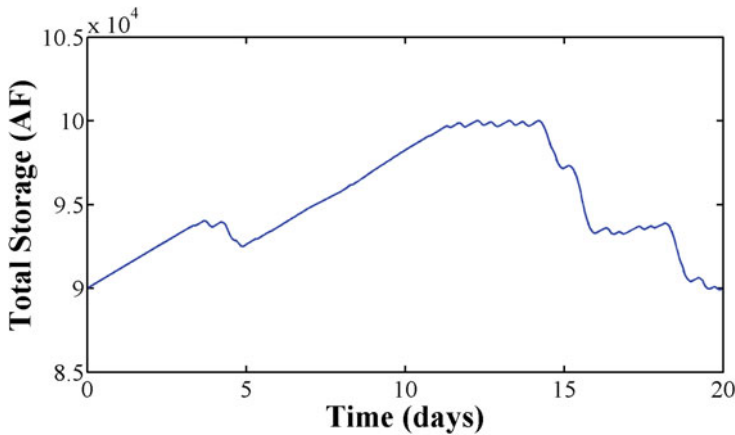


Fig. 5 Results for Case 2 obtained using the proposed approach. **a** Optimized turbine flow and spill flow obtained using the proposed approach; **b** comparison of revenue generated by using the optimized turbine flow and spill flow and setting turbine flow to be equal to spill flow



**Fig. 6** Change in storage level of the reservoir during the simulation period

parameters obtained yield overall higher revenue as compared to setting hourly flow through turbine to be equal to the hourly inflow may not result. Additionally, the change in the reservoir storage level over the optimization period has been shown in Fig. 6. It can be seen that the revenue at the start of the simulation is equal to that at the end of the simulation.

## 5 Conclusions

This paper presents a novel approach for hydroelectric flow optimization. The proposed approach integrates Kriging into the framework of genetic algorithm (GA). This coupling reduces the computational effort associated with conventional GA without affecting the accuracy. The proposed approach has been used for hydroelectric flow optimization. For the model considered, revenue generated is dependent on (a) hourly turbine flow, (b) hourly spill flow, (c) hourly electricity price and (d) storage level of reservoir. Two case studies have been performed by varying the simulation time considered. For the first case, the simulation is run for 50 h. It is observed that the proposed approach yields accurate result at significantly reduced computational cost. On contrary for the second case, the simulation is run for 20 days. Due to huge computational cost involved, it was not possible to generate benchmark solution. Hence, only the results obtained using the proposed approach have been reported. The results obtained are indicative of the fact that the proposed approach can be utilized for optimization of large-scale system from an affordable computational cost.

**Acknowledgements** SB and SC acknowledge the support of MHRD, Govt. of India. RC acknowledges the support of CSIR via grant no. 22(0712)/16/EMR-II.

## References

1. Hou S, Li Q, Long S, Yang X, Li W (2008) Multiobjective optimization of multi-cell sections for the crashworthiness design. *Int J Impact Eng* 35(11):1355–1367
2. Liu X, Wang L, Tang X (2013) Optimized linearization of chord and twist angle profiles for fixed-pitch fixed-speed wind turbine blades. *Renew Energy* 57:111–119
3. Mukherjee I, Ray PK (2006) A review of optimization techniques in metal cutting processes. *Comput Ind Eng* 50(1–2):15–34
4. Gaspar B, Teixeira AP, Soares CG (2014) Assessment of the efficiency of Kriging surrogate models for structural reliability analysis. *Probab Eng Mech.* 37:24–34
5. Mukhopadhyay T, Chakraborty S, Dey S, Adhikari S, Chowdhury R (2016) A critical assessment of Kriging model variants for high-fidelity uncertainty quantification in dynamics of composite shells. *Arch Comput Methods Eng* (Accepted)
6. Kaymaz I (2005) Application of Kriging method to structural reliability problems. *Struct Saf* 27(2):133–151
7. Zhang L, Lu Z, Wang P (2015) Efficient structural reliability analysis method based on advanced Kriging model. *Appl Math Model* 39(2):781–793
8. Knudby A, Jupiter S, Roelfsema C, Lyons M, Phinn S (2013) Mapping coral reef resilience indicators using field and remotely sensed data. *Remote Sens* 5(3):1311–1334
9. Arfaoui M, Inoubli MH (2013) Advantages of using the Kriging interpolator to estimate the gravity surface, comparison and spatial variability of gravity data in the El Kef-Ouargha region (northern Tunisia). *Arab J Geosci* 6(8):3139–3147
10. Thakali L, Kwon TJ, Fu L (2015) Identification of crash hotspots using kernel density estimation and Kriging methods: a comparison. *J Mod Transp* 23(2):93–106
11. Krige DG (1951) A statistical approach to some basic mine valuation problems on the Witwatersrand. *J Chem Met Min Soc South Africa* 52(6):119–139
12. Matheron G (1963) Principles of geostatistics. *Econ Geol* 58(8):1246–1266
13. Cressie NAC (1990) The origins of Kriging. *Math Geol* 22(3):239–252
14. Sacks J, Schiller SB, Welch WJ (1989) Designs for computer experiments. *Technometrics* 31(1):41–47
15. Ibrahim NAB (2012) Modelling of micro hydroelectric system design. University Tun Hussein Onn Malaysia
16. Olsson A, Sandberg G, Dahlblom O (2003) On Latin hypercube sampling for structural reliability analysis. *Struct Saf* 25(1):47–68

# Effect of Nanosilica and Microsilica on Bond and Flexural Behaviour of Reinforced Concrete



Lincy Varghese, V. V. L. Kanta Rao and Lakshmy Parameswaran

**Abstract** Nanosilica is a recent addition to the group of pozzolanic admixtures in concrete, which is recognized as efficient in improving strength and durability of concrete. This paper presents a comparative evaluation of some structural properties, namely bond and flexural behaviour, of nanosilica added high-performance concrete, microsilica added high-performance concrete and a reference concrete. The experimental results show the beneficial effects of nanosilica addition on the structural properties of reinforced concrete. The nanosilica added high-performance concrete showed better concrete–rebar interface, higher bond stress, a fewer number of cracks with lesser crack width, higher ultimate load carrying capacity and an improvement in the ductile nature of concrete, compared to the other two concretes. The study concludes that nanosilica can be a promising pozzolanic admixture for structural concrete applications.

**Keywords** Nanosilica · Microsilica · Reinforced concrete · Bond stress  
Flexural behaviour

## 1 Introduction

The use of supplementary cementitious materials (SCMs) in concrete has been a revolutionary development in concrete technology since 1970s. The addition of SCMs to concrete improves the properties of concrete along with the enhancement of its sustainability. Any improvement in the properties of concrete can reduce the

---

L. Varghese · V. V. L. Kanta Rao (✉) · L. Parameswaran  
Bridge Engineering and Structures Division, Academy of Scientific and Innovative Research,  
CSIR-Central Road Research Institute, New Delhi 110025, India  
e-mail: vvlk Rao.crri@nic.in

L. Varghese  
e-mail: lincyvarghese91@gmail.com

L. Parameswaran  
e-mail: lakshmy.crri@nic.in

overall quantity of the constituent materials during construction (higher strength with the lesser material) and may reduce the cost of maintenance (higher durability delays the need of maintenance). The most researched SCMs are fly ash, silica fume (microsilica), granulated blast furnace slag, rice husk ash, etc., among which the microsilica (mS) was found to have a greater impact on strength and durability improvement, even with a small quantity, compared to the other SCMs. Hence, the use of mS is preferred where high strength and durability requirements are of concern. However, mS is not produced in India and is often imported. In this regard, it is worthwhile to consider expanding the existing frame of SCMs by introducing synthesized SCMs as well, which provides an opportunity for indigenous development of such materials. Nanosilica (nS) is one such synthesized pozzolanic admixture, which is being extensively researched after the introduction of nanotechnology in concrete. It is a nanomaterial, with approximately 99% active silica content and high specific surface area, which can be prepared mainly by the sol–gel process [1]. It was reported from various researches that nS imparts better strength and durability to concrete as compared to other pozzolanic admixtures, through nanolevel refinement of the microstructure of concrete [2–5]. It was also noted that most of the published research pertained to study of properties of nS added plain cement concrete. However, before recommending the use of nS for any practical applications in concrete structures, it is necessary to investigate the effect of the same in reinforced concrete. Considering the application of concrete for construction of bridges, a study of flexural behaviour of concrete is of great importance. In addition, the composite action of any reinforced concrete is possible only if sufficient bond strength exists between reinforcing bars and concrete. Both the above properties of reinforced concrete depend on several characteristics of reinforcement bar and concrete such as strength of concrete, bar diameter, spacing of bars, transverse reinforcement, type of bars, coating on the bar, confinement of concrete around bar. However, the present study attempts to investigate the effect of nS addition on these two properties of reinforced concrete, using one type of steel bar and one grade of concrete and compares the same with those of mS added concrete and reference concrete.

## 2 Experimental Programme

### 2.1 *Characteristics of Materials*

Ordinary Portland cement of 43 grade was used for the study, and its properties were evaluated as per procedures of IS:4031-1988 standard and were found to be conforming to IS:8112-2013. Two mineral admixtures, namely mS and nS, were used as cement replacing materials in the present study. Densified powder-type amorphous mS of grade 920 D [6] and colloidal nS of grade Cembinder 8 [7] with 50% solid content were used. The particle size and shape of mS and nS were

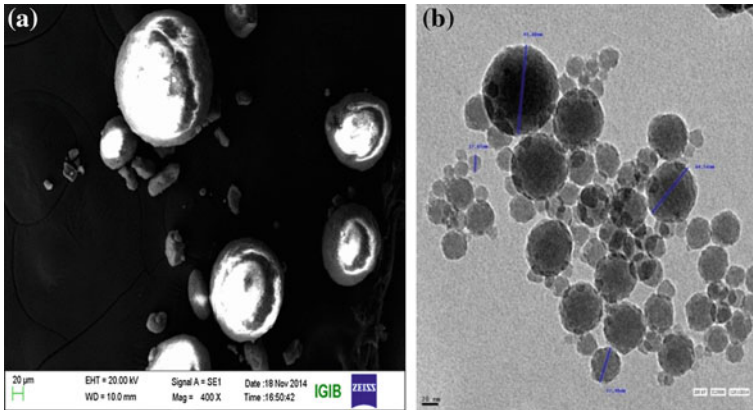


**Fig. 1** a Scanning electron microscopic image of microsilica (M: 400X) b Transmission electron microscopic image of nanosilica (M: 25000X) (M = image magnification)

determined using scanning electron microscopy and transmission electron microscopy, respectively and are shown in Fig. 1. Both mS and nS particles were found to be non-uniform and spherical in shape. The specific gravity of mS was 2.2 [8], and that of nS in colloidal form was 1.38 (measured by density bottle method). The silica content of mS and nS was determined through chemical analysis as per IS:1727-1967, and the same was found to be 86.71 and 92.41%, respectively. The silica content of mS conformed to the requirements of IS:15388-2003.

Crushed granite coarse aggregate of 20 and 10 mm size and crushed fine aggregate available in Delhi region conforming to IS:383-1970 were used. The salient properties of coarse aggregate were determined as per IS:2386-1963, and the results so obtained are summarized in Table 1. The specific gravity, water absorption and silt content of fine aggregate were determined as per IS:2386-1963 (Part III and Part II) and were found to be 2.6, 1 and 13.5%, respectively. The particle size distribution of both coarse aggregate and fine aggregate was determined using sieve analysis and was found to be conforming to the requirements of IS:383-1970; the fine aggregate conformed to the grading curve of Zone II. Tap

**Table 1** Properties of coarse aggregate

Properties	Results
Specific gravity	2.78
Water absorption	0.35%
Bulk density	1690 kg/m <sup>3</sup>
Flakiness index	11.2%
Combined flakiness and elongation index	9.7%
Crushing value	20%
Impact value	18%
Abrasion value	22%



water free from oil, organic materials, and other impurities, conforming to IS:456-2000 was used for concrete mixing and curing. Polycarboxylic ether-based superplasticizer MasterGlenium SKY 8777 [9] conforming to IS:9103-1999 was used.

## 2.2 Mix Proportioning

A concrete mix with a characteristic compressive strength of 40 MPa was designed as per IS:10262-2009, suitable for “very severe” exposure condition, with a durability criterion of maximum rapid chloride permeability at 56 days as 1200 C, and having a workability of 75–125 mm. The proportions of mS and nS were selected based on their maximum efficiency factor level, i.e. 7.5% for mS and 3% for nS [5]. Similar proportions of mS and nS were reported in the literature on mS and nS added concretes [10]. The concretes so prepared were designated as reference concrete (RefCon), mS added high-performance concrete (mS-HPC) and nS added high-performance concrete (nS-HPC). The mix proportions of these concretes are given in Table 2. The superplasticizer content was kept constant at 1.5% by weight of cementitious material for all the mixes.

The mixing of concrete was carried out in a tilting type laboratory rotary mixer. The mS was added to the aggregate mixture just before the addition of cement, and colloidal nS was added by mixing it with half of the mixing water. The slump of all the concrete mixes was found to be in the range of 120–150 mm, which conformed to the requirements of MoRTH: 2013 for concretes for application in reinforced or prestressed concrete structures with highly congested reinforcement such as in bridges. The rapid chloride permeability of the concretes at 56 days was found to be 1856, 385 and 916 C, respectively, for RefCon, mS-HPC and nS-HPC. Thus, the high-performance concrete mixes were found to be satisfying the requirements for the application in reinforced concrete road bridges as per IRC:112-2011.

**Table 2** Proportion of concrete mixes

Materials	Quantity of materials (kg/m <sup>3</sup> )		
	RefCon	mS-HPC	nS-HPC
Cement	420	388.5	407.4
mS	–	31.5	–
nS	–	–	25.2
Water	168	168	155.4
Coarse aggregate	1233	1225	1229
Fine aggregate	649	645	647

### 2.3 Casting of Test Specimens

Cube specimens of size 150 mm were cast for the pull-out test, as per IS:2770-1967. The mould set-up of the specimen is shown in Fig. 2. An HYSD rebar (Fe 500), with an embedment length of 125 mm, was placed vertically along the centre of the specimen. The surface characteristics of the rebar are presented in Table 3.

Beam mould, made of steel, with internal dimensions  $2000 \times 150 \times 250$  mm was used for making RCC specimens for investigating the flexural behaviour of RCC beam, made with three types of concrete, under an imposed load. The under-reinforced beam was designed for a moment resistance of 31.2 kN m as per IS:456-2000. The details of the reinforcement are given in Fig. 3. Electrical strain gauges were pasted at mid- and quarter-points of one of the bottom longitudinal reinforcements. A nominal cover of 30 mm was provided by fixing cover blocks to the reinforcement before placing the same in the mould.

All the test specimens were demoulded after 24 h and subjected to 28 days water curing at  $27 \pm 2$  °C.

**Fig. 2** Mould set-up for bond stress specimen



**Table 3** Surface characteristics of rebar

Parameter	Measured value
Diameter (mm)	20
Rib height(mm)	1.43
Rib width (mm)	0.19
Rib spacing (mm)	20.76
Rib face angle	45°

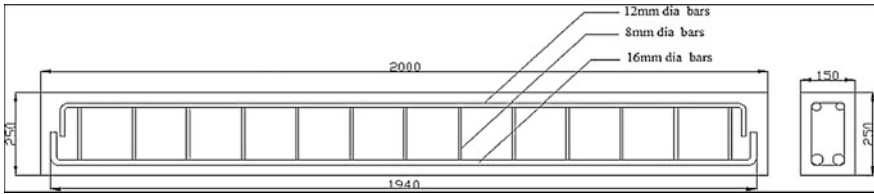


Fig. 3 Reinforcement details of RCC beam

### 2.4 Test Procedure

The bond stress of all the three concrete mixes was determined by conducting a pull-out test as per IS:2770-1967. The test was carried out when the average compressive strength of concrete was between 20–30 MPa. The pull-out test was continued till the failure of the specimens. The bond stress was computed using Eq. (1) at load corresponding to a slippage of 0.025, 0.25 mm and at failure, as given in IS:2770-1967.

$$\text{Bond stress} = \frac{\text{Load at a slippage 0.025 or 0.25 mm or at failure}}{\text{Surface area of embedded length of bar}} \quad (1)$$

The flexural behaviour of the RCC beams was investigated under four-point loading at 56 days. The schematic test set-up of beam is presented in Fig. 4. The beams were supported on roller at one end and rocker at the other end. The span of the beam was 1800 mm. The load was applied using a hydraulic jack and controlled using a calibrated load cell having a capacity of 50 tonne. The load distribution was achieved using symmetrical steel rollers at a distance of 300 mm from the centre. Five dial gauges of sensitivity 0.01 mm were placed to measure the deflections at

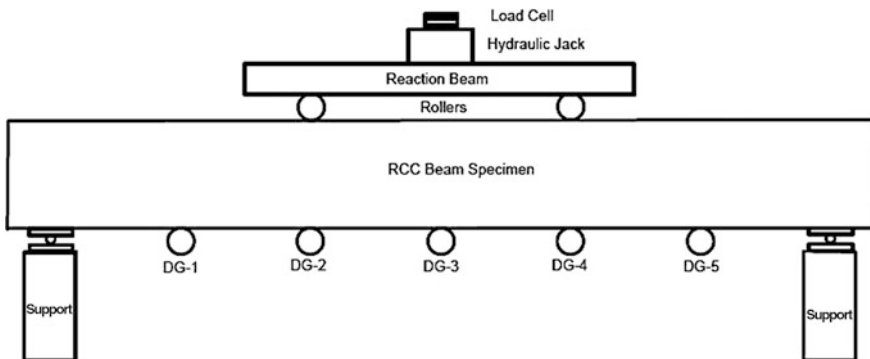


Fig. 4 Schematic diagram of beam test set-up

the mid-span section, quarter-span sections of the beam and near supports. The dial gauges and strain gauges were connected to the “DEWETRON” data acquisition system.

### 3 Results and Discussion

#### 3.1 Bond Stress

The pull-out test was carried out on specimens when the corresponding compressive strengths were ~28 MPa at 3rd, 4th and 5th day, respectively, on nS-HPC, RefCon and mS-HPC. It was noted that mS-HPC was slower in gaining compressive strength at the early age, compared to other two concretes. Load versus slip curves developed from the experimental data are shown in Figs. 5, 6 and 7. The abscissa of the plot indicates the slippage of the steel bar at the free end, and the ordinate is the corresponding load. The rate of slip of the rebar in mS-HPC specimens was comparatively greater than the same in other two concretes at a given load. This may be because in case of RefCon and nS-HPC the slippage of bar could have been resisted by a stronger rebar–concrete interface as the load is transferred, whereas in the case of mS-HPC, the rebar–concrete interface could be weak, possibly due to slower pozzolanic activity of mS during the early age.

The bond stress of concretes was computed using Eq. (1) and is presented in Table 4. It may be noted that the nS-HPC showed the highest bond stress in comparison with that of RefCon and mS-HPC. This could be due to the early strength gain of nS-HPC.

The observed crack pattern on the specimens after failure is shown in Fig. 8. It was observed that the interface between reinforcement and concrete has failed in

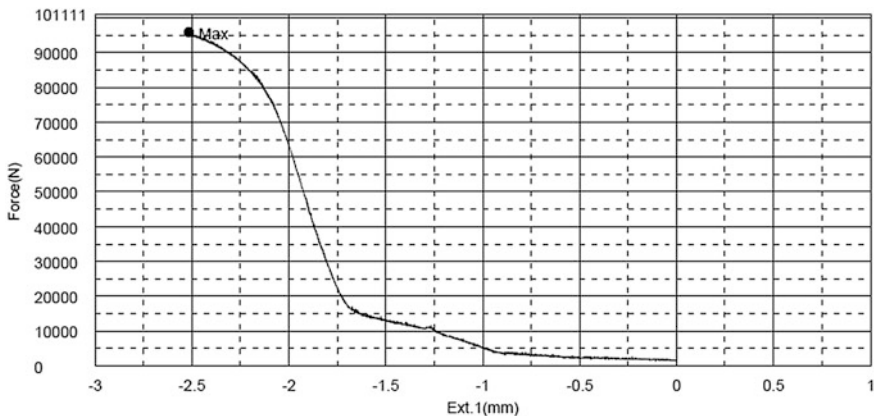


Fig. 5 Load versus slip curve of RefCon

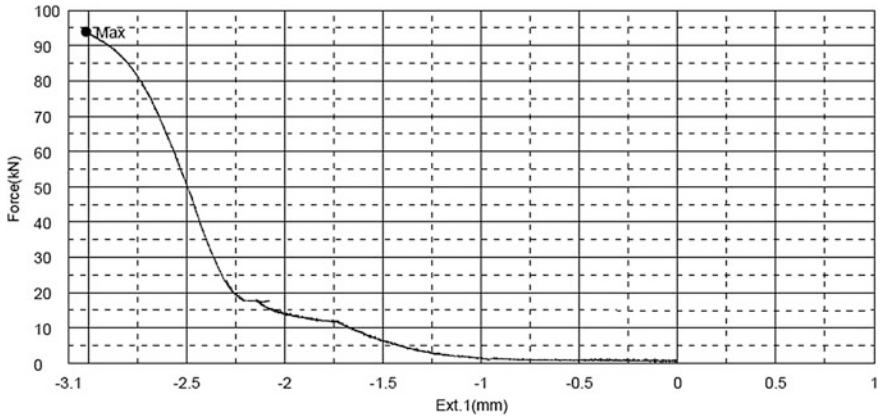


Fig. 6 Load versus slip curve of mS-HPC

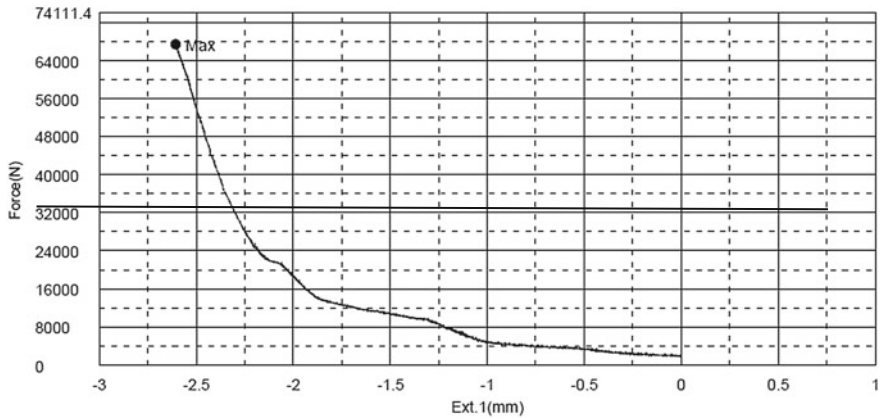


Fig. 7 Load versus slip curve of nS-HPC

Table 4 Estimated bond stress of concrete mixes

Mix	Bond stress (MPa)		
	At 0.025 mm slippage	At 0.25 mm slippage	At failure
RefCon	0.23	0.28	13.84
mS-HPC	0.13	0.15	13.11
nS-HPC	0.31	0.33	14.70

RefCon, with fewer cracks extended onto the concrete mass. While this interface failure was not significant in the case of mS-HPC and nS-HPC, but a number of cracks were visible on the concrete surface extending to the sides. This further justifies the presence of a better bond between concrete and steel, which made the

concrete fail first. At failure, the crack width on mS-HPC was comparatively higher than that of nS-HPC, but nS-HPC exhibited a number of finer cracks. The higher number of finer cracks in nS-HPC specimen could indicate a better rebar–concrete bond, compared to the other two concretes. As the bond between rebar and concrete gets better, the concrete tends to crack first with lesser rebar slippage.

### 3.2 Flexural Behaviour of RCC Beam

At the time of flexural behaviour test of RCC beam (56 days), the mechanical properties of the three concretes are presented in Table 5.

#### 3.2.1 Crack Versus Load

The crack characteristics of the RCC beams were monitored at various loads. The final crack pattern of the three concrete beams is presented in Figs. 9, 10 and 11. The initial crack in RefCon beam was observed at 35 kN, and the same for both

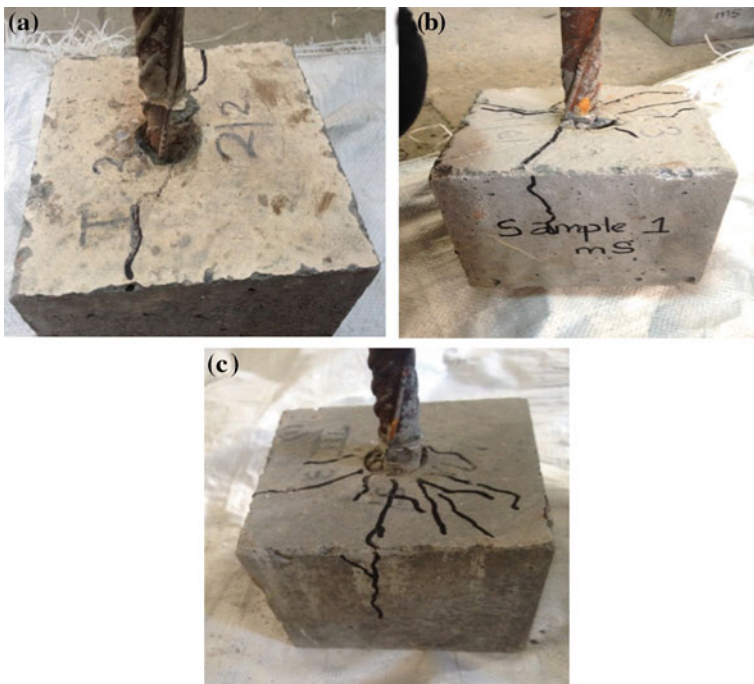


**Fig. 8** Observed crack pattern on specimens after bond stress test **a** RefCon, **b** mS-HPC, **c** nS-HPC

**Table 5** Mechanical properties of concrete

	RefCon	mS-HPC	nS-HPC
Compressive strength (MPa) {150 mm cube}	53.5	63.8	64.4
Split tensile strength (MPa) {300 × 150 mm cylinder}	3.4	4.5	4.5
Flexural strength (MPa){500 × 500 × 100 mm prism}	5.0	6.5	6.7
Elastic modulus (GPa) {300 × 150 mm cylinder}	31.5	37.2	33.7

Note Size of the test specimens is mentioned in { }

mS-HPC and nS-HPC was observed at 40 kN. Figure 12 presents the number of cracks which have developed with increase in load. The total number of cracks initiated with increase of load in RefCon, mS-HPC and nS-HPC beams was 32, 33 and 28, respectively. The width of cracks was measured using a portable crack measuring device and are presented in Fig. 13. From a comparison of Figs. 9, 10, 11, 12 and 13, it was noted that the nS-HPC beam exhibited the least number of cracks, wider crack spacing (in tension zone) as well as lower crack width compared to those of other two concrete beams. This could be due to its higher tensile strength of nS-HPC as can be observed from Table 5.

### 3.2.2 Load Versus Strain

The strain developed at the longitudinal bottom reinforcement during flexural loading was measured through electrical strain gauges fixed to the reinforcement at mid-span and quarter-span of the RCC beams. The observed variation in strain with increase in load is presented in Figs. 14 and 15. Compared to RefCon and mS-HPC beams, the strain was found to be maximum in nS-HPC beam, substantiating the wider crack spacing of nS-HPC as observed from the crack pattern (Figs. 9, 10 and 11). The higher-yielding of longitudinal reinforcement in nS-HPC beam also indicates its ductile nature compared to other two concrete mixes.

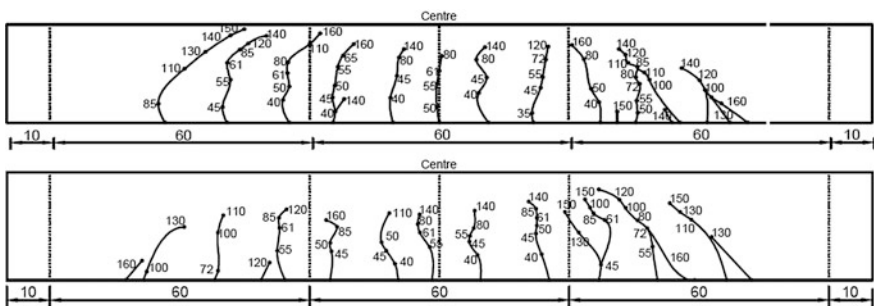


**Fig. 9** Crack pattern of RefCon beam (side 1 and 2)

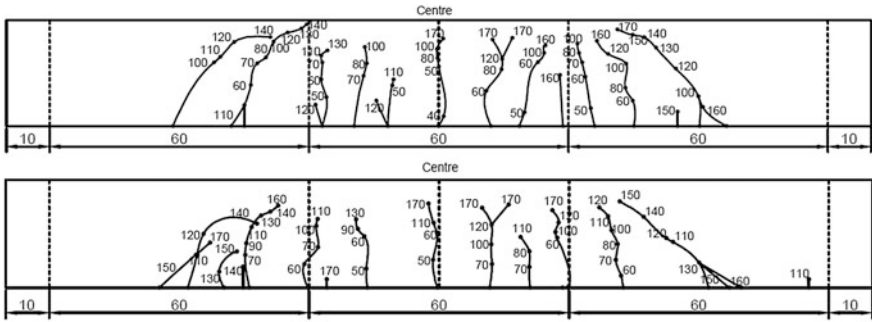


Fig. 10 Crack pattern of mS-HPC beam (side 1 and 2)

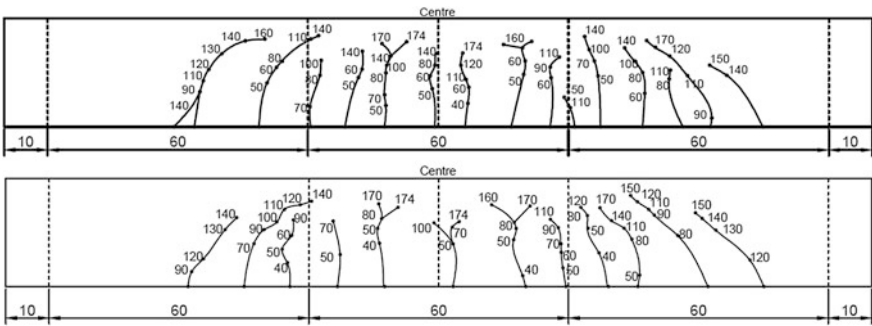
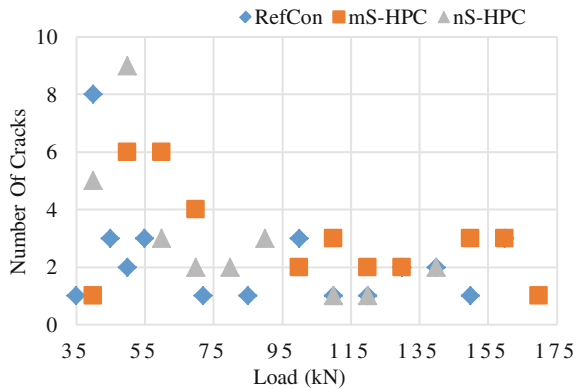


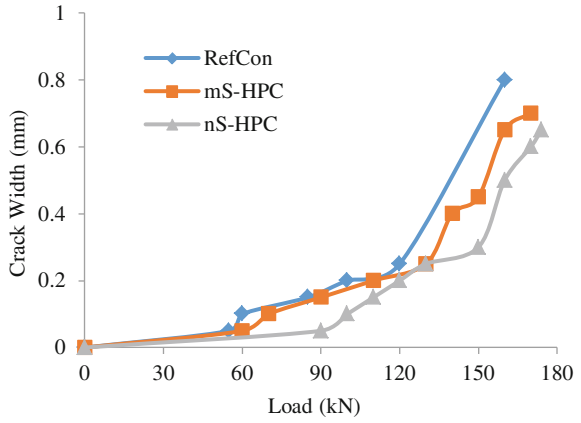
Fig. 11 Crack pattern of nS-HPC beam (side 1 and 2) Note For side 1: right support = rocker; left support = roller and for side 2: right support = roller; left support = rocker

Fig. 12 Number of cracks initiated with increase in load





**Fig. 13** Crack width versus load



**Fig. 14** Load versus strain at mid-span

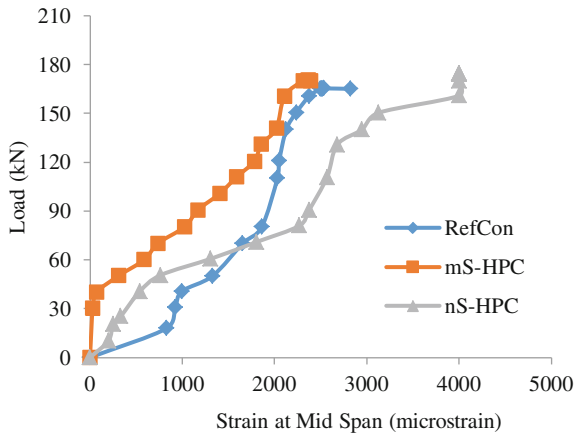


**Fig. 15** Load versus strain at quarter-span

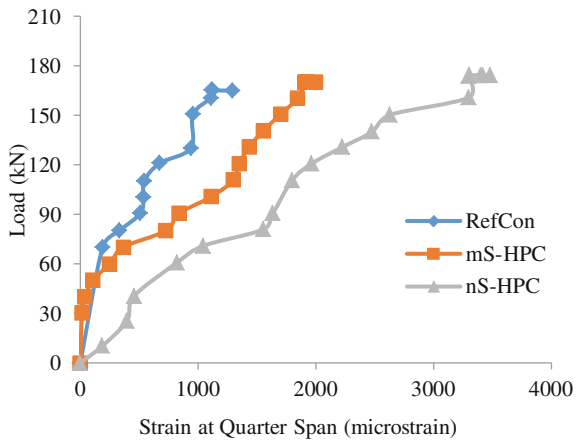
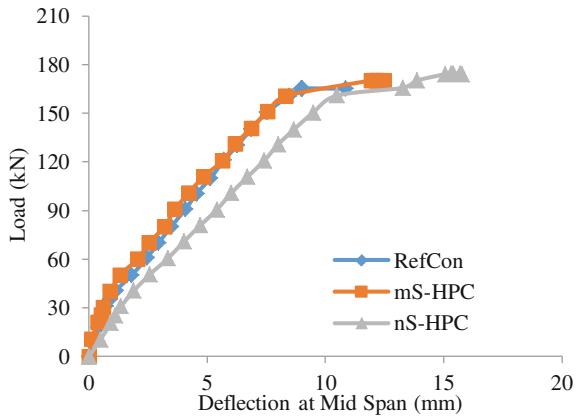


**Fig. 16** Load versus deflection at mid-span



### 3.2.3 Load Versus Deflection

The deflection of the RCC beams with increase in load was measured using dial gauges. Figures 16 and 17 show the measured deflection of beam at mid-span and at quarter-span, respectively, at various applied loads. The ultimate load was observed to be 165, 170 and 174.5 kN, respectively, for RefCon, mS-HPC and nS-HPC beam. The nS-HPC beam showed the highest deflection compared to other two beams, while mS-HPC beam showed the least. This could be due to the highest elastic modulus of mS-HPC compared to that of other two concretes (Table 5). On the other hand, highest deflection of nS-HPC beam can be attributed to the presence of larger amount of gel water in C-S-H (it was reported that nS-HPC produces finer C-S-H compared to mS-HPC [5, 11]—finer the C-S-H higher the quantity of gel water), which could have offered cushioning effect in nS-HPC beam under flexure.

**Fig. 17** Load versus deflection at quarter-span

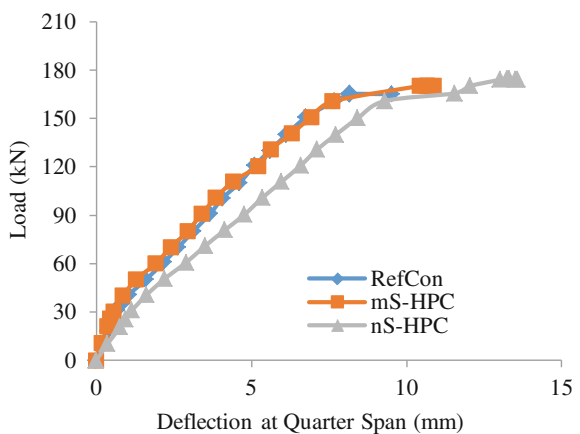
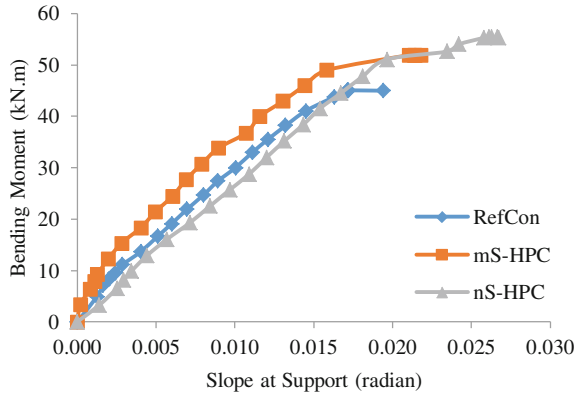


**Fig. 18** Bending moment versus slope at supports



### 3.2.4 Bending Moment Versus Slope

Figure 18 shows the bending moment versus slope of concrete beams at supports. Similar to the load versus deflection pattern, the slope at each particular bending moment of mS-HPC beam was lower than that of RefCon and nS-HPC beams which also support the earlier conclusion that the nS-HPC is more ductile compared to the other two concretes.

## 4 Conclusions

- (i) The bond stress of nS-HPC was found to be highest with a better concrete–rebar interface compared to that of mS-HPC and RefCon.
- (ii) The nS-HPC beam under flexure showed least number of cracks, maximum spacing between cracks and minimum crack width. This was attributed to its higher tensile strength, and yielding of longitudinal bar of nS-HPC beam, indicating its ductile nature.
- (iii) The addition of even a small quantity of nS (3% of cement) in concrete is observed to be a have a considerable effect in modifying the properties of reinforced concrete. Thus makes nS a promising pozzolanic admixture for structural concrete applications.

**Acknowledgements** The authors wish to thank all staff members of Bridge Engineering and Structures Division, CSIR-CRRI for their invaluable help in carrying out the experimental work. Authors also express their sincere gratitude to CSIR-IGIB for helping in Electron Microscopy Imaging. Regards are also due to AkzoNobel and Elkem for providing us with nanosilica and microsilica samples for carrying out this research work. The authors also thank the Director, CSIR-Central Road Research Institute for kindly granting permission to publish this paper.

## References

1. Sobolev K, Flores I, Hermosillo R, Martinez L (2006) Nanotechnology of concrete: recent developments and future perspectives. In: Proceedings of ACI session, Denver, USA
2. Nili M, Ehsani A, Shabani K (2010) Influence of nanosilica and microsilica on concrete performance. In: Proceedings of second international conference on sustainable construction materials and technologies, Ancona, Italy, 28–30 June 2010
3. Quercia G, Brouwers HJH (2010) Application of nanosilica in concrete mixtures. In: 8th Fib Ph.D. symposium in Kgs, Lyngby, Denmark, 20–23 June 2010
4. Maheswaran S, Bhuvaneshwari B, Palani GS, Iyer NR, Kalaiselvan S (2013) An overview on the influence of nanosilica in concrete and a research initiative. *Res J Recent Sci* 2:17–24 International Science Congress Association
5. Lincy V (2015) Experimental investigation on structural properties of nanosilica added high performance concrete. M.Tech dissertation, Academy of Scientific and Innovative Research–Central Road Research Institute, New Delhi
6. Elkem (2015) Product data sheet-microsilica. <http://www.elkem.com>. Accessed on 12 Aug 2015
7. AkzoNobel (2015) Product data sheet-cembinder 8, AkzoNobel pulp and performance chemicals AB: colloidal silica, <http://www.colloidalsilica.com>. Accessed on 15 Oct 2015
8. Holland TC (2005) Silica fume user's manual. Silica Fume Association, US Department of Transportation, Federal Highway Administration FHWA-IF-05-016, Washington
9. BASF (2015) Product data sheet-MasterGlenium SKY 8777. BASF: The Chemical Company. <https://assets.master-builders-solutions.basf.com>. Accessed on 12 Oct 2015
10. Lincy V, Rao VVLK, Lakshmy P (2015) A review on effects of nanosilica and microsilica on microstructure and mechanical properties of concrete. In: Proceedings of 4th Asian conference on Ecstasy of concrete, Kolkata, 2, Oct 2015, pp 355–362
11. Singh LP, Karade SR, Battacharyya SK, Yousuf MM, Ahalawat S (2013) Beneficial role of nanosilica in cement based material—A review. *Constr Build Mater* 47:1069–1077

# Interaction of a Flexible Splitter Plate with Vortex Shedding Past a Rigid Circular Cylinder



Chandan Bose, S. Krishna Kumar, Sunetra Sarkar and Sayan Gupta

**Abstract** This study deals with energy harvesting from vortex-induced vibration (VIV) of a flexible cantilever plate placed in the wake of a rigid cylinder. Conventionally, the plate is designed to resonate with the vortex shedding frequency behind the cylinder at a given flow velocity. The experimental results presented here show that the frequency of the plate oscillations undergoes an abrupt increase from a low value to a higher value at a critical flow velocity. Numerical simulations carried out in the present study suggest that this jump is due to the transition between two modes of wake oscillations in the system, one with a low Strouhal number range accompanied by impeded shedding and the other being the natural vortex shedding with a higher Strouhal number range. It is also found that the mode of vortex shedding depends on the flow velocity as well as the gap between the cylinder and the plate. There exists a critical gap for every flow velocity below which vortex shedding is inhibited resulting in reduced plate vibrations. The results indicate that the position of the plate in the wake affects the shedding frequency significantly and thus the gap between the plate and cylinder needs to be considered as a key parameter in design of such flow-induced energy harvesters.

**Keywords** Energy harvesting · Vortex shedding · Wake · Flexible plate

---

C. Bose · S. Krishna Kumar · S. Gupta  
Department of Applied Mechanics, Indian Institute of Technology Madras,  
Chennai 600036, India  
e-mail: cb.ju.1991@gmail.com

S. Krishna Kumar  
e-mail: skk.89@hotmail.com

S. Gupta  
e-mail: gupta.sayan@gmail.com

S. Sarkar (✉)  
Department of Aerospace Engineering, Indian Institute of Technology Madras,  
Chennai 600036, India  
e-mail: sunetra.sarkar@gmail.com

## 1 Introduction

It is well known that flow past a bluff body causes vortices to be shed from the body into the wake at periodic intervals. The vortex shedding frequency, termed in non-dimensional form as Strouhal number ( $St_f$ ), depends on the Reynolds number of the upstream flow. Vortex shedding behind a bluff body can induce vibrations of the bluff body itself as well as in any flexible structure placed downstream. Since these vibrations may induce instability in the structures, they are often deemed undesirable and need to be controlled. In case of vortex shedding induced vibration, this usually means that the shedding itself has to be suppressed or delayed. On the contrary, energy harvesters exploiting flow-induced vibrations require the vibrations to be heavy enough to yield reasonable quantity of power. The possibility of extracting electrical energy from VIV of flexible structures has been explored by various researchers in the past three decades [1–4]. In either case, a controlled vortex shedding is essential for favourable system behaviour.

Mechanisms causing flow-induced vibrations, like vortex shedding, are influenced not only by the upstream flow impinging on the bluff body but also by its near-field wake topology. The importance of wake in the process has led researchers to experiment with additional structures placed in the wake of primary, usually bluff, structure. Presence of the additional structures in the downstream leads to variation in the wake which feeds back to the vortex shedding of the primary structure. A common idea used in this regard is to use a ‘splitter plate’ attached behind the primary structure, thereby disrupting the flow interactions that would otherwise happen in the wake. In this study, we explore the effect of a downstream flexible plate placed at a distance behind the primary structure (a circular cylinder) on its vortex shedding. It has been seen in the literature [5–7] that the gap between the two structures affects the vortex shedding for a given flow velocity. It was reported that the vortex shedding frequency was also influenced by the presence of downstream structures.

Contrasting with the case of a conventional attached splitter plate in which the plate dimensions are the only parameters influencing shedding, the case of detached plate offers an additional control parameter in the form of gap between the cylinder and the plate. This allows design of systems where the control can be more dynamic and also over a wider range of flow velocities. Several energy harvesting systems based on vortex-induced vibrations of downstream detached flexible structures have been reported in the literature [1, 4]. These systems were designed such that the flexible structure resonated with the vortex shedding behind the rigid cylinder maximising the structural oscillations. An arbitrary gap between the cylinder and the flexible plate was considered and vortex shedding was observed. However, the effect of the gap on the vortex shedding phenomena, and thus the VIV of the flexible structure, was not studied. On the other hand, investigations into the flow dynamics of cylinder-plate systems, outside the energy harvesting community, have shown that presence of downstream structures can suppress vortex shedding behind the cylinder when the gap was smaller than a critical value [5–7]. The critical gap

also varied with the variation in flow velocity. Thus, one can expect that the choice of an optimal gap would be crucial to successful design of VIV energy harvesters. Therefore, there is a crucial need to investigate the underlying fluid–structure interaction dynamics in terms of the vortex interactions with the flexible plate.

In this paper, experimental results demonstrating these phenomena by low-speed wind tunnel tests are presented. A cylinder fixed in its position with a thin flat plate at some distance downstream of it is considered and the effect of the gap on the vortex shedding is studied. An abrupt increase in the frequency of the plate oscillations has been observed as flow velocity is increased. In the absence of sophisticated and costly flow visualisation hardware, numerical simulations of the fluid–structure interaction (FSI) system have been carried out to understand the underlying flow physics. It is seen that the jump in frequency can be attributed to the change in the mode of vortex shedding past the cylinder–plate system.

The remainder of the paper consists of the following sections. Section 2 presents the experimental observations of plate vibrations, and Sect. 3 reports the computational methodology along with the vorticity contours obtained at different Reynolds numbers. Section 4 presents a discussion on these observations and the paper ends with concluding remarks in Sect. 5.

## 2 Experimental Results

### 2.1 Experimental Set-up

A schematic of the harvester has been shown in Fig. 1. The set-up (see Fig. 2) consists of a steel cylinder connected to an aluminium plate via a connecting rod made of hardened steel. The cylinder was 25 cm long and 8 cm wide. The aluminium plate was 17 cm long, i.e. nearly twice the cylinder diameter, 9 cm wide

**Fig. 1** Schematic of the experimental set-up

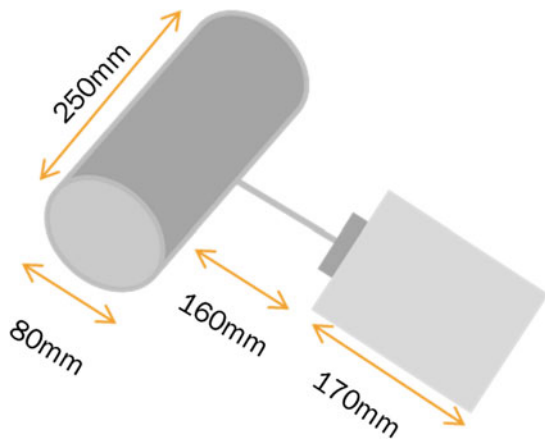


**Fig. 2** Photograph of the experimental set-up in the wind tunnel



and 0.3 mm thick. The gap between the cylinder and plate was 16 cm, i.e. twice the diameter of the cylinder.

Fixed support condition was imposed on the leading edge of plate. The wind tunnel was operated in suction. The flow velocity was varied between 2–14 m/s, corresponding to Reynolds number range of 10000–70000. The walls of the wind tunnel were kept closed throughout the experiment. The displacements are measured using laser displacement sensors at about 3/4th of the length of the plate from the fixed end.

## 2.2 *Experimental Results*

The displacement time histories of the flexible plate measured by the laser sensors are analysed to determine the dominant frequency (say, ' $f_p$ ') in its frequency spectra. The non-dimensional frequency of plate oscillation is calculated using the most dominant frequency as ( $St_p = (f_p L)/U_\infty$ ), where  $L$  is the length of the plate and  $U_\infty$  is the free-stream velocity. Figure 3 shows the variation of  $St_p$  with the Reynolds number ( $Re$ ). The  $St_p$  decreases with increase in  $Re$  and shows an abrupt increase at a  $Re$  value of 500, which is in concurrence with similar change in Strouhal number (say  $St_f$ ) reported in the literature [7]. Figure 4a, b, respectively, show the averaged frequency spectra for the displacement time history before and after the abrupt increase in the frequency. It can be seen that an additional frequency appears in the spectra post the abrupt increase and dominates the system response. The emergence of the new frequency, higher than the primary one, post the jump phenomenon needs to be investigated further.

The profile of the oscillating plate approximately corresponded to that of the first bending mode shape in the pre-jump regime and that of the second bending mode after the jump. The node for the second mode-shaped vibration seemed to be moving towards the plate free tip as the flow velocities increased. It can also be



**Fig. 3**  $St_p$  versus  $Re$

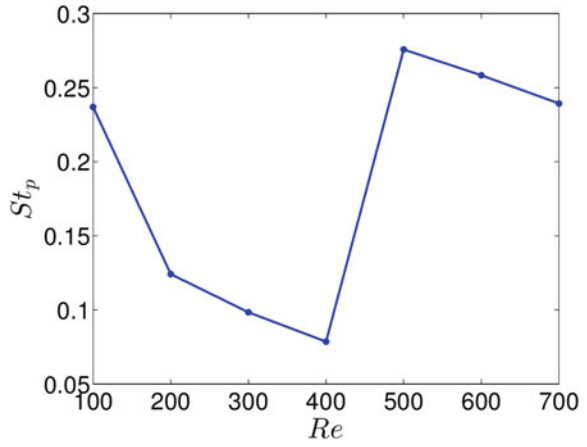
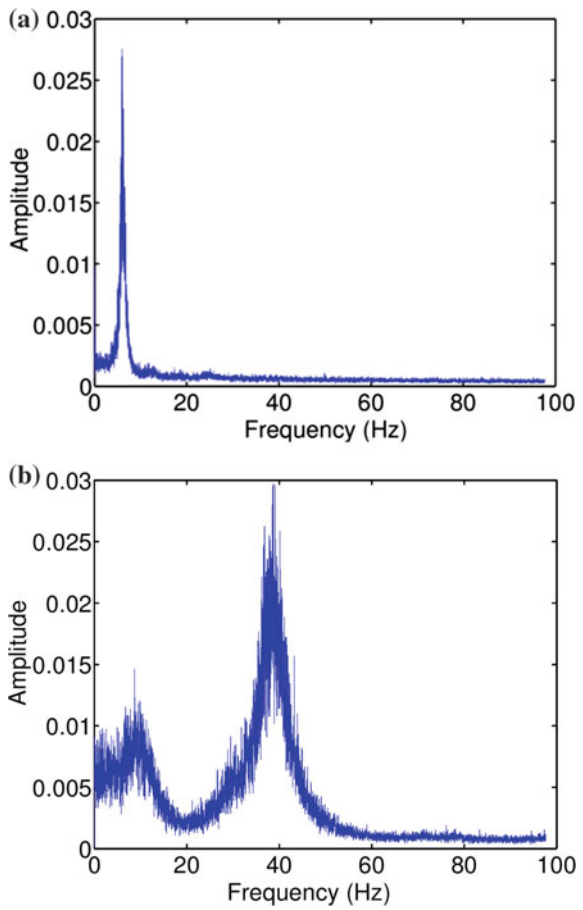


**Fig. 4** Frequency spectra of plate response **a** before jump and **b** after jump



noticed that the higher frequency seems to around 4 times the lower frequency in most cases. This would mean that the transition between two regimes of vortex shedding actually implies a transition from a lower frequency ( $\sim 10$  Hz for aluminium) to its harmonic ( $\sim 40$  Hz for aluminium). Such a transition has not been discussed in available the literature. Hence, this warrants a further study. Investigation of these effects is, however, out of the scope of this study.

It is evident from the results presented here and in [5–7] that the presence of downstream body within the formation region can affect the vortex shedding and induce a frequency higher or lower than that for the case of plain flow past cylinder. To investigate the underlying mechanism of the jump phenomenon, understanding the vortex interactions with the deformable plate is crucial. The flow physics is further investigated through CFD simulations using a finite volume-based solver as an alternative to the expensive and time consuming experimental flow visualisation techniques.

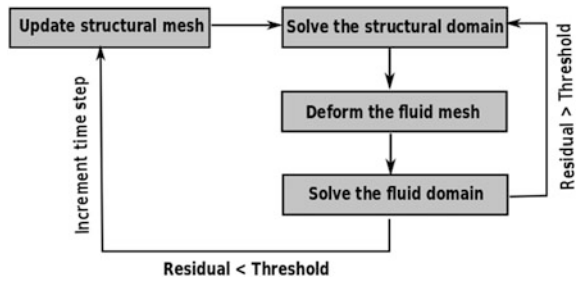
### 3 Computational Methodology and Results

The vortex-induced vibration (VIV) of a chord-wise flexible plate situated in the wake of a rigid cylinder has been simulated in two dimensions using a strongly coupled solver taking the fluid–structure interaction (FSI) effects into consideration. The objective of the simulations performed is to understand the role of vortex shedding between the cylinder and the flexible plate in the abrupt increase in  $St_p$  for variation in Reynolds number. This will enable us to identify an optimum parameter regime to enhance the plate vibration maximising the energy harvesting.

#### 3.1 Governing Equations and Solver Details

A coupled FSI solver is needed to capture the mutual interaction between the unsteady viscous flow generated in the wake of the cylinder and the deformable plate. In the present study, the FSI framework is composed of an incompressible Navier–Stokes solver coupled with a nonlinear elastic structural model by a partitioned approach based strong coupling method. The flow model is a transient solver for incompressible, laminar flow of Newtonian fluids. An arbitrary Lagrangian Eulerian (ALE) formulation [8] has been employed in the present study, to fulfill the requirement of a solution over a time-varying computational domain, by solving the N–S equation on a moving grid. A Laplacian mesh motion strategy [9] has been implemented with variable diffusivity coefficient. The flow solver uses a second-order accurate spatial discretisation and the temporal discretisation is performed using a second-order implicit backward differencing scheme. A variable time stepping technique based on a maximal Courant number has been adopted. The pressure velocity coupling is implemented through PISO (Pressure Implicit

**Fig. 5** Flow chart of the strong coupling algorithm



with Splitting of Operator) algorithm [8]. The absolute error tolerance criteria for pressure and velocity are set to  $10^{-6}$ . The structural part has been solved by a large strain elastic stress analysis solver based on Lagrangian displacement formulation [9]. The absolute tolerance criterion of the structural solver is also taken to be  $10^{-6}$ .

The flow and the structural solver have been integrated by a partitioned approach based strong coupling method. The partitioned approach is employed to separately solve the governing equations of the flow and the structure continua, with two independent solvers [10]. The solution is advanced in time separately over each partition communicating through their common interface by exchanging coupled state variables. Even though the partitioned approach is less stable than the monolithic approach, it is computationally more efficient and hence employed in the present study. The partitioned approach can be implemented in an explicit (weak coupling) or in implicit (strong coupling) manner. The basic difference between strong and weak coupling is that the former is equipped with an extra correction loop which assures the consistency of the mesh deformation with the kinematic and dynamic interface conditions. The variables exchanged from the fluid solver to the structural solver are pressure and viscous force. On the other hand, displacement increment and velocity are the variables fed from the structural solver to the fluid solver. The strong coupling method adopted in the present FSI solver is illustrated through the following flowchart (Fig. 5).

To implement the strong coupling method, a quasi-Newton coupling algorithm with an approximation for the inverse of the residual's Jacobian matrix from a least-square model (abbreviated as IQN-ILS) [11] has been used. The present FSI solver has been already validated extensively by Tukovic et al. [9].

### 3.2 Computational Domain and the Mesh

A rectangular computational domain as shown in Fig. 6 has been used in the present computations. The height and width of the domain are  $10D$  and  $15D$ , respectively, to avoid the wall effects. The gap between the cylinder and the plate and the length of the plate has been fixed as  $2D$  and  $2.5D$ , respectively, whereas the thickness of the plate has been kept as  $0.05D$ . Here,  $D$  is the diameter of

**Fig. 6** Schematic of the computational domain (not to scale)

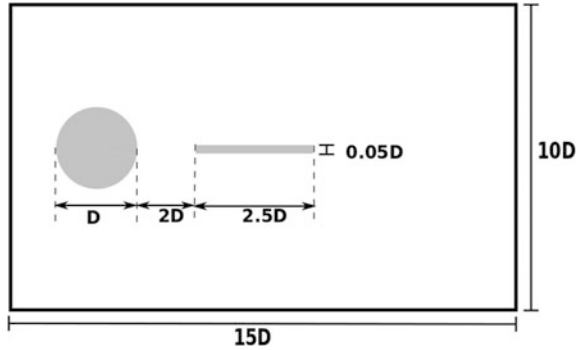
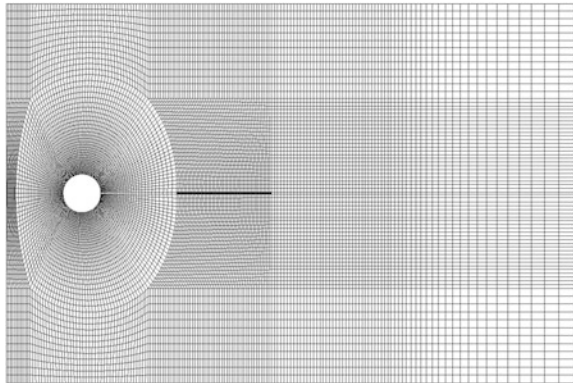


**Fig. 7** Computational grid: structured meshing



the cylinder. Standard boundary conditions have been applied: a zero pressure gradient and a constant free-stream at the inlet; a zero velocity gradient and atmospheric pressure condition at the outlet; no slip and zero normal pressure gradient condition on the horizontal walls and traction boundary condition on the flexible plate. The computational domain is discretised using structured grids as shown in Fig. 7. The mesh containing 89,052 grid points has been finalised through a grid independence test.

### 3.3 Wake Evolution at Different $Re$

For flow past a bluff body with no downstream structures disturbing its wake, vortex shedding occurs at a post-critical  $Re$  resulting in a von Kármán vortex street. It is well known that presence of a downstream plate, commonly called splitter plate attached or detached, affects the occurrence of the vortex shedding [12]. Thus, it can be expected that the steep increase in the  $St_p$  of the flexible plate could be related to a significant change in the flow dynamics past the cylinder-plate system. Since the

**Fig. 8** Vorticity contours at  $Re = 500$  at different time instances

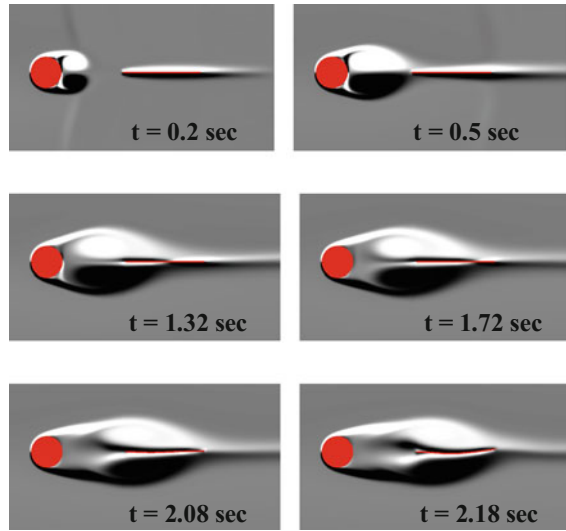
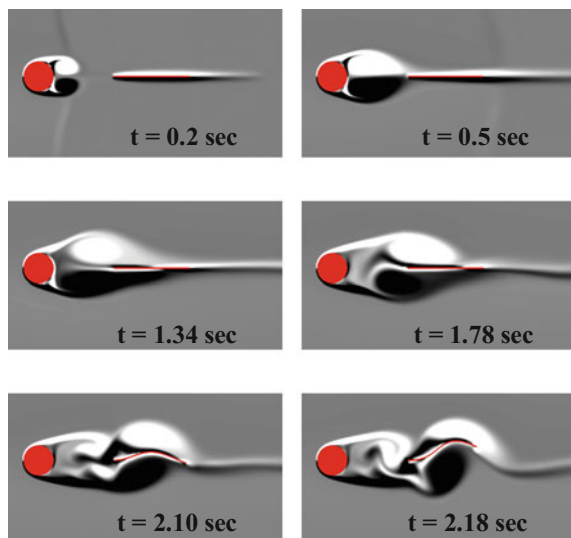
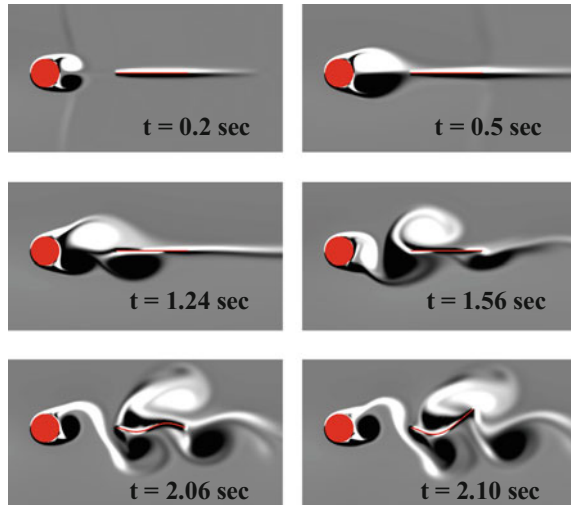


**Fig. 9** Vorticity contours at  $Re = 750$  at different time instances



vortex shedding past the cylinder drives the plate vibrations, any change in shedding frequency would affect the frequency of the plate vibrations. The detailed flow field for a range of Reynolds number were computed using the FSI solver described earlier. Three distinct flow patterns are presented in terms of vorticity contours for  $Re = 500, 750$  and  $1000$  in Figs. 8, 9 and 10 respectively.

**Fig. 10** Vorticity contours at  $Re = 1000$  at different time instances



### 3.3.1 $Re = 500$

At  $Re = 500$ , it is seen that the shear layers form the vortex cores which evolve with time, growing in their strength. For a cylinder without a downstream plate, one would expect these vortex cores to shed eventually in the form of a natural von Kármán vortex street at this Reynolds number. However, the presence of the flexible splitter plate with a gap twice the diameter of the cylinder inhibits the shedding immediately behind the cylinder. Rather, the vortex cores deform by convecting over the flexible plate inducing a moderate vibration in it and subsequently sheds downstream of the plate. It is seen that the plate vibrates in its first mode shape under the impinging vortex cores which is in agreement with our experimental observations.

### 3.3.2 $Re = 750$

At  $Re = 750$ , a marked change begins to appear in the flow pattern. Similar to the previous case, initially the shear layers form the vortex cores which grow in time and approach the plate. However, subsequently the growth in strength of the two vortices doesn't remain equal resulting in an asymmetric impingement on the flexible plate. This induces significant vibrations in the flexible plate which in turn breaks the continuity of the shear layer and stimulates vortex shedding in the gap. It is also noticed that the plate starts to vibrate in its second mode shape with larger displacements.

### 3.3.3 $Re = 1000$

For flows with Reynolds number greater than 750, the interactions between the plate vibration and vortex cores become stronger. The instability in the shear layer takes place even before the vortices fully impinge on the plate.

The vortices are shed in the gap which subsequently triggers the vibration of the plate. In other words, a natural von Kármán shedding starts taking place. Moreover, it is evident that the shedding frequency significantly changes from the previous cases. Besides, vortex-induced vibration of the flexible plate is seen to be enhanced remarkably in terms of its higher mode shapes.

## 4 Discussions

From the flow fields presented above, it is evident that a transition in the mode of vortex shedding happens around  $Re = 750$ . The change from an inhibited vortex shedding to a natural shedding behaviour seems to occur due to interactions between vibrating plate and the unsteady fluid flow.

Vortex shedding behind bluff bodies is usually attributed to the interaction of shear layers. The distance behind the cylinder at which the shear layers mingle resulting in vortex shedding is usually called as ‘vortex formation length’. It is observed through the presented flow fields that the formation length decreases with increasing Reynolds number. For the pre-transition case, the vortex formation length would be greater than  $4.5D$  (the gap + length of the plate) since the interaction between the shear layers happens only beyond that. At the transition, the formation length decreases approximately to  $2D$  in an abrupt manner where the vortices start shedding just within the gap. On the contrary, in the post-transition regime, the formation length is much lower than the gap ( $2D$ ). It has been noted in literature [5, 12] that the frequency of vortex shedding, or equivalently the  $St_f$ , increases when the formation length decreases. Thus, the transition in the mode of vortex shedding might result in a significant increase in the  $St_f$ . Since vortex shedding governs the vibration of the plate, a jump in the  $St_f$  would result in an abrupt increase in the frequency of plate oscillations. This corroborates with the experimental observation of an abrupt increase in  $St_p$  presented in Sect. 2.

It must be noted that the aim of the numerical simulations was to qualitatively investigate the relation between the change in flow field to an abrupt increase in  $St_p$ . The study presented here indicates that it is possible to enhance the plate vibrations and in turn the power output from the plate by harnessing the role of gap in the FSI dynamics. It is thus evident that the present study may help optimise the design of the VIV energy harvester.

## 5 Concluding Remarks

A FSI system consisting of a rigid cylinder and a flexible plate placed with a gap in the downstream has been investigated both experimentally and numerically. The VIV of the flexible downstream plate is of our interest in connection with the prospect of energy harvesting. Experimentally, a significant increase in the frequency of the plate oscillations has been observed. The numerical simulations carried out to understand the underlying FSI dynamics indicate that the abrupt increase in the frequency is connected to a sudden transition in the mode of the vortex shedding past the cylinder. The role played by the gap in this transition implies that a proper choice of the gap is mandatory to ensure natural vortex shedding required for efficient energy harvesting.

## References

1. Allen JJ, Smits AJ (2001) Energy harvesting eel. *J Fluids Struct* 15(3):629–640
2. Wang DA, Chiu CY, Pham HT (2012) Electromagnetic energy harvesting from vibrations induced by Kármán vortex street. *Mechatronics* 22(6):746–756
3. Akaydin HD, Elvin N, Andreopoulos Y (2010) Energy harvesting from highly unsteady flows using piezo-electric materials. *J Intell Mater Struct* 21(13):1263–1278
4. Akaydin HD, Elvin N, Andreopoulos Y (2012) The performance of a self excited fluidic energy harvester. *Smart Mater Struct* 21(2):025007
5. Gerrard JH (1966) The mechanics of the formation region of vortices behind bluff bodies. *J Fluid Mech* 25(02):401–413
6. Ozono S (1999) Flow control of vortex shedding by a short splitter plate asymmetrically arranged downstream of a cylinder. *Phys Fluids* 11:2928–2934
7. Lau YL, So RMC, Leung RCK (2004) Flow-induced vibration of elastic slender structures in a cylinder wake. *J Fluids Struct* 19(8):1061–1083
8. Ferziger J, Peric M (2002) *Computational methods for fluid dynamics*. Springer, Berlin
9. Tukovic Z, Cardiff P, Karac A, Jasak H, Ivankovic A (2014) OpenFOAM library for fluid structure interaction. In: 9th OpenFOAM workshop, Zagreb, Croatia
10. Michler C, Hulshoff SJ, van Brummelen EH, de Borst R (2004) A monolithic approach to fluid-structure interaction. *Comput Fluids* 33(5):839–848
11. Degroote J, Haelterman R, Annerel S, Bruggeman P, Vierendeels J (2010) Performance of partitioned procedures in fluid-structure interaction. *Comput Struct* 88(7):446–457
12. Roshko A (1954) On the drag and shedding frequency of two-dimensional bluff bodies. National Aeronautical and Space Administration (No. TN3169)